Nonequilibrium Green Functions Simulations on the Next Level: Theoretical Advances and Applications to Finite Lattice Systems

Dissertation
zur Erlangung des Doktorgrades
der Mathematisch-Naturwissenschaftlichen Fakultät
der Christian-Albrechts-Universität zu Kiel

vorgelegt von

Niclas Schlünzen

Kiel, 2021

Nothing is more practical
than a good theory.

(Ludwig Boltzmann)

Abstract

This thesis is devoted to the description of correlated finite lattice systems under nonequilibrium conditions. In this context, the lack of small parameters in the corresponding standard many-body equations makes it difficult to construct suitable approximations for theoretical tools, which renders the computation of relevant observables numerically costly and impractical. At the same time, rigorous predictions for the ultrafast dynamics in correlated lattices are highly valuable for the understanding of many state-of-the-art experiments. The nonequilibrium Green functions (NEGF) technique is particularly well-suited to meet the challenging demands that come with the description of the nontrivial interplay between quantum correlations and nonequilibrium effects in excited lattice systems. However, in order to apply the approach on a practically relevant scale, several methodological improvements come to be indispensable. The present thesis contains these theoretical advances of the NEGF method, alongside with—thus accessible—applications to ultracold atoms in optical lattices and excited finite graphene nanostructures.

On a fundamental level, the NEGF foundation is improved by deriving time-reversibility conditions for the underlying equations and by establishing time-reversal symmetry as a numerical stability test. This technique is used to clarify a recent controversy about unphysical attractor-like behavior in NEGF calculations by showing that the observations in question have been caused by insufficient numerical integration methods and time steps. Furthermore, the accuracy of the NEGF description of finite lattice systems is brought to proof in a comprehensive benchmark study with density-matrix-renormalization-group results for moderately-sized 1D and 2D clusters.

Many-body approximations are introduced to the NEGF formalism via the single-particle selfenergy. Here, more sophisticated approximations are reflected as generally more accurate but computationally demanding selfenergy schemes. The publications in this thesis demonstrate how such higher-order approaches are made accessible for practically relevant systems. Additionally, a specific characterization of the respective applicability ranges is given. Beyond that, the third-order approximation (TOA) is established and shown to be accurate for a large range of system parameters. In this thesis, the partial-summation schemes of different selfenergy approximations are further analyzed with respect to the satisfaction of physical conservation laws.

The theoretical capstone of this thesis is the development of the G1–G2 scheme. It is a set of coupled time-diagonal differential equations that follow from a reformulation of basic NEGF relations. As a result, the G1–G2 scheme exhibits a time-linear computational scaling as opposed to the generally cubic and for some cases quadratic time scaling of previous NEGF approaches. This remarkable result leads to accessible speed-up factors of up to 10^4 in practice. The G1–G2 scheme is generalized to higher-order selfenergy

approximations to describe dynamical screening and many-body scattering effects. The G1–G2 formulation of the TOA scheme is included as original content within this thesis.

Based on these methodological advances, the NEGF formalism is applied to different ultrafast many-body-dynamics scenarios. In a first study, it is used to predict the expansion dynamics of initially confined fermion clouds in multi-dimensional lattice systems. Here, the dynamical separation between single particles and coupled particle pairs (doublons) is observed. This behavior was also found in recent optical-lattice experiments. A direct comparison reveals an unprecedented agreement between the measurements and NEGF predictions for the expansion velocity.

Beyond that, the NEGF technique is applied to ion-stopping dynamics in finite graphene-type lattices. In several studies, the interaction processes are analyzed in large detail. The results suggest a strong influence of electronic correlations in the target material onto the energy loss of the incident ion. Furthermore, it is observed that the ion-impact process induces the formation of stable doublons in the lattice. This effect can be amplified by multiple excitations, which constitutes an important insight for ion-sputtering experiments, as well as plasma–solid interface scenarios. Moreover the NEGF approach is used to analyzed Auger effects in irradiated graphene nanoribbons (GNRs).

The thesis is concluded with a brief outlook to ion-stopping simulations with the new-found G1–G2 scheme and a generalization of the approach to the Pariser–Parr–Pople model to describe excited GNR heterostructures.

Kurzfassung

Die vorliegende Arbeit ist der Beschreibung von korrelierten endlichen Gittersystemen im Nichtgleichgewicht gewidmet. In diesem Fall ist es schwierig, geeignete Näherungen für theoretische Methoden zu konstruieren, weil in den entsprechenden Gleichungen der Vielteilchen-Theorie keine Parameter vernachlässigt werden können. Dadurch wird die Berechnung von relevanten Observablen numerisch anspruchsvoll und schwer umsetzbar. Gleichzeitig werden akkurate Beschreibungen der Ultrakurzzeit-Effekte in korrelierten Gittersystemen für das Verständnis vieler moderner Experimente benötigt. Die Nichtgleichgewichts-Greenfunktionen-Methode (NEGF) ist in besonderer Weise geeignet, das Zusammenspiel von Quantenkorrelationen und Nichtgleichgewichtseffekten in angeregten Gittersystemen zu beschreiben. Jedoch sind für die direkte Anwendung auf experimentell relevante Systeme einige methodische Verbesserungen unabdingbar. Diese Arbeit enthält die entsprechenden theoretischen Weiterentwicklungen, sowie die dadurch ermöglichten Anwendungen auf ultrakalte Atome in optischen Gittern und angeregte finite Graphen-Nanostrukturen.

Zur Verbesserung der theoretischen Grundlage der NEGF-Methode wird eine Bedingung für Zeitumkehrsymmetrie in den zugrundeliegenden Gleichungen hergeleitet. Die simulierte Verifikation dieser Symmetrie wird als ein numerischer Stabilitätstest etabliert. Mithilfe dieser Technik wird eine Kontroverse über unphysikalisches attraktorartiges Verhalten in NEGF-Berechnungen aufgeklärt, indem die entsprechenden Beobachtungen zweifelsfrei einer unzureichenden numerischen Integrationstechnik zugeordnet werden. Darüber hinaus wird die Genauigkeit der NEGF-Beschreibung von endlichen Gittersystemen in einer umfassenden Benchmark-Studie mit Ergebnissen der Dichtematrix-Renormierungsgruppen-Methode für mittelgroße 1D- und 2D-Cluster nachgewiesen.

Im NEGF-Formalismus werden Vielteilchen-Näherungen durch die Einteilchen-Selbstenergie dargestellt. Dabei zeigen sich aufwendigere Näherungen in Form von allgemein genaueren, aber rechenintensiveren Selbstenergieschemata. In den Veröffentlichungen dieser Arbeit wird demonstriert, wie solche Näherungen höherer Ordnung für experimentell relevante Systeme anwendbar gemacht werden. Zusätzlich wird jeder dieser Selbstenergienäherungen ein entsprechender Anwendbarkeitsbereich zugewiesen. Darüber hinaus wird die dritte-Ordnung-Näherung (TOA) etabliert und gezeigt, dass diese innerhalb eines großen Parameterbereichs genaue Resultate hervorbringt. Im Rahmen dieser Arbeit werden einige Selbstenergienäherungen unter dem Gesichtspunkt physikalischer Erhaltungssätze weiter analysiert.

Das bedeutendste theoretische Ergebnis dieser Arbeit ist die Entwicklung des G1–G2-Schemas. Dieses besteht aus zwei gekoppelten zeitdiagonalen Differentialgleichungen, welche aus einer Umformulierung elementarer NEGF-Gleichungen hervorgehen. In-

folgedessen weist das G1–G2-Schema eine zeitlineare numerische Skalierung auf, im Kontrast zu der gemeinhin kubischen und in einigen Fällen quadratischen Zeitskalierung vorheriger NEGF-Ansätze. Dieses bemerkenswerte Ergebnis führt zu praktisch erreichbaren Beschleunigungsfaktoren von bis zu 10^4. Das G1–G2-Schema wird um Selbstenergienäherungen höherer Ordnung ergänzt, um dynamische Abschirmung und Vielteilchen-Streuungseffekte beschreiben zu können. Die G1–G2-Formulierung des TOA-Schemas wird im Rahmen dieser Arbeit hergeleitet.

Aufbauend auf diesen methodischen Weiterentwicklungen wird der NEGF-Formalismus auf die Ultrakurzzeitdynamik unterschiedlicher Vielteilchensysteme angewandt. Eine erste Studie behandelt die Expansionsdynamik von anfänglich eingeschlossenen Fermionen in mehrdimensionalen Gittersystemen. Dabei kann die dynamische Aufspaltung in effektive Einteilchen und gekoppelte Teilchenpaare (Doublons) beobachtet werden. Dieses Verhalten wurde ebenfalls in kürzlich durchgeführten Experimenten mit optischen Gittern gefunden. Der direkte Vergleich zwischen den Messungen und den NEGF-Vorhersagen für die Expansionsgeschwindigkeit zeigt eine zuvor unerreichte Übereinstimmung.

Darüber hinaus wird die NEGF-Technik auf endliche graphenartige Gitter angewandt, welche von energetischen Ionen angeregt werden. In mehreren Studien werden die Wechselwirkungsprozesse detailliert analysiert. Die Ergebnisse deuten an, dass die elektronischen Korrelationen im Targetmaterial einen starken Einfluss auf den Energieverlust des einfallenden Ions haben. Weiterhin kann beobachtet werden, dass der Durchstoß des Ions die Bildung von stabilen Doublons im Gitter induziert. Dieser Effekt kann durch Mehrfachanregungen verstärkt werden. Die Erkenntnisse sind wichtig für das Verständnis von Ionen-Sputter-Experimenten sowie für Plasma–Festkörper-Grenzflächenszenarien im Allgemeinen. Außerdem wird der NEGF-Ansatz zur Analyse von Auger-Effekten in bestrahlten Graphen-Nanobändern (GNRs) verwendet.

Die Arbeit schließt mit einem kurzen Ausblick auf Simulationen von Ionen-Abbremsungsprozessen mit dem G1–G2-Schema und einer Verallgemeinerung des Ansatzes auf das Pariser–Parr–Pople Modell zur Beschreibung angeregter GNR-Heterostrukturen.

Table of Contents

Chapter 1

Introduction

Nature has found remarkable ways to arrange the microscopic constituents of matter into the forms and shapes that make up the macroscopic world.

On the one hand, there is the way studied in chemistry and molecular biology, where atoms are combined to molecules, organic compounds, polypeptides, oligomers, and complex macromolecules, such as proteins, lipids and DNA, all of which are interconnected in numerous layers of complexity and self-organization that interfuse and transcend each other—thereby giving rise to the wonders of metabolism as the foundation of life itself.

On the other hand, atoms can directly form uniform macroscopic units. This is the realm of statistical physics.

There are good reasons to study the latter. Many-body systems represent a capital fraction of all visible matter in the universe. Huge accumulated clouds of gas form the basis of the interstellar medium. Gravity-bound plasma clouds collapse to luminous spheroids all over the night sky. Even more exotic forms, such as nuclear matter in neutron stars and the primordial quark–gluon plasma are highly relevant for the understanding of astrophysical concepts. In addition, a plethora of technological advances is based on many-body systems, with conductors and semiconductors leading the way to the current information age. At the same time, the uniformity of many-body systems can have fascinating implications. One example is that microscopic quantum effects on the nanoscale can manifest—bypassing multiple orders of magnitude—as macroscopic phenomena, such as Bose–Einstein condensation, superconductivity, or superfluidity. This holds a tantalizing promise to theorists: a comprehensive description on the fundamental level of interaction between particles allows one to draw conclusions about the full many-body aggregate.

In thermodynamic equilibrium, there has indeed been made tremendous progress in predicting and understanding collective physics over the last decades. Several breakthroughs have led to a near-complete picture in the description of fluid systems [1–3] (with state-of-the-art applications in battery technology [4, 5] or photovoltaics [6, 7]), plasma physics [8] and warm dense matter [9–11] (with paramount importance for nuclear fusion [12, 13]), or condensed-matter phenomena, such as the Kondo effect [14–16] or the quantum Hall effect [17, 18]. This sheer abundance of achievements has been rendered possible by the remarkable strength of statistical physics. The guiding principle of this concept is to disregard the individual information of each particle in favor of more insightful average quantities. Particularly the ensemble-averaged density operator is a key quantity

for probabilistic approaches. With its help, statistical physics has done an excellent job in deriving the basic thermodynamic laws from microscopic equations (see Ref. [19] for a recent discussion). There are several theoretical difficulties in the corresponding description of many-body systems, such as the representation of many-body correlations, i.e. inter-particle interaction effects that are not captured within a mean-field picture. Beyond that, fundamentally different statistical tools are needed to describe collective quantum behavior. For equilibrium situations, these barriers have been overcome to astonishing degree.

However, the assumption of equilibrium is an idealization. Since the universe itself is in a nonequilibrium state, so is ultimately every many-body system in it. The incorporation of nonequilibrium does not only drastically enlarge the space of possible many-body states but also constitutes a conceptual increase of dimensionality—as it is inherently connected to the evolution in time. For quantum systems, time dependence is particularly difficult to theoretically consider and involves propagating the time-dependent Schrödinger or von Neumann equation[1] for a potentially time-dependent Hamiltonian. For sufficiently small external perturbations it is possible to approximate the time-resolved response of the excited system by using equilibrium information via linear-response theory [20]. This approach becomes increasingly inaccurate the more the system is driven out of equilibrium. Only by means of time-dependent quantum ensemble averages [21, 22] it becomes possible (and feasible) to predict the dynamics of large quantum many-body systems in general nonequilibrium states. It should be noted that each system in the ensemble is propagated as an isolated system by this approach [23]. The coupling to the environment is considered through the initial state. The time-dependent statistical approach allows one to take on the extremely rich field of nonequilibrium physics. This includes nonadiabatic and non-Born–Oppenheimer processes [24, 25], such as photoionization, charge transfer, photodissociation of molecules, and collective dynamical correlation effects like, e.g., dynamical-screening processes and Auger effects. Nonequilibrium phenomena are of great importance for various practical applications. In particular, they dominate the short-time behavior following external excitations. This is highly relevant for, e.g., time-resolved, angle-resolved photoemission spectroscopy [26–29] (trARPES) and other laser experiments involving solid materials [30–35], as well as laser heating in plasmas [36, 37]. Likewise, the exposure to ionic radiation can cause intriguing short-time dynamics in, e.g., correlated solids [38–41]. Almost arbitrary nonequilibrium states are regularly generated in experiments with ultracold atoms in optical lattice systems [42–45].

In order to theoretically predict nonequilibrium phenomena, a large number of statistical tools has been developed. An overview is given in the subsequent section followed by a brief introduction to the method at the heart of this thesis—the nonequilibrium Green functions (NEGF) method.

---

[1]The Schrödinger equation for the time-dependent wavefunction is applied for pure-state descriptions. The von Neumann equation, however, can also be used to propagate statistical ensembles, which allows one to describe systems that are coupled to an environment.

1.1 Methods and Theoretical Description

In the classical regime, i.e. when quantum effects are negligible, there exists a variety of frameworks to simulate nonequilibrium many-body systems. To name a few, there are generalizations of molecular-dynamics[2] approaches [50–52], various techniques based on the Boltzmann equation [53, 54], as well as the particle-in-cell (PIC) method [36, 49], which holds a significant share of state-of-the-art high-performance computing capacity [37, 55–63].

For quantum systems in nonequilibrium states most computational methods can be ascribed to one of two basic strategies. The first strategy relies on finding exact or approximate solutions for the time-dependent wavefunction. This includes the coupled-cluster method [64, 65], configuration interaction [66, 67] and the active-space restricted variants [68–70], multi-configurational time-dependent Hartree–Fock [71–74], as well as density-matrix-renormalization-group (DMRG) approaches [75–78]. These methods inherit their numerical scaling behavior from the dimension and size of the N-particle wavefunction and its explicit information. The resulting linear time scaling is highly beneficial for the description of long-time simulations. Beyond that, wavefunction-based approaches remain valid for arbitrary degrees of nonequilibrium and coupling, by construction. However, setting up the wavefunction object becomes increasingly intricate for large many-body systems, which leads to an inevitable exponential scaling with the particle number. This unpleasant fact restricts the applicability of the methods of the first strategy to mostly few-particle systems of picayune practical value [69, 70, 79]. Moreover, wavefunction objects are limited to the representation of pure states. Statistical ensembles of pure states (mixed states) cannot be accounted for within theoretical approaches based on a single wavefunction. For the second strategy, the explicit N-particle information is omitted in favor of the direct propagation of time-dependent ensemble-averaged observables. By this procedure, the time-dependent simulation of larger many-body systems becomes computationally feasible. Commonly used methods following this approach are time-dependent density-functional theory [49, 80–83] (TDDFT), real-time quantum Monte Carlo [84, 85] (RTQMC) and diagrammatic Monte Carlo [86–89] (DiagMC), dynamical mean-field theory [90–93] (DMFT), the framework of reduced density operators [49, 94–100] (RDO), and NEGF theory [23, 101]. TDDFT has a broad, universal applicability and constitutes a valuable tool for systems in the regime of moderate interaction strengths and benign excitations. However, due to the adiabatic approximations within its framework TDDFT is incapable of describing strong nonequilibrium situations. Furthermore, TDDFT lacks a systematic way to accurately treat strong non-local correlation effects. Dynamical Monte Carlo approaches such as DiagMC and RTQMC excel in accuracy for time propagations where numerical ergodicity can be ensured. Particularly for fermions, these Monte Carlo methods are, however, severely hampered by the fermion sign problem and the additional dynamical sign problem. This currently limits the practical utility to very short dynamical simulations. DMFT exactly describes the limits of the interactions strength for vanishing and infinite coupling. Specifically, the many-body problem is mapped to a local impurity

---

[2]For completeness, it is mentioned that there have been efforts to extend molecular dynamics to the quantum realm [46–49].

model. This local description fails to represent strong nonequilibrium situations for intermediate interaction strengths. Beyond that, DMFT is generally constructed for the thermodynamic limit, making it unsuited to describe low-dimensional setups and, most notably, finite systems.

The difficult requirements for an accurate description of correlated nonequilibrium scenarios in finite systems are met by the RDO and NEGF method, which are closely related and introduce quantum kinetic equations. Both approaches exhibit polynomial numerical scalings with the number of time steps and the size of the single-particle basis. As both methods are derived in and inherent to the occupation-number representation they involve a computational effort that does not depend on the particle number—in stark contrast to the tools of the first strategy. Together with the general rise of computer power in the last decades, these properties allow RDO and NEGF schemes to be applied for experimentally relevant time scales and system sizes. One of the key advantages of the quantum kinetic approaches is the unrestricted capability to portray nonequilibrium processes, since they preserve the full generality of time-dependence from the Schrödinger and Heisenberg equation. The NEGF and RDO frameworks both rely on hierarchies of equations of motion (EOMs). While the Bogoliubov–Born–Green–Kirkwood–Yvon (BBGKY) hierarchy for the density operators does only depend on a single time argument, the Martin–Schwinger hierarchy for the Green functions has a more complex time structure with multiple coupled arguments. This conceptual distinction directly causes the main performance differences between both approaches. As such, the numerical scaling with respect to the basis size is superior for the NEGF scheme, whereas the RDO approach can be expressed in a time-linear form—unachievable within conventional NEGF theory. With its more sophisticated time structure, the Green-functions scheme, however, provides a more consistent way to account for dynamical correlations. Furthermore, the NEGF-rooted selfenergy diagram technique constitutes a powerful and highly approachable method to systematically describe correlation effects in general. For this reasons, the NEGF framework is used to describe the correlated nonequilibrium dynamics of finite lattice systems in this thesis.

1.1.1 Basics of the NEGF Technique

The method of nonequilibrium Green functions was established in the 1960s by Schwinger, Keldysh, Kadanoff, Baym and others (cf. Refs. [21, 22, 102, 103]) as an attempt to generalize successful concepts from equilibrium theory to kinetic transport phenomena [104, 105]. It builds up upon groundstate Green-function theory and the Feynman diagram technique by Schwinger, Dyson, and Feynman, as well as the respective generalization to arbitrary thermodynamic equilibrium by Matsubara, Kubo and others [105]. Being more of theoretical interest at first, NEGF theory was primarily used to derive and enhance Boltzmann-type kinetic equations. This changed in the 1980s, when Danielewicz demonstrated that the NEGF equations can themselves be efficiently used for more precise computer simulations [106]. Another major improvement has been the introduction of the generalized Kadanoff–Baym ansatz (GKBA) by Lipavský *et al.* in 1986 [107], with the

help of which the time scaling can be reduced by one order of magnitude. On this footing, the NEGF technique has developed into a flourishing, productive field and a keystone for the elucidation of nonequilibrium phenomena [41, 108–114].

NEGF theory is formulated in second quantization.[3] In this picture, only the occupation numbers of the underlying single-particle orbitals are considered to describe the system's many-body state. The natural choice to modify the states in this regard are the canonical creation $(\hat{c}_i^\dagger)$ and annihilation $(\hat{c}_i)$ operators that add a particle to or remove a particle from the single-particle orbital i. By convention, these operators are defined in such a way, that the quantum statistics for bosons and fermions are automatically accounted for, which constitutes an enormous advantage compared to the behavior of many-body wave functions. In second quantization, any operator can be expressed as a product of a matrix element in the single-particle basis and a series of canonical operators. Regarding the description of closed systems, physical processes are obliged to preserve particle-number conservation. It is, thus, convenient to define symmetric products of canonical operators as scaffoldings and building blocks for arbitrary operators and observables. The nonequilibrium Green function is the most general form of these operator products. The single-particle and two-particle nonequilibrium Green functions are defined as

$$G_{ij}(z, z') = \frac{1}{i\hbar} \left\langle \hat{\mathcal{T}}_\mathcal{C} \left\{ \hat{c}_i(z)\,\hat{c}_j^\dagger(z') \right\} \right\rangle \qquad \text{and} \qquad (1.1)$$

$$G_{ijkl}^{(2)}(z_1, z_2, z_1', z_2') = \frac{1}{(i\hbar)^2} \left\langle \hat{\mathcal{T}}_\mathcal{C} \left\{ \hat{c}_i(z_1)\,\hat{c}_j(z_2)\,\hat{c}_l^\dagger(z_2')\,\hat{c}_k^\dagger(z_1') \right\} \right\rangle, \qquad (1.2)$$

respectively. Within these definitions, two concepts are introduced:

- The statistical averaging is denoted by $\langle \cdot \rangle$. It corresponds to the average of an ensemble of identical isolated quantum systems. The averaging process is carried out using the trace over the single-particle basis and the density matrix operator.

- The time-ordering operator $\hat{\mathcal{T}}_\mathcal{C}\{\cdot\}$ is a superoperator acting on its arguments by arranging them according to the positioning of the contour times z on the time contour $\mathcal{C}$ (see Fig. 1.1). The idea of the time contour goes back to Schwinger [21] and Keldysh [102]. By this procedure, it is possible to describe dynamical quantum expectation values in a most concise formulation.

The single-particle Green function of Eq. (1.1) is a two-time generalization of the density matrix from RDO theory, the information of which is contained as the equal-time limit.[4] By its two-time structure, the Green function additionally contains spectral information and dynamical correlations. From the Heisenberg equation one can derive the EOMs for the canonical operators and eventually for the Green functions. Due to the structure of the Hamiltonian in second quantization the resulting equations for the single-particle

---

[3]At this point, only a brief overview of the central NEGF equations is given and formal details are spared out to improve the comprehensibility. A thorough introduction to the topic can be found in Sec. 2.1.

[4]Broadly speaking, the single-particle Green function [cf. Eq. (1.1)] can be considered as the formalized manifestation of a particle's lifespan, from the time and space of its creation $[\hat{c}_j^\dagger(z')]$ to its annihilation $[\hat{c}_i(z)]$.
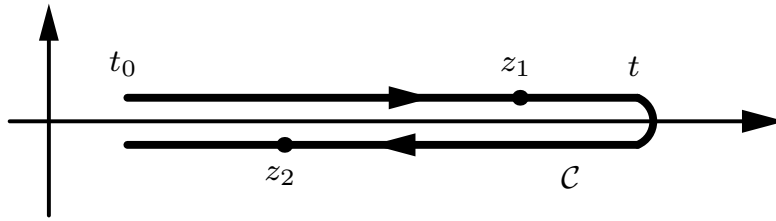
Figure 1.1 – Illustration of a general time contour $\mathcal{C}$. It consists of a causal and an anticausal branch clinging to the real-time axis. In the depicted example, the time z_2 is later than z_1, despite their respective real-time projections being in reverse order.

Green function couple to the two-particle Green function of Eq. (1.2). This behavior continues for all higher-order equations corresponding to the respective N-particle Green functions, defined analogously to Eqs. (1.1) and (1.2). The arising system of coupled equations is known as the Martin–Schwinger hierarchy [115]. It is an exact reformulation of the time-dependent Schrödinger equation in terms of nonequilibrium Green functions. Due to the increasing complexity with each order of the hierarchy, it is unfeasible to solve the system of equations directly. Instead, one focuses on the first-order hierarchy equations and introduces an auxiliary quantity to formally decouple the time evolution of the single-particle Green function from all higher-order equations:

$$\sum_l \left[i\hbar \frac{\mathrm{d}}{\mathrm{d}z} \delta_{il} - h_{il}^{(0)}(z) \right] G_{lj}(z, z') = \delta_{ij} \delta_{\mathcal{C}}(z, z') \pm i\hbar \sum_{lmn} \int_{\mathcal{C}} \mathrm{d}\bar{z}\, w_{ilmn}(z, \bar{z}) G_{mnjl}^{(2)}(z, \bar{z}, z', \bar{z}^+)$$

$$=: \delta_{ij} \delta_{\mathcal{C}}(z, z') + \sum_l \int_{\mathcal{C}} \mathrm{d}\bar{z}\, \Sigma_{il}(z, \bar{z}) G_{lj}(\bar{z}, z') . \qquad (1.3)$$

Here, w and $h^{(0)}$ are the matrix elements of the interaction and the single-particle Hamiltonian. The symbols $\int_{\mathcal{C}}$ and $\delta_{\mathcal{C}}$ correspond to integration[5] along the time contour $\mathcal{C}$ and the Dirac delta function on $\mathcal{C}$. The quantity Σ in Eq. (1.3) is called the (single-particle) selfenergy. It provides the starting point for the introduction of many-body approximations to NEGF theory. Eq. (1.3) and its adjoint are the well-known Keldysh–Kadanoff–Baym equations (KBE). Before discussing the selfenergy and the most common ways to close the KBE for the single-particle Green function, a few observations are made:

- In the noninteracting limit, the last term of Eq. (1.3) vanishes and only the delta-term remains on the right-hand side of the equation. In that case, G (or G_0 to indicate the ideal equation) acts as the inverse of the operator $\left[i\hbar \frac{\mathrm{d}}{\mathrm{d}z} \delta - h^{(0)} \right]$. The resulting equation is precisely of the form that was introduced by George Green in the 1820s [116], with G_0 playing the role of the mathematical Green function. This similarity is indeed the origin of the name Green function for the quantities of Eqs. (1.1) and (1.2).

- The appearance of three different time arguments in Eq. (1.3) has two important

---

[5] The superscript of the contour time $\hat{z}^+$ indicates an infinitesimally larger value to ensure the correct operator ordering by $\hat{\mathcal{T}}_{\mathcal{C}}$.

implications. First, it is a manifestation of the memory structure that is included in G (and also Σ). By this explicit consideration of memory effects the NEGF technique fundamentally differs from Markovian methods, such as traditional Boltzmann-equation approaches. Secondly, the times indicate a cubic scaling with respect to the number of time steps for numerical implementations of the KBE.

- By using the ideal Green function G_0 and its property as the inverse of $\left[i\hbar\frac{d}{dz}\delta - h^{(0)}\right]$, the KBE can be transformed to the following Dyson form:

$$G_{ij}(z, z') = G_{0,ij}(z, z') + \sum_{kl} \int_{\mathcal{C}} d\bar{z}d\bar{\bar{z}}\, G_{0,ik}(z, \bar{z})\Sigma_{kl}(\bar{z}, \bar{\bar{z}})G_{lj}(\bar{\bar{z}}, z') \,. \qquad (1.4)$$

This relation has the same structure as the commonly used Dyson equation from equilibrium Green-functions theory [23, 117],

$$G_{ij}^{\mathrm{R}}(\omega) = G_{0,ij}^{\mathrm{R}}(\omega) + \sum_{kl} G_{0,ik}^{\mathrm{R}}(\omega)\Sigma_{kl}^{\mathrm{R}}(\omega)G_{lj}^{\mathrm{R}}(\omega) \,, \qquad (1.5)$$

to which it is easily transformed by taking the real-time components and performing a Fourier transform with respect to the time difference. Eq. (1.5) and derivational relations are widely used to describe correlated plasmas (for an introductory overview see., e.g., Ref. [117]) and also finite nanostructures have recently been investigated within this approach [118, 119].

The selfenergy Σ in principle contains the full many-body information of the considered system encapsulated in a single-particle quantity. As the computation of the exact selfenergy is practically impossible for larger systems, efficient and suitable approximations are generally required. In NEGF theory, there exist remarkably powerful ways to systematically derive many-body approximations in the form of Hedin's equations for the screened vertex [23, 79, 120], an equivalent scheme for the bare interaction [79, 121], as well as the direct derivation from the Martin–Schwinger hierarchy [23, 122]. All three approaches rely on (but are not limited to) perturbation expansions with respect to the interaction matrix element. The best-established selfenergy approximations can be classified into two categories. The first category consists of approximations that straightforwardly involve all terms up to a given interaction order. This includes the (first-order) **Hartree–Fock** (**HF**) approximation describing many-body effects on a mean-field level. The **second-order Born approximation** (**SOA** or **2B**) incorporates the first terms to capture correlation effects. The more involved **third-order approximation** (**TOA**) can be used to describe even moderate to strong coupling. The second category features the so-called resummation approaches. Here, specific classes of physical processes can be included in the description by use of iterative relations. Due to this procedure, the resulting selfenergy terms are not restricted to a finite interaction order. One of these resummation approaches is the **T-matrix** or ladder **approximation** (**TMA**). It can be constructed to account for scattering processes in the **particle–particle** channel (**TPP**) or the **particle–hole** channel (**TPH**). The resummation of terms describing dynamical-screening effects into a renormalized effective interaction tensor leads to the well-known **GW approximation** (**GWA**). Additionally, there are ways to combine these approaches into collective selfenergy

approximations. One example of this kind is the **fluctuating-exchange approximation** (**FLEX**).

The GKBA [107] is an approximation that employs a different idea. It does not apply to the selfenergy but, instead, to the time structure of the KBE. Overall, the GKBA is an attempt to reduce the number of time integrals during the propagation. This is achieved by adapting Eq. (1.3) only for its time-diagonal limit ($z = z'$) and reconstruct all off-diagonal values of the Green function by the following approximate formula,

$$G_{ij}^{\gtrless}(t, t') = i\hbar \sum_k \left[G_{ik}^{\mathrm{R}}(t, t') G_{kj}^{\gtrless}(t') - G_{ik}^{\gtrless}(t) G_{kj}^{\mathrm{A}}(t, t') \right] . \tag{1.6}$$

This equation relates the real-time components of G, which result from mapping the contour times (cf. Fig. 1.1) back to the real-time branch. The single-time-dependent $G^{\gtrless}(t)$ denotes the equal-time limit and is therefore directly connected to the density matrix. In order to close the system of equations, one needs to find explicit expressions for the propagators $G^{\mathrm{R/A}}$. For the particular example of propagators in HF approximation (HF-GKBA) in combination with a SOA selfenergy, the computation of the GKBA can be realized with a quadratic time scaling, as opposed to the cubic scaling of the two-time KBE [cf. Eq. (1.3)].

The structure of the central equations in NEGF theory not only makes for the advantageous properties regarding the application to correlated nonequilibrium dynamics, but also causes the general limitations of the method. Eq. (1.3) scales with $\mathcal{O}\left(N_{\mathrm{b}}^3 N_{\mathrm{t}}^3\right)$ with respect to the basis size N_{b} and the number of time steps N_{t}. This polynomial scaling allows one to describe small and mesoscopic systems but prohibits the direct application to the macroscopic limit. Likewise, NEGF simulations are limited to short-time propagations, not exceeding the femtosecond time scale. This is not only caused by the cubic (or quadratic for GKBA) time scaling, but also by the general absence of system–environment interaction. For larger time scales, the proper treatment of the coupling to the environment is essential to describe relaxation and energy dissipation [23]. Lastly, the NEGF technique fails to describe systems in the strong-coupling limit, due to the perturbative nature of selfenergy approximations.[6]

Before the author has commenced his PhD research, there has been a shift of interest within a large fraction of the NEGF community. While previous investigations focused on spatially continuous systems, such as atoms and molecules [124–126] or quantum wells [127–129], several authors started to address discrete finite lattice systems instead [109, 130–135]. These systems proved to be a controllable setting for methodological analyses regarding finite-size effects in NEGF approaches. An important observation was made by von Friesen *et al.* in Refs. [109] and [130]. They demonstrated that solving the KBE for strongly excited finite systems can result in an unphysical damping of the density dynamics. The authors explained this behavior as being caused by the interplay between the selfconsistent character of the KBE and the partial summation of scattering terms in the selfenergy. By construction, the GKBA significantly reduces the degree of selfconsistency in the EOMs. For this reason, the method was a suited candidate to approach this artificial behavior. Indeed, Sebastian Hermanns and others could show in Ref. [136] that the GKBA

---

[6]For completeness, it is mentioned that the TPP selfenergy becomes exact in the limit of full/empty bands, regardless of the interaction strength [123].

completely removes the artificial damping property. This publication was also the first to which the author of the present thesis contributed during his early master's studies. In close collaboration with Sebastian Hermanns and later Jan-Philip Joost, the author further developed the NEGF approach to finite lattice systems and provided the application to highly topical experimental concepts.

1.2 Relevant Systems

In this thesis, the NEGF technique is applied to ultracold atoms in optical lattices, as well as finite graphene nanostructures irradiated by ions and laser light. Both system stand out due to the importance of nonequilibrium effects on a short-time scale and the significance of many-body correlations.

The idea to use laser-cooled neutral atoms in artificial light-induced lattice potentials in order to generate a strongly interacting quantum system was introduced in 1998 in Ref. [137]. The ensuing decades have established this concept as a full-fledged and highly successful experimental field (see, e.g., the review articles of Refs. [42–45]). As the basic principle behind this approach, one utilizes the fact that counterpropagating laser beams create a standing wave that contains regular, periodic potential extrema, which act as microtraps for the cold atoms. Due to the high fidelity of laser optics in general, these optical lattices have particularly advantageous characteristics with respect to variability, accuracy, and detection possibilities. One example is the capacity to realize lattice systems in 1D [138, 139], 2D [140, 141] and 3D [142, 143]. Especially the experiments with ultracold fermionic atoms have aroused broader interest, because—depending on the spin states of the atoms—the artificial lattices can be considered a model setup for the electrons in condensed-matter systems. The high controllability allows one to drive the many-body systems to extreme conditions and to design various dynamical excitations [45]. Single-atom resolution has been achieved with the developments of the so-called quantum-gas microscopes for bosons [144, 145] and fermions [146–150]. Thus, optical-lattice experiments provide excellent conditions for comparison with theoretical predictions.

The advent of optical-lattice research has opened up new avenues to study nonequilibrium phenomena in quantum lattice systems (for an overview see Ref. [45]). A particularly interesting example is the expansion of initially confined particle clouds [140, 151–154]. Here, the dynamical behavior strongly depends on the coupling between the particles. In the experiments, the interaction strength can be arbitrarily tuned in a procedure that utilizes Feshbach resonances. Particularly in the regime of moderate and strong coupling strength, the incipient correlated expansion dynamics features a complex interplay of nonequilibrium effects and quantum many-body correlations. A phenomenon that arises under such conditions is, e.g., the *quantum distillation* [155], i.e., the dynamical separation between uncorrelated single particles and coupled particle pairs. Reliable theoretical descriptions of these scenarios are valuable for benchmark purposes, as well as to identify and explain the underlying mechanisms. While for one-dimensional systems such predictions are provided, e.g., by DMRG calculations [154, 156], 2D and 3D dynamics are out of reach for most theoretical approaches.

Graphene was the first stable two-dimensional material that could be isolated in experiments [157], which was honored with the 2010 Nobel prize in physics [158]. It consists of sp^2-hybridized carbon atoms, arranged in a hexagonal, planar configuration. After its discovery, it was shown that the exceptional structure of graphene results in rather exotic behavior, such as the relativistic linear dispersion relation around the K points [159, 160] and the strikingly high carrier mobility [161]. Furthermore, graphene exhibits interesting optical properties that qualify for applications in ultrafast photodetectors [162] and even photovoltaic devices [163–166]. In its planar configuration, graphene is a zero-band-gap semiconductor with the valence and conduction band meeting at the K points. In order to harvest the full potential of graphene in nanoelectronics, great efforts have been put in to induce a finite gap to the material. These attempts utilize the interaction with a suitable substrate [167, 168], the effects of strain to the graphene sheet [169, 170], or stacking two graphene layers to a bilayer aggregate [171]—a path that culminated in the acclaimed recent trend of *twisted bilayer graphene* [172]. Another very promising method to manufacture a band gap to graphene monolayers is the lateral confinement in finite nanostructures [173, 174]. This perspective has directed much attention to the analysis of such finite graphene fragments [175–179]. Furthermore, novel synthesization methods for, e.g., graphene nanoribbons (GNRs) have been developed recently [173, 174, 180–185], which allow for a precise control over size and shape of the products. Due to these advantageous properties, graphene nanostructures are a promising candidate for the application in next-generation nanoelectronics [186–188].

Nonequilibrium situations in graphene typically induce a unique dynamic response behavior that is governed by the high carrier mobility and the 2D connectivity structure. As a result, graphene-based structures feature a remarkable resilience, due to the ultrafast redistribution of local energy excesses. This is, e.g., vividly demonstrated in Ref. [39] for the extremely strong and localized electric fields of highly charged ions. On the other hand, high-energetic ion sputtering is a frequently used method to break the graphene structure and cut finite fragments [189–191]. These conceptually different behaviors give room for an interesting intermediate domain of nonequilibrium physics. Apart from that, graphene-type materials are in the focus of many experiments invoking optical excitations [192–195]. Here, the electrons are driven out of equilibrium by energetic photons, leading to spatial or spectral carrier redistributions. Especially in regard to applications in photodetectors or solar cells, the proper understanding of the peculiarities of graphene is crucial. Studying the nonequilibrium dynamics is particularly interesting for finite graphene nanostructures, where the quantum confinement causes a significant interparticle coupling. The multilayered synergy of correlations and nonequilibrium then fosters the emergence of, e.g., Auger effects, such as the multiplication of excited electrons [33, 35]. Due to the inherent complexity and the lack of small parameters, such processes constitute a delicate objective for any theoretical description.

1.3 Goals and Application

The overall ambition of this thesis is the investigation of correlated nonequilibrium phenomena in ultracold-atom systems and graphene-type nanostructures by means of the NEGF method. In practice, the application of Green functions in this regard constitutes a formidable challenge due to the concrete limitations of the approach. There are three major obstacles that hamper the direct implementation of the method.

To begin with, the theoretical foundation of NEGF theory itself has not been in a sufficient state to enter the uncharted territory of the desired modern applications. This shows in the fact that there has been no concrete evidence for the accuracy of the approach especially in the context of experimentally relevant lattice systems. While the identification of certain scattering-process classes with different many-body approximations has been established on an abstract level, no specific predictions to the actual performance could be made. Furthermore, the NEGF method was short in testing procedures for the numerical stability with mainly energy-conservation checks used in practice. Beyond that, recent observations suggest to fundamentally question the validity of the theoretical build-up: in many cases solution multiplicity was reported for Green-functions techniques [196–201] and a recent paper by Adrian Stan claimed the existence of an unphysical attractor inherent to NEGF theory [202].

Another momentous hurdle stems from the circumstance that the dominant majority of all practically applied NEGF studies does not exceed the second-order level for the selfenergy. Higher-order approximations, such as GWA and TMA were (if at all) only applied for conceptual analyses and toy-model systems (see, e.g., Refs. [109], [130] and [136]). This is by no means surprising, because the implementation of such schemes is quite cumbersome and elaborate. In order to approach the correlated dynamics present in cold-atom experiments or excited finite graphene clusters, these more advanced selfenergies are, however, essential to account for the interparticle coupling. Prior to this thesis, it has not been investigated how the higher-order approximations are set up and efficiently implemented for these applications.

Arguably, the most severe obstacle of applied NEGF theory is the overall cubic time scaling of the KBE [cf. Eq. (1.3)]. It renders the implementation of long-time simulations increasingly costly. In this regard, the special case of GKBA+SOA calculations using HF propagators has a striking advantage as these simulations can be executed with $\mathcal{O}\left(N_{\mathrm{t}}^{2}\right)$ scaling [101]. For the more accurate (and much needed) higher-order selfenergies, however, no such scaling improvement is generated by the GKBA. Naturally, there have been efforts to enhance the technique while maintaining the favourable quadratic time scaling.[7] Nevertheless, these approaches remained unsuited to tackle the strong-coupling situations present in the systems that are described in Sec. 1.2. With the desired scaling aspiration of $\mathcal{O}\left(N_{\mathrm{t}}^{2}\right)$, improving the NEGF method even beyond that barrier was considered an insurmountable task.

In the present thesis, the aforementioned obstacles are directly addressed and successfully overcome by the following three major methodological advances:

---

[7] An interesting example is described in Ref. [203], where static correlations on the second-order level are included for the propagators.

(I) **The theoretical foundation of the NEGF technique is significantly improved.** This is achieved by a thorough benchmark analysis for practically relevant systems that brings the accuracy of the method to proof (Sec. 4.1), by establishing time reversibility as a numerical stability check (Sec. 3.2), by discussing and resolving solution multiplicity on a specific example (Sec. 3.3), and by a scrupulous scrutiny of Ref. [202] that deprives the basis for its far-reaching claims (Sec. 4.1).

(II) **The higher-order selfenergies are rendered practically accessible.** This is achieved by deriving applied equations for the TPP, TPH, GWA, and FLEX selfenergies and proposing efficient numerical solution techniques (Sec. 2.1). Additionally, the novel TOA selfenergy is established and successfully applied (Secs. 2.1.2 and 4.1). These important outcomes are made accessible to the community in two extensive review papers (Sec. 2.1).

(III) **NEGF theory is brought to the ultimate time-scaling limit.** This is achieved by deriving the G1–G2 scheme—an exact reformulation of the HF-GKBA that is based on the time-diagonal elements of the single-particle and two-particle Green functions and scales linearly in time (Sec. 3.1). This scaling is universal for all described selfenergy approximations and allows one to combine the resummation approaches on a deeper, and more systematic level.

Only by conceiving and implementing the above methodological improvements became it possible to apply the NEGF approach to lattice-excitation scenarios on an experimentally relevant length and time scale. This has been indispensable to obtain the key results of the present thesis.

For ultracold atoms in optical lattices, the NEGF technique is used to predict the expansion dynamics of confined fermionic particle clouds, modeled via the Hubbard Hamiltonian [204] in 1D, 2D and 3D. Here, the simulation results show an unprecedented agreement with recent experiments using ultracold fermionic potassium [140]. As part of that, the correct expansion behavior is reproduced on a large range of interaction strengths from strongly attractive to heavily repulsive. Furthermore, the analysis sheds light on the time- and space-resolved build-up of quantum correlations in the system—a hitherto inaccessible perspective for large two-dimensional lattices (Sec. 4.2).

In order to describe finite graphene nanostructures, the NEGF method and exact solving procedures (where applicable) are applied to Hubbard-based hexagonal lattice models. Particularly, the impact of energetic ions piercing through the lattice is analyzed. In such a situation, the electronic redistribution in the target leads to the build-up of net charges that, in turn, influence the incident ions. The simulations evince that typical finite-graphene correlations significantly affect the ion's kinetic-energy progression—in a way that cannot be captured by mean-field approaches. Beyond that, a fascinating novel phenomenon is observed for specific projectile energies: the ion impact induces the formation of stable correlated electron pairs (doublons). By multiple excitation, this effect is suited as an efficient doublon-generation protocol (Secs. 2.2 and 4.3). The importance of nonequilibrium correlation effects in graphene is further confirmed in an additional study of Auger processes in laser-excited GNRs (Sec. 5.1).

The new-found G1–G2 scheme is in itself a central practical outcome of the author's PhD studies. The innovative reformulation idea lifts the NEGF technique onto the level of time-linear evaluation—the scaling capstone for quantum time-evolution methods. With this advantageous numerical behavior, it is possible to achieve speed-up factors of $\mathcal{O}\left(10^4\right)$ in practice. In addition, it is demonstrated that even the precise higher-order many-body approximation are straightforwardly implemented into the G1–G2 scheme, without changing the beneficial time scaling. The new method is set up in a general single-particle basis and adapted for the Hubbard model and the homogeneous electron gas to allow for the investigation of correlated nonequilibrium phenomena on a next level (Sec. 3.1). The development of the G1–G2 formalism has already had seminal impact on the activities of the NEGF community [205, 206].

1.4 Outline: How To Read This Thesis

The present cumulative thesis contains all of the author's publications that are relevant to its scope (a complete list can be found in Sec. 1.5). In order to achieve the most logical structure and the best readability, the respective papers are not included in chronological order, but they are grouped together regarding their topical context. The most important results of this thesis are presented in Chpts. 2 – 4. Chpt. 2 contains three comprehensive review articles that include a detailed introduction to NEGF theory and give an accurate picture of the majority of the key results of this thesis. In Chpt. 3, the theoretical advancements achieved by the author are included, which are crucial to approach modern lattice-dynamics applications. Chpt. 4 contains numerical studies of the NEGF method, as well as the numerical results for ultracold atoms in optical lattices and ion-impact-driven finite graphene clusters. At the beginning of each section, a brief introduction is given to outline the key results of each publication, and to put them into the broader context of this thesis.

For specific papers, the author has included complementing information after the article. These passages contain original results of the present thesis that have not been published before. Concretely, this applies to Secs. 2.1.3 and 2.1.4, which discuss the topic of exchange terms and conserving approximations, as well as to Secs. 3.1.1 and 3.1.2, in which the G1–G2 scheme is further investigated. One important outcome of this original content is the proof of the satisfaction of physical conservation laws for the TOA selfenergy in Sec. 2.1.4. Beyond that, it is demonstrated that the TPH selfenergy is generally not conserving if it is applied with exchange contributions. Another considerable result is presented in Sec. 3.1.2, where the G1–G2 scheme is generalized to the TOA and FLEX approaches.

- **Chapter 2: Review Articles**
  Three extensive review papers cover the NEGF method and its application to correlated finite systems out of equilibrium. Sec. 2.1 focuses on the theoretical foundation and utilization details. Here, Ref. [122] recovers the derivation of the KBE, centers on the TMA scheme, and reviews numerical results in the context of optical-lattice

experiments. Ref. [79] focuses on the derivation and adaptation of efficient selfenergy approximations and discusses their application in practice. Following the article, the author has included a clarification for different uses of the interaction tensor, as well as the additional discussion about conserving approximations, including the important consequences for the TPH selfenergy. Sec. 2.2 contains Ref. [207], a topical review that concentrates on the simulation of ion-impact scenarios on solid surfaces, as well as the GKBA and its recent developments.

- **Chapter 3: Theoretical Developments of the NEGF Formalism**
  This chapter contains all publications that advance individual theoretical topics. Sec. 3.1 deals with the formulation of single-time equations for NEGF. Ref. [114] establishes the G1–G2 scheme by deriving the equations for SOA and GWA and demonstrates the profound numerical advantages. In Ref. [208], the previous derivations are redone in more detail and the scheme is generalized to TPP and TPH. As a combination of these higher-order contributions, the dynamically-screened-ladder (DSL) approximation for Green functions is proposed. Subsequent to the article, the author included a clarification of the handling of exchange terms within the scheme. Furthermore, the generalization of the G1–G2 scheme to TOA and FLEX is shown. Sec. 3.2 is about the derivation of time-reversibility conditions in quantum-kinetic equations. This is published in Ref. [209] for the NEGF method, and in Ref. [210] for the RDO technique. Sec. 3.3 includes Ref. [118], an investigation of a specific example of solution multiplicity in the context of Hubbard-type lattice systems. Here, the observation of a so-called Löwdin symmetry dilemma is reported.

- **Chapter 4: Applications to Correlated Lattice Systems Out of Equilibrium**
  This chapter contains the numerical results of this thesis. In Sec. 4.1, the predictive power of the NEGF method is numerically confirmed. Ref. [211] is written as comment to the recent publication by Adrian Stan [202], in which he seriously questioned the inherent numerical consistency and validity of the basic NEGF equations. The foundation of these claims is thoroughly investigated and unambiguously refuted, being caused by technical errors in the implementation. Ref. [212] is a benchmark analysis in the scope of practically relevant lattice systems that compares the NEGF method with DMRG calculations. Sec. 4.2 contains Ref. [213], an NEGF study of fermionic expansion dynamics in 2D and 3D. The simulations predict the dynamical build-up of correlations and exhibit an unprecedented agreement with experimental measurements for ultracold atoms in 2D optical lattices [140]. Sec. 4.3 deals with the stopping dynamics of energetic ions in hexagonal lattices. In Ref. [214], the influence of electronic lattice correlations on the energy loss of incident hydrogen and helium ions is investigated via the NEGF technique and the model is tested against experimentally supported graphene data. Ref. [41] predicts the ion-induced production of stable double occupation in finite graphene fragments and comparable hexagonal materials. Ref. [215] complements the previous findings by analyzing the different time-dependent energy contributions of the ion–target system in a combined study with TDDFT simulations of proton stopping on an aluminum surface.

- **Chapter 5: Other Works**
  This chapter contains an additional publication that is relevant for this thesis. Ref. [216] is an NEGF study of laser-excited GNRs that focuses on the analysis of Auger processes.

- **Chapter 6: Summary and Outlook**
  This chapter contains a summary and discussion regarding all theoretical improvements and practical applications. Subsequently, an overview of possible future applications of the NEGF method is given. Particularly the G1–G2 scheme features promising possibilities. Preliminary G1–G2 results for ion-stopping in more realistic systems are included. Finally, the G1–G2 scheme is generalized to the Pariser–Parr–Pople model and first test results for laser-excited GNRs are presented.

1.5 List of Publications

The following list contains all publications that are included in this work in chronological order. The contributions of the author to each paper are explicitly stated below the respective entries. Equal contribution of different authors is indicated by the blue font of the author names.

1. **N. Schlünzen**, S. Hermanns, M. Bonitz, and C. Verdozzi, *Dynamics of strongly correlated fermions: Ab initio results for two and three dimensions*, Phys. Rev. B, **93**, 035107 (2016)

   - The author contributed 70% to this work by implementing the T-matrix based NEGF code, performing all simulations, creating all figures and writing substantial parts of the text. 80% of the author's work on this paper have been done during his master's studies. This publication is included on p. 375.

2. **N. Schlünzen** and M. Bonitz, *Nonequilibrium Green Functions Approach to Strongly Correlated Fermions in Lattice Systems*, Contrib. Plasma Phys., **56**, 5 (2016)

   - This work is based the author's master's thesis, which makes for 70% of the paper's content. The author contributed additional 20% to this work by creating several new figures, as well as rewriting and adding large parts of the text. This publication is included on p. 21.

3. K. Balzer, **N. Schlünzen**, and M. Bonitz, *Stopping dynamics of ions passing through correlated honeycomb clusters*, Phys. Rev. B, **94**, 245118 (2016)

   - The author contributed 20% to this work by providing all non-local full NEGF data (second Born, 3rd order, T matrix), all GKBA data and writing parts of the text. This publication is included on p. 386.

4. **N. Schlünzen**, J.-P. Joost, F. Heidrich-Meisner, and M. Bonitz, *Nonequilibrium dynamics in the one-dimensional Fermi-Hubbard model: Comparison of the nonequilibrium Green-functions approach and the density matrix renormalization group method*, Phys. Rev. B, **95**, 165139 (2017)

   - The author contributed 45% to this work by developing most of the NEGF code, providing large parts of the simulation data, creating all figures in collaboration with J.-P.J. and writing substantial parts of the text. This publication is included on p. 360.

   The paper has been selected as *Editors' Suggestion*.

5. M. Scharnke, **N. Schlünzen**, and M. Bonitz, *Time reversal invariance of quantum kinetic equations: Nonequilibrium Green functions formalism*, J. Math. Phys., **58**, 061903 (2017)

   - The author contributed 25% to this work by providing all figures and writing parts of the text. He was also involved in the derivation of the central equations. This publication is included on p. 315.

6. **N. Schlünzen**, J.-P. Joost, and M. Bonitz, *Comment on "On the unphysical solutions of the Kadanoff-Baym equations in linear response: Correlation-induced homogeneous density-distribution and attractors"*, Phys. Rev. B, **96**, 117101 (2017)

   - The author contributed 65% to this work by carrying out all simulations, creating all figures and writing large parts of the text. This publication is included on p. 354.

7. M. Bonitz, M. Scharnke, and **N. Schlünzen**, *Time-reversal invariance of quantum kinetic equations II: Density operator formalism*, Contrib. Plasma Phys., **58**, 1036 (2018)

   - The author contributed 15% to this work by creating all figures and writing parts of the text. This publication is included on p. 323.

8. K. Balzer, M. Rodriguez Rasmussen, **N. Schlünzen**, J.-P. Joost, and M. Bonitz, *Doublon Formation by Ions Impacting a Strongly Correlated Finite Lattice System*, Phys. Rev. Lett., **121**, 267602 (2018)

   - The author contributed 25% to this work by providing all NEGF data, creating the Figs. 4 and S2 and writing parts of the text. This publication is included on p. 399.

9. **N. Schlünzen**, K. Balzer, M. Bonitz, L. Deuchler, and E. Pehlke, *Time-dependent simulation of ion stopping: Charge transfer and electronic excitations*, Contrib. Plasma Phys., **59**, e201800184 (2019)

   - The author contributed 35% to this work by creating Figs. 2 and 3, providing the respective NEGF simulation data and writing substantial parts of the text. This publication is included on p. 409.

10. J.-P. Joost, **N. Schlünzen**, and M. Bonitz, *Femtosecond Electron Dynamics in Graphene Nanoribbons – A Nonequilibrium Green Functions Approach Within an Extended Hubbard Model*, Phys. Status Solidi B, **256**, 1800498 (2019)

    - The author contributed 15% to this work by co-developing the idea, creating Fig. 2, and providing parts of the code. This publication is included on p. 425.

11. M. Bonitz, K. Balzer, **N. Schlünzen**, M. Rodriguez Rasmussen, and J.-P. Joost, *Ion Impact Induced Ultrafast Electron Dynamics in Finite Graphene-Type Hubbard Clusters*, Phys. Status Solidi B, **256**, 1800490 (2019)

    - The author contributed 20% to this work by providing most of the NEGF simulation data and creating Figs. 2, 7, and 8, as well as parts of Figs. 3 and 4. This publication is included on p. 236.

    The paper has been designated as a *feature article*. A modified version of Fig. 7 was featured as the cover picture of the respective issue.

12. **N. Schlünzen**, S. Hermanns, M. Scharnke, and M. Bonitz, *Ultrafast dynamics of strongly correlated fermions - Nonequilibrium Green functions and selfenergy approximations*, J. Phys. Condens. Matter, **32**, 103001 (2020)

    - This work is based on the PhD thesis by Sebastian Hermanns, which makes for 35% of the paper's content. The author contributed 45% to this work by creating all diagrammatic derivations, preparing several figures, providing new simulation data and writing substantial parts of the text. This publication is included on p. 110.

13. **N. Schlünzen**, J.-P. Joost, and M. Bonitz, *Achieving the Scaling Limit for Nonequilibrium Green Functions Simulations*, Phys. Rev. Lett., **124**, 076601 (2020)

    - The author contributed 65% to this work by deriving the differential formulation of the G1–G2 scheme for the SOA and the *GW* approximation. He also implemented the scheme for the Hubbard basis, provided all computational results, created all figures, and wrote large parts of the text. The idea was developed in collaboration with Jan-Philip Joost and Michael Bonitz. This publication is included on p. 255.

14. J.-P. Joost, **N. Schlünzen**, and M. Bonitz, *G1-G2 scheme: Dramatic acceleration of nonequilibrium Green functions simulations within the Hartree-Fock generalized Kadanoff-Baym ansatz*, Phys. Rev. B, **101**, 245101 (2020)

    - The author contributed 45% to this work by deriving the majority of all equations, implementing the code, creating all figures in collaboration with J.-P.J. and writing substantial parts of the text. This publication is included on p. 265.

15. J.-P. Joost, **N. Schlünzen**, S. Hese, M. Bonitz, P. Schmitteckert, C. Verdozzi, and M. Hopjan, *Löwdin's symmetry dilemma within Green functions theory for the one-dimensional Hubbard model*, Contrib. Plasma Phys., **Early View**, DOI: 10.1002/ctpp.202000220 (2021)

    - The author contributed 20% to this work by creating Figs. 1–3 and writing parts of the text. This publication is included on p. 337.

Chapter 2

Review Articles

During his PhD studies, the author had the opportunity to participate in several extensive review papers that cover the topic of Green functions in the context of finite correlated systems out of equilibrium. The original content in these works aims to improve the accessibility of higher-order selfenergies (II) and to support the theoretical foundation of the NEGF method in general (I).

2.1 Advances in NEGF Theory

The topic of NEGF theory with many-body approximations is a multifarious and content-rich field in the description of quantum many-body physics. There are several text books that capture the theory—from the basic concepts to its advanced applications [23, 101, 103, 117, 217]. The following review articles,[1,2] Refs. [122] and [79], aim to profoundly deepen specific topics and to expand the existing instructional literature by adding new perspectives.

2.1.1 The T-Matrix Approach to Optical Lattices

Ultracold atoms in optical lattices are of great importance due to their unique property to mirror charge carriers in a condensed-matter state in a controllable way. In recent years, there have been several important experimental breakthroughs in this field (see, e.g., Ref. [42–45]). However, a proper theoretical description especially for 2D and 3D setups was completely missing [44, 140, 218]. This has been changed due to new advances and adaptions of the NEGF method that have been achieved by the author. In this course, it was possible to obtain remarkable agreement between theory and experiment for fermionic

---

[1]N. Schlünzen and M. Bonitz, Contrib. Plasma Phys., **56**, 5 (2016). Copyright Wiley-VCH Verlag GmbH & Co. KGaA. Reproduced with permission.

[2]N. Schlünzen, S. Hermanns, M. Scharnke, and M. Bonitz, J. Phys. Condens. Matter, **32**, 103001 (2020), reproduced under the Creative Commons Attribution 3.0 licence.

expansion in 2D, for the first time. Therefore, the author was in the unique position to provide a comprehensive review of the theoretical framework supporting the applied NEGF approach. This resulted in Ref. [122]—a selfcontained, in-depth review that covers the derivation of the Kadanoff–Baym equations from basic quantum-dynamical relations, focuses on the (particle–particle) T-matrix approximation, and concludes with applications to ultracold atoms in optical lattices.

After beginning with a broad motivation and an overview of the available quantum-dynamics methods, first, a general introduction to the second quantization and the contour formalism is given (p. 7 ff. in Ref. [122]). Starting from the Heisenberg equation for the canonical operators, next a cohesive derivation of the Martin–Schwinger hierarchy for the N-particle Green function is given in a fully specified, general single-particle basis (p. 13 ff. in Ref. [122]). The truncation of the hierarchy on the one-particle level results in the KBE—the equations of motion for single-particle Green function. Subsequently, the concept of the selfenergy is described and the TPP selfenergy—representing the sum of all ladder diagrams in the particle–particle channel—is motivated from the hierarchy and derived in detail (p. 17 ff. in Ref. [122]). The TPP approximation has proven very successful for the description of expansion dynamics in lattice systems [213]. The theoretical part is closed with the mapping of contour-time quantities to their corresponding real-time components and a motivation and discussion of the generalized Kadanoff–Baym ansatz—an approximation to the time structure of the KBE (p. 23 ff. in Ref. [122]). For the numerical evaluation of the KBE the GKBA can reduce the computational scaling by one order which is highly relevant for practical applications that would be out of reach, otherwise.

The next part is devoted to experiments with ultracold atoms in optical lattices with a particular focus on recent fermionic-expansion results for two-dimensional systems (p. 29 ff. in Ref. [122]). Afterwards, the Hubbard model is introduced and the corresponding single-particle basis is applied to the central equations of the NEGF approach (p. 35 ff. in Ref. [122]). The following section focuses on the numerical implementation of the NEGF equations and gives practical details about numerical integration and propagation schemes (p. 42 ff. in Ref. [122]). Subsequently, different applications of the NEGF method to the Hubbard model are reviewed (p. 59 ff. in Ref. [122]). Of particular importance is the description of expansion setups of ultracold atoms in two-dimensional optical lattices [213], where an unprecedented agreement with the experiments was achieved. This breakthrough was possible thanks to the theoretical developments by the author and is discussed in more detail in Sec. 4.2.

In summary, Ref. [122] gives a comprehensible overview of the foundation and implementation of the central NEGF equations and their application to lattice systems, which is an important outcome of the author's master's- and early PhD studies.

Nonequilibrium Green Functions Approach to Strongly Correlated Fermions in Lattice Systems

N. Schlünzen and **M. Bonitz**[*]

Christian-Albrechts-Universität zu Kiel, Institut für Theoretische Physik und Astrophysik, Leibnizstraße 15, 24098 Kiel, Germany

Quantum dynamics in strongly correlated systems are of high current interest in many fields including dense plasmas, nuclear matter and condensed matter and ultracold atoms. An important model case are fermions in lattice systems that is well suited to analyze, in detail, a variety of electronic and magnetic properties of strongly correlated solids. Such systems have recently been reproduced with fermionic atoms in optical lattices which allow for a very accurate experimental analysis of the dynamics and of transport processes such as diffusion. The theoretical analysis of such systems far from equilibrium is very challenging since quantum and spin effects as well as correlations have to be treated non-perturbatively. The only accurate method that has been successful so far are density matrix renormalization group (DMRG) simulations. However, these simulations are presently limited to one-dimensional (1D) systems and short times. Extension of quantum dynamics simulations to two and three dimensions is commonly viewed as one of the major challenges in this field. Recently we have reported a breakthrough in this area [N. Schlünzen et al., Phys. Rev. B (2016)] where we were able to simulate the expansion dynamics of strongly correlated fermions in a Hubbard lattice following a quench of the confinement potential in 1D, 2D and 3D. The results not only exhibited excellent agreement with the experimental data but, in addition, revealed new features of the short-time dynamics where correlations and entanglement are being build up. The method used in this work are nonequilibrium Green functions (NEGF) which are found to be very powerful in the treatment of fermionic lattice systems filling the gap presently left open by DMRG in 2D and 3D.

In this paper we present a detailed introduction in the NEGF approach and its application to inhomogeneous Hubbard clusters. In detail we discuss the proper strong coupling approximation which is given by T-matrix selfenergies that sum up two-particle scattering processes to infinite order. The efficient numerical implementation of the method is discussed in detail as it has allowed us to achieve dramatic performance gains. This has been the basis for the treatment of more than 100 particles over large time intervals. The numerical results presented in this paper concentrate on the diffusion in 1D to 3D lattices. We find that the expansion dynamics consist of three different phases that are linked with the build-up of correlations. In the long time limit, a universal scaling with the particle number is revealed. By extrapolating the expansion velocities to the macroscopic limit, the obtained results show excellent agreement with recent experiments on ultracold fermions in optical lattices. Moreover we present results for the site-resolved behavior of correlations and entanglement that can be directly compared with experiments using the recently developed atomic microscope technique.

1 Introduction

Transport processes in strongly correlated quantum systems, including carriers of charge, momentum and energy, are of growing interest in the fields of condensed matter [1–3], dense plasmas [4] and, in particular, ultracold gases [5–7]. Many of today's most exciting phenomena in physics, such as high-temperature superconductivity, superfluidity and quantum-Hall physics, to name a few, are driven by quantum transport. While many issues of correlated quantum transport out of equilibrium are still poorly understood, much progress can be made for model systems, most importantly, lattice models. These models, such as the Hubbard model, have been developed to approximately capture the physics of solid-state systems and revealed many robust predictions for the phase diagram and, more recently, also for the transport behavior and nonequilibrium dynamics.

[*] Corresponding author. E-mail: bonitz@physik.uni-kiel.de

While lattice models often constitute only a rough picture of real condensed matter systems, these models have been accurately realized in experiments with ultracold atoms in optical lattices [5, 6, 8–21] and allow for the in-situ study of correlated quantum systems. There is a large body of experimental studies of traditional condensed matter phenomena with optical lattices with an impressive amount of novel predictions. At the same time, there is a striking mismatch on the theory side as most of these predictions (in particular, beyond one-dimensional systems) can currently not be described with *ab initio* quantum methods.

The theoretical description of correlated quantum dynamics is a challenging task which requires the proper simultaneous treatment of nonequilibrium, strong coupling and dimensionality effects. Since the exact solution of the Schrdinger equation scales exponentially with the particle number N [22], one has to find reliable approximations that accurately describe the governing processes. A possible approach is given by the density matrix renormalization group (DMRG) method [23] which has been successfully applied to one-dimensional bosonic [6] and fermionic [7] lattice systems. It is an iterative, variational approach that reduces the size of the Hilbert space to the most relevant effective space. This first-principle method has been generalized to describe time-dependent processes, resulting in the time-dependent DMRG (t-DMRG) and the time evolving block decimation (TEBD) [7, 24]. These methods are constructed to describe one-dimensional lattice systems. While the generalization to two-dimensional systems is a subject of current research [24], the description of higher dimension is out of reach.

Another possible approach which is applicable regardless of the dimensionality D, is given by the time-dependent density functional theory [25] (TDDFT). It is supported by the Hohenberg–Kohn theorem [26] which states that in equilibrium, all observables are functionals of the single-particle density matrix, and can be generalized to nonequilibrium. TDDFT has been applied to fermionic lattice systems of up to three dimensions [27, 28], however, its validity crucially depends on the choice of the exchange-correlation potential v_{xc} which is, in general, unknown. The dynamics in quantum lattice systems can also be described by the dynamical mean-field theory [29] (DMFT). In this approach, the lattice is mapped to a local impurity model. The DMFT becomes exact in the limit of infinitely large interaction strengths. For medium coupling, due to the local character of the method, the description of nonequilibrium processes becomes erroneous.

For the low coupling limit, quantum transport can also be described e.g. by multi-configurational time-dependent Hartree–Fock [30] (MCTDHF) approaches or the coupled cluster theory [31]. However, they fail to describe strong correlations that are of central interest in the following. In this work, we also briefly discuss a model based on the semi-classical Boltzmann equation in relaxation time approximation as it was recently used to simulate fermionic transport [5, 21, 32]. However, since it provides a description under the assumption of local equilibrium it exhibits fundamental problems and large quantitative deviations if applied to nonequilibrium systems.

To overcome the problems of the above-mentioned approaches, in this paper, the nonequilibrium Green functions (NEGF) method is used. The NEGF framework is an *ab-initio* method that is applicable to bosonic and fermionic systems out of equilibrium, regardless of the dimensionality. It can treat arbitrary external fields and excitations and, since the NEGF method is a statistical description, it is applicable to the ground state, to finite temperatures and to arbitrary nonequilibrium situations. The approach is based on the many-particle Green function $G^{(n)}$ which contains the full information on the system and gives rise to a hierarchy of equations (the Martin–Schwinger hierarchy) for all lower order Green functions. The lowest order is given by the Keldysh-Kadanoff–Baym equations (KBE) for the single-particle Green function G which are formally closed by introduction of the selfenergy Σ which accounts for correlation effects. The problem of conserving approximations has been analyzed in great detail in recent years. Here we demonstrate that, for strongly correlated Hubbard clusters out of equilibrium the proper choice of the selfenergy can be derived from a truncation of the hierarchy at the second order in the interaction strength. This provides a set of equations which is solved by the T-matrix, a quantity that sums up scattering processes to infinite order. The corresponding selfenergy in T-matrix approximation (TMA) is analyzed in detail for the Hubbard model and a highly efficient implementation is presented. Furthermore, we analyze the generalized Kadanoff–Baym ansatz (GKBA) that was proposed by Lipavský et al. [33]. This ansatz has recently attracted growing attention [34–37] since it provides a way to reduce the numerical effort of the computation of the time propagation, while still accurately accounting for correlations. In the GKBA, the general two-time Green function is approximately reconstructed from its time-diagonal value.

In the present paper, the NEGF approach with TMA is applied to inhomogeneous, finite fermionic lattice systems of dimension $D = 1, 2, 3$ whereby, both, the full two-time propagation and the GKBA are being used.

A special focus lies on the investigation of diffusion processes where we follow the ideas originally presented in Ref. [37]. Here we substantially extend this analysis of diffusion processes, including the classification with respect to the evolution of correlations, and the dependencies on the particle number, the interaction strength and the dimension. Using the example of the diffusion in two-dimensional fermionic lattices, the NEGF approach with T-matrix approximation allows for comparisons with experimental results of ultracold quantum gases [5]. As was first shown in Refs. [38, 39], NEGF-TMA simulations are perfectly capable to treat strongly correlated fermionic lattice systems, including 2D and 3D and, thus, provide the until now missing *ab inito* quantum method.

The remainder of this his paper is organized as follows. In section 2 the theoretical foundations of the NEGF formalism are described in detail. After a short overview of the second quantization, which is the underlying description of quantum systems, the concept of the time contour is introduced which allows for a simple description of time dependence and statistical averaging. The Martin–Schwinger hierarchy, which determines the many-particle Green function, is derived and the first equations—the KBE—are decoupled to focus on the single-particle Green function. By truncation of the hierarchy, the T-matrix is derived which allows to treat strong correlations. The representation via real-time components, which map the contour quantities back to real space, is described. Finally, the closed time propagation and the related GKBA are derived, whereby, for the latter, the Hartree–Fock propagators are introduced. Section 3 gives a brief introduction in experiments with ultracold atoms in optical lattices. The practical steps to generate potential lattices and to control the interaction between the atoms and underlying physical effects are briefly discussed. Afterwards, diffusion results for an ultracold fermionic gas in a two-dimensional optical lattice are presented.

Section 4 reviews the basics of the Hubbard model, and discusses the physical properties, for simple limiting cases. Furthermore, the particular case of the Hubbard Hamiltonian is used in the formulation of the NEGF framework, providing useful simplifications. Section 5 presents details on the numerical solution of the KBE including higher order integration methods and the time propagation algorithm including the selfconsistent, iterative computation of the T-matrix. The different methods for the generation of the initial state are described and the evaluation of the physical quantities during the propagation is shown. Additionally, the computational demands and the performance of the algorithm and the parallelization on graphics processing units (GPUs) are discussed. Section 6 contains the numerical results for fermionic Hubbard clusters. After performing accuracy tests for small one-dimensional systems, the approach is used to predict diffusion processes for Hubbard lattices of large size in all dimensions. A special focus lies on the classification of the short-time dynamics and the expansion in the long time limit. For the latter, a universal scaling with the particle number is revealed, which is used to extrapolate the expansion velocities to the macroscopic limit, where comparisons with experimental data are possible. The paper concludes with a discussion of the results and outlook in section 7.

2 Nonequilibrium Green functions approach

Before describing the nonequilibrium Green functions formalism and, in particular, the T-matrix approximation, first, a short overview of the second quantization—the underlying description of quantum systems—is given. For a more detailed introduction, the reader is referred to e.g. Ref. [40].

2.1 Second quantization

The second quantization provides a natural formalism to describe quantum particles by transforming the full information of the many-particle state to the occupation numbers of the respective underlying orbitals. It exhibits an inherent description to account for the symmetry of the bosonic and the antisymmetry of fermionic wavefunction, which are caused by the indistinguishability of particles in quantum mechanics. It is called *second* quantization in reference to the formalism of the Schrdinger equation (SE), which is a quantized field-theory itself. The SE determines the wave function $\mid \psi \rangle$ that describes the full many-body state and its dynamics in a Hilbert space $\mathcal{H}$ while each observable O is represented by a corresponding operator $\hat{O} : \mathcal{H} \rightarrow \mathcal{H}$. In contrast, in second quantization, the system state is described in a more abstract space $\mathcal{F}$ that is called Fock space. This representation allows to describe also processes, where the particle numbers of the initial state and the final state differ. For each observable O, the corresponding Fock space operator $\hat{O}^{\mathcal{F}} : \mathcal{F} \rightarrow \mathcal{F}$ determines the corresponding expectation values.

2.1.1   Relation to the Schrödinger equation formalism

To elucidate the connection between the SE and the second quantization formalism and how the respective operators transform, it is convenient to restrict the system to a fixed particle number N_0. If every quantum particle is described by a wave function, each is defined on the same Hilbert space $\mathcal{H}$, due to the indistinguishability of fermions and bosons. The full many-body state $|\psi_{N_0}\rangle$ is, in this case, defined on

$$\mathcal{H}_{N_0} = \text{span}\left\{ |\phi\rangle_{i_1} \otimes |\phi\rangle_{i_2} \otimes \cdots \otimes |\phi\rangle_{i_{N_0}} | (i_1, \ldots, i_{N_0}) \in I_{N_0} \right\} . \tag{1}$$

Here, $\{|\phi\rangle_i | i \in I\}$ specifies a basis set of $\mathcal{H}$. I (I_{N_0}) denotes an index set of cardinality $\dim_{\mathcal{H}}$ ($\dim_{\mathcal{H}_{N_0}}$). In the many-particle state the characteristics of indistinguishable particles are fully taken into account because each state constitutes a superposition of corresponding states that would exist in the case of distinguishable particles. This is formally ensured by the exchange symmetry (antisymmetry) of bosonic (fermionic) states which leads to a smaller Fock space $\mathcal{F}_{N_0} \subset \mathcal{H}_{N_0}$ [41]. The resulting state is uniquely defined by the occupation numbers $\{n_i | i \in I, \sum_i n_i = N_0\}$ of the single-particle states $|\phi\rangle_i$. Therefore, the N_0-particle state $|\psi\rangle_{N_0}$ can be expressed as [42]

$$|\psi_{N_0}\rangle := |n_1, n_2, \ldots\rangle . \tag{2}$$

The full Fock space $\mathcal{F}$, regarding states of all possible particle numbers, emerges as the direct orthogonal sum of all respective Fock spaces of fixed particle number $\mathcal{F}_{N_0}$ [43], i.e. $\mathcal{F} = \bigoplus_{N_0 \in \mathbb{N}} \mathcal{F}_{N_0}$.

Since each state in $\mathcal{F}$ is completely determined by the occupation number, every Fock operator $\hat{O}^{\mathcal{F}}$ can only act as an occupation change. Thus, a very useful basis to define those operators is given by the canonical creation (annihilation) operators $\hat{c}_i^\dagger$ ($\hat{c}_i$). The action of these operators on a Fock state is defined as the insertion or extraction of a single particle in the state $|\phi\rangle_i$. Hence, they connect the N-particle subspace of $\mathcal{F}$ with the $(N+1)$- or the $(N-1)$- particle subspace. In detail, the definition of the actions reads

$$\hat{c}_i^\dagger |n_1, n_2, \ldots, n_i, \ldots\rangle = (\pm 1)^\alpha \sqrt{n_i + 1}\, |n_1, n_2, \ldots, n_i + 1, \ldots\rangle \cdot \begin{cases} 1 & \text{for bosons} \\ \delta_{n_1, 0} & \text{for fermions} \end{cases},$$

$$\hat{c}_i |n_1, n_2, \ldots, n_i, \ldots\rangle = (\pm 1)^\alpha \sqrt{n_i}\, |n_1, n_2, \ldots, n_i - 1, \ldots\rangle \cdot \begin{cases} 1 - \delta_{n_i, 0} & \text{for bosons} \\ \delta_{n_1, 1} & \text{for fermions} \end{cases},$$

$$\tag{3}$$

with $\alpha = \sum_{j=1}^{i-1} n_j$. The upper (lower) sign corresponds to bosons (fermions). From these relations, one can easily derive the commutator relations of the canonical operators for bosons and the anticommutator relations for fermions, respectively,

$$\left[\hat{c}_i^\dagger, \hat{c}_j^\dagger\right]_{\mp} = 0, \qquad \left[\hat{c}_i, \hat{c}_j\right]_{\mp} = 0, \qquad \left[\hat{c}_i, \hat{c}_j^\dagger\right]_{\mp} = \delta_{i,j} . \tag{4}$$

The creation operator can be used to construct any state $|n_1, n_2, \ldots\rangle$ from the vacuum Fock state $|0\rangle$ which is defined as the state, where no orbitals are occupied, i.e. $|0\rangle := |n_1 = 0, n_2 = 0, \ldots\rangle$,

$$|n_1, n_2, \ldots\rangle = \left(\prod_i \frac{1}{\sqrt{n_i!}}\right) \left(\hat{c}_1^\dagger\right)^{n_1} \left(\hat{c}_2^\dagger\right)^{n_2} \ldots |0\rangle . \tag{5}$$

The Fock operators can now be expressed in terms of the canonical creator and annihilator. By basis transformation of the SE operators, for the single-particle operators $\hat{O}_1$ and the two-particle operators $\hat{O}_2$, the corresponding second quantized quantities become

$$\hat{O}_1^{\mathcal{F}} = \sum_{i,j} \left\langle i \left| \hat{O}_1 \right| j \right\rangle \hat{c}_i^\dagger \hat{c}_j =: \sum_{i,j} O_{ij} \hat{c}_i^\dagger \hat{c}_j , \tag{6}$$

$$\hat{O}_2^{\mathcal{F}} = \sum_{i,j,k,l} \left\langle ij \left| \hat{O}_2 \right| kl \right\rangle \hat{c}_i^\dagger \hat{c}_j^\dagger \hat{c}_l \hat{c}_k =: \sum_{i,j,k,l} O_{ijkl} \hat{c}_i^\dagger \hat{c}_j^\dagger \hat{c}_l \hat{c}_k , \tag{7}$$

with the matrix elements O_{ij} and O_{ijkl}. The ordering of the canonical operators in the two-particle equation ensures a correct description of bosonic as well as fermionic particles.

2.1.2   Time evolution

Transport processes in quantum systems and, furthermore, dynamics in general, are inextricably linked with an evolution in time, which can only be described by time-dependent observables $O(t)$ (cf. Eq. (15)). In quantum mechanics, there are three widely used formalisms to treat time evolution: the Schrdinger picture, the Heisenberg picture and the Dirac picture. All formulations lead to the same expectation values for the observables but differ in the attribution of time dependence. In the Schrdinger picture, the entire time information is assigned to the states, i.e. $\frac{d}{dt}|n_S\rangle \neq 0$, whereas the operators remain constant: $\frac{d}{dt}\hat{O}_S \equiv 0$. In the Heisenberg picture, the operators carry the time dependence, i.e. $\frac{d}{dt}\hat{O}_H \neq 0$, while the states are constants of motion: $\frac{d}{dt}|n_H\rangle \equiv 0$. The Dirac picture (or interaction picture) is a formulation, where both operators and states are allowed to be time-dependent, i.e. $\frac{d}{dt}\hat{O}_D \neq 0$, $\frac{d}{dt}|n_D\rangle \neq 0$. All formalisms are equivalent and also apply for operators in second quantization.

The transformation between the introduced pictures can be a by the use of time evolution operators. From the Schrdinger picture to the Heisenberg picture, the states and operators transform as

$$|n_H\rangle = \hat{U}(t_0, t)|n_S(t)\rangle , \quad \hat{O}_H(t) = \hat{U}(t_0, t)\hat{O}_S\hat{U}(t, t_0) , \tag{8}$$

with the time evolution operator [44]

$$\hat{U}(t, t_0) := \begin{cases} \mathcal{T}\left\{ e^{-\frac{i}{\hbar}\int_{t_0}^{t} d\bar{t}\,\hat{H}(\bar{t})} \right\} & \text{if} \quad t \geq t_0 \\ \bar{\mathcal{T}}\left\{ e^{+\frac{i}{\hbar}\int_{t}^{t_0} d\bar{t}\,\hat{H}(\bar{t})} \right\} & \text{if} \quad t < t_0 . \end{cases} \tag{9}$$

for the, in general, time-dependent Hamiltonian $\hat{H}(t)$. Here, $\mathcal{T}$ denotes the causal time-ordering operator which sorts operators in chronological order according to their time arguments $t_1 \leq t_2 \leq \ldots \leq t_k$,

$$\mathcal{T}\left\{ \hat{O}(t_{P(k)})\hat{O}(t_{P(k-1)})\ldots\hat{O}(t_{P(1)}) \right\} = \hat{O}(t_k)\hat{O}(t_{k-1})\ldots\hat{O}(t_1) . \tag{10}$$

This relation holds for all permutations P of $\mathbb{N}_{\leq k}$. $\mathcal{T}$ is is not connected to an observable in the quantum mechanical sense, but it is a superoperator[1]. Analogously, $\bar{\mathcal{T}}$ denotes the anticausal time-ordering operator which also obeys Eq. (10) (if inserted for $\mathcal{T}$), but for times $t_1 \geq t_2 \geq \ldots \geq t_k$. It is easy to see that the time evolution operator obeys the relations

$$\hat{U}(t_1, t_2)\hat{U}(t_2, t_3) = \hat{U}(t_1, t_3) \quad \text{and}$$
$$\hat{U}(t_1, t_2)\hat{U}(t_2, t_1) = \hat{U}(t_1, t_1) = 1 . \tag{12}$$

Thus, since $\hat{U}$ is unitary, $\left(\hat{U}(t_1, t_2)\right)^{\dagger} = \hat{U}(t_2, t_1)$. In the Dirac picture, the Hamiltonian is split into a time-dependent and a static part. The formally transformation depends on the particular choice how the time dependence is attributed.

While the time evolution in the Schrdinger picture is described by the SE, operators in the Heisenberg picture obey the Heisenberg equation (HE) [45],

$$\frac{d\hat{O}_H(t)}{dt} = \frac{i}{\hbar}\left[\hat{H}_H(t), \hat{O}_H(t)\right]_- + \frac{\partial\hat{O}_H(t)}{\partial t} , \tag{13}$$

where $\hat{H}_H(t)$ is the time-dependent Hamiltonian in the Heisenberg picture.

---

[1]   To understand the action of $\mathcal{T}$ in Eq. (9), it is essential to define the operator action of the exponential function by the associated Taylor expansion expression,

$$\mathcal{T}\left\{ e^{-\frac{i}{\hbar}\int_{t_0}^{t} d\bar{t}\,\hat{H}(\bar{t})} \right\} := \sum_{n=0}^{\infty} \frac{(-\frac{i}{\hbar})^n}{n!} \int_{t_0}^{t} dt_1 \int_{t_0}^{t} dt_2 \ldots \int_{t_0}^{t} dt_n \, \mathcal{T}\left\{ \hat{H}(t_1)\hat{H}(t_2)\ldots\hat{H}(t_n) \right\} . \tag{11}$$

On the right-hand side, the sorting of $\mathcal{T}$ is well-defined.

2.1.3   Statistical averaging

In order to obtain statistical averaged expectation values of observables, it is required to define a statistical ensemble, the averaging acts on. In second quantization one has to ensure a correct description of the creation and annihilation processes, which directly demands an ensemble which allows the particle number to vary, if the processes are not balanced. Therefore, the grand canonical ensemble is a convenient choice. It is characterized by the temperature T, the volume V and the chemical potential μ of the system. These three quantities determine the macrostate of the system (T, V, μ). The quantum statistical ensemble is described by the density operator $\hat{\rho} : \mathcal{F} \to \mathcal{F}$. It can be expressed, e.g. in the Heisenberg picture, in spectral representation [46],

$$\hat{\rho}_{\mathrm{H}} = \sum_n p_n |n_{\mathrm{H}}\rangle \langle n_{\mathrm{H}}| \quad \text{with} \tag{14}$$

$$\mathrm{Tr}\left(\hat{\rho}_{\mathrm{H}}\right) = 1, \quad p_n \in [0, 1], \quad \sum_n p_n = 1,$$

where $\hat{\rho}_{\mathrm{H}}$ is time-independent. Here, the $|n_{\mathrm{H}}\rangle$ are the microstates of the system and also eigenstates of the density operator. The trace over $\mathcal{F}$ is denoted by $\mathrm{Tr}\left(\cdot\right)$. This density operator allows for statistical averaging of operators in the Heisenberg picture. Thus, the expectation value of an observable becomes

$$O(t) = \mathrm{Tr}\left(\hat{\rho}_{\mathrm{H}} \hat{O}_{\mathrm{H}}(t)\right). \tag{15}$$

Note that the density operator can also be defined in the Schrdinger picture or the Dirac picture.

2.2   The time contour

The purpose of the following section is to show how statistical averaging of a many-body state and the subsequent time evolution can be combined to a unified description which implies the introduction of a time contour for the evaluation of time-dependent expectation values. The idea of this contour was first presented by Schwinger [47] and Keldysh [48]. In this work, a few steps of the derivation are partly skipped to focus on the most important relations. For a more detailed introduction, the reader is referred to e.g. Ref. [44].

Starting from the time-dependent matrix element of a chosen microstate n, according to Eq. (8), one has

$$O^{(n)}(t) = \left\langle n_{\mathrm{H}} \left| \hat{U}(t_0, t) \hat{O}_{\mathrm{S}} \hat{U}(t, t_0) \right| n_{\mathrm{H}} \right\rangle. \tag{16}$$

Here, one denotes $\langle n_{\mathrm{H}}| =: \langle n_{t_0}|$, $|n_{\mathrm{H}}\rangle =: |n_{t_0}\rangle$ and $\hat{O}_{\mathrm{S}} =: \hat{O}_t$, not to indicate time dependence, but to assign the attributed time of the evolution, leading to

$$O^{(n)}(t) = \left\langle n_{t_0} \left| \bar{\mathcal{T}} \left\{ \mathrm{e}^{-\frac{\mathrm{i}}{\hbar} \int_t^{t_0} \mathrm{d}\bar{t}\, \hat{H}(\bar{t})} \right\} \hat{O}_t \mathcal{T} \left\{ \mathrm{e}^{-\frac{\mathrm{i}}{\hbar} \int_{t_0}^t \mathrm{d}\bar{t}\, \hat{H}(\bar{t})} \right\} \right| n_{t_0} \right\rangle, \tag{17}$$

where the definition of $\hat{U}(t, t_0)$ in Eq. (9) is used. One way to interpret the sequence of the operators in Eq. (17) is the identification with two time branches, a causal and an anticausal one with respect to the time direction. The connection of the two branches leads to a first time contour $\mathcal{C}$. This idea is illustrated in Fig. 1. To distinguish time arguments in the real time space and on $\mathcal{C}$, contour times are denoted $z \in \mathcal{C}$. With this definition, identifying $\mathcal{C}_-$ with the forward branch and $\mathcal{C}_+$ with the backward one, Eq. (17) can be rewritten,

$$O^{(n)}(t) = \left\langle n_{t_0} \left| \mathcal{T}_{\mathcal{C}} \left\{ \mathrm{e}^{-\frac{\mathrm{i}}{\hbar} \int_{\mathcal{C}_+} \mathrm{d}\bar{z}\, \hat{H}(\bar{z})} \right\} \hat{O}_{t_\pm} \mathcal{T}_{\mathcal{C}} \left\{ \mathrm{e}^{-\frac{\mathrm{i}}{\hbar} \int_{\mathcal{C}_-} \mathrm{d}\bar{z}\, \hat{H}(\bar{z})} \right\} \right| n_{t_0} \right\rangle. \tag{18}$$

Here, $\mathcal{T}_{\mathcal{C}}$ is the time ordering operator on the contour, obeying

$$\mathcal{T}_{\mathcal{C}} \left\{ \hat{O}(z_{P(k)}) \hat{O}(z_{P(k-1)}) \ldots \hat{O}(z_{P(1)}) \right\} = (-1)^{F_P} \hat{O}(z_k) \hat{O}(z_{k-1}) \ldots \hat{O}(z_1), \tag{19}$$

for contour times $z_1 \leq z_2 \leq \ldots \leq z_k$. F_P is the number of exchanged fermionic operators of the permutation P and originates from the fermionic commutator relation. The value of $O^{(n)}(t)$ is equal for the insertion of both
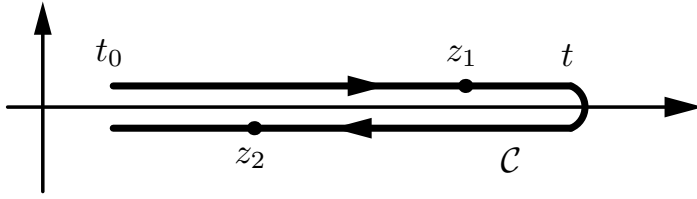
Fig. 1 Illustration of the time branches: the contour $\mathcal{C}$ on the real-time axis consists of a causal branch and an anticausal branch. On $\mathcal{C}$, the time z_2 is later than z_1, although their projections on the real time axis are arranged oppositely.

$\hat{O}_{t_+}$ (on $\mathcal{C}_+$) and $\hat{O}_{t_-}$ (on $\mathcal{C}_-$). Since the times on $\mathcal{C}_+$ are entirely later than the ones on $\mathcal{C}_-$, and, moreover, inside the $\mathcal{T}_\mathcal{C}$ sign, operators can be treated as commuting operators [44], one arrives at

$$O^{(n)}(t) = \left\langle n_{t_0} \left| \mathcal{T}_\mathcal{C} \left\{ e^{-\frac{i}{\hbar} \int_\mathcal{C} d\bar{z}\, \hat{H}(\bar{z})} \hat{O}_{t_\pm} \right\} \right| n_{t_0} \right\rangle . \tag{20}$$

It is convenient to extend the contour $\mathcal{C}$ to $+\infty$, to make it universal and independent of the choice of t. This does not change the form of Eq. (20). Since $\hat{O}_{t_\pm}$ is not explicitly time-dependent (cf. Eq. (16)) one can safely write $\hat{O}_{t_\pm} = \hat{O}_t$. Furthermore, one can also apply Eq. (20) to contour times z,

$$O^{(n)}(z) = \left\langle n_{t_0} \left| \mathcal{T}_\mathcal{C} \left\{ e^{-\frac{i}{\hbar} \int_\mathcal{C} d\bar{z}\, \hat{H}(\bar{z})} \hat{O}_z \right\} \right| n_{t_0} \right\rangle . \tag{21}$$

At this point, the question arises, how ensemble averaging can be combined with the presented time structure. In general, this is achieved by applying the trace over all microstates with the density operator, as shown in Eq. (15). Together with the findings of Eq. (21), the ensemble expectation value for a given observable reads

$$O(z) = \mathrm{Tr} \left(\hat{\rho}_\mathrm{H} \mathcal{T}_\mathcal{C} \left\{ e^{-\frac{i}{\hbar} \int_\mathcal{C} d\bar{z}\, \hat{H}(\bar{z})} \hat{O}_z \right\} \right) , \tag{22}$$

with the density operator $\hat{\rho}_\mathrm{H} = \frac{e^{-\beta \hat{H}(z)}}{Z}$ and the partition function $Z = \mathrm{Tr}\left(e^{-\beta \hat{H}(z)} \right)$. In this work, there are two different ways to treat this ensemble averaging concerning the different system setups that are investigated. In general, one has to compute a nontrivial interacting ground state from which to start the time evolution. Under certain conditions, this can be achieved by the use of the so-called adiabatic switching method, which is presented in the following section[2]. The Hamiltonian of a quantum system in second quantization in the Schrödinger picture generally reads (cf. Eq. (6) and Eq. (7))

$$\hat{H}(t) = \hat{H}_0 + \hat{W} + \hat{F}(t), \quad \text{with} \tag{23}$$

$$\hat{H}_0 = \sum_{i,j} h_{ij}^{(0)} \hat{c}_i^\dagger \hat{c}_j \quad \text{and} \quad \hat{W} = \frac{1}{2} \sum_{i,j,k,l} W_{ijkl} \hat{c}_i^\dagger \hat{c}_j^\dagger \hat{c}_l \hat{c}_k , \tag{24}$$

$\hat{H}_0$ being the single-particle Hamiltonian, $\hat{W}$ the interaction part and $\hat{F}(t)$ a general excitation with $\hat{F}(t) \equiv 0$ for $t < t_0$. For the adiabatic switching method, this Hamiltonian is generalized to

$$\hat{H}_\mathrm{AS}(t) = \hat{H}_0 + f_\mathrm{AS}(t) \left(\hat{W} + \hat{F}(t) \right) , \tag{25}$$

where $f_\mathrm{AS}(t)$ denotes an adiabatic switching function to switch on the interaction. This monotonically increasing function, $f_\mathrm{AS} : \mathbb{R} \to [0, 1]$, has to obey the following relations,

$$\lim_{t \to -\infty} f_{AS}(t) = 0 \quad \text{and} \quad f_\mathrm{AS}(t) = 1 \quad \text{for all} \quad t \geq t_0 . \tag{26}$$

---

[2] The ensemble averaging and the preparation of the interacting initial state can also be done by including a vertical branch into the contour $\mathcal{C}$, describing the imaginary time. This solution is not part of the present work and can be looked up e.g. in Ref. [44]

According to the modified Hamiltonian $\hat{H}_{AS}(t)$, one can define a corresponding time evolution operator $\hat{U}_{AS}(t, t_0)$ similar to Eq. (9). Now the fully interacting density operator can be expressed in the following way,

$$\hat{\rho}_{H} = \hat{U}_{AS}(t_0, -\infty)\hat{\rho}_0\hat{U}_{AS}(-\infty, t_0) \,, \tag{27}$$

where $\hat{\rho}_0$ denotes the non-interacting single-particle density operator corresponding to $\hat{H}_0$. This is the main assumption of the adiabatic switching method. It is mathematically supported by the *Gell-Mann–Low theorem* [49, 50] that requires the existence of a nondegenerate ground state of $\hat{H}_0$. Furthermore, the state of the system after the switch-on is not necessarily the interacting ground state, but an eigenstate of $\hat{H}(t)$ [51]. In practice, the switch-on via $f_{AS}(t)$ has to be performed sufficiently slow to ensure that a nonfluctuating fully interacting state is approached. It has to be checked whether this state is the ground state. It is noteworthy that, in principle, the interaction and excitation Hamiltonian has to be switched off for $t \to \infty$ in a similar way for the adiabatic assumption to be valid. This, however, can be neglected for all practical purposes, since it does not affect the preceding evolution.

Combining Eq. (22) and Eq. (27), one arrives at

$$O(z) = \mathrm{Tr}\left(\hat{\rho}_0\hat{U}_{AS}(-\infty, t_0)\mathcal{T}_{\mathcal{C}}\left\{e^{-\frac{i}{\hbar}\int_{\mathcal{C}} d\bar{z}\,\hat{H}(\bar{z})}\hat{O}_z\right\}\hat{U}_{AS}(t_0, -\infty)\right) \,. \tag{28}$$

Here, the cyclic property of the trace has been used. This equation can be simplified by the introduction of a new time contour which extends $\mathcal{C}$ to $-\infty$. It is illustrated in Fig. 2.
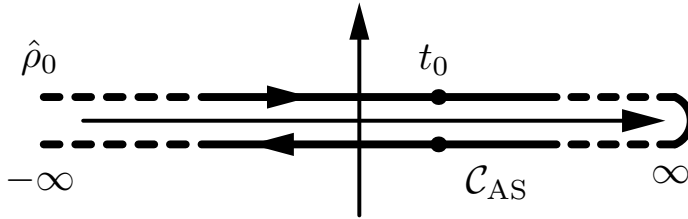
Fig. 2 Time contour for the adiabatic switching method: the contour starts at $-\infty$ with the noninteracting ground state of the system. The interaction is switched on before t_0. The two branches are similar to the ones in Fig. 1.

From now on, $\mathcal{C}$ denotes this generalized adiabatic switching time contour $\mathcal{C}_{AS}$, when the system is prepared in the interacting ground state. Inserting $\mathcal{C}_{AS}$ into Eq. (28) leads to the following simplification,

$$O(z) = \mathrm{Tr}\left(\hat{\rho}_0\mathcal{T}_{\mathcal{C}_{AS}}\left\{e^{-\frac{i}{\hbar}\int_{\mathcal{C}_{AS}} d\bar{z}\,\hat{H}_{AS}(\bar{z})}\hat{O}_z\right\}\right) \,, \tag{29}$$

where $\mathcal{T}_{\mathcal{C}_{AS}}$ is now evaluated on the adiabatic switching contour $\mathcal{C}_{AS}$.

Many of the systems which are studied in this paper, start from a setup with a substantially lower degree of complexity. For instance, the initial state of the systems presented in Sec. 6.2.4 is exactly described by an ideal state (cf. Sec. 5.3.1). In this case, it is not necessary to generate an interacting ground state by adiabatic switching and the time contour can be reduced to two positive branches. This is illustrated in Fig. 3.

When no ground state preparation by adiabatic switching is performed, from now on, $\mathcal{C}$ denotes this reduced time contour $\mathcal{C}_{id}$. The ensemble average from equation Eq. (22) reduces to

$$O(z) = \mathrm{Tr}\left(\hat{\rho}_{id}\mathcal{T}_{\mathcal{C}_{id}}\left\{e^{-\frac{i}{\hbar}\int_{\mathcal{C}_{id}} d\bar{z}\,\hat{H}(\bar{z})}\hat{O}_z\right\}\right) \,, \tag{30}$$

$\hat{\rho}_{id}$ being the density operator of the ideal state (cf. Sec. 5.3) and $\mathcal{T}_{\mathcal{C}_{id}}$ the time ordering operator on $\mathcal{C}_{id}$.

Summarizing, the time contour is a very useful and universal description that combines time evolution and ensemble averaging in a simple way. The specific choice of $\mathcal{C}$, however, depends on the properties of the system.
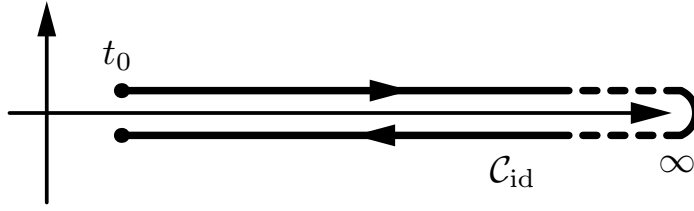
Fig. 3 Time contour for the ideal initial state: the contour $\mathcal{C}$ is only defined for times $t \geq t_0$. The two branches correspond to the ones in Fig. 1.

2.3 The many-particle Green function and the Martin–Schwinger hierarchy

The derivation of the Martin–Schwinger hierarchy, a coupled system of integro-differential equations which describe the motion of a system in terms of all N-particle Green functions, with $N \in \mathbb{N}$, can only briefly discussed here, for a more detailed introduction see e.g. Refs. [43, 44, 52]. The next important step is the time evolution of the canonical operators in the Heisenberg picture obtained from the Heisenberg equation, e.g. [43]

$$i\hbar \frac{d\hat{c}_i(z)}{dz} = \sum_j h_{ij}^{(0)}(z)\hat{c}_j(z) + \sum_{j,k,l} W_{ijkl}(z)\hat{c}_j^\dagger(z)\hat{c}_l(z)\hat{c}_k(z), \tag{31}$$

$$-i\hbar \frac{d\hat{c}_i^\dagger(z)}{dz} = \sum_j \hat{c}_j^\dagger(z)h_{ji}^{(0)}(z) + \sum_{j,k,l} \hat{c}_j^\dagger(z)\hat{c}_k^\dagger(z)\hat{c}_l(z)W_{jkil}(z), \tag{32}$$

for contour times z (for simplicity, the excitation part $\hat{F}(t)$ of the Hamiltonian is omitted, but this derivation can easily be generalized accordingly). The main question which remains after studying the contents of Sec. 2.2, is how $O(z)$ is calculated in particular and, especially, how the exponentials in Eqs. (29) and (30) are evaluated. Since in second quantization, each operator can be expressed in terms of the creation and annihilation operators, it is convenient to introduce the N-particle correlator $\hat{G}^{(N)}$ in the following way,

$$\hat{G}^{(N)}_{i_1\ldots i_N j_1\ldots j_N}(z_1,\ldots,z_N,z_1',\ldots,z_N') :=$$
$$\frac{1}{(i\hbar)^N}\mathcal{T}_\mathcal{C}\left\{\hat{c}_{i_1}(z_1)\ldots\hat{c}_{i_N}(z_N)\hat{c}_{j_N}^\dagger(z_N')\ldots\hat{c}_{j_1}^\dagger(z_1')\right\}. \tag{33}$$

A solution for the evolution of $\hat{G}^{(N)}$ immediately enables the evaluation of any operator $\hat{O}(z)$[3]

$$\mathcal{T}_\mathcal{C}\left\{\hat{O}_1(z_1)\ldots\hat{O}_k(z_k)\right\} =$$
$$\sum_P (\pm 1)^P \Theta_\mathcal{C}^{(k)}\left(z_{P(1)},\ldots,z_{P(k)}\right)\hat{O}_{P(1)}(z_{P(1)})\ldots\hat{O}_{P(k)}(z_{P(k)}). \tag{34}$$

Here, $\Theta_\mathcal{C}^{(k)}(z_1,\ldots,z_k) = \Theta_\mathcal{C}(z_1,z_2)\Theta_\mathcal{C}(z_2,z_3)\ldots\Theta_\mathcal{C}(z_{k-1},z_k)$ is the generalized theta function, $\Theta_\mathcal{C}(z_1,z_2) :=$ $\begin{cases} 1 & \text{if } z_1 > z_2 \\ 0 & \text{otherwise} \end{cases}$ being the Heaviside step function on the contour $\mathcal{C}$. The time derivative of the N-particle correlator becomes

$$\frac{d}{d\mathfrak{z}_k}\hat{G}^{(N)}_{i_1\ldots i_N j_1\ldots j_N}(z_1,\ldots,z_N,z_1',\ldots,z_N') =$$
$$\frac{1}{(i\hbar)^N}\left\{\left(\frac{d}{d\mathfrak{z}_k}\Theta_\mathcal{C}^{(2N)}\right)\prod_i \hat{c}_i \prod_j \hat{c}_j^\dagger + \mathcal{T}_\mathcal{C}\left(\frac{d}{d\mathfrak{z}_k}\prod_i \hat{c}_i \prod_j \hat{c}_j^\dagger\right)\right\}, \tag{35}$$

with $\mathfrak{z} \in \{z, z'\}$ and the symbolic objects

$$\left(\frac{d}{d\mathfrak{z}_k}\Theta_\mathcal{C}^{(2N)}\right)\prod_i \hat{c}_i \prod_j \hat{c}_j^\dagger := \sum_P(\pm 1)^P \left(\frac{d}{d\mathfrak{z}_k}\Theta_\mathcal{C}^{(2N)}\left(z_{P(1)},\ldots,z_{P(2N)}\right)\right)$$
$$\hat{a}_{i_{P(1)}}(z_{P(1)})\ldots\hat{a}_{i_{P(2N)}}(z_{P(2N)}'), \tag{36}$$

---

[3] The canonical operators in Eq. (33) are, in general, not time-dependent, since most operators are integrals of motion.

and

$$
\mathcal{T}_{\mathcal{C}} \left(\frac{\mathrm{d}}{\mathrm{d}_{\mathfrak{z}k}} \prod_i \hat{c}_i \prod_j \hat{c}_j^\dagger \right) :=
$$

$$
\begin{cases}
\mathcal{T}_{\mathcal{C}} \left\{ \hat{c}_{i_1}(z_1) \dots \left(\frac{\mathrm{d}}{\mathrm{d}z_k} \hat{c}_{i_k}(z_k) \right) \dots \hat{c}_{i_N}(z_N) \hat{c}_{j_N}^\dagger(z_N') \dots \hat{c}_{j_1}^\dagger(z_1') \right\} & \text{if} \quad \mathfrak{z} = z \\
\mathcal{T}_{\mathcal{C}} \left\{ \hat{c}_{i_1}(z_1) \dots \hat{c}_{i_N}(z_N) \hat{c}_{j_N}^\dagger(z_N') \dots \left(\frac{\mathrm{d}}{\mathrm{d}z_k'} \hat{c}_{j_k}^\dagger(z_k') \right) \dots \hat{c}_{j_1}^\dagger(z_1') \right\} & \text{if} \quad \mathfrak{z} = z'
\end{cases} \tag{37}
$$

In Eq. (36) the operators $\hat{a}_i$ and the times z_i are defined such that

$$
\hat{a}_{i_m}(z_m) := \begin{cases}
\hat{c}_{i_m}(z_m) & \text{if} \quad m \in \{1, \dots, N\} \\
\hat{c}_{j_{2N-m+1}}^\dagger(z_{2N-m+1}') & \text{if} \quad m \in \{N+1, \dots, 2N\}
\end{cases} . \tag{38}
$$

Eq. (36) can be rearranged by the use of time ordering of permutations and the (anti)commutator expressions of the canonical operators, resulting in [44]

$$
\left(\frac{\mathrm{d}}{\mathrm{d}_{\mathfrak{z}k}} \Theta_{\mathcal{C}}^{(2N)} \right) \prod_i \hat{c}_i \prod_j \hat{c}_j^\dagger =
$$

$$
\begin{cases}
\sum_{l=1}^N (\pm 1)^{k+l} \delta_{i_k, j_l} \delta_{\mathcal{C}}(z_k, z_l') \cdot \\
\mathcal{T}_{\mathcal{C}} \left\{ \hat{c}_{i_1}(z_1) \dots \hat{c}_{i_k}\cancel{(z_k)} \dots \hat{c}_{i_N}(z_N) \hat{c}_{j_N}^\dagger(z_N') \dots \hat{c}_{j_l}^\dagger\cancel{(z_l')} \dots \hat{c}_{j_1}^\dagger(z_1') \right\} & \text{if} \quad \mathfrak{z} = z \\
- \sum_{l=1}^N (\pm 1)^{k+l} \delta_{i_l, j_k} \delta_{\mathcal{C}}(z_l, z_k') \cdot \\
\mathcal{T}_{\mathcal{C}} \left\{ \hat{c}_{i_1}(z_1) \dots \hat{c}_{i_l}\cancel{(z_l)} \dots \hat{c}_{i_N}(z_N) \hat{c}_{j_N}^\dagger(z_N') \dots \hat{c}_{j_k}^\dagger\cancel{(z_k')} \dots \hat{c}_{j_1}^\dagger(z_1') \right\} & \text{if} \quad \mathfrak{z} = z'
\end{cases} . \tag{39}
$$

Here, $\delta_{\mathcal{C}}(z, z')$ denotes the Dirac distribution acting on contour times. Eq. (39) shows that the respective time ordering operators including the subsequent canonical operators can be identified with a $N-1$-particle correlator according to Eq. (33). This is an important finding, because it allows to solve the evolution equations recursively. The time derivatives occurring in Eq. (37) can be replaced by the relations in Eqs. (31) and (32). Due to the structure of the operators therein, one can easily see that in this case an N-particle correlator for the single-particle part and a $N+1$-particle correlator for the interaction part can be identified. This leads to the simple hierarchic equations,

$$
\sum_l \left[\mathrm{i}\hbar \frac{\mathrm{d}}{\mathrm{d}z_k} \delta_{i_k, l} - h_{i_k l}^{(0)}(z_k) \right] \hat{G}_{i_1 \dots l \dots i_N j_1 \dots j_N}^{(N)}(z_1, \dots, z_N, z_1', \dots, z_N')
$$

$$
= \pm \mathrm{i}\hbar \sum_{l,m,n} \int_{\mathcal{C}} \mathrm{d}\bar{z}\, w_{i_k l m n}(z_k, \bar{z}) \hat{G}_{i_1 \dots m \dots i_N n j_1 \dots j_N l}^{(N+1)}(z_1, \dots, z_N, \bar{z}, z_1', \dots, z_N', \bar{z}^+) \tag{40}
$$

$$
+ \sum_{p=1}^N (\pm 1)^{k+p} \delta_{i_k, j_p} \delta_{\mathcal{C}}(z_k, z_p') \hat{G}_{i_1 \dots \cancel{i_k} \dots i_N j_1 \dots \cancel{j_p} \dots j_N}^{(N-1)}(z_1, \dots, \cancel{z_k}, \dots, z_N, z_1', \dots, \cancel{z_p'}, \dots, z_N'),
$$

$$
\sum_l \hat{G}_{i_1 \dots i_N j_1 \dots l \dots j_N}^{(N)}(z_1, \dots, z_N, z_1', \dots, z_N') \left[-\mathrm{i}\hbar \frac{\overleftarrow{\mathrm{d}}}{\mathrm{d}z_k'} \delta_{l, j_k} - h_{l j_k}^{(0)}(z_k') \right]
$$

$$
= \pm \mathrm{i}\hbar \sum_{l,m,n} \int_{\mathcal{C}} \mathrm{d}\bar{z}\, \hat{G}_{i_1 \dots i_N n j_1 \dots l \dots j_N m}^{(N+1)}(z_1, \dots, z_N, \bar{z}^-, z_1', \dots, z_N', \bar{z}) w_{l m j_k n}(\bar{z}, z_k') \tag{41}
$$

$$
+ \sum_{p=1}^N (\pm 1)^{k+p} \delta_{i_p, j_k} \delta_{\mathcal{C}}(z_p, z_k') \hat{G}_{i_1 \dots \cancel{i_p} \dots i_N j_1 \dots \cancel{j_k} \dots j_N}^{(N-1)}(z_1, \dots, \cancel{z_p}, \dots, z_N, z_1', \dots, \cancel{z_k'}, \dots, z_N').
$$

In these equations, the interaction obeys $W_{ijkl}(z) = \int_{\mathcal{C}} \mathrm{d}\bar{z}\, w_{ijkl}(z, \bar{z})$, with

$$
w_{ijkl}(z, \bar{z}) := W_{ijkl}(z) \delta_{\mathcal{C}}(z, \bar{z}). \tag{42}
$$

This additional time dependence allows to include the canonical operators naturally into the correlators. The idea causes also the times $z^{\pm} = z \pm \epsilon, \epsilon \ll 1$ which are defined as infinitesimally larger or smaller to ensure the correct operator ordering. The arrow in $\frac{\overleftarrow{\mathrm{d}}}{\mathrm{d}z'_k}$ denotes an acting of the differential operator to its left.

Finally, one can define the N-particle nonequilibrium Green function including the ensemble averaging (cf. Eqs. (29) and (30)),

$$G^{(N)}_{i_1\ldots i_N j_1\ldots j_N}(z_1,\ldots,z_N,z'_1,\ldots,z'_N) :=$$
$$\mathrm{Tr}\left(\hat{\rho}_{0/\mathrm{id}}\,\hat{G}^{(N)}_{i_1\ldots i_N j_1\ldots j_N}(z_1,\ldots,z_N,z'_1,\ldots,z'_N)\right),\tag{43}$$

where $\hat{\rho}_{0/\mathrm{id}}$ depends on the choice of the time contour. By applying the trace to Eqs. (40) and (41), one can easily see that the N-particle Green function formally obeys the same equations as the N-particle correlator. This leads to the well-known Martin–Schwinger hierarchy [53],

$$\sum_l \left[\mathrm{i}\hbar\frac{\mathrm{d}}{\mathrm{d}z_k}\delta_{i_k,l} - h^{(0)}_{i_k l}(z_k)\right] G^{(N)}_{i_1\ldots l\ldots i_N j_1\ldots j_N}(z_1,\ldots,z_N,z'_1,\ldots,z'_N)$$
$$= \pm\,\mathrm{i}\hbar \sum_{l,m,n} \int_{\mathcal{C}} \mathrm{d}\bar{z}\, w_{i_k lmn}(z_k,\bar{z}) G^{(N+1)}_{i_1\ldots m\ldots i_N n j_1\ldots j_N l}(z_1,\ldots,z_N,\bar{z},z'_1,\ldots,z'_N,\bar{z}^+)\tag{44}$$
$$+ \sum_{p=1}^N (\pm 1)^{k+p}\delta_{i_k,j_p}\delta_{\mathcal{C}}(z_k,z'_p) G^{(N-1)}_{i_1\ldots\cancel{i_k}\ldots i_N j_1\ldots\cancel{j_p}\ldots j_N}(z_1,\ldots,\cancel{z_k},\ldots,z_N,z'_1,\ldots,\cancel{z'_p},\ldots,z'_N),$$

$$\sum_l G^{(N)}_{i_1\ldots i_N j_1\ldots l\ldots j_N}(z_1,\ldots,z_N,z'_1,\ldots,z'_N)\left[-\mathrm{i}\hbar\frac{\overleftarrow{\mathrm{d}}}{\mathrm{d}z'_k}\delta_{l,j_k} - h^{(0)}_{lj_k}(z'_k)\right]$$
$$= \pm\,\mathrm{i}\hbar \sum_{l,m,n} \int_{\mathcal{C}} \mathrm{d}\bar{z}\, G^{(N+1)}_{i_1\ldots i_N n j_1\ldots l\ldots j_N m}(z_1,\ldots,z_N,\bar{z}^-,z'_1,\ldots,z'_N,\bar{z}) w_{lmj_k n}(\bar{z},z'_k)\tag{45}$$
$$+ \sum_{p=1}^N (\pm 1)^{k+p}\delta_{i_p,j_k}\delta_{\mathcal{C}}(z_p,z'_k) G^{(N-1)}_{i_1\ldots\cancel{i_p}\ldots i_N j_1\ldots\cancel{j_k}\ldots j_N}(z_1,\ldots,\cancel{z_p},\ldots,z_N,z'_1,\ldots,\cancel{z'_k},\ldots,z'_N).$$

This hierarchy can, in principle, be solved exactly, starting from the zero-particle Green function $G^{(0)} := 1$. However, since it is, in general, a large (for a macroscopic system, infinitely large) set of coupled integro-differential equations one has to find approximate solutions by truncation of the hierarchy at a certain order.

The N-particle Green function obeys a number of boundary conditions in time which are readily obtained. Let z_{s} (z_{e}) be the starting (ending) time of a contour $\mathcal{C}$. By using the definition in Eq. (43) and Eq. (33), respectively and considering the acting of the time ordering operator of Eq. (34), one finds

$$G^{(N)}_{i_1\ldots i_N j_1\ldots j_N}(z_1,\ldots,z_{\mathrm{s}},\ldots,z_N,z'_1,\ldots,z'_N) = \pm G^{(N)}_{i_1\ldots i_N j_1\ldots j_N}(z_1,\ldots,z_{\mathrm{e}},\ldots,z_N,z'_1,\ldots,z'_N)$$
$$G^{(N)}_{i_1\ldots i_N j_1\ldots j_N}(z_1,\ldots,z_N,z'_1,\ldots,z'_{\mathrm{s}},\ldots,z'_N) = \pm G^{(N)}_{i_1\ldots i_N j_1\ldots j_N}(z_1,\ldots,z_N,z'_1,\ldots,z'_{\mathrm{e}},\ldots,z'_N).\tag{46}$$

These equations are known as the Kubo–Martin–Schwinger (KMS) relations [53, 54].

In order to find equations of motion which are easier to handle than the full hierarchy equations, it is convenient to focus on the first one, describing the motion of the single-particle nonequilibrium Green function, $G^{(1)}_{ij}(z,z') =: G_{ij}(z,z')$, which, from now on, is simply called the Green function,

$$\sum_l \left[\mathrm{i}\hbar\frac{\mathrm{d}}{\mathrm{d}z}\delta_{i,l} - h^{(0)}_{il}(z)\right] G_{lj}(z,z') = \delta_{i,j}\delta_{\mathcal{C}}(z,z')\tag{47}$$
$$\pm\ \mathrm{i}\hbar \sum_{l,m,n} \int_{\mathcal{C}} \mathrm{d}\bar{z}\, w_{ilmn}(z,\bar{z}) G^{(2)}_{mnjl}(z,\bar{z},z',\bar{z}^+),$$

$$\sum_l G_{il}(z, z') \left[-i\hbar \frac{\overleftarrow{\mathrm{d}}}{\mathrm{d}z'} \delta_{l,j} - h_{lj}^{(0)}(z') \right] = \delta_{i,j} \delta_{\mathcal{C}}(z, z') \tag{48}$$

$$\pm i\hbar \sum_{l,m,n} \int_{\mathcal{C}} \mathrm{d}\bar{z}\, G_{inlm}^{(2)}(z, \bar{z}^-, z', \bar{z}) w_{lmjn}(\bar{z}, z').$$

Equations 47 and 48 are the well-known Keldysh-Kadanoff–Baym equations (KBE) [55]. Due to the structure of the hierarchy, they are coupled to the two-particle Green function. In the same manner, one can also find the hierarchy equations for $G_{i_1 i_2 j_1 j_2}^{(2)}(z_1, z_2, z_1', z_2')$,

$$\sum_l \left[i\hbar \frac{\mathrm{d}}{\mathrm{d}z_1} \delta_{i_1,l} - h_{i_1 l}^{(0)}(z_1) \right] G_{l i_2 j_1 j_2}^{(2)}(z_1, z_2, z_1', z_2') = \tag{49}$$

$$\delta_{i_1,j_1} \delta_{\mathcal{C}}(z_1, z_1') G_{i_2 j_2}(z_2, z_2') \quad \pm \quad \delta_{i_1,j_2} \delta_{\mathcal{C}}(z_1, z_2') G_{i_2 j_1}(z_2, z_1')$$

$$\pm i\hbar \sum_{l,m,n} \int_{\mathcal{C}} \mathrm{d}\bar{z}\, w_{i_1 lmn}(z_1, \bar{z})\, G_{m i_2 n j_1 j_2 l}^{(3)}(z_1, z_2, \bar{z}, z_1', z_2', \bar{z}^+),$$

$$\sum_l \left[i\hbar \frac{\mathrm{d}}{\mathrm{d}z_2} \delta_{i_2,l} - h_{i_2 l}^{(0)}(z_2) \right] G_{i_1 l j_1 j_2}^{(2)}(z_1, z_2, z_1', z_2') = \tag{50}$$

$$\delta_{i_2,j_2} \delta_{\mathcal{C}}(z_2, z_2') G_{i_1 j_1}(z_1, z_1') \quad \pm \quad \delta_{i_2,j_1} \delta_{\mathcal{C}}(z_2, z_1') G_{i_1 j_2}(z_1, z_2')$$

$$\pm i\hbar \sum_{l,m,n} \int_{\mathcal{C}} \mathrm{d}\bar{z}\, w_{i_2 lmn}(z_2, \bar{z})\, G_{i_1 mn j_1 j_2 l}^{(3)}(z_1, z_2, \bar{z}, z_1', z_2', \bar{z}^+),$$

$$\sum_l G_{i_1 i_2 l j_2}^{(2)}(z_1, z_2, z_1', z_2') \left[-i\hbar \frac{\overleftarrow{\mathrm{d}}}{\mathrm{d}z_1'} \delta_{l,j_1} - h_{l j_1}^{(0)}(z_1') \right] = \tag{51}$$

$$\delta_{i_1,j_1} \delta_{\mathcal{C}}(z_1, z_1') G_{i_2 j_2}(z_2, z_2') \quad \pm \quad \delta_{i_2,j_1} \delta_{\mathcal{C}}(z_2, z_1') G_{i_1 j_2}(z_1, z_2')$$

$$\pm i\hbar \sum_{l,m,n} \int_{\mathcal{C}} \mathrm{d}\bar{z}\, G_{i_1 i_2 n l j_2 m}^{(3)}(z_1, z_2, \bar{z}^-, z_1', z_2', \bar{z}) w_{lm j_1 n}(\bar{z}, z_1'),$$

$$\sum_l G_{i_1 i_2 j_1 l}^{(2)}(z_1, z_2, z_1', z_2') \left[-i\hbar \frac{\overleftarrow{\mathrm{d}}}{\mathrm{d}z_2'} \delta_{l,j_2} - h_{l j_2}^{(0)}(z_2') \right] = \tag{52}$$

$$\delta_{i_2,j_2} \delta_{\mathcal{C}}(z_2, z_2') G_{i_1 j_1}(z_1, z_1') \quad \pm \quad \delta_{i_1,j_2} \delta_{\mathcal{C}}(z_1, z_2') G_{i_2 j_1}(z_2, z_1')$$

$$\pm i\hbar \sum_{l,m,n} \int_{\mathcal{C}} \mathrm{d}\bar{z}\, G_{i_1 i_2 n j_1 l m}^{(3)}(z_1, z_2, \bar{z}^-, z_1', z_2', \bar{z}) w_{lm j_2 n}(\bar{z}, z_2'),$$

which are coupled to G and $G^{(3)}$.

Finally, since it will become important in the derivation of the T-matrix [cf. Sec. 2.4], we give the second hierarchy equation for the three-particle Green function

$$\sum_l \left[i\hbar \frac{\mathrm{d}}{\mathrm{d}z_2} \delta_{i_2,l} - h_{i_2 l}^{(0)}(z_2) \right] G_{i_1 l i_3 j_1 j_2 j_3}^{(3)}(z_1, z_2, z_3, z_1', z_2', z_3') =$$

$$\pm \delta_{i_2,j_1} \delta_{\mathcal{C}}(z_2, z_1') G_{i_1 i_3 j_2 j_3}^{(2)}(z_1, z_3, z_2', z_3')$$

$$+ \delta_{i_2,j_2} \delta_{\mathcal{C}}(z_2, z_2') G_{i_1 i_3 j_1 j_3}^{(2)}(z_1, z_3, z_1', z_3') \tag{53}$$

$$\pm \delta_{i_2,j_3} \delta_{\mathcal{C}}(z_2, z_3') G_{i_1 i_3 j_1 j_2}^{(2)}(z_1, z_3, z_1', z_2')$$

$$\pm i\hbar \sum_{l,m,n} \int_{\mathcal{C}} \mathrm{d}\bar{z}\, w_{i_2 lmn}(z_2, \bar{z}) G_{i_1 m i_3 n j_1 j_2 j_3 l}^{(4)}(z_1, z_2, z_3, \bar{z}, z_1', z_2', z_3', \bar{z}^+),$$

which couples to the two-particle Green function and the four-particle Green function. Due to the explicit appearance of w in Eqs. (44) and (45), the hierarchy provides a systematic starting point to apply perturbation expansions in terms of the interaction as will be discussed in the following section.

2.4 The selfenergy and the T-matrix

The standard decoupling of the hierarchy in NEGF theory is achieved by introducing the single-particle selfenergy [43, 44, 52, 56] Σ which fulfills the following relations,

$$\pm i\hbar \sum_{l,m,n} \int_{\mathcal{C}} d\bar{z}\, w_{ilmn}(z,\bar{z}) G^{(2)}_{mnjl}(z,\bar{z},z',\bar{z}^+) \quad =: \quad \sum_l \int_{\mathcal{C}} d\bar{z}\, \Sigma_{il}(z,\bar{z}) G_{lj}(\bar{z},z')\,, \tag{54}$$

$$\pm i\hbar \sum_{l,m,n} \int_{\mathcal{C}} d\bar{z}\, G^{(2)}_{inlm}(z,\bar{z}^-,z',\bar{z}) w_{lmjn}(\bar{z},z') \quad =: \quad \sum_l \int_{\mathcal{C}} d\bar{z}\, G_{il}(z,\bar{z}) \Sigma_{lj}(\bar{z},z')\,. \tag{55}$$

By applying these definitions to Eqs. (47) and (48) one arrives at the formally closed KBE,

$$\sum_l \left[i\hbar \frac{d}{dz} \delta_{i,l} - h^{(0)}_{il}(z) \right] G_{lj}(z,z') \quad = \quad \delta_{i,j} \delta_{\mathcal{C}}(z,z') \tag{56}$$

$$+ \sum_l \int_{\mathcal{C}} d\bar{z}\, \Sigma_{il}(z,\bar{z}) G_{lj}(\bar{z},z')\,,$$

$$\sum_l G_{il}(z,z') \left[-i\hbar \frac{\overleftarrow{d}}{dz'} \delta_{l,j} - h^{(0)}_{lj}(z') \right] \quad = \quad \delta_{i,j} \delta_{\mathcal{C}}(z,z') \tag{57}$$

$$+ \sum_l \int_{\mathcal{C}} d\bar{z}\, G_{il}(z,\bar{z}) \Sigma_{lj}(\bar{z},z')\,.$$

In this form, the non-Markovian structure of the equations becomes visible, since the Green function depends on its own history in the integral expression. Equations 56 and 57 are exact, if the selfenergy Σ would be exactly known. In practice, however, one has to use approximate expressions which follow from approximations for the two-particle Green function. In the following we discuss important approximations and how they account for quantum correlations.

2.4.1 The Hartree–Fock selfenergy

It is easy to check that in Eqs. (49) to (52), the first two lines of each equation, which only contain the single-particle Green functions on the right hand site, are fulfilled by

$$G^{(2),\text{HF}}_{i_1 i_2 j_1 j_2}(z_1, z_2, z'_1, z'_2) = G_{i_1 j_1}(z_1, z'_1) G_{i_2 j_2}(z_2, z'_2) \pm G_{i_1 j_2}(z_1, z'_2) G_{i_2 j_1}(z_2, z'_1)\,. \tag{58}$$

Replacing the two-particle Green function by $G^{(2),\text{HF}}$ in Eqs. (47) and (48) leads to the so-called Hartree–Fock approximation. In terms of a perturbative expansion, it corresponds to a truncation at the first order in the interaction w, since all terms originating from the three-particle Green function in Eqs. (49) to (52) are at least of second order in w in the Kadanoff–Baym equations. While generally, the two-particle Green function describes the evolution of two particles, which are "inserted" at times z'_1 and z'_2 and removed at times z_1 and z_2, in the Hartree–Fock approximation, this process is described by the evolution of two independent particles (mean-field approximation). The first KBE in Hartree–Fock approximation attains the following form,

$$\sum_l \left[i\hbar \frac{d}{dz} \delta_{i,l} - h^{(0)}_{il}(z) \right] G_{lj}(z,z') = \quad \delta_{i,j} \delta_{\mathcal{C}}(z,z')$$

$$\pm i\hbar \sum_{l,m,n} \int_{\mathcal{C}} dz d\bar{\bar{z}}\, \delta_{\mathcal{C}}(z,\bar{\bar{z}}) w_{ilmn}(z,\bar{z}) G_{nl}(\bar{z},\bar{z}^+) G_{mj}(\bar{\bar{z}},z') \tag{59}$$

$$+ i\hbar \sum_{l,m,n} \int_{\mathcal{C}} d\bar{z}\, w_{ilmn}(z,\bar{z}) G_{ml}(z,\bar{z}^+) G_{nj}(\bar{z},z')\,.$$

By comparison with Eq. (56), one can identify the Hartree–Fock selfenergy,

$$\Sigma_{ij}^{\mathrm{HF}}(z, z') = \pm i\hbar \delta_{\mathcal{C}}(z, z') \sum_{k,l} \int_{\mathcal{C}} \mathrm{d}\bar{z}\, w_{ikjl}(z, \bar{z}) G_{lk}(\bar{z}, \bar{z}^+) + i\hbar \sum_{k,l} w_{iklj}(z, z') G_{lk}(z, z'^+) \,. \quad (60)$$

(the same expression is found starting from the second KBE, cf. Eqs. (48) and (57)) the Feynman diagrams of which are shown in Fig. 4. The first diagram corresponds to the so-called Hartree (mean-field) term, whereas the second accounts for exchange processes (Fock term).
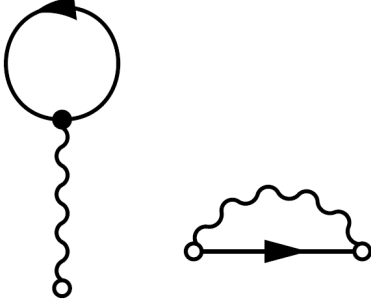
Fig. 4 Diagrammatic representation of the Hartree–Fock selfenergy, Eq. (60). Solid lines correspond to Green functions and wiggly lines to interactions. The empty dots represent the external time indices (z, z'), whereas the filled dots stand for intermediate time points $(\bar{z})$.

The Hartree–Fock approximation is widely used in many-body physics, however, it has been shown frequently (see e.g. Refs. [34,57,58]) that it severely differs from exact results and often fails to capture important qualitative features. This deviation is the manifestation of the omission of correlation effects, so it is necessary to search for a higher order truncation of the hierarchy equations.

2.4.2 The T-matrix. Derivation from the hierarchy

The natural generalization of the expression of the two-particle Green function beyond Hartree-Fock is given by

$$G_{i_1 i_2 j_1 j_2}^{(2)}(z_1, z_2, z'_1, z'_2) =: G_{i_1 i_2 j_1 j_2}^{(2),\mathrm{HF}}(z_1, z_2, z'_1, z'_2) + \Upsilon_{i_1 i_2 j_1 j_2}(z_1, z_2, z'_1, z'_2) \,, \quad (61)$$

which is exact if the two-particle correlation function Υ of $G^{(2)}$ contains the full hierarchy information. To derive an equation of motion for Υ, one has to evaluate

$$\sum_l \left[i\hbar \frac{\mathrm{d}}{\mathrm{d}z_1} \delta_{i_1,l} - h_{i_1 l}^{(0)}(z_1) \right] \Upsilon_{l i_2 j_1 j_2}(z_1, z_2, z'_1, z'_2)$$

$$= \sum_l \left[i\hbar \frac{\mathrm{d}}{\mathrm{d}z_1} \delta_{i_1,l} - h_{i_1 l}^{(0)}(z_1) \right] \left\{ G_{l i_2 j_1 j_2}^{(2)}(z_1, z_2, z'_1, z'_2) \right.$$

$$\left. - G_{l j_1}(z_1, z'_1) G_{i_2 j_2}(z_2, z'_2) \mp G_{l j_2}(z_1, z'_2) G_{i_2 j_1}(z_2, z'_1) \right\}$$

$$\overset{(49)}{\underset{(47)}{=}} \pm i\hbar \sum_{l,m,n} \int_{\mathcal{C}} \mathrm{d}\bar{z}\, w_{i_1 l m n}(z_1, \bar{z}) G_{m i_2 n j_1 j_2 l}^{(3)}(z_1, z_2, \bar{z}, z'_1, z'_2, \bar{z}^+) \quad (62)$$

$$\mp i\hbar G_{i_2 j_2}(z_2, z'_2) \sum_{l,m,n} \int_{\mathcal{C}} \mathrm{d}\bar{z}\, w_{i_1 l m n}(z_1, \bar{z}) G_{m n j_1 l}^{(2)}(z_1, \bar{z}, z'_1, \bar{z}^+)$$

$$- i\hbar G_{i_2 j_1}(z_2, z'_1) \sum_{l,m,n} \int_{\mathcal{C}} \mathrm{d}\bar{z}\, w_{i_1 l m n}(z_1, \bar{z}) G_{m n j_2 l}^{(2)}(z_1, \bar{z}, z'_2, \bar{z}^+) \,.$$

Still, all terms in Eq. (62) are of the same order in the interaction. Therefore, one evaluates

$$\sum_k \left[i\hbar \frac{\mathrm{d}}{\mathrm{d}z_2} \delta_{i_2,k} - h_{i_2 k}^{(0)}(z_2) \right] \sum_l \left[i\hbar \frac{\mathrm{d}}{\mathrm{d}z_1} \delta_{i_1,l} - h_{i_1 l}^{(0)}(z_1) \right] \Upsilon_{l k j_1 j_2}(z_1, z_2, z'_1, z'_2) \,, \quad (63)$$

instead. The added operator only acts on the three-particle Green function and on the single-particle Green functions. With the first and third hierarchy equations, Eq. (47) and Eq. (53), we obtain

$$
\sum_k \left[i\hbar \frac{d}{dz_2} \delta_{i_2,k} - h^{(0)}_{i_2 k}(z_2) \right] \sum_l \left[i\hbar \frac{d}{dz_1} \delta_{i_1,l} - h^{(0)}_{i_1 l}(z_1) \right] \Upsilon_{lkj_1 j_2}(z_1, z_2, z_1', z_2')
$$

$$
= i\hbar \sum_{m,n} w_{i_1 i_2 mn}(z_1, z_2) G^{(2)}_{mn j_1 j_2}(z_1, z_2, z_1', z_2')
$$

$$
+ (i\hbar)^2 \sum_{l,m,n,p,q,r} \int_{\mathcal{C}} dz\, d\bar{z}\, w_{i_1 lmn}(z_1.\bar{z}) w_{i_2 pqr}(z_2, \bar{\bar{z}}) \Bigg\{ G^{(4)}_{mqnr j_1 j_2 lp}(z_1, z_2, \bar{z}, \bar{\bar{z}}, z_1', z_2' \bar{z}^+, \bar{\bar{z}}^+)
$$

$$
- G^{(2)}_{mn j_1 l}(z_1, \bar{z}, z_1', \bar{z}^+) G^{(2)}_{qr j_2 p}(z_2, \bar{\bar{z}}, z_2', \bar{\bar{z}}^+) \mp G^{(2)}_{mn j_2 l}(z_1, \bar{z}, z_2', \bar{z}^+) G^{(2)}_{qr j_1 p}(z_2, \bar{\bar{z}}, z_1', \bar{\bar{z}}^+) \Bigg\}. \tag{64}
$$

In this equation, only one term is of first order in the interaction, while the other ones are of higher order. Thus, at this point, it is reasonable to use a higher order truncation of the hierarchy. Let $\Upsilon^{T^{(0)}}$ and $G^{(2),T^{(0)}}$ be an approximate correlation function and two-particle Green function obeying

$$
\sum_k \left[i\hbar \frac{d}{dz_2} \delta_{i_2,k} - h^{(0)}_{i_2 k}(z_2) \right] \sum_l \left[i\hbar \frac{d}{dz_1} \delta_{i_1,l} - h^{(0)}_{i_1 l}(z_1) \right] \Upsilon^{T^{(0)}}_{lk j_1 j_2}(z_1, z_2, z_1', z_2')
$$

$$
= i\hbar \sum_{m,n} w_{i_1 i_2 mn}(z_1, z_2) G^{(2),T^{(0)}}_{mn j_1 j_2}(z_1, z_2, z_1', z_2'), \tag{65}
$$

where the superscript $T^{(0)}$ denotes that this equation is related to the $T^{(0)}$-matrix approximation, see below. To find an expression for $G^{(2),T^{(0)}}$, we introduce the non-interacting Green function, $G_{ij,0}$ which obeys [cf. Eqs. (47) and (48)]

$$
\sum_l \left[i\hbar \frac{d}{dz} \delta_{i,l} - h^{(0)}_{il}(z) \right] G_{lj,0}(z, z') = \delta_{i,j} \delta_{\mathcal{C}}(z, z'), \tag{66}
$$

$$
\sum_l G_{il,0}(z, z') \left[-i\hbar \frac{\overleftarrow{d}}{dz'} \delta_{l,j} - h^{(0)}_{lj}(z') \right] = \delta_{i,j} \delta_{\mathcal{C}}(z, z'), \tag{67}
$$

and allows us to simplify expressions such as the left-hand side of Eq. (65). In detail, this is done for a reduced term in the following way,

$$
\sum_{l,m} \int_{\mathcal{C}} d\bar{z}\, G_{i_1 m,0}(z_1, \bar{z}) \left[i\hbar \frac{d}{d\bar{z}} \delta_{m,l} - h^{(0)}_{ml}(\bar{z}) \right] \Upsilon_{lk j_1 j_2}(\bar{z}, \bar{\bar{z}}, z_1', z_2')
$$

$$
= - \sum_{l,m} \int_{\mathcal{C}} d\bar{z}\, G_{i_1 m,0}(z_1, \bar{z}) h^{(0)}_{ml}(\bar{z}) \Upsilon_{lk j_1 j_2}(\bar{z}, \bar{\bar{z}}, z_1', z_2')
$$

$$
+ i\hbar \sum_l \int_{\mathcal{C}} d\bar{z}\, G_{i_1 l,0}(z_1, \bar{z}) \frac{d}{d\bar{z}} \Upsilon_{lk j_1 j_2}(\bar{z}, \bar{\bar{z}}, z_1', z_2')
$$

$$
\overset{(*)}{=} - \sum_{l,m} \int_{\mathcal{C}} d\bar{z}\, G_{i_1 m,0}(z_1, \bar{z}) h^{(0)}_{ml}(\bar{z}) \Upsilon_{lk j_1 j_2}(\bar{z}, \bar{\bar{z}}, z_1', z_2')
$$

$$
+ i\hbar \sum_l \left\{ \left[G_{i_1 l}(z_1, \bar{z}) \Upsilon_{lk j_1 j_2}(\bar{z}, \bar{\bar{z}}, z_1', z_2') \right]^{\bar{z}=z_e}_{\bar{z}=z_s} - \int_{\mathcal{C}} d\bar{z}\, G_{i_1 l}(z_1, \bar{z}) \frac{\overleftarrow{d}}{d\bar{z}} \Upsilon_{lk j_1 j_2}(\bar{z}, \bar{\bar{z}}, z_1', z_2') \right\}
$$

$$
\overset{(**)}{=} \sum_{l,m} \int_{\mathcal{C}} \mathrm{d}\bar{z}\, G_{i_1 m,0}(z_1, \bar{z}) \left[-\mathrm{i}\hbar \frac{\overset{\leftarrow}{\mathrm{d}}}{\mathrm{d}\bar{z}} \delta_{m,l} - h_{ml}^{(0)}(\bar{z}) \right] \Upsilon_{lkj_1 j_2}(\bar{z}, \bar{\bar{z}}, z_1', z_2')
$$

$$
\overset{(***)}{=} \sum_{l} \int_{\mathcal{C}} \mathrm{d}\bar{z}\, \delta_{i_1,l} \delta_{\mathcal{C}}(z_1, \bar{z}) \Upsilon_{lkj_1 j_2}(\bar{z}, \bar{\bar{z}}, z_1', z_2') = \Upsilon_{i_1 k j_1 j_2}(z_1, \bar{z}, z_1', z_2'),
$$

(68)

where $(*)$ follows from partial integration, $(**)$ holds since the integrated term vanishes due to the KMS relations Eq. (46), and $(***)$ is obtained from Eq. (67). Similarly, one arrives at

$$
\sum_{k,l,m,n} \int_{\mathcal{C}} \mathrm{d}\bar{z}\mathrm{d}\bar{\bar{z}}\, G_{i_1 m,0}(z_1, \bar{z}) G_{i_2 n,0}(z_2, \bar{\bar{z}})
$$

$$
\left[\mathrm{i}\hbar \frac{\mathrm{d}}{\mathrm{d}\bar{\bar{z}}} \delta_{n,k} - h_{nk}^{(0)}(\bar{\bar{z}}) \right] \left[\mathrm{i}\hbar \frac{\mathrm{d}}{\mathrm{d}\bar{z}} \delta_{m,l} - h_{ml}^{(0)}(\bar{z}) \right] \Upsilon_{lkj_1 j_2}^{T^{(0)}}(\bar{z}, \bar{\bar{z}}, z_1', z_2')
$$

$$
= \Upsilon_{i_1 i_2 j_1 j_2}^{T^{(0)}}(z_2, z_2, z_1', z_2').
$$

(69)

Combining Eqs. (65) and (69) leads to the integral expression for $\Upsilon^{T^{(0)}}$,

$$
\Upsilon_{i_1 i_2 j_1 j_2}^{T^{(0)}}(z_2, z_2, z_1', z_2') =
$$

$$
\mathrm{i}\hbar \sum_{k,l,m,n} \int_{\mathcal{C}} \mathrm{d}\bar{z}\mathrm{d}\bar{\bar{z}}\, G_{i_1 k,0}(z_1, \bar{z}) G_{i_2 l,0}(z_2, \bar{\bar{z}}) w_{klmn}(\bar{z}, \bar{\bar{z}}) G_{mnj_1 j_2}^{(2),T^{(0)}}(\bar{z}, \bar{\bar{z}}, z_1', z_2').
$$

(70)

By inserting back the two-particle Green function of Eq. (61), one finds an expression for $G^{(2),T^{(0)}}$,

$$
G_{i_1 i_2 j_1 j_2}^{(2),T^{(0)}}(z_1, z_2, z_1', z_2') = G_{i_1 i_2 j_1 j_2}^{(2),\mathrm{HF}}(z_1, z_2, z_1', z_2')
$$

$$
+ \mathrm{i}\hbar \sum_{k,l,m,n} \int_{\mathcal{C}} \mathrm{d}\bar{z}\mathrm{d}\bar{\bar{z}}\, G_{i_1 k,0}(z_1, \bar{z}) G_{i_2 l,0}(z_2, \bar{\bar{z}}) w_{klmn}(\bar{z}, \bar{\bar{z}}) G_{mnj_1 j_2}^{(2),T^{(0)}}(\bar{z}, \bar{\bar{z}}, z_1', z_2').
$$

(71)

Eq. (71) is the two-particle equivalent to the Born series of nonequilibrium many-body theory. It is formally equivalent to the Bethe–Salpeter equation in the particle-particle channel [52],

$$
G_{i_1 i_2 j_1 j_2}^{(2)}(z_1, z_2, z_1', z_2') = G_{i_1 i_2 j_1 j_2}^{(2),\mathrm{HF}}(z_1, z_2, z_1', z_2')
$$

(72)

$$
+ \sum_{k,l,m,n} \int_{\mathcal{C}} \mathrm{d}\bar{z}_1 \mathrm{d}\bar{z}_2 \mathrm{d}\bar{z}_3 \mathrm{d}\bar{z}_4\, G_{i_1 k}(z_1, \bar{z}_1) G_{i_2 l}(z_2, \bar{z}_2) \mathcal{K}_{klmn}(\bar{z}_1, \bar{z}_2, \bar{z}_3, \bar{z}_4) G_{mnj_1 j_2}^{(2)}(\bar{z}_3, \bar{z}_4, z_1', z_2').
$$

Here, $\mathcal{K}$ is an integration kernel which sums up all irreducible diagrams in the particle-particle channel. Eq. (71) results from Eq. (72) by inserting

$$
\mathcal{K}_{i_1 i_2 j_1 j_2}(z_1 z_2, z_1' z_2') = \mathrm{i}\hbar w_{i_1 i_2 j_1 j_2}(z_1, z_2) \delta_{\mathcal{C}}(z_1, z_1') \delta_{\mathcal{C}}(z_2, z_2'),
$$

(73)

except for the single-particle Green functions which are non-interacting in Eq. (71). The particle-particle channel can be understood as the restriction to processes where two particles are created and removed simultaneously. The opposite extreme is the particle-hole channel, in which creation and annihilation of single particles occur simultaneously, i.e. a particle and a hole have a coinciding lifetime. It should be mentioned that the particle-particle channel is no additional restriction in the present derivation, since Eq. (71) naturally follows from the truncation of the hierarchy. The particle-hole channel and the associated T-matrix are not discussed in this paper, see e.g. Ref. [59].

Returning to Eq. (71), we define the two-particle Green function in a slightly different way[4],

$$
G_{i_1 i_2 j_1 j_2}^{(2),T}(z_1, z_2, z_1', z_2') := G_{i_1 i_2 j_1 j_2}^{(2),\mathrm{HF}}(z_1, z_2, z_1', z_2')
$$

(74)

$$
+ \mathrm{i}\hbar \sum_{k,l,m,n} \int_{\mathcal{C}} \mathrm{d}\bar{z}\mathrm{d}\bar{\bar{z}}\, G_{i_1 k}(z_1, \bar{z}) G_{i_2 l}(z_2, \bar{\bar{z}}) w_{klmn}(\bar{z}, \bar{\bar{z}}) G_{mnj_1 j_2}^{(2),T}(\bar{z}, \bar{\bar{z}}, z_1', z_2'),
$$

---

[4] In general, an approximate two-particle Green function provides a conserving scheme, if the corresponding Green function fulfills both KBE and obeys the symmetry $G_{ijkl}^{(2)}(t_1, t_2, t_3, t_4) = G_{jilk}^{(2)}(t_2, t_1, t_4, t_3)$ [56]. In the present case, both conditions are fulfilled by construction.

Contrib. Plasma Phys. **56**, No. 1 (2016) / www.cpp-journal.org

21

where the noninteracting Green functions have been replaced by interacting ones. A closer look at Eq. (74) reveals that the recursive structure of the two-particle Green function can be transferred to an auxiliary quantity, T

$$G^{(2),T}_{i_1 i_2 j_1 j_2}(z_1, z_2, z_1', z_2') =: G^{(2),\text{HF}}_{i_1 i_2 j_1 j_2}(z_1, z_2, z_1', z_2') \tag{75}$$

$$\pm i\hbar \sum_{k,l,m,n} \int_{\mathcal{C}} d\bar{z}_1 d\bar{z}_2 d\bar{z}_3 d\bar{z}_4 \, G_{i_1 k}(z_1, \bar{z}_1) G_{i_2 l}(z_2, \bar{z}_2) T_{klmn}(\bar{z}_1, \bar{z}_2, \bar{z}_3, \bar{z}_4) G^{(2),\text{HF}}_{mn j_1 j_2}(\bar{z}_3, \bar{z}_4, z_1', z_2'),$$

the T-matrix in the particle-particle channel. Insertion of Eq. (75) into Eq. (74) leads to

$$G^{(2),T}_{i_1 i_2 j_1 j_2}(z_1, z_2, z_1', z_2') = G^{(2),\text{HF}}_{i_1 i_2 j_1 j_2}(z_1, z_2, z_1', z_2') \tag{76}$$

$$+ i\hbar \sum_{k,l,m,n} \int_{\mathcal{C}} d\bar{z}_1 d\bar{z}_2 \, G_{i_1 k}(z_1 \bar{z}_1) G_{i_2 l}(z_2, \bar{z}_2) w_{klmn}(\bar{z}_1, \bar{z}_2) G^{(2),\text{HF}}_{mn j_1 j_2}(\bar{z}_1 \bar{z}_2, z_1' z_2')$$

$$\pm (i\hbar)^2 \sum_{k,l,m,n,p,q,r,s} \int_{\mathcal{C}} d\bar{z}_1 d\bar{z}_2 d\bar{z}_3 d\bar{z}_4 d\bar{z}_5 d\bar{z}_6 \, G_{i_1 k}(z_1 \bar{z}_1) G_{i_2 l}(z_2, \bar{z}_2) w_{klmn}(\bar{z}_1, \bar{z}_2)$$

$$G_{mp}(\bar{z}_1, \bar{z}_3) G_{nq}(\bar{z}_2, \bar{z}_4) T_{pqrs}(\bar{z}_3 \bar{z}_4, \bar{z}_5 \bar{z}_6) G^{(2),\text{HF}}_{rs j_1 j_2}(\bar{z}_5 \bar{z}_6, z_1' z_2').$$

Finally, comparing with Eq. (75), we identify an expression for the T-matrix,

$$T_{ijkl}(z_1 z_2, z_3 z_4) = \pm w_{ijkl}(z_1, z_2) \delta_{\mathcal{C}}(z_1, z_3) \delta_{\mathcal{C}}(z_2, z_4) \tag{77}$$

$$+ i\hbar \sum_{m,n,p,q} \int_{\mathcal{C}} d\bar{z}_1 d\bar{z}_2 \, w_{ijmn}(z_1, z_2) G_{mp}(z_1, \bar{z}_1) G_{nq}(z_2, \bar{z}_2) T_{pqkl}(\bar{z}_1, \bar{z}_2, z_3, z_4).$$

In a similar manner, one finds that, in the case of the noninteracting Green functions, Eq. (71) and the equivalent to Eq. (75) are fulfilled by

$$T^{(0)}_{ijkl}(z_1 z_2, z_3 z_4) = \pm w_{ijkl}(z_1, z_2) \delta_{\mathcal{C}}(z_1, z_3) \delta_{\mathcal{C}}(z_2, z_4) \tag{78}$$

$$+ i\hbar \sum_{m,n,p,q} \int_{\mathcal{C}} d\bar{z}_1 d\bar{z}_2 \, w_{ijmn}(z_1, z_2) G_{mp,0}(z_1, \bar{z}_1) G_{nq,0}(z_2, \bar{z}_2) T^{(0)}_{pqkl}(\bar{z}_1, \bar{z}_2, z_3, z_4),$$

which is the origin of the naming in Eq. (65).

The name T-matrix originates from scattering theory. A two-particle scattering state of energy E and the relative momentum operator $\hat{p}$ with the eigenvalue $\boldsymbol{k}$ is described by the Lippmann–Schwinger equation [44],

$$|\psi\rangle = |\boldsymbol{k}\rangle + \frac{1}{E - \hat{\boldsymbol{p}}^2/m \pm i\eta} v(\hat{\boldsymbol{r}}) |\psi\rangle, \tag{79}$$

with $m = m_1 = m_2$ being the mass of the particles and η an infinitesimally small parameter. The $v(\hat{\boldsymbol{r}})$ denotes the interaction, evaluated at the relative spatial coordinate $\hat{\boldsymbol{r}}$. This equation is formally equivalent to Eq. (74). The problem is usually solved by introducing the so-called transfer matrix $\hat{T}$ (T-operator) in the following way,

$$|\psi\rangle = |\boldsymbol{k}\rangle + \frac{1}{E - \hat{\boldsymbol{p}}^2/m \pm i\eta} \hat{T} |\boldsymbol{k}\rangle. \tag{80}$$

This equation corresponds to Eq. (75) where $\hat{T}$ obeys

$$\hat{T} = v(\hat{\boldsymbol{r}}) + \hat{T} \frac{1}{E - \hat{\boldsymbol{p}}^2/m \pm i\eta} v(\hat{\boldsymbol{r}}), \tag{81}$$

which is similar to Eq. (77). $\hat{T}$ is called transfer matrix, because it transforms the free scattering-state $|\boldsymbol{k}\rangle$ into the interacting scattering-state $|\psi\rangle$,

$$\hat{T} |\boldsymbol{k}\rangle = v(\hat{\boldsymbol{r}}) |\psi\rangle. \tag{82}$$

Aside from this close analogy, there are qualitative differences. In contrast to scattering theory which considers an isolated pair of two particles the present theory is far more general. First, in the present case our particles are

not necessarily in a pure state. We allow for mixed states which is captured by the involved density matrix and the Green functions derived from it. Second, we consider a many-particle system where the scattering process of two particles is substantially influenced by the surrounding particles. The latter may modify the effective interaction of the pair and, furthermore, limit the available space of scattering states, e.g. by Pauli blocking. Third, the present theory allows for arbitrary non-equilibrium situations given, e.g., by time-dependent fields. Therefore, also the scattering process may change in time. All these effects are captured by the NEGF and their associated equations of motion. For a more detailed discussion see e.g. Refs. [60–63].

2.4.3   The T-matrix selfenergy

The selfenergy in T-matrix approximation is obtained by inserting the two-particle Green function of Eq. (75) into the selfenergy definition, Eq. (54), while the Hartree–Fock part is already solved by Σ^{HF}, so we define $\Sigma_{ij}(z, z') =: \Sigma_{ij}^{\mathrm{HF}}(z, z') + \Sigma_{ij}^{T}(z, z')$ and consider only the remaining part, in the following. After relabeling of indices, we arrive at

$$\sum_k \int_{\mathcal{C}} \mathrm{d}\bar{z} \; \Sigma_{ik}^{T}(z, \bar{z}) G_{kj}(\bar{z}, z') = \tag{83}$$

$$(\mathrm{i}\hbar)^2 \sum_{k,l,m,n,p,q,r} \int_{\mathcal{C}} \mathrm{d}\bar{z}\mathrm{d}\bar{z}_1\mathrm{d}\bar{z}_2\mathrm{d}\bar{z}_3\mathrm{d}\bar{z}_4 \, w_{ilmn}(z, \bar{z}_3) G_{mp}(z, \bar{z}_1) G_{nq}(\bar{z}_3, \bar{z}_2)$$

$$\left[T_{pqkr}(\bar{z}_1, \bar{z}_2, \bar{z}, \bar{z}_4) \pm T_{pqrk}(\bar{z}_1, \bar{z}_2, \bar{z}_4, \bar{z}) \right] G_{rl}(\bar{z}_4, \bar{z}_3) G_{kj}(\bar{z}, z') \, ,$$

which implicitly defines

$$\Sigma_{ik}^{T}(z, \bar{z}) \;\; = \;\; (\mathrm{i}\hbar)^2 \sum_{l,m,n,p,q,r} \int_{\mathcal{C}} \mathrm{d}\bar{z}_1\mathrm{d}\bar{z}_2\mathrm{d}\bar{z}_3\mathrm{d}\bar{z}_4 \, w_{ilmn}(z, \bar{z}_3) G_{mp}(z, \bar{z}_1) G_{nq}(\bar{z}_3, \bar{z}_2)$$

$$\left[T_{pqkr}(\bar{z}_1, \bar{z}_2, \bar{z}, \bar{z}_4) \pm T_{pqrk}(\bar{z}_1, \bar{z}_2, \bar{z}_4, \bar{z}) \right] G_{rl}(\bar{z}_4, \bar{z}_3) \, . \tag{84}$$

At this point, the T-matrix and the corresponding selfenergy are well-defined. However, it is convenient to simplify the expressions. To avoid singularities [64, 65] such as the one in Eq. (77), we define

$$\widetilde{T}_{ijkl}(z_1, z_2, z_3, z_4) := T_{ijkl}(z_1, z_2, z_3, z_4) \mp w_{ijkl}(z_1, z_2)\delta_{\mathcal{C}}(z_1, z_3)\delta_{\mathcal{C}}(z_2, z_4)$$

$$= \mathrm{i}\hbar \sum_{m,n,p,q} \int_{\mathcal{C}} \mathrm{d}\bar{z}_1\mathrm{d}\bar{z}_2 \, w_{ijmn}(z_1, z_2) G_{mp}(z_1, \bar{z}_1) G_{nq}(z_2, \bar{z}_2)$$

$$\left[\widetilde{T}_{pqkl}(\bar{z}_1, \bar{z}_2, z_3, z_4) \pm w_{pqkl}(\bar{z}_1, \bar{z}_2)\delta_{\mathcal{C}}(\bar{z}_1, z_3)\delta_{\mathcal{C}}(\bar{z}_2, z_4) \right]$$

$$= \pm \mathrm{i}\hbar \sum_{m,n,p,k} w_{ijmn}(z_1, z_2) G_{mp}(z_1, z_3) G_{nq}(z_2, z_4) w_{pqkl}(z_3, z_4) \tag{85}$$

$$+ \mathrm{i}\hbar \sum_{m,n,p,q} \int_{\mathcal{C}} \mathrm{d}\bar{z}_1\mathrm{d}\bar{z}_2 \, w_{ijmn}(z_1, z_2) G_{mp}(z_1, \bar{z}_1) G_{nq}(z_2, \bar{z}_2)$$

$$\widetilde{T}_{pqkl}(\bar{z}_1, \bar{z}_2, z_3, z_4) \, .$$

Further, the selfenergy, Eq. (84), suggests to introduce the (anti-)symmetrized T-matrix,

$$\widetilde{T}_{ijkl}^{\pm}(z_1, z_2, z_3, z_4) := \widetilde{T}_{ijkl}(z_1, z_2, z_3, z_4) \pm \widetilde{T}_{ijlk}(z_1, z_2, z_4, z_3)$$

$$= \pm \mathrm{i}\hbar \sum_{m,n,p,q} w_{ijmn}(z_1, z_2) G_{mp}(z_1, z_3) G_{nq}(z_2, z_4) w_{pqkl}(z_3, z_4)$$

$$+ \mathrm{i}\hbar \sum_{m,n,p,q} w_{ijmn}(z_1, z_2) G_{mp}(z_1, z_4) G_{nq}(z_2, z_3) w_{pqlk}(z_4, z_3) \tag{86}$$

$$+ \mathrm{i}\hbar \sum_{m,n,p,q} \int_{\mathcal{C}} \mathrm{d}\bar{z}_1\mathrm{d}\bar{z}_2 \, w_{ijmn}(z_1, z_2) G_{mp}(z_1, \bar{z}_1) G_{nq}(z_2, \bar{z}_2)$$

$$\widetilde{T}_{pqkl}^{\pm}(\bar{z}_1, \bar{z}_2, z_3, z_4) \, ,$$

and replace the original T-matrix in Eq. (84),

$$
\begin{aligned}
\Sigma_{ik}^{T}(z,\bar{z}) &= (\mathrm{i}\hbar)^2 \sum_{l,m,n,p,q,r} \int_{\mathcal{C}} \mathrm{d}\bar{z}_1 \mathrm{d}\bar{z}_2 \mathrm{d}\bar{z}_3 \mathrm{d}\bar{z}_4 \, w_{ilmn}(z,\bar{z}_3) G_{mp}(z,\bar{z}_1) G_{nq}(\bar{z}_3,\bar{z}_2) \\
&\quad \Big[\widetilde{T}_{pqkr}(\bar{z}_1,\bar{z}_2,\bar{z},\bar{z}_4) \pm w_{pqkr}(\bar{z}_1,\bar{z}_2)\delta_{\mathcal{C}}(\bar{z}_1,\bar{z})\delta_{\mathcal{C}}(\bar{z}_2,\bar{z}_4) \\
&\quad \pm \widetilde{T}_{pqrk}(\bar{z}_1,\bar{z}_2,\bar{z}_4,\bar{z}) + w_{pqrk}(\bar{z}_1,\bar{z}_2)\delta_{\mathcal{C}}(\bar{z}_1,\bar{z}_4)\delta_{\mathcal{C}}(\bar{z}_2,\bar{z}) \Big] G_{rl}(\bar{z}_4,\bar{z}_3) . \\
&= \pm (\mathrm{i}\hbar)^2 \sum_{l,m,n,p,q,r} \int_{\mathcal{C}} \mathrm{d}\bar{z}_1 \mathrm{d}\bar{z}_2 \, w_{ilmn}(z,\bar{z}_1) G_{mp}(z,\bar{z}) G_{nq}(\bar{z}_1,\bar{z}_2) w_{pqkr}(\bar{z},\bar{z}_2) G_{rl}(\bar{z}_2,\bar{z}_1) \\
&\quad + (\mathrm{i}\hbar)^2 \sum_{l,m,n,p,q,r} \int_{\mathcal{C}} \mathrm{d}\bar{z}_1 \mathrm{d}\bar{z}_2 \, w_{ilmn}(z,\bar{z}_1) G_{mp}(z,\bar{z}_2) G_{nq}(\bar{z}_1,\bar{z}) w_{pqrk}(\bar{z}_2,\bar{z}) G_{rl}(\bar{z}_2,\bar{z}_1) \\
&\quad + (\mathrm{i}\hbar)^2 \sum_{l,m,n,p,q,r} \int_{\mathcal{C}} \mathrm{d}\bar{z}_1 \mathrm{d}\bar{z}_2 \mathrm{d}\bar{z}_3 \mathrm{d}\bar{z}_4 \, w_{ilmn}(z,\bar{z}_1) G_{mp}(z,\bar{z}_3) G_{nq}(\bar{z}_1,\bar{z}_4) \\
&\qquad\qquad\qquad\qquad \widetilde{T}_{pqkr}^{\pm}(\bar{z}_3,\bar{z}_4,\bar{z},\bar{z}_2) G_{rl}(\bar{z}_2,\bar{z}_1) .
\end{aligned}
\tag{87}
$$

Comparison with Eq. (86), reveals that the selfenergy simplifies to

$$
\Sigma_{ik}^{T}(z,\bar{z}) \;\; = \;\; \mathrm{i}\hbar \sum_{m,n} \int_{\mathcal{C}} \mathrm{d}\bar{z}_1 \mathrm{d}\bar{z}_2 \, \widetilde{T}_{imkn}^{\pm}(z,\bar{z}_1,\bar{z},\bar{z}_2) G_{nm}(\bar{z}_2,\bar{z}_1) .
\tag{88}
$$

Eqs. (86) and (88) provide an iterative scheme to construct the selfenergy in terms of the T-matrix up to arbitrary order which is visualized by Feynman diagrams in Fig. 5. As one can see, there are two types of diagrams – direct ones (first and third) and exchange diagrams (second and fourth). The diagrams illustrate that the T-matrix includes scattering processes of infinite order.
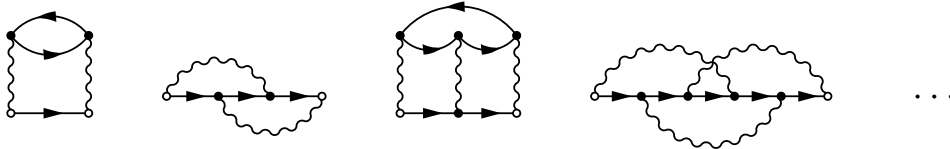
Fig. 5 Diagrammatic representation of the selfenergy in T-matrix approximation: the diagrams which are generated by Eqs. (86) and (88) are shown up to the third order in the interaction (cf. Fig. 4).

The first two lines in Eq. (87) (first two diagrams in Fig. 5) are referred to as second order Born approximation which treat pair interactions up to the second order. This approximation is appropriate for weak to moderate coupling as will be confirmed below.

2.5   The real-time components of contour quantities

In order to map contour quantities[5] onto a scheme which is accessible to numerical calculations, it is useful to introduce the real-time components of two-time contour quantities such as G and Σ. This procedure does not depend on the particular choice of $\mathcal{C}$, because both $\mathcal{C}_{\mathrm{AS}}$ and $\mathcal{C}_{\mathrm{id}}$ lead to the same ordering of contour times (cf. Figs. 2 and 3). It can also be seen that $\widetilde{T}^{\pm}$ in Eq. (86) is a two-time contour quantity, by replacing the interaction

---

[5] The term "contour quantity" is used, if a quantity obeys the Eqs. (101) and (104), or the corresponding equivalent for its tensor rank. This is not true for arbitrary quantities but holds for the T-matrix by construction.

with its definition in Eq. (42),

$$
\begin{aligned}
\widetilde{T}^{\pm}_{ijkl}(z_1, z_2, z_3, z_4) = &\pm i\hbar\delta_{\mathcal{C}}(z_1, z_2)\delta_{\mathcal{C}}(z_3, z_4) \sum_{m,n,p,q} W_{ijmn}(z_1)G_{mp}(z_1, z_3)G_{nq}(z_2, z_4)W_{pqkl}(z_3) \\
&+ i\hbar\delta_{\mathcal{C}}(z_1, z_2)\delta_{\mathcal{C}}(z_4, z_3) \sum_{m,n,p,q} W_{ijmn}(z_1)G_{mp}(z_1, z_4)G_{nq}(z_2, z_3)W_{pqlk}(z_4) \\
&+ i\hbar\delta_{\mathcal{C}}(z_1, z_2) \sum_{m,n,p,q} \int_{\mathcal{C}} d\bar{z}_1 d\bar{z}_2\, W_{ijmn}(z_1)G_{mp}(z_1, \bar{z}_1)G_{nq}(z_2, \bar{z}_2)\widetilde{T}^{\pm}_{pqkl}(\bar{z}_1, \bar{z}_2, z_3, z_4).
\end{aligned}
\tag{89}
$$

In this form, one can easily check that in each iteration of $\widetilde{T}^{\pm}$ also the last two time arguments of the T-matrix become equal, so it is convenient to define the two-time T-matrix,

$$
\widetilde{T}^{\pm}_{ijkl}(z_1, z_2, z_3, z_4) =: \delta_{\mathcal{C}}(z_1, z_2)\delta_{\mathcal{C}}(z_3, z_4)T_{ijkl}(z_1, z_3),
\tag{90}
$$

which obeys

$$
\begin{aligned}
T_{ijkl}(z, z') = &\pm i\hbar \sum_{m,n,p,q} W_{ijmn}(z)G^{\mathrm{H}}_{mnpq}(z, z')W_{pqkl}(z') \\
&+ i\hbar \sum_{m,n,p,q} W_{ijmn}(z)G^{\mathrm{H}}_{mnpq}(z, z')W_{pqlk}(z') \\
&+ i\hbar \sum_{m,n,p,q} \int_{\mathcal{C}} d\bar{z}\, W_{ijmn}(z)G^{\mathrm{H}}_{mnpq}(z, \bar{z})T_{pqkl}(\bar{z}, z'),
\end{aligned}
\tag{91}
$$

with the Hartree-type two-particle Green function $G^{\mathrm{H}}_{ijkl}(z, z') := G_{ik}(z, z')G_{jl}(z, z')$. In this notation, the selfenergy of Eq. (88) can be written as a simple matrix multiplication,

$$
\Sigma^T_{ij}(z, z') = i\hbar \sum_{k,l} T_{ikjl}(z, z')G_{lk}(z', z).
\tag{92}
$$

On the time contour, there are four different ways to order two time arguments, which is shown in Fig. 6.
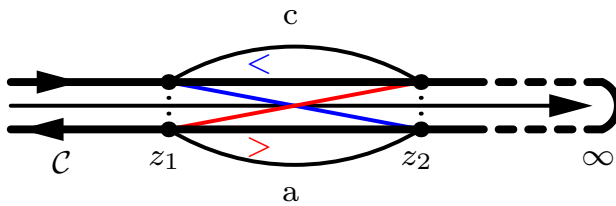
Fig. 6 Illustration of the time ordering on the contour: Two time arguments can either be both placed on the same branch, which leads to causal component (indicated with "c") and the anticausal component (indicated with "a"), or they lie on different branches, which results in the greater component (red), if z_1 (z_2) is on the anticausal (causal) branch, and in the less component (blue) otherwise.

This suggests to represent a two-time contour quantity by its four corresponding real-time components that can be combined into a matrix. Using, as an example, the Green function,

$$
\boldsymbol{G_{ij}}(t_1, t_2) = \begin{pmatrix} G^{\mathrm{c}}_{ij}(t_1, t_2) & G^{<}_{ij}(t_1, t_2) \\ G^{>}_{ij}(t_1, t_2) & G^{\mathrm{a}}_{ij}(t_1, t_2) \end{pmatrix}.
\tag{93}
$$

Here, the components are defined in the following way[6],

$$G_{ij}^{c}(t_1, t_2) = \frac{1}{i\hbar} \left\langle \mathcal{T} \left\{ \hat{c}_i(t_1) \hat{c}_j^\dagger(t_2) \right\} \right\rangle, \tag{94}$$

$$G_{ij}^{<}(t_1, t_2) = \pm \frac{1}{i\hbar} \left\langle \hat{c}_j^\dagger(t_2) \hat{c}_i(t_1) \right\rangle, \tag{95}$$

$$G_{ij}^{>}(t_1, t_2) = \frac{1}{i\hbar} \left\langle \hat{c}_i(t_1) \hat{c}_j^\dagger(t_2) \right\rangle, \tag{96}$$

$$G_{ij}^{a}(t_1, t_2) = \frac{1}{i\hbar} \left\langle \bar{\mathcal{T}} \left\{ \hat{c}_i(t_1) \hat{c}_j^\dagger(t_2) \right\} \right\rangle. \tag{97}$$

Of this set only two components are independent, in non-equilibrium [66]. In this work, the following set of three components is used, as it was suggested in Ref. [67] resulting in the Green function matrix[7],

$$\boldsymbol{G_{ij}}(t_1, t_2) = \begin{pmatrix} G_{ij}^{R}(t_1, t_2) & G_{ij}^{<}(t_1, t_2) \\ 0 & G_{ij}^{A}(t_1, t_2) \end{pmatrix}, \tag{98}$$

with $G_{ij}^{R}(t_1, t_2)$ and $G_{ij}^{A}(t_1, t_2)$ being the retarded and advanced Green functions, which obey

$$\begin{aligned} G_{ij}^{R}(t_1, t_2) &:= G_{ij}^{c}(t_1, t_2) - G_{ij}^{<}(t_1, t_2) = G_{ij}^{>}(t_1, t_2) - G_{ij}^{a}(t_1, t_2) \\ G_{ij}^{A}(t_1, t_2) &:= G_{ij}^{c}(t_1, t_2) - G_{ij}^{>}(t_1, t_2) = G_{ij}^{<}(t_1, t_2) - G_{ij}^{a}(t_1, t_2). \end{aligned} \tag{99}$$

These components can be expressed in a more compact way [44],

$$G_{ij}^{R/A}(t_1, t_2) = G_{ij}^{\delta}(t_1)\delta(t_1, t_2) + \Theta(t_{1/2}, t_{2/1}) \left(G_{ij}^{\gtrless}(t_1, t_2) - G_{ij}^{\lessgtr}(t_1, t_2) \right), \tag{100}$$

where Θ is the Heaviside step function with $\Theta(t_1, t_2) = 1$, if $t_1 > t_2$, and $\Theta(t_1, t_2) = 0$ otherwise, and δ denotes the Dirac distribution. G^{δ} is the time-diagonal contribution. Furthermore, the retarded and advanced components are connected via conjugation

$$G_{ij}^{R}(t_1, t_2) = \left[G_{ji}^{A}(t_2, t_1) \right]^*, \tag{101}$$

which accounts for the overcompleteness. Note that for the particular case of the Green function, the G^{δ} component vanishes [44].

For the case of two two-time contour quantities, $\boldsymbol{B}$ and $\boldsymbol{C}$, the matrix representation allows for a straightforward calculation of the components of their product,

$$\begin{pmatrix} B^{R} & B^{<} \\ 0 & B^{A} \end{pmatrix} \cdot \begin{pmatrix} C^{R} & C^{<} \\ 0 & C^{A} \end{pmatrix} = \begin{pmatrix} B^{R}C^{R} & B^{R}C^{<} + B^{<}C^{A} \\ 0 & B^{A}C^{A} \end{pmatrix}, \tag{102}$$

which are the so-called Langreth–Wilkins rules [67]. It should be noted that Eq. (102) is a symbolic notation. In detail, e.g. the less component transforms as follows[8],

$$\begin{aligned} \left\{ \sum_k \int_{\mathcal{C}} \mathrm{d}\bar{z}\, B_{ik}(z, \bar{z}) C_{kj}(\bar{z}, z') \right\}^{\gtrless} &= \sum_k \int_{t_s}^{\infty} \mathrm{d}\bar{t}\, B_{ik}^{R}(t, \bar{t}) C_{kj}^{\gtrless}(\bar{t}, t') \\ &+ \sum_k \int_{t_s}^{\infty} \mathrm{d}\bar{t}\, B_{ik}^{\gtrless}(t, \bar{t}) C_{kj}^{A}(\bar{t}, t'), \end{aligned} \tag{103}$$

for rank two tensors $\boldsymbol{B}$ and $\boldsymbol{C}$. The general structure for e.g. the T-matrix in Eq. (91) depends on the form of the initial product on the contour $\mathcal{C}$. The time t_s corresponds to the starting point z_s on $\mathcal{C}$. It is either equal to t_0 or,

---

[6] The average $\langle \cdot \rangle = \mathrm{Tr}\left(\hat{\rho}_{0/\mathrm{id}} \cdot \right)$ denotes the trace in the Fock space $\mathcal{F}$ (cf. Eq. (15)) with the respective density operator, corresponding to the choice of the contour $\mathcal{C}$.

[7] It can be obtained by doing a linear transformation of the form $\boldsymbol{G_{ij}} \mapsto \boldsymbol{M}\boldsymbol{\sigma_z}\boldsymbol{G_{ij}}\boldsymbol{M}^{-1}$ with $\boldsymbol{M} = \begin{pmatrix} 1 & 0 \\ 1 & 1 \end{pmatrix}$ and $\boldsymbol{\sigma_z} = \begin{pmatrix} 1 & 0 \\ 0 & -1 \end{pmatrix}$.

[8] The greater component also obeys Eq. (103). This is not derived here, but it can be found in an analogous consideration.

for the adiabatic switching case, in principle, equal to $-\infty$.

For all two-time contour quantities $\boldsymbol{B}$, the components obey the following relation [56],

$$B_{ij}^{\gtrless}(t_1, t_2) = -\left[B_{ji}^{\gtrless}(t_2, t_1)\right]^*, \tag{104}$$

for any two basis indices, whereas the Green functions obey, in addition,

$$n_{ij}(t) = \pm i\hbar G_{ij}^<(t, t^+), \tag{105}$$

$$G_{ij}^>(t, t) - G_{ij}^<(t, t) = \pm \frac{i}{\hbar}\delta_{i,j}, \tag{106}$$

with $n_{ij}(t)$ being the (i, j) density matrix element at time t, i.e. $n_{ij}(t) = \left\langle \hat{c}_j^\dagger(t)\hat{c}_i(t)\right\rangle$, which directly follows from the definitions in Eqs. (95) and (96).

2.6   Time propagation and the generalized Kadanoff–Baym ansatz

With the equations of motion Eqs. (56) and (57), the T-matrix of Eq. (91), the corresponding selfenergy, Eq. (92), (or another many-body approximation such as the second Born approximation) and the mapping of all quantities from the time contour onto real-time components, it is straightforward to calculate the interacting ground state of a quantum system and, subsequently, propagate it in time. In this paper, also a second time propagation method is discussed—the generalized Kadanoff–Baym ansatz (GKBA) that reduces the propagation to the time-diagonal part.

To understand the GKBA in detail, it is convenient to start with Eqs. (56) and (57) in real-time components. From Eq. (103), one gets

$$\sum_l \left[i\hbar\frac{d}{dt}\delta_{i,l} - h_{il}^{(0)}(t)\right]G_{lj}^{\gtrless}(t, t') = \sum_l \int_{t_s}^\infty d\bar{t}\left\{\Sigma_{il}^R(t, \bar{t})G_{lj}^{\gtrless}(\bar{t}, t') + \Sigma_{il}^{\gtrless}(t, \bar{t})G_{lj}^A(\bar{t}, t')\right\}, \tag{107}$$

$$\sum_l G_{il}^{\gtrless}(t, t')\left[-i\hbar\frac{\overleftarrow{d}}{dt'}\delta_{l,j} - h_{lj}^{(0)}(t')\right] = \sum_l \int_{t_s}^\infty d\bar{t}\left\{G_{il}^R(t, \bar{t})\Sigma_{lj}^{\gtrless}(\bar{t}, t') + G_{il}^{\gtrless}(t, \bar{t})\Sigma_{lj}^A(\bar{t}, t')\right\}. \tag{108}$$

Here, it is used that for the greater and less component the contour times $\{z, z'\}$ are located on different branches, i.e. $z \neq z'$. Thus, the time-diagonal part vanishes. For the retarded and advanced components, the equations become

$$\sum_l \left[i\hbar\frac{d}{dt}\delta_{i,l} - h_{il}^{(0)}(t)\right]G_{lj}^{R/A}(t, t') = \delta_{ij}\delta(t, t') + \sum_l \int_{t_s}^\infty d\bar{t}\,\Sigma_{il}^{R/A}(t, \bar{t})G_{lj}^{R/A}(\bar{t}, t') \tag{109}$$

and

$$\sum_l G_{il}^{R/A}(t, t')\left[-i\hbar\frac{\overleftarrow{d}}{dt'}\delta_{l,j} - h_{lj}^{(0)}(t')\right] = \delta_{ij}\delta(t, t') + \sum_l \int_{t_s}^\infty d\bar{t}\,G_{il}^{R/A}(t, \bar{t})\Sigma_{lj}^{R/A}(\bar{t}, t'). \tag{110}$$

In Eqs. (109) and (110), the time-diagonal part does not vanish. In order to isolate the time diagonal properties, one can define

$$\mathcal{R}_{ij}^{\gtrless}(t_1, t_2) := \widetilde{\Theta}(t_1, t_2)G_{ij}^{\gtrless}(t_1, t_2), \tag{111}$$

$$\mathcal{A}_{ij}^{\gtrless}(t_1, t_2) := -\widetilde{\Theta}(t_2, t_1)G_{ij}^{\gtrless}(t_1, t_2). \tag{112}$$

so that

$$G_{ij}^{\gtrless}(t_1, t_2) = \mathcal{R}_{ij}^{\gtrless}(t_1, t_2) - \mathcal{A}_{ij}^{\gtrless}(t_1, t_2). \tag{113}$$

The modified Heaviside function $\widetilde{\Theta}$ is defined in the way that $\widetilde{\Theta}(t_1, t_2) = 1$ if $t_1 \geq t_2$ and $\widetilde{\Theta}(t_1, t_2) = 0$ otherwise.

With these relations, it becomes possible to evaluate the following expression,

$$
\begin{aligned}
&\sum_k \int_{t_s}^\infty \mathrm{d}\bar{t}_1 \, G_{ik}^{\mathrm{R}}(t_1, \bar{t}_1) \Omega_{kj}(\bar{t}_1, t_2) \\
&:= \sum_{k,l} \int_{t_s}^\infty \mathrm{d}\bar{t}_1 \mathrm{d}\bar{t}_2 \, G_{ik}^{\mathrm{R}}(t_1, \bar{t}_1) \left\{ \delta(\bar{t}_1, \bar{t}_2) \left[i\hbar \frac{\mathrm{d}}{\mathrm{d}\bar{t}_2} \delta_{k,l} - h_{kl}^{(0)}(\bar{t}_2) \right] - \Sigma_{kl}^{\mathrm{R}}(\bar{t}_1, \bar{t}_2) \right\} \mathcal{R}_{lj}^{\gtrless}(\bar{t}_2, t_2) \quad (114) \\
&= \mathcal{R}_{ij}^{\gtrless}(t_1, t_2) \,.
\end{aligned}
$$

This can be seen in the same way as in Eq. (68) together with Eq. (110). The enclosed quantity Ω can be evaluated to

$$
\begin{aligned}
&\sum_l \int_{t_s}^\infty \mathrm{d}\bar{t}_2 \left\{ \delta(\bar{t}_1, \bar{t}_2) \left[i\hbar \frac{\mathrm{d}}{\mathrm{d}\bar{t}_2} \delta_{k,l} - h_{kl}^{(0)}(\bar{t}_2) \right] - \Sigma_{kl}^{\mathrm{R}}(\bar{t}_1, \bar{t}_2) \right\} \mathcal{R}_{lj}^{\gtrless}(\bar{t}_2, t_2) \\
&\stackrel{(*)}{=} \sum_l \int_{t_s}^\infty \mathrm{d}\bar{t}_2 \left\{ \delta(\bar{t}_1, \bar{t}_2) i\hbar \delta_{k,l} \left(\delta(\bar{t}_2, t_2) G_{lj}^{\gtrless}(\bar{t}_2, t_2) + \widetilde{\Theta}(\bar{t}_2, t_2) \frac{\mathrm{d}}{\mathrm{d}\bar{t}_2} G_{lj}^{\gtrless}(\bar{t}_2, t_2) \right) \right. \\
&\qquad \left. - \delta(\bar{t}, \bar{t}_2) h_{kl}^{(0)}(\bar{t}_2) \widetilde{\Theta}(\bar{t}_2, t_2) G_{lj}^{\gtrless}(\bar{t}_2, t_2) \right\} \\
&\quad - \sum_l \int_{t_s}^\infty \mathrm{d}\bar{t}_2 \, \widetilde{\Theta}(\bar{t}_2, t_2) \Sigma_{kl}^{\mathrm{R}}(\bar{t}_1, \bar{t}_2) G_{lj}^{\gtrless}(\bar{t}_2, t_2) \\
&\stackrel{(**)}{=} i\hbar \delta(\bar{t}_1, t_2) G_{kj}^{\gtrless}(\bar{t}_1, t_2) + \widetilde{\Theta}(\bar{t}_1, t_2) \sum_l \left[i\hbar \frac{\mathrm{d}}{\mathrm{d}\bar{t}_1} \delta_{k,l} - h_{kl}^{(0)}(\bar{t}_1) \right] G_{lj}^{\gtrless}(\bar{t}_1, t_2) \\
&\quad - \sum_l \int_{t_2}^{\bar{t}_1} \mathrm{d}\bar{t}_2 \, \Sigma_{kl}^{\mathrm{R}}(\bar{t}_1, \bar{t}_2) G_{lj}^{\gtrless}(\bar{t}_2, t_2) \qquad (115) \\
&\stackrel{(107)}{=} i\hbar \delta(\bar{t}_1, t_2) G_{kj}^{\gtrless}(\bar{t}_1, t_2) \\
&\quad + \widetilde{\Theta}(\bar{t}_1, t_2) \sum_l \int_{t_s}^\infty \mathrm{d}\bar{t}_2 \left\{ \Sigma_{kl}^{\mathrm{R}}(\bar{t}_1, \bar{t}_2) G_{lj}^{\gtrless}(\bar{t}_2, t_2) + \Sigma_{kl}^{\gtrless}(\bar{t}_1, \bar{t}_2) G_{lj}^{\mathrm{A}}(\bar{t}_2, t_2) \right\} \\
&\quad - \sum_l \int_{t_2}^{\bar{t}_1} \mathrm{d}\bar{t}_2 \, \Sigma_{kl}^{\mathrm{R}}(\bar{t}_1, \bar{t}_2) G_{lj}^{\gtrless}(\bar{t}_2, t_2) \\
&\stackrel{(***)}{=} i\hbar \delta(\bar{t}_1, t_2) G_{kj}^{\gtrless}(\bar{t}_1, t_2) + \widetilde{\Theta}(\bar{t}_1, t_2) \sum_l \int_{t_s}^{t_2} \mathrm{d}\bar{t}_2 \, \Sigma_{kl}^{\mathrm{R}}(\bar{t}_1, \bar{t}_2) G_{lj}^{\gtrless}(\bar{t}_2, t_2) \\
&\quad + \widetilde{\Theta}(\bar{t}_1, t_2) \sum_l \int_{t_s}^{t_2} \mathrm{d}\bar{t}_2 \, \Sigma_{kl}^{\gtrless}(\bar{t}_1, \bar{t}_2) G_{lj}^{\mathrm{A}}(\bar{t}_2, t_2) \,.
\end{aligned}
$$

In $(*)$, the definition in Eq. (111), the product rule and the relation $\frac{\mathrm{d}}{\mathrm{d}t} \widetilde{\Theta}(t, t') = \delta(t, t')$ are used. In $(**)$, the Dirac distributions are evaluated and the Heaviside functions of the last term cut the integration boundaries (cf. Eq. (100)). In $(***)$, again the Heaviside functions are evaluated and the mutual integration part cancels. Bringing

these results together with Eq. (114), one finds

$$
\begin{aligned}
\mathcal{R}_{ij}^{\gtrless}(t_1, t_2) \;=\; &\pm \sum_k G_{ik}^{\mathrm{R}}(t_1, t_2)\mathfrak{n}_{kj}^{\gtrless}(t_2) \\
&+ \sum_{k,l} \int_{t_2}^{t_1} \mathrm{d}\bar{t}_1 \int_{t_s}^{t_2} \mathrm{d}\bar{t}_2\, G_{ik}^{\mathrm{R}}(t_1, \bar{t}_1)\Sigma_{kl}^{\mathrm{R}}(\bar{t}_1, \bar{t}_2)G_{lj}^{\gtrless}(\bar{t}_2, t_2) \\
&+ \sum_{k,l} \int_{t_2}^{t_1} \mathrm{d}\bar{t}_1 \int_{t_s}^{t_2} \mathrm{d}\bar{t}_2\, G_{ik}^{\mathrm{R}}(t_1, \bar{t}_1)\Sigma_{k,l}^{\gtrless}(\bar{t}_1, \bar{t}_2)G_{lj}^{\mathrm{A}}(\bar{t}_2, t_2)\,.
\end{aligned}
\tag{116}
$$

In agreement with Eqs. (105) and (106), $\mathfrak{n}^{\gtrless}$ are defined as

$$
\mathfrak{n}_{ij}^{<}(t) = n_{ij}(t) \quad \text{and} \quad \mathfrak{n}_{ij}^{>}(t) = n_{ij}(t) - \delta_{i,j}\,.
\tag{117}
$$

Similarly, one finds for $\mathcal{A}^{<}$, in combination with the advanced component of the less Green function,

$$
\begin{aligned}
\mathcal{A}_{ij}^{\gtrless}(t_1, t_2) \;=\; &\pm \sum_k \mathfrak{n}_{ik}^{\gtrless}(t_1)G_{kj}^{\mathrm{A}}(t_1, t_2) \\
&- \sum_{k,l} \int_{t_s}^{t_1} \mathrm{d}\bar{t}_1 \int_{t_1}^{t_2} \mathrm{d}\bar{t}_2\, G_{ik}^{\gtrless}(t_1, \bar{t}_1)\Sigma_{kl}^{\mathrm{A}}(\bar{t}_1, \bar{t}_2)G_{lj}^{\mathrm{A}}(\bar{t}_2, t_2) \\
&- \sum_{k,l} \int_{t_s}^{t_1} \mathrm{d}\bar{t}_1 \int_{t_1}^{t_2} \mathrm{d}\bar{t}_2\, G_{ik}^{\mathrm{R}}(t_1, \bar{t}_1)\Sigma_{k,l}^{\gtrless}(\bar{t}_1, \bar{t}_2)G_{lj}^{\mathrm{A}}(\bar{t}_2, t_2)\,.
\end{aligned}
\tag{118}
$$

Finally, by applying Eq. (113), one obtains an expression for the less Green function that explicitly depends on the values on the time diagonal,

$$
\begin{aligned}
G_{ij}^{\gtrless}(t_1, t_2) \;=\; &\pm \sum_k \left[G_{ik}^{\mathrm{R}}(t_1, t_2)\mathfrak{n}_{kj}^{\gtrless}(t_2) - \mathfrak{n}_{ik}^{\gtrless}(t_1)G_{kj}^{\mathrm{A}}(t_1, t_2) \right] \\
&+ \sum_{k,l} \int_{t_2}^{t_1} \mathrm{d}\bar{t}_1 \int_{t_s}^{t_2} \mathrm{d}\bar{t}_2\, G_{ik}^{\mathrm{R}}(t_1, \bar{t}_1)\Sigma_{kl}^{\mathrm{R}}(\bar{t}_1, \bar{t}_2)G_{lj}^{\gtrless}(\bar{t}_2, t_2) \\
&+ \sum_{k,l} \int_{t_2}^{t_1} \mathrm{d}\bar{t}_1 \int_{t_s}^{t_2} \mathrm{d}\bar{t}_2\, G_{ik}^{\mathrm{R}}(t_1, \bar{t}_1)\Sigma_{k,l}^{\gtrless}(\bar{t}_1, \bar{t}_2)G_{lj}^{\mathrm{A}}(\bar{t}_2, t_2) \\
&+ \sum_{k,l} \int_{t_s}^{t_1} \mathrm{d}\bar{t}_1 \int_{t_1}^{t_2} \mathrm{d}\bar{t}_2\, G_{ik}^{\gtrless}(t_1, \bar{t}_1)\Sigma_{kl}^{\mathrm{A}}(\bar{t}_1, \bar{t}_2)G_{lj}^{\mathrm{A}}(\bar{t}_2, t_2) \\
&+ \sum_{k,l} \int_{t_s}^{t_1} \mathrm{d}\bar{t}_1 \int_{t_1}^{t_2} \mathrm{d}\bar{t}_2\, G_{ik}^{\mathrm{R}}(t_1, \bar{t}_1)\Sigma_{k,l}^{\gtrless}(\bar{t}_1, \bar{t}_2)G_{lj}^{\mathrm{A}}(\bar{t}_2, t_2)\,.
\end{aligned}
\tag{119}
$$

Neglect of the integral terms leads to the generalized Kadanoff–Baym ansatz (GKBA) [33],

$$
G_{ij}^{\gtrless}(t_1, t_2) \;\approx\; \pm \sum_k \left[G_{ik}^{\mathrm{R}}(t_1, t_2)\mathfrak{n}_{kj}^{\gtrless}(t_2) - \mathfrak{n}_{ik}^{\gtrless}(t_1)G_{kj}^{\mathrm{A}}(t_1, t_2) \right]\,.
\tag{120}
$$

By applying this equation, one is able to reconstruct the non-time-diagonal values of the Green function from the density matrix n of the system and the propagator functions $G^{\mathrm{R/A}}$. The GKBA obeys particle number conservation and exhibits an inherently causal structure. Furthermore, it is also a full nonequilibrium approach, as it has been shown in Ref. [68].

We underline that this result differs from the original Kadanoff–Baym ansatz which is exact in equilibrium [56,68]

$$
G_{ij}^{<}(t_1, t_2) \;\approx\; \pm \sum_k f_{ik}\left(\frac{t_1 + t_2}{2}\right)\left(G_{kj}^{\mathrm{R}}(t_1, t_2) - G_{kj}^{\mathrm{A}}(t_1, t_2)\right)\,,
\tag{121}
$$

with f being the Wigner distribution function. In systems far from equilibrium, this ansatz fails because f only depends on the "center-of-mass" time, which violates causality.

In order to use the GKBA, Eq. (120), to calculate the Green function one has to make a choice for the propagators $G^{R/A}$. Generally, these functions obey Eqs. (109) and (110), the solution of which is of the same complexity as the full propagation equation of $G^{\gtrless}$. To overcome this bottleneck, a further approximation is introduced. In this paper, the propagators are chosen to obey the KBE in Hartree–Fock approximation, Eq. (60), leading to the expressions,

$$
\begin{aligned}
G_{ij}^{\mathrm{HF,R}}(t_1, t_2) &= -\mathrm{i}\Theta(t_1, t_2) \left[\exp\left(-\frac{\mathrm{i}}{\hbar} \int_{t_2}^{t_1} \mathrm{d}\bar{t}\, h^{\mathrm{eff}}(\bar{t}) \right) \right]_{ij}, \\
G_{ij}^{\mathrm{HF,A}}(t_1, t_2) &= +\mathrm{i}\Theta(t_2, t_1) \left[\exp\left(-\frac{\mathrm{i}}{\hbar} \int_{t_2}^{t_1} \mathrm{d}\bar{t}\, h^{\mathrm{eff}}(\bar{t}) \right) \right]_{ij},
\end{aligned}
\tag{122}
$$

that depend on the effective Hartree–Fock Hamiltonian h^{eff} which, in turn, only depends on the time-dependent density matrix n[9]. Together with Eq. (120), the non-time-diagonal part of $G^{\gtrless}$ can now be reconstructed solely from n. Using the HF propagators the resulting KBE preserve total energy conservation if the selfenergy of the full two-time KBE was conserving, as was shown in Ref. [34].

To summarize the theoretical part of this paper, the main approximation in this work is the selfenergy of the Kadanoff–Baym equations, cf. Eqs. (56) and (57). In this paper the selfenergy is mainly evaluated in T-matrix approximation, Eqs. (91) and (92). While in most cases we will perform full two-time calculations, in some case, we will compare to the Hartree-Fock GKBA, Eq. (120) with Hartree–Fock propagators, Eq. (122).

3   Experiments with ultracold atoms in optical lattices

The main results of the present paper concern the dynamics of fermionic lattice systems. These are, by construction, model systems for solid state physics. However, the behaviour of quantum particles in lattices can also be directly observed in experiments which is the topic of ultracold atoms in optical lattices.

At very low temperatures, of the order of nanokelvin, atoms reveal their full quantum properties. When the atomic de-Broglie wavelength exceeds the interparticle distance, the quantum statistics govern the behaviour of the system. That is why the experiments in the field of ultracold atoms are of growing interest in the past 20 years [8, 12, 16]. Even so, the physics of ultracold atoms constitute a comparatively young research field. Due to the very challenging experimental realization, the breakthrough was not before 1995, when the observation of Bose–Einstein condensation in ultracold gases became possible [9–11]. The study of ultracold gases requires a trapping of the (neutral) atoms, which, in the early stage, was mainly achieved by magnetic traps. The main idea of such a trap, is to apply an inhomogeneous magnetic field to atoms that causes a splitting of the spectral lines due to the Zeeman effect. The shift in the energy actuates the *weak-field-seekers*[10] to drift toward the minima in the field. Since this affects only a small subset of the atoms, the use of the alternative optical dipole traps has soon become popular. The concept of optical traps is discussed in Sec. 3.1. With these traps, it became possible to generate lattice systems of ultracold atoms. Since then, a variety of experimental results for both bosonic and fermionic atoms in optical lattices has been published [5, 6, 13–15, 17]. The main advantage of this method is given by the large degree of control over the system. Today, one is able to manipulate the interaction strength between the particles [5,6] and the potential depth of the lattice sites [13,14,17]. Even inhomogeneous and time-dependent potentials on the lattice can be realized [5,6]. This is the reason why ultracold atoms in optical lattices are well suited to study transport and diffusion processes. In addition, the detection techniques have been steadily improving [8]. By reaching the single-site resolution [5], the accuracy of the observations became precise enough to allow for comparisons with theoretical predictions for lattice systems.

---

[9] There are also other choices for $G^{R/A}$. For instance, damped propagators have been tested in Refs. [43, 69] and it was shown that they violate total energy conservation. Recently, the authors of Ref. [35] presented propagators that are connected to the second order Born approximation.

[10] Atoms with total spin $\boldsymbol{S}$, so that the change in the energy $\Delta E_B = -g_{\mathrm{S}}\mu_{\mathrm{B}}\boldsymbol{S}\cdot\boldsymbol{B} < 0$ are called *weak-field-seekers* [18]. Here, g_{S} is the Landé g-factor, μ_{B} is the Bohr magneton and $\boldsymbol{B}$ is the magnetic field. This leads to an effective spatial potential, in which *weak-field-seekers* drift to minima of the field.

3.1   Realization of optical lattices

When the oscillating electric light field provided by a laser interacts with an atom, it induces an alternating dipole moment in it. At the same time, this dipole moment interacts with the electric field itself. This fact is used in the so-called optical dipole trap. The time-dependent electric field of a laser $\boldsymbol{E}(\boldsymbol{r}, t)$, in the presence of an atom, leads to the induced dipole moment [16]

$$d_i(t) = \sum_{j=x,y,z} \alpha_{ij}(\omega_{\mathrm{L}}) E_j(\boldsymbol{r}, t), \tag{123}$$

following the oscillations of the laser field. Here, ω_{L} is the laser frequency and $\alpha_{ij}(\omega_{\mathrm{L}})$ denotes the matrix element of the polarizability tensor of the atom. Eq. (123) only holds, if ω_{L} is far away from an atomic resonance frequency. Due to the standard quadratical Stark effect, the electronic energy of the atom undergoes a shift of the form $\Delta E = -\boldsymbol{d} \cdot \boldsymbol{E}$. Because of the spatial inhomogeneity, an effective optical potential arises,

$$V_{\mathrm{dip}}(\boldsymbol{r}) = -\boldsymbol{d} \cdot \boldsymbol{E} \propto |\boldsymbol{E}(\boldsymbol{r})|^2. \tag{124}$$

These are the basic physical processes to trap neutral atoms in laser fields. By overlapping two counter-propagating laser beams, an optical standing wave emerges. In this way, the spatial positions of the field minima become time-independent. Thus, the atoms in this system form a static, one-dimensional chain, which represents the simplest optical lattice, where the static field minima correspond to the lattice sites as is schematically depicted in Fig. 7 on the left.
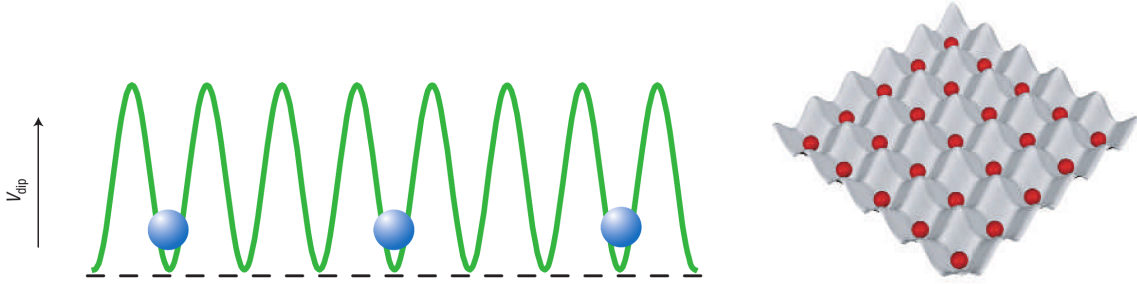

Fig. 7 Optical lattice systems in $D = 1, 2$: The left (right) figure shows a schematic illustration of a one-(two-)dimensional optical lattice. The points represent the ultracold atoms, whereas the line (surface) corresponds to the optical potential V_{dip} in Eq. (124). The graphics are taken from Ref. [8].

Adding more laser fields of the same frequency allows to generate two- (see right part of Fig. 7) and three-dimensional lattices.

The bottom-up generation of an ultracold atom arrangement exhibits a multitude of manipulation possibilities. The amplitude of the laser wave directly enters the lattice potential depth. Thus, by modifying the amplitude, one can control the probability of the atoms to hop between the sites. The lattice depth is usually given in units of the recoil energy $E_{\mathrm{r}} = \frac{\hbar^2 |\boldsymbol{k}_{\mathrm{L}}|^2}{2m}$, m being the mass of a neutral atom and $\boldsymbol{k}_{\mathrm{L}}$ the wave vector of the laser light [8]. The frequency of the electric field ω_{L} determines the interparticle distance in the lattice and by overlapping different frequencies, it becomes possible to construct additional inhomogeneous potentials. The effective wavelength of the standing wave can, e.g., be enlarged by interfering two laser beams at an angle less than $180°$. Even the interaction strength of the atoms can be controlled via magnetically tuned Feshbach resonances [12].

Feshbach resonances can occur during the scattering process of two atoms, if the energy of a bound molecular state is close to the free atom energy. The physical origin can be understood from Fig. 8. Let $V_{\mathrm{bg}}(R)$ be the background potential, describing the potential of the scattering between two initially free atoms depending on the interparticle distance R. $V_{\mathrm{c}}(R)$ is the potential curve of a bound molecular state between the atoms. Both potentials exhibit the shape of an anharmonic oscillator. Considering a collision process with the relatively small energy E, $V_{\mathrm{bg}}(R)$ acts as an energetically open channel, since the energy is large enough to leave the potential. $V_{\mathrm{c}}(R)$ is referred to as closed channel, since in a bound state the particles with energy E cannot escape from the minimum. A Feshbach resonance occurs when the scattering state in the open channel is energetically close to a bound molecular state in the closed channel. In this case, a strong coupling between the two channels sets in, which changes the effective scattering length.
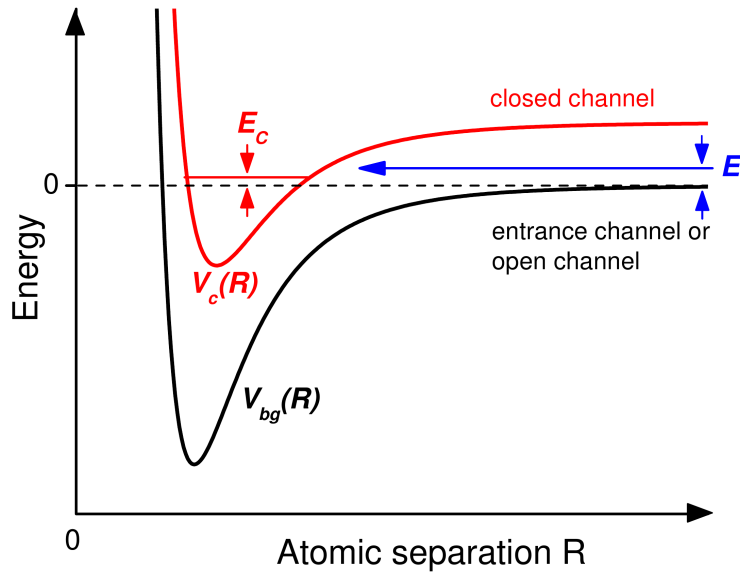
Fig. 8 Basic two-channel model for a Feshbach resonance: The black curve corresponds to the background potential, while the red curve describes the potential of the bound state. Colliding atoms with energy E can resonantly couple to a molecular bound state with energy Ec. The graphic is taken from Ref. [12].
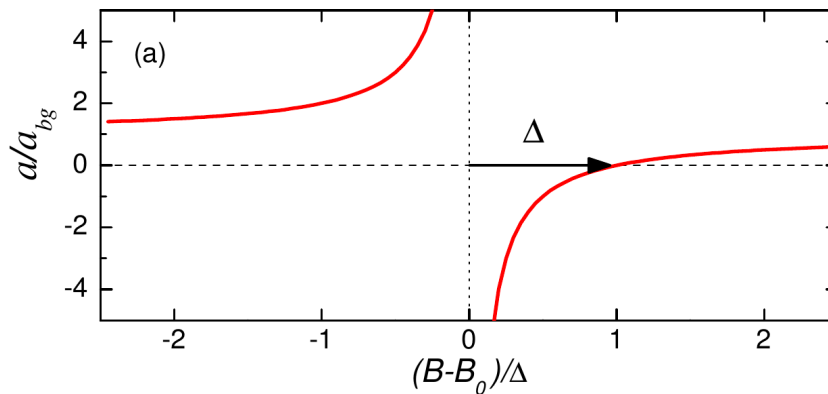
Fig. 9 Connection between the scattering length and the magnetic field: The red curve corresponds to the scattering length of Eq. (125). The graphic is taken from Ref. [12].

The energy position of the channels can be controlled by applying a magnetic field to the system that causes a shift in the energy levels due to the Zeeman effect. If the corresponding magnetic moments of the atoms are different, it is possible to regulate the energy difference between the channels. Thus, the scattering length changes with varying magnetic field. This effect is called *magnetically tuned Feshbach resonance*. The connection between the magnetic field B and the scattering length a can be described by a simple formula [19],

$$a(B) = a_{\text{bg}} \left(1 - \frac{\Delta}{B - B_0} \right) . \tag{125}$$

Here, a_{bg} is the scattering length corresponding to $V_{\text{bg}}(R)$, the parameter Δ is called *resonance width* and B_0 is the magnetic field associated with the Feshbach resonance, where the scattering length diverges. Eq. (125) is illustrated in Fig. 9. As one can see, $a(B)$ approaches the background scattering length for $B \to \pm\infty$, diverges at $B = B_0$ with a sign flip and crosses zero at $B = B_0 + \Delta$. Since the scattering length a corresponds the interaction strength between the atoms, one can achieve perfect interaction control by modulating the magnetic field.

The purpose of the next section is to show some measurements of transport properties of ultracold fermionic atoms in two-dimensional optical lattices that have been published by Schneider et al. [5]. These results are representative for the wide range of experiments with quantum gases in lattices.

3.2   Diffusion results for fermions in two-dimensional lattices

Spatially inhomogeneous density setups provide a suitable way to trigger transport processes and, in particular, diffusive expansion. Therefore, Schneider et al. [5] used a strong circular harmonic trap to confine fermions in the center of a two-dimensional optical lattice. By switching off the potential, the particles begin to expand in the lattice. This is schematically illustrated in Fig. 10. The diffusive expansion results in different geometric structures depend on the strength of the interaction between the particles.
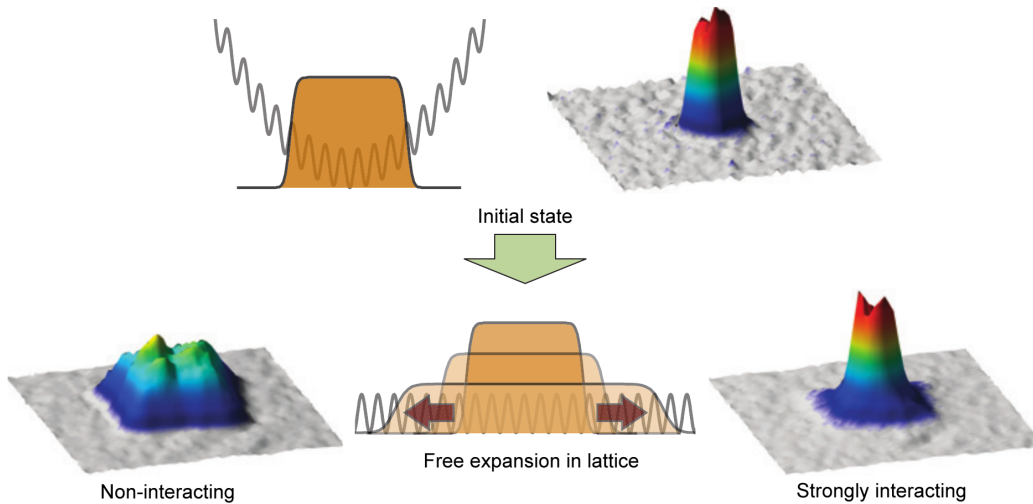

Fig. 10 Schematic illustration of the expansion setups: Initially confined fermionic clouds expand freely in the lattice after the switch-off of the confinement potential. Different interaction strengths lead to stable cores of varying degree and dissimilar geometric shapes of the expanding clouds. The graphic is taken from Ref. [5].

In detail, to experimentally simulate electronic properties, they used a balanced spin mixture of the two lowest hyperfine states of fermionic potassium ^{40}K. These states can be described by $|F, m_F\rangle = |9/2, -9/2\rangle$ and $|9/2, -7/2\rangle$, F being the quantum number of the total angular momentum and m_F the corresponding magnetic quantum number. In total, each experiment involved $N = 2 - 3 \cdot 10^5$ atoms at an initial temperature of $T/T_F = 0.13$, T_F being the Fermi temperature. The Feshbach resonance for the used spin states is parameterized by $B_0 = 202.1$ G and the resonance width $\Delta = (7.0 \pm 0.2)$ G.

This experimental setup is very well suited to investigate the effects of the interaction strength. In Fig. 11, the resulting density distributions in the lattice after a certain expansion time (25 ms) are shown for different interaction strengths.

Here, U and J denote the interaction strength and hopping amplitude of the corresponding Hubbard description (see Sec. 4). The occupation of the lattice sites varies from large (red) to small (blue). One can see that, in general, the density expands toward a square shape due to the square symmetry of the lattice. However, for increasing interaction strength, the core of the particle cloud remains stable in its initial, circular shape. Schneider et al. [5] pointed out that this bimodal behaviour of the expansion goes together with ballistic particles in the outer region and highly interacting atoms in the center of the lattice. The interesting, nontrivial expansion of the core has been analyzed in more detail by measuring the so-called "core expansion velocity", cf. Sec. 6.2.4 which is depicted in Fig. 12.

As one can see, the core expansion velocity has a positive maximum for $U/J = 0$ and decreases rapidly for increasing positive or negative interaction strength[11]. It even reveals a zero-crossing toward slightly negative core

---

[11] The symmetric behaviour with respect to attractive and repulsive interaction is a nontrivial property of the Hubbard model. For more information, the reader is referred to Refs. [5, 20]

expansion velocities, which corresponds to a shrinking of the core, whereupon it slowly converges to zero. The core shrinking can be understood as the consequence of an effectively frozen, strongly interacting core that "[...] dissolves by emitting ballistic particles [...], similarly to a melting ball of ice." [5]. The influence of the lattice potential depth seems not to systematically affect the expansion.
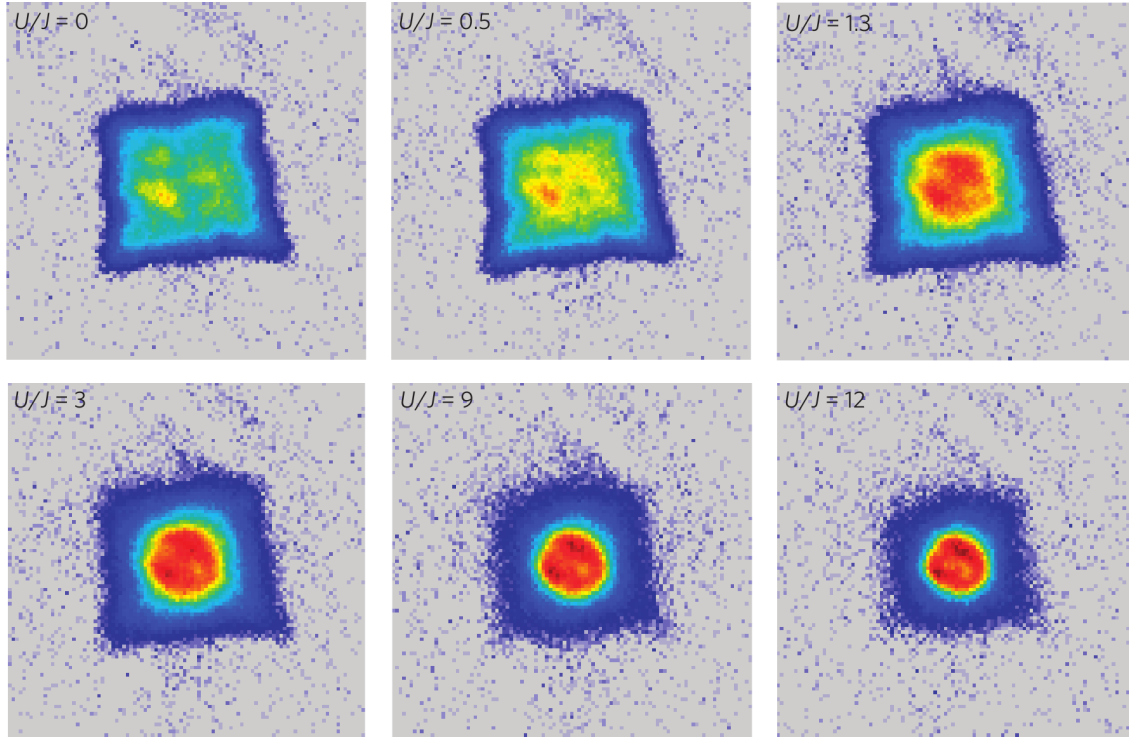
Fig. 11 Resulting density distributions for different interaction strengths: From upper left to lower right, the density profiles after 25 ms of expansion in the lattice are shown for $U/J = 0, 0.5, 1.3, 3, 9, 12$. The color scheme corresponds to the density on the lattice sites, where red (blue) denotes large (small) occupation. While the shape of the outer region is constantly squared through all setups, the core varies from a squared shape for vanishing interaction to a circular shape at larger interaction strengths. The graphic is taken from Ref. [5].

3.3 Simulation results of the fermion diffusion using a relaxation-time model

As mentioned in the introduction, until recently, there were no accurate quantum simulations available that would be able to describe the experimental expansion results in a two-dimensional optical lattice. Various models have been applied and a comparison to the experiments is of high interest as it reveals the applicability limits of various theoretical approaches. The red curve in Fig. 12 corresponds to the theoretical prediction of a semi-classical Markovian Boltzmann equation in relaxation time approximation (RTA) that is described in Refs. [5, 21, 32],

$$\partial_t f_{\boldsymbol{k}} + \nabla_{\boldsymbol{k}} \epsilon_{\boldsymbol{k}} \nabla_{\boldsymbol{r}} + \boldsymbol{F}(\boldsymbol{r}) \nabla_{\boldsymbol{k}} f_{\boldsymbol{k}} = -\frac{1}{\tau(\boldsymbol{n})} \left(f_{\boldsymbol{k}} - f_{\boldsymbol{k}}^0(\boldsymbol{n}) \right) . \tag{126}$$

Here, $f_{\boldsymbol{k}}$ denotes the nonequilibrium distribution function, $f_{\boldsymbol{k}}^0$ is the Fermi function in equilibrium, $\epsilon_{\boldsymbol{k}}$ denotes the dispersion relation of the non-interacting Hubbard model (cf. Eq. (137)) and $\boldsymbol{F}(\boldsymbol{r})$ is an external field. The time τ is the so-called relaxation time. Eq. (126) accounts for a drift, an external field and the scattering, whereby for the latter, in general, the full collision integral has to be solved. In the described approach, Eq. (126) is solved in two steps. First, the equation is linearized, which is only valid if the system is in local equilibrium [21], and second, using a variational method, the effective diffusion coefficient is calculated which determines the value of the relaxation time τ [5, 21]. As one can see, the approach captures the qualitative behaviour of the experiments—the reduction of the fermion expansion speed with the interaction strength.

Fig. 12 Dependence of the core expansion velocity: The core expansion velocities are shown for different interaction streng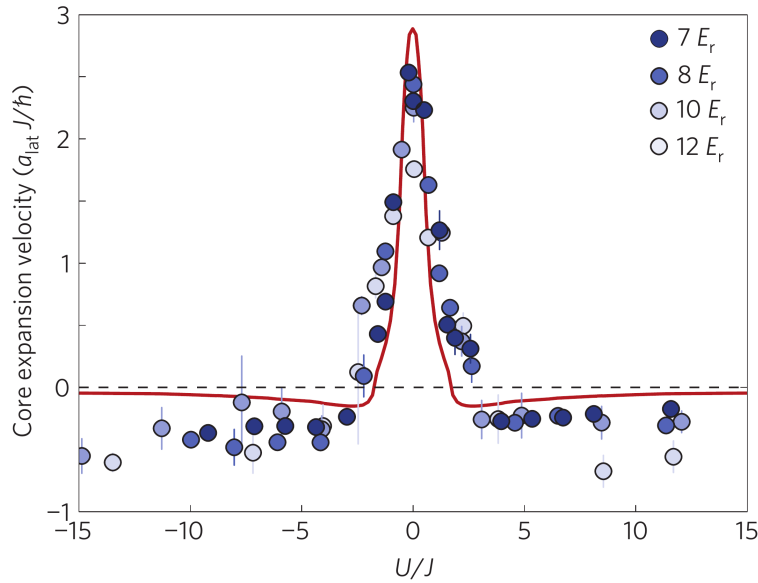ths $U/J \in [-15, 15]$. The blue colors correspond to different lattice potential depths from $7E_r$ to $12E_r$. The red line shows the predicted results, provided by a semiclassical Boltzmann equation simulation in relaxation time approximation. The graphic is taken from Ref. [5].

However, this semiclassical approach exhibits substantial quantitative deviations: it systematically underestimates the core expansion velocity in the low-coupling regime and even fails to reproduce the ideal system ($U = 0$). At the same time, this model overestimates the expansion velocity for larger interaction strengths, and it cannot reproduce the zero crossing of the core expansion velocity. This rather poor agreement is, of course, not surprising [5] given the approximations involved in deriving the semi-classical Boltzmann equation, e.g. Ref. [43]: This model completely neglects quantum effects in the dynamics (classical limit for the external force), and it is dissipative (irreversible) whereas the experimental system is almost perfectly isolated and should exhibit unitary time-reversible dynamics. Further, the RTA collision term violates total energy conservation and forces, by construction, relaxation to the equilibrium momentum distribution of an ideal Fermi gas – in striking contrast to the behavior of strongly correlated fermions. Finally, the RTA ansatz assumes validity of linear response, i.e. it can only describe the final stage of the dynamics where correlations are being build up already and the system is close to equilibrium.

The present non-equilibrium Green functions approach allows us to systematically overcome all these deficiencies. In fact, the KBE constitute generalized quantum kinetic equations that are unitary (time-reversible), conserve total energy and fully capture quantum dynamics effects. The semi-classical Boltzmann equation is readily derived from the KBE with a number of drastic (but well controlled) additional approximations that reveal the applicability limits of the Boltzmann equation, e.g. Refs. [43, 55]. It is, therefore, of high interest to apply the KBE to the experimental setup and perform a detailed comparison. Thereby, good agreement is not obvious from the beginning since the KBE simulations involve an approximation for the correlation effects (via the selfenergy) and they treat only a finite system that is much smaller than the experimental setup. We will show in Sec. 6 that the T-matrix selfenergy is, in fact, the proper many-body approximation that allows us to capture the interaction effects governing the experiment. We will further see that the issue of the limited particle number in the simulation can be efficiently overcome by analyzing the scaling of the collective properties with the particle number and performing an extrapolation to the macroscopic limit. A key to the realization of this procedure is a highly efficient computational scheme which we discuss in Sec. 5.

To tackle the experimental setup with NEGF simulations we first need to apply the Green functions formalism to the fermionic Hubbard model since this model was found to accurately describe fermionic ultra-cold atom ensembles in optical lattices [6, 8, 16]. Before developing the NEGF approach to transport processes in Hubbard lattice systems we recall, in the next section, several basic properties of this model.

4 The Hubbard model

The purpose of this section is to introduce the Hubbard model, to discuss its main properties and to specify the relevant quantities of the NEGF approach, introduced in Sec. 2, to the context of the Hubbard Hamiltonian. This model was proposed in 1963 in Ref. [70] with the goal to describe fundamental correlation effects in solid state physics in a simplified way. The model has been applied to a variety of systems and processes and provides a deep understanding of many properties of lattice systems and the underlying processes. It correctly predicts the existence of the so-called Mott insulator, where electrical conduction is suppressed by the strong repulsion between the electrons, and the model can be straightforwardly generalized [71–73]. The simplicity of the Hubbard model allows for a study with a multitude of analytical techniques, but exact solutions can only be found for systems of low dimensions and small particle numbers.

The basic concept of the Hubbard model is illustrated in Fig. 13. When identical atoms with non-degenerate orbitals form a solid state lattice, the outermost orbitals overlap significantly and produce a single band, in which the electrons can move. In the low energy regime, the orbitals of the inner shells can be considered frozen, since the overlap with the orbitals of other atoms vanishes. Electrons in the corresponding shells mainly modify the effective potential of the nucleus by screening effects. The Hubbard model focuses on the description of the (small) overlap between the outermost shells which results in a tunneling between the atoms. The resulting system can be described by lattice sites at the atomic positions that can be occupied by only two electrons each, corresponding to one electronic orbital. The tunneling probability shows up as a hopping amplitude for the electrons describing their transitions from one lattice sight to the next. In the Hubbard model, the interaction is considered to be on-site, i.e. only electrons at the same lattice site can interact. The contrast to the long-range Coulomb interaction can be justified by assuming that the electrons of the inner shells shield the potential of the active electron. Thus, an effectively screened potential emerges that can be considered fallen off at all lattice sites in the vicinity (extensions to interaction between electrons on different sites are straightforward, but will not be considered here).
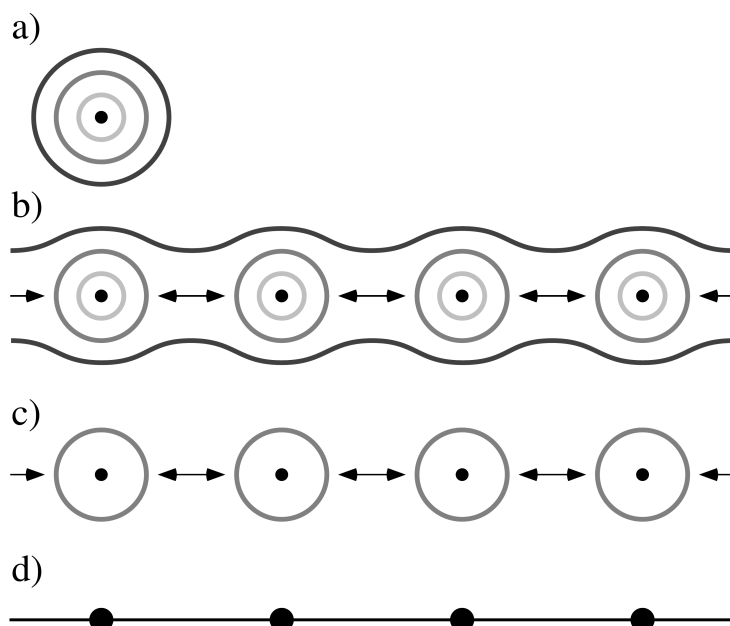
Fig. 13 Illustration of the assumptions of the Hubbard model: a) A single atom with multiple electrons in nondegenerate orbitals. b) Identical atoms form a solid state lattice. The overlap of the outermost orbitals generates a single band, in which the electrons become itinerant. c) Electrons on the inner orbitals are considered localized at the atom positions and only show up as an effective screened potential, while the electrons of the outermost shell have a non-negligible possibility to tunnel between the atoms. d) The system reduces to effective lattice sites, with a single electronic orbital each site. Electrons can only interact at the same site and the tunneling is considered as a hopping between the atom positions. The graphic is taken from Ref. [74].

4.1 The Hubbard Hamiltonian

With the assumptions presented in the preceding section, the Hubbard Hamiltonian in second quantization is determined by the matrix elements of the single-particle and interaction part (cf. Eqs. (23) to (24)). Therefore, one has to decouple the spatial and spin coordinates, $\{i\} \rightarrow \{i, \sigma\}$, with the lattice site position i and the electronic spin $\sigma \in \{\uparrow, \downarrow\}$, leading to

$$h^{(0)}_{ij,\alpha\beta} = -J\delta_{\langle i,j\rangle}\delta_{\alpha,\beta} \quad \text{and} \quad W_{ijkl,\alpha\beta\gamma\delta} = U\delta_{i,j}\delta_{i,k}\delta_{i,l}\delta_{\alpha,\gamma}\delta_{\beta,\delta}\bar{\delta}_{\alpha,\beta} \,. \tag{127}$$

Here, $\bar{\delta}_{\alpha,\beta} := 1 - \delta_{\alpha,\beta}$ and $\delta_{\langle i,j\rangle} := 1$ if the sites i, j are neighboring sites and $\delta_{\langle i,j\rangle} := 0$ otherwise. In Eq. (127), J denotes the hopping amplitude and U is the on-site interaction strength. The full Hamiltonian (without excitation) becomes,

$$
\begin{aligned}
\hat{H} &= -J\sum_{i,j}\sum_{\alpha,\beta}\delta_{\langle i,j\rangle}\delta_{\alpha,\beta}\hat{c}^{\dagger}_{i,\alpha}\hat{c}_{j,\beta} + \frac{U}{2}\sum_{i,j,k,l}\sum_{\alpha,\beta,\gamma,\delta}\delta_{i,j}\delta_{i,k}\delta_{i,l}\delta_{\alpha,\gamma}\delta_{\beta,\delta}\hat{c}^{\dagger}_{i,\alpha}\hat{c}^{\dagger}_{j,\beta}\hat{c}_{l,\delta}\hat{c}_{k,\gamma}\bar{\delta}_{\alpha,\beta} \\
&= -J\sum_{\langle i,j\rangle}\sum_{\alpha}\hat{c}^{\dagger}_{i,\alpha}\hat{c}_{j,\alpha} + \frac{U}{2}\sum_{i}\sum_{\alpha\neq\beta}\hat{c}^{\dagger}_{i,\alpha}\hat{c}^{\dagger}_{i,\beta}\hat{c}_{i,\beta}\hat{c}_{i,\alpha} \,,
\end{aligned}
\tag{128}
$$

$\sum_{\langle i,j\rangle}$ being a short notation for the summation over all neighboring sites i, j. The summation of the interaction part can be further reduced to

$$
\begin{aligned}
\sum_{i}\sum_{\alpha\neq\beta}\hat{c}^{\dagger}_{i,\alpha}\hat{c}^{\dagger}_{i,\beta}\hat{c}_{i,\beta}\hat{c}_{i,\alpha} &= \sum_{i}\left\{\hat{c}^{\dagger}_{i,\uparrow}\hat{c}^{\dagger}_{i,\downarrow}\hat{c}_{i,\downarrow}\hat{c}_{i,\uparrow} + \hat{c}^{\dagger}_{i,\downarrow}\hat{c}^{\dagger}_{i,\uparrow}\hat{c}_{i,\uparrow}\hat{c}_{i,\downarrow}\right\} \\
&= 2\sum_{i}\hat{c}^{\dagger}_{i,\uparrow}\hat{c}_{i,\uparrow}\hat{c}^{\dagger}_{i,\downarrow}\hat{c}_{i,\downarrow} = 2\sum_{i}\hat{n}^{\uparrow}_{i}\hat{n}^{\downarrow}_{i} \,,
\end{aligned}
\tag{129}
$$

where, for the second line, the last anticommutator relation for fermions in Eq. (4) is used, which gives zero for different spin indices. Having this, Eq. (128) can be written in the form

$$\hat{H} = -J\sum_{\langle i,j\rangle}\sum_{\alpha}\hat{c}^{\dagger}_{i,\alpha}\hat{c}_{j,\alpha} + U\sum_{i}\hat{n}^{\uparrow}_{i}\hat{n}^{\downarrow}_{i} \,, \tag{130}$$

which is known as the Hubbard Hamiltonian. To account for time-dependent single-particle excitations (cf. Eq. (23)), it useful to introduce a generalized time-dependent Hubbard Hamiltonian,

$$\hat{H}(t) = -J\sum_{\langle i,j\rangle}\sum_{\alpha}\hat{c}^{\dagger}_{i,\alpha}\hat{c}_{j,\alpha} + U\sum_{i}\hat{n}^{\uparrow}_{i}\hat{n}^{\downarrow}_{i} + \sum_{i,j}\sum_{\alpha,\beta}F_{ij,\alpha\beta}(t)\hat{c}^{\dagger}_{i,\alpha}\hat{c}_{j,\beta} \,. \tag{131}$$

Moreover, if the Hubbard system is solved with the aforementioned NEGF approach (see Sec. 2), one has to consider the adiabatic switching in the Hamiltonian (cf. Eq. (25)). Thereto, one defines a time-dependent interaction[12]

$$U(t) := f_{\text{AS}}(t)U \,, \tag{132}$$

leading to

$$\hat{H}(t) = -J\sum_{\langle i,j\rangle}\sum_{\alpha}\hat{c}^{\dagger}_{i,\alpha}\hat{c}_{j,\alpha} + U(t)\sum_{i}\hat{n}^{\uparrow}_{i}\hat{n}^{\downarrow}_{i} + \sum_{i,j}\sum_{\alpha,\beta}F_{ij,\alpha\beta}(t)\hat{c}^{\dagger}_{i,\alpha}\hat{c}_{j,\beta} \,. \tag{133}$$

When applied to a solid state system, as motivated in Sec. 4, the Hubbard Hamiltonian is not valid, if the width of the conduction band is too large, so that the electrons are not mainly localized at the atomic orbitals. It is not valid, if there is a significantly large percentage of hopping processes with a greater displacement than between neighboring sites. It is also not valid, if the interaction has a long effective range, so that the interaction between particles on different sites cannot be neglected. When applied to an ultracold atom system on an optical lattice, the Hubbard Hamiltonian is not valid, if the lattice potential depth is too small (see Sec. 3.1), leading to

---

[12] In the case of an excitation, this is also possible, because $f_{\text{AS}} = 1$ for all $t \geq t_0$ and $F_{ij,\alpha\beta}(t) = 0$ for all $t < t_0$.

large on-site displacement and to more than two particles per site. It is also not valid, if the laser amplitude is inhomogeneous, which manifests as a position-dependent hopping amplitude. Finally, if there is hopping with a large displacement, which can occur for too small wavelengths, the Hubbard Hamiltonian also fails to describe the system accurately.

To get a better insight into the properties of the Hubbard model, it is useful to discuss a few special cases. In Sec. 4.2, the limiting cases for $U = 0$ and $J = 0$ are studied and the two-site Hubbard model is discussed in Sec. 4.3.

4.2 Limiting cases

If one considers a Hubbard system with vanishing interaction strength U and without external excitation, the Hamiltonian transforms into (cf. Eq. (133))

$$\hat{H}_{U=0} = -J \sum_{\langle i,j \rangle} \sum_{\alpha} \hat{c}_{i,\alpha}^{\dagger} \hat{c}_{j,\alpha} \,. \tag{134}$$

The problem is usually solved in the reciprocal space. The transformation of the canonical operators reads [75],

$$\hat{c}_{i,\sigma}^{\dagger} = \frac{1}{\sqrt{\prod_{d=1}^{D} N_d}} \sum_{i} \mathrm{e}^{-\mathrm{i}\boldsymbol{k}\cdot\boldsymbol{i}} \hat{c}_{k,\sigma}^{\dagger} \,, \qquad \hat{c}_{i,\sigma} = \frac{1}{\sqrt{\prod_{d=1}^{D} N_d}} \sum_{i} \mathrm{e}^{\mathrm{i}\boldsymbol{k}\cdot\boldsymbol{i}} \hat{c}_{k,\sigma} \,. \tag{135}$$

Assuming periodic boundary conditions in every Cartesian direction d, the quasi-momentum k_d takes the values $k_d = \frac{2\pi n_d}{N_d} - \pi$, with $n_d \in \{0, 1, \dots, N_d - 1\}$, N_d being the number of lattice sites in the direction d. Thus, the Hamiltonian of Eq. (134) in a D-dimensional system becomes,

$$
\begin{aligned}
\hat{H}_{U=0} &= -J \sum_{\langle \boldsymbol{i},\boldsymbol{j} \rangle} \sum_{\sigma} \hat{c}_{\boldsymbol{i},\sigma}^{\dagger} \hat{c}_{\boldsymbol{j},\sigma} = -\frac{J}{\prod_{d=1}^{D} N_d} \sum_{\boldsymbol{k},\boldsymbol{k}'} \sum_{\langle \boldsymbol{i},\boldsymbol{j} \rangle} \sum_{\sigma} \mathrm{e}^{-\mathrm{i}\boldsymbol{k}\cdot\boldsymbol{i}} \mathrm{e}^{\mathrm{i}\boldsymbol{k}'\cdot\boldsymbol{j}} \hat{c}_{\boldsymbol{k},\sigma}^{\dagger} \hat{c}_{\boldsymbol{k}',\sigma} \\
&= -\frac{J}{\prod_{d=1}^{D} N_d} \sum_{\boldsymbol{k},\boldsymbol{k}'} \sum_{\boldsymbol{i}} \sum_{\sigma} \hat{c}_{\boldsymbol{k},\sigma}^{\dagger} \hat{c}_{\boldsymbol{k}',\sigma} \\
&\quad \mathrm{e}^{\mathrm{i}\boldsymbol{k}\cdot\boldsymbol{i}} \sum_{d=1}^{D} \left(\mathrm{e}^{-\mathrm{i}\left(k_1' i_1 + \dots + k_d'(i_d - 1) + \dots + k_D' i_D \right)} + \mathrm{e}^{\mathrm{i}\left(k_1' i_1 + \dots + k_d'(i_d + 1) + \dots + k_D' i_D \right)} \right) \\
&= -J \sum_{\boldsymbol{k},\boldsymbol{k}'} \sum_{\sigma} \hat{c}_{\boldsymbol{k},\sigma}^{\dagger} \hat{c}_{\boldsymbol{k}',\sigma} \sum_{d=1}^{D} \left(\mathrm{e}^{-\mathrm{i}k_d'} + \mathrm{e}^{\mathrm{i}k_d'} \right) \underbrace{\frac{1}{\prod_{d=1}^{D} N_d} \sum_{\boldsymbol{i}} \mathrm{e}^{-\mathrm{i}\boldsymbol{i}\cdot\left(\boldsymbol{k}-\boldsymbol{k}' \right)}}_{\delta_{\boldsymbol{k},\boldsymbol{k}'}} \\
&= \sum_{\boldsymbol{k}} \sum_{\sigma} -J \hat{n}_{\boldsymbol{k}}^{\sigma} \sum_{d=1}^{D} \left(2\cos\left(k_d \right) \right) = \sum_{\boldsymbol{k}} \sum_{\sigma} \epsilon_{\boldsymbol{k}} \hat{n}_{\boldsymbol{k}}^{\sigma} \,,
\end{aligned}
\tag{136}
$$

where

$$\epsilon_{\boldsymbol{k}} := -2J \sum_{d=1}^{D} \cos\left(k_d \right) \tag{137}$$

is the dispersion relation for the energy for discrete $\boldsymbol{k}$. The structure of these expressions leads to the conclusion that the electrons behave like free waves in the lattice. This is exactly the result that one obtains in the tight-binding approximation. Having the dispersion relation for D-dimensional Hubbard system, one can define the energy bandwidth. Since $\cos : [-\pi, \pi) \to [-1, 1]$, the full range of possible energies for dimension D becomes

$$b(D) = 4JD \,. \tag{138}$$

This definition of the bandwidth is usually taken as a reference value to compare systems of different dimensions, even in the interacting case, where the actual bandwidth values can slightly differ, cf. Sec. 4.3.

The other extreme case of the Hubbard model corresponds to vanishing hopping amplitude. In this case, there is

no process that couples the different lattice sites. Thus, each site can be considered separately with the resulting single-site Hamiltonian

$$\hat{H}_{J=0} = U\hat{n}^{\uparrow}\hat{n}^{\downarrow} . \tag{139}$$

On each site, four different spin states can be realized, $\sigma \in \{|0\rangle, |\uparrow\rangle, |\downarrow\rangle, |\uparrow\downarrow\rangle\}$. These states are eigenstates of $\hat{H}_{J=0}$. In the grand canonical ensemble with inverse temperature $\beta = 1/k_B T$, the partition function is given by

$$
\begin{aligned}
Z &= \mathrm{Tr}\left(\mathrm{e}^{-\beta\left[\hat{H}_{J=0} - \mu\left(\hat{n}^{\uparrow} + \hat{n}^{\downarrow}\right)\right]}\right) = \sum_{\sigma} \left\langle \sigma \left| \mathrm{e}^{-\beta\left[\hat{H}_{J=0} - \mu\left(\hat{n}^{\uparrow} + \hat{n}^{\downarrow}\right)\right]} \right| \sigma \right\rangle \\
&= 1 + 2\mathrm{e}^{\beta\mu} + \mathrm{e}^{2\beta\mu - \beta U} ,
\end{aligned}
\tag{140}
$$

where, for the trace $\mathrm{Tr}(\cdot)$, the eigenstates of $\hat{n}^{\uparrow}$ and $\hat{n}^{\downarrow}$ were used. A characteristic behaviour of the Hubbard model can be found by considering the average occupation $\langle \hat{n} \rangle = \left\langle \hat{n}^{\uparrow} + \hat{n}^{\downarrow} \right\rangle$,

$$\langle \hat{n} \rangle = \frac{1}{Z} \sum_{\sigma} \left\langle \sigma \left| \left(\hat{n}^{\uparrow}\hat{n}^{\downarrow}\right) \mathrm{e}^{-\beta\left[\hat{H}_{J=0} - \mu\left(\hat{n}^{\uparrow} + \hat{n}^{\downarrow}\right)\right]} \right| \sigma \right\rangle = \frac{2}{Z}\left(\mathrm{e}^{\beta\mu} + \mathrm{e}^{2\beta\mu - \beta U}\right) .$$

For $U = 1$, this expression is graphically shown in Fig. 14 for different inverse temperatures β. One can see the so-called Hubbard gap, which accounts for the fact that the energy gain for adding a particle into the system becomes more and more step-like, the higher β.
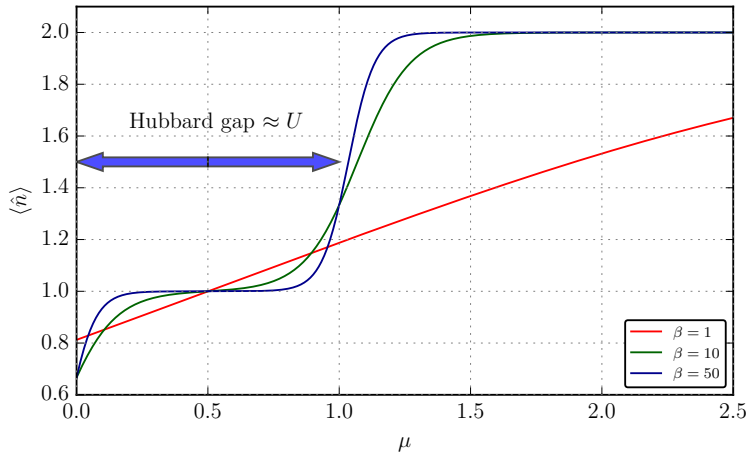
Fig. 14 Illustration of the Hubbard gap for $U = 1$: The average occupation $\langle \hat{n} \rangle$ in the $J = 0$ limit of the Hubbard model is shown for varying chemical potential μ and different values of the inverse temperature $\beta = 1, 10, 50$. If the temperature approaches zero, $\langle \hat{n} \rangle$ becomes a step function that corresponds to the energy U gained when a particle is added into the system.

4.3 The Hubbard dimer

After discussing the limiting cases of the Hubbard model, it is useful, to study a simple system that includes both nonvanishing hopping and interaction. Therefore, one can consider the Hubbard dimer, which is a two-site Hubbard chain. As an example, the case of half-filling ($N = 2$) with $N^{\uparrow} = N^{\downarrow} = 1$ is chosen. The possible states in this system read

$$
\begin{aligned}
|\uparrow, \downarrow\rangle &= \hat{c}_{2,\downarrow}^{\dagger}\hat{c}_{1,\uparrow}^{\dagger}|0\rangle , \\
|\downarrow, \uparrow\rangle &= \hat{c}_{1,\downarrow}^{\dagger}\hat{c}_{2,\uparrow}^{\dagger}|0\rangle , \\
|\downarrow\uparrow, \cdot\rangle &= \hat{c}_{1,\downarrow}^{\dagger}\hat{c}_{1,\uparrow}^{\dagger}|0\rangle , \\
|\cdot, \downarrow\uparrow\rangle &= \hat{c}_{2,\downarrow}^{\dagger}\hat{c}_{2,\uparrow}^{\dagger}|0\rangle .
\end{aligned}
\tag{141}
$$

With this basis set, the Hamiltonian of Eq. (130) attains the form

$$
H = \begin{pmatrix} 0 & 0 & -J & -J \\ 0 & 0 & +J & +J \\ -J & +J & U & 0 \\ -J & +J & 0 & U \end{pmatrix} .
\tag{142}
$$

This Hamiltonian can be solved by diagonalization, which yields four energy eigenvalues and the corresponding eigenvectors,

$$
E^{\pm} = \frac{U}{2} \pm \frac{\sqrt{U^2 + 16J^2}}{2} , \quad \psi^{\pm} = \frac{\pm \left(|\downarrow, \uparrow\rangle - |\uparrow, \downarrow\rangle\right) + \frac{E^{\pm}}{2J} \left(|\downarrow\uparrow, \cdot\rangle + |\cdot, \downarrow\uparrow\rangle\right)}{\sqrt{2 + \frac{1}{2}\left(\frac{E^{\pm}}{J}\right)^2}} ,
$$

$$
E^0 = 0 , \qquad \psi^0 = \frac{|\uparrow, \downarrow\rangle + |\downarrow, \uparrow\rangle}{\sqrt{2}} ,
\tag{143}
$$

$$
E^U = U , \qquad \psi^U = \frac{|\cdot, \downarrow\uparrow\rangle - |\downarrow\uparrow, \cdot\rangle}{\sqrt{2}} .
$$

The U-dependence of the obtained energies is depicted in Fig. 15. As one can see, for $U = 0$, the energy range is exactly the bandwidth for a one-dimensional setup from Eq. (138) and grows with increasing interaction strength. In the limit $U \to \infty$, the four energies become pairwise degenerate, i.e. E^- goes to zero and E^+ approaches E^U.
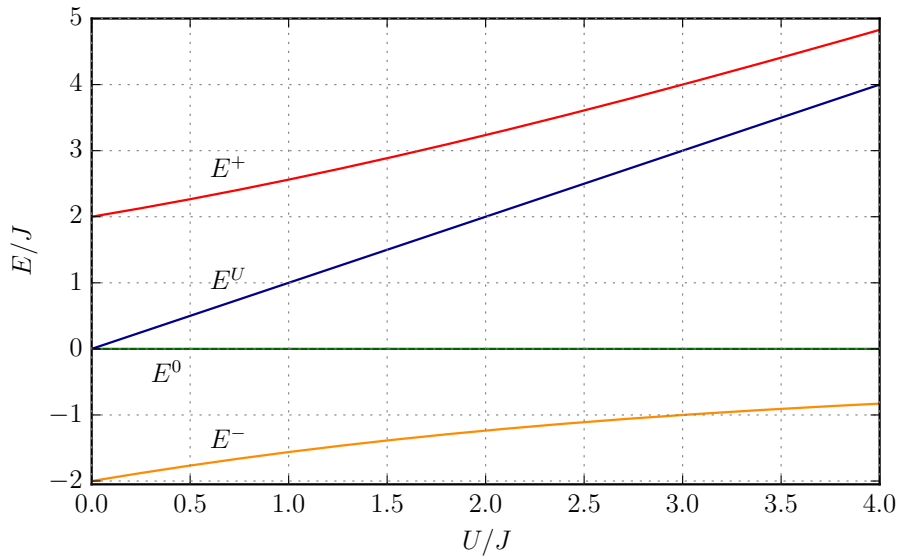
Fig. 15 Energies of the Hubbard dimer: The eigenenergies of the half-filled, two-site Hubbard system of Eq. (143) are shown for varying interaction strength U. In the strong interaction limit, E^+ approaches E^U and E^- goes to E^0.

4.4 Application of NEGF to the Hubbard model

To apply the NEGF approach to finite Hubbard clusters in non-equilibrium, one has to replace the interaction according to Eq. (127). Doing so, the T-matrix of Eq. (91) becomes (again with decoupled spatial and spin

coordinates)

$$
\begin{aligned}
&T_{ijkl,\alpha\beta\gamma\delta}(z,z') \\
&= -\mathrm{i}\hbar \sum_{m,n,p,q} \sum_{\varepsilon,\vartheta,\kappa,\lambda} U(z)\delta_{i,j}\delta_{i,m}\delta_{i,n}\delta_{\alpha,\varepsilon}\delta_{\beta,\vartheta}\bar{\delta}_{\alpha,\beta} G^{\mathrm{H}}_{mnpq,\varepsilon\vartheta\kappa\lambda}(z,z') U(z')\delta_{p,q}\delta_{p,k}\delta_{p,l}\delta_{\kappa,\gamma}\delta_{\lambda,\delta}\bar{\delta}_{\kappa,\lambda} \\
&\quad + \mathrm{i}\hbar \sum_{m,n,p,q} \sum_{\varepsilon,\vartheta,\kappa,\lambda} U(z)\delta_{i,j}\delta_{i,m}\delta_{i,n}\delta_{\alpha,\varepsilon}\delta_{\beta,\vartheta}\bar{\delta}_{\alpha,\beta} G^{\mathrm{H}}_{mnpq,\varepsilon\vartheta\kappa\lambda}(z,z') U(z')\delta_{p,q}\delta_{p,l}\delta_{p,k}\delta_{\kappa,\delta}\delta_{\lambda,\gamma}\bar{\delta}_{\kappa,\lambda} \\
&\quad + \mathrm{i}\hbar \sum_{m,n,p,q} \sum_{\varepsilon,\vartheta,\kappa,\lambda} \int_{\mathcal{C}} \mathrm{d}\bar{z}\, U(z)\delta_{i,j}\delta_{i,m}\delta_{i,n}\delta_{\alpha,\varepsilon}\delta_{\beta,\vartheta}\bar{\delta}_{\alpha,\beta} G^{\mathrm{H}}_{mnpq,\varepsilon\vartheta\kappa\lambda}(z,\bar{z}) T_{pqkl,\kappa\lambda\gamma\delta}(\bar{z},z') \\
&= -\mathrm{i}\hbar U(z)\delta_{i,j}\bar{\delta}_{\alpha,\beta} G^{\mathrm{H}}_{iikk,\alpha\beta\gamma\delta}(z,z') U(z')\delta_{k,l}\bar{\delta}_{\gamma,\delta} + \mathrm{i}\hbar U(z)\delta_{i,j}\bar{\delta}_{\alpha,\beta} G^{\mathrm{H}}_{iikk,\alpha\beta\delta\gamma}(z,z') U(z')\delta_{k,l}\bar{\delta}_{\gamma,\delta} \\
&\quad + \mathrm{i}\hbar \sum_{p,q} \sum_{\kappa,\lambda} \int_{\mathcal{C}} \mathrm{d}\bar{z}\, U(z)\delta_{i,j}\bar{\delta}_{\alpha,\beta} G^{\mathrm{H}}_{ijpq,\alpha\beta\kappa\lambda}(z,\bar{z}) T_{pqkl,\kappa\lambda\gamma\delta}(\bar{z},z') \,.
\end{aligned}
$$

$$(144)$$

The Hubbard Hamiltonian does, in general, not allow for spin flips. This can especially be seen in the single-particle Hamiltonian in Eq. (127). Therefore, every Green function has to conserve spin, i.e. $G_{ij,\alpha\beta}(z,z') = G_{ij,\alpha\alpha}(z,z')\delta_{\alpha,\beta}$. By applying this relation to Eq. (92), i.e.

$$
\begin{aligned}
\Sigma^{T}_{ij,\alpha\beta}(z,z') &= \mathrm{i}\hbar \sum_{k,l} \sum_{\gamma,\delta} T_{ikjl,\alpha\gamma\beta\delta}(z,z') G_{lk,\delta\delta}(z',z)\delta_{\delta,\gamma} \\
&= \mathrm{i}\hbar \sum_{k,l} \sum_{\gamma} T_{ikjl,\alpha\gamma\beta\gamma}(z,z') G_{lk,\gamma\gamma}(z',z)\,,
\end{aligned}
$$

$$(145)$$

it is obvious that the T-matrix has only nonvanishing contributions for equal second and fourth spin arguments. For the two-particle Hartree Green function, spin conservation results in $G^{\mathrm{H}}_{ijkl,\alpha\beta\gamma\delta}(z,z') = G^{\mathrm{H}}_{ijkl,\alpha\beta\alpha\beta}(z,z') \delta_{\alpha,\gamma}\delta_{\beta,\delta}$. Thus, Eq. (144) transforms into

$$
\begin{aligned}
T_{ijkl,\alpha\beta\gamma\beta}(z,z') &= -\mathrm{i}\hbar U(z)\delta_{i,j}\bar{\delta}_{\alpha,\beta} G^{\mathrm{H}}_{iikk,\alpha\beta\alpha\beta}(z,z')\delta_{\alpha,\gamma} U(z')\delta_{k,l} \\
&\quad + \mathrm{i}\hbar U(z)\delta_{i,j}\bar{\delta}_{\alpha,\beta} G^{\mathrm{H}}_{iikk,\alpha\beta\alpha\beta}(z,z')\delta_{\alpha,\beta} U(z')\delta_{k,l} \underbrace{\delta_{\beta,\gamma}\bar{\delta}_{\gamma,\beta}}_{=0} \\
&\quad + \mathrm{i}\hbar \sum_{p,q} \int_{\mathcal{C}} \mathrm{d}\bar{z}\, U(z)\delta_{i,j}\bar{\delta}_{\alpha,\beta} G^{\mathrm{H}}_{ijpq,\alpha\beta\alpha\beta}(z,\bar{z}) T_{pqkl,\alpha\beta\gamma\beta}(\bar{z},z') \\
&= \delta_{i,j}\bar{\delta}_{\alpha,\beta} \Bigg(-\mathrm{i}\hbar U(z) G^{\mathrm{H}}_{iikk,\alpha\beta\alpha\beta}(z,z')\delta_{\alpha,\gamma} U(z')\delta_{k,l} \\
&\quad + \mathrm{i}\hbar \sum_{p,q} \int_{\mathcal{C}} \mathrm{d}\bar{z}\, U(z) G^{\mathrm{H}}_{ijpq,\alpha\beta\alpha\beta}(z,\bar{z}) T_{pqkl,\alpha\beta\gamma\beta}(\bar{z},z') \Bigg) \,.
\end{aligned}
$$

$$(146)$$

Hence, the full series of exchange diagrams from the T-matrix does not contribute for the Hubbard model. From Eq. (146), one can see that, for each iteration, also $k = l$ and $\gamma = \alpha$ are fulfilled. Therefore, it is convenient to introduce a reduced T-matrix,

$$
T_{ijkl,\alpha\beta\gamma\beta}(z,z') =: T_{ik,\alpha\beta}(z,z')\delta_{i,j}\delta_{k,l}\delta_{\alpha,\gamma}\delta_{\beta,\delta}\bar{\delta}_{\alpha,\beta}\,,
$$

$$(147)$$

with

$$
\begin{aligned}
T_{ij,\alpha\beta}(z,z') &= -\mathrm{i}\hbar U(z) G^{\mathrm{H}}_{ij,\alpha\beta}(z,z') U(z') \\
&\quad + \mathrm{i}\hbar \sum_{k} \int_{\mathcal{C}} \mathrm{d}\bar{z}\, U(z) G^{\mathrm{H}}_{ik,\alpha\beta}(z,\bar{z}) T_{kj,\alpha\beta}(\bar{z},z')\,.
\end{aligned}
$$

$$(148)$$

Finally, since

$$
\begin{aligned}
G_{ij,\uparrow\downarrow}^{\mathrm{H}}(z,z') &= G_{ij,\uparrow\uparrow}(z,z')G_{ij,\downarrow\downarrow}(z,z') = G_{ij,\downarrow\downarrow}(z,z')G_{ij,\uparrow\uparrow}(z,z') \\
&= G_{ij,\downarrow\uparrow}^{\mathrm{H}}(z,z')
\end{aligned}
\tag{149}
$$

and, therefore, also

$$
T_{ij,\uparrow\downarrow}(z,z') = T_{ij,\downarrow\uparrow}(z,z')\,,
\tag{150}
$$

it is convenient to define

$$
G_{ij}^{\mathrm{H}}(z,z') := G_{ij,\uparrow\downarrow}^{\mathrm{H}}(z,z') \quad \text{and} \quad T_{ij}(z,z') := T_{ij,\uparrow\downarrow}(z,z')\,,
\tag{151}
$$

leading to

$$
T_{ij}(z,z') = -\mathrm{i}\hbar U(z)G_{ij}^{\mathrm{H}}(z,z')U(z') + \mathrm{i}\hbar \sum_k \int_{\mathcal{C}} \mathrm{d}\bar{z}\, U(z)G_{ik}^{\mathrm{H}}(z,\bar{z})T_{kj}(\bar{z},z')\,.
\tag{152}
$$

This is the definition of the T-matrix in the Hubbard model. With the last definitions, $G_{ij}^{\sigma}(z,z') := G_{ij,\sigma\sigma}(z,z')$ and $\Sigma_{ij}^{\sigma}(z,z') := \Sigma_{ij,\sigma\sigma}(z,z')$, one can simplify the selfenergy of Eq. (145) to

$$
\Sigma_{ij}^{T,\uparrow(\downarrow)}(z,z') = \mathrm{i}\hbar T_{ij}(z,z')G_{ji}^{\downarrow(\uparrow)}(z',z)\,.
\tag{153}
$$

Since in Eq. (152) the T-matrix is a matrix with two indices, one can obtain the corresponding real-time components in exactly the same way as for G or Σ. In order to obtain a structure which only depends on single-particle contour quantities, it is appropriate to define

$$
\Phi_{ij}(z,z') := \mathrm{i}\hbar G_{ij}^{\mathrm{H}}(z,z')\,,
\tag{154}
$$

which obeys the symmetry relations of the Eqs. (101) and (104). Thus, Eq. (152) attains the form

$$
T_{ij}(z,z') = -U(z)\Phi_{ij}(z,z')U(z') + \sum_k \int_{\mathcal{C}} \mathrm{d}\bar{z}\, U(z)\Phi_{ik}(z,\bar{z})T_{kj}(\bar{z},z')\,.
\tag{155}
$$

By applying Eqs. (102) and (103), one finds

$$
\begin{aligned}
T_{ij}^{\mathrm{R/A}}(t,t') &= -U(t)\Phi_{ij}^{\mathrm{R/A}}(t,t')U(t') \\
&\quad + \sum_k \int_{t_{\mathrm{s}}}^{\infty} \mathrm{d}\bar{t}\, U(t)\Phi_{ik}^{\mathrm{R/A}}(t,\bar{t})T_{kj}^{\mathrm{R/A}}(\bar{t},t')\,,
\end{aligned}
\tag{156}
$$

$$
\begin{aligned}
T_{ij}^{\gtrless}(t,t') &= -U(t)\Phi_{ij}^{\gtrless}(t,t')U(t') \\
&\quad + \sum_k \int_{t_{\mathrm{s}}}^{\infty} \mathrm{d}\bar{t}\, U(t)\Phi_{ik}^{\mathrm{R}}(t,\bar{t})T_{kj}^{\gtrless}(\bar{t},t') \\
&\quad + \sum_k \int_{t_{\mathrm{s}}}^{\infty} \mathrm{d}\bar{t}\, U(t)\Phi_{ik}^{\gtrless}(t,\bar{t})T_{kj}^{\mathrm{A}}(\bar{t},t')\,.
\end{aligned}
\tag{157}
$$

The real-time components of the quantity Φ, related to the two-particle Hartree Green function become, by definition[13] in Eq. (100)

$$
\begin{aligned}
\Phi_{ij}^{\gtrless}(t,t') &= \mathrm{i}\hbar G_{ij}^{\uparrow,\gtrless}(t,t')G_{ij}^{\downarrow,\gtrless}(t,t')\,, \\
\Phi_{ij}^{\mathrm{R}}(t,t') &= \Theta(t,t')\left[\Phi_{ij}^{>}(t,t') - \Phi_{ij}^{<}(t,t')\right]\,, \\
\Phi_{ij}^{\mathrm{A}}(t,t') &= \Theta(t',t)\left[\Phi_{ij}^{<}(t,t') - \Phi_{ij}^{>}(t,t')\right]\,.
\end{aligned}
\tag{158}
$$

---

[13] The time-diagonal component Φ^{δ} vanishes due to $G^{\delta} = 0$ [44].

Because of the order of the time arguments [67], we obtain for the selfenergy

$$\Sigma_{ij}^{T,\uparrow(\downarrow),\gtrless}(t,t') = i\hbar T_{ij}^{\gtrless}(t,t')G_{ji}^{\downarrow(\uparrow),\lessgtr}(t',t)\,, \tag{159}$$

for the less and greater components, which will be used in Sec. 5. Finally, we formulate the KBE for the Hubbard case. For the greater and less components of Eqs. (107) and (108) together with Eq. (127), we arrive at (the selfenergy also contains the Hartree–Fock contribution)

$$\sum_l \left[i\hbar\frac{\mathrm{d}}{\mathrm{d}t}\delta_{i,l} + J\delta_{\langle i,l\rangle}\right]G_{lj}^{\sigma,\gtrless}(t,t') = \sum_l \int_{t_{\mathrm{s}}}^{\infty}\mathrm{d}\bar{t}\left\{\Sigma_{il}^{\sigma,\mathrm{R}}(t,\bar{t})G_{lj}^{\sigma,\gtrless}(\bar{t},t') + \Sigma_{il}^{\sigma,\gtrless}(t,\bar{t})G_{lj}^{\sigma,\mathrm{A}}(\bar{t},t')\right\}, \tag{160}$$

$$\sum_l G_{il}^{\sigma,\gtrless}(t,t')\left[-i\hbar\frac{\overleftarrow{\mathrm{d}}}{\mathrm{d}t'}\delta_{l,j} + J\delta_{\langle l,j\rangle}\right] = \sum_l \int_{t_{\mathrm{s}}}^{\infty}\mathrm{d}\bar{t}\left\{G_{il}^{\sigma,\mathrm{R}}(t,\bar{t})\Sigma_{lj}^{\sigma,\gtrless}(\bar{t},t') + G_{il}^{\sigma,\gtrless}(t,\bar{t})\Sigma_{lj}^{\sigma,\mathrm{A}}(\bar{t},t')\right\}. \tag{161}$$

In order to describe the dynamics of the considered systems, we want to solve the Eqs. (160) and (161) for the Green functions. To this end, at each time step, we need to evaluate the integrals on the right-hand side, which require the knowledge of the selfenergy of Eq. (159) and thus the T-matrix. The latter is obtained by solving the Eqs. (156) and (157). Special care must be taken here since the T-matrix depends on itself. To account for this, we compute the advanced, the less and the greater component of T in an iterative procedure that leads to convergence.

5   Numerical algorithms and implementation details

This section is devoted to the presentation of the numerical algorithms that are used to solve the dynamics of Hubbard models within the introduced NEGF approach with the needed efficiency. Before discussing the details of the numerical propagation, it is convenient to look at numerical integration methods to keep the large computational effort manageable.

5.1   Numerical integration

The numerical implementation of the NEGF approach is governed by the numerical evaluation of time integrals, as one can see in Eqs. (160), (161), (156) and (157). For the evaluation of integral expressions, a variety of numerical methods exists but the structure of the time propagation (cf. Sec. 5.2) requires a restriction to methods with equidistant stepping. A convenient higher order integration scheme is given by the so-called Newton–Cotes formulas that are briefly summarized below, for a detailed derivation, see Apps. A to E.

Assuming a function $f : [a,b] \to \mathbb{C}, x \mapsto f(x)$ with $a,b \in \mathbb{R}$, the one-dimensional integration problem starts with the integral expression

$$I(f) = \int_a^b \mathrm{d}x\, f(x)\,. \tag{162}$$

With Newton–Cotes integration, $I(f)$ can be approximated by an expression that only depends on values for discrete sampling points $f_i := f(x_i)$ with $x_i = a + i\frac{b-a}{n}$, $n \in \mathbb{N}$, $i \in [0,n]$,

$$I(f) \quad\approx\quad nh\sum_{i=0}^{n}f_i w_i^n \qquad \text{with} \qquad w_i^n := \int_0^1 \mathrm{d}\hat{x}\prod_{\substack{j=0\\j\neq i}}^{n}\frac{n\hat{x}-j}{i-j} \quad, \tag{163}$$

where $h := \frac{x_n - x_0}{n}$ (see App. A for a derivation). The w_i^n, which only depend on the order n, are the so-called universal weight factors for the closed Newton–Cotes formulas. They can be calculated analytically, which is shown in App. B. The resulting weights for chosen orders n are listed in Tab. 1. The error of Eq. (163) is of the order $\mathcal{O}\left(h^{n+2}\left|f^{(n+1)}\right|\right)$, if n is odd and of the order $\mathcal{O}\left(h^{n+3}\left|f^{(n+2)}\right|\right)$, if n is even. In principle, it is always possible to integrate over n sampling points with n-th order integration. Practically, it turns out that the weight factors for $n \geq 8$ become progressively negative. To avoid numerical cancellation effects that can

occur by summation with alternating sign [76], it is convenient not to use these higher order formulas. Instead, integration with a large number of sampling points $\{x_0, \ldots, x_N\}$, $N \in \mathbb{N}$ can be achieved by combining blocks of lower order integration.

If $N = kn$, $k \in \mathbb{N}$ for a chosen n, the integration can easily be done by combining only segments of the integration order n. In general, this is not possible, so that one has to mix blocks of different order. In every case, one can define the number of blocks $a_N(\widetilde{n})$ that attributes a number of segments to the integration order $\widetilde{n}$. In this work, the function f and its derivatives are considered to be of similar shape throughout $[x_0, x_N]$. Therefore, it is convenient to arrange the $a_N(\widetilde{n})$ blocks in such a way that the points $[x_{\sum_{\hat{n}=\tilde{n}+1}^{n} a_N(\hat{n})\cdot\hat{n}}, x_{\sum_{\hat{n}=\tilde{n}}^{n} a_N(\hat{n})\cdot\hat{n}}]$ are integrated in $\widetilde{n}$-th order, if $a_N(\widetilde{n}) > 0$, i.e. the first points are integrated with the highest order and so forth. In total, the full integral can be expressed in the following way (see App. C),

$$
\begin{aligned}
I(f) \quad \approx \quad & \sum_{\tilde{n}=1}^{n} \tilde{n}h \Bigg[f_{\sum_{\hat{n}=\tilde{n}+1}^{n} a_N(\hat{n})\cdot\hat{n}} w_0^{\tilde{n}} + f_{\sum_{\hat{n}=\tilde{n}}^{n} a_N(\hat{n})\cdot\hat{n}} w_{\tilde{n}}^{\tilde{n}} \\
& + \sum_{i=1}^{a_N(\hat{n})\cdot\hat{n}-1} f_{i+\sum_{\hat{n}=\tilde{n}+1}^{n} a_N(\hat{n})\cdot\hat{n}} \left(w_{i \bmod \tilde{n}}^{\tilde{n}} + \delta_{i \bmod \tilde{n}} w_{\tilde{n}}^{\tilde{n}} \right) \Bigg].
\end{aligned}
\tag{164}
$$

The correctness of the numerical integration is crucially depending on the choice of the segmentation, i.e. on $a_N(\widetilde{n})$. As an example, if one treats as many points as possible with n-th order integration, i.e. $a_N(n) = \lfloor \frac{N}{n} \rfloor$[14] and the remaining points with $\widetilde{n} = N \bmod n$, i.e. $a_N(N \bmod n) = 1$ (in the following referred to as *primitive scheme*), one gets an inhomogeneous error order for consecutive N, due to the last block that has an arbitrary integration order. A better scheme to choose the $a_N(\widetilde{n})$ is given by

$$
a_N(\tilde{n}) =
\begin{cases}
\left\lfloor \left(\frac{N}{\tilde{n}-1} - \lfloor \frac{N}{\tilde{n}} \rfloor - 1 \right)(\tilde{n}-1) \right\rfloor, & \lfloor \frac{N}{\tilde{n}-1} \rfloor > \lfloor \frac{N}{\tilde{n}} \rfloor \wedge N \bmod \tilde{n} \neq 0 \wedge (a_N(\tilde{n}+1) = 0 \vee \tilde{n} = n) \\
\frac{N}{\tilde{n}}, & \lfloor \frac{N}{\tilde{n}-1} \rfloor > \lfloor \frac{N}{\tilde{n}} \rfloor \wedge N \bmod \tilde{n} = 0 \wedge (a_N(\tilde{n}+1) = 0 \vee \tilde{n} = n) \\
\frac{N-(\tilde{n}+1)a_N(\tilde{n}+1)}{\tilde{n}}, & a_N(\tilde{n}+1) \neq 0 \wedge (a_N(\tilde{n}+2) = 0 \vee \tilde{n}+1 = n) \\
0, & \text{otherwise}
\end{cases}
\tag{165}
$$

primitive scheme
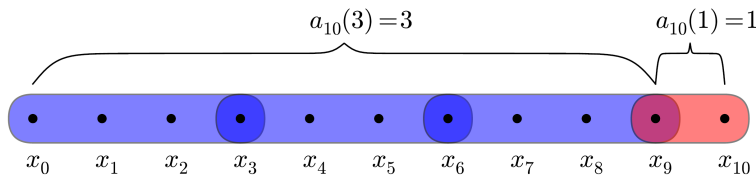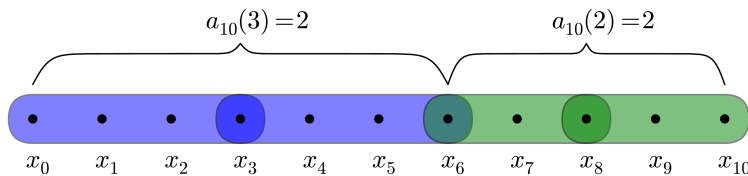

optimal order scheme

Fig. 16 Higher order integration scheme comparison: For an exemplary setup with $N = 10$ and $n = 3$, the block structure of the primitive- (top) and optimal order-scheme (bottom) are schematically illustrated.

---

[14] Here, $\lfloor a \rfloor$ denotes the so-called floor function, i.e. $\lfloor a \rfloor = \max\{\hat{a} \in \mathbb{Z} | \hat{a} \leq a\}$.

It can be called *optimal order scheme*. The difference between the two schemes is illustrated in Fig. 16. Considering the example for $n = 3$ and $N = 10$, in the primitive scheme (top), one treats the points $x_0 \ldots x_9$ (blue area) via integration for $\tilde{n} = 3$. The remaining points $x_9 \ldots x_{10}$ (red area) can only be integrated with $\tilde{n} = 1$, which leads to the unfavorable low integration order $\mathcal{O}\left(h^3 \left|f''\right|\right)$. In the optimal order scheme (bottom), only the points $x_0 \ldots x_6$ are integrated with $\tilde{n} = 3$, although one could include more points in this area. The advantage of this procedure arises from the circumstance that the remaining points $x_6 \ldots x_{10}$ (green area) fit the $\tilde{n} = 2$ type integration, which gives the maximum possible total order $\mathcal{O}\left(h^5 \left|f^{(4)}\right|\right)$. In general, for sufficiently large N, the order of the error becomes homogeneous in the optimal order scheme, since only blocks with $\tilde{n} = n$ or $\tilde{n} = n - 1$ are included. In detail, for odd n, it becomes $\mathcal{O}\left(h^{n+2} \left|f^{(n+1)}\right|\right)$ and for even n, it varies between $\mathcal{O}\left(h^{n+3} \left|f^{(n+2)}\right|\right)$ and $\mathcal{O}\left(h^{n+1} \left|f^{(n)}\right|\right)$ for $N \geq N_n^{\mathrm{FO}} = (n-1)(n-2)$ (see App. D).

The dissimilar quality of the introduced higher order integration schemes becomes apparent in Fig. 17, where the test function $f(x) = \sin(x)$ is integrated in the way $F(x) := \int_0^x \mathrm{d}s\, f(s) = 1 - \cos(x)$ for $n = 1, 2, 3, 4, 5$. The total deviation

$$\Delta F(x) := \left| I_n^{\mathrm{num}}(N) - F(x) \right| \tag{166}$$

and the estimated error are shown depending on the integration boundary x, which corresponds to the number of sampling points $N + 1$. As one can easily see, in the primitive scheme, the errors are strongly inhomogeneous in the whole range. In the optimal order scheme, however, the errors converge especially for odd n. Therefore, the latter is clearly superior and favorable.
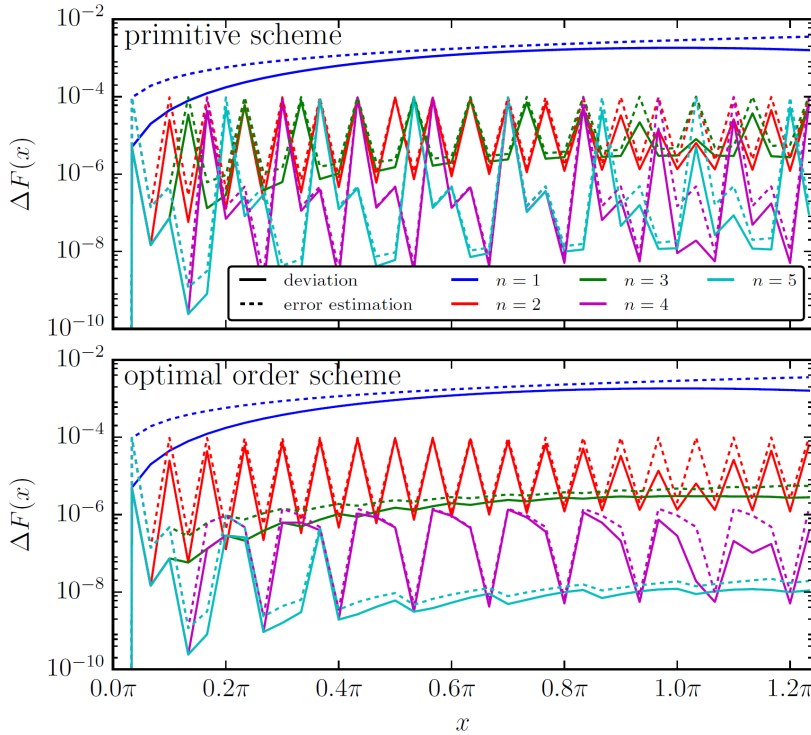
Fig. 17 Errors for different integration orders: The total deviation ΔF is plotted as a function of x with logarithmically scaled ordinate and the resolution step $h = \frac{\pi}{30}$. The solid lines correspond to the deviation, whereas the dashed lines belong to the estimated error terms according to Eq. (285). The blue (red, green, magenta, cyan) curve corresponds to $n = 1 (2, 3, 4, 5)$. The upper graph is calculated using the primitive scheme of higher order integration, while the lower one is calculated via the optimal order scheme.

In this paper, it is required to numerically calculate the integrals for a given resolution which is defined by the propagation structure (see Sec. 5.2). This can, of course, be achieved by application of the introduced optimal order scheme. It is not always necessary to integrate with the accuracy obtained for a high integration order n

with respect to the resolution h. In these cases, one can decide not to use every sampling point for the integration, thus, to increase the resolution step h to reduce the numerical effort of the calculation. However, the integral boundaries still correspond to the stepping of high resolution. For that purpose, one needs to generalize the integration scheme to time points that do not match the equidistant raster. Therefore, it is convenient, to consider integration on $[a, b]$ while $a < x_0$ and/or $b > x_N$. The values $f(a)$ and $f(b)$ are also known. If one considers, for instance, the case $a < x_0$, the integral between a and x_0 can be numerically approximated by (see App. E for a derivation)

$$I(f)\Big|_a^{x_0} \approx h\left(f(a)w_a^{n,\mathrm{gr}} + \sum_{i=0}^{n-1} f_i w_i^{n,\mathrm{gr}}\right),\tag{167}$$

with the generalized raster weight factors

$$w_i^{n,\mathrm{gr}} = \frac{d}{h}\int_0^1 d\bar{x}\,\frac{\bar{x}}{i\frac{h}{d}+1}\prod_{\substack{j=0\\j\neq i}}^{n-1}\frac{\frac{d}{h}(\bar{x}-1)-j}{i-j}, \qquad w_a^{n,\mathrm{gr}} = \frac{d}{h}\int_0^1 d\bar{x}\prod_{j=0}^{n-1}\left(1 - \frac{\bar{x}}{j\frac{h}{d}+1}\right)\tag{168}$$

Here, d is defined as $d := x_0 - a$. The resulting values of the generalized raster weights for selected values of n and d can be found in Tab. 3. For the case $b > x_N$, the same weight factors apply.

point sampling scheme

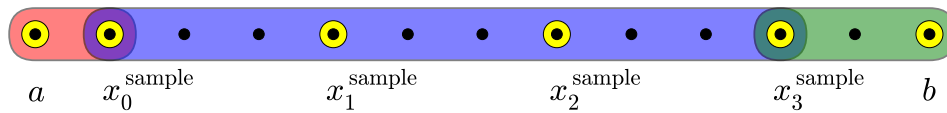**Fig. 18** Point sampling in the generalized raster integration: For a setup with $r_{\mathrm{sample}} = 3$, $a = x_0^{\mathrm{sample}} - h$ and $b = x_3^{\mathrm{sample}} + 2h$, the generalized raster scheme is illustrated schematically. The blue area corresponds to the closed optimal order integration, whereas the red and the green area belong to margin integration. The yellow marked points are actually used as sampling points.

The obtained generalized integration rules can now be used to increase the resolution step. Let r_{sample} define the chosen points in the way that $x_i^{\mathrm{sample}} = x_0 + i r_{\mathrm{sample}} h$ (i.e. use every r_{sample}-th old sampling point). If the integration boundaries a and b are not contained in the x_i^{sample}, the remaining margin integrals are treated according to Eq. (167). This is illustrated in Fig. 18 for the example $r_{\mathrm{sample}} = 3$, $a = x_0^{\mathrm{sample}} - h$ and $b = x_3^{\mathrm{sample}} + 2h$. The blue region is integrated with the standard optimal order scheme of closed integration for the respective n, but with the resolution step $r_{\mathrm{sample}} \cdot h = 3h$. The yellow marked points denote the sampling points actually used. The red and the green area are treated with generalized raster integration for the respective n according to Eq. (167). In this case that means that for the interval $\left[a, x_0^{\mathrm{sample}}\right]$ (red) the weight factors for the resolution step $3h$ are calculated for $\frac{d}{3h} = \frac{1}{3}$. For the interval $\left[x_3^{\mathrm{sample}}, b\right]$ (green), the weight factors are calculated for $\frac{d}{3h} = \frac{2}{3}$. In principle, one can also think about an extrapolation of the margin points, but it turns out that this would provide larger error terms [65] (of the same order).

To illustrate the obtained efficiency inherent in the introduced approach, the CPU runtime for the evaluation of $F(x) = \int_0^x ds\,\sin(s)$ is analyzed for two different test cases. The first setup belongs to the primitive first order integration with no use of an enlarged sampling ratio r_{sample}, i.e. $n = 1$ and $r_{\mathrm{sample}} = 1$. In the second setup, however, integration is done with $n = 5$, $r_{\mathrm{sample}} = 10$ and the optimal order- as well as the generalized raster-scheme. The deviations for these setups are shown in Fig. 19 in the upper graph. For small x, one can see that the actual deviation as well as the error estimation are higher for the more sophisticated approach (red), which is due to the small amount of sampling points. But once the final integration order is reached, the deviations of the efficient approach are constantly below the results of the primitive integration (blue), although almost every tenth sampling point is included in the calculation. Therefore, the introduced approach provides very accurate results.
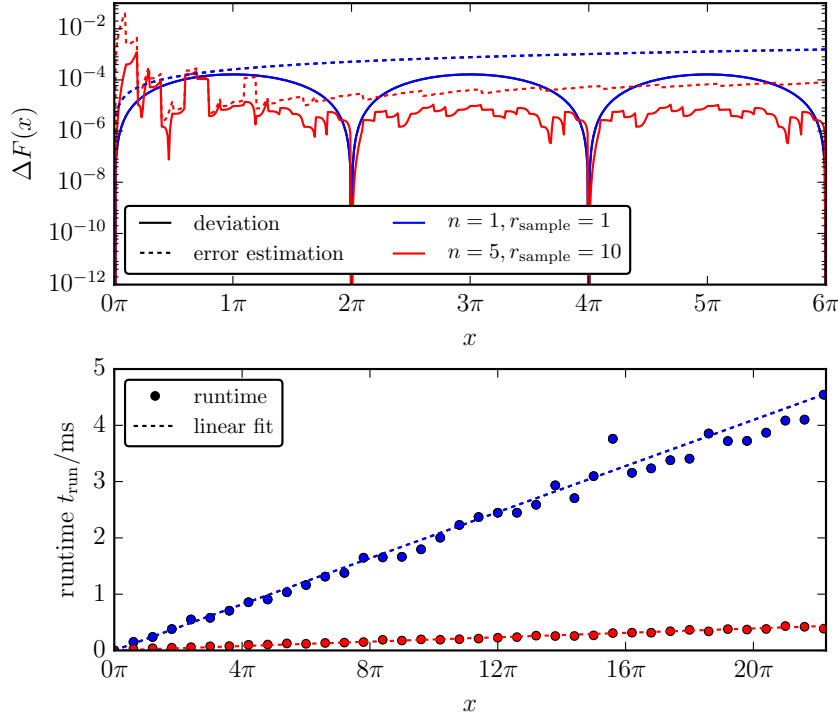
Fig. 19 Comparison between primitive and improved integration: In the top graph, the deviations for $n = 1$, $r_{\text{sample}} = 1$ (blue) and $n = 5$, $r_{\text{sample}} = 10$ (red) are plotted in the same way as in Fig. 17. In the bottom graph, the CPU runtime is shown as a function of x. The dots belong to measured runtimes, whereas the dashed lines correspond to linear fits. For both setups, the step width is $h = \frac{\pi}{100}$.

Obviously, the periodicity of the deviations is due to the periodicity of the test function $f(x) = \sin(x)$. In the lower graph, the actual CPU runtime (dots) is plotted for both setups. The dashed lines correspond to linear fits. One can easily see that the improved algorithm provides a runtime that scales much better than the primitive one. For obvious reasons, the speed-up of the improved algorithm is of the order of the sampling ratio r_{sample}, because only every r_{sample}-th sampling point is used. Thus, in this example, not only the integration quality is improved, but also the CPU runtime scaling is optimized significantly.

5.2 Time propagation algorithms

In this section, for both the full propagation and the time-diagonal propagation according to the GKBA, the respective algorithm for a numerical solution of the equations of motion is described. To start with, there are two more simplifications that are used in this work. Considering the selfenergy in Hartree–Fock approximation of Eq. (60) for the Hubbard case (Eq. (127) and $G_{ij,\alpha\beta}(t,t') = G_{ij,\alpha\alpha}(t,t')\delta_{\alpha,\beta}$),

$$
\begin{aligned}
\Sigma^{\text{HF}}_{ij,\alpha\beta}(z,z') &= -i\hbar\delta_{\mathcal{C}}(z,z') \sum_{k,l}\sum_{\gamma,\delta} \int_{\mathcal{C}} d\bar{z}\, U(z)\delta_{\mathcal{C}}(z,\bar{z})\delta_{i,k}\delta_{i,j}\delta_{i,l}\delta_{\alpha,\beta}\delta_{\gamma,\delta}\bar{\delta}_{\alpha,\gamma}G_{lk,\delta\gamma}(\bar{z},\bar{z}^+) \\
&\quad +i\hbar\sum_{k,l}\sum_{\gamma,\delta} U(z)\delta_{\mathcal{C}}(z,z')\delta_{i,k}\delta_{i,l}\delta_{i,j}\delta_{\alpha,\delta}\delta_{\gamma,\beta}\bar{\delta}_{\alpha,\gamma}\delta_{\delta,\gamma}G_{lk,\delta\gamma}(z,z'^+) \\
&= -i\hbar\delta_{\mathcal{C}}(z,z')\delta_{i,j}\delta_{\alpha,\beta}\sum_{\gamma} U(z)\bar{\delta}_{\alpha,\gamma}G_{ii,\gamma\gamma}(z,z^+) \\
&\quad +i\hbar\delta_{\mathcal{C}}(z,z')\delta_{i,j}\underbrace{\bar{\delta}_{\alpha,\beta}\delta_{\alpha,\beta}}_{=0}U(z)G_{ii,\alpha\beta}(z,z'^+)\,,
\end{aligned}
\tag{169}
$$

one can see that the exchange Fock term cancels again (cf. Eq. (146)). Therefore, one can replace $\Sigma^{\text{HF}}_{ij,\alpha\beta}(z, z') =:$ $\delta_{\mathcal{C}}(z, z')\delta_{i,j}\delta_{\alpha,\beta}\Sigma^{\text{HF},\alpha}_i(z)$, with

$$\Sigma^{\text{HF},\uparrow(\downarrow)}_i(z) = -\mathrm{i}\hbar U(z) G^{\downarrow(\uparrow)}_{ii}(z, z^+)\,. \tag{170}$$

Since this is no longer a two-time quantity, it can be directly written in the real-time space,

$$\Sigma^{\text{HF},\uparrow(\downarrow)}_i(t) = U(t) n^{\downarrow(\uparrow)}_i(t)\,, \tag{171}$$

where $n^\sigma_i(t) := n^\sigma_{ii}(t)$ (cf. Eq. (105)). Due to its very simple structure, it can be accounted by introducing an effective single-particle Hamiltonian,

$$h^{\text{eff}}_{ij,\alpha\beta}(t) = -J\delta_{\langle i,j\rangle}\delta_{\alpha,\beta} + \delta_{i,j}\delta_{\alpha,\beta}U(t)\sum_\gamma \bar\delta_{\alpha,\gamma} n^\gamma_i(t) \tag{172}$$

that can be further simplified by $h^{\text{eff}}_{ij,\alpha\beta}(t) =: h^{\text{eff},\alpha}_{ij}(t)\delta_{\alpha,\beta}$ with

$$h^{\text{eff},\uparrow(\downarrow)}_{ij}(t) = -J\delta_{\langle i,j\rangle} + \delta_{i,j}U(t) n^{\downarrow(\uparrow)}_i(t)\,. \tag{173}$$

Using this modified single-particle Hamiltonian, the new equations of motion of Eqs. (160) and (161) become

$$\sum_l \left[\mathrm{i}\hbar\frac{\mathrm{d}}{\mathrm{d}t}\delta_{i,l} - h^{\text{eff},\sigma}_{il}(t)\right] G^{\sigma,\gtrless}_{lj}(t, t') = \tag{174}$$

$$\sum_l \int^\infty_{t_{\mathrm{s}}} \mathrm{d}\bar t \left\{\Sigma^{\sigma,\text{R}}_{il}(t, \bar t) G^{\sigma,\gtrless}_{lj}(\bar t, t') + \Sigma^{\sigma,\gtrless}_{il}(t, \bar t) G^{\sigma,\text{A}}_{lj}(\bar t, t')\right\}\,,$$

$$\sum_l G^{\sigma,\gtrless}_{il}(t, t') \left[-\mathrm{i}\hbar\frac{\overleftarrow{\mathrm{d}}}{\mathrm{d}t'}\delta_{l,j} - h^{\text{eff},\sigma}_{lj}(t')\right] = \tag{175}$$

$$\sum_l \int^\infty_{t_{\mathrm{s}}} \mathrm{d}\bar t \left\{G^{\sigma,\text{R}}_{il}(t, \bar t)\Sigma^{\sigma,\gtrless}_{lj}(\bar t, t') + G^{\sigma,\gtrless}_{il}(t, \bar t)\Sigma^{\sigma,\text{A}}_{lj}(\bar t, t')\right\}\,,$$

where the selfenergy Σ only contains contributions beyond Hartree–Fock level.

The second simplification concerns the spin subspace. Apparently, neither the Hamiltonian (cf. Eq. (133)) nor Eqs. (174) and (175) provide a special treatment for any spin orientation σ. In other words, if the initial state is symmetric with respect to spin-up ($\uparrow$) and spin-down ($\downarrow$) particles, this symmetry will be retained for all times and spatial positions, i.e.

$$G^{\uparrow,\gtrless}_{ij}(t, t') = G^{\downarrow,\gtrless}_{ij}(t, t') \quad \forall i, j, t, t'\,. \tag{176}$$

Since, in this work, only systems and setups with spin symmetry are studied (cf. Sec. 6), it is convenient to neglect the spin indices and define

$$G^\gtrless_{ij}(t, t') := G^{\uparrow,\gtrless}_{ij}(t, t') = G^{\downarrow,\gtrless}_{ij}(t, t')\,, \tag{177}$$

which only depend on the Hubbard site indices and the times. Consequently, all other quantities can be expressed in a spin-independent way, too.

5.2.1 Computation of the time propagators

For the numerical solution of the propagation problem, it is essential to compute time propagators, to couple quantities of successive time steps (see Sec. 5.2.2). Additionally, those directly enter the evaluation of the Hartree–Fock propagators introduced in Sec. 2.6. The description is based on Ref. [77]. Assuming a time T and a small time step $\Delta \ll 1$, one can define the time propagator to connect T with $T + \Delta$ (cf. Eq. (9)),

$$X_{ij}(T + \Delta, T) \quad := \quad \left[\exp\left(-\frac{\mathrm{i}}{\hbar}\int^{T+\Delta}_T \mathrm{d}\bar t\, h^{\text{eff}}(\bar t)\right)\right]_{ij} \approx \left[\exp\left(-\frac{\mathrm{i}}{\hbar}h^{\text{eff}}(T)\Delta\right)\right]_{ij} =: \mathcal{U}_{ij}(T)\,.$$

Here, h^{eff} is assumed approximately not to change between T and $T + \Delta$. For the other time direction, one obtains

$$
X_{ij}^*(T, T + \Delta) \quad := \quad \left[\exp\left(\frac{\mathrm{i}}{\hbar} \int_{T+\Delta}^{T} \mathrm{d}\bar{t}\, h^{\text{eff}}(\bar{t}) \right) \right]_{ij} \approx \left[\exp\left(-\frac{\mathrm{i}}{\hbar} h^{\text{eff}}(T)\Delta \right) \right]_{ij} = \mathcal{U}_{ij}(T) \, .
$$

To find the matrix elements of the exponential, one can use the fact that the exponential of a diagonal matrix is given by the diagonal matrix of the exponentials of the diagonal elements [78]. Furthermore, for two quadratic, invertible matrices A and B, the relation $\mathrm{e}^{BAB^{-1}} = B\mathrm{e}^{A}B^{-1}$ holds [78]. Therefore, if $\left[-\frac{\mathrm{i}}{\hbar} h^{\text{eff}}(T)\Delta \right]$ is diagonalized by $B \left[-\frac{\mathrm{i}}{\hbar} h^{\text{eff}}(T)\Delta \right] B^{-1} =: D$, the exponential is given by

$$
\mathcal{U}_{ij}(T) = \left[B^{-1} \mathcal{D} \left(\mathrm{e}^{D_{11}}, \mathrm{e}^{D_{22}}, \dots, \mathrm{e}^{D_{N_sN_s}} \right) B \right]_{ij} , \tag{178}
$$

where N_s is the number of Hubbard sites and $\mathcal{D}$ is defined as

$$
\mathcal{D}\left(a_1, a_2, \dots, a_n \right) := \begin{pmatrix} a_1 & 0 & \cdots & 0 \\ 0 & a_2 & \cdots & 0 \\ \vdots & \vdots & \ddots & \vdots \\ 0 & 0 & \cdots & a_n \end{pmatrix} . \tag{179}
$$

In the same manner, one finds that

$$
\mathcal{V}_{ij}(T) := \left[\left(h^{\text{eff}}(T) \right)^{-1} \left(1 - \exp\left(-\frac{\mathrm{i}}{\hbar} h^{\text{eff}}(T)\Delta \right) \right) \right]_{ij} \tag{180}
$$

can be evaluated via

$$
\mathcal{V}_{ij}(T) = \left[B^{-1} \mathcal{D} \left(\frac{1 - \mathrm{e}^{D_{11}}}{D_{11}}, \frac{1 - \mathrm{e}^{D_{22}}}{D_{22}}, \dots, \frac{1 - \mathrm{e}^{D_{N_sN_s}}}{D_{N_sN_s}} \right) B \right]_{ij} . \tag{181}
$$

The propagation quantities $\mathcal{U}$ and $\mathcal{V}$ are both used in Sec. 5.2.2. By comparison with Eq. (122), one finds that the Hartree–Fock propagators can be expressed via

$$
G_{ij}^{\text{HF,R}}(t_1, t_2) = -\mathrm{i}\Theta(t_1, t_2) X_{ij}(t_1, t_2), \qquad G_{ij}^{\text{HF,A}}(t_1, t_2) = +\mathrm{i}\Theta(t_2, t_1) X_{ij}(t_1, t_2). \tag{182}
$$

In the propagation scheme using the GKBA, they are evaluated for $X_{ij}(\bar{t}, T)$ with $\bar{t} \leq T$. This quantity can be transformed as

$$
\begin{aligned}
X_{ij}(\bar{t}, T) &= \left[\exp\left(-\frac{\mathrm{i}}{\hbar} \int_{T}^{\bar{t}} \mathrm{d}t\, h^{\text{eff}}(t) \right) \right]_{ij} \\
&= \left[\exp\left(\frac{\mathrm{i}}{\hbar} \int_{\bar{t}}^{T-\Delta} \mathrm{d}t\, h^{\text{eff}}(t) + \frac{\mathrm{i}}{\hbar} \int_{T-\Delta}^{T} \mathrm{d}t\, h^{\text{eff}}(t) \right) \right]_{ij} \\
&= \left[\exp\left(-\frac{\mathrm{i}}{\hbar} \int_{T-\Delta}^{\bar{t}} \mathrm{d}t\, h^{\text{eff}}(t) \right) \exp\left(\frac{\mathrm{i}}{\hbar} h^{\text{eff}}(T)\Delta \right) \right]_{ij} + \mathcal{O}\left(\Delta^2 \right) \\
&\approx \sum_k X_{ik}(\bar{t}, T - \Delta) \mathcal{U}_{kj}^*(T) .
\end{aligned} \tag{183}
$$

Here, again, $\Delta \ll 1$ is assumed. By this scheme, it can be avoided to diagonalize for every $\bar{t}$ in each propagation step T. Furthermore, by iterative insertion of Eq. (183), the time ordering is fulfilled, which is essential for the algorithm.

5.2.2 Time-stepping algorithm

To find an algorithm to propagate the equations of motion of Eqs. (174) and (175), one needs to compute the expressions appearing in the collision integral that contain the selfenergy. If one writes the Kadanoff–Baym equations as

$$\sum_l \left[i\hbar \frac{d}{dt}\delta_{i,l} - h_{il}^{\text{eff}}(t) \right] G_{lj}^<(t,t') \;=\; I_{ij}^{(1),<}(t,t'), \tag{184}$$

$$\sum_l G_{il}^>(t,t') \left[-i\hbar \frac{\overleftarrow{d}}{dt'}\delta_{l,j} - h_{lj}^{\text{eff}}(t') \right] \;=\; I_{ij}^{(2),>}(t,t'), \tag{185}$$

the collision integrals $I^{(1),<}$ and $I^{(2),>}$ obey

$$
\begin{aligned}
I_{ij}^{(1),<}(t,t') &:= \sum_l \int_{t_{\text{s}}}^\infty d\bar{t} \left\{ \Sigma_{il}^{\text{R}}(t,\bar{t}) G_{lj}^<(\bar{t},t') + \Sigma_{il}^<(t,\bar{t}) G_{lj}^{\text{A}}(\bar{t},t') \right\}, \\
I_{ij}^{(2),>}(t,t') &:= \sum_l \int_{t_{\text{s}}}^\infty d\bar{t} \left\{ G_{il}^{\text{R}}(t,\bar{t}) \Sigma_{lj}^>(\bar{t},t') + G_{il}^>(t,\bar{t}) \Sigma_{lj}^{\text{A}}(\bar{t},t') \right\}.
\end{aligned}
\tag{186}
$$

It should be noted that the relations above are formulated for special cases. Due to the relation of Eq. (104), i.e. $G_{ij}^{\gtrless}(t,t') = -\left[G_{ji}^{\gtrless}(t',t) \right]^*$, one only needs to solve one equation per real-time component. Furthermore, it is sufficient to compute $I_{ij}^{(1),<}(t,t')$ for $t < t'$ (denoted as $I_{ij}^{(1),<}(t < t')$) and $I_{ij}^{(2),>}(t,t')$ for $t > t'$ (denoted as $I_{ij}^{(2),>}(t > t')$). The Green function for switched time arguments is obtained from the symmetry relation.

Following Ref. [64], for given $G_{ij}^<(t < T)$, $G_{ij}^>(T > t')$ and $G_{ij}^<(T,T)$, the values after a small time step Δ can be obtained in a simple scheme via three propagation equations that agree with Eqs. (184) and (185),

$$G_{ij}^<(t < T+\Delta) \;=\; \sum_l \left\{ G_{il}^<(t < T)\mathcal{U}_{jl}^*(T) - I_{il}^{(1),<}(t < T)\mathcal{V}_{jl}^*(T) \right\}, \tag{187}$$

$$G_{ij}^>(T+\Delta > t') \;=\; \sum_l \left\{ \mathcal{U}_{il}(T) G_{lj}^>(T > t') - \mathcal{V}_{il}(T) I_{lj}^{(2),>}(T > t') \right\}, \tag{188}$$

$$G_{ij}^<(T+\Delta, T+\Delta) \;=\; \sum_{lm} \left\{ \mathcal{U}_{il}(T) \left[G_{lm}^<(T,T) + \mathcal{W}_{lm}(T) \right] \mathcal{U}_{jm}^*(T) \right\}, \tag{189}$$

where

$$
\begin{aligned}
&\mathcal{W}_{lm}(T) := \sum_{n=0}^\infty w_{lm}^{(n)}(T), \qquad w_{lm}^{(n)}(T) := \frac{i\Delta}{n+1} \left[\left[h^{\text{eff}}(T), w^{(n-1)}(T) \right]_- \right]_{lm}, \\
&w_{lm}^{(0)}(T) := i\Delta \left(I_{lm}^{(1),<}(T,T) - I_{lm}^{(2),>}(T,T) \right)
\end{aligned}
\tag{190}
$$

and $\mathcal{U}, \mathcal{V}$ are obtained from Eqs. (178) and (181). These equations are provided by an explicit Euler integration [65]. In Sec. 5.1, it has been shown that for the numerical evaluation of integrals, not every sampling point must be used. In Eqs. (187) and (188), t and t' denote times with a larger time step, i.e. $t_{i+1} - t_i = r_{\text{sample}}\Delta$. This procedure also allows to store the Green function only for times t, t'. In $\mathcal{W}$, the summation can be truncated at any n, leading to an error of the order $\mathcal{O}(\Delta^{n+2})$. In this work, only the leading term is considered. The three propagation equations lead to a simple, causal propagation stepping scheme that is illustrated in Fig. 20. Starting from $G^{\gtrless}(t_{\text{s}}, t_{\text{s}})$, one can consecutively obtain $G^{\gtrless}$ in the full two-time plane.

Due to their appearance in Eqs. (187) and (188), one has to express the collision integral contributions of Eq. (186) only in terms of $G_{ij}^<(t_1 < t_2)$ and $G_{ij}^>(t_1 > t_2)$. By replacing the retarded and advanced components by

their definition in Eq. (100), one has

$$
\begin{aligned}
I_{il}^{(1),<}(\mathfrak{t} < T) &:= \sum_k G_{ik}^{\delta}(\mathfrak{t}) \Sigma_{kl}^{<}(\mathfrak{t} < T) - \sum_k G_{ik}^{<}(\mathfrak{t} < T) \Sigma_{kl}^{\delta}(T) \\
&\quad + \int_{t_s}^{\mathfrak{t}} d\bar{\mathfrak{t}} \sum_k \left\{ \left(G_{ik}^{>}(\mathfrak{t} > \bar{\mathfrak{t}}) - G_{ik}^{<}(\mathfrak{t} > \bar{\mathfrak{t}}) \right) \Sigma_{kl}^{<}(\bar{\mathfrak{t}} < T) \right\} \\
&\quad + \int_{t_s}^{T} d\bar{\mathfrak{t}} \sum_k \left\{ G_{ik}^{<}(\mathfrak{t}, \bar{\mathfrak{t}}) \left(\Sigma_{kl}^{<}(\bar{\mathfrak{t}} < T) - \Sigma_{kl}^{>}(\bar{\mathfrak{t}} < T) \right) \right\}, \\
I_{lj}^{(2),>}(T > \mathfrak{t}') &:= \sum_k \Sigma_{lk}^{\delta}(T) G_{kj}^{>}(T > \mathfrak{t}') - \sum_k \Sigma_{lk}^{>}(T > \mathfrak{t}') G_{kj}^{\delta}(\mathfrak{t}') \\
&\quad + \int_{t_s}^{T} d\bar{\mathfrak{t}} \sum_k \left\{ \left(\Sigma_{lk}^{>}(T > \bar{\mathfrak{t}}) - \Sigma_{lk}^{<}(T > \bar{\mathfrak{t}}) \right) G_{kj}^{>}(\bar{\mathfrak{t}}, \mathfrak{t}') \right\} \\
&\quad + \int_{t_s}^{\mathfrak{t}'} d\bar{\mathfrak{t}} \sum_k \left\{ \Sigma_{lk}^{>}(T > \bar{\mathfrak{t}}) \left(G_{kj}^{<}(\bar{\mathfrak{t}} < \mathfrak{t}') - G_{kj}^{>}(\bar{\mathfrak{t}} < \mathfrak{t}') \right) \right\}.
\end{aligned}
\tag{191}
$$

The time-diagonal component Σ^{δ} can always be expressed in terms of G^{δ} which is equal to zero as already mentioned in Sec. 2.5. Therefore, the first lines of Eq. (191) vanish. In order to force the time order, one can split the integration, yielding

$$
\begin{aligned}
I_{il}^{(1),<}(\mathfrak{t} < T) &= \int_{t_s}^{\mathfrak{t}} d\bar{\mathfrak{t}} \sum_k \left\{ \left(G_{ik}^{>}(\mathfrak{t} > \bar{\mathfrak{t}}) - G_{ik}^{<}(\mathfrak{t} > \bar{\mathfrak{t}}) \right) \Sigma_{kl}^{<}(\bar{\mathfrak{t}} < T) \right\} \\
&\quad + \int_{t_s}^{\mathfrak{t}} d\bar{\mathfrak{t}} \sum_k \left\{ G_{ik}^{<}(\mathfrak{t} > \bar{\mathfrak{t}}) \left(\Sigma_{kl}^{<}(\bar{\mathfrak{t}} < T) - \Sigma_{kl}^{>}(\bar{\mathfrak{t}} < T) \right) \right\} \\
&\quad + \int_{\mathfrak{t}}^{T} d\bar{\mathfrak{t}} \sum_k \left\{ G_{ik}^{<}(\mathfrak{t} < \bar{\mathfrak{t}}) \left(\Sigma_{kl}^{<}(\bar{\mathfrak{t}} < T) - \Sigma_{kl}^{>}(\bar{\mathfrak{t}} < T) \right) \right\}, \\
I_{lj}^{(2),>}(T > \mathfrak{t}') &= \int_{t_s}^{\mathfrak{t}'} d\bar{\mathfrak{t}} \sum_k \left\{ \left(\Sigma_{lk}^{>}(T > \bar{\mathfrak{t}}) - \Sigma_{lk}^{<}(T > \bar{\mathfrak{t}}) \right) G_{kj}^{>}(\bar{\mathfrak{t}} < \mathfrak{t}') \right\} \\
&\quad \int_{\mathfrak{t}'}^{T} d\bar{\mathfrak{t}} \sum_k \left\{ \left(\Sigma_{lk}^{>}(T > \bar{\mathfrak{t}}) - \Sigma_{lk}^{<}(T > \bar{\mathfrak{t}}) \right) G_{kj}^{>}(\bar{\mathfrak{t}} > \mathfrak{t}') \right\} \\
&\quad + \int_{t_s}^{\mathfrak{t}'} d\bar{\mathfrak{t}} \sum_k \left\{ \Sigma_{lk}^{>}(T > \bar{\mathfrak{t}}) \left(G_{kj}^{<}(\bar{\mathfrak{t}} < \mathfrak{t}') - G_{kj}^{>}(\bar{\mathfrak{t}} < \mathfrak{t}') \right) \right\}.
\end{aligned}
\tag{192}
$$

Cancelling out the terms appearing twice leads to

$$
\begin{aligned}
I_{il}^{(1),<}(\mathfrak{t} < T) &= \int_{t_s}^{\mathfrak{t}} d\bar{\mathfrak{t}} \sum_k \left\{ G_{ik}^{>}(\mathfrak{t} > \bar{\mathfrak{t}}) \Sigma_{kl}^{<}(\bar{\mathfrak{t}} < T) - G_{ik}^{<}(\mathfrak{t} > \bar{\mathfrak{t}}) \Sigma_{kl}^{>}(\bar{\mathfrak{t}} < T) \right\} \\
&\quad + \int_{\mathfrak{t}}^{T} d\bar{\mathfrak{t}} \sum_k \left\{ G_{ik}^{<}(\mathfrak{t} < \bar{\mathfrak{t}}) \Sigma_{kl}^{<}(\bar{\mathfrak{t}} < T) - G_{ik}^{<}(\mathfrak{t} < \bar{\mathfrak{t}}) \Sigma_{kl}^{>}(\bar{\mathfrak{t}} < T) \right\}, \\
I_{lj}^{(2),>}(T > \mathfrak{t}') &= \int_{t_s}^{\mathfrak{t}'} d\bar{\mathfrak{t}} \sum_k \left\{ \Sigma_{lk}^{>}(T > \bar{\mathfrak{t}}) G_{kj}^{<}(\bar{\mathfrak{t}} < \mathfrak{t}') - \Sigma_{lk}^{<}(T > \bar{\mathfrak{t}}) G_{kj}^{>}(\bar{\mathfrak{t}} < \mathfrak{t}') \right\} \\
&\quad + \int_{\mathfrak{t}'}^{T} d\bar{\mathfrak{t}} \sum_k \left\{ \Sigma_{lk}^{>}(T > \bar{\mathfrak{t}}) G_{kj}^{<}(\bar{\mathfrak{t}} < \mathfrak{t}') - \Sigma_{lk}^{>}(T > \bar{\mathfrak{t}}) G_{kj}^{>}(\bar{\mathfrak{t}} < \mathfrak{t}') \right\}.
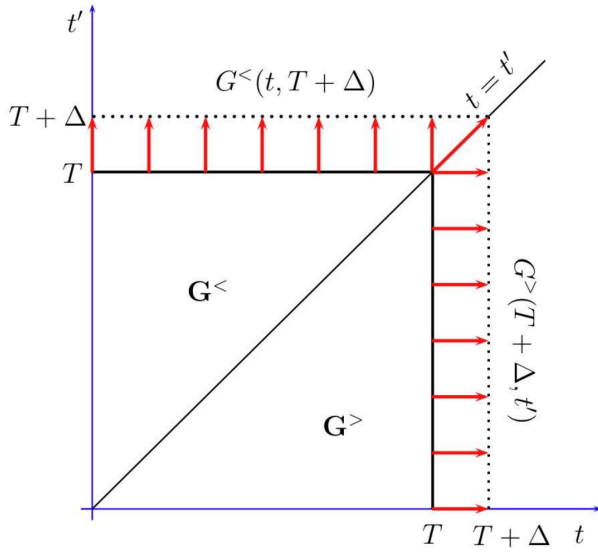\end{aligned}
\tag{193}
$$

Fig. 20 Propagation stepping overview: The three directions of propagation are illustrated in the two-time plane. The upper left propagation for $G^<$ corresponds to Eq. (187), while the lower right propagation for $G^>$ corresponds to Eq. (188). The time diagonal time stepping is given by Eq. (189). The graphic is taken from Ref. [64].

By using the symmetry relations of Eq. (104), one arrives at

$$
\begin{aligned}
I_{il}^{(1),<}(\mathfrak{t} < T) = &\int_{t_s}^{\mathfrak{t}} d\bar{\mathfrak{t}} \sum_k \left\{ G_{ik}^>(\mathfrak{t} > \bar{\mathfrak{t}}) \Sigma_{kl}^<(\bar{\mathfrak{t}} < T) - \left(G_{ki}^<(\bar{\mathfrak{t}} < \mathfrak{t}) \Sigma_{lk}^>(T > \bar{\mathfrak{t}}) \right)^* \right\} \\
&+ \int_{\mathfrak{t}}^{T} d\bar{\mathfrak{t}} \sum_k \left\{ G_{ik}^<(\mathfrak{t} < \bar{\mathfrak{t}}) \Sigma_{kl}^<(\bar{\mathfrak{t}} < T) + G_{ik}^<(\mathfrak{t} < \bar{\mathfrak{t}}) \left(\Sigma_{lk}^>(T > \bar{\mathfrak{t}}) \right)^* \right\},
\end{aligned}
$$

$$
\begin{aligned}
I_{lj}^{(2),>}(T > \mathfrak{t}') = &\int_{t_s}^{\mathfrak{t}'} d\bar{\mathfrak{t}} \sum_k \left\{ \Sigma_{lk}^>(T > \bar{\mathfrak{t}}) G_{kj}^<(\bar{\mathfrak{t}} < \mathfrak{t}') - \left(\Sigma_{kl}^<(\bar{\mathfrak{t}} < T) G_{jk}^>(\mathfrak{t}' > \bar{\mathfrak{t}}) \right)^* \right\} \\
&+ \int_{\mathfrak{t}'}^{T} d\bar{\mathfrak{t}} \sum_k \left\{ \Sigma_{lk}^>(T > \bar{\mathfrak{t}}) G_{kj}^<(\bar{\mathfrak{t}} < \mathfrak{t}') + \Sigma_{lk}^>(T > \bar{\mathfrak{t}}) \left(G_{jk}^>(\mathfrak{t}' > \bar{\mathfrak{t}}) \right)^* \right\},
\end{aligned}
\tag{194}
$$

which only depends on quantities of known time order. Therefore, the propagation is closed, if $\Sigma_{ij}^<(t_1 < t_2)$ and $\Sigma_{ij}^>(t_1 > t_2)$ only depend on $G_{ij}^<(t_1 < t_2)$ and $G_{ij}^>(t_1 > t_2)$.

For the time-diagonal time stepping in Eq. (189), in a similar manner, one obtains

$$
\begin{aligned}
I_{il}^{(1),<}(T,T) &= \int_{t_s}^{T} d\bar{\mathfrak{t}} \sum_k \left\{ G_{ik}^>(T > \bar{\mathfrak{t}}) \Sigma_{kl}^<(\bar{\mathfrak{t}} < T) - \left(G_{ki}^<(\bar{\mathfrak{t}} < T) \Sigma_{lk}^>(T > \bar{\mathfrak{t}}) \right)^* \right\}, \\
I_{lj}^{(2),>}(T,T) &= \int_{t_s}^{T} d\bar{\mathfrak{t}} \sum_k \left\{ \Sigma_{lk}^>(T > \bar{\mathfrak{t}}) G_{kj}^<(\bar{\mathfrak{t}} < T) - \left(\Sigma_{kl}^<(\bar{\mathfrak{t}} < T) G_{jk}^>(T > \bar{\mathfrak{t}}) \right)^* \right\} \\
&= - \left(I_{jl}^{(1),<}(T,T) \right)^*,
\end{aligned}
\tag{195}
$$

leading to $G_{ij}^<(T+\Delta,\, T+\Delta)$. The value for $G_{ij}^>(T+\Delta,\, T+\Delta)$ can be obtained by the symmetry on the time diagonal of Eq. (106).

In the case of the GKBA, one only needs to propagate along the time diagonal, i.e. one needs to solve Eqs. (189), (190) and (195). The Green functions on the full two-time plane can be reconstructed via (cf. Eqs. (120) and (182))

$$
\begin{aligned}
G_{ij}^<(\mathfrak{t} < T) &= \hbar \sum_k G_{ik}^<(\mathfrak{t},\mathfrak{t}) X_{kj}(\mathfrak{t} < T), \\
G_{ij}^>(T > \mathfrak{t}') &= \hbar \sum_k \left(X_{ki}(\mathfrak{t}' < T) \right)^* G_{kj}^>(\mathfrak{t}',\mathfrak{t}'),
\end{aligned}
\tag{196}
$$

where $t_1, t_2 \in \{T, \mathfrak{t}, \mathfrak{t}', \bar{\mathfrak{t}}\}$.

5.2.3   Calculation of the selfenergy

The validity of the propagation stepping scheme from the last section crucially depends on the correct evaluation of the selfenergy. Due to the appearance in Eqs. (194) and (195), Σ is only required for $\Sigma_{kl}^<(\bar{t} < T)$ and $\Sigma_{lk}^>(T > \bar{t})$. In the case of the T-matrix selfenergy of Eq. (159), one arrives at

$$
\begin{aligned}
\Sigma_{kl}^{T,<}(\bar{t} < T) &= i\hbar T_{kl}^<(\bar{t} < T) G_{lk}^>(T > \bar{t}) \\
\Sigma_{lk}^{T,>}(T > \bar{t}) &= -i\hbar \left(T_{kl}^>(\bar{t} < T) \right)^* G_{kl}^<(\bar{t} < T).
\end{aligned}
\tag{197}
$$

Here, the symmetry relation for the T-matrix of Eq. (104) is applied[15]. The T-matrix is given by (cf. Eq. (157))

$$
\begin{aligned}
T_{kl}^{\gtrless}(\bar{t} < T) = &- U(\bar{t}) \Phi_{kl}^{\gtrless}(\bar{t} < T) U(T) \\
&+ \sum_m \int_{t_s}^{\bar{t}} d\bar{t}_2\, U(\bar{t}) \Phi_{km}^R(\bar{t} > \bar{t}_2) T_{ml}^{\gtrless}(\bar{t}_2 < T) \\
&+ \sum_m \int_{t_s}^{T} d\bar{t}_2\, U(\bar{t}) \Phi_{km}^{\gtrless}(\bar{t}, \bar{t}_2) T_{ml}^A(\bar{t}_2 < T).
\end{aligned}
\tag{198}
$$

Again, by splitting the integration, one can find a form in which every time order is unique,

$$
\begin{aligned}
T_{kl}^<(\bar{t} < T) = &- U(\bar{t}) \Phi_{kl}^<(\bar{t} < T) U(T) \\
&+ \sum_m \int_{t_s}^{\bar{t}} d\bar{t}_2\, U(\bar{t}) \Phi_{km}^R(\bar{t} > \bar{t}_2) T_{ml}^<(\bar{t}_2 < T) \\
&- \sum_m \int_{t_s}^{\bar{t}} d\bar{t}_2\, U(\bar{t}) \left(\Phi_{mk}^<(\bar{t}_2 < \bar{t}) \right)^* T_{ml}^A(\bar{t}_2 < T) \\
&+ \sum_m \int_{\bar{t}}^{T} d\bar{t}_2\, U(\bar{t}) \Phi_{km}^<(\bar{t} < \bar{t}_2) T_{ml}^A(\bar{t}_2 < T), \\
T_{kl}^>(\bar{t} < T) = &\, U(\bar{t}) \left(\Phi_{lk}^>(T > \bar{t}) \right)^* U(T) \\
&+ \sum_m \int_{t_s}^{\bar{t}} d\bar{t}_2\, U(\bar{t}) \Phi_{km}^R(\bar{t} > \bar{t}_2) T_{ml}^>(\bar{t}_2 < T) \\
&+ \sum_m \int_{t_s}^{\bar{t}} d\bar{t}_2\, U(\bar{t}) \Phi_{km}^>(\bar{t} > \bar{t}_2) T_{ml}^A(\bar{t}_2 < T) \\
&- \sum_m \int_{\bar{t}}^{T} d\bar{t}_2\, U(\bar{t}) \left(\Phi_{mk}^>(\bar{t}_2 > \bar{t}) \right)^* T_{ml}^A(\bar{t}_2 < T).
\end{aligned}
\tag{199}
$$

For the contour quantity of the Hartree Green function, one has, cf. Eq. (158),

$$
\begin{aligned}
\left(\Phi_{mk}^<(\bar{t}_2 < \bar{t}) \right)^* &= (i\hbar)^* \left(G_{mk}^<(\bar{t}_2 < \bar{t}) \right)^* \left(G_{mk}^<(\bar{t}_2 < \bar{t}) \right)^* \\
&= (-i\hbar) \left(-G_{km}^<(\bar{t} > \bar{t}_2) \right) \left(-G_{km}^<(\bar{t} > \bar{t}_2) \right) = -\Phi_{km}^<(\bar{t} > \bar{t}_2),
\end{aligned}
$$

which is used in Eq. (199). The retarded and advanced components of Φ can also be obtained from Eq. (158),

$$
\begin{aligned}
\Phi_{ij}^R(t > t') &= i\hbar\Theta(t, t') \left[G_{ij}^>(t > t') G_{ij}^>(t > t') - \left(G_{ji}^<(t' < t) \right)^* \left(G_{ji}^<(t' < t) \right)^* \right], \\
\Phi_{ij}^A(t < t') &= i\hbar\Theta(t', t) \left[G_{ij}^<(t < t') G_{ij}^<(t < t') - \left(G_{ji}^>(t' > t) \right)^* \left(G_{ji}^>(t' > t) \right)^* \right].
\end{aligned}
\tag{200}
$$

Both components of the T-matrix—less and greater—depend on $T_{ml}^A(\bar{t}_2 < T)$. From Eq. (156), one gets

$$
\begin{aligned}
T_{ml}^A(\bar{t}_2 < T) = &- U(\bar{t}_2) \Phi_{ml}^A(\bar{t}_2 < T) U(T) \\
&+ \sum_n \int_{\bar{t}_2}^{T} d\bar{t}_3\, U(\bar{t}_2) \Phi_{mn}^A(\bar{t}_2 < \bar{t}_3) T_{nl}^A(\bar{t}_3 < T).
\end{aligned}
\tag{201}
$$

---

[15] It should be noted that $T_{kl}^>(\bar{t} < T)$ is used instead of $T_{lk}^>(T > \bar{t})$. This is advantageous in the following transformations.

At this point, all appearing quantities are already contained in the propagation approach. The T-matrix, however, depends on itself in all components. Therefore, one has to develop a scheme to solve the equations iteratively. As a starting point, the advanced T-matrix is a convenient choice, since it only depends on G, U and itself. The time-diagonal value can immediately be found,

$$T_{ml}^{\mathrm{A}}(T,T) = -U(T)\Phi_{ml}^{\mathrm{A}}(T,T)U(T)\,, \tag{202}$$

since the integral term vanishes. Let $\bar{\Delta} := r_{\mathrm{sample}}\Delta$ be the enlarged time step due to the integration scheme of Sec. 5.1. To ensure that, in each propagation step, the same sampling points are used, one has to compute $T_{ml}^{\mathrm{A}}(\mathfrak{t}^{\max} < T)$ first, with $\mathfrak{t}^{\max} := \lfloor \frac{T}{r_{\mathrm{sample}}} \rfloor r_{\mathrm{sample}}$. Therefore, one can set $\mathfrak{T} = \mathfrak{t}^{\max}$ and solve

$$
\begin{aligned}
T_{ml}^{\mathrm{A},(N+1)}(\mathfrak{T} < T) \;=\; & -U(\mathfrak{T})\Phi_{ml}^{\mathrm{A}}(\mathfrak{T} < T)U(T) \\
& + \sum_n \int_{\mathfrak{T}}^{T} \mathrm{d}\bar{\mathfrak{t}}_3\, U(\mathfrak{T})\Phi_{mn}^{\mathrm{A}}(\mathfrak{T} < \bar{\mathfrak{t}}_3)T_{nl}^{\mathrm{A},(N)}(\bar{\mathfrak{t}}_3 < T)
\end{aligned}
\tag{203}
$$

via numerical integration. In doing so, the sampling points for $T_{ml}^{\mathrm{A}}(T,T)$ and $T_{nl}^{\mathrm{A},(N)}(\mathfrak{T} < T)$ appear. The first is already obtained from Eq. (202) and the latter can be solved by iteration over N. Let $\epsilon \ll 1$ be a threshold accuracy. One can consider the iteration process converged if

$$\sum_{ml} \left| T_{ml}^{\mathrm{A},(N)}(\mathfrak{T} < T) - T_{ml}^{\mathrm{A},(N-1)}(\mathfrak{T} < T) \right| < \epsilon\,. \tag{204}$$

For the next time step, $\mathfrak{T}$ is set to $\mathfrak{T} \rightarrow \mathfrak{T} - \bar{\Delta}$ and, again, Eq. (204) is solved by iteration. This scheme has to be continued until $\mathfrak{T} = t_{\mathrm{s}}$.

A very similar process can be applied to the less and greater components of the T-matrix. Starting from

$$
\begin{aligned}
T_{kl}^{<}(t_{\mathrm{s}} < T) = & -U(t_{\mathrm{s}})\Phi_{kl}^{<}(t_{\mathrm{s}} < T)U(T) \\
& + \sum_m \int_{t_{\mathrm{s}}}^{T} \mathrm{d}\bar{\mathfrak{t}}_2\, U(t_{\mathrm{s}})\Phi_{km}^{<}(t_{\mathrm{s}} < \bar{\mathfrak{t}}_2)T_{ml}^{\mathrm{A}}(\bar{\mathfrak{t}}_2 < T)\,, \\
T_{kl}^{>}(t_{\mathrm{s}} < T) = & \,U(t_{\mathrm{s}})\left(\Phi_{lk}^{>}(T > t_{\mathrm{s}})\right)^{*} U(T) \\
& - \sum_m \int_{t_{\mathrm{s}}}^{T} \mathrm{d}\bar{\mathfrak{t}}_2\, U(t_{\mathrm{s}})\left(\Phi_{mk}^{>}(\bar{\mathfrak{t}}_2 > t_{\mathrm{s}})\right)^{*} T_{ml}^{\mathrm{A}}(\bar{\mathfrak{t}}_2 < T)\,,
\end{aligned}
\tag{205}
$$

one can set $\mathfrak{T} = t_{\mathrm{s}} + \bar{\Delta}$ and iterate the following equations,

$$
\begin{aligned}
T_{kl}^{<,(N+1)}(\mathfrak{T} < T) = & -U(\mathfrak{T})\Phi_{kl}^{<}(\mathfrak{T} < T)U(T) \\
& + \sum_m \int_{t_{\mathrm{s}}}^{\mathfrak{T}} \mathrm{d}\bar{\mathfrak{t}}_2\, U(\mathfrak{T})\Phi_{km}^{\mathrm{R}}(\mathfrak{T} > \bar{\mathfrak{t}}_2)T_{ml}^{<,(N)}(\bar{\mathfrak{t}}_2 < T) \\
& - \sum_m \int_{t_{\mathrm{s}}}^{\mathfrak{T}} \mathrm{d}\bar{\mathfrak{t}}_2\, U(\mathfrak{T})\left(\Phi_{mk}^{<}(\bar{\mathfrak{t}}_2 < \mathfrak{T})\right)^{*} T_{ml}^{\mathrm{A}}(\bar{\mathfrak{t}}_2 < T) \\
& + \sum_m \int_{\mathfrak{T}}^{T} \mathrm{d}\bar{\mathfrak{t}}_2\, U(\mathfrak{T})\Phi_{km}^{<}(\mathfrak{T} < \bar{\mathfrak{t}}_2)T_{ml}^{\mathrm{A}}(\bar{\mathfrak{t}}_2 < T)\,, \\
T_{kl}^{>,(N+1)}(\mathfrak{T} < T) = & \,U(\mathfrak{T})\left(\Phi_{lk}^{>}(T > \mathfrak{T})\right)^{*} U(T) \\
& + \sum_m \int_{t_{\mathrm{s}}}^{\mathfrak{T}} \mathrm{d}\bar{\mathfrak{t}}_2\, U(\mathfrak{T})\Phi_{km}^{\mathrm{R}}(\mathfrak{T} > \bar{\mathfrak{t}}_2)T_{ml}^{>,(N)}(\bar{\mathfrak{t}}_2 < T) \\
& + \sum_m \int_{t_{\mathrm{s}}}^{\mathfrak{T}} \mathrm{d}\bar{\mathfrak{t}}_2\, U(\mathfrak{T})\Phi_{km}^{>}(\mathfrak{T} > \bar{\mathfrak{t}}_2)T_{ml}^{\mathrm{A}}(\bar{\mathfrak{t}}_2 < T) \\
& - \sum_m \int_{\mathfrak{T}}^{T} \mathrm{d}\bar{\mathfrak{t}}_2\, U(\mathfrak{T})\left(\Phi_{mk}^{>}(\bar{\mathfrak{t}}_2 > \mathfrak{T})\right)^{*} T_{ml}^{\mathrm{A}}(\bar{\mathfrak{t}}_2 < T)\,,
\end{aligned}
\tag{206}
$$

until $T^{\gtrless}$ is converged, i.e.

$$
\sum_{kl} \left| T_{kl}^{\gtrless,(N)}(\mathfrak{T} < T) - T_{kl}^{\gtrless,(N-1)}(\mathfrak{T} < T) \right| < \epsilon \,. \tag{207}
$$

Subsequently, $\mathfrak{T}$ is set to $\mathfrak{T} \to \mathfrak{T} + \bar{\Delta}$ to proceed with Eq. (206). This scheme has to be continued, until $\mathfrak{T} = \mathfrak{t}^{\max}$. In the final step, $\mathfrak{T}$ is set to $\mathfrak{T} \to T$ and, again, Eq. (206) has to be iterated.

In this way, the less and greater components of the T-matrix can be computed, leading to a selfenergy according to Eq. (197) that can be included in the collision integral, as shown in Sec. 5.2.2. Finally, it should be noted that the second order Born approximation is recovered, if $T^<$ and $T^>$ are set equal to the first lines in Eq. (206).

5.2.4　Overview of propagation algorithms

Bringing the considerations of the last three sections together, there are several important quantities and computation steps that have to be regarded in each propagation step. If the quantities are only used in the full two-time propagation, the step is shown in blue and for quantities that are merely used for the GKBA, the step is shown in red. Mutual steps are shown in black.

- compute $\mathcal{U}(T)$ from $G^<(\mathfrak{t},\mathfrak{t})$, $\mathfrak{t} \in \left\{ t_\mathrm{s}, t_\mathrm{s} + \bar{\Delta}, \ldots, \mathfrak{t}^{\max} \right\}$ according to Eq. (178)

- compute $\mathcal{V}(T)$ from $G^<(\mathfrak{t},\mathfrak{t})$, $\mathfrak{t} \in \left\{ t_\mathrm{s}, t_\mathrm{s} + \bar{\Delta}, \ldots, \mathfrak{t}^{\max} \right\}$ according to Eq. (181)

- compute $X(\mathfrak{t},T)$ from $\mathcal{U}(T)$ for all $\mathfrak{t} \in \left\{ t_\mathrm{s}, t_\mathrm{s} + \bar{\Delta}, \ldots, \mathfrak{t}^{\max} \right\}$ according to Eq. (183)

- compute $G^<(\mathfrak{t} < T)$ and $G^>(T > \mathfrak{t})$ from $X(\mathfrak{t},T)$ for all $\mathfrak{t} \in \left\{ t_\mathrm{s}, t_\mathrm{s} + \bar{\Delta}, \ldots, \mathfrak{t}^{\max} \right\}$ according to Eq. (196)

- compute $T^\mathrm{A}(\mathfrak{T} < T)$ iteratively for $\mathfrak{T} \in \left\{ T, \mathfrak{t}^{\max}, \mathfrak{t}^{\max} - \bar{\Delta}, \ldots, t_\mathrm{s} \right\}$ from $G^{\gtrless}$ according to Eq. (204)

- compute $T^{\gtrless}(\mathfrak{T} < T)$ iteratively for $\mathfrak{T} \in \left\{ t_\mathrm{s}, t_\mathrm{s} + \bar{\Delta}, \ldots, \mathfrak{t}^{\max}, T \right\}$ from $T^\mathrm{A}(\mathfrak{T} < T)$ and $G^{\gtrless}$ according to Eq. (206)

- compute $\Sigma^{T,<}(\bar{\mathfrak{t}} < T)$ and $\Sigma^{T,>}(T > \bar{\mathfrak{t}})$ for $\bar{\mathfrak{t}} \in \left\{ t_\mathrm{s}, t_\mathrm{s} + \bar{\Delta}, \ldots, \mathfrak{t}^{\max}, T \right\}$ from $G^<(\bar{\mathfrak{t}} < T)$, $G^>(T > \bar{\mathfrak{t}})$ and $T^{\gtrless}(\mathfrak{T} < T)$ according to Eq. (197)

- compute the collision integrals $I^{(1),<}(\mathfrak{t} < T)$ and $I^{(2),>}(T > \mathfrak{t}')$ for $\mathfrak{t}, \mathfrak{t}' \in \left\{ t_\mathrm{s}, t_\mathrm{s} + \bar{\Delta}, \ldots, \mathfrak{t}^{\max} \right\}$ from $\Sigma^{T,<}(\bar{\mathfrak{t}} < T)$, $\Sigma^{T,>}(T > \bar{\mathfrak{t}})$ and $G^{\gtrless}$ according to Eq. (194)

- compute the collision integral $I^{(1),<}(T,T)$ from $\Sigma^{T,<}(\bar{\mathfrak{t}} < T)$, $\Sigma^{T,>}(T > \bar{\mathfrak{t}})$, $G^<(\bar{\mathfrak{t}} < T)$ and $G^>(T > \bar{\mathfrak{t}})$ according to Eq. (195)

- compute the Green functions $G^<(\mathfrak{t} < T + \Delta)$ and $G^>(T + \Delta > \mathfrak{t}')$ for $\mathfrak{t}, \mathfrak{t}' \in \left\{ t_\mathrm{s}, t_\mathrm{s} + \bar{\Delta}, \ldots, \mathfrak{t}^{\max} \right\}$ from $\mathcal{U}(T), \mathcal{V}(T), I^{(1),<}(\mathfrak{t} < T), I^{(1),>}(T > \mathfrak{t}'), G^<(\mathfrak{t} < T)$ and $G^>(T > \mathfrak{t}')$ according to Eqs. (187) and (188)

- compute the Green function $G^<(T + \Delta, T + \Delta)$ from $\mathcal{U}(T), I^{(1),<}(T,T)$ and $G^<(T,T)$ according to Eqs. (189) and (190)

- save the Green function $G^<(T + \Delta, T + \Delta)$, if $\lfloor \frac{T+\Delta}{r_\mathrm{sample}} \rfloor r_\mathrm{sample} = T + \Delta$

- save $G^<(\mathfrak{t} < T + \Delta)$ and $G^>(T + \Delta > \mathfrak{t}')$ ($G^<(\mathfrak{t} < T)$ and $G^>(T > \mathfrak{t}')$), if $\lfloor \frac{T+\Delta}{r_\mathrm{sample}} \rfloor r_\mathrm{sample} = T + \Delta$ ($\lfloor \frac{T}{r_\mathrm{sample}} \rfloor r_\mathrm{sample} = T$)

5.3　Generation of the initial state

In this section, the generation of the initial state is discussed. The details about the adiabatic switching method that was presented in Sec. 2 are described in Sec. 5.3.2. The generation of the Hartree–Fock state that leads to the noninteracting ground state, in the case of the adiabatic switching, and to the ideal state, for full doubly occupied setups, is discussed in Sec. 5.3.1.

5.3.1 Generation of the Hartree–Fock state

The underlying ensemble in the NEGF approach can be considered to have a fixed particle number, since it is conserved by all approximations of Secs. 2 and 5.1 [44, 68]. In the noninteracting limit, this would correspond to a canonical ensemble that is described by the density operator

$$\hat{\rho}_0 = \frac{\mathrm{e}^{-\beta \hat{H}_0}}{\mathrm{Tr}\left(\mathrm{e}^{-\beta \hat{H}_0}\right)} \,, \tag{208}$$

β being the inverse temperature. However, a fixed particle number cannot allow for the natural action of the canonical operators which connect the N-particle space with the $(N \pm 1)$-particle space. Therefore, one can use the grand-canonical ensemble, instead. In this choice of an ensemble, the properties are determined by β and the chemical potential μ. To nevertheless achieve a subspace with a constant particle number, one can choose μ in such a way that, in the ground state, the average particle number $\langle N \rangle_0$ is equal to the desired N. This corresponds to an effective canonical ensemble, at least for sufficiently large β. To allow for the generation of interacting ground states, one can generalize the ensemble to the effective Hartree–Fock Hamiltonian of Eq. (173) that depends on the density itself. To find the initial density matrix, one can apply the iterative scheme that is presented below. To find the density matrix for the M-th step, one has to diagonalize the Hamiltonian $h_{ij}^{\mathrm{eff},(M)}(t_{\mathrm{s}})$ that depends on $n_i^{(M)}(t_{\mathrm{s}})$ to get the eigenbasis. If $D^{(M)}$ is a diagonal matrix with

$$D^{(M)} = B^{(M)} h_{ij}^{\mathrm{eff},(M)}(t_{\mathrm{s}}) \left(B^{(M)}\right)^{-1}, \tag{209}$$

then $D_{11}^{(M)}, D_{22}^{(M)}, \ldots, D_{N_{\mathrm{s}} N_{\mathrm{s}}}^{(M)}$ are the eigenvalues of $h_{ij}^{\mathrm{eff},(M)}(t_{\mathrm{s}})$. At this point, one can choose the chemical potential μ such that

$$N(\beta, \mu, D) = \sum_k f(D_{kk}^{(M)} - \mu) \tag{210}$$

is equal to the desired particle number. Here, $f(D_{kk}^{(M)} - \mu) = \left(\exp\left(\beta(D_{kk}^{(M)} - \mu)\right) + 1\right)^{-1}$ is the Fermi–Dirac distribution. Having found the matching μ, one obtains the corresponding density matrix in the Hubbard basis by

$$\widetilde{n}_{ij}^{(M+1)}(t_{\mathrm{s}}) = \left[\left(B^{(M)}\right)^{-1} \mathcal{D}(f(D_{11}^{(M)} - \mu), f(D_{22}^{(M)} - \mu), \ldots, f(D_{N_{\mathrm{s}} N_{\mathrm{s}}}^{(M)} - \mu)) B^{(M)}\right]_{ij}. \tag{211}$$

The iterative procedure can be started from an arbitrary density matrix $n_{ij}^{(0)}(t_{\mathrm{s}})$. It is convenient to not directly use $\widetilde{n}_{ij}^{(M+1)}(t_{\mathrm{s}})$ for the next iteration, but to mix the density matrices as follows

$$n_{ij}^{(M+1)}(t_{\mathrm{s}}) = \alpha n_{ij}^{(M)}(t_{\mathrm{s}}) + (1 - \alpha)\widetilde{n}_{ij}^{(M+1)}(t_{\mathrm{s}}), \tag{212}$$

where, $\alpha \in [0, 1)$ denotes a mixing parameter that accelerates the convergence. The iteration process can be considered converged, if

$$\sum_{ij} \left| n_{ij}^{(M)}(t_{\mathrm{s}}) - n_{ij}^{(M-1)}(t_{\mathrm{s}}) \right| < \epsilon. \tag{213}$$

After convergence, the time propagation can be started by setting $G_{ij}^<(t_{\mathrm{s}}, t_{\mathrm{s}}) = \frac{\mathrm{i}}{\hbar} n_{ij}(t_{\mathrm{s}})$, cf. Eq. (105).

In the case of $U = 0$, the resulting density matrix corresponds to the noninteracting ground state, from which the interacting ground state can be generated by adiabatic switching (see Sec. 5.3.2). In principle, it is also possible to start the time propagation of any setup from the Hartree–Fock state that, in general, differs from the exact interacting ground state. Furthermore, one can include additional potential terms into the Hamiltonian to realize, e.g., a harmonic confinement.

In this paper, mainly setups that are initially completely determined by the occupation of a smaller subsystem are considered. In these cases, the above-mentioned procedure can be applied for this subset of Hubbard sites and the density matrix can be augmented to the full size by adding zero in all unknown matrix elements afterwards. This

corresponds to an excitation of the form of a confinement quench, since the restriction on the subset is equivalent to an infinitely strong potential on the unoccupied sites. Depending on the density of the initially occupied sites, the Hartree–Fock solution can lead to an approximative result, or, for exclusively doubly occupied sites, to an exact density matrix. This is the case, because the Hartree–Fock state gives the exact total energy for this setup.

5.3.2   Realization of the adiabatic switching

As was shown in Sec. 2.2, the generation of an interacting initial state can be achieved by the adiabatic switching method. According to Eq. (132), this leads to an effectively time-dependent interaction strength $U(t) = U f_{AS}(t)$. In general, the switch-on procedure has to start from $t_s = -\infty$, to ensure that no additional energy is transferred to the system. In practice, t_s has to be made finite, which is justified, if the resulting additional energies are sufficiently small. Also, in general, $f_{AS}(t)$ has to fulfill the adiabatic condition, i.e.

$$f_{AS}^{-1} \frac{\partial f_{AS}}{\partial t} = \text{const} , \tag{214}$$

which leads to the expression [44] $f_{AS}(t) = \exp\left(-(t - t_0)\right)$. For numerical reasons, one has to ensure that the total change of f_{AS} is small for $t \to t_s$ and $t \to t_0$, to avoid artificial fluctuations caused by the integration procedures due to a gap at t_s and a kink at t_0. These conditions are precisely fulfilled by the choice [79]

$$
\begin{aligned}
f_{AS}^{\tau, t_H}(t) &= \exp\left\{ -\frac{A_{t_H}^{\tau}}{t/(2t_H)} \exp\left(\frac{B_{t_H}^{\tau}}{t/(2t_H) - 1}\right) \right\} , \\
B_{t_H}^{\tau} &:= \frac{t_H}{\tau \ln(2)} - \frac{1}{2} , \qquad A_{t_H}^{\tau} := \frac{\ln(2)}{2} e^{2B_{t_H}^{\tau}} ,
\end{aligned}
\tag{215}
$$

where $t_H := \frac{t_0 - t_s}{2}$ and τ is a free parameter to control the slope of the function. The shape of f_{AS}^{τ, t_H} for different τ is shown in Fig. 21. It should be noted that the function is asymmetric with respect to t_H unlike e.g. the Fermi–Dirac distribution.
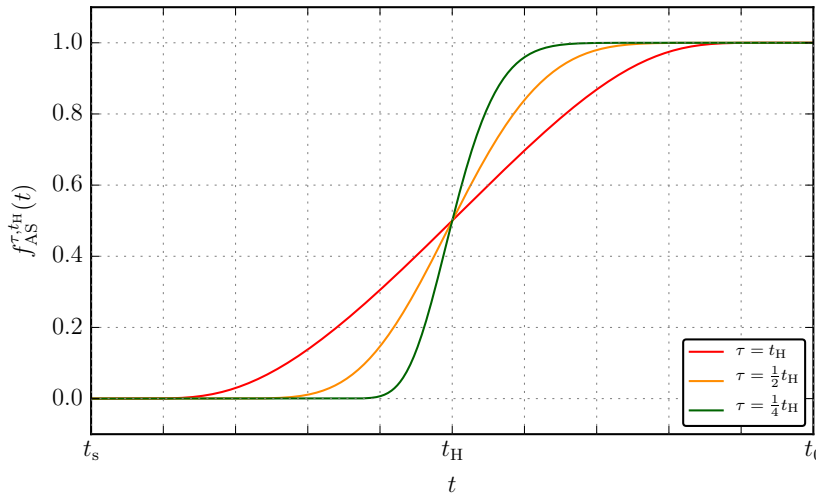

Fig. 21 Illustration of the adiabatic switching function: The shape of f_{AS}^{τ, t_H} in Eq. (215) is shown for $\frac{\tau}{t_H} = 1, \frac{1}{2}, \frac{1}{4}$. The functions go to zero for $t \to t_s$ and to one for $t \to t_0$. The functions are asymmetric with respect to t_H.

We underline that the adiabatic switching method is well-tested, see e.g Refs. [77, 80] and allows for reliable and accurate simulations.

5.4   Evaluation of physical observables

During the propagation, one has access to the full Green function and to the different collision integrals. From these quantities, one can compute many relevant physical observables. The most important one, for the study of

nonequilibrium transport processes, is the time-dependent single-particle density matrix

$$n_{ij}^{\uparrow(\downarrow)}(t) = -i\hbar G_{ij}^{<}(t,t) \,. \tag{216}$$

It should be noted that $n_i^{\uparrow(\downarrow)}(t)$ gives the density for spin-up or spin-down particles. The total occupation is given by $n_i(t) := n_i^{\uparrow}(t) + n_i^{\downarrow}(t)$. Almost the entire transport analysis is based on $n_{ij}(t)$ and $n_i(t) = n_{ii}(t)$ in particular. The energy contributions that sum up to the total energy can also be obtained. They are given by

- the kinetic energy $E_{\text{kin}}(t)$ that corresponds to $\hat{H}_0$,

$$E_{\text{kin}}(t) = \Re\left[\text{Tr}\left(h^{(0)} n(t) \right) \right] \,, \tag{217}$$

- the potential energy $E_{\text{pot}}(t)$ that corresponds to the excitation of the system $\hat{F}(t)$,

$$E_{\text{pot}}(t) = \Re\left[\text{Tr}\left(F(t) n(t) \right) \right] \,, \tag{218}$$

- the Hartree–Fock energy $E_{\text{HF}}(t)$ that corresponds to the Hartree–Fock selfenergy $\Sigma^{\text{HF}}(t)$,

$$E_{\text{HF}}(t) = \frac{1}{2}\Re\left[\text{Tr}\left(\Sigma^{\text{HF}}(t) n(t) \right) \right] \,, \tag{219}$$

- the correlation energy $E_{\text{corr}}(t)$ which can be obtained from the time-diagonal collision integral $I^{(1),<}(t,t)$,

$$E_{\text{corr}}(t) = \frac{1}{2}\Im\left[\text{Tr}\left(I^{(1),<}(t,t) \right) \right] \,. \tag{220}$$

Consequently, the total energy $E_{\text{tot}}(t)$ is given by

$$E_{\text{tot}}(t) = E_{\text{kin}}(t) + E_{\text{pot}}(t) + E_{\text{HF}}(t) + E_{\text{corr}}(t) \,. \tag{221}$$

A very interesting quantity that provides insight into the correlations and quantum behaviour of the particles is the local entanglement entropy [81, 82]

$$
\begin{aligned}
S_i(t) = &-2\left(\frac{n_i(t)}{2} - n_{ii}^{(2)}(t) \right) \log_2\left(\frac{n_i(t)}{2} - n_{ii}^{(2)}(t) \right) - n_{ii}^{(2)}(t) \log_2 n_{ii}^{(2)}(t) \\
&- \left(1 - n_i(t) + n_{ii}^{(2)}(t) \right) \log_2\left(1 - n_i(t) + n_{ii}^{(2)}(t) \right) \,,
\end{aligned}
\tag{222}
$$

where $n_{ii}^{(2)}(t)$ is the double occupation of site i that is accessible in the NEGF approach according to

$$n_{ii}^{(2)}(t) = \frac{1}{2U(t)}\left(\Re\left[\Sigma_i^{\text{HF}}(t) n_i(t) \right] + \Im\left[I_{ii}^{(1),<}(t,t) \right] \right) \,. \tag{223}$$

$S_i(t)$ can be understood as a measure of the complexity of the many-body state. It quantifies the overlap of particles at site i with particles on all other sites. The total entanglement entropy can be found by applying the trace,

$$S(t) := \sum_i S_i(t) \,. \tag{224}$$

The single-particle part, S_{sp}, follows from the replacement $n_{ii}^{(2)}(t) \to n_i^{\uparrow}(t) n_i^{\downarrow}(t) = \left(\frac{n_i(t)}{2} \right)^2$, in Eq. (222). This is obtained from Eqs. (171) and (223) with the assumption that $I_{ii}^{(1),<}(t,t) = 0$. Thus, S_{sp} becomes

$$
\begin{aligned}
S_{\text{sp}}(t) := \sum_i \Bigg[&-2\left(\frac{n_i(t)}{2} - \left(\frac{n_i(t)}{2} \right)^2 \right) \log_2\left(\frac{n_i(t)}{2} - \left(\frac{n_i(t)}{2} \right)^2 \right) \\
&- \left(\frac{n_i(t)}{2} \right)^2 \log_2\left(\frac{n_i(t)}{2} \right)^2 \\
&- \left(1 - n_i(t) + \left(\frac{n_i(t)}{2} \right)^2 \right) \log_2\left(1 - n_i(t) + \left(\frac{n_i(t)}{2} \right)^2 \right) \Bigg] \,.
\end{aligned}
\tag{225}
$$

Consequently, one can define the correlation part of the entanglement entropy S_{corr} according to

$$S_{\text{corr}}(t) := S(t) - S_{\text{sp}}(t) \,. \tag{226}$$

Although the factorization of the two-particle density yields the formally non-interacting result, $n_i^{\uparrow}(t)n_i^{\downarrow}(t)$, the single-particle densities are computed from the full Green functions. Therefore, this expression and, also the corresponding entropy, $S_{\text{sp}}(t)$, contain interaction effects [38].

Another quantity that is studied in this work is the occupation in the quasi-momentum space $n_k(t)$ which is obtained by a discrete Fourier transform [44,65] (k is the quasi-momentum),

$$n_k(t) = \frac{1}{N_{\text{s}}} \sum_{ij} e^{-iki} e^{ikj} n_{ij}(t) \,. \tag{227}$$

5.5　Computational demands and parallelization

We now briefly discuss computational aspects. In particular, it is crucial to know how the required computer memory CPU time scale with the basis size N_{s} and the number of propagation steps N_t. Furthermore, we discuss how the code can be accelerated by massive parallelization. The required main memory of KBE calculations is dominated by the storage of the less and greater Green functions, both depending on two times arguments, as shown in Sec. 5.2.4. Since one has to store only $G_{ij}^{<}(\mathfrak{t} < \mathfrak{t}')$ and $G_{ij}^{>}(\mathfrak{t} > \mathfrak{t}')$, the required memory $M_{r_{\text{sample}}}(N_{\text{s}}, N_t)$ reduces to (assuming double-precision complex numbers, i.e. 16 Bytes)

$$M_{r_{\text{sample}}}(N_{\text{s}}, N_t) = 16\,\text{Bytes} \cdot 2 \cdot \frac{1}{2} \cdot N_{\text{s}}^2 \cdot \left(\frac{N_t}{r_{\text{sample}}}\right)^2 \,. \tag{228}$$

Here, the factor 2 corresponds to the two components and the factor $\frac{1}{2}$ accounts for the triangular matrix structure of the time arguments. Note that, compared to a primitive integration scheme, the memory is reduced by a factor r_{sample}^{-2}, cf. Sec. 5.1.

The scaling of the CPU time can be estimated from the number of coupled integrations/summations in the propagation scheme of Sec. 5.2.4. In all cases, the leading contribution arises from the evaluation of the T-matrix which scales with $\mathcal{O}\left(N_{\text{s}}^3 \cdot \left(\frac{N_t}{r_{\text{sample}}}\right)^2\right)$, leading to a total performance $P_{r_{\text{sample}}}(N_{\text{s}}, N_t)$ scaling of the order

$$P_{r_{\text{sample}}}(N_{\text{s}}, N_t) \propto \mathcal{O}\left(N_{\text{s}}^3 \cdot N_t \left(\frac{N_t}{r_{\text{sample}}}\right)^2\right) \,. \tag{229}$$

Again, the CPU time is reduced by a factor r_{sample}^{-2}, with the improved integration scheme[16] Note that neither the memory demand nor the performance scheme depends on the particle number N.

The complex algorithms introduced in the present section constitute a large number of independent computational steps. For example, each matrix multiplication of the form

$$C_{ij}(t, t') = \sum_k \int_{t_1}^{t_2} d\bar{t}\, A_{ik}(t, \bar{t}) B_{kj}(\bar{t}, t') \tag{230}$$

can be parallelized with respect to i, j, t, t' leading to a massive speed-up when executed on an appropriate architecture. In this work, all simulation were performed on graphics processing units (GPUs) provided by accelerator cards of the types

- NVIDIA®Tesla®K20m

---

[16] It should be noted that in the case of the second order Born approximation combined with a propagation scheme according to the GKBA, the memory and performance scaling are further reduced to

$$M_{r_{\text{sample}}}^{\text{SBA}}(N_{\text{s}}, N_t) = 16\,\text{Bytes} \cdot N_{\text{s}}^2 \cdot \frac{N_t}{r_{\text{sample}}} \quad \text{and} \quad P_{r_{\text{sample}}}^{\text{SBA}}(N_{\text{s}}, N_t) \propto \quad \mathcal{O}\left(N_{\text{s}}^3 \cdot N_t \frac{N_t}{r_{\text{sample}}}\right) \,.$$

- NVIDIA®GeForce®GTX TITAN

- NVIDIA®GeForce®GTX TITAN Black.

The above-mentioned properties and the use of parallelization allow us to access a broad parameter range in terms of N_s and N_t that is sketched in Fig. 22. The grey dots correspond to actual simulations which have been performed. The blue area shows where calculations are possible within the introduced approach. It can be seen that it is possible to perform simulations with up to several hundreds of Hubbard sites or propagation times up to $T/J^{-1} = \mathcal{O}(10^3)$.
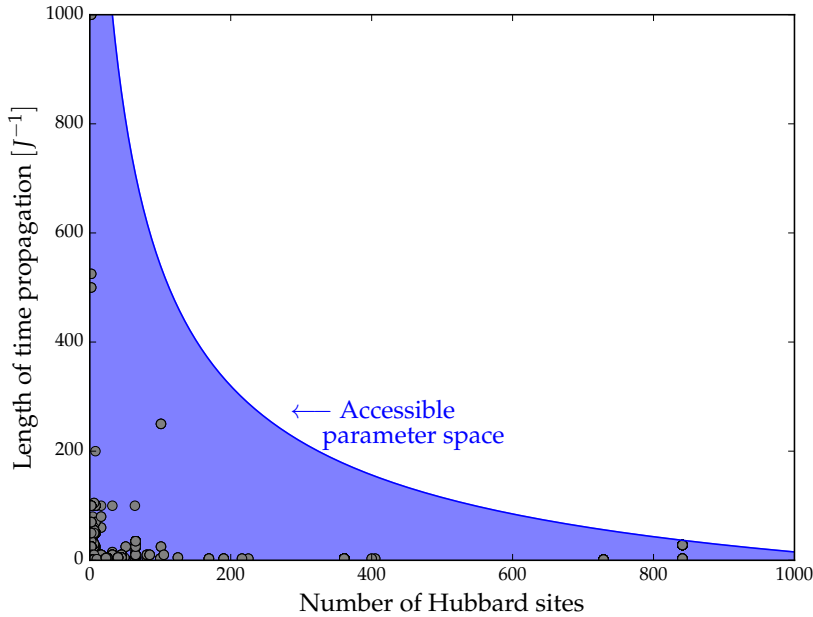
Fig. 22 Illustration of the accessible parameter space: The parameter space spanned by the length of the time propagation $T = N_t \Delta$ and the number of Hubbard sites N_s is shown. The grey dots correspond to actual calculations and the blue area denotes the accessible parameter space for runtimes up to one week.

To summarize the numerical and computational details of this paper, the presented algorithms start with the generation of an initial state by diagonalization of the effective Hartree–Fock Hamiltonian and a possible adiabatic switch-on of the interaction which is followed by the time propagation. It is dominated by the evaluation of the T-matrix and the collision integral, to propagate in the full two-time plane or only on the time-diagonal for the GKBA. The computation is facilitated by an efficient higher order integration scheme and massive parallelization on GPUs. Eventually, during the propagation, access to many nontrivial physical observables is achieved.

6 Numerical Results from NEGF simulations

In this section, the introduced NEGF approach is applied to the Hubbard model and studied for a variety of setups. In particular the dependence of the dynamics on the interaction strength U, the particle number N and the system dimensionality D is analyzed. Our T-matrix calculations are compared to exact results (where available), mean-field calculations and other many-body approximations. A special focus lies on the quantification of transport processes in Hubbard systems, in particular, on the diffusion in two-dimensional fermionic lattice systems. Here we will observe excellent agreement with experimental results for ultra-cold atoms which confirms the quality of our NEGF results and gives us confidence about their predictive capability for new results that have not yet been accessible to experiments. In the first part of this section we test our NEGF approach for simple systems comparing to other methods considering, both, the ground state and the dynamics following an excitation.

The main part of the results is devoted to the analysis of nonequilibrium diffusion processes in lattices that are

triggered by an inhomogeneous initial state, in which the density is confined either on the edge or at the center of the system. The resulting diffusive expansion is studied in a large parameter range with respect to interaction strength and particle number. For the case of diffusion from the center, also the effects of the dimensionality are considered. Due to its efficient computation, the approach allows us to analyze systems up to mesoscopic size on the order of $N_S = 100$ lattice sites.

For all results shown below we set $\hbar \to 1$. Furthermore, the interaction strength U and the hopping amplitude J are combined to a normalized interaction strength $U \to \frac{U}{J}$. Similarly, all energies and the time t will be given in units of J and J^{-1}, respectively. In all our calculations, the total energy and the particle number are conserved within the numerical precision which is guaranteed by choosing the time step Δ sufficiently small. All systems are considered at zero temperature.

6.1 Validity tests of the approach

In order to apply the introduced approach to large systems that are out of reach for ab-initio methods, it is essential to first check the validity of the used approximations. A suitable test case are small one-dimensional Hubbard chain for which exact results provided by the *configuration interaction* method [22] (CI) are available the CPU effort of which, however, scales exponentially with the particle number.

6.1.1 Comparison of ground state results

The simplest test case is the Hubbard dimer ($N_s = 2$) which, in equilibrium, can be solved analytically, cf. Sec. 4.3. Using the NEGF approach, the interacting ground state for $N^\uparrow = N^\downarrow = 2$ is obtained via adiabatic switching, cf. Sec. 5.3.2, and the accuracy is evaluated via the total energy of the ensuing state $E_{\mathrm{GS}} := E_{\mathrm{tot}}(t_0)$, which approaches the ground state energy. The results of the corresponding calculations are depicted in Fig. 23 for $U \in [0.5, 4]$ and different many-body approximations.
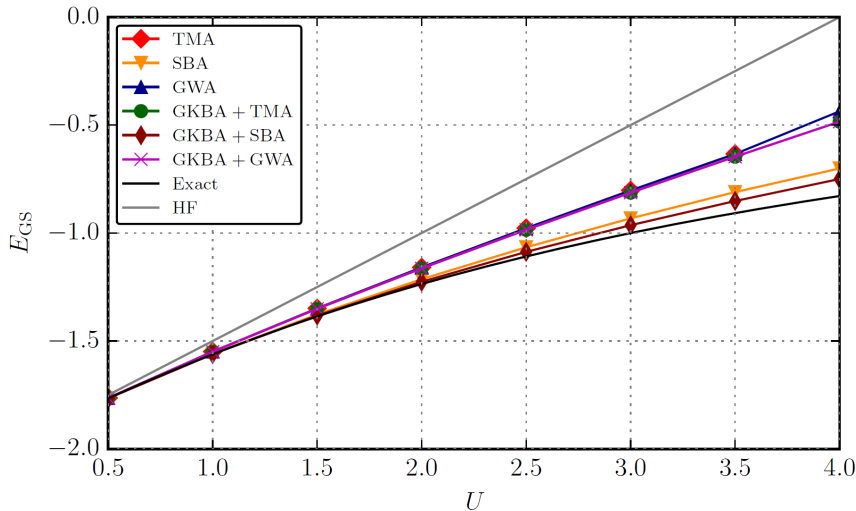

Fig. 23 Comparison of the ground state energies for the Hubbard dimer: The obtained ground state energies after the adiabatic switching are shown for varying interaction strength U and different many-body approximations. The exact solution (black) corresponds to E^- of Eq. (143).

The exact ground state energy (E^-) of Eq. (143) (black) and the Hartree–Fock (HF, gray) solution increasingly differ with U while the results for the T-matrix approximation (TMA), the second order Born approximation (SBA) and the GW-approximation (GWA)[17] lie in-between. Interestingly, the exact energy is best approached by the GKBA+SBA result which shows a very good agreement within the whole range of U. The energies obtained by the full two-time calculation combined with the second Born selfenergy are slightly higher for large interaction

---

[17] The GWA is the simplest possibility to include an effective screening [44] in the interaction of quantum particles. For more information about the approximation, the reader is referred to Refs. [44, 57, 58].

strengths. The calculations using the TMA and the GWA provide almost identical results for both the full and the GKBA propagation.

To understand this unexpected ordering of the various approximate results, one has to focus on the differences of the selfenergies. Up to the second order in the interaction, TMA, GWA and SBA provide the same expressions which causes the qualitatively better solutions compared to HF which neglects correlations. However, in the third order, there are differences, as shown by the Feynman diagrams in Fig. 24. The first one is contained in our (particle-particle) T-matrix selfenergy, cf. Fig. 5, whereas the second one corresponds to the particle-hole channel [59]. In the particular case of half-filling, due to the particle-hole symmetry the two diagrams give exactly the same contribution but with opposite sign [83], thus the sum over all third order Hubbard diagrams vanishes. Therefore, the second Born approximation is effectively of third order in the interaction. Therefore, in the case of the present T-matrix implementation where only one of these diagrams is considered, the leading term beyond second Born gives an unbalanced contribution which explains the behaviour in Fig. 23. In the case of the GWA, the included diagram of the third order is unphysical in the Hubbard model due to the contradictory spin properties of the interactions [39, 44]
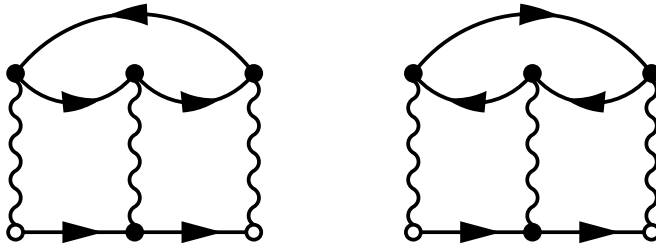

Fig. 24 Third order diagrams of the Hubbard model: The left diagram is contained in the particle-particle channel, while the right one corresponds to the particle-hole channel. For half-filling and a symmetric setup, the sum of both contributions vanishes. Only the left diagram is contained in the T-matrix description.

This example demonstrates that for very small systems and, in particular, at half filling, series-based many-body approximations such as the T-matrix have to be used with care, or the set of diagrams has to be properly expanded. With increasing system size and away from half-filling, i.e. in the low (or high) density limit [58], in contrast, the present T-matrix approximation yields excellent results. This can be seen in Sec. 6.1.2. As a final remark we note that that the GKBA and the full two-time propagation provide results of comparable accuracy, cf. Fig. 23, which confirms the validity of the former [68]. For more tests of the GKBA, see Ref. [34]. A more detailed insight into the general performance and accuracy of the NEGF approach with TMA is gained by considering non-equilibrium processes and dynamics which is the subject of the next section.

6.1.2 Excitation dynamics of small Hubbard clusters

To initiate nontrivial dynamics we consider a sudden potential switch on the first Hubbard site, i.e. an excitation of the form

$$\hat{F}(t) = \sum_{i,j} \sum_{\alpha,\beta} F^{w_0}_{ij,\alpha\beta}(t)\hat{c}^\dagger_{i,\alpha}\hat{c}_{j,\beta} \quad \text{with} \quad F^{w_0}_{ij,\alpha\beta}(t) = \delta_{i,1}\delta_{j,1}\delta_{\alpha,\beta}\Theta\left(t-t_0\right)w_0 \,. \tag{231}$$

The relaxation of a half-filled Hubbard dimer following a strong quench with a large amplitude $w_0 = 8$ is shown in Fig. 25 for different many-body approximations [57]. The initial state is prepared using adiabatic switching. The results are compared to exact diagonalization results (black line) that exhibit strong undamped oscillations. While for all methods the density on the first site oscillates, in the cases of full two-time propagations, it subsequently exhibits damping toward a constant value. This is observed for the Born approximation (orange) as well as for the T-matrix (red dashed line) where the latter is in perfect agreement with earlier independent TMA results from Ref. [57] which gives strong confirmation for the correctness of our implementation.

This unphysical damping is not observed for the Hartree-Fock-GKBA propagations. The reason for the artificial steady state is expected to lie in the self-consistency, which leads to unphysical additional peaks in the spectral function, in the case of small systems. This has been studied in more detail in Refs. [34, 57, 58]. This explanation is confirmed by the present findings, since the GKBA provides a significantly lower degree of self-consistency by construction. From Fig. 25 one can also see that the GKBA+TMA result is superior to all other approximative methods. This is not contradictory to the considerations of Sec. 6.1.1, since the symmetry of the system and also the particle-hole symmetry is broken due to the local excitation. Therefore, the third order diagrams do not vanish any longer.
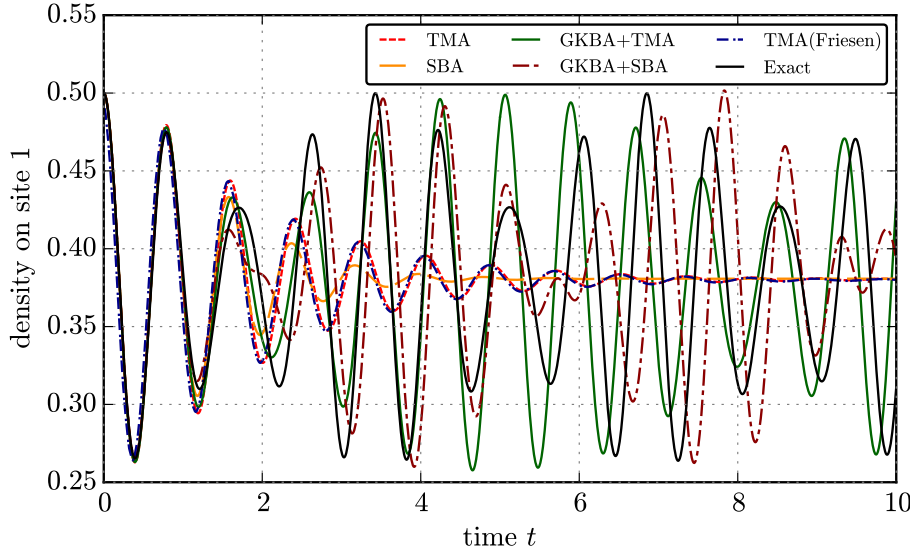

Fig. 25 Nonlinear response of a Hubbard dimer with $U = 1$: the evolution of the density on the first site is shown for a very strong excitation at $t = 0$, according to Eq. (231) with $w_0 = 8$. The initial state is prepared by adiabatic switching. The exact solution (black) is obtained from CI calculations. The blue line corresponds to the TMA calculation with full propagation in Ref. [57].

In the following, we test the reliability of the approach for systems with larger interaction strength $U = 4$ and varying filling $n := \frac{N}{N_s} = \frac{1}{2}, \frac{1}{6}$ for the case of a six-site Hubbard chain and two excitation strengths: $w_0 = 1$ and $w_0 = 5$, cf. Fig. 26. In all cases, the first site is initially depopulated, due to the on-site potential, and subsequently oscillates. The highest frequency is found for strong excitation and low density. One can see that the T-matrix based methods provide the best agreement with the exact results. Especially the GKBA propagation with T-matrix selfenergy provides a density evolution that is very close to the exact one, whereas the results from HF and GKBA+SBA fail to describe the evolution for large interaction and strong excitation in particular.

As already explained in Sec. 6.1.1, the T-matrix performs best in the low density regime which is confirmed by the results of Fig. 26. The higher accuracy of the GKBA+TMA approach for short times is again explained by the lower degree of selfconsistency, cf. Sec. 6.1.1. Note that the T-matrix performs significantly better than the GWA, which is also a series-based many-body approximation. This indicates that the predominant physical processes in this system are better described by the diagrams of Fig. 5. The GW-approximation which is constructed to describe dynamical screening effects of the interaction is not well suited for the Hubbard model, where the interaction acts locally.

To summarize, the T-matrix provides an accurate description of many-body processes, in particular in the regime of low or high density. The GKBA and the full two-time propagation are, in general, of comparable accuracy. These findings allow us to apply the introduced approach to larger systems in order to describe transport processes.
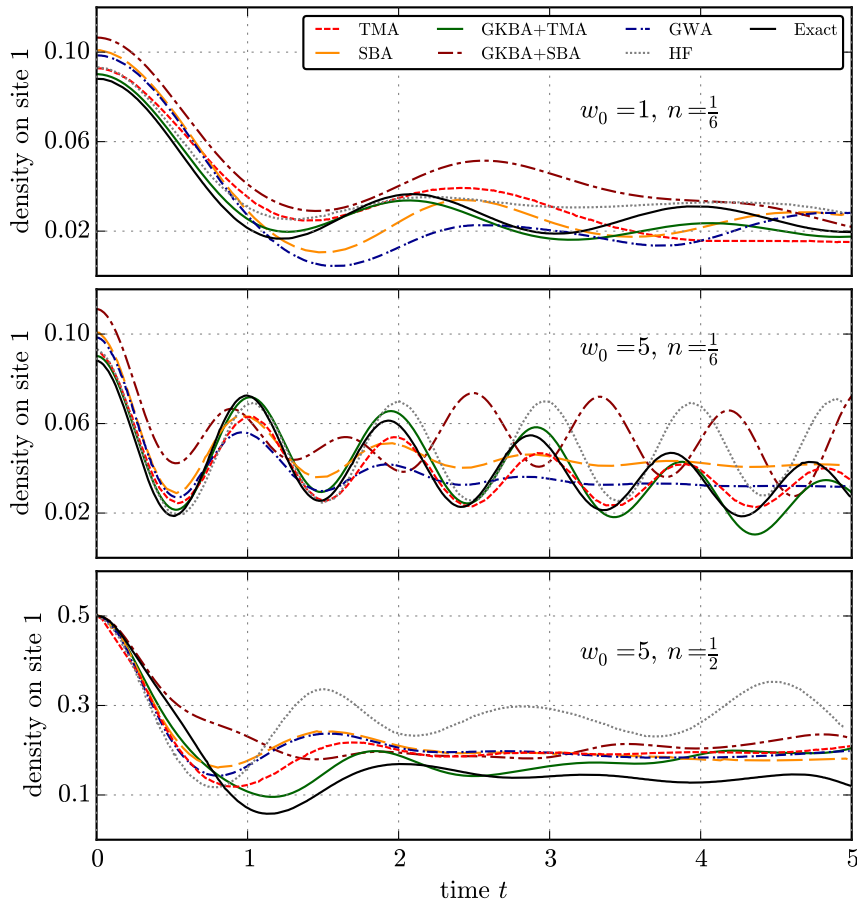
Fig. 26 Nonlinear response of the six-site Hubbard chain: the evolution of the density on the first site after the excitation from Eq. (231) is shown for different many-body approximations and $U = 4$. Top: $w_0 = 1$, $n = 1/6$; Center: $w_0 = 5$, $n = 1/6$; Bottom: $w_0 = 5$, $n = 1/2$. All simulations start from the adiabatic switching ground state. The exact solutions are provided by CI calculations. The results for GWA and HF are taken from Ref. [57].

6.2 Transport results in one, two and three dimensions

The theoretical description of nonequilibrium quantum transport processes in lattice systems has attained growing interest in the last years, since recent experiments with ultracold atoms have provided accurate data (see Sec. 3). In this paper, the evolution of initially confined fermions is considered. To quantitatively describe the time-dependent transport of the particles, it is useful to introduce a few physical quantities which are all calculated from the single-particle density $n(t)$. We define all transport quantities in a general way such that they apply to all dimensions $D = 1, 2, 3$. Therefore, the index of each Hubbard site is expressed as a D-dimensional vector.

6.2.1 Nonequilibrium transport quantities

The collective drift of the particle "cloud" is measured by the motion of the center-of-mass position $\boldsymbol{s}(t)$ which is defined as

$$\boldsymbol{s}(t) = \frac{1}{N} \sum_{\boldsymbol{i}} n_{\boldsymbol{i}}(t)\boldsymbol{i} . \tag{232}$$

To quantify the expansion of the particle cloud, it is useful to compute the time-dependent mean squared displacement $R^2(t)$ in the following way,

$$R^2(t) = \frac{1}{N} \sum_{\boldsymbol{i}} n_{\boldsymbol{i}}(t) \|\boldsymbol{i} - \boldsymbol{s}(t)\|^2 \,. \tag{233}$$

To find a comparable measure for particle clouds of different sizes we define the cloud diameter $d(t)$ adjusted for the initial width $R^2(t_0)$,

$$d(t) = \sqrt{R^2(t) - R^2(t_0)} \,. \tag{234}$$

Finally, the expansion velocity $v_{\exp}(t)$ is identified with the time derivative of the diameter,

$$v_{\exp}(t) = \frac{\mathrm{d}}{\mathrm{d}t} d(t) \,. \tag{235}$$

6.2.2   Simple limiting cases of diffusion processes

Before proceeding with the computational analysis of diffusion in finite Hubbard clusters let us recall two limiting cases. The first is the case of a classical system. If the particles are non-interacting they move on straight trajectories with constant speed and linearly growing coordinates (ballistic motion), as a single free particle would. In other words, the square of the distance from any initial point $\mathbf{r}(t_0)$ grows quadratically with time. In an interacting classical system, this distance is averaged over all particles, and the diffusion processes is described by the mean squared displacement (MSD) [84, 85]

$$\langle |\mathbf{r}(t) - \mathbf{r}(t_0)^2| \rangle = 2D\mathcal{D}t \,. \tag{236}$$

Collisions reduce the mobility of the particles, leading to a characteristic *linear* scaling of the MSD with time, where $\mathcal{D}$ is the diffusion coefficient. This is an equilibrium result following from the Green-Kubo relations. Alternatively one can follow the nonequilibrium process of the expansion of an inhomogeneous density distribution by solving the diffusion equation

$$\frac{\partial n}{\partial t} = \mathcal{D}\Delta n \,. \tag{237}$$

For an initially strongly localized density the solution is a Gaussian with a time-dependent width (variance) that exactly reproduces the result (236). While this linear scaling of the MSD with t is usually derived within gasdynamic or hydrodyanamic models, it can be extended to strongly interacting systems by means of computer simulations (molecular dynamics). Then the above results remain valid, but the diffusion coefficient rapidly decreases with the coupling strength, e.g. Refs. [86, 87]. At the same time, if their exist large-scale collective modes in the system, diffusion can be "anomalous", i.e. the MSD scales faster or slower than t, corresponding to "superdiffusion" or "subdiffusion", respectively, cf. e.g. Ref. [88] and references therein.

A second well known solvable example is the case of a single free quantum particle. If the particle is modelled by a Gaussian wave packet in momentum space,

$$\psi(k) = C \exp\left\{ -\frac{\sigma^2}{4}(k - k_0)^2 \right\}, \tag{238}$$

quantum dynamics yields the well-known expansion of this wave packet where the width in coordinate space (coordinate variance, MSD) grows in time according to

$$\sigma_x^2(t) = \frac{\sigma^2}{4} + \frac{\hbar^2}{m^2\sigma^2} t^2 \,. \tag{239}$$

Thus for non-interacting quantum particles the MSD grows, for long time, proportional to t^2, exactly like in the classical ballistic case. For short times, deviations occur that are due to the Heisenberg uncertainty.

For the case of finite Hubbard cluster, the cloud diameter, $d(t)$, introduced above, corresponds to the square root of the MSD, i.e. to $\sigma_x(t)$. We will see in Secs. 6.2.3 and 6.2.4 that $d(t)$ also approaches a linear in t

growth, for sufficiently long time. This corresponds to a constant expansion velocity which, however, depends in a nontrivial way on the interaction strength U and the system dimensionality. With increasing coupling the particle mobility (and the effective diffusion coefficient) are reduced, as in the classical case (see above). In the case of quantum particles on a lattice, here an additional effect is possible that is related to the formation of fermion pairs (doublons) the propagation of which may decouple from the mean expansion velocity.

6.2.3 Diffusion in an inhomogeneously filled Hubbard chain

To test the applicability of the NEGF approach to the description of transport processes, it is convenient to consider a Hubbard chain, where the density is initially localized in one half (e.g. the leftmost sites) whereas the remaining sites are empty. From this non-equilibrium state, the propagation starts and diffusion sets in. For the following simulations, the GKBA+TMA method is used, cf. Ref. [37].
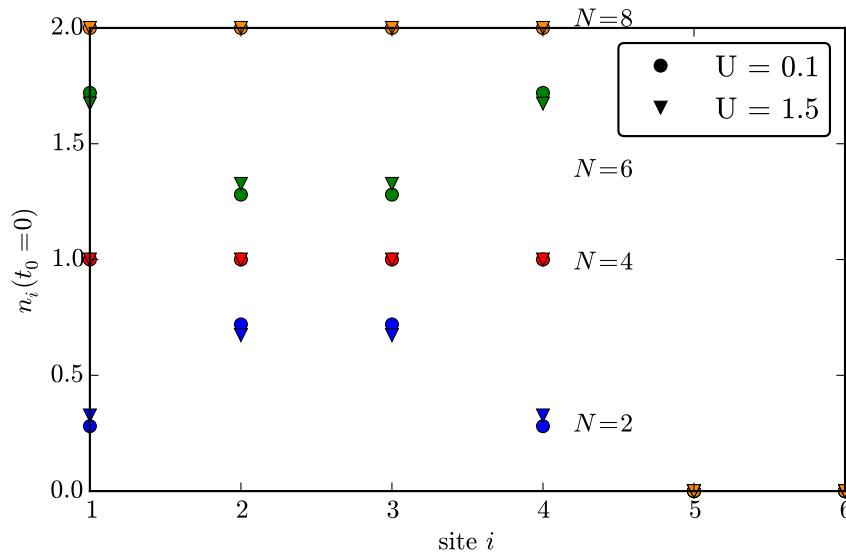

Fig. 27 Illustration of the initial setups for the diffusion for the one-dimensional Hubbard chain: the initial density of the leftmost six sites is shown for different particle numbers and interaction strengths. The orange (green, red, blue) symbols correspond to $N = 8(6, 4, 2)$. The circles denote the results for $U = 0.1$ and the triangles correspond to $U = 1.5$. The initial state is obtained from a Hartree–Fock calculation. The graphic is taken from Ref. [37].

In all calculations, the system consists of $N_s = 18$ Hubbard sites, and the expansion is analyzed for different fillings of the initial state and varying interaction strength U. All simulations start from the interacting Hartree–Fock state, cf. Sec. 5.3.1, which is shown in Fig. 27 for several cases. The occupation at the beginning of the propagation ($t = t_0 = 0$) is depicted for the leftmost six lattice sites. As one can see, for half-filling (red) and doubly occupied sites (orange), the density shape is homogeneous which is explained by the particle-hole symmetry in the latter case. However, the densities reveal a concave shape for $N = 6$ (green), and a convex shape for $N = 2$ (blue). This is a finite-size effect that is caused by the restricted mobility on the particles on the outermost sites. The density distributions are almost independent of the interaction strength. The curved occupation shape is slightly more pronounced for the weak interaction $U = 0.1$ (circles) than for $U = 1.5$ (triangles). This is caused by the repulsive character of the interaction.

The choice of the Hartree–Fock ground state which is assumed to be sufficiently accurate for small interaction strengths $U \leq 2$, allows for a longer effective propagation time, since the adiabatic switching can be omitted.

The evolution of the density is depicted in Fig. 28 for four cases. The occupation corresponds to the color scheme that shows the evolution in time (abscissa) for all lattice sites (ordinate). The upper graphs describe the density for the small particle number $N = 2$ with $U = 0.1$ (left) and $U = 1.5$ (right), while the lower ones correspond to the initially doubly-occupied setup ($N = 8$). In all cases, the evolution can be described by two different regimes. The first one which corresponds to small occupation (violet), reveals a "light-cone" like density spreading in time which is unchanged in all considered setups.
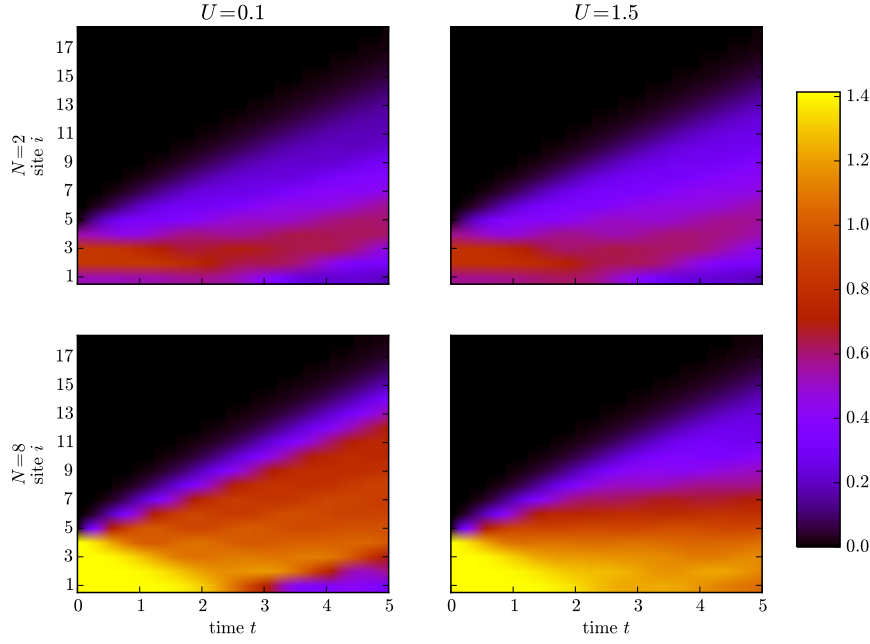
Fig. 28 Illustration of the expansion: the time evolution of the square root of the density $\sqrt{n_i(t)}$ (color scheme) is shown for consecutively numbered Hubbard sites (ordinate). The upper graphs show the low-density results ($N = 2$) for $U = 0.1$ (left) and $U = 1.5$ (right). The lower graphs show high-density results ($N = 8$). The graphic is taken from Ref. [37].

The second regime belongs to the regions of large density which is shown in red/orange. It is much more pronounced in the lower cases with large filling. While the second regime remains almost unchanged for $N = 2$ with respect to the interaction strength, it provides a significantly slower evolution in the $U = 1.5$ case for the larger particle number. The different velocities of the regimes for large interaction and filling suggests to identify the first regime with effective single-particles and the second regime with an effective double-occupation state. This corresponds to the appearance of so-called doublons which appear for very large interaction strengths [89, 90]. The electrons of doubly occupied sites are forced to form a stable bosonic quasiparticle due to strong interactions. This behaviour can be explained with the specific energy structure of the Hubbard model. The large total energy of a system which contains doubly occupied sites could not be conserved, if the electrons would separate, since the kinetic energy gain could not compensate the energy loss. Formally, the behaviour is explained by the effective doublon Hamiltonian [89, 91]

$$\hat{\mathcal{H}}_{\mathrm{D}} = \frac{J^2}{U} \sum_{\langle i,j \rangle} \hat{c}^\dagger_{i,\uparrow} \hat{c}^\dagger_{i,\downarrow} \hat{c}_{j,\uparrow} \hat{c}_{j,\downarrow} + \sum_{i,j} V_{ij} \hat{c}^\dagger_{i,\uparrow} \hat{c}^\dagger_{i,\downarrow} \hat{c}_{i,\uparrow} \hat{c}_{i,\downarrow} \hat{c}^\dagger_{j,\downarrow} \hat{c}^\dagger_{j,\uparrow} \hat{c}_{j,\uparrow} \hat{c}_{j,\downarrow} , \tag{240}$$

where $V_{ij} = \begin{cases} \infty & \text{if } i = j \\ -\frac{J^2}{U} & \text{otherwise} \end{cases}$. It can be found by expanding the Hubbard Hamiltonian of Eq. (130) in terms of U^{-1} and neglecting terms of the order $\mathcal{O}(U^{-2})$. The doublon Hamiltonian does not couple to states with different number of doubly-occupied sites which explains the stability. Furthermore the effective hopping amplitude is proportional to $\frac{1}{U}$ which is the reason for the reduced velocity for increasing interaction strength. The same underlying processes apply for the setups of Fig. 28 for smaller U.

To quantify the observed processes in detail, the introduced transport quantities of Sec. 6.2.1 are computed. The results are shown in Figs. 29 and 30 for a small parameter study. In both figures, the evolution of the center-of-mass position $s_x(t)$ of Eq. (232) (top row), the cloud diameter $d(t)$ of Eq. (234) (middle row) and the expansion velocity $v_{\exp}(t)$ (top row) are depicted. In Fig. 29 the results are shown for different N while the columns correspond to $U = 0.1$ (left) and $U = 1.5$.
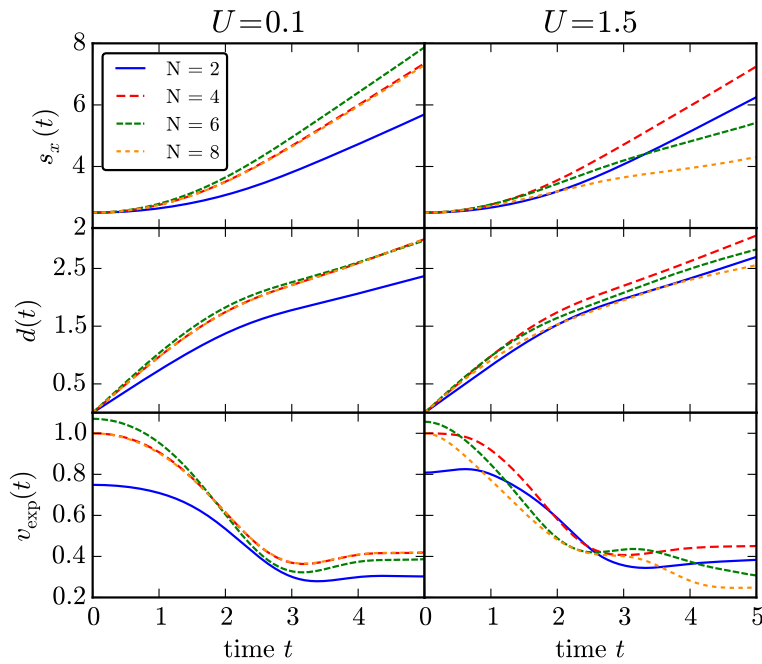
Fig. 29 Time evolution of the transport quantities for different particle numbers: center-of-mass (top row), cloud diameter (middle row) and expansion velocity (bottom row) following the initial states of Fig. 27 are shown for $N = 2, 4, 6, 8$. The left (right) column corresponds to $U = 0.1$ ($U = 1.5$).
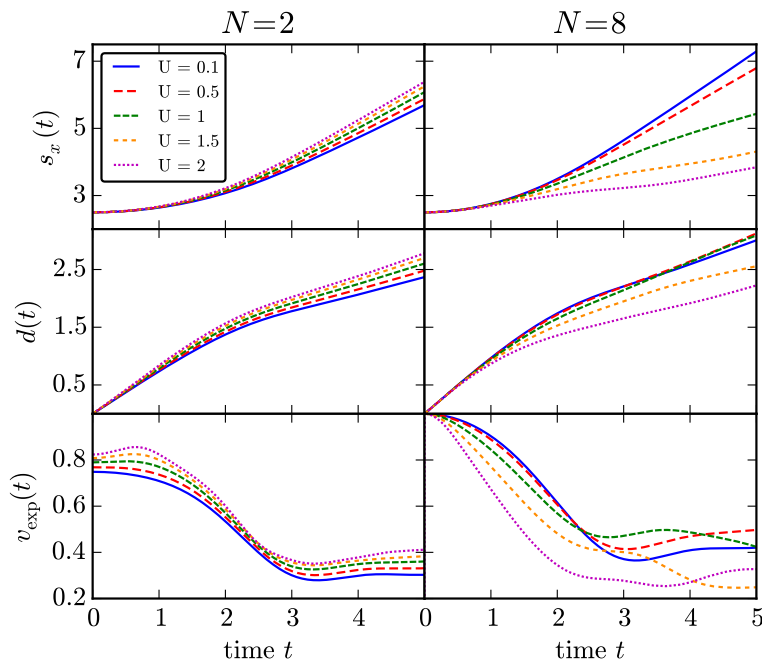
Fig. 30 Evolution of the transport quantities for different interactions strengths: The same quantities as in Fig. 29 are shown for $U = 0.1, 0.5, 1, 1.5, 2$. The first column corresponds to $N = 2$ and the second to $N = 8$. The graphic is taken from Ref. [37].

The columns in Fig. 30 belong to $N = 2$ (left) and $N = 8$ (right) while the colors denote the values of U, respectively. It can be seen that for all cases, the center-of-mass position increases in time which is caused by the

reflection at the wall, due to the missing hopping term at the first site. Likewise, the cloud diameter increases for all setups which corresponds to a diffusive expansion of the particles. The expansion velocity initially decreases, for all cases, and saturates afterwards with small fluctuations. The decrease is caused by the ongoing reflections at the wall and ends when all particles drift in the same direction (cf. Fig. 28). It can also be seen that the diameter growth approaches a linear curve, for all cases. This corresponds to a mean squared displacement which scales quadratically in time, in contrast to the classical case, cf. Eq. (236).

These simulations reveal the following general observations regarding the dependence on the particle number and the interaction strength:

(i) For small U, the diffusion quantities only depend on the initial state.

(ii) For $U = 1.5$ the quantities are in a nontrivial order with respect to N.

(iii) For small density, the expansion is nearly unaffected by the interaction.

(iv) For $N = 8$, the transport coefficients decrease with increasing interaction strength.

For noninteracting particles, it does not matter how large the density on adjacent sites is. Therefore, when initially the density in the outer region is higher than in the inner region, the particles are more likely to move along the Hubbard chain and vice versa, which is the reason for (i). For $U = 1.5$ the above-mentioned behaviour is in competition with the lowered expansion velocity, for large N, due to the doublon-like behaviour, cf. Eq. (240), which explains (ii). It is apparent that, for small densities, interactions become less important, which is the origin of (iii). Finally, (iv) corresponds again to the effective doublon velocity which decreases with increasing U.

In order to quantitatively explain the initial values of the expansion velocities, we compute the free expansion velocity $v_{\exp}^{(0)}$ of Hubbard systems that is obtained from the dispersion relation for the noninteracting case, Eq. (137). The general group velocity of a wave is given by [84]

$$v_{\mathrm{g}} = \frac{\mathrm{d}\omega}{\mathrm{d}\boldsymbol{k}} = \frac{1}{\hbar}\frac{\mathrm{d}\epsilon_{\boldsymbol{k}}}{\mathrm{d}\boldsymbol{k}} \ . \tag{241}$$

With v_{g}, the free expansion velocity becomes

$$
\begin{aligned}
v_{\exp}^{(0)} &= \sqrt{\langle v_{\mathrm{g}}^2 \rangle} = \sqrt{\left\langle \left(\frac{1}{\hbar}\frac{\mathrm{d}\epsilon_{\boldsymbol{k}}}{\mathrm{d}\boldsymbol{k}} \right)^2 \right\rangle} = \frac{2J}{\hbar}\sqrt{\left\langle \sum_{d=1}^{D} \sin^2(k_d) \right\rangle} \\
&= \frac{2J}{\hbar}\sqrt{\frac{1}{2\pi}\sum_{d=1}^{D}\int_{-\pi}^{\pi}\mathrm{d}k_d\,\sin^2(k_d)} = \frac{2J}{\hbar}\sqrt{\frac{D}{2}} = \frac{J}{\hbar}\sqrt{2D} \ .
\end{aligned}
\tag{242}
$$

Therefore, the free expansion velocity is equal to $v_{\exp}^{(0)} = \sqrt{2}$. Due to the geometry of the setup, this value is reduced to $v_{\exp}(t_0 = 0) = 1$, for setups with an initially homogeneous density distribution, after which the interaction further reduces $v_{\exp}$. Due to the inhomogeneous initial state, for $N = 2$ and $N = 6$, the value differs.

The results of the last section have shown that the introduced NEGF approach with TMA is well suited to describe transport processes in Hubbard lattices. Furthermore, it predicts reasonable physical behaviour which agrees with the theoretical expectations, in limiting cases. Therefore, it is applicable also for larger systems and higher dimensions.

6.2.4　Diffusion from the lattice center for $1D$, $2D$ and $3D$

This section is devoted to a detailed study of diffusion and expansion processes in large Hubbard lattice systems. The NEGF approach with TMA is used to simulate the evolution of circularly confined fermions Ref. [38]. The effects of different particle numbers and varying interaction strengths are analyzed for dimensions $D = 1, 2, 3$. A special focus lies on the two-dimensional results since here experimental results are available [5] that have been reviewed in Sec. 3.2.

Diffusion setups

All considered setups start from a state in which all initially occupied lattice sites are doubly-occupied. The corresponding particles are arranged within a $(D-1)$-sphere for each dimension, i.e. for $D = 1$, the central sites are occupied, for $D = 2$, the particles form a circle and for $D = 3$, they form a sphere. This corresponds to an initial potential $V_{\boldsymbol{i}}^R$ and the excitation, cf. Eq. (133),

$$F_{\boldsymbol{ij},\alpha\beta}(t) = \delta_{\boldsymbol{i},\boldsymbol{j}} V_{\boldsymbol{i}}^R(t), \tag{243}$$

where $V_{\boldsymbol{i}}^R(t) = \Theta(t_0, t) \begin{cases} 0 & \text{if } |\boldsymbol{i} - \boldsymbol{s}(t_0)| < R \\ \infty & \text{otherwise} \end{cases}$. Due to the lattices, the projection of the $(D-1)$-spheres onto the square geometry are not perfectly continuous for finite particle numbers. In Fig. 31, the density distributions of typical systems for $D = 1$ (left), $D = 2$ (middle) and $D = 3$ (right) are illustrated. The above-mentioned shapes of the initial occupations are shown in the first row. The second row shows possible density distributions after chosen evolution times. It can be seen that the particles symmetrically expand from the central confinement toward the periphery of the systems.
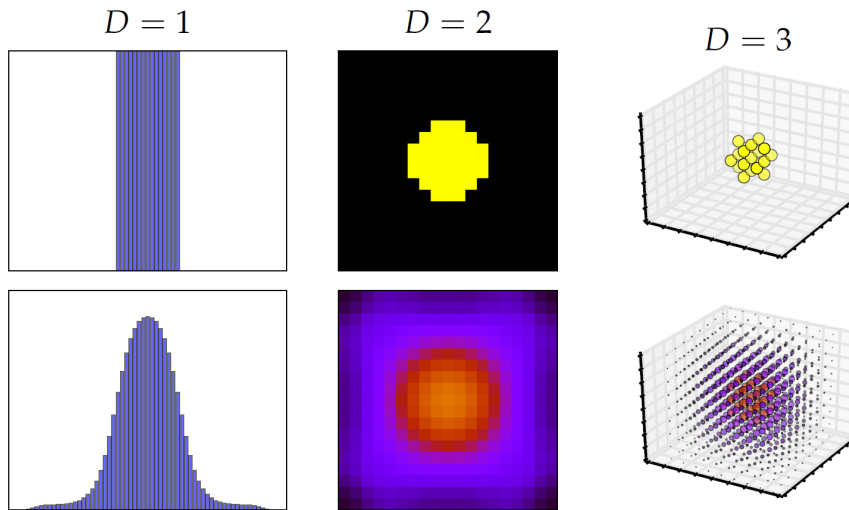

Fig. 31 Illustration of the expansion processes for all dimensions: The density distribution in a typical one- (left column), two- (middle) and three-dimensional (right) system. The upper row corresponds to the initial state whereas the lower row shows density shape after a certain propagation time. All simulations start from circularly confined fermion pairs at the center of the lattice. The results are obtained from TMA calculations with full two-time propagation.

Since a state containing only doubly-occupied sites is exactly described by ideal particles, the initial state is directly obtained from calculating the Hartree–Fock state of the occupied sub-system, as was discussed in Sec. 5.3.1. The expansion, following the confinement quench, is simulated using our NEGF approach with the T-matrix selfenergy and both time propagation schemes. In order to study the dependence on the particle number, the radius R of the initial particle clouds is varied. Additionally, the expansion is studied for different U. All in all, the systems are considered for setups of particle numbers in the range $N \in [2, 114]$ and interaction strengths in the range $U \in [0, 8]$. For systems of dimension $D = 1$, a Hubbard chain of 65 sites is used. In the case $D = 2$ ($D = 3$) the Hubbard lattice consists of $19 \times 19 = 361$ ($9 \times 9 \times 9 = 729$) sites. Using the example of two-dimensional systems, in Fig. 32 the density evolution of selected systems is shown. The columns from left to right correspond to the time evolution with the step $\Delta t = 1$. In the three rows, the expansion is shown for three particle numbers, $N = 2, 26, 72$, for $U = 1$, while the last row corresponds to $N = 72$ and $U = 4$. As one can see, the expansion toward the periphery of the system is governed by the transition from the circular distribution to a squared density shape which is due to the geometry of the lattice. The smaller the particle number N the more "fractal" is the distribution of the particles which is a finite-size effect. In the case of strong interaction ($U = 4$), the core region of the density remains almost constant in the circular shape.

The general trends of the expansion are in agreement with the obtained results of Sec. 6.2.3. The stability of the central region for strong interaction corresponds to the identification with effective doublons, according to Eq. (240). Furthermore, the obtained density evolutions are in very good qualitative agreement with the experimental results of Fig. 11. Apparently, the expansion processes start from a universal phase in which the diffusion is only possible for the particles at the edge of the cloud since the fermions at the center are initially effectively frozen due to Pauli blocking [7, 34, 92]. With ongoing evolution, the expansion processes become more complex and exhibit nontrivial dependencies on N and U. To quantify those, the diffusion quantities of Sec. 6.2.1 are applied.

The expansion processes

For illustration, in the following, the results for $2D$ systems are shown. Considering the simplest setup with a single initially doubly-occupied site, i.e. $N = 2$, allows to compare the expansion results with the exact solution which is obtained from CI calculations. In Fig. 33, the evolution of the diameter (top) of Eq. (234) and the expansion velocity (bottom) of Eq. (235) are shown[18] for $U = 0.1, 1, 2, 3, 4$. The short dashed lines belong to the full propagation with TMA, the long dashed lines to the GKBA propagation with TMA and the solid line to the exact results. As one can see, for all interaction strengths, the expansion starts with the free expansion velocity $v_{\exp}^{(0)} = 2$, cf. Eq. (242). Both quantities share a common initial phase, for all U. After a short time, the quantities begin to deviate, for the different U, which goes together with a decrease in $v_{\exp}$. Subsequently, the diameters approach a linear increase with t reflecting a constant expansion velocity.
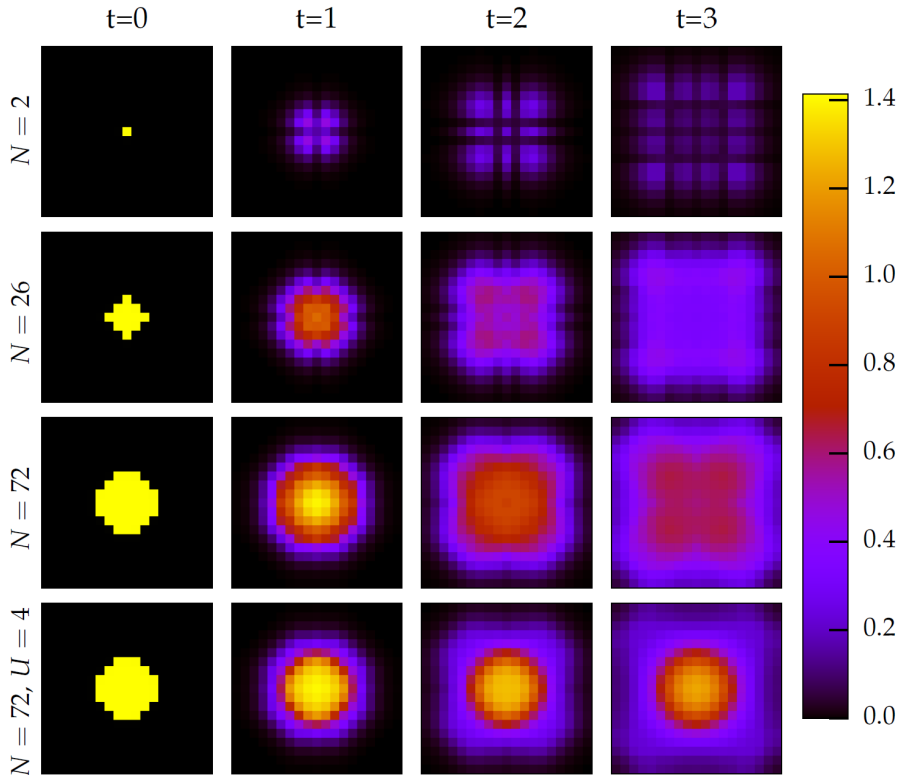
Fig. 32 Illustration of the different $2D$ setups: The time evolution of the density is shown for representative systems from left to right in steps of $\Delta t = 1$. The first three rows correspond to $U = 1$ and different particle numbers $N = 2, 26, 72$. The last row belongs to $N = 72$ and $U = 4$. For all setups, the evolution starts from initially circularly confined fermions in a two-dimensional 19×19 Hubbard lattice. The color code corresponds to the square root of the density $\sqrt{n_i(t)}$. The results are obtained from two-time TMA calculations.

---

[18] Due to the symmetry of the setup, the center-of-mass position s has to be time-independent which is fulfilled within numerical precision.

The decrease of the expansion velocities with U is caused by the reduced mobility of interacting fermions which form a correlated many-body state at the center of the system. This corresponds to the effective doublons which are discussed in Sec. 6.2.3. Regarding the accuracy of the different methods, one notices that for $U \leq 2$ the results obtained by TMA and GKBA+TMA calculations and the exact solution are almost indistinguishable. For the largest considered interaction strength, all obtained results lie within a range of 10%. This accounts for the high accuracy of the introduced approach and, in particular, of the T-matrix approximation. Furthermore, it confirms the findings of the former sections since on all sites, the density is predominantly either near double occupation or very low, i.e. away from half-filling [58].
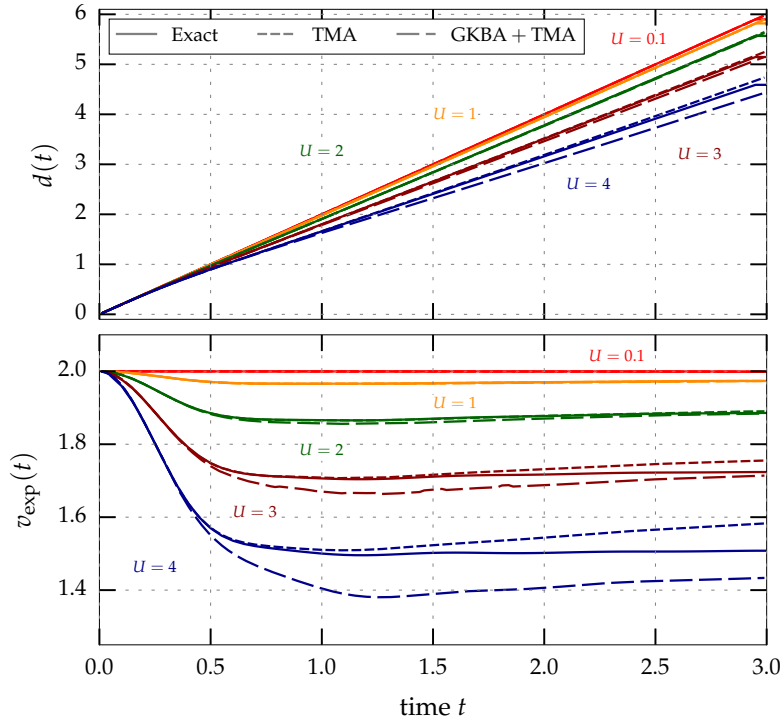

Fig. 33 Time evolution of two fermions in a two-dimensional lattice: The upper graph shows the time-dependent behaviour of the diameter for $N = 2$ according to Eq. (234). The corresponding expansion velocity of Eq. (235) is depicted in the lower graph. The solid lines belong to the exact solution obtained from CI calculations. The short dashed lines are obtained from NEGF calculation with TMA and full propagation while the long dashed lines correspond to the GKBA propagation. The results for $U = 0.1$ (1, 2, 3, 4) are shown in red (orange, green, brown, blue).

The shape of the expansion velocities is in agreement with the results of the previous section. To understand the underlying processes that cause the change in the expansion in more detail, it is helpful to look at the evolution of the energies and entanglement entropies of the systems. For the $N = 2$ setup with the interaction strength $U = 4$, the dynamics of $E_{\mathrm{sp}} := E_{\mathrm{HF}}$, E_{corr}, S_{sp} and S_{corr} (cf. Eqs. (219), (220), (225) and (226)) are shown in the left graph of Fig. 34. The depicted results belong to a TMA simulation with full propagation. The evolution of the energy and entropy contributions suggests the identification with three different time phases. The first phase is governed by the build-up of the single-particle entropy and the decrease of E_{sp}, while S_{corr} and E_{corr} are equal to zero. This leads to a decrease in the expansion velocity v_{exp} (cf. the right graph of Fig. 34). Since S_{sp} starts from zero, the build-up corresponds to a transition from a state of independent particles to an interacting many-body state. The inflection time τ_{sp} of S_{sp} can be used as a representative time for the first phase. It followed by a second phase, in which the single-particle quantities start to saturate, which causes the v_{exp} to converge, and E_{corr} and S_{corr} are build up instead. This build-up partly prolongs the saturation of $E_{\mathrm{sp}}/S_{\mathrm{sp}}$ and determines the final value of the expansion velocity. A characteristic time for the time scale of the second phase is given by the inflection point τ_{corr} of S_{corr} Subsequently, in a third phase, the correlation quantities and v_{exp} are saturated, whereas S_{sp} (E_{sp}) continues to increase (decrease) until $E_{\mathrm{sp}} = 0$.

For the considered two-dimensional systems with $N = 2$, the characteristic times τ_{sp} and τ_{corr} are depicted in the right graph of Fig. 34 for varying interaction strength. It can be seen that all τ_{sp} coincide with the reflection points of the expansion velocity. Furthermore, all τ_{corr} correspond to the onset of convergence which confirms the suggestions above. One can also see that the positions of all τ depend on the value of U. To analyze this dependence in more detail and also consider the effects of different particle numbers N, the characteristic times τ are computed within the whole parameter range. In Fig. 35, τ_{sp} (τ_{corr}) is shown in the full (N, U)-plane in the upper (lower) color map. The graphs in the upper and lower left and in the middle correspond to sections for $U = 1$ and $N = 74$. As one can see, both τ_{sp} and τ_{corr} increase for increasing particle number and decreasing interaction strength. Additionally, for N and U, τ_{corr} is one order of magnitude larger than τ_{sp}, which is remarkable since it contrasts the observations in equilibrium where the correlation time is always small compared to the single-particle time scale [43]. The long characteristic time τ_{corr} in the present case results from the ongoing formation of the diffusion front which only allows for the build-up of correlations.
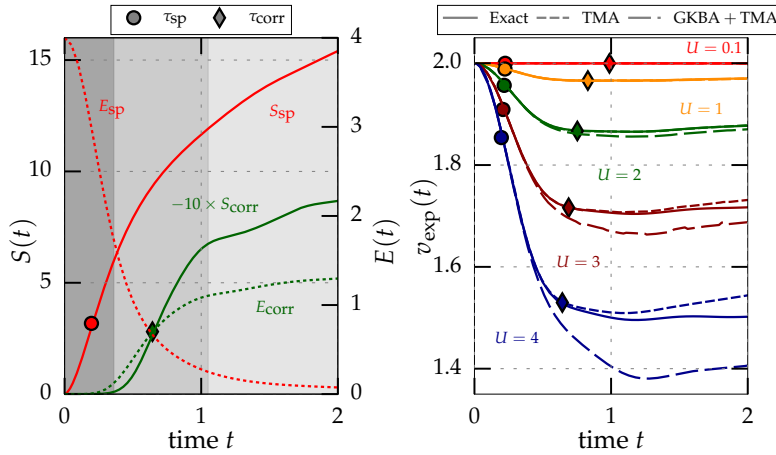

Fig. 34 Illustration of the expansion phases: the left graph shows the evolution the single-particle energy $E_{sp} = E_{HF}$ and entanglement entropy S_{sp} (red), as well as the correlation energy E_{corr} and entanglement entropy $-10 \times S_{corr}$ (green), for a setup of $N = 2$, $D = 2$ and $U = 4$. The circle (diamond) denotes the inflection time of the single-particle (correlation) entanglement entropy. The quantities are obtained from a TMA calculation with full propagation. The three gray shades mark the different expansion phases. The right graph shows the expansion velocities for the setup of $N = 2$ and $D = 2$ similar to the bottom graph of Fig. 33. Additionally, the inflection times of the corresponding single-particle and correlation entanglement entropy are shown in a similar way as in the left graph. The inflection times correspond to the full two-time TMA calculation.

The dependence of τ_{sp} and τ_{corr} on the particle number can be understood from the local build-up of energy and entanglement entropy. Since, at the start of the expansion, the particles can only move at the edge of the fermionic cloud, the local entanglement entropy (cf. Eq. (222)) is first produced in this region. During the ongoing expansion the outer doubly occupied sites are depopulated which causes a further build-up of entanglement toward the center of the cloud. For small particle numbers N, these entropy regions quickly overlap which obstructs the further production of entanglement entropy and, thus, causes a small inflection time τ. The dependence of both characteristic times τ on the interaction strength is explained by the increased effective scattering length for increasing U. This causes a faster build-up of entanglement and energy and results in a smaller τ. The given description of the underlying physical processes is also valid for systems of dimension $D = 1$ and $D = 3$.

It is also instructive to compare the T-matrix results with the findings of other many-body approximations. In Fig. 36, the evolution of the expansion velocity is shown for a typical two-dimensional setup of $N = 58$ and $U = 2.5$. The orange curve corresponds to a Hartree–Fock calculation. The red and green curves belong to T-matrix calculations for a full propagation and using the GKBA. The blue and brown curves are calculated using the second order Born approximation, while for the latter, the GKBA is applied. It can be seen that for all methods, the expansion velocity starts from the free value $v_{exp}^{(0)}$. In the case of the Hartree–Fock calculation, v_{exp} only slightly decreases and quickly converges. The correlated methods, however, accordingly continue to decay. Subsequently, v_{exp} divides with respect to the selfenergy into a branch with second Born based methods

and a branch with T-matrix based ones. With ongoing expansion, each branch further divides with respect to the propagation type. Interestingly, for SBA, GKBA+SBA and TMA, the final value of $v_{\exp}$ differs by less than 10% while the GKBA+TMA result is slightly lower. The strong deviation of the HF solution shows that a reliable description of diffusion processes requires a proper treatment of correlations. By comparison with the behaviour for $N = 2$ in Fig. 33, where the exact solution is possible, one can conclude that the T-matrix based methods approach provide reliable results which approach the exact solutions for small to medium times best. At the time scale of the convergence the full two-time propagation seems to be slightly favorable.

From Figs. 33 and 36 one finds that the expansion velocities converge to constant values for all considered setups. This is, in particular, in agreement with the results of Sec. 6.2.3. The asymptotic values of $v_{\exp}$ can be used to describe the expansion in the long time limit.
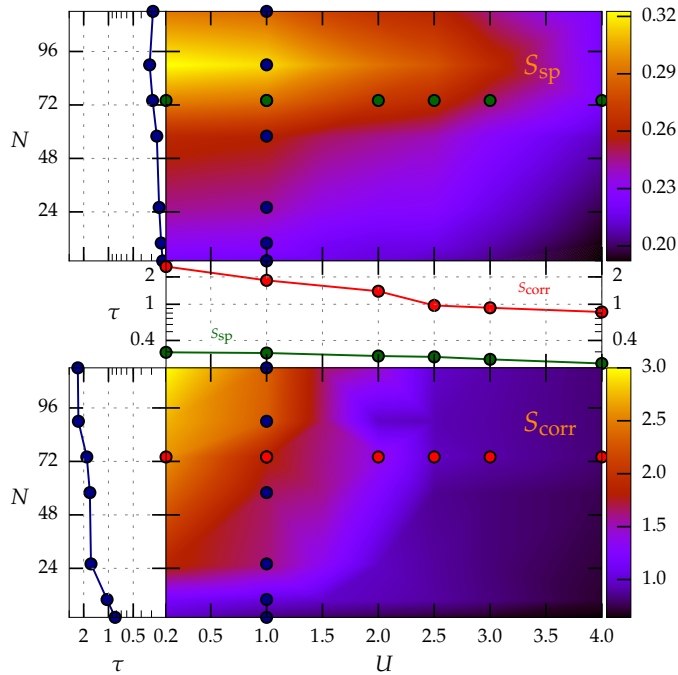

Fig. 35 Illustration of the representative times τ in the full (N, U)-plane for $D = 2$: the upper color map shows the dependence of the inflection time of single-particle entropy $\tau_{\rm sp}$ in the (N, U)-plane while the lower one belongs to $\tau_{\rm corr}$. For selected N and U which are marked in the color maps the corresponding sections are depicted logarithmically in the upper left, the middle and the lower left graph. For $U = 1$, $\tau_{\rm sp}$ ($\tau_{\rm corr}$) shown for varying N in the upper (lower) left graph. In the middle graph $\tau_{\rm sp}$ (green) and $\tau_{\rm corr}$ (red) are depicted for $N = 74$ and varying U. The results are obtained using the full propagation with the TMA.

The long time limit and the universal scaling

In order to describe processes on an experimentally accessible time scale [5], it is required to extrapolate $v_{\exp}(t)$. Let $v_{\exp}^{\infty}$ be the asymptotic expansion velocity with

$$v_{\exp}^{\infty} := \lim_{t \to \infty} v_{\exp}(t). \tag{244}$$

It can be computed from the time evolution of the expansion velocity $v_{\exp}$ by averaging over all values after a certain time $t_{\rm avg}$, where $v_{\exp}(t > t_{\rm avg})$ remains constant. Numerically, this time $t_{\rm avg}$ can be found by applying a condition to the relative change of $v_{\exp}$ which reads

$$\left| \frac{1}{v_{\exp}(t)} \cdot \frac{{\rm d}v_{\exp}}{{\rm d}t}(t) \right| < \epsilon, \tag{245}$$

for all $t > t_{\text{avg}}$. Here, ϵ denotes a small parameter ($\epsilon \ll 1$) to allow for deviations that are caused by numerical fluctuations. For a perfectly converged expansion velocity the condition is satisfied for $\epsilon = 0$. In practice, ϵ is typically of the order $\sim \mathcal{O}(10^{-3})$. The estimator for v_{exp}^{∞} on a discretized time space is given by

$$v_{\text{exp}}^{\infty} = \frac{1}{N_{\text{avg}}} \sum_{t > t_{\text{avg}}} v_{\text{exp}}(t), \tag{246}$$

where N_{avg} is the number of time steps with $t > t_{\text{avg}}$. This procedure is schematically illustrated in Fig. 37, where a typical shape of v_{exp} is depicted (red) and the considered values to calculate v_{exp}^{∞} are marked in blue. The final value of the asymptotic expansion velocity is shown as the black dashed line. To quantify the error of v_{exp}^{∞}, the standard deviation $\sigma\left(v_{\text{exp}}^{\infty}\right)$ of the averaging process is used [78].
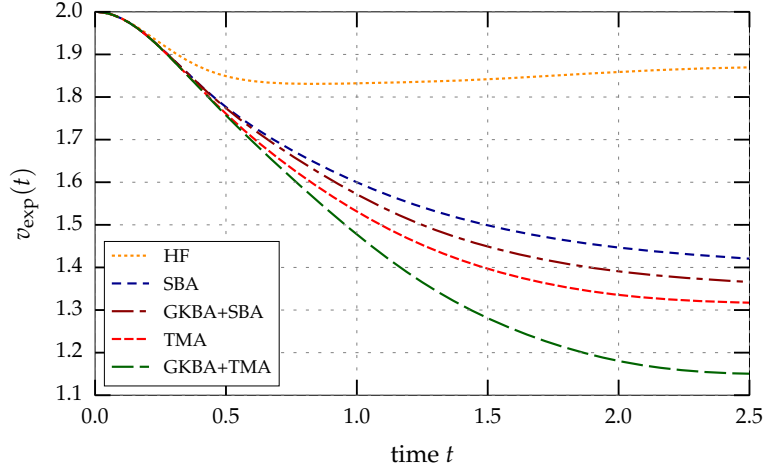
Fig. 36 Comparison of the different many-body approximations: the evolution of the expansion velocity v_{exp} is depicted for a typical setup of $N = 58$, $D = 2$ and $U = 2.5$. The Hartree–Fock result is shown in orange. The blue (red) curve corresponds to a full two-time propagation with a selfenergy in second Born (T-matrix) approximation. The brown and green lines belong to a GKBA propagation with SBA and TMA.
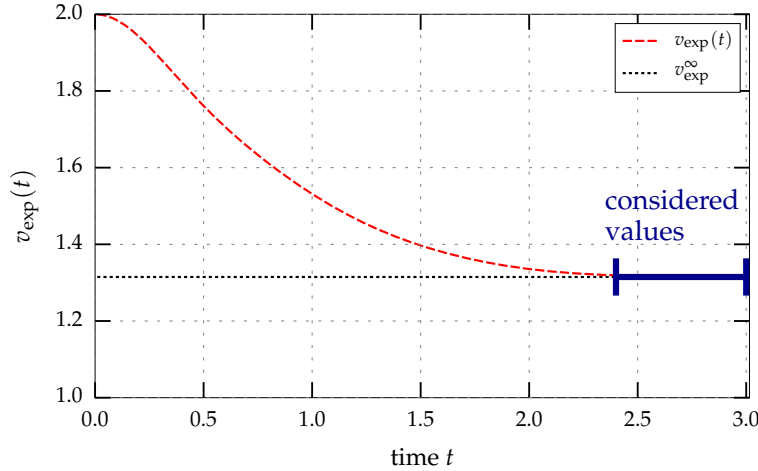
Fig. 37 Schematic illustration of the estimation of the asymptotic expansion velocity: The red curve corresponds to v_{exp} for a typical system with $N = 58$, $U = 2$ and $D = 2$. The region in which v_{exp} fulfills the condition of Eq. (245) is shown in blue, resulting in the value for v_{exp}^{∞} (black) according to Eq. (246). The results are obtained from a full propagation using the TMA.

The dynamics of the long time limit result from the initial behaviour which is shown in the previous section. Hence, the dependencies on N and U of the initial expansion phases manifest also in v_{exp}^{∞}. In the following, the

influences of the finite particle number are analyzed. Additionally, the effects of the dimension of the system are studied. In the left graph of Fig. 38, the asymptotic expansion velocity is shown for varying $N^{-1/2}$ and different interaction strengths and dimensions. The colors correspond to the values of $U = 1, 2, 3$, whereas the dimensions $D = 1, 2, 3$ are labelled in the figure. As one can see, $v_{\mathrm{exp}}^{\infty}$ decreases with increasing (decreasing) particle number ($N^{-1/2}$) and with increasing interaction strength. The results for the three-dimensional systems exhibit the largest asymptotic expansion velocities, while for $D = 1$, the values of $v_{\mathrm{exp}}^{\infty}$ become the smallest.

Fig. 38 Dependencies of the asymptotic expansion velocity: the left graph shows $v_{\mathrm{exp}}^{\infty}$ for varying particle numbers $N^{-1/2}$. The colors and 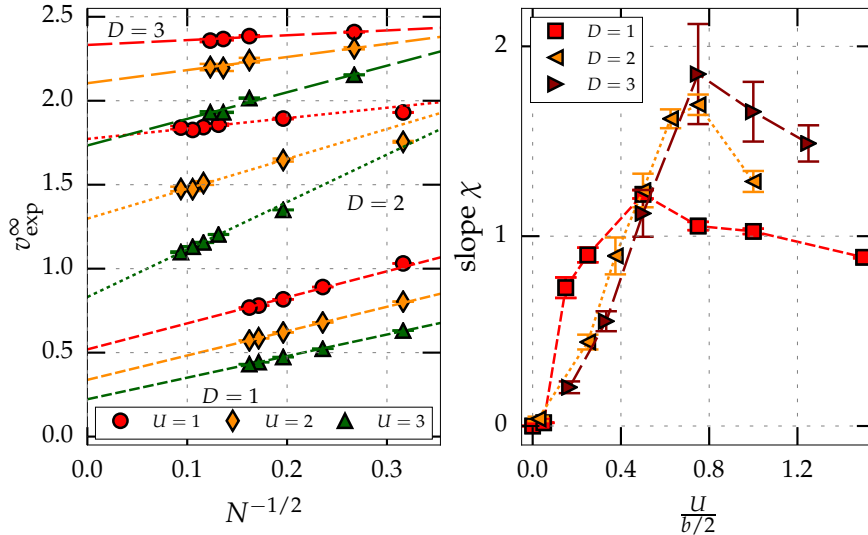symbols correspond to different interactions strengths $U = 1, 2, 3$, where the errors are smaller than the symbol size. The results for different system dimensions $D = 1, 2, 3$ are labelled in the figure. The lines correspond to linear fits according to Eq. (247). The right graph shows the dependence of the slope χ of Eq. (247) for varying bandwidth-normalized interaction strengths and different dimensions. All results are obtained from TMA calculations with the full two-time propagation. The graphic is taken from Ref. [38].

The behaviour for varying interaction strength is in agreement with the previous findings and caused by the various mobility of the interacting, correlated central fermions. The increase of $v_{\mathrm{exp}}^{\infty}$ with respect to the dimension D is due to the enlarged number of degrees of freedom, which can also be seen from the free expansion velocity $v_{\mathrm{exp}}^{(0)}$ of Eq. (242) which increases with D. The dependence on the particle number reveals a very interesting behaviour. For all dimensions and all interaction strengths, $v_{\mathrm{exp}}^{\infty}$ exhibits a linear scaling with $N^{-1/2}$ for sufficiently large N. In detail, this scaling is described by

$$v_{\mathrm{exp}}^{\infty}(U, N, D) - V_{\mathrm{exp}}(U, D) = \chi(U, D) N^{-1/2} \,, \tag{247}$$

where V_{exp} and χ no longer depend on the particle number. This is a striking observation, as it is a nontrivial property of the Hubbard model. By performing fits for the asymptotic expansion velocities in the full parameter space according to Eq. (247) and using V_{exp} and χ as free parameters[19], one obtains linear fit curves which are depicted in the left graph of Fig. 38. The fit procedure provides estimations for the slope χ and V_{exp} which is the macroscopic expansion velocity. Thus, it is possible to extrapolate the expansion velocities to the macroscopic limit. This extrapolation is part of Sec. 6.2.4.

The slope χ exhibits an interesting behaviour with respect to the interaction strength and the dimension. Its behaviour is depicted in the right graph of Fig. 38. For a better comparability, χ is shown for varying bandwidth-normalized interaction strengths $\frac{U}{b/2}$ (cf. Eq. (138)). The red (orange, brown) curve corresponds to $D = 1$ (2, 3). As one can see, for all dimensions the slope χ vanishes for $U = 0$ and increases to a maximum below $U = b/2$. For further increasing interaction strength, χ again decreases. The behaviour in the noninteracting limit is a

---

[19] The error terms $\sigma(v_{\mathrm{exp}}^{\infty})$ are also included in the fit process, resulting in error expressions for the slope χ and the macroscopic expansion velocity V_{exp}.

consequence of the ballistic expansion of independent particles. Thus, in this case, v_{exp}^{∞} does not depend on the particle number. In the limit $U \to \infty$, all particles are effectively frozen in a stable doublon cloud, which means that the particles do not expand at all. Thus, v_{exp}^{∞} vanishes for all N which explains the behaviour of the slope. The behaviour between these limits is quantitatively similar for all dimensions D when the bandwidth-normalized interaction strength is considered.
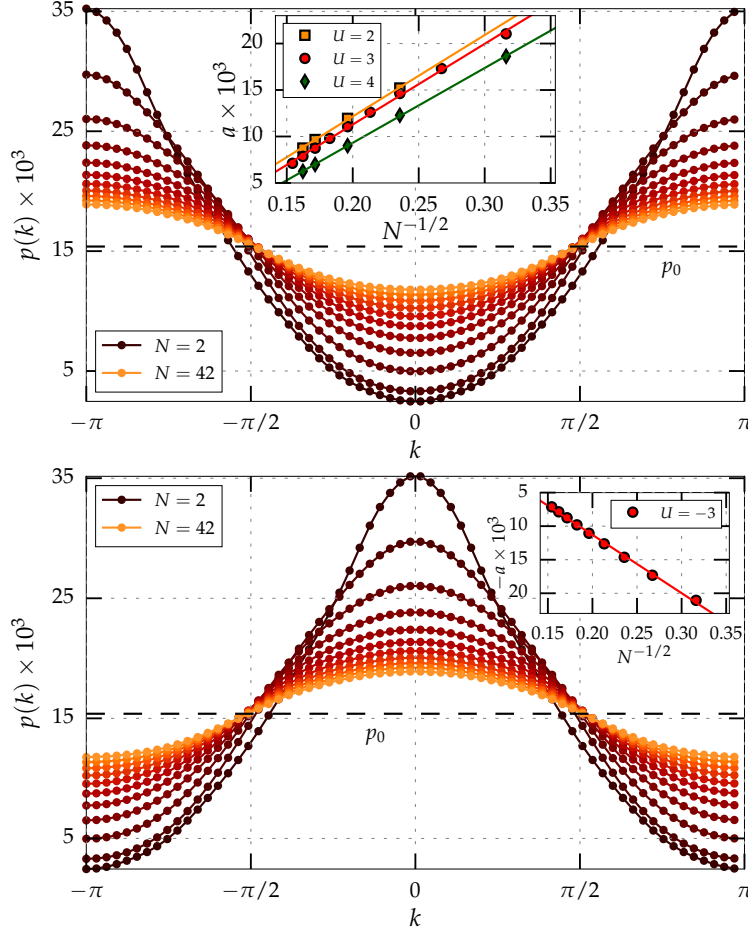
Fig. 39 Dependence of the quasi-momentum distribution on the particle number: the occupation probability $p(k)$ in the quasi-momentum space is shown at $t = 9.5$ for a one-dimensional system with $U = 3$ (top) and $U = -3$ (bottom) for different particle numbers $N = 2, \ldots, 42$ (colors). The dashed line corresponds to the initial distribution $p_0(k)$ which is constant for all N. The insets show the amplitude a of the distribution for varying particle number $N^{-1/2}$ and $U = 2, 3, 4(-3)$. The symbols correspond to actual results, whereas the lines denote linear fits. All results are obtained from a TMA calculation with full propagation. The graphic is taken from Ref. [38].

The obtained universal scaling with the particle number (see Eq. (247)) is not only visible in the asymptotic expansion velocity. It can also be seen from the density in the quasi-momentum space (cf. Eq. (227)). It corresponds to a Hamiltonian of the form [44]

$$
\begin{aligned}
\tilde{H}(t) = \sum_{\boldsymbol{k}} \sum_{\sigma=\uparrow,\downarrow} \epsilon_{\boldsymbol{k}} \, \hat{c}_{\boldsymbol{k},\sigma}^{\dagger} \hat{c}_{\boldsymbol{k},\sigma} &+ \sum_{\boldsymbol{k},\boldsymbol{p}} \sum_{\sigma=\uparrow,\downarrow} \tilde{V}_{\boldsymbol{k}\boldsymbol{p}}^{R}(t) \hat{c}_{\boldsymbol{k},\sigma}^{\dagger} \hat{c}_{\boldsymbol{p},\sigma} \\
&+ \frac{U}{N_{\text{s}}} \sum_{\boldsymbol{k},\boldsymbol{p},\boldsymbol{q}} \hat{c}_{\boldsymbol{p}+\boldsymbol{q},\uparrow}^{\dagger} \hat{c}_{\boldsymbol{k}-\boldsymbol{q},\downarrow}^{\dagger} \hat{c}_{\boldsymbol{p},\uparrow} \hat{c}_{\boldsymbol{k},\downarrow} ,
\end{aligned}
\tag{248}
$$

where $\epsilon_{\boldsymbol{k}}$ is the dispersion relation of Eq. (137) and $V_{\boldsymbol{kp}}^{R}$ is the transform of $V_{\boldsymbol{s}}^{R}(t)$ (cf. Eq. (243)). Let p be the quasi-momentum occupation probability which is defined by

$$p(\boldsymbol{k}, t) := \frac{n_{\boldsymbol{k}}(t)}{N} . \tag{249}$$

In Fig. 39, $p(k) := p(\boldsymbol{k})$ is shown for a one-dimensional system with $U = 3$ (top) and $U = -3$ (bottom) at the time $t = 9.5$ for different particle numbers $N = 2, \dots, 42$ which are represented by the color scheme. The dashed line corresponds to the initial distribution $p_0(k)$. The time is chosen in such a way that for all considered setups, the expansion velocity is converged. As one can see, for all N the distribution oscillates around p_0. The favoured occupation for large k can be described by a thermal distribution at effectively negative temperatures for positive U and vice versa (see Refs. [5, 20, 21] for further information). The amplitudes a of the oscillations monotonically decrease with the particle number. For sufficiently large N, one observes that the occupation probabilities obey

$$p(k) = \frac{1}{N_{\mathrm{s}}} - a \cos(k) . \tag{250}$$

By performing a fit, one can compute values of the amplitude a. The resulting dependence on U and N is illustrated in the insets of Fig. 39, where a is shown for varying $N^{-1/2}$. It can be seen that for all interaction strengths U, the amplitude a exhibits a linear scaling. The recovery of the scaling of Eq. (247) in the quasi-momentum distribution again confirms its universality.

Extrapolation and comparison with experiments
The inherent scaling of the asymptotic expansion velocity with the particle number can be used to extrapolate it to the macroscopic limit. From Eq. (247), one obtains the macroscopic expansion velocity V_{exp}. Using the example of two-dimensional systems, the resulting dependence on the interaction strength is shown in Fig. 40. The colors correspond to different many-body approximations. Again, the decreasing mobility of the particles in an interacting many-body state for increasing U is observed. The ordering of the different methods is in agreement to the findings of Fig. 36 and shows again that a proper treatment of correlations is essential for the description of diffusion processes in quantum systems.
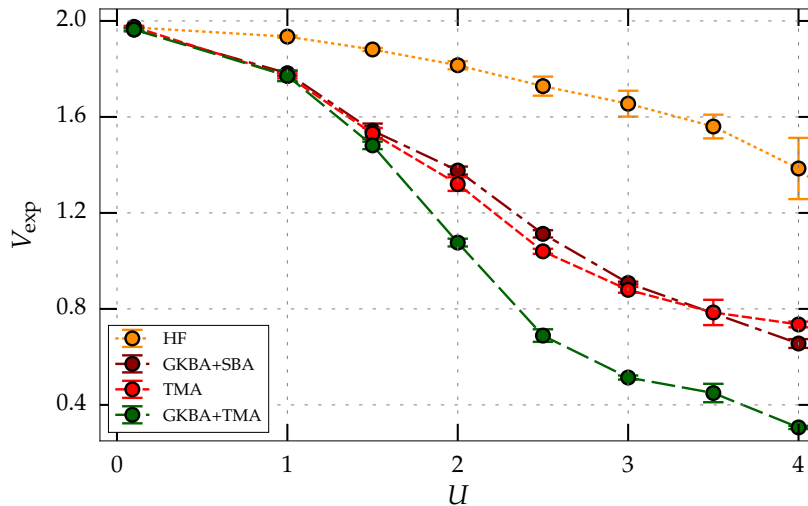
Fig. 40 U-dependence of the asymptotic expansion velocity: the obtained V_{exp} of Eq. (247) is shown for two-dimensional systems of varying interaction strengths U. The resulting behaviour is depicted for different many-body approximations.

Since the introduced approach is capable of reliably describing macroscopic transport processes, this allows to compare with experimental results of observations on ultracold atoms in optical lattices. In particular the fermionic diffusion in two-dimensional lattices which has been measured by Schneider et al. [5] (cf. Sec. 3.2)

is well suited for comparisons. The setups of Sec. 6.2.4 are very similar to the ones studied in Ref. [5]. They only slightly differ in the choice of the initial confinement[20]. In the experiments, Schneider et al. [5] used a strong harmonic trap, whereas the confinement provided by V_i^R (cf. Eq. (243)) is infinitely strong. Therefore, it is necessary to study the influence of the initial state on the asymptotic expansion.

Similar to V_i^R, one can define the harmonic confinement as

$$V_i^k(t) = \Theta(t_0, t)\, \gamma_k \, |i - s(t_0)|^2 \,, \tag{251}$$

with the curvature γ_k. To ensure comparability for different particle numbers, one can choose

$$\gamma_k(N) = \frac{k}{N} \tag{252}$$

which results in similar shapes of the density distributions. To test the influence of the confinement, the NEGF approach with GKBA and SBA is used for one-dimensional systems. Since the initial states in a harmonic trap are not ideal, the adiabatic switching method is used to prepare the interacting ground state. The resulting asymptotic expansion velocities v_{exp}^∞ for $U = 1$ are shown in Fig. 41 for varying particle number $N^{-1/2}$. The colors correspond to four different choices for k. The brown circles belong to the infinitely strong confinement V_i^R, whereas the red (orange, green) circles correspond to $k = 3$ (5,10). The insets show the density distributions of the initial states for $N = 26$. As one can see, even though the density profiles are affected by the differently strong confinements, the asymptotic expansion velocities only slightly change. Furthermore, the universal scaling with the particle number applies also for lower k which is illustrated by linear fits in Fig. 41. The macroscopic expansion velocity V_{exp} changes by less than 10% in the considered setups. Thus, one finds that the asymptotic expansion only slightly depends on the initial confinement. This has also been seen by the authors of Ref. [93]. Since Schneider et al. [5] used very strong harmonic traps to initially confine the particles, the description with V_i^R is justified.
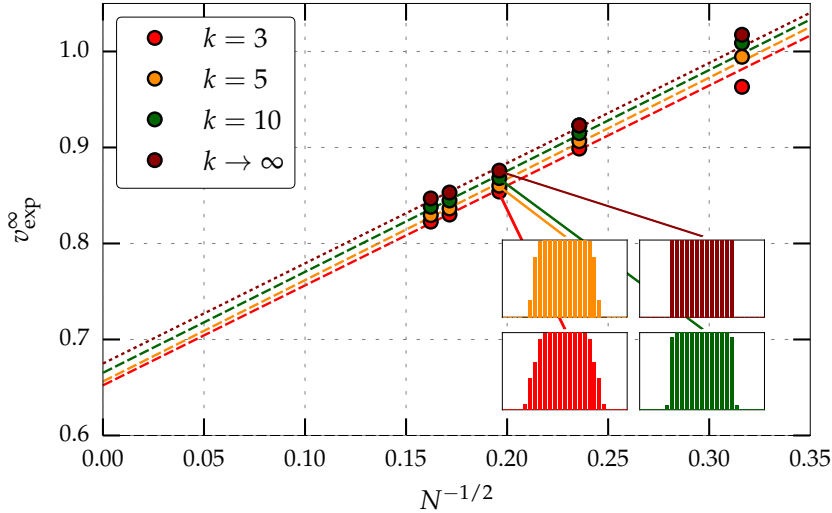
Fig. 41 Illustration of the asymptotic expansion for different initial confinements: for one-dimensional systems with $U = 1$, the obtained v_{exp}^∞ are depicted for varying particle numbers $N^{-1/2}$. The colors correspond to differently strong harmonic traps for the initial state. The circles denote results from GKBA+SBA calculations. The interacting ground state is prepared by adiabatic switching. The lines correspond to linear fits. The insets show the density distributions of the initial states for $N = 26$, according to the confinement of Eq. (251). The graphic is taken from Ref. [38].

Unfortunately, V_{exp} has not been directly measured in the experiments but the very closely related core expansion velocity C_{exp}. In agreement with Ref. [5], it is calculated in the following way. For two-dimensional

---

[20] The temperature of $T/T_{\text{F}} = 0.13$ in the experiments is sufficiently low to simulate the ground state at $T = 0$ (cf. Sec. 3.2) which is considered in this work.

systems, for each time step, the density profile is averaged azimuthally. From the resulting effectively one-dimensional density distribution, half width at half maximum $R_{\mathrm{HWHM}}(t)$ is used as a measure of the core width. The asymptotic core expansion velocity $c_{\mathrm{exp}}^{\infty}$ is obtained by fitting $R_{\mathrm{HWHM}}(t)$ to (cf. Eqs. (234) and (235))

$$R_{\mathrm{HWHM}}(t) = \sqrt{\left(R_{\mathrm{HWHM}}^{0}\right)^{2} + \left(c_{\mathrm{exp}}^{\infty} t\right)^{2}} \tag{253}$$

for all $t > t_{\mathrm{avg}}$ (cf. Eq. (245)). Here, the initial core width R_{HWHM}^{0} and $c_{\mathrm{exp}}^{\infty}$ denote free fitting parameters. From the experimental findings of Fig. 12 and from the results of Fig. 42, one finds that the core of the density distribution starts to shrink for large U. In these cases one applies

$$R_{\mathrm{HWHM}}(t) = \sqrt{\left(R_{\mathrm{HWHM}}^{0}\right)^{2} - \left(c_{\mathrm{exp}}^{\infty} t\right)^{2}} \tag{254}$$

instead. The resulting $c_{\mathrm{exp}}^{\infty}$ is then considered the speed of contraction of the core region. Due to its very close resemblance to $v_{\mathrm{exp}}^{\infty}$, $c_{\mathrm{exp}}^{\infty}$ reveals the same scaling with $N^{-1/2}$ which allows for an extrapolation to the macroscopic core expansion velocity C_{exp} according to Eq. (247).

For the T-matrix based methods, the resulting C_{exp} for two-dimensional systems as well as the experimental results of Schneider et al. [5] (cf. Fig. 12) are shown in Fig. 42 for varying interaction strengths U. The TMA (GKBA+TMA) calculation is shown in red (green), the plus-signs correspond to the experimental results for different lattice depths and the dashed, gray curve belongs to the results of Boltzmann equation in relaxation time approximation (cf. Sec. 3.2). In fact, the NEGF results exhibit a surprisingly good agreement with the experiment data in the full interaction range. Even the mentioned zero-crossing at $U \approx 3, -3$ is accurately described. As already discussed in Sec. 3.2, the core shrinking corresponds to a strongly interacting fermionic cloud which emits ballistic single-particles. Since the finite lattice depth seems not to systematically affect the resulting expansion velocities, this dependence can be neglected. Regarding the accuracy of the two propagation methods, the full two-time calculation seems to be slightly favorable for medium to large U.
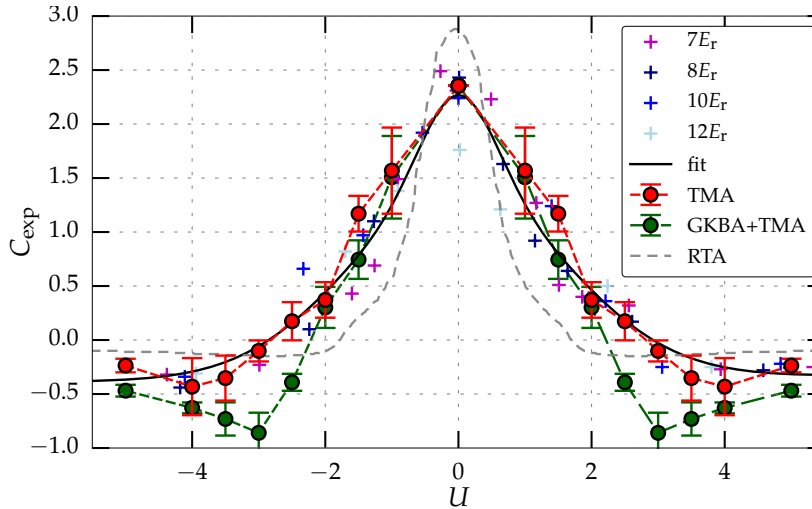
Fig. 42 Comparison with experimental results: the macroscopic core expansion velocity C_{exp} is shown for varying interaction strengths. The red (green) circles and error bars correspond to TMA calculations with full (GKBA) propagation. The plus-signs belong to the experimental results of Schneider et al. [5] (cf. Fig. 12) for different lattice depths. The dashed, gray curve corresponds to the results of the Boltzmann equation in relaxation time approximation which is discussed in Sec. 3.2. The black line is a fit through the experimental points to guide the eye.

Compared to the results of the RTA approach, the T-matrix results show a way better agreement with the experiments, especially for the zero-crossing which is predicted for significantly lower interaction strengths in RTA. This deviation accounts for the strong nonequilibrium situation of the systems, which is governed by the competition and interplay between ballistic, independent single-particles and strongly interacting, correlated fermions that form a complex many-body state. Due to the linearization of the Boltzmann equation in RTA, only systems

in local equilibrium can be described [21], whereas in the NEGF approach, the mentioned processes are fully taken into account.

7 Conclusions & Outlook

Summary

In this paper, the nonequilibrium Green functions (NEGF) method with the T-matrix approximation (TMA) for the selfenergy has been used to describe the dynamics of fermionic lattice systems. The main goal was to present theoretical and computational details of the recently reported simulations [38]. We have given a selfcontained introduction into the method of NEGF and derived their equations of motion—the Keldysh–Kadanoff Baym equations (KBE). We then discussed in detail relevant approximations for the selfenergy and concentrated on the derivation of the T-matrix selfenergy that is appropriate to model fermions on a Hubbard lattice.

Using the generalized Kadanoff–Baym ansatz [33] (GKBA), the less component of the Green function for different times $G^<(t, t')$ which, in general, is the solution of the full KBE, is approximately expressed by the density matrix and the propagators $G^{R/A}$. For the latter, the Hartree–Fock propagators $G^{HF,R/A}$, have been used. Despite its simplicity, the GKBA provides a full nonequilibrium description [68] which is often comparable in accuracy to the full two-time approach.

After the theoretical derivations we demonstrated how to efficiently realize NEGF simulations on modern computer hardware. We discussed optimized integration and time propagation schemes, together with parallelization approaches. All these recent advances have made it possible to perform NEGF-TMA simulations for rather large Hubbard systems that were recently far out of reach. With these optimizations we can now treat Hubbard clusters of several hundred sites of any dimensionality for rather long times, although a compromise between the number of sites and propagation time has to be made.

We have presented numerical results for transport processes in finite Hubbard systems. These include the diffusion from the boundary of one-dimensional Hubbard chains and diffusion from a doubly occupied central region. The latter case was of particular interest since this setup was studied in recent 2D experiments of ultracold fermionic atoms [5], where a potential quench was applied. We investigated this scenario for all dimensions, particle numbers in the range $2 \le N \le 114$ and interaction strengths of $0 \le U \le 8$. These system sizes are out of reach for most correlated ab-initio methods. Studying the short-time dynamics suggests to identify three phases which are linked to the build-up of entanglement. In particular, the correlation time scale is observed for significantly larger times than the single-particle time scale which is in striking contrast to homogeneous systems [43]. In the long time limit, the expansion velocities reveal a universal scaling with the particle number—independent of the interaction strength and the dimensionality. This has allowed us to extrapolate the expansion velocities to the macroscopic limit and to directly compare the experimental results. The experimental core expansion velocity could be reproduced with surprising accuracy in the whole range of coupling strengths, including the position of its zero-crossing.

Aside from reproducing the experimental results for the final stage of the expansion, our simulations have also revealed many details that have not been reported in experiments before. One example is the short-time behavior of the pair correlations and the entanglement in the system. Another prediction can be made for the details of the spatial formation of the correlations.

Single-site-resolved results

The present NEGF simulations are performed for a fully inhomogeneous case. Unlike hydrodynamic approaches, here no spatial averaging is performed, so the full microscopic spatial resolution is retained. While the dynamics of simple one-particle observables, such as the density, has been studied in detail before, the simulations also give access to other quantities that are directly sensitive to pair correlations. These quantities include the double occupations, the local entropy and the pair correlation function, $\delta n_s^{\uparrow\downarrow} = n_s^{\uparrow\downarrow} - n_s^\uparrow n_s^\downarrow$. An example of the dynamics of these quantities is shown in Fig. 43 [38]. Studying these quantities promises much deeper insight in the physics of strongly correlated fermions on all time scales. Moreover, recently site-resolved measurements on fermionic Hubbard lattices became possible [...] which can be directly compared to these simulations.
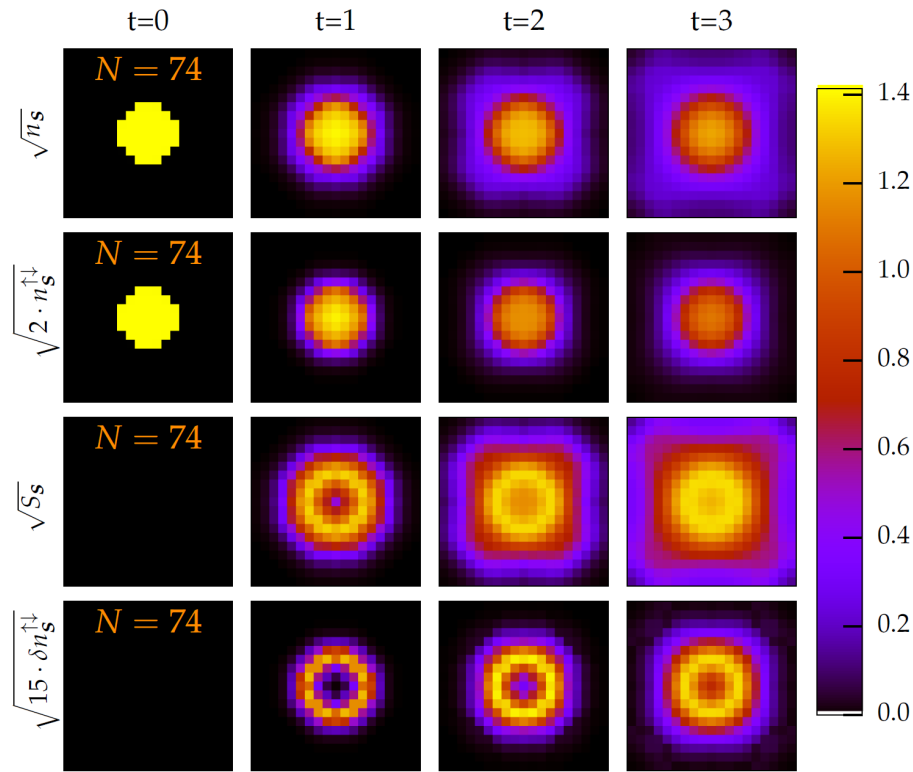
Fig. 43 Time and lattice site resolved fermion expansion dynamics in a 2D Hubbard lattice with 19×19 sites at $U = 4$. Top row: square root of density n_s for $N = 74$. Rows $2 - 4$: square root of double occupation, entropy density S_s and the pair correlation function, $\delta n_s^{\uparrow\downarrow} = n_s^{\uparrow\downarrow} - n_s^{\uparrow} n_s^{\downarrow}$. The graphic is taken from Ref. [38].

Outlook

As we demonstrated, the presented NEGF approach is perfectly applicable to a variety of problems of strong correlation physics in condensed matter systems and, equivalently, to fermionic atoms in optical lattices. In particular, situations far from equilibrium, including various quenches or excitation by electromagnetic radiation, can be accurately studied. Possible topics of the future research include

- Regarding the description of ultracold atoms in lattice systems, the NEGF framework can be used to compute other important transport quantities, such as the electrical- and the heat conductivity, as well as magnetic properties. Furthermore, the initial state, the system geometry and the dimension can be varied to investigate interesting nonequilibrium behaviour.

- An interesting question for future analysis is the behavior of correlated fermions on longer time scales and the approach of the asymptotic state. Whether this state coincides with a thermodynamic equilibrium state and what the relevant time scales and dominant collective modes are, is interesting from a fundamental and applied point of view.

- Since the NEGF approach is universal, it is possible to generalize the method to the description of bosons, in particular in lattice systems, for which many experimental results for ultracold atoms have been published whereas ab-initio quantum simulations for higher dimensions are still missing. To this end, one has to regard the right spin properties of the Bose–Hubbard interaction, which result in nonvanishing exchange diagrams. Furthermore, the bosonic sign in the NEGF theory and the Bose–Einstein statistics in the generation of the Hartree–Fock state have to be considered. Finally, to describe Bose-Einstein condensation one has to include anomalous propagators.

- The NEGF framework can also be generalized to more realistic lattice models such as the extended Hubbard model and the Pariser–Parr–Pople model [44], where interaction between particles on different lattice sites is considered, or to models with next-nearest neighbor hopping.

This work was motivated by the impressive progress in the field of strongly correlated fermionic lattice systems out of equilibrium. In particular, recent experiments with ultracold fermionic atoms in optical lattices open new prospects for studying correlation phenomena with unprecedented space and time resolution. The experimental advances have led to a growing need for accurate theoretical models that are capable to treat the quantum dynamics in two and three dimensions for sufficiently long times. While exact diagonalization methods can treat only very small systems other *ab initio* methods, such as DMRG, are currently limited to one-dimensional setups.

This striking mismatch between experiment and theory that is frequently being re-iterated in the experimental literature has now been removed. As was demonstrated in this paper, with nonequilibrium Green functions it is now possible to study experimentally relevant situations and achieve surprisingly close agreement.

Appendix

A   Derivation of the closed Newton–Cotes formulas

Starting from the integral expression of Eq. (162), one has to find a numerical expression which only depends on $f(x)$. Since for all polynomials

$$p : [a, b] \rightarrow \mathbb{R}, \, x \mapsto \sum_{i=0}^{N} a_i x^i, \, N \in \mathbb{N}, \tag{255}$$

the integration can easily be carried out analytically, it is convenient to express $f(x)$ approximately by such a polynomial.

To find an approximate expression for $f(x)$, in this work, equidistant sampling points are used, $x_i \in [a, b], i \in [0, n], n \in \mathbb{N}$, for which f produces the values $f_i := f(x_i)$. For these pairs of values $\{x_i, f_i\}$ there is a unique polynomial of degree at most n that interpolates the points f_i. This polynomial is called the Lagrange polynomial [65]

$$L_n(x) = \sum_{i=0}^{n} f_i l_i(x), \qquad \text{with} \tag{256}$$

$$l_i(x) = \prod_{\substack{j=0 \\ j \neq i}}^{n} \frac{x - x_j}{x_i - x_j}. \tag{257}$$

If the function f is $n + 1$ times continuously differentiable on $[a, b]$, there exists $\xi \in [a, b]$ such that

$$L_n(x) - f(x) = \frac{f^{(n+1)}(\xi)}{(n+1)!} \prod_{i=0}^{n} (x - x_i) \tag{258}$$

for all $x \in [a, b]$ [94, 95]. This equation can be used to estimate the error of the polynomial interpolation. Since the relation

$$\max_{\chi \in [a,b]} \left\{ \left| f^{(n+1)}(\chi) \right| \right\} \geq f^{n+1}(\xi) \tag{259}$$

holds, one can define the maximum error $\Delta \widetilde{L}_n(x, a, b)$,

$$L_n(x) - f(x) \leq \Delta \widetilde{L}_n(x, a, b) := \max_{\chi \in [a,b]} \left\{ \left| f^{(n+1)}(\chi) \right| \right\} \frac{\prod_{i=0}^{n} (x - x_i)}{(n+1)!} . \tag{260}$$

Assuming $x_0 = a$ and $x_n = b$, one obtains the closed Newton–Cotes formulas by simply integrating over the respective Lagrange polynomials. Consequently, one approximates the integral

$$
\begin{aligned}
I(f) \approx I(L_n) &= \int_a^b \mathrm{d}x \, L_n(x) \\
&= \int_{x_0}^{x_n} \mathrm{d}x \sum_{i=0}^{n} f_i \prod_{\substack{j=0 \\ j \neq i}}^{n} \frac{x - x_j}{x_i - x_j} \\
&= \sum_{i=0}^{n} f_i \int_{x_0}^{x_n} \mathrm{d}x \prod_{\substack{j=0 \\ j \neq i}}^{n} \frac{x - x_j}{x_i - x_j} \\
&= (x_n - x_0) \sum_{i=0}^{n} f_i \int_0^1 \mathrm{d}\hat{x} \prod_{\substack{j=0 \\ j \neq i}}^{n} \frac{\hat{x} - \hat{x}_j}{\hat{x}_i - \hat{x}_j} ,
\end{aligned}
\tag{261}
$$

with $\hat{x} = \frac{x - x_0}{x_n - x_0}$ and $\hat{x}_i = \frac{x_i - x_0}{x_n - x_0}$. Since the x_i are assumed to be equidistant, i.e. $x_i = x_0 + ih$ with the step width $h = \frac{x_n - x_0}{n}$, one obtains

$$\hat{x}_i = \frac{i}{n} \qquad \text{and} \qquad \frac{\hat{x} - \hat{x}_j}{\hat{x}_i - \hat{x}_j} = \frac{\hat{x} - \frac{j}{n}}{\frac{i}{n} - \frac{j}{n}} = \frac{n\hat{x} - j}{i - j} . \tag{262}$$

Eq. (261) can be written in the form

$$I(L_n) = nh \sum_{i=0}^{n} f_i w_i^n , \qquad \text{with} \tag{263}$$

$$w_i^n := \int_0^1 \mathrm{d}\hat{x} \prod_{\substack{j=0 \\ j \neq i}}^{n} \frac{n\hat{x} - j}{i - j} . \tag{264}$$

To estimate the validity of these formulas, one can consider Eqs. (258) and (260), from which one can easily see that the errors of the closed Newton–Cotes formulas are given by integration over the error of the respective Lagrange polynomial, i.e.

$$\int_a^b \mathrm{d}x \, L_n(x) - \int_a^b \mathrm{d}x \, f(x) \leq \int_a^b \mathrm{d}x \, \Delta \widetilde{L}_n(x, a, b) =: \Delta L_n(a, b) . \tag{265}$$

The so-defined integration error $\Delta L_n(a,b)$ can be simplified using the substitution $s = n\left(\frac{x-x_0}{x_n-x_0} - \frac{1}{2}\right)$,

$$\Delta L_n(a,b) = \max_{\chi\in[a,b]}\left\{\frac{\left|f^{(n+1)}(\chi)\right|}{(n+1)!}\right\}\int_{x_0}^{x_n}\mathrm{d}x\prod_{i=0}^{n}(x-x_i) \tag{266}$$

$$= \max_{\chi\in[a,b]}\left\{\frac{\left|f^{(n+1)}(\chi)\right|}{(n+1)!}\right\}h^{n+2}\int_{-\frac{n}{2}}^{\frac{n}{2}}\mathrm{d}s\prod_{i=-\frac{n}{2}}^{\frac{n}{2}}(s-i)\ . \tag{267}$$

Therefore, the error $\Delta L_n(a,b,h)$ is of the order $\sim\mathcal{O}(h^{n+2}\left|f^{(n+1)}\right|)$.

For the function $g(s) = \prod_{i=-\frac{n}{2}}^{\frac{n}{2}}(s-i)$, there exist two different symmetry relations. For odd n the relation $g(-s) = g(s)$ holds, while for even n one obtains $g(-s) = -g(s)$. Since the integral boundaries in Eq. (267) are also symmetric, the integration error term vanishes for even n. Since this formula only calculates the leading error term, this means that one has to estimate the error for even n with the interpolation error for $n+1$, which is $\Delta\widetilde{L}_{n+1}(a,b,h)$. Finally, $\Delta L_n(a,b,h)$ becomes

$$\Delta L_n(a,b,h) = \begin{cases} \max_{\chi\in[a,b]}\left\{\left|f^{(n+1)}(\chi)\right|\right\}\frac{h^{n+2}}{(n+1)!}\int_{-\frac{n}{2}}^{\frac{n}{2}}\mathrm{d}s\prod_{i=-\frac{n}{2}}^{\frac{n}{2}}(s-i), & n\,\text{odd} \\ \max_{\chi\in[a,b]}\left\{\left|f^{(n+2)}(\chi)\right|\right\}\frac{h^{n+3}}{(n+2)!}\int_{-\frac{n}{2}}^{\frac{n}{2}}\mathrm{d}s\prod_{i=-\frac{n}{2}-1}^{\frac{n}{2}}(s-i), & n\,\text{even} \end{cases}, \tag{268}$$

or

$$\Delta L_n(a,b,h) = \begin{cases} \mathcal{O}\left(h^{n+2}\left|f^{(n+1)}\right|\right), & n\,\text{odd} \\ \mathcal{O}\left(h^{n+3}\left|f^{(n+2)}\right|\right), & n\,\text{even} \end{cases}, \tag{269}$$

respectively. The resulting weights and error terms of the closed Newton–Cotes formulas up to the order $n=6$ are listed in Tab. 1.

Table 1   Weight factors and error terms of the closed Newton–Cotes formulas: The weight factors w_i^n of Eq. (163) and the error terms $\Delta L_n(x,a,b)$ according to Eq. (268) are listed up to the order $n=6$.

n	w_i^n							ΔL_n
1	$\frac{1}{2}$	$\frac{1}{2}$						$-\frac{1}{12}h^3\max_{\chi\in[a,b]}\left\{\left|f''(\chi)\right|\right\}$
2	$\frac{1}{6}$	$\frac{4}{6}$	$\frac{1}{6}$					$-\frac{1}{90}h^5\max_{\chi\in[a,b]}\left\{\left|f^{(4)}(\chi)\right|\right\}$
3	$\frac{1}{8}$	$\frac{3}{8}$	$\frac{3}{8}$	$\frac{1}{8}$				$-\frac{3}{80}h^5\max_{\chi\in[a,b]}\left\{\left|f^{(4)}(\chi)\right|\right\}$
4	$\frac{7}{90}$	$\frac{32}{90}$	$\frac{12}{90}$	$\frac{32}{90}$	$\frac{7}{90}$			$-\frac{8}{945}h^7\max_{\chi\in[a,b]}\left\{\left|f^{(6)}(\chi)\right|\right\}$
5	$\frac{19}{288}$	$\frac{75}{288}$	$\frac{50}{288}$	$\frac{50}{288}$	$\frac{75}{288}$	$\frac{19}{288}$		$-\frac{275}{12096}h^7\max_{\chi\in[a,b]}\left\{\left|f^{(6)}(\chi)\right|\right\}$
6	$\frac{41}{840}$	$\frac{216}{840}$	$\frac{27}{840}$	$\frac{272}{840}$	$\frac{27}{840}$	$\frac{216}{840}$	$\frac{41}{840}$	$-\frac{9}{1400}h^9\max_{\chi\in[a,b]}\left\{\left|f^{(8)}(\chi)\right|\right\}$

B   Analytical computation of polynomial integrals

For the numerical solution of integrals with the use of Newton–Cotes formulas, it is necessary to compute expressions of the form,

$$\int_0^1\mathrm{d}a\prod_{i=0}^{n}(a-b_i)\ . \tag{270}$$

To make such a term accessible to calculations on a computer, one can perform the following transformations,

$$
\prod_{i=0}^{n} (a - b_i) = (a - b_0)(a - b_1)\ldots(a - b_n) \tag{271}
$$

$$
\begin{aligned}
= \; & a^{n+1} - a^n (b_0 + \cdots + b_n) \\
& + a^{n-1}(b_0 b_1 + \cdots + b_0 b_n + b_1 b_2 + \cdots + b_1 b_n + \cdots + b_{n-1} b_n) \\
& + \ldots \\
& + (-1)^{n+1} a^0 (b_0 b_1 \cdots b_n)
\end{aligned} \tag{272}
$$

$$
\begin{aligned}
= \; & (-1)^0 \, a^{n+1} \frac{1}{0!} + (-1)^1 \, a^n \frac{1}{1!} \sum_{k_0=0}^{n} b_{k_0} \\
& + (-1)^2 \, a^{n-1} \frac{1}{2!} \sum_{k_0 \neq k_1}^{n} b_{k_0} b_{k_1} + \ldots \\
& + (-1)^{n+1} a^0 \frac{1}{(n+1)!} \sum_{\substack{k_0 \neq k_1 \\ \neq \cdots \neq k_n}}^{n} b_{k_0} b_{k_1} \ldots b_{k_n}
\end{aligned} \tag{273}
$$

$$
= \sum_{i=0}^{n+1} (-1)^{n+1-i} a^i \frac{1}{(n+1-i)!} \sum_{\substack{k_0 \neq k_1 \neq \ldots \\ \neq k_{n-i}}}^{n} \left(\prod_{j=0}^{n-i} b_{k_j} \right). \tag{274}
$$

In this form, the integration can easily be done,

$$
\int_0^1 \mathrm{d}a \prod_{i=0}^{n} (a - b_i) = \left[\sum_{i=0}^{n+1} (-1)^{n+1-i} \frac{1}{i+1} a^{i+1} \frac{1}{(n+1-i)!} \sum_{\substack{k_0 \neq k_1 \neq \ldots \\ \neq k_{n-i}}}^{n} \left(\prod_{j=0}^{n-i} b_{k_j} \right) \right]_0^1 \tag{275}
$$

$$
= \sum_{i=0}^{n+1} \frac{(-1)^{n+1-i}}{i+1} \frac{1}{(n+1-i)!} \sum_{\substack{k_0 \neq k_1 \neq \ldots \\ \neq k_{n-i}}}^{n} \left(\prod_{j=0}^{n-i} b_{k_j} \right). \tag{276}
$$

The last expression can be evaluated numerically which is readily implemented.

C The extended integration formulas

The closed Newton–Cotes formulas of degree n can only include $n+1$ sampling points. The easiest way to include more points is to separate the interval into regions with $n+1$ points. With $N = kn$, $k \in \mathbb{N}$ and $x_0 = a$, $x_N = b$, one can split the integral in the following way,

$$
\begin{aligned}
I(f) = \int_a^b \mathrm{d}x \, f(x) = \; & \int_{x_0}^{x_n} \mathrm{d}x \, f(x) + \int_{x_n}^{x_{2n}} \mathrm{d}x \, f(x) + \ldots \\
& + \int_{x_{(k-2)n}}^{x_{(k-1)n}} \mathrm{d}x \, f(x) + \int_{x_{(k-1)n}}^{x_N} \mathrm{d}x \, f(x).
\end{aligned} \tag{277}
$$

Each of the resulting integration terms can be approximated by a closed Newton–Cotes formula, as shown in App. A. Therefore, one obtains

$$
\begin{aligned}
I(f) \; \approx \; & nh \sum_{j=1}^{k} \sum_{i=0}^{n} f_{(j-1)n+i} w_i^n \\
= \; & nh \left[f_0 w_0^n + f_N w_n^n + \sum_{i=1}^{N-1} f_i \left(w_{i \bmod n}^n + \delta_{i \bmod n} w_n^n \right) \right].
\end{aligned} \tag{278}
$$

Here, δ_m is defined as $\delta_m = \begin{cases} 1, & m = 0 \\ 0, & m \neq 0 \end{cases}$.

Considering, e.g., $n = 1$, one obtains the extended trapezoidal rule,

$$I(f) \approx h \left[\frac{f_0 + f_N}{2} + \sum_{j=1}^{N-1} f_j \right] . \tag{279}$$

Since the integral term can be divided into several terms as shown in Eq. (277), the respective error can be expressed in the same way. Using the error formula for a single Newton–Cotes integration of Eq. (268), one obtains the error of the extended Newton–Cotes formulas $\Delta L_n^{\text{ext}}(a, b, h, N)$,

$$\sum_{j=1}^{k} \Delta L_n(x_{(j-1)n}, x_{jn}, h) \overset{(*)}{\leq} k \Delta L_n(x_0, x_N, h) = \frac{N}{n} \Delta L_n(a, b, h) =: \Delta L_n^{\text{ext}}(a, b, h, N) . \tag{280}$$

The relation $(*)$ holds because

$$\max_{\chi \in [a,b]} \left\{ \left| f^{(m)}(\chi) \right| \right\} \geq \max_{\chi \in \left[x_{(j-1)n}, x_{jn} \right]} \left\{ \left| f^{(m)}(\chi) \right| \right\} \tag{281}$$

for all $m \in \mathbb{N}$, $j \leq k$.
$\Delta L_n^{\text{ext}}(a, b, h, N)$ can be written as

$$\Delta L_n^{\text{ext}}(a, b, h, N) = \begin{cases} \max_{\chi \in [a,b]} \left\{ \left| f^{(n+1)}(\chi) \right| \right\} \frac{N h^{n+2}}{n(n+1)!} \int_{-\frac{n}{2}}^{\frac{n}{2}} \mathrm{d}s \prod_{i=-\frac{n}{2}}^{\frac{n}{2}} (s-i), & n \text{ odd} \\ \max_{\chi \in [a,b]} \left\{ \left| f^{(n+2)}(\chi) \right| \right\} \frac{N h^{n+3}}{n(n+2)!} \int_{-\frac{n}{2}}^{\frac{n}{2}} \mathrm{d}s \prod_{i=-\frac{n}{2}-1}^{\frac{n}{2}} (s-i), & n \text{ even} \end{cases}, \tag{282}$$

or

$$\Delta L_n^{\text{ext}}(a, b, h, N) = \begin{cases} \mathcal{O}\left(N h^{n+2} \left| f^{(n+1)} \right| \right), & n \text{ odd} \\ \mathcal{O}\left(N h^{n+3} \left| f^{(n+2)} \right| \right), & n \text{ even} \end{cases} . \tag{283}$$

Since the extended Newton–Cotes formulas of Eq. (278) are only applicable for a fitting number of sampling points (i.e. $N = kn$, $k \in \mathbb{N}$), it is useful to develop a scheme that enables integration for all $N \in \mathbb{N}$. Therefore, the number of blocks $a_N(\tilde{n})$ for the respective order $\tilde{n} \leq n$ is introduced. Since, in this paper, f and its derivatives are considered to be of similar shape throughout $[x_0, x_N]$, it is convenient to arrange the blocks as presented in Sec. 5.1, i.e. the points $[x_{\sum_{\hat{n}=\tilde{n}+1}^{n} a_N(\hat{n}) \cdot \hat{n}}, x_{\sum_{\hat{n}=\tilde{n}}^{n} a_N(\hat{n}) \cdot \hat{n}}]$ are treated via the extended Newton–Cotes formula for $\tilde{n}$, if $a_N(\tilde{n}) > 0$. For the total integral, that means (Eq. (278))

$$\begin{aligned} I(f) & \approx & I_n^{\text{closed}}(a_N) \\ & := & \sum_{\tilde{n}=1}^{n} \tilde{n} h \left[f_{\sum_{\hat{n}=\tilde{n}+1}^{n} a_N(\hat{n}) \cdot \hat{n}} w_0^{\tilde{n}} + f_{\sum_{\hat{n}=\tilde{n}}^{n} a_N(\hat{n}) \cdot \hat{n}} w_{\tilde{n}}^{\tilde{n}} \right. \\ & & \left. + \sum_{i=1}^{a_N(\hat{n}) \cdot \hat{n} - 1} f_{i + \sum_{\hat{n}=\tilde{n}+1}^{n} a_N(\hat{n}) \cdot \hat{n}} \left(w_{i \bmod \tilde{n}}^{\tilde{n}} + \delta_{i \bmod \tilde{n}} w_{\tilde{n}}^{\tilde{n}} \right) \right] . \end{aligned} \tag{284}$$

The error that results from this procedure can be estimated using Eq. (282) and demanding $\Delta L_n^{\text{ext}}(x, x, h, 0) = 0$:

$$\begin{aligned} \Delta L_n^{\text{ext}}(x_0, x_N, h, N) & = & \sum_{\tilde{n}=1}^{n} \Delta L_{\tilde{n}}^{\text{ext}}\left(x_{\sum_{\hat{n}=\tilde{n}+1}^{n} a_N(\hat{n}) \cdot \hat{n}}, x_{\sum_{\hat{n}=\tilde{n}}^{n} a_N(\hat{n}) \cdot \hat{n}}, h, a_N(\tilde{n}) \cdot \tilde{n} \right) \\ & \overset{(**)}{\leq} & \sum_{\tilde{n}=1}^{n} \Delta L_{\tilde{n}}^{\text{ext}}(x_0, x_N, h, a_N(\tilde{n}) \cdot \tilde{n}) . \end{aligned} \tag{285}$$

Table 2 Final order check: The adjacent points of N_n^{FO}, their block structure and their respective answer to the question, whether the final order is achieved are listed.

N	$a_N(n)$	$a_N(n-1)$	$a_N(n-2)$	final order achieved
$N_n^{\text{FO}} - 1$	0	$n-3$	1	no
N_n^{FO}	0	$n-2$	0	yes
$N_n^{\text{FO}} + 1$	1	$n-3$	0	yes
$\vdots$	$\vdots$	$\vdots$	$\vdots$	$\vdots$
$N_n^{\text{FO}} + n - 2$	$n-2$	0	0	yes
$N_n^{\text{FO}} + n - 1$	0	$n-1$	0	yes
$\vdots$	$\vdots$	$\vdots$	$\vdots$	$\vdots$

Here, the relation $(**)$ holds because

$$\max_{\chi \in [x_0, x_N]} \left\{ \left| f^{(m)}(\chi) \right| \right\} \geq \max_{\chi \in [x_p, x_q]} \left\{ \left| f^{(m)}(\chi) \right| \right\} \tag{286}$$

for all $m \in \mathbb{N}$ and $p, q \in [0, N]$. Notice that Eq. (285) gives the correct error for any choice of $a_N(\tilde{n})$.

D   Details on the optimal order scheme

The integration order of the optimal order scheme that is introduced in Sec. 5.1 can be found by combining Eqs. (282) and (285). It is evident that for a consecutive series of N, the error terms are of the same order, once the point is reached, where there are enough sampling points to integrate only with $\tilde{n} = n$ and $\tilde{n} = n - 1$.

In general, a homogeneous order for increasing N can only be achieved by choosing an odd n. In this case, it becomes $\mathcal{O}\left(h^{n+2} \left| f^{(n+1)} \right| \right)$. For even n, however, the arising order varies between $\mathcal{O}\left(h^{n+3} \left| f^{(n+2)} \right| \right)$ and $\mathcal{O}\left(h^{n+1} \left| f^{(n)} \right| \right)$. The minimum value for N, where integration solely with $\tilde{n} = n$ and $\tilde{n} = n - 1$ is possible, and thus the final order is reached, is given by

$$N_n^{\text{FO}} = (n-1)(n-2) \qquad . \tag{287}$$

To show this, one has to discuss the different adjacent cases. As mentioned before, the final order is achieved, if

$$\left(a_N(n) \neq 0 \vee a_N(n-1) \neq 0 \right) \wedge \left(a_N(\tilde{n}) = 0 \,\forall\, \tilde{n} \leq n-2 \right) \qquad . \tag{288}$$

By applying Eq. (165) to N, one gets the $a_N(\tilde{n})$ that are listed in Tab. 2. It turns out that for any n, N_n^{FO} exactly gives the minimum value for N, so that the final order of integration is ensured.

E   Integration with generalized raster boundaries

Based on the Lagrange polynomial in Eqs. (256) and (257), one can find an expression that estimates the integral between the border (a or b) and the first or last sampling point (x_0 or x_N). Considering, e.g., $a < x_0$ and $b = x_N$, then the closed integration is done for $[x_0, x_N]$ as shown in Sec. 5.1 and the interval $[a, x_0]$ is left. In this instance, the Lagrange polynomial, build up from the points $a, x_0 \ldots x_{n-1}$ can be integrated from a to x_0. Let d denote the length of this interval, $d = x_0 - a$. In analogy to App. A, the resulting weight factors can be calculated as

follows:

$$
\begin{aligned}
I(f)\Big|_a^{x_0} \approx I(L_n)\Big|_a^{x_0} &= \int_a^{x_0} \mathrm{d}x \left[f_a \prod_{j=0}^{n-1} \frac{x-x_j}{a-x_j} + \sum_{i=0}^{n-1} f_i \frac{x-a}{x_i-a} \prod_{\substack{j=0 \\ j\neq i}}^{n-1} \frac{x-x_j}{x_i-x_j} \right] \quad (289) \\
&= f_a \int_{x_0-d}^{x_0} \mathrm{d}x \prod_{j=0}^{n-1} \frac{x-x_j}{x_0-d-x_j} \\
&\quad + \sum_{i=0}^{n-1} f_i \int_{x_0-d}^{x_0} \mathrm{d}x \frac{x-x_0+d}{x_i-x_0+d} \prod_{\substack{j=0 \\ j\neq i}}^{n-1} \frac{x-x_j}{x_i-x_j} \quad (290) \\
&= d f_a \int_0^1 \mathrm{d}\bar{x} \prod_{j=0}^{n-1} \left(1-\frac{\bar{x}}{\bar{x}_j}\right) \\
&\quad + d \sum_{i=0}^{n-1} f_i \int_0^1 \mathrm{d}\bar{x} \frac{\bar{x}}{\bar{x}_i} \prod_{\substack{j=0 \\ j\neq i}}^{n-1} \frac{\bar{x}-\bar{x}_j}{\bar{x}_i-\bar{x}_j} \,, \quad (291)
\end{aligned}
$$

with $\bar{x} = \frac{x-x_0}{d}+1$ and $\bar{x}_i = \frac{x_i-x_0}{d}+1$. Assuming, again, equidistant x_i, i.e. $x_i = x_0 + ih$, one obtains

$$
\bar{x}_i = i\frac{h}{d}+1 \qquad \text{and} \qquad \frac{\bar{x}-\bar{x}_j}{\bar{x}_i-\bar{x}_j} = \frac{\frac{d}{h}(\bar{x}-1)-j}{i-j} \,. \quad (292)
$$

Eq. (291) can be written in the form

$$
I(L_n)\Big|_a^{x_0} = h\left(f(a) w_a^{n,\mathrm{gr}} + \sum_{i=0}^{n-1} f_i w_i^{n,\mathrm{gr}} \right) \,, \quad (293)
$$

with the generalized raster weight factors

$$
w_i^{n,\mathrm{gr}} = \frac{d}{h} \int_0^1 \mathrm{d}\bar{x} \frac{\bar{x}}{i\frac{h}{d}+1} \prod_{\substack{j=0 \\ j\neq i}}^{n-1} \frac{\frac{d}{h}(\bar{x}-1)-j}{i-j} \,, \quad (294)
$$

$$
w_a^{n,\mathrm{gr}} = \frac{d}{h} \int_0^1 \mathrm{d}\bar{x} \prod_{j=0}^{n-1} \left(1-\frac{\bar{x}}{j\frac{h}{d}+1}\right) \,. \quad (295)
$$

For n up to the order $n=4$, the resulting weights as well as the respective error terms (see below) are shown in Tab. 3. Due to symmetry reasons, the same weight factors are obtained for $a = x_0$ and $b > x_N$, but in reverse order. An error estimation can be found by integration over the corresponding error term of the Lagrange polynomial (cf. Eq. (260)),

$$
\begin{aligned}
\Delta L_n^{\mathrm{gr}}\left(a,b,h,\frac{d}{h}\right) &:= \int_a^{x_0} \mathrm{d}x \max_{\chi\in[a,b]}\left\{\left|f^{(n+1)}(\chi)\right|\right\} \frac{(x-a)\prod_{i=0}^{n-1}(x-x_i)}{(n+1)!} \\
&= \max_{\chi\in[a,b]}\left\{\left|f^{(n+1)}(\chi)\right|\right\} \frac{h^{n+2}}{(n+1)!}\left(\frac{d}{h}\right)^2 \int_0^1 \mathrm{d}\bar{x}\,\bar{x}\prod_{i=0}^{n-1}\left[\frac{d}{h}(\bar{x}-1)-i\right] \,. \quad (296)
\end{aligned}
$$

To estimate the total error of the integration in $[a,b]$ for, e.g., $a < x_0$ and $b > x_N$, one can separate the error term in the same way as the integral,

$$
\int_a^b \mathrm{d}x\, f(x) = \int_a^{x_0} \mathrm{d}x\, f(x) + \int_{x_0}^{x_N} \mathrm{d}x\, f(x) + \int_{x_N}^b \mathrm{d}x\, f(x) \quad (297)
$$

and the respective numerical expression

$$I_n^{\text{num}}(N) := I(L_n)\Big|_a^{x_0} + I_n^{\text{closed}}(a_N) + I(L_n)\Big|_{x_N}^b \tag{298}$$

into three parts,

$$
\begin{aligned}
\Delta L_n^{\text{ext,gr}}(a,b,h,N) \quad &:= \quad \Delta L_{\min(N-1,n)}^{\text{gr}}\left(a,x_N,h,\frac{x_0-a}{h}\right) + \Delta L_n^{\text{ext}}(x_0,x_N,h,N) \\
&\quad + \Delta L_{\min(N-1,n)}^{\text{gr}}\left(x_0,b,h,\frac{b-x_N}{h}\right) \tag{299} \\
&\leq \quad \Delta L_{\min(N-1,n)}^{\text{gr}}\left(a,b,h,\frac{x_0-a}{h}\right) + \Delta L_n^{\text{ext}}(a,b,h,N) \\
&\quad + \Delta L_{\min(N-1,n)}^{\text{gr}}\left(a,b,h,\frac{b-x_N}{h}\right). \tag{300}
\end{aligned}
$$

The final order for the complete integration is obtained when $N \geq N_n^{\text{FO}} \wedge N \geq n+1$. Therefore, it is convenient to define the new $N_n^{\text{FO,gr}}$,

$$N_n^{\text{FO,gr}} = \max\left(N_n^{\text{FO}}, n+1\right). \tag{301}$$

Table 3 Weight factors of the generalized raster integration: For n up to $n=4$ and $d=\frac{1}{2}$, the generalized raster weight factors of Eq. (168) and the respective error terms according to Eq. (296) are listed.

n	$\frac{d}{h}$	$w_a^{n,\text{gr}}$	$w_i^{n,\text{gr}}$				ΔL_n^{gr}
0	$\frac{1}{2}$	$\frac{1}{2}$	-				$\frac{1}{8}h^2 \max_{\chi \in [a,b]}\left\{|f'(\chi)|\right\}$
1	$\frac{1}{2}$	$\frac{1}{4}$	$\frac{1}{4}$				$-\frac{1}{96}h^3 \max_{\chi \in [a,b]}\left\{|f''(\chi)|\right\}$
2	$\frac{1}{2}$	$\frac{16}{72}$	$\frac{21}{72}$	$-\frac{1}{72}$			$\frac{5}{1152}h^4 \max_{\chi \in [a,b]}\left\{\left|f^{(3)}(\chi)\right|\right\}$
3	$\frac{1}{2}$	$\frac{40}{192}$	$\frac{61}{192}$	$-\frac{6}{192}$	$\frac{1}{192}$		$-\frac{113}{46080}h^5 \max_{\chi \in [a,b]}\left\{\left|f^{(4)}(\chi)\right|\right\}$
4	$\frac{1}{2}$	$\frac{40192}{201600}$	$\frac{68005}{201600}$	$-\frac{10255}{201600}$	$\frac{3423}{201600}$	$-\frac{565}{201600}$	$\frac{41}{25600}h^6 \max_{\chi \in [a,b]}\left\{\left|f^{(5)}(\chi)\right|\right\}$

If $N > N_n^{\text{FO,gr}}$, the resulting total error is of the order

$$
\begin{aligned}
\Delta L_n^{\text{ext,gr}}(a,b,h,N) \quad &= \quad \mathcal{O}\left(h^{n+2}\left|f^{(n+1)}\right|\right) + \mathcal{O}\left(h^{n+2}\left|f^{(n+1)}\right|\right) + \mathcal{O}\left(h^{n+2}\left|f^{(n+1)}\right|\right) \\
&= \quad \mathcal{O}\left(h^{n+2}\left|f^{(n+1)}\right|\right) \tag{302}
\end{aligned}
$$

for odd n and varies between

$$
\begin{aligned}
\Delta L_n^{\text{ext,gr}}(a,b,h,N) \quad &= \quad \mathcal{O}\left(h^{n+2}\left|f^{(n+1)}\right|\right) + \mathcal{O}\left(h^{n+1}\left|f^{(n)}\right|\right) + \mathcal{O}\left(h^{n+2}\left|f^{(n+1)}\right|\right) \\
&= \quad \mathcal{O}\left(h^{n+1}\left|f^{(n)}\right|\right) \tag{303}
\end{aligned}
$$

and

$$
\begin{aligned}
\Delta L_n^{\text{ext,gr}}(a,b,h,N) \quad &= \quad \mathcal{O}\left(h^{n+2}\left|f^{(n+1)}\right|\right) + \mathcal{O}\left(h^{n+3}\left|f^{(n+2)}\right|\right) + \mathcal{O}\left(h^{n+2}\left|f^{(n+1)}\right|\right) \\
&= \quad \mathcal{O}\left(h^{n+2}\left|f^{(n+1)}\right|\right) \tag{304}
\end{aligned}
$$

for even n.

References

[1] E. Pavarini, D. Vollhardt, A. Lichtenstein, and E. Koch, The LDA+ DMFT approach to strongly correlated materials (Verlag des Forschungszentrum Jülich, 2011).

[2] A.-M. Uimonen, E. Khosravi, A. Stan, G. Stefanucci, S. Kurth, R. van Leeuwen, and E. Gross, Phys. Rev. B **84**, 115103 (2011).

[3] K. Balzer, M. Bonitz, R. van Leeuwen, A. Stan, and N.E. Dahlen, Phys. Rev. B **79**, 245306 (2009).

[4] H. Whitley, C.R. Scullard, L. Benedict, J. Castor, A. Randles, J. Glosli, D. Richards, M. Desjarlais, and F. Graziani, Contrib. Plasma Phys. **55**, 192 (2015).

[5] U. Schneider, L. Hackermüller, J.P. Ronzheimer, S. Will, S. Braun, T. Best, I. Bloch, E. Demler, S. Mandt, D. Rasch, et al., Nat. Phys. **8**, 213 (2012).

[6] J.P. Ronzheimer, M. Schreiber, S. Braun, S.S. Hodgman, S. Langer, I.P. McCulloch, F. Heidrich-Meisner, I. Bloch, and U. Schneider, Phys. Rev. Lett. **110**, 205301 (2013).

[7] J. Kajala, F. Massel, and P. Törmä, Phys. Rev. Lett. **106**, 206401 (2011).

[8] I. Bloch, Nat. Phys. **1**, 23 (2005).

[9] K.B. Davis, M.-O. Mewes, M.R. Andrews, N. Van Druten, D. Durfee, D. Kurn, and W. Ketterle, Phys. Rev. Lett. **75**, 3969 (1995).

[10] M.H. Anderson, J.R. Ensher, M.R. Matthews, C.E. Wieman, and E.A. Cornell, Science **269**, 198 (1995).

[11] C.C. Bradley, C. Sackett, J. Tollett, and R.G. Hulet, Phys. Rev. Lett. **75**, 1687 (1995).

[12] C. Chin, R. Grimm, P. Julienne, and E. Tiesinga, Rev. Mod. Phys. **82**, 1225 (2010).

[13] M. Cheneau, P. Barmettler, D. Poletti, M. Endres, P. Schauß, T. Fukuhara, C. Gross, I. Bloch, C. Kollath, and S. Kuhr, Nature **481**, 484 (2012).

[14] S. Trotzky, Y.-A. Chen, A. Flesch, I. P. McCulloch, U. Schollwöck, J. Eisert, and I. Bloch, Nat. Phys. **8**, 325 (2012).

[15] S. Will, D. Iyer, and M. Rigol, Nat. Commun. **6**, (2015).

[16] M. Lewenstein, A. Sanpera, and V. Ahufinger, Ultracold atoms in optical lattices: simulating quantum manybody systems (OUP Oxford, 2012).

[17] X. Zhang, C.-L. Hung, S.-K. Tung, and C. Chin, Science **335**, 1070 (2012).

[18] J. Denschlag, D. Cassettari, and J. Schmiedmayer, Phys. Rev. Lett. **82**, 2014 (1999).

[19] A. Moerdijk, B. Verhaar, and A. Axelsson, Phys. Rev. A **51**, 4852 (1995).

[20] U. Schneider, Interacting fermionic atoms in optical lattices—a quantum simulator for condensed matter physics, PhD thesis (Johannes Gutenberg-Universität Mainz, 2010).

[21] S. Mandt, Transport and non-equilibrium dynamics in optical lattices. from expanding atomic clouds to negative absolute temperatures, PhD thesis (Universität zu Köln, 2012).

[22] C.J. Cramer, Essentials of computational chemistry: theories and models (John Wiley & Sons, 2013).

[23] S. R. White, Phys. Rev. Lett. **69**, 2863 (1992).

[24] U. Schollwöck, Matrix product state algorithms: DMRG, TEBD and relatives, in Strongly correlated systems (Springer, 2013), pp. 6798.

[25] E. Runge and E.K. Groß, Phys. Rev. Lett. **52**, 997 (1984).

[26] P. Hohenberg and W. Kohn, Phys. Rev. **136**, B864 (1964).

[27] D. Karlsson, A. Privitera, and C. Verdozzi, Phys. Rev. Lett. **106**, 116401 (2011).

[28] C. Verdozzi, D. Karlsson, M.P. von Friesen, C.-O. Almbladh, and U. von Barth, Chem. Phys. **391**, 37 (2011).

[29] A. Georges, G. Kotliar, W. Krauth, and M.J. Rozenberg, Rev. Mod. Phys. **68**, 13 (1996).

[30] D. Hochstuhl, S. Bauch, and M. Bonitz, Multiconfigurational time-dependent Hartree-Fock calculations for photoionization of one-dimensional Helium, in J. Phys. Conf. Ser. Vol. 220, 1 (IOP Publishing, p. 012019) (2010).

[31] R.J. Bartlett, Annu. Rev. Phys. Chem. **32**, 359 (1981).

[32] J. M. Ziman, Electrons and phonons: the theory of transport phenomena in solids (Oxford University Press, 1960).

[33] P. Lipavský, V. Špička, and B. Velický, Phys. Rev. B **34**, 6933 (1986).

[34] S. Hermanns, N. Schlünzen, and M. Bonitz, Phys. Rev. B **90**, 125111 (2014).

[35] S. Latini, E. Perfetto, A.-M. Uimonen, R. van Leeuwen, and G. Stefanucci, Phys. Rev. B **89**, 075306 (2014).

[36] E. Perfetto, A.-M. Uimonen, R. van Leeuwen, and G. Stefanucci, Phys. Rev. A **92**, 033419 (2015).

[37] M. Bonitz, N. Schlünzen, and S. Hermanns, Contrib. Plasma Phys. **55**, 152 (2015).

[38] N. Schlünzen, S. Hermanns, M. Bonitz, and C. Verdozzi, Phys. Rev. B **93**, 035107 (2016).

[39] N. Schlünzen, Nonequilibrium Green functions analysis of electron dynamics in strongly correlated lattice systems, Masters thesis (Christian-Albrechts-Universität zu Kiel, Germany, Sept. 2015).

[40] G.D. Mahan, Many-particle physics (Springer Science & Business Media, 2013).

[41] W. Greiner and J. Reinhardt, Field quantization (Springer, Berlin, Heidelberg, 1996).

[42] F. Schwabl, Quantenmechanik für Fortgeschrittene (QM II) (Springer, 2008).

[43] M. Bonitz, Quantum kinetic theory (B.G. Teubner, Leipzig, 1998).

[44] G. Stefanucci and R. v. Leeuwen, Nonequilibrium many-body theory of quantum systems: a modern introduction (Cambridge University Press, Cambridge, pp 600, 2013).

[45] A. Messiah and J. Streubel, Albert Messiah: Quantenmechanik, Bd. 1 (De Gruyter, 1991).

[46] M. Bonitz and D. Semkat, Introduction to computational methods in many body physics (Rinton Press, 2006).
[47] J. Schwinger, J. Math. Phys. **2**, 407 (1961).
[48] L.V. Keldysh, Sov. Phys. JETP **20**, 1307 (1965).
[49] M. Gell-Mann and F. Low, Phys. Rev. **84**, 350 (1951).
[50] A. Fetter and J. Walecka, Quantum theory of many-particle systems, Dover Books on Physics (Dover Publications, 2003).
[51] M. Born and V. Fock, German, Z. Phys. **51**, 165 (1928).
[52] D. Kremp, T. Bornath, M. Schlanges, and W. Kraeft, Quantum statistics of nonideal plasmas, Springer Series on Atomic, Optical, and Plasma Physics (Springer, Berlin, Heidelberg, 2006).
[53] P.C. Martin and J. Schwinger, Phys. Rev. **115**, 1342 (1959).
[54] R. Kubo, J. Phys. Soc. Jpn. **12**, 570 (1957).
[55] L. Kadanoff and G. Baym, Quantum statistical mechanics: Greens function methods in equilibrium and nonequilibrium problems, Frontiers in physics (W.A. Benjamin, 1962).
[56] K. Balzer and M. Bonitz, Nonequilibrium Green's Functions Approach to Inhomogeneous Systems, Vol. 867, Lecture Notes in Physics (Springer, Berlin, Heidelberg, 2013).
[57] M. von Friesen, C. Verdozzi, and C.-O. Almbladh, Phys. Rev. B **82**, 155108 (2010).
[58] M.P. von Friesen, C. Verdozzi, and C.-O. Almbladh, Phys. Rev. Lett. **103**, 176404 (2009).
[59] P. Romaniello, F. Bechstedt, and L. Reining, Phys. Rev. B **85**, 155131 (2012).
[60] D. Kremp, M. Bonitz, W. Kraeft, and M. Schlanges, Ann. Phys. **258**, 320 (1997).
[61] D. Gericke, S. Kosse, M. Schlanges, and M. Bonitz, Phys. Rev. B **59**, 10639 (1999).
[62] D. Semkat, D. Kremp, and M. Bonitz, J. Math. Phys. **41**, 7458 (2000).
[63] D. Semkat, D. Kremp, and M. Bonitz, Contrib. Plasma Phys. **42**, 31 (2002).
[64] A. Stan, N.E. Dahlen, and R. van Leeuwen, J. Chem. Phys. **130**, 224101 (2009).
[65] W.H. Press, S.A. Teukolsky, W.T. Vetterling, and B.P. Flannery, Numerical recipes 3rd edition: the art of scientific computing, 3rd ed. (Cambridge University Press, New York, NY, USA, 2007).
[66] L.V. Keldysh, Zh. Eksp. Teor. Fiz. **47**, 1515 (1964); Sov. Phys. JETP **20**, 1018 (1965).
[67] D.C. Langreth and J.W. Wilkins, Phys. Rev. B **6**, 3189 (1972).
[68] V. Špička, B. Velický, and A. Kalvová, Physica E **29**, 154 (2005).
[69] M. Bonitz, D. Semkat, and H. Haug, EPJ B **9**, 309 (1999).
[70] J. Hubbard, Electron correlations in narrow energy bands, in Proceedings of the royal society of london a: mathematical, physical and engineering sciences, Vol. 276, 1365 (The Royal Society, pp. 238257, 1963).
[71] A. Altland and B.D. Simons, Condensed matter field theory (Cambridge University Press, 2010).
[72] D. Baeriswyl, D.K. Campbell, J.M. Carmelo, F. Guinea, and E. Louis, The Hubbard model: its physics and mathematical physics, Vol. 343 (Springer Science & Business Media, 2013).
[73] A. Montorsi, The Hubbard Model: A Reprint Volume (World Scientific, 1992).
[74] H. Tasaki, J. Phys. Condens. Matter **10**, 4353 (1998).
[75] A. Tomas, C.-C. Chang, Z. Bai, R. Scalettar, J. Perez, C.-R. Lee, S. Chiesa, I. Yamazaki, M. Jarrell, E. Khatami, C. Varney, W. Chen, E. DAzevedo, T. Maier, S. Savrasov, and K. Tomko, Elementary Introduction to the Hubbard Model, quest.ucdavis.edu/tutorial/hubbard7.pdf.
[76] G. Dahlquist and Å. Björck, Numerical methods, Dover Books on Mathematics (Dover Publications, 2003).
[77] S. Hermanns, Nonequilibrium Greens function approach to Hubbard nano-clusters using the generalized KadanoffBaym ansatz, Diploma thesis (Christian-Albrechts-Universität zu Kiel, Germany, Aug. 2012).
[78] I. Bronstein and K. Semendjajew, Taschenbuch der Mathematik, 25 (1991).
[79] M. Watanabe and W.P. Reinhardt, Phys. Rev. Lett. **65**, 3301 (1990).
[80] S. Hermanns, K. Balzer, and M. Bonitz, The non-equilibrium Green function approach to inhomogeneous quantum many-body systems using the generalized KadanoffBaym ansatz, Phys. Scripta 2012, 014036 (2012).
[81] D. Larsson and H. Johannesson, Phys. Rev. Lett. **95**, 196406 (2005).
[82] M.P. von Friesen, C. Verdozzi, and C.-O. Almbladh, Europhys. Lett. **95**, 27005 (2011).
[83] F. Gebhard, E. Jeckelmann, S. Mahlert, S. Nishimoto, and R.M. Noack, Fourth-order perturbation theory for the half-filled Hubbard model in infinite dimensions, EPJ B 36, 491-509 (2003).
[84] C. Gerthsen and D. Meschede, Gerthsen Physik (Springer, 2010).
[85] T. Ott, Transport and waves in strongly coupled Coulomb and Yukawa one-component plasmas, PhD thesis (Christian-Albrechts-Universität zu Kiel, 2012).
[86] J. Daligault, Phys. Rev. Lett. **96**, 065003 (2006).
[87] T. Ott and M. Bonitz, Phys. Rev. Lett. **107**, 135003 (2011).
[88] T. Ott and M. Bonitz, Phys. Rev. Lett. **103**, 195001 (2009).
[89] A. MacDonald, S. Girvin, and D.t. Yoshioka, Phys. Rev. B **37**, 9753 (1988).
[90] L. Oesinghaus, Stabilität und Dynamik von Doublons im Hubbard-Modell, Bachelor thesis (Christian-Albrechts-Universität zu Kiel, Germany, 2013).
[91] A. Rosch, D. Rasch, B. Binz, and M. Vojta, Phys. Rev. Lett. **101**, 265301 (2008).
[92] D. Lacroix, S. Hermanns, C. Hinz, and M. Bonitz, Phys. Rev. B **90**, 125112 (2014).
[93] L. Vidmar, S. Langer, I. McCulloch, U. Schneider, U. Schollwöck, and F. Heidrich-Meisner, Phys. Rev. B **88**, 235117 (2013).
[94] R. Plato, Numerische Mathematik kompakt, Vieweg Studium (Vieweg Verlag, Friedr, & Sohn Verl.-Ges. mbH, 2009).
[95] J. De Villiers, Mathematics of approximation, English (Atlantis Press, Amsterdam; Paris, 2012).

2.1.2 Efficient Selfenergy Approximations for Correlated Systems

The astonishing advance of computer power in the last decades has proved to be a godsend for numerical applications. At the same time, increasingly precise experimental measurements have demonstrated the importance of nontrivial quantum correlations in condensed-matter systems (see, e.g., Ref. [140, 154, 192–195]). While the accurate description of correlated setups is heavily demanding for most quantum-simulation tools, NEGF theory provides an eminently suitable way to systematically incorporate correlation effects by the choice of the selfenergy. The author's group has demonstrated that more complex and accurate selfenergy approximations have come within reach for experimentally relevant systems through massive parallelization on computing clusters and GPUs [212, 213]. This involvement in these theoretical advances has made it possible to provide a consistent and comprehensive review that makes this challenging topic accessible even to non-experts. In this sense, Ref. [79] is an extensive review article with a twofold purpose: to give an overview of recent applications of NEGF approaches, and to shed light on the selfenergy and its many-body approximations—from the derivations to their application in different single-particle bases.

The introductory part summarizes the developments regarding strongly correlated quantum systems, applicable theoretical methods to describe correlated dynamics, and the NEGF method in particular. Following this, the theoretical foundation of Green functions is presented, covering second quantization, different single-particle basis choices, the contour formalism, and the Martin–Schwinger hierarchy (p. 4 ff. in Ref. [79]). After the selfenergy and its equations of motion are introduced (p. 12 ff. in Ref. [79]) two equivalent schemes for the derivation of selfenergy approximations are presented: Hedin's equations for the dynamically screened vertex, and the counterpart set of equations for the bare vertex (p.14 ff.). Afterwards, important resulting approximations for the selfenergy are summarized and the GKBA is discussed (p. 16 ff. in Ref. [79]).

In the next part, several applications for NEGF approaches are reviewed and the different performances of the selfenergy approximations are compared, starting with groundstate energies and spectra for Hubbard systems (p. 20 ff. in Ref. [79]). Subsequently, various nonequilibrium-dynamics setups are discussed (p. 26 ff. in Ref. [79]), which feature prominently in the publications included in the present thesis—among others, one-dimensional relaxation dynamics from nonequilibrium initial states (see Sec. 4.1), two-dimensional expansion of fermionic particle clouds that lead to the build-up of doublons (see Sec. 4.2), and the electronic response following a charged-particle impact in hexagonal lattices (see Sec. 4.3).

The last and central part addresses the selfenergy and its different flavors, mirroring the pool of diagrammatic many-body approximations (p. 36 ff. in Ref. [79]). Successively, each selfenergy variant is derived in an instructive and highly ostensive way, where the formal relations and their diagrammatic illustrations are presented side by side to achieve maximal comprehensibility. This is followed, individually, by the respective specification of the final selfenergy in a general single-particle basis, a diagonal basis, and the Hubbard basis for bosons and fermions. Ensuing the above-mentioned scheme based on Hedin's equations, the Hartree–Fock approximation (p. 36 ff. in Ref. [79]), the second-order terms

(p. 38 ff. in Ref. [79]), the third-order contributions (p. 41 ff. in Ref. [79]), and the GW approximation are described (p. 55 ff. in Ref. [79]). The bare-vertex iteration scheme leads to the particle–particle T matrix (p. 61 ff. in Ref. [79]) and to the related particle–hole T-matrix approximation (p. 72 ff. in Ref. [79]).

In a nutshell, Ref. [79] is meant as instructional material and reference work for the selfenergy in NEGF theory, discusses its approximations in theory and application, and summarizes some of the key results of the present thesis.

Topical Review

Ultrafast dynamics of strongly correlated fermions—nonequilibrium Green functions and selfenergy approximations

N Schlünzen, S Hermanns, M Scharnke[1] and M Bonitz[2]

Institut für Theoretische Physik und Astrophysik, Christian-Albrechts-Universität zu Kiel, D-24098 Kiel, Germany

E-mail: bonitz@theo-physik.uni-kiel.de

CrossMark

Abstract

This article presents an overview on recent progress in the theory of nonequilibrium Green functions (NEGF). We discuss applications of NEGF simulations to describe the femtosecond dynamics of various finite fermionic systems following an excitation out of equilibrium. This includes the expansion dynamics of ultracold atoms in optical lattices following a confinement quench and the excitation of strongly correlated electrons in a solid by the impact of a charged particle. NEGF, presently, are the only *ab initio* quantum approach that is able to study the dynamics of correlations for long times in two and three dimensions. However, until recently, NEGF simulations have mostly been performed with rather simple selfenergy approximations such as the second-order Born approximation (SOA). While they correctly capture the qualitative trends of the relaxation towards equilibrium, the reliability and accuracy of these NEGF simulations has remained open, for a long time.

Here we report on recent tests of NEGF simulations for finite lattice systems against exact-diagonalization and density-matrix-renormalization-group benchmark data. The results confirm the high accuracy and predictive capability of NEGF simulations—provided selfenergies are used that go beyond the SOA and adequately include strong correlation and dynamical-screening effects. With an extended arsenal of selfenergies that can be used effectively, the NEGF approach has the potential of becoming a powerful simulation tool with broad areas of new applications including strongly correlated solids and ultracold atoms. The present review aims at making such applications possible. To this end we present a selfcontained introduction to the theory of NEGF and give an overview on recent numerical applications to compute the ultrafast relaxation dynamics of correlated fermions. In the second part we give a detailed introduction to selfenergies beyond the SOA. Important examples are the third-order approximation, the GW approximation, the T-matrix approximation and the fluctuating-exchange approximation. We give a comprehensive summary of the explicit selfenergy expressions for a variety of systems of practical relevance, starting from the most general expressions (general basis) and the Feynman diagrams, and including also the important cases of diagonal basis sets, the Hubbard model and the differences occuring for bosons and fermions. With these details, and information on

---

[1] Present address: Imperial College London, Department of Materials, Exhibition Road, SW7 2AZ.

[2] Author to whom any correspondence should be addressed.

the computational effort and scaling with the basis size and propagation duration, readers will be able to choose the proper basis set and straightforwardly implement and apply advanced selfenergy approximations to a broad class of systems.

Keywords: nonequilibrium Green functions (NEGF), strongly correlated materials, Hubbard model, seflenergy, T matrix, GW approximation

(Some figures may appear in colour only in the online journal)

Contents

1. Introduction

Strong correlation effects, arising when the interaction energy of a many-particle system exceeds the single-particle energy, are ubiquitous in nature and laboratory systems. Examples are the interior of dwarf stars or giant planets, the quark–gluon plasma, e.g. [1, 2] or electrons in strongly correlated materials, e.g. [3]. In classical systems strong correlations exist e.g. in electrolytes [4], in ultracold plasmas [5, 6], or in complex plasmas where they lead to fluid-like or crystalline behavior of charged particles, for an overview see [7]. Even though there exist many similarities in the static and dynamic properties between classical and quantum systems [8], the latter have a number of peculiarities and require dedicated theoretical approaches. Therefore, in the present article, we will concentrate only on quantum systems.

1.1. Strong correlations in quantum systems

In recent years strong correlations in quantum systems have come into the focus in a variety of fields. The first example are dense plasmas as they exist in the interior of giant planets, dwarf stars or neutron stars. Similar conditions are also generated in the laboratory by compression of matter by means of shock waves, ion beams or high-intensity lasers [9, 10]. This typically leads to situations where the electrons are quantum degenerate whereas the heavy particles exhibit only weak quantum behavior. This peculiar state of highly excited nonideal matter has been termed 'warm dense matter' or high-energy density matter, e.g. [11]. The range of electron densities where correlation effects are important is characterized by values of the Brueckner parameter exceeding unity, i.e. $r_s = \bar{r}/a_B > 1$, where $\bar{r}$ denotes the mean interparticle distance and a_B the Bohr radius. In warm dense matter in thermodynamic equilibrium, temperatures are in the range of $0.1 \lesssim \Theta = \frac{T}{T_F} \lesssim 10$ (with the Fermi temperature T_F) which means that electrons are highly excited and ground-state approaches fail. Here, the method of choice are first-principle approaches such as path-integral Monte Carlo simulations [12–14], for a recent overview, see [15].

The second example are condensed-matter systems where strong electronic correlations are of high importance in many materials, e.g. [3, 16]. Examples are transition metals and their oxids, rare-earth metals or cuprate superconductors. Here the standard mean-field description fails and correlated approaches such as dynamical mean-field theory [16] or Hubbard-type model Hamiltonians, e.g. [17] are being used.

The third example of strong correlation effects are ultracold fermionic and bosonic atoms. In particular ultracold atoms in optical lattices have allowed one to study correlation effects experimentally with unprecedented accuracy, e.g. [18]. Moreover, with the advent of atomic microscopes even single-site spatial resolution has been achieved [19–21].

In Hubbard-type systems, the coupling strength is given by the ratio of the on-site interaction to the hopping amplitude, U/J. In the present paper we consider ratios in the range from zero (ideal system) to five. The latter will be referred to as strongly correlated system even though much larger values are also being studied [22–24].

1.2. Nonequilibrium correlation dynamics following rapid external excitation

There is a large variety of excitation scenarios that drive a many-body system rapidly out of equilibrium. This includes excitation by laser pulses—from the infrared, over the optical and ultraviolet to the x-ray range. Time-resolved optical diagnostics (pump–probe spectroscopy) has evolved as a powerful experimental tool to probe the time evolution of atoms, molecules and materials that has been covered in many textbooks. Another method that provides spatially localized excitations is the impact of charged particles that may lead to surface modifications, heating or excitations of the electronic degrees of freedom, e.g. [25–27]. For correlated atoms in optical lattices, additional excitation schemes have been developed. This includes rapid changes of confinement potentials (confinement quench) [23, 28], rapid changes of the pair interaction (interaction quench) via Feshbach resonance [29] or periodic modulation of the lattice depth (lattice-modulation spectroscopy), e.g. [30–32].

All these methods have seen a rapid development in recent years and allow for accurate diagnostic of the time evolution of many-body systems. This, on the other hand, requires extensive theory developments in order to achieve detailed comparisons with and explanation of experimental observations.

1.3. Theoretical approaches to computing nonequilibrium dynamics in correlated quantum systems

The theoretical approaches that have been applied most extensively in the field of correlated lattice systems are exact diagonalization (CI) [33–35], density-matrix renormalization group (DMRG) methods [36–38], diagrammatic Monte Carlo [39–41], real-time quantum Monte Carlo (RTQMC) [42, 43], reduced-density-matrix approaches [44–46], and time-dependent density-functional theory (TDDFT) [47–51]. However, each of these methods has fundamental problems and limitations. CI faces an exponential increase of the CPU time with the system size and applies only for small systems. RTQMC can only treat short evolution times due to the dynamic fermion sign problem. DMRG is accurate at strong coupling but has difficulties at moderate and weak coupling and is, moreover, restricted to 1D systems, e.g. [22]. Finally, TDDFT has no dimensional restrictions, but it is not able to accurately treat electronic correlations in a systematic way. Besides, the simulations usually involve the adiabatic approximation which neglects memory effects and may make the results

unreliable. Presently, there are intense activities underway to improve each of these approaches.

1.4. Nonequilibrium Green functions (NEGF)

There exists an independent approach to the dynamics of correlated systems that originates in quantum-field theory. It is based on nonequilibrium Green functions (NEGF) that were introduced by Keldysh [52] and Baym and Kadanoff [53]. This approach has been extremely successful and extensively applied in many fields of physics, including semiconductor optics [54–57], semiconductor quantum transport [58–61], nuclear physics [62–64], laser plasmas [65, 66], high-energy physics [67–69], and small atoms and molecules [70–72]. For text-book discussions, see [54, 55, 73–75].

NEGF have only recently been applied to finite correlated lattice systems out of equilibrium [51, 74, 76, 77]. This method is not suffering from most of the limitations of the other approaches and has achieved remarkable results. Benchmarks against CI simulations for small systems, cold-atom experiments [28] and DMRG data [22] have shown impressive accuracy of the approach for many observables, for details see section 3. Of course there is a price to pay: NEGF methods are complicated and computationally very expensive. A recent overview on the NEGF results for the dynamics of fermionic lattice systems can be found in [78], and a recent overview on different NEGF applications is given in [79].

At this point it is useful to have a look at the conceptual basis of nonequilibrium Green functions. This approach is internally consistent. It obeys conservation laws and the dynamics are time-reversible [80]. NEGF simulations depend on a single input quantity—the selfenergy Σ (this is analogous to DFT which depends only on the accuracy of the exchange–correlation potential). Would Σ be known exactly, the NEGF method would be exact. In practice, of course, aside from a few model cases, the exact Σ is not known and one has to resort to approximations. In the majority of applications to closed correlated many-body systems (neglecting the coupling to phonons or other bosonic degrees of freedom) just two approximations are used: the Hartree–Fock selfenergy and the second-order Born approximation that incorporates correlations to lowest order. These approximations are well studied and their numerical application can be considered routine.

At the same time, the excellent quantitative agreement with benchmark data that was mentioned above could only be achieved by applying more complex selfenergy approximations that adequateley take into account both, the coupling strength and the filling (density) of the system. However, even though a number of improved approximations such as the T-matrix selfenergy, that describes strong coupling and bound-state formation, or the GW approximation, that describes dynamical screening, are known for more than half a century, their application is often still very challenging. Unfortunately, in most publications the presentation of these approximations is rather sketchy, and often does not include all details about the spin degrees of freedom or general basis representations. Moreover, there is a high need for additional approximations,

for instance, selfenergies that couple dynamical screening and strong coupling (including the FLEX approximation) or perturbation results that go beyond the second-Born approximation that have occasionally been used in the literature, but usually not under nonequilibrium conditions.

Thus, limited availability of a broad class of selfenergy approximations, including their representations for commonly used situations, can be considered a major bottleneck for further progress in nonequilibrium Green functions and their applications to many fields of many-body physics. It is a goal of the present review, to fill this gap.

1.5. Outline of this review

This article is organized as follows. In section 2 we present a brief but selfcontained introduction into the concepts of nonequilibrium Green functions including the equations of motion for the NEGF—the Keldysh–Kadanoff–Baym equations. This is followed by an introduction to the Hubbard model for strongly correlated systems and the transformation of the NEGF into a Hubbard basis. We then introduce the selfenergy Σ and the two main approaches for deriving approximations for Σ: the first is based on an expansion in terms of the bare pair interaction whereas the second uses the screened interaction, as the basic ingredient (Hedin's equations). We then present an overview of the main selfenergy approximations that follow from those two schemes. This is followed, in section 3, by a summary of representative numerical applications to the dynamics of strongly correlated fermions under various excitation conditions which illustrate the performance of the different approximations for Σ. In the second part of the review that contains sections 4 and 5 we return to the governing equations for the selfenergy where the former (latter) is devoted to the expansion in terms of unscreened (screened) pair potentials. In each of the two sections the relevant approximations for Σ will be presented first in the most general form (general basis) which is then specified to various practically relevant representations including the basis where the interaction potential is diagonal and the Hubbard basis. Finally, a summary and outlook is presented in section 6.

2. Basics of nonequilibrium Green functions

This section gives an overview about the theoretical foundations of the NEGF method and focuses on the interconnection between and classification of common approximation schemes. As far as we are aware, it provides the first comprehensive overview of the relevant equations in a fully general basis representation[3]. From this, the common cases of a diagonal basis such as the coordinate basis and the Hubbard basis for fermions and bosons are deduced. Alongside the development of the theory, the numerical scaling of the different approximation techniques will be detailed to enable a suitable choice with respect to the achievable simulation duration and basis size. In section 2.1, the representation of states

---

[3] For the particle–particle T-matrix approximation, a thorough derivation for a general basis set was presented in [78].

of indistinguishable quantum particles such as electrons in the so-called *Fock space* is discussed. The underlying notion of the *second quantization* allows for a suitable description of the dynamics for these particles in terms of canonical operators which perform the creation and annihilation in a chosen basis comprised of single-particle orbitals. Section 2.2 explores several possible sets of basis functions and their numerical suitability for different classes of systems. As a special case, the description of bosons and fermions in the basis set of the Hubbard model [81] is described.

For general time-dependent problems, it turns out to be advantageous to work on a complex time-contour (Schwinger–Keldysh contour), that is introduced in section 2.4. The central quantity on the time-contour—the single-particle Green function—which gives access to all single-particle observables, the single-particle spectrum and some two-particle quantities, is defined in section 2.5. The equations of motion for the Green functions are a set of integro-differential equations, which are mutually coupled, constituting a hierarchy between Green functions of different particle number, the Martin–Schwinger hierarchy (MSH). A suitable reformulation of the MSH has been given in [82], where a set of five contour quantities is introduced, which also obey coupled equations of motion, the solutions of which yield the same Green function as the solution of the MSH. The representations of these equations in a general basis set are given in section 2.8. Since the exact solution of either set of equations is numerically impossible for most realistic systems, approximation techniques have to be employed. The approaches presented in this work are based on the common building block of the so-called *selfenergy* the purpose of which is to capture all relevant many-body effects. How it can be approximately determined using both perturbative and non-perturbative methods is detailed at the end of this section.

2.1. Dynamics of indistinguishable quantum particles in second quantization

The physical properties of all quantum particles are determined by their nature as excitations of an underlying field. These fields are quantized, i.e. they can only accommodate an integral number of elementary excitations, which are identified with the quantum particles. If only a single particle is excited, its state can be described by a wavefunction $|\Psi\rangle$, defined on a single-particle Hilbert space $\mathcal{H}$ over the field of complex numbers $\mathbb{C}$, which is assumed to be of finite dimension[4]. For excitations of more than one particle, the indistinguishability of quantum particles has to be taken into account properly. Experimentally, it has been found that quantum particles either carry *bosonic* or *fermionic* statistics, i.e. obey either the Fermi–Dirac [83, 84] or the Bose–Einstein [85] distribution. The group of fermions, which all have half-integer spin, contains the quarks and leptons, such as the electron, whereas phonons, *W*- and *Z* gauge-particles, gluons and the

recently experimentally verified Higgs particle are bosons. Particles that are composed of elementary fermions or bosons can be of either bosonic[5] (e.g. mesons, pions, kaons, excitons, biexcitons) or fermionic (baryons [69], nucleons, trions etc) type, depending on the number of fermions involved. In the theoretical description, the spin statistics amounts to the many-body wavefunction being totally symmetric, for bosons, or totally anti-symmetric, for fermions with respect to interchange of two particles. How these statistics are conveniently built into the description of the many-body system, is detailed in the following.

To be able to treat states of varying particle number on an equal footing, it is convenient to define the so-called Fock space $\mathcal{F}_\sigma^\mathcal{H}$ induced by the single-particle Hilbert space $\mathcal{H}$ as the (completion—indicated as overline—of the) direct sum of (anti-)symmetrized n-fold tensor products of $\mathcal{H}$,

$$\mathcal{F}_\sigma^\mathcal{H} = \overline{\bigoplus_{n=0}^\infty S_\sigma \mathcal{H}^{\otimes n}} = \overline{\mathbb{C} \oplus \mathcal{H} \oplus S_\sigma(\mathcal{H} \otimes \mathcal{H}) \oplus \dots}, \quad (1)$$

with ($\mathbb{N}_0$ being the natural numbers with zero)

$$\mathcal{H}^{\otimes n} = \overbrace{\mathcal{H} \otimes \mathcal{H} \otimes \cdots \otimes \mathcal{H}}^{n \text{ times}} \quad \text{for all } n \in \mathbb{N}_0. \quad (2)$$

The operator S_σ symmetrizes or anti-symmetrizes tensors for bosonic ($\sigma = +$) or fermionic ($\sigma = -$) particles. To define its action, it is suitable to fix a single-particle orbital basis of $\mathcal{H}$,

$$\mathcal{B}^{\text{sp}} = \left\{ |b_i\rangle, i \in I \right\}, \quad (3)$$

for an index set I of cardinality $\dim_\mathcal{H}$. With this, for every $n \in \mathbb{N}_0$ and basis elements $|b_1\rangle, \dots, |b_n\rangle \in \mathcal{B}^{\text{sp}}$, the action of S_σ on the standard tensor product is given by

$$S_+\left(|b_1\rangle \otimes \dots \otimes |b_n\rangle\right) \quad (4)$$
$$= \frac{1}{\sqrt{n! \prod_{p=0}^\infty n_p!}} \sum_{s \in \text{Sym}_n} |b_{s(1)}\rangle \otimes \dots \otimes |b_{s(n)}\rangle =: |b_1\rangle \circ \dots \circ |b_n\rangle$$

and

$$S_-\left(|b_1\rangle \otimes \dots \otimes |b_n\rangle\right) \quad (5)$$
$$= \frac{1}{\sqrt{n!}} \sum_{s \in \text{Sym}_n} \text{sign}\left(s\right) |b_{s(1)}\rangle \otimes \dots \otimes |b_{s(n)}\rangle =: |b_1\rangle \wedge \dots \wedge |b_n\rangle,$$

for bosons and fermions, respectively. Here, Sym_n denotes the n-body permutation group (or symmetric group), which performs a permutation among the state labels b_i. The n_p is the total number of particles in state p (note that for fermions the occupation is forced to $n_p = 0, 1$ due to the Pauli exclusion and thus $n_p! = 1$). Note that it is sufficient to define the (anti-)symmetrization operator only for basis elements, since it is linear. For example, a general fermionic anti-symmetrized state $|\Psi_2^-\rangle$ on the two-fold tensor product $\mathcal{H} \otimes \mathcal{H}$ is of the form

---

[4] In practice, this does not constitute a restriction, since the Hilbert space is either already of finite dimension or has to be approximated as such anyway to make a numerical treatment possible.

[5] Note that the Bose character is only approximate, and deviations may appear on short length scales on the order of the interparticle distance.

$$|\Psi_2^-\rangle = \sum_{i<j\in I} c_{ij}|b_i\rangle \wedge |b_j\rangle \quad \text{for } |b_i\rangle, |b_j\rangle \in \mathcal{B}^{\text{sp}}, \quad (6)$$

for $c_{ij} \in \mathbb{C}$. Here, the antisymmetric tensor product $|b_i\rangle \wedge |b_j\rangle$ is given in terms of the standard tensor product as

$$|b_i\rangle \wedge |b_j\rangle = \frac{1}{\sqrt{2}}\Big(|b_i\rangle \otimes |b_j\rangle + \big(-1\big)|b_j\rangle \otimes |b_i\rangle\Big). \quad (7)$$

Note that $|b_i\rangle \wedge |b_i\rangle = 0$, which reflects that, due to the Pauli exclusion principle, no two fermions can occupy the same state. With this, a general state in the Fock space $\mathcal{F}_\sigma^{\mathcal{H}}$, a *Fock state* $|\Psi^\sigma\rangle$, which is a superposition of states with a different number of particles, can be written as

$$|\Psi^\sigma\rangle = c_0|0\rangle \oplus \sum_{i\in I} c_i|b_i\rangle \oplus \sum_{i\leqslant j\in I} c_{ij}|b_i\rangle \otimes_\sigma |b_j\rangle \oplus \dots, \quad (8)$$

for $c_0, c_i, c_{ij} \in \mathbb{C}$, where the short-hand notation

$$\otimes_\sigma = \begin{cases} \circ & \text{for bosons,} \\ \wedge & \text{for fermions,} \end{cases} \quad (9)$$

has been introduced. The first state, $|0\rangle$, is the vacuum state, which is the state of zero physical particles and of the lowest possible energy, E^{vac}—in the context of this article, $E^{\text{vac}} = 0$ is assumed[6].

With the concept of Fock states that are suitable to describe systems with a varying particle number, it is most natural to define operators[7] that create $\big(\hat{c}^\dagger[|b_i\rangle] =: \hat{c}_i^\dagger\big)$ or remove $\big(\hat{c}[|b_i\rangle] =: \hat{c}_i\big)$ a particle in a given single-particle orbital $|b_i\rangle$. To characterize their action, it is sufficient to define the action on all (anti-)symmetrized n-particle subspaces of $\mathcal{F}_\sigma^{\mathcal{H}}$ defined in a fashion similar to equation (2),

$$\mathcal{H}^{\otimes_\sigma n} = \overbrace{\mathcal{H} \otimes_\sigma \mathcal{H} \otimes_\sigma \dots \mathcal{H}}^{n \text{ times}}, \quad (10)$$

as

$$\hat{c}_i^\dagger \overbrace{\Big(|b_1\rangle \otimes_\sigma \dots \otimes_\sigma |b_n\rangle\Big)}^{\in \mathcal{H}^{\otimes_\sigma n}} = \overbrace{|b_i\rangle \otimes_\sigma |b_1\rangle \otimes_\sigma \dots \otimes_\sigma |b_n\rangle}^{\in \mathcal{H}^{\otimes_\sigma n+1}}$$

and

$$\hat{c}_i \overbrace{\Big(|b_1\rangle \otimes_\sigma \dots \otimes_\sigma |b_n\rangle\Big)}^{\in \mathcal{H}^{\otimes_\sigma n}}$$

$$= \underbrace{\sum_{k\in I} \sigma^k \langle b_i|b_k\rangle |b_1\rangle \otimes_\sigma \dots \otimes_\sigma |b_k\rangle \otimes_\sigma \dots \otimes_\sigma |b_n\rangle}_{\in \mathcal{H}^{\otimes_\sigma n-1}}. \quad (11)$$

Note that, for the case of fermions, action of the operators $\hat{c}_i$ ($\hat{c}_i^\dagger$) on an n-particle state may give rise to a sign change depending on the location of the orbital 'i' in the state. This depends on the choice of ordering of single-particle orbitals in the n-particle state. This will be made explicit for the example of occupation-number representation presented below.

With these equations, the (anti-)commutator between the creation operators and annihilation operators as well as between one creation and one annihilation operator for fermions (bosons) is easily worked out,

$$\left[\hat{c}_i^\dagger, \hat{c}_j^\dagger\right]_\mp = 0, \quad \left[\hat{c}_i, \hat{c}_j\right]_\mp = 0, \quad \left[\hat{c}_i, \hat{c}_j^\dagger\right]_\mp = \langle b_i|b_j\rangle. \quad (12)$$

Here, $\left[a, b\right]_\mp$ denotes the commutator $(ab - ba)$ for bosons and the anti-commutator $(ab + ba)$ for fermions. Note that we used a general description that allows for a non-orthogonal set, $\{|b_i\rangle\}$, of single-particle basis states. In the special case of an orthonormal basis, $\langle b_i|b_j\rangle = \delta_{ij}$, and one recovers, in the final expression δ_{ij} which is familiar from many text books.

Now we make a transition from the abstract representation of n-particle states to the occupation-number representation that is commonly used in the literature. First, the general single-particle orbitals are replaced by (orthogonal) eigenfunctions of the one-particle Hamiltonian $\hat{H}^0$, $|b_i\rangle \rightarrow |i\rangle$ where $\hat{H}^0|i\rangle = \epsilon_i|i\rangle$ and $\epsilon_{i-1} \leqslant \epsilon_i \leqslant \epsilon_{i+1}$ for all i. Together with the occupation n_i of the ith orbital, the n-particle state (see equations (4) and (5)) can then be written as

$$|n_1, n_2, \dots\rangle := |1\rangle \otimes_\sigma |2\rangle \otimes_\sigma \dots$$

and represents the bosonic (fermionic) permanents (Slater determinants) of single-particle orbitals. Having that, the actions of the creation and annihilation operators (now with $(n \pm 1)$-particle states sorted by energy) is then given by

$$\hat{c}_i^\dagger|n_1, n_2, \dots, n_i, \dots\rangle = \sigma^\alpha \sqrt{n_i+1}|n_1, n_2, \dots, n_i+1, \dots\rangle \cdot \begin{cases} 1 & \text{for bosons} \\ \delta_{n_i 0} & \text{for fermions} \end{cases},$$

$$\hat{c}_i|n_1, n_2, \dots, n_i, \dots\rangle = \sigma^\alpha \sqrt{n_i}|n_1, n_2, \dots, n_i-1, \dots\rangle \cdot \begin{cases} 1 & \text{for bosons} \\ \delta_{n_i 1} & \text{for fermions} \end{cases},$$

with $\alpha = \sum_{j=1}^{i-1} n_j$ accounting for the fermionic sign change due to the resorting of orbitals. Note that the Kronecker-delta terms for the fermionic cases again account for the Pauli exclusion principle. The above canonical operators again fulfill the (anti-)commutation relations from equation (12) for an orthogonal basis set, i.e. with $\left[\hat{c}_i, \hat{c}_j^\dagger\right]_\mp = \delta_{ij}$.

The creation and annihilation operators form a basis for all operators acting on the space $\mathcal{F}_\sigma^{\mathcal{H}}$. For instance, general single-particle and two-particle operators $\hat{O}^{(1)}$, $\hat{O}^{(2)}$ are given as linear superpositions[8]

$$\hat{O}^{(1)} = \sum_{mn} o_{mn}^{(1)} \hat{c}_m^\dagger \hat{c}_n, \quad (13)$$

---

[6] In quantum chromodynamics and quantum electrodynamics, the lowest energy state may not have zero energy and allow for quantum fluctuations [86].
[7] As the notation indicates, $\hat{c}^\dagger$ and $\hat{c}$ are indeed pairwise conjugated operators, i.e. $\hat{c}^\dagger = \left[\hat{c}\right]^\dagger$.

[8] From now on, if not stated otherwise, all sums run over the complete basis set.

$$\hat{O}^{(2)} = \sum_{mnpq} o^{(2)}_{mnpq} \hat{c}^\dagger_m \hat{c}^\dagger_n \hat{c}_p \hat{c}_q, \qquad (14)$$

where the matrix elements are

$$o^{(1)}_{mn} = \left\langle b_m \middle| \hat{o}^{(1)} \middle| b_n \right\rangle, \qquad o^{(2)}_{mnpq} = \left\langle b_m b_n \middle| \hat{o}^{(2)} \middle| b_p b_q \right\rangle. \qquad (15)$$

As a special case, the Hamiltonian, which carries the specific geometries of the studied systems as well as any external (time-dependent) potentials and forces driving the dynamics transforms to

$$\hat{H}(t) = \underbrace{\sum_{mn} h_{mn} \hat{c}^\dagger_m \hat{c}_n}_{\hat{H}^0} + \underbrace{\frac{1}{2} \sum_{mnpq} w_{mnpq} \hat{c}^\dagger_m \hat{c}^\dagger_n \hat{c}_p \hat{c}_q}_{\hat{W}} + \underbrace{\sum_{mn} f_{mn}(t) \hat{c}^\dagger_m \hat{c}_n}_{\hat{F}(t)}, \qquad (16)$$

containing the single-particle part $\hat{H}^0$, the interaction $\hat{W}$ and the time-dependent single-particle excitation part $\hat{F}(t)$. Since all quantities discussed in this section are formulated in terms of the single-particle basis $\mathcal{B}^{\mathrm{sp}}$ (see equation (3)), its suitable choice is vital for the numerical implementation to achieve the best possible performance. A strategy for the selection of a set of basis functions is detailed in the next section.

2.2. Choice of the one-particle basis

Selecting a single-particle basis (see equation (3)) constitutes the first step in the process of the theoretical modeling of a system. With this basis $\mathcal{B}^{\mathrm{sp}}$ or an equivalent choice $\mathcal{C}^{\mathrm{sp}} = \left\{ |c_j\rangle, j \in J \right\}$, elements $|\Psi\rangle$ of the single-particle Hilbert space $\mathcal{H}$ can be expanded as

$$|\Psi\rangle = \sum_{i \in I} b_i |b_i\rangle = \sum_{j \in J} c_j |c_j\rangle, \qquad (17)$$

where I (J) is an index set of cardinality $\dim_{\mathcal{H}}$. For Hilbert spaces of infinite dimension, I has to be substituted by a finite set I' to make a numerical treatment possible, which renders equation (17) only approximately valid. For the formulation of the Hamiltonian, according to equation (16), the matrix elements h_{km}, w_{klmn}, $f_{km}(t)$ have to be specified. Once they are given in the natural basis of the studied system, they can be transformed into another single-particle basis $\mathcal{C}^{\mathrm{sp}}$ by

$$h^{\mathcal{C}}_{km} = \sum_{r=1}^{\dim_{\mathcal{H}}} \sum_{s=1}^{\dim_{\mathcal{H}}} b^*_{rk} h^{\mathcal{B}}_{rs} b_{sm}, \qquad (18)$$

with the expansion of the new basis functions $|c_i\rangle$ in terms of the old $|b_i\rangle$ given as

$$\langle c_i| = \sum_{r=1}^{\dim_{\mathcal{H}}} b^*_{ri} \langle b_r|, \qquad (19)$$

$$|c_i\rangle = \sum_{s=1}^{\dim_{\mathcal{H}}} |b_s\rangle b_{si}, \qquad (20)$$

with the transformation matrix elements

$$b_{si} = \langle b_s | c_i \rangle, \qquad b^*_{ri} = \langle b_r | c_i \rangle^*. \qquad (21)$$

With these transformations, the basis can be chosen to suit the numerical needs. To this end, two criteria can be formulated which characterize how well numerically tractable a set of basis functions is. First, it should consist of as few basis functions as possible to achieve the accuracy demanded, i.e. it describes single-particle orbitals that are as close as possible to the true orbitals occupied by the particles. To work out the other criterion, one notices that, according to equation (16), the interaction—a central quantity in any exact treatment as well as the selfenergy approximations discussed later in this article—is represented by a fourth-order tensor w_{klmn} in a general basis. This structure is numerically prohibitive since it involves at least a scaling of $\mathcal{O}\left(N_{\mathrm{b}}^4\right)$, where N_{b} is the dimension of the basis set. Fortunately, the interaction tensor can be brought into a diagonal representation, where it is characterized by a second-order tensor, i.e. is of the structure

$$w_{klmn} = \delta_{kn} \delta_{lm} w_{kl}. \qquad (22)$$

In practice, this diagonalization can be achieved by choosing a quadrature rule for the integrals involved in the computation of the interaction matrix elements (see equation (15)) and construction of a (finite-element) discrete variable representation upon it [74, 87, 88]. For details, the reader is referred to [71, 89], where various aspects of different choices of quadratures and their implementation are discussed. Accordingly, the second criterion is that the basis functions are chosen such that the interaction matrix elements are (approximately) diagonal in the sense of equation (22). Unfortunately, both criteria are often 'orthogonal' to each other, and the user has to choose between them. While physically motivated basis sets achieve a good representation with only a small number of basis functions, they entail a dense fourth-order tensorial structure of the interaction matrix elements. In contrast, discrete-variable-representation basis sets provide the latter in diagonal form, but the basis functions are 'general purpose' and the worse representation of physical states requires their number to be comparably large. As a rule of thumb, it can be stated that, for small systems, which require only few basis functions, physical basis sets are preferable while, for large systems, for instance in the description of photoemission experiments on atoms, molecules or solids [88, 90, 91], a grid-based approach is often favorable. In both cases, a close look at the structure of the equations at hand provides a more thorough basis for the decision. As an example, looking ahead to equations (189) and (190) versus equations (176) and (183), the index structure of the selfenergy—the central quantity in Green function based calculations—for example, in the important second-order Born (2B) approximation, looks like (omitting time arguments and scalar factors)

$$\Sigma^{(2),\mathrm{diagonal}}_{ij} \sim \sum_{np} G_{in} w_{ip} G_{np} G_{pj} w_{nj} \pm \sum_{pr} G_{ij} w_{ip} G_{rp} G_{pr} w_{rj}, \qquad (23)$$

$$\Sigma_{ij}^{(2)} \sim \sum_{mnpqrs} G_{mn} w_{ipqm} G_{sp} G_{qr} \left(w_{nrjs} \pm w_{rnjs} \right), \quad (24)$$

in a diagonal basis versus general basis representation. At first glance, the diagonal case of equation (23) suggests a scaling of $\mathcal{O}\left(N_{\mathrm{b}}^4\right)$ stemming from the two external indices i, j and the summation over the two internal indices, whereas in the case of full interaction, according to equation (24), the summation over six internal indices (m, n, p, q, r, s) prompts a scaling of $\mathcal{O}\left(N_{\mathrm{b}}^8\right)$, which would strongly favor the former over the latter. A quick reordering, though, lets one rewrite equations (23) and (24) as

$$\Sigma_{ij}^{(2),\mathrm{diagonal}} \sim \sum_n G_{in} w_{nj} \sum_p w_{ip} G_{np} G_{pj} \pm G_{ij} \sum_p w_{ip} \sum_r G_{pr} G_{rp} w_{rj}, \quad (25)$$

$$\Sigma_{ij}^{(2)} \sim \sum_{mpq} w_{ipqm} \sum_s G_{sp} \sum_r G_{qr} \sum_n G_{mn} \left(w_{nrjs} \pm w_{rnjs} \right). \quad (26)$$

This elucidates that, for diagonal interaction, $\Sigma_{ij}^{(2),\mathrm{diagonal}}$ indeed scales as $\mathcal{O}\left(N_{\mathrm{b}}^4\right) + \mathcal{O}\left(N_{\mathrm{b}}^3\right) = \mathcal{O}\left(N_{\mathrm{b}}^4\right)$, whereas, $\Sigma_{ij}^{(2)}$ scales as $\mathcal{O}\left(N_{\mathrm{b}}^5\right) + \mathcal{O}\left(N_{\mathrm{b}}^5\right) + \mathcal{O}\left(N_{\mathrm{b}}^5\right) + \mathcal{O}\left(N_{\mathrm{b}}^5\right) = \mathcal{O}\left(N_{\mathrm{b}}^5\right)$, in contrast[9]. Thus, the preferable basis choice strongly depends on the respective basis sizes needed.

2.3. The Hubbard model

Since it plays an important role underlying the applications in section 3, the special case of the Hubbard basis and the associated Hubbard model is briefly discussed here. The Hubbard model has been introduced by *John Hubbard*, a British physicist, in 1963 [81] to describe the physics—especially the transition between conducting and insulating behavior—of electrons in narrow energy bands of solid-state systems such as transition-metal oxides. At the heart of the Hubbard model is the observation that, in narrow *d*- and *f*-bands, the electrons are mostly located at the nuclei—where they interact—and only rarely move between different positions on the lattice. Therefore, Hubbard proposed to describe these systems in terms of 'sites' between which the electrons 'hop' with a given amplitude *J*. At each site, which, in the model, contains one orbital for spin-up and one orbital for spin-down orientation, the electrons experience a repulsion by electrons in the other orbital of strength *U*. Accordingly, the Hubbard model can be described by the generic Hamiltonian, see equation (16), with matrix elements (written in the representation in terms of spin-orbitals $|i\alpha\rangle$, with site i and spin α),

$$h_{i\alpha j\beta} = -J\delta_{\langle ij\rangle}\delta_{\alpha\beta} - \mu\delta_{ij}\delta_{\alpha\beta}\hat{c}_{i\alpha}^\dagger\hat{c}_{i\alpha}, \quad (27)$$

$$w_{i\alpha j\beta k\gamma l\delta} = U\delta_{il}\delta_{\alpha\delta}\delta_{jk}\delta_{\beta\gamma}\delta_{ij}, \quad (28)$$

$$f_{i\alpha j\beta}\left(t\right) = \delta_{ij}\delta_{\alpha\beta}f_{i\alpha}\left(t\right), \quad (29)$$

where $\delta_{\langle ij\rangle} = 1$, exactly if the sites i, j are nearest neighbors. The term

$$-\mu\delta_{ij}\delta_{\alpha\beta}\hat{c}_{i\alpha}^\dagger\hat{c}_{i\alpha} \quad (30)$$

describes the chemical energy induced by a chemical potential μ. The time-dependent excitation matrices $f_{i\alpha j\beta}\left(t\right)$ for all processes considered in this work are both, on-site $\left(\delta_{ij}\right)$ and spin-conserving $\left(\delta_{\alpha\beta}\right)$. Inserting equations (27)–(29) into the general form of equation (16), one arrives at

$$
\begin{aligned}
\hat{H}\left(t\right) = &-J \sum_{m\epsilon n\zeta} \delta_{\langle mn\rangle}\delta_{\epsilon\zeta}\hat{c}_{m\epsilon}^\dagger\hat{c}_{n\zeta} + \frac{U}{2} \sum_{m\epsilon n\zeta p\eta q\theta} \delta_{mq}\delta_{\epsilon\theta}\delta_{np}\delta_{\zeta\eta}\delta_{mn}\hat{c}_{m\epsilon}^\dagger\hat{c}_{n\zeta}^\dagger\hat{c}_{p\eta}\hat{c}_{q\theta} \\
&+ \sum_{m\epsilon n\zeta} \delta_{mn}\delta_{\epsilon\zeta}f_{m\epsilon n\zeta}\left(t\right)\hat{c}_{m\epsilon}^\dagger\hat{c}_{n\zeta} - \mu\sum_{m\epsilon}\hat{c}_{m\epsilon}^\dagger\hat{c}_{m\epsilon} \\
= &-J \sum_{\langle m,n\rangle} \sum_\epsilon \hat{c}_{m\epsilon}^\dagger\hat{c}_{n\epsilon} + \frac{U}{2} \sum_m \sum_{\epsilon\zeta} \hat{c}_{m\epsilon}^\dagger\hat{c}_{m\zeta}^\dagger\hat{c}_{m\zeta}\hat{c}_{m\epsilon} \\
&+ \sum_{m\epsilon} f_{m\epsilon}\left(t\right)\hat{c}_{m\epsilon}^\dagger\hat{c}_{m\epsilon} - \mu\sum_{m\epsilon}\hat{c}_{m\epsilon}^\dagger\hat{c}_{m\epsilon}.
\end{aligned}
\quad (31)
$$

Here, $\langle m, n\rangle$ denotes the summation over nearest-neighbor sites.

The formal derivation of the Hubbard Hamiltonian [81] starts with the continuous-space Hamiltonian for a periodic solid-state system for which the wavefunctions attain the form of Bloch waves. These Bloch functions can be expanded in the basis of Wannier functions which are spatially localized. For the resulting atomic orbitals, to recover equation (31), now only overlap between neighboring atoms and interaction between on-atom orbitals are assumed. The Hubbard basis, which formally is a set of Wannier states, can thus be understood as set of localized on-site orbitals with a short-range overlap to the nearest neighbors. For more details see, e.g. [92, 93] for bosons and [94] for fermions.

The following results differ for the cases of fermions and bosons, respectively, so we provide both cases separately. With the canonical commutation relations, see equation (12), for bosons, the interaction term can be rewritten as

$$
\begin{aligned}
\hat{W}_{\mathrm{bosons}}^{\mathrm{Hubbard}} &= \frac{U}{2} \sum_m \sum_{\epsilon\zeta} \hat{c}_{m\epsilon}^\dagger\hat{c}_{m\zeta}^\dagger\hat{c}_{m\zeta}\hat{c}_{m\epsilon} = \frac{U}{2} \sum_m \sum_{\epsilon\zeta} \hat{c}_{m\epsilon}^\dagger\hat{c}_{m\zeta}^\dagger\hat{c}_{m\epsilon}\hat{c}_{m\zeta} \\
&= \frac{U}{2} \sum_m \sum_{\epsilon\zeta} \hat{c}_{m\epsilon}^\dagger\hat{c}_{m\epsilon}\hat{c}_{m\zeta}^\dagger\hat{c}_{m\zeta} - \frac{U}{2} \sum_m \sum_\epsilon \hat{c}_{m\epsilon}^\dagger\hat{c}_{m\epsilon} \\
&=: \frac{U}{2} \sum_m \sum_{\epsilon\zeta} \hat{n}_{m\epsilon}\hat{n}_{m\zeta} - \frac{U}{2} \sum_m \sum_\epsilon \hat{n}_{m\epsilon} \\
&= \frac{U}{2} \sum_m \sum_{\epsilon\neq\zeta} \hat{n}_{m\epsilon}\hat{n}_{m\zeta} + \frac{U}{2} \sum_m \sum_\epsilon \hat{n}_{m\epsilon}\left(\hat{n}_{m\epsilon} - 1\right).
\end{aligned}
\quad (32)
$$

The special case of spin-0 bosons results in the Bose–Hubbard interaction,

$$\hat{W}_{\mathrm{bosons},0}^{\mathrm{Hubbard}} = \frac{U}{2} \sum_m \hat{n}_m\left(\hat{n}_m - 1\right), \quad (33)$$

and the corresponding Bose–Hubbard Hamiltonian (without time-dependent excitation),

---

[9] As one notices, the ordering of the terms in equations (25) and (26) is not unique but there exists no ordering which results in a better scaling.

$$\hat{H}_{\text{spin-0}}^{\text{Bose-Hubbard}} = -J \sum_{\langle m,n \rangle} \hat{c}_m^\dagger \hat{c}_n + \frac{U}{2} \sum_m \hat{n}_m \left(\hat{n}_m - 1 \right) - \mu \sum_m \hat{n}_m. \tag{34}$$

Next consider fermions. Now, due to the Pauli exclusion principle, equation (28) can be rewritten as

$$w_{i\alpha j\beta k\gamma l\delta} = U \delta_{il} \delta_{\alpha\delta} \delta_{jk} \delta_{\beta\gamma} \delta_{ij} \bar{\bar{\delta}}_{\alpha\beta}, \tag{35}$$

with $\bar{\bar{\delta}}_{\alpha\beta} = 1 - \delta_{\alpha\beta}$. Consequently, the interaction part $\hat{W}$ of the Hamiltonian becomes

$$\hat{W}_{\text{fermions}}^{\text{Hubbard}} = \frac{U}{2} \sum_m \sum_{\epsilon \neq \zeta} \hat{c}_{m\epsilon}^\dagger \hat{c}_{m\zeta}^\dagger \hat{c}_{m\zeta} \hat{c}_{m\epsilon} = -\frac{U}{2} \sum_m \sum_{\epsilon \neq \zeta} \hat{c}_{m\epsilon}^\dagger \hat{c}_{m\zeta}^\dagger \hat{c}_{m\epsilon} \hat{c}_{m\zeta}$$
$$= \frac{U}{2} \sum_m \sum_{\epsilon \neq \zeta} \hat{c}_{m\epsilon}^\dagger \hat{c}_{m\epsilon} \hat{c}_{m\zeta}^\dagger \hat{c}_{m\zeta} = \frac{U}{2} \sum_m \sum_{\epsilon \neq \zeta} \hat{n}_{m\epsilon} \hat{n}_{m\zeta}. \tag{36}$$

For the special case of spin-$\frac{1}{2}$ fermions, this expression simplifies to

$$\hat{W}_{\text{fermions},1/2}^{\text{Hubbard}} = \frac{U}{2} \sum_m \left(\hat{n}_{m\uparrow} \hat{n}_{m\downarrow} + \hat{n}_{m\downarrow} \hat{n}_{m\uparrow} \right) = U \sum_m \hat{n}_{m\uparrow} \hat{n}_{m\downarrow} \tag{37}$$

and the (Fermi–)Hubbard Hamiltonian (again without time-dependent excitation) is given by

$$\hat{H}_{\text{spin-1/2}}^{\text{Fermi-Hubbard}} = -J \sum_{\langle m,n \rangle} \sum_{\epsilon \in \{\uparrow,\downarrow\}} \hat{c}_{m\epsilon}^\dagger \hat{c}_{n\epsilon} + U \sum_m \hat{n}_{m\uparrow} \hat{n}_{m\downarrow} - \mu \sum_m \left(\hat{n}_{m\uparrow} + \hat{n}_{m\downarrow} \right).$$

One notices that the Hubbard interaction $w_{i\alpha j\beta k\gamma l\delta}$ is highly diagonal, which is very advantageous for the numerical treatment—a property which has contributed greatly to the recurring popularity of the Hubbard model in computational physics in the last decade, e.g. [28, 51, 77, 95–98]. Accordingly, for the example of the second-order selfenergy that was presented above in equation (23) and which will be treated in full detail in section 4, the expression in the Hubbard basis reads, see equation (198),

$$\Sigma_{i\downarrow(\uparrow)j\downarrow(\uparrow)}^{(2),2,0,\text{Hubbard,f},1/2}(z_1, z_2) = \pm \left(i\hbar \right)^2 G_{i\downarrow(\uparrow)j\downarrow(\uparrow)}(z_1, z_2)$$
$$U(z_1) G_{i\uparrow(\downarrow)j\uparrow(\downarrow)}(z_1, z_2) G_{j\uparrow(\downarrow)i\uparrow(\downarrow)}(z_2, z_1) U(z_2). \tag{38}$$

This expression only scales as $\mathcal{O}\left(N_{\text{b}}^2 \right)$, since it involves no matrix multiplications, compared to the scaling for a general basis, with $\mathcal{O}\left(N_{\text{b}}^5 \right)$, and of $\mathcal{O}\left(N_{\text{b}}^4 \right)$, in a diagonal basis. Here, the arguments $z_{1,2}$ denote times that are situated on the Schwinger–Keldysh contour that naturally emerges in nonequilibrium quantum statistics and which we introduce next.

2.4. Time-dependence of observables and the Schwinger–Keldysh time-contour

The purpose of the formalism of second quantization, introduced in the last section, is to provide a suitable framework for the description of quantum many-particle systems, in particular, for time-dependent processes. Here, one is mostly interested in the expectation values of operators of the form

of equations (13) and (14), at any given time t. With the time-dependent many-particle wavefunction, $|\Psi(t)\rangle$, i.e. the solution of the time-dependent Schrödinger equation, the expectation value can be computed as

$$O(t) = \langle \Psi(t) | \hat{O}(t) | \Psi(t) \rangle \tag{39}$$
$$= \left\langle \Psi_0 \left| \hat{\mathcal{T}}_{\text{a}} \left\{ \exp \left(\frac{1}{i\hbar} \int_t^{t_0} d\bar{t} \, \hat{H}(\bar{t}) \right) \right\} \hat{O}(t) \hat{\mathcal{T}}_{\text{c}} \left\{ \exp \left(-\frac{1}{i\hbar} \int_t^{t_0} d\bar{t} \, \hat{H}(\bar{t}) \right) \right\} \right| \Psi_0 \right\rangle,$$

where the operators $\left(\hat{\mathcal{T}}_{\text{a}} \right) \hat{\mathcal{T}}_{\text{c}}$ are the (anti-)chronological time-ordering superoperators, which rearrange the operators acted on such that the latest (earliest) times are moved to the left-hand side to account for (anti-)causality. A more concise formulation can be achieved by introducing an oriented contour $\mathcal{C}$ which starts from t_0, extends to the turning point t and then reaches back to t_0,

$$\mathcal{C} = \underbrace{\left(t_0, t \right)}_{\mathcal{C}^-} \bigoplus \underbrace{\left(t, t_0 \right)}_{\mathcal{C}^+}, \tag{40}$$

with a forward branch $\mathcal{C}^-$ and a backward branch $\mathcal{C}^+$, depicted in figure 1. Henceforth, a general time on the contour $\mathcal{C}$ will be denoted as z and $z_\pm$ to refer to a time lying on one of the branches. Accordingly, an operator $\hat{O}$ can be extended to the contour, having possibly different values on both branches,

$$\hat{O}(z) = \begin{cases} \hat{O}_-(z) & \text{if } z \in \mathcal{C}^- \\ \hat{O}_+(z) & \text{if } z \in \mathcal{C}^+ \end{cases}. \tag{41}$$

With this definition, one can define a contour time-ordering superoperator $\hat{\mathcal{T}}_{\mathcal{C}}$ which moves operators at later contour times ahead of operators at earlier contour times. As a consequence, its action agrees with that of $\hat{\mathcal{T}}_{\text{c}}$, for all times $z_- \in \mathcal{C}^-$, and with that of $\hat{\mathcal{T}}_{\text{a}}$, for all times $z_+ \in \mathcal{C}^+$. Furthermore, time integrals are extended in a natural way to the contour by defining

$$\int_{z_1}^{z_2} d\bar{z} \, \hat{O}(\bar{z}) := \begin{cases} \int_{t_1}^{t_2} d\bar{t} \, \hat{O}_-(\bar{t}) & \text{if } z_1, z_2 \in \mathcal{C}^- \\ \int_{t_1}^{t} d\bar{t} \, \hat{O}_-(\bar{t}) + \int_t^{t_2} d\bar{t} \, \hat{O}_+(\bar{t}) & \text{if } z_1 \in \mathcal{C}^-, z_2 \in \mathcal{C}^+ \\ \int_{t_1}^{t_2} d\bar{t} \, \hat{O}_+(\bar{t}) & \text{if } z_1, z_2 \in \mathcal{C}^+ \end{cases},$$

assuming z_1 is later than z_2. Using the contour integral, one can reformulate equation (39) for operators which have the same value on both branches, i.e. $\hat{O}_- = \hat{O}_+ =: \hat{O}_\pm$, as

$$O(t) = \left\langle \Psi_0 \left| \hat{\mathcal{T}}_{\mathcal{C}} \left\{ \exp \left(\frac{1}{i\hbar} \int_{\mathcal{C}^+} d\bar{z} \, \hat{H}(\bar{z}) \right) \hat{O}_\pm(t) \exp \left(\frac{1}{i\hbar} \int_{\mathcal{C}^-} d\bar{z} \, \hat{H}(\bar{z}) \right) \right\} \right| \Psi_0 \right\rangle, \tag{42}$$

which, taking into account the action $\hat{\mathcal{T}}_{\mathcal{C}}$, can be further simplified to

$$O(t) = \left\langle \Psi_0 \left| \hat{\mathcal{T}}_{\mathcal{C}} \left\{ \exp \left(\frac{1}{i\hbar} \int_{\mathcal{C}} d\bar{z} \, \hat{H}(\bar{z}) \right) \hat{O}_\pm(t) \right\} \right| \Psi_0 \right\rangle. \tag{43}$$
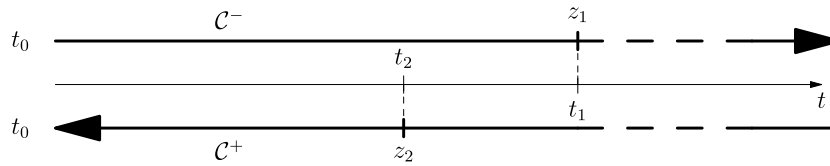
Figure 1. Schwinger–Keldysh contour $\mathcal{C}$. The forward-branch $\mathcal{C}^-$ extends from the initial time t_0 to the current time t, bends and leads back to t_0 along the backward $\mathcal{C}^+$-branch. Note that the projections of the contour times $z_1 < z_2$ on the real axis obey the inverse relationship $t_1 > t_2$.
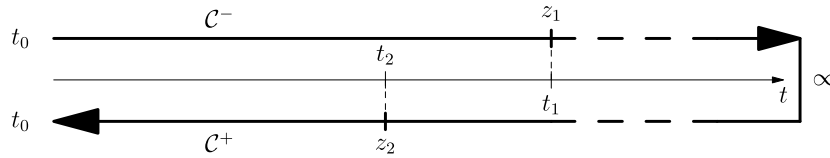
Figure 2. Schwinger–Keldysh contour $\mathcal{C}$ extended to ∞. The forward-branch $\mathcal{C}^-$ spans from the initial time t_0 to ∞, bends and leads back to t_0 along the backward $\mathcal{C}^+$-branch.

On both branches, the contour Hamiltonian $\hat{H}\left(\bar{z}\right)$ is set equal to its definition in equation (16) for the corresponding real-time argument.

An undesirable feature of the introduced contour is that it seemingly depends on the value of t. This can be remedied by extending the contour to $t \rightarrow \infty$, for which the above expressions, in particular equation (43), hold again, since the additional two integral parts cancel. The corresponding contour is depicted in figure 2. Finally, one notices that equation (43) is also true for all contour times z,

$$O(z) = \left\langle \Psi_0 \middle| \hat{\mathcal{T}}_{\mathcal{C}} \left\{ \exp\left(\frac{1}{i\hbar} \int_{\mathcal{C}} \mathrm{d}\bar{z}\, \hat{H}\left(\bar{z}\right) \right) \hat{O}\left(z\right) \right\} \middle| \Psi_0 \right\rangle. \tag{44}$$

It should be noted that in equation (44) the operator $\hat{O}\left(z\right)$ might not bare an explicit time dependence. The indication of the time argument is, however, useful to ensure the correct placement during the time-ordering process of $\hat{\mathcal{T}}_{\mathcal{C}}$.

The contour $\mathcal{C}$ was introduced by Keldysh in 1964 [52] who showed that, with this modified time axis all expressions of ground-state and thermodynamic Green functions, including Feynman's diagram technique, are naturally transferred to arbitrary nonequilibrium situations. The historical context of the development of this method of real-type (Keldysh) Green functions has been reviewed by Keldysh himself, for details see [99].

2.5. Nonequilibrium Green functions and their equations of motion

To compute time-dependent operator expectation values, there are two immediate choices at hand, following equation (39): one can either solve the first or the second line. The first option requires the solution of the equation of motion for the time-dependent wavefunction $|\Psi\left(t\right)\rangle$, which is the Schrödinger equation. This is the road taken by wavefunction-based methods like full configuration interaction [100, 101], multiconfigurational time-dependent Hartree–Fock

[89, 102, 103], generalized active-space configuration interaction [91, 104], exact diagonalization [95], coupled-cluster methods [105] and density-matrix renormalization group based approaches [106–111].

The other way is to follow the second line and to work with the (known) initial wavefunction $|\Psi_0\rangle$[10] and develop an equation of motion for the term

$$\hat{\mathcal{T}}_{\mathcal{C}} \left\{ \exp\left(\frac{1}{i\hbar} \int_{\mathcal{C}} \mathrm{d}\bar{z}\, \hat{H}\left(\bar{z}\right) \right) \hat{O}\left(z\right) \right\}, \tag{45}$$

according to equations (43) and (44), respectively. Approaches relying on this method are, among others, time-dependent Hartree–Fock [112], reduced-density-matrix theory [44, 113], density-functional theory [51, 114–116], dynamical mean-field theory (DMFT) [117–120] and the method of Green functions [28, 71, 72, 77, 78, 96, 98, 121–129], which is the topic of this article. In principle, both approaches are equivalent and yield the same results. The main difference is the set of available approximation techniques and, foremost, the numerical scaling behavior with respect to the maximal simulation time, particle number, basis size and interaction strength. The wavefunction-based methods, in general, can cope with huge basis sets with a number of basis functions, depending on the system at hand, ranging from thousands to millions and interaction strengths from weak to strong coupling. Additionally, they offer a linear scaling of the numerical effort with the simulation time. The trade-off is the exponential scaling of the numerical effort with the particle number rendering the simulation of systems with more than a few particles impossible [91, 104].

In contrast, the second group of methods, which relies on the equation of motion for the creation and annihilation operators, are not limited by the particle number. The scaling with the basis size is worse compared to the other group but still polynomial and the scaling with the total simulation time is at least quadratic for methods going beyond Hartree–Fock (which has a linear scaling). Apart from DMFT, which is also good for very strong interactions but can simulate only

---

[10] It will be shown in section 2.11 that, actually, the knowledge of the ideal, i.e. non-interacting, initial state is sufficient.

short time-spans, all methods of the second group, including Green functions, are mostly suited for small interaction strengths. In the following, the theory behind the Green functions method will be summarized. For a more in-detail derivation, see, e.g. [73, 74]. In the following section, the definition of the Green functions, their equations of motion and the determination of time-dependent observables from them will be discussed.

The direct computation of the time-dependent values of operators according to equation (44) involves the evaluation of the time-ordered exponential, which is impractical apart from very small basis sizes due to the dimensionality of the Hamiltonian. One strategy to bypass the direct evaluation of the exponential is to introduce the contour Heisenberg picture, which will be described in the following. Similar as for standard time, one can define the time-evolution operator $\hat{U}\left(z_2, z_1\right)$ on the contour,

$$
\hat{U}\left(z_2, z_1\right) =
\begin{cases}
\hat{\mathcal{T}}_{\mathcal{C}}\left\{\exp\left(\dfrac{1}{i\hbar}\displaystyle\int_{z_1}^{z_2} d\bar{z}\,\hat{H}\left(\bar{z}\right)\right)\right\} & \text{if } z_2 \text{ later than } z_1, \\[2mm]
\hat{\mathcal{T}}_{\mathcal{C}}^{\mathrm{a}}\left\{\exp\left(-\dfrac{1}{i\hbar}\displaystyle\int_{z_2}^{z_1} d\bar{z}\,\hat{H}\left(\bar{z}\right)\right)\right\} & \text{if } z_2 \text{ earlier than } z_1,
\end{cases}
\tag{46}
$$

where, in the second line, the anti-chronological time-ordering operator $\hat{\mathcal{T}}_{\mathcal{C}}^{\mathrm{a}}$ has been introduced, which places operators with later contour times to the right. The contour time-evolution operator has the usual properties, i.e. fulfills

$$
i\hbar\frac{d}{dz_1}\hat{U}\left(z_1, z_0\right) = \hat{H}\left(z_1\right)\hat{U}\left(z_1, z_0\right), \tag{47}
$$

$$
i\hbar\frac{d}{dz_1}\hat{U}\left(z_0, z_1\right) = -\hat{U}\left(z_0, z_1\right)\hat{H}\left(z_1\right). \tag{48}
$$

With this, equation (44) can be cast into the form

$$
O(z_1) = \left\langle \Psi_0\middle|\hat{U}\left(z_{0^+}, z_{0^-}\right)\hat{U}\left(z_{0^-}, z_1\right)\hat{O}\left(z_1\right)\hat{U}\left(z_1, z_{0^-}\right)\middle|\Psi_0\right\rangle, \tag{49}
$$

where z_{0^-} and z_{0^+} represent the start (end) of the contour. Equation (49) suggests to introduce the contour Heisenberg picture

$$
\hat{O}_{\mathrm{H}}\left(z_1\right) := \hat{U}\left(z_{0^-}, z_1\right)\hat{O}\left(z_1\right)\hat{U}\left(z_1, z_{0^-}\right), \tag{50}
$$

with the equation of motion

$$
i\hbar\frac{d}{dz_1}\hat{O}_{\mathrm{H}}\left(z_1\right) = \left[\hat{O}_{\mathrm{H}}\left(z_1\right), \hat{H}_{\mathrm{H}}\left(z_1\right)\right]_- + \partial_{z_1}\hat{O}_{\mathrm{H}}\left(z_1\right). \tag{51}
$$

Using the commutator relations, see equation (12), the contour equations of motion for the canonical creation and annihilation operators for systems described by the Hamiltonian in equation (16) are readily found,

$$
i\hbar\frac{d}{dz_1}\hat{c}_i\left(z_1\right) = \sum_n\left(h_{in}\left(z_1\right) + f_{in}\left(z_1\right)\right)\hat{c}_n\left(z_1\right) \tag{52}
$$
$$
+ \sum_{npq} w_{inpq}\left(z_1\right)\hat{c}_n^\dagger\left(z_1\right)\hat{c}_p\left(z_1\right)\hat{c}_q\left(z_1\right),
$$

$$
-i\hbar\frac{d}{dz_1}\hat{c}_i^\dagger\left(z_1\right) = \sum_m\hat{c}_m^\dagger\left(z_1\right)\left(h_{mi}\left(z_1\right) + f_{mi}\left(z_1\right)\right) \tag{53}
$$
$$
+ \sum_{mnp}\hat{c}_m^\dagger\left(z_1\right)\hat{c}_n^\dagger\left(z_1\right)\hat{c}_p\left(z_1\right)w_{mnpi}\left(z_1\right),
$$

where

$$
\hat{c}\left(z_1\right) := \hat{c}_{\mathrm{H}}\left(z_1\right), \quad \hat{c}^\dagger\left(z_1\right) := \hat{c}_{\mathrm{H}}^\dagger\left(z_1\right). \tag{54}
$$

These equations can be used to derive equations for operator correlators, such as already encountered in equation (44). For N operators, they are of the form

$$
\hat{k}\left(z_1 \ldots z_N\right) = \hat{\mathcal{T}}_{\mathcal{C}}\left\{\hat{O}_1\left(z_1\right)\ldots\hat{O}_N\left(z_N\right)\right\}. \tag{55}
$$

Remembering that any operator can be expressed in terms of the canonical operators, a special role is played by the correlators of these operators. From equations (13) and (14), it is evident that especially those with the same number of creation and annihilation operators are of interest, since they give direct access to observables. Thus it is useful to define the correlator of N annihilation and creation operators,

$$
\hat{G}_{i_1\ldots i_N j_1\ldots j_N}^{(N)}\left(z_1 \cdots z_N, z_1' \cdots z_N'\right) \tag{56}
$$
$$
:= \frac{1}{\left(i\hbar\right)^N}\hat{\mathcal{T}}_{\mathcal{C}}\left\{\hat{c}_{i_1}\left(z_1\right)\ldots\hat{c}_{i_N}\left(z_N\right)\hat{c}_{j_1}^\dagger\left(z_1'\right)\ldots\hat{c}_{j_N}^\dagger\left(z_N'\right)\right\},
$$

with $2N$ contour time arguments. Using some contour calculus, not repeated here (for details see [73, 78]), and the contour Heisenberg equations, one can derive their equations of motion, which couple the N-particle correlator to the $(N-1)$- and $(N+1)$-particle correlators,

$$
\sum_l\left[i\hbar\frac{d}{dz_k}\delta_{i_k l} - h_{i_k l}\left(z_k\right)\right]\hat{G}_{i_1\ldots l\ldots i_N j_1\ldots j_N}^{(N)}\left(z_1 \cdots z_N, z_1' \cdots z_N'\right)
$$
$$
= \pm i\hbar\sum_{lmn}\int_{\mathcal{C}} d\bar{z}\, w_{i_k lmn}\left(z_k, \bar{z}\right)\hat{G}_{i_1\ldots m\ldots i_N n j_1\ldots j_N m}^{(N+1)}\left(z_1 \cdots z_N, \bar{z}, z_1' \cdots z_N', \bar{z}\right)
$$
$$
+ \sum_p\left(\pm\right)^{k+p}\delta_{i_k j_p}\delta_{\mathcal{C}}\left(z_k, z_p'\right)
$$
$$
\hat{G}_{i_1\ldots\slashed{i}\ldots i_N j_1\ldots\slashed{j}\ldots j_N}^{(N-1)}\left(z_1 \cdots \slashed{z}_k \cdots z_N, z_1' \cdots \slashed{z}_p' \cdots z_N'\right), \tag{57}
$$

$$
\sum_l\hat{G}_{i_1\ldots i_N j_1\ldots l\ldots j_N}^{(N)}\left(z_1 \cdots z_N, z_1' \cdots z_N'\right)\left[-i\hbar\frac{\overleftarrow{d}}{dz_k'}\delta_{l j_k} - h_{l j_k}\left(z_k'\right)\right]
$$
$$
= \pm i\hbar\sum_{lmn}\int_{\mathcal{C}} d\bar{z}\,\hat{G}_{i_1\ldots i_N n j_1\ldots l\ldots j_N m}^{(N+1)}\left(z_1 \cdots z_N, \bar{z}, z_1' \cdots z_N', \bar{z}\right)w_{lmj_k n}\left(\bar{z}, z_k'\right)
$$
$$
+ \sum_p\left(\pm\right)^{k+p}\delta_{i_p j_k}\delta_{\mathcal{C}}\left(z_p, z_k'\right)
$$
$$
\hat{G}_{i_1\ldots\slashed{i}\ldots i_N j_1\ldots\slashed{j}\ldots j_N}^{(N-1)}\left(z_1 \cdots \slashed{z}_p \cdots z_N, z_1' \cdots \slashed{z}_k' \cdots z_N'\right). \tag{58}
$$

Here, the crossed-out indices (times) have to be omitted for the respective $(N-1)$-particle correlators. The expectation value of the operator $\hat{G}^{(N)}$ in the initial state Ψ_0 yields the N-particle Green function $G^{(N)}$,

$$G^{(N)} = \left\langle \Psi_0 \left| \hat{G}^{(N)} \right| \Psi_0 \right\rangle. \qquad (59)$$

Note that in equations (57) and (58), the bare interaction is written as a two-time quantity—a generalization that would become important e.g. in the context of retarded and advanced relativistic potentials. However, in this work, the bare interaction is always considered single-time-dependent, i.e.

$$w_{ijkl}\left(z_1, z_2\right) = \delta_{\mathcal{C}}\left(z_1, z_2\right) w_{ijkl}\left(z_1\right). \qquad (60)$$

Nevertheless, the two-time structure of w is often used for the illustration via Feynman diagrams (see section 2.8).

　The equations of motion for the Green functions are directly generated from the equations for the underlying operators by taking the expectation value, which corresponds to replacing all correlator operators in equations (57) and (58) by the respective Green functions,

$$\hat{G}^{(N)} \longrightarrow G^{(N)}. \qquad (61)$$

These mutually coupled equations form a hierarchy, the *Martin–Schwinger hierarchy* [130]. The solution of the full hierarchy gives access to all observables of the studied system and, by virtue of the connections to the $(N-1)$-particle and $(N+1)$-particle spaces, also spectral information is available. Thus, as a subset, the solution of the hierarchy incorporates the solution of the N-particle Schrödinger equation. Unfortunately and as expected, the effort for the full solution of the hierarchy also scales exponentially with the particle number. For the one-particle Green function $G^{(1)}$, which will be simply called the Green function G in the following, the equations of motion, the *Keldysh–Kadanoff–Baym equations* (KBE), read

$$\sum_l \left[i\hbar \frac{\mathrm{d}}{\mathrm{d}z_1} \delta_{il} - h_{il}\left(z_1\right) \right] G_{lj}\left(z_1, z_2\right) \qquad (62)$$
$$= \delta_{\mathcal{C}}\left(z_1, z_2\right)\delta_{ij} \pm i\hbar \sum_{lmn} w_{ilnm}\left(z_1\right) G^{(2)}_{mnjl}\left(z_1, z_1, z_2, z_{1+}\right),$$

$$\sum_l G_{il}\left(z_1, z_2\right) \left[-i\hbar \frac{\overleftarrow{\mathrm{d}}}{\mathrm{d}z_2} \delta_{lj} - h_{lj}\left(z_2\right) \right] \qquad (63)$$
$$= \delta_{\mathcal{C}}\left(z_1, z_2\right)\delta_{ij} \pm i\hbar \sum_{lmn} G^{(2)}_{inlm}\left(z_1, z_{2-}, z_2, z_2\right) w_{lmnj}\left(z_2\right).$$

Note that the short-hand notation $z_\pm := z \pm \epsilon \; (\epsilon \to +0)$ has been introduced here to facilitate the correct ordering of the operators under $\hat{\mathcal{T}}_{\mathcal{C}}$. One notices that even the determination of the one-particle Green functions requires the solution of all other hierarchy equations as well, due to the coupling to the two-particle Green function (which, in turn couples to the three-particle Green function, and so on).

2.6. Definition of the selfenergy

To decouple the Martin–Schwinger hierarchy, approximations are necessary. This requires to find a functional relation of $G^{(n)}$ in terms of $G^{(n-1)}$ that is based on physical considerations

about the dominant processes. Alternatively, one can apply perturbation theory in terms of the particle interaction. If the knowledge of the single-particle Green function is sufficient for the physical problem at hand, it is suitable to introduce the so-called single-particle *selfenergy* Σ, which allows one to (formally) decouple the time-evolution of the Green function from those of the $(N > 1)$-particle Green functions and obtain a closed equation for the one-particle Green function. The selfenergy is implicitly defined as

$$\pm i\hbar \sum_{lmn} w_{ilnm}\left(z_1\right) G^{(2)}_{mnjl}\left(z_1, z_1, z_2, z_{1+}\right)$$
$$=: \sum_l \int_{\mathcal{C}} \mathrm{d}z_3 \, \Sigma_{il}\left(z_1, z_3\right) G_{lj}\left(z_3, z_2\right), \qquad (64)$$

$$\pm i\hbar \sum_{lmn} G^{(2)}_{inlm}\left(z_1, z_{2-}, z_2, z_2\right) w_{lmnj}\left(z_1\right)$$
$$=: \sum_l \int_{\mathcal{C}} \mathrm{d}z_3 \, G_{il}\left(z_1, z_3\right) \Sigma_{lj}\left(z_3, z_2\right). \qquad (65)$$

Note that the Σ resulting from the first definition (equation (64)) also fulfills equation (65) and vice versa. This feature is not self-evident but follows from the built-in properties of the KBE and, in particular, the two-particle Green function (see, e.g. [73]). With this, equations (62) and (63) transform into

$$\sum_l \left[i\hbar \frac{\mathrm{d}}{\mathrm{d}z_1} \delta_{il} - h_{il}\left(z_1\right) \right] G_{lj}\left(z_1, z_2\right)$$
$$= \delta_{\mathcal{C}}\left(z_1, z_2\right)\delta_{ij} + \sum_l \int_{\mathcal{C}} \mathrm{d}z_3 \, \Sigma_{il}\left(z_1, z_3\right) G_{lj}\left(z_3, z_2\right), \quad (66)$$

$$\sum_l G_{il}\left(z_1, z_2\right) \left[-i\hbar \frac{\overleftarrow{\mathrm{d}}}{\mathrm{d}z_2} \delta_{lj} - h_{lj}\left(z_2\right) \right]$$
$$= \delta_{\mathcal{C}}\left(z_1, z_2\right)\delta_{ij} + \sum_l \int_{\mathcal{C}} \mathrm{d}z_3 \, G_{il}\left(z_1, z_3\right) \Sigma_{lj}\left(z_3, z_2\right). \quad (67)$$

These equations contain the two main quantities in Green functions theory, both depending on two contour times z_1, z_2: the (single-particle) selfenergy $\Sigma\left(z_1, z_2\right)$ and the (single-particle) Green function $G\left(z_1, z_2\right)$ itself.

　It is apparent from equations (64) and (65) that Σ directly follows from the functional form of the two-particle Green function $G^{(2)}$. It can be shown from the functional-derivative technique [53, 73, 131] that

$$G^{(2)}_{ijkl}\left(z_1, z_2, z_3, z_{2+}\right) = G_{ik}\left(z_1, z_3\right) G_{jl}\left(z_2, z_{2+}\right) \pm \frac{\partial G_{ik}\left(z_1, z_3\right)}{\partial U_{jl}\left(z_2\right)},$$

where U is a small perturbation of the Hamiltonian. From this, it can be seen that the exact $G^{(2)}$ can always be written as a functional of G and, thus, also the exact selfenergy Σ. Similarly, for every conserving approximation of $G^{(2)}$ one obtains $\Sigma\left[G\right]$.
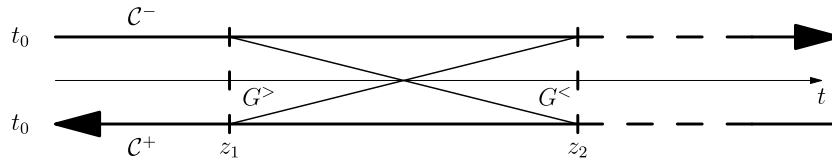
Figure 3. Subordinated Green functions on $\mathcal{C}$ with the forward branch $\mathcal{C}^-$ and the backward branch $\mathcal{C}^+$. The positions of the two time arguments of $G\left(z_1, z_2\right)$ for the '$\gtrless$' components, which can lie an both parts of the contour, are depicted.

Before turning to the self-consistent determination of $\Sigma\left[G\right]$ in section 2.8, and several approximation strategies thereof in section 4, a mapping technique for single-particle contour quantities onto real-time quantities is detailed in section 2.7.

2.7. Keldysh–Kadanoff–Baym equations (KBE)

For the actual computation of expressions containing integrals and products of contour quantities, a mapping to ordinary real-time quantities has to be used. A suitable technique has been provided by *Langreth* and *Wilkins* [132]. Since, in this work, only single-particle correlators like the (single-particle) Green function and selfenergy are of concern, the following technique will only deal with terms of the form (see equation (55)),

$$k\left(z_1, z_2\right) = \left\langle \Psi_0 \Big| \hat{\mathcal{T}}_\mathcal{C}\left\{\hat{O}_1\left(z_1\right)\hat{O}_2\left(z_2\right)\right\} \Big| \Psi_0 \right\rangle, \quad (68)$$

with the restriction that the operators have to obey

$$\hat{O}_- = \hat{O}_+, \quad (69)$$

i.e. they have the same values for contour arguments on the upper and lower branch. The appearance of the contour-ordering operator $\hat{\mathcal{T}}_\mathcal{C}$ in equation (68) suggest to split k into

$$k\left(z_1, z_2\right) = \delta_\mathcal{C}\left(z_1, z_2\right)k^\delta(z_1) + \Theta_\mathcal{C}\left(z_1, z_2\right)k^>\left(z_1, z_2\right)$$
$$+ \Theta_\mathcal{C}\left(z_2, z_1\right)k^<\left(z_1, z_2\right), \quad (70)$$

with

$$k^>\left(z_1, z_2\right) = \left\langle \Psi_0 \Big| \hat{O}_1\left(z_1\right)\hat{O}_2\left(z_2\right) \Big| \Psi_0 \right\rangle, \quad (71)$$

$$k^<\left(z_1, z_2\right) = \pm\left\langle \Psi_0 \Big| \hat{O}_2\left(z_2\right)\hat{O}_1\left(z_1\right) \Big| \Psi_0 \right\rangle, \quad (72)$$

where the $\pm$ stands for bosonic/fermionic operators. Both functions, '<' and '>', obey

$$k^\gtrless\left(z_{1+}, z_2\right) = k^\gtrless\left(z_{1-}, z_2\right),$$
$$k^\gtrless\left(z_1, z_{2+}\right) = k^\gtrless\left(z_1, z_{2-}\right), \quad (73)$$

where $z_{1/2\pm} = t_{1/2\pm}$ are the projections on the backward/forward branch of the contour, and the relations are depicted in figure 3. With that, only two linearly independent quantities remain and it is thus natural to define the so-called real-time '<' and '>' Keldysh components

$$k^>\left(t_1, t_2\right) := k\left(t_{1+}, t_{2-}\right) = k^>\left(t_{1+}, t_{2-}\right), \quad (74)$$

$$k^<\left(t_1, t_2\right) := k\left(t_{1-}, t_{2+}\right) = k^<\left(t_{1-}, t_{2+}\right) \quad (75)$$

and the δ component

$$k^\delta\left(t_1\right) := k\left(t_{1-}, t_{1-}\right) = k\left(t_{1+}, t_{1+}\right)$$
$$= k^\delta\left(t_{1+}, t_{1+}\right) = k^\delta\left(t_{1-}, t_{1-}\right). \quad (76)$$

For convenience, two more (redundant) components, the retarded and advanced component, can be defined as

$$k^\mathcal{R}\left(t_1, t_2\right) = \delta\left(t_1, t_2\right)k^\delta\left(t_1\right) + \Theta\left(t_1, t_2\right)\left[k^>\left(t_1, t_2\right) - k^<\left(t_1, t_2\right)\right], \quad (77)$$

$$k^\mathcal{A}\left(t_1, t_2\right) = \delta\left(t_1, t_2\right)k^\delta\left(t_1\right) + \Theta\left(t_2, t_1\right)\left[k^<\left(t_1, t_2\right) - k^>\left(t_1, t_2\right)\right]. \quad (78)$$

With these components, the real-time expressions for two common concatenations of Keldysh functions, i.e. functions satisfying equations (70) and (73), the convolution and the product, can be worked out. For the convolution

$$c\left(z_1, z_2\right) = \int_\mathcal{C} \mathrm{d}z_3\, a\left(z_1, z_3\right)b\left(z_3, z_2\right), \quad (79)$$

one has

$$c^\gtrless\left(t_1, t_2\right) = \int_{t_0}^{t_1} \mathrm{d}t_3\, a^\mathcal{R}\left(t_1, t_3\right)b^\gtrless\left(t_3, t_2\right) + \int_{t_0}^{t_2} \mathrm{d}t_3\, a^\gtrless\left(t_1, t_3\right)b^\mathcal{A}\left(t_3, t_2\right) \quad (80)$$

and

$$c^\mathcal{R}\left(t_1, t_2\right) = \int_{t_2}^{t_1} \mathrm{d}t_3\, a^\mathcal{R}\left(t_1, t_3\right)b^\mathcal{R}\left(t_3, t_2\right), \quad (81)$$

$$c^\mathcal{A}\left(t_1, t_2\right) = \int_{t_1}^{t_2} \mathrm{d}t_3\, a^\mathcal{A}\left(t_1, t_3\right)b^\mathcal{A}\left(t_3, t_2\right). \quad (82)$$

For the product of type

$$c\left(z_1, z_2\right) = a\left(z_1, z_2\right)b\left(z_2, z_1\right), \quad (83)$$

with $a^\delta = 0 = b^\delta$, one arrives at

$$c^\gtrless\left(t_1, t_2\right) = a^\gtrless\left(t_1, t_2\right)b^\lessgtr\left(t_2, t_1\right) \quad (84)$$

and

$$
\begin{aligned}
c^{\mathcal{R}/\mathcal{A}}\left(t_1,t_2\right) &= a^{\mathcal{R}/\mathcal{A}}\left(t_1,t_2\right)b^<\left(t_2,t_1\right) + a^<\left(t_1,t_2\right)b^{\mathcal{A}/\mathcal{R}}\left(t_2,t_1\right) \\
&= a^{\mathcal{R}/\mathcal{A}}\left(t_1,t_2\right)b^>\left(t_2,t_1\right) + a^>\left(t_1,t_2\right)b^{\mathcal{A}/\mathcal{R}}\left(t_2,t_1\right),
\end{aligned}
\tag{85}
$$

while for the product of type

$$
c\left(z_1,z_2\right) = a\left(z_1,z_2\right)b\left(z_1,z_2\right),
\tag{86}
$$

with $a^\delta = 0 = b^\delta$, one has

$$
c^\gtrless\left(t_1,t_2\right) = a^\gtrless\left(t_1,t_2\right)b^\gtrless\left(t_1,t_2\right)
\tag{87}
$$

and

$$
\begin{aligned}
c^{\mathcal{R}/\mathcal{A}}\left(t_1,t_2\right) &= a^{\mathcal{R}/\mathcal{A}}\left(t_1,t_2\right)b^<\left(t_1,t_2\right) + a^>\left(t_1,t_2\right)b^{\mathcal{R}/\mathcal{A}}\left(t_1,t_2\right) \\
&= a^{\mathcal{R}/\mathcal{A}}\left(t_1,t_2\right)b^>\left(t_1,t_2\right) + a^<\left(t_1,t_2\right)b^{\mathcal{R}/\mathcal{A}}\left(t_1,t_2\right).
\end{aligned}
\tag{88}
$$

With these definitions, the KBE in component representation read

$$
\begin{aligned}
\sum_l & \left[i\hbar\frac{d}{dt_1}\delta_{il} - h_{il}\left(t_1\right)\right]G^\gtrless_{lj}\left(t_1,t_2\right) \\
&= \sum_l\int_{t_0}^{t_1}dt_3\,\Sigma^{\mathcal{R}}_{il}\left(t_1,t_3\right)G^\gtrless_{lj}\left(\bar{t},t'\right) + \int_{t_0}^{t_2}dt_3\,\Sigma^\gtrless_{il}\left(t_1,t_3\right)G^{\mathcal{A}}_{lj}\left(\bar{t},t'\right) \\
&= \sum_l\int_{t_0}^{t_1}dt_3\left(\Sigma^>_{il}\left(t_1,t_3\right)-\Sigma^<_{il}\left(t_1,t_3\right)\right)G^\gtrless_{lj}\left(\bar{t},t'\right) \\
&\quad + \sum_l\int_{t_0}^{t_2}dt_3\,\Sigma^\gtrless_{il}\left(t_1,t_3\right)\left(G^<_{lj}\left(\bar{t},t'\right)-G^>_{lj}\left(\bar{t},t'\right)\right)
\end{aligned}
\tag{89}
$$

and

$$
\begin{aligned}
\sum_l & G^\gtrless_{il}\left(t_1,t_2\right)\left[-i\hbar\frac{\overleftarrow{d}}{dt_2}\delta_{lj} - h_{lj}\left(t_2\right)\right] \\
&= \sum_l\int_{t_0}^{t_1}dt_3\,G^{\mathcal{R}}_{il}\left(t_1,t_3\right)\Sigma^\gtrless_{lj}\left(t_3,t_2\right) + \int_{t_0}^{t_2}dt_3\,G^\gtrless_{il}\left(t_1,t_3\right)\Sigma^{\mathcal{A}}_{lj}\left(t_3,t_2\right) \\
&= \sum_l\int_{t_0}^{t_1}dt_3\left(G^>_{il}\left(t_1,t_3\right)-G^<_{il}\left(t_1,t_3\right)\right)\Sigma^\gtrless_{lj}\left(t_3,t_2\right) \\
&\quad + \sum_l\int_{t_0}^{t_2}dt_3\,G^\gtrless_{il}\left(t_1,t_3\right)\left(\Sigma^<_{lj}\left(t_3,t_2\right)-\Sigma^>_{lj}\left(t_3,t_2\right)\right).
\end{aligned}
\tag{90}
$$

Note the missing $\delta_{\mathcal{C}}$ in the '$\gtrless$' components of equations (89) and (90) compared to equations (66) and (67), which, as it is a time-diagonal function, only enters the retarded and advanced components.

2.8. Basic equations for deriving selfenergy approximations

In this brief section, a coupled set of equations of motions for five dynamical quantities, two of which are the Green function and the selfenergy, is summarized. It has been first presented by *Lars Hedin* in 1965 [82] in association with the *GW* method, which will be discussed in more detail in section 5. If solved exactly, the set of Hedin's equations yields the same G as the solution of the Martin–Schwinger hierarchy[11] and provides multiple starting points for approximate solution schemes. To determine the solution for $G\left(z_1,z_2\right)$, its equations of motion, the KBE, see equations (66) and (67), have to be solved. This can be either done directly in their differential form, or in the integral form, which reads

$$
\begin{aligned}
G_{ij}\left(z_1,z_2\right) &= G^{(0)}_{ij}\left(z_1,z_2\right) \\
&+ \int_{\mathcal{C}}dz_3dz_4\sum_{mn}G^{(0)}_{im}\left(z_1,z_3\right)\Sigma_{mn}\left(z_3,z_4\right)G_{nj}\left(z_4,z_2\right),
\end{aligned}
\tag{91}
$$

with the reference Green function $G^{(0)}$ that is the solution of the ideal pair of equations

$$
\sum_l\left[i\hbar\frac{d}{dz_1}\delta_{il} - h_{il}\left(z_1\right)\right]G_{lj}\left(z_1,z_2\right) = \delta_{\mathcal{C}}\left(z_1,z_2\right)\delta_{ij},
\tag{92}
$$

$$
\sum_l G_{il}\left(z_1,z_2\right)\left[-i\hbar\frac{\overleftarrow{d}}{dz_2}\delta_{lj} - h_{lj}\left(z_2\right)\right] = \delta_{\mathcal{C}}\left(z_1,z_2\right)\delta_{ij}.
\tag{93}
$$

Note that $G^{(0)}$ does not refer to zero particles, but to the property that it is of zeroth order with respect to the interaction w.

At this point, a more compact notation is introduced that focuses on the time structure of the upcoming quantities and uses the corresponding Feynman diagrams to exemplify the underlying connections. Thereto, the basis indices are skipped and the contour-time arguments are replaced by bare numbers $(z_1 \mapsto 1)$. The occuring integrations are implicitly determined by times, the corresponding vertices of which are fully connected (i.e. two Green functions and one interaction or an equivalent connectivity state). As it is usually done in the context of Feynman diagrams the bare interaction is used as a two-time quantity, see equation (60). This notation will be used extensively in sections 4 and 5 to simplify the derivations of the selfenergy approximations. For equation (91) this notation reads as follows,

$$
\begin{aligned}
G\left(1,2\right) &= G^{(0)}\left(1,2\right) \\
&+ G^{(0)}\left(1,3\right)\Sigma\left(3,4\right)G\left(4,2\right)
\end{aligned}
\tag{94}
$$

---

[11] Although, to the knowledge of the authors, no strict proof exists that shows the equivalence of the solutions for G of Hedin's equation versus that from the Martin–Schwinger hierarchy, both approaches agree for all practically relevant approximations. It is, however, worth mentioning that it is proven, e.g. in [73] that the original variational approach of Hedin and the diagrammatic techniques are fully equivalent.

Equation (91) (and (94), respectively) is referred to as the *Dyson equation* for the one-particle Green function. Comparing the KBE, see equations (66) and (67), to the Dyson equation, see equation (91), the question may arise whether the solution of one or the other is numerically more favorable. Realizing that the determination of $G^{(0)}$ via equations (92) and (93) is of $\mathcal{O}\left(N_b^2\right)$ and $\mathcal{O}\left(N_t^2\right)$, whereas the solution of the full G via equation (91) involves two separable time integrations and matrix multiplications, it is of order $\mathcal{O}\left(N_b^3\right)$ and $\mathcal{O}\left(N_t^3\right)$, which is the same scaling as the solution of the KBE, although the prefactors are higher for the Dyson equation. In section 4, though, it will be shown that in an expansion of Σ and, particularly, G with respect to the order of the interaction, only the Dyson equation allows for a strict order-per-order expansion scheme.

Both, the Dyson equation and the KBE, depend on the knowledge of the selfenergy Σ. It can be decomposed into two parts[12],

$$\Sigma_{ij}\left(z_1, z_2\right) = \Sigma_{ij}^{H}\left(z_1, z_2\right) + \Sigma_{ij}^{xc}\left(z_1, z_2\right), \qquad (95)$$

$$\begin{aligned}\Sigma(1,2) &= \pm i\hbar\delta(1,2)w(1,3)G(3,3^+) \\ &+ i\hbar w(1,3)G(1,4)\Lambda(4,2,3)\end{aligned} \qquad (99)$$

$$\begin{aligned}\Lambda(1,2,3) &= \delta(1,2^+)\delta(3,2) \\ &+ \frac{\delta\Sigma(1,2)}{\delta G(4,5)}G(4,6)G(7,5)\Lambda(6,7,3)\end{aligned} \qquad (100)$$

with the (static) time-diagonal Hartree part, Σ^{H},

$$\Sigma_{ij}^{H}\left(z_1, z_2\right) = \pm i\hbar\delta_{\mathcal{C}}\left(z_1, z_2\right)\sum_{mn} w_{mijn}\left(z_1\right)G_{nm}\left(z_1, z_{1+}\right), \qquad (96)$$

and the exchange–correlation part, Σ^{xc}. To determine Σ^{xc}, there exist two commonly used equivalent formally exact approaches. Approach I regards the selfenergy as a functional of the bare interaction, $\Sigma^{xc} = \Sigma^{xc}[w]$, whereas approach II treats it as a functional of the screened interaction W, i.e. $\Sigma^{xc} = \Sigma^{xc}[W]$, where the screening arises from the dynamic redistribution of the other particles in the system. Both techniques rely on a so-called *vertex function*, named either Λ or Γ, in the two cases, which involves the derivatives of either

[12] The same decomposition is used in density-functional theory.

Σ or Σ^{xc} with respect to G to determine the vertex function and, with it, Σ^{xc}. With the coupled equations for Σ^{xc} and the vertex function, both approaches yield a systematic means to generate all selfenergy terms by iteration. We now summarize both approaches.

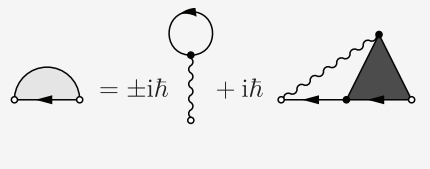(I). With the bare interaction, w, one has

$$\Sigma_{ij}^{xc}\left(z_1, z_2\right) = i\hbar\sum_{mpq} w_{ipqm}\left(z_1\right)\int_{\mathcal{C}}dz_3 \sum_n G_{mn}\left(z_1, z_3\right)\Lambda_{nqpj}\left(z_3, z_2, z_1\right). \qquad (97)$$

The *bare vertex* Λ is self-consistently given as the solution of

$$\begin{aligned}\Lambda_{ijkl}\left(z_1, z_2, z_3\right) &= \delta_{\mathcal{C}}\left(z_1, z_{2+}\right)\delta_{\mathcal{C}}\left(z_3, z_2\right)\delta_{ik}\delta_{jl} \\ &+ \int_{\mathcal{C}}dz_4 dz_5 \sum_{mn}\frac{\delta\Sigma_{il}\left(z_1, z_2\right)}{\delta G_{mn}\left(z_4, z_5\right)}\int_{\mathcal{C}}dz_6 \sum_p G_{mp}\left(z_4, z_6\right) \\ &\int_{\mathcal{C}}dz_7 \sum_q G_{qn}\left(z_7, z_5\right)\Lambda_{pjkq}\left(z_6, z_7, z_3\right).\end{aligned} \qquad (98)$$
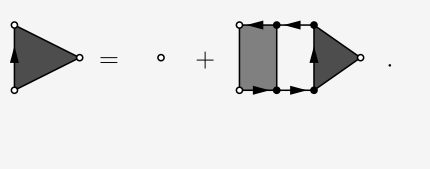
In the compact notation this set of equations becomes,

(II). Using the screened interaction, W, as a basis for the expansion, the exchange–correlation selfenergy reads, see equation (97),

$$\begin{aligned}\Sigma_{ij}^{xc}\left(z_1, z_2\right) &= i\hbar\int_{\mathcal{C}}dz_3 \sum_{mpq} W_{ipqm}\left(z_1, z_3\right) \\ &\times \int_{\mathcal{C}}dz_4 \sum_n G_{mn}\left(z_1, z_4\right)\Gamma_{nqpj}\left(z_4, z_2, z_3\right), \quad (101)\end{aligned}$$

where W obeys

$$W_{ijkl}\left(z_1, z_2\right) = W_{ijkl}^{bare}\left(z_1, z_2\right) + W_{ijkl}^{ns}\left(z_1, z_2\right), \quad (102)$$

with the bare interaction

$$W_{ijkl}^{bare}\left(z_1, z_2\right) = \delta_{\mathcal{C}}\left(z_1, z_2\right)w_{ijkl}\left(z_1\right), \qquad (103)$$

and the non-singular (ns) induced part

$$W_{ijkl}^{ns}\left(z_1,z_2\right)=\sum_{mn}w_{imnl}\left(z_1\right)\int_{\mathcal{C}}\mathrm{d}z_3\sum_{pq}P_{nqpm}\left(z_1,z_3\right)W_{pjkq}\left(z_3,z_2\right).$$

(104)

The occurring polarizability P is given by

$$P_{ijkl}\left(z_1,z_2\right)=\pm\mathrm{i}\hbar\int_{\mathcal{C}}\mathrm{d}z_3\sum_{m}G_{im}\left(z_1,z_3\right)$$

$$\times\int_{\mathcal{C}}\mathrm{d}z_4\sum_{n}G_{nl}\left(z_4,z_1\right)\Gamma_{mjkn}\left(z_3,z_4,z_2\right). \quad (105)$$

The screened vertex function Γ—which Σ^{xc} and P depend on—is governed by
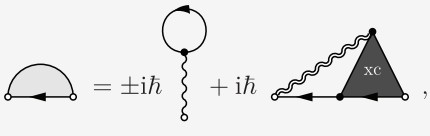
$$\Gamma_{ijkl}\left(z_1,z_2,z_3\right)=\delta_{\mathcal{C}}\left(z_1,z_{2^+}\right)\delta_{\mathcal{C}}\left(z_3,z_2\right)\delta_{ik}\delta_{jl}$$

$$+\int_{\mathcal{C}}\mathrm{d}z_4\mathrm{d}z_5\sum_{mn}\frac{\delta\Sigma_{il}^{\mathrm{xc}}\left(z_1,z_2\right)}{\delta G_{mn}\left(z_4,z_5\right)}\int_{\mathcal{C}}\mathrm{d}z_6\sum_{p}G_{mp}\left(z_4,z_6\right)$$

$$\int_{\mathcal{C}}\mathrm{d}z_7\sum_{q}G_{qn}\left(z_7,z_5\right)\Gamma_{pjkq}\left(z_6,z_7,z_3\right). \quad (106)$$
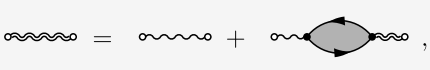
To summarize, Hedin's equations are repeated in the compact notation,
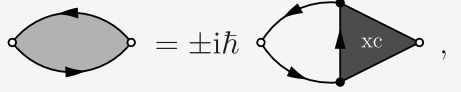
2.9. Summary of selfenergy approximations

We now list the selfenergies that will be discussed in this paper and briefly summarize their respective strengths and weaknesses. For approach I.) that starts with the bare interaction, equation (97), we will consider:

– The particle–particle T-matrix approximation (TPP)
  The TPP selfenergy sums up the diagrams of the Born series. This process is computationally expensive, which, therefore, restricts the applicability range of the approximation to systems of moderate basis size. The TPP is a moderate- to strong-coupling approximaton, that becomes exact in the limit of low (large) density. It, thus, performes best away from half-filling.
– The particle–hole T-matrix approximation (TPH)
  The TPH selfenergy sums up a series of particle–hole diagrams, which is of comparable numercial complexity as the TPP. It is specifically designed to describe systems around half-filling, i.e. where the particle and hole densities are close to each other. For these cases, it provides accurate results for moderate to strong interaction strengths. For the application to electronic Hubbard systems, the TPH will later be called electron–hole T-matrix approximation (TEH).

$$\Sigma\left(1,2\right)=\pm\mathrm{i}\hbar\delta\left(1,2\right)w\left(1,3\right)G\left(3,3^+\right)$$
$$+\mathrm{i}\hbar W\left(1,3\right)G\left(1,4\right)\Gamma\left(4,2,3\right)$$

(107)

$$W\left(1,2\right)=w\left(1,2\right)$$
$$+w\left(1,3\right)P\left(3,4\right)W\left(4,2\right)$$

(108)

$$P\left(1,2\right)=\pm\mathrm{i}\hbar G\left(1,3\right)G\left(4,1\right)\Gamma\left(3,4,2\right)$$

(109)
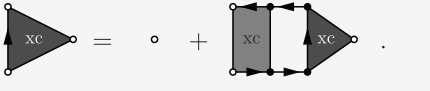
$$\Gamma\left(1,2,3\right)=\delta\left(1,2^+\right)\delta\left(3,2\right)$$
$$+\frac{\delta\Sigma^{\mathrm{xc}}\left(1,2\right)}{\delta G\left(4,5\right)}G\left(4,6\right)G\left(7,5\right)\Gamma\left(6,7,3\right)$$

(110)

Table 1. Main selfenergy approximations, abbreviations and section where the approximation is being introduced and discussed.

Abbreviation	Selfenergy	
HF	Hartree–Fock approximation: $\Sigma = \Sigma^{\mathrm{H}} + \Sigma^{\mathrm{F}}$	Section 4.1
SOA	Second-order approximation: $\Sigma = \Sigma^{(2)}$	Section 4.2
TOA	Third-order approximation: $\Sigma = \Sigma^{(3)}$	Section 4.3
GWA	GW approximation: $\Sigma = \Sigma^{GW}$	Section 5.2
TPP	Particle–particle T-matrix approximation: $\Sigma = \Sigma^{T^{\mathrm{pp}}}$	Section 5.3
TPH	Particle–hole T-matrix approximation: $\Sigma = \Sigma^{T^{\mathrm{ph}}}$	Section 5.3
FLEX	Fluctuating-exchange approximation: $\Sigma = \Sigma^{\mathrm{FLEX}}$	Section 5.5

For approach (II.) that starts with the screened interaction, equation (101), we will consider:

– The Hartree–Fock (HF) approximation
The HF selfenergy results from a perturbative expansion up to first order in the interaction. It is equivalent to a description on the mean-field level. Due to its simplicity, it is numerically easy to use and applicable to large systems and long simulation times. However, it only gives accurate results in the weak-coupling regime.
– The second-order (Born) approximation (SOA)
The SOA selfenergy consists of all diagrams up to second order in the interaction. It provides the easiest way to include correlation effects in a NEGF calculation. Due to its basic structure, the combination with the GKBA (see section 2.10) leads to a favorable numerical scaling, which opens its applicability to a wide range of systems. The SOA gives accurate results for weak to moderate coupling strengths.
– The third-order approximation (TOA)
The TOA selfenergy combines all possible selfenergy contributions up to third order in the interaction. It is much more involved than the SOA rendering the simulations numerically costly. Thus, the applicability range of the TOA is restricted to problems with a moderate basis size. In return, the TOA remains accurate even in the regime of moderate to strong coupling.
– The GW approximation (GWA)
The GW selfenergy provides the easiest way to describe dynamical-screening effects by summing up the polarization-bubble diagram series. The resummation process is computationally demanding which narrows the class of the systems that can be treated, although there are some scaling advantages for problems that require a diagonal (i.e. with a two-index interaction matrix, see equation (22)) basis set. The GWA can be considered a moderate-to strong-coupling approximation, which is particularly accurate around half filling, where the contributions of particles and holes coincide.

Finally, a combination of some of the above results leads to:

– The fluctuating-exchange approximation (FLEX)
The FLEX selfenergy merges the diagram series of the TPP, the TPH and the GWA. It, therefore, has the highest computational demands of the presented selfenergy approximations. By combining the advantages of its ingredients, it is applicable for all filling factors and up to strong interaction strengths.

An overview of the selfenergies and the abbreviations that are being used is given in table 1. The respective applicability ranges are schematically illustrated in figure 4. The shown results are motivated from experience with lattice calculations but are expected to be qualitatively valid also in a more general context. The illustration demonstrates a fundamental difference between perturbative approximations (HF, SOA, TOA) on the one hand and partial diagram summations (GW, TPP, TEH), on the other. While the former are not intrinsically density dependent, the latter show (by construction) very specific application scopes with respect to the filling. FLEX is not shown but should be qualitatively equivalent to the unification of GWA/TEH/TPP. It has not yet been tested extensively and is, therefore, skipped here. The detailed derivation of the selfenergy expressions will be given later in sections 4 and 5. A thorough comparison of the respective performance of the presented selfenergy approximations is given in section 3.

2.10. The generalized Kadanoff–Baym Ansatz

To compute the time-dependent single-particle Green functions, either the KBE, see equations (66) and (67), or the Dyson equation, see equation (91) have to be solved, which both scale cubically with respect to the time duration. An approximate way to transform the scaling to a quadratic one, has been proposed by Lipavský *et al* and was named *generalized Kadanoff–Baym ansatz* (GKBA), for details about the derivation see [133] by Lipavský *et al* and [125, 127, 128, 134]. The approximation starts from an exact reformulation of the Dyson equation, the '<' component of which reads

$$G_{ij}^{<}\left(t_1, t_2\right) = -\mathrm{i}\hbar \sum_k G_{ik}^{\mathcal{R}}\left(t_1, t_2\right) G_{kj}^{<}\left(t_2, t_2\right) \tag{111}$$

$$+ \int_{t_2}^{t_1} \mathrm{d}t_3 \int_{t_0}^{t_2} \mathrm{d}t_4 \sum_{kl} G_{ik}^{\mathcal{R}}\left(t_1, t_3\right) \Sigma_{kl}^{<}\left(t_3, t_4\right) G_{lj}^{\mathcal{A}}\left(t_4, t_2\right)$$

$$+ \int_{t_2}^{t_1} \mathrm{d}t_3 \int_{t_0}^{t_2} \mathrm{d}t_4 \sum_{kl} G_{ik}^{\mathcal{R}}\left(t_1, t_3\right) \Sigma_{kl}^{\mathcal{R}}\left(t_3, t_4\right) G_{lj}^{<}\left(t_4, t_2\right)$$

$$+ \mathrm{i}\hbar \sum_k G_{ik}^{<}\left(t_1, t_1\right) G_{kj}^{\mathcal{A}}\left(t_1, t_2\right)$$

$$- \int_{t_0}^{t_1} \mathrm{d}t_3 \int_{t_1}^{t_2} \mathrm{d}t_4 \sum_{kl} G_{ik}^{\mathcal{R}}\left(t_1, t_3\right) \Sigma_{kl}^{<}\left(t_3, t_4\right) G_{lj}^{\mathcal{A}}\left(t_4, t_2\right)$$

$$- \int_{t_0}^{t_1} \mathrm{d}t_3 \int_{t_1}^{t_2} \mathrm{d}t_4 \sum_{kl} G_{ik}^{<}\left(t_1, t_3\right) \Sigma_{kl}^{\mathcal{A}}\left(t_3, t_4\right) G_{lj}^{\mathcal{A}}\left(t_4, t_2\right),$$
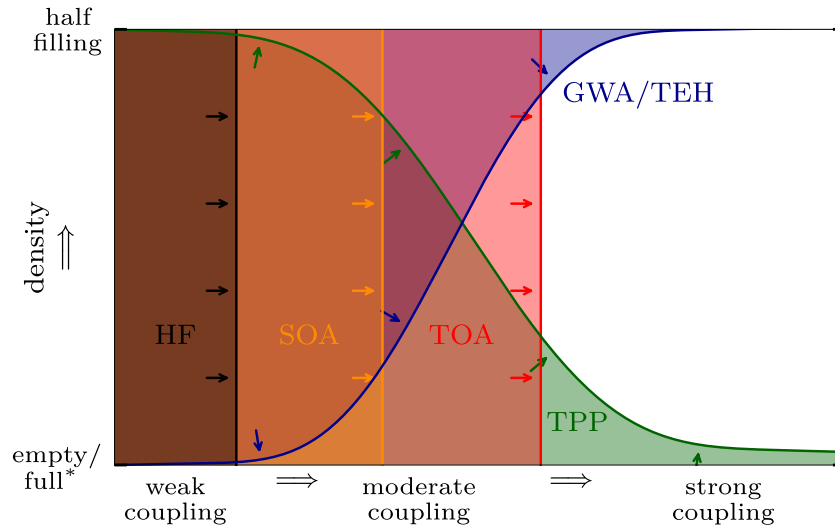
Figure 4. Illustration of the applicability ranges of the considered selfenergy approximations. The colored areas schematically demonstrate the parameter ranges—with respect to the density and the interaction strength—where the respective approximations give reliable results. *The empty–full symmetry is a property of the Hubbard model.

and analogously for the '>' component. The GKBA approximates these terms by only retaining the non-integral contributions, which can be considered a simultaneous perturbative expansion of G with respect to Σ and to the spectral structure conveyed by the off-diagonal elements of both quantities. It reads,

$$G_{ij}^{\gtrless}\left(t_1,t_2\right) = -\mathrm{i}\hbar \sum_k \left\{ G_{ik}^{\mathcal{R}}\left(t_1,t_2\right) G_{kj}^{\gtrless}\left(t_2,t_2\right) + G_{ik}^{\gtrless}\left(t_1,t_1\right) G_{kj}^{\mathcal{A}}\left(t_1,t_2\right) \right\}$$
$$= \sum_k A_{ik}\left(t_1,t_2\right) \left\{ \Theta\left(t_1,t_2\right) G_{kj}^{\gtrless}\left(t_2,t_2\right) + \Theta\left(t_2,t_1\right) G_{kj}^{\gtrless}\left(t_1,t_1\right) \right\},$$
$$(112)$$

where, in the second line, the spectral function

$$A_{ij}\left(t_1,t_2\right) = \mathrm{i}\hbar \left\{ G_{ij}^{>}\left(t_1,t_2\right) - G_{ij}^{<}\left(t_1,t_2\right) \right\}, \quad (113)$$

has been introduced. The approximated '$\gtrless$' components are used in the right-hand sides of the KBE which, thereby, need to be propagated only along the time diagonal. To achieve the overall reduction to a quadratic scaling, though, the GKBA has to be accompanied by a second-order selfenergy and another approximation concerning the retarded and advanced components, which, unapproximated, obey equations of similar complexity as the original KBE, i.e. with cubic scaling. In this work, the propagators, and with that the spectral function, will be approximated on the HF level. Another possibility, employed in [135], is to use approximate correlated propagators. The GKBA has several important benefits: It preserves the causal structure of the KBE and it conserves important constants of motion, whenever the chosen selfenergy approximation does [98]. Further, it cures certain damping-induced artifacts for small systems [77, 122], an example of which will be further explored in section 3.4. For a recent discussion, see [27].

2.11. Interacting initial state

To compute the time evolution of the single-particle Green function according to equations (66) and (67), the initial state represented by $G\left(t_0,t_0\right)$ has to be calculated. It is determined by the environment of the system. If the system is isolated, i.e. is described by a pure state, $G\left(t_0,t_0\right)$ is the fully interacting initial state. For a system embedded into a bath with which it exchanges particles or energy, the initial state is strongly influenced by the equilibrium between degrees of freedom of the system and the bath. Under the assumption that the interaction between both is weak and dominantly uncorrelated a suitable ensemble, for instance the canonical or grand-canonical ensemble, determines the occupation of the energy levels in the initial state of the system. For both cases of systems, whether connected to a bath or isolated, there exist several methodologies to generate the interacting initial state, some of which will be detailed in the next sections including the method of adiabatic switch-on of the interaction in section 2.11.2, which is used throughout this work.

2.11.1. Extension of the contour to finite temperatures. One possibility to include the description of the interacting initial state, in equilibrium with a bath or isolated, is to augment the original contour, comprised of a forward and a backward branch $\mathcal{C}^+$, $\mathcal{C}^-$, by a 'vertical' branch $\mathcal{C}^{\mathrm{M}}$ of complex time arguments ranging along the imaginary axis from z_0 to $z_0 - \mathrm{i}\hbar\beta$. Here β is the inverse temperature of the bath (or equal to ∞ for an isolated system at zero temperature). The reasoning behind this can be understood by considering the following observations for quantum systems in contact with an environment. The simplest way to treat the interaction of the system with the environment is statistically, i.e. by assigning bath-induced weights w_n (i.e. probabilities, with $0 \leqslant w_n \leqslant 1$ and $\sum_n w_n = 1$) of finding the system in one of its eigenstates $|n\rangle$. With this, the ensemble average of an observable $\hat{O}\left(t_0\right)$ in such a mixed state is defined as

$$O(t_0) = \sum_n w_n \left\langle n \middle| \hat{O}\left(t_0\right) \middle| n \right\rangle. \quad (114)$$
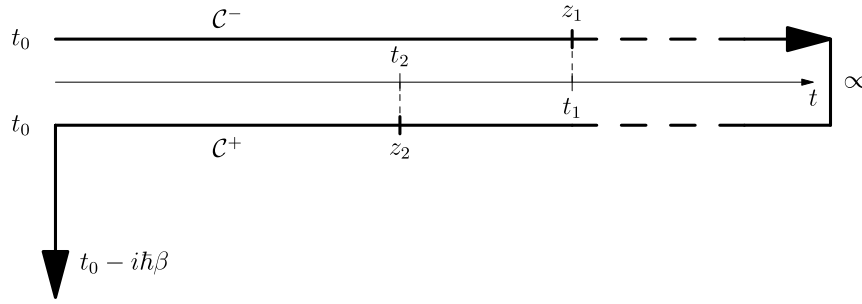
Figure 5. Schwinger–Keldysh contour $\mathcal{C}$ extended to the imaginary axis. The forward-branch $\mathcal{C}^-$ spans from the initial time t_0 to ∞, bends and leads back to t_0 along the backward $\mathcal{C}^+$-branch. Then it continues along the imaginary branch $\mathcal{C}^{\mathrm{M}}$ to $t_0 - \mathrm{i}\hbar\beta$, where β is the inverse temperature.

Note that equation (114) is a natural generalization of a pure state $|n\rangle = |\Psi_k\rangle$, to which it reduces if $w_n = \delta_{k,n}$. With equation (114), the statistical density-matrix operator $\hat{\rho}$ can be defined[13],

$$\hat{\rho} = \sum_n w_n |n\rangle\langle n|, \qquad (115)$$

with which equation (114) can be rewritten as

$$O(t_0) = \mathrm{Tr}\left[\hat{\rho}\hat{O}\left(t_0\right)\right]. \qquad (116)$$

The trace Tr is to be understood as acting on the full Fock space $\mathcal{F}_\sigma^{\mathcal{H}}$. For the grand-canonical ensemble (GCE), which describes a system which exchanges energy (characterized by inverse temperature β) and particles (characterized by the chemical potential μ) with its environment, the density-matrix operator $\hat{\rho}$ reads

$$\hat{\rho} = \frac{\exp\left(-\beta\hat{H}_{\mathrm{M}}\right)}{Z^{\mathrm{GCE}}}, \qquad (117)$$

with the corresponding Hamiltonian, $\hat{H}_{\mathrm{M}} = \hat{H} - \mu\hat{N}$, and the partition function $Z^{\mathrm{GCE}} = \mathrm{Tr}\left[\exp\left(-\beta\hat{H}_{\mathrm{M}}\right)\right]$. For the GCE, equation (116) becomes

$$O(t_0) = \frac{\mathrm{Tr}\left[\exp\left(-\beta\hat{H}_{\mathrm{M}}\right)\hat{O}\left(t_0\right)\right]}{Z^{\mathrm{GCE}}}. \qquad (118)$$

With this result, equation (44) can be specialized to

$$O(z) = \frac{\mathrm{Tr}\left[\exp\left(-\beta\hat{H}_{\mathrm{M}}\right)\hat{\mathcal{T}}_\mathcal{C}\left\{\exp\left(\frac{1}{\mathrm{i}\hbar}\int_\mathcal{C}\mathrm{d}z_3\,\hat{H}\left(z_3\right)\hat{O}\left(z\right)\right)\right\}\right]}{\mathrm{Tr}\left[\exp\left(-\beta\hat{H}_{\mathrm{M}}\right)\right]}. \qquad (119)$$

Using

$$\hat{\mathcal{T}}_\mathcal{C}\left\{\exp\left(\frac{1}{\mathrm{i}\hbar}\int_\mathcal{C}\mathrm{d}z_3\,\hat{H}\left(z_3\right)\right)\right\} = \hat{1}, \qquad (120)$$

and introducing the vertical part of the contour $\mathcal{C}^{\mathrm{M}}$ running from z_0 to $z_0 - \mathrm{i}\hbar\beta$ with the identity

$$\exp\left(-\beta\hat{H}_{\mathrm{M}}\right) = \exp\left(-\frac{\mathrm{i}}{\hbar}\int_{\mathcal{C}^{\mathrm{M}}}\mathrm{d}z_3\,\hat{H}_{\mathrm{M}}\right), \qquad (121)$$

we arrive at

$$O(z)$$
$$= \frac{\mathrm{Tr}[\exp\left(-\frac{\mathrm{i}}{\hbar}\int_{\mathcal{C}^{\mathrm{M}}}\mathrm{d}z_3\,\hat{H}_{\mathrm{M}}\right)\hat{\mathcal{T}}_\mathcal{C}\left\{\exp\left(-\frac{\mathrm{i}}{\hbar}\int_\mathcal{C}\mathrm{d}z_3\,\hat{H}\left(z_3\right)\right)\hat{O}\left(z\right)\right\}]}{\mathrm{Tr}[\exp\left(-\frac{\mathrm{i}}{\hbar}\int_{\mathcal{C}^{\mathrm{M}}}\mathrm{d}z_3\,\hat{H}_{\mathrm{M}}\right)\hat{\mathcal{T}}_\mathcal{C}\left\{\exp\left(-\frac{\mathrm{i}}{\hbar}\int_\mathcal{C}\mathrm{d}z_3\,\hat{H}\left(z_3\right)\right)\right\}]}. \qquad (122)$$

From this structure, the contour extension idea can be directly derived. If one defines

$$\hat{H}\big|_{\mathcal{C}^{\mathrm{M}}} \equiv \hat{H}_{\mathrm{M}}, \quad \hat{O}\big|_{\mathcal{C}^{\mathrm{M}}} \equiv \hat{O}\left(t_0\right) \qquad (123)$$

and redefines the contour $\mathcal{C}$ as

$$\mathcal{C} = \mathcal{C}^- \bigoplus \mathcal{C}^+ \bigoplus \mathcal{C}^{\mathrm{M}}, \qquad (124)$$

so that every point on the vertical track is defined as 'later' than all points on the forward and backward branches, equation (122) can be recast as

$$O(z) = \frac{\mathrm{Tr}\left[\hat{\mathcal{T}}_\mathcal{C}\left\{\exp\left(-\frac{\mathrm{i}}{\hbar}\int_\mathcal{C}\mathrm{d}z_3\,\hat{H}\left(z_3\right)\right)\hat{O}\left(z\right)\right\}\right]}{\mathrm{Tr}\left[\hat{\mathcal{T}}_\mathcal{C}\left\{\exp\left(-\frac{\mathrm{i}}{\hbar}\int_\mathcal{C}\mathrm{d}z_3\,\hat{H}\left(z_3\right)\right)\right\}\right]}. \qquad (125)$$

The corresponding contour is depicted in figure 5. With this, definition (125) correctly reproduces the time-dependent expectation values in accordance with equation (44) for $z \in \mathcal{C}^- \bigoplus \mathcal{C}^+$ and the ensemble average for $z \in \mathcal{C}^{\mathrm{M}}$, agreeing with equation (118). Note though that this treatment of the system-bath interaction is only valid for times smaller than its relaxation time as the bath only directly influences the initial state and not any time-dependent excitations during the propagation [73].

2.11.2. Adiabatic switch-on of interactions. If one is mainly interested in the evolution of isolated systems

---

[13] The concept of the density operator was introduced by Landau and von Neumann. For a general nonequilibrium approach, see [136].
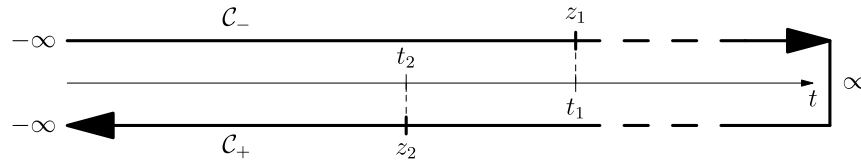
Figure 6. Schwinger–Keldysh contour $\mathcal{C}^{\mathrm{AS}}$ with adiabatic switch-on of the interactions. The starting and end point is now $-\infty$.

described by a pure state, a suitable procedure is the generation of the non-interacting state of the system, which is known for most systems and a subsequent sufficiently slow ramp-up of the interaction strength from zero to the desired value. Provided the *Gell-Mann–Low theorem* holds [137], which assures the existence of some limites, and the non-interacting ground state is non-degenerate, it follows that the state of the system after switch-on of the interaction is an eigenstate of the fully interacting Hamiltonian. It remains to be checked—e.g. by comparison with other methods—that it is the ground state. Under the adiabatic-switching protocol, the Hamiltonian of equation (16) is replaced by

$$\hat{H}^{\mathrm{AS}}\left(t\right) = \underbrace{\sum_{mn} h_{mn}\hat{c}_m^\dagger \hat{c}_n}_{\hat{H}^0} + \underbrace{\frac{1}{2} f^{\mathrm{AS}}\left(t\right) \sum_{mnpq} w_{mnpq}\, \hat{c}_m^\dagger \hat{c}_n^\dagger \hat{c}_p \hat{c}_q}_{\hat{W}^{\mathrm{AS}}\left(t\right)}$$
$$+ \underbrace{\sum_{mn} f_{mn}\left(t\right)\hat{c}_m^\dagger \hat{c}_n}_{\hat{F}\left(t\right)}, \qquad (126)$$

where the monotonically increasing switching function $f^{\mathrm{AS}} : \mathbb{R} \longrightarrow [0,1]$ satisfies

$$\lim_{t \to -\infty} f^{\mathrm{AS}}\left(t\right) = 0, \quad f^{\mathrm{AS}}\left(t\right) = 1, \quad \text{for } t \geqslant t_0. \quad (127)$$

To achieve a high fidelity of the final state the switch-on process has to be performed slow enough and as smooth as possible. Here, the use of the function [138]

$$f_{\mathrm{AS}}^{\tau, t_{\mathrm{H}}}\left(t\right) = \exp\left(-\frac{A_{t_{\mathrm{H}}}^\tau}{t/\left(2t_{\mathrm{H}}\right)} \exp\left(\frac{B_{t_{\mathrm{H}}}^\tau}{t/\left(2t_{\mathrm{H}}\right) - 1}\right)\right),$$
$$B_{t_{\mathrm{H}}}^\tau = \frac{t_{\mathrm{H}}}{\tau \ln 2} - \frac{1}{2}, \qquad A_{t_{\mathrm{H}}}^\tau = \frac{\ln 2}{2}\exp\left(2B_{t_{\mathrm{H}}}^\tau\right), \quad (128)$$

is superior compared to an approach based on a Fermi function, since it provides a very small relative change for values near the beginning and the end of the switch-on process. The free parameters τ and t_{H}, the halftime (chosen as $t_{\mathrm{H}} = t_0/2$ for $t \in \left[0, t_0\right]$), control the steepness and the duration of the switch-on. Using the adiabatic-switching methodology, the time-contour attains the form depicted in figure 6.

A third option to include initial correlation is via an additional collision integral or selfenergy term [27, 136, 139, 140]. For completeness, we also mention that similar problems arise by use of the GKBA [136].

3. Applications: numerical results for fermionic lattice systems

This section discusses some applications of the approximation strategies detailed in the previous section. All simulations described in this section have been performed for spin-1/2 fermions in the Hubbard model, see section 2.3, for zero temperature. After providing an overview of the algorithm for the numerical solution of the KBE in section 3.1, results for the correlated ground state of Hubbard nano-clusters are presented in section 3.3. The ground-state energy and spectral function are used as benchmarks to compare the performance of the selfenergy approximations listed in section 2.9 for different filling factors and interaction strengths. Subsequently, in section 3.4, the behavior of the approximation strategies in the simulation of the time-dependent response of Hubbard clusters to external excitations is studied. A special focus lies on excitations that strongly drive the system out of equilibrium. There, the occurrence of a particular weakness of selfconsistent approaches, the so-called correlation-induced damping [122], is analyzed for all approximations and it is demonstrated how it can be overcome to a large extent by application of the GKBA, in section 3.4.

3.1. Algorithm for the solution of the Keldysh–Kadanoff–Baym equations (KBE)

This section gives an overview of the algorithm to calculate the solution of the KBE, see equations (89) and (90), for spin-1/2 fermions. Both equations need to be equipped with the initial value $G^{\gtrless}\left(t_0, t_0\right)$, which are the Green functions of the—in general, correlated—initial state. These Green functions are, in turn, generated from the ones of the ideal ground state, $G^{(0),\gtrless}$, via the *adiabatic-switching method* described in section 2.11.2. The '$\gtrless$' components of the ideal Green function directly follow from the ideal one-particle density matrix $n^{(0)}$ via the relations

$$G_{ij}^{(0),<} = -\frac{1}{i\hbar} n_{ji}^{(0)}, \qquad (129)$$

$$G_{ij}^{(0),>} = \frac{1}{i\hbar}\left(\delta_{ij} - n_{ji}^{(0)}\right), \qquad (130)$$

where the second follows from the more general relation for an arbitrary time t,

$$G_{ij}^{>}\left(t, t\right) = \frac{1}{i\hbar}\delta_{ij} + G_{ij}^{<}\left(t, t\right). \qquad (131)$$

Since, here, only zero-temperature applications are considered, the ideal fermionic density matrix can be found by

diagonalization of the single-particle part of the Hamiltonian, $\hat{H}^0$, see equation (16). The density matrix $n^{\hat{H}^0}$ in the eigenbasis of $\hat{H}^0$ is diagonal and, for N particles, reads (sorted by the eigenvalues, starting from the smallest one)

$$n_{ij}^{\hat{H}^0} = \delta_{ij} \begin{cases} 1, & \text{if } i \leqslant N \\ 0, & \text{else} \end{cases}. \qquad (132)$$

After transformation into the Hubbard basis, this yields the ideal density matrix $n_{ji}^{(0)}$ and, via equations (129) and (130), the components of the ideal Green function. Using $G_{ij}^{(0),\gtrless}$ as initial values, following equation (126), the KBE are propagated along both time-directions simultaneously switching on the interaction with the switching function, see equation (128), i.e. the solutions of

$$\sum_l \left[\mathrm{i}\hbar \frac{\mathrm{d}}{\mathrm{d}t_1} \delta_{il} - h_{il}(t_1) \right] G_{lj}^{\gtrless}(t_1, t_2) \qquad (133)$$

$$= \sum_l \int_{t_s}^{t_1} \mathrm{d}t_3 \left[\Sigma_{il}^{>}(t_1, t_3) - \Sigma_{il}^{<}(t_1, t_3) \right] G_{lj}^{\gtrless}(\bar{t}, t')$$

$$+ \sum_l \int_{t_s}^{t_2} \mathrm{d}t_3 \, \Sigma_{il}^{\gtrless}(t_1, t_3) \left[G_{lj}^{<}(\bar{t}, t') - G_{lj}^{>}(\bar{t}, t') \right],$$

and

$$\sum_l G_{il}^{\gtrless}(t_1, t_2) \left[-\mathrm{i}\hbar \frac{\overleftarrow{\mathrm{d}}}{\mathrm{d}t_2} \delta_{lj} - h_{lj}(t_2) \right] \qquad (134)$$

$$= \sum_l \int_{t_s}^{t_1} \mathrm{d}t_3 \left[G_{il}^{>}(t_1, t_3) - G_{il}^{<}(t_1, t_3) \right] \Sigma_{lj}^{\gtrless}(t_3, t_2)$$

$$+ \sum_l \int_{t_s}^{t_2} \mathrm{d}t_3 \, G_{il}^{\gtrless}(t_1, t_3) \left[\Sigma_{lj}^{<}(t_3, t_2) - \Sigma_{lj}^{>}(t_3, t_2) \right],$$

for all values $t_1, t_2 \in \left[t_s, t_0 \right]$, are computed, where t_s is the starting time of the adiabatic switching. The interaction matrix in the selfenergy terms for the chosen approximation, on the right-hand sides are replaced by (see sections 4 and 5)

$$w_{ijkl} \longrightarrow f_{\mathrm{AS}}^{\tau, t_{\mathrm{H}}}(t) w_{ijkl}, \qquad (135)$$

where the switching parameters t_{H} and τ are chosen such that the resulting state is converged with respect to the relevant observables. In practice, values of $\tau = 19.0 \, J^{-1}$ and $t_{\mathrm{H}} = 25.0 \, J^{-1}$ have been found sufficient for all calculations. After the switching is completed, the system is in the correlated ground state[14] described by $G^{\gtrless}(t_0, t_0)$. The information about the correlations in the system is encoded in the values of the Green functions for all time-points during the switching. That is why all integrals occurring in the solution of the KBE for physically relevant times have to extend along the whole

[14] As already pointed out in section 2.11.2, it has to be checked externally, e.g. by comparison with other methods, that the final state of the adiabatic switching is indeed the ground state.

time-plane including the adiabatic-switching part, i.e. equations (133) and (134) have to be used also for $t_1, t_2 > t_0$. It has to be noted that any time-dependent excitation of the system has to occur after the switching is finished and that the values of G with at least one argument in the switching region cannot be used for the determination of observables, as detailed in section 3.2.

For the numerical solution of the KBE, standard approaches for the solution of ordinary differential equations (ODEs), such as Runge–Kutta methods [141], can be employed upon appropriately discretizing the two-time plane. Thereto, a time-stepping scheme has to be used to propagate the Green function starting from $G^{\gtrless}(t_0, t_0)$ along both time directions in the two-time plane and along the time diagonal (for more details, see, e.g. [70, 78]). Further, an integration routine for the right-hand sides of equations (133) and (134) is required. Here, the approach detailed in [78] has been employed for all calculations. As a general note, the use of higher-order methods for the solution of the ODEs and the integrals, i.e. methods where the error scales with a high power of the time step such that time steps of the order of $10^{-2} J^{-1}$–$10^{-1} J^{-1}$ are possible, is especially advisable to achieve performance and accuracy, since the right-hand sides of the KBE are numerically very expensive. The accuracy of the simulations can be monitored by verifying the conservation laws, in particular of the density and total energy [142] and time-reversibility [80]. Needless to say, these accuracy tests are compulsory to ensure the generation of reasonable and physical results; the numerical behavior that follows from a violation of these laws can easily get uncontrolled and strongly depends on the choice of the numerical methods [142]. More details to a proper numerical treatment in the context of nonequilibrium Green functions are given, e.g. in [74, 78, 136, 143].

During the evaluation of the selfenergy, for the resummation approaches presented in section 2.9, one has to face a specific type of equations—namely, the Volterra equations of the second kind. In the case of the GW approximation, one has the Dyson-type equation for the screened interaction (see equations (102)–(104)), whereas for the T-matrix approximations, one gets the respective Lippmann–Schwinger equations (see equations (345) and (383)). There are two general procedures to solve these equations. We demonstrate both on the example of the screened interaction. From equation (309) (advanced components for spin-0 bosons) one gets

$$W_{ij}^{\mathrm{ns,b},0,\mathcal{A}}(t_1, t_2) = \Phi_{ij}^{GW,\mathrm{b},0,\mathcal{A}}(t_1, t_2)$$

$$+ U(t_1) \int_{t_1}^{t_2} \mathrm{d}t_3 \sum_p G_{ipip}^{\mathrm{F},\mathcal{A}}(t_1, t_3) W_{pj}^{\mathrm{ns,b},0,\mathcal{A}}(t_3, t_2).$$

For the first procedure, the equation is solved by *iteration*. For that, one uses Φ as a starting value for W by inserting it into the integral term to calculate a refined W (which can then be used as the next starting value). This procedure is repeated until the change $\left| W^{(n)} - W^{(n-1)} \right|$ (with the number of iterations n) falls below a chosen threshold and W can be considered to be converged. This algorithm is explained in more detail, e.g. in

[78] for the particle–particle T matrix. The second procedure to solve the equation is done via *inversion*. After applying the inverse Fock Green function from the left and some resorting of terms, the equation takes the following form,

$$W_{ij}^{\text{ns,b,0},\mathcal{A}}\left(t_1, t_2\right) = \left\{ \left[\left(G^{\text{F},\mathcal{A}}\right)^{-1} - U\left(t_1\right) \right]^{-1} \right\}_{ij} \left(t_1, t_2\right) \times U\left(t_1\right) U\left(t_2\right).$$

With that, there is no longer a time integration or an index sum to be done, but, instead, two numerical inversions on the full two-time plane have to be calculated. More details to the inversion scheme for time-dependent Green functions can be found, e.g. in [144]. Both procedures have upsides and drawbacks. For the iteration scheme, it can become increasingly numerically tough to achieve convergence during the propagation, while for the inversion scheme, the computations on the two-time plane can become very resource-demanding. For most results in this paper, the iteration procedure is used.

It should be mentioned that, instead of using the KBE, the numerical solution of the Dyson equation (equation (91)) gives an equivalent way to propagate the Green functions. This can also be achieved either via iteration or inversion (see, e.g. [144] for details).

3.2. Important time-dependent observables

This section briefly describes how important physical observables can be obtained from the time-dependent Green functions and additionally from the right-hand sides of the KBE, see equations (133) and (134), the so-called collision integrals. As detailed in the equation (129), the '$<$' component of the Green function of the interacting ground state is directly linked to the density matrix. This relation also holds true for the time-dependent density matrix $n_{ij}\left(t\right)$, which describes the single-particle response of the system subject to a time-dependent excitation, reading

$$G_{ij}^{<}\left(t, t\right) = -\frac{1}{i\hbar} n_{ji}\left(t\right). \tag{136}$$

Apart from the time-dependent occupations of the Hubbard sites, which are given by the diagonal elements of the time-dependent density matrix, the latter also permits the calculation of several energy contributions:

– the kinetic energy,

$$E_{\text{kin}}\left(t\right) = \text{Re}\left(\sum_{mn} h_{mn} n_{nm}\left(t\right)\right), \tag{137}$$

– the energy induced by a time-dependent excitation $f_{mn}\left(t\right)$,

$$E_{\text{ex}}\left(t\right) = \text{Re}\left(\sum_{mn} f_{mn}\left(t\right) n_{nm}\left(t\right)\right). \tag{138}$$

– The mean interaction energy is also available. Its calculation requires knowledge of the two-particle Green function and is given by (with contour times)

$$E_{\text{int}}\left(z_1\right) = \pm i\hbar \sum_{klmn} w_{klnm}\left(z_1\right) G_{mnkl}^{(2)}\left(z_1, z_1, z_{1+}, z_{1+}\right)$$

$$= \sum_{kl} \int_{\mathcal{C}} \text{d}z_3 \, \Sigma_{kl}\left(z_1, z_3\right) G_{lk}\left(z_3, z_1\right).$$

It is, thus, the trace over the time-diagonal contribution of the collision integral. The real-time expression for the interaction energy can then be found by performing the trace over the right-hand side of equation (89) and includes—in contrast to equations (137) and (138)—the full two-time Green functions,

$$E_{\text{int}}\left(t\right) = -\frac{i\hbar}{2} \sum_{kl} \int_{t_0}^{t} \text{d}\bar{t} \left[\Sigma_{kl}^{>}\left(t, \bar{t}\right) - \Sigma_{kl}^{<}\left(t, \bar{t}\right) \right] G_{lk}^{<}\left(\bar{t}, t\right) \tag{139}$$

$$- \frac{i\hbar}{2} \sum_{kl} \int_{t_0}^{t} \text{d}\bar{t} \, \Sigma_{kl}^{<}\left(t, \bar{t}\right) \left[G_{lk}^{<}\left(\bar{t}, t\right) - G_{lk}^{>}\left(\bar{t}, t\right) \right]$$

$$= -\frac{i\hbar}{2} \sum_{kl} \int_{t_0}^{t} \text{d}\bar{t} \left\{ \Sigma_{kl}^{>}\left(t, \bar{t}\right) G_{lk}^{<}\left(\bar{t}, t\right) - \Sigma_{kl}^{<}\left(t, \bar{t}\right) G_{lk}^{>}\left(\bar{t}, t\right) \right\}.$$

The possibility to compute the interaction energy (a two-particle quantity) from a single-particle function is a unique feature of the Green functions approach (in contrast, in reduced-density-operator theory this requires the two-particle density operator [136]).

The availability of information off the time diagonal in the one-particle Green function allows, furthermore, to gain insight into the $(N + 1)$- and $(N - 1)$ particle spaces by means of the single-particle spectral function, already encountered in equation (113). If an N-particle system is prepared in the ground state $|\Psi_0^{(N)}\rangle$ with energy $E_0^{(N)}$ (or any other N-particle energy eigenstate), e.g. via adiabatic switching, and afterwards propagated without additional excitations, the '$\gtrless$' components of the two-time Green functions obey

$$G_{ji}^{<}\left(t_1, t_2\right) = \mp i\hbar \sum_{m} Q_m(j) Q_m^*(i) \exp\left(\frac{1}{i\hbar} \left(E_m^{(N-1)} - E_0^{(N)} \right) \left(t_2 - t_1\right) \right), \tag{140}$$

$$G_{ji}^{>}\left(t_1, t_2\right) = i\hbar \sum_{m} P_m(j) P_m^*(i) \exp\left(\frac{1}{i\hbar} \left(E_m^{(N+1)} - E_0^{(N)} \right) \left(t_1 - t_2\right) \right), \tag{141}$$

where the amplitudes $Q_m(i)$, $P_m(i)$ are defined as

$$P_m(i) = \left\langle \Psi_0^{(N)} \middle| \hat{c}_i \middle| \Psi_m^{(N+1)} \right\rangle, \tag{142}$$

$$Q_m(i) = \left\langle \Psi_m^{(N-1)} \middle| \hat{c}_i \middle| \Psi_0^{(N)} \right\rangle. \tag{143}$$

They are the overlap matrix elements of the $(N - 1)$- and $(N + 1)$-particle states of energy E_m with the state which originates from removing/adding one particle in the ith basis state from/to the N-particle state. By Fourier transforming and via the knowledge of $E_0^{(N)}$, the $(N - 1)$- and $(N + 1)$-particle energies can be determined from the propagation of the two-time Green function of the N-particle system. In other words, the correlation function $G^{<}$ contains information about the occupied states of the N-particle system and the transition

energies to the $N − 1$-particle system. In contrast, $G^>$ contains information about the unoccupied states ('holes') of the N-particle system and the transition energies to the $N + 1$-particle system when one of the unoccupied states is being filled.

The combination of both functions directly yields the *spectral function*,

$$A_{ji}(t_1, t_2) = i\hbar \left\{ G_{ji}^> \left(t_1, t_2 \right) - G_{ji}^< \left(t_1, t_2 \right) \right\}. \quad (144)$$

Aside from the two-particle energy, see equation (139), the single-particle Green function gives also access to another two-particle quantity—the *local two-particle density*. Indeed, via the collision integral, the time-dependent double-occupations, $n_i^{(2)} \left(t \right) = \langle \hat{n}_{i\uparrow}(t)\hat{n}_{i\downarrow}(t) \rangle$, i.e. the probability that one electron with spin up and another with spin down simultaneously occupy the same spatial orbital on a Hubbard site 'i', can be computed as

$$n_i^{(2)} \left(t \right) = \frac{1}{2U} \sum_l \int_{t_0}^t d\bar{t} \left\{ \Sigma_{il}^> \left(t, \bar{t} \right) G_{li}^< \left(\bar{t}, t \right) - \Sigma_{il}^< \left(t, \bar{t} \right) G_{li}^> \left(\bar{t}, t \right) \right\}, \quad (145)$$

which becomes obvious when taking into account the relation between the selfenergy and the two-particle Green function, see equations (64) and (65). Further, the *two-particle local density correlation* (pair-correlation function) can be computed by subtracting the uncorrelated (mean-field) expression of the two-particle density which (for the Hubbard model) is nothing but the product of two single-particle densities,

$$\delta n_i^{(2)}(t) = n_i^{(2)}(t) - n_{i\uparrow}(t)n_{i\downarrow}(t). \quad (146)$$

This quantity is identical to zero if the system is uncorrelated and thus directly measures effects beyond Hartree–Fock. A quantity that also measures the space-resolved correlations in a many-body system is the local entanglement entropy [28],

$$S_i(t) = -2 \left(\frac{n_i}{2} - n_i^{(2)} \right) \log_2 \left(\frac{n_i}{2} - n_i^{(2)} \right) - n_i^{(2)} \log_2 n_i^{(2)}$$
$$- \left(1 - n_i + n_i^{(2)} \right) \log_2 \left(1 - n_i + n_i^{(2)} \right). \quad (147)$$

We now turn to a survey of recent computational results that were obtained with the involvement of (some of) the authors. Our focus is on comparison of different selfenergy approximations and on tests of their accuracy.

3.3. Numerical results for the correlated ground state

In this section, numerical results for the interacting ground-state energies are presented. As an example, we consider a six-site Hubbard model for which exact results can be obtained. Our main interest is to test the performance of the different selfenergy approximation schemes introduced in sections 4 and 5 with respect to filling level n (i.e. density) and interaction strength, U/J, of the system, by comparison with exact calculations.

Following the adiabatic-switching algorithm of section 2.11.2, the system is initially prepared in the non-interacting ground state for $N_\uparrow = N_\downarrow = 1, 2, 3$ particles,

i.e. filling levels $n = 1/6$, $n = 1/3$ and $n = 0.5$. Using the switching function (128) with parameters $\tau = 19.0 J^{-1}$ and $t_H = 25.0 J^{-1}$, ensuing, the interaction U is ramped up to the final values $U = 0.1, 0.5, 1.0$ and 2.0. In table 1, we list the selfenergy approximations that are being used and compared.

3.3.1. Results for the ground-state energy. We begin with a detailed analysis of the ground-state energy to understand the quality of the different selfenergy approximation, in dependence on the coupling strength and the filling. Starting with $U = 0.1J$, which is very close to an ideal system, the results for $N_\uparrow = N_\downarrow = 1, 2, 3$ are listed in the second columns of tables 2–4, respectively.

For all three filling factors, the Hartree results differ from the exact results in the third decimal place, while all methods beyond Hartree agree up to the fourth decimal place. This can be explained by the fact that the Hartree approximation is only correct up to the first order in the interaction strength, while all other methods agree up to the second order in the interaction with each other and the exact solution. For both smaller-than-half-filling factors, the results of the non-Hartree methods behave similarly. The best results, which agree up to at least 5 decimal places with the exact result, are achieved by the third-order and the FLEX approximations, which are both correct up the third order in the interaction strength.

On the other hand, when only one of the two third-order selfenergy contributions is included, the particle–particle and electron–hole T-matrix approximations (TPP, TEH), do not improve the result significantly compared to the second-order approximation (SOA) for $n = 1/3$, although, for $n = 1/6$, the particle–particle T matrix performs better than the electron–hole T matrix, since the latter contributes less as the electronic density is comparatively small. For $U = 0.1J$, the GW approximation shows no difference to the SOA results, since both approximations only differ in the fourth order, as the GWA has no third-order diagram, see equation (316). For half filling, $n = 0.5$, all correlated methods (i.e. all methods except Hartree), apart from the T matrices, agree with each other and with the exact solution up to 5 decimal places. This is explained by the so-called particle–hole symmetry in the Hubbard model [145], which only occurs at half filling. In this particular case there is an exact cancellation of all electron–hole and particle–particle T-matrix terms of odd orders in the interaction and equality of all even order terms. Therefore, for half filling, SOA and TOA yield exactly the same results and agree with GWA and FLEX up to the fourth order in the interaction.

For the increased but still small interaction strength $U = 0.5J$, the results for $N_\uparrow = N_\downarrow = 1, 2, 3 (n = 1/6, 1/3, 0.5)$ are shown in the third columns of tables 2–4, respectively. Here, the Hartree results differ from the exact result already in the second decimal place. In contrast, all correlated methods agree with the exact result in the second decimal place. Compared to the $U = 0.1J$ results, only the TOA remains close to the exact solution whereas all other methods show more pronounced deviations. For $n = 1/6$, FLEX and TPP yield comparably good results. Further, TEH is worse compared

Table 2. Ground-state energies, E_{gs}/J, for $N_s = 6$ sites and 1/6 filling, i.e. $N_\uparrow = N_\downarrow = 1$, for different couplings and for different selfenergy approximations. Approximations are ordered by E_{gs} for the smallest U. In each column, the two results that are closest to the exact one are typed bold.

Σ	$U/J = 0.1$	$U/J = 0.5$	$U/J = 1.0$	$U/J = 2.0$
H	−0.533 604	−0.449 56	−0.347 18	−0.149 39
TPP	**− 0.534 067**	−0.459 81	−0.382 91	−0.263 19
Exact	**− 0.534 073**	**− 0.460 65**	**− 0.388 10**	**− 0.288 20**
TOA	**− 0.534 075**	**− 0.460 48**	**− 0.385 45**	**− 0.267 38**
FLEX	−0.534 076	**− 0.461 29**	−0.396 85	−0.360 59
SOA	−0.534 084	−0.461 64	**− 0.394 72**	**− 0.325 14**
GWA	−0.534 084	−0.461 81	−0.397 23	−0.350 68
TEH	−0.534 093	−0.462 93	−0.405 35	−0.390 65

Table 3. Ground-state energies, E_{gs}/J, for $N_s = 6$ sites and 1/3 filling, i.e. $N_\uparrow = N_\downarrow = 2$, for different couplings and for different selfenergy approximations. Approximations are ordered by E_{gs} for the smallest U. In each column, the two results that are closest to the exact one are typed bold.

Σ	$U/J = 0.1$	$U/J = 0.5$	$U/J = 1.0$	$U/J = 2.0$
H	−2.642 487	−2.359 48	−2.009 67	−1.318 91
TPP	**− 2.643 354**	−2.379 63	−2.083 69	−1.573 67
Exact	**− 2.643 367**	**− 2.381 07**	**− 2.093 67**	**− 1.633 42**
TOA	**− 2.643 367**	**− 2.380 93**	**− 2.091 82**	**− 1.614 55**
FLEX	−2.643 368	**− 2.381 74**	−2.104 24	−1.761 67
SOA	−2.643 376	−2.382 08	**− 2.100 58**	**− 1.670 92**
GWA	−2.643 376	−2.382 26	−2.103 57	−1.713 03
TEH	−2.643 390	−2.384 00	−2.117 46	−1.803 34

to its particle–particle counterpart, and GWA is worse than the SOA. For $n = 1/3$, FLEX becomes better than TPP, showing the increasing importance of the third-order electron–hole contribution. For half filling, the GWA result is the closest to the exact solution, closely followed by the equal results of the SOA and TOA. This gives a first hint that, at $U = 0.5J$, the fourth- and possibly higher-order terms gain influence, although among the approximations containing fourth-order and higher terms, only the GWA gives improved energies compared to second-/third-order perturbative results.

For the higher interaction strengths $U/J = 1.0$ and $U/J = 2.0$, the results are shown in the fourth and fifth columns of tables 2–4, respectively. Compared to the results for $U = 0.5J$, the relative order of the performance of the different selfenergy approximations remains the same, but the absolute differences to the exact results increase. Summarizing the results for the ground-state energies, it is evident that, away from half filling, the TOA outperforms all other perturbative and non-perturbative selfenergy approximations, at least in the covered range of coupling parameters $U/J = 0.1 \ldots 2.0$. For half filling, on the other hand, the best results are obtained from the *GW* approximation.

3.3.2. Results for the spectral function in the ground state. Let us now consider another important quantity of the correlated ground state, which goes beyond the description of

Table 4. Ground-state energies, E_{gs}/J, for $N_s = 6$ sites, and half filling, i.e. $N_\uparrow = N_\downarrow = 3$, for different couplings and for different selfenergy approximations. Approximations are ordered by E_{gs} for the smallest U. In each column, the two results that are closest to the exact one are typed bold.

Σ	$U/J = 0.1$	$U/J = 0.5$	$U/J = 1.0$	$U/J = 2.0$
H	−6.837 918	−6.237 92	−5.487 91	−3.987 91
TPP	**− 6.839 299**	−6.269 49	−5.601 73	−4.368 96
Exact	**− 6.839 331**	**− 6.273 22**	−5.628 89	**− 4.546 31**
TOA	**− 6.839 331**	−6.272 85	−5.623 56	−4.485 69
SOA	−6.839 331	**− 6.272 85**	**− 5.623 56**	**− 4.485 69**
GWA	−6.839 331	**− 6.273 47**	**− 5.632 59**	**− 4.586 04**
FLEX	−6.839 334	−6.274 71	−5.649 23	−4.716 30
TEH	−6.839 363	−6.277 41	−5.661 04	−4.735 47

the lowest energy level: the single-particle spectral function, that was introduced in section 3.2. For an N-particle system, it shows the transition energies into the $(N − 1)$-particle as well as the $(N + 1)$-particle system, i.e. the single-particle removal and addition energies. The removal energies are carried by the off-timediagonal values of $G^<$, while the addition energies are similarly encoded in $G^>$. They can be made visible by transforming into relative and center-of-mass time and, afterwards, Fourier transforming with respect to the relative time. Comparing with equations (140) and (141), one expects peaks at the energy levels of $(N \pm 1)$-particle systems shifted by the ground-state energy of the N-particle system.

For the six-site Hubbard system of interaction strength $U = 1J$, the performance of the different selfenergy approximations is studied for the three filling factors $n = 1/6, 1/3$ and $1/2$. The results are compared with exact excitation spectra of the relevant $(N \pm 1)$-particle systems, which in turn are generated by excitation with a δ-kick and subsequent Fourier transform of the time-dependent density evolution.

For $n = 1/6$, the results are shown in figure 7. The frequency axis of the spectrum is shifted such that all removal energies, corresponding to $G^<$, have negative values while the addition energies, corresponding to $G^>$, have positive energies. Since the spectrum of the $(N − 1)$-particle system only contains one spin-up or spin-down particle[15] it has no interaction effects and, thus, is ideal. This corresponds to the '<'-part of the spectrum having only one spectral line which matches the exact result (blue line) for every approximation including Hartree(–Fock). Analyzing the '>' part of the spectrum which belongs to the system with two particles of one spin-direction and one particle of the other, one can separate two sets of spectral lines. The three spectral lines belonging to the lowest addition energies are in exact agreement throughout all approximations including Hartree and, thus, indicate mostly uncorrelated states. The position of the peak for the next higher addition energy begins to differ between the approximations. The best agreement with the exact solution is reached by the

---

[15] As the fermionic Hubbard Hamiltonian contains no terms which are different for up or down spin-orientation, a system with N spin-up and M spin-down particles behaves like the system with M spin-up particles and N spin-down particles.

Figure 7. Six-site Hubbard cluster with $U = J$ at one-sixth filling. Spectral function generated from different selfenergy approximations: brown full line: third-order approximation (TOA), crimson dashed line: second-order approximation (SOA), green dashed line: particle–particle T matrix (TPP), yellow dashed line: electron–hole T matrix (TEH), blue dashed line: GW approximation (GWA), purple semi-dashed line: fluctuating-exchange approximation (FLEX), gray full line: Hartree–Fock approximation (HF). For comparison: Exact excitation spectra of the systems with $N^\uparrow = 1$, $N^\downarrow = 0$ (blue) and $N^\uparrow = 2$, $N^\downarrow = 1$ (red). The spectra are shifted such that $E = 0$ lies in the center between the highest removal energy and the lowest addition energy.
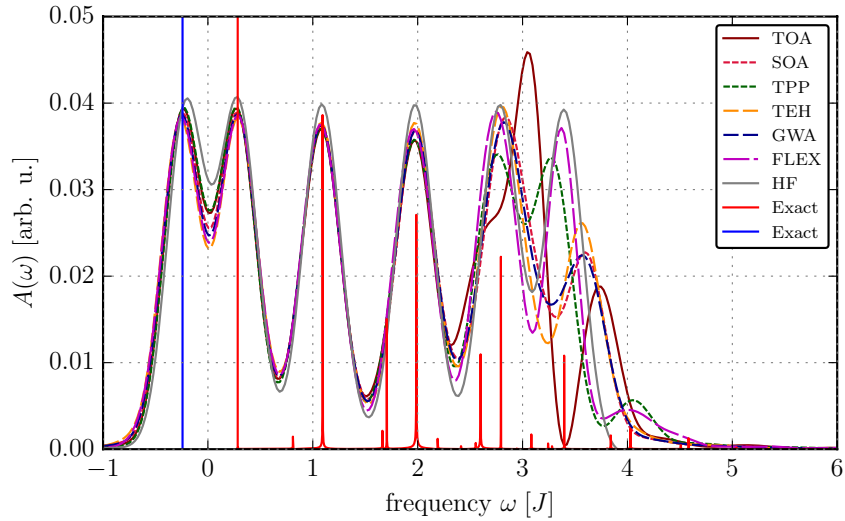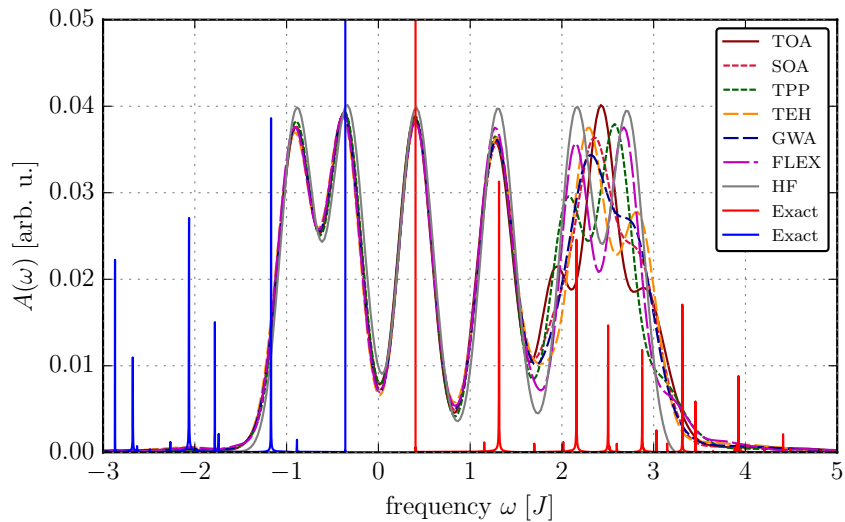

Figure 8. Six-site Hubbard cluster with $U = J$ at one-third filling. Spectral function generated from different selfenergy approximations: brown full line: third-order approximation (TOA), crimson dashed line: second-order approximation (SOA), green dashed line: particle–particle T matrix (TPP), yellow dashed line: electron–hole T matrix (TEH), blue dashed line: GW approximation (GWA), purple semi-dashed line: fluctuating-exchange approximation (FLEX), gray full line: Hartree–Fock approximation (HF). For comparison: Excitation spectra of the systems with $N^\uparrow = 2$, $N^\downarrow = 1$ (blue) and $N^\uparrow = 3$, $N^\downarrow = 2$ (red). The spectra are shifted such that $E = 0$ lies in the center between the highest removal energy and the lowest addition energy.

GWA followed by SOA, TEH and HF. The positions for TPP and FLEX are slightly shifted to lower energies. For TOA, the peak position cannot be easily distinguished with the shown spectral resolution, but the knee-structure within the left slope of the peak for the next higher energy suggests that the accuracy is comparable to that of the other approximations. Unlike any other tested approximation, though, the TOA is able to show the energy level just above $\omega/J \approx 3$. The next-higher energy level at $\omega/J \approx 3.3$ is best captured by the FLEX approximation followed by TPP, which slightly shifts to lower energies. The SOA, GWA and the TEH show this peak shifted to higher energies. For the TOA, it remains questionable if

the peak at $\omega/J \approx 3.8$ is to be attributed to exact energy level at $\omega/J \approx 3.3$ or if it shows the energy level at $\omega/J \approx 3.9$. The level just above $\omega/J \approx 4$ is only shown by the TPP and FLEX approximations, which indicates that these states embody a high degree of correlation. Summing up the findings for one-sixth filling, the best overall results are achieved by the TPP and FLEX approximation, with the latter performing slightly better. In addition, the TOA shows energy levels which are not captured by any other approximation.

For $n = 0.33$, the results are shown in figure 8. Two removal energy levels with a large amplitude and one with a small amplitude are visible. It is noteworthy that the removal
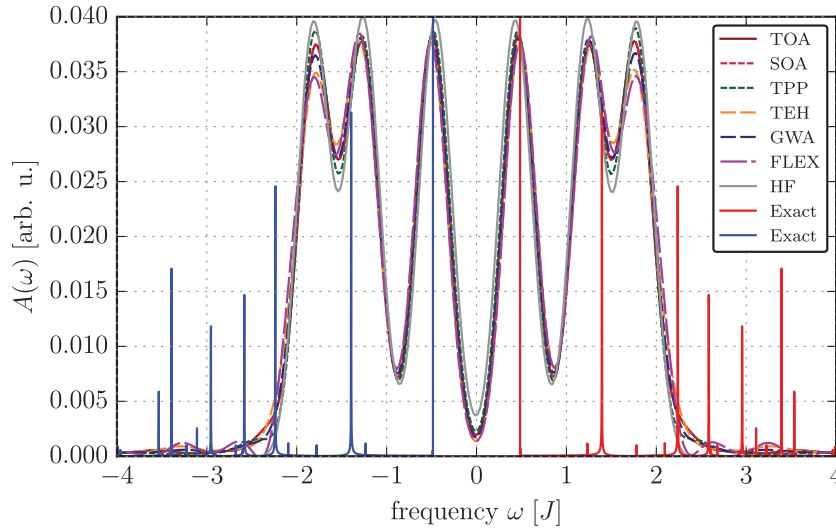
Figure 9. Six-site Hubbard cluster with $U = J$ at half filling. Spectral function generated from different selfenergy approximations: brown full line: third-order approximation (TOA), crimson dashed line: second-order approximation (SOA), green dashed line: particle–particle T matrix (TPP), yellow dashed line: electron–hole T matrix (TEH), blue dashed line: GW approximation (GWA), purple semi-dashed line: fluctuating-exchange approximation (FLEX), gray full line: Hartree–Fock approximation (HF). For comparison: Excitation spectra of the systems with $N^\uparrow = 3$, $N^\downarrow = 2$ (blue) and $N^\uparrow = 4$, $N^\downarrow = 3$ (red). The spectra are shifted such that $E = 0$ lies in the center between the highest removal energy and the lowest addition energy.

energies of the one-third filled Hubbard cluster connect to, i.e. that of two and one particle of both spin-directions, respectively, is the same the addition energies of the one-sixth filled cluster connect to. Comparing with the right part of figure 7, one immediately recognizes that the shown energy levels are not the same. For $n = 1/3$, the destination energy levels are levels 1, 2 and 6, while, for $n = 1/6$, the levels 1, 3, 6 and higher levels are reached. Thus, the combined information of both fillings can be used to gain insight into the energy spectrum of the intermediate system that differs by one particle to both. Concerning the quality of the approximations for the removal energy levels, all approximation agree with each other and with the exact solution, indicating that the states belonging to the removal energies are mainly uncorrelated. For the addition energies, the same is true for the first two levels. Starting from just above $\omega/J \approx 2$, there are many close-lying energy levels in the range up to $\omega/J \approx 4$, which renders an attribution to the different approximations difficult. In general, confirming the trend found for $n = 1/6$, the FLEX approximation yields results which very well agree with the exact energy levels, while the TOA reveals correct energy levels not found with the other approximations.

Turning to the results for half filling, shown in figure 9, one immediately recognizes two peculiarities of this setup. First, the removal and addition part of the spectrum is symmetric with respect to $E = 0$. This is, again, due to the occurrence of particle–hole symmetry [145]. Second, comparing the quality of the different approximations, one can discern only minor differences at energy levels farther away from $E = 0$, which are most pronounced for the FLEX approximation. As a special note, the good performance of the Hartree approximation for the spectral function indicates that the use of the GKBA with Hartree propagators is justified for half filling and explains the excellent results that could be achieved [77, 128, 146].

Summarizing the ability of NEGF methods to describe the spectral function of Hubbard clusters, one can state that the overall agreement for small to medium interaction strength is good and especially via combination of different approximation methods as well as probing from both systems with adjacent number of particles, one can gain a large part of the spectral information.

3.4. Time evolution following an external excitation

After analyzing simulation results for the correlated ground state and the quality of different selfenergy approximations, we now turn to time-dependent simulations. Thereby the ground-state data serve as the initial condition of the system prior to the excitation. The dynamics of the system which is driven out of equilibrium by an external excitation are studied numerically using the correlated selfenergy approximations that were described in sections 4 and 5. Thereby we focus on separate dynamics studies following different types of excitations.

Again, the motivation here is to analyze the accuracy of different approximations by performing tests against benchmark data. These include exact-diagonalization (CI) calculations that are possible for small systems; examples are given in sections 3.4.4 and 3.4.5. For larger systems, comparisons with time-dependent density-matrix renormalization group (DMRG) simulations can be performed, (see sections 3.4.1 and 3.4.2) which, however, are restricted to one-dimensional systems, due to the present limitations of DMRG. Finally, comparisons can be made to experiments with ultracold atoms, see section 3.4.1.

3.4.1. Time evolution following a confinement quench. A rather simple excitation of a finite system is to start with a
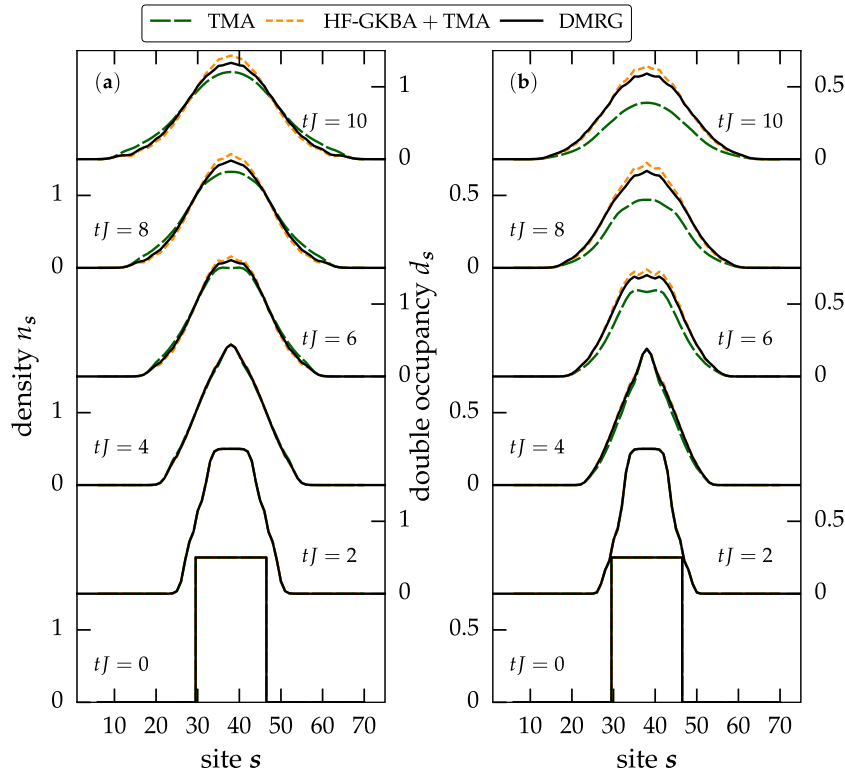
Figure 10. Symmetric 1D sudden expansion of a Hubbard chain of $N = 34$ fermions at $U = J$. Time evolution of (a) density n_s and (b) double occupancy d_s for six times (from bottom to top): $tJ = 0, 2, 4, 6, 8, 10$. Solid lines: DMRG, long dashes: TMA (two-time NEGF with T-matrix selfenergy), dashed lines: T matrix with HF-GKBA. From [22].

spatially localized configuration that is achieved by a strong confinement potential and then to rapidly remove the confinement at some time $t = 0$. This resembles classical diffusion experiments where a localized particle density expands into vacuum. Such a configuration of a quantum system is straightforwardly realized with ultracold atoms in a trap or an optical lattice. An example of a rapid expansion of cold fermionic atoms was presented by Schneider *et al* in [147].

With the NEGF approach it is fairly straightforward to simulate such an expansion scenario of atoms on an optical lattice because the latter accurately reproduces the Hubbard Hamiltonian (27) with onsite interaction. In the present experiment a two-dimensional geometry was used. Before presenting NEGF results for this setup we focus on benchmark calculations where comparison with DMRG simulations were performed. In [22], expansion simulations for $N = 34$ fermions in a one-dimensional configuration of 75 Hubbard sites have been carried out. Initially, the 17 central sites were doubly occupied whereas the outer sites were empty, see the bottom row (left column) of figure 10. The expansion dynamics are quite interesting and differ significantly from the classical case due to the rectangular shape of the initial density profile. Furthermore, the expansion of fermions is constrained by the Pauli principle, i.e. the innermost particles cannot move until the fermions at the edge have (partially) emptied their sites.

In figure 10 three sets of simulations are presented. The full lines are time-dependent DMRG results, see [22] for details. In addition, the authors show NEGF results with particle–particle T-matrix selfenergies (here TMA) in order to accurately

simulate strong-correlation effects. One set of results is from a full two-time simulation (TMA, green dashes), the other one, from a single-time approximation using the GKBA with Hartree–Fock propagators (HF-GKBA+TMA, yellow dashes). In the present simulations the coupling was moderate, $U/J = 1$ and, not surprisingly, the agreement of the NEGF results for the density profile with DMRG is excellent. An interesting observation is that the two-time simulations show a faster dynamics than the one-time approximation (HF-GKBA).

A more sensitive quantity than the density is the local doublon number, equation (145), which is plotted in the right column of figure 10. Here the agreement with the DMRG data is similar. While the two-time result for $d_s(t)$ shows stronger deviations than the single-particle density, the HF-GKBA exhibits the same high accuracy for both quantities. A very interesting observation is that the exact (DMRG) result is enclosed by the two-time and GKBA results. This behavior was confirmed for a broad range of coupling parameters, self-energy approximations and in many other setups as well, e.g. [22]. This has important implications for the use of NEGF simulations for more complex systems where independent benchmark data are not available.

Returning to the physics of the expansion of fermions—one of the most interesting questions is how the expansion speed depends on the interaction strength U/J (i.e. on the correlations in the system). A particularly interesting theoretical prediction was [95] that fermions that are in doubly occupied lattice sites ('doublons') should expand slower compared to
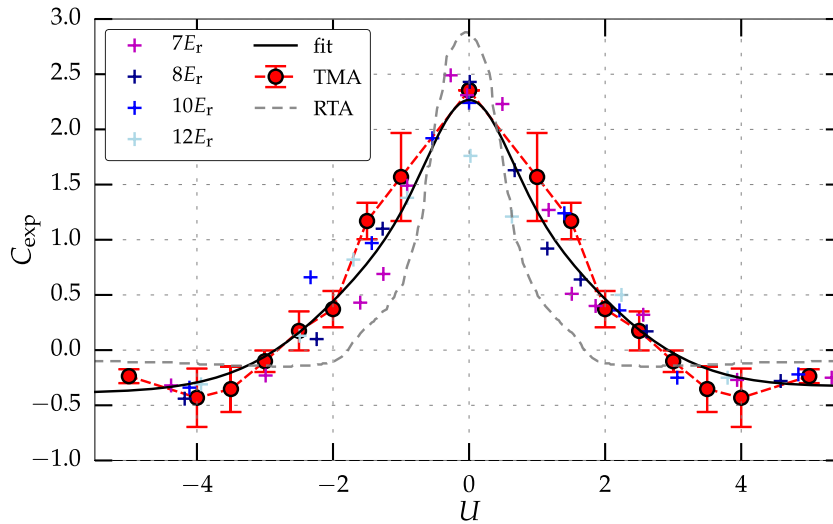
Figure 11. Asymptotic core (half width at half maximum of the density) expansion velocity C_{exp}. Plus signs: experimental results for different lattice depths in units of the recoil energy E_r; gray dashed line: relaxation-time approximation model of [147]; red circles: two-time NEGF results with T-matrix selfenergies, the error bars denote the statistical uncertainty due to the extrapolation with respect to time and particle number (see text). The black line is a fit through the experimental points to guide the eye. From [28].

singly occupied sites ('singlons') giving rise to a spatial separation of the two components ('quantum distillation'). A first test can be made by comparing the two columns of figure 10. There, indeed, the doublon expansion is slightly slower than that of the total density, in particular, for the initial time frames (see the lowest three rows). Here, however, the interaction is comparably weak and the effect is small.

Such a peculiar separated expansion of doublons and singlons was, in fact, observed experimentally for strongly correlated fermionic atoms in [147]. They demonstrated that, when the system is initially in a fully doubly occupied configuration, after removal of the confinement, doublons remain dominantly in the trap center. Moreover, the expansion speed of this central part ('core') decreases when the coupling strength U/J increases. The experimental results for the 'core expansion velocity' C_{exp} are reproduced in figure 11 by the full black line. Interestingly, C_{exp} even becomes negative which means that the 'core shrinks'. Furthermore, the result is exactly the same for attractive and repulsive interaction (negative and positive U, respectively), which is an exact property of the Hubbard model.

Figure 11 also contains results from a semiclassical kinetic simulation in relaxation-time approximation (grey dashed curve [147]) which reproduces the overall trend but exhibits very strong deviations, for most values of U. It is, therefore, of high interest to apply the NEGF approach to this problem since, due to the 2D geometry, DMRG simulations are not possible. Such NEGF simulations were developed by three of the present authors and published in [28]. To correctly describe strong-coupling effects, the second-Born approximation cannot be applied. Instead, T-matrix selfenergies were used. An advantage in these simulations is that the initial state is uncorrelated (it is an Hartree–Fock state), so no adiabatic switching needs to be done. This is particularly important since the simulations have to be sufficiently long to reach the regime where the expansion velocity approaches a constant value ('hydrodynamic stage').

The present NEGF simulations with particle–particle T-matrix selfenergies were carried out for a broad range of particle numbers, up to about $N = 100$ particles on a 2D lattice of 19×19 sites. It turned out that the expansion velocity shows a simple scaling with N, so an extrapolation to the thermodynamics limit, $N \to \infty$ (the experiments used several hundred thousands of atoms) was possible. At the same time, the statistical error of the extrapolation provides a measure of the numerical uncertainty of the macroscopic results [78]. These results are also included in figure 11 by the red dots and the associated error bars. Obviously, the agreement with the experiment, over the whole range of coupling parameters, is impressive. These have been the first and so far the only quantum-dynamics simulations that allow for a direct comparison with cold-atom experiments in two dimensions. Moreover, in [28] results for three-dimensional lattice configurations were presented and the dependence of the expansion velocity on the dimensionality was analyzed.

The time-dependent NEGF simulations provide extensive additional information on the expansion dynamics. From the nonequilibrium Green functions it is straightforward to obtain full space (site)-resolved information. An example is shown in figure 12 where the time evolution of various quantities with single-site resolution is presented [28]. This includes the density (first three rows), the doublon density (row 4, equation (145)), the doublon correlation function, (equation (146)) and the entanglement entropy, (equation (147)). The latter two quantities are of particular interest, as they allow to separate the effect of the buildup of correlations in the system: as mentioned above, the initial state is uncorrelated, and with removal of the confinement correlations start to form at the cluster edge and then spread in and outward. These simulation results can be directly compared to experiments with ultracold atoms where single-site resolution has been achieved with quantum-gas microscopes [19–21]. More details on the present simulations can be found in [78].
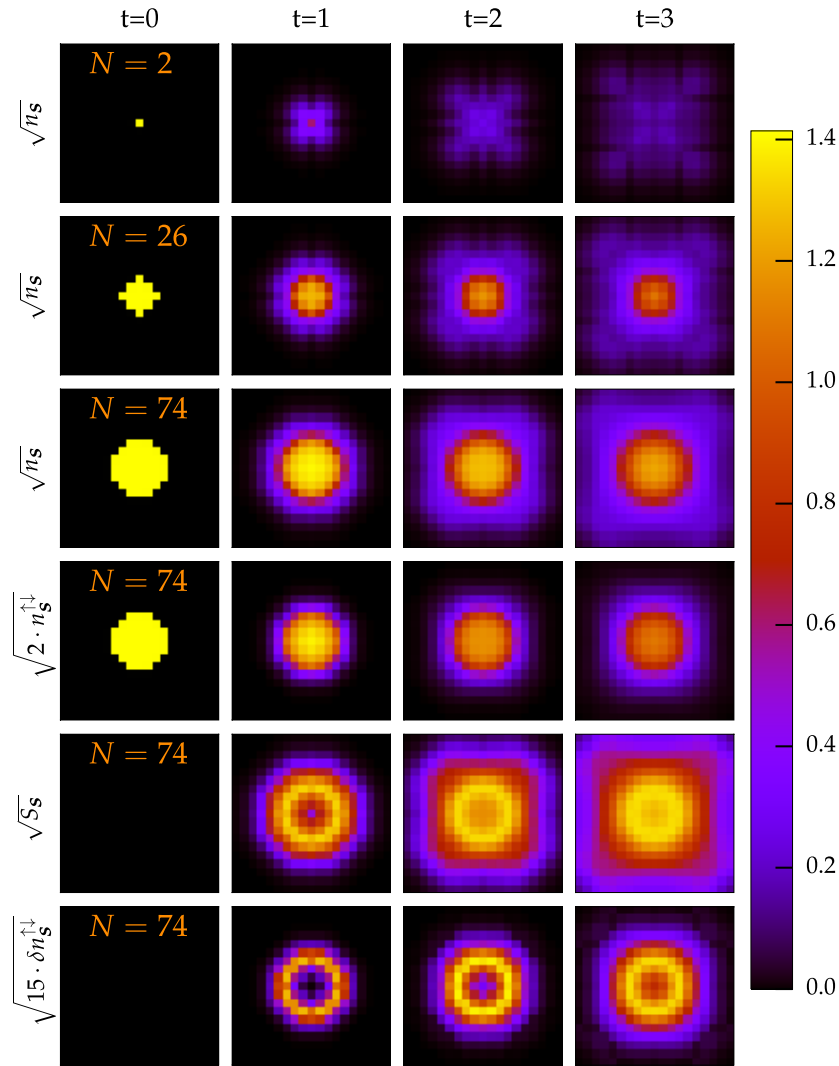
Figure 12. Site-resolved expansion dynamics in a 2D 19×19 Hubbard lattice at $U/J = 4$ for four times (in units of J^{-1}). Top three rows: square root of density n_s for $N = 2$, $N = 26$, and $N = 74$, respectively. Rows 4–6: square root of double occupation, local entanglement entropy S_s, equation (147), and the pair-correlation function $\delta n_s^{\uparrow\downarrow} = \delta n_s^{(2)}$, equation (146). From [28].

Concluding this section, we note that the present NEGF simulations with T-matrix selfenergies are rather costly and require large computer resources. In particular, simulations for large U become increasingly difficult which explains the choice of the maximum U-values displayed in figure 11. To reach large coupling values, improved computational approaches and, possibly, further improved selfenergy approximations, have to be developed.

3.4.2. Time evolution starting from a charge-density-wave state. Next, we focus on the time evolution of correlated electrons after a confinement quench starting from a different initial state than before. In [22] the authors considered a state of alternating doubly occupied and empty sites which will be called 'charge-density-wave state' (CDW). After removal of the confinement density can spread to the originally empty sites. To compare with benchmark data from DMRG simulations the simulations are limited to 1D geometry. In [22] extensive NEGF–DMRG comparisons

have been carried out. Here we show some typical results, see figure 13.

The first question to answer for the NEGF simulations is again the proper choice of the selfenergy. Since, again, correlation effects and, in particular, large values of U/J are of interest, the second-Born approximation is not appropriate. The particle–particle T matrix that showed impressive results in the diffusion setup of section 3.4.1 is not expected to work well here. The reason is that the T-matrix selfenergy treats interaction effects accurately on the two-particle level but neglects three-particle effects. It is, therefore, expected to be adequate for low densities. In application to Hubbard systems, this corresponds to low (or, due to particle–hole symmetry, high) filling factors. In the diffusion setup, the filling factor is low, except for the initial dynamics in the core region.

In contrast, in the present CDW setup the entire system is initially at half filling and remains at half filling. There, the particle–particle T matrix is inaccurate. At half filling we found in section 3.3 that the third-order approximation (TOA)
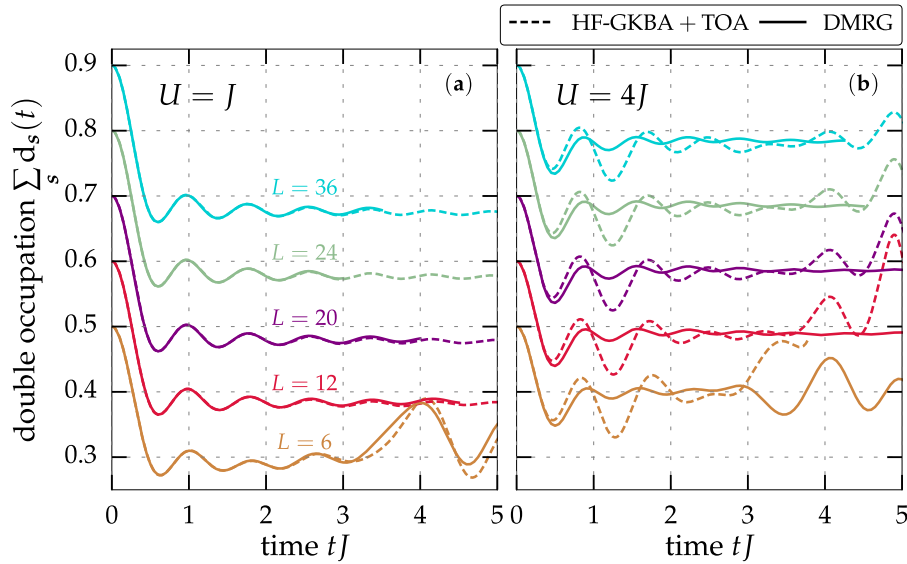
Figure 13. Charge-density wave excitation (the initial state conists of alternating doubly occupied and empty lattice sites): time evolution of the total double occupation, see equation (145) for two coupling strengths and five different systems sizes, $L = 6, \ldots 36$. Comparison of DMRG (full lines) and NEGF with third-order selfenergies within the single-time HF-GKBA scheme.

provides much more accurate data for the ground-state energy. It is, therefore, expected that also the dynamics will be treated more accurately within TOA selfenergies. Consequently, this selfenergy is being used, in addition to applying the HF-GKBA. The results are shown in figure 13 for two values of the coupling strength and five different chain lengths, in the range of $L = 6$ and $L = 36$. Note that we do not show the dynamics of the densities—there the agreement is excellent— but we focus on the more sensitive double occupations, equation (145), summed over the entire cluster.

For moderate coupling, $U/J = 1$, left column, the NEGF results are practically indistinguishable from the DMRG data. Only for the smallest system and for long times, small deviations are visible. For the case of larger coupling $U/J = 4$ significantly larger deviations are observed. While the overall trends, such as the mean value of the total double occupation, $d(t)$, is well reproduced for the initial time interval, the oscillations of $d(t)$ occur with a slightly modified frequency, and the amplitude of the HF-GKBA results is substantially larger than in the DMRG data. Also, the 'density revival' seen in small systems at weak coupling (bottom curve of left column) which seems to be present also at larger coupling (bottom right DMRG curve) seems to be amplified by the HF-GKBA. Most interestingly, the agreement of the NEGF data with the DMRG systematically improves with increasing system size. For more details, the reader is referred to [22].

3.4.3. Time evolution following a charged-particle impact. Let us now consider a very different type of excitation that is caused by the impact of an energetic projectile in a correlated Hubbard cluster. The interaction of the projectile with the electrons of the cluster is particularly strong for a charged particle. This type of excitation differs from the quenches above by its strongly localized character: typically only the few nearest neighbors of the impact point will be strongly affected. Depending on the velocity of the projectile, the interaction is

also localized in time where the interaction duration is controlled by the initial velocity of the projectile.

The associated energy loss of the projectile ('stopping power') has been studied experimentally and theoretically for many years, for an overview see e.g. [148], and broad purpose numerical simulation tools (e.g. SRIM) were developed, e.g. [149]. These models are based on extensive averages and experimental input. Moreover, they assume that the solid can be treated as following the excitation adiabatically. More recently, time-dependent simulations have provided very detailed information on the complex physical processes. This mostly concerns time-dependent DFT simulations, e.g. [150, 151]. At the same time, TD-DFT does not allow one to reliably describe electronic correlation effects and the dynamics of correlations. Therefore, NEGF simulations are of high interest.

Time-dependent NEGF simulations of ion stopping were first presented by Balzer *et al* in [26]. Here we summarize a few representative results. To investigate electronic correlation effects one can apply an NEGF–Ehrenfest approach where the dynamics of the projectile are treated classically. The corresponding electronic Hamiltonian is given by

$$\hat{H}_{\mathrm{e}} = - J \sum_{\langle i,j \rangle, \sigma} c_{i\sigma}^{\dagger} c_{j\sigma} + U \sum_{i} \left(n_{i\uparrow} - \frac{1}{2} \right) \left(n_{i\downarrow} - \frac{1}{2} \right)$$
$$- \frac{Z_{\mathrm{p}} e^2}{4\pi \epsilon_0} \sum_{i,\sigma} \frac{c_{i\sigma}^{\dagger} c_{i\sigma}}{|\vec{r}_{\mathrm{p}}(t) - \vec{R}_i|}, \tag{148}$$

which, in addition to the standard Hubbard Hamiltonian, now includes the Coulomb interaction between a Z_p-fold charged ion and all electrons of the target. The trajectory of the projectile, $\vec{r}_{\mathrm{p}}(t)$, is obtained by solving Newton's equation where the force is given by the total force from the interaction with all electrons. By solving the coupled Keldysh–Kadanoff–Baym equations for the electrons and Newton's equation for the projectile one obtains the time-dependent energy exchange
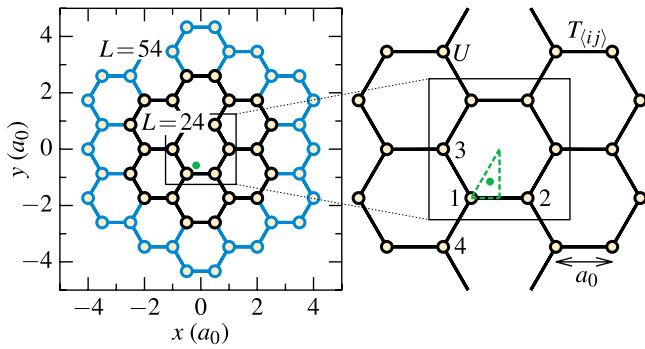
Figure 14. Sketch of the lattice structure of circular honeycomb clusters with $L = 24$ (black) and $L = 54$ sites (blue). The green point indicates the position where the projectile hits the lattice plain. From [26].

between the ion and the electrons. The energy loss of the projectile follows from the asymptotic values for long times after and before the impact,

$$S_e[E_{\text{kin}}] = m_p \frac{\dot{r}_p^2(t \to -\infty)}{2} - m_p \frac{\dot{r}_p^2(t \to +\infty)}{2}. \quad (149)$$

Before starting the time-dependent simulations, again, the initial state has to be generated. Here two approximations are considered: (A) the initial state is a Hartree–Fock state and (B) the initial state is correlated and generated by adiabatic switching. From a computational stand point, (A) is advantageous, whereas (B) is more accurate but requires a substantially increased total computation duration.

The dependence of the energy loss on the initial kinetic energy, E_{kin}, of the projectile is plotted in figure 15 and show the characteristic single-peak behavior. For very fast projectiles, the interaction duration vanishes, and so does the energy exchange. On the other hand, for very slow projectiles, the initial kinetic energy is small. Therefore, obviously, a maximum exists, for an optimal choice of E_{kin}. For the present honeycomb clusters (see figure 14) this peak is in the range of 10 keV.

Since no spatial homogeneity is assumed, the energy loss can be compared in finite clusters of different size. In figure 15 Balzer et al [26] compare the energy loss of a proton of the same energy in two clusters (see the sketch in figure 14) of size $L = 24$ (inner cluster) and $L = 54$ (complete cluster). Clearly, the energy loss increases with cluster size because more electrons are being excited by the projectile.

Next, the role of interaction effects in the substrate on the stopping power is analyzed. This can be achieved by comparing mean-field (Hartree) simulations with different coupling parameters U/J as well as Hartree simulations to correlated NEGF results. Obviously, one should expect that interaction effects will be of minor importance at large projecticle energies because, in this case, the kinetic energy exceeds the interaction energy (weak coupling). This is indeed observed in all simulations shown in figure 15. At energies exceeding 200 keV the differences between different approximations quickly vanish. In contrast, for lower impact energies and, in particular, for energies below the peak energy (moderate to strong coupling), strong deviations are observed. The general
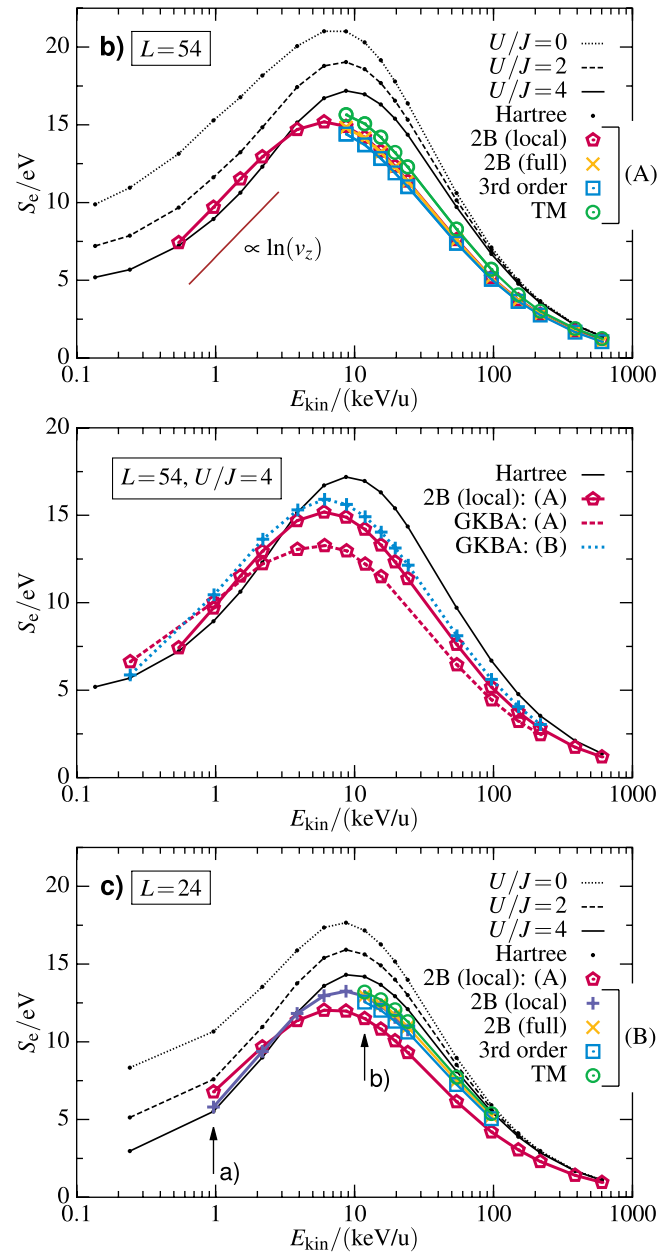
Figure 15. Energy loss S_e, equation (149), for protons passing through the honeycomb clusters of figure 14 of size $L = 54$ (panels (a) and (b)) and $L = 24$ (panel (c)). In all panels, the value of the onsite interaction U/J is encoded in the line style, the symbols correspond to NEGF results, and the black lines indicate the results of the Hartree approximation. The shortcuts stand for 2B (3rd order): second-order Born (third-order) approximation, TM: particle–particle T matrix, local: local approximation of the selfenergy, $\Sigma_{ij} \to \Sigma_i \delta_{ij}$. From [26].

trend is that, with increasing U/J the stopping power decreases, regardless of the chosen selfenergy approximation. A comparison of Hartree and correlated simulations reveals that correlations, at large energies, tend to make the system 'more rigid' which reduces the stopping power. Interestingly, at low impact energies, $E_{\text{kin}} \lesssim 3$ keV the situation changes and correlation effects lead to an increase of the stopping power. The explanation is that for slow projectiles the excitation energy can be resonant with electronic transitions in the material and lead, in
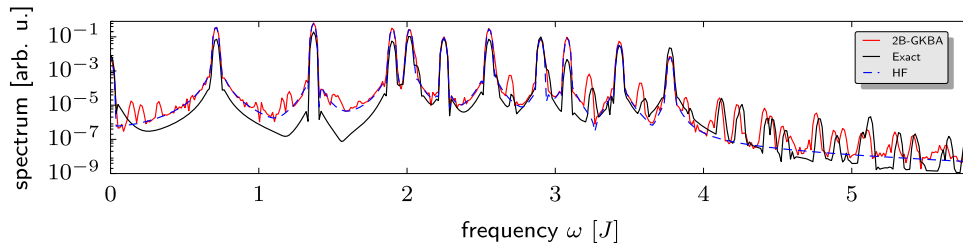
Figure 16. Spectral function of an 8-site Hubbard cluster at $U/J = 0.1$ computed via Fourier transform after a single-particle potential kick, equation (150). NEGF simulations with second-order Born selfenergies (Hartree–Fock-GKBA) are compared to Hartree and exact diagonalization results. From [77].

particular, to the excitation of doublons (see equation (145)) which is not possible in a mean-field description [152].

Let us now discuss the influence of different selfenergy approximations. Figure 15 contains a large variety of approximations. Note, however, that these calculations are quite expensive and become increasingly more difficult when the impact energy decreases because then the required simulation duration grows. Therefore, most results were obtained for large impact energies where the differences between different approximations are small. In [26] the authors performed simulations using second-order Born (2B), third-order and particle–particle T-matrix (TM) selfenergies. The differences are small with the T matrix yielding the largest stopping power. Comparing two-time simulations and single-time simulations within the HF-GKBA (top two frames of figure 15), the GKBA leads to a slight reduction of the stopping power. However, this comparison has only been done for a few cases, and more simulations are required to obtain a systematic picture. Also, the effect of initial correlations has not yet been fully clarified.

More recently, a special correlation effect has been investigated: the formation of local electronic double occupations, equation (145), due to the ion impact [152]. There it was shown that, at low projectile energies, electrons may be efficiently excited across the Hubbard gap (e.g. at half filling) which gives rise to an enhancement of the stopping power. This effect has been explored in more detail in [27, 153].

To summarize this section: NEGF simulations coupled to an Ehrenfest description of a classical ion have been shown to be a powerful tool to model the energy transfer between a projectile and correlated target. They allow for a fully time-resolved analysis and deep insight into the electronic transitions that can be triggered by the ion impact. At the same time, these simulations are very expensive at low impact energies and further optimization is needed. Interesting future questions include the quantum treatment of the projectile and of the electronic excitations in the ion as well as possible charge transfer processes between projectile and substrate [153, 154].

3.4.4. Time evolution following a short enhancement ('kick') of the single-particle potential. We now consider another excitation scenario where an external single-particle potential is turned on for a very short time only (see equation (31)),

$$f_{i\sigma}\left(t\right) = f_{i,0}\, \delta(t - t_0). \tag{150}$$

Such a very short excitation, is spectrally (energetically) broad which means that a broad range of energetic transitions will be

excited. Following the time-dependent dynamics of a suitable observable $B(t)$ one can easily reconstruct the spectral information contained in it, via Fourier transformation. It turns out that this is a very efficient way to obtain high-quality spectral information, provided the propagation can be extended to sufficiently long times, to avoid windowing effects in the Fourier transform. If, furthermore, the excitation is weak, i.e. linear response applies, then one accurately probes the properties of the unperturbed system, e.g. the ground state or the equilibrium properties.

This approach was first used in NEGF simulations by Kwong *et al* to compute the optical absorption of a semiconductor [155]. There, the frequency-resolved absorption coefficient was obtained, after applying a short optical laser pulse, from Fourier transforming the interband polarization $P(t)$, for details, see [136]. Similarly, it was shown that one can obtain the dynamical structure factor and dielectric function of a correlated system (e.g. electron gas or plasma) by applying a short monochromatic electric field with wavenumber q, i.e. a time-local excitation of (in the context of the uniform electron gas) $f(r, t) = U_0(t) \cos(qr)$, that excites a density modulation $\delta n(r, t)$ of wavelength $2\pi/q$ which yields the linear dynamic density-response function $\chi(q, \omega)$ [156]. As a consequence one obtains results for the dynamic dielectric function and for the dynamic structure factor that selfconsistently include correlation effects thereby obeying the relevant sum rules.

After successful applications to macroscopic systems this method was also used for finite systems. Van Leeuwen *et al* computed the optical absorption of atoms by Fourier transforming the time-dependent dipole transition signal [70]. The method can also be applied to compute, via time-dependent NEGF simulations, the spectrum of electronic excitations of finite correlated systems. Balzer *et al* considered a four electron model quantum well and showed the second-order Born selfenergies yield accurate results for the electronic double excitations [124]. Similar results were obtained by Säkinen *et al* [157].

Here we illustrate this approach for a small Hubbard cluster of 8 sites and coupling strength $U/J = 0.1$. In the simulations of Hermanns *et al* [77] the excitation was local on one site, i.e. in equation (150) the excitation amplitude was $f_{i,0} = w_0 \delta_{i1}$. Choosing a very small amplitude, $w_0 = 0.01J$, the system remained well inside the linear-response regime. Performing a very long simulation of duration $T = 1000J^{-1}$ provided an accurate excitation spectrum. The selfenergy was used on the second-order Born level, which is adequate
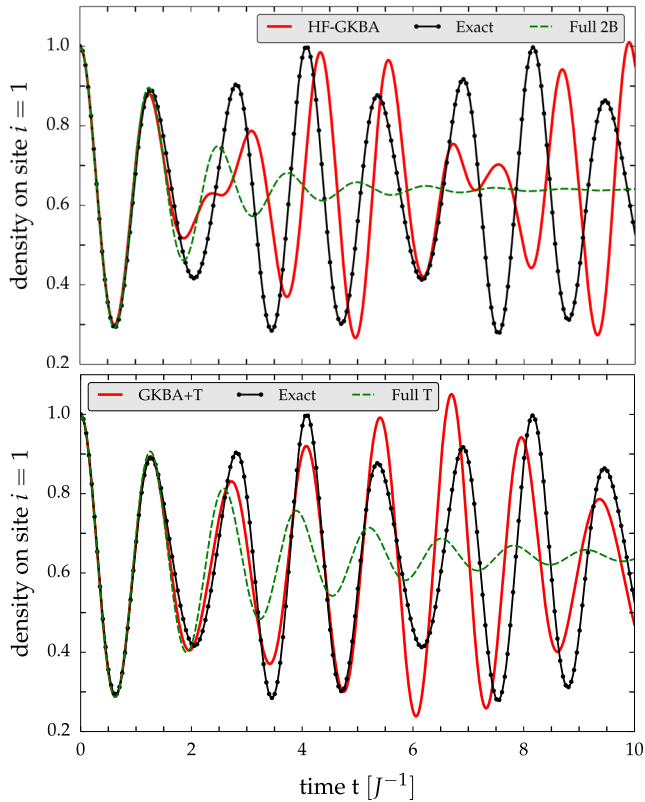
Figure 17. Half-filled Hubbard dimer for $U = J$. Density evolution on the first site following a sudden switch-on of the onsite potential (equation (151)) of strength $w_0 = 5.0J$ on site $i = 1$. Black line with dots: exact results; green dashed line: two-time NEGF result, and red full line: HF-GKBA. Top figure: NEGF and GKBA with second-order Born selfenergy (Full 2B). Bottom figure: NEGF and GKBA with T-matrix selfenergy (Full T). From [77].

for the present weak-coupling case. To achieve the desired long simulation duration a single-time simulation (with the Hartree–Fock GKBA) was carried out. The result is shown in figure 16 where the NEGF result is compared to an exact-diagonalization calculation. Obviously, the agreement is excellent. The NEGF simulations accurately reproduce the exact spectrum over a broad range of energies and practically capture all peaks. This agreement extends over an impressive seven orders of magnitude (note the logarithmic scale). Small deviations are visible for increasing frequency where peak shapes exhibit slight deviations. This calculation also allows to clearly single out correlation effects and explore the limitations of the mean-field result (see the blue curves labeled HF). While HF well captures the low-frequency peaks, it entirely misses peaks occuring above $\omega \sim 3.8J$. But also at lower energy, many peaks are missing, e.g. at $\omega/J \approx 2.7, 3.2$ and 3.6 that are associated to double excitations.

This result confirms the power of this approach and the capability of NEGF simulations to obtain accurate ground-state (or equilibrium) spectra via time propagation. These results can, of course, be directly compared to independent pure ground-state (or equilibrium) simulations, e.g. within the framework of the Bethe–Salpeter equation for the Matsubara Green function. The comparison of the two approaches reveals that [156] time-dependent NEGF simulations with a

selfenergy Σ correspond to Bethe–Salpeter results with a two-particle kernel $K_{\mathrm{BSE}} = \delta\Sigma/\delta G$. For text-book discussions, see [73, 136].

3.4.5. Time evolution following a strong rapid quench of the onsite potential. We now turn to the final example of time-dependent excitation that is very different from the previous cases. This section investigates the dynamics of small Hubbard clusters that are driven out of equilibrium by a very strong sudden quench of the on-site potential of the form

$$f_{i\sigma}(t) = \Theta(t, t_0)\delta_{i1}w_0, \tag{151}$$

where throughout this section the value $w_0 = 5J$ is used. Thus at $t = 0$ site $i = 1$ is very strongly excited by a constant potential. This excitation, initially, drives a depletion of this site which is followed by a subsequent oscillation of the electronic density throughout the system. Such strong excitations of this form (equation (151)) of very small Hubbard clusters were studied in detail by Verdozzi and co-workers [121, 122] using selfconsistent two-time solutions of the KBE. They made a surprising observation: in contrast to the exact solution (which is easily found for these small systems), the NEGF dynamics of the density oscillations are strongly damped. The authors of these papers explained this artifact by the selfconsistency of the solution of the Dyson equation (or the KBE) which contains selfenergy contribution to arbitrary orders (powers). This leads to a series of peaks in the spectral function that are not present in the exact result. They also observed that the effect is particularly strong for small clusters.

In the following we illustrate this effect for a few examples. In particular, we are interested in (1) how this damping behavior depends on the chosen selfenergy approximation, (2) on the filling and (3) how results from the HF-GKBA behave. To this end we focus on very small systems containing just two electrons on two and four sites, corresponding to half and quarter filling, respectively. The case of a half-filled Hubbard dimer, with an interaction of $U = J$ and excitation strength of $w_0 = 5.0J$, is shown in figure 17 [77]. There, three of us analyzed the time evolution of the density on the first (excited) site, comparing the exact result to selfconsistent two-time NEGF simulations and also single-time GKBA calculations with HF propagators. As expected, the exact solution exhibits undamped oscillations of the density because electrons periodically move between the two sites after an initial depletion of the first site. Consider now the result of fully selfconsistent solutions of the KBE with second-order selfenergy (top figure). Here, reasonably good agreement with the exact solution is only observed for the first 1.5 oscillation periods. For later times the oscillation period becomes smaller and the oscillations quickly damp, reaching an artificial steady state that is not present in the exact result. It is now of interest to reduce the level of selfconsistency for which different approximations can be considered [158]. Here we followed a different and more systematic strategy: we applied the Hartree–Fock-GKBA propagators as described in section 2.10. The results for the case of second-order Born selfenergies are also included in the top part of figure 17. Evidently, application of
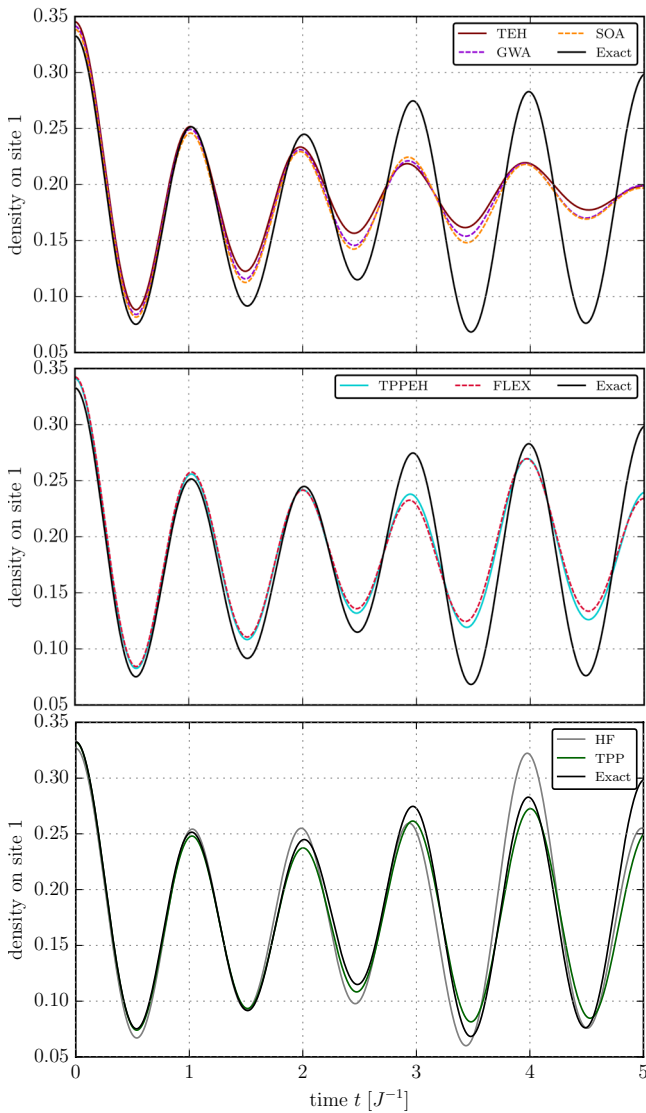
Figure 18. One quarter-filled four-site Hubbard cluster for $U = 1.5J$. Density evolution of the first (driven) site following a sudden switch-on of an onsite potential of strength $w_0 = 5.0J$. The selfenergy approximations are given in the inset. Top (middle): strongly (moderately) damped methods, bottom: undamped results.

the HF-GKBA indeed 'cures' the artificial damping and qualitatively agrees with the exact solution. The quantitative agreement, though, can only be considered satisfactory for the first five oscillation periods up to 6 inverse hopping amplitudes. While the exact oscillation period is roughly reproduced, the GKBA exhibits several phase changes that are not present in the exact dynamics.

To further improve the agreement with the exact results we then combined the HF-GKBA with a higher-order non-perturbative selfenergy. Results for the particle–particle T-matrix approximation, both, for two-time solutions and in combinations with the HF-GKBA, are shown in the bottom part of figure 17. In this case, the GKBA achieves very good agreement with the exact result. The first four periods are reproduced very accurately, whereas for later times a slight dephasing is observed. In contrast, the full two-time solution of the KBE with the particle–particle T matrix is quickly damped, as in

the case of the second-order Born approximation (Full 2B, SOA, top figure). At the same time, the T-matrix result is better than the second-Born approximation which is explained by the moderate coupling strength. Based on these results we conclude that the HF-GKBA, if used with the proper selfenergy, provides an excellent method to solve the problem of artificial damping of two-time simulations in the case of very strong excitation.

We now turn to the case of a four-site fermionic Hubbard model with one quarter filling, and an interaction strength of $U = 1.5J$. The excitation is the same as before. For this setup, *Friesen et al* [158] reported the particle–particle T matrix to show very good agreement with the exact solution, while the GW approximation performed much worse. Here, the same setup is re-examined using all selfenergy approximations that were introduced in sections 4 and 5. We observe that the selfenergies can be categorized into three groups based on the amount of artificial damping they exhibit. The three most strongly damped methods, which quickly start to deviate from the exact result are the electron–hole T matrix, the GW approximation and the second-order Born selfenergy and are shown in the top part of figure 18.

For all three methods, the damping sets in after the second oscillation period, and the amplitude quickly drops to roughly one third of the exact amplitude. For the fluctuating-exchange approximation (FLEX) and the similarly constructed approximation combining only the electron–hole and the particle–particle T matrix (TPPEH), the results are shown in the middle part of figure 18. Here, one notices only a slight damping, and the overall agreement with the exact result is significantly improved, compared to the first group of selfenergies approximations. The third group of methods that do not exhibit conceivable damping, in the present situation, are the particle–particle T matrix and, by construction, the uncorrelated Hartree(–Fock) approximation. The corresponding results are shown in the bottom part of figure 18. Both methods are in good agreement with the exact result, but the quality of the T-matrix approximation is much better than that of the uncorrelated Hartree approximation. The superior quality of the particle–particle T matrix, in the present case, is of course arising from the low density in the system as was noted also in the previous sections. For higher density the situation changes. Most importantly, we conclude that the artificial damping in strongly excited finite systems is not a generic feature of all two-time simulations but is observed for selfenergy approximations that most strongly deviate from the exact Hamiltonian. In addition, we have seen before that the artificial damping is removed almost completely by invoking the GKBA with Hartree–Fock propagators.

3.5. Discussion of the numerical results and outlook

We conclude the overview of numerical solutions of the KBE in equilibrium and nonequilibrium with a brief summary of the main findings and an outlook. In section 3.3 it has been shown that, for the interacting ground state, the order-by-order expansion with respect to the interaction strength yields good results, already with the second-order approximation

(SOA). The results significantly improve further when also the third-order terms are taken into account (TOA). On the other hand, the non-perturbative expansions, such as the particle–particle and particle–hole T-matrix approximations and the GW approximation, as well as combinations of several non-perturbative approximations, do, in general, not reach the same accuracy. Concerning the single-particle spectrum, both, perturbative and non-perturbative methods, yield good results and especially with the combination of the results for all available methods, most of the spectral information can be computed.

For time-dependent processes involving strong excitations, the GKBA has been found to be a valuable tool to mitigate correlation-induced damping. Combined with the particle–particle T matrix, which has shown to produce excellent results in full calculations for lower filling factors, it yields a density evolution which is close to the exact solution. With the great variety of available selfenergy approximations, covered in sections 4 and 5 both, with and without application of the GKBA, a powerful toolset is available to study systems of arbitrary dimension and large particle numbers, where currently no exact methods are available.

In section 3.4 we considered the dynamics of small- and intermediate-size Hubbard clusters in response to various kinds of excitations ranging from short to long and weak to strong. Where comparisons with benchmark data were available NEGF calculations have obtained very good agreement, provided the proper selfenergy approximation has been chosen. This means that Σ has to be chosen such that it matches both the coupling strength and filling (density). While, at weak coupling, the second-order Born approximation is adequate, at moderate coupling, $U \gtrsim J$, this approximation shows significant deviations and there is even no guarantee that it captures the dominant trends. Therefore, it is crucial to have a sufficiently large arsenal of selfenergy approximations available that can be used in a flexible manner. Thus, we can conclude that NEGF simulations have, indeed, reached a level of accuracy where reliable predictions can be made. For an efficient use of the proper selfenergies, it is crucial to have explicit results for each approximation available that can be rapidly implemented. This will be discussed in great detail in the next sections.

Before doing this we note that time-dependent NEGF simulations have seen a dramatic surge in activity in many areas. Even though the most accurate and best tested results were obtained for lattice models, as discussed above, there exist many further applications that are outside the scope of this article but should be briefly mentioned, together with a few relevant references. Indeed, second-order Born simulations were reported for electrons in quantum dots [159, 160], the laser excitation of small atoms and molecules [70–72]. Interestingly, second-order Born calculations were shown to be applicable also to the photoionization of larger atoms such as krypton [161] and to well reproduce two-electron processes such as Auger ionization [162]. Other finite systems the relaxation dynamics of which were recently studied include

graphene-type clusters such as graphene nanoribbons [163]. Correlation effects of particular interest here are, e.g. carrier multiplication effects.

While in the applications listed above the electronic system was typically treated as isolated, in many cases the coupling to the environment (bath) has to be included. Examples are transport problems. Since the bath is typically much larger than the physical system of interest with time scales often well separated from those of the system, suitable procedures to eliminate the bath degrees of freedom are of high interest. An important example is transport through nanoscale systems where it is often advantageous to eliminate the effect of the leads. Here a highly efficient solution within the NEGF scheme is provided by an embedding approach [164], for a text-book discussion see [73]. This approach has been extended to the photoionization of atoms [161] and charge transfer processes between atoms and a solid surface [27, 154].

Due to the success of these NEGF simulations we expect that the number and scope of applications will continue to increase over the next years. Further progress requires new developments in several directions. One is certainly the use of improved more realistic models. Here we mention the idea to combine NEGF simulations with an *ab initio* basis set that is provided by a Kohn–Sham simulation. This concept is realized, e.g. within the Yambo code of Marini *et al*, e.g. [165, 166, 189]. A major problem for these approaches is the large basis size which leads to very large requirements of CPU time and computer memory.

One approach that allows to mitigate these problems, at least partially, is the generalized Kadanoff–Baym ansatz (GKBA) that was introduced in section 2.10. We have seen throughout the present section that the GKBA, combined with Hartree–Fock propagators, indeed provides the expected major savings of resource. Moreover, in many cases it yields excellent results that may be not worse than the full two-time simulation, e.g. [77]. This, however, does not mean that two-time simulations become obsolete. In contrast, as we have seen from the comparison to DMRG results in sections 3.4.1 and 3.4.2, in many cases, the exact result is enclosed between those of the two-time NEGF and the time-diagonal GKBA. Thus, both types of simulations should be developed in parallel.

Future developments in this field should also aim at improving the GKBA simulations. Part of the problems of the GKBA will be overcome if, instead of Hartree–Fock propagators, correlated propagators are being used. Here, we mention recent promising proposals of [27, 167]. Furthermore, it will also be important to include correlated initial states into GKBA simulations and to develop efficient schemes that reduce the associated computational overhead, e.g. [27, 168–170].

Finally, all of the NEGF applications discussed above crucially depend on the availability of a large arsenal of selfenergy approximations and their optimization for special basis sets. In the remainder of this paper, we present a detailed overview of practical formulas that are ready to use in NEGF simulations.

4. Selfenergy approximations I: perturbation expansions

To study time-dependent observables of the system of interest by solving the Keldysh–Kadanoff–Baym equations, one has to know the '<' and '>' components of the two-time Green function, $G^{\lessgtr}\left(t_1, t_2\right)$. These components can be generated from the solution of the contour Dyson equation, which is the first equation of Hedin's equations, see equation (91). Its main ingredient is the selfenergy Σ. It is of great importance, both, from a physical point of view—since it incorporates all different classes of inter-particle effects and processes—as well as from the computational view—since a large portion of the numerical resources is consumed for its determination. Σ is the solution of the second Hedin equation, equation (95), which, in turn, is dependent on the third to fifth Hedin equation, equations (102), (105) and (106), and, in turn, also on the Dyson equation via the Green function entering it. Since the selfenergy, by iteration of Hedin's equations, consists of an infinite number of terms, a strategy has to be used to reach a good approximation with only a small finite subset. The two most common approaches are detailed in the following. The first applies a perturbative approach with respect to the interaction strength, i.e. with respect to the powers of the potential w, whereas the second uses a resummation idea. The resummation involves (infinitely many) diagrams in all orders of the interaction strength belonging to certain topological classes, namely the particle–particle, the particle–hole T-matrix approximation (TPP, TEH), the GW approximation (GWA), or a combination of all of them or some subsets. The present section 4 deals with the expansion in orders of the interaction strength where we systematically study selfenergies of first, second and third order. After this, in section 5, the resummation approaches, are introduced and discussed for all relevant special cases. In these two sections we introduce all selfenergies that were applied in the calculations of section 3.

In the remainder of this section we focus on the expansion of the selfenergy with respect to the number of interaction factors w involved. This means that the nth order approximation contains only terms with no more than n interactions. This procedure has two sources of reasoning behind it. First, for small interaction strength (in units of the single-particle energy), higher-order processes with more interaction factors usually have small amplitudes. Second, even for larger coupling strength, higher-order terms also contain several Green functions corresponding to the correlated creation and annihilation of several particles. The strength of these correlations is not directly coupled to the interaction strength and, therefore, a lower-order approximation may give good results even for stronger interactions.

Regarding the treatment of the Green functions occuring in the expansion of the selfenergy, three different approaches are common. In the *free-particle approach*, the Green function is expanded with respect to the number of occurrences of the interaction. That way, the selfenergy is eventually considered as a functional of the bare interaction and the non-interacting Green function: $\Sigma\left[G^{(0)}, w\right]$. This treatment is consistent to the expansion scheme of the selfenergy itself (and the other quantities in Hedin's equations) in this section. That way, it is ensured that the nth order approximation contains no terms of higher order in w. In the *self-consistent approach* instead, the selfenergy is treated as a functional of the interacting Green function and the bare interaction: $\Sigma\left[G, w\right]$. Here, one starts from the non-interacting Green function $G^{(0)}$ and computes the selfenergy according to equation (95), within the chosen approximation. Then, the Dyson equation is evaluated, taking $G = G^{(0)}$ on the right-hand side. With the resulting G, the selfenergy is reevaluated. This procedure is continued iteratively until convergence is reached. During this process terms of all orders in w are produced. Nonetheless, these terms are valid terms of order higher than n, so it cannot be answered beforehand which method is superior. We also mention a third framework—the *screened approach*—which appears to be the most native treatment of Hedin's equations. Here, the selfenergy is considered as a functional of the screened interaction and the interacting Green function: $\Sigma\left[G, W\right]$ (see, e.g. [73] for details). This treatment gives rise to several high-order resummation ideas, starting from the GW approximation (see section 5.2).

In the remainder of this section, the two approaches based on the bare interaction will be analyzed in detail by considering selfenergies up to the third order in w, i.e. Hartree–Fock (HF), second-order Born approximation (SOA) and third-order approximation (TOA). These approximations will be systematically deduced from Hedin's equations[16]; first, for a general basis. After this, each result will be specified to two important cases: a basis where the interaction is diagonal ('diagonal basis') and the Hubbard basis. For all three basis representations we present the quantities first on the Keldysh contour and then we derive the '$\gtrless$' and retarded/advanced components. In addition, we separately present the results for bosons and fermions. In cases when there are differences for different spin projections, the different cases will be specified separately. In addition to the formulas we present the graphical representation in terms of Feynman diagrams that will be introduced in figure 19.

4.1. First-order terms. Hartree and Fock selfenergies

To determine the first-order contributions to Σ, one starts from the second Hedin equation, equation (95). The first term, the Hartree term Σ^{H}, is of first order, since it contains one w. It was already given in equation (96) and is repeated here for consistency,

$$\Sigma_{ij}^{\mathrm{H}}\left(z_1, z_2\right) = \pm \mathrm{i}\hbar \delta_{\mathcal{C}}\left(z_1, z_2\right) \sum_{mn} w_{mijn}\left(z_1\right) G_{nm}\left(z_1, z_{1^+}\right). \tag{152}$$

---

[16] It may seem more 'native' to deduce the order-wise selfenergy approximations from the bare-vertex approach I (equations (97) and (98)). Since both approaches are fully equivalent we, instead, use approach II (equations (101)–(106)), because it nicely demonstrates the interdependent mechanics of Hedin's equations and gives additional insights to the involved quantities.
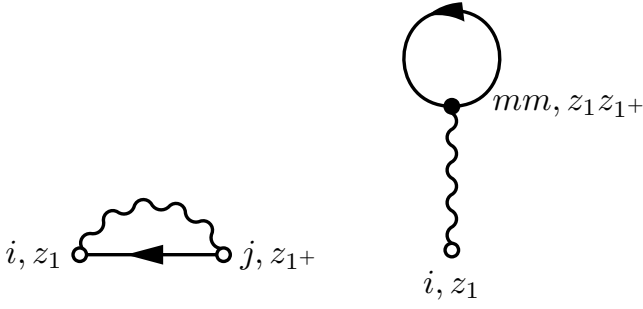
Figure 19. First-order diagrams in the diagonal basis. Left: Fock diagram, $\Sigma^{\text{F,diagonal}}$. Right: Hartree diagram, $\Sigma^{\text{H,diagonal}}$. Both diagrams are time-diagonal.

Since this expression contains a contour delta function, $\delta_{\mathcal{C}}$, the only non-vanishing Keldysh component is

$$\Sigma^{\text{H},\delta}_{ij}\left(t_1\right) = \Sigma^{\text{H}}_{ij}\left(z_1, z_1\right) = \pm i\hbar \sum_{mn} w_{mijn}\left(z_1\right) G_{nm}\left(z_1, z_{1+}\right)$$

$$= \pm i\hbar \sum_{mn} w_{mijn}\left(t_1\right) G^<_{nm}\left(t_1, t_1\right). \quad (153)$$

The second first-order term belongs to Σ^{xc}, see equation (95), and is generated by the first-order term $W^{(1)}$ of equation (102),

$$W^{(1)}_{ijkl}\left(z_1, z_2\right) = W^{\text{bare}}_{ijkl}\left(z_1, z_2\right) = \delta_{\mathcal{C}}\left(z_1, z_2\right) w_{ijkl}\left(z_1\right), \quad (154)$$

and the zeroth order vertex $\Gamma^{(0)}$, see equation (106),

$$\Gamma^{(0)}_{ijkl}\left(z_1, z_2, z_3\right) = \delta_{\mathcal{C}}\left(z_1, z_{2+}\right) \delta_{\mathcal{C}}\left(z_3, z_2\right) \delta_{ik}\delta_{jl}. \quad (155)$$

This yields the *Fock term*, Σ^{F}, which is of time-diagonal structure as the Hartree term and is given by

$$\Sigma^{\text{F}}_{ij}\left(z_1, z_2\right) = \Sigma^{\text{xc}}_{ij}\left(W^{(1)} \equiv W^{\text{bare}}, \Gamma^{(0)}\right) \quad (156)$$

$$= i\hbar \delta_{\mathcal{C}}\left(z_1, z_2\right) \sum_{mn} w_{injm}\left(z_1\right) G_{mn}\left(z_1, z_{1+}\right).$$

The δ component (prefactor of the delta function) is given by

$$\Sigma^{\text{F},\delta}_{ij}\left(t_1\right) = \Sigma^{\text{F}}_{ij}\left(z_1, z_1\right) = i\hbar \sum_{mn} w_{injm}\left(t_1\right) G^<_{mn}\left(t_1, t_1\right). \quad (157)$$

Because there is no further term stemming from $W^{(0)}$ and $\Gamma^{(1)}$, since $W^{(0)} \equiv 0$, the final result for the first-order selfenergy $\Sigma^{(1)}$ is given by

$$\Sigma^{(1)} = \Sigma^{\text{H}} + \Sigma^{\text{F}}, \quad (158)$$

which both are time-diagonal. For the *non-selfconsistent treatment*, the Green functions appearing in Σ^{H} and Σ^{F} are taken as free Green functions, i.e. $G \longrightarrow G^{(0)}$. Otherwise, all expressions remain the same. There are no additional terms containing higher-order Green functions in first order.

4.1.1. Diagonal basis. In a basis where the interactions are diagonal, $w_{ijkl} = \delta_{il}\delta_{jk}w_{ij}$, the first-order terms read

$$\Sigma^{\text{H,diagonal}}_{ij}\left(z_1, z_2\right) = \pm i\hbar \delta_{\mathcal{C}}\left(z_1, z_2\right) \delta_{ij} \sum_{m} w_{mi}\left(z_1\right) G_{mm}\left(z_1, z_{1+}\right),$$

$$\quad (159)$$

$$\Sigma^{\text{F,diagonal}}_{ij}\left(z_1, z_2\right) = i\hbar \delta_{\mathcal{C}}\left(z_1, z_2\right) w_{ij}\left(z_1\right) G_{ij}\left(z_1, z_{1+}\right), \quad (160)$$

with the δ components

$$\Sigma^{\text{H,diagonal},\delta}_{ij}\left(t_1\right) = \pm i\hbar \delta_{ij} \sum_{m} w_{mi}\left(t_1\right) G^<_{mm}\left(t_1, t_1\right), \quad (161)$$

$$\Sigma^{\text{F,diagonal},\delta}_{ij}\left(t_1\right) = i\hbar w_{ij}\left(t_1\right) G^<_{ij}\left(t_1, t_1\right). \quad (162)$$

Feynman diagrams. The structure of the selfenergy contributions can be suitably visualized by using Feynman diagrams [171]. In this diagrammatic representation, Green functions are depicted as solid lines with an arrow pointing from the second argument to the first argument (since the creation operator in G has the second argument and the annihilation operator has the first argument). The interaction is represented by a wiggly line which has two endpoints (in the diagonal basis). Employing the Feynman diagram technique, the two first-order contributions to the selfenergy are depicted in figure 19.

4.1.2. Hubbard basis. For the Hubbard basis, introduced in section 2.3, the first-order selfenergy terms can be directly worked out. Here we separately consider the cases of bosons and fermions (superscripts $\mathfrak{b}$ and $\mathfrak{f}$, respectively), see equations (28) and (35). For bosons we obtain[17]

$$\Sigma^{\text{H},\mathfrak{b}}_{i\alpha j\alpha}\left(z_1, z_2\right) = i\hbar \delta_{\mathcal{C}}\left(z_1, z_2\right) \delta_{ij} \sum_{\epsilon} U\left(z_1\right) G_{i\epsilon i\epsilon}\left(z_1, z_{1+}\right),$$

$$\quad (163)$$

$$\Sigma^{\text{F},\mathfrak{b}}_{i\alpha j\alpha}\left(z_1, z_2\right) = i\hbar \delta_{\mathcal{C}}\left(z_1, z_2\right) \delta_{ij} U\left(z_1\right) G_{i\alpha i\alpha}\left(z_1, z_{1+}\right), \quad (164)$$

with the δ components

$$\Sigma^{\text{H},\mathfrak{b},\delta}_{i\alpha j\alpha}\left(t_1\right) = i\hbar \delta_{ij} \sum_{\epsilon} U\left(t_1\right) G^<_{i\epsilon i\epsilon}\left(t_1, t_1\right), \quad (165)$$

$$\Sigma^{\text{F},\mathfrak{b},\delta}_{i\alpha j\alpha}\left(t_1\right) = i\hbar \delta_{ij} U\left(t_1\right) G^<_{i\alpha i\alpha}\left(t_1, t_1\right). \quad (166)$$

On the other hand, for fermions one obtains the following Hartree terms

$$\Sigma^{\text{H},\mathfrak{f}}_{i\alpha j\alpha}\left(z_1, z_2\right) = -i\hbar \delta_{\mathcal{C}}\left(z_1, z_2\right) \delta_{ij} \sum_{\epsilon \neq \alpha} U\left(z_1\right) G_{i\epsilon i\epsilon}\left(z_1, z_{1+}\right),$$

$$\quad (167)$$

$$\Sigma^{\text{H},\mathfrak{f},\delta}_{i\alpha j\alpha}\left(t_1\right) = -i\hbar \delta_{ij} \sum_{\epsilon \neq \alpha} U\left(t_1\right) G^<_{i\epsilon i\epsilon}\left(t_1, t_1\right), \quad (168)$$

whereas the fermionic Fock terms vanish exactly in the Hubbard basis, $\Sigma^{\text{F},\mathfrak{f}}_{i\alpha j\alpha}\left(z_1, z_2\right) \equiv \Sigma^{\text{F},\mathfrak{f},\delta}_{i\alpha j\alpha}\left(t_1\right) \equiv 0$.

We also consider the important special cases of spin-0 bosons and spin-1/2 fermions, respectively (the spin is indicated

---

[17] From here, we use a generalized time-dependent Hubbard interaction $U\left(z\right) \left[U\left(t\right)\right]$. This is particularly useful in the context of the adiabatic switching (see equation (126)), where the switching function can be included as $f^{\text{AS}}\left(t\right) U \to U\left(t\right)$.

by an additional superscript). For spin-0 bosons the terms attain the form

$$\Sigma_{ij}^{\mathrm{H,b,0}}\left(z_1\right) = i\hbar\delta_{\mathcal{C}}\left(z_1,z_2\right)\delta_{ij}U\left(z_1\right)G_{ii}\left(z_1,z_{1+}\right),$$

$$\Sigma_{ij}^{\mathrm{F,b,0}}\left(z_1\right) = i\hbar\delta_{\mathcal{C}}\left(z_1,z_2\right)\delta_{ij}U\left(z_1\right)G_{ii}\left(z_1,z_{1+}\right),$$

$$\Sigma_{ij}^{\mathrm{H,b,0,\delta}}\left(t_1\right) = i\hbar\delta_{ij}U\left(t_1\right)G_{ii}^{<}\left(t_1,t_1\right),$$

$$\Sigma_{ij}^{\mathrm{F,b,0,\delta}}\left(t_1\right) = i\hbar\delta_{ij}U\left(t_1\right)G_{ii}^{<}\left(t_1,t_1\right),$$

whereas for spin-1/2 fermions the results are

$$\Sigma_{i\uparrow j\uparrow}^{\mathrm{H,f,1/2}}\left(z_1\right) = -i\hbar\delta_{\mathcal{C}}\left(z_1,z_2\right)\delta_{ij}U\left(z_1\right)G_{i\downarrow i\downarrow}\left(z_1,z_{1+}\right),$$

$$\Sigma_{i\downarrow j\downarrow}^{\mathrm{H,f,1/2}}\left(z_1\right) = -i\hbar\delta_{\mathcal{C}}\left(z_1,z_2\right)\delta_{ij}U\left(z_1\right)G_{i\uparrow i\uparrow}\left(z_1,z_{1+}\right),$$

$$\Sigma_{i\uparrow j\uparrow}^{\mathrm{H,f,1/2,\delta}}\left(t_1\right) = -i\hbar\delta_{ij}U\left(t_1\right)G_{i\downarrow i\downarrow}^{<}\left(t_1,t_1\right),$$

$$\Sigma_{i\downarrow j\downarrow}^{\mathrm{H,f,1/2,\delta}}\left(t_1\right) = -i\hbar\delta_{ij}U\left(t_1\right)G_{i\uparrow i\uparrow}^{<}\left(t_1,t_1\right),$$

where the fermionic Fock terms are again zero. The corresponding diagrams for spin-0 bosons and spin-1/2 fermions are shown in figures 20 and 21, respectively.

4.2. Second-order terms. Second-Born approximation (SOA)

We now return to equations (95) and (101), and investigate the selfconsistent second-order contribution,

$$\Sigma^{(2)} = \Sigma^{\mathrm{xc},(2)}. \tag{169}$$

The second-order terms of $\Sigma^{\mathrm{xc},(2)}$ can only be of either one of two forms

$$\Sigma^{(2),2,0} = \Sigma^{\mathrm{xc},(2)}\left(W^{(2)},\Gamma^{(0)}\right), \qquad \Sigma^{(2),1,1} = \Sigma^{\mathrm{xc},(2)}\left(W^{(1)},\Gamma^{(1)}\right), \tag{170}$$
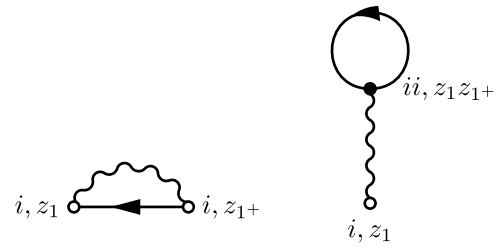

Figure 20. First-order diagrams in Hubbard basis for spin-0 bosons. Left: Fock diagram, $\Sigma^{\mathrm{F,b,0}}$. Right: Hartree diagram, $\Sigma^{\mathrm{H,b,0}}$. Note that both diagrams coincide for the Hubbard basis.
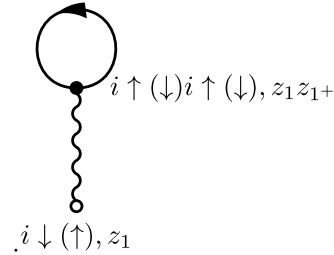
Figure 21. First-order (Hartree) diagram in Hubbard basis for spin-1/2 fermions, $\Sigma^{\mathrm{H,f,1/2}}$.

where the superscripts refer to the orders of W and Γ. The first term involves $W^{(2)}$, the structure of which is determined from equation (102),

$$W^{(2)} = W^{\mathrm{ns}}\left(P^{(0)},W^{(1)}\right), \tag{171}$$

where the zeroth order polarization is

$$P^{(0)} = P\left(\Gamma^{(0)}\right), \tag{172}$$

which is explicitly given by[18]

$$
\begin{aligned}
P^{(0)}\left(1,2\right) &= \pm i\hbar G\left(1,3\right)G\left(4,1\right) \\
&\quad \delta\left(3,4^{+}\right)\delta\left(2,4\right) \\
&= \pm i\hbar G\left(1,2\right)G\left(2,1\right)
\end{aligned}
$$

$$\tag{173}$$

Inserting this result into equation (171) and, employing equation (104), one arrives at

$$
\begin{aligned}
W^{(2)}\left(1,2\right) &= w\left(1,3\right)P^{(0)}\left(3,4\right) \\
&\quad W^{(1)}\left(4,2\right) \\
&= \pm i\hbar w\left(1,3\right)G\left(3,4\right) \\
&\quad G\left(4,3\right)w\left(4,2\right)
\end{aligned}
$$

$$\tag{174}$$

[18] For the purpose of better understanding, the following derivations are given in the simplified notation, as introduced in section 2.8. The way to the first second-order selfenergy term in the full notation is presented in the supplemental material 20 in section 1.1.1.

With this, $\Sigma^{(2),2,0}$ can be calculated as, (see equation (101)),

$$
\begin{aligned}
&\Sigma^{(2),2,0}(1,2) \\
&= i\hbar W^{(2)}(1,3)G(1,4) \\
&\quad \Gamma^{(0)}(4,2,3) \\
&= \pm(i\hbar)^2 w(1,3)G(3,4) \\
&\quad G(4,3)w(4,2)G(1,2)
\end{aligned}
\qquad\qquad
\text{}
\tag{175}
$$

or, in the full extended notation,

$$
\Sigma_{ij}^{(2),2,0}(z_1,z_2) = \pm(i\hbar)^2 \sum_{mn} G_{mn}(z_1,z_2) \sum_{st} G_{st}(z_1,z_2)
$$
$$
\times \sum_r w_{irsm}(z_1) \sum_u w_{tnju}(z_2) G_{ur}(z_2,z_1).
\tag{176}
$$

The other second-order selfenergy term, $\Sigma_{ij}^{(2),1,1}$, requires the first-order term of the vertex Γ, the structure of which is

$$
\Gamma^{(1)} = \Gamma\left(\delta\Sigma^{\text{xc},(1)}/\delta G, \Gamma^{(0)}\right),
\tag{177}
$$

and involves the functional derivative of $\Sigma^{\text{xc},(1)}$ with respect to G,

$$
\frac{\delta\Sigma_{ij}^{\text{xc},(1)}(z_1,z_2)}{\delta G_{rs}(z_5,z_6)} = \frac{\delta\Sigma_{ij}^{\text{xc},(1),\text{F}}(z_1,z_2)}{\delta G_{rs}(z_5,z_6)}.
\tag{178}
$$

Employing equation (156), one finds[19]

$$
\begin{aligned}
&\frac{\delta\Sigma^{\text{xc},(1)}(1,2)}{\delta G(5,6)} = i\hbar w(1,2)\frac{\delta G(1,2)}{\delta G(5,6)} \\
&= i\hbar\delta(1,5)\delta(2,6)w(1,2)
\end{aligned}
\qquad\qquad
\text{}
\tag{179}
$$

where the functional derivative with respect to G, in the diagrams, corresponds to cutting the G-line (or, more generally, all G-lines one by one) which is symbolized by the scissors. In case of different arguments of the Green functions, the result is

$$
\frac{\delta G(1,2)}{\delta G(5,6)} = \delta(1,5)\delta(2,6)
\qquad\qquad
\text{}
\tag{180}
$$

Using equations (179) and (155), one arrives at

$$
\begin{aligned}
&\Gamma^{(1)}(1,2,3) \\
&= \frac{\delta\Sigma^{\text{xc},(1)}(1,2)}{\delta G(4,5)}G(4,6) \\
&\quad G(7,5)\Gamma^{(0)}(6,7,3) \\
&= i\hbar w(1,2)G(1,3)G(3,2)
\end{aligned}
\qquad\qquad
\text{}
\tag{181}
$$

[19] For the full-notation derivation, see section 1.1.2 of the supplement 20.

Inserting this result, together with equation (154), yields

$$
\begin{aligned}
&\Sigma^{(2),1,1}\left(1,2\right)\\
&= i\hbar W^{(1)}\left(1,3\right)G\left(1,4\right)\\
&\quad \Gamma^{(1)}\left(4,2,3\right)\\
&= \left(i\hbar\right)^2 w\left(1,3\right)G\left(1,4\right)\\
&\quad w\left(4,2\right)G\left(4,3\right)G\left(3,2\right)
\end{aligned}
$$

(182)

or, in the full notation,

$$
\begin{aligned}
\Sigma_{ij}^{(2),1,1}\left(z_1,z_2\right) &= \left(i\hbar\right)^2 \sum_{mpq} w_{ipqm}\left(z_1\right)\sum_n G_{mn}\left(z_1,z_2\right)\\
&\times \sum_{rs} w_{nsjr}\left(z_2\right)G_{rp}\left(z_2,z_1\right)G_{qs}\left(z_1,z_2\right).
\end{aligned}
$$

(183)

This is the final result that is still written on the Keldysh contour, i.e. is an equation for Keldysh matrices. The corresponding matrix elements ('>', '<', retarded and advanced components) of the selfconsistent second-order selfenergy contributions $\Sigma_{ij}^{(2),2,0}$ and $\Sigma_{ij}^{(2),1,1}$ are straightforwardly extracted, applying the Langreth rules:

$$
\begin{aligned}
\Sigma_{ij}^{(2),2,0,\gtrless}\left(t_1,t_2\right) &= \pm\left(i\hbar\right)^2 \sum_{mn} G_{mn}^{\gtrless}\left(t_1,t_2\right)\sum_{st} G_{st}^{\gtrless}\left(t_1,t_2\right)\\
&\times \sum_r w_{irsm}\left(t_1\right)\sum_u w_{tnju}\left(t_2\right)G_{ur}^{\lessgtr}\left(t_2,t_1\right),
\end{aligned}
$$

(184)

$$
\begin{aligned}
\Sigma_{ij}^{(2),1,1,\gtrless}\left(t_1,t_2\right) &= \left(i\hbar\right)^2 \sum_{mpq} w_{ipqm}\left(t_1\right)\sum_n G_{mn}^{\gtrless}\left(t_1,t_2\right)\\
&\times \sum_{rs} w_{nsjr}\left(t_2\right)G_{rp}^{\lessgtr}\left(t_2,t_1\right)G_{qs}^{\gtrless}\left(t_1,t_2\right).
\end{aligned}
$$

(185)

All the above results were obtained within the selfconsistent framework, where all expressions contain full, interacting Green functions. As we noted in the beginning of this section, alternatively one can perform a non-selfconsistent treatment, where all Green functions are replaced by non-interacting functions. In that case, the possible second-order classes are

$$
\Sigma^{(2),(2),2,0,0} = \Sigma^{\mathrm{xc},(2)}\left(W^{(2)},G^{(0)},\Gamma^{(0)}\right) \equiv \Sigma^{(2),2,0}\left(G\to G^{(0)}\right),
$$

(186)

$$
\Sigma^{(2),(2),1,0,1} = \Sigma^{\mathrm{xc},(2)}\left(W^{(1)},G^{(0)},\Gamma^{(1)}\right) \equiv \Sigma^{(2),1,1}\left(G\to G^{(0)}\right)
$$

(187)

and

$$
\Sigma^{(2),\{H,0\},1} = \Sigma^{H,0}\left(G^{(1)}\right), \qquad \Sigma^{(2),\{F,0\},1} = \Sigma^{F,0}\left(G^{(1)}\right).
$$

(188)

A detailed list of these contributions, including all Keldysh matrix components for all considered basis sets, is given in the supplemental material[20] in section 2.

4.2.1. Diagonal basis. For a basis where the interaction is diagonal, $w_{ijkl} = \delta_{il}\delta_{jk}w_{ij}$, the selfconsistent second-order selfenergy terms, (see equations (176) and (183)), simplify to

$$
\Sigma_{ij}^{(2),2,0,\mathrm{diagonal}}\left(z_1,z_2\right)
$$

(189)

$$
= \pm\left(i\hbar\right)^2 G_{ij}\left(z_1,z_2\right)\sum_s w_{is}\left(z_1\right)\sum_t G_{st}\left(z_1,z_2\right)G_{ts}\left(z_2,z_1\right)w_{tj}\left(z_2\right),
$$

$$
\Sigma_{ij}^{(2),1,1,\mathrm{diagonal}}\left(z_1,z_2\right)
$$

(190)

$$
= \left(i\hbar\right)^2 \sum_p w_{ip}\left(z_1\right)\sum_n G_{in}\left(z_1,z_2\right)w_{nj}\left(z_2\right)G_{np}\left(z_2,z_1\right)G_{pj}\left(z_1,z_2\right),
$$

with the corresponding Keldysh matrix components

$$
\Sigma_{ij}^{(2),2,0,\mathrm{diagonal},\gtrless}\left(t_1,t_2\right)
$$

(191)

$$
= \pm\left(i\hbar\right)^2 G_{ij}^{\gtrless}\left(t_1,t_2\right)\sum_s w_{is}\left(t_1\right)\sum_t G_{st}^{\gtrless}\left(t_1,t_2\right)G_{ts}^{\lessgtr}\left(t_2,t_1\right)w_{tj}\left(t_2\right),
$$

$$
\Sigma_{ij}^{(2),1,1,\mathrm{diagonal},\gtrless}\left(t_1,t_2\right)
$$

(192)

$$
= \left(i\hbar\right)^2 \sum_p w_{ip}\left(t_1\right)\sum_n G_{in}^{\gtrless}\left(t_1,t_2\right)w_{nj}\left(t_2\right)G_{np}^{\lessgtr}\left(t_2,t_1\right)G_{pj}^{\gtrless}\left(t_1,t_2\right).
$$

The Feynman diagrams for these expressions are shown in figure 22.

4.2.2. Hubbard basis. For the Hubbard basis, we give the selfconsistent second-order selfenergy contributions first for bosons

$$
\Sigma_{i\alpha j\alpha}^{(2),2,0,\mathrm{Hubbard},\flat}\left(z_1,z_2\right)
$$

(193)

$$
= \left(i\hbar\right)^2 G_{i\alpha j\alpha}\left(z_1,z_2\right)U\left(z_1\right)\sum_\epsilon G_{i\epsilon j\epsilon}\left(z_1,z_2\right)G_{j\epsilon i\epsilon}\left(z_2,z_1\right)U\left(z_2\right),
$$

[20] See supplemental material at (stacks.iop.org/JPhysCM/32/103001/mmedia) for the derivations of the selfenegies in a general (non-diagonal) basis set and for the non-selfconsistent selfenergy contributions in second order.
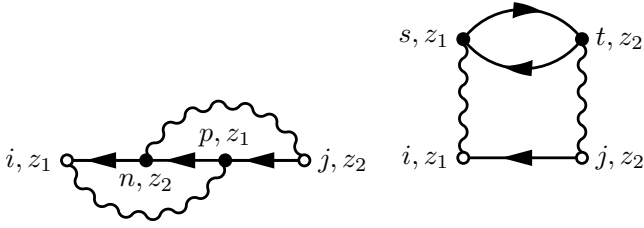
Figure 22. Selfconsistent second-order diagrams in the diagonal basis. Left: Exchange diagram $\Sigma^{(2),1,1,\text{diagonal}}$. Right: Direct diagram, $\Sigma^{(2),2,0,\text{diagonal}}$.
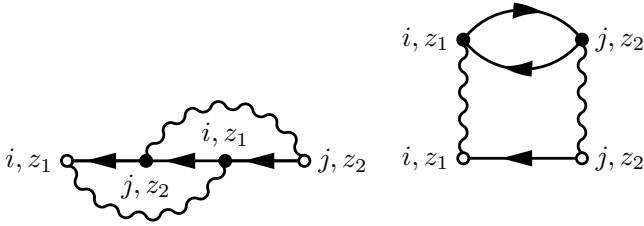

Figure 23. Selfconsistent second-order diagrams for spin-0 bosons in the Hubbard basis. Left: Exchange diagram $\Sigma^{(2),1,1,\text{Hubbard},\mathfrak{b},0}$. Right: Direct diagram, $\Sigma^{(2),2,0,\text{Hubbard},\mathfrak{b},0}$. Note that both diagrams coincide for the Hubbard basis.
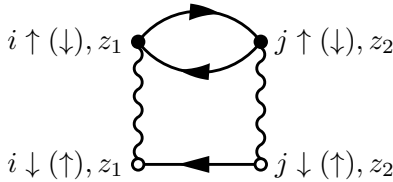

Figure 24. Selfconsistent second-order diagram for spin-1/2 fermions in the Hubbard basis, $\Sigma^{(2),2,0,\text{Hubbard},\mathfrak{f},1/2}$.

$$\Sigma^{(2),1,1,\text{Hubbard},\mathfrak{b}}_{i\alpha j\alpha}\left(z_1, z_2\right) \tag{194}$$
$$= \left(\mathrm{i}\hbar\right)^2 U\left(z_1\right) G_{i\alpha j\alpha}\left(z_1, z_2\right) U\left(z_2\right) G_{j\alpha i\alpha}\left(z_2, z_1\right) G_{i\alpha j\alpha}\left(z_1, z_2\right).$$

Similarly, we obtain for fermions:

$$\Sigma^{(2),2,0,\text{Hubbard},\mathfrak{f}}_{i\alpha j\alpha}\left(z_1, z_2\right) \tag{195}$$
$$= -\left(\mathrm{i}\hbar\right)^2 G_{i\alpha j\alpha}\left(z_1, z_2\right) U\left(z_1\right) \sum_{\epsilon \neq \alpha} G_{i\epsilon j\epsilon}\left(z_1, z_2\right) G_{j\epsilon i\epsilon}\left(z_2, z_1\right) U\left(z_2\right),$$

whereas the second expression vanishes, $\Sigma^{(2),1,1,\text{Hubbard},\mathfrak{f}}_{i\alpha j\alpha}\left(z_1, z_2\right) \equiv 0$.

The corresponding '$\gtrless$' Keldysh matrix components read, for bosons,

$$\Sigma^{(2),2,0,\text{Hubbard},\mathfrak{b},\gtrless}_{i\alpha j\alpha}\left(t_1, t_2\right)$$
$$= \left(\mathrm{i}\hbar\right)^2 G^{\gtrless}_{i\alpha j\alpha}\left(t_1, t_2\right) U\left(t_1\right) \sum_{\epsilon} G^{\gtrless}_{i\epsilon j\epsilon}\left(t_1, t_2\right) G^{\lessgtr}_{j\epsilon i\epsilon}\left(t_2, t_1\right) U\left(t_2\right),$$
$$\Sigma^{(2),1,1,\text{Hubbard},\mathfrak{b},\gtrless}_{i\alpha j\alpha}\left(t_1, t_2\right)$$
$$= \left(\mathrm{i}\hbar\right)^2 U\left(t_1\right) G^{\gtrless}_{i\alpha j\alpha}\left(t_1, t_2\right) U\left(t_2\right) G^{\lessgtr}_{j\alpha i\alpha}\left(t_2, t_1\right) G^{\gtrless}_{i\alpha j\alpha}\left(t_1, t_2\right).$$

Analogously, we have, for fermions,

$$\Sigma^{(2),2,0,\text{Hubbard},\mathfrak{f},\gtrless}_{i\alpha j\alpha}\left(t_1, t_2\right) = -\left(\mathrm{i}\hbar\right)^2 G^{\gtrless}_{i\alpha j\alpha}\left(t_1, t_2\right) U\left(t_1\right) \sum_{\epsilon \neq \alpha}$$
$$G^{\gtrless}_{i\epsilon j\epsilon}\left(t_1, t_2\right) G^{\lessgtr}_{j\epsilon i\epsilon}\left(t_2, t_1\right) U\left(t_2\right)$$

and, as before, $\Sigma^{(2),1,1,\text{Hubbard},\mathfrak{f},\gtrless}_{i\alpha j\alpha}\left(t_1, t_2\right) \equiv 0$.

We again consider the special cases of spin-0 bosons and spin-1/2 fermions, respectively. For spin-0 bosons, the self-consistent second-order contributions are given by

$$\Sigma^{(2),2,0,\text{Hubbard},\mathfrak{b},0}_{ij}\left(z_1, z_2\right) \tag{196}$$
$$= \left(\mathrm{i}\hbar\right)^2 G_{ij}\left(z_1, z_2\right) U\left(z_1\right) G_{ij}\left(z_1, z_2\right) G_{ji}\left(z_2, z_1\right) U\left(z_2\right),$$

$$\Sigma^{(2),1,1,\text{Hubbard},\mathfrak{b},0}_{ij}\left(z_1, z_2\right) \tag{197}$$
$$= \left(\mathrm{i}\hbar\right)^2 U\left(z_1\right) G_{ij}\left(z_1, z_2\right) U\left(z_2\right) G_{ji}\left(z_2, z_1\right) G_{ij}\left(z_1, z_2\right).$$

Similarly, for spin-1/2 fermions we obtain

$$\Sigma^{(2),2,0,\text{Hubbard},\mathfrak{f},1/2}_{i\downarrow(\uparrow)j\downarrow(\uparrow)}\left(z_1, z_2\right)$$
$$= -\left(\mathrm{i}\hbar\right)^2 G_{i\downarrow(\uparrow)j\downarrow(\uparrow)}\left(z_1, z_2\right) U\left(z_1\right) G_{i\uparrow(\downarrow)j\uparrow(\downarrow)}\left(z_1, z_2\right)$$
$$G_{j\uparrow(\downarrow)i\uparrow(\downarrow)}\left(z_2, z_1\right) U\left(z_2\right). \tag{198}$$

The Feynman diagrams of the self-consistent second-order selfenergy contributions for spin-0 bosons and spin-1/2 fermions are depicted in figures 23 and 24, respectively.

Consider again the corresponding '>' and '<' Keldysh matrix components. For spin-0 bosons, we have

$$\Sigma^{(2),2,0,\text{Hubbard},\mathfrak{b},0,\gtrless}_{ij}\left(t_1, t_2\right)$$
$$= \left(\mathrm{i}\hbar\right)^2 G^{\gtrless}_{ij}\left(t_1, t_2\right) U\left(t_1\right) G^{\gtrless}_{ij}\left(t_1, t_2\right) G^{\lessgtr}_{ji}\left(t_2, t_1\right) U\left(t_2\right),$$
$$\Sigma^{(2),1,1,\text{Hubbard},\mathfrak{b},0,\gtrless}_{ij}\left(t_1, t_2\right)$$
$$= \left(\mathrm{i}\hbar\right)^2 U\left(t_1\right) G^{\gtrless}_{ij}\left(t_1, t_2\right) U\left(t_2\right) G^{\lessgtr}_{ji}\left(t_2, t_1\right) G^{\gtrless}_{ij}\left(t_1, t_2\right).$$

In similar manner, we find the correlation components for spin-1/2 fermions:

$$\Sigma^{(2),2,0,\text{Hubbard},\mathfrak{f},1/2,\gtrless}_{i\downarrow(\uparrow)j\downarrow(\uparrow)}\left(t_1, t_2\right) = -\left(\mathrm{i}\hbar\right)^2 G^{\gtrless}_{i\downarrow(\uparrow)j\downarrow(\uparrow)}\left(t_1, t_2\right)$$
$$U\left(t_1\right) G^{\gtrless}_{i\uparrow(\downarrow)j\uparrow(\downarrow)}\left(t_1, t_2\right) G^{\lessgtr}_{j\uparrow(\downarrow)i\uparrow(\downarrow)}\left(t_2, t_1\right) U\left(t_2\right),$$

whereas the second contribution vanishes, as before.

4.3. Third-order selfenergy (TOA)

After discussing the frequently used first- and second-order contributions, we now turn to the selfenergy approximations

that are of third order in the interaction. We have seen in the results section 3 that, in many cases, the third order provides surprisingly accurate results. On the other hand, this approximation has not been discussed in the literature before. Therefore, we discuss the third-order approximation and its different variants in detail below.

The structure of the selfconsistent third-order contributions to the selfenergy can again be deduced from equation (101). There is a total of three terms that contribute to the third-order selfenergy

$$\Sigma^{(3),3,0} = \Sigma^{\mathrm{xc}}\Big(W^{(3)}, \Gamma^{(0)}\Big), \tag{199}$$

$$\Sigma^{(3),2,1} = \Sigma^{\mathrm{xc}}\Big(W^{(2)}, \Gamma^{(1)}\Big), \tag{200}$$

$$\Sigma^{(3),1,2} = \Sigma^{\mathrm{xc}}\Big(W^{(1)}, \Gamma^{(2)}\Big). \tag{201}$$

For the first class, in turn, there exist two contributions to $W^{(3)}$:

$$W^{(3),0,2} = W^{\mathrm{ns}}\Big(P^{(0)}, W^{(2)}\Big), \qquad W^{(3),1,1} = W^{\mathrm{ns}}\Big(P^{(1)}, W^{(1)}\Big). \tag{202}$$

Using equation (104), together with equation (174), one finds[21]

$$
\begin{aligned}
&W^{(3),0,2}\big(1,2\big)\\
&= w\big(1,3\big)P^{(0)}\big(3,4\big)\\
&\quad W^{(2)}\big(4,2\big)\\
&= \big(\mathrm{i}\hbar\big)^2 w\big(1,3\big)G\big(3,4\big)G\big(4,3\big)\\
&\quad w\big(4,5\big)G\big(5,6\big)G\big(6,5\big)w\big(6,2\big)
\end{aligned}
\tag{203}
$$

Combining this with equation (155), the first term of the first third-order selfenergy class, $\Sigma^{(3),3,0}$, becomes

$$
\begin{aligned}
&\Sigma^{(3),\{3;0,2\},0}\big(1,2\big)\\
&= \mathrm{i}\hbar W^{(3),0,2}\big(1,3\big)G\big(1,4\big)\\
&\quad \Gamma^{(0)}\big(4,2,3\big)\\
&= \big(\mathrm{i}\hbar\big)^3 G\big(1,2\big)w\big(1,3\big)G\big(3,4\big)G\big(4,3\big)\\
&\quad w\big(4,5\big)G\big(5,6\big)G\big(6,5\big)w\big(6,2\big)
\end{aligned}
\tag{204}
$$

or, in the full notation,

$$
\begin{aligned}
\Sigma^{(3),\{3;0,2\},0}_{ij}\big(z_1,z_2\big)
&= \big(\mathrm{i}\hbar\big)^3 \sum_{mn} G_{mn}\big(z_1,z_2\big) \sum_{rs} w_{irsm}\big(z_1\big) \int_{\mathcal{C}} \mathrm{d}z_3 \sum_{tu} G_{st}\big(z_1,z_3\big) G_{ur}\big(z_3,z_1\big)\\
&\quad \times \sum_{vw} w_{tvwu}\big(z_3\big) \sum_{xy} G_{wx}\big(z_3,z_2\big) G_{yv}\big(z_2,z_3\big) w_{xnjy}\big(z_2\big).
\end{aligned}
\tag{205}
$$

---

[21] The corresponding equations in the full notation are given in section 1.2.1 of the supplement 20.

For the second class of the interaction, $W^{(3),1,1}$, contributing to equation (199), the first-order contribution to the polarization is needed, which is given by[22], (see equations (105) and (181)),

$$
\begin{aligned}
P^{(1)}\big(1,2\big) \\
= \pm \mathrm{i}\hbar G\big(1,3\big)G\big(4,1\big)\Gamma^{(1)}\big(3,4,2\big) \\
= \pm \big(\mathrm{i}\hbar\big)^2 G\big(1,3\big)G\big(4,1\big) \\
w\big(3,4\big)G\big(3,2\big)G\big(2,4\big)
\end{aligned}
\qquad
\begin{aligned}
&\mapsto \pm \mathrm{i}\hbar \\
&= \pm \big(\mathrm{i}\hbar\big)^2
\end{aligned}
\tag{206}
$$

Inserting this result back, one finds, using equation (104),

$$
\begin{aligned}
W^{(3),1,1}\big(1,2\big) \\
= w\big(1,3\big)P^{(1)}\big(3,4\big)W^{(1)}\big(4,2\big) \\
= \pm \big(\mathrm{i}\hbar\big)^2 w\big(1,3\big)G\big(3,5\big)G\big(6,3\big) \\
w\big(5,6\big)G\big(5,4\big)G\big(4,6\big)w\big(4,2\big)
\end{aligned}
\qquad
\begin{aligned}
&\mapsto \\
&= \pm \big(\mathrm{i}\hbar\big)^2
\end{aligned}
\tag{207}
$$

With these results, the second term of the class $\Sigma^{(3),3,0}$ is found, using equations (101) and (155),

$$
\begin{aligned}
\Sigma^{(3),\{3;1,1\},0}\big(1,2\big) \\
= \mathrm{i}\hbar W^{(3),1,1}\big(1,3\big)G\big(1,4\big) \\
\Gamma^{(0)}\big(4,2,3\big) \\
= \pm \big(\mathrm{i}\hbar\big)^3 w\big(1,3\big)G\big(3,5\big)G\big(6,3\big) \\
w\big(5,6\big)G\big(5,4\big)G\big(4,6\big)w\big(4,2\big)G\big(1,2\big)
\end{aligned}
\qquad
\begin{aligned}
&\mapsto \mathrm{i}\hbar \\
&= \pm \big(\mathrm{i}\hbar\big)^3
\end{aligned}
\tag{208}
$$

or, in the full notation,

$$
\begin{aligned}
\Sigma_{ij}^{(3),\{3;1,1\},0}\big(z_1,z_2\big) \\
= \pm \big(\mathrm{i}\hbar\big)^3 \sum_{mn} G_{mn}\big(z_1,z_2\big) \sum_{rs} w_{irsm}\big(z_1\big) \int_{\mathcal{C}} \mathrm{d}z_3 \sum_t G_{st}\big(z_1,z_3\big) \sum_u G_{ur}\big(z_3,z_1\big) \\
\times \sum_{vw} w_{twuv}\big(z_3\big) \sum_{xy} G_{vx}\big(z_3,z_2\big) G_{yw}\big(z_2,z_3\big) w_{xnjy}\big(z_2\big).
\end{aligned}
\tag{209}
$$

---

[22] The corresponding equations in the full notation are given in section 1.2.2 of the supplement 20.

We continue with the second class, $\Sigma^{(3),2,1}$, which is straightforwardly worked out[23] by combining equations (174) and (181),

$$
\begin{aligned}
\Sigma^{(3),2,1}\left(1,2\right) &= i\hbar W^{(2)}\left(1,3\right) \\
&\quad G\left(1,4\right)\Gamma^{(1)}\left(4,2,3\right) \\
&= \pm\left(i\hbar\right)^{3} w\left(1,5\right)G\left(5,6\right)G\left(6,5\right) \\
&\quad w\left(6,3\right)G\left(1,4\right)w\left(4,2\right)G\left(4,3\right)G\left(3,2\right)
\end{aligned}
$$

(210)

or, in the full notation,

$$
\begin{aligned}
\Sigma_{ij}^{(3),2,1}&\left(z_1,z_2\right) \\
&= \pm\left(i\hbar\right)^{3}\int_{\mathcal{C}} dz_3 \sum_{mrs} w_{irsm}\left(z_1\right)\sum_{tu} G_{st}\left(z_1,z_3\right)G_{ur}\left(z_3,z_1\right)\sum_{pq} w_{tpqu}\left(z_3\right) \\
&\quad \times \sum_{n} G_{mn}\left(z_1,z_2\right)\sum_{vw} w_{nwjv}\left(z_2\right)G_{vp}\left(z_2,z_3\right)G_{qw}\left(z_3,z_2\right).
\end{aligned}
$$

(211)

For the third class $\Sigma^{(3),1,2}$, the second-order contributions to the vertex, $\Gamma^{(2)}$, have to be computed. There are two structural classes to consider:

$$
\Gamma^{(2),1,1} = \Gamma\left(\delta\Sigma^{xc,(1)}/\delta G, \Gamma^{(1)}\right),
$$

(212)

$$
\Gamma^{(2),2,0} = \Gamma\left(\delta\Sigma^{xc,(2)}/\delta G, \Gamma^{(0)}\right).
$$

(213)

For the class $\Gamma^{(2),1,1}$, there exists a single contribution[24], which is found by employing equations (179) and (181),

$$
\begin{aligned}
\Gamma^{(2),1,1}\left(1,2,3\right) &= \frac{\delta\Sigma^{xc,(1)}\left(1,2\right)}{\delta G\left(4,5\right)} \\
&\quad G\left(4,6\right)G\left(7,5\right)\Gamma^{(1)}\left(6,7,3\right) \\
&= \left(i\hbar\right)^{2} w\left(1,2\right)G\left(1,6\right) \\
&\quad G\left(7,2\right)w\left(6,7\right)G\left(6,3\right)G\left(3,7\right)
\end{aligned}
$$

(214)

This enables the computation of $\Sigma^{(3),1,\{2;1,1\}}$ with equations (101) and (154),

$$
\begin{aligned}
\Sigma^{(3),1,\{2;1,1\}}\left(1,2\right) &= i\hbar W^{(1)}\left(1,3\right) \\
&\quad G\left(1,4\right)\Gamma^{(2),1,1}\left(4,2,3\right) \\
&= \left(i\hbar\right)^{3} w\left(1,3\right)G\left(1,4\right)w\left(4,2\right)G\left(4,5\right) \\
&\quad G\left(6,2\right)w\left(5,6\right)G\left(5,3\right)G\left(3,6\right)
\end{aligned}
$$

(215)

---

[23] The corresponding equations in the full notation are given in section 1.2.3 of the supplement 20.

[24] The corresponding equations in the full notation are given in section 1.2.4 of the supplement 20.

i.e. in the full notation,

$$
\Sigma_{ij}^{(3),1,\{2;1,1\}}\left(z_1, z_2\right)
$$

$$
= \left(i\hbar\right)^3 \sum_{mpq} w_{ipqm}\left(z_1\right) \sum_n G_{mn}\left(z_1, z_2\right) \sum_{rs} w_{nsjr}\left(z_2\right) \int_{\mathcal{C}} dz_3 \sum_t G_{rt}\left(z_2, z_3\right)
$$

$$
\times \sum_u G_{us}\left(z_3, z_2\right) \sum_{vw} w_{twuv}\left(z_3\right) G_{vp}\left(z_3, z_1\right) G_{qw}\left(z_1, z_3\right). \tag{216}
$$

The vertex class $\Gamma^{(2),2,0}$ has six members stemming from the derivatives with respect to each of the three Green functions in both second-order contributions to $\Sigma^{(2)}$, see equations (176) and (183),

$$
\Gamma^{(2),\{2;2,0\},0} = \Gamma\left(\delta\Sigma^{(2),2,0}/\delta G, \Gamma^{(0)}\right), \tag{217}
$$

$$
\Gamma^{(2),\{2;1,1\},0} = \Gamma\left(\delta\Sigma^{(2),1,1}/\delta G, \Gamma^{(0)}\right). \tag{218}
$$

For the first terms, one finds[25]

$$(219)$$

Inserting equation (176), the occurring derivative evaluates to

$$(220)$$

With that, the resulting vertex splits up into three parts labeled 'A', 'B' and 'C':

$$(221)$$

[25] The corresponding equations in the full notation are given in section 1.2.5 of the supplement 20.

$$\Gamma^{(2),\{2;2,0\},0,\mathrm{B}}\big(1,2,3\big)$$

$$= \frac{\delta\Sigma^{(2),2,0,\mathrm{B}}\big(1,2\big)}{\delta G\big(4,5\big)}G\big(4,3\big)G\big(3,5\big)$$

$$= \pm\big(\mathrm{i}\hbar\big)^2 w\big(1,4\big)G\big(5,4\big)$$

$$w\big(5,2\big)G\big(1,2\big)G\big(4,3\big)G\big(3,5\big)$$

(222)

$$\Gamma^{(2),\{2;2,0\},0,\mathrm{C}}\big(1,2,3\big)$$

$$= \frac{\delta\Sigma^{(2),2,0,\mathrm{C}}\big(1,2\big)}{\delta G\big(4,5\big)}G\big(4,3\big)G\big(3,5\big)$$

$$= \pm\big(\mathrm{i}\hbar\big)^2 w\big(1,5\big)G\big(5,4\big)$$

$$w\big(4,2\big)G\big(1,2\big)G\big(4,3\big)G\big(3,5\big)$$

(223)

Similarly, one finds

$$\Gamma^{(2),\{2;1,1\},0}\big(1,2,3\big) =$$

$$\frac{\delta\Sigma^{(2),1,1}\big(1,2\big)}{\delta G\big(4,5\big)}G\big(4,3\big)G\big(3,5\big)$$

(224)
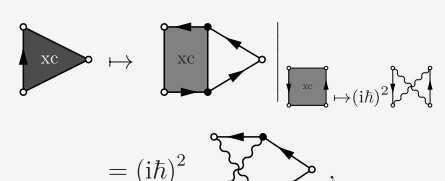
Inserting equation (183), the occurring derivative evaluates to
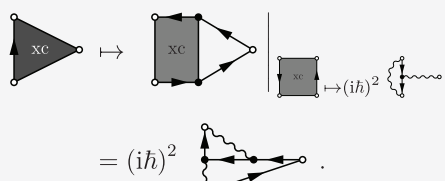
$$\frac{\delta\Sigma^{(2),1,1}\big(1,2\big)}{\delta G\big(4,5\big)} = \big(\mathrm{i}\hbar\big)^2 \frac{\delta\big(w\big(1,6\big)G\big(1,7\big)w\big(7,2\big)G\big(7,6\big)G\big(6,2\big)\big)}{\delta G\big(4,5\big)}$$

$$= \big(\mathrm{i}\hbar\big)^2 \delta\big(1,4\big)w\big(1,6\big)w\big(5,2\big)G\big(5,6\big)G\big(6,2\big)$$

$$+ \big(\mathrm{i}\hbar\big)^2 w\big(1,5\big)G\big(1,4\big)w\big(4,2\big)G\big(5,2\big)$$

$$+ \big(\mathrm{i}\hbar\big)^2 \delta\big(2,5\big)w\big(1,4\big)G\big(1,7\big)w\big(7,2\big)G\big(7,4\big)$$

(225)

Again, three vertex contributions A, B and C are generated:

$$
\begin{aligned}
&\Gamma^{(2),\{2;1,1\},0,A}(1,2,3) \\
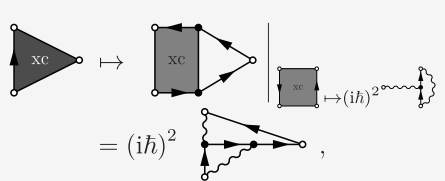&= \frac{\delta\Sigma^{(2),1,1,A}(1,2)}{\delta G(4,5)}G(4,3)G(3,5) \\
&= (i\hbar)^2 w(1,6)w(5,2)G(5,6) \\
&\quad G(6,2)G(1,3)G(3,5)
\end{aligned}
$$

(226)

$$
\begin{aligned}
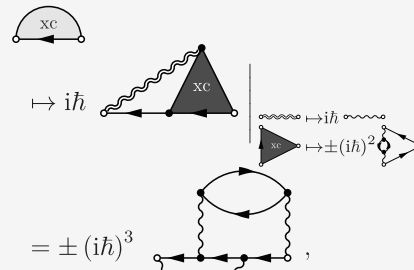&\Gamma^{(2),\{2;1,1\},0,B}(1,2,3) \\
&= \frac{\delta\Sigma^{(2),1,1,B}(1,2)}{\delta G(4,5)}G(4,3)G(3,5) \\
&= (i\hbar)^2 w(1,5)G(1,4)w(4,2) \\
&\quad G(5,2)G(4,3)G(3,5)
\end{aligned}
$$

(227)

$$
\begin{aligned}
&\Gamma^{(2),\{2;1,1\},0,C}(1,2,3) \\
&= \frac{\delta\Sigma^{(2),1,1,C}(1,2)}{\delta G(4,5)}G(4,3)G(3,5) \\
&= (i\hbar)^2 w(1,4)G(1,7)w(7,2) \\
&\quad G(7,4)G(4,3)G(3,2)
\end{aligned}
$$

(228)

With this result, the corresponding selfenergy terms[26] can be computed by combining equations (101) and (154) with equations (221)–(228),

$$
\begin{aligned}
&\Sigma^{(3),1,\{2;\{2;2,0\},0,A\}}(1,2) = i\hbar W^{(1)}(1,3) \\
&\quad G(1,4)\Gamma^{(2),\{2;2,0\},0,A}(4,2,3) \\
&= \pm(i\hbar)^3 w(1,3)G(1,4)w(4,6) \\
&\quad G(6,7)G(7,6)w(7,2)G(4,3)G(3,2)
\end{aligned}
$$

(229)

$$\Sigma^{(3),1,\{2;\{2;2,0\},0,\text{B}\}}\left(1,2\right) = \mathrm{i}\hbar W^{(1)}\left(1,3\right)$$
$$G\left(1,4\right)\Gamma^{(2),\{2;2,0\},0,\text{B}}\left(4,2,3\right)$$
$$= \pm\left(\mathrm{i}\hbar\right)^{3} w\left(1,3\right) G\left(1,4\right) w\left(4,5\right)$$
$$G\left(6,5\right) w\left(6,2\right) G\left(4,2\right) G\left(5,3\right) G\left(3,6\right)$$

(230)

$$\Sigma^{(3),1,\{2;\{2;2,0\},0,\text{C}\}}\left(1,2\right) = \mathrm{i}\hbar W^{(1)}\left(1,3\right)$$
$$G\left(1,4\right)\Gamma^{(2),\{2;2,0\},0,\text{C}}\left(4,2,3\right)$$
$$= \pm\left(\mathrm{i}\hbar\right)^{3} w\left(1,3\right) G\left(1,4\right) w\left(4,6\right)$$
$$G\left(6,5\right) w\left(5,2\right) G\left(4,2\right) G\left(5,3\right) G\left(3,6\right)$$

(231)

$$\Sigma^{(3),1,\{2;\{2;1,1\},0,\text{A}\}}\left(1,2\right) = \mathrm{i}\hbar W^{(1)}\left(1,3\right)$$
$$G\left(1,4\right)\Gamma^{(2),\{2;1,1\},0,\text{A}}\left(4,2,3\right)$$
$$= \left(\mathrm{i}\hbar\right)^{3} w\left(1,3\right) G\left(1,4\right) w\left(4,6\right) w\left(5,2\right)$$
$$G\left(5,6\right) G\left(6,2\right) G\left(4,3\right) G\left(3,5\right)$$

(232)

$$\Sigma^{(3),1,\{2;\{2;1,1\},0,\text{B}\}}\left(1,2\right) = \mathrm{i}\hbar W^{(1)}\left(1,3\right)$$
$$G\left(1,4\right)\Gamma^{(2),\{2;1,1\},0,\text{B}}\left(4,2,3\right)$$
$$= \left(\mathrm{i}\hbar\right)^{3} w\left(1,3\right) G\left(1,4\right) w\left(4,6\right) G\left(4,5\right)$$
$$w\left(5,2\right) G\left(6,2\right) G\left(5,3\right) G\left(3,6\right)$$

(233)

$$\Sigma^{(3),1,\{2;\{2;1,1\},0,C\}}(1,2) = i\hbar W^{(1)}(1,3)$$
$$G(1,4)\Gamma^{(2),\{2;1,1\},0,C}(4,2,3)$$
$$= (i\hbar)^3 w(1,3)G(1,4)w(4,5)G(4,6)$$
$$w(6,2)G(6,5)G(5,3)G(3,2)$$

(234)

In the full notation, these contributions read,

$$\Sigma_{ij}^{(3),1,\{2;\{2;2,0\},0,A\}}(z_1,z_2) = \pm(i\hbar)^3 \sum_{mpq} w_{ipqm}(z_1)$$

(235)

$$\times \int_{\mathcal{C}} dz_4 \sum_n G_{mn}(z_1,z_4) \sum_{rsuv} G_{uv}(z_4,z_2) \sum_t w_{ntur}(z_4)$$

$$\times \sum_w w_{vsjw}(z_2) G_{wt}(z_2,z_4) G_{rp}(z_4,z_1) G_{qs}(z_1,z_2),$$

$$\Sigma_{ij}^{(3),1,\{2;\{2;2,0\},0,B\}}(z_1,z_2)$$

(236)

$$= \pm(i\hbar)^3 \sum_{mpq} w_{ipqm}(z_1) \int_{\mathcal{C}} dz_4 \sum_n G_{mn}(z_1,z_4) \sum_{rs}\sum_{tu} G_{tu}(z_4,z_2)$$

$$\times \sum_v w_{nvrt}(z_4) \sum_w w_{sujw}(z_2) G_{wv}(z_2,z_4) G_{rp}(z_4,z_1) G_{qs}(z_1,z_2),$$

$$\Sigma_{ij}^{(3),1,\{2;\{2;2,0\},0,C\}}(z_1,z_2)$$

(237)

$$= \pm(i\hbar)^3 \sum_{mpq} w_{ipqm}(z_1) \int_{\mathcal{C}} dz_4 \sum_n G_{mn}(z_1,z_4) \sum_{rs}\sum_{tu} G_{tu}(z_4,z_2)$$

$$\times \sum_{vw} G_{vw}(z_4,z_2) w_{nsvt}(z_4) w_{wujr}(z_2) G_{rp}(z_2,z_1) G_{qs}(z_1,z_4),$$

$$\Sigma_{ij}^{(3),1,\{2;\{2;1,1\},0,A\}}(z_1,z_2)$$

(238)

$$= (i\hbar)^3 \sum_{mpq} w_{ipqm}(z_1) \int_{\mathcal{C}} dz_4 \sum_n G_{mn}(z_1,z_4) \sum_{rs}\sum_{tu} w_{ntur}(z_4)$$

$$\times \sum_{vw} w_{swjv}(z_2) G_{vt}(z_2,z_4) G_{uw}(z_4,z_2) G_{rp}(z_4,z_1) G_{qs}(z_1,z_2),$$

$$\Sigma_{ij}^{(3),1,\{2;\{2;1,1\},0,B\}}(z_1,z_2)$$

(239)

$$= (i\hbar)^3 \sum_{mpq} w_{ipqm}(z_1) \int_{\mathcal{C}} dz_4 \sum_n G_{mn}(z_1,z_4) \sum_{rs}\sum_{tv} w_{nsvt}(z_4)$$

$$\times \sum_u G_{tu}(z_4,z_2) \sum_w w_{uwjr}(z_2) G_{vw}(z_4,z_2) G_{rp}(z_2,z_1) G_{qs}(z_1,z_4),$$

$$\Sigma_{ij}^{(3),1,\{2;\{2;1,1\},0,C\}}(z_1,z_2)$$

(240)

$$= (i\hbar)^3 \sum_{mpq} w_{ipqm}(z_1) \int_{\mathcal{C}} dz_4 \sum_n G_{mn}(z_1,z_4) \sum_{rs}\sum_{tv} w_{nvrt}(z_4)$$

$$\times \sum_u G_{tu}(z_4,z_2) \sum_w w_{usjw}(z_2) G_{wv}(z_2,z_4) G_{rp}(z_4,z_1) G_{qs}(z_1,z_2).$$

'>' and '<' Keldysh coomponents: Let us now turn to the '$\gtrless$' components which are the central ingredient for

the numerical implementation. For all third-order selfenergy terms these components can be computed in a generic fashion, splitting all integrals at the points where the arguments of each Green function change their relative ordering on the contour. Consider first the '<' component, to $\Sigma_{ij}^{(3),1,\{2;\{2;2,0\},0,B\}}(z_1,z_2)$. The result consists of three terms, (see equation (74)),

$$\Sigma_{ij}^{(3),1,\{2;\{2;2,0\},0,B\},<}(t_1,t_2) = \Sigma_{ij}^{(3),1,\{2;\{2;2,0\},0,B\},<}(z_{1-},z_{2+})$$

$$= \pm(i\hbar)^3 \sum_{mpq} w_{ipqm}(z_{1-})$$

$$\times \left\{ I_{mpq}^{1,<}(z_{1-},z_{2+}) + I_{mpq}^{2,<}(z_{1-},z_{2+}) + I_{mpq}^{3,<}(z_{1-},z_{2+}) \right\},$$

(241)

with the three terms given by

$$I_{mpq}^{1,<}(z_{1-},z_{2+}) = \int_{z_{0-}}^{z_{1-}} dz_4 \sum_n G_{mn}^>(z_{1-},z_4)$$

(242)

$$\times \sum_{rs}\sum_{tu} G_{tu}^<(z_4,z_{2+}) \sum_v w_{nvrt}(z_4)$$

$$\times \sum_w w_{sujw}(z_{2+}) G_{wv}^>(z_{2+},z_4) G_{rp}^<(z_4,z_{1-}) G_{qs}^<(z_{1-},z_{2+}),$$

$$I_{mpq}^{2,<}(z_{1-},z_{2+}) = \int_{z_{1-}}^{z_{2+}} dz_4 \sum_n G_{mn}^<(z_{1-},z_4)$$

(243)

$$\times \sum_{rs}\sum_{tu} G_{tu}^<(z_4,z_{2+}) \sum_v w_{nvrt}(z_4)$$

$$\times \sum_w w_{sujw}(z_{2+}) G_{wv}^>(z_{2+},z_4) G_{rp}^>(z_4,z_{1-}) G_{qs}^<(z_{1-},z_{2+}),$$

$$I_{mpq}^{3,<}(z_{1-},z_{2+}) = \int_{z_{2+}}^{z_{0+}} dz_4 \sum_n G_{mn}^<(z_{1-},z_4)$$

(244)

$$\sum_{rs}\sum_{tu} G_{tu}^>(z_4,z_{2+}) \sum_v w_{nvrt}(z_4)$$

$$\sum_w w_{sujw}(z_{2+}) G_{wv}^<(z_{2+},z_4) G_{rp}^>(z_4,z_{1-}) G_{qs}^<(z_{1-},z_{2+}).$$

We now transform these expression to real-time integrals:

$$\Sigma_{ij}^{(3),1,\{2;\{2;2,0\},0,B\},<}(t_1,t_2) = \pm(i\hbar)^3 \sum_{mpq} w_{ipqm}(t_1)$$

$$\times \left\{ I_{mpq}^{1,<}(t_1,t_2) + I_{mpq}^{2,<}(t_1,t_2) + I_{mpq}^{3,<}(t_1,t_2) \right\},$$

(245)

with the corresponding results for the three contributions

$$
I^{1,<}_{mpq}\left(t_1,t_2\right) = \int_{t_0}^{t_1} dt_4 \sum_n G^{>}_{mn}\left(t_1,t_4\right) \tag{246}
$$
$$
\times \sum_{rs}\sum_{tu} G^{<}_{tu}\left(t_4,t_2\right)\sum_v w_{nvrt}\left(t_4\right)
$$
$$
\times \sum_w w_{sujw}\left(t_2\right) G^{>}_{wv}\left(t_2,t_4\right) G^{<}_{rp}\left(t_4,t_1\right) G^{<}_{qs}\left(t_1,t_2\right),
$$

$$
I^{2,<}_{mpq}\left(t_1,t_2\right) = \int_{t_1}^{t_2} dt_4 \sum_n G^{<}_{mn}\left(t_1,t_4\right) \tag{247}
$$
$$
\times \sum_{rs}\sum_{tu} G^{<}_{tu}\left(t_4,t_2\right)\sum_v w_{nvrt}\left(t_4\right)
$$
$$
\times \sum_w w_{sujw}\left(t_2\right) G^{>}_{wv}\left(t_2,t_4\right) G^{>}_{rp}\left(t_4,t_1\right) G^{<}_{qs}\left(t_1,t_2\right),
$$

$$
I^{3,<}_{mpq}\left(t_1,t_2\right) = \int_{t_2}^{t_0} dt_4 \sum_n G^{<}_{mn}\left(t_1,t_4\right) \tag{248}
$$
$$
\times \sum_{rs}\sum_{tu} G^{>}_{tu}\left(t_4,t_2\right)\sum_v w_{nvrt}\left(t_4\right)
$$
$$
\times \sum_w w_{sujw}\left(t_2\right) G^{<}_{wv}\left(t_2,t_4\right) G^{>}_{rp}\left(t_4,t_1\right) G^{<}_{qs}\left(t_1,t_2\right).
$$

For the '>' component, we find analogously

$$
\Sigma^{(3),1,\{2;\{2;2,0\},0,B\},>}_{ij}\left(t_1,t_2\right) = \Sigma^{(3),1,\{2;\{2;2,0\},0,B\},>}_{ij}\left(z_{1+},z_{2-}\right)
$$
$$
= \pm\left(i\hbar\right)^3 \sum_{mpq} w_{ipqm}\left(z_{1+}\right)
$$
$$
\times \left\{ I^{1,>}_{mpq}\left(z_{1+},z_{2-}\right) + I^{2,>}_{mpq}\left(z_{1+},z_{2-}\right) + I^{3,>}_{mpq}\left(z_{1+},z_{2-}\right)\right\}, \tag{249}
$$

which, again, consists of three terms:

$$
I^{1,>}_{mpq}\left(z_{1+},z_{2-}\right) = \int_{z_{0-}}^{z_{2-}} dz_4 \sum_n G^{>}_{mn}\left(z_{1+},z_4\right) \tag{250}
$$
$$
\times \sum_{rs}\sum_{tu} G^{<}_{tu}\left(z_4,z_{2-}\right)\sum_v w_{nvrt}\left(z_4\right)
$$
$$
\times \sum_w w_{sujw}\left(z_{2-}\right) G^{>}_{wv}\left(z_{2-},z_4\right) G^{<}_{rp}\left(z_4,z_{1+}\right) G^{>}_{qs}\left(z_{1+},z_{2-}\right),
$$

$$
I^{2,>}_{mpq}\left(z_{1+},z_{2-}\right) = \int_{z_{2-}}^{z_{1+}} dz_4 \sum_n G^{>}_{mn}\left(z_{1+},z_4\right) \tag{251}
$$
$$
\times \sum_{rs}\sum_{tu} G^{>}_{tu}\left(z_4,z_{2-}\right)\sum_v w_{nvrt}\left(z_4\right)
$$
$$
\times \sum_w w_{sujw}\left(z_{2-}\right) G^{<}_{wv}\left(z_{2-},z_4\right) G^{<}_{rp}\left(z_4,z_{1+}\right) G^{>}_{qs}\left(z_{1+},z_{2-}\right),
$$

$$
I^{3,>}_{mpq}\left(z_{1+},z_{2-}\right) = \int_{z_{1+}}^{z_{0+}} dz_4 \sum_n G^{<}_{mn}\left(z_{1+},z_4\right) \tag{252}
$$
$$
\times \sum_{rs}\sum_{tu} G^{>}_{tu}\left(z_4,z_{2-}\right)\sum_v w_{nvrt}\left(z_4\right)
$$
$$
\times \sum_w w_{sujw}\left(z_{2-}\right) G^{<}_{wv}\left(z_{2-},z_4\right) G^{>}_{rp}\left(z_4,z_{1+}\right) G^{>}_{qs}\left(z_{1+},z_{2-}\right).
$$

Transforming, again, to real-time integrals, we obtain

$$
\Sigma^{(3),1,\{2;\{2;2,0\},0,B\},>}_{ij}\left(t_1,t_2\right) = \pm\left(i\hbar\right)^3 \sum_{mpq} w_{ipqm}\left(t_1\right)
$$
$$
\times \left\{ I^{1,>}_{mpq}\left(t_1,t_2\right) + I^{2,>}_{mpq}\left(t_1,t_2\right) + I^{3,>}_{mpq}\left(t_1,t_2\right)\right\}, \tag{253}
$$

with the three contributions becoming

$$
I^{1,>}_{mpq}\left(t_1,t_2\right) = \int_{t_0}^{t_2} dt_4 \sum_n G^{>}_{mn}\left(t_1,t_4\right) \tag{254}
$$
$$
\times \sum_{rs}\sum_{tu} G^{<}_{tu}\left(t_4,t_2\right)\sum_v w_{nvrt}\left(t_4\right)
$$
$$
\times \sum_w w_{sujw}\left(t_2\right) G^{>}_{wv}\left(t_2,t_4\right) G^{<}_{rp}\left(t_4,t_1\right) G^{>}_{qs}\left(t_1,t_2\right),
$$

$$
I^{2,>}_{mpq}\left(t_1,t_2\right) = \int_{t_2}^{t_1} dt_4 \sum_n G^{>}_{mn}\left(t_1,t_4\right) \tag{255}
$$
$$
\times \sum_{rs}\sum_{tu} G^{>}_{tu}\left(t_4,t_2\right)\sum_v w_{nvrt}\left(t_4\right)
$$
$$
\times \sum_w w_{sujw}\left(t_2\right) G^{<}_{wv}\left(t_2,t_4\right) G^{<}_{rp}\left(t_4,t_1\right) G^{>}_{qs}\left(t_1,t_2\right),
$$

$$
I^{3,>}_{mpq}\left(t_1,t_2\right) = \int_{t_1}^{t_0} dt_4 \sum_n G^{<}_{mn}\left(t_1,t_4\right) \tag{256}
$$
$$
\times \sum_{rs}\sum_{tu} G^{>}_{tu}\left(t_4,t_2\right)\sum_v w_{nvrt}\left(t_4\right)
$$
$$
\times \sum_w w_{sujw}\left(t_2\right) G^{<}_{wv}\left(t_2,t_4\right) G^{>}_{rp}\left(t_4,t_1\right) G^{>}_{qs}\left(t_1,t_2\right).
$$

Non-selfconsistent expansion: We now briefly discuss how the above results change in the case that all expressions are expanded in terms of noninteracting Green functions. The additional non-selfconsistent diagrams are of either of the structures

$$
\Sigma^{(3)}\left(G \longrightarrow G^{(0)}\right), \qquad \text{(10 terms)}
$$
$$
\Sigma^{(2)}\left(G^{(0)} \longrightarrow G^{(0)}\Sigma^{(1)}G^{(0)}\right), \qquad (6\cdot 2 = 12 \text{ terms})
$$
$$
\Sigma^{H}/\Sigma^{F}\left(G^{(0)} \longrightarrow G^{(0)}\Sigma^{(2)}G^{(0)}\right), \qquad (2\cdot 6 = 12 \text{ terms})
$$
$$
\Sigma^{H}/\Sigma^{F}\left(G^{(0)} \longrightarrow G^{(0)}\Sigma^{(1)}G^{(0)}\Sigma^{(1)}G^{(0)}\right), \quad (2\cdot 2\cdot 2 = 8 \text{ terms})
$$

This makes a total of 42 non-selfconsistent third-order terms.

4.3.1. Diagonal basis. In a diagonal basis, the selfconsistent third-order selfenergy contributions become

$$
\Sigma^{(3),\{3;0,2\},0,\text{diag}}_{ij}\left(z_1,z_2\right) \tag{257}
$$
$$
= \left(i\hbar\right)^3 G_{ij}\left(z_1,z_2\right)\sum_r w_{ir}\left(z_1\right)\int_C dz_3 \sum_t G_{rt}\left(z_1,z_3\right) G_{tr}\left(z_3,z_1\right)
$$
$$
\times \sum_v w_{tv}\left(z_3\right)\sum_x G_{vx}\left(z_3,z_2\right) G_{xv}\left(z_2,z_3\right) w_{xj}\left(z_2\right),
$$

$$\Sigma_{ij}^{(3),\{3;1,1\},0,\mathrm{diag}}\left(z_1,z_2\right) \tag{258}$$

$$= \pm\left(\mathrm{i}\hbar\right)^3 G_{ij}\left(z_1,z_2\right) \sum_r w_{ir}\left(z_1\right) \int_{\mathcal{C}} \mathrm{d}z_3 \sum_t G_{rt}\left(z_1,z_3\right) \sum_u G_{ur}\left(z_3,z_1\right)$$

$$\times w_{tu}\left(z_3\right) \sum_x G_{tx}\left(z_3,z_2\right) G_{xu}\left(z_2,z_3\right) w_{xj}\left(z_2\right),$$

$$\Sigma_{ij}^{(3),2,1,\mathrm{diag}}\left(z_1,z_2\right)$$

$$= \pm\left(\mathrm{i}\hbar\right)^3 \int_{\mathcal{C}} \mathrm{d}z_3 \sum_r w_{ir}\left(z_1\right) \sum_t G_{rt}\left(z_1,z_3\right) G_{tr}\left(z_3,z_1\right) \sum_p w_{tp}\left(z_3\right)$$

$$\times \sum_n G_{in}\left(z_1,z_2\right) w_{nj}\left(z_2\right) G_{np}\left(z_2,z_3\right) G_{pj}\left(z_3,z_2\right), \tag{259}$$

$$\Sigma_{ij}^{(3),1,\{2;1,1\},\mathrm{diag}}\left(z_1,z_2\right)$$

$$= \left(\mathrm{i}\hbar\right)^3 \sum_p w_{ip}\left(z_1\right) \sum_n G_{in}\left(z_1,z_2\right) w_{nj}\left(z_2\right) \int_{\mathcal{C}} \mathrm{d}z_3 \sum_t G_{nt}\left(z_2,z_3\right)$$

$$\times \sum_u G_{uj}\left(z_3,z_2\right) w_{tu}\left(z_3\right) G_{tp}\left(z_3,z_1\right) G_{pu}\left(z_1,z_3\right), \tag{260}$$

Now we again provide the three contributions labeled 'A, B, C', respectively:

$$\Sigma_{ij}^{(3),1,\{2;\{2;2,0\},0,\mathrm{A}\},\mathrm{diag}}\left(z_1,z_2\right) \tag{261}$$

$$= \pm\left(\mathrm{i}\hbar\right)^3 \sum_p w_{ip}\left(z_1\right) \int_{\mathcal{C}} \mathrm{d}z_4 \sum_n G_{in}\left(z_1,z_4\right) \sum_{tv} G_{tv}\left(z_4,z_2\right)$$

$$\times w_{nt}\left(z_4\right) w_{vj}\left(z_2\right) G_{vt}\left(z_2,z_4\right) G_{np}\left(z_4,z_1\right) G_{pj}\left(z_1,z_2\right),$$

$$\Sigma_{ij}^{(3),1,\{2;\{2;2,0\},0,\mathrm{B}\},\mathrm{diag}}\left(z_1,z_2\right) \tag{262}$$

$$= \pm\left(\mathrm{i}\hbar\right)^3 \sum_p w_{ip}\left(z_1\right) \int_{\mathcal{C}} \mathrm{d}z_4 \sum_n G_{in}\left(z_1,z_4\right) \sum_{rs} G_{nj}\left(z_4,z_2\right)$$

$$\times w_{nr}\left(z_4\right) w_{sj}\left(z_2\right) G_{sr}\left(z_2,z_4\right) G_{rp}\left(z_4,z_1\right) G_{ps}\left(z_1,z_2\right),$$

$$\Sigma_{ij}^{(3),1,\{2;\{2;2,0\},0,\mathrm{C}\},\mathrm{diag}}\left(z_1,z_2\right) \tag{263}$$

$$= \pm\left(\mathrm{i}\hbar\right)^3 \sum_p w_{ip}\left(z_1\right) \int_{\mathcal{C}} \mathrm{d}z_4 \sum_n G_{in}\left(z_1,z_4\right) \sum_{rs} G_{nj}\left(z_4,z_2\right)$$

$$\times G_{sr}\left(z_4,z_2\right) w_{ns}\left(z_4\right) w_{rj}\left(z_2\right) G_{rp}\left(z_2,z_1\right) G_{ps}\left(z_1,z_4\right)$$

and, similarly, for the second class of selfenergy contributions:

$$\Sigma_{ij}^{(3),1,\{2;\{2;1,1\},0,\mathrm{A}\},\mathrm{diag}}\left(z_1,z_2\right) \tag{264}$$

$$= \left(\mathrm{i}\hbar\right)^3 \sum_p w_{ip}\left(z_1\right) \int_{\mathcal{C}} \mathrm{d}z_4 \sum_n G_{in}\left(z_1,z_4\right) \sum_{st} w_{nt}\left(z_4\right)$$

$$\times w_{sj}\left(z_2\right) G_{st}\left(z_2,z_4\right) G_{tj}\left(z_4,z_2\right) G_{np}\left(z_4,z_1\right) G_{ps}\left(z_1,z_2\right),$$

$$\Sigma_{ij}^{(3),1,\{2;\{2;1,1\},0,\mathrm{B}\},\mathrm{diag}}\left(z_1,z_2\right) \tag{265}$$

$$= \left(\mathrm{i}\hbar\right)^3 \sum_p w_{ip}\left(z_1\right) \int_{\mathcal{C}} \mathrm{d}z_4 \sum_n G_{in}\left(z_1,z_4\right) \sum_{rs} w_{ns}\left(z_4\right)$$

$$\times G_{nr}\left(z_4,z_2\right) w_{rj}\left(z_2\right) G_{sj}\left(z_4,z_2\right) G_{rp}\left(z_2,z_1\right) G_{ps}\left(z_1,z_4\right),$$

$$\Sigma_{ij}^{(3),1,\{2;\{2;1,1\},0,\mathrm{C}\},\mathrm{diag}}\left(z_1,z_2\right) \tag{266}$$

$$= \left(\mathrm{i}\hbar\right)^3 \sum_p w_{ip}\left(z_1\right) \int_{\mathcal{C}} \mathrm{d}z_4 \sum_n G_{in}\left(z_1,z_4\right) \sum_r w_{nr}\left(z_4\right)$$

$$\times \sum_u G_{nu}\left(z_4,z_2\right) w_{uj}\left(z_2\right) G_{ur}\left(z_2,z_4\right) G_{rp}\left(z_4,z_1\right) G_{pj}\left(z_1,z_2\right).$$

The corresponding Keldysh matrix components as well as the non-selfconsistent selfenergy contributions can be worked out in analogy to those in the non-diagonal basis. The diagrams of the selfconsistent third-order selfenergy contributions in a diagonal basis are shown in figure 25.

4.3.2. Hubbard basis. Spin-0 bosons. For the Hubbard basis we separately consider spin-0 bosons and spin-1/2 fermions. For the case of spin-0 bosons, the third-order selfenergy contributions separate into two classes. The first is given by

$$\Sigma_{ij}^{(3),\{3;0,2\},0,\mathrm{b},0}\left(z_1,z_2\right) = \Sigma_{ij}^{(3),\{3;1,1\},0,\mathrm{b},0}\left(z_1,z_2\right)$$

$$= \Sigma_{ij}^{(3),2,1,\mathrm{b},0}\left(z_1,z_2\right) = \Sigma_{ij}^{(3),1,\{2;1,1\},\mathrm{b},0}\left(z_1,z_2\right)$$

$$= \Sigma_{ij}^{(3),1,\{2;\{2;2,0\},0,\mathrm{A}\},\mathrm{b},0}\left(z_1,z_2\right) = \Sigma_{ij}^{(3),1,\{2;\{2;2,0\},0,\mathrm{B}\},\mathrm{b},0}\left(z_1,z_2\right)$$

$$= \Sigma_{ij}^{(3),1,\{2;\{2;1,1\},0,\mathrm{A}\},\mathrm{b},0}\left(z_1,z_2\right) = \Sigma_{ij}^{(3),1,\{2;\{2;1,1\},0,\mathrm{C}\},\mathrm{b},0}\left(z_1,z_2\right)$$

$$= \left(\mathrm{i}\hbar\right)^3 G_{ij}\left(z_1,z_2\right) U\left(z_1\right) \int_{\mathcal{C}} \mathrm{d}z_3 \sum_t G_{it}\left(z_1,z_3\right) G_{ti}\left(z_3,z_1\right)$$

$$\times U\left(z_3\right) G_{tj}\left(z_3,z_2\right) G_{jt}\left(z_2,z_3\right) U\left(z_2\right), \tag{267}$$

and the second is given by

$$\Sigma_{ij}^{(3),1,\{2;\{2;2,0\},0,\mathrm{C}\},\mathrm{b},0}\left(z_1,z_2\right) = \Sigma_{ij}^{(3),1,\{2;\{2;1,1\},0,\mathrm{B}\},\mathrm{b},0}\left(z_1,z_2\right)$$

$$= \left(\mathrm{i}\hbar\right)^3 U\left(z_1\right) \int_{\mathcal{C}} \mathrm{d}z_4 \sum_n G_{in}\left(z_1,z_4\right) G_{nj}\left(z_4,z_2\right)$$

$$\times G_{nj}\left(z_4,z_2\right) U\left(z_4\right) U\left(z_2\right) G_{ji}\left(z_2,z_1\right) G_{in}\left(z_1,z_4\right). \tag{268}$$

The corresponding diagrams are shown in figure 26.

Let us now turn to the Hubbard result for spin-1/2 fermions. In this case only the terms with the superscripts 'B' and 'C' exist which are denoted by $\Sigma^{(3),1,\{2;\{2;2,0\},0,\mathrm{B}\},\mathrm{f},1/2}$ and $\Sigma^{(3),1,\{2;\{2;2,0\},0,\mathrm{C}\},\mathrm{f},1/2}$, respectively. The 'B'-terms are given by

$$\Sigma_{i\uparrow j\uparrow}^{(3),1,\{2;\{2;2,0\},0,\mathrm{B}\},\mathrm{f},1/2}\left(z_1,z_2\right) \tag{269}$$

$$= -\left(\mathrm{i}\hbar\right)^3 U\left(z_1\right) \int_{\mathcal{C}} \mathrm{d}z_4 \sum_n G_{i\uparrow n\uparrow}\left(z_1,z_4\right) G_{n\uparrow j\uparrow}\left(z_4,z_2\right)$$

$$\times U\left(z_4\right) U\left(z_2\right) G_{j\downarrow n\downarrow}\left(z_2,z_4\right) G_{n\downarrow i\downarrow}\left(z_4,z_1\right) G_{i\downarrow j\downarrow}\left(z_1,z_2\right),$$

$$\Sigma_{i\downarrow j\downarrow}^{(3),1,\{2;\{2;2,0\},0,\mathrm{B}\},\mathrm{f},1/2}\left(z_1,z_2\right) \tag{270}$$

$$= -\left(\mathrm{i}\hbar\right)^3 U\left(z_1\right) \int_{\mathcal{C}} \mathrm{d}z_4 \sum_n G_{i\downarrow n\downarrow}\left(z_1,z_4\right) G_{n\downarrow j\downarrow}\left(z_4,z_2\right)$$

$$\times U\left(z_4\right) U\left(z_2\right) G_{j\uparrow n\uparrow}\left(z_2,z_4\right) G_{n\uparrow i\uparrow}\left(z_4,z_1\right) G_{i\uparrow j\uparrow}\left(z_1,z_2\right),$$
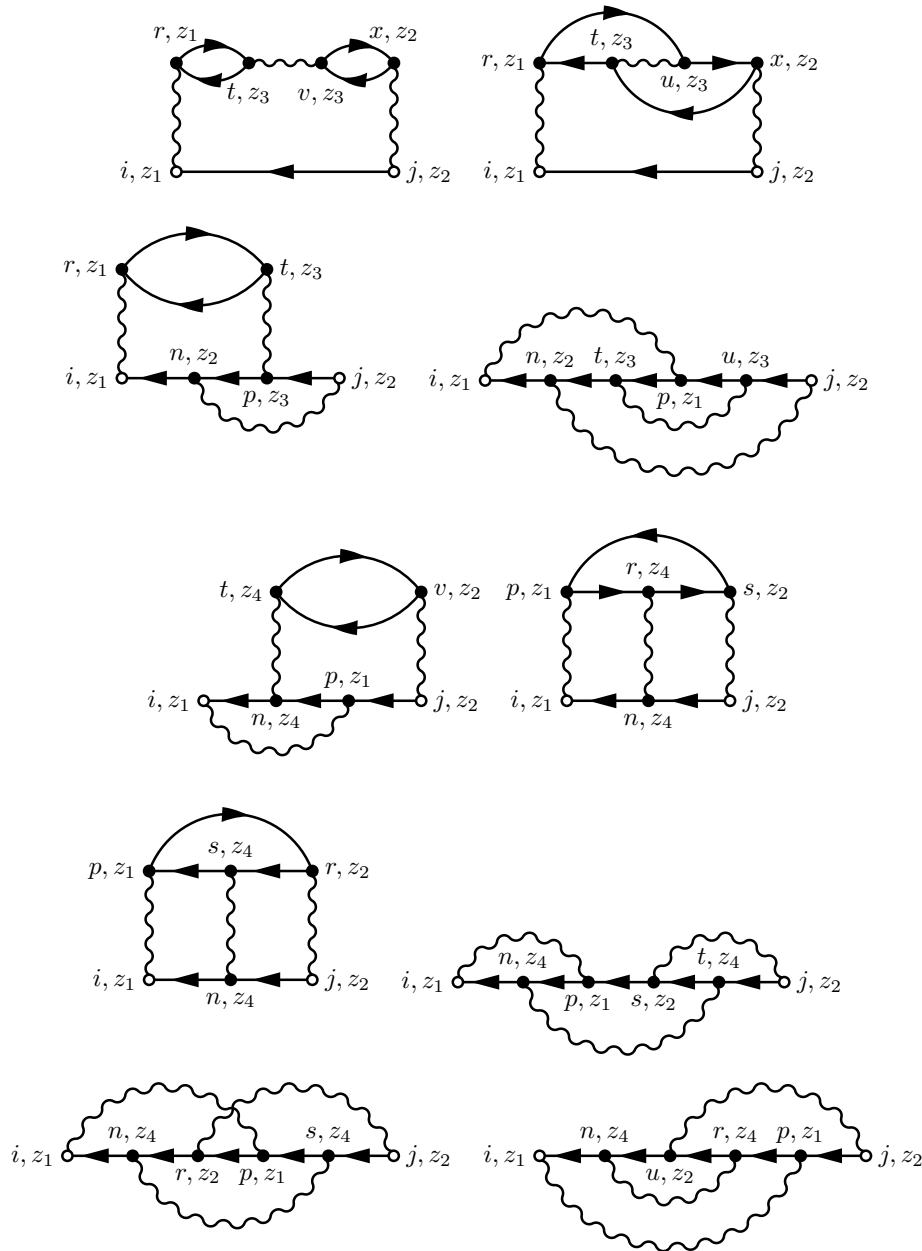
Figure 25. Third-order diagrams in diagonal basis from left to right. First row: $\Sigma^{(3),\{3;0,2\},0,\text{diag}}$, $\Sigma^{(3),\{3;1,1\},0,\text{diag}}$ Second row: $\Sigma^{(3),2,1,\text{diag}}$, $\Sigma^{(3),1,\{2;1,1\},\text{diag}}$ Third row: $\Sigma^{(3),1,\{2;\{2;2,0\},0,A\},\text{diag}}$, $\Sigma^{(3),1,\{2;\{2;2,0\},0,B\},\text{diag}}$ Fourth row: $\Sigma^{(3),1,\{2;\{2;2,0\},0,C\},\text{diag}}$, $\Sigma^{(3),1,\{2;\{2;1,1\},0,A\},\text{diag}}$ Fifth row: $\Sigma^{(3),1,\{2;\{2;1,1\},0,B\},\text{diag}}$, $\Sigma^{(3),1,\{2;\{2;1,1\},0,C\},\text{diag}}$.

and, for the 'C'-terms, we find

$$\Sigma^{(3),1,\{2;\{2;2,0\},0,C\},\mathfrak{f},1/2}_{i\uparrow j\uparrow}\left(z_1,z_2\right) \tag{271}$$

$$= -\left(i\hbar\right)^3 U\left(z_1\right) \int_{\mathcal{C}} dz_4 \sum_n G_{i\uparrow n\uparrow}\left(z_1,z_4\right) G_{n\uparrow j\uparrow}\left(z_4,z_2\right)$$

$$\times U\left(z_4\right) U\left(z_2\right) G_{n\downarrow j\downarrow}\left(z_4,z_2\right) G_{i\downarrow n\downarrow}\left(z_1,z_4\right) G_{j\downarrow i\downarrow}\left(z_2,z_1\right),$$

$$\Sigma^{(3),1,\{2;\{2;2,0\},0,C\},\mathfrak{f},1/2}_{i\downarrow j\downarrow}\left(z_1,z_2\right) \tag{272}$$

$$= -\left(i\hbar\right)^3 U\left(z_1\right) \int_{\mathcal{C}} dz_4 \sum_n G_{i\downarrow n\downarrow}\left(z_1,z_4\right) G_{n\downarrow j\downarrow}\left(z_4,z_2\right)$$

$$\times U\left(z_4\right) U\left(z_2\right) G_{n\uparrow j\uparrow}\left(z_2,z_4\right) G_{i\uparrow n\uparrow}\left(z_4,z_1\right) G_{j\uparrow i\uparrow}\left(z_1,z_2\right),$$

whereas the 'A' terms vanish, as well as all other contributions in third order. The corresponding Feynman diagrams are shown in figure 27.

4.4. Selfenergies of orders higher than three

All terms of orders higher than three can be generated similarly as was demonstrated above for the lower orders. So we only outline the main steps. As before, one computes all possible permutations of the quantities involved in Hedin's equations that lead to the desired total order. An approach that is suitable for a systematic recursive algorithm, starts by eliminating the polarizability from Hedin's equations, yielding, for the selfenergy and the screened potential (see equation (95)–(106)),
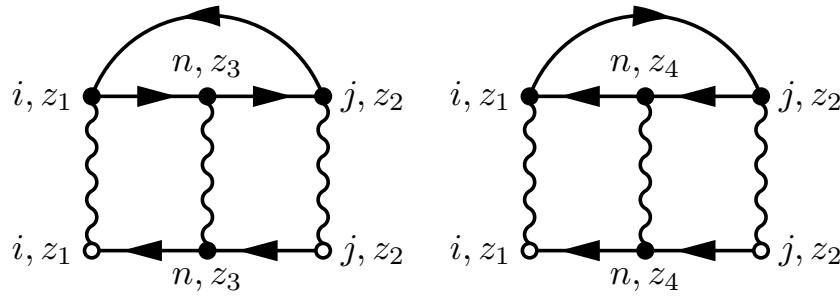
Figure 26. Third-order diagrams in the Hubbard basis for spin-0 bosons. Left: first equivalence class of $\Sigma^{(3),\{3;0,2\},0,\text{diag}}$, $\Sigma^{(3),\{3;1,1\},0,\text{diag}}$, $\Sigma^{(3),2,1,\text{diag}}$, $\Sigma^{(3),1,\{2;1,1\},\text{diag}}$, $\Sigma^{(3),1,\{2;\{2;2,0\},0,A\},\text{diag}}$, $\Sigma^{(3),1,\{2;\{2;2,0\},0,B\},\text{diag}}$, $\Sigma^{(3),1,\{2;\{2;1,1\},0,A\},\text{diag}}$ and $\Sigma^{(3),1,\{2;\{2;1,1\},0,C\},\text{diag}}$. Right: Second equivalence class of $\Sigma^{(3),1,\{2;2,0,C\},\text{diag}}$ and $\Sigma^{(3),1,\{2;1,1,B\},\text{diag}}$.

$$
\Sigma_{ij}\left(z_1, z_2\right) = \Sigma_{ij}^{\text{H}}\left(z_1, z_2\right) + i\hbar \int_{\mathcal{C}} \mathrm{d}z_3 \sum_{mpq} W_{ipqm}\left(z_1, z_3\right)
$$
$$
\times \int_{\mathcal{C}} \mathrm{d}z_4 \sum_n G_{mn}\left(z_1, z_4\right) \Gamma_{nqpj}\left(z_4, z_2, z_3\right),
\tag{273}
$$

$$
W_{ijkl}\left(z_1, z_2\right) = \delta_{\mathcal{C}}\left(z_1, z_2\right) w_{ijkl}\left(z_1\right)
\tag{274}
$$
$$
\pm i\hbar \sum_{mn} w_{imnl}\left(z_1\right) \int_{\mathcal{C}} \mathrm{d}z_3 \sum_{pq} \int_{\mathcal{C}} \mathrm{d}z_4 \sum_r G_{nr}\left(z_1, z_4\right)
$$
$$
\times \int_{\mathcal{C}} \mathrm{d}z_5 \sum_s G_{sm}\left(z_5, z_1\right) \Gamma_{rqps}\left(z_4, z_5, z_3\right) W_{pjkq}\left(z_3, z_2\right)
$$

and, for the vertex function,

$$
\Gamma_{ijkl}\left(z_1, z_2, z_3\right) = \delta_{\mathcal{C}}\left(z_1, z_{2+}\right) \delta_{\mathcal{C}}\left(z_3, z_2\right) \delta_{ik}\delta_{jl}
$$
$$
+ \int_{\mathcal{C}} \mathrm{d}z_4 \mathrm{d}z_5 \sum_{mn} \frac{\delta \Sigma_{il}^{\text{xc}}\left(z_1, z_2\right)}{\delta G_{mn}\left(z_4, z_5\right)} \int_{\mathcal{C}} \mathrm{d}z_6 \sum_p G_{mp}\left(z_4, z_6\right)
$$
$$
\times \int_{\mathcal{C}} \mathrm{d}z_7 \sum_q G_{qn}\left(z_7, z_5\right) \Gamma_{pjkq}\left(z_6, z_7, z_3\right).
\tag{275}
$$

With this set of three coupled equations, the following recursive algorithm can be applied to calculate the Nth order selfenergy contributions:

(i) Initialize $\Sigma^{(1)} = \Sigma^{\text{H}}$, see equation (273),
(ii) Initialize $W^{(1)} = w$, see equation (274),
(iii) Initialize $\Gamma = \Gamma^{(0)}$, see equation (275),
(iv) Loop over $n = 1 \ldots N$:

(a) If $n > 1$: Loop over all orders $m = 1 \ldots (n-1)$:

– Loop over all selfenergy contributions $\Sigma^{(m)}$ of order m:
– Loop over all vertex contributions $\Gamma^{(n-1-m)}$ of order $n - 1 - m$:
– Calculate the new vertex contribution $\Gamma^{(n-1)}$ of order $m + n - 1 - m = n - 1$, from $\Sigma^{(m)}$ and $\Gamma^{(n-1-m)}$, via equation (275),

(b) If $n > 1$: Loop over all orders $m = 1 \ldots (n-1)$:

– Loop over all contributions to the screened interaction $W^{(m)}$ of order m:
– Loop over all vertex contributions $\Gamma^{(n-1-m)}$ of order $n - 1 - m$:
– Calculate the new contribution to the screened interaction $W^{(n)}$ of order $1 + m + n - 1 - m = n$, from w, $W^{(m)}$ and $\Gamma^{(n-1-m)}$, via equation (274)

(c) Loop over all orders $m = 1 \ldots n$:

– Loop over all contributions to the screened interaction $W^{(m)}$ of order m:
– Loop over all vertex contributions $\Gamma^{(n-m)}$ of order $n - m$:
– Calculate the new selfenergy contribution $\Sigma^{(n)}$ from $W^{(m)}$ and $\Gamma^{(n-m)}$ of order $m + n - m = n$ via equation (273).

A similar algorithm yielding the diagrams with respect to the bare interaction, w, can be deduced, replacing the full vertex Γ by the bare vertex Λ, see equations (97) and (98). Further, the generation of the non-selfconsistent diagrams is straightforward by inclusion of the Dyson equation and, additionally, taking into account the order of the Green functions in the respective equations.

With this we conclude the discussion of the perturbative approaches to the selfenergy.

5. Selfenergy approximations II: diagram resummation. *GW*, *T* matrix, FLEX

In this section we discuss an alternative to the perturbative expansion of the selfenergy in terms of the interaction strength that was presented in section 4. The perturbation expansion is expected to become questionable or, at least, inefficient with increasing interaction strength. This was confirmed in the section 3 where we demonstrated that a number of non-perturbative approaches, such as the *GW* approximation, the *T*-matrix approximation or the FLEX approach are significantly more accurate, in many cases.

Thus, when perturbation expansions fail, a more appropriate approach consists in diagram resummation techniques that sum an entire infinite perturbation series and which is in the focus of the present section. The underlying idea is to take into consideration one or several classes of terms with a recursive structure which occur in all orders of the interaction, based on physical intuition about their importance. In fact such resummation approaches have a long history. For example the T-matrix approximation has been successfully applied in scattering theory and in nuclear physics. On the other hand, the concept of dynamical screening (GW approximation) has been employed for electrolytes and plasmas. The major advance provided by Green functions theory is the extension of the concept to arbitrary nonequilibrium situations.

GW approximation. Starting from the notion of the screened interaction, W, the simplest choice is the GW approximation [82] which centers around treating W exactly according to equation (102) while taking the screened vertex Γ only in zeroth-order approximation. This leads to the familiar concept of dynamical screening and plasmon dynamics which is of particular importance for long-range Coulomb interaction in dense plasmas [136] or molecules. The resulting structure of the selfenergy approximation is discussed in the ensuing section 5.2.

T-matrix approximation. In contrast to GW, the T-matrix approximation, treats the interaction only at the level of the bare interaction, but focuses instead on a good representation of the bare vertex functions Λ. This approximation sums the entire Born series and is, thus expected to be more accurate than the second-Born approximation, at strong coupling. The T-matrix approximation exists in two flavors—the particle–particle T-matrix approximation (TPP) and the particle–hole T-matrix approximation (TPH).

Combination of strong coupling and dynamical screening. Furthermore, several other approaches have been introduced that mix screened and bare interaction [172]. An example for this group is the second-order screened-exchange (SOSEX) approximation [105, 172, 173], which takes the second-order exchange diagram, see equation (183), and replaces one of the bare interactions w by the screened interaction W. Doing that, the total complexity is still of $\mathcal{O}\left(N_{\mathrm{t}}^3\right)$, since the determination of the selfenergy, the computation of the screened interaction according to equation (104) and the

solution of the KBE, (see equations (66) and (67)), all scale as $\mathcal{O}\left(N_{\mathrm{t}}^3\right)$.

Another possible way is to combine several existing approximations. Thereby one has to correct for possible double counting. This strategy is pursued in the so-called fluctuating-exchange (FLEX) approximation which adds the diagrams of third and higher order of the GW approximation and both T matrices to the second-order diagrams, which are taken only once. The FLEX approximation which will be detailed in section 5.5 can be seen as a the starting term of the more sophisticated plaquet theory [174–180], where one uses coupled equations for the vertex functions in the particle–particle and particle–hole channels.

Before discussing in detail the GW approximation, the T-matrix approximation and the FLEX approximation, in Sections 5.2, 5.3 and 5.5, respectively, we investigate in some detail the two-particle Green function $G^{(2)}$. We start by introducing the Hartree and the Fock approximation for $G^{(2)}$ in section 5.1, since they will be used later.

5.1. Mean field. Hartree and Fock approximations for $G^{(2)}$

In the following, the two simplest approximations for the two-particle Green function are defined which will are the starting point for simplifying the expressions occuring in the resummation approaches. Those are the Hartree Green function, $G^{(2),\mathrm{H}}$, and the Fock Green function, $G^{(2),\mathrm{F}}$.
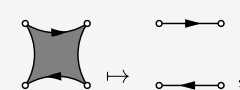
$G^{(2),\mathrm{H}}$ corresponds to the approximation that two particles are uncorrelated. Then the two-particle Green function $G^{(2)}$ is approximated as
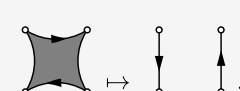
$$G^{(2)}_{ijkl}\left(z_1,z_2,z_3,z_4\right) \equiv G^{(2),\mathrm{H}}_{ijkl}\left(z_1,z_2,z_3,z_4\right) := G_{ik}\left(z_1,z_3\right)G_{jl}\left(z_2,z_4\right). \tag{276}$$

This approximation applies to classical and quantum many-particle systems alike. In contrast, an additional approximation that exists only in the case of quantum systems and reflects the indistinguishability of quantum particles (exchange effects of bosons or fermions) is the Fock approximations which, is denoted as $G^{(2),\mathrm{F}}$ and reads

$$G^{(2)}_{ijkl}\left(z_1,z_2,z_3,z_4\right) \equiv G^{(2),\mathrm{F}}_{ijkl}\left(z_1,z_2,z_3,z_4\right) := \pm G_{il}\left(z_1,z_4\right)G_{jk}\left(z_2,z_3\right). \tag{277}$$

For better illustration both two-particle quantities are repeated in the compact notation:

$$\begin{aligned} G^{(2)}\left(1,2,3,4\right) &\approx G^{(2),\mathrm{H}}\left(1,2,3,4\right) \\ &:= G\left(1,3\right)G\left(2,4\right) \end{aligned} \qquad\qquad \text{} \tag{278}$$

$$\begin{aligned} G^{(2)}\left(1,2,3,4\right) &\approx G^{(2),\mathrm{F}}\left(1,2,3,4\right) \\ &:= \pm G\left(1,4\right)G\left(2,3\right) \end{aligned} \qquad\qquad \text{} \tag{279}$$

Following the above considerations, in a quantum system the mean-field approximation for $G^{(2)}$ is the sum of the Hartree and Fock contributions.

In the resummation expansions presented in this section, both quantities play a central role. However, in most cases, we will only need simpler two-time versions of the two-particle functions, G^{H} and G^{F}, respectively These expressions follow by setting equal two pairs of time-arguments and adding a dimensionality factor $i\hbar$. This leads to (we skip the superscript '(2)' since it is clear that a function with four basis indices refers to a two-particle Green function)

$$G^{\mathrm{H}}_{ijkl}\left(z_1,z_2\right) := i\hbar G^{(2),\mathrm{H}}_{ijkl}\left(z_1,z_1,z_2,z_2\right) \equiv i\hbar G_{ik}\left(z_1,z_2\right) G_{jl}\left(z_1,z_2\right),$$
(280)

whereas, for the Fock approximation, one has

$$G^{\mathrm{F}}_{ijkl}\left(z_1,z_2\right) = i\hbar G^{(2),\mathrm{F}}_{ijkl}\left(z_1,z_2,z_1,z_2\right) \equiv \pm i\hbar G_{il}\left(z_1,z_2\right) G_{jk}\left(z_2,z_1\right).$$
(281)

We now provide the Keldysh matrix components of equations (280) and (281). For the Hartree function, we have the following '$\gtrless$' and advanced/retarded components:

$$G^{\mathrm{H},\gtrless}_{ijkl}\left(t_1,t_2\right) = i\hbar G^{\gtrless}_{ik}\left(t_1,t_2\right) G^{\gtrless}_{jl}\left(t_1,t_2\right),$$

$$G^{\mathrm{H},\mathcal{A}/\mathcal{R}}_{ijkl}\left(t_1,t_2\right) = \mp i\hbar \Theta[\pm(t_2 - t_1)]$$
$$- \left[G^{>}_{ik}\left(t_1,t_2\right) G^{>}_{jl}\left(t_1,t_2\right) G^{<}_{ik}\left(t_1,t_2\right) G^{<}_{jl}\left(t_1,t_2\right) \right].$$

Similarly, for the Fock two-particle function follows

$$G^{\mathrm{F},\gtrless}_{ijkl}\left(t_1,t_2\right) = \pm i\hbar G^{\gtrless}_{il}\left(t_1,t_2\right) G^{\lessgtr}_{jk}\left(t_2,t_1\right),$$

$$G^{\mathrm{F},\mathcal{A}/\mathcal{R}}_{ijkl}\left(t_1,t_2\right) = \mp i\hbar \Theta[\pm(t_2 - t_1)]$$
$$\left[G^{>}_{il}\left(t_1,t_2\right) G^{<}_{jk}\left(t_2,t_1\right) - G^{<}_{il}\left(t_1,t_2\right) G^{>}_{jk}\left(t_2,t_1\right) \right].$$

5.2. Polarization bubble resummation. GW approximation

The GW approximation aims at treating long-range interaction effects that lead to dynamical screening and collective excitations (plasmons). These effects are of particular relevance for charged many-particle systems, including ionized gases (plasmas), the electron gas in metals, electron-hole plasmas in semiconductors and so on. In fact, many-body approximations that go beyond the static second-Born approximation, on one hand, and beyond the statical-screening concept of Debye and Hückel, on the other hand, have a long tradition in plasma physics. In fact kinetic equations with collision integrals the include a complete resummation of all polarization diagrams have been derived in the 1960s by Lenard and Balescu [181, 182] and analyzed in detail by Klimontovich [183] and many others. A quantum derivation within density-operator theory (BBGKY-hierarchy) and a discussion of its relation to Green functions can be found in [136].

The Green functions approach to dynamical screening and collective excitation is based on Hedin's equations for the screened interaction W according to equation (104) with the zeroth order vertex $\Gamma^{(0)}$. The set of equations is given by the Dyson equation[27] (see equation (91))

$$G\left(1,2\right) = G^{(0)}\left(1,2\right)$$
$$+ G^{(0)}\left(1,3\right) \Sigma\left(3,4\right) G\left(4,2\right)$$

(282)

the equation for the selfenergy (see equation (95))

$$\Sigma\left(1,2\right) = \Sigma^{\mathrm{H}}\left(1,2\right) + \Sigma^{\mathrm{xc}}\left(1,2\right)$$

(283)

with

$$\Sigma^{\mathrm{xc}}\left(1,2\right)$$
$$= i\hbar W\left(1,3\right) G\left(1,4\right) \Gamma^{(0)}\left(4,2,3\right)$$
$$= i\hbar W\left(1,2\right) G\left(1,2\right)$$

(284)

[27] The corresponding equations in the full notation are given in section 1.3 of the supplement 20.

the zeroth-order polarizability (see equation (173))

$$
\begin{aligned}
P^{(0)}\big(1,2\big) &= \pm\mathrm{i}\hbar G\big(1,3\big)G\big(4,1\big) \\
&\quad \Gamma^{(0)}\big(3,4,2\big) \\
&= \pm\mathrm{i}\hbar G\big(1,2\big)G\big(2,1\big)
\end{aligned}
\tag{285}
$$

and the screened interaction (see equations (102) and (104))

$$
\begin{aligned}
W\big(1,2\big) &= w\big(1,2\big) \\
&\quad + w\big(1,3\big)P^{(0)}\big(3,4\big)W\big(4,2\big) \\
&= w\big(1,2\big) \\
&\quad \pm\mathrm{i}\hbar w\big(1,3\big)G\big(3,4\big)G\big(4,3\big)W\big(4,2\big)
\end{aligned}
\tag{286}
$$

To solve this set of equations, one has to determine the selfconsistent solution of equation (286). Due to the time-diagonal structure (i.e. due to the time delta function) of the bare interaction (see equation (60)) the computational solution of equation (286) in the displayed form becomes ill-defined. Therefore, it is advantageous to eliminate the singular bare interaction by defining the 'non-singular' part of the interaction (or the induced potential which will be labeled with the superscript 'ns')

$$
\begin{aligned}
W^{\mathrm{ns}}\big(1,2\big) &:= W\big(1,2\big) - W^{\mathrm{bare}}\big(1,2\big) \\
&= W\big(1,2\big) - w\big(1,2\big)
\end{aligned}
\tag{287}
$$

Using this and, by comparison with equation (156), one arrives at

$$
\begin{aligned}
\Sigma^{GW}\big(1,2\big) &= \Sigma^{\mathrm{H}}\big(1,2\big) + \mathrm{i}\hbar W\big(1,2\big)G\big(1,2\big) \\
&= \Sigma^{\mathrm{H}}\big(1,2\big) + \mathrm{i}\hbar w\big(1,2\big)G\big(1,2\big) + \mathrm{i}\hbar W^{\mathrm{ns}}\big(1,2\big)G\big(1,2\big) \\
&=: \Sigma^{\mathrm{H}}\big(1,2\big) + \Sigma^{\mathrm{F}}\big(1,2\big) + \Sigma^{GW,\mathrm{corr}}\big(1,2\big)
\end{aligned}
\tag{288}
$$

Thus the full selfenergy in the *GW* approximation contains, in addition to the Hartree–Fock selfenergy, a correlation contribution which is denoted $\Sigma_{ij}^{GW,\mathrm{corr}}$ and which will be in the focus of the subsequent analysis.

For the non-singular part of the screened interaction, we have

$$
\begin{aligned}
&W^{\mathrm{ns}}(1,2) \\
&= \pm i\hbar w(1,3) G(3,4) G(4,3) w(4,2) \\
&\quad \pm i\hbar w(1,3) G(3,4) G(4,3) W^{\mathrm{ns}}(4,2)
\end{aligned}
\qquad (289)
$$

Returning to the full notation and the single-time interaction one can use the definition of G^{F} in equation (281) to simplify equation (289) to

$$
W^{\mathrm{ns}}_{ijkl}\left(z_1, z_2\right) = \Phi^{GW}_{ijkl}\left(z_1, z_2\right) + \sum_{mn} w_{imnl}\left(z_1\right) \int_{\mathcal{C}} \mathrm{d}z_3 \sum_{pq}
$$
$$
G^{\mathrm{F}}_{nqmp}\left(z_1, z_3\right) W^{\mathrm{ns}}_{pjkq}\left(z_3, z_2\right), \qquad (290)
$$

$$
\Phi^{GW}_{ijkl}\left(z_1, z_2\right) =: \sum_{mn} w_{imnl}\left(z_1\right) \sum_{pq} G^{\mathrm{F}}_{nqmp}\left(z_1, z_2\right) w_{pjkq}\left(z_2\right), \qquad (291)
$$

where we introduced the short notation Φ for the second-Born contribution to the screened potential.

Finally, we provide the correlation components of equation (288)

$$
\Sigma^{GW,\mathrm{corr},\gtrless}_{ij}\left(t_1, t_2\right) = i\hbar \sum_{mp} W^{\mathrm{ns},\gtrless}_{ipjm}\left(t_1, t_2\right) G^{\gtrless}_{mp}\left(t_1, t_2\right), \qquad (292)
$$

which require knowledge of the correlation components of the non-singular screened potential equation (290), that are given by

$$
W^{\mathrm{ns},\gtrless}_{ijkl}\left(t_1, t_2\right) = \Phi^{GW,\gtrless}_{ijkl}\left(t_1, t_2\right) + \sum_{mn} w_{imnl}\left(t_1\right) \sum_{pq} \qquad (293)
$$
$$
\left(\int_{t_0}^{t_1} \mathrm{d}t_3\, G^{\mathrm{F},\mathcal{R}}_{nqmp}\left(t_1, t_3\right) W^{\mathrm{ns},\gtrless}_{pjkq}\left(t_3, t_2\right) + \int_{t_0}^{t_2} \mathrm{d}t_3\, G^{\mathrm{F},\gtrless}_{nqmp}\left(t_1, t_3\right) W^{\mathrm{ns},\mathcal{A}}_{pjkq}\left(t_3, t_2\right) \right),
$$

as well as of the advanced/retarded components,

$$
W^{\mathrm{ns},\mathcal{A}/\mathcal{R}}_{ijkl}\left(t_1, t_2\right) = \Phi^{GW,\mathcal{A}/\mathcal{R}}_{ijkl}\left(t_1, t_2\right) \qquad (294)
$$
$$
+ \sum_{mn} w_{imnl}\left(t_1\right) \int_{t_{1/2}}^{t_{2/1}} \mathrm{d}t_3 \sum_{pq} G^{\mathrm{F},\mathcal{A}/\mathcal{R}}_{nqmp}\left(t_1, t_3\right) W^{\mathrm{ns},\mathcal{A}/\mathcal{R}}_{pjkq}\left(t_3, t_2\right).
$$

In the integration limits, in the notation $t_{1/2}$, the first (second) subscript refers to the advanced (retarded) function.

5.2.1. Diagonal basis. In a diagonal basis set, equation (290) simplifies to

$$
W^{\mathrm{ns,diag}}_{ijkl}\left(z_1, z_2\right) = \delta_{il}\delta_{jk}\Phi^{GW,\mathrm{diag}}_{ijji}\left(z_1, z_2\right) \qquad (295)
$$
$$
+ \delta_{il} \sum_m w_{im}\left(z_1\right) \int_{\mathcal{C}} \mathrm{d}z_3 \sum_{pq} G^{\mathrm{F}}_{mpmq}\left(z_1, z_3\right) W^{\mathrm{ns,diag}}_{pjkq}\left(z_3, z_2\right).
$$

$$
\Phi^{GW,\mathrm{diag}}_{ijji}\left(z_1, z_2\right) =: \sum_m w_{im}\left(z_1\right) \sum_p G^{\mathrm{F}}_{mpmp}\left(z_1, z_2\right) w_{pj}\left(z_2\right), \qquad (296)
$$

where we again used the function Φ, equation (291). By iteration, it becomes evident that $W^{\mathrm{ns,diag}}$ and $\Phi^{GW,\mathrm{diag}}_{ijji}$ are always of the form

$$
W^{\mathrm{ns,diag}}_{ijkl}\left(z_1, z_2\right) = \delta_{il}\delta_{jk} W^{\mathrm{ns,diag}}_{ijji}\left(z_1, z_2\right) =: \delta_{il}\delta_{jk} W^{\mathrm{ns,diag}}_{ij}\left(z_1, z_2\right), \qquad (297)
$$
$$
\Phi^{GW,\mathrm{diag}}_{ijkl}\left(z_1, z_2\right) = \delta_{il}\delta_{jk} \Phi^{GW,\mathrm{diag}}_{ijji}\left(z_1, z_2\right) =: \delta_{il}\delta_{jk} \Phi^{GW,\mathrm{diag}}_{ij}\left(z_1, z_2\right). \qquad (298)
$$

With this, for a diagonal basis, equation (290) attains the form

$$
W^{\mathrm{ns,diag}}_{ij}\left(z_1, z_2\right) = \Phi^{GW,\mathrm{diag}}_{ij}\left(z_1, z_2\right) \qquad (299)
$$
$$
+ \sum_m w_{im}\left(z_1\right) \int_{\mathcal{C}} \mathrm{d}z_3 \sum_p G^{\mathrm{F}}_{mpmp}\left(z_1, z_3\right) W^{\mathrm{ns,diag}}_{pj}\left(z_3, z_2\right).
$$

The correlation part of the selfenergy, equation (288), reads

$$
\Sigma^{GW,\mathrm{corr}}_{ij}{}^{,\mathrm{diag}}\left(z_1, z_2\right) = +i\hbar W^{\mathrm{ns,diag}}_{ij}\left(z_1, z_2\right) G_{ij}\left(z_1, z_2\right). \qquad (300)
$$

The first four terms of the *GW* selfenergy (mean field plus correlation selfenergy) are shown diagrammatically in figure 28. The sum continues to infinite order (infinite number of polarization bubbles).

The relevant components of the Keldysh matrix read (see equations (293) and (294)),

$$
W^{\mathrm{ns,diag},\gtrless}_{ij}\left(t_1, t_2\right) = \Phi^{GW,\mathrm{diag},\gtrless}_{ij}\left(t_1, t_2\right) + \sum_{mp} w_{im}\left(t_1\right) \qquad (301)
$$
$$
\left(\int_{t_0}^{t_1} \mathrm{d}t_3\, G^{\mathrm{F},\mathcal{R}}_{mpmp}\left(t_1, t_3\right) W^{\mathrm{ns,diag},\gtrless}_{pj}\left(t_3, t_2\right) \right.
$$
$$
\left. + \int_{t_0}^{t_2} \mathrm{d}t_3\, G^{\mathrm{F},\gtrless}_{mpmp}\left(t_1, t_3\right) W^{\mathrm{ns,diag},\mathcal{A}}_{pj}\left(t_3, t_2\right) \right),
$$

$$
W^{\mathrm{ns,diag},\mathcal{A}/\mathcal{R}}_{ij}\left(t_1, t_2\right) = \Phi^{GW,\mathrm{diag},\mathcal{A}/\mathcal{R}}_{ij}\left(t_1, t_2\right) \qquad (302)
$$
$$
+ \sum_{mp} w_{im}\left(t_1\right) \int_{t_{1/2}}^{t_{2/1}} \mathrm{d}t_3\, G^{\mathrm{F},\mathcal{A}/\mathcal{R}}_{mpmp}\left(t_1, t_3\right) W^{\mathrm{ns,diag},\mathcal{A}/\mathcal{R}}_{pj}\left(t_3, t_2\right),
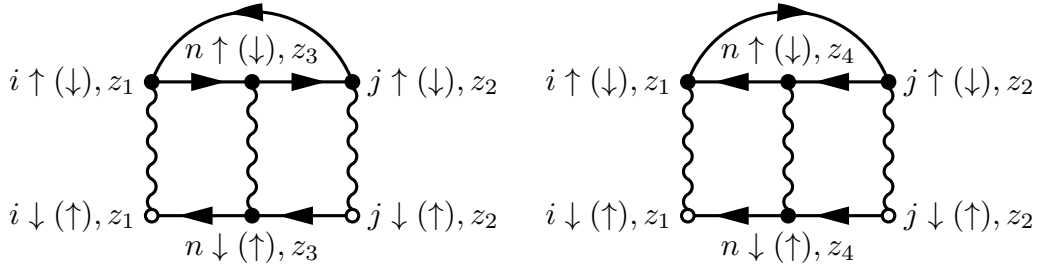$$

Figure 27. Third-order diagrams in Hubbard basis for spin-1/2 fermions. Left: $\Sigma^{(3),1,\{2;\{2;2,0\},0,B\},f,1/2}$. Right: $\Sigma^{(3),1,\{2;\{2;2,0\},0,C\},f,1/2}$.
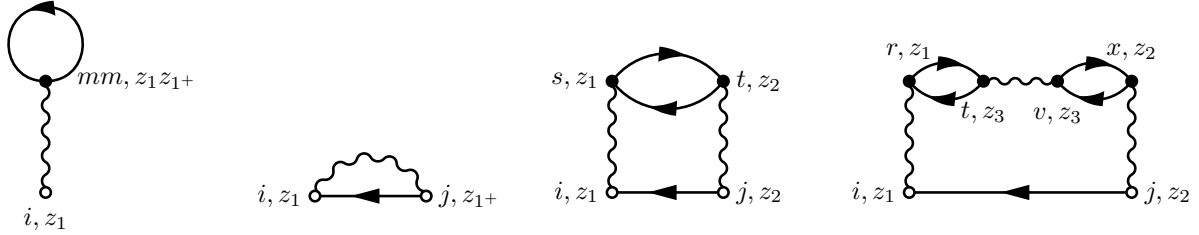

Figure 28. The first four terms of the GW selfenergy, including Hartree and Fock terms, in a diagonal basis.

and (see equation (292)),

$$\Sigma_{ij}^{GW,\text{corr,diag},\gtrless}\left(t_1,t_2\right) = i\hbar W_{ij}^{\text{ns,diag},\gtrless}\left(t_1,t_2\right)G_{ij}^{\gtrless}\left(t_1,t_2\right). \quad (303)$$

5.2.2. Hubbard basis.

In the Hubbard basis, see section 2.3, the GW approximation simplifies considerably. We start by presenting the equations for bosons:

$$W_{i\alpha j\beta}^{\text{ns,b}}\left(z_1,z_2\right) = \Phi_{ij}^{GW,\text{b}}\left(z_1,z_2\right) \quad (304)$$
$$+ U\left(z_1\right)\int_{\mathcal{C}}\mathrm{d}z_3\sum_{p\epsilon}G_{i\epsilon p\epsilon i\epsilon p\epsilon}^{\text{F}}\left(z_1,z_3\right)W_{p\epsilon j\beta}^{\text{ns,b}}\left(z_3,z_2\right),$$

$$\Phi_{ij}^{GW,\text{b}}\left(z_1,z_2\right) =: U\left(z_1\right)\sum_{\epsilon}G_{i\epsilon j\epsilon i\epsilon j\epsilon}^{\text{F}}\left(z_1,z_2\right)U\left(z_2\right), \quad (305)$$

and the correlation selfenergy on the Keldysh contour is

$$\Sigma_{i\alpha j\alpha}^{GW,\text{corr,b}}\left(z_1,z_2\right) = i\hbar W_{i\alpha j\alpha}^{\text{ns,b}}\left(z_1,z_2\right)G_{i\alpha j\alpha}\left(z_1,z_2\right). \quad (306)$$

The Keldysh matrix components of the screened potential in the Hubbard basis become

$$W_{i\alpha j\beta}^{\text{ns,b},\gtrless}\left(t_1,t_2\right) = \Phi_{ij}^{GW,\text{b},\gtrless}\left(t_1,t_2\right)$$
$$+ U\left(t_1\right)\int_{t_0}^{t_1}\mathrm{d}t_3\sum_{p\epsilon}G_{i\epsilon p\epsilon i\epsilon p\epsilon}^{\text{F},\mathcal{R}}\left(t_1,t_3\right)W_{p\epsilon j\beta}^{\text{ns,b},\gtrless}\left(t_3,t_2\right)$$
$$+ U\left(t_1\right)\int_{t_0}^{t_2}\mathrm{d}t_3\sum_{p\epsilon}G_{i\epsilon p\epsilon i\epsilon p\epsilon}^{\text{F},\gtrless}\left(t_1,t_3\right)W_{p\epsilon j\beta}^{\text{ns,b},\mathcal{A}}\left(t_3,t_2\right),$$

$$W_{i\alpha j\beta}^{\text{ns,b},\mathcal{A}/\mathcal{R}}\left(t_1,t_2\right) = \Phi_{ij}^{GW,\text{b},\mathcal{A}/\mathcal{R}}\left(t_1,t_2\right)$$
$$+ U\left(t_1\right)\int_{t_{1/2}}^{t_{2/1}}\mathrm{d}t_3\sum_{p\epsilon}G_{i\epsilon p\epsilon i\epsilon p\epsilon}^{\text{F},\mathcal{A}/\mathcal{R}}\left(t_1,t_3\right)W_{p\epsilon j\beta}^{\text{ns,b},\mathcal{A}/\mathcal{R}}\left(t_3,t_2\right),$$

and the '$\gtrless$' components of the correlation selfenergy (306) are

$$\Sigma_{i\alpha j\alpha}^{GW,\text{corr,b},\gtrless}\left(t_1,t_2\right) = i\hbar W_{i\alpha j\alpha}^{\text{ns,b},\gtrless}\left(t_1,t_2\right)G_{i\alpha j\alpha}^{\gtrless}\left(t_1,t_2\right). \quad (307)$$

For the special case of spin-0 bosons, the screened potential on the Keldysh contour has the form

$$W_{ij}^{\text{ns,b},0}\left(z_1,z_2\right) = \Phi_{ij}^{GW,\text{b},0}\left(z_1,z_2\right) + U\left(z_1\right)$$
$$\int_{\mathcal{C}}\mathrm{d}z_3\sum_{p}G_{ipip}^{\text{F}}\left(z_1,z_3\right)W_{pj}^{\text{ns,b},0}\left(z_3,z_2\right),$$

$$\Phi_{ij}^{GW,\text{b},0}\left(z_1,z_2\right) =: U\left(z_1\right)G_{ijij}^{\text{F}}\left(z_1,z_2\right)U\left(z_2\right), \quad (308)$$

and the correlation selfenergy in GW approximation becomes

$$\Sigma_{ij}^{GW,\text{corr,b},0}\left(z_1,z_2\right) = i\hbar W_{ij}^{\text{ns,b},0}\left(z_1,z_2\right)G_{ij}\left(z_1,z_2\right).$$

The '$>$', '$<$' and advanced/retarded matrix components become

$$W_{ij}^{\text{ns,b},0,\gtrless}\left(t_1,t_2\right) = \Phi_{ij}^{GW,\text{b},0,\gtrless}\left(t_1,t_2\right)$$
$$+ U\left(t_1\right)\int_{t_0}^{t_1}\mathrm{d}t_3\sum_{p}G_{ipip}^{\text{F},\mathcal{R}}\left(t_1,t_3\right)W_{pj}^{\text{ns,b},0,\gtrless}\left(t_3,t_2\right)$$
$$+ U\left(t_1\right)\int_{t_0}^{t_2}\mathrm{d}t_3\sum_{p}G_{ipip}^{\text{F},\gtrless}\left(t_1,t_3\right)W_{pj}^{\text{ns,b},0,\mathcal{A}}\left(t_3,t_2\right),$$

$$W_{ij}^{\text{ns,b},0,\mathcal{A}/\mathcal{R}}\left(t_1,t_2\right) = \Phi_{ij}^{GW,\text{b},0,\mathcal{A}/\mathcal{R}}\left(t_1,t_2\right) \quad (309)$$
$$+ U\left(t_1\right)\int_{t_{1/2}}^{t_{2/1}}\mathrm{d}t_3\sum_{p}G_{ipip}^{\text{F},\mathcal{A}/\mathcal{R}}\left(t_1,t_3\right)W_{pj}^{\text{ns,b},0,\mathcal{A}/\mathcal{R}}\left(t_3,t_2\right)$$

and, for the '$\gtrless$' components of the correlation selfenergy, we have
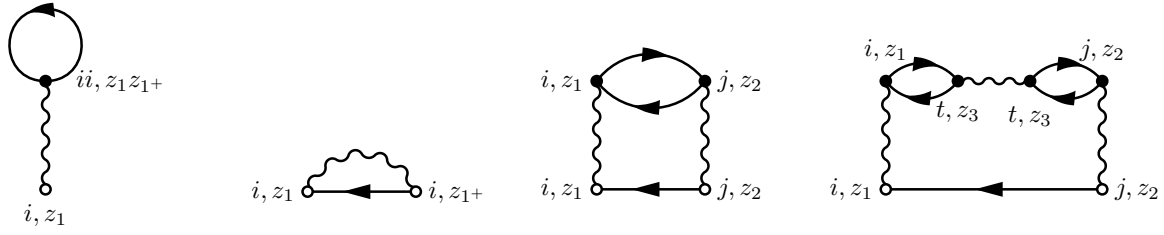
Figure 29. The first four terms of the *GW* selfenergy (Hartree, Fock and correlation part) in the Hubbard basis for spin-0 bosons.

$$\Sigma_{ij}^{GW,\text{corr},\mathfrak{b},0,\gtrless}\left(t_1,t_2\right) = \mathrm{i}\hbar W_{ij}^{\text{ns},\mathfrak{b},0,\gtrless}\left(t_1,t_2\right) G_{ij}^{\gtrless}\left(t_1,t_2\right).$$

The diagrammatic representation of the leading terms for spin-0 bosons in the Hubbard basis is shown in figure 29.

Let us now turn to fermions. In that case the equations on the Keldysh contour attain the form

$$W_{i\alpha j\beta}^{\text{ns},\mathfrak{f}}\left(z_1,z_2\right) = \Phi_{ij\alpha\beta}^{GW,\mathfrak{f}}\left(z_1,z_2\right) \tag{310}$$

$$+ U\left(z_1\right)\int_{\mathcal{C}}\mathrm{d}z_3 \sum_p \sum_{\epsilon\neq\alpha} G_{i\epsilon p\epsilon i\epsilon p\epsilon}^{\text{F}}\left(z_1,z_3\right) W_{p\epsilon j\beta}^{\text{ns},\mathfrak{f}}\left(z_3,z_2\right)$$

$$\Phi_{ij\alpha\beta}^{GW,\mathfrak{f}}\left(z_1,z_2\right) =: \sum_{\epsilon\neq\{\alpha,\beta\}} U\left(z_1\right) G_{i\epsilon j\epsilon i\epsilon j\epsilon}^{\text{F}}\left(z_1,z_2\right) U\left(z_2\right), \tag{311}$$

whereas the correlation part of the selfenergy becomes

$$\Sigma_{i\alpha j\alpha}^{GW,\text{corr},\mathfrak{f}}\left(z_1,z_2\right) = \mathrm{i}\hbar W_{i\alpha j\alpha}^{\text{ns},\mathfrak{f}}\left(z_1,z_2\right) G_{i\alpha j\alpha}\left(z_1,z_2\right).$$

The Keldysh matrix components of the screened potential are now

$$W_{i\alpha j\beta}^{\text{ns},\mathfrak{f},\gtrless}\left(t_1,t_2\right) = \Phi_{ij\alpha\beta}^{GW,\mathfrak{f},\gtrless}\left(t_1,t_2\right)$$

$$+ U\left(t_1\right)\int_{t_0}^{t_1}\mathrm{d}t_3 \sum_p \sum_{\epsilon\neq\alpha} G_{i\epsilon p\epsilon i\epsilon p\epsilon}^{\text{F},\mathcal{R}}\left(t_1,t_3\right) W_{p\epsilon j\beta}^{\text{ns},\mathfrak{f},\gtrless}\left(t_3,t_2\right)$$

$$+ U\left(t_1\right)\int_{t_0}^{t_2}\mathrm{d}t_3 \sum_p \sum_{\epsilon\neq\alpha} G_{i\epsilon p\epsilon i\epsilon p\epsilon}^{\text{F},\gtrless}\left(t_1,t_3\right) W_{p\epsilon j\beta}^{\text{ns},\mathfrak{f},\mathcal{A}}\left(t_3,t_2\right),$$

$$W_{i\alpha j\beta}^{\text{ns},\mathfrak{f},\mathcal{A}/\mathcal{R}}\left(t_1,t_2\right) = \Phi_{ij\alpha\beta}^{GW,\mathfrak{f},\mathcal{A}/\mathcal{R}}\left(t_1,t_2\right)$$

$$+ U\left(t_1\right)\int_{t_{1/2}}^{t_{2/1}}\mathrm{d}t_3 \sum_p \sum_{\epsilon\neq\alpha} G_{i\epsilon p\epsilon i\epsilon p\epsilon}^{\text{F},\mathcal{A}/\mathcal{R}}\left(t_1,t_3\right) W_{p\epsilon j\beta}^{\text{ns},\mathfrak{f},\mathcal{A}/\mathcal{R}}\left(t_3,t_2\right).$$

The *GW* selfenergy has now the following correlation components

$$\Sigma_{i\alpha j\alpha}^{GW,\text{corr},\mathfrak{f},\gtrless}\left(t_1,t_2\right) = \mathrm{i}\hbar W_{i\alpha j\alpha}^{\text{ns},\mathfrak{f},\gtrless}\left(t_1,t_2\right) G_{i\alpha j\alpha}^{\gtrless}\left(t_1,t_2\right).$$

For the special case of spin-$\frac{1}{2}$-fermions, the equations for the screened interaction require some care. Since the particles can

have two spin projections, there are four different screened potentials each obeying its own equation which, in turn, are coupled. To underline these details we use different colors for the four potentials:

$$W_{i\uparrow j\uparrow}^{\text{ns},\mathfrak{f},1/2}\left(z_1,z_2\right) = \Phi_{ij\uparrow}^{GW,\mathfrak{f},1/2}\left(z_1,z_2\right) + U\left(z_1\right)\int_{\mathcal{C}}\mathrm{d}z_3 \sum_m G_{i\downarrow m\downarrow i\downarrow m\downarrow}^{\text{F}}\left(z_1,z_3\right) W_{m\downarrow j\uparrow}^{\text{ns},\mathfrak{f},1/2}\left(z_3,z_2\right),$$

$$\Phi_{ij\uparrow}^{GW,\mathfrak{f},1/2}\left(z_1,z_2\right) =: U\left(z_1\right) G_{i\downarrow j\downarrow i\downarrow j\downarrow}^{\text{F}}\left(z_1,z_2\right) U\left(z_2\right),$$

$$W_{i\downarrow j\uparrow}^{\text{ns},\mathfrak{f},1/2}\left(z_1,z_2\right) = U\left(z_1\right)\int_{\mathcal{C}}\mathrm{d}z_3 \sum_m G_{i\uparrow m\uparrow i\uparrow m\uparrow}^{\text{F}}\left(z_1,z_3\right) W_{m\uparrow j\uparrow}^{\text{ns},\mathfrak{f},1/2}\left(z_3,z_2\right), \tag{312}$$

$$W_{i\downarrow j\downarrow}^{\text{ns},\mathfrak{f},1/2}\left(z_1,z_2\right) = \Phi_{ij\downarrow}^{GW,\mathfrak{f},1/2}\left(z_1,z_2\right) + U\left(z_1\right)\int_{\mathcal{C}}\mathrm{d}z_3 \sum_m G_{i\uparrow m\uparrow i\uparrow m\uparrow}^{\text{F}}\left(z_1,z_3\right) W_{m\uparrow j\downarrow}^{\text{ns},\mathfrak{f},1/2}\left(z_3,z_2\right),$$

$$\Phi_{ij\downarrow}^{GW,\mathfrak{f},1/2}\left(z_1,z_2\right) =: U\left(z_1\right) G_{i\uparrow j\uparrow i\uparrow j\uparrow}^{\text{F}}\left(z_1,z_2\right) U\left(z_2\right),$$

$$W_{i\uparrow j\downarrow}^{\text{ns},\mathfrak{f},1/2}\left(z_1,z_2\right) = U\left(z_1\right)\int_{\mathcal{C}}\mathrm{d}z_3 \sum_m G_{i\downarrow m\downarrow i\downarrow m\downarrow}^{\text{F}}\left(z_1,z_3\right) W_{m\downarrow j\downarrow}^{\text{ns},\mathfrak{f},1/2}\left(z_3,z_2\right). \tag{313}$$

Interestingly, the equations for the screened potentials with different spin combinations, equations (312) and (313), do not contain a contribution from the bare interaction.

The correlation selfenergies of fermions with spin up and down read, respectively,

$$\Sigma_{i\uparrow j\uparrow}^{GW,\text{corr},\mathfrak{f},1/2}\left(z_1,z_2\right) = \mathrm{i}\hbar W_{i\uparrow j\uparrow}^{\text{ns},\mathfrak{f},1/2}\left(z_1,z_2\right) G_{i\uparrow j\uparrow}\left(z_1,z_2\right), \tag{314}$$

$$\Sigma_{i\downarrow j\downarrow}^{GW,\text{corr},\mathfrak{f},1/2}\left(z_1,z_2\right) = \mathrm{i}\hbar W_{i\downarrow j\downarrow}^{\text{ns},\mathfrak{f},1/2}\left(z_1,z_2\right) G_{i\downarrow j\downarrow}\left(z_1,z_2\right). \tag{315}$$

The diagrammatic representation of the leading terms for spin-1/2 fermions in the Hubbard basis is shown in figure 30. One recognizes a special structure of these equations for spin-$\frac{1}{2}$-fermions. The selfenergy $\left(\Sigma_{i\uparrow j\uparrow}^{GW,\mathfrak{f},1/2} \big/ \Sigma_{i\downarrow j\downarrow}^{GW,\mathfrak{f},1/2}\right)$, which couples only contributions of the same spin, also directly depends only on the same-spin parts of the screened interaction $\left(W_{i\uparrow j\uparrow}^{\text{ns},\mathfrak{f},1/2} G_{i\uparrow j\uparrow} \big/ W_{i\downarrow j\downarrow}^{\text{ns},\mathfrak{f},1/2} G_{i\downarrow j\downarrow}\right)$, see equations (314) and (315). The same-spin screened interaction, in turn, depends on the screened interaction with different spin orientations $\left(W_{m\downarrow j\uparrow}^{\text{ns},\mathfrak{f},1/2} \big/ W_{m\uparrow j\downarrow}^{\text{ns},\mathfrak{f},1/2}\right)$, which itself couples back to the same-spin part.
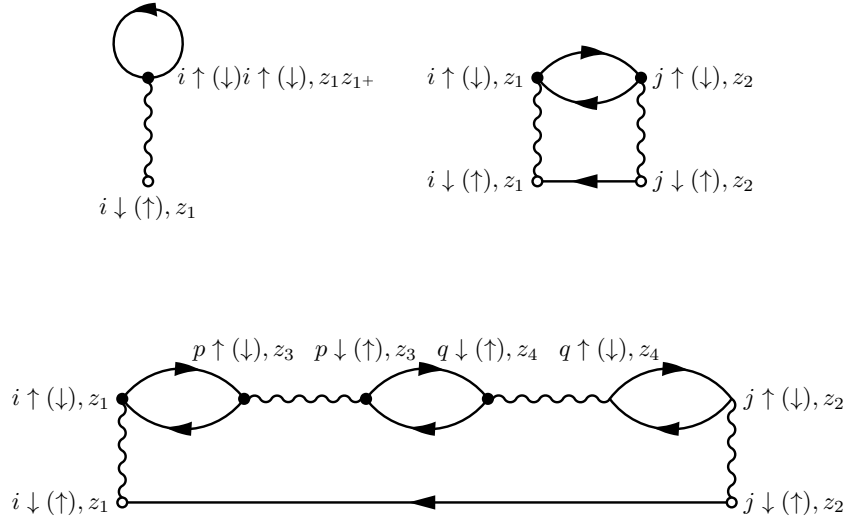
Figure 30. The first three terms of the GW selfenergy (mean field plus correlation term) in the Hubbard basis for spin-1/2 fermions. Note that the Fock term equals zero.

Finally, we present the respective '$\gtrless$' and retarded/advanced Keldysh components of the screened potential for all four spin combinations:

$$W_{i\uparrow j\uparrow}^{\mathrm{ns,f},1/2,\gtrless}\left(t_1,t_2\right) = \Phi_{ij\uparrow}^{GW,\mathfrak{f},1/2,\gtrless}\left(t_1,t_2\right)$$
$$+ U\left(t_1\right)\int_{t_0}^{t_1}\mathrm{d}t_3 \sum_m G_{i\downarrow m\downarrow i\downarrow m\downarrow}^{\mathrm{F},\mathcal{R}}\left(t_1,t_3\right)W_{m\downarrow j\uparrow}^{\mathrm{ns,f},1/2,\gtrless}\left(t_3,t_2\right)$$
$$+ U\left(t_1\right)\int_{t_0}^{t_2}\mathrm{d}t_3 \sum_m G_{i\downarrow m\downarrow i\downarrow m\downarrow}^{\mathrm{F},\gtrless}\left(t_1,t_3\right)W_{m\downarrow j\uparrow}^{\mathrm{ns,f},1/2,\mathcal{A}}\left(t_3,t_2\right),$$

$$W_{i\uparrow j\uparrow}^{\mathrm{ns,f},1/2,\mathcal{A}/\mathcal{R}}\left(t_1,t_2\right) = \Phi_{ij\uparrow}^{GW,\mathfrak{f},1/2,\mathcal{A}/\mathcal{R}}\left(t_1,t_2\right)$$
$$+ U\left(t_1\right)\int_{t_{1/2}}^{t_{2/1}}\mathrm{d}t_3 \sum_m G_{i\downarrow m\downarrow i\downarrow m\downarrow}^{\mathrm{F},\mathcal{A}/\mathcal{R}}\left(t_1,t_3\right)W_{m\downarrow j\uparrow}^{\mathrm{ns,f},1/2,\mathcal{A}/\mathcal{R}}\left(t_3,t_2\right),$$

$$W_{i\downarrow j\uparrow}^{\mathrm{ns,f},1/2,\gtrless}\left(t_1,t_2\right) = U\left(t_1\right)\int_{t_0}^{t_1}\mathrm{d}t_3 \sum_m G_{i\uparrow m\uparrow i\uparrow m\uparrow}^{\mathrm{F},\mathcal{R}}\left(t_1,t_3\right)W_{m\uparrow j\uparrow}^{\mathrm{ns,f},1/2,\gtrless}\left(t_3,t_2\right)$$
$$+ U\left(t_1\right)\int_{t_0}^{t_2}\mathrm{d}t_3 \sum_m G_{i\uparrow m\uparrow i\uparrow m\uparrow}^{\mathrm{F},\gtrless}\left(t_1,t_3\right)W_{m\uparrow j\uparrow}^{\mathrm{ns,f},1/2,\mathcal{A}}\left(t_3,t_2\right),$$

$$W_{i\downarrow j\uparrow}^{\mathrm{ns,f},1/2,\mathcal{A}/\mathcal{R}}\left(t_1,t_2\right) = U\left(t_1\right)\int_{t_{1/2}}^{t_{2/1}}\mathrm{d}t_3 \sum_m G_{i\uparrow m\uparrow i\uparrow m\uparrow}^{\mathrm{F},\mathcal{A}/\mathcal{R}}\left(t_1,t_3\right)W_{m\uparrow j\uparrow}^{\mathrm{ns,f},1/2,\mathcal{A}/\mathcal{R}}\left(t_3,t_2\right),$$

$$W_{i\downarrow j\downarrow}^{\mathrm{ns,f},1/2,\gtrless}\left(t_1,t_2\right) = \Phi_{ij\downarrow}^{GW,\mathfrak{f},1/2,\gtrless}\left(t_1,t_2\right)$$
$$+ U\left(t_1\right)\int_{t_0}^{t_1}\mathrm{d}t_3 \sum_m G_{i\uparrow m\uparrow i\uparrow m\uparrow}^{\mathrm{F},\mathcal{R}}\left(t_1,t_3\right)W_{m\uparrow j\downarrow}^{\mathrm{ns,f},1/2,\gtrless}\left(t_3,t_2\right)$$
$$+ U\left(t_1\right)\int_{t_0}^{t_2}\mathrm{d}t_3 \sum_m G_{i\uparrow m\uparrow i\uparrow m\uparrow}^{\mathrm{F},\gtrless}\left(t_1,t_3\right)W_{m\uparrow j\downarrow}^{\mathrm{ns,f},1/2,\mathcal{A}}\left(t_3,t_2\right),$$

$$W_{i\downarrow j\downarrow}^{\mathrm{ns,f},1/2,\mathcal{A}/\mathcal{R}}\left(t_1,t_2\right) = \Phi_{ij\downarrow}^{GW,\mathfrak{f},1/2,\mathcal{A}/\mathcal{R}}\left(t_1,t_2\right)$$
$$+ U\left(t_1\right)\int_{t_{1/2}}^{t_{2/1}} \mathrm{d}t_3 \sum_m G_{i\uparrow m\uparrow i\uparrow m\uparrow}^{\mathrm{F},\mathcal{A}/\mathcal{R}}\left(t_1,t_3\right)W_{m\uparrow j\downarrow}^{\mathrm{ns,f},1/2,\mathcal{A}/\mathcal{R}}\left(t_3,t_2\right),$$

$$W_{i\uparrow j\downarrow}^{\mathrm{ns,f},1/2,\gtrless}\left(t_1,t_2\right) = U\left(t_1\right)\int_{t_0}^{t_1} \mathrm{d}t_3 \sum_m G_{i\downarrow m\downarrow i\downarrow m\downarrow}^{\mathrm{F},\mathcal{R}}\left(t_1,t_3\right)W_{m\downarrow j\downarrow}^{\mathrm{ns,f},1/2,\gtrless}\left(t_3,t_2\right)$$
$$+ U\left(t_1\right)\int_{t_0}^{t_2} \mathrm{d}t_3 \sum_m G_{i\downarrow m\downarrow i\downarrow m\downarrow}^{\mathrm{F},\gtrless}\left(t_1,t_3\right)W_{m\downarrow j\downarrow}^{\mathrm{ns,f},1/2,\mathcal{A}}\left(t_3,t_2\right)$$

$$W_{i\uparrow j\downarrow}^{\mathrm{ns,f},1/2,\mathcal{A}/\mathcal{R}}\left(t_1,t_2\right) = U\left(t_1\right)\int_{t_{1/2}}^{t_{2/1}} \mathrm{d}t_3 \sum_m G_{i\downarrow m\downarrow i\downarrow m\downarrow}^{\mathrm{F},\mathcal{A}/\mathcal{R}}\left(t_1,t_3\right)W_{m\downarrow j\downarrow}^{\mathrm{ns,f},1/2,\mathcal{A}/\mathcal{R}}\left(t_3,t_2\right).$$

The correlation components of the selfenergy read

$$\Sigma_{i\uparrow j\uparrow}^{GW,\mathrm{corr},\mathfrak{f},\gtrless}\left(t_1,t_2\right) = \mathrm{i}\hbar W_{i\uparrow j\uparrow}^{\mathrm{ns,f},\gtrless}\left(t_1,t_2\right)G_{i\uparrow j\uparrow}^{\gtrless}\left(t_1,t_2\right),$$

(316)

$$\Sigma_{i\downarrow j\downarrow}^{GW,\mathrm{corr},\mathfrak{f},\gtrless}\left(t_1,t_2\right) = \mathrm{i}\hbar W_{i\downarrow j\downarrow}^{\mathrm{ns,f},\gtrless}\left(t_1,t_2\right)G_{i\downarrow j\downarrow}^{\gtrless}\left(t_1,t_2\right).$$

(317)

With this we conclude the discussion of the GW approximation. As mentioned before the strength of this approximation is the account of long-range screening effects and collective excitations (plasmons) which is of particular relevance for systems with Coulomb interaction. As we have seen in section 3, the GW approximation has an impressively high accuracy, in many cases. At the same time, the GW approximation does not take into account strong-coupling effects since it includes only terms of second order in the (screened) interaction. Effects of multiple scattering are, thus, missing.
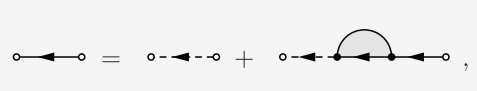
The inclusion of these effects for the case of a static pair interaction is the goal of the T-matrix approximation that is studied in section 5.3. On the other hand, to account for multiple scattering and dynamical screening simultaneously, is the goal of the FLEX scheme that is discussed in section 5.5.

5.3. Strong coupling. T-matrix approximation. Particle–particle and particle–hole T matrices

The goal of the T-matrix approximation is to capture effects of multiple scattering that are important in strongly coupled systems, but are missing in the second-Born approximation. The solution is to sum all higher-order Born terms up what leads to an effective interaction. In contrast to the GW approximation, the T-matrix approximation takes only the bare interaction, w, into account (at least in its standard versions), neglecting dynamical screening, and aims, instead, at a good approximation of the bare vertex function Λ. The goal here is to accurately capture multiple scattering effects. Thus, its constitutive equations are the Dyson equation[28],
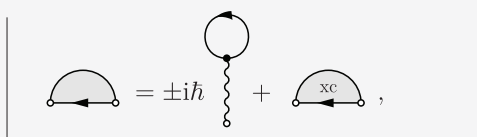
$$G(1,2) = G^{(0)}(1,2) + G^{(0)}(1,3)\Sigma(3,4)G(4,2)$$

(318)

the equation for the selfenergy, see equations (95) and (97),
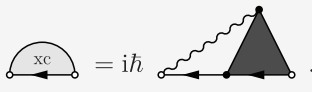
$$\Sigma(1,2) = \Sigma^{\mathrm{H}}(1,2) + \Sigma^{\mathrm{xc}}(1,2)$$
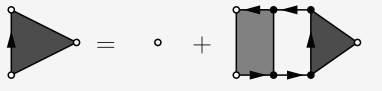
(319)

---

[28] The corresponding equations in the full notation are given in section 1.4 of the supplement 20.
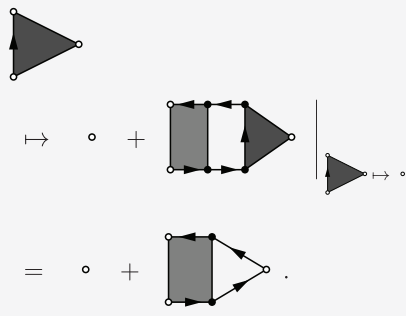
with the exchange–correlation selfenergy (all contributions beyond Hartree) given by

$$
\begin{aligned}
\Sigma^{\mathrm{xc}}\!\left(1,2\right) \\
= \mathrm{i}\hbar w\!\left(1,3\right)G\!\left(1,4\right)\Lambda\!\left(4,2,3\right)
\end{aligned}
\qquad
\text{(320)}
$$
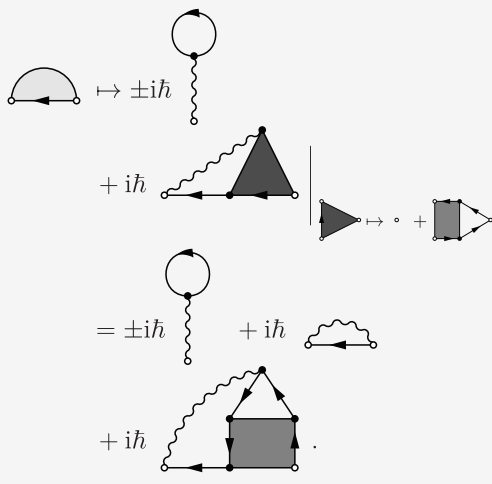
The bare vertex Λ is self-consistently given as the solution of the integral equation

$$
\begin{aligned}
\Lambda\!\left(1,2,3\right) = \delta\!\left(1,2^{+}\right)\delta\!\left(3,2\right) \\
+ \frac{\delta\Sigma\!\left(1,2\right)}{\delta G\!\left(4,5\right)}G\!\left(4,6\right)G\!\left(7,5\right)\Lambda\!\left(6,7,3\right)
\end{aligned}
\qquad
\text{(321)}
$$

If these equations are iterated *ad infinitum*, all selfenergy terms will be generated. To break the circular dependence between equations (320) and (321), the *T*-matrix approximation starts by taking the bare vertex on the right-hand side of equation (321) only in zeroth order, transforming it into

$$
\begin{aligned}
\Lambda^{\mathrm{cl}}\!\left(1,2,3\right) = \delta\!\left(1,2^{+}\right)\delta\!\left(3,2\right) \\
+ \frac{\delta\Sigma^{\mathrm{cl}}\!\left(1,2\right)}{\delta G\!\left(4,5\right)}G\!\left(4,6\right)G\!\left(7,5\right)\Lambda^{(0)}\!\left(6,7,3\right) \\
= \delta\!\left(1,2^{+}\right)\delta\!\left(3,2\right) \\
+ \frac{\delta\Sigma^{\mathrm{cl}}\!\left(1,2\right)}{\delta G\!\left(4,5\right)}G\!\left(4,3\right)G\!\left(3,5\right)
\end{aligned}
\qquad
\text{(322)}
$$

This closure of the equation for Λ allows to systematically generate results for the selfenergy which we will denote by the superscript 'cl'. Using this result in equation (319), we obtain (see equation (156))

$$
\begin{aligned}
\Sigma^{\mathrm{cl}}\!\left(1,2\right) \\
= \Sigma^{\mathrm{H}}\!\left(1,2\right) \\
+ \mathrm{i}\hbar w\!\left(1,3\right)G\!\left(1,4\right)\Lambda^{\mathrm{cl}}\!\left(4,2,3\right) \\
= \Sigma^{\mathrm{H}}\!\left(1,2\right) + \Sigma^{\mathrm{F}}\!\left(1,2\right) \\
+ \mathrm{i}\hbar w\!\left(1,3\right)G\!\left(1,4\right)\frac{\delta\Sigma^{\mathrm{cl}}\!\left(4,2\right)}{\delta G\!\left(5,6\right)} \\
G\!\left(5,3\right)G\!\left(3,6\right)
\end{aligned}
\qquad
\text{(323)}
$$

To solve for $\delta \Sigma^{cl}/\delta G$, we differentiate the whole equation with respect to G:

$$\frac{\delta \Sigma^{cl}(1,2)}{\delta G(7,8)} = \pm i\hbar \delta(1,2)\delta(7,8)w(1,7) + i\hbar \delta(1,7)\delta(2,8)w(1,2)$$

$$+ i\hbar \delta(1,7)w(1,3)\frac{\delta \Sigma^{cl}(8,2)}{\delta G(5,6)}G(5,3)G(3,6)$$

$$+ i\hbar w(1,8)G(1,4)\frac{\delta \Sigma^{cl}(4,2)}{\delta G(7,6)}G(8,6)$$

$$+ i\hbar w(1,7)G(1,4)\frac{\delta \Sigma^{cl}(4,2)}{\delta G(5,8)}G(5,7)$$

$$+ i\hbar w(1,3)G(1,4)\frac{\delta \Sigma^{cl}(4,2)}{\delta G(5,6)\delta G(7,8)}G(5,3)G(3,6)$$

(324)
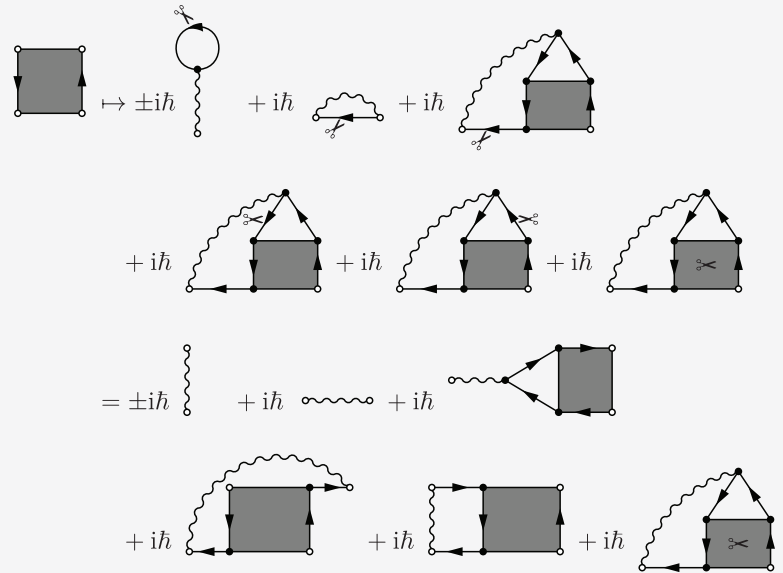
This equation is still very complicated. Therefore, to make further progress, we transform equation (324) into a closed equation for $\frac{\delta \Sigma^{cl}}{\delta G}$ by neglecting the term $\frac{\delta \Sigma^{cl}_{nj}(z_4,z_2)}{\delta G_{rs}(z_5,z_6)\delta G_{tu}(z_7,z_8)}$. The first iteration yields the second-order terms

$$\frac{\delta\Sigma^{\mathrm{cl},(2)}\big(1,2\big)}{\delta G\big(7,8\big)} \approx \mathrm{i}\hbar\delta\big(1,7\big)w\big(1,3\big)\frac{\delta\Sigma^{\mathrm{cl},(1)}\big(8,2\big)}{\delta G\big(5,6\big)}G\big(5,3\big)G\big(3,6\big)$$

$$+ \mathrm{i}\hbar w\big(1,8\big)G\big(1,4\big)\frac{\delta\Sigma^{\mathrm{cl},(1)}\big(4,2\big)}{\delta G\big(7,6\big)}G\big(8,6\big)$$

$$+ \mathrm{i}\hbar w\big(1,7\big)G\big(1,4\big)\frac{\delta\Sigma^{\mathrm{cl},(1)}\big(4,2\big)}{\delta G\big(5,8\big)}G\big(5,7\big)$$

$$= \pm\big(\mathrm{i}\hbar\big)^2\delta\big(1,7\big)\delta\big(8,2\big)w\big(1,3\big)w\big(2,5\big)G\big(5,3\big)G\big(3,5\big)$$

$$+ \big(\mathrm{i}\hbar\big)^2\delta\big(1,7\big)w\big(1,3\big)w\big(8,2\big)G\big(8,3\big)G\big(3,2\big)$$

$$\pm \big(\mathrm{i}\hbar\big)^2 w\big(1,8\big)G\big(1,2\big)w\big(2,7\big)G\big(8,7\big)$$

$$+ \big(\mathrm{i}\hbar\big)^2 w\big(1,8\big)G\big(1,7\big)w\big(7,2\big)G\big(8,2\big)$$

$$\pm \big(\mathrm{i}\hbar\big)^2 w\big(1,7\big)G\big(1,2\big)w\big(2,8\big)G\big(8,7\big)$$

$$+ \big(\mathrm{i}\hbar\big)^2\delta\big(2,8\big)w\big(1,7\big)G\big(1,4\big)w\big(4,2\big)G\big(4,7\big)$$

(325)
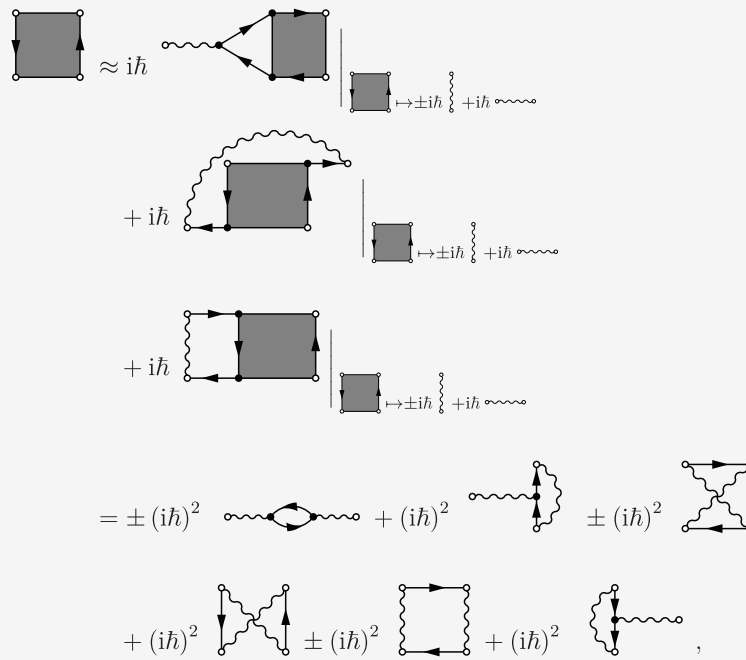
recovering equations (220) and (225) from the derivation of the third-order selfenergy guided by Hedin's equations. Note that, for the first iteration, $\frac{\delta\Sigma^{\mathrm{cl}}_{nj}(z_4,z_2)}{\delta G_{rs}(z_5,z_6)\delta G_{tu}(z_7,z_8)}$ is exactly equal to zero, thus equation (325) is also exact up to second order in w.

Considering equation (324), in the following, each of the three leading higher-order terms will be treated separately, starting off its particular diagrammatic series. Looking back at equations (324) and (325), it is convenient to choose a common starting point for all series, leading to the same first- and second-order selfenergy contributions,

$$\Sigma^{\mathrm{cl},(1)}\big(1,2\big) = \Sigma^{\mathrm{H}}\big(1,2\big) + \Sigma^{\mathrm{F}}\big(1,2\big)$$

(326)

$$
\begin{aligned}
&\Sigma^{\mathrm{cl},(2)}\big(1,2\big)\\
&= i\hbar w\big(1,3\big)G\big(1,4\big)\frac{\delta\Sigma^{\mathrm{cl},(1)}\big(4,2\big)}{\delta G\big(5,6\big)}\\
&\quad G\big(5,3\big)G\big(3,6\big)\\
&= \pm\big(i\hbar\big)^2 w\big(1,3\big)G\big(1,2\big)w\big(2,5\big)\\
&\quad G\big(5,3\big)G\big(3,5\big)\\
&\quad + \big(i\hbar\big)^2 w\big(1,3\big)G\big(1,4\big)w\big(4,2\big)\\
&\quad G\big(4,3\big)G\big(3,2\big)
\end{aligned}
$$

(327)

which agree with the exact first and second-order terms, already encountered in equations (158), (176) and (183).

The first diagram series (A) is generated by decoupling the first higher-order contribution of the derivation of the selfenergy in equation (324), leading to

$$
\begin{aligned}
&\frac{\delta\Sigma^{\mathrm{cl,A}}\big(1,2\big)}{\delta G\big(7,8\big)}\\
&= \pm i\hbar\delta\big(1,2\big)\delta\big(7,8\big)w\big(1,7\big)\\
&\quad + i\hbar\delta\big(1,7\big)\delta\big(2,8\big)w\big(1,2\big)\\
&\quad + i\hbar\delta\big(1,7\big)w\big(1,3\big)\frac{\delta\Sigma^{\mathrm{cl,A}}\big(8,2\big)}{\delta G\big(5,6\big)}\\
&\quad G\big(5,3\big)G\big(3,6\big)
\end{aligned}
$$

(328)

The corresponding third-order selfenergy terms of series A follow by insertion of the respective second-order derivative terms in equation (325) as

$$
\begin{aligned}
&\Sigma^{\mathrm{cl,A}(3)}\big(1,2\big)\\
&= i\hbar w\big(1,3\big)G\big(1,4\big)\frac{\delta\Sigma^{\mathrm{cl,A}(2)}\big(4,2\big)}{\delta G\big(5,6\big)}\\
&\quad G\big(5,3\big)G\big(3,6\big)\\
&= \pm\big(i\hbar\big)^3 w\big(1,3\big)G\big(1,4\big)w\big(4,5\big)w\big(2,6\big)\\
&\quad G\big(6,5\big)G\big(5,6\big)G\big(4,3\big)G\big(3,2\big)\\
&\quad + \big(i\hbar\big)^3 w\big(1,3\big)G\big(1,4\big)w\big(4,5\big)w\big(6,2\big)\\
&\quad G\big(6,5\big)G\big(5,2\big)G\big(4,3\big)G\big(3,6\big)
\end{aligned}
$$

(329)

At this point it is convenient to go back to the full notation and, particularly, the single-time interaction, to estimate the numerical effort of computationally solving the first diagrammatic series. By introducing the kernel K in the following way,

$$
K^{\mathrm{A}}_{ijkl}\big(z_1,z_2,z_3,z_4\big) := \pm\frac{\delta\Sigma^{\mathrm{cl,A}}_{ik}\big(z_1,z_3\big)}{\delta G_{lj}\big(z_4,z_2\big)},
$$

(330)

we arrive at a closed equation for $K_{ijkl}^{\text{A}}\left(z_1, z_2, z_3, z_4\right)$,

$$
\begin{aligned}
K_{ijkl}^{\text{A}}\left(z_1, z_2, z_3, z_4\right) = &\pm i\hbar \delta_{\mathcal{C}}\left(z_1, z_3\right)\delta_{\mathcal{C}}\left(z_1, z_4\right)\delta_{\mathcal{C}}\left(z_{1+}, z_2\right)w_{ijkl}^{\pm}\left(z_1\right) \\
&+ i\hbar \delta_{\mathcal{C}}\left(z_1, z_4\right)\sum_{pq} w_{ipql}\left(z_1\right) \\
&\times \int_{\mathcal{C}} \mathrm{d}z_5 \mathrm{d}z_6 \sum_{rs} K_{jskr}^{\text{A}}\left(z_2, z_6, z_3, z_5\right)G_{rp}\left(z_5, z_1\right)G_{qs}\left(z_1, z_6\right),
\end{aligned}
$$

(331)

where we introduced the (anti-)symmetrized interaction, $w_{ijkl}^{\pm}\left(z_1\right) := w_{ijkl}\left(z_1\right) \pm w_{jikl}\left(z_1\right)$. Iterating this equation, starting from

$$
K_{ijkl}^{\text{A},(1)}\left(z_1, z_2, z_3, z_4\right) = \pm i\hbar \delta_{\mathcal{C}}\left(z_1, z_3\right)\delta_{\mathcal{C}}\left(z_1, z_4\right)\delta_{\mathcal{C}}\left(z_{1+}, z_2\right)w_{ijkl}^{\pm}\left(z_1\right),
$$

we have, for the second iteration,

$$
\begin{aligned}
K_{ijkl}^{\text{A},(2)}\left(z_1, z_2, z_3, z_4\right) &= i\hbar \delta_{\mathcal{C}}\left(z_1, z_4\right)\sum_{pq} w_{ipql}\left(z_1\right) \\
&\times \int_{\mathcal{C}} \mathrm{d}z_5 \mathrm{d}z_6 \sum_{rs} K_{jskr}^{\text{A},(1)}\left(z_2, z_6, z_3, z_5\right)G_{rp}\left(z_5, z_1\right)G_{qs}\left(z_1, z_6\right) \\
&= \pm\left(i\hbar\right)^2 \delta_{\mathcal{C}}\left(z_1, z_4\right)\delta_{\mathcal{C}}\left(z_2, z_3\right)\sum_{pq} w_{ipql}\left(z_1\right)\sum_{rs} w_{jskr}^{\pm}\left(z_2\right)G_{rp}\left(z_2, z_1\right)G_{qs}\left(z_1, z_2\right).
\end{aligned}
$$

Similarly, we obtain the third and fourth iterations,

$$
\begin{aligned}
K_{ijkl}^{\text{A},(3)}\left(z_1, z_2, z_3, z_4\right) &= i\hbar \delta_{\mathcal{C}}\left(z_1, z_4\right)\sum_{pq} w_{ipql}\left(z_1\right) \\
&\times \int_{\mathcal{C}} \mathrm{d}z_5 \mathrm{d}z_6 \sum_{rs} K_{jskr}^{\text{A},(2)}\left(z_2, z_6, z_3, z_5\right)G_{rp}\left(z_5, z_1\right)G_{qs}\left(z_1, z_6\right) \\
&= \pm i\hbar \delta_{\mathcal{C}}\left(z_1, z_4\right)\sum_{pq} w_{ipql}\left(z_1\right)\sum_{rs} K_{jskr}^{\text{A},(2)}\left(z_2, z_3, z_3, z_2\right)G_{rp}\left(z_2, z_1\right)G_{qs}\left(z_1, z_3\right),
\end{aligned}
$$

$$
\begin{aligned}
K_{ijkl}^{\text{A},(4)}\left(z_1, z_2, z_3, z_4\right) &= i\hbar \delta_{\mathcal{C}}\left(z_1, z_4\right)\sum_{pq} w_{ipql}\left(z_1\right) \\
&\times \int_{\mathcal{C}} \mathrm{d}z_5 \mathrm{d}z_6 \sum_{rs} K_{jskr}^{\text{A},(3)}\left(z_2, z_6, z_3, z_5\right)G_{rp}\left(z_5, z_1\right)G_{qs}\left(z_1, z_6\right) \\
&= i\hbar \delta_{\mathcal{C}}\left(z_1, z_4\right)\sum_{pq} w_{ipql}\left(z_1\right)\int_{\mathcal{C}} \mathrm{d}z_6 \sum_{rs} K_{jskr}^{\text{A},(3)}\left(z_2, z_6, z_3, z_2\right)G_{rp}\left(z_2, z_1\right)G_{qs}\left(z_1, z_6\right),
\end{aligned}
$$

and a similar structure for the higher orders. It is noteworthy that the computation of the fourth- and higher-order iterations are of complexity $\mathcal{O}\left(N_{\text{t}}^4\right)$, since, due to the appearance of the delta function, $\delta_{\mathcal{C}}\left(z_1, z_4\right)$,

$$
K_{ijkl}^{\text{A},(N)}\left(z_1, z_2, z_3, z_4\right) = \delta_{\mathcal{C}}\left(z_1, z_4\right)K_{ijkl}^{\text{A},(N)}\left(z_1, z_2, z_3, z_1\right),
$$

(332)

and the right-hand side contains one integral over an intermediate time, which typically limits the applicability of this approximation to very short time scales. Therefore, series A is usually omitted in efficient quantum-many-body frameworks.

The second approximation (B) is generated by the second higher-order contribution of $\frac{\delta\Sigma_{ij}^{\rm cl}}{\delta G}$ in equation (324), leading to

$$
\begin{aligned}
\frac{\delta\Sigma^{\rm cl,B}(1,2)}{\delta G(7,8)} &= \pm\mathrm{i}\hbar\,\delta(1,2)\,\delta(7,8)\,w(1,7)\\
&\quad + \mathrm{i}\hbar\,\delta(1,7)\,\delta(2,8)\,w(1,2)\\
&\quad + \mathrm{i}\hbar\,w(1,8)\,G(1,4)\frac{\delta\Sigma^{\rm cl,B}(4,2)}{\delta G(7,6)}G(8,6)
\end{aligned}
$$

(333)

Using the respective second-order derivative terms in equation (325) one obtains the third-order selfenergy contributions of series B,

$$
\begin{aligned}
\Sigma^{\rm cl,B(3)}(1,2) &= \mathrm{i}\hbar\,w(1,3)\,G(1,4)\frac{\delta\Sigma^{\rm cl,B(2)}(4,2)}{\delta G(5,6)}\\
&\quad\ G(5,3)\,G(3,6)\\
&= \pm(\mathrm{i}\hbar)^3 w(1,3)\,G(1,4)\,w(4,6)\,G(4,2)\\
&\quad\ w(2,5)\,G(6,5)\,G(5,3)\,G(3,6)\\
&\quad + (\mathrm{i}\hbar)^3 w(1,3)\,G(1,4)\,w(4,6)\,G(4,5)\\
&\quad\ w(5,2)\,G(6,2)\,G(5,3)\,G(3,6)
\end{aligned}
$$

(334)

In the full notation with the single-time interaction we again introduce a kernel K for the series B:

$$
K_{ijkl}^{\rm B}\big(z_1,z_2,z_3,z_4\big) := \pm\frac{\delta\Sigma_{ik}^{\rm cl,B}(z_1,z_3)}{\delta G_{lj}(z_4,z_2)},
\tag{335}
$$

which obeys the equation of motion

$$
\begin{aligned}
K_{ijkl}^{\rm B}\big(z_1,z_2,z_3,z_4\big) &= \pm\mathrm{i}\hbar\,\delta_{\mathcal{C}}(z_1,z_3)\,\delta_{\mathcal{C}}(z_1,z_4)\,\delta_{\mathcal{C}}(z_{1+},z_2)\,w_{ijkl}^{\pm}(z_1)\\
&\quad + \mathrm{i}\hbar\,\delta_{\mathcal{C}}(z_1,z_2)\sum_{mq}w_{ijqm}(z_1)\int_{\mathcal{C}}\mathrm{d}z_5\sum_n G_{mn}(z_1,z_5)\\
&\quad\ \times\int_{\mathcal{C}}\mathrm{d}z_6\sum_s K_{nskl}^{\rm B}(z_5,z_6,z_3,z_4)\,G_{qs}(z_1,z_6).
\end{aligned}
$$

Iterating, starting again from the first iteration,

$$
K_{ijkl}^{\rm B,(1)}\big(z_1,z_2,z_3,z_4\big) = \pm\mathrm{i}\hbar\,\delta_{\mathcal{C}}(z_1,z_3)\,\delta_{\mathcal{C}}(z_1,z_4)\,\delta_{\mathcal{C}}(z_{1+},z_2)\,w_{ijkl}^{\pm}(z_1),
$$

we find, for the second iteration,

$$
\begin{aligned}
K_{ijkl}^{\rm B,(2)}\big(z_1,z_2,z_3,z_4\big) &= \mathrm{i}\hbar\,\delta_{\mathcal{C}}(z_1,z_2)\sum_{mq}w_{ijqm}(z_1)\int_{\mathcal{C}}\mathrm{d}z_5\sum_n G_{mn}(z_1,z_5)\\
&\quad \times\int_{\mathcal{C}}\mathrm{d}z_6\sum_s K_{nskl}^{\rm B,(1)}(z_5,z_6,z_3,z_4)\,G_{qs}(z_1,z_6)\\
&= \mathrm{i}\hbar\,\delta_{\mathcal{C}}(z_1,z_2)\,\delta_{\mathcal{C}}(z_3,z_4)\sum_{mq}w_{ijqm}(z_1)\sum_n G_{mn}(z_1,z_3)\sum_s\\
&\quad K_{nskl}^{\rm B,(1)}(z_3,z_3,z_3,z_3)\,G_{qs}(z_1,z_3)
\end{aligned}
$$

(336)

and, for the third iteration,

$$K_{ijkl}^{B,(3)}\left(z_1,z_2,z_3,z_4\right) = i\hbar\delta_{\mathcal{C}}\left(z_1,z_2\right)\sum_{mq}w_{ijqm}\left(z_1\right)\int_{\mathcal{C}}dz_5\sum_{n}G_{mn}\left(z_1,z_5\right)$$

$$\times\int_{\mathcal{C}}dz_6\sum_{s}K_{nskl}^{B,(2)}\left(z_5,z_6,z_3,z_4\right)G_{qs}\left(z_1,z_6\right)$$

$$= i\hbar\delta_{\mathcal{C}}\left(z_1,z_2\right)\delta_{\mathcal{C}}\left(z_3,z_4\right)\sum_{mq}w_{ijqm}\left(z_1\right)\int_{\mathcal{C}}dz_5\sum_{n}G_{mn}\left(z_1,z_5\right)$$

$$\times\sum_{s}K_{nskl}^{B,(2)}\left(z_5,z_5,z_3,z_3\right)G_{qs}\left(z_1,z_5\right). \tag{337}$$

In similar manner higher orders are derived. The structure of this approximation is such that the computation of all terms scales as $\mathcal{O}\left(N_t^3\right)$ since, due to the two delta functions, we have, for each iteration order (N),

$$K_{ijkl}^{B,(N)}\left(z_1,z_2,z_3,z_4\right) = \delta_{\mathcal{C}}\left(z_1,z_2\right)\delta_{\mathcal{C}}\left(z_3,z_4\right)K_{ijkl}^{B,(N)}\left(z_1,z_2\right),$$

and one integration on the right-hand side. With this, one finds (see equation (337)),

$$K_{ijkl}^{B}\left(z_1,z_3\right) = \delta_{\mathcal{C}}\left(z_1,z_3\right)K_{ijkl}^{B,(1)}\left(z_1,z_1\right) \tag{338}$$

$$+ \sum_{mq}w_{ijqm}\left(z_1\right)\int_{\mathcal{C}}dz_5\sum_{ns}G_{mqns}^{H}\left(z_1,z_5\right)K_{nskl}^{B}\left(z_5,z_3\right),$$

where equation (280) has been used, in the last line. To simplify the following expressions further, it is useful to eliminate the contributions with the delta function by introducing the non-singular kernel (superscript 'ns')[29] (see equations (338) and (336)), according to

$$K_{ijkl}^{B,ns}\left(z_1,z_2\right) := K_{ijkl}^{B}\left(z_1,z_2\right) - \delta_{\mathcal{C}}\left(z_1,z_2\right)K_{ijkl}^{B,(1)}\left(z_1,z_1\right)$$

$$= K_{ijkl}^{B}\left(z_1,z_2\right) \mp i\hbar\delta_{\mathcal{C}}\left(z_1,z_2\right)w_{ijkl}^{\pm}\left(z_1\right). \tag{339}$$

It obeys its own equation where no singular terms appear anymore (see equation (338)),

$$K_{ijkl}^{B,ns}\left(z_1,z_2\right) = \sum_{mq}w_{ijqm}\left(z_1\right)\int_{\mathcal{C}}dz_5\sum_{ns}G_{mqns}^{H}\left(z_1,z_5\right)$$

$$\times\left\{K_{nskl}^{B,ns}\left(z_5,z_2\right) \pm i\hbar\delta_{\mathcal{C}}\left(z_5,z_2\right)w_{nskl}^{\pm}\left(z_2\right)\right\}$$

$$= \pm i\hbar\sum_{mq}w_{ijqm}\left(z_1\right)\sum_{ns}G_{mqns}^{H}\left(z_1,z_2\right)w_{nskl}^{\pm}\left(z_2\right)$$

$$+ \sum_{mq}w_{ijqm}\left(z_1\right)\int_{\mathcal{C}}dz_5\sum_{ns}G_{mqns}^{H}\left(z_1,z_5\right)K_{nskl}^{B,ns}\left(z_5,z_2\right). \tag{340}$$

The corresponding selfenergy reads, (see equation (323)),

$$\Sigma_{ij}^{cl,B}\left(z_1,z_2\right) = \Sigma_{ij}^{H}\left(z_1,z_2\right) + \Sigma_{ij}^{F}\left(z_1,z_2\right) + \Sigma_{ij}^{cl,corr,B}\left(z_1,z_2\right) \tag{341}$$

$$\Sigma_{ij}^{cl,corr,B}\left(z_1,z_2\right) =: \pm i\hbar\sum_{mpq}w_{ipqm}\left(z_1\right)\int_{\mathcal{C}}dz_3\sum_{n}G_{mn}\left(z_1,z_3\right)$$

$$\int_{\mathcal{C}}dz_4dz_5\sum_{rs}K_{nsjr}^{B}\left(z_3,z_5,z_2,z_4\right)G_{rp}\left(z_4,z_1\right)G_{qs}\left(z_1,z_5\right), \tag{342}$$

[29] This follows the procedure applied for the GWA, section 5.2.

where we defined the correlation part of the selfenergy via the additional superscript 'corr'. Inserting the expression for K^B, we find

$$\Sigma_{ij}^{cl,corr,B}\left(z_1,z_2\right) = \pm i\hbar\sum_{mpq}w_{ipqm}\left(z_1\right)\int_{\mathcal{C}}dz_3\sum_{n}G_{mn}\left(z_1,z_3\right)$$

$$\times\sum_{rs}G_{qs}\left(z_1,z_3\right)K_{nsjr}^{B}\left(z_3,z_2\right)G_{rp}\left(z_2,z_1\right),$$

which, by insertion of equation (339), transforms to

$$\Sigma_{ij}^{cl,corr,B}\left(z_1,z_2\right) = \pm\sum_{mpq}w_{ipqm}\left(z_1\right)\int_{\mathcal{C}}dz_3\sum_{nrs}G_{mqns}^{H}\left(z_1,z_3\right)$$

$$\times\left\{K_{nsjr}^{B,ns}\left(z_3,z_2\right)\pm i\hbar\delta_{\mathcal{C}}\left(z_3,z_2\right)w_{nsjr}^{\pm}\left(z_2\right)\right\}G_{rp}\left(z_2,z_1\right).$$

After restructuring, one has

$$\Sigma_{ij}^{cl,corr,B}\left(z_1,z_2\right) = \pm\left(\pm i\hbar\sum_{mpq}w_{ipqm}\left(z_1\right)\sum_{nrs}G_{mqns}^{H}\left(z_1,z_3\right)w_{nsjr}^{\pm}\left(z_2\right)\right.$$

$$+\sum_{mpq}w_{ipqm}\left(z_1\right)\int_{\mathcal{C}}dz_3\sum_{nrs}G_{mqns}^{H}\left(z_1,z_3\right)$$

$$\left.K_{nsjr}^{B,ns}\left(z_3,z_2\right)\right)G_{rp}\left(z_2,z_1\right).$$

Looking at equation (340), it is obvious that the right-hand side already contains the first iteration of the recursion equation, so we simply have

$$\Sigma_{ij}^{cl,corr,B}\left(z_1,z_2\right) = \pm\sum_{pr}K_{ipjr}^{B,ns}\left(z_1,z_2\right)G_{rp}\left(z_2,z_1\right). \tag{343}$$

With the definition

$$i\hbar T_{ijkl}^{pp}\left(z_1,z_2\right) := \pm K_{ijkl}^{B,ns}\left(z_1,z_2\right), \tag{344}$$

the coupled solution of, equations (340) and (343) becomes,

$$T_{ijkl}^{pp}\left(z_1,z_2\right) = \Phi_{ijkl}^{pp}\left(z_1,z_2\right) \tag{345}$$

$$+\sum_{mq}w_{ijqm}\left(z_1\right)\sum_{ns}\int_{\mathcal{C}}dz_5\,G_{mqns}^{H}\left(z_1,z_5\right)T_{nskl}^{pp}\left(z_5,z_2\right),$$

$$\Phi_{ijkl}^{pp}\left(z_1,z_2\right) =: \sum_{mq}w_{ijqm}\left(z_1\right)\sum_{ns}G_{mqns}^{H}\left(z_1,z_2\right)w_{nskl}^{\pm}\left(z_2\right), \tag{346}$$

where we introduced an abbreviation for the first term that contains the second-Born approximation (as we did before for the *GW* approximation).

Thus, according to equation (343), the correlation part of the selfenergy in the so-called (particle–particle) *T*-matrix approximation is given by

$$\Sigma_{ij}^{pp}\left(z_1,z_2\right) := \Sigma_{ij}^{T^{pp},corr}\left(z_1,z_2\right) = i\hbar\sum_{pr}T_{ipjr}^{pp}\left(z_1,z_2\right)G_{rp}\left(z_2,z_1\right). \tag{347}$$

The *T* matrix relates to a similar quantity in scattering theory, which is called *transfer matrix* there. It describes an interacting scattering state of a system selfconsistently in terms of a free state of two particles which undergo multiple (in general, infinitely many) scattering events with each other, which can be resummed into the transfer matrix acting on the two particles. Looking at equations (345)

and (347), the same interpretation is possible, since G^{H} describes a particle pair, and their scattering is governed by T^{pp}.

The Keldysh correlation components of the particle–particle T matrix read

$$
T^{\mathrm{pp},\gtrless}_{ijkl}\left(t_1,t_2\right) = \Phi^{\mathrm{pp},\gtrless}_{ijkl}\left(t_1,t_2\right) + \sum_{mq} w_{ijqm}\left(t_1\right)\sum_{ns} \tag{348}
$$

$$
\times \left(\int_{t_0}^{t_1} dt_5\, G^{\mathrm{H},\mathcal{R}}_{mqns}\left(t_1,t_5\right) T^{\mathrm{pp},\gtrless}_{nskl}\left(t_5,t_2\right) + \int_{t_0}^{t_2} dt_5\, G^{\mathrm{H},\gtrless}_{mqns}\left(t_1,t_5\right) T^{\mathrm{pp},\mathcal{A}}_{nskl}\left(t_5,t_2\right) \right),
$$

where $\Phi^{\mathrm{pp},\gtrless}$ is the '$\gtrless$' component of Φ^{pp} that is obtained from equation (346) by replacing $G^{\mathrm{H}} \to G^{\mathrm{H},\gtrless}$. Analogously, we have for the advanced/retarded Keldysh component and

$$
T^{\mathrm{pp},\mathcal{A}/\mathcal{R}}_{ijkl}\left(t_1,t_2\right) = \Phi^{\mathrm{pp},\mathcal{A}/\mathcal{R}}_{ijkl}\left(t_1,t_2\right)
$$

$$
+ \sum_{mq} w_{ijqm}\left(t_1\right)\sum_{ns} \int_{t_{1/2}}^{t_{2/1}} dt_5\, G^{\mathrm{H},\mathcal{A}/\mathcal{R}}_{mqns}\left(t_1,t_5\right) T^{\mathrm{pp},\mathcal{A}/\mathcal{R}}_{nskl}\left(t_5,t_2\right),
$$

where $\Phi^{\mathrm{pp},\mathcal{A}/\mathcal{R}}$ again follows from Φ^{pp} by replacing $G^{\mathrm{H}} \to G^{\mathrm{H},\mathcal{A}/\mathcal{R}}$, and in the notation $t_{1/2}$ the first (second) subscript refers to the advanced (retarded) function. For the correlation components of the particle–particle T-matrix selfenergy (347), we have

$$
\Sigma^{\mathrm{pp},\gtrless}_{ij}\left(t_1,t_2\right) = i\hbar \sum_{pr} T^{\mathrm{pp},\gtrless}_{ipjr}\left(t_1,t_2\right) G^{\lessgtr}_{rp}\left(t_2,t_1\right).
$$

5.3.1. Particle–particle T matrix in a diagonal basis. In a basis with diagonal interaction, $w_{ijkl} = \delta_{il}\delta_{jk} w_{ij}$, equation (345) attains the form

$$
T^{\mathrm{pp,diag}}_{ijkl}\left(z_1,z_2\right) =: \Phi^{\mathrm{pp,diag}}_{ijkl}\left(z_1,z_2\right) \tag{349}
$$

$$
+ w_{ij}\left(z_1\right) \sum_{ns} \int_{\mathcal{C}} dz_5\, G^{\mathrm{H}}_{ijns}\left(z_1,z_5\right) T^{\mathrm{pp,diag}}_{nskl}\left(z_5,z_2\right),
$$

where the diagonal basis version of equation (346) is

$$
\Phi^{\mathrm{pp,diag}}_{ijkl}\left(z_1,z_2\right) = w_{ij}\left(z_1\right)\left\{ G^{\mathrm{H}}_{ijlk}\left(z_1,z_2\right) \pm G^{\mathrm{H}}_{ijkl}\left(z_1,z_2\right)\right\} w_{lk}\left(z_2\right). \tag{350}
$$

The correlation part of the selfenergy, corresponding to equation (347), reads

$$
\Sigma^{\mathrm{pp,diag}}_{ij}\left(z_1,z_2\right) = i\hbar \sum_{pr} T^{\mathrm{pp,diag}}_{ipjr}\left(z_1,z_2\right) G_{rp}\left(z_2,z_1\right). \tag{351}
$$

The leading contributions to the selfenergy for a diagonal basis are shown in figure 31. The respective Keldysh matrix components are

$$
T^{\mathrm{pp,diag},\gtrless}_{ijkl}\left(t_1,t_2\right) = \Phi^{\mathrm{pp,diag},\gtrless}_{ijkl}\left(t_1,t_2\right)
$$

$$
+ w_{ij}\left(t_1\right)\left(\int_{t_0}^{t_1} dt_5 \sum_{ns} G^{\mathrm{H},\mathcal{R}}_{ijns}\left(t_1,t_5\right) T^{\mathrm{pp,diag},\gtrless}_{nskl}\left(t_5,t_2\right) \right.
$$

$$
\left. + \int_{t_0}^{t_2} dt_5\, G^{\mathrm{H},\gtrless}_{ijns}\left(t_1,t_5\right) T^{\mathrm{pp,diag},\mathcal{A}}_{nskl}\left(t_5,t_2\right) \right), \tag{352}
$$

$$
T^{\mathrm{pp,diag},\mathcal{A}/\mathcal{R}}_{ijkl}\left(t_1,t_2\right) = \Phi^{\mathrm{pp,diag},\mathcal{A}/\mathcal{R}}_{ijkl}\left(t_1,t_2\right) \tag{353}
$$

$$
+ w_{ij}\left(t_1\right) \sum_{ns} \int_{t_{1/2}}^{t_{2/1}} dt_5\, G^{\mathrm{H},\mathcal{A}/\mathcal{R}}_{ijns}\left(t_1,t_5\right) T^{\mathrm{pp,diag},\mathcal{A}/\mathcal{R}}_{nskl}\left(t_5,t_2\right)
$$

and, finally, the diagonal version of the correlation selfenergy (347) becomes

$$
\Sigma^{\mathrm{pp,diag},\gtrless}_{ij}\left(t_1,t_2\right) = \sum_{pr} T^{\mathrm{pp,diag},\gtrless}_{ipjr}\left(t_1,t_2\right) G^{\lessgtr}_{rp}\left(t_2,t_1\right).
$$

5.3.2. Particle–particle T matrix in the Hubbard basis. In the Hubbard basis the expressions for the T matrix simplify further. We start from the case of bosons. In the bosonic Hubbard basis, the particle–particle T matrix reads

$$
T^{\mathrm{pp},\flat}_{i\alpha j\beta k\alpha l\beta}\left(z_1,z_2\right) = \delta_{ij}\delta_{kl} \Phi^{\mathrm{pp},\flat}_{i\alpha i\beta k\alpha k\beta}\left(z_1,z_2\right) \tag{354}
$$

$$
+ \delta_{ij} U\left(z_1\right) \sum_{ns} \int_{\mathcal{C}} dz_5\, G^{\mathrm{H}}_{i\alpha i\beta n\alpha s\beta}\left(z_1,z_5\right) T^{\mathrm{pp},\flat}_{n\alpha s\beta k\alpha l\beta}\left(z_5,z_2\right),
$$

where the bosonic Hubbard version of the function Φ^{pp} is given by

$$
\Phi^{\mathrm{pp},\flat}_{i\alpha i\beta k\alpha k\beta}\left(z_1,z_2\right) =: 2U\left(z_1\right) G^{\mathrm{H}}_{i\alpha i\beta k\alpha k\beta}\left(z_1,z_2\right) U\left(z_2\right). \tag{355}
$$

For the correlation part of the selfenergy, we now have

$$
\Sigma^{\mathrm{pp},\flat}_{i\alpha j\alpha}\left(z_1,z_2\right) = i\hbar \sum_{pr}\sum_{\epsilon} T^{\mathrm{pp},\flat}_{i\alpha p\epsilon j\alpha r\epsilon}\left(z_1,z_2\right) G_{r\epsilon p\epsilon}\left(z_2,z_1\right).
$$

From these equations it is evident that the equality

$$
\Phi^{\mathrm{pp},\flat}_{i\alpha j\beta k\alpha l\beta}\left(z_1,z_2\right) = \delta_{ij}\delta_{kl} \Phi^{\mathrm{pp},\flat}_{i\alpha i\beta k\alpha k\beta}\left(z_1,z_2\right) =: \delta_{ij}\delta_{kl} \Phi^{\mathrm{pp},\flat}_{ik\alpha\beta}\left(z_1,z_2\right), \tag{356}
$$

implies $T^{\mathrm{pp},\flat}_{i\alpha j\beta k\alpha l\beta}\left(z_1,z_2\right) =: \delta_{ij}\delta_{kl} T^{\mathrm{pp},\flat}_{ik\alpha\beta}\left(z_1,z_2\right)$, which is verified by iteration. Regarding the notation, one has to bear in mind that $T^{\mathrm{pp},\flat}_{ik\alpha\beta}$ and $G^{\mathrm{H}}_{ik\alpha\beta} := G^{\mathrm{H}}_{i\alpha i\beta k\alpha k\beta}$ are quantities of all four spin-space orbitals $|i\alpha\rangle, |i\beta\rangle, |k\alpha\rangle, |k\beta\rangle$. With this, the equations become

$$
T^{\mathrm{pp},\flat}_{ik\alpha\beta}\left(z_1,z_2\right) = \Phi^{\mathrm{pp},\flat}_{ik\alpha\beta}\left(z_1,z_2\right)
$$

$$
+ U\left(z_1\right) \sum_{n} \int_{\mathcal{C}} dz_5\, G^{\mathrm{H}}_{in\alpha\beta}\left(z_1,z_5\right) T^{\mathrm{pp},\flat}_{nk\alpha\beta}\left(z_5,z_2\right),
$$

and the correlation selfenergy is

$$
\Sigma^{\mathrm{pp},\flat}_{i\alpha j\alpha}\left(z_1,z_2\right) = i\hbar \sum_{\epsilon} T^{\mathrm{pp},\flat}_{ij\alpha\epsilon}\left(z_1,z_2\right) G_{j\epsilon i\epsilon}\left(z_2,z_1\right).
$$

The Keldysh '$\gtrless$' matrix components of the selfenergy and the T matrix read

$$
\Sigma^{\mathrm{pp},\flat,\gtrless}_{i\alpha j\alpha}\left(t_1,t_2\right) = i\hbar \sum_{\epsilon} T^{\mathrm{pp},\flat,\gtrless}_{ij\alpha\epsilon}\left(t_1,t_2\right) G^{\lessgtr}_{j\epsilon i\epsilon}\left(t_2,t_1\right),
$$

$$
T^{\mathrm{pp},\flat,\gtrless}_{ik\alpha\beta}\left(t_1,t_2\right) = \Phi^{\mathrm{pp},\flat,\gtrless}_{ik\alpha\beta}\left(t_1,t_2\right) + U\left(t_1\right) \sum_{n} \tag{357}
$$

$$
\left(\int_{t_0}^{t_1} dt_5\, G^{\mathrm{H},\mathcal{R}}_{in\alpha\beta}\left(t_1,t_5\right) T^{\mathrm{pp},\gtrless}_{nk\alpha\beta}\left(t_5,t_2\right) + \int_{t_0}^{t_2} dt_5\, G^{\mathrm{H},\gtrless}_{in\alpha\beta}\left(t_1,t_5\right) T^{\mathrm{pp},\mathcal{A}}_{nk\alpha\beta}\left(t_5,t_2\right) \right),
$$
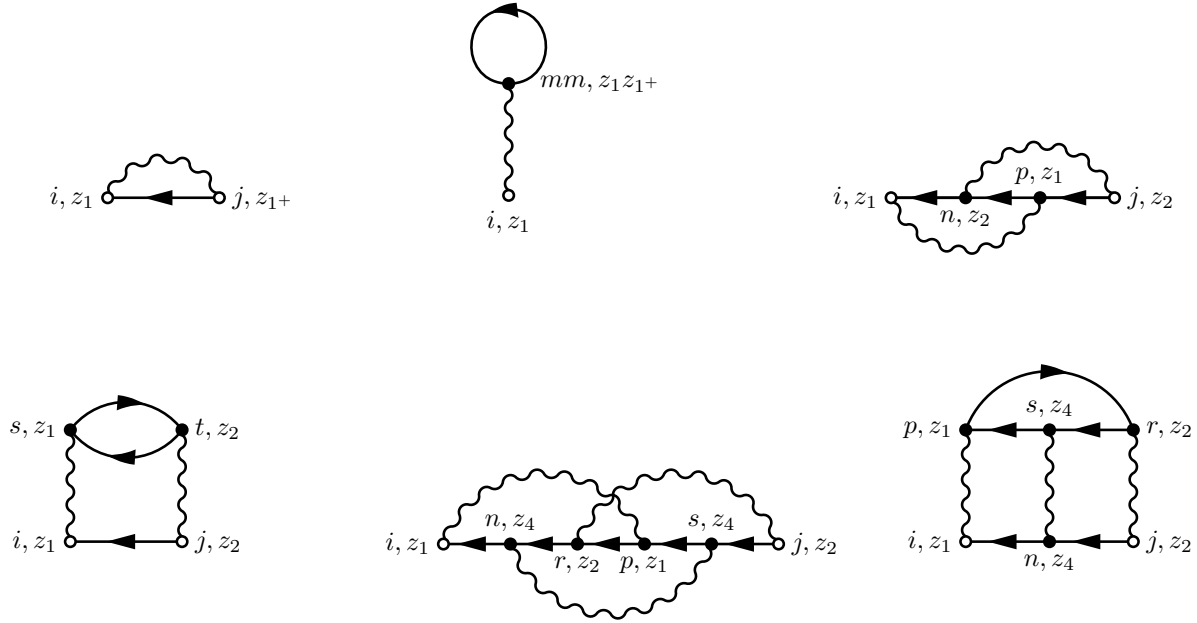
Figure 31. Leading terms of the particle–particle T-matrix selfenergy, $\Sigma^{\mathrm{pp,diag}}$ (including first-order terms), in a diagonal basis.

whereas the advanced/retarded component is given by

$$T^{\mathrm{pp,b},\mathcal{A}/\mathcal{R}}_{ik\alpha\beta}\left(t_1,t_2\right) = \Phi^{\mathrm{pp,b},\mathcal{A}/\mathcal{R}}_{ik\alpha\beta}\left(t_1,t_2\right) \tag{358}$$

$$+ U\left(t_1\right)\sum_n \int_{t_{1/2}}^{t_{1/2}} \mathrm{d}t_5\, G^{\mathrm{H},\mathcal{A}/\mathcal{R}}_{in\alpha\beta}\left(t_1,t_5\right) T^{\mathrm{pp},\mathcal{A}/\mathcal{R}}_{nk\alpha\beta}\left(t_5,t_2\right).$$

In the special case of spin-0 bosons, there is no spin index, and we have

$$T^{\mathrm{pp,b},0}_{ik}\left(z_1,z_2\right) = \Phi^{\mathrm{pp,b},0}_{ik}\left(z_1,z_2\right)$$

$$+ U\left(z_1\right)\sum_n \int_{\mathcal{C}} \mathrm{d}z_5\, G^{\mathrm{H}}_{in}\left(z_1,z_5\right) T^{\mathrm{pp,b},0}_{nk}\left(z_5,z_2\right),$$

and the correlation part of the selfenergy reduces to

$$\Sigma^{\mathrm{pp,b},0}_{ij}\left(z_1,z_2\right) = \mathrm{i}\hbar T^{\mathrm{pp,b},0}_{ij}\left(z_1,z_2\right) G_{ji}\left(z_2,z_1\right). \tag{359}$$

The ' $\gtrless$ ' components of the correlation selfenergy are

$$\Sigma^{\mathrm{pp,b},0,\gtrless}_{ij}\left(t_1,t_2\right) = \mathrm{i}\hbar T^{\mathrm{pp,b},0,\gtrless}_{ij}\left(t_1,t_2\right) G^{\lessgtr}_{ji}\left(t_2,t_1\right), \tag{360}$$

with the Keldysh components of the T matrix given by

$$T^{\mathrm{pp,b},0,\gtrless}_{ik}\left(t_1,t_2\right) = \Phi^{\mathrm{pp,b},0,\gtrless}_{ik}\left(t_1,t_2\right) + U\left(t_1\right)\sum_n$$

$$\times \left(\int_{t_0}^{t_1} \mathrm{d}t_5\, G^{\mathrm{H},\mathcal{R}}_{in}\left(t_1,t_5\right) T^{\mathrm{pp,b},0,\gtrless}_{nk}\left(t_5,t_2\right) \right.$$

$$\left. + \int_{t_0}^{t_2} \mathrm{d}t_5\, G^{\mathrm{H},\gtrless}_{in}\left(t_1,t_5\right) T^{\mathrm{pp,b},0,\mathcal{A}}_{nk}\left(t_5,t_2\right) \right), \tag{361}$$

$$T^{\mathrm{pp,b},0,\mathcal{A}/\mathcal{R}}_{ik}\left(t_1,t_2\right) = \Phi^{\mathrm{pp,b},0,\mathcal{A}/\mathcal{R}}_{ik}\left(t_1,t_2\right) \tag{362}$$

$$+ U\left(t_1\right)\sum_n \int_{t_{1/2}}^{t_{2/1}} \mathrm{d}t_5\, G^{\mathrm{H},\mathcal{A}/\mathcal{R}}_{in}\left(t_1,t_5\right) T^{\mathrm{pp,b},0,\mathcal{A}/\mathcal{R}}_{nk}\left(t_5,t_2\right).$$

The corresponding diagrams are shown in figure 32.

Fermions. Let us now consider the results for the T-matrix approximation for the fermionic Hubbard model. The correlation part of the selfenergy[30] is

$$\Sigma^{\mathrm{pp,f}}_{i\alpha j\alpha}\left(z_1,z_2\right) = \mathrm{i}h \sum_{pr}\sum_{\epsilon} T^{\mathrm{pp,f}}_{i\alpha p\epsilon j\alpha r\epsilon}\left(z_1,z_2\right) G_{r\epsilon p\epsilon}\left(z_2,z_1\right),$$

and the equation of motion for the T matrix reads

$$T^{\mathrm{pp,f}}_{i\alpha j\beta k\alpha l\beta}\left(z_1,z_2\right) = U\left(z_1\right)\delta_{ij}\delta_{kl}\bar{\delta}_{\alpha\beta} \tag{363}$$

$$\times \left\{ G^{\mathrm{H}}_{i\alpha i\beta k\beta k\alpha}\left(z_1,z_2\right)\delta_{\alpha\beta} - G^{\mathrm{H}}_{i\alpha i\beta k\alpha k\beta}\left(z_1,z_2\right)\delta_{\alpha\alpha}\delta_{\beta\beta} \right\} U\left(z_2\right)$$

$$+ U\left(z_1\right)\bar{\delta}_{\alpha\beta}\delta_{ij}\sum_{ns} \int_{\mathcal{C}} \mathrm{d}z_5\, G^{\mathrm{H}}_{i\alpha i\beta n\alpha s\beta}\left(z_1,z_5\right) T^{\mathrm{pp,f}}_{n\alpha s\beta k\alpha l\beta}\left(z_5,z_2\right).$$

After cancellations, the equation becomes

$$T^{\mathrm{pp,f}}_{i\alpha j\beta k\alpha l\beta}\left(z_1,z_2\right) = \bar{\delta}_{\alpha\beta}\delta_{ij}\delta_{kl}\Phi^{\mathrm{pp,f}}_{iikk\alpha\beta}\left(z_1,z_2\right) \tag{364}$$

$$+ U\left(z_1\right)\bar{\delta}_{\alpha\beta}\delta_{ij}\sum_{ns} \int_{\mathcal{C}} \mathrm{d}z_5\, G^{\mathrm{H}}_{i\alpha i\beta n\alpha s\beta}\left(z_1,z_5\right) T^{\mathrm{pp,f}}_{n\alpha s\beta k\alpha l\beta}\left(z_5,z_2\right),$$

$$\Phi^{\mathrm{pp,f}}_{iikk\alpha\beta}\left(z_1,z_2\right) =: -U\left(z_1\right) G^{\mathrm{H}}_{i\alpha i\beta k\alpha k\beta}\left(z_1,z_2\right) U\left(z_2\right), \tag{365}$$

where we again introduced the function Φ^{pp}. Similar as for bosons, by iteration starting with

$$\Phi^{\mathrm{pp,f}}_{i\alpha j\beta k\alpha l\beta}\left(z_1,z_2\right) = \bar{\delta}_{\alpha\beta}\delta_{ij}\delta_{kl}\Phi^{\mathrm{pp,f}}_{iikk\alpha\beta}\left(z_1,z_2\right) =: \bar{\delta}_{\alpha\beta}\delta_{ij}\delta_{kl}\Phi^{\mathrm{pp,f}}_{ik\alpha\neq\beta}\left(z_1,z_2\right),$$

the particle–particle T matrix is also of the structure

$$T^{\mathrm{pp,f}}_{i\alpha j\beta k\alpha l\beta}\left(z_1,z_2\right) := \bar{\delta}_{\alpha\beta}\delta_{ij}\delta_{kl}T^{\mathrm{pp,f}}_{iikk\alpha\beta}\left(z_1,z_2\right) =: \delta_{ij}\delta_{kl}\bar{\delta}_{\alpha\beta}T^{\mathrm{pp,f}}_{ik\alpha\neq\beta}\left(z_1,z_2\right).$$

[30] The total selfenergy contains the Hartree selfenergy. There is no Fock term.
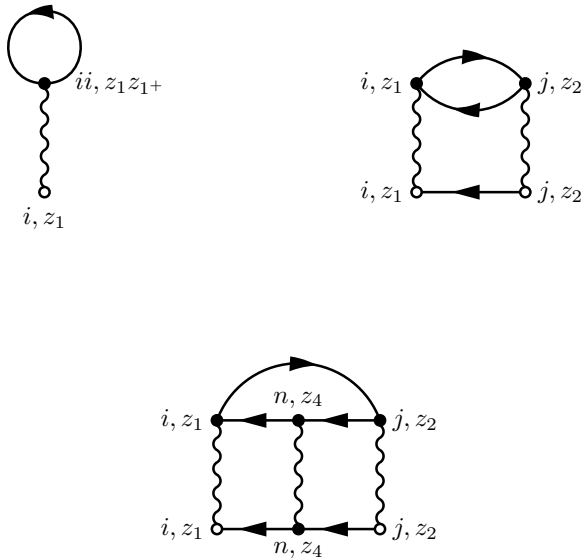
Figure 32. Leading terms of $\Sigma^{\mathrm{pp},\mathfrak{b},0}$ (including first-order terms) in the Hubbard basis for spin-0 bosons. Each term carries a factor of two.

Figure 33. Leading terms of $\Sigma^{\mathrm{pp},\mathfrak{f},1/2}$ (including first-order terms) in the Hubbard basis for spin-1/2 fermions.

The resulting equations for the T matrix and the correlation selfenergy read

$$T^{\mathrm{pp},\mathfrak{f}}_{ik\alpha\neq\beta}\left(z_1,z_2\right) = \Phi^{\mathrm{pp},\mathfrak{f}}_{ik\alpha\neq\beta}\left(z_1,z_2\right) \tag{366}$$
$$+ U\left(z_1\right) \sum_n \int_{\mathcal{C}} \mathrm{d}z_5\, G^{\mathrm{H}}_{in\alpha\neq\beta}\left(z_1,z_5\right) T^{\mathrm{pp},\mathfrak{f}}_{nk\alpha\neq\beta}\left(z_5,z_2\right),$$

$$\Sigma^{\mathrm{pp},\mathfrak{f}}_{i\alpha j\alpha}\left(z_1,z_2\right) = \mathrm{i}\hbar \sum_{\epsilon\neq\alpha} T^{\mathrm{pp},\mathfrak{f}}_{ij\alpha\neq\epsilon}\left(z_1,z_2\right) G_{j\epsilon i\epsilon}\left(z_2,z_1\right). \tag{367}$$

The '$\gtrless$' components of the selfenergy are given by

$$\Sigma^{\mathrm{pp},\mathfrak{f},\gtrless}_{i\alpha j\alpha}\left(t_1,t_2\right) = \mathrm{i}\hbar \sum_{\epsilon\neq\alpha} T^{\mathrm{pp},\mathfrak{f},\gtrless}_{ij\alpha\neq\epsilon}\left(t_1,t_2\right) G^{\lessgtr}_{j\epsilon i\epsilon}\left(t_2,t_1\right),$$

whereas the Keldysh components of the T matrix are

$$T^{\mathrm{pp},\mathfrak{f},\gtrless}_{ik\alpha\neq\beta}\left(t_1,t_2\right) = \Phi^{\mathrm{pp},\mathfrak{f},\gtrless}_{ik\alpha\neq\beta}\left(t_1,t_2\right)$$
$$+ U\left(t_1\right) \sum_n \left(\int_{t_0}^{t_1} \mathrm{d}t_5\, G^{\mathrm{H},\mathcal{R}}_{in\alpha\neq\beta}\left(t_1,t_5\right) T^{\mathrm{pp},\mathfrak{f},\gtrless}_{nk\alpha\neq\beta}\left(t_5,t_2\right) \right.$$
$$\left. + \int_{t_0}^{t_2} \mathrm{d}t_5\, G^{\mathrm{H},\gtrless}_{in\alpha\neq\beta}\left(t_1,t_5\right) T^{\mathrm{pp},\mathfrak{f},\mathcal{A}}_{nk\alpha\neq\beta}\left(t_5,t_2\right) \right), \tag{368}$$

and

$$T^{\mathrm{pp},\mathfrak{f},\mathcal{A}/\mathcal{R}}_{ik\alpha\neq\beta}\left(t_1,t_2\right) = \Phi^{\mathrm{pp},\mathfrak{f},\mathcal{A}/\mathcal{R}}_{ik\alpha\neq\beta}\left(t_1,t_2\right)$$
$$+ U\left(t_1\right) \sum_n \int_{t_{1/2}}^{t_{2/1}} \mathrm{d}t_5\, G^{\mathrm{H},\mathcal{A}/\mathcal{R}}_{in\alpha\neq\beta}\left(t_1,t_5\right) T^{\mathrm{pp},\mathfrak{f},\mathcal{A}/\mathcal{R}}_{nk\alpha\neq\beta}\left(t_5,t_2\right).$$

In the special case of spin-$\frac{1}{2}$ fermions, we have

$$\Phi^{\mathrm{pp},\mathfrak{f},1/2}_{ik\alpha\neq\beta}\left(z_1,z_2\right) =: \Phi^{\mathrm{pp},\mathfrak{f},1/2}_{ik}\left(z_1,z_2\right),$$
$$G^{\mathrm{H}}_{ik\alpha\neq\beta}\left(z_1,z_2\right) =: G^{\mathrm{H}}_{ik}\left(z_1,z_2\right),$$

and, consequently, $T^{\mathrm{pp},\mathfrak{f},1/2}_{ik\alpha\neq\beta}\left(z_1,z_2\right) =: T^{\mathrm{pp},\mathfrak{f},1/2}_{ik}\left(z_1,z_2\right)$, holds. With this, one arrives at

$$T^{\mathrm{pp},\mathfrak{f},1/2}_{ik}\left(z_1,z_2\right) = \Phi^{\mathrm{pp},\mathfrak{f},1/2}_{ik}\left(z_1,z_2\right) \tag{369}$$
$$+ U\left(z_1\right) \sum_n \int_{\mathcal{C}} \mathrm{d}z_5\, G^{\mathrm{H}}_{in}\left(z_1,z_5\right) T^{\mathrm{pp},\mathfrak{f},1/2}_{nk}\left(z_5,z_2\right),$$

and obtains for the spin up and spin down selfenergies

$$\Sigma^{\mathrm{pp},\mathfrak{f},1/2}_{i\uparrow j\uparrow}\left(z_1,z_2\right) = \mathrm{i}\hbar T^{\mathrm{pp},\mathfrak{f},1/2}_{ij}\left(z_1,z_2\right) G_{j\downarrow i\downarrow}\left(z_2,z_1\right),$$
$$\Sigma^{\mathrm{pp},\mathfrak{f},1/2}_{i\downarrow j\downarrow}\left(z_1,z_2\right) = \mathrm{i}\hbar T^{\mathrm{pp},\mathfrak{f},1/2}_{ij}\left(z_1,z_2\right) G_{j\uparrow i\uparrow}\left(z_2,z_1\right).$$

The '$\gtrless$' components of the selfenergy are given by

$$\Sigma^{\mathrm{pp},\mathfrak{f},1/2,\gtrless}_{i\uparrow j\uparrow}\left(t_1,t_2\right) = \mathrm{i}\hbar T^{\mathrm{pp},\mathfrak{f},1/2,\gtrless}_{ij}\left(t_1,t_2\right) G^{\lessgtr}_{j\downarrow i\downarrow}\left(t_2,t_1\right),$$
$$\Sigma^{\mathrm{pp},\mathfrak{f},1/2,\gtrless}_{i\downarrow j\downarrow}\left(t_1,t_2\right) = \mathrm{i}\hbar T^{\mathrm{pp},\mathfrak{f},1/2,\gtrless}_{ij}\left(t_1,t_2\right) G^{\lessgtr}_{j\uparrow i\uparrow}\left(t_2,t_1\right),$$

and the corresponding '$\gtrless$' Keldysh components of the T matrix are

$$T^{\mathrm{pp},\mathfrak{f},1/2,\gtrless}_{ik}\left(t_1,t_2\right) = \Phi^{\mathrm{pp},\mathfrak{f},1/2,\gtrless}_{ik}\left(t_1,t_2\right) \tag{370}$$
$$+ U\left(t_1\right) \sum_n \int_{t_0}^{t_1} \mathrm{d}t_5\, G^{\mathrm{H},\mathcal{R}}_{in}\left(t_1,t_5\right) T^{\mathrm{pp},\mathfrak{f},1/2,\gtrless}_{nk}\left(t_5,t_2\right)$$
$$+ U\left(t_1\right) \sum_n \int_{t_0}^{t_2} \mathrm{d}t_5\, G^{\mathrm{H},\gtrless}_{in}\left(t_1,t_5\right) T^{\mathrm{pp},\mathfrak{f},1/2,\mathcal{A}}_{nk}\left(t_5,t_2\right),$$

whereas the advanced and retarded components become

$$T^{\mathrm{pp},\mathfrak{f},1/2,\mathcal{A}/\mathcal{R}}_{ik}\left(t_1,t_2\right) = \Phi^{\mathrm{pp},\mathfrak{f},1/2,\mathcal{A}/\mathcal{R}}_{ik}\left(t_1,t_2\right) \tag{371}$$
$$+ U\left(t_1\right) \sum_n \int_{t_{1/2}}^{t_{2/1}} \mathrm{d}t_5\, G^{\mathrm{H},\mathcal{A}/\mathcal{R}}_{in}\left(t_1,t_5\right) T^{\mathrm{pp},\mathfrak{f},1/2,\mathcal{A}/\mathcal{R}}_{nk}\left(t_5,t_2\right).$$

Finally, the corresponding Feynman diagrams are shown in figure 33.

5.4. Particle–hole T-matrix approximation

Returning to equation (324) and taking the third approximation (C), we have

$$
\begin{aligned}
&\frac{\delta \Sigma^{\mathrm{cl,C}}\left(1,2\right)}{\delta G\left(7,8\right)} \\
&= \pm \mathrm{i}\hbar \delta\left(1,2\right)\delta\left(7,8\right)w\left(1,7\right) \\
&\quad + \mathrm{i}\hbar \delta\left(1,7\right)\delta\left(2,8\right)w\left(1,2\right) \\
&\quad + \mathrm{i}\hbar w\left(1,7\right)G\left(1,4\right)\frac{\delta \Sigma^{\mathrm{cl,C}}\left(4,2\right)}{\delta G\left(5,8\right)}G\left(5,7\right)
\end{aligned}
$$

(372)

The corresponding third-order selfenergy terms follow as (see equation (325))

$$
\begin{aligned}
&\Sigma^{\mathrm{cl,C(3)}}\left(1,2\right) \\
&= \mathrm{i}\hbar w\left(1,3\right)G\left(1,4\right)\frac{\delta \Sigma^{\mathrm{cl,C(2)}}\left(4,2\right)}{\delta G\left(5,6\right)} \\
&\quad G\left(5,3\right)G\left(3,6\right) \\
&= \pm\left(\mathrm{i}\hbar\right)^{3}w\left(1,3\right)G\left(1,4\right)G\left(4,2\right)w\left(4,5\right) \\
&\quad w\left(2,6\right)G\left(6,5\right)G\left(5,3\right)G\left(3,6\right) \\
&\quad + \left(\mathrm{i}\hbar\right)^{3}w\left(1,3\right)G\left(1,4\right)w\left(4,5\right)G\left(4,6\right) \\
&\quad w\left(6,2\right)G\left(6,5\right)G\left(5,3\right)G\left(3,2\right)
\end{aligned}
$$

(373)

The Kernel of series C is again introduced in the full notation with the single-time interaction,

$$
K_{ijkl}^{\mathrm{C}}\left(z_1,z_2,z_3,z_4\right) := \pm \frac{\delta \Sigma_{ik}^{\mathrm{cl,C}}\left(z_1,z_3\right)}{\delta G_{lj}\left(z_4,z_2\right)},
$$

and obeys the equation

$$
\begin{aligned}
K_{ijkl}^{\mathrm{C}}\left(z_1,z_2,z_3,z_4\right) &= \pm \mathrm{i}\hbar \delta_{\mathcal{C}}\left(z_1,z_3\right)\delta_{\mathcal{C}}\left(z_1,z_4\right)\delta_{\mathcal{C}}\left(z_{1+},z_2\right)w_{ijkl}^{\pm}\left(z_1\right) \\
&\quad + \mathrm{i}\hbar \delta_{\mathcal{C}}\left(z_1,z_4\right)\sum_{mp}w_{iplm}\left(z_1\right)\int_{\mathcal{C}}\mathrm{d}z_5\sum_{n}G_{mn}\left(z_1,z_5\right) \\
&\quad \times \int_{\mathcal{C}}\mathrm{d}z_6\sum_{r}K_{njkr}^{\mathrm{C}}\left(z_5,z_2,z_3,z_6\right)G_{rp}\left(z_6,z_1\right).
\end{aligned}
$$

Iterating as before, starting with

$$
K_{ijkl}^{\mathrm{C,(1)}}\left(z_1,z_2,z_3,z_4\right) = \pm \mathrm{i}\hbar \delta_{\mathcal{C}}\left(z_1,z_3\right)\delta_{\mathcal{C}}\left(z_1,z_4\right)\delta_{\mathcal{C}}\left(z_{1+},z_2\right)w_{ijkl}^{\pm}\left(z_1\right),
$$

(374)

we arrive at

$$
\begin{aligned}
K_{ijkl}^{\mathrm{C,(2)}}\left(z_1,z_2,z_3,z_4\right) &= \mathrm{i}\hbar \delta_{\mathcal{C}}\left(z_1,z_4\right)\sum_{mp}w_{iplm}\left(z_1\right)\int_{\mathcal{C}}\mathrm{d}z_5\sum_{n}G_{mn}\left(z_1,z_5\right) \\
&\quad \times \int_{\mathcal{C}}\mathrm{d}z_6\sum_{r}K_{njkr}^{\mathrm{C,(1)}}\left(z_5,z_2,z_3,z_6\right)G_{rp}\left(z_6,z_1\right).
\end{aligned}
$$

(375)

Use of the δ-structure of $K^{\mathrm{C,(1)}}$, leads to

$$
\begin{aligned}
K_{ijkl}^{\mathrm{C,(2)}}\left(z_1,z_2,z_3,z_4\right) &= \mathrm{i}\hbar \delta_{\mathcal{C}}\left(z_1,z_4\right)\delta_{\mathcal{C}}\left(z_2,z_3\right) \\
&\quad \sum_{mp}w_{iplm}\left(z_1\right)\sum_{n}G_{mn}\left(z_1,z_2\right) \\
&\quad \times \sum_{r}K_{njkr}^{\mathrm{C,(1)}}\left(z_2,z_2,z_2,z_2\right)G_{rp}\left(z_2,z_1\right),
\end{aligned}
$$

(376)

$$
\begin{aligned}
K_{ijkl}^{\mathrm{C,(3)}}\left(z_1,z_2,z_3,z_4\right) &= \mathrm{i}\hbar \delta_{\mathcal{C}}\left(z_1,z_4\right)\sum_{mp}w_{iplm}\left(z_1\right)\int_{\mathcal{C}}\mathrm{d}z_5\sum_{n}G_{mn}\left(z_1,z_5\right) \\
&\quad \times \int_{\mathcal{C}}\mathrm{d}z_6\sum_{r}K_{njkr}^{\mathrm{C,(2)}}\left(z_5,z_2,z_3,z_6\right)G_{rp}\left(z_6,z_1\right) \\
&= \mathrm{i}\hbar \delta_{\mathcal{C}}\left(z_1,z_4\right)\delta_{\mathcal{C}}\left(z_2,z_3\right)\sum_{mp}w_{iplm}\left(z_1\right)\int_{\mathcal{C}}\mathrm{d}z_5\sum_{n}G_{mn}\left(z_1,z_5\right) \\
&\quad \times \sum_{r}K_{njkr}^{\mathrm{C,(2)}}\left(z_5,z_2,z_2,z_5\right)G_{rp}\left(z_5,z_1\right).
\end{aligned}
$$

(377)

The structure again remains the same for higher orders, so that this approximation lies within $\mathcal{O}\left(N_{\mathrm{t}}^3\right)$ due to

$$K_{ijkl}^{\mathrm{C},(N)}\left(z_1,z_2,z_3,z_4\right) =: \delta_{\mathcal{C}}\left(z_1,z_4\right)\delta_{\mathcal{C}}\left(z_2,z_3\right)K_{ijkl}^{\mathrm{C},(N)}\left(z_1,z_2\right),$$

and one integration on the right-hand side. With this, we arrive at (see equation (374))

$$K_{ijkl}^{\mathrm{C}}\left(z_1,z_2\right) = \delta_{\mathcal{C}}\left(z_1,z_2\right)K_{ijkl}^{\mathrm{C},(1)}\left(z_1,z_1\right) + i\hbar\sum_{mp}w_{iplm}\left(z_1\right)$$
$$\times \int_{\mathcal{C}}\mathrm{d}z_5\sum_n G_{mn}\left(z_1,z_5\right)\sum_r K_{njkr}^{\mathrm{C}}\left(z_5,z_2\right)G_{rp}\left(z_5,z_1\right).$$
(378)

To simplify, we again go over to a non-singular kernel

$$K_{ijkl}^{\mathrm{C,ns}}\left(z_1,z_2\right) := K_{ijkl}^{\mathrm{C}}\left(z_1,z_2\right) - \delta_{\mathcal{C}}\left(z_1,z_2\right)K_{ijkl}^{\mathrm{C},(1)}\left(z_1,z_1\right)$$
$$= K_{ijkl}^{\mathrm{C}}\left(z_1,z_2\right) \mp i\hbar\delta_{\mathcal{C}}\left(z_1,z_2\right)w_{ijkl}^{\pm}\left(z_1\right).$$
(379)

This quantity obeys the equation (see equation (377))

$$K_{ijkl}^{\mathrm{C,ns}}\left(z_1,z_2\right) = i\hbar\sum_{mp}w_{iplm}\left(z_1\right)\int_{\mathcal{C}}\mathrm{d}z_5\sum_n G_{mn}\left(z_1,z_5\right)\sum_r G_{rp}\left(z_5,z_1\right)$$
$$\times \left\{K_{njkr}^{\mathrm{C,ns}}\left(z_5,z_2\right) \pm i\hbar\delta_{\mathcal{C}}\left(z_5,z_2\right)w_{njkr}^{\pm}\left(z_2\right)\right\}.$$
(380)

Restructuring, this implies

$$K_{ijkl}^{\mathrm{C,ns}}\left(z_1,z_2\right) = \pm\left(i\hbar\right)^2\sum_{mp}w_{iplm}\left(z_1\right)\sum_n G_{mn}\left(z_1,z_2\right)\sum_r G_{rp}\left(z_2,z_1\right)w_{njkr}^{\pm}\left(z_2\right)$$
$$+ i\hbar\sum_{mp}w_{iplm}\left(z_1\right)\int_{\mathcal{C}}\mathrm{d}z_5\sum_n G_{mn}\left(z_1,z_5\right)\sum_r G_{rp}\left(z_5,z_1\right)K_{njkr}^{\mathrm{C,ns}}\left(z_5,z_2\right)$$

and, finally,

$$K_{ijkl}^{\mathrm{C,ns}}\left(z_1,z_2\right) = i\hbar\sum_{mp}w_{iplm}\left(z_1\right)\sum_{nr}G_{mrpn}^{\mathrm{F}}\left(z_1,z_2\right)w_{njkr}^{\pm}\left(z_2\right)$$
$$\pm \sum_{mp}w_{iplm}\left(z_1\right)\int_{\mathcal{C}}\mathrm{d}z_5\sum_{nr}G_{mrpn}^{\mathrm{F}}\left(z_1,z_5\right)K_{njkr}^{\mathrm{C,ns}}\left(z_5,z_2\right),$$
(381)

where in the last line, equation (281) has been used.

With this, the correlation selfenergy reads[31], (see equation (323))

$$\Sigma_{ij}^{\mathrm{cl,corr,C}}\left(z_1,z_2\right) = \pm i\hbar\sum_{mpq}w_{ipqm}\left(z_1\right)\int_{\mathcal{C}}\mathrm{d}z_3\sum_n G_{mn}\left(z_1,z_3\right)$$
$$\times \int_{\mathcal{C}}\mathrm{d}z_4\mathrm{d}z_5\sum_{rs}K_{nsjr}^{\mathrm{C}}\left(z_3,z_5,z_2,z_4\right)G_{rp}\left(z_4,z_1\right)G_{qs}\left(z_1,z_5\right).$$

Using equation (379), we arrive at

$$\Sigma_{ij}^{\mathrm{cl,corr,C}}\left(z_1,z_2\right) = \pm i\hbar\sum_{mpqs}w_{ipqm}\left(z_1\right)G_{qs}\left(z_1,z_2\right)$$
$$\sum_{nr}\int_{\mathcal{C}}\mathrm{d}z_3\,G_{mn}\left(z_1,z_3\right)G_{rp}\left(z_3,z_1\right)$$
$$\times \left\{K_{nsjr}^{\mathrm{C,ns}}\left(z_3,z_2\right) \pm i\hbar\delta_{\mathcal{C}}\left(z_3,z_2\right)w_{nsjr}^{\pm}\left(z_2\right)\right\}.$$

Evaluating this expression further, we find

$$\Sigma_{ij}^{\mathrm{cl,corr,C}}\left(z_1,z_2\right) = \pm\sum_{qs}G_{qs}\left(z_1,z_2\right)$$
$$\times \left(i\hbar\sum_{pm}w_{ipqm}\left(z_1\right)\sum_{rn}G_{mrpn}^{\mathrm{F}}\left(z_1,z_2\right)w_{nsjr}^{\pm}\left(z_2\right)\right.$$
$$\left.\pm \sum_{pm}w_{ipqm}\left(z_1\right)\int_{\mathcal{C}}\mathrm{d}z_3\sum_{rn}G_{mrpn}^{\mathrm{F}}\left(z_1,z_3\right)K_{nsjr}^{\mathrm{C,ns}}\left(z_3,z_2\right)\right).$$

As for the particle–particle T matrix, the right-hand side already contains the first iteration of equation (381) and, thus, we can simplify

$$\Sigma_{ij}^{\mathrm{cl,corr,C}}\left(z_1,z_2\right) = \pm\sum_{qs}G_{qs}\left(z_1,z_2\right)K_{isjq}^{\mathrm{C,ns}}\left(z_1,z_2\right). \quad (382)$$

Defining $i\hbar T_{ijkl}^{\mathrm{ph}}\left(z_1,z_2\right) := \pm K_{ijkl}^{\mathrm{C,ns}}\left(z_1,z_2\right)$, and solving equations (381) and (382), we have

$$T_{ijkl}^{\mathrm{ph}}\left(z_1,z_2\right) = \Phi_{ijkl}^{\mathrm{ph}}\left(z_1,z_2\right) \quad (383)$$
$$\pm \sum_{mp}w_{iplm}\left(z_1\right)\int_{\mathcal{C}}\mathrm{d}z_5\sum_{nr}G_{mrpn}^{\mathrm{F}}\left(z_1,z_5\right)T_{njkr}^{\mathrm{ph}}\left(z_5,z_2\right),$$

$$\Phi_{ijkl}^{\mathrm{ph}}\left(z_1,z_2\right) = \pm\sum_{mp}w_{iplm}\left(z_1\right)\sum_{nr}G_{mrpn}^{\mathrm{F}}\left(z_1,z_2\right)w_{njkr}^{\pm}\left(z_2\right),$$
(384)

where we again defined the proper function Φ^{ph} corresponding to the first iteration (second-Born approximation).

With these definitions, we obtain the correlation selfenergy

$$\Sigma_{ij}^{\mathrm{ph}}\left(z_1,z_2\right) := \Sigma_{ij}^{T^{\mathrm{ph},\mathrm{corr}}}\left(z_1,z_2\right) = i\hbar\sum_{qs}G_{qs}\left(z_1,z_2\right)T_{isjq}^{\mathrm{ph}}\left(z_1,z_2\right),$$

which is the so-called *particle–hole T-matrix approximation*[32] (TPH). In contrast to the particle–particle T matrix, which describes the recurrent scattering of a pair of particles, the particle–hole T matrix describes the (multiple) scattering of a particle–hole pair. The Keldysh components of the particle–hole T matrix read

$$T_{ijkl}^{\mathrm{ph},\gtrless}\left(t_1,t_2\right) = \Phi_{ijkl}^{\mathrm{ph},\gtrless}\left(t_1,t_2\right) \pm \sum_{mp}w_{iplm}\left(t_1\right)\sum_{nr} \quad (385)$$
$$\left(\int_{t_0}^{t_1}\mathrm{d}t_5\,G_{mrpn}^{\mathrm{F},\mathcal{R}}\left(t_1,t_5\right)T_{njkr}^{\mathrm{ph},\gtrless}\left(t_5,t_2\right) + \int_{t_0}^{t_2}\mathrm{d}t_5\,G_{mrpn}^{\mathrm{F},\gtrless}\left(t_1,t_5\right)T_{njkr}^{\mathrm{ph},\mathcal{A}}\left(t_5,t_2\right)\right),$$

and

$$T_{ijkl}^{\mathrm{ph},\mathcal{A}/\mathcal{R}}\left(t_1,t_2\right) = \Phi_{ijkl}^{\mathrm{ph},\mathcal{A}/\mathcal{R}}\left(t_1,t_2\right) \quad (386)$$
$$\pm \sum_{mp}w_{iplm}\left(t_1\right)\sum_{nr}\int_{t_{1/2}}^{t_{2/1}}\mathrm{d}t_5\,G_{mrpn}^{\mathrm{H},\mathcal{A}/\mathcal{R}}\left(t_1,t_5\right)T_{njkr}^{\mathrm{ph},\mathcal{A}/\mathcal{R}}\left(t_5,t_2\right).$$

For the '$\gtrless$' components of the selfenergy, we have

$$\Sigma_{ij}^{\mathrm{ph},\gtrless}\left(t_1,t_2\right) = \sum_{qs}G_{qs}^{\gtrless}\left(t_1,t_2\right)T_{isjq}^{\mathrm{ph},\gtrless}\left(t_1,t_2\right).$$

---

[31] The total selfenergy contains, in addition the mean-field terms $\Sigma_{ij}^{\mathrm{H}}\left(z_1,z_2\right) + \Sigma_{ij}^{\mathrm{F}}\left(z_1,z_2\right)$.

[32] In the context of the Fermi–Hubbard model for electrons, the particle–hole T matrix will later be called *electron–hole T matrix* (TEH).

5.4.1. Particle–hole T matrix in a diagonal basis.

For diagonal basis sets with $w_{ijkl} = \delta_{il}\delta_{jk}w_{ij}$, equations (383) and (385) become

$$T_{ijkl}^{\text{ph,diag}}\left(z_1, z_2\right) = \Phi_{ijkl}^{\text{ph,diag}}\left(z_1, z_2\right) \pm w_{il}\left(z_1\right)$$
$$\int_{\mathcal{C}} \mathrm{d}z_5 \sum_{nr} G_{irln}^{\text{F}}\left(z_1, z_5\right) T_{njkr}^{\text{ph,diag}}\left(z_5, z_2\right),$$

$$\Phi_{ijkl}^{\text{ph,diag}}\left(z_1, z_2\right) =: \pm w_{il}\left(z_1\right) \left\{ \delta_{jk} \sum_n \right.$$
$$\left. G_{inln}^{\text{F}}\left(z_1, z_2\right) w_{nj}\left(z_2\right) \pm G_{ijlk}^{\text{F}}\left(z_1, z_2\right) w_{jk}\left(z_2\right) \right\},$$

where we defined the diagonal version of the particle–hole function Φ^{ph}. Then the selfenergy in the diagonal basis becomes

$$\Sigma_{ij}^{\text{ph,diag}}\left(z_1, z_2\right) = \mathrm{i}\hbar \sum_{qs} G_{qs}\left(z_1, z_2\right) T_{isjq}^{\text{ph,diag}}\left(z_1, z_2\right).$$

The '$\gtrless$' Keldysh components are

$$T_{ijkl}^{\text{ph,diag},\gtrless}\left(t_1, t_2\right) = \Phi_{ijkl}^{\text{ph,diag},\gtrless}\left(t_1, t_2\right) \pm w_{il}\left(t_1\right) \sum_{nr}$$
$$\times \left(\int_{t_0}^{t_1} \mathrm{d}t_5 \, G_{irln}^{\text{F},\mathcal{R}}\left(t_1, t_5\right) T_{njkr}^{\text{ph,diag},\gtrless}\left(t_5, t_2\right) \right.$$
$$\left. + \int_{t_0}^{t_2} \mathrm{d}t_5 \, G_{irln}^{\text{F},\gtrless}\left(t_1, t_5\right) T_{njkr}^{\text{ph,diag},\mathcal{A}}\left(t_5, t_2\right) \right), \quad (387)$$

whereas, for the advanced/retarded T matrices we obtain

$$T_{ijkl}^{\text{ph,diag},\mathcal{A/R}}\left(t_1, t_2\right) = \Phi_{ijkl}^{\text{ph,diag},\mathcal{A/R}}\left(t_1, t_2\right) \quad (388)$$
$$\pm w_{il}\left(t_1\right) \sum_{nr} \int_{t_{1/2}}^{t_{2/1}} \mathrm{d}t_5 \, G_{irln}^{\text{F},\mathcal{A/R}}\left(t_1, t_5\right) T_{njkr}^{\text{ph,diag},\mathcal{A/R}}\left(t_5, t_2\right).$$

For the '$\gtrless$' components of the selfenergy, we have

$$\Sigma_{ij}^{\text{ph,diag},\gtrless}\left(t_1, t_2\right) = \mathrm{i}\hbar \sum_{qs} G_{qs}^{\gtrless}\left(t_1, t_2\right) T_{isjq}^{\text{ph,diag},\gtrless}\left(t_1, t_2\right). \quad (389)$$

The diagrammatic representation of the first terms of the particle–hole T matrix is given in figure 34.

5.4.2. Particle–hole T matrix in the Hubbard basis.

For the bosonic Hubbard basis, the particle–hole T matrix reads

$$T_{i\alpha j\beta k\alpha l\beta}^{\text{ph,}\flat}\left(z_1, z_2\right) = \delta_{il}\delta_{jk} U\left(z_1\right) \left\{ \delta_{\alpha\beta} G_{i\alpha j\alpha i\alpha j\alpha}^{\text{F}}\left(z_1, z_2\right) \right.$$
$$\left. + G_{i\alpha j\beta i\beta j\alpha}^{\text{F}}\left(z_1, z_2\right) \right\} U\left(z_2\right)$$
$$+ \delta_{il} U\left(z_1\right) \int_{\mathcal{C}} \mathrm{d}z_5 \sum_{nr} G_{i\alpha r\beta i\beta n\alpha}^{\text{F}}\left(z_1, z_5\right) T_{n\alpha j\beta k\alpha r\beta}^{\text{ph,}\flat}\left(z_5, z_2\right).$$

Introducing the function Φ^{ph}, as before, this expression becomes

$$T_{i\alpha j\beta k\alpha l\beta}^{\text{ph,}\flat}\left(z_1, z_2\right) =: \delta_{il}\delta_{jk} \Phi_{i\alpha j\beta i\alpha j\beta}^{\text{ph,}\flat}\left(z_1, z_2\right)$$
$$+ \delta_{il} U\left(z_1\right) \int_{\mathcal{C}} \mathrm{d}z_5 \sum_{nr} G_{i\alpha r\beta i\beta n\alpha}^{\text{F}}\left(z_1, z_5\right) T_{n\alpha j\beta k\alpha r\beta}^{\text{ph,}\flat}\left(z_5, z_2\right).$$

By iteration, starting from
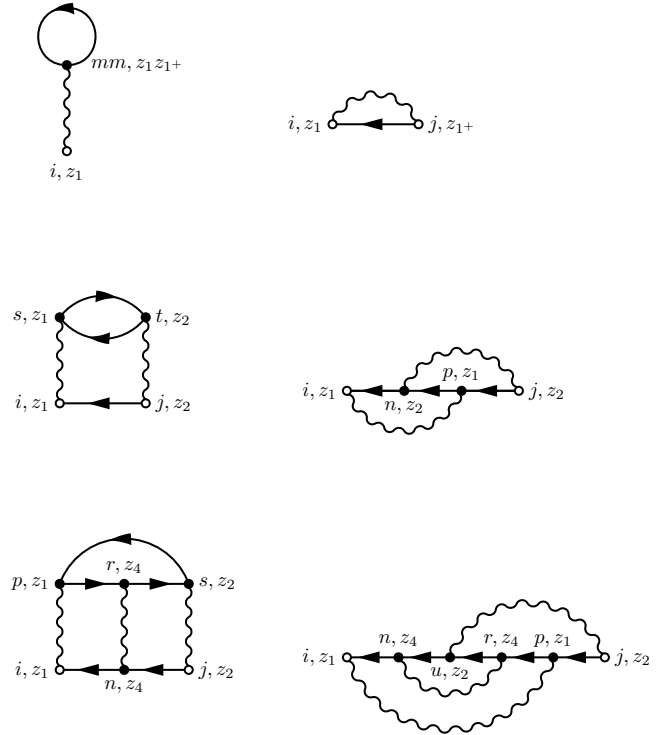
Figure 34. The first six terms of the particle–hole T-matrix selfenergy (including first-order terms) in a diagonal basis.

$$\Phi_{i\alpha j\beta k\alpha l\beta}^{\text{ph,}\flat}\left(z_1, z_2\right) = \delta_{il}\delta_{jk} \Phi_{i\alpha j\beta j\alpha i\beta}^{\text{ph,}\flat}\left(z_1, z_2\right) =: \delta_{il}\delta_{jk} \Phi_{ij\alpha\beta}^{\text{ph,}\flat}\left(z_1, z_2\right),$$

it is evident that the particle–hole T matrix is also of the structure

$$T_{i\alpha j\beta k\alpha l\beta}^{\text{ph,}\flat}\left(z_1, z_2\right) =: \delta_{il}\delta_{jk} T_{ij\alpha\beta}^{\text{ph,}\flat}\left(z_1, z_2\right).$$

Thus the governing equation for the T matrix becomes

$$T_{ij\alpha\beta}^{\text{ph,}\flat}\left(z_1, z_2\right) = \Phi_{ij\alpha\beta}^{\text{ph,}\flat}\left(z_1, z_2\right) \quad (390)$$
$$+ U\left(z_1\right) \int_{\mathcal{C}} \mathrm{d}z_5 \sum_n G_{i\alpha n\beta i\beta n\alpha}^{\text{F}}\left(z_1, z_5\right) T_{nj\alpha\beta}^{\text{ph,}\flat}\left(z_5, z_2\right),$$

and the resulting correlation selfenergy reads

$$\Sigma_{i\alpha j\alpha}^{\text{ph,}\flat}\left(z_1, z_2\right) = \mathrm{i}\hbar \sum_{\epsilon} G_{i\epsilon j\epsilon}\left(z_1, z_2\right) T_{ij\alpha\epsilon}^{\text{ph}}\left(z_1, z_2\right). \quad (391)$$

The '$\gtrless$' components of the correlation selfenergy are given by

$$\Sigma_{i\alpha j\alpha}^{\text{ph,}\flat,\gtrless}\left(t_1, t_2\right) = \mathrm{i}\hbar \sum_{\epsilon} G_{i\epsilon j\epsilon}^{\gtrless}\left(t_1, t_2\right) T_{ij\alpha\epsilon}^{\text{ph,}\gtrless}\left(t_1, t_2\right), \quad (392)$$

with the '$\gtrless$' components of the T matrix:

$$T_{ij\alpha\beta}^{\text{ph,}\flat,\gtrless}\left(t_1, t_2\right) = \Phi_{ij\alpha\beta}^{\text{ph,}\flat,\gtrless}\left(t_1, t_2\right)$$
$$+ U\left(t_1\right) \left(\int_{t_0}^{t_1} \mathrm{d}t_5 \sum_n G_{i\alpha n\beta i\beta n\alpha}^{\text{F},\mathcal{R}}\left(t_1, t_5\right) T_{nj\alpha\beta}^{\text{ph,}\flat,\gtrless}\left(t_5, t_2\right) \right.$$
$$\left. + \int_{t_0}^{t_2} \mathrm{d}t_5 \sum_n G_{i\alpha n\beta i\beta n\alpha}^{\text{F},\gtrless}\left(t_1, t_5\right) T_{nj\alpha\beta}^{\text{ph,}\flat,\mathcal{A}}\left(t_5, t_2\right) \right), \quad (393)$$
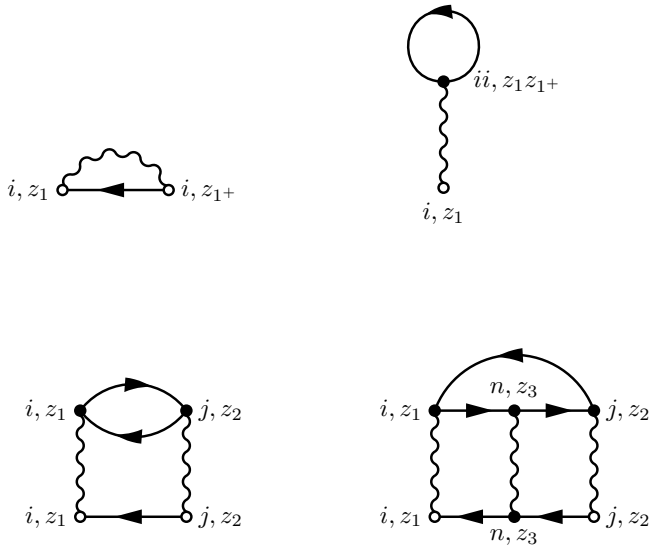
Figure 35. Leading terms of $\Sigma^{\mathrm{ph,b,0}}$ (including first-order terms) in the Hubbard basis for spin-0 bosons. Each term carries a factor of two.

and the advanced/retarded components,

$$
T^{\mathrm{ph,b},\mathcal{A}/\mathcal{R}}_{ij\alpha\beta}\left(t_1,t_2\right) = \Phi^{\mathrm{ph,b},\mathcal{A}/\mathcal{R}}_{ij\alpha\beta}\left(t_1,t_2\right) \tag{394}
$$
$$
+ U\left(t_1\right)\int_{t_{1/2}}^{t_{2/1}}\mathrm{d}t_5 \sum_n G^{\mathrm{F},\mathcal{A}/\mathcal{R}}_{i\alpha n\beta i\beta n\alpha}\left(t_1,t_5\right)T^{\mathrm{ph,b},\mathcal{A}/\mathcal{R}}_{nj\alpha\beta}\left(t_5,t_2\right).
$$

For spin-0 bosons, the equations simplify to

$$
T^{\mathrm{ph,b,0}}_{ij}\left(z_1,z_2\right) = \Phi^{\mathrm{ph,b,0}}_{ij}\left(z_1,z_2\right)
$$
$$
+ U\left(z_1\right)\int_{\mathcal{C}}\mathrm{d}z_5 \sum_n G^{\mathrm{F}}_{inin}\left(z_1,z_5\right)T^{\mathrm{ph,b,0}}_{nj}\left(z_5,z_2\right)
$$

and the correlation selfenergy is

$$
\Sigma^{\mathrm{ph,b,0}}_{ij}\left(z_1,z_2\right) = \mathrm{i}\hbar G_{ij}\left(z_1,z_2\right)T^{\mathrm{ph,b,0}}_{ij}\left(z_1,z_2\right), \tag{395}
$$

with the '$\gtrless$' components

$$
\Sigma^{\mathrm{ph,b,0},\gtrless}_{ij}\left(t_1,t_2\right) = \mathrm{i}\hbar G^{\gtrless}_{ij}\left(t_1,t_2\right)T^{\mathrm{ph,b,0},\gtrless}_{ij}\left(t_1,t_2\right). \tag{396}
$$

The '$\gtrless$' components of the T matrix that enter this expression are given by

$$
T^{\mathrm{ph,b,0},\gtrless}_{ij}\left(t_1,t_2\right) = \Phi^{\mathrm{ph,b,0},\gtrless}_{ij}\left(t_1,t_2\right)
$$
$$
+ U\left(t_1\right)\Bigg(\int_{t_0}^{t_1}\mathrm{d}t_5 \sum_n G^{\mathrm{F},\mathcal{R}}_{inin}\left(t_1,t_5\right)T^{\mathrm{ph,b,0},\gtrless}_{nj}\left(t_5,t_2\right)
$$
$$
+ \int_{t_0}^{t_2}\mathrm{d}t_5 \sum_n G^{\mathrm{F},\gtrless}_{inin}\left(t_1,t_5\right)T^{\mathrm{ph,b,0},\mathcal{A}}_{nj}\left(t_5,t_2\right)\Bigg), \tag{397}
$$

and the advanced/retarded components are

$$
T^{\mathrm{ph,b,0},\mathcal{A}/\mathcal{R}}_{ij}\left(t_1,t_2\right) = \Phi^{\mathrm{ph,b,0},\mathcal{A}/\mathcal{R}}_{ij}\left(t_1,t_2\right) \tag{398}
$$
$$
+ U\left(t_1\right)\int_{t_{1/2}}^{t_{2/1}}\mathrm{d}t_5 \sum_n G^{\mathrm{F},\mathcal{A}/\mathcal{R}}_{inin}\left(t_1,t_5\right)T^{\mathrm{ph,b,0},\mathcal{A}/\mathcal{R}}_{nj}\left(t_5,t_2\right).
$$

The leading terms of the corresponding diagrams are shown in figure 35.

For fermionic particles and holes, the particle–hole T matrix satisfies

$$
T^{\mathrm{ph,f}}_{i\alpha j\beta k\alpha l\beta}\left(z_1,z_2\right) = \delta_{il}\delta_{jk}\bar{\delta}_{\alpha\beta}U\left(z_1\right) \tag{399}
$$
$$
\times\Big\{-\delta_{\alpha\beta}G^{\mathrm{F}}_{i\alpha j\alpha i\alpha j\alpha}\left(z_1,z_2\right) + G^{\mathrm{F}}_{i\alpha j\beta i\beta j\alpha}\left(z_1,z_2\right)\Big\}U\left(z_2\right)
$$
$$
- \delta_{il}\bar{\delta}_{\alpha\beta}U\left(z_1\right)\int_{\mathcal{C}}\mathrm{d}z_5 \sum_{nr} G^{\mathrm{F}}_{i\alpha r\beta i\beta n\alpha}\left(z_1,z_5\right)T^{\mathrm{ph,f}}_{n\alpha j\beta k\alpha r\beta}\left(z_5,z_2\right).
$$

Evaluating the terms, we have

$$
T^{\mathrm{ph,f}}_{i\alpha j\beta k\alpha l\beta}\left(z_1,z_2\right) = \delta_{il}\delta_{jk}\bar{\delta}_{\alpha\beta}U\left(z_1\right)G^{\mathrm{F}}_{i\alpha j\beta i\beta j\alpha}\left(z_1,z_2\right)U\left(z_2\right)
$$
$$
- \delta_{il}\bar{\delta}_{\alpha\beta}U\left(z_1\right)\int_{\mathcal{C}}\mathrm{d}z_5 \sum_{nr} G^{\mathrm{F}}_{i\alpha r\beta i\beta n\alpha}\left(z_1,z_5\right)T^{\mathrm{ph,f}}_{n\alpha j\beta k\alpha r\beta}\left(z_5,z_2\right),
$$

which, with the introduction of the function Φ^{ph}, becomes

$$
T^{\mathrm{ph,f}}_{i\alpha j\beta k\alpha l\beta}\left(z_1,z_2\right) =: \delta_{il}\delta_{jk}\bar{\delta}_{\alpha\beta}\Phi^{\mathrm{ph,f}}_{i\alpha j\beta i\alpha j\beta}\left(z_1,z_2\right) \tag{400}
$$
$$
- \delta_{il}\bar{\delta}_{\alpha\beta}U\left(z_1\right)\int_{\mathcal{C}}\mathrm{d}z_5 \sum_{nr} G^{\mathrm{F}}_{i\alpha r\beta i\beta n\alpha}\left(z_1,z_5\right)T^{\mathrm{ph,f}}_{n\alpha j\beta k\alpha r\beta}\left(z_5,z_2\right).
$$

Again by iteration, starting from $\Phi^{\mathrm{ph,f}}_{i\alpha j\beta k\alpha l\beta}\left(z_1,z_2\right) =: \delta_{il}\delta_{jk}\bar{\delta}_{\alpha\beta}\Phi^{\mathrm{ph,f}}_{ij\alpha\neq\beta}\left(z_1,z_2\right)$, it follows $T^{\mathrm{ph,f}}_{i\alpha j\beta k\alpha l\beta}\left(z_1,z_2\right) =: \delta_{il}\delta_{jk}\bar{\delta}_{\alpha\beta}T^{\mathrm{ph,f}}_{ij\alpha\neq\beta}\left(z_1,z_2\right)$. With this, equation (400) simplifies to

$$
T^{\mathrm{ph,f}}_{ij\alpha\neq\beta}\left(z_1,z_2\right) = \Phi^{\mathrm{ph,f}}_{ij\alpha\neq\beta}\left(z_1,z_2\right) \tag{401}
$$
$$
- U\left(z_1\right)\int_{\mathcal{C}}\mathrm{d}z_5 \sum_n G^{\mathrm{F}}_{i\alpha n\beta i\beta n\alpha}\left(z_1,z_5\right)T^{\mathrm{ph,f}}_{nj\alpha\neq\beta}\left(z_5,z_2\right).
$$

The corresponding correlation selfenergy becomes[33]

$$
\Sigma^{\mathrm{ph,f}}_{i\alpha j\alpha}\left(z_1,z_2\right) = \mathrm{i}\hbar \sum_{\epsilon\neq\alpha} G_{i\epsilon j\epsilon}\left(z_1,z_2\right)T^{\mathrm{ph,f}}_{ij\alpha\neq\epsilon}\left(z_1,z_2\right). \tag{402}
$$

The Keldysh components of the T matrix read

$$
T^{\mathrm{ph,f},\gtrless}_{ij\alpha\neq\beta}\left(t_1,t_2\right) = \Phi^{\mathrm{ph,f},\gtrless}_{ij\alpha\neq\beta}\left(t_1,t_2\right) \tag{403}
$$
$$
- U\left(t_1\right)\Bigg(\int_{t_0}^{t_1}\mathrm{d}t_5 \sum_n G^{\mathrm{F},\mathcal{R}}_{i\alpha n\beta i\beta n\alpha}\left(t_1,t_5\right)T^{\mathrm{ph,f},\gtrless}_{nj\alpha\neq\beta}\left(t_5,t_2\right)
$$
$$
+ \int_{t_0}^{t_2}\mathrm{d}t_5 \sum_n G^{\mathrm{F},\gtrless}_{i\alpha n\beta i\beta n\alpha}\left(t_1,t_5\right)T^{\mathrm{ph,f},\mathcal{A}}_{nj\alpha\neq\beta}\left(t_5,t_2\right)\Bigg),
$$

$$
T^{\mathrm{ph,f},\mathcal{A}/\mathcal{R}}_{ij\alpha\neq\beta}\left(t_1,t_2\right) = \Phi^{\mathrm{ph,f},\mathcal{A}/\mathcal{R}}_{ij\alpha\neq\beta}\left(t_1,t_2\right) \tag{404}
$$
$$
- U\left(t_1\right)\int_{t_{1/2}}^{t_{2/1}}\mathrm{d}t_5 \sum_n G^{\mathrm{F},\mathcal{A}/\mathcal{R}}_{i\alpha n\beta i\beta n\alpha}\left(t_1,t_5\right)T^{\mathrm{ph,f},\mathcal{A}/\mathcal{R}}_{nj\alpha\neq\beta}\left(t_5,t_2\right).
$$

For the correlation selfenergy, the '$\gtrless$' components read

---

[33] The total selfenergy contains, in addition, the Hartree selfenergy, $\Sigma^{\mathrm{H,f}}_{i\alpha j\alpha}\left(z_1,z_2\right)$.
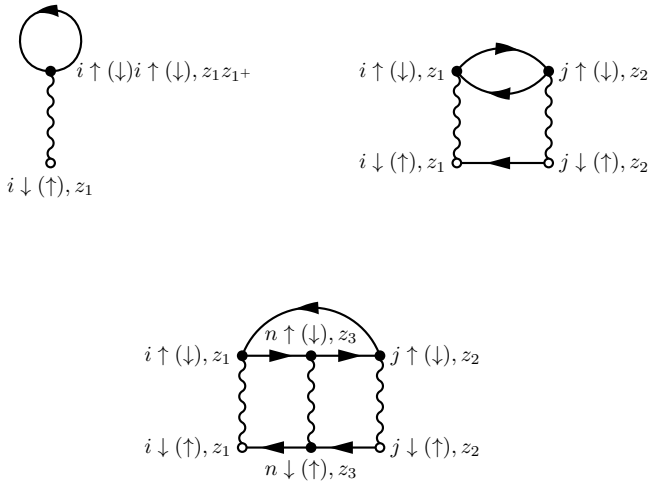
Figure 36. Leading terms of $\Sigma^{\mathrm{eh,f,1/2}}$ (including first-order terms) in the Hubbard basis for spin-1/2 fermions.

$$\Sigma^{\mathrm{ph,f},\gtrless}_{i\alpha j\alpha}\left(t_1, t_2\right) = i\hbar \sum_{\epsilon \neq \alpha} G^{\gtrless}_{i\epsilon j\epsilon}\left(t_1, t_2\right) T^{\mathrm{ph,f},\gtrless}_{ij\alpha \neq \epsilon}\left(t_1, t_2\right).$$

For spin-$\frac{1}{2}$ fermions, we now switch to the name *electron–hole T matrix* (TEH), since the quantity is predominantly used for (effective) electrons. We get

$$T^{\mathrm{eh,f,1/2}}_{ij\uparrow\downarrow}\left(z_1, z_2\right) = T^{\mathrm{eh,f,1/2}}_{ij\downarrow\uparrow}\left(z_1, z_2\right) =: T^{\mathrm{eh,f,1/2}}_{ij}\left(z_1, z_2\right)$$
$$= \Phi^{\mathrm{eh,f,1/2}}_{ij}\left(z_1, z_2\right) - U\left(z_1\right) \int_{\mathcal{C}} dz_5 \sum_n G^{\mathrm{F}}_{in}\left(z_1, z_5\right) T^{\mathrm{eh,f,1/2}}_{nj}\left(z_5, z_2\right),$$

where we have defined

$$\Phi^{\mathrm{eh,f,1/2}}_{ij}\left(z_1, z_2\right) := \Phi^{\mathrm{eh,f,1/2}}_{ij\uparrow\downarrow}\left(z_1, z_2\right) = \Phi^{\mathrm{eh,f,1/2}}_{ij\downarrow\uparrow}\left(z_1, z_2\right),$$
$$G^{\mathrm{F}}_{in}\left(z_1, z_2\right) := G^{\mathrm{F}}_{i\uparrow n\downarrow i\downarrow n\uparrow}\left(z_1, z_2\right) = G^{\mathrm{F}}_{i\downarrow n\uparrow i\uparrow n\downarrow}\left(z_1, z_2\right). \tag{405}$$

The correlation selfenergy reads

$$\Sigma^{\mathrm{eh,f,1/2}}_{i\downarrow(\uparrow)j\downarrow(\uparrow)}\left(z_1, z_2\right) = i\hbar G_{i\uparrow(\downarrow)j\uparrow(\downarrow)}\left(z_1, z_2\right) T^{\mathrm{eh,f,1/2}}_{ij}\left(z_1, z_2\right). \tag{406}$$

The first terms of the diagrammatic representation are shown in figure 36.

The '$\gtrless$' components of the electron–hole T matrix are

$$T^{\mathrm{eh,f,1/2},\gtrless}_{ij}\left(t_1, t_2\right) = \Phi^{\mathrm{eh,f,1/2},\gtrless}_{ij}\left(t_1, t_2\right) \tag{407}$$
$$- U\left(t_1\right) \Bigg(\int_{t_0}^{t_1} dt_5 \sum_n G^{\mathrm{F},\mathcal{R}}_{in}\left(t_1, t_5\right) T^{\mathrm{eh,f,1/2},\gtrless}_{nj}\left(t_5, t_2\right)$$
$$+ \int_{t_0}^{t_2} dt_5 \sum_n G^{\mathrm{F},\gtrless}_{in}\left(t_1, t_5\right) T^{\mathrm{eh,f,1/2},\mathcal{A}}_{nj}\left(t_5, t_2\right) \Bigg),$$

and the advanced/retarded components become

$$T^{\mathrm{eh,f,1/2},\mathcal{A}/\mathcal{R}}_{ij}\left(t_1, t_2\right) = \Phi^{\mathrm{eh,f,1/2},\mathcal{A}/\mathcal{R}}_{ij}\left(t_1, t_2\right) \tag{408}$$
$$- U\left(t_1\right) \int_{t_{1/2}}^{t_{2/1}} dt_5 \sum_n G^{\mathrm{F},\mathcal{A}/\mathcal{R}}_{in}\left(t_1, t_5\right) T^{\mathrm{eh,f,1/2},\mathcal{A}/\mathcal{R}}_{nj}\left(t_5, t_2\right).$$

The '$\gtrless$' components of the correlation selfenergy read

$$\Sigma^{\mathrm{eh,f,1/2},\gtrless}_{i\downarrow(\uparrow)j\downarrow(\uparrow)}\left(t_1, t_2\right) = i\hbar G^{\gtrless}_{i\uparrow(\downarrow)j\uparrow(\downarrow)}\left(t_1, t_2\right) T^{\mathrm{eh,f,1/2},\gtrless}_{ij}\left(t_1, t_2\right).$$

With this we conclude the discussion of the T-matrix approximation. After considering separately the standard approximations—the particle–particle and particle–hole T matrix, we briefly mention the limitations and possible extensions. The present approximations were based on the static pair interaction. While we took into account multiple scattering processes to all orders, on the other hand, dynamical-screening effects (as described by the GW approximation in section 5.2), have been neglected completely. An approximate combination of dynamical-screening and strong-coupling effects is, therefore, considered in the next section.

5.5. Fluctuating-exchange approximation (FLEX)

The idea to combine strong-coupling and dynamical-screening effects goes back several decades. A discussion in the frame of Green functions is summarized in [184]. An alternative approach has been presented within density-operator theory. The solution for the pair-correlation operator that includes both, ladder and polarization terms leads to the screened-ladder approximation, e.g. [136]. However, implementing these approximations for nonequilibrium situations is presently not computationally feasible. Therefore, it is reasonable to employ a simpler approach where contributions of both approximations are taken into account approximately. This idea was first realized for classical plasmas by Gould and DeWitt [185]. They had the idea to simultaneously include strong-coupling and dynamical-screening effects in a kinetic equation by simply adding the Boltzmann (B) and Lenard–Balescu (LB) collision integrals,

$$I^{\mathrm{GDW}} = I^{\mathrm{B}} + I^{\mathrm{LB}} - I^{\mathrm{L}}, \tag{409}$$

where the Boltzmann collision integral includes the entire Born series and Lenard–Balescu the entire ring-diagram sum [181, 182]. In the Green functions language the former corresponds to the T-matrix approximation and the latter to GW. Subtraction of the Landau integral, I^{L}, is necessary to avoid double counting of terms. The Landau integral corresponds to the static second-Born approximation (collision integrals of second order in the pair potential) which are contained (as the lowest iteration orders) in both, the T matrix and the dynamically screened potential, see [186] for a recent discussion and further references.

Extension of this idea to quantum systems directly leads to the fluctuating-exchange approximation (FLEX). The idea behind FLEX is to construct an approximation that includes both flavors of the T matrix as well as the GW approximation thereby neglecting cross-terms that mix the three different approximations. To avoid double counting, the common to all three second-order terms are subtracted twice in the correlation contribution. Thereby, the resulting FLEX selfenergy becomes

$$\Sigma^{\mathrm{FLEX}} = \Sigma^{\mathrm{H}} + \Sigma^{\mathrm{F}} + \Sigma^{\mathrm{FLEX,corr}}.$$
$$\Sigma^{\mathrm{FLEX,corr}} = \Sigma^{GW,\mathrm{corr}} + \Sigma^{\mathrm{pp}} + \Sigma^{\mathrm{eh}} - 2\Sigma^{(2)} \tag{410}$$
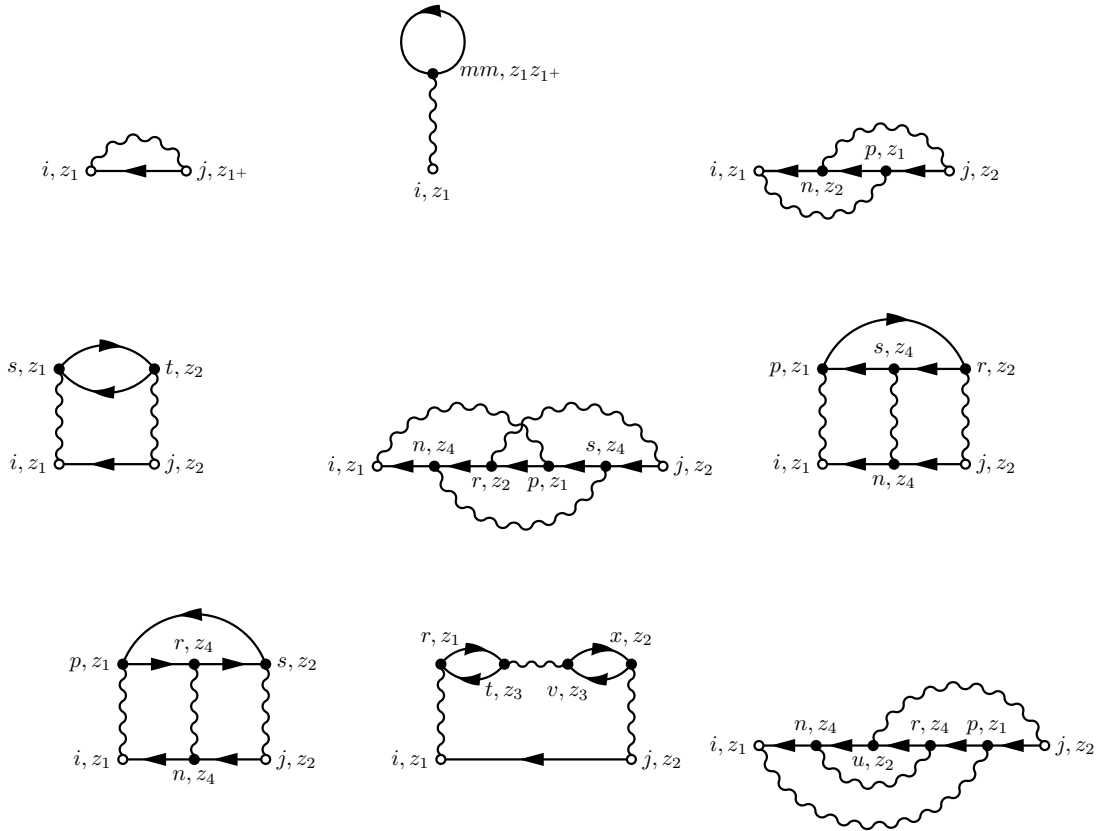
Figure 37. Leading terms of $\Sigma^{\text{FLEX,diag}}$ in a diagonal basis.

where equation (410) directly corresponds to the Gould–DeWitt approach, equation (409). This scheme can be applied in an arbitrary basis representation. The diagrammatic representation of the leading terms for a diagonal basis, and for spin-0 bosons as well as spin-1/2 fermions in the Hubbard basis are shown in figures 37–39, respectively.

We have implemented this scheme for a fermionic Hubbard basis and found excellent performance. Numerical results for the ground-state properties and for nonequilibrium dynamics were presented in section 3 and confirm that this is a powerful and highly accurate approximation.

6. Discussion and outlook

6.1. Summary of numerical results

In this article, an overview of recent progress in the dynamics of correlated fermions out of equilibrium has been given. The theoretical framework in the focus was nonequilibrium (real-time) Green functions that were introduced 55 years ago by Keldysh, in the Soviet Union, and Baym and Kadanoff, in the U.S. For more than two decades the method of NEGF was primarily a tool to systematically derive Boltzmann-type quantum-kinetic equations and improvements thereof. Only after the work of Danielewicz two decades later [187] it became a practical option to use the NEGF technique for numerical simulations. However, the computational effort that exceeds that of other many-body approaches by far, remained a major obstacle. The next step forward occured in the second half of the 1990s where important effects in semiconductor
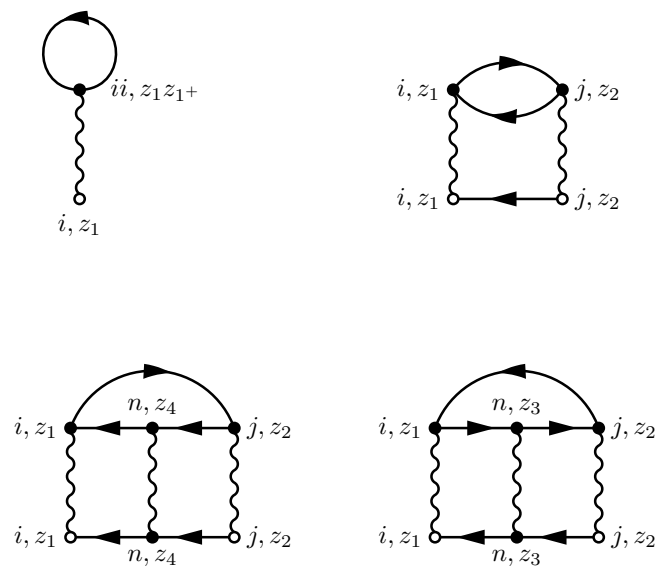
Figure 38. Leading terms of $\Sigma^{\text{FLEX,}\flat,0}$ in the Hubbard basis for spin-0 bosons.

optics and transport, in nuclear matter and laser plasmas could be explained for the first time by using NEGF methods, for details see the text books [54, 55, 131, 136]. Not only were new approximations derived but also the number of groups that attempted numerical solutions increased rapidly.

The next spike of activity came 10 years later when NEGF methods were first applied to finite spatially inhomogenous systems including electrons in atoms, molecules or quantum dots [71, 73, 188]. NEGF simulations with second-order Born
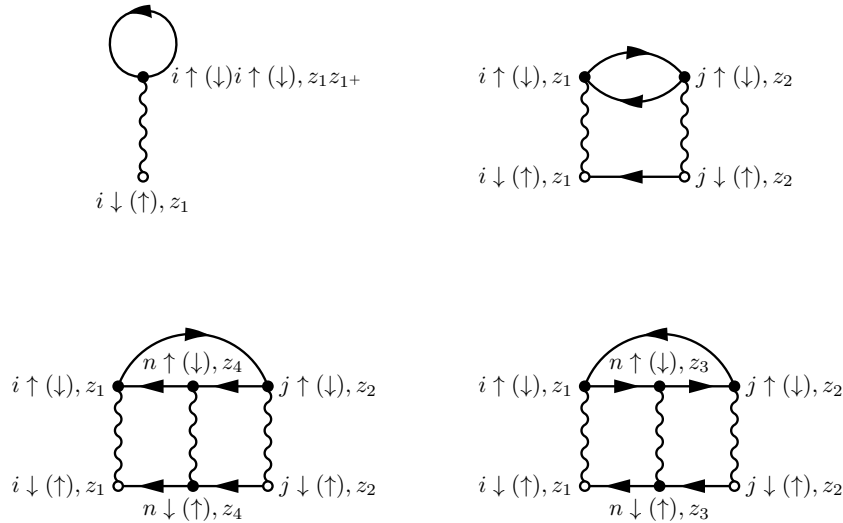
Figure 39. Leading terms of $\Sigma^{\text{FLEX,f,1/2}}$ in the Hubbard basis for spin-1/2 fermions.

selfenergies (SOA) were able to reproduce the qualitative features of the excitation and ionization dynamics of optically excited few-electron systems. Another new application concerned finite Hubbard-type lattice models [77, 121, 122]. The simplicity of the basis allowed, for the first time, to systematically study strongly correlated systems in nonequilibrium with selfenergies beyond the simple second-Born approximation. This has allowed for NEGF applications in the fields of strongly correlated solids and cold atoms [28, 78, 152].

Still it remained unclear what level of accuracy NEGF simulations can provide and whether they are an approach that is competitive with other many-body methods. This question was answered in a series of papers where small Hubbard clusters were treated with NEGF simulations that could be compared to exact-diagonalization calculations [77, 158]. Recently the first systematic test of various selfenergy approximations was reported by two of the present authors by comparing to DMRG benchmark simulations for 1D Hubbard systems [22]. The result was that, indeed, NEGF simulations are a highly accurate tool if, in each case, the proper selfenergy approximation is being used. The choice is dictated, primarily, by the coupling strength and the particle density (filling factor). With that NEGF simulations have reached the level of a predictive tool where the main observables can be accurately computed—with an error not exceeding the order of 10% . . . 20%. This allows extensions of the system size, system geometry and the simulation duration to situations that are out of the reach of alternative methods such as CI, DMRG or real-time quantum Monte Carlo.

Thus, NEGF simulations have the potential of becoming a broadly used tool in many fields of physics including atomic and molecular physics, condensed-matter physics, nuclear matter, warm dense matter and cold atomic and molecular gases. This requires not only codes that efficiently solve the Keldysh–Kadanoff–Baym equations but also a quick, easy and reliable use of the entire arsenal of selfenergy approximations. The present article attempted to pave the way for such applications focusing on the latter task.

To this end, we gave a short selfcontained introduction to the theory of NEGF in section 2 and an overview on recent numerical results for the dynamics of finite Hubbard systems in section 3. There a variety of selfenergy approximations was used that included, in addition to the commonly used Hartree–Fock and second-order Born approximation (SOA), also the third-order approximation (TOA), the particle–particle and particle–hole T matrices (TPP, TPH), the GW and the FLEX approximations, and their accuracy was investigated. The first tests concerned the interacting ground-state properties, in particular, the ground-state energy and the spectral function of small Hubbard clusters of varying coupling strength and filling. The best results were obtained for the perturbative approaches, i.e. the second-order and especially the third-order approximations, the latter being applied for the first time to the Hubbard model, in this article. For small and medium fillings, the TOA ground-state energies were, by far, the most accurate, and the TOA outperformed all previously applied approximations. For half filling, though, the TOA exactly agrees with the SOA due to particle–hole symmetry and, consequently, yields no improvement over it.

We then analyzed the spectral properties of small Hubbard clusters by computing the single-particle spectral function via the solution of the full two-time KBE. Here, the best results were achieved with the FLEX approximation, for all filling factors. Additionally, the TOA shows single-particle energy transitions which are not contained in any other approximation. Thus, by taking into account the full set of approximation methods, most of the relevant energy levels of the systems differing by one particle from the analyzed system can be determined.

Finally, the performance of the different selfenergies in various time-dependent setups, was investigated. We showed results for the time evolution following a confinement quench that was motivated by recent experiments with fermionic atoms. The NEGF results using the particle–particle T-matrix selfenergy agreed very well with the experiment. The second setup used a one-dimensional charge-density-wave state as initial state. Here, by comparison with DMRG simulations the best results were obtained for third-order selfenergies. The third setup were finite graphene-type honeycomb clusters that were exposed to the impact of energetic ions. Here

we compared, among others, second-order Born selfenergies and HF-GKBA simulations. The fourth type of excitation was a rapid weak change of the lattice potential. The subsequent (linear-response) dynamics allowed to compute the spectral function of the system.

Finally, we considered a strong excitation of the system where the lattice potential of one site was changed. Here previous studies have indicated problems in the dynamics of the NEGF, in particular, a strongly damped behavior that is absent in exact-diagonalization calculations [122]. This behavior was found to vary strongly for different selfenergy approximations. We also compared two-time and single-time simulations within the HF-GKBA. The latter almost completely removed the damping.

6.2. Summary of Selfenergy approximations

In the second part of this review, a detailed overview of approximation strategies for the single-particle selfenergy within the framework of nonequilibrium Green functions has been presented. Here we followed two strategies. The first is a perturbative approach with respect to the interaction strength that, i.a. gives rise to the Born series. After reproducing the familiar and broadly used second-order Born approximation we derived the third-order selfenergy (TOA). This approximation contains all terms that are of third order in the interaction strength including, in particular, the relevant ladder-type and polarization diagrams. This important new approximation was derived for all relevant system types, starting from a general basis representation. Additionally, for the special cases of a basis, in which the interaction is diagonal, as well as for the fermionic and bosonic Hubbard basis with a scalar interaction, the corresponding selfenergy terms with Keldysh components have been derived.

The second strategy was a non-perturbative approach where the selfenergies are derived using resummations of infinite partial series. Here our starting point was the set of Hedin's equations from which we derived the GW approximation. The closely related set of integral equations for the bare interaction and vertex led us to the particle–particle and the particle–hole T matrix. In each case we presented all details of the formulas that are needed for an efficient numerical implementation. As before, the results were summarized for general basis sets, for the case of a diagonal potential and for the Hubbard basis. The presentation was concluded by a discussion of the fluctuating-exchange (FLEX) approximation that involves the combination of the terms from both T matrices and GW.

6.3. Outlook

With the set of selfenergies that were introduced in this review a powerful arsenal of approximations is available. In addition to two-time results that are obtained from the full Keldysh–Kadanoff–Baym equations, also the single-time version is available. Here the basis is the Hartree–Fock-GKBA that, in many cases was found to be complementary to the KBE. The HF-GKBA removes the artificial damping for two-time

simulations but does not yield spectral information. It has been successfully combined with most of the selfenergies discussed in this paper, which confirms the attractive properties of this approximation. Moreover, comparisons with DMRG benchmark data indicated that the exact result is typically enclosed between KBE and HF-GKBA. This means that, if both simulations are performed independently, accurate predictions are possible even in the absence of benchmark data.

An important further development will consist in combining the GKBA with propagators beyond Hartree–Fock, i.e. correlated propagators [27]. This is expected to improve the spectral content of single-time simulations and bringing the GKBA simulations closer to the exact result.

The presently available selfenergies have been found to work well for arbitrary filling parameters and weakly to moderately correlated Fermi systems, within the Hubbard model this corresponds to $U/J \lesssim 8$. For larger couplings the present implementation failed to converge. Here it will be important to attempt modified implementations to extend the range of accessible coupling strengths. In addition, it is of high interest to derive higher-order selfenergy approximations, along the lines outlined in this article. For example, for half filling, the implementation of the fourth-order terms, following the algorithm presented in section 4.4, could achieve significant improvements, as was done successfully for homogeneous systems by Gebhard *et al* in [145]. One important obstacle to the application of the fourth-order terms, though, is the numerical downside of a quartic scaling with the propagation time, which will probably limit the applicability to small system sizes and short propagation times. If achievable, though, it opens the way to many new approximation strategies and resummations starting from the fourth-order terms similar to the (third-order-starting) T matrices. Furthermore, the equations for the screened interaction W, see equation (104), and the polarizability P, see equation (105), can be solved exactly in fourth order for a given approximation of the vertex function.

ORCID iDs

M Bonitz ● https://orcid.org/0000-0001-7911-0656

References

[1] Müller B and Nagle J L 2006 Results from the relativistic heavy ion collider *Annu. Rev. Nucl. Part. Sci.* **56** 93
[2] Filinov V, Bonitz M, Ivanov Y, Skokov V, Levashov P and Fortov V 2009 Equation of state of strongly coupled quark–gluon plasma—path integral Monte Carlo results *Contrib. Plasma Phys.* **49** 536

[3] Kotliar G and Vollhardt D 2004 Strongly correlated materials: insights from dynamical mean-field theory *Phys. Today* **57** 53

[4] Falkenhagen H 1971 *Theorie der Elektrolyte* (Leipzig: S. Hirzel)

[5] Wineland D J, Bergquist J, Itano W M, Bollinger J and Manney C 1987 Atomicion Coulomb clusters in an ion trap *Phys. Rev. Lett.* **59** 2935

[6] Drewsen M, Jensen I, Lindballe J, Nissen N, Martinussen R, Mortensen A, Staanum P and Voigt D 2003 Ion Coulomb crystals: a tool for studying ion processes *Int. J. Mass Spectrom.* **229** 83

[7] Bonitz M, Henning C and Block D 2010 Complex plasmas: a laboratory for strong correlations *Rep. Prog. Phys.* **73** 066501

[8] Bonitz M *et al* 2008 Classical and quantum Coulomb crystals *Phys. Plasmas* **15** 055704

[9] Gomez M R *et al* 2014 Experimental demonstration of fusion-relevant conditions in magnetized liner inertial fusion *Phys. Rev. Lett.* **113** 155003

[10] Hurricane O A *et al* 2016 Inertially confined fusion plasmas dominated by alpha-particle self-heating *Nat. Phys.* **12** 800

[11] Glenzer S H *et al* 2016 Matter under extreme conditions experiments at the linac coherent light source *J. Phys. B: At. Mol. Opt. Phys.* **49** 092001

[12] Brown E W, DuBois J L, Holzmann M and Ceperley D M 2013 Exchangecorrelation energy for the three-dimensional homogeneous electron gas at arbitrary temperature *Phys. Rev. B* **88** 081102

[13] Filinov V S, Fortov V E, Bonitz M and Moldabekov Z 2015 Fermionic pathintegral Monte Carlo results for the uniform electron gas at finite temperature *Phys. Rev. E* **91** 033108

[14] Schoof T, Groth S, Vorberger J and Bonitz M 2015 *Ab initio* thermodynamic results for the degenerate electron gas at finite temperature *Phys. Rev. Lett.* **115** 130402

[15] Dornheim T, Groth S and Bonitz M 2018 The uniform electron gas at warm dense matter conditions *Phys. Rep.* **744** 1

[16] Kotliar G, Savrasov S Y, Haule K, Oudovenko V S, Parcollet O and Marianetti C A 2006 Electronic structure calculations with dynamical mean-field theory *Rev. Mod. Phys.* **78** 865

[17] Essler F H, Frahm H, Göhmann F, Klümper A and Korepin V E 2005 *The One-Dimensional Hubbard Model* (Cambridge: Cambridge University Press)

[18] Bloch I 2014 *Quantum Information and Coherence* (*Scott Graduation Services*) ed E Andersson and P Öhberg (New York: Springer) pp 31–63

[19] Cheuk L W, Nichols M A, Okan M, Gersdorf T, Ramasesh V V, Bakr W S, Lompe T and Zwierlein M W 2015 Quantum-gas microscope for fermionic atoms *Phys. Rev. Lett.* **114** 193001

[20] Parsons M F, Huber F, Mazurenko A, Chiu C S, Setiawan W, Wooley-Brown K, Blatt S and Greiner M 2015 Site-resolved imaging of fermionic Li 6 in an optical lattice *Phys. Rev. Lett.* **114** 213002

[21] Haller E, Hudson J, Kelly A, Cotta D A, Peaudecerf B, Bruce G D and Kuhr S 2015 Single-atom imaging of fermions in a quantum-gas microscope *Nat. Phys.* **11** 738

[22] Schlünzen N, Joost J-P, Heidrich-Meisner F and Bonitz M 2017 Nonequilibrium dynamics in the one-dimensional Fermi–Hubbard model: comparison of the nonequilibrium Green-functions approach and the density matrix renormalization group method *Phys. Rev. B* **95** 165139

[23] Schneider U *et al* 2012 Fermionic transport and out-of-equilibrium dynamics in a homogeneous Hubbard model with ultracold atoms *Nat. Phys.* **8** 213

[24] Ronzheimer J P, Schreiber M, Braun S, Hodgman S S, Langer S, McCulloch I P, Heidrich-Meisner F, Bloch I and Schneider U 2013 Expansion dynamics of interacting bosons in homogeneous lattices in one and two dimensions *Phys. Rev. Lett.* **110** 205301

[25] Gruber E *et al* 2016 Ultrafast electronic response of graphene to a strong and localized electric field *Nat. Commun.* **7** 13948

[26] Balzer K, Schlünzen N and Bonitz M 2016 Stopping dynamics of ions passing through correlated honeycomb clusters *Phys. Rev. B* **94** 245118

[27] Bonitz M, Balzer K, Schlünzen N, Rasmussen M R and Joost J-P 2019 Ion impact induced ultrafast electron dynamics in finite graphene-type hubbard clusters *Phys. Status Solidi* b **256** 1800490

[28] Schlünzen N, Hermanns S, Bonitz M and Verdozzi C 2016 Dynamics of strongly correlated fermions: *ab initio* results for two and three dimensions *Phys. Rev. B* **93** 035107

[29] Schecter M and Kamenev A 2012 Forming doublons by a quantum quench *Phys. Rev. A* **85** 043623

[30] Greif D, Tarruell L, Uehlinger T, Jördens R and Esslinger T 2011 Probing nearestneighbor correlations of ultracold fermions in an optical lattice *Phys. Rev. Lett.* **106** 145302

[31] Tokuno A, Demler E and Giamarchi T 2012 Doublon production rate in modulated optical lattices *Phys. Rev. A* **85** 053601

[32] Dirks A, Mikelsons K, Krishnamurthy H and Freericks J 2014 Theoretical description of coherent doublon creation via lattice modulation spectroscopy *Phys. Rev. A* **89** 021602

[33] Noack R M and Manmana S R 2005 Diagonalization- and numerical renormalizationgroup- based methods for interacting quantum systems *AIP Conf. Proc.* **789** 93

[34] Rigol M, Dunjko V and Olshanii M 2008 Thermalization and its mechanism for generic isolated quantum systems *Nature* **452** 854

[35] Prelovšek P and Bonca J 2013 Ground state and finite temperature Lanczos methods *Springer Ser. Solid-State Sci.* **176** 1

[36] Vidal G 2004 Efficient simulation of one-dimensional quantum many-body systems *Phys. Rev. Lett.* **93** 040502

[37] Daley A J, Kollath C, Schollwöck U and Vidal G 2004 Time-dependent densitymatrix renormalization-group using adaptive effective Hilbert spaces *J. Stat. Mech.* P04005

[38] White S R and Feiguin A E 2004 Real-time evolution using the density matrix renormalization group *Phys. Rev. Lett.* **93** 076401

[39] Prokof'ev N V and Svistunov B V 1998 Polaron problem by diagrammatic quantum Monte Carlo *Phys. Rev. Lett.* **81** 2514

[40] Werner P, Oka T and Millis A J 2009 Diagrammatic Monte Carlo simulation of nonequilibrium systems *Phys. Rev. B* **79** 035320

[41] Kozik E, Houcke K V, Gull E, Pollet L, Prokof'ev N, Svistunov B and Troyer M 2010 Diagrammatic Monte Carlo for correlated fermions *Europhys. Lett.* **90** 10004

[42] Rubtsov A N, Savkin V V and Lichtenstein A I 2005 Continuous-time quantum Monte Carlo method for fermions *Phys. Rev. B* **72** 035122

[43] Gull E, Millis A J, Lichtenstein A I, Rubtsov A N, Troyer M and Werner P 2011 Continuous-time Monte Carlo methods for quantum impurity models *Rev. Mod. Phys.* **83** 349

[44] Akbari A, Hashemi M J, Rubio A, Nieminen R M and van Leeuwen R 2012 Challenges in truncating the hierarchy of time-dependent reduced density matrices equations *Phys. Rev. B* **85** 235121

[45] Lacroix D, Hermanns S, Hinz C M and Bonitz M 2014 Ultrafast dynamics of finite Hubbard clusters: a stochastic mean-field approach *Phys. Rev. B* **90** 125112

[46] Krönke S and Schmelcher P 2018 Born–Bogoliubov–Green–Kirkwood–Yvon hierarchy for ultracold bosonic systems *Phys. Rev. A* **98** 013629

[47] Runge E and Gross E K U 1984 Density-functional theory for time-dependent systems *Phys. Rev. Lett.* **52** 997

[48] Marques M and Gross E 2004 Time-dependent density functional theory *Annu. Rev. Phys. Chem.* **55** 427

[49] Onida G, Reining L and Rubio A 2002 Electronic excitations: density-functional versus many-body Green's-function approaches *Rev. Mod. Phys.* **74** 601

[50] van Leeuwen R 2001 Key concepts in time-dependent density-functional theory *Int. J. Mod. Phys.* B **15** 1969

[51] Verdozzi C, Karlsson D, Puig von Friesen M, Almbladh C-O and von Barth U 2011 Some open questions in TDDFT: clues from lattice models and Kadanoff–Baym dynamics *Chem. Phys.* **391** 37

[52] Keldysh L 1965 Diagram technique for nonequilibrium processes *Sov. Phys. JETP* **20** 1018
Keldysh L 1964 Diagram technique for nonequilibrium processes *Zh. Eksp. Teor. Fiz.* **47** 1515

[53] Kadanoff L and Baym G 1962 *Quantum Statistical Mechanics* (New York: Benjamin)

[54] Schäfer W and Wegener M 2002 *Semiconductor Optics and Transport Phenomena* (Berlin: Springer)

[55] Haug H and Jauho A-P 2008 *Quantum Kinetics in Transport and Optics of Semiconductors* (Berlin: Springer)

[56] Seebeck J, Nielsen T R, Gartner P and Jahnke F 2005 Polarons in semiconductor quantum dots and their role in the quantum kinetics of carrier relaxation *Phys. Rev.* B **71** 125327

[57] Lorke M, Nielsen T R, Seebeck J, Gartner P and Jahnke F 2006 Quantum kinetic effects in the optical absorption of semiconductor quantum-dot systems *J. Phys.: Conf. Ser.* **35** 182

[58] Rammer J and Smith H 1986 Quantum field-theoretical methods in transport theory of metals *Rev. Mod. Phys.* **58** 323

[59] Meir Y and Wingreen N S 1992 Landauer formula for the current through an interacting electron region *Phys. Rev. Lett.* **68** 2512

[60] Jauho A P, Wingreen N S and Meir Y 1994 Time-dependent transport in interacting and noninteracting resonant-tunneling systems *Phys. Rev.* B **50** 5528

[61] Stefanucci G and Almbladh C O 2004 Time-dependent partition-free approach in resonant tunneling systems *Phys. Rev.* B **69** 195318

[62] Köhler H S 1995 Memory and correlation effects in nuclear collisions *Phys. Rev.* C **51** 3232

[63] Köhler H S 2006 Beyond the quasi-particle picture in nuclear matter calculations using Green's function techniques *J. Phys.: Conf. Ser.* **35** 384

[64] Rios A, Barker B, Buchler M and Danielewicz P 2011 Towards a nonequilibrium Green's function description of nuclear reactions: one-dimensional mean-field dynamics *Ann. Phys., NY* **326** 1274

[65] Kremp D, Bornath T, Bonitz M and Schlanges M 1999 Quantum kinetic theory of plasmas in strong laser fields *Phys. Rev.* E **60** 4725

[66] Bonitz M, Bornath T, Kremp D, Schlanges M and Kraeft W D 1999 Quantum kinetic theory for laser plasmas. dynamical screening in strong fields *Contrib. Plasma Phys.* **39** 329

[67] Garny M and Müller M M 2009 Kadanoff-Baym equations with non-Gaussian initial conditions: the equilibrium limit *Phys. Rev.* D **80** 085011

[68] Herranen M, Kainulainen K and Rahkila P M 2010 Coherent quasiparticle approximation (cqpa) and nonlocal coherence *J. Phys.: Conf. Ser.* **220** 012007

[69] Garny M, Kartavtsev A and Hohenegger A 2013 Leptogenesis from first principles in the resonant regime *Ann. Phys., NY* **328** 26

[70] Stan A, Dahlen N E and Robert van Leeuwen 2009 Time propagation of the Kadanoff–Baym equations for inhomogeneous systems *J. Chem. Phys.* **130** 224101

[71] Balzer K, Bauch S and Bonitz M 2010 Efficient grid-based method in nonequilibrium Green's function calculations: application to model atoms and molecules *Phys. Rev.* A **81** 022510

[72] Balzer K, Bauch S and Bonitz M 2010 Time-dependent second-order Born calculations for model atoms and molecules in strong laser fields *Phys. Rev.* A **82** 033427

[73] Stefanucci G and van Leeuwen R 2013 *Nonequilibrium Many-Body Theory of Quantum Systems* (Cambridge: Cambridge University Press)

[74] Balzer K and Bonitz M 2013 *Nonequilibrium Green's Functions Approach to Inhomogeneous Systems* (*Lecture Notes in Physics* vol 867) (Berlin: Springer)

[75] Kamenev A 2011 *Field Theory of Non-Equilibrium Systems* (Cambridge: Cambridge University Press)

[76] van Leeuwen R, Tuovinen R and Bonitz M 2013 Progress in nonequilibrium Green's functions V (PNGF V) *J. Phys.: Conf. Ser.* **427** 011001

[77] Hermanns S, Schlünzen N and Bonitz M 2014 Hubbard nanoclusters far from equilibrium *Phys. Rev.* B **90** 125111

[78] Schlünzen N and Bonitz M 2016 Nonequilibrium Green functions approach to strongly correlated fermions in lattice systems *Contrib. Plasma Phys.* **56** 5

[79] Hirsbrunner M R, Philip T M, Basa B, Kim Y, Park M J and Gilbert M J 2019 A review of modeling interacting transient phenomena with non-equilibrium Green functions *Rep. Prog. Phys.* **82** 046001

[80] Scharnke M, Schlünzen N and Bonitz M 2017 Time reversal invariance of quantum kinetic equations: nonequilibrium Green functions formalism *J. Math. Phys.* **58** 061903

[81] Hubbard J 1963 Electron correlations in narrow energy bands *Proc. R. Soc.* A **276** 238

[82] Hedin L 1965 New method for calculating the one-particle Green's function with application to the electron–gas problem *Phys. Rev.* **139** A796

[83] Fermi E 1926 Sulla quantizzazione del gas perfetto monoatomico *Rend. Lincei* **3** 145

[84] Dirac P A M 1926 On the theory of quantum mechanics *Proc. R. Soc.* A **112** 661

[85] Bose 1924 Plancks Gesetz und Lichtquantenhypothese *Z. Phys.* **26** 178

[86] Cao T Y 2004 *Conceptual Foundations of Quantum Field Theory* (Cambridge: Cambridge University Press)

[87] Balzer K, Bauch S and Bonitz M 2010 Finite elements and the discrete variable representation in nonequilibrium Green's function calculations. Atomic and molecular models *J. Phys.: Conf. Ser.* **220** 012020

[88] Larsson H R, Bauch S, Sörensen L K and Bonitz M 2016 Correlation effects in strong-field ionization of heteronuclear diatomic molecules *Phys. Rev.* A **93** 013426

[89] Hochstuhl D, Hinz C M and Bonitz M 2014 Time-dependent multiconfiguration methods for the numerical simulation of photoionization processes of many-electron atoms *Eur. Phys. J. Spec. Top.* **223** 177

[90] Eckstein M and Kollar M 2008 Measuring correlated electron dynamics with timeresolved photoemission spectroscopy *Phys. Rev.* B **78** 245113

[91] Bauch S, Sörensen L K and Madsen L B 2014 Time-dependent generalized-activespace configuration-interaction approach to photoionization dynamics of atoms and molecules *Phys. Rev.* A **90** 062508

[92] Jaksch D and Zoller P 2005 The cold atom Hubbard toolbox *Ann. Phys., NY* **315** 52 (special issue)

[93] Jaksch D, Bruder C, Cirac J I, Gardiner C W and Zoller P 1998 Cold bosonic atoms in optical lattices *Phys. Rev. Lett.* **81** 3108

[94] Liu W V, Wilczek F and Zoller P 2004 Spin-dependent Hubbard model and a quantum phase transition in cold atoms *Phys. Rev.* A **70** 033603

[95] Heidrich-Meisner F, Manmana S R, Rigol M, Muramatsu A, Feiguin A E and Dagotto E 2009 Quantum distillation: dynamical generation of low-entropy states of strongly correlated fermions in an optical lattice *Phys. Rev.* A **80** 041603

[96] Balzer K and Eckstein M 2014 Auxiliary Hamiltonian representation of the nonequilibrium Dyson equation *Phys. Rev.* B **89** 035148

[97] Mandt S 2014 Damping of Bloch oscillations: Variational solutions of the Boltzmann equation beyond linear response *Phys. Rev.* A **90** 053624

[98] Bonitz M, Hermanns S and Balzer K 2013 Dynamics of Hubbard nano-clusters following strong excitation *Contrib. Plasma Phys.* **53** 778

[99] Bonitz M, Jauho A-P, Sadovskii M and Tikhodeev S 2019 In memoriam Leonid V. Keldysh *Phys. Status Solidi* b **256** 1800600

[100] Bauch S, Balzer K and Bonitz M 2010 Electronic correlations in double ionization of atoms in pump-probe experiments *Europhys. Lett.* **91** 53001

[101] Bauch S and Bonitz M 2012 Theoretical description of field-assisted postcollision interaction in Auger decay of atoms *Phys. Rev.* A **85** 053416

[102] Hochstuhl D, Bauch S and Bonitz M 2010 Multiconfigurational time-dependent Hartree–Fock calculations for photoionization of one-dimensional Helium *J. Phys.: Conf. Ser.* **220** 012019

[103] Hochstuhl D and Bonitz M 2011 Two-photon ionization of helium studied with the multiconfigurational time-dependent Hartree–Fock method *J. Chem. Phys.* **134** 084106

[104] Hochstuhl D and Bonitz M 2012 Time-dependent restricted-active-space configuration-interaction method for the photoionization of many-electron atoms *Phys. Rev.* A **86** 053424

[105] Freeman D L 1977 Coupled-cluster expansion applied to the electron gas: inclusion of ring and exchange effects *Phys. Rev.* B **15** 5512

[106] White S R 1992 Density matrix formulation for quantum renormalization groups *Phys. Rev. Lett.* **69** 2863

[107] Rausch R and Potthoff M 2016 Multiplons in the two-hole excitation spectra of the one-dimensional Hubbard model *New J. Phys.* **18** 023033

[108] Riegger L, Orso G and Heidrich-Meisner F 2015 Interaction quantum quenches in the one-dimensional Fermi–Hubbard model with spin imbalance *Phys. Rev.* A **91** 043623

[109] Okumura M, Onishi H, Yamada S and Machida M 2010 Dynamics of attractively interacting fermi atoms in one-dimensional optical lattices: non-equilibrium simulations of fermion superfluidity *Physica* C **470** S949 (*Proc. 9th Int. Conf. on Materials and Mechanisms of Superconductivity*)

[110] Langer S, Schuetz M J A, McCulloch I P, Schollwöck U and Heidrich- Meisner F 2012 Expansion velocity of a one-dimensional, two-component Fermi gas during the sudden expansion in the ballistic regime *Phys. Rev.* A **85** 043618

[111] Keßler S, McCulloch I P and Marquardt F 2013 Creation and dynamics of remote spin-entangled pairs in the expansion of strongly correlated fermions in an optical lattice *New J. Phys.* **15** 053043

[112] Zhang B, Yuan J and Zhao Z 2015 DMTDHF A full dimensional time-dependent Hartree–Fock program for diatomic molecules in strong laser fields *Comput. Phys. Commun.* **194** 84

[113] Lackner F, Brezinová I, Sato T, Ishikawa K L and Burgdörfer J 2015 Propagating two-particle reduced density matrices without wave functions *Phys. Rev.* A **91** 023412

[114] Boström E, Mikkelsen A and Verdozzi C 2016 Time-resolved spectroscopy at surfaces and adsorbate dynamics: insights from a model-system approach *Phys. Rev.* B **93** 195416

[115] Hopjan M, Karlsson D, Ydman S, Verdozzi C and Almbladh C-O 2016 Merging features from Green's functions and time dependent density functional theory: a route to the description of correlated materials out of equilibrium? *Phys. Rev. Lett.* **116** 236402

[116] Karlsson D, Privitera A and Verdozzi C 2011 Time-dependent density-functional theory meets dynamical mean-field theory: real-time dynamics for the 3D Hubbard model *Phys. Rev. Lett.* **106** 116401

[117] Byczuk K and Vollhardt D 2008 Correlated bosons on a lattice: dynamical meanfield theory for Bose–Einstein condensed and normal phases *Phys. Rev.* B **77** 235106

[118] Eckstein M, Hackl A, Kehrein S, Kollar M, Moeckel M, Werner P and Wolf F 2009 New theoretical approaches for correlated systems in nonequilibrium *Eur. Phys. J. Spec. Top.* **180** 217

[119] Biermann S 2014 Dynamical screening effects in correlated electron materials—a progress report on combined many-body perturbation and dynamical mean field theory: 'GW+DMFT' *J. Phys.: Condens. Matter* **26** 173202

[120] Ayral T, Biermann S and Werner P 2013 Screening and nonlocal correlations in the extended Hubbard model from self-consistent combined GW and dynamical mean field theory *Phys. Rev.* B **87** 125149

[121] von Friesen M P, Verdozzi C and Almbladh C-O 2010 Kadanoff-Baym equations and approximate double occupancy in a Hubbard dimer (arXiv:1009.2917)

[122] von Friesen M P, Verdozzi C and Almbladh C-O 2009 Successes and failures of Kadanoff–Baym dynamics in Hubbard nanoclusters *Phys. Rev. Lett.* **103** 176404

[123] Lani G, Romaniello P and Reining L 2012 Approximations for many-body Green's functions: insights from the fundamental equations *New J. Phys.* **14** 013056

[124] Balzer K, Hermanns S and Bonitz M 2012 Electronic double excitations in quantum wells: solving the two-time Kadanoff-Baym equations *Europhys. Lett.* **98** 67002

[125] Balzer K, Hermanns S and Bonitz M 2013 The generalized Kadanoff–Baym ansatz. Computing nonlinear response properties of finite systems *J. Phys.: Conf. Ser.* **427** 012006

[126] Balzer K, Wolf F A, McCulloch I P, Werner P and Eckstein M 2015 Nonthermal melting of Neel order in the Hubbard model *Phys. Rev.* X **5** 031039

[127] Hermanns S, Balzer K and Bonitz M 2012 The non-equilibrium Green function approach to inhomogeneous quantum many-body systems using the generalized Kadanoff–Baym ansatz *Phys. Scr.* **2012** 014036

[128] Hermanns S, Balzer K and Bonitz M 2013 Few-particle quantum dynamics—comparing nonequilibrium Green functions with the generalized Kadanoff–Baym ansatz to density operator theory *J. Phys.: Conf. Ser.* **427** 012008

[129] Sangalli D and Marini A 2015 Complete collisions approximation to the Kadanoff–Baym equation: a first-principles implementation *J. Phys.: Conf. Ser.* **609** 12006

[130] Martin P C and Schwinger J 1959 Theory of many-particle systems. I *Phys. Rev.* **115** 1342

[131] Kremp D, Schlanges M and Kraeft W 2005 *Quantum Statistics of Nonideal Plasmas* (Berlin: Springer)

[132] Langreth D C 1976 *Linear and Nonlinear Electron Transport in Solids* (*NATO Advanced Study Institutes Series* vol 17)

ed J T Devreese and V E van Doren (New York: Springer) pp 3–32

[133] Lipavský P, Špička V and Velický B 1986 Generalized Kadanoff–Baym ansatz for deriving quantum transport equations *Phys. Rev.* B **34** 6933

[134] Špička V, Velický B and Kalvová A 2005 Long and short time quantum dynamics: I. Between Green's functions and transport equations *Physica* E **29** 154

[135] Perfetto E, Uimonen A-M, van Leeuwen R and Stefanucci G 2015 Firstprinciples nonequilibrium Green's-function approach to transient photoabsorption: application to atoms *Phys. Rev.* A **92** 033419

[136] Bonitz M 2016 *Quantum Kinetic Theory* (*Teubner-Texte zur Physik*) 2nd edn (New York: Springer)

[137] Gell-Mann M and Low F 1951 Bound states in quantum field theory *Phys. Rev.* **84** 350

[138] Watanabe M and Reinhardt W 1990 Direct dynamical calculation of entropy and free energy by adiabatic switching *Phys. Rev. Lett.* **65** 3301

[139] Semkat D, Kremp D and Bonitz M 1999 Kadanoff–Baym equations with initial correlations *Phys. Rev.* E **59** 1557

[140] Semkat D, Kremp D and Bonitz M 2000 Kadanoff–Baym equations and non- Markovian Boltzmann equation in generalized T-matrix approximation *J. Math. Phys.* **41** 7458

[141] Butcher J C 2008 *Numerical Methods for Ordinary Differential Equations* (New York: Wiley)

[142] Schlünzen N, Joost J-P and Bonitz M 2017 Comment on 'On the unphysical solutions of the Kadanoff-Baym equations in linear response: correlation-induced homogeneous density-distribution and attractors' *Phys. Rev.* B **96** 117101

[143] Bonitz M and Semkat D 2006 *Introduction to Computational Methods in Many Body Physics* (Paramus: Rinton Press Inc.)

[144] Talarico N W, Maniscalco S and Lo Gullo N 2019 A scalable numerical approach to the solution of the Dyson equation for the non-equilibrium single-particle Green's function *Phys. Status Solidi* b **256** 1800501

[145] Gebhard F, Jeckelmann E, Mahlert S, Nishimoto S and Noack R M 2003 Fourthorder perturbation theory for the half-filled Hubbard model in infinite dimensions *Eur. Phys. J.* B **36** 491

[146] Latini S, Perfetto E, Uimonen A-M, van Leeuwen R and Stefanucci G 2014 Charge dynamics in molecular junctions: nonequilibrium Green's function approach made fast *Phys. Rev.* B **89** 075306

[147] Schneider V, Strunskus T, Elbahri M and Faupel F 2015 Light-induced conductance switching in azobenzene based near-percolated single wall carbon nanotube/polymer composites *Carbon* **90** 94

[148] Sigmund P 2006 *Particle Penetration and Radiation Effects* (New York: Springer)

[149] Ziegler J F, Biersack J P and Littmark U 1996 *The Stopping and Range of Ions in Solids* (New York: Pergamon)

[150] Zhao S, Kang W, Xue J, Zhang X and Zhang P 2015 Comparison of electronic energy loss in graphene and BN sheet by means of time-dependent density functional theory *J. Phys.: Condens. Matter* **27** 025401

[151] Ojanperä A, Krasheninnikov A V and Puska M 2014 Electronic stopping power from first-principles calculations with account for core electron excitations and projectile ionization *Phys. Rev.* B **89** 035120

[152] Balzer K, Rasmussen M R, Schlünzen N, Joost J-P and Bonitz M 2018 Doublon formation by ions impacting a strongly correlated finite lattice system *Phys. Rev. Lett.* **121** 267602

[153] Schlünzen N, Balzer K, Bonitz M, Deuchler L and Pehlke E 2019 Time-dependent simulation of ion stopping: charge transfer and electronic excitations *Contrib. Plasma Phys.* **59** e201800184

[154] Bonitz M *et al* 2019 Towards an integrated modeling of the plasma-solid interface *Front. Chem. Sci. Eng.* **13** 201

[155] Kwong N H, Bonitz M, Binder R and Köhler H S 1998 Semiconductor Kadanoff–Baym equation results for optically excited electron–hole plasmas in quantum wells *Phys. Status Solidi* b **206** 197

[156] Kwong N-H and Bonitz M 2000 Real-time Kadanoff–Baym approach to plasma oscillations in a correlated electron gas *Phys. Rev. Lett.* **84** 1768

[157] Säkkinen N, Peng Y, Appel H and van Leeuwen R 2015 Many-body Green's function theory for electron–phonon interactions: the Kadanoff–Baym approach to spectral properties of the Holstein dimer *J. Chem. Phys.* **143** 234102

[158] von Friesen M, Verdozzi C and Almbladh C-O 2010 Kadanoff–Baym dynamics of Hubbard clusters: performance of many-body schemes, correlation-induced damping and multiple steady and quasi-steady states *Phys. Rev.* B **82** 155108

[159] Balzer K, Bonitz M, van Leeuwen R, Stan A and Dahlen N E 2009 Nonequilibrium Green's function approach to strongly correlated few-electron quantum dots *Phys. Rev.* B **79** 245306

[160] Balzer K and Bonitz M 2009 Nonequilibrium properties of strongly correlated artificial atoms—a Green's functions approach *J. Phys. A: Math. Theor.* **42** 214020

[161] Perfetto E, Uimonen A-M, van Leeuwen R and Stefanucci G 2016 Time-resolved photoabsorption in finite systems: a first-principles negf approach *J. Phys.: Conf. Ser.* **696** 012004

[162] Covito F, Perfetto E, Rubio A and Stefanucci G 2018 Real-time dynamics of Auger wave packets and decays in ultrafast charge migration processes *Phys. Rev.* A **97** 061401

[163] Joost J-P, Schlünzen N and Bonitz M 2019 Femtosecond electron dynamics in graphene nanoribbons—a nonequilibrium Green functions approach within an extended Hubbard model *Phys. Status Solidi* b **256** 1800498

[164] Myöhänen P, Stan A, Stefanucci G and van Leeuwen R 2009 Kadanoff–Baym approach to quantum transport through interacting nanoscale systems: from the transient to the steady-state regime *Phys. Rev.* B **80** 115107

[165] Marini A NEGF with Kohn–Sham orbitals, Yambo-code: www.yambo-code.org

[166] Marini A, Hogan C, Grüning M and Varsano D 2009 Yambo: an *ab initio* tool for excited state calculations *Comput. Phys. Commun.* **180** 1392

[167] Hopjan M and Verdozzi C 2019 Initial correlated states for the generalized Kadanoff–Baym Ansatz without adiabatic switching-on of interactions in closed systems *Eur. Phys. J. Spec. Top.* **227** 1939

[168] Karlsson D, van Leeuwen R, Perfetto E and Stefanucci G 2018 The generalized Kadanoff-Baym ansatz with initial correlations *Phys. Rev.* B **98** 115148

[169] Hopjan M 2018 Theoretical developments for the real-time description and control of nanoscale systems *PhD Thesis* Lund University

[170] Semkat D, Kremp D and Bonitz M 2002 Generalized T-matrix approximation in quantum kinetic equations *Contrib. Plasma Phys.* **42** 31

[171] Feynman R P 1949 The theory of positrons *Phys. Rev.* **76** 749

[172] Romaniello P, Bechstedt F and Reining L 2012 Beyond the GW approximation: combining correlation channels *Phys. Rev.* B **85** 155131

[173] Grüneis A, Marsman M, Harl J, Schimka L and Kresse G 2009 Making the random phase approximation to electronic correlation accurate *J. Chem. Phys.* **131** 154115

[174] Bickers N E, Scalapino D J and White S R 1989 Conserving approximations for strongly correlated electron systems: Bethe-Salpeter equation and dynamics for the two-dimensional Hubbard model *Phys. Rev. Lett.* **62** 961

[175] Bickers N E and Scalapino D J 1989 Conserving approximations for strongly fluctuating electron systems. I. Formalism and calculational approach *Ann. Phys., NY* **193** 206

[176] Bickers N E and White S R 1991 Conserving approximations for strongly fluctuating electron systems. II. Numerical results and parquet extension *Phys. Rev.* B **43** 8044

[177] van Leeuwen R, Dahlen N E and Stan A 2006 Total energies from variational functionals of the Green function and the renormalized four-point vertex *Phys. Rev.* B **74** 195105

[178] Babu S and Brown G E 1973 Quasiparticle interaction in liquid 3He *Ann. Phys., NY* **78** 1

[179] Dominicis C D and Martin P C 1964 Stationary entropy principle and renormalization in normal and superfluid systems. I. Algebraic formulation *J. Math. Phys.* **5** 14

[180] Dominicis C D and Martin P C 1964 Stationary entropy principle and renormalization in normal and superfluid systems. II. Diagrammatic formulation *J. Math. Phys.* **5** 31

[181] Lenard A 1960 On Bogoliubov's kinetic equation for a spatially homogeneous plasma *Ann. Phys., NY* **10** 390

[182] Balescu R 1960 Irreversible processes in ionized gases *Phys. Fluids* **3** 52

[183] Klimontovich Y 1982 *Kinetic Theory of Nonideal Gases and Nonideal Plasmas* (Oxford: Pergamon)

[184] Kraeft W, Kremp D, Ebeling W and Röpke G 1986 *Quantum Statistics of Charged Particle Systems* (Berlin: Akademieverlag)

[185] Gould H A and DeWitt H E 1967 Convergent kinetic equation for a classical plasma *Phys. Rev.* **155** 68

[186] Whitley H D, Alastuey A, Gaffney J, Cauble R, Kraeft W and Bonitz M 2015 A tribute to pioneers of strongly coupled plasmas: Hugh E DeWitt, Bernard Jancovici and Forrest J Rogers *Contrib. Plasma Phys.* **55** 102

[187] Danielewicz P 1984 Quantum theory of nonequilibrium processes II. Application to nuclear collisions *Ann. Phys., NY* **152** 305

[188] Dahlen N E and van Leeuwen R 2007 Solving the Kadanoff-Baym equations for inhomogeneous systems: application to atoms and molecules *Phys. Rev. Lett.* **98** 153004

[189] Sangalli D *et al* 2019 *J. Phys.: Condens. Matter* **31** 325902

Supplement Material for Manuscript "Ultrafast Dynamics of Strongly Correlated Fermions — Nonequilibrium Green Functions and Selfenergy Approximations"

N. Schlünzen, S. Hermanns, M. Scharnke, and M. Bonitz

Institut für Theoretische Physik und Astrophysik, Christian-Albrechts-Universität zu Kiel, D-24098 Kiel, Germany

1. Derivations in full notation

For the following derivations we repeat several equations from the main text. From Hedin's equations (or the respective scheme for the bare interaction) we rewrite the Dyson equation [main text: Eq. (91)],

$$
G_{ij}\big(z_1, z_2\big) = G_{ij}^{(0)}\big(z_1, z_2\big) + \tag{1}
$$
$$
+ \int_{\mathcal{C}} \mathrm{d}z_3 \mathrm{d}z_4 \sum_{mn} G_{im}^{(0)}\big(z_1, z_3\big) \Sigma_{mn}\big(z_3, z_4\big) G_{nj}\big(z_4, z_2\big),
$$

the selfenergy [main text: Eqs. (95), (97) and (101)],

$$
\Sigma_{ij}\big(z_1, z_2\big) = \Sigma_{ij}^{\mathrm{H}}\big(z_1, z_2\big) + \Sigma_{ij}^{\mathrm{xc}}\big(z_1, z_2\big), \tag{2}
$$

$$
\Sigma_{ij}^{\mathrm{xc}}\big(z_1, z_2\big) = \mathrm{i}\hbar \sum_{mpq} w_{ipqm}\big(z_1\big) \int_{\mathcal{C}} \mathrm{d}z_3 \sum_n G_{mn}\big(z_1, z_3\big) \Lambda_{nqpj}\big(z_3, z_2, z_1\big), \tag{3}
$$

$$
\Sigma_{ij}^{\mathrm{xc}}\big(z_1, z_2\big) = \mathrm{i}\hbar \int_{\mathcal{C}} \mathrm{d}z_3 \sum_{mpq} W_{ipqm}\big(z_1, z_3\big) \times \tag{4}
$$
$$
\int_{\mathcal{C}} \mathrm{d}z_4 \sum_n G_{mn}\big(z_1, z_4\big) \Gamma_{nqpj}\big(z_4, z_2, z_3\big),
$$

the interaction [main text: Eqs. (102)-(104)],

$$
W_{ijkl}\big(z_1, z_2\big) = W_{ijkl}^{\mathrm{bare}}\big(z_1, z_2\big) + W_{ijkl}^{\mathrm{ns}}\big(z_1, z_2\big), \tag{5}
$$

$$
W_{ijkl}^{(1)}\big(z_1, z_2\big) = W_{ijkl}^{\mathrm{bare}}\big(z_1, z_2\big) = \delta_{\mathcal{C}}\big(z_1, z_2\big) w_{ijkl}\big(z_1\big), \tag{6}
$$

$$W^{\text{ns}}_{ijkl}\left(z_1, z_2\right) = \sum_{mn} w_{imnl}\left(z_1\right) \int_{\mathcal{C}} \mathrm{d}z_3 \sum_{pq} P_{nqpm}\left(z_1, z_3\right) W_{pjkq}\left(z_3, z_2\right), \qquad (7)$$

and the polarizability [main text: Eq. (105)],

$$P_{ijkl}\left(z_1, z_2\right) = \pm i\hbar \int_{\mathcal{C}} \mathrm{d}z_3 \sum_{m} G_{im}\left(z_1, z_3\right) \times \qquad (8)$$

$$\int_{\mathcal{C}} \mathrm{d}z_4 \sum_{n} G_{nl}\left(z_4, z_1\right) \Gamma_{mjkn}\left(z_3, z_4, z_2\right).$$

The first-order selfenergy reads [main text: Eq. (158)]

$$\Sigma^{(1)}_{ij}\left(z_1, z_2\right) = \Sigma^{\text{H}}_{ij}\left(z_1, z_2\right) + \Sigma^{\text{F}}_{ij}\left(z_1, z_2\right), \qquad (9)$$

with [main text: Eq. (156)]

$$\Sigma^{\text{F}}_{ij}\left(z_1, z_2\right) = \Sigma^{\text{xc}}_{ij}\left(W^{(1)} \equiv W^{\text{bare}}, \Gamma^{(0)}\right) = \qquad (10)$$

$$= i\hbar \delta_{\mathcal{C}}\left(z_1, z_2\right) \sum_{mn} w_{injm}\left(z_1\right) G_{mn}\left(z_1, z_{1+}\right).$$

The zeroth-order screened vertex becomes [main text: Eq. (155)]

$$\Gamma^{(0)}_{ijkl}\left(z_1, z_2, z_3\right) = \delta_{\mathcal{C}}\left(z_1, z_{2+}\right) \delta_{\mathcal{C}}\left(z_3, z_2\right) \delta_{ik} \delta_{jl}. \qquad (11)$$

1.1. Second-order selfenergy contributions

1.1.1. Direct second-order selfenergy

The first second-order selfenergy term involves $W^{(2)}$, which structurally is given by, cf. Eq. (5),

$$W^{(2)} = W^{\text{ns}}\left(P^{(0)}, W^{(1)}\right). \qquad (12)$$

The structure of the zeroth-order term of the polarization is

$$P^{(0)} = P\left(\Gamma^{(0)}\right). \qquad (13)$$

Thus, it is given by

$$P^{(0)}_{ijkl}\left(z_1, z_2\right) = \pm i\hbar \int_{\mathcal{C}} \mathrm{d}z_3 \sum_{m} G_{im}\left(z_1, z_3\right) \qquad (14)$$

$$\int_{\mathcal{C}} \mathrm{d}z_4 \sum_{n} G_{nl}\left(z_4, z_1\right) \delta_{\mathcal{C}}\left(z_3, z_{4+}\right) \delta_{\mathcal{C}}\left(z_2, z_4\right) \delta_{mk} \delta_{jn}$$

$$= \pm i\hbar G_{ik}\left(z_1, z_2\right) G_{jl}\left(z_2, z_1\right).$$

Inserting this result into Eq. (12), one arrives at

$$W_{ijkl}^{(2)}\left(z_1, z_2\right) = \sum_{mn} w_{imnl}\left(z_1\right) \tag{15}$$

$$\int_{\mathcal{C}} dz_3 \sum_{pq} \left(\pm i\hbar G_{np}\left(z_1, z_3\right) G_{qm}\left(z_3, z_1\right)\right) \delta_{\mathcal{C}}\left(z_3, z_2\right) w_{pjkq}\left(z_3\right)$$

and, employing Eq. (7), finally, one has

$$W_{ijkl}^{(2)}\left(z_1, z_2\right) \tag{16}$$

$$= \pm i\hbar \sum_{mn} w_{imnl}\left(z_1\right) \sum_{pq} G_{np}\left(z_1, z_2\right) G_{qm}\left(z_2, z_1\right) w_{pjkq}\left(z_2\right).$$

With this, $\Sigma^{(2),2,0}$ can be calculated as, cf. Eq. (4),

$$\Sigma_{ij}^{(2),2,0}\left(z_1, z_2\right) \tag{17}$$

$$= i\hbar \int_{\mathcal{C}} dz_3 \sum_{mpq} \left(\pm i\hbar \sum_{rs} w_{irsm}\left(z_1\right) \sum_{tu} G_{st}\left(z_1, z_3\right) G_{ur}\left(z_3, z_1\right) w_{tpqu}\left(z_3\right)\right)$$

$$\int_{\mathcal{C}} dz_4 \sum_n G_{mn}\left(z_1, z_4\right) \delta_{\mathcal{C}}\left(z_4, z_{2+}\right) \delta_{\mathcal{C}}\left(z_3, z_2\right) \delta_{np} \delta_{qj}.$$

Evaluating the terms, one arrives at

$$\Sigma_{ij}^{(2),2,0}\left(z_1, z_2\right) \tag{18}$$

$$= \pm \left(i\hbar\right)^2 \sum_{mn} G_{mn}\left(z_1, z_2\right) \sum_{st} G_{st}\left(z_1, z_2\right)$$

$$\sum_r w_{irsm}\left(z_1\right) \sum_u w_{tnju}\left(z_2\right) G_{ur}\left(z_2, z_1\right).$$

1.1.2. Exchange–correlation second-order selfenergy

The other second-order selfenergy term, $\Sigma_{ij}^{(2),1,1}$, requires the first-order term of the vertex Γ, the structure of which is

$$\Gamma^{(1)} = \Gamma\left(\delta\Sigma^{\mathrm{xc},(1)}/\delta G, \Gamma^{(0)}\right). \tag{19}$$

This term involves the functional derivative of $\Sigma^{\mathrm{xc},(1)}$ with respect to G. One has

$$\frac{\delta\Sigma_{ij}^{\mathrm{xc},(1)}\left(z_1, z_2\right)}{\delta G_{rs}\left(z_5, z_6\right)} = \frac{\delta\Sigma_{ij}^{\mathrm{xc},(1),\mathrm{F}}\left(z_1, z_2\right)}{\delta G_{rs}\left(z_5, z_6\right)}. \tag{20}$$

Employing Eq. (10), one finds

$$\frac{\delta\Sigma_{ij}^{\mathrm{xc},(1)}\left(z_1, z_2\right)}{\delta G_{rs}\left(z_5, z_6\right)} = i\hbar\delta_{\mathcal{C}}\left(z_1, z_2\right) \sum_{mn} w_{injm}\left(z_1\right) \frac{\delta G_{mn}\left(z_1, z_{1+}\right)}{\delta G_{rs}\left(z_5, z_6\right)} \tag{21}$$

$$= i\hbar\delta_{\mathcal{C}}\left(z_1, z_2\right) \delta_{\mathcal{C}}\left(z_1, z_5\right) \delta_{\mathcal{C}}\left(z_1, z_6\right) w_{isjr}\left(z_1\right),$$

where

$$\frac{\delta G_{ij}\big(z_1, z_2\big)}{\delta G_{mn}\big(z_5, z_6\big)} = \delta_{\mathcal{C}}\big(z_1, z_5\big)\delta_{\mathcal{C}}\big(z_2, z_6\big)\delta_{im}\delta_{jn} \tag{22}$$

has been applied. With this,

$$\Gamma^{(1)}_{ijkl}\big(z_1, z_2, z_3\big) \tag{23}$$
$$= \int_{\mathcal{C}} \mathrm{d}z_4 \mathrm{d}z_5 \sum_{mn} \frac{\delta \Sigma^{\mathrm{xc},(1)}_{il}\big(z_1, z_2\big)}{\delta G_{mn}\big(z_4, z_5\big)} \int_{\mathcal{C}} \mathrm{d}z_6 \sum_p G_{mp}\big(z_4, z_6\big)$$
$$\int_{\mathcal{C}} \mathrm{d}z_7 \sum_q G_{qn}\big(z_7, z_5\big)\Gamma^{(0)}_{pjkq}\big(z_6, z_7, z_3\big).$$

Using Eq. (21), one has

$$\Gamma^{(1)}_{ijkl}\big(z_1, z_2, z_3\big) \tag{24}$$
$$= \mathrm{i}\hbar\delta_{\mathcal{C}}\big(z_1, z_2\big) \sum_{mn} w_{inlm}\big(z_1\big) \int_{\mathcal{C}} \mathrm{d}z_6 \sum_p G_{mp}\big(z_1, z_6\big)$$
$$\int_{\mathcal{C}} \mathrm{d}z_7 \sum_q G_{qn}\big(z_7, z_1\big)\Gamma^{(0)}_{pjkq}\big(z_6, z_7, z_3\big).$$

With Eq. (11), finally,

$$\Gamma^{(1)}_{ijkl}\big(z_1, z_2, z_3\big) \tag{25}$$
$$= \mathrm{i}\hbar\delta_{\mathcal{C}}\big(z_1, z_2\big) \sum_{mn} w_{inlm}\big(z_1\big)G_{mk}\big(z_1, z_3\big)G_{jn}\big(z_3, z_1\big)$$

ensues. Inserting this result yields

$$\Sigma^{(2),1,1}_{ij}\big(z_1, z_2\big) \tag{26}$$
$$= \mathrm{i}\hbar \int_{\mathcal{C}} \mathrm{d}z_3 \sum_{mpq} W^{(1)}_{ipqm}\big(z_1, z_3\big) \int_{\mathcal{C}} \mathrm{d}z_4 \sum_n G_{mn}\big(z_1, z_4\big)\Gamma^{(1)}_{nqpj}\big(z_4, z_2, z_3\big).$$

Employing Eqs. (6) and (25), one arrives at

$$\Sigma^{(2),1,1}_{ij}\big(z_1, z_2\big) \tag{27}$$
$$= \mathrm{i}\hbar \sum_{mpq} w_{ipqm}\big(z_1\big) \int_{\mathcal{C}} \mathrm{d}z_4 \sum_n G_{mn}\big(z_1, z_4\big)\Gamma^{(1)}_{nqpj}\big(z_4, z_2, z_1\big)$$
$$= \big(\mathrm{i}\hbar\big)^2 \sum_{mpq} w_{ipqm}\big(z_1\big) \sum_n G_{mn}\big(z_1, z_2\big) \sum_{rs} w_{nsjr}\big(z_2\big)G_{rp}\big(z_2, z_1\big)G_{qs}\big(z_1, z_2\big).$$

1.2. Third-order selfenergy contributions

1.2.1. Third-order term: $\Sigma_{ij}^{(3),\{3;0,2\},0}$

Using Eq. (7), one finds

$$
W_{ijkl}^{(3),0,2}\big(z_1, z_2\big) \tag{28}
$$
$$
= \sum_{mn} w_{imnl}\big(z_1\big) \int_{\mathcal{C}} dz_3 \sum_{pq} \big(\pm i\hbar G_{np}\big(z_1, z_3\big) G_{qm}\big(z_3, z_1\big)\big) W_{pjkq}^{(2)}\big(z_3, z_2\big).
$$

Employing Eq. (15) yields

$$
W_{ijkl}^{(3),0,2}\big(z_1, z_2\big) \tag{29}
$$
$$
= \sum_{mn} w_{imnl}\big(z_1\big) \int_{\mathcal{C}} dz_3 \sum_{pq} \big(\pm i\hbar G_{np}\big(z_1, z_3\big) G_{qm}\big(z_3, z_1\big)\big)
$$
$$
\bigg(\pm i\hbar \sum_{rs} w_{prsq}\big(z_3\big) \sum_{tu} G_{st}\big(z_3, z_2\big) G_{ur}\big(z_2, z_3\big) w_{tjku}\big(z_2\big)\bigg).
$$

Evalutating and reordering, one has

$$
W_{ijkl}^{(3),0,2}\big(z_1, z_2\big) \tag{30}
$$
$$
= \big(i\hbar\big)^2 \sum_{mn} w_{imnl}\big(z_1\big) \int_{\mathcal{C}} dz_3 \sum_{pq} G_{np}\big(z_1, z_3\big) G_{qm}\big(z_3, z_1\big) \sum_{rs} w_{prsq}\big(z_3\big)
$$
$$
\sum_{tu} G_{st}\big(z_3, z_2\big) G_{ur}\big(z_2, z_3\big) w_{tjku}\big(z_2\big).
$$

With this, the first term of the first third-order selfenergy class, $\Sigma^{(3),3,0}$, becomes

$$
\Sigma_{ij}^{(3),\{3;0,2\},0}\big(z_1, z_2\big) \tag{31}
$$
$$
= i\hbar \int_{\mathcal{C}} dz_3 \sum_{mpq} W_{ipqm}^{(3),0,2}\big(z_1, z_3\big) \int_{\mathcal{C}} dz_4 \sum_{n} G_{mn}\big(z_1, z_4\big) \Gamma_{nqpj}^{(0)}\big(z_4, z_2, z_3\big).
$$

Using Eq. (11), one has

$$
\Sigma_{ij}^{(3),\{3;0,2\},0}\big(z_1, z_2\big) \tag{32}
$$
$$
= \big(i\hbar\big)^3 \sum_{mn} G_{mn}\big(z_1, z_2\big) \sum_{rs} w_{irsm}\big(z_1\big) \int_{\mathcal{C}} dz_3 \sum_{tu} G_{st}\big(z_1, z_3\big) G_{ur}\big(z_3, z_1\big)
$$
$$
\sum_{vw} w_{tvwu}\big(z_3\big) \sum_{xy} G_{wx}\big(z_3, z_2\big) G_{yv}\big(z_2, z_3\big) w_{xnjy}\big(z_2\big).
$$

1.2.2. Third-order term: $\Sigma_{ij}^{(3),\{3;1,1\},0}$

For the second class of the interaction, $W^{(3),1,1}$, the first-order contribution to the polarizability is needed, which is given by, cf. Eqs. (8) and (25),

$$
P_{ijkl}^{(1)}\big(z_1, z_2\big) = P_{ijkl}\big(z_1, z_2\big)\big(\Gamma^{(1)}\big) \tag{33}
$$
$$
= \pm i\hbar \int_{\mathcal{C}} dz_3 \sum_{m} G_{im}\big(z_1, z_3\big) \int_{\mathcal{C}} dz_4 \sum_{n} G_{nl}\big(z_4, z_1\big) \Gamma_{mjkn}^{(1)}\big(z_3, z_4, z_2\big).
$$

Employing Eq. (25), one arrives at

$$
P_{ijkl}^{(1)}\big(z_1, z_2\big) \tag{34}
$$
$$
= \pm\big(i\hbar\big)^2 \int_{\mathcal{C}} dz_3 \sum_m G_{im}\big(z_1, z_3\big) \sum_n G_{nl}\big(z_3, z_1\big)
$$
$$
\sum_{pq} w_{mqnp}\big(z_3\big) G_{pk}\big(z_3, z_2\big) G_{jq}\big(z_2, z_3\big).
$$

Inserting this result back, one finds, using Eq. (7),

$$
W_{ijkl}^{(3),1,1}\big(z_1, z_2\big) = \sum_{mn} w_{imnl}\big(z_1\big) \int_{\mathcal{C}} dz_3 \sum_{pq} P_{nqpm}^{(1)}\big(z_1, z_3\big) W_{pjkq}^{(1)}\big(z_3, z_2\big)
$$
$$
= \sum_{mn} w_{imnl}\big(z_1\big) \int_{\mathcal{C}} dz_3 \sum_{pq} \bigg(\pm\big(i\hbar\big)^2 \int_{\mathcal{C}} dz_4 \sum_r G_{nr}\big(z_1, z_4\big) \sum_s G_{sm}\big(z_4, z_1\big)
$$
$$
\sum_{tu} w_{rust}\big(z_4\big) G_{tp}\big(z_4, z_3\big) G_{qu}\big(z_3, z_4\big)\bigg) \delta_{\mathcal{C}}\big(z_3, z_2\big) w_{pjkq}\big(z_2\big). \tag{35}
$$

After reordering, one has

$$
W_{ijkl}^{(3),1,1}\big(z_1, z_2\big) \tag{36}
$$
$$
= \pm\big(i\hbar\big)^2 \sum_{mn} w_{imnl}\big(z_1\big) \int_{\mathcal{C}} dz_3 \sum_r G_{nr}\big(z_1, z_3\big) \sum_s G_{sm}\big(z_3, z_1\big)
$$
$$
\sum_{tu} w_{rust}\big(z_3\big) \sum_{pq} G_{tp}\big(z_3, z_2\big) G_{qu}\big(z_2, z_3\big) w_{pjkq}\big(z_2\big).
$$

With these results, the second term of the class $\Sigma^{(3),3,0}$ is found, using Eq. (4),

$$
\Sigma_{ij}^{(3),\{3;1,1\},0}\big(z_1, z_2\big) \tag{37}
$$
$$
= i\hbar \int_{\mathcal{C}} dz_3 \sum_{mpq} W_{ipqm}^{(3),1,1}\big(z_1, z_3\big) \int_{\mathcal{C}} dz_4 \sum_n G_{mn}\big(z_1, z_4\big) \Gamma_{nqpj}^{(0)}\big(z_4, z_2, z_3\big).
$$

Using Eq. (11), one finds

$$
\Sigma_{ij}^{(3),\{3;1,1\},0}\big(z_1, z_2\big) \tag{38}
$$
$$
= \pm\big(i\hbar\big)^3 \sum_{mn} G_{mn}\big(z_1, z_2\big) \sum_{rs} w_{irsm}\big(z_1\big) \int_{\mathcal{C}} dz_3 \sum_t G_{st}\big(z_1, z_3\big) \sum_u G_{ur}\big(z_3, z_1\big)
$$
$$
\sum_{vw} w_{twuv}\big(z_3\big) \sum_{xy} G_{vx}\big(z_3, z_2\big) G_{yw}\big(z_2, z_3\big) w_{xnjy}\big(z_2\big).
$$

1.2.3. Third-order term: $\Sigma_{ij}^{(3),2,1}$

Continuing with the second class $\Sigma^{(3),2,1}$, it is directly worked out by combining Eqs. (15)

and (25),

$$\Sigma_{ij}^{(3),2,1}\left(z_1, z_2\right) = i\hbar \int_{\mathcal{C}} dz_3 \sum_{mpq} W_{ipqm}^{(2)}\left(z_1, z_3\right) \tag{39}$$

$$\int_{\mathcal{C}} dz_4 \sum_n G_{mn}\left(z_1, z_4\right) \Gamma_{nqpj}^{(1)}\left(z_4, z_2, z_3\right).$$

Inserting Eq. (25) yields

$$\Sigma_{ij}^{(3),2,1}\left(z_1, z_2\right) \tag{40}$$

$$= \pm \left(i\hbar\right)^3 \int_{\mathcal{C}} dz_3 \sum_{mrs} w_{irsm}\left(z_1\right) \sum_{tu} G_{st}\left(z_1, z_3\right) G_{ur}\left(z_3, z_1\right) \sum_{pq} w_{tpqu}\left(z_3\right)$$

$$\sum_n G_{mn}\left(z_1, z_2\right) \sum_{vw} w_{nwjv}\left(z_2\right) G_{vp}\left(z_2, z_3\right) G_{qw}\left(z_3, z_2\right).$$

1.2.4. Third-order term: $\Sigma_{ij}^{(3),1,\{2;1,1\}}$

For the single contribution to the class $\Gamma^{(2),1,1}$, one finds, employing Eqs. (21) and (25),

$$\Gamma_{ijkl}^{(2),1,1}\left(z_1, z_2, z_3\right) = \int_{\mathcal{C}} dz_4 dz_5 \sum_{mn} \frac{\delta \Sigma_{il}^{\mathrm{xc},(1)}\left(z_1, z_2\right)}{\delta G_{mn}\left(z_4, z_5\right)} \int_{\mathcal{C}} dz_6 \sum_p G_{mp}\left(z_4, z_6\right)$$

$$\int_{\mathcal{C}} dz_7 \sum_q G_{qn}\left(z_7, z_5\right) \Gamma_{pjkq}^{(1)}\left(z_6, z_7, z_3\right). \tag{41}$$

Evaluating the derivative yields

$$\Gamma_{ijkl}^{(2),1,1}\left(z_1, z_2, z_3\right) \tag{42}$$

$$= i\hbar \delta_{\mathcal{C}}\left(z_1, z_2\right) \sum_{mn} w_{inlm}\left(z_1\right) \int_{\mathcal{C}} dz_6 \sum_p G_{mp}\left(z_1, z_6\right)$$

$$\int_{\mathcal{C}} dz_7 \sum_q G_{qn}\left(z_7, z_1\right) \Gamma_{pjkq}^{(1)}\left(z_6, z_7, z_3\right).$$

Employing Eq. (25), one finds

$$\Gamma_{ijkl}^{(2),1,1}\left(z_1, z_2, z_3\right) \tag{43}$$

$$= \left(i\hbar\right)^2 \delta_{\mathcal{C}}\left(z_1, z_2\right) \sum_{mn} w_{inlm}\left(z_1\right) \int_{\mathcal{C}} dz_6 \sum_p G_{mp}\left(z_1, z_6\right)$$

$$\sum_q G_{qn}\left(z_6, z_1\right) \sum_{rs} w_{psqr}\left(z_6\right) G_{rk}\left(z_6, z_3\right) G_{js}\left(z_3, z_6\right).$$

This enables the computation of $\Sigma^{(3),1,\{2;1,1\}}$ with Eqs. (4) and (6),

$$\Sigma_{ij}^{(3),1,\{2;1,1\}}\left(z_1, z_2\right) \tag{44}$$

$$= i\hbar \int_{\mathcal{C}} dz_3 \sum_{mpq} W_{ipqm}^{(1)}\left(z_1, z_3\right) \int_{\mathcal{C}} dz_4 \sum_n G_{mn}\left(z_1, z_4\right) \Gamma_{nqpj}^{(2),1,1}\left(z_4, z_2, z_3\right)$$

$$= i\hbar \sum_{mpq} w_{ipqm}\left(z_1\right) \int_{\mathcal{C}} dz_4 \sum_n G_{mn}\left(z_1, z_4\right) \Gamma_{nqpj}^{(2),1,1}\left(z_4, z_2, z_1\right).$$

Using Eq. (43), one arrives at

$$\Sigma_{ij}^{(3),1,\{2;1,1\}}\left(z_1, z_2\right) \tag{45}$$

$$= \left(i\hbar\right)^3 \sum_{mpq} w_{ipqm}\left(z_1\right) \sum_n G_{mn}\left(z_1, z_2\right) \sum_{rs} w_{nsjr}\left(z_2\right) \int_{\mathcal{C}} dz_3 \sum_t G_{rt}\left(z_2, z_3\right)$$

$$\sum_u G_{us}\left(z_3, z_2\right) \sum_{vw} w_{twuv}\left(z_3\right) G_{vp}\left(z_3, z_1\right) G_{qw}\left(z_1, z_3\right).$$

1.2.5. Second-order vertex terms

For the first terms, one finds

$$\Gamma_{ijkl}^{(2),\{2;2,0\},0}\left(z_1, z_2, z_3\right) = \int_{\mathcal{C}} dz_4 dz_5 \sum_{mn} \frac{\delta \Sigma_{il}^{(2),2,0}\left(z_1, z_2\right)}{\delta G_{mn}\left(z_4, z_5\right)} \int_{\mathcal{C}} dz_6 \sum_p G_{mp}\left(z_4, z_6\right)$$

$$\int_{\mathcal{C}} dz_7 \sum_q G_{qn}\left(z_7, z_5\right) \Gamma_{pjkq}^{(0)}\left(z_6, z_7, z_3\right) \tag{46}$$

$$= \int_{\mathcal{C}} dz_4 dz_5 \sum_{mn} \frac{\delta \Sigma_{il}^{(2),2,0}\left(z_1, z_2\right)}{\delta G_{mn}\left(z_4, z_5\right)} G_{mk}\left(z_4, z_3\right) G_{jn}\left(z_3, z_5\right).$$

Inserting Eq. (18), the term attains the form

$$\Gamma_{ijkl}^{(2),\{2;2,0\},0}\left(z_1, z_2, z_3\right) = \pm\left(i\hbar\right)^2 \int_{\mathcal{C}} dz_4 dz_5 \tag{47}$$

$$\sum_{mn} \frac{\delta\left(\sum_{pq} G_{pq}\left(z_1, z_2\right) \sum_{st} G_{st}\left(z_1, z_2\right) \sum_r w_{irsp}\left(z_1\right) \sum_u w_{tqlu}\left(z_2\right) G_{ur}\left(z_2, z_1\right)\right)}{\delta G_{mn}\left(z_4, z_5\right)}$$

$$G_{mk}\left(z_4, z_3\right) G_{jn}\left(z_3, z_5\right).$$

Evaluating the derivative, one has

$$\Gamma_{ijkl}^{(2),\{2;2,0\},0}\left(z_1, z_2, z_3\right) = \Gamma_{ijkl}^{(2),\{2;2,0\},0,\mathrm{A}}\left(z_1, z_2, z_3\right) \tag{48}$$

$$+ \Gamma_{ijkl}^{(2),\{2;2,0\},0,\mathrm{B}}\left(z_1, z_2, z_3\right) + \Gamma_{ijkl}^{(2),\{2;2,0\},0,\mathrm{C}}\left(z_1, z_2, z_3\right),$$

with

$$\Gamma_{ijkl}^{(2),\{2;2,0\},0,\text{A}}\left(z_1, z_2, z_3\right) \tag{49}$$

$$= \pm\left(\mathrm{i}\hbar\right)^2 \sum_{mn}\sum_{st} G_{st}\left(z_1, z_2\right) \sum_{r} w_{irsm}\left(z_1\right)$$

$$\sum_{u} w_{tnlu}\left(z_2\right) G_{ur}\left(z_2, z_1\right) G_{mk}\left(z_1, z_3\right) G_{jn}\left(z_3, z_2\right)$$

and

$$\Gamma_{ijkl}^{(2),\{2;2,0\},0,\text{B}}\left(z_1, z_2, z_3\right) \tag{50}$$

$$\pm\left(\mathrm{i}\hbar\right)^2 \sum_{mn}\sum_{pq} G_{pq}\left(z_1, z_2\right) \sum_{r} w_{irmp}\left(z_1\right)$$

$$\sum_{u} w_{nqlu}\left(z_2\right) G_{ur}\left(z_2, z_1\right) G_{mk}\left(z_1, z_3\right) G_{jn}\left(z_3, z_2\right)$$

as well as

$$\Gamma_{ijkl}^{(2),\{2;2,0\},0,\text{C}}\left(z_1, z_2, z_3\right) \tag{51}$$

$$\pm\left(\mathrm{i}\hbar\right)^2 \sum_{mn}\sum_{pq} G_{pq}\left(z_1, z_2\right) \sum_{st} G_{st}\left(z_1, z_2\right)$$

$$w_{insp}\left(z_1\right) w_{tqlm}\left(z_2\right) G_{mk}\left(z_2, z_3\right) G_{jn}\left(z_3, z_1\right).$$

Similarly, one finds

$$\Gamma_{ijkl}^{(2),\{2;1,1\},0}\left(z_1, z_2, z_3\right) = \int_{\mathcal{C}} \mathrm{d}z_4 \mathrm{d}z_5 \sum_{mn} \frac{\delta\Sigma_{il}^{(2),1,1}\left(z_1, z_2\right)}{\delta G_{mn}\left(z_4, z_5\right)} \int_{\mathcal{C}} \mathrm{d}z_6 \sum_{p} G_{mp}\left(z_4, z_6\right)$$

$$\int_{\mathcal{C}} \mathrm{d}z_7 \sum_{q} G_{qn}\left(z_7, z_5\right) \Gamma_{pjkq}^{(0)}\left(z_6, z_7, z_3\right). \tag{52}$$

Inserting Eq. (27) yields

$$\Gamma_{ijkl}^{(2),\{2;1,1\},0}\left(z_1, z_2, z_3\right) = \left(\mathrm{i}\hbar\right)^2 \int_{\mathcal{C}} \mathrm{d}z_4 \mathrm{d}z_5 \tag{53}$$

$$\sum_{mn} \frac{\delta\left(\sum\limits_{prs} w_{irsp}\left(z_1\right) \sum\limits_{q} G_{pq}\left(z_1, z_2\right) \sum\limits_{tu} w_{qult}\left(z_2\right) G_{tr}\left(z_2, z_1\right) G_{su}\left(z_1, z_2\right)\right)}{\delta G_{mn}\left(z_4, z_5\right)}$$

$$G_{mk}\left(z_4, z_3\right) G_{jn}\left(z_3, z_5\right),$$

which, after evaluation of the derivative, yields

$$\Gamma_{ijkl}^{(2),\{2;1,1\},0}\left(z_1, z_2, z_3\right) = \Gamma_{ijkl}^{(2),\{2;1,1\},0,\text{A}}\left(z_1, z_2, z_3\right) \tag{54}$$

$$+ \Gamma_{ijkl}^{(2),\{2;1,1\},0,\text{B}}\left(z_1, z_2, z_3\right) + \Gamma_{ijkl}^{(2),\{2;1,1\},0,\text{C}}\left(z_1, z_2, z_3\right),$$

with

$$\Gamma_{ijkl}^{(2),\{2;1,1\},0,\mathrm{A}}\left(z_1, z_2, z_3\right) \tag{55}$$
$$= \left(\mathrm{i}\hbar\right)^2 \sum_{mn} \sum_{rs} w_{irsm}\left(z_1\right) \sum_{tu} w_{nult}\left(z_2\right) G_{tr}\left(z_2, z_1\right)$$
$$G_{su}\left(z_1, z_2\right) G_{mk}\left(z_1, z_3\right) G_{jn}\left(z_3, z_2\right)$$

and

$$\Gamma_{ijkl}^{(2),\{2;1,1\},0,\mathrm{B}}\left(z_1, z_2, z_3\right) \tag{56}$$
$$+ \left(\mathrm{i}\hbar\right)^2 \sum_{mn} \sum_{ps} w_{insp}\left(z_1\right) \sum_q G_{pq}\left(z_1, z_2\right) \sum_u w_{qulm}\left(z_2\right)$$
$$G_{su}\left(z_1, z_2\right) G_{mk}\left(z_2, z_3\right) G_{jn}\left(z_3, z_1\right)$$

as well as

$$\Gamma_{ijkl}^{(2),\{2;1,1\},0,\mathrm{C}}\left(z_1, z_2, z_3\right) \tag{57}$$
$$+ \left(\mathrm{i}\hbar\right)^2 \sum_{mn} \sum_{pr} w_{irmp}\left(z_1\right) \sum_q G_{pq}\left(z_1, z_2\right) \sum_t w_{qnlt}\left(z_2\right)$$
$$G_{tr}\left(z_2, z_1\right) G_{mk}\left(z_1, z_3\right) G_{jn}\left(z_3, z_2\right).$$

1.2.6. Third-order terms: $\Sigma_{ij}^{(3),1,2}$

With this result, the corresponding selfenergy terms can be computed,

$$\Sigma_{ij}^{(3),1,\{2;\{2;2,0\},0,\mathrm{A}\}}\left(z_1, z_2\right) \tag{58}$$
$$= \mathrm{i}\hbar \int_{\mathcal{C}} \mathrm{d}z_3 \sum_{mpq} W_{ipqm}^{(1)}\left(z_1, z_3\right) \int_{\mathcal{C}} \mathrm{d}z_4 \sum_n G_{mn}\left(z_1, z_4\right) \Gamma_{nqpj}^{(2),\{2;2,0\},0,\mathrm{A}}\left(z_4, z_2, z_3\right)$$
$$= \mathrm{i}\hbar \sum_{mpq} w_{ipqm}\left(z_1\right) \int_{\mathcal{C}} \mathrm{d}z_4 \sum_n G_{mn}\left(z_1, z_4\right) \Gamma_{nqpj}^{(2),\{2;2,0\},0,\mathrm{A}}\left(z_4, z_2, z_1\right).$$

Inserting Eq. (49), one arrives at

$$\Sigma_{ij}^{(3),1,\{2;\{2;2,0\},0,\mathrm{A}\}}\left(z_1, z_2\right) = \pm\left(\mathrm{i}\hbar\right)^3 \sum_{mpq} w_{ipqm}\left(z_1\right) \tag{59}$$

$$\int_{\mathcal{C}} \mathrm{d}z_4 \sum_n G_{mn}\left(z_1, z_4\right) \sum_{rsuv} G_{uv}\left(z_4, z_2\right) \sum_t w_{ntur}\left(z_4\right)$$
$$\sum_w w_{vsjw}\left(z_2\right) G_{wt}\left(z_2, z_4\right) G_{rp}\left(z_4, z_1\right) G_{qs}\left(z_1, z_2\right).$$

For the second term, one has

$$\Sigma_{ij}^{(3),1,\{2;\{2;2,0\},0,\mathrm{B}\}}\left(z_1, z_2\right) \tag{60}$$
$$= \mathrm{i}\hbar \sum_{mpq} w_{ipqm}\left(z_1\right) \int_{\mathcal{C}} \mathrm{d}z_4 \sum_n G_{mn}\left(z_1, z_4\right) \Gamma_{nqpj}^{(2),\{2;2,0\},0,\mathrm{B}}\left(z_4, z_2, z_1\right).$$

Using Eq. (50) yields

$$\Sigma_{ij}^{(3),1,\{2;\{2;2,0\},0,B\}}(z_1, z_2) \tag{61}$$
$$= \pm(i\hbar)^3 \sum_{mpq} w_{ipqm}(z_1) \int_{\mathcal{C}} dz_4 \sum_n G_{mn}(z_1, z_4) \sum_{rs} \sum_{tu} G_{tu}(z_4, z_2)$$
$$\sum_v w_{nvrt}(z_4) \sum_w w_{sujw}(z_2) G_{wv}(z_2, z_4) G_{rp}(z_4, z_1) G_{qs}(z_1, z_2).$$

The third term is given by

$$\Sigma_{ij}^{(3),1,\{2;\{2;2,0\},0,C\}}(z_1, z_2) \tag{62}$$
$$= i\hbar \sum_{mpq} w_{ipqm}(z_1) \int_{\mathcal{C}} dz_4 \sum_n G_{mn}(z_1, z_4) \Gamma_{nqpj}^{(2),\{2;2,0\},0,C}(z_4, z_2, z_1).$$

With Eq. (51), one finds

$$\Sigma_{ij}^{(3),1,\{2;\{2;2,0\},0,C\}}(z_1, z_2) \tag{63}$$
$$= \pm(i\hbar)^3 \sum_{mpq} w_{ipqm}(z_1) \int_{\mathcal{C}} dz_4 \sum_n G_{mn}(z_1, z_4) \sum_{rs} \sum_{tu} G_{tu}(z_4, z_2)$$
$$\sum_{vw} G_{vw}(z_4, z_2) w_{nsvt}(z_4) w_{wujr}(z_2) G_{rp}(z_2, z_1) G_{qs}(z_1, z_4).$$

For the other class, one has

$$\Sigma_{ij}^{(3),1,\{2;\{2;1,1\},0,A\}}(z_1, z_2) \tag{64}$$
$$= i\hbar \int_{\mathcal{C}} dz_3 \sum_{mpq} W_{ipqm}^{(1)}(z_1, z_3) \int_{\mathcal{C}} dz_4 \sum_n G_{mn}(z_1, z_4) \Gamma_{nqpj}^{(2),\{2;1,1\},0,A}(z_4, z_2, z_3)$$
$$= i\hbar \sum_{mpq} w_{ipqm}(z_1) \int_{\mathcal{C}} dz_4 \sum_n G_{mn}(z_1, z_4) \Gamma_{nqpj}^{(2),1,1,A}(z_4, z_2, z_1).$$

Inserting Eq. (55) yields

$$\Sigma_{ij}^{(3),1,\{2;\{2;1,1\},0,A\}}(z_1, z_2) \tag{65}$$
$$= (i\hbar)^3 \sum_{mpq} w_{ipqm}(z_1) \int_{\mathcal{C}} dz_4 \sum_n G_{mn}(z_1, z_4) \sum_{rs} \sum_{tu} w_{ntur}(z_4)$$
$$\sum_{vw} w_{swjv}(z_2) G_{vt}(z_2, z_4) G_{uw}(z_4, z_2) G_{rp}(z_4, z_1) G_{qs}(z_1, z_2).$$

Similarly, the second term reads

$$\Sigma_{ij}^{(3),1,\{2;\{2;1,1\},0,B\}}(z_1, z_2) \tag{66}$$
$$= i\hbar \sum_{mpq} w_{ipqm}(z_1) \int_{\mathcal{C}} dz_4 \sum_n G_{mn}(z_1, z_4) \Gamma_{nqpj}^{(2),\{2;1,1\},0,B}(z_4, z_2, z_1).$$

With Eq. (56), one has

$$
\Sigma_{ij}^{(3),1,\{2;\{2;1,1\},0,\mathrm{B}\}}\big(z_1, z_2\big) \tag{67}
$$
$$
= \big(\mathrm{i}\hbar\big)^3 \sum_{mpq} w_{ipqm}\big(z_1\big) \int_{\mathcal{C}} \mathrm{d}z_4 \sum_n G_{mn}\big(z_1, z_4\big) \sum_{rs}\sum_{tv} w_{nsvt}\big(z_4\big)
$$
$$
\sum_u G_{tu}\big(z_4, z_2\big) \sum_w w_{uwjr}\big(z_2\big) G_{vw}\big(z_4, z_2\big) G_{rp}\big(z_2, z_1\big) G_{qs}\big(z_1, z_4\big).
$$

For the third term, one finds

$$
\Sigma_{ij}^{(3),1,\{2;\{2;1,1\},0,\mathrm{C}\}}\big(z_1, z_2\big) \tag{68}
$$
$$
= \mathrm{i}\hbar \sum_{mpq} w_{ipqm}\big(z_1\big) \int_{\mathcal{C}} \mathrm{d}z_4 \sum_n G_{mn}\big(z_1, z_4\big) \Gamma_{nqpj}^{(2),\{2;1,1\},0,\mathrm{C}}\big(z_4, z_2, z_1\big).
$$

Employing Eq. (57), one arrives at

$$
\Sigma_{ij}^{(3),1,\{2;\{2;1,1\},0,\mathrm{C}\}}\big(z_1, z_2\big) \tag{69}
$$
$$
= \big(\mathrm{i}\hbar\big)^3 \sum_{mpq} w_{ipqm}\big(z_1\big) \int_{\mathcal{C}} \mathrm{d}z_4 \sum_n G_{mn}\big(z_1, z_4\big) \sum_{rs}\sum_{tv} w_{nvrt}\big(z_4\big)
$$
$$
\sum_u G_{tu}\big(z_4, z_2\big) \sum_w w_{usjw}\big(z_2\big) G_{wv}\big(z_2, z_4\big) G_{rp}\big(z_4, z_1\big) G_{qs}\big(z_1, z_2\big).
$$

1.3. Resummation approaches: GW approximation

The GW approximation solves Hedin's equation for the screened interaction W according to Eq. (7) with the zeroth-order vertex $\Gamma^{(0)}$. The set of equations is given by the Dyson equation, cf. Eq. (1),

$$
G_{ij}\big(z_1, z_2\big) = G_{ij}^{(0)}\big(z_1, z_2\big) \tag{70}
$$
$$
+ \int_{\mathcal{C}} \mathrm{d}z_3 \mathrm{d}z_4 \sum_{mn} G_{im}^{(0)}\big(z_1, z_3\big) \Sigma_{mn}\big(z_3, z_4\big) G_{nj}\big(z_4, z_2\big),
$$

the equation for the selfenergy [cf. Eq. (2)]

$$
\Sigma_{ij}\big(z_1, z_2\big) = \Sigma_{ij}^{\mathrm{H}}\big(z_1, z_2\big) + \Sigma_{ij}^{\mathrm{xc}}\big(z_1, z_2\big), \tag{71}
$$

with

$$
\Sigma_{ij}^{\mathrm{xc}}\big(z_1, z_2\big) = \mathrm{i}\hbar \int_{\mathcal{C}} \mathrm{d}z_3 \sum_{mpq} W_{ipqm}\big(z_1, z_3\big) \tag{72}
$$
$$
\int_{\mathcal{C}} \mathrm{d}z_4 \sum_n G_{mn}\big(z_1, z_4\big) \Gamma_{nqpj}^{(0)}\big(z_4, z_2, z_3\big)
$$
$$
= \mathrm{i}\hbar \sum_{mp} W_{ipjm}\big(z_1, z_2\big) G_{mp}\big(z_1, z_2\big),
$$

the zeroth-order polarizability, cf. Eq. (14),

$$P_{ijkl}\big(z_1, z_2\big) = P_{ijkl}^{(0)}\big(z_1, z_2\big) = \pm i\hbar G_{ik}\big(z_1, z_2\big) G_{jl}\big(z_2, z_1\big), \tag{73}$$

the zeroth-order vertex, cf. Eq. (11),

$$\Gamma_{ijkl}\big(z_1, z_2, z_3\big) = \Gamma_{ijkl}^{(0)}\big(z_1, z_2, z_3\big) = \delta_{\mathcal{C}}\big(z_1, z_{2+}\big)\delta_{\mathcal{C}}\big(z_3, z_2\big)\delta_{ik}\delta_{jl} \tag{74}$$

and the screened interaction [cf. Eqs. (5) and (7)]

$$W_{ijkl}\big(z_1, z_2\big) = \delta_{\mathcal{C}}\big(z_1, z_2\big) w_{ijkl}\big(z_1\big) + W_{ijkl}^{\mathrm{ns}}\big(z_1, z_2\big), \tag{75}$$

with

$$W_{ijkl}^{\mathrm{ns}}\big(z_1, z_2\big) \tag{76}$$
$$= \sum_{mn} w_{imnl}\big(z_1\big) \int_{\mathcal{C}} \mathrm{d}z_3 \sum_{pq} P_{nqpm}^{(0)}\big(z_1, z_3\big) W_{pjkq}\big(z_3, z_2\big)$$
$$= \pm i\hbar \sum_{mn} w_{imnl}\big(z_1\big) \int_{\mathcal{C}} \mathrm{d}z_3 \sum_{pq} G_{np}\big(z_1, z_3\big) G_{qm}\big(z_3, z_1\big) W_{pjkq}\big(z_3, z_2\big).$$

To solve this set of equations, one has to determine the selfconsistent solution of Eq. (75). Thereto, it is more suitable to eliminate the singular bare interaction by using

$$W_{ijkl}^{\mathrm{ns}}\big(z_1, z_2\big) = W_{ijkl}\big(z_1, z_2\big) - W_{ijkl}^{\mathrm{bare}}\big(z_1, z_2\big) \tag{77}$$
$$= W_{ijkl}\big(z_1, z_2\big) - \delta_{\mathcal{C}}\big(z_1, z_2\big) w_{ijkl}\big(z_1\big).$$

The selfenergy [cf. Eqs. (71) and (72)] in terms of W^{ns} is then given by

$$\Sigma_{ij}^{\mathrm{GW}}\big(z_1, z_2\big) = \Sigma_{ij}^{\mathrm{H}}\big(z_1, z_2\big) + i\hbar \sum_{mp} W_{ipjm}\big(z_1, z_2\big) G_{mp}\big(z_1, z_2\big)$$
$$= \Sigma_{ij}^{\mathrm{H}}\big(z_1, z_2\big) + i\hbar \sum_{mp} w_{ipjm}\big(z_1\big) G_{mp}\big(z_1, z_{1+}\big) \delta_{\mathcal{C}}\big(z_1, z_2\big)$$
$$+ i\hbar \sum_{mp} W_{ipjm}^{\mathrm{ns}}\big(z_1, z_2\big) G_{mp}\big(z_1, z_2\big). \tag{78}$$

Using Eq. (10), the expression simplifies to

$$\Sigma_{ij}^{\mathrm{GW}}\big(z_1, z_2\big) \tag{79}$$
$$= \Sigma_{ij}^{\mathrm{H}}\big(z_1, z_2\big) + \Sigma_{ij}^{\mathrm{F}}\big(z_1, z_2\big) + i\hbar \sum_{mp} W_{ipjm}^{\mathrm{ns}}\big(z_1, z_2\big) G_{mp}\big(z_1, z_2\big)$$
$$=: \Sigma_{ij}^{\mathrm{H}}\big(z_1, z_2\big) + \Sigma_{ij}^{\mathrm{F}}\big(z_1, z_2\big) + \Sigma_{ij}^{\mathrm{GW,corr}}\big(z_1, z_2\big).$$

For the screened interaction, one has

$$
W_{ijkl}^{\mathrm{ns}}\left(z_1, z_2\right) \tag{80}
$$

$$
= \pm i\hbar \sum_{mn} w_{imnl}\left(z_1\right) \sum_{pq} G_{np}\left(z_1, z_2\right) G_{qm}\left(z_2, z_1\right) w_{pjkq}\left(z_2\right)
$$

$$
\pm i\hbar \sum_{mn} w_{imnl}\left(z_1\right) \int_{\mathcal{C}} \mathrm{d}z_3 \sum_{pq} G_{np}\left(z_1, z_3\right) G_{qm}\left(z_3, z_1\right) W_{pjkq}^{\mathrm{ns}}\left(z_3, z_2\right).
$$

1.4. Resummation approaches: T matrix

In contrast to the GW approximation, the T matrix is an approximation, which takes only the bare interaction w into account and aims instead at a good approximation of the bare vertex function Λ. Thus, its constitutive equations are the Dyson equation,

$$
G_{ij}\left(z_1, z_2\right) = \tag{81}
$$

$$
G_{ij}^{(0)}\left(z_1, z_2\right) + \int_{\mathcal{C}} \mathrm{d}z_3 \mathrm{d}z_4 \sum_{mn} G_{im}^{(0)}\left(z_1, z_3\right) \Sigma_{mn}\left(z_3, z_4\right) G_{nj}\left(z_4, z_2\right),
$$

the equation for the selfenergy, cf. Eqs. (2) and (3),

$$
\Sigma_{ij}\left(z_1, z_2\right) = \Sigma_{ij}^{\mathrm{H}}\left(z_1, z_2\right) + \Sigma_{ij}^{\mathrm{xc}}\left(z_1, z_2\right), \tag{82}
$$

with

$$
\Sigma_{ij}^{\mathrm{xc}}\left(z_1, z_2\right) \tag{83}
$$

$$
= i\hbar \sum_{mpq} w_{ipqm}\left(z_1\right) \int_{\mathcal{C}} \mathrm{d}z_3 \sum_n G_{mn}\left(z_1, z_3\right) \Lambda_{nqpj}\left(z_3, z_2, z_1\right).
$$

The bare vertex Λ is self-consistently given as the solution of

$$
\Lambda_{ijkl}\left(z_1, z_2, z_3\right) = \delta_{\mathcal{C}}\left(z_1, z_{2^+}\right) \delta_{\mathcal{C}}\left(z_3, z_2\right) \delta_{ik} \delta_{jl} \tag{84}
$$

$$
+ \int_{\mathcal{C}} \mathrm{d}z_4 \mathrm{d}z_5 \sum_{mn} \frac{\delta \Sigma_{il}\left(z_1, z_2\right)}{\delta G_{mn}\left(z_4, z_5\right)} \int_{\mathcal{C}} \mathrm{d}z_6 \sum_p G_{mp}\left(z_4, z_6\right)
$$

$$
\int_{\mathcal{C}} \mathrm{d}z_7 \sum_q G_{qn}\left(z_7, z_5\right) \Lambda_{pjkq}\left(z_6, z_7, z_3\right).
$$

If these equations are iterated ad infinitum, all selfenergy terms will be generated. To break the circular dependence between Eqs. (83) and (84), the T-matrix approximation starts by taking the bare vertex on the right-hand side of Eq. (84) only in zeroth order,

$$
\Lambda_{ijkl}^{(0)}\left(z_1, z_2, z_3\right) = \delta_{\mathcal{C}}\left(z_1, z_{2^+}\right) \delta_{\mathcal{C}}\left(z_3, z_2\right) \delta_{ik} \delta_{jl}, \tag{85}
$$

transforming it into

$$\Lambda^{\mathrm{cl}}_{ijkl}\left(z_1, z_2, z_3\right) = \delta_{\mathcal{C}}\left(z_1, z_{2^+}\right)\delta_{\mathcal{C}}\left(z_3, z_2\right)\delta_{ik}\delta_{jl} \tag{86}$$
$$+ \int_{\mathcal{C}} \mathrm{d}z_4 \mathrm{d}z_5 \sum_{mn} \frac{\delta\Sigma^{\mathrm{cl}}_{il}\left(z_1, z_2\right)}{\delta G_{mn}\left(z_4, z_5\right)} G_{mk}\left(z_4, z_3\right)G_{jn}\left(z_3, z_5\right).$$

To arrive at a closed equation, this result is used in Eq. (82), yielding

$$\Sigma^{\mathrm{cl}}_{ij}\left(z_1, z_2\right) = \Sigma^{\mathrm{H}}_{ij}\left(z_1, z_2\right) + \Sigma^{\mathrm{xc}}_{ij}\left(z_1, z_2\right) \tag{87}$$
$$= \Sigma^{\mathrm{H}}_{ij}\left(z_1, z_2\right) + \mathrm{i}\hbar \sum_{mpq} w_{ipqm}\left(z_1\right) \int_{\mathcal{C}} \mathrm{d}z_3 \sum_{n} G_{mn}\left(z_1, z_3\right)\Lambda^{\mathrm{cl}}_{nqpj}\left(z_3, z_2, z_1\right).$$

Inserting Eq. (86), one has

$$\Sigma^{\mathrm{cl}}_{ij}\left(z_1, z_2\right) = \pm\mathrm{i}\hbar\delta_{\mathcal{C}}\left(z_1, z_2\right) \sum_{mn} w_{mijn}\left(z_1\right)G_{nm}\left(z_1, z_{1^+}\right) \tag{88}$$
$$+ \mathrm{i}\hbar \sum_{mn} w_{injm}\left(z_1\right)G_{mn}\left(z_1, z_{1^+}\right)\delta_{\mathcal{C}}\left(z_1, z_2\right)$$
$$+ \mathrm{i}\hbar \sum_{mpq} w_{ipqm}\left(z_1\right) \int_{\mathcal{C}} \mathrm{d}z_3 \sum_{n} G_{mn}\left(z_1, z_3\right)$$
$$\int_{\mathcal{C}} \mathrm{d}z_4 \mathrm{d}z_5 \sum_{rs} \frac{\delta\Sigma^{\mathrm{cl}}_{nj}\left(z_3, z_2\right)}{\delta G_{rs}\left(z_4, z_5\right)} G_{rp}\left(z_4, z_1\right)G_{qs}\left(z_1, z_5\right).$$

This term can be restructured to yield

$$\Sigma^{\mathrm{cl}}_{ij}\left(z_1, z_2\right) \tag{89}$$
$$= \mathrm{i}\hbar\delta_{\mathcal{C}}\left(z_1, z_2\right) \sum_{mn} G_{mn}\left(z_1, z_{1^+}\right)w^{\pm}_{injm}\left(z_1\right)$$
$$+ \mathrm{i}\hbar \sum_{mpq} w_{ipqm}\left(z_1\right) \int_{\mathcal{C}} \mathrm{d}z_3 \sum_{n} G_{mn}\left(z_1, z_3\right)$$
$$\int_{\mathcal{C}} \mathrm{d}z_4 \mathrm{d}z_5 \sum_{rs} \frac{\delta\Sigma^{\mathrm{cl}}_{nj}\left(z_3, z_2\right)}{\delta G_{rs}\left(z_4, z_5\right)} G_{rp}\left(z_4, z_1\right)G_{qs}\left(z_1, z_5\right),$$

with the (anti-)symmetrized potential $w^{\pm}_{ijkl}\left(z_1\right) := w_{ijkl}\left(z_1\right) \pm w_{jikl}\left(z_1\right)$. Using Eq. (10) again, one finds

$$\Sigma^{\mathrm{cl}}_{ij}\left(z_1, z_2\right) \tag{90}$$
$$= \Sigma^{\mathrm{H}}_{ij}\left(z_1, z_2\right) + \Sigma^{\mathrm{F}}_{ij}\left(z_1, z_2\right) + \mathrm{i}\hbar \sum_{mpq} w_{ipqm}\left(z_1\right) \int_{\mathcal{C}} \mathrm{d}z_3 \sum_{n} G_{mn}\left(z_1, z_3\right)$$
$$\int_{\mathcal{C}} \mathrm{d}z_4 \mathrm{d}z_5 \sum_{rs} \frac{\delta\Sigma^{\mathrm{cl}}_{nj}\left(z_3, z_2\right)}{\delta G_{rs}\left(z_4, z_5\right)} G_{rp}\left(z_4, z_1\right)G_{qs}\left(z_1, z_5\right).$$

Taking the derivative with respect to G, one arrives at

$$\frac{\delta \Sigma_{ij}^{cl}\left(z_1, z_2\right)}{\delta G_{tu}\left(z_6, z_7\right)} = i\hbar \delta_{\mathcal{C}}\left(z_1, z_2\right) \delta_{\mathcal{C}}\left(z_1, z_6\right) \delta_{\mathcal{C}}\left(z_{1^+}, z_7\right) w_{iujt}^{\pm}\left(z_1\right)$$
$$\left(\frac{\delta \Sigma_{ij}^{cl,A}\left(z_1, z_2\right)}{\delta G_{tu}\left(z_6, z_7\right)} + \frac{\delta \Sigma_{ij}^{cl,B}\left(z_1, z_2\right)}{\delta G_{tu}\left(z_6, z_7\right)} \right.$$
$$\left. + \frac{\delta \Sigma_{ij}^{cl,C}\left(z_1, z_2\right)}{\delta G_{tu}\left(z_6, z_7\right)} + \frac{\delta \Sigma_{ij}^{cl,D}\left(z_1, z_2\right)}{\delta G_{tu}\left(z_6, z_7\right)} \right), \tag{91}$$

with

$$\frac{\delta \Sigma_{ij}^{cl,A}\left(z_1, z_2\right)}{\delta G_{tu}\left(z_6, z_7\right)} \tag{92}$$
$$= i\hbar \delta_{\mathcal{C}}\left(z_1, z_6\right) \sum_{pq} w_{ipqt}\left(z_1\right)$$
$$\int_{\mathcal{C}} dz_4 dz_5 \sum_{rs} \frac{\delta \Sigma_{uj}^{cl}\left(z_7, z_2\right)}{\delta G_{rs}\left(z_4, z_5\right)} G_{rp}\left(z_4, z_1\right) G_{qs}\left(z_1, z_5\right),$$

$$\frac{\delta \Sigma_{ij}^{cl,B}\left(z_1, z_2\right)}{\delta G_{tu}\left(z_6, z_7\right)} \tag{93}$$
$$= i\hbar \delta_{\mathcal{C}}\left(z_1, z_7\right) \sum_{mq} w_{iuqm}\left(z_1\right) \int_{\mathcal{C}} dz_3 \sum_{n} G_{mn}\left(z_1, z_3\right)$$
$$\int_{\mathcal{C}} dz_5 \sum_{s} \frac{\delta \Sigma_{nj}^{cl}\left(z_3, z_2\right)}{\delta G_{ts}\left(z_6, z_5\right)} G_{qs}\left(z_1, z_5\right)$$

and

$$\frac{\delta \Sigma_{ij}^{cl,C}\left(z_1, z_2\right)}{\delta G_{tu}\left(z_6, z_7\right)} \tag{94}$$
$$= i\hbar \delta_{\mathcal{C}}\left(z_1, z_6\right) \sum_{mp} w_{iptm}\left(z_1\right) \int_{\mathcal{C}} dz_3 \sum_{n} G_{mn}\left(z_1, z_3\right)$$
$$\int_{\mathcal{C}} dz_4 \sum_{r} \frac{\delta \Sigma_{nj}^{cl}\left(z_3, z_2\right)}{\delta G_{ru}\left(z_4, z_7\right)} G_{rp}\left(z_4, z_1\right),$$

as well as

$$\frac{\delta \Sigma_{ij}^{\text{cl,D}}\big(z_1, z_2\big)}{\delta G_{tu}\big(z_6, z_7\big)} \tag{95}$$

$$= i\hbar \sum_{mpq} w_{ipqm}\big(z_1\big) \int_{\mathcal{C}} dz_3 \sum_{n} G_{mn}\big(z_1, z_3\big)$$

$$\int_{\mathcal{C}} dz_4 dz_5 \sum_{rs} \frac{\delta \Sigma_{nj}^{\text{cl}}\big(z_3, z_2\big)}{\delta G_{rs}\big(z_4, z_5\big) \delta G_{tu}\big(z_6, z_7\big)} G_{rp}\big(z_4, z_1\big) G_{qs}\big(z_1, z_5\big) .$$

Neglecting $\frac{\delta \Sigma_{nj}^{\text{cl}}(z_3, z_2)}{\delta G_{rs}(z_4, z_5) \delta G_{tu}(z_6, z_7)}$ as an approximation, Eq. (91) becomes a closed equation for $\frac{\delta \Sigma^{\text{cl}}}{\delta G}$. The first iteration yields the second-order terms

$$\frac{\delta \Sigma_{ij}^{\text{cl,(2)}}\big(z_1, z_2\big)}{\delta G_{tu}\big(z_6, z_7\big)} \approx \frac{\delta \Sigma_{ij}^{\text{cl,(2),A}}\big(z_1, z_2\big)}{\delta G_{tu}\big(z_6, z_7\big)} \tag{96}$$

$$+ \frac{\delta \Sigma_{ij}^{\text{cl,(2),B}}\big(z_1, z_2\big)}{\delta G_{tu}\big(z_6, z_7\big)} + \frac{\delta \Sigma_{ij}^{\text{cl,(2),C}}\big(z_1, z_2\big)}{\delta G_{tu}\big(z_6, z_7\big)} ,$$

with

$$\frac{\delta \Sigma_{ij}^{\text{cl,(2),A}}\big(z_1, z_2\big)}{\delta G_{tu}\big(z_6, z_7\big)} \tag{97}$$

$$= \big(i\hbar\big)^2 \delta_{\mathcal{C}}\big(z_1, z_6\big) \delta_{\mathcal{C}}\big(z_2, z_7\big) \sum_{pq} w_{ipqt}\big(z_1\big)$$

$$\sum_{rs} w_{usjr}^{\pm}\big(z_2\big) G_{rp}\big(z_2, z_1\big) G_{qs}\big(z_1, z_2\big)$$

and

$$\frac{\delta \Sigma_{ij}^{\text{cl,(2),B}}\big(z_1, z_2\big)}{\delta G_{tu}\big(z_6, z_7\big)} \tag{98}$$

$$= \big(i\hbar\big)^2 \delta_{\mathcal{C}}\big(z_1, z_7\big) \delta_{\mathcal{C}}\big(z_2, z_6\big) \sum_{mq} w_{iuqm}\big(z_1\big)$$

$$\sum_{n} G_{mn}\big(z_1, z_2\big) \sum_{s} w_{nsjt}^{\pm}\big(z_2\big) G_{qs}\big(z_1, z_2\big)$$

as well as

$$\frac{\delta \Sigma_{ij}^{\text{cl,(2),C}}\big(z_1, z_2\big)}{\delta G_{tu}\big(z_6, z_7\big)} \tag{99}$$

$$= \big(i\hbar\big)^2 \delta_{\mathcal{C}}\big(z_1, z_6\big) \delta_{\mathcal{C}}\big(z_2, z_7\big) \sum_{mp} w_{iptm}\big(z_1\big)$$

$$\sum_{n} G_{mn}\big(z_1, z_2\big) \sum_{r} w_{nujr}^{\pm}\big(z_2\big) G_{rp}\big(z_2, z_1\big) .$$

Note that, for the first iteration, $\frac{\delta\Sigma_{ij}^{\text{cl,D}}(z_1,z_2)}{\delta G_{tu}(z_6,z_7)}$ is exactly equal to zero, thus Eq. (96) is also exact up to second order in w. In the following, each of the three terms will be considered separately. To start with, one recognizes that all three terms yield the same first and second-order contributions to the selfenergy, which read

$$\Sigma_{ij}^{\text{cl,(1)}}\big(z_1,z_2\big) = \Sigma_{ij}^{\text{H}}\big(z_1,z_2\big) + \Sigma_{ij}^{\text{F}}\big(z_1,z_2\big) \tag{100}$$

$$\Sigma_{ij}^{\text{cl,(2)}}\big(z_1,z_2\big) = \big(i\hbar\big)^2 \sum_{mpq} w_{ipqm}\big(z_1\big) \sum_n G_{mn}\big(z_1,z_2\big) \tag{101}$$

$$\sum_{rs} w_{nsjr}^{\pm}\big(z_2\big) G_{rp}\big(z_2,z_1\big) G_{qs}\big(z_1,z_2\big)$$

and agree with the exact first and second-order terms, already encountered in Eqs. (9), (18) and (27). The third-order contributions to Σ^{cl} from the second-order terms in Eq. (96) are given by

$$\Sigma_{ij}^{\text{cl,(3),A}}\big(z_1,z_2\big) = i\hbar \sum_{mpq} w_{ipqm}\big(z_1\big) \int_{\mathcal{C}} dz_3 \sum_n G_{mn}\big(z_1,z_3\big) \tag{102}$$

$$\int_{\mathcal{C}} dz_4 dz_5 \sum_{rs} \frac{\delta\Sigma_{nj}^{\text{cl,(2),A}}\big(z_3,z_2\big)}{\delta G_{rs}\big(z_4,z_5\big)} G_{rp}\big(z_4,z_1\big) G_{qs}\big(z_1,z_5\big)\,.$$

Inserting the second-order term yields

$$\Sigma_{ij}^{\text{cl,(3),A}}\big(z_1,z_2\big) = \big(i\hbar\big)^3 \sum_{mpq} w_{ipqm}\big(z_1\big) \int_{\mathcal{C}} dz_3 \sum_n G_{mn}\big(z_1,z_3\big) \tag{103}$$

$$\sum_{rs}\sum_{tu} w_{ntur}\big(z_3\big) \sum_{vw} w_{swjv}^{\pm}\big(z_2\big)$$

$$G_{vt}\big(z_2,z_3\big) G_{uw}\big(z_3,z_2\big) G_{rp}\big(z_3,z_1\big) G_{qs}\big(z_1,z_2\big)\,.$$

For the second third-order selfenergy term, one has

$$\Sigma_{ij}^{\text{cl,(3),B}}\big(z_1,z_2\big) = i\hbar \sum_{mpq} w_{ipqm}\big(z_1\big) \int_{\mathcal{C}} dz_3 \sum_n G_{mn}\big(z_1,z_3\big) \tag{104}$$

$$\int_{\mathcal{C}} dz_4 dz_5 \sum_{rs} \frac{\delta\Sigma_{nj}^{\text{cl,(2),B}}\big(z_3,z_2\big)}{\delta G_{rs}\big(z_4,z_5\big)} G_{rp}\big(z_4,z_1\big) G_{qs}\big(z_1,z_5\big)\,.$$

which evaluates to

$$\Sigma_{ij}^{\text{cl,(3),B}}\big(z_1,z_2\big) = \big(i\hbar\big)^3 \sum_{mpq} w_{ipqm}\big(z_1\big) \int_{\mathcal{C}} dz_3 \sum_n G_{mn}\big(z_1,z_3\big) \tag{105}$$

$$\sum_{rs}\sum_{tu} w_{nsut}\big(z_3\big) \sum_v G_{tv}\big(z_3,z_2\big) \sum_w w_{vwjr}^{\pm}\big(z_2\big)$$

$$G_{uw}\big(z_3,z_2\big) G_{rp}\big(z_2,z_1\big) G_{qs}\big(z_1,z_3\big)\,.$$

The third term reads

$$\Sigma_{ij}^{\text{cl},(3),\text{C}}\left(z_1, z_2\right) = i\hbar \sum_{mpq} w_{ipqm}\left(z_1\right) \int_{\mathcal{C}} dz_3 \sum_n G_{mn}\left(z_1, z_3\right) \tag{106}$$

$$\int_{\mathcal{C}} dz_4 dz_5 \sum_{rs} \frac{\delta \Sigma_{nj}^{\text{cl},(2),\text{C}}\left(z_3, z_2\right)}{\delta G_{rs}\left(z_4, z_5\right)} G_{rp}\left(z_4, z_1\right) G_{qs}\left(z_1, z_5\right). $$

$$\tag{107}$$

Using the second-order result, one arrives at

$$\Sigma_{ij}^{\text{cl},(3),\text{C}}\left(z_1, z_2\right) = i\hbar \sum_{mpq} w_{ipqm}\left(z_1\right) \int_{\mathcal{C}} dz_3 \sum_n G_{mn}\left(z_1, z_3\right) \tag{108}$$

$$\sum_{rs} \sum_{tu} w_{nurt}\left(z_3\right) \sum_v G_{tv}\left(z_3, z_2\right) \sum_w w_{vsjw}^{\pm}\left(z_2\right)$$

$$G_{wu}\left(z_2, z_3\right) G_{rp}\left(z_3, z_1\right) G_{qs}\left(z_1, z_2\right). $$

2. Non-selfconsistent second-order selfenergy contributions

2.1. General basis

The first two classes are just the same as in the selfconsistent approximation, cf. Eqs. (176) and (183) of the main text, with the replacement $G \to G^{(0)}$. Likewise, their components follow directly from Eqs. (184) and (185) of the main text. For the third and fourth class, one needs the contributions to $G^{(1)}$, which are

$$G_{ij}^{(1),\{\text{H},0\},0}\left(z_1, z_2\right) \tag{109}$$

$$= \int_{\mathcal{C}} dz_3 dz_4 \sum_{mn} G_{im}^{(0)}\left(z_1, z_3\right) \Sigma_{mn}^{\text{H},0}\left(z_3, z_4\right) G_{nj}^{(0)}\left(z_4, z_2\right)$$

$$= \pm i\hbar \int_{\mathcal{C}} dz_3 \sum_{mn} G_{im}^{(0)}\left(z_1, z_3\right) \sum_{pq} w_{pmnq}\left(z_3\right) G_{qp}^{(0)}\left(z_3, z_{3+}\right) G_{nj}^{(0)}\left(z_3, z_2\right)$$

and

$$G_{ij}^{(1),\{\text{F},0\},0}\left(z_1, z_2\right) \tag{110}$$

$$= \int_{\mathcal{C}} dz_3 dz_4 \sum_{mn} G_{im}^{(0)}\left(z_1, z_3\right) \Sigma_{mn}^{\text{F},0}\left(z_3, z_4\right) G_{nj}^{(0)}\left(z_4, z_2\right)$$

$$= i\hbar \int_{\mathcal{C}} dz_3 \sum_{mn} G_{im}^{(0)}\left(z_1, z_3\right) \sum_{pq} w_{mqnp}\left(z_3\right) G_{pq}^{(0)}\left(z_3, z_{3+}\right) G_{nj}^{(0)}\left(z_3, z_2\right). $$

With these results, the additional non-selfconsistent contributions are

$$\Sigma_{ij}^{(2),\{H,0\},\{1,\{H,0\},0\}}\left(z_1, z_2\right) = \pm i\hbar \delta_{\mathcal{C}}\left(z_1, z_2\right) \sum_{mn} w_{mijn}\left(z_1\right) G_{nm}^{(1),\{H,0\},0}\left(z_1, z_{1^+}\right)$$

$$= \left(i\hbar\right)^2 \delta_{\mathcal{C}}\left(z_1, z_2\right) \sum_{mn} w_{mijn}\left(z_1\right) \tag{111}$$

$$\int_{\mathcal{C}} dz_3 \sum_{pq} G_{np}^{(0)}\left(z_1, z_3\right) \sum_{rs} w_{rpqs}\left(z_3\right) G_{sr}^{(0)}\left(z_3, z_{3^+}\right) G_{qm}^{(0)}\left(z_3, z_{1^+}\right),$$

as well as

$$\Sigma_{ij}^{(2),\{H,0\},\{1,\{F,0\},0\}}\left(z_1, z_2\right) = \pm i\hbar \delta_{\mathcal{C}}\left(z_1, z_2\right) \sum_{mn} w_{mijn}\left(z_1\right) G_{nm}^{(1),\{F,0\},0}\left(z_1, z_{1^+}\right)$$

$$= \pm \left(i\hbar\right)^2 \delta_{\mathcal{C}}\left(z_1, z_2\right) \sum_{mn} w_{mijn}\left(z_1\right) \tag{112}$$

$$\int_{\mathcal{C}} dz_3 \sum_{pq} G_{np}^{(0)}\left(z_1, z_3\right) \sum_{rs} w_{psqr}\left(z_3\right) G_{rs}^{(0)}\left(z_3, z_{3^+}\right) G_{qm}^{(0)}\left(z_3, z_{1^+}\right)$$

and

$$\Sigma_{ij}^{(2),\{F,0\},\{1,\{H,0\},0\}}\left(z_1, z_2\right) = i\hbar \delta_{\mathcal{C}}\left(z_1, z_2\right) \sum_{mn} w_{injm}\left(z_1\right) G_{mn}^{(1),\{H,0\},0}\left(z_1, z_{1^+}\right)$$

$$= \pm \left(i\hbar\right)^2 \delta_{\mathcal{C}}\left(z_1, z_2\right) \sum_{mn} w_{nimj}\left(z_1\right) \tag{113}$$

$$\int_{\mathcal{C}} dz_3 \sum_{pq} G_{mp}^{(0)}\left(z_1, z_3\right) \sum_{rs} w_{rpqs}\left(z_3\right) G_{sr}^{(0)}\left(z_3, z_{3^+}\right) G_{qn}^{(0)}\left(z_3, z_{1^+}\right),$$

as well as

$$\Sigma_{ij}^{(2),\{F,0\},\{1,\{F,0\},0\}}\left(z_1, z_2\right) = i\hbar \delta_{\mathcal{C}}\left(z_1, z_2\right) \sum_{mn} w_{injm}\left(z_1\right) G_{mn}^{(1),\{F,0\},0}\left(z_1, z_{1^+}\right)$$

$$= \left(i\hbar\right)^2 \delta_{\mathcal{C}}\left(z_1, z_2\right) \sum_{mn} w_{nimj}\left(z_1\right) \tag{114}$$

$$\int_{\mathcal{C}} dz_3 \sum_{pq} G_{mp}^{(0)}\left(z_1, z_3\right) \sum_{rs} w_{psqr}\left(z_3\right) G_{rs}^{(0)}\left(z_3, z_{3^+}\right) G_{qn}^{(0)}\left(z_3, z_{1^+}\right).$$

The corresponding components are all time-diagonal and read

$$\Sigma_{ij}^{(2),\{H,0\},\{1,\{H,0\},0\},\delta}\left(t_1\right) \tag{115}$$

$$= \left(i\hbar\right)^2 \sum_{mn} w_{mijn}\left(t_1\right) \Bigg($$

$$\int_{t_0}^{t_1} dt_3 \sum_{pq} G_{np}^{(0),>}\left(t_1, t_3\right) \sum_{rs} w_{rpqs}\left(t_3\right) G_{sr}^{(0),<}\left(t_3, t_3\right) G_{qm}^{(0),<}\left(t_3, t_1\right)$$

$$+ \int_{t_1}^{t_0} dt_3 \sum_{pq} G_{np}^{(0),<}\left(t_1, t_3\right) \sum_{rs} w_{rpqs}\left(t_3\right) G_{sr}^{(0),<}\left(t_3, t_3\right) G_{qm}^{(0),>}\left(t_3, t_1\right) \Bigg)$$

and

$$\Sigma_{ij}^{(2),\{H,0\},\{1,\{F,0\},0\},\delta}\left(t_1\right) \tag{116}$$

$$= \pm\left(i\hbar\right)^2 \sum_{mn} w_{mijn}\left(t_1\right)\Bigg($$

$$\int_{t_0}^{t_1} dt_3 \sum_{pq} G_{np}^{(0),>}\left(t_1,t_3\right) \sum_{rs} w_{psqr}\left(t_3\right) G_{rs}^{(0),<}\left(t_3,t_3\right) G_{qm}^{(0),<}\left(t_3,t_1\right)$$

$$+ \int_{t_1}^{t_0} dt_3 \sum_{pq} G_{np}^{(0),<}\left(t_1,t_3\right) \sum_{rs} w_{psqr}\left(t_3\right) G_{rs}^{(0),<}\left(t_3,t_3\right) G_{qm}^{(0),>}\left(t_3,t_1\right)\Bigg),$$

as well as

$$\Sigma_{ij}^{(2),\{F,0\},\{1,\{H,0\},0\},\delta}\left(t_1\right) \tag{117}$$

$$= \pm\left(i\hbar\right)^2 \sum_{mn} w_{nimj}\left(t_1\right)\Bigg($$

$$\int_{t_0}^{t_1} dt_3 \sum_{pq} G_{mp}^{(0),>}\left(t_1,t_3\right) \sum_{rs} w_{rpqs}\left(t_3\right) G_{sr}^{(0),<}\left(t_3,t_3\right) G_{qn}^{(0),<}\left(t_3,t_1\right)$$

$$+ \int_{t_1}^{t_0} dt_3 \sum_{pq} G_{mp}^{(0),<}\left(t_1,t_3\right) \sum_{rs} w_{rpqs}\left(t_3\right) G_{sr}^{(0),<}\left(t_3,t_3\right) G_{qn}^{(0),>}\left(t_3,t_1\right)\Bigg)$$

and

$$\Sigma_{ij}^{(2),\{F,0\},\{1,\{F,0\},0\},\delta}\left(t_1\right) \tag{118}$$

$$= \left(i\hbar\right)^2 \sum_{mn} w_{nimj}\left(t_1\right)\Bigg($$

$$\int_{t_0}^{t_1} dt_3 \sum_{pq} G_{mp}^{(0),>}\left(t_1,t_3\right) \sum_{rs} w_{psqr}\left(t_3\right) G_{rs}^{(0),<}\left(t_3,t_3\right) G_{qn}^{(0),<}\left(t_3,t_1\right)$$

$$+ \int_{t_1}^{t_0} dt_3 \sum_{pq} G_{mp}^{(0),<}\left(t_1,t_3\right) \sum_{rs} w_{psqr}\left(t_3\right) G_{rs}^{(0),<}\left(t_3,t_3\right) G_{qn}^{(0),>}\left(t_3,t_1\right)\Bigg).$$

2.2. Diagonal basis

For $w_{ijkl} = \delta_{il}\delta_{jk}w_{ij}$, the non-selfconsistent selfenergy terms attain the form, cf. Eqs. (189) and (191) of the main text,

$$\Sigma_{ij}^{(2),(2),2,0,0,\text{diagonal}}\left(z_1,z_2\right) \tag{119}$$

$$\equiv \Sigma_{ij}^{(2),2,0,\text{diagonal}}\left(z_1,z_2\right)\left(G \to G^{(0)}\right)$$

and

$$\Sigma_{ij}^{(2),(2),1,0,1,\text{diagonal}}\left(z_1,z_2\right) \tag{120}$$

$$\equiv \Sigma_{ij}^{(2),1,1,\text{diagonal}}\left(z_1,z_2\right)\left(G \to G^{(0)}\right),$$

as well as

$$\Sigma_{ij}^{(2),\{H,0\},\{1,\{H,0\},0\},\text{diagonal}}\left(z_1, z_2\right) \tag{121}$$

$$= \left(i\hbar\right)^2 \delta_{\mathcal{C}}\left(z_1, z_2\right) \delta_{ij} \sum_m w_{mi}\left(z_1\right)$$

$$\int_{\mathcal{C}} dz_3 \sum_p G_{mp}^{(0)}\left(z_1, z_3\right) G_{pm}^{(0)}\left(z_3, z_{1+}\right) \sum_r w_{rp}\left(z_3\right) G_{rr}^{(0)}\left(z_3, z_{3+}\right)$$

and

$$\Sigma_{ij}^{(2),\{H,0\},\{1,\{F,0\},0\},\text{diagonal}}\left(z_1, z_2\right) \tag{122}$$

$$= \pm \left(i\hbar\right)^2 \delta_{\mathcal{C}}\left(z_1, z_2\right) \delta_{ij} \sum_m w_{mi}\left(z_1\right)$$

$$\int_{\mathcal{C}} dz_3 \sum_p G_{mp}^{(0)}\left(z_1, z_3\right) \sum_q w_{pq}\left(z_3\right) G_{pq}^{(0)}\left(z_3, z_{3+}\right) G_{qm}^{(0)}\left(z_3, z_{1+}\right).$$

Further,

$$\Sigma_{ij}^{(2),\{F,0\},\{1,\{H,0\},0\},\text{diagonal}}\left(z_1, z_2\right) \tag{123}$$

$$= \pm \left(i\hbar\right)^2 \delta_{\mathcal{C}}\left(z_1, z_2\right) w_{ij}\left(z_1\right)$$

$$\int_{\mathcal{C}} dz_3 \sum_p G_{ip}^{(0)}\left(z_1, z_3\right) \sum_r w_{rp}\left(z_3\right) G_{rr}^{(0)}\left(z_3, z_{3+}\right) G_{pj}^{(0)}\left(z_3, z_{1+}\right)$$

and

$$\Sigma_{ij}^{(2),\{F,0\},\{1,\{F,0\},0\},\text{diagonal}}\left(z_1, z_2\right) \tag{124}$$

$$= \left(i\hbar\right)^2 \delta_{\mathcal{C}}\left(z_1, z_2\right) w_{ij}\left(z_1\right)$$

$$\int_{\mathcal{C}} dz_3 \sum_p G_{ip}^{(0)}\left(z_1, z_3\right) \sum_q w_{pq}\left(z_3\right) G_{pq}^{(0)}\left(z_3, z_{3+}\right) G_{qj}^{(0)}\left(z_3, z_{1+}\right).$$

The components read [cf. Eqs. (191) and (192) of the main text]

$$\Sigma_{ij}^{(2),(2),2,0,0,\text{diagonal},\gtrless}\left(t_1, t_2\right) \equiv \Sigma_{ij}^{(2),2,0,\text{diagonal},\gtrless}\left(t_1, t_2\right)\left(G \to G^{(0)}\right), \tag{125}$$

$$\Sigma_{ij}^{(2),(2),1,0,1,\text{diagonal},\gtrless}\left(t_1, t_2\right) \equiv \Sigma_{ij}^{(2),1,1,\text{diagonal},\gtrless}\left(t_1, t_2\right)\left(G \to G^{(0)}\right), \tag{126}$$

as well as [cf. Eq. (115) to Eq. (119)]

$$\Sigma_{ij}^{(2),\{H,0\},\{1,\{H,0\},0\},\text{diagonal},\delta}\left(t_1\right) \tag{127}$$

$$= \left(i\hbar\right)^2 \delta_{ij} \sum_m w_{mi}\left(t_1\right)\Bigg($$

$$\int_{t_0}^{t_1} dt_3 \sum_p G_{mp}^{(0),>}\left(t_1, t_3\right) \sum_r w_{rp}\left(t_3\right) G_{rr}^{(0),<}\left(t_3, t_3\right) G_{pm}^{(0),<}\left(t_3, t_1\right)$$

$$+ \int_{t_1}^{t_0} dt_3 \sum_p G_{mp}^{(0),<}\left(t_1, t_3\right) \sum_r w_{rp}\left(t_3\right) G_{rr}^{(0),<}\left(t_3, t_3\right) G_{pm}^{(0),>}\left(t_3, t_1\right)\Bigg)$$

and

$$\Sigma_{ij}^{(2),\{H,0\},\{1,\{F,0\},0\},\delta}\left(t_1\right) \tag{128}$$

$$= \pm\left(i\hbar\right)^2 \delta_{ij} \sum_m w_{mi}\left(t_1\right)\Bigg(

\int_{t_0}^{t_1} dt_3\, G_{mr}^{(0),>}\left(t_1,t_3\right) \sum_{rs} w_{rs}\left(t_3\right) G_{rs}^{(0),<}\left(t_3,t_3\right) G_{sm}^{(0),<}\left(t_3,t_1\right)$$

$$+ \int_{t_1}^{t_0} dt_3\, G_{mr}^{(0),<}\left(t_1,t_3\right) \sum_{rs} w_{rs}\left(t_3\right) G_{rs}^{(0),<}\left(t_3,t_3\right) G_{sm}^{(0),>}\left(t_3,t_1\right)\Bigg).$$

Further,

$$\Sigma_{ij}^{(2),\{F,0\},\{1,\{H,0\},0\},\text{diagonal},\delta}\left(t_1,t_2\right) \tag{129}$$

$$= \pm\left(i\hbar\right)^2 w_{ji}\left(t_1\right)\Bigg(

\int_{t_0}^{t_1} dt_3 \sum_p G_{ip}^{(0),>}\left(t_1,t_3\right) \sum_{rs} w_{rp}\left(t_3\right) G_{rr}^{(0),<}\left(t_3,t_3\right) G_{pj}^{(0),<}\left(t_3,t_1\right)$$

$$+ \int_{t_1}^{t_0} dt_3 \sum_p G_{ip}^{(0),<}\left(t_1,t_3\right) \sum_{rs} w_{rp}\left(t_3\right) G_{rr}^{(0),<}\left(t_3,t_3\right) G_{pj}^{(0),>}\left(t_3,t_1\right)\Bigg)$$

and

$$\Sigma_{ij}^{(2),\{F,0\},\{1,\{F,0\},0\},\delta}\left(t_1\right) \tag{130}$$

$$= \left(i\hbar\right)^2 \sum_n w_{ji}\left(t_1\right)\Bigg(

\int_{t_0}^{t_1} dt_3\, G_{ir}^{(0),<}\left(t_1,t_3\right) \sum_{rs} w_{rs}\left(t_3\right) G_{rs}^{(0),<}\left(t_3,t_3\right) G_{sj}^{(0),>}\left(t_3,t_1\right)$$

$$+ \int_{t_1}^{t_0} dt_3\, G_{ir}^{(0),>}\left(t_1,t_3\right) \sum_{rs} w_{rs}\left(t_3\right) G_{rs}^{(0),<}\left(t_3,t_3\right) G_{sj}^{(0),<}\left(t_3,t_1\right)\Bigg).$$

2.3. Hubbard basis

In the Hubbard basis, the non-selfconsistent contributions attain the form

$$\Sigma_{i\alpha j\alpha}^{(2),(2),2,0,0,\text{Hubbard},\flat}\left(z_1,z_2\right) \tag{131}$$

$$\equiv \Sigma_{i\alpha j\alpha}^{(2),2,0,\text{Hubbard},\flat}\left(z_1,z_2\right)\left(G \to G^{(0)}\right)$$

and

$$\Sigma_{i\alpha j\alpha}^{(2),(2),1,0,1,\text{Hubbard},\flat}\left(z_1,z_2\right) \tag{132}$$

$$\equiv \Sigma_{i\alpha j\alpha}^{(2),1,1,\text{Hubbard},\flat}\left(z_1,z_2\right)\left(G \to G^{(0)}\right),$$

as well as

$$\Sigma_{i\alpha j\alpha}^{(2),\{H,0\},\{1,\{H,0\},0\},\text{Hubbard},\mathfrak{b}}\left(z_1, z_2\right) \tag{133}$$

$$= \left(\mathrm{i}\hbar\right)^2 \delta_{\mathcal{C}}\left(z_1, z_2\right)\delta_{ij}\sum_{\epsilon} U\left(z_1\right)$$

$$\int_{\mathcal{C}} \mathrm{d}z_3 \sum_p G_{i\epsilon p\epsilon}^{(0)}\left(z_1, z_3\right)G_{p\epsilon i\epsilon}^{(0)}\left(z_3, z_{1+}\right)\sum_{\zeta} U\left(z_3\right)G_{p\zeta p\zeta}^{(0)}\left(z_3, z_{3+}\right)$$

and

$$\Sigma_{i\alpha j\alpha}^{(2),\{H,0\},\{1,\{F,0\},0\},\text{Hubbard},\mathfrak{b}}\left(z_1, z_2\right) \tag{134}$$

$$= \left(\mathrm{i}\hbar\right)^2 \delta_{\mathcal{C}}\left(z_1, z_2\right)\delta_{ij}\sum_{\epsilon} U\left(z_1\right)$$

$$\int_{\mathcal{C}} \mathrm{d}z_3 \sum_p G_{i\epsilon p\epsilon}^{(0)}\left(z_1, z_3\right)U\left(z_3\right)G_{p\epsilon p\epsilon}^{(0)}\left(z_3, z_{3+}\right)G_{p\epsilon i\epsilon}^{(0)}\left(z_3, z_{1+}\right).$$

Further,

$$\Sigma_{i\alpha j\alpha}^{(2),\{F,0\},\{1,\{H,0\},0\},\text{Hubbard},\mathfrak{b}}\left(z_1, z_2\right) \tag{135}$$

$$= \left(\mathrm{i}\hbar\right)^2 \delta_{\mathcal{C}}\left(z_1, z_2\right)\delta_{ij}U\left(z_1\right)$$

$$\int_{\mathcal{C}} \mathrm{d}z_3 \sum_p G_{i\alpha p\alpha}^{(0)}\left(z_1, z_3\right)U\left(z_3\right)\sum_{\epsilon} G_{p\epsilon p\epsilon}^{(0)}\left(z_3, z_{3+}\right)G_{p\alpha i\alpha}^{(0)}\left(z_3, z_{1+}\right)$$

and

$$\Sigma_{i\alpha j\alpha}^{(2),\{F,0\},\{1,\{F,0\},0\},\text{Hubbard},\mathfrak{b}}\left(z_1, z_2\right) \tag{136}$$

$$= \left(\mathrm{i}\hbar\right)^2 \delta_{\mathcal{C}}\left(z_1, z_2\right)\delta_{ij}U\left(z_1\right)$$

$$\int_{\mathcal{C}} \mathrm{d}z_3 \sum_p G_{i\alpha p\alpha}^{(0)}\left(z_1, z_3\right)U\left(z_1\right)G_{p\alpha p\alpha}^{(0)}\left(z_1, z_{1+}\right)G_{p\alpha i\alpha}^{(0)}\left(z_3, z_{1+}\right),$$

for bosons, and

$$\Sigma_{i\alpha j\alpha}^{(2),(2),2,0,0,\text{Hubbard},\mathfrak{f}}\left(z_1, z_2\right) \tag{137}$$

$$\equiv \Sigma_{i\alpha j\alpha}^{(2),2,0,\text{Hubbard},\mathfrak{f}}\left(z_1, z_2\right)\left(G \rightarrow G^{(0)}\right)$$

and

$$\Sigma_{i\alpha j\alpha}^{(2),(2),1,0,1,\text{Hubbard},\mathfrak{f}}\left(z_1, z_2\right) \tag{138}$$

$$\equiv \Sigma_{i\alpha j\alpha}^{(2),1,1,\text{Hubbard},\mathfrak{f}}\left(z_1, z_2\right)\left(G \rightarrow G^{(0)}\right),$$

as well as

$$\Sigma_{i\alpha j\alpha}^{(2),\{H,0\},\{1,\{H,0\},0\},\text{Hubbard},\mathfrak{f}}\left(z_1, z_2\right) \tag{139}$$

$$= \left(i\hbar\right)^2 \delta_{\mathcal{C}}\left(z_1, z_2\right)\delta_{ij}\sum_{\epsilon\neq\alpha} U\left(z_1\right)$$

$$\int_{\mathcal{C}} dz_3 \sum_p G_{i\epsilon p\epsilon}^{(0)}\left(z_1, z_3\right) G_{p\epsilon i\epsilon}^{(0)}\left(z_3, z_{1^+}\right)\sum_{\zeta\neq\epsilon} U\left(z_3\right) G_{p\zeta p\zeta}^{(0)}\left(z_3, z_{3^+}\right),$$

$$\Sigma_{i\alpha j\alpha}^{(2),\{H,0\},\{1,\{F,0\},0\},\text{Hubbard},\mathfrak{f}}\left(z_1, z_2\right) \equiv 0 \tag{140}$$

and

$$\Sigma_{i\alpha j\alpha}^{(2),\{F,0\},\{1,\{H,0\},0\},\text{Hubbard},\mathfrak{f}}\left(z_1, z_2\right) \equiv 0\,, \tag{141}$$

$$\Sigma_{i\alpha j\alpha}^{(2),\{F,0\},\{1,\{F,0\},0\},\text{Hubbard},\mathfrak{f}}\left(z_1, z_2\right) \equiv 0\,, \tag{142}$$

for fermions. The components read

$$\Sigma_{i\alpha j\alpha}^{(2),(2),2,0,0,\text{Hubbard},\mathfrak{b},\gtrless}\left(t_1, t_2\right) \tag{143}$$

$$\equiv \Sigma_{i\alpha j\alpha}^{(2),2,0,\text{Hubbard},\mathfrak{b},\gtrless}\left(t_1, t_2\right)\left(G \to G^{(0)}\right),$$

$$\Sigma_{i\alpha j\alpha}^{(2),(2),1,0,1,\text{Hubbard},\mathfrak{b},\gtrless}\left(t_1, t_2\right) \tag{144}$$

$$\equiv \Sigma_{i\alpha j\alpha}^{(2),1,1,\text{Hubbard},\mathfrak{b},\gtrless}\left(t_1, t_2\right)\left(G \to G^{(0)}\right),$$

$$\Sigma_{i\alpha j\alpha}^{(2),(2),2,0,0,\text{Hubbard},\mathfrak{f},\gtrless}\left(t_1, t_2\right) \tag{145}$$

$$\equiv \Sigma_{i\alpha j\alpha}^{(2),2,0,\text{Hubbard},\mathfrak{f},\gtrless}\left(t_1, t_2\right)\left(G \to G^{(0)}\right),$$

$$\Sigma_{i\alpha j\alpha}^{(2),(2),1,0,1,\text{Hubbard},\mathfrak{f},\gtrless}\left(t_1, t_2\right) \tag{146}$$

$$\equiv \Sigma_{i\alpha j\alpha}^{(2),1,1,\text{Hubbard},\mathfrak{f},\gtrless}\left(t_1, t_2\right)\left(G \to G^{(0)}\right),$$

as well as

$$\Sigma_{i\alpha j\alpha}^{(2),\{H,0\},\{1,\{H,0\},0\},\text{Hubbard},\mathfrak{b},\delta}\left(t_1, t_2\right) \tag{147}$$

$$= \left(i\hbar\right)^2 \delta_{ij}\sum_{\epsilon} U\left(t_1\right)\bigg($$

$$\int_{t_0}^{t_1} dt_3 \sum_p G_{i\epsilon p\epsilon}^{(0),>}\left(t_1, t_3\right) G_{p\epsilon i\epsilon}^{(0),<}\left(t_3, t_1\right)\sum_{\zeta} U\left(t_3\right) G_{p\zeta p\zeta}^{(0),<}\left(t_3, t_3\right)$$

$$+ \int_{t_1}^{t_0} dt_3 \sum_p G_{i\epsilon p\epsilon}^{(0),<}\left(t_1, t_3\right) G_{p\epsilon i\epsilon}^{(0),>}\left(t_3, t_1\right)\sum_{\zeta} U\left(t_3\right) G_{p\zeta p\zeta}^{(0),<}\left(t_3, t_3\right)\bigg)$$

and

$$
\Sigma_{i\alpha j\alpha}^{(2),\{H,0\},\{1,\{F,0\},0\},\text{Hubbard},\flat,\delta}\left(t_1,t_2\right) \tag{148}
$$

$$
= \left(\mathrm{i}\hbar\right)^2 \delta_{ij} \sum_{\epsilon} U\left(t_1\right) \Bigg(
$$

$$
\int_{t_0}^{t_1} \mathrm{d}t_3 \sum_{p} G_{i\epsilon p\epsilon}^{(0),>}\left(t_1,t_3\right) U\left(t_3\right) G_{p\epsilon p\epsilon}^{(0),<}\left(t_3,t_3\right) G_{p\epsilon i\alpha}^{(0),<}\left(t_3,t_1\right)
$$

$$
+ \int_{t_1}^{t_0} \mathrm{d}t_3 \sum_{p} G_{i\epsilon p\epsilon}^{(0),<}\left(t_1,t_3\right) U\left(t_3\right) G_{p\epsilon p\epsilon}^{(0),<}\left(t_3,t_3\right) G_{p\epsilon i\epsilon}^{(0),>}\left(t_3,t_1\right) \Bigg).
$$

Further,

$$
\Sigma_{i\alpha j\alpha}^{(2),\{F,0\},\{1,\{H,0\},0\},\text{Hubbard},\flat,\delta}\left(t_1,t_2\right) \tag{149}
$$

$$
= \left(\mathrm{i}\hbar\right)^2 \delta_{ij} U\left(z_1\right) \Bigg(
$$

$$
\int_{t_0}^{t_1} \mathrm{d}t_3 \sum_{p} G_{i\alpha p\alpha}^{(0),>}\left(t_1,t_3\right) U\left(t_3\right) \sum_{\epsilon} G_{p\epsilon p\epsilon}^{(0),<}\left(t_3,t_3\right) G_{p\alpha i\alpha}^{(0),<}\left(t_3,t_1\right)
$$

$$
+ \int_{t_1}^{t_0} \mathrm{d}t_3 \sum_{p} G_{i\alpha p\alpha}^{(0),<}\left(t_1,t_3\right) U\left(t_3\right) \sum_{\epsilon} G_{p\epsilon p\epsilon}^{(0),<}\left(t_3,t_3\right) G_{p\alpha i\alpha}^{(0),>}\left(t_3,t_1\right) \Bigg)
$$

and

$$
\Sigma_{i\alpha j\alpha}^{(2),\{F,0\},\{1,\{F,0\},0\},\text{Hubbard},\flat,\delta}\left(t_1,t_2\right) \tag{150}
$$

$$
= \left(\mathrm{i}\hbar\right)^2 \delta_{ij} U\left(t_1\right) \Bigg(
$$

$$
\int_{t_0}^{t_1} \mathrm{d}t_3 \sum_{p} G_{i\alpha p\alpha}^{(0),>}\left(t_1,t_3\right) U\left(t_3\right) G_{p\alpha p\alpha}^{(0),<}\left(t_3,t_3\right) G_{p\alpha i\alpha}^{(0),<}\left(t_3,t_1\right)
$$

$$
+ \int_{t_1}^{t_0} \mathrm{d}t_3 \sum_{p} G_{i\alpha p\alpha}^{(0),<}\left(t_1,t_3\right) U\left(t_3\right) G_{p\alpha p\alpha}^{(0),<}\left(t_3,t_3\right) G_{p\alpha i\alpha}^{(0),>}\left(t_3,t_1\right) \Bigg)
$$

and

$$
\Sigma_{i\alpha j\alpha}^{(2),\{H,0\},\{1,\{H,0\},0\},\text{Hubbard},\mathfrak{f},\delta}\left(t_1,t_2\right) \tag{151}
$$

$$
= \left(\mathrm{i}\hbar\right)^2 \delta_{ij} \sum_{\epsilon\neq\alpha} U\left(t_1\right) \Bigg(
$$

$$
\int_{t_0}^{t_1} \mathrm{d}t_3 \sum_{p} G_{i\epsilon p\epsilon}^{(0),>}\left(t_1,t_3\right) G_{p\epsilon i\epsilon}^{(0),<}\left(t_3,t_1\right) \sum_{\zeta\neq\epsilon} U\left(t_3\right) G_{p\zeta p\zeta}^{(0),<}\left(t_3,t_3\right)
$$

$$
+ \int_{t_1}^{t_0} \mathrm{d}t_3 \sum_{p} G_{i\epsilon p\epsilon}^{(0),<}\left(t_1,t_3\right) G_{p\epsilon i\epsilon}^{(0),>}\left(t_3,t_1\right) \sum_{\zeta\neq\epsilon} U\left(t_3\right) G_{p\zeta p\zeta}^{(0),<}\left(t_3,t_3\right) \Bigg).
$$

2.4. Spin-0 bosons/spin-1/2 fermions

For the specific bosonic and fermionic cases, one has

$$
\Sigma_{ij}^{(2),(2),2,0,0,\text{Hubbard},\flat,0}\left(z_1, z_2\right) \tag{152}
$$
$$
\equiv \Sigma_{ij}^{(2),2,0,\text{Hubbard},\flat,0}\left(z_1, z_2\right)\left(G \to G^{(0)}\right)
$$

and

$$
\Sigma_{ij}^{(2),(2),1,0,1,\text{Hubbard},\flat,0}\left(z_1, z_2\right) \tag{153}
$$
$$
\equiv \Sigma_{ij}^{(2),1,1,\text{Hubbard},\flat,0}\left(z_1, z_2\right)\left(G \to G^{(0)}\right),
$$

as well as

$$
\Sigma_{ij}^{(2),\{\text{H},0\},\{1,\{\text{H},0\},0\},\text{Hubbard},\flat,0}\left(z_1, z_2\right) \tag{154}
$$
$$
= \Sigma_{ij}^{(2),\{\text{H},0\},\{1,\{\text{F},0\},0\},\text{Hubbard},\flat,0}\left(z_1, z_2\right)
$$
$$
= \Sigma_{ij}^{(2),\{\text{F},0\},\{1,\{\text{H},0\},0\},\text{Hubbard},\flat,0}\left(z_1, z_2\right)
$$
$$
= \Sigma_{ij}^{(2),\{\text{F},0\},\{1,\{\text{F},0\},0\},\text{Hubbard},\flat,0}\left(z_1, z_2\right)
$$
$$
= \left(\mathrm{i}\hbar\right)^2 \delta_{\mathcal{C}}\left(z_1, z_2\right)\delta_{ij}U\left(z_1\right)
$$
$$
\int_{\mathcal{C}} \mathrm{d}z_3 \sum_p G_{ip}^{(0)}\left(z_1, z_3\right)G_{pi}^{(0)}\left(z_3, z_{1+}\right)U\left(z_3\right)G_{pp}^{(0)}\left(z_3, z_{3+}\right),
$$

for spin-0 bosons, and

$$
\Sigma_{i\alpha j\alpha}^{(2),(2),2,0,0,\text{Hubbard},\mathfrak{f},1/2}\left(z_1, z_2\right) \tag{155}
$$
$$
\equiv \Sigma_{i\alpha j\alpha}^{(2),2,0,\text{Hubbard},\mathfrak{f},1/2}\left(z_1, z_2\right)\left(G \to G^{(0)}\right)
$$

and

$$
\Sigma_{i\alpha j\alpha}^{(2),(2),1,0,1,\text{Hubbard},\mathfrak{f},1/2}\left(z_1, z_2\right) \tag{156}
$$
$$
\equiv \Sigma_{i\alpha j\alpha}^{(2),1,1,\text{Hubbard},\mathfrak{f},1/2}\left(z_1, z_2\right)\left(G \to G^{(0)}\right),
$$

as well as

$$
\Sigma_{i\uparrow j\uparrow}^{(2),\{\text{H},0\},\{1,\{\text{H},0\},0\},\text{Hubbard},\mathfrak{f},1/2}\left(z_1, z_2\right) \tag{157}
$$
$$
= \left(\mathrm{i}\hbar\right)^2 \delta_{\mathcal{C}}\left(z_1, z_2\right)\delta_{ij}U\left(z_1\right)
$$
$$
\int_{\mathcal{C}} \mathrm{d}z_3 \sum_p G_{i\downarrow p\downarrow}^{(0)}\left(z_1, z_3\right)G_{p\downarrow i\downarrow}^{(0)}\left(z_3, z_{1+}\right)U\left(z_3\right)G_{p\uparrow p\uparrow}^{(0)}\left(z_3, z_{3+}\right)
$$

and

$$\Sigma_{i\downarrow j\downarrow}^{(2),\{H,0\},\{1,\{H,0\},0\},\mathrm{Hubbard},\mathfrak{f},1/2}\left(z_1,z_2\right) \tag{158}$$

$$= \left(\mathrm{i}\hbar\right)^2 \delta_{\mathcal{C}}\left(z_1,z_2\right)\delta_{ij}U\left(z_1\right)$$

$$\int_{\mathcal{C}}\mathrm{d}z_3 \sum_p G_{i\uparrow p\uparrow}^{(0)}\left(z_1,z_3\right)G_{p\uparrow i\uparrow}^{(0)}\left(z_3,z_{1+}\right)U\left(z_3\right)G_{p\downarrow p\downarrow}^{(0)}\left(z_3,z_{3+}\right),$$

for spin-1/2 fermions. The corresponding components read

$$\Sigma_{ij}^{(2),(2),2,0,0,\mathrm{Hubbard},\mathfrak{b},0,\gtrless}\left(t_1,t_2\right) \tag{159}$$

$$\equiv \Sigma_{ij}^{(2),2,0,\mathrm{Hubbard},\mathfrak{b},0,\gtrless}\left(t_1,t_2\right)\left(G \to G^{(0)}\right),$$

$$\Sigma_{ij}^{(2),(2),1,0,1,\mathrm{Hubbard},\mathfrak{b},0,\gtrless}\left(t_1,t_2\right) \tag{160}$$

$$\equiv \Sigma_{ij}^{(2),1,1,\mathrm{Hubbard},\mathfrak{b},0,\gtrless}\left(t_1,t_2\right)\left(G \to G^{(0)}\right),$$

$$\Sigma_{i\alpha j\alpha}^{(2),(2),2,0,0,\mathrm{Hubbard},\mathfrak{f},1/2,\gtrless}\left(t_1,t_2\right) \tag{161}$$

$$\equiv \Sigma_{i\alpha j\alpha}^{(2),2,0,\mathrm{Hubbard},\mathfrak{f},1/2,\gtrless}\left(t_1,t_2\right)\left(G \to G^{(0)}\right),$$

$$\Sigma_{i\alpha j\alpha}^{(2),(2),1,0,1,\mathrm{Hubbard},\mathfrak{f},1/2,\gtrless}\left(t_1,t_2\right) \tag{162}$$

$$\equiv \Sigma_{i\alpha j\alpha}^{(2),1,1,\mathrm{Hubbard},\mathfrak{f},1/2,\gtrless}\left(t_1,t_2\right)\left(G \to G^{(0)}\right),$$

as well as

$$\Sigma_{ij}^{(2),\{H,0\},\{1,\{H,0\},0\},\mathrm{Hubbard},\mathfrak{b},0,\delta}\left(t_1,t_2\right) \tag{163}$$

$$= \Sigma_{ij}^{(2),\{H,0\},\{1,\{F,0\},0\},\mathrm{Hubbard},\mathfrak{b},0,\delta}\left(t_1,t_2\right)$$

$$= \Sigma_{ij}^{(2),\{F,0\},\{1,\{H,0\},0\},\mathrm{Hubbard},\mathfrak{b},0,\delta}\left(t_1,t_2\right)$$

$$= \Sigma_{ij}^{(2),\{F,0\},\{1,\{F,0\},0\},\mathrm{Hubbard},\mathfrak{b},0,\delta}\left(t_1,t_2\right)$$

$$= \left(\mathrm{i}\hbar\right)^2 \delta_{ij}U\left(t_1\right)\Bigg($$

$$\int_{t_0}^{t_1}\mathrm{d}t_3 \sum_p G_{ip}^{(0),>}\left(t_1,t_3\right)G_{pi}^{(0),<}\left(t_3,t_1\right)U\left(t_3\right)G_{pp}^{(0),<}\left(t_3,t_3\right)$$

$$+\int_{t_1}^{t_0}\mathrm{d}t_3 \sum_p G_{ip}^{(0),<}\left(t_1,t_3\right)G_{pi}^{(0),>}\left(t_3,t_1\right)U\left(t_3\right)G_{pp}^{(0),<}\left(t_3,t_3\right)\Bigg),$$

for spin-0 bosons, and

$$\Sigma_{i\uparrow j\uparrow}^{(2),\{H,0\},\{1,\{H,0\},0\},\text{Hubbard},\mathfrak{f},1/2,\delta}\left(t_1,t_2\right) \tag{164}$$

$$= \left(i\hbar\right)^2 \delta_{ij} U\left(t_1\right)\Bigg($$

$$\int_{t_0}^{t_1} dt_3 \sum_p G_{i\downarrow p\downarrow}^{(0),>}\left(t_1,t_3\right) G_{p\downarrow i\downarrow}^{(0),<}\left(t_3,t_1\right) U\left(t_3\right) G_{p\uparrow p\uparrow}^{(0),<}\left(t_3,t_3\right)$$

$$+ \int_{t_1}^{t_0} dt_3 \sum_p G_{i\downarrow p\downarrow}^{(0),<}\left(t_1,t_3\right) G_{p\downarrow i\downarrow}^{(0),>}\left(t_3,t_1\right) U\left(t_3\right) G_{p\uparrow p\uparrow}^{(0),<}\left(t_3,t_3\right)\Bigg),$$

as well as

$$\Sigma_{i\downarrow j\downarrow}^{(2),\{H,0\},\{1,\{H,0\},0\},\text{Hubbard},\mathfrak{f},1/2,\delta}\left(t_1,t_2\right) \tag{165}$$

$$= \left(i\hbar\right)^2 \delta_{ij} U\left(t_1\right)\Bigg($$

$$\int_{t_0}^{t_1} dt_3 \sum_p G_{i\uparrow p\uparrow}^{(0),>}\left(t_1,t_3\right) G_{p\uparrow i\uparrow}^{(0),<}\left(t_3,t_1\right) U\left(t_3\right) G_{p\downarrow p\downarrow}^{(0),<}\left(t_3,t_3\right)$$

$$+ \int_{t_1}^{t_0} dt_3 \sum_p G_{i\uparrow p\uparrow}^{(0),<}\left(t_1,t_3\right) G_{p\uparrow i\uparrow}^{(0),>}\left(t_3,t_1\right) U\left(t_3\right) G_{p\downarrow p\downarrow}^{(0),<}\left(t_3,t_3\right)\Bigg),$$

for spin-1/2 fermions.

2.1.3 Representations of the Interaction Tensor

Despite of all care and diligence, there are occasionally ambiguous definitions circulating within the NEGF community and, to some degree, also in the publications of this thesis. This section is used to clarify such ambiguities regarding the pair-interaction tensor.

2.1.3.1 The General Single-Particle Basis

As the alert reader certainly noticed, Refs. [122] and [79] make use of different formulations of the general second-quantization Hamiltonian. Given the canonical creation $\left(\hat{c}_i^\dagger\right)$ and annihilation $\left(\hat{c}_i\right)$ operators (in a general, orthonormal single-particle basis), which obey the following (anti-)commutation relations,[3]

$$\left[\hat{c}_i^\dagger, \hat{c}_j^\dagger\right]_\mp = 0\,, \quad \left[\hat{c}_i, \hat{c}_j\right]_\mp = 0\,, \quad \left[\hat{c}_i, \hat{c}_j^\dagger\right]_\mp = \delta_{ij}\,, \tag{2.1}$$

the Hamiltonian (time dependence and single-particle excitations are neglected)

$$\hat{H} = \sum_{ij} h_{ij}\hat{c}_i^\dagger\hat{c}_j + \frac{1}{2}\sum_{ijkl} w_{ijkl}\hat{c}_i^\dagger\hat{c}_j^\dagger\hat{c}_l\hat{c}_k\,, \tag{2.2}$$

is used in Eqs. (23)–(24) of Ref. [122] to describe a system of interacting identical particles. Here, h_{ij} is the ideal single-particle Hamiltonian and w_{ijkl} is the matrix element of the two-particle interaction. In contrast, in Eq. (16) of Ref. [79] the Hamiltonian

$$\hat{H} = \sum_{ij} h_{ij}\hat{c}_i^\dagger\hat{c}_j + \frac{1}{2}\sum_{ijkl} \mathsf{w}_{ijkl}\hat{c}_i^\dagger\hat{c}_j^\dagger\hat{c}_k\hat{c}_l \tag{2.3}$$

is used (the fontstyle of the interaction matrix is altered to disambiguate the definitions). Note that the last two annihilation operators in Eq. (2.3) are interchanged, compared to Eq. (2.2). Indeed, both Hamiltonians incorporate different definitions for the interaction matrix. To demonstrate this, first, the position–spin $\mathbf{x}$ is introduced that comprises the position $\boldsymbol{r}$ and the spin σ as $|\mathbf{x}\rangle = |\boldsymbol{r}\sigma\rangle$. With the single-particle basis functions $|i\rangle = |\varphi_i\rangle$, the standard way to define the two-particle interaction tensor is given by

$$w_{ijkl} \coloneqq \int \mathrm{d}\mathbf{x}\mathrm{d}\mathbf{x}'\, \varphi_i^*(\mathbf{x})\varphi_j^*(\mathbf{x}')v(\mathbf{x}, \mathbf{x}')\varphi_k(\mathbf{x})\varphi_l(\mathbf{x}')\,, \tag{2.4}$$

which can be found in many text books (see, e.g., Refs. [219–222]) and is also used in Eq. (2.2) and Ref. [122], respectively. The most common choice of the two-body interaction potential $v(\mathbf{x}, \mathbf{x}')$ is the Coulomb potential $v_{\mathrm{C}}(\mathbf{x}, \mathbf{x}') \propto |\boldsymbol{r} - \boldsymbol{r}'|^{-1}$. For this case, Eq. (2.4) is referred to as *Coulomb integral* or *two-electron integral* if electrons are described. Recently, it has become increasingly popular within the NEGF community to use—opposed to

---

[3]Here and below, the $\mp$ sign refers to bosons/fermions.

the standard definition—the following modified two-particle interaction matrix (see, e.g., Refs. [23, 108, 223, 224]):

$$\mathsf{w}_{ijkl} := \int \mathrm{d}\mathbf{x}\mathrm{d}\mathbf{x}' \, \varphi_i^*(\mathbf{x})\varphi_j^*(\mathbf{x}')v(\mathbf{x},\mathbf{x}')\varphi_k(\mathbf{x}')\varphi_l(\mathbf{x}) = \mathsf{w}_{ijlk} \,, \tag{2.5}$$

to allow for the more intuitively structured Hamiltonian of Eq. (2.3). The interaction matrix in the general basis is a central quantity of Ref. [79]. In order to achieve the highest possible impact the definition of Eq. (2.5) has been applied to conform to the aforementioned emerging trend.[4]

It should be mentioned that, by using the (anti-)commutator property of Eq. (2.1) for the annihilation operators, the Hamiltonian of Eq. (2.2) can be transformed to

$$\hat{H} = \sum_{ij} h_{ij}\hat{c}_i^\dagger\hat{c}_j \pm \frac{1}{2}\sum_{ijkl} w_{ijkl}\hat{c}_i^\dagger\hat{c}_j^\dagger\hat{c}_k\hat{c}_l \,, \tag{2.6}$$

which, compared to Eq. (2.3), could suggest the equality between $\pm w_{ijkl}$ and w_{ijkl}. The equality holds, yet, only for the terms in the Hamiltonians and not the interaction matrix itself. It implies, however, that $\pm w_{ijkl}$ and w_{ijkl} lead to the same interaction energy, which hints towards an (anti-)symmetrized usage of the interaction matrix in the exact solution or consistent approximations.

It is an important implication of the two definitions (2.4) and (2.5), that the typical diagonal representation of the interaction matrix within the same single-particle basis is found in different ways. While the second-order tensor for w is reached via $w_{ijkl} = \delta_{ik}\delta_{jl}w_{ij}$, the differing definition of w leads to $\mathsf{w}_{ijkl} = \delta_{il}\delta_{jk}w_{ij}$. Therefore, it is of crucial importance to keep track of the respective interaction choice when handling the NEGF equations or any second-quantization framework in general.

2.1.3.2 The Fermi-Hubbard Basis

Unrelated to the discussion above, there are two common ways to define the Hubbard interaction for electronic systems. Based on the general, non-diagonal interaction matrix, both definitions can be formulated as (lattices-site positions, $ijkl$, and spin indices, $\alpha\beta\gamma\delta$,

---

[4]The above-mentioned difference between the definitions of the interaction matrix must not be confused with the difference between the "physicist's notation",

$$\langle ij|kl \rangle := \int \mathrm{d}\mathbf{x}\mathrm{d}\mathbf{x}' \, \varphi_i^*(\mathbf{x})\varphi_j^*(\mathbf{x}')v_{\mathrm{C}}(\mathbf{x},\mathbf{x}')\varphi_k(\mathbf{x})\varphi_l(\mathbf{x}') = w_{ijkl} \,,$$

and the "chemist's (or Mulliken) notation",

$$[ij|kl] := \int \mathrm{d}\mathbf{x}\mathrm{d}\mathbf{x}' \, \varphi_i^*(\mathbf{x})\varphi_j(\mathbf{x})v_{\mathrm{C}}(\mathbf{x},\mathbf{x}')\varphi_k^*(\mathbf{x}')\varphi_l(\mathbf{x}') = w_{ikjl} \,,$$

for the Coulomb integral that are widely used in quantum chemistry (see, e.g., Ref. [222]).

are explicitly specified; time dependence is omitted)[5]

$$w_{ijkl}^{\alpha\beta\gamma\delta} = U\delta_{ik}\delta_{jl}\delta_{ij}\delta_{\alpha\gamma}\delta_{\beta\delta}\mathcal{P}_{\alpha\beta}\,, \tag{2.7}$$

where U is the on-site Hubbard interaction. The two treatments differ in the question whether or not explicit Pauli blocking is applied. If so, $\mathcal{P}$ is set to $\mathcal{P}_{\alpha\beta} = 1 - \delta_{\alpha\beta}$ and accounts for the fact that no electrons of the same spin can occupy the same lattice site; if not, $\mathcal{P}$ is set to $\mathcal{P}_{\alpha\beta} = 1$. These treatments are sometimes called *spin dependent* ($\mathcal{P}_{\alpha\beta} = 1 - \delta_{\alpha\beta}$) and *spin independent* ($\mathcal{P}_{\alpha\beta} = 1$) (see, e.g., Ref. [109]). In the following, it is demonstrated that both choices for $\mathcal{P}$ lead to the same interaction part $\hat{W}$ and, thus, to the same (Fermi-)Hubbard Hamiltonian. Starting from the general form in second quantization [cf. Eq. (2.2)] and inserting the definition of Eq. (2.7) leads to:

$$
\begin{aligned}
\hat{W} &= \frac{1}{2}\sum_{\substack{ijkl\\\alpha\beta\gamma\delta}} w_{ijkl}^{\alpha\beta\gamma\delta}\hat{c}_{i,\alpha}^\dagger\hat{c}_{j,\beta}^\dagger\hat{c}_{l,\delta}\hat{c}_{k,\gamma} = \frac{1}{2}\sum_{\substack{ijkl\\\alpha\beta\gamma\delta}} \left(U\delta_{ik}\delta_{jl}\delta_{ij}\delta_{\alpha\gamma}\delta_{\beta\delta}\mathcal{P}_{\alpha\beta}\right)\hat{c}_{i,\alpha}^\dagger\hat{c}_{j,\beta}^\dagger\hat{c}_{l,\delta}\hat{c}_{k,\gamma}\\
&= \frac{1}{2}U\sum_{i,\alpha\beta}\mathcal{P}_{\alpha\beta}\hat{c}_{i,\alpha}^\dagger\hat{c}_{i,\beta}^\dagger\hat{c}_{i,\beta}\hat{c}_{i,\alpha}\,.
\end{aligned}\tag{2.8}
$$

For the case of explicit Pauli blocking ($\mathcal{P}_{\alpha\beta} = 1 - \delta_{\alpha\beta}$) Eq. (2.8) is further transformed to

$$
\begin{aligned}
\hat{W} &= \frac{1}{2}U\sum_{i,\alpha\neq\beta}\hat{c}_{i,\alpha}^\dagger\hat{c}_{i,\beta}^\dagger\hat{c}_{i,\beta}\hat{c}_{i,\alpha}\\
&= \frac{1}{2}U\sum_{i,\alpha\neq\beta}\hat{c}_{i,\alpha}^\dagger\hat{c}_{i,\alpha}\hat{c}_{i,\beta}^\dagger\hat{c}_{i,\beta} = \frac{1}{2}U\sum_{i,\alpha\neq\beta}\hat{n}_i^\alpha\hat{n}_i^\beta\,,
\end{aligned}\tag{2.9}
$$

where the anticommutation relations for the canonical operators [see Eq. (2.1)] and the occupation-number operator $\hat{n}_i^\alpha := \hat{c}_{i,\alpha}^\dagger\hat{c}_{i,\alpha}$ have been used in the last line. Inserting the explicit electronic spin $\sigma \in \{\uparrow,\downarrow\}$ leads to

$$\hat{W} = \frac{1}{2}U\sum_i\left(\hat{n}_i^\uparrow\hat{n}_i^\downarrow + \hat{n}_i^\downarrow\hat{n}_i^\uparrow\right) = U\sum_i\hat{n}_i^\uparrow\hat{n}_i^\downarrow\,, \tag{2.10}$$

which is the widely used standard form that appears in the Hubbard Hamiltonian (see, e.g., Refs. [79, 122]). Going back to Eq. (2.8), the spin-independent treatment is carried out by inserting $\mathcal{P}_{\alpha\beta} = 1$. In this case, the anticommutation relations of Eq. (2.1) lead to additional terms:

$$
\begin{aligned}
\hat{W} &= \frac{1}{2}U\sum_{i,\alpha\beta}\hat{c}_{i,\alpha}^\dagger\hat{c}_{i,\beta}^\dagger\hat{c}_{i,\beta}\hat{c}_{i,\alpha} = \frac{1}{2}U\sum_{i,\alpha\beta}\left(\hat{c}_{i,\alpha}^\dagger\hat{c}_{i,\alpha}\hat{c}_{i,\beta}^\dagger\hat{c}_{i,\beta} - \delta_{\alpha\beta}\hat{c}_{i,\alpha}^\dagger\hat{c}_{i,\beta}\right)\\
&= \frac{1}{2}U\sum_{i,\alpha\beta}\left(\hat{n}_i^\alpha\hat{n}_i^\beta - \delta_{\alpha\beta}\hat{n}_i^\alpha\right)\,.
\end{aligned}\tag{2.11}
$$

---

[5]Here, the standard interaction matrix is applied [cf. Eq. (2.4)]. For the modified definition [cf. Eq. (2.5)], the Hubbard interaction is found via

$$\mathsf{w}_{ijkl}^{\alpha\beta\gamma\delta} = U\delta_{il}\delta_{jk}\delta_{ij}\delta_{\alpha\delta}\delta_{\beta\gamma}\mathcal{P}_{\alpha\beta}\,.$$

For an electronic system one finds

$$\hat{W} = \frac{1}{2}U\sum_i \left(\hat{n}_i^{\uparrow}\hat{n}_i^{\uparrow} + \hat{n}_i^{\uparrow}\hat{n}_i^{\downarrow} + \hat{n}_i^{\downarrow}\hat{n}_i^{\uparrow} + \hat{n}_i^{\downarrow}\hat{n}_i^{\downarrow} - \hat{n}_i^{\uparrow} - \hat{n}_i^{\downarrow} \right) , \qquad (2.12)$$

which—due to the idempotence of the occupation-number operator $\left(\hat{n}_i^{\sigma}\hat{n}_i^{\sigma} = \hat{n}_i^{\sigma} \right)$—is easily transformed to

$$\hat{W} = \frac{1}{2}U\sum_i \left(\hat{n}_i^{\uparrow}\hat{n}_i^{\downarrow} + \hat{n}_i^{\downarrow}\hat{n}_i^{\uparrow} \right) = U\sum_i \hat{n}_i^{\uparrow}\hat{n}_i^{\downarrow} , \qquad (2.13)$$

again and recovers Eq. (2.10).

Having found that the Hubbard Hamiltonian is independent of the choice of $\mathcal{P}$, it is obvious that the exact solution for any Hubbard system does not depend on $\mathcal{P}$ as well. The picture is different, however, for certain many-body approximations. In NEGF theory, it has been reported, e.g., for the GW selfenergy, that both treatments lead to different results [109]. To decide whether or not an approximation is affected by $\mathcal{P}$, it is expedient to consider the (anti-)symmetrized interaction matrix in a general one-particle basis (see, e.g., Refs. [79, 122]),

$$w_{ijkl}^{\pm} := w_{ijkl} \pm w_{ijlk} , \qquad (2.14)$$

and its equivalent in the (Fermi-)Hubbard basis,

$$w_{ijkl}^{-,\alpha\beta\gamma\delta} = U\delta_{ik}\delta_{jl}\delta_{ij} \left(\delta_{\alpha\gamma}\delta_{\beta\delta}\mathcal{P}_{\alpha\beta} - \delta_{\alpha\delta}\delta_{\beta\gamma}\mathcal{P}_{\alpha\beta} \right) . \qquad (2.15)$$

For $\alpha \neq \beta$, either choice of $\mathcal{P}$ results in $\mathcal{P}_{\alpha\beta} = 1$, by construction, whereas for $\alpha = \beta$, the expression in parentheses in Eq. (2.15) vanishes in either case. Hence, the antisymmetrized interaction matrix

$$w_{ijkl}^{-,\alpha\beta\gamma\delta} = U\delta_{ik}\delta_{jl}\delta_{ij} \left(\delta_{\alpha\gamma}\delta_{\beta\delta} - \delta_{\alpha\delta}\delta_{\beta\gamma} \right) \qquad (2.16)$$

is unaffected by the choice of $\mathcal{P}$. This implies that every selfenergy approximation that can be constructed in terms of $w^{\pm}$ in a general single-particle basis remains unchanged. This is, e.g., the case for all order-truncated approximations, such as HF, SOA, and TOA, but not for the GW approximation, which confirms the result of Ref. [109].

2.1.4 Conserving Approximations and the Φ Functional

While Ref. [79] discusses many aspects of the selfenergy and covers a variety of different approximations, it is, nevertheless, instructive to place special emphasis on another characteristic of selfenergy approximations: the satisfaction of physical conservation laws. As this is a fundamental property of major importance, it is unsurprising that conserving schemes are frequently used as a starting point for derivations of many-body approximations [23, 103, 225–228]. It is a remarkable feature of the selfenergy and the single-particle Green function that the important conservation laws for density, momentum,

angular momentum, and total energy can be matched to a universal form.[6] In 1962, Baym [225] demonstrated a close connection between the conservation laws and the so-called Φ functional which is related to the works of Luttinger and Ward [229]. In the language of many-body theory, the Φ functional is constructed by using only skeletonic vacuum diagrams, i.e. scattering diagrams that are fully connected and not representable through resummation procedures of smaller units. As Φ contains the condensed scattering information encapsulated in a specific integrated connectivity structure, one is tempted to quote from Ref. [230]: "Φ (...) is a unique shape made of integrated information—a shape that is maximally irreducible—the shape of understanding".[7] The striking benefit of Φ becomes apparent in the fact that the selfenergy satisfies all above conservation laws if it fulfills a single, condensed condition—Φ derivability; the selfenergy has to be educible as the functional derivative of Φ with respect to the single-particle Green function G. While, in principle, the way to construct conserving approximation within NEGF theory is well-known, it becomes increasingly complex when higher-order approximations are addressed. For some of these approximations, particularly the TOA and the TPH, the concept of Φ derivability has, to the knowledge of the author, not been discussed in detail before. This shortcoming is rectified in Sec. 2.1.4.1 for the case of the TOA selfenergy, and in Sec. 2.1.4.2 for the TPH approximation, where also other resummation approaches are discussed. In particular, the latter case has important implications for the general applicability.

2.1.4.1 Third-Order Selfenergy

As discussed before, the great value of the graphical Feynman-diagram technique is the unique convertibility back to mathematical expressions while being intuitively accessible. To reduce complexity and increase the comprehensibility, the discussion of different Φ functionals and their respective derivatives is, thus, only given diagrammatically. There are six distinct skeletonic vacuum diagrams that are of third order in the interaction (cf., e.g., Ref. [234]), which are illustrated in Fig. 2.1 in the parentheses. The functional derivative with respect to the single-particle Green function has a one-to-one correspondence to the Feynman-diagram technique, as it corresponds to a cut through one Green-function line, leaving the corresponding (previously connected) vertices as external indices. If the initial quantity consists of multiple Green functions, the product rule results in the sum of several diagrams, each one cut at a different respective G. Fig. 2.1 shows how the third-order contributions of the Φ functional generate the ten third-order selfenergy diagrams by functional derivative. As one can see, the high symmetry of the first four Φ diagrams leads to six congruent selfenergy terms each (note the prefactors of the Φ terms). This

---

[6]The interested reader is referred to Ref. [23] which contains a comprehensible, well-written introduction to the Φ functional and its properties.

[7]Apparently, the author has used an out-of-context quote from integrated-information theory (IIT)—a research field of neuroscience—to point at the strong analogy in this context. In IIT, Φ is used as the symbol for integrated information, which is assumed to be both, foundation and manifestation of consciousness [231–233].
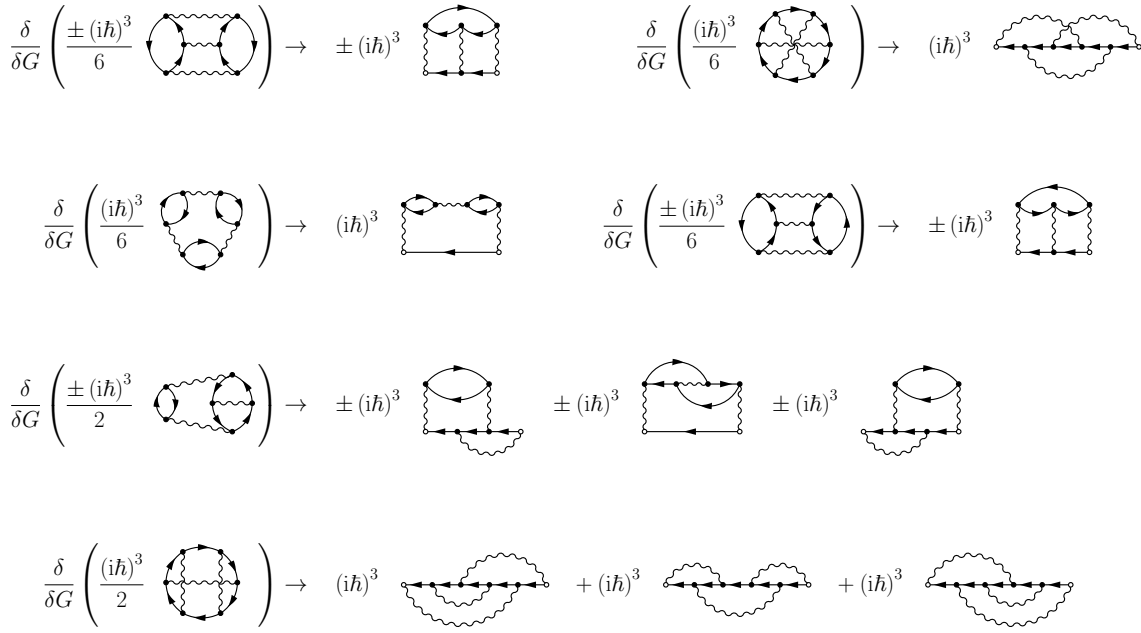
Figure 2.1 – Third-order Φ diagrams (in parentheses) and their corresponding selfenergy terms, which result from removing a single Green-function line from the Φ diagrams. Prefactors are given explicitly.

implies that every selfenergy diagram in the first two rows can be used individually in conserving approximations, as it is Φ derivable on its own. In contrast, the remaining two third-order Φ terms break into inhomogeneous parts (cf. the two bottom rows of Fig. 2.1). As a consequence, the resulting groups of three selfenergy diagrams have to be included collectively to be Φ compensated and to ensure a conserving approach. The TOA scheme, which is described in Ref. [79], consists of all ten third-order selfenergy diagrams and, therefore, is Φ compensated by construction. The partial inclusion of diagrams, however, is expected to cause conservation problems since any incomplete subset of the Φ-compensated diagram groups is not Φ derivable.

The interdependence of the selfenergy contributions can be made explicit by using an additional property, which is equivalent to Φ derivability. If the Φ functional is cut not only once but at two different G lines, this generates the two-particle kernel K, which is, thus, the functional derivative of the selfenergy [23],

$$K_{ijkl}(z_1, z_2, z_3, z_4) = \pm \frac{\Phi}{\delta G_{ki}(z_3, z_1)\delta G_{lj}(z_4, z_2)} = \pm \frac{\delta \Sigma_{ik}(z_1, z_3)}{\delta G_{lj}(z_4, z_2)}. \qquad (2.17)$$

It is a direct consequence following from the symmetry of the two-particle Green function $G^{(2)}_{ijkl}(z_1, z_2, z_3, z_4) = G^{(2)}_{jilk}(z_2, z_1, z_4, z_3)$ that the kernel has to obey [23]

$$K_{ijkl}(z_1, z_2, z_3, z_4) = K_{jilk}(z_2, z_1, z_4, z_3), \qquad (2.18)$$

which leads to the following symmetry:

$$\frac{\delta \Sigma_{ik}(z_1, z_3)}{\delta G_{lj}(z_4, z_2)} = \frac{\delta \Sigma_{jl}(z_2, z_4)}{\delta G_{ki}(z_3, z_1)}. \qquad (2.19)$$
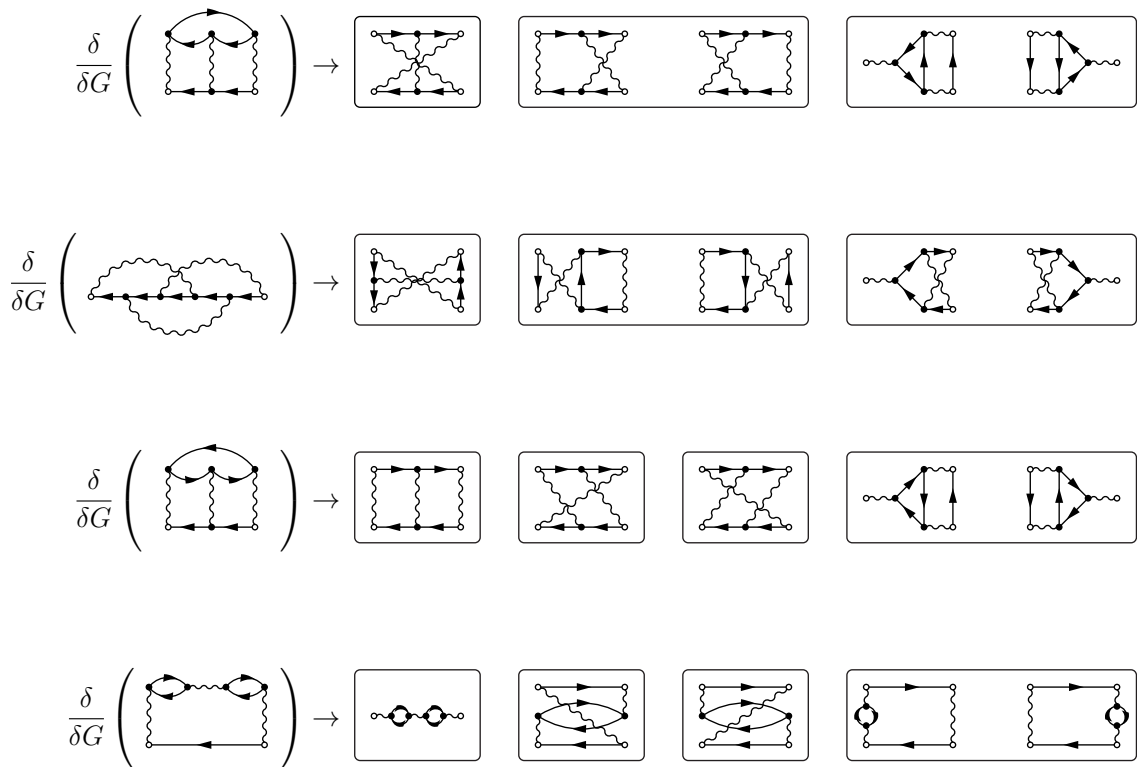
Figure 2.2 – Φ-derivable third-order selfenergy diagrams and their corresponding two-particle-kernel terms. Black frames indicate the kernel-diagram pairs that transition into each other under 180° rotation and, thus, obey Eq. (2.19). Individually framed kernel diagrams are rotational invariant on their own. Prefactors are omitted for better readability.

In the language of the Feynman-diagram technique, Eq. (2.19) has a very simple translation; if Σ is a conserving (Φ-derivable) approximation the respective kernel diagrams $\frac{\delta\Sigma}{\delta G}$ have to be invariant under rotation by an angle of 180°.

For the first four third-order selfenergy diagrams of Fig. 2.1, the corresponding kernel diagrams are illustrated in Fig. 2.2. As expected, the symmetry of Eq. (2.19) holds for each selfenergy term, separately. While the rotation by 180° leaves some kernel diagrams unchanged (individually framed), there are other ones that form symmetric pairs, in which the diagrams transition into each other (framed pairs).

The behavior is different for the Φ-compensated selfenergy diagram groups of Fig. 2.1. The two-particle-kernel diagrams that correspond to the respective third-order selfenergy group without a Green-function loop are illustrated in Fig. 2.3. Some of the kernel terms (black frame) directly obey Eq. (2.19) on their own. For all other kernel contributions the mirrored diagram pairs are distributed across multiple lines: the second line compensates contributions of the first line (red, blue), as well as the third line (yellow, pink), whereas the third line compensates terms of the first line (lightblue, green). Thus, to form a conserving approximation, all three selfenergy diagrams have to be included collectively which agrees with the previous result in the context of Φ derivability (cf. Fig. 2.1).
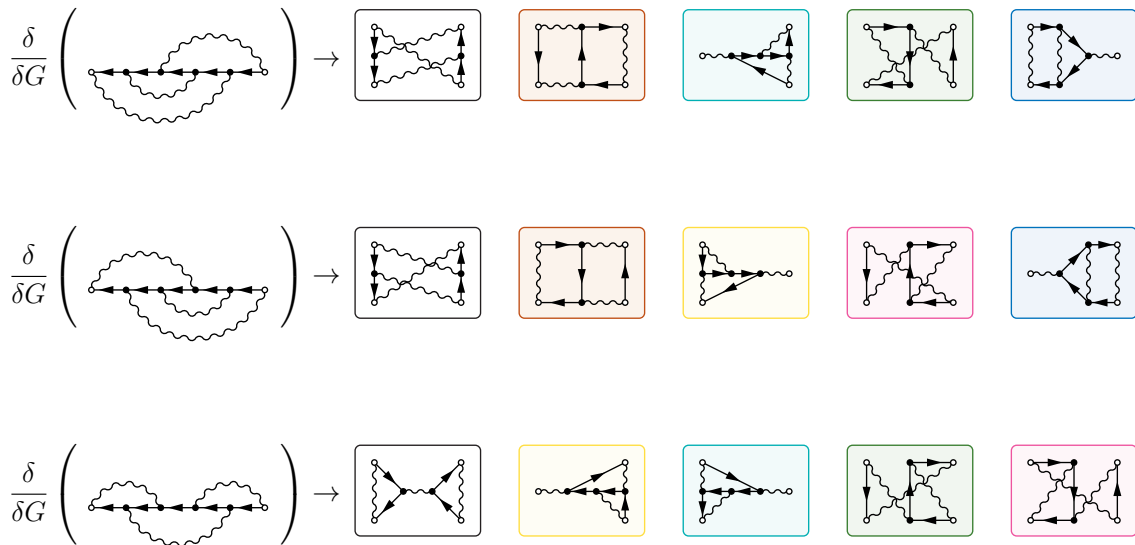
Figure 2.3 – Φ-compensated third-order selfenergy diagram group without Green-function loop, and their corresponding two-particle-kernel terms. Kernel diagrams framed in black remain unchanged under 180° rotation. Diagrams with the same color transition into each other when flipped. Prefactors are omitted for better readability.

A similar picture is found for the Φ-compensated, third-order selfenergy diagram group with one Green-function loop (cf. the third line of Fig. 2.1). The respective two-particle-kernel diagrams are shown in Fig. 2.4. Again, Eq. (2.19) is only fulfilled if all three selfenergy diagrams are combined. Here, the first line couples to the second line via the red and lightblue terms, and to the third line via the green and blue contributions. The second and third line are interconnected through the yellow and pink diagrams.

The above discussion for the third-order selfenergy diagrams points towards problems for some of the resummation approximations presented in Ref. [79], as the TOA already contains their respective third-order terms. The property of Φ derivability for these approximations is addressed in the following section.

2.1.4.2 Resummation Selfenergies and the Case of TPH

For the long-established TPP and GW approximations, the corresponding Φ functionals are well known and can be found, e.g., in Ref. [23]. The nth-order Φ diagrams for GW (first line) and the particle–particle ladder (second and third line) are repeated in Fig. 2.5 together with their respective selfenergy diagrams that follow from the functional derivative with respect to G. It is worth mentioning that the T matrix, which consists of a direct and an exchange term, leads to two separate Φ diagrams. In this case, both nth-order selfenergy diagrams of the resummation series are Φ derivable on their own. This is a consequence following from the high symmetry of the corresponding Φ diagrams that—being cut at any Green-function line—produce only a single type of selfenergy diagram.

For the TPH approximation, however, this behavior is only found for the direct
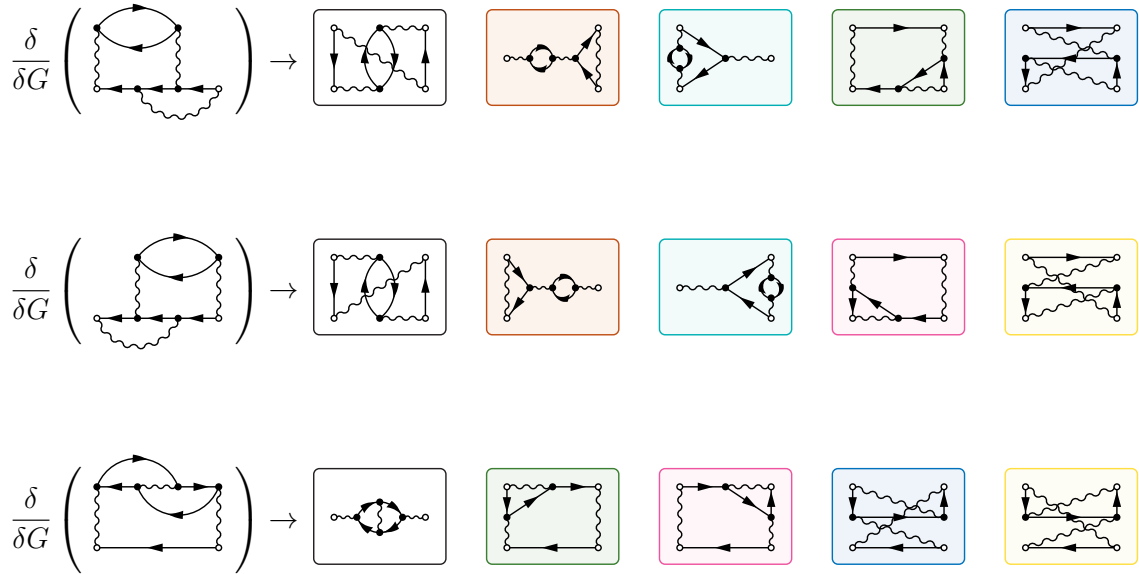
Figure 2.4 – Φ-compensated third-order selfenergy diagram group with one Green-function loop, and their corresponding two-particle-kernel terms. Kernel diagrams framed in black remain unchanged under 180° rotation. Diagrams with the same color transition into each other when flipped. Prefactors are omitted for better readability.

terms of the T matrix and their respective Φ. The nth-order Φ diagram and the resulting selfenergy contribution is presented in the fourth line of Fig. 2.5. As one can see, it differs from the direct TPP counterpart only by the direction of one Green-function loop. The exchange terms of the TPH approximation (cf. Ref. [79]) are—when considered isolated—not Φ derivable. The nth-order selfenergy diagram that corresponds to the TPH exchange series, follows, instead, from a Φ diagram that gives rise to various other selfenergy contributions that are not considered within the approximation. This is illustrated in Fig. 2.6. Here, the first (TPH-representable) selfenergy diagram is accompanied by its mirrored counterpart, as well as several other contributions that balance the interaction lines between the two sides.

One has to conclude that the TPH approximation in the way presented in Ref. [79] is not Φ compensated and, thus, violates physical conservation laws for a general single-particle basis. Hence, it is advisable to reduce all uses of the approximation to the direct, Φ-derivable terms. It is presumably an interesting topic of future research to combine all selfenergy terms of Fig. 2.6 into a generalized, conserving particle–hole T matrix. Furthermore, it should be noted that for the Hubbard basis the exchange terms of the TPH approximation vanish [79]. Thus, all produced TPH results for the Hubbard model within the publications of this thesis are not affected by conservation issues and remain valid. Finally, it should be mentioned that an analogous consideration for the potential exchange terms of the GW series leads to similar results (not shown in detail). The inclusion of exchange diagrams within an NEGF scheme with GW approximation is, therefore, not recommended. The same holds true for the FLEX selfenergy, which is a combination of the TPP, TPH and GWA schemes (cf. Ref. [79]). To summarize the results of this section, an overview of conserving approximations within the NEGF framework is shown in Tab. 2.1.
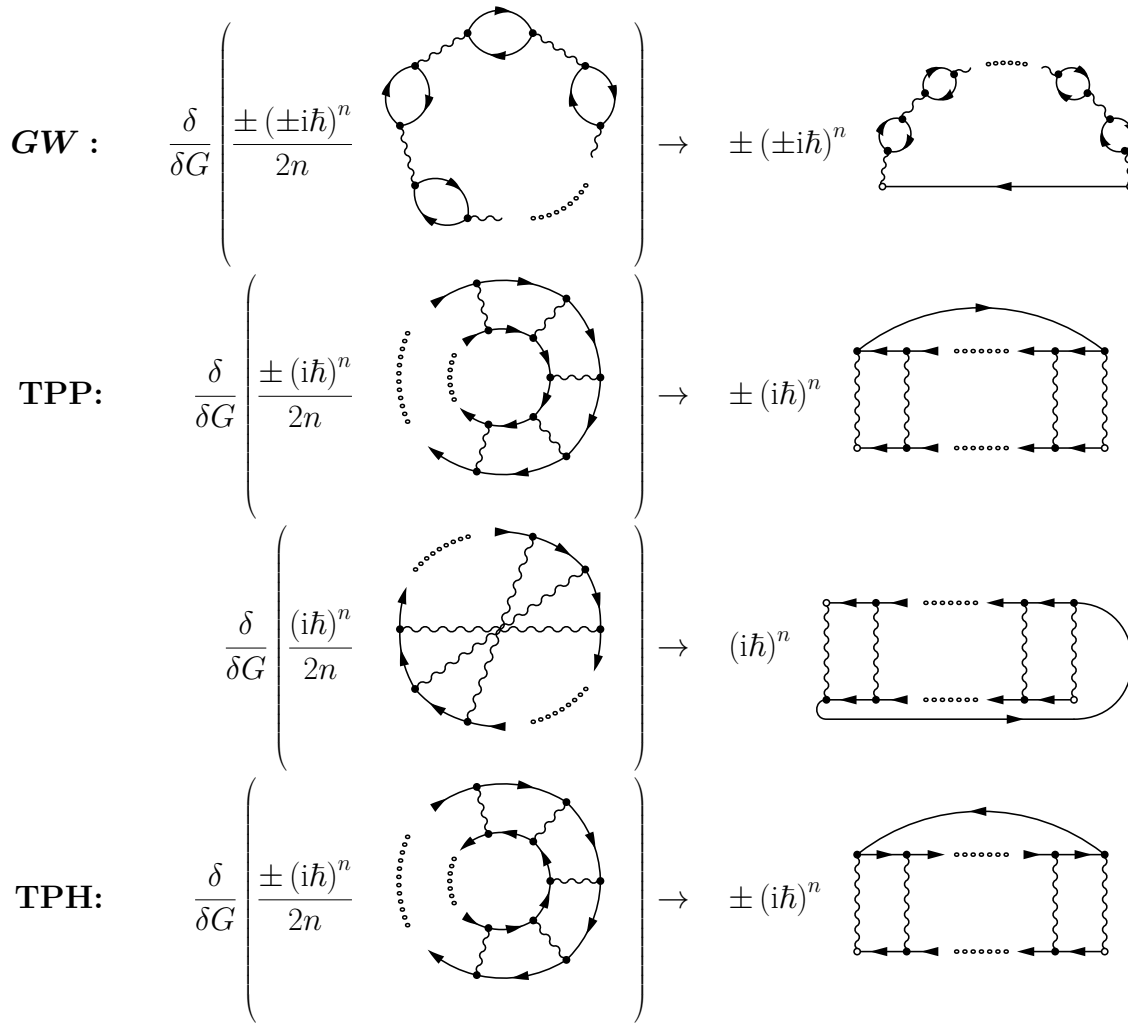
Figure 2.5 – Illustration of the nth-order Φ diagrams of the GW, TPP and the (direct) TPH approximation, as well as their corresponding selfenergy diagrams. Dotted lines indicate structural continuation until n occurrences of the interaction are reached. The prefactors are given explicitly.
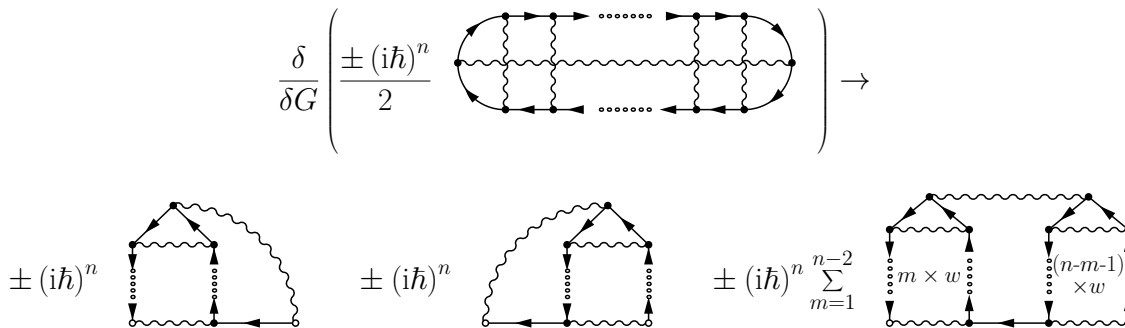
Figure 2.6 – Illustration of the nth-order Φ diagram that gives rise to the TPH exchange selfenergy contributions. Dotted lines indicate structural continuation until n occurrences of the interaction are reached. In the last selfenergy diagram the number of interaction lines is explicitly specified. The prefactors are given explicitly.

Φ compensated	Φ incomplete
HF	TPH + exchange
SOA	GWA + exchange
TOA	FLEX + exchange
TPP direct	
TPP + exchange	
TPH direct	
GWA direct	
FLEX direct	

Table 2.1 – Overview of conserving and unbalanced approximations. As in the main text, "Φ compensated" refers to Φ-derivable, conserving approximations that contain all selfenergy diagrams that originate from a specific choice of the Φ functional. In contrast, "Φ incomplete" refers to approximations that include at least one unbalanced subset of a Φ-derivable selfenergy-diagram group and, thus, violate physical conservation laws.

2.2 Ion Stopping in Correlated Materials: A Green-Functions Perspective

The conference proceedings following the 2018 meeting "Progress in Nonequilibrium Green's Functions VII" (PNGF VII) in Frascati, Italy contain a variety of interesting works on several topics, including theoretical developments for the Dyson equation [235, 236], the GKBA [207, 237, 238], and the NEGF method in general [239, 240], as well as experimentally relevant applications for magnetic skyrmions [241], graphene nanoribbons [216] (see Sec. 5.1), quantum-well photovoltaics [242], and ion-impact processes on solids [207] (see Sec. 4.3). Especially the last topic is of high interest as ion-impact scenarios play an important role, e.g., in ion sputtering on surfaces [243] and, in particular, as measuring the kinetic-energy loss of the ions can be used as a diagnostic tool for electronic structures [244]. From a theoretical point of view, the description of ion-stopping situations is particularly challenging as it requires to properly treat the intriguingly intricate interplay between nonequilibrium processes and correlations. This obstacle can be overcome by using the NEGF method. Since the author's group has significantly advanced the corresponding theoretical foundations [41, 214, 215] (see Sec. 4.3) it was possible to review the NEGF approach for ion-impact scenarios as a whole and provide a roadmap for future adaptions and theoretical developments. As a feature article[8] within the above-mentioned proceedings, the following Ref. [207], is a topical review that discusses NEGF theory and applications, developments of the GKBA, and, most notably, the simulation of ion-impact processes on solid surfaces. In addition, Ref. [207] contains original content in the form of further results and theoretical advancements.

Following a short introduction, Ref. [207] starts with the description of a simple but expedient model to describe the dynamics of charged-particle impacts on a surface (Sec. 2 of Ref. [207]). It is based on the versatile Hubbard model [204], which has been used to explain a large number of interesting effects in condensed matter, including band magnetism, the Mott metal–insulator transition, and superconductivity [245]. This description of Hubbard-type lattice models is combined with a classically treated ion, which interacts with the (quantum) lattice electrons. The subsequent section (Sec. 3 of Ref. [207]) gives a brief recapitulation of the central NEGF equations, discusses different selfenergy approximations, and focuses particularly on the GKBA. Here, benchmark results against DMRG calculations (see Sec. 4.1) are shown, the use of correlated propagators is addressed, and the proper treatment of initial correlations, giving rise to the possibility of restarting from a previously generated system state, is described. Coming back to the application of ion stopping, or, more precisely, ion deceleration on surfaces, the next section (Sec. 4 of Ref. [207]) reviews results of energy-loss calculations on finite, hexagonal quantum dots, where electronic correlations emerge as a red-shifted, reduced stopping-power maximum. In Ref. [41], it was shown that the exposure of 2D lattice systems with incident charged particles can be an efficient mechanism to induce electronic double occupation in the lattice.

This novel connection is demonstrated and elaborated in the next part of Ref. [207] and an analytical model based on a Landau–Zener approach is used to explain the increased doublon number. Additionally, the effect of multiple successive ion impacts is analyzed for the local double occupation which shows a correlation-spreading velocity, and the spectral function where an increased excitation to the upper Hubbard band is observed. Finally, a generalized approach to include charge-transfer processes is presented (Sec. 5 of Ref. [207], see also Refs. [246, 247]) which is based on an embedding-selfenergy scheme. As part of this, first numerical test calculations are shown.

Ion Impact Induced Ultrafast Electron Dynamics in Finite Graphene-Type Hubbard Clusters

Michael Bonitz,* Karsten Balzer, Niclas Schlünzen, Maximilian Rodriguez Rasmussen, and Jan-Philip Joost

Strongly correlated systems of fermions have an interesting phase diagram arising from the Hubbard gap. Excitation across the gap leads to the formation of doubly occupied lattice sites (doublons) which offers interesting electronic and optical properties. Moreover, when the system is driven out of equilibrium interesting collective dynamics may arise that are related to the spatial propagation of doublons. Here, a novel mechanism that was recently proposed by the authors [Balzer et al., Phys. Rev. Lett. 121, 267602 (2018)] is verified by exact diagonalization and nonequilibrium Green functions (NEGF) simulations – fermionic doublon creation by the impact of energetic ions. The formation of a nonequilibrium steady state with homogeneous doublon distribution is reported. The effect should be particularly important for correlated finite systems, such as graphene nanoribbons, and directly observable with fermionic atoms in optical lattices. It is demonstrated that doublon formation and propagation in correlated lattice systems can be accurately simulated with NEGF. In addition to two-time results, single-time results within the generalized Kadanoff–Baym ansatz (GKBA) with Hartree–Fock propagators (HF-GKBA) is presented. Finally systematic improvements of the GKBA that use correlated propagators (correlated GKBA) and a correlated initial state are discussed.

1. Introduction

The interaction of energetic charged particles with solid bodies is a phenomenon common to hot gases, plasmas, as well as astrophysical systems, including the solar wind and cosmic rays. When charged particles hit a solid surface, they deposit energy and momentum and may cause substantial surface modification the details of which strongly depend on the particle energy and the material properties. In low-temperature plasma physics, this process is routinely used to clean surfaces from adsorbates or modify them via sputtering, for example ref. [1] or as a source of secondary electrons.[2] On the other hand, ions impacting a solid can be used as a diagnostic tool of the electronic structure of the material by measuring the energy loss (or stopping power or stopping range) as a function of impact energy.[3]

From the theory side, the interaction of ions with a solid surface has been studied with a variety of approaches including scattering theory[4] or uniform electron gas models.[5] More recently, ab initio simulations of ion stopping based on time-dependent density functional theory (TDDFT) became available for metals,[6] semimetals,[7] or boron nitride and graphene sheets[8] and other materials. These simulations account primarily for valence electron excitation. Good results for the stopping power of high energy ions in matter are also provided by the SRIM code[9] that uses the binary collision approximation in combination with an averaging over a large range of experimental situations. Thus presently two main questions remain open: i) how does the stopping power change in correlated materials and what is the effect of the correlation strength? ii) How does the stopping power change when the system size is reduced or the geometry of the target is altered? And what is the role of electronic correlations in finite systems?

The motivation for these questions is fueled by the recent progress in nanostructured materials, clusters or finite nano-size systems. A particularly exciting example are finite honeycomb clusters or graphene nanoribbons (GNR). GNR hold the promise that they overcome the limitations of graphene arising from its semimetallic character. In contrast, GNR have been shown to have a finite bandgap $E_G(L)$ arising from the quantum confinement.[10,11] Over a broad range of system widths L, the band gap increases nearly proportional with L^{-1}.[12] Typical values for the bandgap are found to be $E_G \leq 2.5\,\mathrm{eV}$ according to tight-binding and DFT calculations.[13] Taking into account quasiparticle corrections results in a significantly larger gap of $E_G \leq 5.5\,\mathrm{eV}$.[10] In electronic structure measurements for GNRs on substrates bandgaps

Prof. M. Bonitz, N. Schlünzen, M. Rodriguez Rasmussen, J.-P. Joost
Institut für Theoretische Physik und Astrophysik
Christian-Albrechts-Universität zu Kiel
24098 Kiel, Germany
E-mail: bonitz@theo-physik.uni-kiel.de

Dr. K. Balzer
Rechenzentrum
Christian-Albrechts-Universität zu Kiel
24098 Kiel, Germany

The ORCID identification number(s) for the author(s) of this article can be found under https://doi.org/10.1002/pssb.201800490.

of $E_G \sim 2.4 - 3.5 \text{eV}$ were found.[14–16] The finite band gap makes the material semiconducting which is crucial for applications in electronics and optics. Recent progress in synthetization methods of GNR,[17–19] has drastically increased the number of exciting experiments over the past few years.[20–23] Therefore, an accurate theoretical description of these systems in nonequilibrium and especially of their time-resolved correlation effects is needed.

However, finite graphene nanostructures, especially when driven out of equilibrium, are extremely complex, inhomogeneous systems that put high requirements on theory. The two-dimensional geometry of the graphene honeycomb lattice has to be modeled, and the correlated nonequilibrium dynamics of the system have to be accurately described for up to several femtoseconds within a reasonable amount of computing time. Due to the limitations of time-dependent density functional theory to weakly correlated systems and the difficulties of density matrix renormalization group (DMRG) approaches to treat two-dimensional systems, nonequilibrium Green functions (NEGF) have emerged as the first choice to provide such a description. This method has recently been shown to accurately describe the dynamics of finite strongly correlated lattice systems, for example, refs. [24–26] where both two-time simulations and single-time dynamics within the generalized Kadanoff–Baym ansatz (GKBA[27]) were presented.[28] Furthermore, in our recent work,[29,30] we have shown that the NEGF approach is well capable to treat the correlated electron dynamics in lattice systems that is initiated by the impact of charged projectiles and, thus, is able to answer questions i) and ii) that were raised above.

The goal of this article is to present recent results on NEGF simulations of finite correlated lattice systems with a particular focus on doublon creation and propagation following the impact of one or several charged particles. We also discuss how to include the description of charge transfer processes between projectile and target that is observed at low impact velocities. Finally, we discuss theoretical issues that are related to the GKBA and to its extension to include correlated propagators.

The remainder of this article is organized as follows. In Section 2, we introduce the Hubbard model and the description of the interaction of the charged projectile with the electronic system. This is followed, in Section 3, by a brief introduction into the NEGF approach and the GKBA and a discussion of its further improvements. The main results are presented in Section 4 and include numerical data from two-time NEGF and GKBA simulations as well as analytical results for a representative two-site system, cf. Section 4.3. We conclude by presenting an embedding approach to treat the charge transfer between projectile and solid, in Section 5, and by an outlook, in Section 6.

2. Model

We consider a 1D or 2D system with moderate to strong electronic correlations that is modeled by a Hubbard hamiltonian (1) with hopping amplitude J [$\langle i,j \rangle$ denotes nearest neighbors] and onsite interaction strength U.

Michael Bonitz is a full professor of Theoretical Physics at Kiel University, Germany. His research interests are plasma physics, warm dense matter, correlated electrons in solids, many-body physics, and ab initio simulations. He has authored over 350 papers and is author or editor of 10 books. He is recipient of the Gustav-Hertz prize of the German Physical Society, fellow of the American Physical Society and doctor honoris causa of the Russian Academy of Sciences.
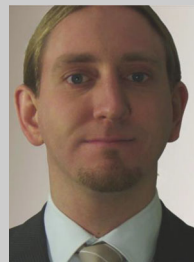
Karsten Balzer obtained his PhD degree in Physics at Kiel University, Germany in 2011, working in the group of Prof. Michael Bonitz on the solution of the two-time Keldysh-Kadanoff-Baym equations for spatially inhomogeneous quantum systems. From 2012 to 2014 he joined, as Postdoc, the group of Prof. Martin Eckstein at the Max Planck Institute for the Structure and Dynamics of Matter (MPSD/CFEL) in Hamburg and developed advanced numerical methods in nonequilibrium dynamical mean-field theory. Currently he is employed as consultant for scientific and high-performance computing at the Computing Centre of Kiel University.

$$
\begin{aligned}
H_e = & -J\sum_{\langle i,j \rangle,\sigma} c_{i\sigma}^\dagger c_{j\sigma} + U\sum_i \left(n_{i\uparrow} - \frac{1}{2} \right)\left(n_{i\downarrow} - \frac{1}{2} \right) \\
& - \frac{Z_p e^2}{4\pi\varepsilon_0}\sum_{i,\sigma} \frac{c_{i\sigma}^\dagger c_{i\sigma}}{|\mathbf{r}_p(t) - \mathbf{R}_i|} + \sum_{\langle i,j \rangle,\sigma} W_{ij}(t) c_{i\sigma}^\dagger c_{j\sigma}
\end{aligned}
\tag{1}
$$

The strength of correlations is measured by the ratio U/J. For finite graphene clusters (nanoribbons) a typical value is $U/J = 3.5$.[31] For other 2D materials larger values are possible. Similarly, such finite clusters are straightforwardly realized from fermionic atoms in optical lattices where U/J can be very large. Here, we will mostly consider moderate values, $U/J = 4$ but also a few applications where $U/J = 10\ldots15$. The latter cases are treated by exact diagonalization (CI) methods, for small systems, and the former with nonequilibrium Green functions, see Section 3.

The second line of Equation (1) contains the coupling of the lattice electrons located at coordinate $\mathbf{R}_i$ with a positively charged projectile of charge Z_p that is treated classically (Ehrenfest dynamics) by solving Newton's equation for the trajectory $\mathbf{r}_p(t)$ under the influence of all Coulomb forces with the lattice electrons. The final term allows to improve the model by accounting for modification of the hopping rates due to the projectile according to $W_{ij}(t) = \gamma\big[W_{ii}(t) + W_{jj}(t)\big]/2$, where W_{ii} is the magnitude of the
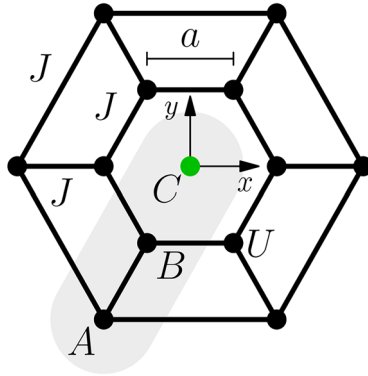
Figure 1. Sketch of a honeycomb cluster of $L = 12$ sites and distance between sites a, showing the hopping and on-site interaction parameters in the hamiltonian (1). The dimer model of Section 4.3 consists of the representative sites A and B.

Coulomb potential of the projectile at lattice site "i," and γ is a phenomenological parameter of the order unity.[29]

Although the Hubbard model permits any geometry, here we will concentrate on single-layer honeycomb clusters, due to their relevance for graphene-type structures. A sketch of such a system is shown in **Figure 1**. For the special case of high symmetry, as in this figure, it is tempting to consider a reduced dimer model that consists only of sites A and B. This model can be solved analytically, even in the presence of a time-dependent external perturbation (such as a charged projectile[30]), and this will be summarized in Section 4.3.

Of course, the Hubbard model (1) represents a strong simplification compared to graphene. Nevertheless, fairly accurate parameters can be obtained from DFT simulations. On the other hand, this model can be exactly realized with ultracold atoms in optical lattices. A first improvement to the model is achieved by using strongly reduced hopping rates at the cluster edge (due to the larger distances and to the termination with other atoms). We have tested this effect in ref. [30] and verified that this does not significantly change the response of the cluster to a projectile compared to the results that are presented below. A further improved description of graphene-type finite-size structures can be achieved via an *extended Hubbard model* where one includes also hopping beyond the nearest neighbor sites and non-vanishing orbital overlap, which is described in detail in ref. [31] but will not be used here.

3. Nonequilibrium Green Functions Formalism

The method of nonequilibrium (real-time) Green functions is a very powerful approach to quantum many-body systems out of equilibrium, cf. refs. [32,33]. The method successfully overcomes the limitations of the quantum Boltzmann equation, such as the restriction to times larger than the correlation time and fundamental problems such as failure for strongly correlated systems, incorrect conservation laws (e.g., conservation of kinetic energy instead of total energy) and relaxation toward an equilibrium state of an ideal gas (Fermi, Bose, or Maxwell distribution) instead of the one of an interacting system, for a detailed discussion, see refs. [34–38]. An extensive overview on

recent applications that span condensed matter physics, nuclear physics, laser plasmas, etc., can be found in the proceedings of the PNGF conferences.[39–44]

3.1. Basic Concepts

The NEGF method is formulated in second quantization (for textbook or review discussions, see for example, refs. [24,33,45]), in terms of creation (annihilation) operators $c_{i\sigma}^\dagger$ ($c_{i\sigma}$) for electrons in a single-particle orbital $|i\rangle$ with spin projection σ that obey the standard fermionic anti-commutation relations. Below we will consider a spatially inhomogeneous lattice configuration where i labels the spatial coordinates of individual lattice points.

The central quantity that determines all time-dependent observables is the one-particle NEGF

$$G_{ij\sigma}(t, t') = -i\hbar \langle T_C c_{i\sigma}(t) c_{j\sigma}^\dagger(t') \rangle \tag{2}$$

where the expectation value is computed with the equilibrium density operator of the system, and times are running along the Keldysh contour C, with T_C denoting ordering of operators on C.[32,46] The NEGF obeys the two-time Keldysh–Kadanoff–Baym equations (KBE)[33]

$$\sum_k \left[i\hbar \partial_t \delta_{ik} - \bar{h}_{ik\sigma}(t) \right] G_{kj\sigma}(t, t')$$
$$= \delta_C(t - t') \delta_{ij} + \sum_k \int_C ds \Sigma_{ik\sigma}(t, s) G_{kj\sigma}(s, t') \tag{3}$$

$$\sum_k G_{ik\sigma}(t, , t') \left[-i\hbar \overleftarrow{\partial}_{t'} \delta_{kj} - \bar{h}_{kj\sigma}(t') \right]$$
$$= \delta_C(t - t') \delta_{ij} + \sum_k \int_C ds G_{kj\sigma}(t, s) \Sigma_{ik\sigma}(s, t') \tag{4}$$

where we do not consider spin changes. The hamiltonian $\bar{h}(t)$ contains kinetic, potential, and mean field energy [including the projectile contributions in the second line of Equation (1)], whereas correlation effects are contained in the selfenergy Σ.

For numerical applications the Equation (3) for the Keldysh matrix Green function have to be rewritten for the correlation functions $G^{\gtrless}$:

$$\sum_l \left[i\hbar \partial_t \delta_{il} - \bar{h}_{il}(t) \right] G_{lj}^{\gtrless}(t, t') = I_{ij}^{(1)\gtrless}(t, t') \tag{5}$$

$$\sum_l G_{il}^{\gtrless}(t, t') \left[-i\hbar \overleftarrow{\partial}_{t'} \delta_{lj} - \bar{h}_{lj}(t') \right] = I_{ij}^{(2)\gtrless}(t, t') \tag{6}$$

with the collision integrals given by

$$I_{ij}^{(1)\gtrless}(t, t') =$$
$$\sum_l \int_{t_s}^\infty d\bar{t} \left\{ \Sigma_{il}^R(t, \bar{t}) G_{lj}^{\gtrless}(\bar{t}, t') + \Sigma_{il}^{\gtrless}(t, \bar{t}) G_{lj}^A(\bar{t}, t') \right\} \tag{7}$$

$$I_{ij}^{(2)\gtrless}(t,t') =$$
$$\sum_l \int_{t_s}^{\infty} d\bar{t}\left\{ G_{il}^{R}(t,\bar{t})\Sigma_{lj}^{\gtrless}(\bar{t},t') + G_{il}^{\gtrless}(t,\bar{t})\Sigma_{lj}^{A}(\bar{t},t') \right\} \tag{8}$$

where the retarded and advanced functions are given by

$$G_{ij}^{R/A}(t,t') = \pm\Theta[\pm(t-t')]\left\{ G_{ij}^{>}(t,t') - G_{ij}^{<}(t,t') \right\}$$
$$\Sigma_{ij}^{R/A}(t,t') = \pm\Theta[\pm(t-t')]\left\{ \Sigma_{ij}^{>}(t,t') - \Sigma_{ij}^{<}(t,t') \right\} \tag{9}$$

Note that the correlation effects that are contained in the collision integrals $I^{1,2\gtrless}$ lead to memory effects, that is, time integrations over the past, starting from a start time t_s. In most of the simulations presented below, we will start at t_s with an uncorrelated system and slowly switch on the interaction ("adiabatic switching"[28,47]) which produces, at time t_0, a correlated ground state from which the excitation of the system starts. We return to the discussion of a correlated initial state in Section 3.4.

The system (3)–(9) is a closed set of equations for the dynamics of the NEGF once a selfenergy approximation $\Sigma[G]$ has been chosen. This issue is discussed in the following section.

3.2. Selfenergies

In this work we use the following selfenergy approximations to account for the electron–electron interaction. We consider Hartree-Fock (HF) contributions (i.e., mean field, note that, for Hubbard systems, the Fock terms are absent) and correlation effects. The latter are described on the level of the second Born (2B) and the T-matrix approximation (TM) where the former (latter) is adequate at weak (moderate) coupling.[25,26] Moreover, we also consider the third-order approximation[24,48] that includes all bubble and ladder-type diagrams to third order. The corresponding selfenergy diagrams are shown in **Figure 2**.

The KBE (3) are solved on the $t-t'$-plane as described in refs. [24,49]. Due to the time integration involved in the collision integrals (memory) the numerical effort increases cubically with the simulation duration T_{tot}. The effort is particularly high for the GW and T-matrix approximations since for the effective interaction, an additional integral equation has to be solved, for example, ref. [24]. One way to reduce the computational effort is the restriction to the propagation along the time diagonal via the generalized Kadanoff–Baym ansatz (GKBA), proposed in ref. [27]. The GKBA reduces the computational effort of NEGF simulations with second order Born selfenergies from a scaling $\sim T_{tot}^3$ with the total simulation duration to $\sim T_{tot}^2$ as was confirmed in ref. [47]. The GKBA has the additional attractive feature that it reduces the degree of selfconsistency in the NEGF simulations[28] and "cures" the artificial damping behavior of two-time simulations
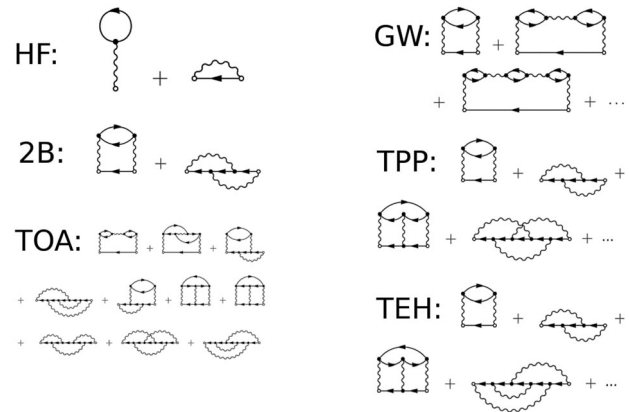
Figure 2. Feynman diagrams for the selfenergy approximations used in this work: Hartree–Fock (HF), Second order Born approximation (2B), particle–particle and particle–hole T-matrix (TPP, TEH), and third order approximation (TOA) which contains all diagrams with three interaction lines from GW, TPP, and TEH.

observed in small systems at very strong excitation,[50] for computational aspects, see also ref. [51].

3.3. Generalized Kadanoff–Baym Ansatz: Extension to Correlated Propagators

Instead of propagating the Green functions in the two-time plane one can perform a propagation along the diagonal, $T = (t + t')/2$, only. The equation for $G^<$ is a commutator equation – the first equation of the BBGKY-hierarchy for the reduced density operators[34]:

$$i\hbar\partial_T G_{ij}^{<}(T,T) = \left[\bar{h}(T), G^{<}(T,T)\right]_{ij} + I_{ij}(T)$$
$$[A,B]_{ij} = \sum_k \left(A_{ik}B_{kj} - B_{ik}A_{kj} \right) \tag{10}$$

$$I_{ij}(T) = \sum_k \int_{t_0}^{T} d\bar{t}\{\Sigma_{ik}^{>}(T,\bar{t})G_{kj}^{<}(\bar{t},T) - \Sigma_{ik}^{<}(T,\bar{t})G_{kj}^{>}(\bar{t},T) + \text{h.c.}\} \tag{11}$$

To compute the collision integral I, the Green functions $G^{\gtrless}(t,t')$ are required also away from the diagonal. In fact, due to the symmetry $G_{ij}^{\gtrless}(t,t') = -[G_{ji}^{\gtrless}(t',t)]^*$ values for $t \geq t'$ are sufficient. With the GKBA the following "reconstruction" approximation is made[27]

$$G_{ij}^{\gtrless}(t,t') = i\hbar\sum_k G_{ik}^{R}(t,t')G_{kj}^{\gtrless}(t',t'), \quad t \geq t' \tag{12}$$

and with $G^{\gtrless}(t,t')$ also $\Sigma^{\gtrless}(t,t')$ are known. While the diagonal value $G_{kj}^{\gtrless}(t',t')$ is available from the solution of Equation (10), the retarded function has to be provided as an external input. Among the different approaches in macroscopic systems we mention the

use of ideal propagators ("Free GKBA" or FGKBA), and quasiparticle propagators, that are exponentially decaying as a function of $|t - t'|$ (QP-GKBA) which have been used extensively in semiconductor optics and transport, in particular, by the groups of Haug, Banyai, and Jahnke, for example, refs. [52–55] and references therein. For strong field physics in semiconductors and laser plasmas the gauge-invariant FGKBA has been introduced.[53,56–58] The GKBA has also been used with propagators taken from a full two-time simulation (2t-GKBA) in ref. [59] which confirmed the good quality of the ansatz (12). A revival of the interest in the GKBA occured with the NEGF study of finite systems about a decade ago, for example, ref. [45] and references therein. Here very good results were obtained with Hartree-Fock propagators (HF-GKBA).[49,60–62]

Although earlier studies used the GKBA together with lowest order correlated selfenergies (second Born approximation) we recently demonstrated that the HF-GKBA can also be successfully used together with mored advanced approximations such as the T-matrix, GW and third-order selfenergies, cf. Section 3.2. The most thorough test of the HF-GKBA (and of two-time NEGF simulations), so far, was performed in ref. [26] by benchmarks against quasi-exact DMRG simulations for 1D systems which are summarized in **Figure 3**. For weak and moderate coupling very good agreement with DMRG was obtained, if the HF-GKBA was combined with the adequate selfenergy: second order Born for $U/J \leq 1$ and T-matrix for $U/J \leq 4$ at weak (or high) filling. Around half filling the third order approximation showed the best behavior. This agreement is observed for all observables including densities and energies and even for very sensitive quantities such as the average double occupation, Equation (24), that is shown in Figure 3. While the NEGF simulations are more efficient than DMRG at

Figure 3. Benchmarks of the HF-GKBA against DMRG for a 1D charge density wave state of doublons (site occupations alternate 2, 0, 2 …). System-size dependence and long-time evolution of the average double occupancy, Equation (24), for (a) $U = J$ and (b) $U = 4J$ and chain lengths $L = 6, 12, 20, 24, 36$. Full lines: DMRG, short dashes: HF-GKBA + TMA. The insets, in addition, show HF-GKBA + TOA results (long dashes). For better visibility, curves for different L are shifted vertically by 0.1. After ref. [26].

weak and moderate coupling (cf. the accessible simulation durations in Figure 3), for strong coupling, $U = 10$, in contrast to DMRG, no NEGF simulations were possible, indicating complementary applicability ranges of the two methods.[26] In addition, NEGF have the remarkable advantage of being completely flexible in terms of system dimensionality and geometry which makes them an ideal approach to treat finite correlated systems such as GNR.

Despite the success of the HF-GKBA, it also has problems. While it removes most of the over-damping artifacts of two-time NEGF simulations (see above), it often underestimates the damping present in the exact dynamics and does not correctly reproduce the high-frequency features, cf. Figure 3. Also, due to the HF-propagators, the spectral function produced by the HF-GKBA is uncorrelated. There have been early attempts to modify the free propators by an exponential damping, $G^R \sim e^{-\gamma|t-t'|}$ (cf. QP-GKBA above). However this choice of propagators violates energy conservation [as opposed to the FKGBA and HF-GKBA] due to a very slow ($1/\omega^2$) decay of the propagators in frequency space. This behavior was improved in ref. [63] by the use of non-Lorentzian damping factors, $G^R \sim 1/\cosh^a[\omega(t - t')]$, where ω is a characteristic frequency (phonon or plasmon frequency) and a is a positive fit parameter, but energy conservation is still violated. For a recent discussion of the reconstruction problem, see ref. [64].

Here we outline a systematic approach toward an improved version of the GKBA that goes beyond the HF-GKBA. The idea is to start from the equation of motion for the retarded propagators (Dyson equation)

$$G_{ij}^R(t, t') = G_{HF,ij}^R(t, t') + \sum_k \int_{t'}^t d\tilde{t} G_{HF,ik}^R(t, \tilde{t}) \tilde{I}_{kj}^R(\tilde{t}, t')$$

$$\tilde{I}_{ij}^R(t, t') = \sum_k \int_{t'}^t dt'' \tilde{\Sigma}_{ik}^R(t, t'') G_{kj}^R(t'', t)$$

(13)

where $\tilde{\Sigma}$ is a conserving selfenergy that may be different from the one used in I_{ij}.[28] Since our main goal is to improve the single-time simulations beyond the HF-GKBA and to include damping effects, we may regard correlation effects in the GKBA as small corrections to $G_{HFij}^R(t, t')$. While the HF-GKBA corresponds to the neglect of the integral in (13), an approximate treatment of the integral will be called *correlated GKBA* (C-GKBA). For this we propose several approximations that are listed in increasing order of accuracy, assuming that $\tilde{\Sigma}$ corresponds to weak correlations, that is, small $\tilde{U}/J$:

a) replacement of all propagators in the integral (13) by ideal propagators, $G^R \rightarrow G_{id}^R$;

b) replacement of all propagators in the integral (13) by HF propagators, $G^R \rightarrow G_{HF}^R$. The result $G^{R,(1)}$ can be understood as first step of an iteration series that starts with $G^{R,(0)} \equiv G_{HF}^R$;

c) higher order iterations, $G^{R,(l)}$, $l \geq 2$, that use $G^{R,(l-1)}$ in the integral term;

d) linearization of the collision integral in the correlated G^R. This means, products of retarded functions are replaced

according to $G_{ik}^R G_{kj}^R \rightarrow G_{HF,ik}^R G_{kj}^R + G_{ik}^R G_{HF,kj}^R$ and similarly, for more complex products;
e) 2t-GKBA: exact solution of the Dyson equation for $G^R(t, t')$,[59] see above.

Note that the Dyson Equation (13) for G^R is not closed since the selfenergy $\tilde{\Sigma}^R$, in general, also contains $G^{\gtrless}$. However, in the spirit of perturbation theory, we can always reconstruct $G^{\gtrless}$ via $G^{R/A}$ applying again the GKBA (12).

This is a systematic scheme to incorporate correlations in the propagators. The drawback of the C-GKBA is, of course, that the evaluation of the integral term in Equation (13) is costly, scaling as T_{tot}^3. However, this effort is warranted by the expected improved accuracy of the observables and spectral properties as compared to two-time NEGF simulations, on the one hand, and HF-GKBA results, on the other. The analytical and numerical properties of the C-GKBA are presently under investigation. Finally, we note that recently also improvements that take into account corrections beyond the GKBA have been studied for stationary transport problems by Kalvova et al.[65] A modified reconstruction problem where the GKBA is applied also to the off-diagonal propagation ("extended GKBA") was recently proposed by Hopjan et al.[66,67] but the relation to the original reconstruction scheme of ref. [27] remains open.

3.4. Initial Correlations for NEGF and GKBA: Restart Capability

Until now we have only considered situations where, at the "initial" time where the evolution starts, the system is uncorrelated. This is, of course, a special case. In general, at this time, the system may be characterized by non-vanishing pair correlations c_{12} which may have a profound effect on the dynamics. The generalization of the KBE to include finite initial correlations goes back to Danielewicz[68] who derived a collision integral I^{IC} that is due to c_{12}. Alternative derivations have been given by Kremp et al.[56,69] who also derived initial correlation contributions to the selfenergy. In these articles also numerical results were given that demonstrate the effect of initial correlations. Text book discussions can be found in refs. [34,45,70]. Despite these early results and similar theoretical and numerical results for density operators, for example, ref. [34], numerical results for the GKBA have not been proposed so far. Only recently, two papers appeared that presented solutions for this problem.[67,71]

Here we present an alternative approach that is based on ref. [72] that provides a complementary and more general view on this issue. In Equation (3) we introduced, on the right-hand side, the collision integral that involves the correlation selfenergy or, alternatively, the correlation part of the two-particle Green function $G^{(2)}$

$$\int d2 V(1-2) G^{(2)}(12, 1'2^+) = \int_C d\bar{1} \Sigma(1, \bar{1}) G(\bar{1}, 1') \quad (14)$$

$$= I(1, 1'; -\infty) \equiv I(1, 1'; t_0) + I^{IC}(1, 1') \quad (15)$$

Here $1 = (\mathbf{r}_1, s_1, t_1)$, V is a general interaction potential, and the third argument of I explicitly denotes the initial moment of the time evolution. When the evolution starts at $-\infty$, the system is assumed to be uncorrelated initially and, due to collisions, correlations are being build up until, at a finite time t_0, they reach a value $c(t_0)$. This can be real dynamics driven by an external excitation. Alternatively, if one is interested in a correlated initial state, the evolution from $-\infty$ to t_0 can be generated "artificially" by adiabatically switching on the interaction, starting from an uncorrelated state, for example, ref. [28], or via including an imaginary track into the Keldysh contour, for example, refs. [45,49]. Even though the start of the dynamics is, in practice, set to a finite value, $-\infty \rightarrow t_-$ with $c(t_-) = 0$, both scenarios involve a time integration over the past in the r.h.s. of Equation (14) which is computationally costly, in particular for long propagation times.

This expensive time integration from t_- to t_0 can, in fact, be avoided in many cases[56,71] as we show now. The r.h.s. of Equation (15) indicates that the collision integral can be identically rewritten as a scattering integral I, in which the evolution starts at t_0, plus an additional collision integral I^{IC} that contains the initial correlations $c(t_0)$, for a detailed discussion, see ref. [72]. In that reference explicit results for a homogeneous system were given. Using the momentum representation (plane wave basis) the additional collision integral becomes, for second order Born selfenergy (the extension to the T-matrix approximation was presented in ref. [69]),

$$I_{p_1}^{IC,2B}(t, t') = -2i\hbar^5 V_0 \sum_{p_2 \bar{p}_1 \bar{p}_2} V_{p_1 - \bar{p}_1} \delta_{p_1 + p_2, \bar{p}_1 + \bar{p}_2}$$
$$\times G_{\bar{p}_1}^R(t, t_0) G_{\bar{p}_2}^R(t, t_0) c_{\bar{p}_1, \bar{p}_2, p_1, p_2}(t_0) G_{\bar{p}_1}^A(t_0, t') G_{\bar{p}_2}^A(t_0, t')$$
$$(16)$$

where V_0 is the volume. This is the first crucial step and one realizes that Equation (16) does, indeed, not contain a time integral. The second important step is to derive the initial correlation function $c(t_0)$. This is done by going back to the connection between the two-particle Green function and the selfenergy, Equation (14), and to specialize this to the desired time moment, $t = t' \rightarrow t_0$. This leads to the following general relation

$$I_{p_1}^{IC}(t_0, t_0) = -2i\hbar V_0 \sum_{p_2 \bar{p}_1 \bar{p}_2} V_{p_1 - \bar{p}_1} \delta_{p_1 + p_2, \bar{p}_1 + \bar{p}_2} \times c_{\bar{p}_1, \bar{p}_2, p_1, p_2}(t_0)$$
$$(17)$$

$$= \int_{t_-}^{t_0} d\bar{t} \left\{ \Sigma_{p_1}^>(t_0, \bar{t}) G_{p_1}^<(\bar{t}, t_0) - \Sigma_{p_1}^<(t_0, \bar{t}) G_{p_1}^>(\bar{t}, t_0) \right\}$$

which constitutes an equation for the matrix $c(t_0)$ in terms of the selfenergy and the correlation functions built up from the uncorrelated state at t_-. An explicit result for $c(t_0)$ can be obtained for direct second order Born selfenergies (first 2B diagram in Figure 2), for $\bar{p}_1 + \bar{p}_2 = p_1 + p_2$ (the other matrix elements are equal to zero),

$$c_{\bar{p}_1, \bar{p}_2, p_1, p_2}^{2B}(t_0) = \frac{i\hbar}{V_0} \int_{t_-}^{t_0} d\bar{t} V_{p_1 - \bar{p}_1}$$
$$\times \left\{ G_{\bar{p}_1}^>(t_0, \bar{t}) G_{\bar{p}_2}^>(t_0, \bar{t}) G_{p_1}^<(\bar{t}, t_0) G_{p_2}^<(\bar{t}, t_0) - (> \leftrightarrow <) \right\}$$
$$(18)$$

which was presented in ref. [72] for the general case of NEGF propagation in the two-time plane.

Expression (18) is immediately rewritten for the case of propagation along the time diagonal within the GKBA scheme, cf. Section 3.3, by replacing the functions $G^{\gtrless}$ via (12),

$$
c^{2B,GKBA}_{\bar{p}_1,\bar{p}_2,p_1,p_2}(t_0) = \frac{i\hbar}{V_0} \int_{t_-}^{t_0} d\bar{t} V_{p_1-\bar{p}_1}
$$
$$
\times G^R_{\bar{p}_1}(t_0,\bar{t}) G^R_{\bar{p}_2}(t_0,\bar{t}) G^A_{p_1}(\bar{t},t_0) G^A_{p_2}(\bar{t},t_0) \tag{19}
$$
$$
\times \left\{ f^>_{\bar{p}_1}(t_0) f^>_{\bar{p}_2}(t_0) f^<_{p_1}(t_0) f^<_{p_2}(t_0) - (> \leftrightarrow <) \right\}
$$

where $f^>(t_0)$ is the Wigner function of the initial state, and $f^> = 1 \pm f^<$. If HF propagators are chosen this agrees with the result of ref. [71], but improved propagators can also be used, as was discussed in Section 3.3. Since the distribution functions are taken at a fixed time, the time integral in Equation (19) involves only the propagators. For HF propagators it can be done analytically whereas for more complicated propagators numerical integration remains to be done, but only once, prior to the start of the time propagation.

Another approach is to derive $c(t)$, Equation (18), from the Bethe-Salpeter equation for $G^{(2)}$. For any choice of the selfenergy $\Sigma(G)$ it is, in principle, possible to find the functional $G^{(2)}[G]$, as was explicitly demonstrated for the Born approximation in ref. [73]. With the GKBA this also provides the result for $c^{GKBA}(t_0)$, Equation (19). In fact, the result for $c^{GKBA}(t_0)$ with HF propagators does not require NEGF input at all. It follows directly from density operator theory within the single-time BBGKY-hierarchy where it has been computed for a variety of many-particle approximations including second order Born, T-matrix[38,69] or GW approximation.[34]

Finally we note that this approach of computing the quantum dynamics within the two-time NEGF or single-time GKBA scheme by starting from a correlated state at a finite time t_0 has another important application. Indeed, the pair correlation $c(t_0)$ is not necessarily that of the ground state or the equilibrium state, but it is arbitrary, as long as it fulfills condition (17) as was shown in ref. [72]. For example, it can be the correlations that have been built up during a previous real dynamics, for $t \leq t_0$, and which can be used to restart (continue) the evolution, for $t \geq t_0$, cf. ref. [72]. This is possible in cases when a unique solution of Equation (17) for the entire matrix of c exists.

3.5. NEGF-Ehrenfest Approach to Ion Stopping

Let us now come back to the problem of ion stopping and the associated electronic correlation effects in finite graphene-type clusters that we discussed above in Sections 1 and 2. For the numerical analysis, we use the Kadanoff–Baym Equations (3) with the electronic hamiltonian (1). The impacting ion acts as a time-dependent external attractive potential for all electrons. This potential is sharply peaked as a function of time, reaching its maximum (negative) value when the projectile traverses the honeycomb layer. The energy loss of the ion is treated classically via solution of Newton's equation (Ehrenfest dynamics). Processes of charge transfer between target and projectile which

are important at low impact velocities will be considered separately, in Section 5.

From the NEGF all time-dependent single-particle observables can be computed according to

$$
\langle \hat{A} \rangle(t) = -i\hbar \sum_{ij} A_{ij} G^<_{ji}(t,t) \tag{20}
$$

including the single-particle energy and the site-resolved density, $n_{i\sigma} = \langle \hat{n}_{i\sigma}(t) \rangle$. Another important quantity is the time-resolved photoemission spectrum[74]

$$
A^<(\omega, T) = -i\hbar \sum_i \int dt dt' S_\kappa(t-T) S_\kappa(t'-T)
$$
$$
\times e^{-i\omega(t-t')} G^<_{ii}(t,t') \tag{21}
$$

which measures the occupied states of the system. It allows for a direct comparison with time-resolved (pump-probe) photoemission experiments where S_κ mimicks a Gaussian probe pulse of width κ,

$$
S_\kappa(t) = \frac{1}{\kappa\sqrt{2\pi}} \exp\left(-\frac{t^2}{2\kappa^2}\right)
$$

The energy exchange between projectile and the cluster can be computed from the increase of the total energy of the electrons or, equivalently, from the energy loss of the projectile,

$$
S_e = m_p \frac{\dot{r}_p^2(t \to +\infty)}{2} - m_p \frac{\left(\dot{r}_p^2 t \to +\infty\right)}{2} \tag{22}
$$

which is just the difference of kinetic energies far away from the target before and after the impact. With this we assume that the interaction between different projectiles or with a surrounding plasma medium is negligible. Further, we do not resolve internal degrees of freedom of the projectile. Also two-particle expectation values such as the correlation energy and the double occupation d_i are accessible in the NEGF approach taking advantage of the two-time information in G and Σ. Thus we compute the expectation value of the site-resolve doublon number, its cluster-average and the long-time limit of the latter, after passing of the projectile, according to

$$
d_i(t) = \langle \hat{n}_{i\uparrow}(t) \hat{n}_{i\downarrow}(t) \rangle
$$
$$
= -\frac{i\hbar}{U} \sum_k \int_C ds \Sigma_{ik}(t,s) G_{ki}(s,t) \tag{23}
$$

$$
d_{av}(t) = \frac{1}{L} \sum_{i=1}^L d_i(t), \quad d_{av}^\infty = \lim_{t \to \infty} \frac{1}{\Delta t} \int_t^{t+\Delta t} d\bar{t} \, d_{av}(\bar{t}) \tag{24}
$$

4. Results

We now turn to the results for the time-resolved coupled electron-projectile dynamics. A detailed investigation has been

presented in refs. [30,75] some results of which are briefly summarized here and complemented with additional data. For small clusters, $L \leq 12$, we have performed exact diagonalization calculations whereas for larger systems we solved the Keldysh–Kadanoff–Baym Equation (3) for the NEGF. In the latter case the accuracy of the results is determined by the choice of the selfenergy Σ. In this article, we present simulations within the second order Born approximation using the HF-GKBA, cf. Section 3.3 and selected data with more advanced selfenergies that were introduced in Section 3.2. Prior to the NEGF simulations we have performed detailed numerical convergence tests that include particle number and energy conservation[51] and time reversibility.[76,77] In addition, for small systems we have performed tests against exact diagonalization calculations. Further tests of the present code (T-matrix selfenergy) include comparisons with cold atom experiments[25] where excellent agreement was found. Finally we mention extensive benchmarks against density matrix renormalization group (DMRG) calculations,[26] a typical example − for the GKBA − was shown above in Figure 3. An important outcome of the benchmarks of ref. [26] was that the exact result is often enclosed between the two-time simulations and the HF-GKBA. From this we can conclude that the present NEGF stopping simulations are reliable and have predictive power.

4.1. Energy Loss of the Projectile

Let us start with the total energy loss of the projectile, Equation (22), as a function of impact energy which is shown in **Figure 4**, for the case of a proton. The overall behavior is well-known: the energy loss vanishes, both, for very low and very high impact energies. An optimum projectile-target interaction is observed at intermediate impact energies, in the range of several keV per mass unit u. The decrease at large energies is due to the reduced interaction duration and is consistent with the standard non-relativistic Bethe formula, for example, ref. [3], and with linear response treatments (based on the density–density correlations and dynamic structure factor). Not surprisingly, here correlations in the material have very little influence which can be seen in the convergence of the curves for different U. In the opposite limit, the energy available for transfer to the target is small. At the same time, in the range left of the maximum the influence of the target properties on the energy loss is significant: here the curves for different coupling strength U differ significantly.

This overall trend of the energy loss (stopping power) is well reproduced with our NEGF simulations, and the results agree well with other approaches, such as TDDFT and the SRIM code, at high energies. On the other hand, in the low energy range the situation is less clear. One reason is that, previously, most attention focused on high-energy particle beams or hot plasmas. Only more recently low projectile energies in the range of several hundred or tens of eV attracted interest because this is the typical energy range in low-temperature plasmas and surface physics, for example, ref. [2]. In this range, correlation effects in the target (the value of U/J in our model) play a crucial role, and also size and geometry effects are expected to be relevant. The influence of system size is clearly seen in our simulations, compare parts (a) and
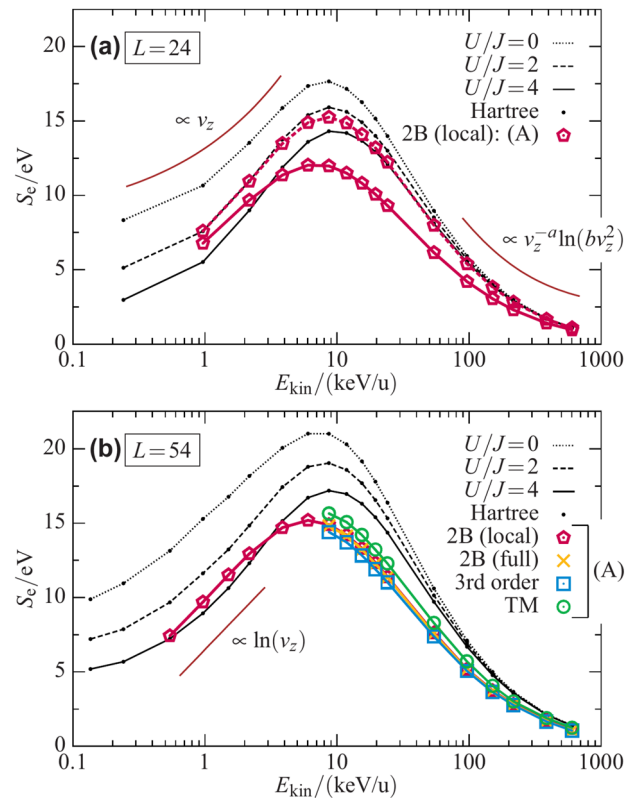
Figure 4. Energy loss of a proton with initial energy E_{kin} during passage through a honeycomb cluster [cf. Figure 1] of size $L = 24$ (top) and $L = 54$ (bottom). Local 2B denotes the local approximation for the second Born selfenergy ($\Sigma_{ij} = \delta_{ij}\Sigma_i$). Reproduced with permission.[29] Copyright 2016, American Physical Society.

(b) of Figure 4: with increasing size of the cluster more electrons are excited by the projectile and, hence, the energy deposition, S_e, grows.

With the increasing role of correlations, also the requirements for theory increase. For NEGF simulations, this means that the proper choice of the selfenergy becomes important, whereas, at high impact energy, the difference between different selfenergy approximations is rather small, cf. Figure 4(b). At the same time, reducing the impact energy increases the interaction time and, thus, also the simulation duration in our nonequilibrium approach grows rapidly. For this reason, in the range of $1 keV/u$ and below, so far, mostly local second order Born simulations (assuming $\Sigma_{ij} \sim \Sigma_i \delta_{ij}$) were performed. A comparison to mean field (Hartree) simulations clearly signals the importance of correlations for the stopping for strongly correlated materials, cf. curves for $U/J = 4$ in Figure 4(a).

4.2. Ion Impact Induced Doublon Excitation

A particularly interesting observation is that the deviation of the correlated simulations from the mean field result changes sign. While for high energy, correlations seem to lower the energy deposition, at impact energies below approximately $3 keV/u$, correlation effects enhance the stopping power. This is a

surprising effect, and one may speculate that this is due to an increase of the correlation energy. To verify this hypothesis we analyze, in the following, the doublon number, Equation (23), that is induced by the projectile. In fact, the total number of doublons or its cluster average, d_{av}, Equation (24), minus the mean field result,

$$d_i^{\mathrm{H}} = \langle \hat{n}_{i\uparrow}(t) \rangle \langle \hat{n}_{i\downarrow}(t) \rangle = n_{i\uparrow}(t) n_{i\downarrow}(t) \qquad (25)$$

is proportional to the correlation energy in the system.

The numerical analysis for the system in Figure 1 confirms, indeed, that a charged projectile with an impact energy in the range of a few hundred electron volts may create a significant number of doublons.[30] Details of this analysis are shown in **Figure 5** for the case of strong correlations ($U/J = 10$). In part (a), we show the electron densities at two lattice sites B and A adjacent to the impact point. During the impact of the projectile ($t = t_0$) electrons from the second nearest site (A) are attracted toward the nearest site B whereas the mean density remains constant. After the projectile has left, both densities, with some retardation, return to their initial values. Consider now the associated dynamics of the mean double occupations at sites A and B. While here, too, doublons are transferred from site A to B, the mean value, d_{av} increases significantly. Most importantly, after the projectile has left, d_{av} does not return to its initial value but remains at a significantly larger value. We conclude that the projectile has deposited correlation energy in the system that remains stored there. This is also confirmed by comparison with the uncorrelated average doublon number, Equation (25), which follows the average density and, hence, remains almost constant. In a quantum-mechanical language, under the action of the projectile, the electron system undergoes a transition to an excited state that is associated with a higher double occupation.[30] This explanation is directly confirmed by a representative dimer model that is discussed in Section 4.3.

4.3. Analytical Dimer Model

For a qualitative examination of the doublon generation in the system of Figure 1, the simplest possible setup is a dimer consisting of only the two sites, A and B, being driven by a pulsed attractive external potential. Since we expect that the excitation of doublons is governed only by the potential difference on sites A and B, it is sufficient to consider the excitation only on one site (B). The time dependence of the excitation is chosen as

$$W(t) = -W_0 \exp^{-(t-t_0)^2/2\tau^2} \qquad (26)$$

which closely resembles a positively charged projectile passing close to one site, where the two parameters W_0 and τ have clear implication as the amplitude (proportional to the charge of the ion) and the interaction duration (proportional to one over the velocity), respectively. For sufficiently large U this can lead to a significant and lasting increase of the mean double occupation d_{av}^∞, Equation (24). However d_{av}^∞ strongly depends on W_0 and τ, as is confirmed by exact diagonalization results that are shown in **Figure 6**. For an excitation amplitude W_0 smaller than U, the Hubbard-gap prevents the creation of doublons. For $W_0 > U$ doublon production is possible, and for larger W_0, oscillations caused by transient Bloch oscillations are observed,[30] the frequency of which grows with W_0. Interestingly, the envelopes of these curves are very similar to the stopping-power curves, cf. Figure 4. There the total energy gain of the electrons was plotted versus kinetic energy of the projectile which here corresponds to the inverse of τ^2. The results of Figure 6 reflect the fraction of the projectile energy that is transferred into an increase of the double occupation in the target, and a detailed analysis of the different energy contributions remains to be performed in future work. The most notable result is, that for an optimal choice of τ and W_0 a permanent increase of the double occupation of up to 0.5 per site can be achieved.

We have shown in ref. [30] that the dimer model captures the excitation physics not only qualitatively correctly. Using a Landau–Zener[78,79] approach the probability for doublon excitation of our model agrees even semi-quantitatively with

Figure 5. Time-dependent response of a strongly correlated finite honeycomb cluster of Figure 1 for $U/J = 10$ to a charged projectile with charge $Z = 2$ penetrating through the center (point C in Figure 1). a) The densities on sites A (dashed line) and B (full) closest to the projectile. b) Site-averaged double occupation, Equation (24). Exact diagonalization results, after ref. [30].
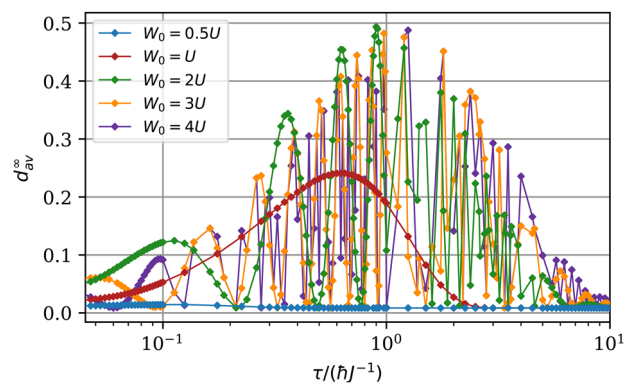
Figure 6. Asymptotic value of the average double occupation, Equation (24), of the dimer versus τ (proportional to the inverse projectile velocity) for $U = 15$ and different excitation amplitudes, W_0. When W_0 exceeds U, doublons are excited and remain in the system.

the simulation results for the $L = 12$ cluster of Figure 1 and shows the correct trends also for other systems, including the optimal coupling strength and projectile velocity that maximize the induced doublon number.

4.4. Doublon Dynamics Excited by Multiple Ion Impacts

The average doublon number in the system can be further increased by repeating the impact once or even more often. The analysis presented in ref. [30] showed that this allows to achieve an asymptotic average doublon number of $d_{av} = 0.25$ and even larger. A representative example is shown in **Figure 7**. At each impact the projectile rapidly increases d_i at the impact point, at the expense of the doublon number at the two nearest neighbor sites. This is followed by a spreading of $d_i(t)$ along the chain (notice the wave fronts). At the same time, with each successive impact, the average doublon number can be systematically increased which can be seen from the increasing doublon level in the foreground. In that figure the excitation is intentionally kept localized at the same central site [keeping only a single term in the sum over "i" in Equation (1)] in order to monitor the propagation of the doublon occupation along the cluster. Note that, when one restores the long-range ion–electron interaction (all terms in the sum over "i"), this gives rise to even larger values of d_{av}^∞.[30]

The ion induced nonequilibrium dynamics of the electron system can also be tracked in the spectral function which can be directly measured in photoemission experiments. In **Figure 8** we plot the photoemission spectrum, Equation (21), that gives information about the occupied energies. The projectiles induce transitions of electrons into the upper Hubbard band corresponding to $\omega > 0$. With each successive impact the spectral weight (corresponding to the fraction of electrons) in the upper Hubbard band grows, cf. the shaded areas.

As in the case of a single impact, Figure 5, also after multiple impacts, the many-electron system remains in the excited state characterized by a significantly increased average doublon occupation d_{av}^∞, after all projectiles have left. This stationary nonequilibrium state will be stable until additional dissipation

channels (e.g., to phononic degrees of freedom) set in and is another example of a pre-thermalized state, for example, refs. [80,81]. In contrast to previous spatially homogeneous doublon excitation scenarios that used time-dependent electric fields or a modulation of the lattice depth, for example, ref. [82], here a local excitation is used that has much more degrees of freedom, including timing and locations of the impacts, and a potential to achieve higher doublon numbers and an increased stopping power.

5. Embedding Scheme to Capture Charge Transfer Dynamics Between Projectile and Target

So far we have considered only the case of high projectile velocities where the feedback from the surface to the ion is small and restricted to a reduction of its velocity whereas quantum effects are neglected. On the other hand, when the impact velocity is reduced, the interaction duration of the projectile with the lattice increases and electron transfer between both systems may occur.
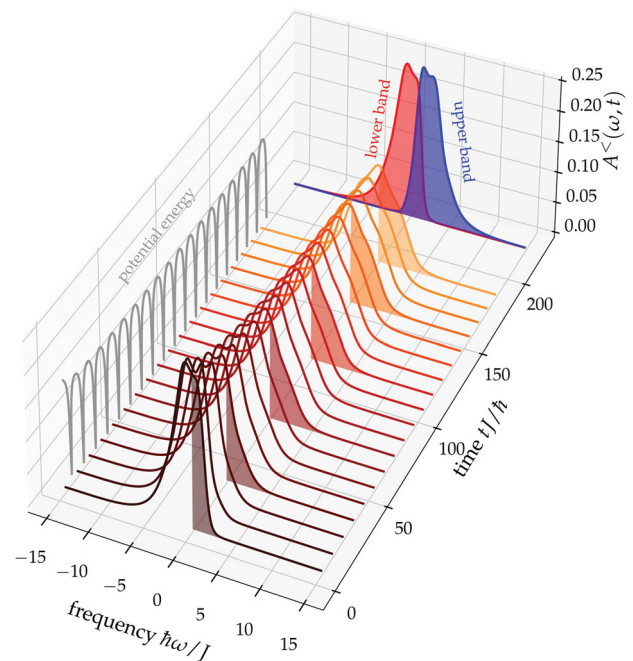
Figure 8. Time evolution of the spectral function of the occupied states, $A^<$ (photoemission spectrum), for the honeycomb cluster with $L = 12$ sites, Figure 1, and $U/J = 4$, from a two-time NEGF simulation with second order Born selfenergies. The cluster is excited by 20 equidistant ion impacts (at times 10, 20, … 200) in the center using a Coulomb potential for the electron–projectile interaction, cf. Equation (1) and the grey line on the left. The projectiles lead to an increased occupation of the upper Hubbard band corresponding to $\omega > 0$, cf. the shaded areas. The spectra are shown at times 5, 15, … 195 with a width of the probe pulse [cf. Equation (21)] of $\kappa = 2.5\hbar/J$ which causes a spectral broadening. For comparison, we also present the results of an unexcited cluster, where only the lower Hubbard band is occupied, depicted by the red filled area corresponding to $A^<$, whereas the unoccupied upper Hubbard band ($A^>$) is shown by the blue area.

Figure 7. Time evolution of the site-resolved doublon number, $d_i(t)$, Equation (23), for a 1D cluster with $L = 24$ sites (periodic boundary conditions) and $U/J = 4$. The cluster is excited by ten ion impacts in the center (at site 12) using the Gaussian model (26). The increase of $d_{av}^\infty(t)$ can be seen from the slope of the surface. Note the logarithmic scale.

Quantum transitions inside the projectile and charge transfer have been studied approximately with quantum kinetic models (Newns-Anderson model) where the projectile was treated as a few level system.[83] Furthermore, there have been a number of TDDFT studies of ions impinging onto correlated materials such as graphene or boron nitride (BN)[7,8] and on finite systems such as metal clusters,[84,85] carbon nanostructures,[86] or graphene fragments[87] (for more references see ref. [2]), where quantum transitions inside the projectile are taken into account. However, the uncertainties in the quality of the adiabatic LDA and the model parameters in the Newns-Anderson model, respectively, as well as the neglect of correlation effects in the material[2] make it desirable to develop an independent many-body approach to this problem.

Here, we present a nonequilibrium Green functions approach for the electron transfer dynamics between projectile and a strongly correlated solid. We start from the second-quantized many-body Hamiltonian for the electrons in the plasma–solid interface and separate the system into a plasma (p) and solid surface part (s) [we denote $\Omega = \{p, s\}$ and do not write the spin index explicitly],

$$
\begin{aligned}
H_{\text{interface}} = & \sum_{\alpha\beta \in \Omega} \sum_{ij} H_{ij}^{\alpha\beta}(t) c_i^{\alpha\dagger} c_j^{\beta} \\
& + \frac{1}{2} \sum_{\alpha\beta\gamma\delta \in \Omega} \sum_{ijkl} W_{ijkl}^{\alpha\beta\gamma\delta} c_i^{\alpha\dagger} c_j^{\beta\dagger} c_k^{\gamma} c_l^{\delta}
\end{aligned}
\tag{27}
$$

Here, the operator $c_i^{\alpha\dagger}$ $\left(c_i^{\alpha}\right)$ creates (annihilates) an electron in the state i of part α. The one-particle Hamiltonian $H(t)$ contains the kinetic and the time-dependent potential energy of electrons, and W accounts for all possible electron–electron Coulomb interactions within and between the two parts.

Considering individual energetic plasma ions, which penetrate into the solid, undergo scattering and stopping in the surface layers or are reflected, we describe the system (27) by a one-particle nonequilibrium Green function (2), $G_{ij}^{\alpha\beta}(t, t')$, which now has an additional 2×2 matrix structure ($\alpha, \beta = \{p, s\}$),

$$
G_{ij}^{\alpha\beta}(t, t') = -i\hbar \langle T_C c_i^{\alpha}(t) c_j^{\beta\dagger}(t') \rangle
\tag{28}
$$

$$
\rho_{ij}^{\alpha\beta}(t) = -i\hbar G_{ji}^{\beta\alpha}(t, t^+)
\tag{29}
$$

for example, refs. [45,88], and the time-diagonal elements provide the density matrix (29). The diagonal elements, ρ_{ij}^{pp} $\left[\rho_{ij}^{ss}\right]$, refer to the plasma part, describing the dynamics of free electrons and electrons bound in the ion [to the solid part, describing electrons in bound states of the solid surface]. Moreover, the density matrix component ρ_{ij}^{ps} is related to charge transfer processes between plasma and solid and will be of special interest in the following.

The equations of motion for the NEGF are the generalization of Equation (3) to the plasma–solid interface,

$$
\begin{aligned}
& i\hbar\partial_t G_{ij}^{\alpha\beta}(t, t') - \sum_{\delta \in \Omega, k} H_{ik}^{\alpha\delta}(t) G_{kj}^{\delta\beta}(t, t') \\
& = \delta_{ij}^{\alpha\beta} \delta_C(t, t') + \sum_{\delta \in \Omega, k} \int_C d\bar{t} \Sigma_{ik}^{\alpha\delta}[W, G](t, \bar{t}) G_{kj}^{\delta\beta}(\bar{t}, t')
\end{aligned}
\tag{30}
$$

where the self-energy $\Sigma^{\alpha\beta}(t, t')$ describes the interaction between the electrons and with phonons. Even though a complete solution of the KBE (30) for real materials and with a full quantum treatment of the plasma electrons is out of reach, these equations provide the rigorous starting point for the development of consistent approximations. In the following, we show how it is possible to include the electronic states of the ion via an embedding self-energy approach that was previously applied to quantum transport and photoionization problems, for example, refs. [89,90], for a text book discussion, see ref. [45]. Here the embedding approach allows us to study resonant (neutralization and ionization) processes at the plasma–solid interface. While this embedding approach is based on a formal decoupling of the surface and plasma parts of the KBE, it retains one-electron charge transfer in the Hamiltonian H^{sp}, cf. Equation (33), see below. A closed description of the solid can be maintained if correlations in the plasma part and the feedback of the solid on the plasma can be neglected, that is, for $\Sigma^{sp} \approx \Sigma^{pp} \approx 0$. This is usually well fulfilled in plasmas, except for plasmas at or beyond atmospheric pressure or in warm dense matter[91] where small correlation corrections should be taken into account. Then, the KBE (3) for the plasma part simplify to

$$
\sum_k \{i\hbar\partial_t \delta_{ik} - H_{ik}^{pp}(t)\} g_{kj}^{pp}(t, t') = \delta_{ij}\delta_C(t, t')
\tag{31}
$$

where the solution $g^{pp}(t, t')$ denotes the NEGF of the electrons inside the plasma ions [here we do not consider processes involving free electrons in the plasma phase because they do not contribute to charge transfer except for heavy particle induced secondary electron emission], whereas the time dependence of $H^{pp}(t)$ accounts for possible parametric changes of the energy levels (e.g., as function of the distance of the ion from the surface).

The main result of the embedding procedure is a closed equation for $G^{ss}(t, t')$:

$$
\begin{aligned}
& \sum_k \{i\hbar\partial_t \delta_{ik} - H_{ik}^{ss}(t)\} G_{kj}^{ss}(t, t') = \delta_{ij}\delta_C(t, t') \\
& \sum_k \int_C d\bar{t} \{\Sigma_{ik}^{ct}(t, \bar{t}) + \Sigma_{ik}^{ss}[G^{ss}](t, \bar{t})\} G_{kj}^{ss}(\bar{t}, t')
\end{aligned}
\tag{32}
$$

to be complemented with the adjoint equation, with the charge transfer (or embedding) self-energy that involves the charge transfer hamiltonian

$$
\Sigma_{ij}^{ct}(t, t') = \sum_{kl} H_{ik}^{sp}(t) g_{kl}^{pp}(t, t') H_{lj}^{ps}(t')
\tag{33}
$$

$$
H_{ij}^{sp}(t) = \int d^3r \phi_i^s(\mathbf{r}) \left(\hat{T} + \hat{V}\right) \phi_j^p(\mathbf{r}; t)
\tag{34}
$$

Equation (32) shows how the many-body description of an isolated (but correlated) solid is altered by the presence of the electronic states of a plasma ion (or neutral), with the latter giving rise to an additional self-energy $\Sigma^{ct}(t, t')$. While, for $\Sigma^{ct} = 0$, the KBE (32) conserve the particle number and total energy [for a conserving approximation of the self-energy Σ^{ss},

such as the ones discussed in Section 3.2], the inclusion of the embedding self-energy explicitly allows for time-dependent changes of the particle number (and energy) in the solid and, thus, accounts for ion charging and neutralization effects. For the practical solution of Equation (32), the charge transfer Hamiltonian $H^{sp}(t)$ has to be computed by selecting the relevant electronic transitions between solid and plasma and computing the matrix elements of the kinetic and potential energy operators $\hat{T}$ and $\hat{V}$, with the electronic single-particle wave functions ϕ^s (ϕ^p) in the solid (ion).

A first test of this embedding scheme is shown in **Figure 9**, where a correlated Hubbard chain (for simplicity only the last site is correlated) is coupled to a single active energy level $\varepsilon_p = J$ of an approaching ion *via* the charge transfer hamilton $H_i^{sp}(t) = \delta_{iL}\Gamma(t)$, cf. the sketch on top of Figure 9. The time dependence of H_i^{sp} is approximated by $\Gamma(t) = \Gamma_0 e^{-(t-t_0)^2/(2\tau^2)}$,

and the initial occupation of the energy level ε_p is set to $n_\sigma = 0.269$.

The charge transfer from the chain to the ion, seen in the reduction of the total electron number in the chain, $N_\sigma(t) = \sum_i n_{i\sigma}(t)$, is shown as a function of time in Figure 9 (a). The reduction of N_σ is found to be nearly proportional to the ion charge (amplitude Γ_0) up to the resonance condition $\Gamma_0 = J$. Thus, as expected, a highly charged ion will be more strongly neutralized. For $\Gamma_0 > J$, away from resonance, the net transfer of charge will decrease again. The neutralization time is given by the interaction duration τ which is inversely proportional to the projectile velocity. The dependence of the magnitude of the charge transfer on τ is analyzed in Figure 9(c) and again confirms the expected trend: the charge transfer increases with τ, i.e., is larger for slower projectiles, whereas for $\tau \lesssim 0.1\hbar/J$ it is negligible. Figure 9(b) shows the spatial propagation of the removed charge (hole) along the chain as a function of time (the distortion of the dip is due to reflections from the edge of the chain). Again one sees that, in the presence of correlations, the propagation speed is reduced, in agreement with simulations of fermion propagation in optical lattices.[24,25]

Finally, we can analyze the effect of correlations in the target on the charge transfer. As can be seen in Figure 9(a) and (c), an increase of electron–electron correlations reduces the charge transfer, which is a consequence of the reduced mobility of the electrons in the chain. An increase of the interaction strength from zero to $U = 4/J$, which is a realistic range for graphene nanoribbons, reduces the charge transfer by about 20%, in the present setup.

In conclusion, we have demonstrated a NEGF approach to charge transfer between a plasma ion and a strongly correlated finite electron system. The next task is to derive improved data for the energy levels and occupations of the projectile. Further, the resonant charge transfer, studied in this section, and the energy deposition and electronic excitation of the target that were discussed in Section 4, should be integrated into a single model to take into account the mutual influences of both processes.

Figure 9. Numerical illustration of the embedding scheme. An initially half-filled tight-binding chain ($L = 10$ sites, nearest-neighbor hopping J, Hubbard interaction strength U on the last site, and inverse temperature $\beta_s = 100J^{-1}$) is interacting with an external energy level $\varepsilon_p = J$ via a time-dependent coupling $\Gamma(t) = \Gamma_0 e^{-(t-t_0^2)/(2\tau^2)}$, cf. bottom of part (b), giving rise to the transfer of charge. The initial occupation of the energy level is given by $n_\sigma = 0.269$ (corresponding to a Fermi distribution with an inverse temperature $\beta_p = 1J^{-1}$). a) Time evolution of the total particle number $N_\sigma(t)$ for different U and Γ_0, computed from Equation (32) with a local second Born self-energy ($\Sigma_{ij} = \delta_{ij}\Sigma_i$); $\tau = 1\hbar J^{-1}$. b) Local electron densities $n_{l\sigma}(t)$ and correlation part of the double occupation $d_L^{cor}(t) = d_L(t) - d_L^H(t)$ on the last site $l = L = 10$ for $U = 3$, $\Gamma_0 = 1J$ and $\tau = 1\hbar J^{-1}$; for times $t - t_0 \lesssim -5$ the time evolution of $d_L^{cor}(t)$ corresponds to the ground state preparation by adiabatic switching (AS). c) Final values of the particle number $N_\sigma(t \to \infty)$ as function of the interaction time τ for different U and Γ_0.

6. Summary and Discussion

In this article, we studied correlated inhomogeneous finite graphene-type Hubbard clusters. Our results are expected to be relevant for ultracold fermionic atoms in optical lattices as well as for electrons in graphene clusters and nanoribbons. We considered the electronic response to a spatially and temporally localized excitation by a charged particle. Using a nonequilibrium Green functions approach we computed, via an Ehrenfest approach, the time-dependent interaction of the projectile with the many-electron system and the dependence of the energy transfer on the impact energy.[29] An interesting observation was that, at low projectile energies, correlation effects lead to an enhanced energy transfer. Our analysis revealed that the ion impact causes a transition of the system across the Hubbard gap leading to the formation of doubly occupied lattice sites (doublons).[30] We investigated the spatial propagation of the doublon number across the cluster. Eventually a homogeneous nonequilibrium steady state is reached that is long lived and may

have interesting electronic and optical properties. A physically intuitive picture was given in terms of an analytical model for a two-site system where the doublon formation is explained in terms of a twofold passage of an avoided crossing (Landau-Zener picture[30]). The effect should be of relevance for graphene nanoribbons and be particularly important for strongly correlated finite systems. For an experimental observation the best candidates are fermionic atoms in optical lattices. There the projectile impact can be easily mimicked by a proper time-dependent modulation of the lattice potentials nearest to the "impact" point.

We demonstrated that doublon formation and propagation in correlated finite lattice systems can be accurately simulated with NEGF. In addition to two-time results we presented single-time results within the generalized Kadanoff–Baym ansatz (GKBA) with Hartree–Fock propagators (HF-GKBA). To further improve the accuracy of GKBA calculations in the future, we introduced the correlated GKBA (C-GKBA) that allows to systematically incorporate correlation effects in the propagators $G^{R/A}$. Moreover, we discussed how to systematically take into account initial correlations in the GKBA and presented an idea that is complementary to recent results for equilibrium correlations.[67,71]

Aside from an accurate treatment of correlation effects, quantitatively reliable NEGF results also require to improve the underlying model. One way to go beyond the present one-band Hubbard model is to use an extended Hubbard model as demonstrated in ref. [31], or to perform ab initio *NEGF* simulations using a Kohn-Sham basis, for example, on the basis of the Yambo code.[92]

Acknowledgments

Conflict of Interest

The authors declare no conflict of interest.

Keywords

[1] I. Adamovich, S. D. Baalrud, A. Bogaerts, P. J. Bruggeman, M. Cappelli, V. Colombo, U. Czarnetzki, U. Ebert, J. G. Eden, P. Favia, D. B. Graves, S. Hamaguchi, G. Hieftje, M. Hori, I. D. Kaganovich, U. Kortshagen, M. J. Kushner, N. J. Mason, S. Mazouffre, S. M. Thagard, H.-R. Metelmann, A. Mizuno, E. Moreau, A. B. Murphy, B. A. Niemira, G. S. Oehrlein, Z. L. Petrovic, L. C. Pitchford, Y.-K. Pu, S. Rauf, O. Sakai, S. Samukawa, S. Starikovskaia, J. Tennyson, K. Terashima,

[2] M. M. Turner, M. C. M. van de Sanden, A. Vardelle, *J. Phys. D: Appl. Phys.* **2017**, *50*, 323001.

[2] M. Bonitz, V. Filinov, J. Abraham, K. Balzer, H. Kaehlert, E. Pehlke, F. X. Bronold, M. Pamperin, M. Becker, D. Loffhagen, H. Fehske, *Front. Chem. Sci. Eng.* **2019**, accepted for publication; arXiv:1809.02473.

[3] P. Sigmund, *Particle Penetration and Radiation Effects*. Springer, Berlin, Heidelberg **2006**. https://www.springer.com/de/book/9783540317135

[4] I. Nagy, B. Apagyi, *Phys. Rev. A* **1998**, *58*, R1653.

[5] J. M. Pitarke, R. H. Ritchie, P. M. Echenique, *Phys. Rev. B* **1995**, *52*, 13883.

[6] M. Quijada, A. G. Borisov, I. Nagy, R. D. Muiño, P. M. Echenique, *Phys. Rev. A* **2007**, *75*, 042902.

[7] A. Ojanperä, A. V. Krasheninnikov, M. Puska, *Phys. Rev. B* **2014**, *89*, 035120.

[8] S. Zhao, W. Kang, J. Xue, X. Zhang, P. Zhang, *J. Phys.: Condens. Matter* **2015**, *27*, 025401.

[9] J. F. Ziegler, M. Ziegler, J. Biersack, *Nucl. Instrum. Methods Phys. Res. B* **2010**, *268*, 1818, 19th International Conference on Ion Beam Analysis.

[10] L. Yang, C.-H. Park, Y.-W. Son, M. L. Cohen, S. G. Louie, *Phys. Rev. Lett.* **2007**, *99*, 186801.

[11] M. Y. Han, B. Özyilmaz, Y. Zhang, P. Kim, *Phys. Rev. Lett.* **2007**, *98*, 206805.

[12] K. Nakada, M. Fujita, G. Dresselhaus, M. S. Dresselhaus, *Phys. Rev. B* **1996**, *54*, 17954.

[13] Y.-W. Son, M. L. Cohen, S. G. Louie, *Phys. Rev. Lett.* **2006**, *97*, 216803.

[14] P. Ruffieux, J. Cai, N. C. Plumb, L. Patthey, D. Prezzi, A. Ferretti, E. Molinari, X. Feng, K. Müllen, C. A. Pignedoli, R. Fasel, *ACS Nano* **2012**, *6*, 6930.

[15] H. Söde, L. Talirz, O. Gröning, C. A. Pignedoli, R. Berger, X. Feng, K. Müllen, R. Fasel, P. Ruffieux, *Phys. Rev. B* **2015**, *91*, 045429.

[16] S. Wang, L. Talirz, C. A. Pignedoli, X. Feng, K. Müllen, R. Fasel, P. Ruffieux, *Nat. Commun.* **2016**, *7*, 11507.

[17] J. Bai, X. Duan, Y. Huang, *Nano Lett.* **2009**, *9*, 2083.

[18] L. Jiao, X. Wang, G. Diankov, H. Wang, H. Dai, *Nat. Nanotechnol.* **2010**, *5*, 321.

[19] A. Kimouche, M. M. Ervasti, R. Drost, S. Halonen, A. Harju, P. M. Joensuu, J. Sainio, P. Liljeroth, *Nat. Commun.* **2015**, *6*, 10177.

[20] S. A. Jensen, R. Ulbricht, A. Narita, X. Feng, K. Müllen, T. Hertel, D. Turchinovich, M. Bonn, *Nano Lett.* **2013**, *13*, 5925.

[21] I. Gierz, F. Calegari, S. Aeschlimann, M. Chávez Cervantes, C. Cacho, R. T. Chapman, E. Springate, S. Link, U. Starke, C. R. Ast, A. Cavalleri, *Phys. Rev. Lett.* **2015**, *115*, 086803.

[22] B. V. Senkovskiy, A. V. Fedorov, D. Haberer, M. Farjam, K. A. Simonov, A. B. Preobrajenski, N. Mårtensson, N. Atodiresei, V. Caciuc, S. Blügel, A. Rosch, N. I. Verbitskiy, M. Hell, D. V. Evtushinsky, R. German, T. Marangoni, P. H. M. van Loosdrecht, F. R. Fischer, A. Grüneis, *Adv. Electron. Mater.* **2017**, *3*, 1600490.

[23] I. Ivanov, Y. Hu, S. Osella, U. Beser, H. I. Wang, D. Beljonne, A. Narita, K. Müllen, D. Turchinovich, M. Bonn, *J. Am. Chem. Soc.* **2017**, *139*, 7982.

[24] N. Schlünzen, M. Bonitz, *Contrib. Plasma Phys.* **2016**, *56*, 5.

[25] N. Schlünzen, S. Hermanns, M. Bonitz, C. Verdozzi, *Phys. Rev. B* **2016**, *93*, 035107.

[26] N. Schlünzen, J.-P. Joost, F. Heidrich-Meisner, M. Bonitz, *Phys. Rev. B* **2017**, *95*, 165139.

[27] P. Lipavský, V. Špička, B. Velický, *Phys. Rev. B* **1986**, *34*, 6933.

[28] S. Hermanns, N. Schlünzen, M. Bonitz, *Phys. Rev. B* **2014**, *90*, 125111.

[29] K. Balzer, N. Schlünzen, M. Bonitz, *Phys. Rev. B* **2016**, *94*, 245118.

[30] K. Balzer, M. Rodriguez Rasmussen, N. Schlünzen, J. P. Joost, M. Bonitz, *Phys. Rev. Lett.* **2018**, *121*, 267602.

[31] J.-P. Joost, N. Schlünzen, M. Bonitz, *Phys. Status Solidi B* **2019**, *256*, 1800498 (this issue).

[32] L. Keldysh, *Soviet Phys. JETP* **1965**, *20*, 1018 (Zh. Eksp. Teor. Fiz. **1964**, *47*, 1515).

[33] L. Kadanoff, G. Baym, *Quantum Statistical Mechanics*. Benjamin, New York **1962**.

[34] M. Bonitz, *Quantum Kinetic Theory, Teubner-Texte zur Physik*, 2nd edition. Springer, International Publishing, Switzerland **2016**. https://www.springer.com/de/book/9783319241197

[35] M. Bonitz, D. Kremp, *Phys. Lett. A* **1996**, *212*, 83.

[36] M. Bonitz, D. Kremp, D. C. Scott, R. Binder, W. D. Kraeft, H. S. Köhler, *J. Phys.: Condens. Matter* **1996**, *8*, 6057.

[37] M. Bonitz, *Phys. Lett. A* **1996**, *221*, 85.

[38] D. Kremp, M. Bonitz, W. Kraeft, M. Schlanges, *Ann. Phys. (NY)* **1997**, *258*, 320.

[39] M. Bonitz, R. Nareyka, D. Semkat, *Progress in Nonequilibrium Green's Functions: Proceedings of the Conference "Kadanoff-Baym Equations: Progress and Perspectives for Many-body Physics" (Rostock, Germany, 20–24 September 1999)*. World Scientific, Singapore **2000**.

[40] M. Bonitz, D. Semkat, *Progress in Nonequilibrium Green's Functions II*. World Scientific, Singapore **2003**.

[41] M. Bonitz, A. Filinov, *J. Phys. Conf. Ser.* **2006**, *35*. http://iopscience.iop.org/issue/1742-6596/35/1

[42] M. Bonitz, K. Balzer, *J. Phys. Conf. Ser.* **2010**, *220*, 011001.

[43] R. van Leeuwen, R. Tuovinen, M. Bonitz, *J. Phys. Conf. Ser.* **2013**, *427*, 011001.

[44] C. Verdozzi, A. Wacker, C.-O. Almbladh, M. Bonitz, *J. Phys. Conf. Ser.* **2016**, *696*, 011001.

[45] G. Stefanucci, R. van Leeuwen, *Nonequilibrium Many-Body Theory of Quantum Systems*. Cambridge University Press, Cambridge **2013**.

[46] M. Bonitz, A. Jauho, M. Sadovskii, S. Tikhodeev, *Phys. Status Solidi B* **2019**, *256*, 1800600 (this issue).

[47] S. Hermanns, K. Balzer, M. Bonitz, *Phys. Scr.* **2012**, *2012*, 014036.

[48] S. Hermanns, *Nonequilibrium Green functions. Selfenergy approximation techniques*, Ph.D. thesis, Kiel University, Kiel, Germany **2016**, unpublished.

[49] K. Balzer, M. Bonitz, *Nonequilibrium Green's Functions Approach to Inhomogeneous Systems*, Number 867 in Lecture Notes in Physics. Springer, Berlin, Heidelberg **2013**.

[50] M. P. von Friesen, C. Verdozzi, C.-O. Almbladh, *Phys. Rev. B* **2010**, *82*, 155108.

[51] N. Schlünzen, J.-P. Joost, M. Bonitz, *Phys. Rev. B* **2017**, *96*, 117101.

[52] L. Bányai, D. B. T. Thoai, E. Reitsamer, H. Haug, D. Steinbach, M. U. Wehner, M. Wegener, T. Marschner, W. Stolz, *Phys. Rev. Lett.* **1995**, *75*, 2188.

[53] H. Haug, A.-P. Jauho, *Quantum Kinetics in Transport and Optics of Semiconductors*. Springer, Berlin, Heidelberg **2008**.

[54] M. Lorke, T. R. Nielsen, J. Seebeck, P. Gartner, F. Jahnke, *J. Phys. Conf. Ser.* **2006**, *35*, 182.

[55] J. Seebeck, T. R. Nielsen, P. Gartner, F. Jahnke, *Phys. Rev. B* **2005**, *71*, 125327.

[56] D. Kremp, T. Bornath, M. Bonitz, M. Schlanges, *Phys. Rev. E* **1999**, *60*, 4725.

[57] M. Bonitz, T. Bornath, D. Kremp, M. Schlanges, W. D. Kraeft, *Contrib. Plasma Phys.* **1999**, *39*, 329.

[58] H. Haberland, M. Bonitz, D. Kremp, *Phys. Rev. E* **2001**, *64*, 026405.

[59] N. Kwong, M. Bonitz, R. Binder, H. Köhler, *Phys. Status Solidi B* **1998**, *206*, 197.

[60] S. Hermanns, K. Balzer, M. Bonitz, *J. Phys. Conf. Ser.* **2013**, *427*, 012008.

[61] K. Balzer, S. Hermanns, M. Bonitz, *J. Phys. Conf. Ser.* **2013**, *427*, 012006.

[62] M. Bonitz, S. Hermanns, K. Balzer, *Contrib. Plasma Phys.* **2013**, *53*, 778.

[63] M. Bonitz, D. Semkat, H. Haug, *Eur. Phys. J. B* **1999**, *9*, 309.

[64] V. Spicka, B. Velicky, A. Kalvova, *Int. J. Mod. Phys. B* **2014**, *28*, 1430013.

[65] A. Kalvova, B. Velicky, V. Spicka, *EPL (Europhys. Lett.)* **2018**, *121*, 67002.

[66] M. Hopjan, *Theoretical developments for the real-time description and control of nanoscale systems*, PhD thesis, Lund University, Faculty of Science, Department of Physics, Division of Mathematical Physics, **2018**.

[67] M. Hopjan, C. Verdozzi, *Eur. Phys. J. Spec. Top.* **2019**, https://doi.org/10.1140/epjst/e2018-800054-3.

[68] P. Danielewicz, *Ann. Phys. (NY)* **1984**, *152*, 305.

[69] D. Semkat, D. Kremp, M. Bonitz, *J. Math. Phys.* **2000**, *41*, 7458.

[70] D. Kremp, M. Schlanges, W. Kraeft, *Quantum Statistics of Nonideal Plasmas*. Springer, Berlin, Heidelberg **2005**.

[71] D. Karlsson, R. van Leeuwen, E. Perfetto, G. Stefanucci, *Phys. Rev. B* **2018**, *98*, 115148.

[72] D. Semkat, M. Bonitz, D. Kremp, *Contrib. Plasma Phys.* **2003**, *43*, 321.

[73] M. Bonitz, S. Hermanns, K. Kobusch, K. Balzer, *J. Phys. Conf. Ser.* **2013**, *427*, 012002.

[74] M. Eckstein, M. Kollar, *Phys. Rev. B* **2008**, *78*, 245113.

[75] K. Balzer, N. Schlünzen, M. Bonitz, *Phys. Rev. B* **2016**, *94*, 245118.

[76] M. Scharnke, N. Schlünzen, M. Bonitz, *J. Math. Phys.* **2017**, *58*, 061903.

[77] M. Bonitz, M. Scharnke, N. Schlünzen, *Contrib. Plasma Phys.* **2018**, *58*, 1036.

[78] L. D. Landau, *Phys. Z. Sowjetunion* **1932**, *2*, 46.

[79] C. Zener, *Proc. R. Soc. Lond. A, Math. Phys. Eng. Sci.* **1932**, *137*, 696.

[80] M. Kollar, F. A. Wolf, M. Eckstein, *Phys. Rev. B* **2011**, *84*, 054304.

[81] A. V. Joura, J. K. Freericks, A. I. Lichtenstein, *Phys. Rev. B* **2015**, *91*, 245153.

[82] A. Tokuno, E. Demler, T. Giamarchi, *Phys. Rev. A* **2012**, *85*, 053601.

[83] M. Pamperin, F. X. Bronold, H. Fehske, *Phys. Rev. B* **2015**, *91*, 035440.

[84] C. L. Moss, C. M. Isborn, X. Li, *Phys. Rev. A* **2009**, *80*, 024503.

[85] A. Castro, M. Isla, J. I. Martínez, J. A. Alonso, *Chem. Phys.* **2012**, *399*, 130.

[86] A. V. Krasheninnikov, Y. Miyamoto, D. Tománek, *Phys. Rev. Lett.* **2007**, *99*, 016104.

[87] S. Bubin, B. Wang, S. Pantelides, K. Varga, *Phys. Rev. B* **2012**, *85*, 235435.

[88] K. Balzer, M. Bonitz, *Nonequilibrium Green's Functions Approach to Inhomogeneous Systems*. Springer, Berlin, Heidelberg **2013**.

[89] P. Myöhänen, A. Stan, G. Stefanucci, R. van Leeuwen, *Phys. Rev. B* **2009**, *80*, 115107.

[90] E. Perfetto, A.-M. Uimonen, R. van Leeuwen, G. Stefanucci, *J. Phys. Conf. Ser.* **2016**, *696*, 012004.

[91] T. Dornheim, S. Groth, M. Bonitz, *Phys. Rep.* **2018**, *744*, 1.

[92] A. Marini, C. Hogan, M. Grüning, D. Varsano, *Comput. Phys. Commun.* **2009**, *180*, 1392.

Chapter 3

Theoretical Developments of the NEGF Formalism

Several methodological improvements have been required for the NEGF method to be applicable in the context of practically relevant correlated lattice systems. In the following, it is demonstrated how the NEGF technique is brought to its ultimate scaling limit (III). Furthermore, serious theoretical shortcomings are eradicated to put the method on a more solid foundation (I).

3.1 Single-Time Equations for the NEGF: the G1–G2 Scheme

In 1986, Lipavský *et al.* published a seminal paper [107] that opened the path to experimentally relevant long-time NEGF simulations by introducing the GKBA. Particularly the greatly advantageous tandem of the second-order selfenergy and the HF-GKBA (SOA-HF-GKBA) has become a workhorse for NEGF calculations (see, e.g., Refs. [101, 129, 136]). While the full two-time NEGF equations yield a computational scaling of $\mathcal{O}\left(N_\mathrm{t}^3\right)$, where N_t is the number of time steps, the SOA-HF-GKBA drops this scaling to $\mathcal{O}\left(N_\mathrm{t}^2\right)$. The increase of computational power has brought about a second rise of GKBA-related activity during the last decade with a variety of successful applications including atoms [126], metallic clusters [248], semiconductors [249], ultracold atoms in optical lattices (see Sec. 4.2), biologically relevant molecules [250], carbon allotropes [113], two-dimensional layered materials [110, 112] as well as ion stopping in hexagonal lattices (see Secs. 2.2 and 4.3).

At the same time, it has become clear that a description on the second-order level is not sufficient to correctly predict the time evolution of strongly correlated systems [79, 109, 130, 212, 213]. However, the usage of higher-order selfenergies and powerful resummation techniques for the GKBA reverts to the unfavorable time scaling of $\mathcal{O}\left(N_\mathrm{t}^3\right)$. This drastically reduces the applicability of the GKBA to strongly correlated systems of practical relevance,

such as heterostructures of graphene nanoribbons [119, 251], irradiated krypton[1] [252], and exotic warm dense matter (WDM) [9–11]. Therefore, much effort has been put into developments to improve and extend the GKBA. A natural generalization is to replace the Hartree–Fock propagators with higher-order choices for the retarded and advanced Green functions which is discussed, e.g., in Refs. [203, 207]. Additionally, the relation between the NEGF equations with the HF-GKBA and the independent RDO theory has been analyzed in Refs. [96, 134] on the second-order level from the RDO perspective. In recent years, also the optimized treatment of initial correlations has attracted considerable interest [207, 253, 254]. Particularly Refs. [207] and [253] demonstrated a way to restart a HF-GKBA simulation after the build-up of correlations by replacing the preceding time evolution by an initial, time-local term. Motivated by this research, the author, in close collaboration with Jan-Philip Joost, asked the question: "Can we achieve $\mathcal{O}\left(N_\mathrm{t}^1\right)$ scaling for HF-GKBA simulations?" Astonishingly, the answer is yes. This raises the applicability of the method onto a next level, thereby opening up the way towards previously unfeasible investigations. The research in this course then addressed different integral and differential formulations, recovered the link to the RDO theory,[2] and led to the following publications,[3,4] Refs. [114] and [208].

Ref. [114] introduces the G1–G2 scheme—a time-linear reformulation of the HF-GKBA from the perspective of nonequilibrium Green functions. It is demonstrated for the second-order selfenergy and, for the first time, for the GW approximation, that a time-local set of equations can be found if the collision terms are computed from the time-diagonal two-particle Green function instead of the original selfenergy integral. The complete set of coupled differential equations for the single-particle and two-particle Green function (hence the name G1–G2 scheme) involves no additional approximation, but contains the full information of the two-time correlation selfenergy. To facilitate a simple, universal applicability, the equations are given for a general single-particle basis, as well as the Hubbard model and the homogeneous electron gas—the latter being of central importance for WDM applications mentioned above. Ref. [114] also analyzes the numerical scaling of the new-found scheme with respect to the number of time steps and the size of the single-particle basis—with a striking outcome: the G1–G2 scheme turns out to be numerically favorable compared to the ordinary HF-GKBA for nearly all cases of practical relevance. A remarkable observation is made for the GW approximation describing dynamical-screening effects, where the time scaling is reduced from $\mathcal{O}\left(N_\mathrm{t}^3\right)$ to $\mathcal{O}\left(N_\mathrm{t}^1\right)$, leading to practical achievable speed-up factors of up to 10^4. Furthermore, while the test calculations for the Hubbard model perfectly agree with the HF-GKBA results, the G1–G2 description even reveals superior numerical accuracy for comparable integration methods. Additionally, Ref. [114] demonstrates that previously inaccessible two-particle quantities, such as the pair-distribution function and the pair-correlation function, are within reach for the new

---

[1]It is demonstrated in Ref. [126] that the experimentally validated transition to Kr^{3+} is not captured by the second-order selfenergy.

[2]In RDO theory, time-local equations for the single-particle and two-particle reduced density matrix are known on different approximation levels [96].

[3]N. Schlünzen, J.-P. Joost, and M. Bonitz, Phys. Rev. Lett., **124**, 076601 (2020). Copyright by the American Physical Society. Reproduced with permission.

[4]J.-P. Joost, N. Schlünzen, and M. Bonitz, Phys. Rev. B, **101**, 245101 (2020). Copyright by the American Physical Society. Reproduced with permission.

method, due to the explicit evaluation of the time-diagonal two-particle Green function. These quantities are of great practical relevance as they are measured experimentally, e.g., for ultracold gases in optical lattices to indicate long-range correlations [146]. In addition, two-particle correlation quantities constitute a conceptual barrier for many other quantum simulation tools, such as DFT-based approaches [255].

The advantageous numerical scaling of the G1–G2 scheme will allow for simulations on an experimentally relevant (long-)time scale for systems that have been out of reach, so far. It has already been directly applied to generalize stopping-power simulations (cf. Secs. 2.2 and 4.3) to more realistic setups, which will be shown in a future publication [256]. Given the popularity of the SOA-HF-GKBA in particular, it is expected that the results of Ref. [114] will have a profound and lasting impact on the NEGF community. Indeed, new research by other groups in this field has already been inspired by the new formalism [205, 206].

As a follow-up publication to Ref. [114], Ref. [208] is meant to be a reference work for the G1–G2 scheme with the purpose to extensively explain, deepen, and generalize the method. As a starting point, the derivation of the SOA-G1–G2 for a general single-particle basis is redone in a step-by-step manner and with more details.[5] Likewise, the GW-G1–G2 scheme is recovered in Sec. IV of Ref. [208] where special emphasis is given to the inverse dielectric function, which obeys a Schrödinger equation. The generalizations of the G1–G2 scheme for the direct parts of both T-matrix approximations presented in Sec. V of Ref. [208] have been derived solely by the author. The extension to corresponding exchange terms for the particle–particle T-matrix approximation[6] have been carried out by Jan-Philip Joost. For both ladder approximations, the respective nonequilibrium Møller operator [257, 258]—which can be understood as a renormalization core that transforms the bare interaction into the corresponding T matrix—is found to also obey a Schrödinger equation. Again, all resulting equations are specified for a general single-particle basis, the Hubbard basis, and the homogeneous electron gas. Furthermore, it is discussed how initial correlations are incorporated within the G1–G2 formalism for several different groundstate methods (Sec. III E of Ref. [208]). The remarkably simple structure of the two-particle EOMs from the different selfenergy expressions allows for an additional generalization by including all above-mentioned approximations into a combined approach—the dynamically-screened-ladder (DSL) approximation (Sec. VI of Ref. [208]). An equivalent of this approach can be systematically derived in RDO theory [96]. From a numerical perspective, Ref. [208] also discusses a complementary formulation of the equations for the time-diagonal two-particle Green function by utilizing a symmetry relation between the particle- and hole-density matrix (Sec. VII of Ref. [208]). It turns out that, for the case of the Hubbard basis, this alternative form yields an improved numerical scaling with the basis size of $\mathcal{O}\left(N_{\mathrm{b}}^4\right)$ compared to the $\mathcal{O}\left(N_{\mathrm{b}}^5\right)$ scaling reported in Ref. [114]. The theoretically derived scaling behaviors with the simulation time and the system size are reproduced by numerical test calculations for the Hubbard model. The results again confirm the advantageous character of the G1–G2 scheme compared to the original HF-GKBA for all considered selfenergy choices. Lastly, the numerical results of the DSL-G1–G2 approach

---

[5]In this progress, also a time-linear integration-based scheme to solve the SOA-HF-GKBA equations is presented and elaborated in the appendix of Ref. [208].

[6]An additional inspection of the particle–hole exchange terms is discussed in Sec. 3.1.1.

accurately match the results [259] for the Wang–Cassing approximation[7] [261] from RDO theory that is based on neglecting all three-particle correlations.

---

[7]The Wang–Cassing approximation is also referred to as Valdemoro approximation after Ref. [260].

Achieving the Scaling Limit for Nonequilibrium Green Functions Simulations

Niclas Schlünzen, Jan-Philip Joost⬤, and Michael Bonitz⬤
Institut für Theoretische Physik und Astrophysik, Christian-Albrechts-Universität zu Kiel, D-24098 Kiel, Germany

The dynamics of strongly correlated fermions following an external excitation reveals extremely rich collective quantum effects. Examples are fermionic atoms in optical lattices, electrons in correlated materials, and dense quantum plasmas. Presently, the only quantum-dynamics approach that rigorously describes these processes in two and three dimensions is the nonequilibrium Green functions (NEGF) method. However, NEGF simulations are computationally expensive due to their T^3 scaling with the simulation duration T. Recently, T^2 scaling was achieved with the generalized Kadanoff-Baym ansatz (GKBA), for second-order Born (SOA) selfenergies, which has substantially extended the scope of NEGF simulations. Here we demonstrate that GKBA-NEGF simulations can be performed with order T^1 scaling, both for SOA and GW selfenergies, and point out the remarkable capabilities of this approach.

Strongly correlated fermion systems are attracting increasing interest in many fields including dense plasmas [1,2], warm dense matter [3,4], strongly correlated materials [5,6], ultracold atoms [7,8], and atoms and molecules in strong radiation fields [9,10]. Of particular relevance are the relaxation phenomena that occur following an external excitation such as a rapid change ("quench") of the confinement or the interaction strength, the impact of charged particles [11,12], or the photoionization of atoms by lasers or free-electron lasers [13,14]. Many theoretical approaches to the dynamics of strongly correlated fermions are limited either to one-dimensional systems (density-matrix renormalization-group simulations, DMRG) or short times (quantum Monte Carlo). The first quantum simulations of the expansion of correlated fermions in two and three dimensions were recently achieved using nonequilibrium Green functions (NEGF) [8] and exhibited very good agreement with experiments. The high accuracy of NEGF simulations was also demonstrated by comparison to DMRG [15]. However, these NEGF simulations are hampered by an unfavorable scaling with the simulation duration according to T^3 resulting from the two-time structure of the NEGF and the memory effects in the collision integral (see below).

This behavior can be relieved by applying the generalized Kadanoff-Baym ansatz (GKBA) [16,17], which reduces the dynamics of the NEGF $G(t, t')$ to propagation along the time diagonal $t = t'$. It could be demonstrated that, indeed, the expected improvement of the scaling, $N_t^3 \rightarrow N_t^2$ (in the following we will use the number of discretization time steps $N_t = T/\Delta t$), can be achieved in practice for the selfenergy in the second-order Born approximation (SOA) [18,19] where initial correlation effects can be treated even more efficiently [20,21]. It could further be shown that this approximation, in

many cases, does not lead to a loss of accuracy [10,15,22]. For these reasons, NEGF simulations using the GKBA with Hartree-Fock propagators (HF-GKBA) [cf. Eqs. (6) and (7) below] have become a powerful tool for studying the quantum dynamics in many fields, including optically excited semiconductors [23–25], excitonic insulators [26], quantum transport and molecular junctions [27,28], laser-excited plasmas [29,30] and atoms [10,13], strongly correlated electrons [22], and fermionic atoms in optical lattices [15,31]. In recent years, significant effort was devoted to improve the GKBA, see, e.g., Refs. [17,20–22,27,32–34]. Nevertheless, the quadratic scaling with N_t still makes the approach much less efficient than competing methods that scale linearly with N_t, such as molecular dynamics, fluid theory, time-dependent density-functional theory within the adiabatic approximation, or Boltzmann-type (Markovian) kinetic equations.

In this Letter we demonstrate that the same linear scaling with N_t, which is the ultimate limit in time-dependent simulations, can be achieved for NEGF simulations within the HF-GKBA. This allows for unprecedented long simulations as well as for high-quality energy spectra that are computed via Fourier transformation of time-dependent quantities, see, e.g., Refs. [35–37]. We demonstrate this efficiency gain, compared to the original HF-GKBA, for finite Hubbard clusters and predict an even stronger gain for a basis in which the Green function and selfenergy are diagonal, such as for spatially homogeneous systems. Moreover, our approach allows one to compute additional quantities that are not directly accessible in standard NEGF schemes, such as the time-dependent pair-distribution function, the static and dynamic structure factor, and various correlation functions. Finally, we prove that linear scaling can be achieved also for more advanced

selfenergies, such as GW, where all existing schemes scale as N_t^3.

Theory.—We consider a general many-particle system with the Hamiltonian

$$H(t) = \sum_{ij} h_{ij}(t)\hat{c}_i^\dagger \hat{c}_j + \frac{1}{2}\sum_{ijkl} w_{ijkl}\hat{c}_i^\dagger \hat{c}_j^\dagger \hat{c}_l \hat{c}_k, \quad (1)$$

containing a single-particle contribution $\hat{h}$ and a pair interaction $\hat{w}$. The matrix elements are computed with an orthonormal system of single-particle orbitals $|i\rangle$. The creation ($\hat{c}_i^\dagger$) and annihilation ($\hat{c}_i$) operators of particles in state $|i\rangle$ define the one-body nonequilibrium Green functions (correlation functions; here and below "$\pm$" refers to bosons and fermions) $G_{ij}^<(t,t') = \pm(i/\hbar)\langle \hat{c}_j^\dagger(t')\hat{c}_i(t)\rangle$ and $G_{ij}^>(t,t') = (i/\hbar)\langle \hat{c}_i(t)\hat{c}_j^\dagger(t')\rangle$, where the averaging is performed with the correlated unperturbed density operator of the system. The response of the system (1) to an external excitation is described by the Keldysh-Kadanoff-Baym equations (KBE) on the time diagonal [16,19] where the Green function reduces to the single-particle density matrix, $\pm i\hbar G_{ij}^<(t,t) = n_{ij}(t)$,

$$\frac{\partial n_{ij}(t)}{\partial t} - \frac{1}{i\hbar}\sum_k [h_{ik}^{\text{HF}}(t), n_{kj}(t)] = \pm[I + I^\dagger]_{ij}(t), \quad (2)$$

with a mean-field Hamiltonian h^{HF}. Here I is the collision integral that takes into account interaction effects beyond Hartree-Fock, including scattering and dissipation, which we will treat in leading order, i.e., within the SOA [19,38]:

$$I_{ij}(t) = (i\hbar)^2 \sum_{mnp} w_{imnp}(t) \sum_{kqrs} \int_{t_0}^t d\bar{t}\, w_{qrsk}^\pm(\bar{t})$$
$$\times [G_{nq}^>(t,\bar{t})G_{pr}^>(t,\bar{t})G_{sm}^<(\bar{t},t)G_{kj}^<(\bar{t},t) - (> \leftrightarrow <)], \quad (3)$$

where we defined $w_{qrsj}^\pm \equiv w_{qrsj} \pm w_{qrjs} = \pm w_{qrjs}^\pm$. Clearly, the computational effort to solve Eqs. (2) and (3) scales with the number of time steps as N_t^2.

We now demonstrate that, in the HF-GKBA approximation, Eqs. (2) and (3) can be reformulated such that the effort is reduced to N_t^1 scaling. First, we introduce an auxiliary four-index function $\mathcal{G}$,

$$I_{ij}(t) = \pm i\hbar \sum_{mnp} w_{imnp}(t)\mathcal{G}_{npjm}(t), \quad (4)$$

$$\mathcal{G}_{npjm}(t) = i\hbar \sum_{kqrs} \int_{t_0}^t d\bar{t}\, w_{qrsk}^\pm(\bar{t})$$
$$\times [G_{nq}^>(t,\bar{t})G_{pr}^>(t,\bar{t})G_{sj}^<(\bar{t},t)G_{km}^<(\bar{t},t) - (> \leftrightarrow <)], \quad (5)$$

where the replacement $k \leftrightarrow s$ is used to match Eq. (3). Comparing Eq. (4) with the first equation of the Martin-Schwinger hierarchy for the many-particle Green functions [39] reveals that $\mathcal{G}(t)$ is nothing but the time-diagonal element of the two-particle Green function, and Eq. (5) is its explicit form in the second-Born approximation [40]. Next, we introduce the GKBA [16,19] (summation over k is implied)

$$G_{ij}^{\gtrless}(t,t') = \pm G_{ik}^R(t,t')n_{kj}^{\gtrless}(t') \mp n_{ik}^{\gtrless}(t)G_{kj}^A(t,t'), \quad (6)$$

$$G^{R/A}(t,t') = \Theta[+/-(t-t')]\{G^\gtrless(t,t') - G^\lessgtr(t,t')\},$$
$$n_{ij}^<(t) = n_{ij}(t), \qquad n_{ij}^>(t) = n_{ij}(t) - \delta_{ij}, \quad (7)$$

with Hartree-Fock propagators (HF-GKBA), $G^{R/A} \to G^{R/A,\text{HF}}$ and apply it to each Green function in Eq. (5):

$$\mathcal{G}_{npjm}^{\text{GKBA}}(t) = i\hbar \sum_{abcdkqrs} \int_{t_0}^t d\bar{t}\, w_{qrsk}^\pm(\bar{t})$$
$$\times \mathcal{U}_{npab}^{(2)}(t,\bar{t})\Phi_{qrcd}^{absk}(\bar{t})\mathcal{U}_{cdjm}^{(2)}(\bar{t},t). \quad (8)$$

Here we introduced the abbreviations

$$\Phi_{qrcd}^{absk}(t) = \Phi_{qrcd}^{absk>}(t) - \Phi_{qrcd}^{absk<}(t),$$
$$\Phi_{qrcd}^{absk\gtrless}(t) = n_{qa}^\gtrless(t)n_{rb}^\gtrless(t)n_{cs}^\lessgtr(t)n_{dk}^\lessgtr(t), \quad (9)$$

and the two-particle time-evolution operator $\mathcal{U}^{(2)}$ is given in the Supplemental Material [41].

Finally, we remove the time integral in Eq. (8) by differentiating with respect to time which yields

$$i\hbar \frac{d}{dt}\mathcal{G}_{npjm}^{\text{GKBA}}(t) - [h^{(2)\text{HF}}, \mathcal{G}^{\text{GKBA}}]_{npjm}(t)$$
$$= \frac{1}{(i\hbar)^2}\sum_{kqrs} w_{qrsk}^\pm(t)\Phi_{qrjm}^{npsk}(t), \quad (10)$$

where $h_{ijkl}^{(2)\text{HF}}(t) = \delta_{jl}h_{ik}^{\text{HF}}(t) + \delta_{ik}h_{jl}^{\text{HF}}(t)$. With this we have shown that NEGF theory within the HF-GKBA can be brought to a memory-less form (10) which, indeed, changes the scaling from quadratic to linear with N_t. This was achieved by introducing the two-particle Green function on the time diagonal $\mathcal{G}$ and by solving coupled time-local equations for $G(t,t)$ and $\mathcal{G}(t)$. We, therefore, will refer to this as the "G1–G2" scheme. In fact, the one-to-one correspondence of NEGF theory within the HF-GKBA to time-local equations has been observed before [18,42]. In Ref. [42] it was also shown how to include arbitrary initial correlations, by supplementing Eq. (10) with an initial value, $\mathcal{G}^{\text{GKBA}}(t_0) = \mathcal{G}_0$. In Eq. (8) this gives rise to an additional homogeneous solution that leads to an additional collision integral in the time-diagonal KBE (2), in agreement with recent results [20,21].

TABLE I. Scaling of the CPU time with the number of time steps N_t and basis dimension N_b of the traditional non-Markovian HF-GKBA and the present time-local scheme (G1–G2), for three relevant basis sets, for SOA and GW selfenergies.

Basis and pair potential	SOA		GW	
	Old	G1–G2	Old	G1–G2
General: w_{ijkl}	$\mathcal{O}(N_b^5 N_t^2)$	$\mathcal{O}(N_b^5 N_t^1)$	$\mathcal{O}(N_b^6 N_t^3)$	$\mathcal{O}(N_b^6 N_t^1)$
Hubbard: U	$\mathcal{O}(N_b^3 N_t^2)$	$\mathcal{O}(N_b^5 N_t^1)$	$\mathcal{O}(N_b^3 N_t^3)$	$\mathcal{O}(N_b^5 N_t^1)$
Jellium: $v_{|q|}$	$\mathcal{O}(N_b^3 N_t^2)$	$\mathcal{O}(N_b^3 N_t^1)$	$\mathcal{O}(N_b^3 N_t^3)$	$\mathcal{O}(N_b^3 N_t^1)$

FIG. 1. Comparison of the numerical accuracy of the ordinary HF-GKBA and the G1–G2 scheme with SOA selfenergies, for a four-site Hubbard chain with $U/J = 1.5$, excited by a rapid potential change of amplitude $w_0 = 0.1J$ at site one. (a) Density evolution at the first lattice site, $n_1(t)$. (b) Density difference between both methods, $\Delta n_1(t) = n_1^{\text{G1–G2}}(t) - n_1^{\text{ordinary}}(t)$. (c) Deviation from total-energy conservation for two time steps. Both NEGF implementations are based on a fourth-order integration scheme with the same time step with the initial state being prepared via adiabatic switching [22,31].

In the following we analyze the G1–G2 scheme more in detail. One readily confirms that the CPU time required to solve Eq. (10), for a general basis of dimension N_b, scales as $\mathcal{O}(N_b^5 N_t^1)$ [43]. In contrast, the original HF-GKBA scales as $\mathcal{O}(N_b^5 N_t^2)$ and, thus a dramatic speedup is expected, for any N_b [45]. At the same time, for many practical applications optimized basis sets are being used for which the scaling of both schemes has to be established separately. We, therefore, consider below two representative examples—the *Hubbard* basis and the uniform electron gas. The scaling for all three cases is summarized in Table I.

Hubbard basis.—The (Fermi-)Hubbard model is a key system in the theory of strongly correlated electrons in solids, see, e.g., Refs. [46,47], and it is being directly realized with fermionic atoms in optical lattices, see, e.g., Refs. [7,48,49]. It is defined by the Hubbard Hamiltonian

$$\hat{H}(t) = -J\sum_{\langle i,j\rangle}\sum_{\alpha} \hat{c}_{i\alpha}^{\dagger}\hat{c}_{j\alpha} + U(t)\sum_{i}\hat{n}_i^{\uparrow}\hat{n}_i^{\downarrow}, \quad (11)$$

which includes hopping processes between nearest-neighbor sites $\langle i, j\rangle$ with amplitude J and an on-site interaction U, and α labels the spin projection. The integral (4) reads, $I_{ij}^{\uparrow(\downarrow)}(t) = -i\hbar U(t)\mathcal{G}_{iiji}^{\uparrow(\downarrow)}(t)$, and the equation of motion (10) for $\mathcal{G}$ simplifies to [50]

$$i\hbar\frac{d}{dt}\mathcal{G}_{npjm}^{\uparrow(\downarrow)}(t) - [h_{\uparrow(\downarrow)}^{(2)\text{HF}}, \mathcal{G}^{\uparrow(\downarrow)}]_{npjm}(t) = (i\hbar)^2\sum_k U(t)$$
$$\times [G_{nk}^{\uparrow(\downarrow)>}(t,t)G_{pk}^{\downarrow(\uparrow)>}(t,t)G_{kj}^{\uparrow(\downarrow)<}(t,t)G_{km}^{\downarrow(\uparrow)<}(t,t) - > \leftrightarrow <].$$

The numerical effort to solve this equation scales as $\mathcal{O}(N_b^5 N_t^1)$, whereas the original HF-GKBA solution scales as $\mathcal{O}(N_b^3 N_t^2)$, cf. Table I. It turns out that, for the Hubbard model, the new scheme exhibits the most unfavorable scaling with N_b, as compared to the standard scheme and will become advantageous only for sufficiently large N_t. For this reason we choose this case for numerical tests. In Fig. 1 we study the dynamics of a small Hubbard cluster and find excellent agreement between both schemes for all observables, which is demonstrated for the density on site one in Figs. 1(a) and 1(b). An even more sensitive accuracy

test is the conservation of total energy. Here, the G1–G2 scheme turns out to be even more accurate than the standard HF-GKBA scheme if both use the same time step Δt, cf. Fig. 1(c). We now compare in Fig. 2 the CPU time required by both schemes for Hubbard systems with $N_b = 2$ and $N_b = 10$. Our results clearly confirm the quadratic (linear) scaling with N_t of the original HF-GKBA (G1–G2) scheme as well as the predicted scaling with N_b: when going from $N_b = 2$ to $N_b = 10$, "break even" is achieved for N_t approximately $(10/2)^2 = 25$ times larger, for SOA selfenergies.

The uniform electron gas [(UEG), jellium] is a key model for many-body physics, plasma, and condensed-matter physics allowing one to describe important features
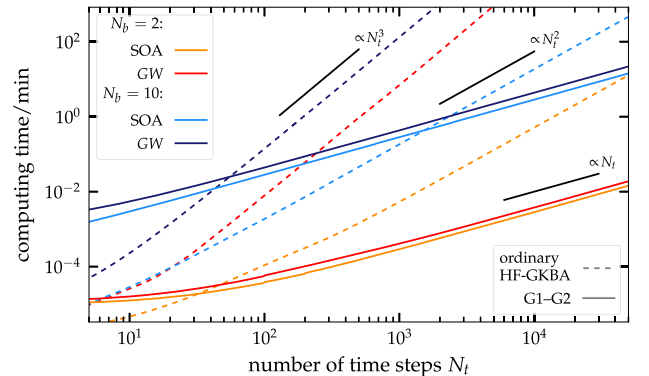
FIG. 2. Log-log comparison of the computational effort of the ordinary HF-GKBA (dashes) and the G1–G2 scheme (full lines) for Hubbard clusters as a function of propagation time N_t. Colors denote system size and the selfenergy approximation.

of the laser-driven nonequilibrium dynamics of electrons in metals [51], warm dense matter [4], and quantum plasmas [2,29], as well as of electron-hole plasmas in semiconductors; see, e.g., Refs. [25,52–54]. Because of homogeneity, a momentum (plain-wave) basis is advantageous where the Green function becomes diagonal: $G_{pq}(t,t') := \delta_{pq} G_p(t,t')$, for momenta $\boldsymbol{p}$, $\boldsymbol{q}$. The Hamiltonian of the UEG in second quantization reads [3]

$$\hat{H}(t) = \sum_{\boldsymbol{p}\alpha} \frac{\boldsymbol{p}^2}{2m} \hat{c}^\dagger_{\boldsymbol{p}\alpha} \hat{c}_{\boldsymbol{p}\alpha} + \sum_{\boldsymbol{p}\boldsymbol{p}'\boldsymbol{q}\alpha\beta} v_{|\boldsymbol{q}|} \hat{c}^\dagger_{\boldsymbol{p}+\boldsymbol{q}\alpha} \hat{c}^\dagger_{\boldsymbol{p}'-\boldsymbol{q}\beta} \hat{c}_{\boldsymbol{p}'\beta} \hat{c}_{\boldsymbol{p}\alpha},$$

with the Coulomb matrix element $v_{|\boldsymbol{q}|} = (4\pi e^2/|\boldsymbol{q}|^2)$. The integral (4) becomes $I_{\boldsymbol{p},\sigma}(t) = \pm i\hbar \sum_{\bar{\boldsymbol{p}},\boldsymbol{q},\alpha} v_{|\boldsymbol{q}|}(t) \mathcal{G}^{\sigma\alpha}_{\boldsymbol{p}\bar{\boldsymbol{p}}\boldsymbol{q}}(t)$, whereas the two-particle Green's function $\mathcal{G}$ obeys

$$i\hbar \frac{d}{dt} \mathcal{G}^{\sigma\alpha}_{\boldsymbol{p}\bar{\boldsymbol{p}}\boldsymbol{q}}(t) - \mathcal{G}^{\sigma\alpha}_{\boldsymbol{p}\bar{\boldsymbol{p}}\boldsymbol{q}}(t)(h^{\mathrm{HF}}_{\boldsymbol{p}-\boldsymbol{q},\sigma} + h^{\mathrm{HF}}_{\bar{\boldsymbol{p}}+\boldsymbol{q},\alpha} - h^{\mathrm{HF}}_{\boldsymbol{p},\sigma} - h^{\mathrm{HF}}_{\bar{\boldsymbol{p}},\alpha})$$
$$= (i\hbar)^2 \{ v_{|\boldsymbol{q}|}(t) \pm \delta_{\sigma,\alpha} v_{|\boldsymbol{p}-\boldsymbol{q}-\bar{\boldsymbol{p}}|}(t) \}$$
$$\times [G^>_{\boldsymbol{p}-\boldsymbol{q},\sigma}(t,t) G^>_{\bar{\boldsymbol{p}}+\boldsymbol{q},\alpha}(t,t) G^<_{\boldsymbol{p},\sigma}(t,t) G^<_{\bar{\boldsymbol{p}},\alpha}(t,t) - (> \leftrightarrow <)]. \quad (12)$$

Interestingly, Eq. (12) scales as $\mathcal{O}(N_b^3 N_t^1)$ vs $\mathcal{O}(N_b^3 N_t^2)$, for the standard HF-GKBA, cf. Table I, and the G1–G2 scheme brings about a dramatic acceleration, independent of basis size.

Spectra and two-particle observables.—In addition to accelerating the time evolution, the G1–G2 scheme gives also access to more accurate spectral information. While within the HF-GKBA spectral functions are treated on the Hartree-Fock level, correlation effects in energy spectra can be recovered by investigating the temporal response of the system to a short weak external excitation (linear response), see, e.g., Refs. [35–37]. This is demonstrated in Fig. 3 where the energy spectrum is retrieved via Fourier transform of the density evolution in a Hubbard system. Here the long propagation time enabled by the G1–G2 scheme allows us to resolve correlation effects in the spectra, in particular broadening and shift of peaks as well as the emergence of new states at high energies.

Furthermore, the G1–G2 scheme allows one to compute several quantities that are difficult or even impossible to access within standard NEGF schemes. This includes the nonequilibrium pair-distribution function (PDF) $g(\boldsymbol{r}_1, \sigma_1; \boldsymbol{r}_2, \sigma_2; t)$ and its Fourier transform—the static structure factor. Moreover, dynamic quantities, such as the density- and spin-correlation functions or velocity-autocorrelation functions and the related transport coefficients—the dynamic structure factor, diffusion and absorption coefficients, and the dynamical conductivity within and beyond linear response—are becoming directly accessible. In Fig. 4, we show, as an example, the time evolution of the pair-correlation function (PCF, i.e., the
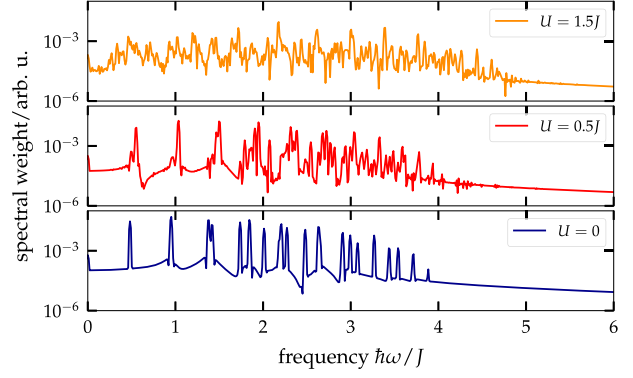
FIG. 3. Excitation spectrum of a 12-site Hubbard chain for three coupling strengths U due to a rapid potential change of amplitude $w_0 = 0.01J$ at site one. The spectrum is obtained via Fourier transform of the density $n_1(t)$ computed with the G1–G2 scheme up to $T = 600\hbar/J$. The initial state is prepared using adiabatic switching.

correlated part or the PDF) relative to site 1, $\delta g_{i\uparrow,1\downarrow} = g_{i\uparrow,1\downarrow} - n_{i\uparrow} n_{1\downarrow}$, for a 20-site Hubbard system after an interaction quench, $U/J = 0 \to 2$. Initially the system is ideal, corresponding to $\delta g \equiv 0$, and correlations emerge rapidly and spread with constant speed throughout the system. Changing U does not affect this speed, but the amplitude of the distance-dependent oscillations is proportional to U.

Extension to advanced selfenergies.—Finally, we test the G1–G2 scheme for the HF-GKBA with GW selfenergies which are known to be significantly more accurate than SOA, in particular, at stronger coupling [38,44]. At the same time existing GW simulations out of equilibrium scale as N_t^3. Remarkably, we observe that the present G1–G2 scheme achieves order N_t^1 scaling, as is summarized for
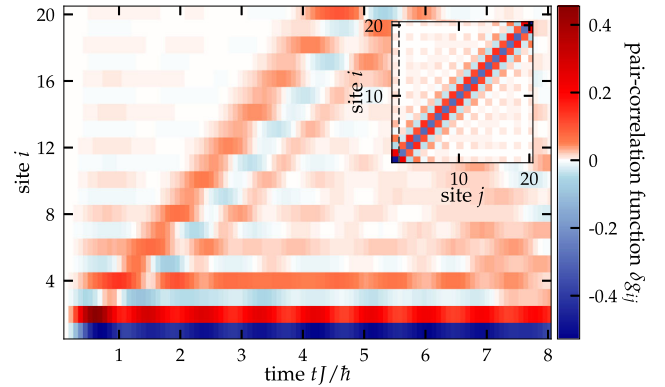
FIG. 4. Time evolution of the PCF relative to site 1, $\delta g_{i\uparrow,1\downarrow}(t)$, for a spatially homogeneous spin-symmetric 20-site Hubbard chain following an interaction quench $U/J = 0 \to 2$ at $t = 0$. Sign-alternating correlations emerge rapidly and approach the correlated ground state (GS). Inset shows $\delta g^{\mathrm{GS}}_{i\uparrow,j\downarrow}$, for $U/J = 2$, computed via adiabatic switching. The dashed line corresponds to data in the main figure.

different basis sets in Table I (details are given in Ref. [41], and similar results are observed for T-matrix selfenergies). The huge computational advantage brought about by G1–G2-GW simulations becomes evident also in Fig. 2; even for Hubbard systems the G1–G2 scheme is advantageous, except for very short simulations. This indicates that a large class of problems is now becoming accessible for accurate NEGF simulations that had remained out of reach so far.

Summary and discussion.—We have implemented an alternative approach to NEGF simulations within the HF-GKBA that is memory-free and achieves the ultimate limit of linear scaling with the propagation duration T, as opposed to the common HF-GKBA approach with SOA (GW) selfenergies that is of order T^2 (T^3). This is achieved by solving coupled time-local equations for $G(t, t)$ and the time-diagonal two-particle Green function $\mathcal{G}(t)$. With this G1–G2 scheme we also established a direct link to the independent reduced-density-matrix (RDM) approach that has become popular in recent years in many fields, see, e.g., Refs. [42,55–60]. Applying our derivation allows one to identify those RDM approximations that are equivalent to common selfenergies in NEGF theory what enables one to make use of the full power of Feynman diagrams in RDM theory. We expect that the demonstrated astonishing scaling of the G1–G2 scheme will make highly accurate NEGF simulations of many nonequilibrium processes such as in laser-excited correlated systems achievable.

———

[1] W. Ebeling, V. Fortov, and V. Filinov, *Quantum Statistics of Dense Gases and Nonideal Plasmas*, Springer Series in Plasma Science and Technology (Springer International Publishing, Cham, 2017).

[2] D. Kremp, M. Schlanges, and W. Kraeft, *Quantum Statistics of Nonideal Plasmas* (Springer, Berlin, Heidelberg, 2005).

[3] T. Dornheim, S. Groth, and M. Bonitz, The uniform electron gas at warm dense matter conditions, Phys. Rep. **744**, 1 (2018).

[4] P. Ndione, S. Weber, B. Rethfeld, and D. Gericke, Density response to short-pulse excitation in gold, Contrib. Plasma Phys. **59**, e201800186 (2019).

[5] S. A. Jensen, R. Ulbricht, A. Narita, X. Feng, K. Müllen, T. Hertel, D. Turchinovich, and M. Bonn, Ultrafast photoconductivity of graphene nanoribbons and carbon nanotubes, Nano Lett. **13**, 5925 (2013).

[6] J.-P. Joost, N. Schlünzen, and M. Bonitz, Femtosecond electron dynamics in graphene nanoribbons a nonequilibrium Green functions approach within an extended Hubbard model, Phys. Status Solidi B **256**, 1800498 (2019).

[7] U. Schneider, L. Hackermüller, J. P. Ronzheimer, S. Will, S. Braun, T. Best, I. Bloch, E. Demler, S. Mandt, D. Rasch, and A. Rosch, Fermionic transport and out-of-equilibrium dynamics in a homogeneous Hubbard model with ultracold atoms, Nat. Phys. **8**, 213 (2012).

[8] N. Schlünzen, S. Hermanns, M. Bonitz, and C. Verdozzi, Dynamics of strongly correlated fermions: *Ab initio* results for two and three dimensions, Phys. Rev. B **93**, 035107 (2016).

[9] C. F. de Morisson Faria and X. Liu, Electron–electron correlation in strong laser fields, J. Mod. Opt. **58**, 1076 (2011).

[10] F. Covito, E. Perfetto, A. Rubio, and G. Stefanucci, Benchmarking nonequilibrium Green's functions against configuration interaction for time-dependent Auger decay processes, Eur. Phys. J. B **91**, 216 (2018).

[11] K. Balzer, N. Schlünzen, and M. Bonitz, Stopping dynamics of ions passing through correlated honeycomb clusters, Phys. Rev. B **94**, 245118 (2016).

[12] K. Balzer, M. R. Rasmussen, N. Schlünzen, J.-P. Joost, and M. Bonitz, Doublon Formation by Ions Impacting a Strongly Correlated Finite Lattice System, Phys. Rev. Lett. **121**, 267602 (2018).

[13] E. Perfetto, A.-M. Uimonen, R. van Leeuwen, and G. Stefanucci, First-principles nonequilibrium Green's-function approach to transient photoabsorption: Application to atoms, Phys. Rev. A **92**, 033419 (2015).

[14] K. Balzer, S. Bauch, and M. Bonitz, Time-dependent second-order Born calculations for model atoms and molecules in strong laser fields, Phys. Rev. A **82**, 033427 (2010).

[15] N. Schlünzen, J.-P. Joost, F. Heidrich-Meisner, and M. Bonitz, Nonequilibrium dynamics in the one-dimensional Fermi-Hubbard model: Comparison of the nonequilibrium Green-functions approach and the density matrix renormalization group method, Phys. Rev. B **95**, 165139 (2017).

[16] P. Lipavský, V. Špička, and B. Velický, Generalized Kadanoff-Baym ansatz for deriving quantum transport equations, Phys. Rev. B **34**, 6933 (1986).

[17] A. Kalvova, B. Velicky, and V. Spicka, Beyond the generalized Kadanoff-Baym ansatz, Phys. Status Solidi B **256**, 1800594 (2019).

[18] S. Hermanns, K. Balzer, and M. Bonitz, Few-particle quantum dynamics—Comparing nonequilibrium Green functions with the generalized Kadanoff-Baym ansatz to density operator theory, J. Phys. Conf. Ser. **427**, 012008 (2013).

[19] K. Balzer and M. Bonitz, *Nonequilibrium Green's Functions Approach to Inhomogeneous Systems* (Springer, Berlin, Heidelberg, 2013).

[20] D. Karlsson, R. van Leeuwen, E. Perfetto, and G. Stefanucci, The generalized Kadanoff-Baym ansatz with initial correlations, Phys. Rev. B **98**, 115148 (2018).

[21] M. Bonitz, K. Balzer, N. Schlünzen, M. R. Rasmussen, and J.-P. Joost, Ion impact induced ultrafast electron dynamics in finite graphene-type Hubbard clusters, Phys. Status Solidi B **256**, 1800490 (2019).

[22] S. Hermanns, N. Schlünzen, and M. Bonitz, Hubbard nanoclusters far from equilibrium, Phys. Rev. B **90**, 125111 (2014).

[23] L. Bányai, Q. T. Vu, B. Mieck, and H. Haug, Ultrafast Quantum Kinetics of Time-Dependent RPA-Screened Coulomb Scattering, Phys. Rev. Lett. **81**, 882 (1998).

[24] M. Lorke, T. R. Nielsen, J. Seebeck, P. Gartner, and F. Jahnke, Quantum kinetic effects in the optical absorption of

semiconductor quantum-dot systems, J. Phys. Conf. Ser. **35,** 182 (2006).

[25] Y. Murakami, M. Schüler, S. Takayoshi, and P. Werner, Ultrafast nonequilibrium evolution of excitonic modes in semiconductors, arXiv:1907.06799.

[26] R. Tuovinen, D. Golez, M. Schüler, P. Werner, M. Eckstein, and M. A. Sentef, Adiabatic preparation of a correlated symmetry-broken initial state with the generalized Kadanoff–Baym ansatz, Phys. Status Solidi B **256,** 1800469 (2019).

[27] S. Latini, E. Perfetto, A.-M. Uimonen, R. van Leeuwen, and G. Stefanucci, Charge dynamics in molecular junctions: Nonequilibrium Green's function approach made fast, Phys. Rev. B **89,** 075306 (2014).

[28] A. Kalvova, B. Velicky, and V. Spicka, Generalized master equation for a molecular bridge improved by vertex correction to the generalized Kadanoff–Baym ansatz, Europhys. Lett. **121,** 67002 (2018).

[29] D. Kremp, T. Bornath, M. Bonitz, and M. Schlanges, Quantum kinetic theory of plasmas in strong laser fields, Phys. Rev. E **60,** 4725 (1999).

[30] H. Haberland, M. Bonitz, and D. Kremp, Harmonics generation in electron-ion collisions in a short laser pulse, Phys. Rev. E **64,** 026405 (2001).

[31] N. Schlünzen and M. Bonitz, Nonequilibrium Green functions approach to strongly correlated Fermions in lattice systems, Contrib. Plasma Phys. **56,** 5 (2016).

[32] M. Hopjan and C. Verdozzi, Initial correlated states for the generalized Kadanoff–Baym Ansatz without adiabatic switching-on of interactions in closed systems, Eur. Phys. J. Spec. Top. **227,** 1939 (2019).

[33] R. Tuovinen, F. Covito, and M. A. Sentef, Efficient computation of the second-Born self-energy using tensor-contraction operations, J. Chem. Phys. **151,** 174110 (2019).

[34] E. Perfetto and G. Stefanucci, The dissection algorithm for the second-born self-energy, Phys. Status Solidi B **256,** 1800573 (2019).

[35] N.-H. Kwong and M. Bonitz, Real-time Kadanoff-Baym Approach to Plasma Oscillations in a Correlated Electron Gas, Phys. Rev. Lett. **84,** 1768 (2000).

[36] N. E. Dahlen and R. van Leeuwen, Solving the Kadanoff–Baym Equations for Inhomogeneous Systems: Application to Atoms and Molecules, Phys. Rev. Lett. **98,** 153004 (2007).

[37] M. Bonitz, S. Hermanns, and K. Balzer, Dynamics of Hubbard nano-clusters following strong excitation, Contrib. Plasma Phys. **53,** 778 (2013).

[38] G. Stefanucci and R. van Leeuwen, *Nonequilibrium Many-Body Theory of Quantum Systems* (Cambridge University Press, Cambridge, England, 2013).

[39] P. C. Martin and J. Schwinger, Theory of many-particle systems. I, Phys. Rev. **115,** 1342 (1959).

[40] M. Bonitz, S. Hermanns, K. Kobusch, and K. Balzer, Nonequilibrium Green function approach to the pair distribution function of quantum many-body systems out of equilibrium, J. Phys. Conf. Ser. **427,** 012002 (2013).

[41] See Supplemental Material at http://link.aps.org/supplemental/10.1103/PhysRevLett.124.076601 for the definition of the two-particle time-evolution operator $\mathcal{U}^{(2)}$ and the derivation of the G1–G2 formulas in *GW* approximation.

[42] M. Bonitz, *Quantum Kinetic Theory*, Teubner-Texte zur Physik, 2nd ed. (Springer, Cham, 2016).

[43] The scaling reduction $\mathcal{O}(N_b^8) \rightarrow \mathcal{O}(N_b^5)$ is achieved by reordering the occurring tensor contractions, cf. Eq. (9), [44].

[44] N. Schlünzen, S. Hermanns, M. Scharnke, and M. Bonitz, Ultrafast dynamics of strongly correlated fermions—Nonequilibrium Green functions and selfenergy approximations, J. Phys. Condens. Matter **32,** 103001 (2020).

[45] For comparison, the numerical effort of the above-mentioned initial-correlations scheme [20,21] scales as $\mathcal{O}(N_b^5 N_{t^*}^2)$, where N_{t^*} denotes the number of time steps after the buildup of correlations. On the other hand, a scaling of the same order as our G1–G2 scheme has been achieved, e.g., in Ref. [13] by invoking the (drastic) Markov approximation to the GKBA equations, whereas the G1–G2 scheme is an identical reformulation of the original HF-GKBA.

[46] J. Hubbard and B. H. Flowers, Electron correlations in narrow energy bands, Proc. R. Soc. A **276,** 238 (1963).

[47] D. Baeriswyl, D. Campbell, J. Carmelo, F. Guinea, and E. Louis, *The Hubbard Model: Its Physics and Mathematical Physics*, Nato Science Series B (Springer, New York, 2013).

[48] T. Esslinger, Fermi-Hubbard physics with atoms in an optical lattice, Annu. Rev. Condens. Matter Phys. **1,** 129 (2010).

[49] L. Tarruell and L. Sanchez-Palencia, Quantum simulation of the Hubbard model with ultracold fermions in optical lattices, C.R. Phys. **19,** 365 (2018).

[50] The matrix $\mathcal{G}_{npjm}$ occurs with two spin combinations $(\uparrow, \downarrow)$ that are defined by the two possible combinations of spins on the right-hand side.

[51] B. Y. Mueller and B. Rethfeld, Relaxation dynamics in laser-excited metals under nonequilibrium conditions, Phys. Rev. B **87,** 035139 (2013).

[52] N. H. Kwong, M. Bonitz, R. Binder, and H. S. Köhler, Semiconductor Kadanoff-Baym equation results for optically excited electronhole plasmas in quantum wells, Phys. Status Solidi B **206,** 197 (1998).

[53] R. Binder, H. S. Köhler, M. Bonitz, and N. Kwong, Memory effects in the momentum orientation relaxation of electron hole plasmas in semiconductors, Phys. Rev. B **55,** 5110 (1997).

[54] H. Haug and A.-P. Jauho, *Quantum Kinetics in Transport and Optics of Semiconductors* (Springer, Berlin, Heidelberg, 2008).

[55] V. M. Axt and A. Stahl, A dynamics-controlled truncation scheme for the hierarchy of density matrices in semiconductor optics, Z. Phys. B **93,** 195 (1994).

[56] H. Nakatsuji and K. Yasuda, Direct Determination of the Quantum-Mechanical Density Matrix Using the Density Equation, Phys. Rev. Lett. **76,** 1039 (1996).

[57] S. Krönke and P. Schmelcher, Born-Bogoliubov-Green-Kirkwood-Yvon hierarchy for ultracold bosonic systems, Phys. Rev. A **98,** 013629 (2018).

[58] A. Akbari, M. J. Hashemi, A. Rubio, R. M. Nieminen, and R. van Leeuwen, Challenges in truncating the hierarchy of time-dependent reduced density matrices equations, Phys. Rev. B **85,** 235121 (2012).

[59] P. Schuck and M. Tohyama, Self-consistent RPA and the time-dependent density matrix approach, Eur. Phys. J. A **52,** 307 (2016).

[60] F. Lackner, I. Březinová, T. Sato, K. L. Ishikawa, and J. Burgdörfer, High-harmonic spectra from time-dependent two-particle reduced-density-matrix theory, Phys. Rev. A **95,** 033414 (2017).

Supplementary material for manuscript "Achieving the Scaling Limit for Nonequilibrium Green Functions Simulations"

Niclas Schlünzen, Jan-Philip Joost, and Michael Bonitz

This supplement contains additional information on 1.) the time-evolution operators $\mathcal{U}(t, t')$, and 2.) the derivation of the G1–G2 formulas in GW approximation.

1 Time-evolution operators

The two-particle time-evolution operator appearing in Eq. (8) of the manuscript is defined as

$$\mathcal{U}^{(2)}_{npab}(t, t') \;\; := \;\; \mathcal{U}_{na}(t, t')\mathcal{U}_{pb}(t, t') \,, \tag{S1}$$

where $\mathcal{U}(t, t')$ obeys a Schrödinger equation,

$$i\hbar\frac{\mathrm{d}}{\mathrm{d}t}\mathcal{U}_{na}(t, t') - \sum_b h^{\mathrm{HF}}_{nb}(t)\mathcal{U}_{ba}(t, t') = 0 \,, \tag{S2}$$

$$i\hbar\frac{\mathrm{d}}{\mathrm{d}t'}\mathcal{U}_{na}(t, t') + \sum_b \mathcal{U}_{nb}(t, t')h^{\mathrm{HF}}_{ba}(t') = 0 \,.$$

Note that the retarded/advanced propagators of Eq. (6) of the main text are related to $\mathcal{U}$ via

$$\mathcal{U}_{ij}(t, t') = G^{\mathrm{R}}_{ij}(t, t') - G^{\mathrm{A}}_{ij}(t, t') \,. \tag{S3}$$

2 Derivation of the G1–G2 scheme for GW selfenergies

In the GW approximation, the selfenergy has the form [1],

$$\Sigma^{\gtrless}_{ij}(t, t') = i\hbar \sum_{kl} W^{\gtrless}_{ilkj}(t, t')G^{\gtrless}_{kl}(t, t') \,, \tag{S4}$$

where, W is the dynamically screened interaction, which can be expressed in terms of the inverse dielectric function [2],

$$W^{\gtrless}_{ijkl}(t, t') = \sum_{mn} w_{imkn}(t)\varepsilon^{-1,\gtrless}_{mjnl}(t, t') \,. \tag{S5}$$

The collision integral in Eq. (2) of the manuscript then becomes,

$$I_{ij}(t) = \sum_k \int_{t_0}^t \mathrm{d}\bar{t}\left[\Sigma^{>}_{ik}(t, \bar{t})G^{<}_{kj}(\bar{t}, t) - \Sigma^{<}_{ik}(t, \bar{t})G^{>}_{kj}(\bar{t}, t)\right] \tag{S6}$$

$$= i\hbar \sum_{klmnp} w_{imkn}(t) \int_{t_0}^t \mathrm{d}\bar{t}\left[\varepsilon^{-1,>}_{mlnp}(t, \bar{t})G^{>}_{kl}(t, \bar{t})G^{<}_{pj}(\bar{t}, t) - \varepsilon^{-1,<}_{mlnp}(t, \bar{t})G^{<}_{kl}(t, \bar{t})G^{>}_{pj}(\bar{t}, t)\right] \,. \tag{S7}$$

With Eq. (4) of the main text one finds the following expression for the time-diagonal element of the two-particle Green function,

$$\mathcal{G}_{npjm}(t) = \pm\sum_{kl} \int_{t_0}^t \mathrm{d}\bar{t}\left[\varepsilon^{-1,>}_{mkpl}(t, \bar{t})G^{>}_{nk}(t, \bar{t})G^{<}_{lj}(\bar{t}, t) - \varepsilon^{-1,<}_{mkpl}(t, \bar{t})G^{<}_{nk}(t, \bar{t})G^{>}_{lj}(\bar{t}, t)\right] \,. \tag{S8}$$

By construction, the interaction tensors obey the following symmetries [2],

$$w_{ijkl}(t) = w_{jilk}(t) \,, \tag{S9}$$

$$W_{ijkl}^{\gtrless}(t,t') = W_{jilk}^{\lessgtr}(t',t) \,. \tag{S10}$$

Using that, the dynamical screening is included in ε^{-1} via the recursive equation,

$$\varepsilon_{ijkl}^{-1,\gtrless}(t,t') = \pm \, \mathrm{i}\hbar \sum_{mn} w_{mjnl}(t') G_{km}^{\gtrless}(t,t') G_{ni}^{\lessgtr}(t',t) \tag{S11}$$

$$\pm \, \mathrm{i}\hbar \sum_{mnpq} w_{jplq}(t') \Bigg[\int_{t_0}^{t} \mathrm{d}\bar{t} \left(G_{km}^{>}(t,\bar{t}) G_{ni}^{<}(\bar{t},t) - G_{km}^{<}(t,\bar{t}) G_{ni}^{>}(\bar{t},t) \right) \varepsilon_{pmqn}^{-1,\lessgtr}(t',\bar{t})$$

$$+ \int_{t_0}^{t'} \mathrm{d}\bar{t} \, G_{km}^{\gtrless}(t,\bar{t}) G_{ni}^{\lessgtr}(\bar{t},t) \left(\varepsilon_{pmqn}^{-1,>}(t',\bar{t}) - \varepsilon_{pmqn}^{-1,<}(t',\bar{t}) \right) \Bigg] \,.$$

Applying the HF-GKBA [cf. Eq. (6) and (7) of the main text] leads to the following expressions for $\mathcal{G}^{\mathrm{GKBA}}$,

$$\mathcal{G}_{npjm}^{\mathrm{GKBA}}(t) = \pm \sum_{klrs} \int_{t_0}^{t} \mathrm{d}\bar{t} \, \mathcal{U}_{nr}(t,\bar{t}) \Big[\varepsilon_{mkpl}^{-1,>}(t,\bar{t}) n_{rk}^{>}(\bar{t}) n_{ls}^{<}(\bar{t}) - \varepsilon_{mkpl}^{-1,<}(t,\bar{t}) n_{rk}^{<}(\bar{t}) n_{ls}^{>}(\bar{t}) \Big] \mathcal{U}_{sj}(\bar{t},t) \,, \tag{S12}$$

as well as for $\varepsilon_{\mathrm{GKBA}}^{-1} \to \varepsilon^{-1}$,

$$\varepsilon_{ijkl}^{-1,\gtrless}(t \geq t') \tag{S13}$$

$$= \pm \, \mathrm{i}\hbar \sum_{mnpq} w_{mjnl}(t') \mathcal{U}_{kp}(t,t') n_{pm}^{\gtrless}(t') n_{nq}^{\lessgtr}(t') \mathcal{U}_{qi}(t',t)$$

$$\pm \, \mathrm{i}\hbar \sum_{mnpqab} w_{jalb}(t') \Bigg[\int_{t_0}^{t} \mathrm{d}\bar{t} \, \mathcal{U}_{kp}(t,\bar{t}) \left(n_{pm}^{>}(\bar{t}) n_{nq}^{<}(\bar{t}) - n_{pm}^{<}(\bar{t}) n_{nq}^{>}(\bar{t}) \right) \mathcal{U}_{qi}(\bar{t},t) \varepsilon_{ambn}^{-1,\lessgtr}(t',\bar{t})$$

$$+ \int_{t_0}^{t'} \mathrm{d}\bar{t} \, \mathcal{U}_{kp}(t,\bar{t}) n_{pm}^{\gtrless}(\bar{t}) n_{nq}^{\lessgtr}(\bar{t}) \mathcal{U}_{qi}(\bar{t},t) \left(\varepsilon_{ambn}^{-1,>}(t',\bar{t}) - \varepsilon_{ambn}^{-1,<}(t',\bar{t}) \right) \Bigg] \,,$$

where $\mathcal{U}$ is given by Eq. (S2). With Eq. (S13), also the derivative of ε^{-1} is readily found,

$$\frac{\mathrm{d}}{\mathrm{d}t} \varepsilon_{ijkl}^{-1,\gtrless}(t \geq t') = \frac{1}{\mathrm{i}\hbar} \sum_{m} h_{km}^{\mathrm{HF}}(t) \varepsilon_{ijml}^{-1,\gtrless}(t \geq t') - \frac{1}{\mathrm{i}\hbar} \sum_{m} \varepsilon_{mjkl}^{-1,\gtrless}(t \geq t') h_{mi}^{\mathrm{HF}}(t)$$

$$\pm \frac{1}{\mathrm{i}\hbar} \sum_{mnab} w_{manb}(t) \Big[n_{km}^{>}(t) n_{ni}^{<}(t) - n_{km}^{<}(t) n_{ni}^{>}(t) \Big] \varepsilon_{ajbl}^{-1,\gtrless}(t \geq t') \,. \tag{S14}$$

Finally, the derivative of $\mathcal{G}^{\mathrm{GKBA}}$ can be set up,

$$\frac{\mathrm{d}}{\mathrm{d}t} \mathcal{G}_{npjm}^{\mathrm{GKBA}}(t) = \pm \frac{1}{(\mathrm{i}\hbar)^2} \sum_{kl} \Big[\varepsilon_{mkpl}^{-1,>}(t,t) n_{nk}^{>}(t) n_{lj}^{<}(t) - \varepsilon_{mkpl}^{-1,<}(t,t) n_{nk}^{<}(t) n_{lj}^{>}(t) \Big]$$

$$\pm \sum_{klrs} \int_{t_0}^{t} \mathrm{d}\bar{t} \left(\frac{\mathrm{d}}{\mathrm{d}t} \mathcal{U}_{nr}(t,\bar{t}) \right) \Big[\varepsilon_{mkpl}^{-1,>}(t,\bar{t}) n_{rk}^{>}(\bar{t}) n_{ls}^{<}(\bar{t}) - \varepsilon_{mkpl}^{-1,<}(t,\bar{t}) n_{rk}^{<}(\bar{t}) n_{ls}^{>}(\bar{t}) \Big] \mathcal{U}_{sj}(\bar{t},t)$$

$$\pm \sum_{klrs} \int_{t_0}^{t} \mathrm{d}\bar{t} \, \mathcal{U}_{nr}(t,\bar{t}) \Bigg[\left(\frac{\mathrm{d}}{\mathrm{d}t} \varepsilon_{mkpl}^{-1,>}(t,\bar{t}) \right) n_{rk}^{>}(\bar{t}) n_{ls}^{<}(\bar{t}) - \left(\frac{\mathrm{d}}{\mathrm{d}t} \varepsilon_{mkpl}^{-1,<}(t,\bar{t}) \right) n_{rk}^{<}(\bar{t}) n_{ls}^{>}(\bar{t}) \Bigg] \mathcal{U}_{sj}(\bar{t},t)$$

$$\pm \sum_{klrs} \int_{t_0}^{t} \mathrm{d}\bar{t} \, \mathcal{U}_{nr}(t,\bar{t}) \Big[\varepsilon_{mkpl}^{-1,>}(t,\bar{t}) n_{rk}^{>}(\bar{t}) n_{ls}^{<}(\bar{t}) - \varepsilon_{mkpl}^{-1,<}(t,\bar{t}) n_{rk}^{<}(\bar{t}) n_{ls}^{>}(\bar{t}) \Big] \left(\frac{\mathrm{d}}{\mathrm{d}t} \mathcal{U}_{sj}(\bar{t},t) \right) \,. \tag{S15}$$

With the introduction of the following auxiliary function [3],

$$P_{npjm}(t) = \pm \sum_{cd} \Big[n_{pd}^{>}(t) n_{cm}^{<}(t) - n_{pd}^{<}(t) n_{cm}^{>}(t) \Big] \sum_{rs} w_{drcs}(t) \mathcal{G}_{nsjr}^{\mathrm{GKBA}}(t) \,, \tag{S16}$$

Eq. (S15) can eventually be exactly brought to the following time-local form that is used in the G1–G2 scheme,

$$\mathrm{i}\hbar \frac{\mathrm{d}}{\mathrm{d}t} \mathcal{G}_{npjm}^{\mathrm{GKBA}}(t) - \left[h^{(2),\mathrm{HF}}, \mathcal{G}^{\mathrm{GKBA}} \right]_{npjm}(t)$$

$$= \frac{1}{(\mathrm{i}\hbar)^2} \sum_{kqrs} w_{qrsk}(t) \Big[n_{nq}^{>}(t) n_{pr}^{>}(t) n_{sj}^{<}(t) n_{km}^{<}(t) - n_{nq}^{<}(t) n_{pr}^{<}(t) n_{sj}^{>}(t) n_{km}^{>}(t) \Big]$$

$$+ P_{npjm}(t) + P_{pnmj}(t) \,. \tag{S17}$$

2

References

[1] N. Schlünzen, S. Hermanns, M. Scharnke, and M. Bonitz, Ultrafast dynamics of strongly correlated fermions – Nonequilibrium Green functions and selfenergy approximations, J. Phys. Condens. Matter **32** (10), 103001 (2020)

[2] G. Stefanucci and R. van Leeuwen, *Nonequilibrium Many-Body Theory of Quantum Systems*, (Cambridge University Press, Cambridge, 2013)

[3] M. Bonitz, *Quantum Kinetic Theory*, 2nd ed. (Springer, Cham, 2016)

G1-G2 scheme: Dramatic acceleration of nonequilibrium Green functions simulations within the Hartree-Fock generalized Kadanoff-Baym ansatz

Jan-Philip Joost ◉, Niclas Schlünzen, and Michael Bonitz ◉*

Institut für Theoretische Physik und Astrophysik, Christian-Albrechts-Universität zu Kiel, D-24098 Kiel, Germany

The time evolution in quantum many-body systems after external excitations is attracting high interest in many fields, including dense plasmas, correlated solids, laser-excited materials, or fermionic and bosonic atoms in optical lattices. The theoretical modeling of these processes is challenging, and the only rigorous quantum-dynamics approach that can treat correlated fermions in two and three dimensions is nonequilibrium Green functions (NEGF). However, NEGF simulations are computationally expensive due to their T^3 scaling with the simulation duration T. Recently, T^2 scaling was achieved with the generalized Kadanoff-Baym ansatz (GKBA), for the second-order Born (SOA) self energy, which has substantially extended the scope of NEGF simulations. In a recent Letter [Schlünzen *et al.*, [Phys. Rev. Lett. **124**, 076601 (2020)](#)]. we demonstrated that GKBA-NEGF simulations can be efficiently mapped onto coupled time-local equations for the single-particle and two-particle Green functions on the time diagonal, hence the method has been called the G1-G2 scheme. This allows one to perform the same simulations with order T^1 scaling, both for SOA and *GW* self energies giving rise to a dramatic speedup. Here we present more details on the G1-G2 scheme, including derivations of the basic equations including results for a general basis, for Hubbard systems, and for jellium. Also, we demonstrate how to incorporate initial correlations into the G1-G2 scheme. Further, the derivations are extended to a broader class of self energies, including the T matrix in the particle-particle and particle-hole channels and the dynamically-screened-ladder approximation. Finally, we demonstrate that, for all self energies, the CPU-time scaling of the G1-G2 scheme with the basis dimension N_b can be improved compared to our first report: The overhead compared to the original GKBA is not more than an additional factor N_b, even for Hubbard systems.

DOI: [10.1103/PhysRevB.101.245101](#)

I. INTRODUCTION

Nonequilibrium Green functions (NEGF) [1–3] have proven highly successful in simulations of the dynamics of correlated many-body systems. This is due to a number of attractive properties that include conservation laws and the existence of systematic approximation schemes that are based on Feynman diagrams. Moreover, NEGF allow for a rigorous derivation of quantum kinetic equations and for their systematic improvement; for recent overviews, see the text books [4–6].

While early computational applications focused on spatially homogeneous systems such as nuclear matter [7,8], optically excited semiconductors [4,9], and dense plasmas [10,11], during the last 15 years the scope of applications has substantially broadened. This includes the excitation and ionization dynamics of small atoms and molecules [12–14], the correlated-electron dynamics in the Hubbard model [15–17], the dynamics of fermionic atoms [18,19], and the stopping of

ions in correlated materials [20–22]. This success was caused, among other things, by progress in the numerical solution of the basic equations of NEGF—the Keldysh-Kadanoff-Baym equations (KBE) [12,23–25]. Furthermore, improved time propagation and integration schemes led to an increase in efficiency and accuracy of the simulations [26,27]. Moreover, the implementation of more advanced self energies, such as the T-matrix self energy, further increased the accuracy and predictive capability; for a recent review, see Ref. [28]. In particular, very good agreement with cold-atom experiments [18] and with *ab initio* density-matrix-renormalization-group (DMRG) simulations were reported [27]. A particular advantage of NEGF simulation is that they are well capable to treat strong electronic correlations, in contrast to density-functional theory (DFT), and that they are neither restricted to 1D systems, such as DMRG, nor to short times, such as continuous-time quantum Monte Carlo [29].

The main disadvantage of NEGF is their high numerical effort. The majority of many-body methods, including time-dependent DFT (TDDFT), Boltzmann-type quantum kinetic equations, hydrodynamics or semiclassical molecular dynamic—and even the exact solution of the time-dependent Schrödinger equation—require a simulation time that grows linearly with the physical time. In contrast, for NEGF, the propagation in the two-time plane, together with the memory integration in the scattering contributions, gives rise to a N_t^3

*bonitz@theo-physik.uni-kiel.de

scaling, where N_t is the propagation time (number of time steps). A substantial acceleration is possible when the generalized Kadanoff-Baym ansatz (GKBA) is applied [30] which restricts the propagation to a time stepping along the time diagonal. If combined with Hartree-Fock propagators (HF-GKBA) [31–33] the CPU-time scaling can be reduced to N_t^2, which has given rise to a drastic increase of the number of HF-GKBA simulations in recent years, see, e.g., Refs. [17,27,34–38]. However, this improved scaling is achieved only for the simplest self energy—the second-Born approximation (SOA). If the HF-GKBA is applied to improved self energies, such as the T-matrix self energy [19,27], which is required for strongly correlated systems [18], or the GW self energy [28] which is required to capture dynamical-screening effects, the CPU-time scaling is again increased to N_t^3.

In a recent Letter we reported a breakthrough for NEGF simulations within the HF-GKBA scheme: We demonstrated that *time-linear scaling*, i.e., a CPU time that is of order N_t^1, can be achieved if the equations of motion are properly reformulated, without any approximations. The alternative approach solves the time-local equations for the time-diagonal single- and two-particle Green functions and was called the G1-G2 scheme [39]. While the equivalence of the HF-GKBA to time-local equations was pointed out before [5,40], a comparison of the numerical behavior of both approaches was performed only in Ref. [39]. There we reported N_t^1 scaling for SOA and GW self energies and any type of single-particle basis. The scaling was demonstrated for small Hubbard clusters which turned out to be the most unfavorable case because the CPU time of the G1-G2 scheme was found to grow by a factor N_b^2 faster than for the standard HF-GKBA approach, where N_b is the dimension of the single-particle basis.

In this paper we present extensive additional results for the G1-G2 scheme. First, we present all necessary details for the derivation of the equation of motion for the time-diagonal two-particle Green function. The results are derived for a general basis, for the Hubbard model, and for jellium. Second, we discuss how initial correlations can be incorporated. Third, we extend the analysis to other self energies: the T-matrix approximation in the particle-particle (TPP) and particle-hole (TPH) channels and the dynamically-screened-ladder (DSL) approximation. Fourth, numerical results are presented for all self-energy approximations which clearly confirm the N_t^1 scaling, not only asymptotically, but already for rather small simulation durations, $N_t \lesssim 30$. Finally, we re-evaluate the N_b dependence of the CPU time and report an additional optimization that reduces the overhead of the new scheme from N_b^2 to only N_b^1, for the Hubbard model, for all self energies.

This paper is organized as follows: In Sec. II we summarize the main required formulas of NEGF theory and the properties of the two-particle Green function. In Sec. III we present the basic formulas for the G1-G2 scheme, for the case of the SOA self energy—separately for a general basis, the Hubbard basis, and for jellium. The same analysis is then extended to GW and T-matrix self energies in Secs. IV and V and to the screened-ladder approximation in Sec. VI. Finally, the analysis of the scaling behavior with N_t and N_b for all self energies and numerical results are presented in Sec. VII.

II. THEORETICAL FRAMEWORK

A. Keldysh-Kadanoff-Baym equations and two-particle Green function

We consider a nonequilibrium quantum many-particle system with the generic Hamiltonian

$$\hat{H}(t) = \sum_{ij} h_{ij}^{(0)}(t)\hat{c}_i^\dagger \hat{c}_j + \frac{1}{2}\sum_{ijkl} w_{ijkl}(t)\hat{c}_i^\dagger \hat{c}_j^\dagger \hat{c}_l \hat{c}_k, \quad (1)$$

containing a single-particle contribution $h^{(0)}$ and a pair interaction w. Note the twofold time dependencies of the Hamiltonian. The time dependence of the single-particle contribution $h^{(0)}$ covers the interaction with external electromagnetic fields, lasers, or particle impact (stopping) [20], or the variation (quench) of a confinement potential [18,41]. While the interaction potential w is time independent in most cases, a time dependence has to be taken into account when modeling interactions quenches (e.g., in cold-atom experiments) or for the numerical preparation of a correlated initial state via "adiabatic switching," cf. Sec. III E. Thus, for the sake of generality of our derivations, we will retain the full time dependence throughout this paper.

The matrix elements of the Hamiltonian are computed with a complete orthonormal system of single-particle orbitals $|i\rangle$. The creation ($\hat{c}_i^\dagger$) and annihilation ($\hat{c}_i$) operators of particles in state $|i\rangle$ define the one-body nonequilibrium Green function (correlation function) for contour-time arguments z on the Keldysh contour $\mathcal{C}$ [28] (examples of the contour are shown in Fig. 1),

$$G_{ij}(z, z') = \frac{1}{i\hbar}\langle \mathcal{T}_{\mathcal{C}}\{\hat{c}_i(z)\hat{c}_j^\dagger(z')\}\rangle. $$

Here, $\mathcal{T}_{\mathcal{C}}$ is the time-ordering operator on the contour, and the averaging is performed with the correlated unperturbed density operator of the system. The equations of motion (EOMs) for the NEGF are the Keldysh-Kadanoff-Baym equations [43]

$$\sum_k \left[i\hbar\frac{d}{dz}\delta_{ik} - h_{ik}^{(0)}(z) \right] G_{kj}(z, z')$$

$$= \delta_{ij}\delta_{\mathcal{C}}(z, z') \pm i\hbar \sum_{klp} \int_{\mathcal{C}} d\bar{z}\, w_{iklp}(z, \bar{z}) G_{lpjk}^{(2)}(z, \bar{z}, z', \bar{z}^+), $$

$$(2)$$

$$\sum_k G_{ik}(z, z') \left[-i\hbar\frac{\overleftarrow{d}}{dz'}\delta_{kj} - h_{kj}^{(0)}(z') \right]$$

$$= \delta_{ij}\delta_{\mathcal{C}}(z, z') \pm i\hbar \sum_{klp} \int_{\mathcal{C}} d\bar{z}\, G_{iklp}^{(2)}(z, \bar{z}^-, z', \bar{z}) w_{lpjk}(\bar{z}, z'). $$

$$(3)$$

Here, the times $z^\pm := z \pm \epsilon$ differ from z by an infinitesimally small positive constant ϵ to avoid ambiguities in the time ordering of field-operator products. Furthermore, a two-time version of the interaction potential is introduced using the delta function on the Keldysh contour, $w_{ijkl}(z, z') = \delta_{\mathcal{C}}(z, z')w_{ijkl}(z)$, see, e.g., Refs. [6,19,28]. The KBE couple to the two-particle Green function (terms on the

(a)

(b)
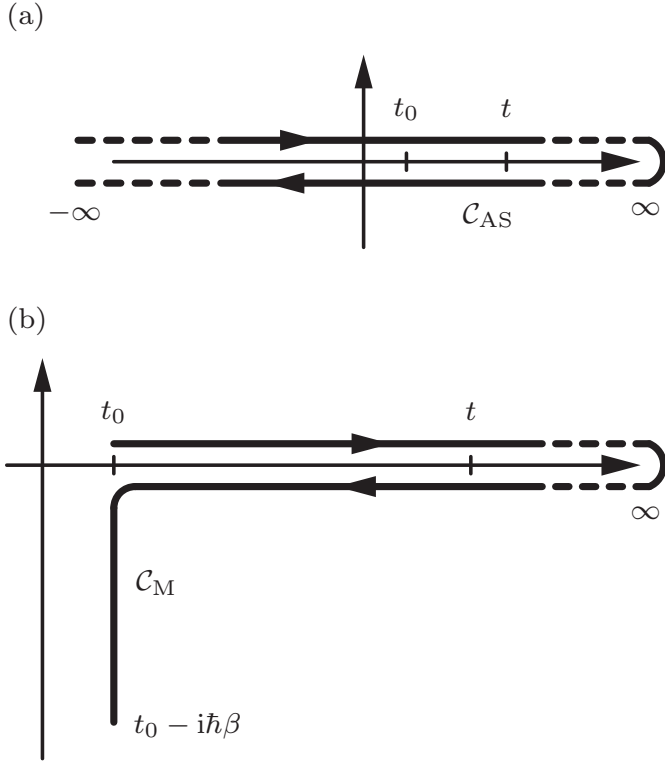
FIG. 1. Two examples of the Keldysh "round-trip" time contour that are used in NEGF theory to treat initial correlations, see, e.g., Ref. [2]. (a) Contour $\mathcal{C}_{AS}$ containing an initial real-time interval (from $-\infty$ to t_0) to adiabatically "switch on" the pair interaction, starting from an uncorrelated state. (b) Contour $\mathcal{C}_M$ with an imaginary branch allowing us to include thermodynamic-equilibrium correlations via Green functions which have one time argument on the real branch and one on the imaginary branch [33,42].

r.h.s.) which is defined by

$$G_{ijkl}^{(2)}(z_1, z_2, z_3, z_4) = \frac{1}{(i\hbar)^2} \langle \mathcal{T}_{\mathcal{C}}\{\hat{c}_i(z_1)\hat{c}_j(z_2)\hat{c}_l^\dagger(z_4)\hat{c}_k^\dagger(z_3)\}\rangle$$

and contains a mean-field (Hartree-Fock) and a correlation contribution

$$G_{ijkl}^{(2)}(z_1, z_2, z_3, z_4) = G_{ijkl}^{(2),H}(z_1, z_2, z_3, z_4) \pm G_{ijkl}^{(2),F}(z_1, z_2, z_3, z_4)$$
$$+ G_{ijkl}^{(2),corr}(z_1, z_2, z_3, z_4). \tag{4}$$

The Eqs. (2) and (3) for the one-particle NEGF are formulated on the Keldysh contour, cf. Fig. 1. They are equivalent to equations for Keldysh Green function matrices of real-time arguments where the matrix components differ by the location of the time arguments on the contour; for details see the text books [6,33]. Our G1-G2 scheme involves the special case of two-particle functions that depend either on one or two times and their real-time components that we define as follows:

$$\mathcal{G}_{ijkl}^H(z, z') := G_{ijkl}^{(2),H}(z, z, z', z') = G_{ik}(z, z')G_{jl}(z, z'),$$

$$\mathcal{G}_{ijkl}^F(z, z') := G_{ijkl}^{(2),F}(z, z, z', z') = G_{il}(z, z')G_{jk}(z', z),$$

$$\mathcal{G}_{ijkl}^{corr}(z, z') := G_{ijkl}^{(2),corr}(z, z, z', z^+),$$

$$\mathcal{G}_{ijkl}^{H,\gtrless}(t, t') := G_{ik}^{\gtrless}(t, t')G_{jl}^{\gtrless}(t, t'),$$

$$\mathcal{G}_{ijkl}^{F,\gtrless}(t, t') := G_{il}^{\gtrless}(t, t')G_{jk}^{\lessgtr}(t', t),$$

$$\mathcal{G}_{ijkl}^{H,\gtrless}(t) := \mathcal{G}_{ijkl}^{H,\gtrless}(t, t),$$

$$\mathcal{G}_{ijkl}^{F,\gtrless}(t) := \mathcal{G}_{ijkl}^{F,\gtrless}(t, t),$$

$$\mathcal{G}_{ijkl}(t) := \mathcal{G}_{ijkl}^{corr,<}(t, t). \tag{5}$$

The time-diagonal two-particle Green function $\mathcal{G}(t)$, defined by Eq. (5), is the central quantity of the G1-G2 scheme. In general, and for all self-energy approximations considered in this work, it obeys the following (pair-) exchange symmetries,

$$\mathcal{G}_{ijkl}(t) = \mathcal{G}_{jilk}(t), \tag{6}$$

$$\mathcal{G}_{ijkl}(t) = [\mathcal{G}_{klij}(t)]^*. \tag{7}$$

B. Time-diagonal KBE

In the following we are interested in the dynamics of the real-time components $G^{\gtrless}(t, t')$ and, in particular, the properties of $G_{ij}^{\gtrless}(t) := G_{ij}^{\gtrless}(t, t)$ on the real-time diagonal. The EOM for $G^<(t)$ has the form [19,44]

$$i\hbar \frac{d}{dt} G_{ij}^<(t) - [h^{HF}, G^<]_{ij}(t) = [I + I^\dagger]_{ij}(t), \tag{8}$$

$$I(t) = \mathcal{I}(t) + \mathcal{I}^{IC}(t), \tag{9}$$

where I is the collision integral of the kinetic equation that, in general, consists of the dynamical collision integral $\mathcal{I}$ and the initial-correlation contribution $\mathcal{I}^{IC}$ which includes pair correlations existing in the system at the initial time $t = t_0$. In NEGF theory initial correlations can be described [6,21], e.g., by including contributions from the imaginary track of the Keldysh contour (lower part of Fig. 1) or via building up initial correlations dynamically via a prior dynamics that starts from an uncorrelated state ("adiabatic switching," upper part of Fig. 1). We will discuss this issue more in detail below, in Sec. III E where we also show how initial correlations are taken into account in the G1-G2 scheme. For now we focus on the first collision integral, i.e., $I(t) = \mathcal{I}(t)$, assuming that the system is prepared in an uncorrelated (ideal) initial state at time t_0. In that case the buildup of dynamical correlations is described by

$$I_{ij}(t) = \pm i\hbar \sum_{klp} w_{iklp}(t)\mathcal{G}_{lpjk}(t)$$

$$= \sum_k \int_{t_0}^t d\bar{t}[\Sigma_{ik}^>(t, \bar{t})G_{kj}^<(\bar{t}, t) - \Sigma_{ik}^<(t, \bar{t})G_{kj}^>(\bar{t}, t)]. \tag{10}$$

Here, the first line follows directly from the r.h.s. of Eqs. (2) and (3), where the time integral has been taken with the help of the delta function in the two-time potential. In the second line the two-particle Green function has been eliminated by introducing the correlation self-energy functions $\Sigma^{\gtrless}$ [the notion "correlation self energy" means that the Hartree-Fock self-energy contributions have been subtracted from $\Sigma^{\gtrless}$; they are included in the Hamiltonian h^{HF} on the l.h.s., cf. Eq. (12)]— which is the standard approach in the NEGF framework. The self energy is the only unknown function in the theory. If it was known exactly, the description of the dynamics would be

exact. This is, of course, not the case in most situations and, thus, approximations are required. In the following sections we will consider several key approximations that are currently broadly used in various fields of many-body physics. Note that for the approximations studied in this paper, the self energies $\Sigma^{\gtrless}(t, t')$ are nonsingular functions. This means, the collision integral $I_{ij}(t)$ in Eq. (10) vanishes for $t \to t_0$.

Before we start the analysis with the second-order Born approximation for the self energy, in Sec. III, we summarize a few important properties of Eq. (8). First, on the time diagonal the less component of the NEGF can be written as

$$G_{ij}^<(t) = G_{ij}^>(t) - \frac{1}{i\hbar}\delta_{ij} = \pm\frac{1}{i\hbar}n_{ij}(t), \qquad (11)$$

where n_{ij} is the single-particle density matrix. Further, as was noted above, in Eq. (8) the mean-field part of the two-particle Green function, cf. Eq. (4) (or, equivalently, the self energy), is included in an effective single-particle Hartree-Fock Hamiltonian which is defined as [28]

$$h_{ij}^{\mathrm{HF}}(t) = h_{ij}^{(0)}(t) \pm i\hbar \sum_{kl} w_{ikjl}^{\pm}(t)G_{lk}^<(t, t), \qquad (12)$$

where we introduced the (anti-)symmetrized interaction potential which we define via its four-dimensional matrix with respect to the single-particle basis

$$w_{ijkl}^{\pm}(t) := w_{ijkl}(t) \pm w_{ijlk}(t). $$

The interaction tensor obeys the same symmetries as $\mathcal{G}(t)$ [cf. Eqs. (6) and (7)]:

$$w_{ijkl}(t) = w_{jilk}(t), \qquad (13)$$

$$w_{ijkl}(t) = [w_{klij}(t)]^*, \qquad (14)$$

which also leads to

$$w_{ijkl}^{\pm}(t) = \pm w_{ijlk}^{\pm}(t). $$

III. SECOND-ORDER BORN SELF ENERGY

In the following we introduce the G1-G2 scheme for the simplest case of choosing the self energy in the second-Born approximation [19],

$$\Sigma_{ij}^{\gtrless}(t, t') = \pm(i\hbar)^2 \sum_{klpqrs} w_{iklp}(t)w_{qrjs}^{\pm}(t')$$
$$\times G_{lq}^{\gtrless}(t, t')G_{pr}^{\gtrless}(t, t')G_{sk}^{\lessgtr}(t', t). $$

With that, the collision integral of the time-diagonal equation (10) transforms into:

$$I_{ij}(t) = \pm(i\hbar)^2 \sum_{klpqrsu} w_{iklp}(t) \int_{t_0}^t d\bar{t}\, w_{qrsu}^{\pm}(\bar{t})$$
$$\times [G_{lq}^>(t, \bar{t})G_{pr}^>(t, \bar{t})G_{uk}^<(\bar{t}, t)G_{sj}^<(\bar{t}, t)$$
$$- G_{lq}^<(t, \bar{t})G_{pr}^<(t, \bar{t})G_{uk}^>(\bar{t}, t)G_{sj}^>(\bar{t}, t)]$$
$$= \pm(i\hbar)^2 \sum_{klpqrsu} w_{iklp}(t) \int_{t_0}^t d\bar{t}\, w_{qrsu}^{\pm}(\bar{t})$$
$$\times [\mathcal{G}_{lpqr}^{\mathrm{H},>}(t, \bar{t})\mathcal{G}_{sujk}^{\mathrm{H},<}(\bar{t}, t) - \mathcal{G}_{lpqr}^{\mathrm{H},<}(t, \bar{t})\mathcal{G}_{sujk}^{\mathrm{H},>}(\bar{t}, t)]$$

$$= \pm(i\hbar)^2 \sum_{klpqrsu} w_{iklp}(t) \int_{t_0}^t d\bar{t}\, w_{qrsu}^{\pm}(\bar{t})$$
$$\times [\mathcal{G}_{ljqs}^{\mathrm{F},>}(t, \bar{t})\mathcal{G}_{urkp}^{\mathrm{F},<}(\bar{t}, t) - \mathcal{G}_{ljqs}^{\mathrm{F},<}(t, \bar{t})\mathcal{G}_{urkp}^{\mathrm{F},>}(\bar{t}, t)], $$

where we presented several equivalent formulations that will be used below. At this point, it is possible to identify $\mathcal{G}$ [cf. Eq. (10)] in SOA,

$$\mathcal{G}_{ijkl}(t) = i\hbar \sum_{pqrs} \int_{t_0}^t d\bar{t}\, w_{pqrs}^{\pm}(\bar{t})$$
$$\times [\mathcal{G}_{ijpq}^{\mathrm{H},>}(t, \bar{t})\mathcal{G}_{rskl}^{\mathrm{H},<}(\bar{t}, t) - \mathcal{G}_{ijpq}^{\mathrm{H},<}(t, \bar{t})\mathcal{G}_{rskl}^{\mathrm{H},>}(\bar{t}, t)]. \qquad (15)$$

A. $\mathcal{G}$ within the GKBA

The G1-G2 scheme is a reformulation of the ordinary solution of the time-diagonal KBE in the HF-GKBA. When applying the GKBA the time-off-diagonal elements of the less and greater NEGF are reconstructed from the time-diagonal value via [19]

$$G_{ij}^{\gtrless}(t, t') = i\hbar \sum_k [G_{ik}^{\mathrm{R}}(t, t')G_{kj}^{\gtrless}(t') - G_{ik}^{\gtrless}(t)G_{kj}^{\mathrm{A}}(t, t')], \qquad (16)$$

with the retarded and advanced Green functions that are defined by

$$G_{ij}^{\mathrm{R}}(t, t') = \Theta(t - t')[G_{ij}^>(t, t') - G_{ij}^<(t, t')],$$
$$G_{ij}^{\mathrm{A}}(t, t') = -\Theta(t' - t)[G_{ij}^>(t, t') - G_{ij}^<(t, t')],$$

where $G^{\mathrm{R}}(t, t')$ [$G^{\mathrm{A}}(t, t')$] is nonzero only for $t \geqslant t'$ ($t \leqslant t'$). We now show that, in the reconstruction expression (16), the individual functions $G^{\mathrm{R/A}}$ can be eliminated in favor of their difference

$$\mathcal{U}_{ij}(t, t') = G_{ij}^{\mathrm{R}}(t, t') - G_{ij}^{\mathrm{A}}(t, t'). \qquad (17)$$

In the case of the HF-GKBA the propagator $\mathcal{U}(t, t')$ has the properties of a time-evolution operator, as is shown in Appendix A. It possesses the group property [Eq. (A4)] and obeys a Schrödinger equation, cf. Eqs. (A6) and (A7), with the initial value

$$\mathcal{U}_{ij}(t, t) = G_{ij}^{\mathrm{R}}(t, t) - G_{ij}^{\mathrm{A}}(t, t) = G_{ij}^>(t) - G_{ij}^<(t) = \frac{1}{i\hbar}\delta_{ij}. \qquad (18)$$

We now demonstrate the appearance of $\mathcal{U}$ by rewriting Eq. (16) separately, for $t = t'$ and $t > t'$,

$$G_{ij}^{\gtrless}(t' = t) = i\hbar \sum_k \left[\underbrace{G_{ik}^{\mathrm{R}}(t, t)G_{kj}^{\gtrless}(t)}_{=G_{ik}^{\gtrless}(t)G_{kj}^{\mathrm{R}}(t,t)} - G_{ik}^{\gtrless}(t)G_{kj}^{\mathrm{A}}(t, t) \right]$$

$$= i\hbar \sum_k G_{ik}^{\gtrless}(t)\left[G_{kj}^{\mathrm{R}}(t, t) - G_{kj}^{\mathrm{A}}(t, t) \right],$$

$$G_{ij}^{\gtrless}(t' < t) = -i\hbar \sum_k G_{ik}^{\gtrless}(t')G_{kj}^{\mathrm{A}}(t', t)$$

$$= i\hbar \sum_k G_{ik}^{\gtrless}(t')\left[\underbrace{G_{kj}^{\mathrm{R}}(t', t)}_{=0} - G_{kj}^{\mathrm{A}}(t', t) \right].$$

Similar relations can be found for $t \leqslant t'$. These results can be combined to an alternative form of the GKBA

$$G_{ij}^{\gtrless}(t' \leqslant t) = i\hbar \sum_k G_{ik}^{\gtrless}(t')\mathcal{U}_{kj}(t', t), \quad (19)$$

$$G_{ij}^{\gtrless}(t \geqslant t') = i\hbar \sum_k \mathcal{U}_{ik}(t, t')G_{kj}^{\gtrless}(t'). \quad (20)$$

Using the results of Eqs. (19) and (20), for the Green functions [taking into account that in the collision integral only $G^{>}(t \geqslant \bar{t})$ and $G^{<}(\bar{t} \leqslant t)$ appear], we reformulate Eq. (15) for the two-particle Green function on the time diagonal (cf. Appendix A 1)

$$\mathcal{G}_{ijkl}(t) = i\hbar \sum_{pqrsuvxy} \int_{t_0}^{t} d\bar{t} \, w_{pqrs}^{\pm}(\bar{t})$$
$$\times \mathcal{U}_{ijuv}^{(2)}(t, \bar{t})\Phi_{pqxy}^{uvrs}(\bar{t})\mathcal{U}_{xykl}^{(2)}(\bar{t}, t),$$

where we introduced short notations for the two-particle propagator $\mathcal{U}^{(2)}$ and define the occupation factors $\Phi^{\gtrless}$,

$$\mathcal{U}_{ijkl}^{(2)}(t, t') = \mathcal{U}_{ik}(t, t')\mathcal{U}_{jl}(t, t') = \mathcal{U}_{jilk}^{(2)}(t, t'), \quad (21)$$

$$\Phi_{pqrs}^{ijkl}(t) = \Phi_{pqrs}^{ijkl,>}(t) - \Phi_{pqrs}^{ijkl,<}(t),$$

$$\Phi_{pqrs}^{ijkl,\gtrless}(t) = (i\hbar)^4 \mathcal{G}_{ijpq}^{H,\gtrless}(t)\mathcal{G}_{klrs}^{H,\lessgtr}(t)$$
$$= (i\hbar)^4 \mathcal{G}_{ikrp}^{F,\gtrless}(t)\mathcal{G}_{jlsq}^{F,\gtrless}(t) = (i\hbar)^4 \mathcal{G}_{ilsp}^{F,\gtrless}(t)\mathcal{G}_{kjqr}^{F,\lessgtr}(t).$$

A more compact and intuitive notation can be achieved by introducing the two-particle source term

$$\Psi_{ijkl}^{\pm}(t) = \frac{1}{(i\hbar)^2} \sum_{pqrs} w_{pqrs}^{\pm}(t)\Phi_{pqkl}^{ijrs}(t),$$

which results in

$$\mathcal{G}_{ijkl}(t) = (i\hbar)^3 \sum_{pqrs} \int_{t_0}^{t} d\bar{t} \, \mathcal{U}_{ijpq}^{(2)}(t, \bar{t})\Psi_{pqrs}^{\pm}(\bar{t})\mathcal{U}_{rskl}^{(2)}(\bar{t}, t) \quad (22)$$

and allows for a straightforward interpretation: Pair correlations $\mathcal{G}_{ijkl}$ existing in the system at time t are due to pair correlations existing at all times $\bar{t}$ with $t_0 \leqslant \bar{t} \leqslant t$ that are time evolved with the propagators $\mathcal{U}^{(2)}$. The function $\Psi^{\pm}$ has the meaning of pair correlations produced in the system via two-particle scattering per unit time. The appearance of two propagators indicates that $\mathcal{G}_{ijkl}(t)$ does not obey a Schrödinger-type equation but a commutator equation, that we will derive below, in Sec. III B. There we will also show that the time integral in Eq. (22) can be eliminated.

B. Time-linear differential solution for $\mathcal{G}$: SOA-G1-G2 equations for a general basis

There are two ways to transform Eq. (22) into a scheme that scales linearly with propagation time. The first is based on the integral representation for $\mathcal{G}$ while the second uses, instead, coupled time-local differential equations for $G^{<}(t)$ and $\mathcal{G}(t)$. Here and throughout this paper we will concentrate on the second approach as it turns out to be more efficient. The first approach is discussed, for completeness, in Appendix B.

In the following we first derive the differential equation scheme (G1-G2 scheme) for a general single-particle basis that corresponds to the generic Hamiltonian defined in Eq. (1), where spin degrees of freedom are included in the basis index. Below we will separately consider the special cases of a Hubbard basis and the jellium model for electrons where the two spin projections will be indicated explicitly. In order to find the differential equation for $\mathcal{G}$, the EOMs for the retarded/advanced Green functions in HF-GKBA along both time directions are repeated [19]:

$$i\hbar \frac{d}{dt}G_{ij}^{R/A}(t, t') = \sum_k h_{ik}^{HF}(t)G_{kj}^{R/A}(t, t') + \delta_{ij}\delta(t, t')$$

$$i\hbar \frac{d}{dt}G_{ij}^{R/A}(t', t) = -\sum_k G_{ik}^{R/A}(t', t)h_{kj}^{HF}(t) - \delta_{ij}\delta(t, t').$$
$$(23)$$

For the two-particle propagators similar Schrödinger-type EOMs hold as shown in Appendix A 3,

$$\frac{d}{dt}\mathcal{U}_{ijkl}^{(2)}(t, t') = \frac{1}{i\hbar} \sum_{pq} h_{ijpq}^{(2),HF}(t)\mathcal{U}_{pqkl}^{(2)}(t, t'), \quad (24)$$

$$\frac{d}{dt}\mathcal{U}_{ijkl}^{(2)}(t', t) = -\frac{1}{i\hbar} \sum_{pq} \mathcal{U}_{ijpq}^{(2)}(t', t)h_{pqkl}^{(2),HF}(t), \quad (25)$$

where we define the two-particle Hartree-Fock Hamiltonian as the sum of two single-particle parts:

$$h_{ijkl}^{(2),HF}(t) = \delta_{jl}h_{ik}^{HF}(t) + \delta_{ik}h_{jl}^{HF}(t). \quad (26)$$

With that we now compute the time derivative of the time-diagonal two-particle Green function within the HF-GKBA (22), $\mathcal{G}$, which contains two parts,

$$\frac{d}{dt}\mathcal{G}_{ijkl}(t) = \left[\frac{d}{dt}\mathcal{G}_{ijkl}(t)\right]_{\int} + \left[\frac{d}{dt}\mathcal{G}_{ijkl}(t)\right]_{\mathcal{U}^{(2)}}.$$

The first contribution ($\int$) originates from the integration boundaries,

$$\left[\frac{d}{dt}\mathcal{G}_{ijkl}(t)\right]_{\int} = (i\hbar)^3 \sum_{pqrs} \mathcal{U}_{ijpq}^{(2)}(t, t)\Psi_{pqrs}^{\pm}(t)\mathcal{U}_{rskl}^{(2)}(t, t)$$

$$= \frac{1}{i\hbar}\Psi_{ijkl}^{\pm}(t), \quad (27)$$

where the latter equation holds due to the identity [cf. Eqs. (18) and (21)]

$$\mathcal{U}_{ijkl}^{(2)}(t, t) = \frac{1}{(i\hbar)^2}\delta_{ik}\delta_{jl}.$$

The second contribution to the derivative results from the time dependence of the integrand, i.e., of $\mathcal{U}^{(2)}$,

$$\left[\frac{d}{dt}\mathcal{G}_{ijkl}(t)\right]_{\mathcal{U}^{(2)}} = (i\hbar)^3 \sum_{pqrs} \int_{t_0}^{t} d\bar{t} \, \Psi_{pqrs}^{\pm}(\bar{t})$$

$$\times \left\{\left[\frac{d}{dt}\mathcal{U}_{ijpq}^{(2)}(t, \bar{t})\right]\mathcal{U}_{rskl}^{(2)}(\bar{t}, t) + \mathcal{U}_{ijpq}^{(2)}(t, \bar{t})\left[\frac{d}{dt}\mathcal{U}_{rskl}^{(2)}(\bar{t}, t)\right]\right\},$$

and, using the results from Eqs. (24) and (25), we obtain

$$
\left[\frac{d}{dt}\mathcal{G}_{ijkl}(t)\right]_{\mathcal{U}^{(2)}} = (i\hbar)^3 \sum_{pqrs}\int_{t_0}^{t}d\bar{t}
$$

$$
\times \Bigg\{ \left[\frac{1}{i\hbar}\sum_{uv}h^{(2),\mathrm{HF}}_{ijuv}(t)\mathcal{U}^{(2)}_{uvpq}(t,\bar{t})\right]\Psi^{\pm}_{pqrs}(\bar{t})\mathcal{U}^{(2)}_{rskl}(\bar{t},t)
$$

$$
+ \mathcal{U}^{(2)}_{ijpq}(t,\bar{t})\Psi^{\pm}_{pqrs}(\bar{t})\left[-\frac{1}{i\hbar}\sum_{uv}\mathcal{U}^{(2)}_{rsuv}(\bar{t},t)h^{(2),\mathrm{HF}}_{uvkl}(t)\right]\Bigg\},
$$

where we identify $\mathcal{G}$ again, to get

$$
\left[\frac{d}{dt}\mathcal{G}_{ijkl}(t)\right]_{\mathcal{U}^{(2)}} = \frac{1}{i\hbar}\sum_{pq}h^{(2),\mathrm{HF}}_{ijpq}(t)\,\mathcal{G}_{pqkl}(t)
$$

$$
-\frac{1}{i\hbar}\sum_{lf}\mathcal{G}_{ijpq}(t)\,h^{(2),\mathrm{HF}}_{pqkl}(t). \qquad (28)
$$

With that, the full derivative of the time-diagonal two-particle Green function is obtained by adding up the results of Eqs. (27) and (28) [45]

$$
i\hbar\frac{d}{dt}\mathcal{G}_{ijkl}(t) - \left[h^{(2),\mathrm{HF}},\mathcal{G}\right]_{ijkl}(t) = \Psi^{\pm}_{ijkl}(t). \qquad (29)
$$

We now summarize the equations of the G1-G2 scheme for the second-order Born self energy, for a general basis. The scheme consists of the equation for the time-diagonal element of the single-particle Green function, cf. Eq. (8),

$$
i\hbar\frac{d}{dt}G^{<}_{ij}(t) = [h^{\mathrm{HF}}, G^{<}]_{ij}(t) + [I + I^{\dagger}]_{ij}(t), \qquad (30)
$$

$$
I_{ij}(t) = \pm i\hbar\sum_{klp}w_{iklp}(t)\mathcal{G}_{lpjk}(t), \qquad (31)
$$

coupled to Eq. (29)—the EOM of the time-diagonal element of the two-particle Green function. Equations (29), (30), and (31) constitute a closed system of time-local differential equations, for which the computational effort for a numerical implementation scales linearly with time. This was achieved by eliminating the non-Markovian (memory) structure of the collision integral. All transformations so far introduce no further approximations resulting in an exact reformulation of the standard HF-GKBA, as was demonstrated in Ref. [39]. The linear scaling with N_t, as opposed to the quadratic scaling of the standard HF-GKBA in SOA, is the basis for a potentially dramatic speedup of NEGF simulations. The price to pay is the need to compute the entire matrix of the time-diagonal two-particle Green function, the effort for which only depends on the basis dimension N_b. This will be analyzed in detail in Sec. VII.

In a similar manner as for the SOA self energy, a time-local equation for $\mathcal{G}$ corresponding to more advanced self energies can be derived for which the speedup of the G1-G2 scheme is even larger. This will be demonstrated in the subsequent sections. But before that, we consider the G1-G2 scheme in SOA for two important special cases of basis sets—the Hubbard basis and the spatially uniform jellium model (plane-wave basis).

C. SOA-G1-G2 equations for the Hubbard model

The Hubbard model [46] is among the fundamental models in condensed-matter physics, in particular, for the analysis of strong electronic correlations. More recently it has been widely used to study the behavior of fermionic and bosonic atoms in optical lattices [47] and, in particular, time-dependent correlation phenomena, see, e.g, Refs. [16,17,41,48]. For the Fermi-Hubbard model, the general pair-interaction matrix element becomes ($\bar{\delta}_{\alpha\beta} := 1 - \delta_{\alpha\beta}$)

$$
w^{\alpha\beta\gamma\delta}_{ijkl}(t) = U(t)\delta_{ij}\delta_{ik}\delta_{il}\delta_{\alpha\gamma}\delta_{\beta\delta}\bar{\delta}_{\alpha\beta}, \qquad (32)
$$

with the on-site interaction U and the spin projection labeled by greek indices. Recall that we allow for a time dependence of the interaction to capture the adiabatic-switching protocol of initial correlations (see Sec. III E) as well as nonequilibrium processes such as an interaction quench, cf. the discussion of Eq. (1) above. The kinetic-energy matrix is replaced by a hopping Hamiltonian,

$$
h^{(0)}_{ij} = -\delta_{\langle i,j\rangle}J,
$$

which includes hopping processes between nearest-neighbor sites $\langle i, j\rangle$ with amplitude J. Thus, the total Hamiltonian is given by

$$
\hat{H}(t) = -J\sum_{\langle i,j\rangle}\sum_{\alpha}\hat{c}^{\dagger}_{i\alpha}\hat{c}_{j\alpha} + U(t)\sum_{i}\hat{n}^{\uparrow}_{i}\hat{n}^{\downarrow}_{i}. \qquad (33)
$$

Extensions to more complicated models, going beyond the nearest-neighbor single-band case are straightforward but will not be considered here.

The time-diagonal EOM for the single-particle Green function, Eq. (8), takes the following form (from here we give all Hubbard equations for the spin-up component; the spin-down equations follow from the replacement $\uparrow \leftrightarrow \downarrow$.)

$$
i\hbar\frac{d}{dt}G^{<,\uparrow}_{ij}(t) = [h^{\mathrm{HF},\uparrow}, G^{<,\uparrow}]_{ij}(t) + [I + I^{\dagger}]^{\uparrow}_{ij}(t), \qquad (34)
$$

$$
I^{\uparrow}_{ij}(t) = -i\hbar U(t)\mathcal{G}^{\uparrow\downarrow\uparrow\downarrow}_{iiji}(t), \qquad (35)
$$

where for electrons there exist two collision integrals, $I^{\uparrow}$ and $I^{\downarrow}$, that enter the single-particle EOMs. The Hartree-Fock Hamiltonian in Eq. (34) in the Hubbard basis becomes [cf. Eq. (12)]:

$$
h^{\mathrm{HF},\uparrow}_{ij}(t) = h^{(0)}_{ij} - i\hbar\delta_{ij}U(t)G^{<,\downarrow}_{ii}(t).
$$

The equation for the time-diagonal two-particle Green function, Eq. (29), now reads

$$
i\hbar\frac{d}{dt}\mathcal{G}^{\uparrow\downarrow\uparrow\downarrow}_{ijkl}(t) - \left[h^{(2),\mathrm{HF}}_{\uparrow\downarrow}, \mathcal{G}^{\uparrow\downarrow\uparrow\downarrow}\right]_{ijkl}(t)
$$

$$
= \frac{1}{(i\hbar)^2}U(t)\Phi^{\uparrow\downarrow\uparrow\downarrow}_{ijkl}(t) =: \Psi^{\uparrow\downarrow\uparrow\downarrow}_{ijkl}(t), \qquad (36)
$$

where

$$
h^{(2),\mathrm{HF}}_{ijkl,\uparrow\downarrow}(t) = \delta_{jl}h^{\mathrm{HF},\uparrow}_{ik}(t) + \delta_{ik}h^{\mathrm{HF},\downarrow}_{jl}(t), \qquad (37)
$$

and

$$
\Phi_{ijkl}^{\uparrow\downarrow\uparrow\downarrow}(t) := (i\hbar)^4 \sum_p \big[G_{ip}^{>,\uparrow}(t) G_{jp}^{>,\downarrow}(t) G_{pk}^{<,\uparrow}(t) G_{pl}^{<,\downarrow}(t)
$$
$$
- G_{ip}^{<,\uparrow}(t) G_{jp}^{<,\downarrow}(t) G_{pk}^{>,\uparrow}(t) G_{pl}^{>,\downarrow}(t) \big] . \quad (38)
$$

The Eqs. (34) and (36) together with their spin-down counterparts form a coupled system of four equations. For SOA, no further spin combinations of $\mathcal{G}$ contribute. Numerical examples will be presented in Sec. VII.

D. SOA-G1-G2 equations for jellium

As the second example we consider the jellium Hamiltonian [49],

$$
\hat{H}(t) = \sum_{p\alpha} \frac{p^2}{2m} \hat{c}_{p\alpha}^\dagger \hat{c}_{p\alpha} + \sum_{pp'q\alpha\beta} v_{|q|}(t) \hat{c}_{p+q\alpha}^\dagger \hat{c}_{p'-q\beta}^\dagger \hat{c}_{p'\beta} \hat{c}_{p\alpha} ,
$$
$$
\quad (39)
$$

with the vector-sized momenta p, p', q and the Coulomb matrix element $v_{|q|} = \frac{4\pi e^2}{|q|^2}$ [we again allow for a time-dependent pair interaction to also describe adiabatic-switching processes, cf. the discussion of Eq. (1) above]. This model is of relevance for the electron gas in metals [50,51], for electron-hole plasmas in semiconductors [4], and for dense quantum plasmas, e.g., Refs. [5,10], as well as for model development [49,51]. The matrix element of the pair interaction in a plane-wave basis is

$$
w_{k_1 k_2 k_3 k_4}^{\alpha\beta\gamma\delta}(t) = \delta_{\alpha\gamma} \delta_{\beta\delta} \delta(k_1 + k_2 - k_3 - k_4) v_{|k_1-k_3|}(t) , \quad (40)
$$

where v_q denotes the spatial Fourier transform of the pair potential, and the delta function arises from momentum conservation (spatial homogeneity).

The EOM for the single-particle Green function, Eq. (8), is now

$$
i\hbar \frac{d}{dt} G_p^{<,\alpha}(t) = [I + I^\dagger]_p^\alpha(t) , \quad (41)
$$

with

$$
I_p^\alpha(t) = \pm i\hbar \sum_{\bar{p},q} \sum_\beta v_{|q|}(t) \mathcal{G}_{p\bar{p}q}^{\alpha\beta}(t) ,
$$

where we defined

$$
\mathcal{G}_{p,\bar{p},q}^{\alpha\beta}(t) := \mathcal{G}_{p-q,\bar{p}+q,p,\bar{p}}^{\alpha\beta\alpha\beta}(t) , \quad (42)
$$

and the equation for the time-diagonal two-particle Green function becomes

$$
i\hbar \frac{d}{dt} \mathcal{G}_{p\bar{p}q}^{\alpha\beta}(t) - \mathcal{G}_{p\bar{p}q}^{\alpha\beta}(t) \big(h_{p-q}^{\mathrm{HF},\alpha} + h_{\bar{p}+q}^{\mathrm{HF},\beta} - h_p^{\mathrm{HF},\alpha} - h_{\bar{p}}^{\mathrm{HF},\beta} \big)(t)
$$
$$
= \frac{1}{(i\hbar)^2} \big[v_{|q|}(t) \pm \delta_{\alpha\beta} v_{|p-q-\bar{p}|}(t) \big] \Phi_{p\bar{p}q}^{\alpha\beta}(t)
$$
$$
=: \Psi_{p\bar{p}q}^{\pm,\alpha\beta}(t) , \quad (43)
$$

where

$$
h_p^{\mathrm{HF},\alpha}(t) = \frac{p^2}{2m} + i\hbar \sum_{\bar{p}} v_{|p-\bar{p}|}(t) G_{\bar{p}}^{<,\alpha}(t) ,
$$

and

$$
\Phi_{p\bar{p}q}^{\alpha\beta}(t) = (i\hbar)^4 \big[G_{p-q}^{>,\alpha}(t) G_{\bar{p}+q}^{>,\beta}(t) G_p^{<,\alpha}(t) G_{\bar{p}}^{<,\beta}(t)
$$
$$
- G_{p-q}^{<,\alpha}(t) G_{\bar{p}+q}^{<,\beta}(t) G_p^{>,\alpha}(t) G_{\bar{p}}^{>,\beta}(t) \big] .
$$

This result agrees with the one derived in Refs. [5,32].

E. Initial pair correlations in the G1-G2 scheme

We conclude this section by returning to the question of initial correlations in NEGF theory that we briefly discussed in the context of Eq. (8) and analyze how they show up in the present G1-G2 scheme. For NEGF theory and the GKBA, the question of initial correlations has been extensively discussed before, see, e.g., Refs. [6,7,11,52], for more recent investigations, see Refs. [21,36,53]. As we mentioned below Eq. (10), the collision integral $I(t) = \mathcal{I}(t)$ vanishes for $t \to t_0$ which is correct only for a system that is uncorrelated at the initial time t_0. In the presence of finite initial correlations, one also has to consider the second contribution of the collision integral, Eq. (9), with $\lim_{t\to t_0} I(t) = \mathcal{I}^{\mathrm{IC}}(t_0)$. In NEGF theory there are three common equivalent approaches to take into account initial correlations and to derive the additional collision integral $\mathcal{I}^{\mathrm{IC}}(t)$:

(i): Derivation of an additional self energy Σ^{IC} that depends on initial correlations. This self energy can be shown to be singular, i.e., it contains a delta function $\delta(t, t_0)$ which gives rise to a finite value of the time integral from t_0 to t in $I(t)$, in the limit $t \to t_0$. This approach has been developed in Refs. [5,10,52,54], where also explicit expressions for the second-order Born and T-matrix approximations for the self energy have been derived.

(ii): Incorporation of thermodynamic-equilibrium initial correlations given by an imaginary-time Green function (Matsubara function). This leads to an extension of the Keldysh time contour $\mathcal{C}$ that is shown in the lower part of Fig. 1. When making the transition from the Green function on this contour to real-time quantities, i.e., from Eqs. (2) and (3) to the equations of motion for $G^{\gtrless}(t, t')$, an additional collision integral appears that involves the mixed Green functions $G(t, \tau)$ and $G(\tau, t)$ where the argument t runs along the real-time part of the contour and τ along the imaginary-time branch of $\mathcal{C}_{\mathrm{M}}$. This approach was introduced by Danielewicz [7] and is explained in detail in Refs. [6,33].

(iii): Incorporation of arbitrary initial correlations at time $t = t_0$ that are computed via a preceding time evolution that starts from an uncorrelated initial state in the remote past ($t \to -\infty$). This is the "adiabatic-switching" procedure that was discussed already by Keldysh [1,2]. There the interaction is smoothly turned on, i.e., $w_{ijkl}(t) = f(t) w_{ijkl}$, where the scalar function $f(t)$ starts from zero and approaches one at t_0. Correspondingly, the contour is extended to real times well before t_0 (see the contour $\mathcal{C}_{\mathrm{AS}}$ in the upper part of Fig. 1) and the collision integral I again has a finite value at $t = t_0$. For recent applications of this approach, see Refs. [17,28,55].

It is characteristic for these NEGF approaches [except for (i)] that the correlated initial state is prepared without explicitly specifying the two-particle Green function $G^{(2)}$ or the pair-correlation function. This is in line with the standard

NEGF approach to formally eliminate the two-particle Green function in favor of the single-particle self energy.

In contrast, the G1-G2 scheme recovers the two-particle Green function on the time diagonal $\mathcal{G}(t)$ from the collision integral $I(t)$. Its equation is solved simultaneously with the equation for the single-particle NEGF. This allows for a different and more straightforward approach to initial correlations as we discuss in the remainder of this section.

As shown in Ref. [5], the previous expression (22) for $\mathcal{G}(t)$ is only a particular solution of the inhomogeneous differential equation (29), whereas the complete solution contains, in addition, the general solution of the homogeneous equations (corresponding to the neglect of $\Psi^{\pm}$) which is directly related to initial correlations and which we denote $\mathcal{G}^{\mathrm{IC}}(t)$. Thus the total solution becomes

$$\mathcal{G}(t) \rightarrow \mathcal{G}(t) + \mathcal{G}^{\mathrm{IC}}(t), \qquad (44)$$

$$\mathcal{G}^{\mathrm{IC}}_{ijkl}(t) = (i\hbar)^4 \sum_{pqrs} \mathcal{U}^{(2)}_{ijpq}(t, t_0)\, \mathcal{G}^0_{pqrs}\, \mathcal{U}^{(2)}_{rskl}(t_0, t). \qquad (45)$$

For the special case $t = t_0$, the first term in Eq. (44) vanishes but the second reduces exactly to the initial correlation, $\mathcal{G}^{\mathrm{IC}}(t_0) = \mathcal{G}^0$. Thus, we have identified the initial conditions for the differential equations (30), for $G^<(t)$, and (29), for $\mathcal{G}(t)$. Recalling the definitions (11) and (5), the former is related to the initial value of the single-particle density matrix and the latter to the initial value of the correlated part of the two-particle density matrix $n^0_{ijkl} := n_{ijkl}(t_0)$:

$$G^{0,<}_{ij} = \pm \frac{1}{i\hbar} n_{ij}(t_0) =: \pm \frac{1}{i\hbar} n^0_{ij},$$

$$\mathcal{G}^0_{ijkl} = \frac{1}{(i\hbar)^2} \left\{ n^0_{ijkl} - n^0_{ik} n^0_{jl} \mp n^0_{il} n^0_{jk} \right\},$$

i.e., to pair correlations existing in the system at the initial time $t = t_0$. The two expressions, (45) and (22), can be combined into the total solution for the time-diagonal two-particle Green function according to

$$\mathcal{G}_{ijkl}(t) = (i\hbar)^4 \sum_{pqrs} \int_{t_0}^{t} d\bar{t}\, \mathcal{U}^{(2)}_{ijpq}(t, \bar{t})$$

$$\times \left[\delta(t_0, \bar{t}) \mathcal{G}^0_{pqrs} + \frac{1}{i\hbar} \Psi^{\pm}_{pqrs}(\bar{t}) \right] \mathcal{U}^{(2)}_{rskl}(\bar{t}, t). \qquad (46)$$

Mathematically, of course, arbitrary initial conditions can be used to time evolve the differential equations for $G^<(t)$ and $\mathcal{G}(t)$. At the same time, however, restrictions should be imposed by selecting only physically realistic correlations (see below). An important example is initial correlations that correspond to the correlated ground state or thermodynamic-equilibrium state. This can be achieved using concept (iii) above to adiabatically turn on the interaction, starting from an uncorrelated system in the remote past. This results in the following "initial" pair-correlation function (corresponding to the second-Born approximation)

$$\mathcal{G}^0_{ijkl} = (i\hbar)^3 \sum_{pqrs} \int_{-\infty}^{t_0} d\bar{t}\, \mathcal{U}^{(2)}_{ijpq}(t_0, \bar{t}) \Psi^{\pm}_{pqrs}(\bar{t}) \mathcal{U}^{(2)}_{rskl}(\bar{t}, t_0). \qquad (47)$$

In practice, a sufficiently long but finite adiabatic-switching time has to be chosen to generate the correlated ground state [19]. Inserting the adiabatic-switching result (47) into the general expression for the time-dependent initial-correlation contribution, Eq. (45), we obtain

$$\mathcal{G}^{\mathrm{IC}}_{ijkl}(t) = (i\hbar)^3 \sum_{pqrs} \int_{-\infty}^{t_0} d\bar{t}\, \mathcal{U}^{(2)}_{ijpq}(t, \bar{t}) \Psi^{\pm}_{pqrs}(\bar{t}) \mathcal{U}^{(2)}_{rskl}(\bar{t}, t),$$

where we took into account the group property of the two-particle propagators, cf. Appendix A 2. Interestingly, this result is of exactly the same mathematical form as the collision-induced contribution, Eq. (22), except for the limits of the time integration, which are t_0 and t, in the latter case. This means, in the case of initial correlations that are produced via adiabatic switching, both contributions to the two-particle function can be combined into

$$\mathcal{G}_{ijkl}(t) = (i\hbar)^3 \sum_{pqrs} \int_{-\infty}^{t} d\bar{t}\, \mathcal{U}^{(2)}_{ijpq}(t, \bar{t}) \Psi^{\pm}_{pqrs}(\bar{t}) \mathcal{U}^{(2)}_{rskl}(\bar{t}, t), \qquad (48)$$

which is a special case of the general result (46). This result also shows that the "initial" point t_0 is arbitrary: The dynamics that started at $-\infty$ can be interrupted at any time $t_1 \in (-\infty, t]$, and the result (48) for $\mathcal{G}(t_1)$ can be used as the new "initial" correlation $\mathcal{G}^0$, whereas the collision-induced contribution now contains an integral running from t_1 to t. Of course, the dynamics are time reversible: Starting at time t and changing the Hamiltonian $\hat{H}(t + \bar{t}) \rightarrow -\hat{H}(t - \bar{t})$ will return the system to the same initial state at t_1 [56].

While expression (47) was based on adiabatic switching, in principle, the initial value for $\mathcal{G}^0$ can be generated by other methods [e.g. (i) and (ii) above], as long as certain physical restrictions are satisfied, as was discussed, e.g., in Refs. [21,57]. The result can be summarized as follows: In a closed (isolated) system, only such pair correlations are physically relevant that are produced for the same system within the same many-body approximations as the subsequent dynamics. In contrast, initial correlations that are produced by different approximations will, in general, lead to discontinuities in the dynamics, for $t > t_0$. This has relevance in open systems, in cases where the initial state is produced externally, by a separate process such as an interaction quench, e.g., Refs. [10,58–60] or a spin switch [61,62]. When the general result, Eq. (46), is inserted into the kinetic equation (30), this will give rise to the total collision integral, $I(t)$, Eq. (9), where the term containing $\Psi^{\pm}$ will produce the dynamical collision integral $\mathcal{I}(t)$, whereas the term containing $\mathcal{G}^0$ will give rise to the second contribution $\mathcal{I}^{\mathrm{IC}}(t)$, in agreement with the discussion above.

With this we succeeded to derive the complete formal solution for the time-diagonal two-particle Green function that is equivalent to the coupled system of differential equations for $G^<(t)$ and $\mathcal{G}(t)$ [Eqs. (30) and (29)] with the initial conditions $G^{<0}$ and $\mathcal{G}^0$, respectively. While the results in Eqs. (46) and (48) hold for the second-Born approximation for the self energy, this functional form is generally valid. The main difference, for more complicated self energies, is the explicit form of the two-particle propagators. For the additional approximations considered in this work [GW (Sec. IV),

T matrix (Sec. V)] the respective expressions are presented in Appendix D.

IV. *GW* SELF ENERGY

The static second-Born approximation that was considered above neglects screening effects and the dynamics of screening. These effects are captured by the *GW* approximation for which the self energy is given by

$$\Sigma_{ij}^{\gtrless}(t,t') = i\hbar \sum_{kl} W_{ilkj}^{\gtrless}(t,t') G_{kl}^{\gtrless}(t,t').$$ (49)

Here, W is the dynamically screened interaction, which can be expressed in terms of the bare interaction and the inverse dielectric function,

$$W_{ijkl}^{\gtrless}(t,t') = \sum_{pq} w_{ipkq}(t) \varepsilon_{pjql}^{-1,\gtrless}(t,t'),$$ (50)

which allows us to transform the self energy (49) into

$$\Sigma_{ij}^{\gtrless}(t,t') = i\hbar \sum_{klpq} w_{ipkq}(t) \varepsilon_{plqj}^{-1,\gtrless}(t,t') G_{kl}^{\gtrless}(t,t').$$

The collision integral of the time-diagonal equation then becomes

$$I_{ij}(t) = \sum_k \int_{t_0}^t d\bar{t} \left[\Sigma_{ik}^{>}(t,\bar{t}) G_{kj}^{<}(\bar{t},t) - \Sigma_{ik}^{<}(t,\bar{t}) G_{kj}^{>}(\bar{t},t) \right]$$

$$= i\hbar \sum_{klpqr} w_{ipkq}(t) \int_{t_0}^t d\bar{t}$$

$$\times \left[\varepsilon_{plqr}^{-1,>}(t,\bar{t}) \mathcal{G}_{krjl}^{F,>}(t,\bar{t}) - \varepsilon_{plqr}^{-1,<}(t,\bar{t}) \mathcal{G}_{krjl}^{F,<}(t,\bar{t}) \right].$$

Recalling the definition (10), we identify the time-diagonal element of the two-particle Green function in *GW* approximation,

$$\mathcal{G}_{ijkl}(t) = \pm \sum_{pq} \int_{t_0}^t d\bar{t} \left[\varepsilon_{lpjq}^{-1,>}(t,\bar{t}) \mathcal{G}_{iqkp}^{F,>}(t,\bar{t}) - \varepsilon_{lpjq}^{-1,<}(t,\bar{t}) \mathcal{G}_{iqkp}^{F,<}(t,\bar{t}) \right].$$

By construction, the screened-interaction tensor obeys the following symmetry [cf. Eq. (13)],

$$W_{ijkl}^{\gtrless}(t,t') = W_{jilk}^{\lessgtr}(t',t).$$ (51)

From Hedin's equations [63] we derive the following relation for the dynamically screened interaction W from which we subtract the singular part, i.e., $W_{ijkl}^{\gtrless}(t,t') \to W_{ijkl}^{\gtrless}(t,t') - w_{ijkl}\delta(t-t')$ [28],

$$W_{ijkl}^{\gtrless}(t,t') = \pm i\hbar \sum_{pqrs} w_{ipkq}(t) w_{rjsl}(t') \mathcal{G}_{qspr}^{F,\gtrless}(t,t')$$

$$\pm i\hbar \sum_{pqrs} w_{ipkq}(t)$$

$$\times \left[\int_{t_0}^t d\bar{t} \left(\mathcal{G}_{qspr}^{F,>}(t,\bar{t}) - \mathcal{G}_{qspr}^{F,<}(t,\bar{t}) \right) W_{rjsl}^{\gtrless}(\bar{t},t') \right.$$

$$\left. + \int_{t_0}^{t'} d\bar{t} \, \mathcal{G}_{qspr}^{F,\gtrless}(t,\bar{t}) \left(W_{rjsl}^{<}(\bar{t},t') - W_{rjsl}^{>}(\bar{t},t') \right) \right].$$ (52)

By comparison with Eq. (50) and using the symmetry of Eq. (51) one can identify a recursive equation for ε^{-1},

$$\varepsilon_{ijkl}^{-1,\gtrless}(t,t') = \pm i\hbar \sum_{pq} w_{pjql}(t') \mathcal{G}_{kqip}^{F,\gtrless}(t,t')$$

$$\pm i\hbar \sum_{pqrs} w_{jrls}(t')$$

$$\times \left[\int_{t_0}^t d\bar{t} \left(\mathcal{G}_{kqip}^{F,>}(t,\bar{t}) - \mathcal{G}_{kqip}^{F,<}(t,\bar{t}) \right) \varepsilon_{rpsq}^{-1,\gtrless}(t',\bar{t}) \right.$$

$$\left. + \int_{t_0}^{t'} d\bar{t} \, \mathcal{G}_{kqip}^{F,\gtrless}(t,\bar{t}) \left(\varepsilon_{rpsq}^{-1,>}(t',\bar{t}) - \varepsilon_{rpsq}^{-1,<}(t',\bar{t}) \right) \right].$$

The time-diagonal equation for the inverse dielectric function can be further simplified,

$$\varepsilon_{ijkl}^{-1,\gtrless}(t,t) = \pm i\hbar \sum_{pq} w_{pjql}(t) \mathcal{G}_{kqip}^{F,\gtrless}(t) \pm i\hbar \sum_{pqrs} w_{jrls}(t)$$

$$\times \int_{t_0}^t d\bar{t} \left(\mathcal{G}_{kqip}^{F,>}(t,\bar{t}) \varepsilon_{rpsq}^{-1,>}(t,\bar{t}) \right.$$

$$\left. - \mathcal{G}_{kqip}^{F,<}(t,\bar{t}) \varepsilon_{rpsq}^{-1,<}(t,\bar{t}) \right)$$

$$= \pm i\hbar \sum_{pq} w_{pjql}(t) \mathcal{G}_{kqip}^{F,\gtrless}(t)$$

$$+ i\hbar \sum_{pq} w_{pjql}(t) \mathcal{G}_{kqip}(t).$$ (53)

A. *GW* approximation within the HF-GKBA

We now apply the HF-GKBA [cf. (16) and (17)] and obtain the following expressions for $\mathcal{G}$,

$$\mathcal{G}_{ijkl}(t) = \pm (i\hbar)^2 \sum_{pqrs} \int_{t_0}^t d\bar{t}\, \mathcal{U}_{ir}(t,\bar{t}) \left[\varepsilon_{lpjq}^{-1,>}(t,\bar{t}) \mathcal{G}_{rqsp}^{F,>}(\bar{t}) \right.$$

$$\left. - \varepsilon_{lpjq}^{-1,<}(t,\bar{t}) \mathcal{G}_{rqsp}^{F,<}(\bar{t}) \right] \mathcal{U}_{sk}(\bar{t},t),$$

as well as for ε^{-1},

$$\varepsilon_{ijkl}^{-1,\gtrless}(t \geqslant t')$$

$$= \pm (i\hbar)^3 \sum_{pqrs} w_{pjql}(t') \mathcal{U}_{kr}(t,t') \mathcal{G}_{rqsp}^{F,\gtrless}(t') \mathcal{U}_{si}(t',t)$$

$$\pm (i\hbar)^3 \sum_{pqrsuv} w_{jrls}(t') \left[\int_{t_0}^t d\bar{t}\, \mathcal{U}_{ku}(t,\bar{t}) \right.$$

$$\times \left(\mathcal{G}_{uqvp}^{F,>}(\bar{t}) - \mathcal{G}_{uqvp}^{F,<}(\bar{t}) \right) \mathcal{U}_{vi}(\bar{t},t) \varepsilon_{rpsq}^{-1,\lessgtr}(t',\bar{t})$$

$$+ \int_{t_0}^{t'} d\bar{t}\, \mathcal{U}_{ku}(t,\bar{t}) \mathcal{G}_{uqvp}^{F,\gtrless}(\bar{t}) \mathcal{U}_{vi}(\bar{t},t)$$

$$\left. \times \left(\varepsilon_{rpsq}^{-1,>}(t',\bar{t}) - \varepsilon_{rpsq}^{-1,<}(t',\bar{t}) \right) \right],$$ (54)

where $\mathcal{U}$ obeys Eqs. (A6) and (A7). By using the symmetry relation of Eq. (51) we easily find an expression for the time derivative of the off-diagonal inverse dielectric

function,

$$
\frac{d}{dt} \varepsilon_{ijkl}^{-1,\gtrless}(t \geqslant t')
$$

$$
= \frac{1}{i\hbar} \sum_p \left\{ h_{kp}^{\mathrm{HF}}(t) \varepsilon_{ijpl}^{-1,\gtrless}(t \geqslant t') - \varepsilon_{pjkl}^{-1,\gtrless}(t \geqslant t') h_{pi}^{\mathrm{HF}}(t) \right\}
$$

$$
\pm i\hbar \sum_{pqrs} w_{prqs}(t) \left[\mathcal{G}_{kqip}^{\mathrm{F},>}(t) - \mathcal{G}_{kqip}^{\mathrm{F},<}(t) \right] \varepsilon_{rjsl}^{-1,\gtrless}(t \geqslant t')
$$

$$
= \frac{1}{i\hbar} \sum_{pq} \left[\mathfrak{h}_{pkqi}^{\varepsilon,\mathrm{HF}}(t) + \mathfrak{h}_{pkqi}^{\varepsilon,\mathrm{corr}}(t) \right] \varepsilon_{pjql}^{-1,\gtrless}(t \geqslant t'),
$$

where we introduced the modified two-particle Hartree-Fock Hamiltonian

$$
\mathfrak{h}_{ijkl}^{\varepsilon,\mathrm{HF}}(t) = \delta_{il} h_{jk}^{\mathrm{HF}}(t) - \delta_{jk} h_{il}^{\mathrm{HF}}(t),
$$

which matches the index structure of the effective quasi-Hamiltonian, defined as

$$
\mathfrak{h}_{ijkl}^{\varepsilon,\mathrm{corr}}(t) = \pm (i\hbar)^2 \sum_{pq} w_{qipk}(t) \left[\mathcal{G}_{jplq}^{\mathrm{F},>}(t) - \mathcal{G}_{jplq}^{\mathrm{F},<}(t) \right]. \quad (55)
$$

Combining these Hamiltonians into a single one,

$$
\mathfrak{h}_{ijkl}^{\varepsilon}(t) = \mathfrak{h}_{ijkl}^{\varepsilon,\mathrm{HF}}(t) + \mathfrak{h}_{ijkl}^{\varepsilon,\mathrm{corr}}(t), \quad (56)
$$

we observe that the inverse dielectric function, within the *GW*-HF-GKBA, obeys a time-dependent two-particle Schrödinger equation,

$$
i\hbar \frac{d}{dt} \varepsilon_{ijkl}^{-1,\gtrless}(t \geqslant t') = \sum_{pq} \mathfrak{h}_{pkqi}^{\varepsilon}(t) \varepsilon_{pjql}^{-1,\gtrless}(t \geqslant t'), \quad (57)
$$

with the Hamiltonian (56), that is equivalent to the rather complicated integral equation (54). In the following, we demonstrate that, for the *GW*-HF-GKBA, again, a time-local G1-G2 scheme can be derived which retains time-linear scaling [39].

B. *GW*-G1-G2 equations for a general basis

To derive the G1-G2 scheme, we compute the time derivative of $\mathcal{G}$, yielding

$$
\frac{d}{dt} \mathcal{G}_{ijkl}(t) = \left[\frac{d}{dt} \mathcal{G}_{ijkl}(t) \right]_{\int} + \left[\frac{d}{dt} \mathcal{G}_{ijkl}(t) \right]_{\varepsilon} + \left[\frac{d}{dt} \mathcal{G}_{ijkl}(t) \right]_{\mathcal{U}}, \quad (58)
$$

where the first contribution, which originates from the derivative of the integration boundaries, is given by

$$
\left[\frac{d}{dt} \mathcal{G}_{ijkl}(t) \right]_{\int}
$$

$$
= \pm \sum_{pq} \left[\varepsilon_{lpjq}^{-1,>}(t,t) \mathcal{G}_{iqkp}^{\mathrm{F},>}(t) - \varepsilon_{lpjq}^{-1,<}(t,t) \mathcal{G}_{iqkp}^{\mathrm{F},<}(t) \right]
$$

$$
= i\hbar \sum_{pqrs} w_{rpsq}(t) \left[\mathcal{G}_{jslr}^{\mathrm{F},>}(t) \mathcal{G}_{iqkp}^{\mathrm{F},>}(t) - \mathcal{G}_{jslr}^{\mathrm{F},<}(t) \mathcal{G}_{iqkp}^{\mathrm{F},<}(t) \right]
$$

$$
\pm i\hbar \sum_{pqrs} w_{rpsq}(t) \mathcal{G}_{jslr}(t) \left[\mathcal{G}_{iqkp}^{\mathrm{F},>}(t) - \mathcal{G}_{iqkp}^{\mathrm{F},<}(t) \right]
$$

$$
= \frac{1}{i\hbar} \Psi_{ijkl}(t) - \frac{1}{i\hbar} \sum_{pq} \mathcal{G}_{qjpl}(t) \left[\mathfrak{h}_{qkpi}^{\varepsilon,\mathrm{corr}}(t) \right]^*.
$$

Here, the two-particle source term is defined as

$$
\Psi_{ijkl}(t) = \frac{1}{(i\hbar)^2} \sum_{pqrs} w_{pqrs}(t) \Phi_{pqkl}^{ijrs}(t).
$$

The second contribution to Eq. (58), resulting from the time derivative of ε^{-1}, is given by

$$
\left[\frac{d}{dt} \mathcal{G}_{ijkl}(t) \right]_{\varepsilon}
$$

$$
= \pm (i\hbar)^2 \sum_{pqrs} \int_{t_0}^{t} d\bar{t}\, \mathcal{U}_{ir}(t,\bar{t}) \left[\left(\frac{d}{dt} \varepsilon_{lpjq}^{-1,>}(t,\bar{t}) \right) \mathcal{G}_{rqsp}^{\mathrm{F},>}(\bar{t}) \right.
$$

$$
\left. - \left(\frac{d}{dt} \varepsilon_{lpjq}^{-1,<}(t,\bar{t}) \right) \mathcal{G}_{rqsp}^{\mathrm{F},<}(\bar{t}) \right] \mathcal{U}_{sk}(\bar{t},t)
$$

$$
= \frac{1}{i\hbar} \sum_{pq} \left[\mathfrak{h}_{pjql}^{\varepsilon,\mathrm{HF}}(t) + \mathfrak{h}_{pjql}^{\varepsilon,\mathrm{corr}}(t) \right] \mathcal{G}_{iqkp}(t),
$$

whereas the third contribution to Eq. (58), which stems from the derivative of the propagators, is

$$
\left[\frac{d}{dt} \mathcal{G}_{ijkl}(t) \right]_{\mathcal{U}}
$$

$$
= \pm (i\hbar)^2 \sum_{pqrs} \int_{t_0}^{t} d\bar{t} \left(\frac{d}{dt} \mathcal{U}_{ir}(t,\bar{t}) \right) \left[\varepsilon_{lpjq}^{-1,>}(t,\bar{t}) \mathcal{G}_{rqsp}^{\mathrm{F},>}(\bar{t}) \right.
$$

$$
\left. - \varepsilon_{lpjq}^{-1,<}(t,\bar{t}) \mathcal{G}_{rqsp}^{\mathrm{F},<}(\bar{t}) \right] \mathcal{U}_{sk}(\bar{t},t)
$$

$$
\pm (i\hbar)^2 \sum_{pqrs} \int_{t_0}^{t} d\bar{t}\, \mathcal{U}_{ir}(t,\bar{t}) \left[\varepsilon_{lpjq}^{-1,>}(t,\bar{t}) \mathcal{G}_{rqsp}^{\mathrm{F},>}(\bar{t}) \right.
$$

$$
\left. - \varepsilon_{lpjq}^{-1,<}(t,\bar{t}) \mathcal{G}_{rqsp}^{\mathrm{F},<}(\bar{t}) \right] \left(\frac{d}{dt} \mathcal{U}_{sk}(\bar{t},t) \right)
$$

$$
= \frac{1}{i\hbar} \sum_p \left[h_{ip}^{\mathrm{HF}}(t) \mathcal{G}_{pjkl}(t) - \mathcal{G}_{ijpl}(t) h_{pk}^{\mathrm{HF}}(t) \right]
$$

$$
= -\frac{1}{i\hbar} \sum_{pq} \mathcal{G}_{qjpl}(t) \left[\mathfrak{h}_{qkpi}^{\varepsilon,\mathrm{HF}}(t) \right]^*.
$$

Finally, the three contributions to the derivative of $\mathcal{G}$ are combined to reveal

$$
i\hbar \frac{d}{dt} \mathcal{G}_{ijkl}(t) = \Psi_{ijkl}(t) + \sum_{pq} \left\{ \mathfrak{h}_{qjpl}^{\varepsilon}(t) [\mathcal{G}_{qkpi}(t)]^* \right.
$$

$$
\left. - \mathcal{G}_{qjpl}(t) \left[\mathfrak{h}_{qkpi}^{\varepsilon}(t) \right]^* \right\}, \quad (59)
$$

where $\mathfrak{h}^{\varepsilon}(t)$ was defined in Eq. (56). With this we have obtained the equations of the G1-G2 scheme for the *GW* approximation. For $\mathfrak{h}^{\varepsilon,\mathrm{corr}}(t) \equiv 0$, we recover the equations from the SOA, cf. Eq. (29), since the remaining Hamiltonian contribution can be expressed as a commutator. Equation (59) is the most compact formulation that visualizes the intrinsic structure of $\mathcal{G}$ in the *GW* approximation.

For practical use, it is convenient to separate the correlation contributions from the mean-field terms via the introduction of an additional quantity:

$$
i\hbar \frac{d}{dt} \mathcal{G}_{ijkl}(t) - \left[h^{(2),\mathrm{HF}}, \mathcal{G} \right]_{ijkl}(t)
$$

$$
= \Psi_{ijkl}(t) + \Pi_{ijkl}(t) - [\Pi_{lkji}(t)]^*, \quad (60)
$$

where polarization effects are included in

$$\Pi_{ijkl}(t) = \sum_{pq} \mathfrak{h}^{\varepsilon,\mathrm{corr}}_{qjpl}(t) \mathcal{G}_{ipkq}(t) \,. \tag{61}$$

Equation (59) agrees with the polarization approximation of density-matrix theory, cf. Refs. [5,64]. In the Markov limit this leads to the quantum generalization of the Balescu-Lenard kinetic equation [65–67].

Here, we have employed the standard definition of *GW* in NEGF theory, which is widely used in literature (see, e.g., Refs. [15,28,68]), in which the screened interaction [Eq. (52)] does not include exchange terms. The generalization to also describe exchange processes is, however, straightforwardly carried out. For the G1-G2 scheme, this is achieved by simply replacing $\Psi_{ijkl}(t)$ by $\Psi^{\pm}_{ijkl}(t)$ in Eqs. (59) and (60).

Again we have succeeded to eliminate all time integrations which means that Eq. (59) can be solved with an effort that is first order in N_t. Note that the conventional HF-GKBA scheme with *GW* self energy scales as N_t^3 indicating a huge advantage of the G1-G2 formulation [39]. More computational details will be given below, in Sec. VII.

C. *GW*-G1-G2 equations for the Hubbard model

For the Hubbard system [cf. Eq. (33)] we again use the interaction matrix of Eq. (32). With that, the equations of motion (60) become,

$$i\hbar \frac{d}{dt} \mathcal{G}^{\uparrow\downarrow\uparrow\downarrow}_{ijkl}(t) - \left[h^{(2),\mathrm{HF}}_{\uparrow\downarrow}, \mathcal{G}^{\uparrow\downarrow\uparrow\downarrow} \right]_{ijkl}(t)$$
$$= \Psi^{\uparrow\downarrow\uparrow\downarrow}_{ijkl}(t) + \Pi^{\uparrow\downarrow\uparrow\downarrow}_{ijkl}(t) - [\Pi^{\uparrow\downarrow\uparrow\downarrow}_{lkji}(t)]^* \quad \text{and} \tag{62}$$

$$i\hbar \frac{d}{dt} \mathcal{G}^{\uparrow\uparrow\uparrow\uparrow}_{ijkl}(t) - \left[h^{(2),\mathrm{HF}}_{\uparrow\uparrow}, \mathcal{G}^{\uparrow\uparrow\uparrow\uparrow} \right]_{ijkl}(t)$$
$$= \Pi^{\uparrow\uparrow\uparrow\uparrow}_{ijkl}(t) - [\Pi^{\uparrow\uparrow\uparrow\uparrow}_{lkji}(t)]^* \,, \tag{63}$$

where we introduced the polarization terms,

$$\Pi^{\uparrow\downarrow\uparrow\downarrow}_{ijkl}(t) = -(i\hbar)^2 U(t) \sum_p [G^{>,\downarrow}_{jp}(t) G^{<,\downarrow}_{pl}(t)$$
$$- G^{<,\downarrow}_{jp}(t) G^{>,\downarrow}_{pl}(t)] \mathcal{G}^{\uparrow\uparrow\uparrow\uparrow}_{ipkp}(t), \tag{64}$$

$$\Pi^{\uparrow\uparrow\uparrow\uparrow}_{ijkl}(t) = -(i\hbar)^2 U(t) \sum_p [G^{>,\uparrow}_{jp}(t) G^{<,\uparrow}_{pl}(t)$$
$$- G^{<,\uparrow}_{jp}(t) G^{>,\uparrow}_{pl}(t)] \mathcal{G}^{\uparrow\downarrow\uparrow\downarrow}_{ipkp}(t) \,. \tag{65}$$

Notice that there are two separate spin combinations (four when considering $\uparrow \leftrightarrow \downarrow$) for the two-particle Green function that enter Eqs. (62) and (63). Due to the cross coupling in the two polarization terms, they cannot be solved independently [28,69]. Numerical results for the *GW*-G1-G2 scheme are presented in Sec. VII.

D. *GW*-G1-G2 equations for jellium

For the uniform electron gas [cf. Eq. (39)] we again use the interaction matrix of Eq. (40) and define

$$\Pi^{\alpha\beta}_{\boldsymbol{p},\bar{\boldsymbol{p}},\boldsymbol{q}}(t) := \Pi^{\alpha\beta\alpha\beta}_{\boldsymbol{p}-\boldsymbol{q},\bar{\boldsymbol{p}}+\boldsymbol{q},\boldsymbol{p},\bar{\boldsymbol{p}}}(t) \,.$$

With that, the equation (60) for the time-diagonal two-particle Green function [recall the definition (42)] becomes

$$i\hbar \frac{d}{dt} \mathcal{G}^{\alpha\beta}_{\boldsymbol{p}\bar{\boldsymbol{p}}\boldsymbol{q}}(t) - \mathcal{G}^{\alpha\beta}_{\boldsymbol{p}\bar{\boldsymbol{p}}\boldsymbol{q}}(t) \big(h^{\mathrm{HF},\alpha}_{\boldsymbol{p}-\boldsymbol{q}} + h^{\mathrm{HF},\beta}_{\bar{\boldsymbol{p}}+\boldsymbol{q}} - h^{\mathrm{HF},\alpha}_{\boldsymbol{p}} - h^{\mathrm{HF},\beta}_{\bar{\boldsymbol{p}}} \big)(t)$$
$$= \underbrace{\frac{1}{(i\hbar)^2} v_{|\boldsymbol{q}|}(t) \Phi^{\alpha\beta}_{\boldsymbol{p}\bar{\boldsymbol{p}}\boldsymbol{q}}(t) + \Pi^{\alpha\beta}_{\boldsymbol{p},\bar{\boldsymbol{p}},\boldsymbol{q}}(t)}_{=: \Psi^{\alpha\beta}_{\boldsymbol{p}\bar{\boldsymbol{p}}\boldsymbol{q}}(t)} - \left[\Pi^{\beta\alpha}_{\bar{\boldsymbol{p}}+\boldsymbol{q},\boldsymbol{p}-\boldsymbol{q},\boldsymbol{q}}(t) \right]^*,$$

with the momentum representation of the polarization term, given by

$$\Pi^{\alpha\beta}_{\boldsymbol{p},\bar{\boldsymbol{p}},\boldsymbol{q}}(t) = \pm (i\hbar)^2 \big[G^{>,\beta}_{\bar{\boldsymbol{p}}+\boldsymbol{q}}(t) G^{<,\beta}_{\bar{\boldsymbol{p}}}(t) - G^{<,\beta}_{\bar{\boldsymbol{p}}+\boldsymbol{q}}(t) G^{>,\beta}_{\bar{\boldsymbol{p}}}(t) \big]$$
$$\times v_{|\boldsymbol{q}|}(t) \sum_{\boldsymbol{k},\sigma} \mathcal{G}^{\alpha\sigma}_{\boldsymbol{p}\boldsymbol{k}\boldsymbol{q}}(t) \,. \tag{66}$$

As we will discuss in Sec. VII, the *GW* equations for jellium can be solved particularly efficiently.

V. *T*-MATRIX SELF ENERGIES

We next turn to the case of strong coupling where the second-Born approximation is not applicable. It is well known that the entire Born series can be summed up, giving rise to the *T*-matrix (or binary-collision or ladder) approximation. Here we first consider the case of a static pair interaction. The extension to a dynamically screened *T* matrix will be considered in Sec. VI. We start by considering, in Sec. V A, the *T* matrix in the particle-particle channel after which we analyze, in Sec. V B, the *T* matrix in the particle-hole channel.

A. *T* matrix in the particle-particle channel

For the particle-particle *T* matrix, the self energy has the form [3,19],

$$\Sigma^{\gtrless}_{ij}(t,t') = i\hbar \sum_{kl} T^{\mathrm{pp},\gtrless}_{ikjl}(t,t') G^{\lessgtr}_{lk}(t',t) \,. \tag{67}$$

Here, the *T* matrix is expressed as

$$T^{\mathrm{pp},\gtrless}_{ijkl}(t,t') = \sum_{pq} w_{ijpq}(t) \Omega^{\mathrm{pp},\gtrless}_{pqkl}(t,t') \,, \tag{68}$$

which allows us to rewrite the self energy (67):

$$\Sigma^{\gtrless}_{ij}(t,t') = i\hbar \sum_{klpq} w_{ikpq}(t) \Omega^{\mathrm{pp},\gtrless}_{pqjl}(t,t') G^{\lessgtr}_{lk}(t',t) \,. \tag{69}$$

In Eqs. (68) and (69) the quantity Ω^{pp} is the nonequilibrium generalization of the Møller operator from scattering theory [70,71]. The collision integral (10) of the time-diagonal equation then becomes,

$$I_{ij}(t) = i\hbar \sum_{klpqr} w_{ipqr}(t) \int_{t_0}^t d\bar{t} \big[\Omega^{\mathrm{pp},>}_{qrkl}(t,\bar{t}) \mathcal{G}^{\mathrm{H},<}_{kljp}(\bar{t},t)$$
$$- \Omega^{\mathrm{pp},<}_{qrkl}(t,\bar{t}) \mathcal{G}^{\mathrm{H},>}_{kljp}(\bar{t},t) \big]$$
$$= \pm i\hbar \sum_{klp} w_{iklp}(t) \mathcal{G}_{kpjl}(t) \,,$$

which results in the following expression for the time-diagonal element of the two-particle Green function,

$$\mathcal{G}_{ijkl}(t) = \pm \sum_{pq} \int_{t_0}^{t} d\bar{t} \left[\Omega_{ijpq}^{\mathrm{pp},>}(t,\bar{t}) \mathcal{G}_{pqkl}^{\mathrm{H},<}(\bar{t},t) - \Omega_{ijpq}^{\mathrm{pp},<}(t,\bar{t}) \mathcal{G}_{pqkl}^{\mathrm{H},>}(\bar{t},t) \right].$$

By construction, the T matrix obeys the following symmetry [cf. Eq. (14)],

$$T_{ijkl}^{\mathrm{pp},\gtrless}(t,t') = -\left[T_{klij}^{\mathrm{pp},\gtrless}(t',t) \right]^*. \tag{70}$$

The T matrix sums up the particle-particle collisions via the recursive equation (nonequilibrium Lippmann-Schwinger equation; compared to the standard definition of the T matrix, here the singular part has been subtracted [19,28]),

$$T_{ijkl}^{\mathrm{pp},\gtrless}(t,t') = \pm i\hbar \sum_{pqrs} w_{ijpq}(t) \mathcal{G}_{pqrs}^{\mathrm{H},\gtrless}(t,t') w_{rskl}^{\pm}(t') + i\hbar \sum_{pqrs} w_{ijpq}(t) \left\{ \int_{t_0}^{t} d\bar{t} \left[\mathcal{G}_{pqrs}^{\mathrm{H},>}(t,\bar{t}) \right. \right.$$

$$\left. \left. - \mathcal{G}_{pqrs}^{\mathrm{H},<}(t,\bar{t}) \right] T_{rskl}^{\mathrm{pp},\gtrless}(\bar{t},t') + \int_{t_0}^{t'} d\bar{t} \, \mathcal{G}_{pqrs}^{\mathrm{H},\gtrless}(t,\bar{t}) \left[T_{rskl}^{\mathrm{pp},<}(\bar{t},t') - T_{rskl}^{\mathrm{pp},>}(\bar{t},t') \right] \right\}.$$

Following this and using the symmetries of Eqs. (14) and (70) the relation for the Møller operator is readily derived,

$$\Omega_{ijkl}^{\mathrm{pp},\gtrless}(t,t') = \pm i\hbar \sum_{pq} \mathcal{G}_{ijpq}^{\mathrm{H},\gtrless}(t,t') w_{pqkl}^{\pm}(t') + i\hbar \sum_{pqrs} \left\{ \int_{t_0}^{t} d\bar{t} \left[\mathcal{G}_{ijpq}^{\mathrm{H},>}(t,\bar{t}) - \mathcal{G}_{ijpq}^{\mathrm{H},>}(t,\bar{t}) \right] w_{pqrs}(\bar{t}) \Omega_{rskl}^{\mathrm{pp},\gtrless}(\bar{t},t') \right.$$

$$\left. + \int_{t_0}^{t'} d\bar{t} \, \mathcal{G}_{ijpq}^{\mathrm{H},\gtrless}(t,\bar{t}) w_{pqrs}(\bar{t}) \left[\Omega_{rskl}^{\mathrm{pp},<}(\bar{t},t') - \Omega_{rskl}^{\mathrm{pp},>}(\bar{t},t') \right] \right\}$$

$$= \pm i\hbar \sum_{pq} \mathcal{G}_{ijpq}^{\mathrm{H},\gtrless}(t,t') w_{pqkl}^{\pm}(t') + i\hbar \sum_{pqrs} \left\{ \int_{t_0}^{t} d\bar{t} \, \Omega_{rspq}^{\mathrm{pp},\gtrless}(t',\bar{t}) \left[\mathcal{G}_{pqij}^{\mathrm{H},<}(\bar{t},t) - \mathcal{G}_{pqij}^{\mathrm{H},>}(\bar{t},t) \right] \right.$$

$$\left. + \int_{t_0}^{t'} d\bar{t} \left[\Omega_{rspq}^{\mathrm{pp},>}(t',\bar{t}) - \Omega_{rspq}^{\mathrm{pp},<}(t',\bar{t}) \right] \mathcal{G}_{pqij}^{\mathrm{H},\gtrless}(\bar{t},t) \right\}^* w_{rskl}(t').$$

The time-diagonal equation for Ω^{pp} can be further simplified,

$$\Omega_{ijkl}^{\mathrm{pp},\gtrless}(t,t) = \pm i\hbar \sum_{pq} \mathcal{G}_{ijpq}^{\mathrm{H},\gtrless}(t) w_{pqkl}^{\pm}(t) + i\hbar \sum_{pqrs} \left[\int_{t_0}^{t} d\bar{t} \left(\Omega_{pqrs}^{\mathrm{pp},>}(t,\bar{t}) \mathcal{G}_{rsij}^{\mathrm{H},<}(\bar{t},t) - \Omega_{pqrs}^{\mathrm{pp},<}(t,\bar{t}) \mathcal{G}_{rsij}^{\mathrm{H},>}(\bar{t},t) \right) \right]^* w_{pqkl}(t)$$

$$= \pm i\hbar \sum_{pq} \mathcal{G}_{ijpq}^{\mathrm{H},\gtrless}(t) w_{pqkl}^{\pm}(t) \pm i\hbar \sum_{pq} \left[\mathcal{G}_{pqij}(t) \right]^* w_{pqkl}(t).$$

1. T^{pp} approximation within the HF-GKBA

We now apply the HF-GKBA [cf. Eqs. (16) and (17)] and find the following expressions for $\mathcal{G}$,

$$\mathcal{G}_{ijkl}(t) = \pm (i\hbar)^2 \sum_{pqrs} \int_{t_0}^{t} d\bar{t} \left[\Omega_{ijpq}^{\mathrm{pp},>}(t,\bar{t}) \mathcal{G}_{pqrs}^{\mathrm{H},<}(\bar{t}) - \Omega_{ijpq}^{\mathrm{pp},<}(t,\bar{t}) \mathcal{G}_{pqrs}^{\mathrm{H},>}(\bar{t}) \right] \mathcal{U}_{rskl}^{(2)}(\bar{t},t),$$

as well as for Ω^{pp},

$$\Omega_{ijkl}^{\mathrm{pp},\gtrless}(t \geqslant t') = \pm (i\hbar)^3 \sum_{pqrs} \mathcal{U}_{ijrs}^{(2)}(t,t') \mathcal{G}_{rspq}^{\mathrm{H},\gtrless}(t') w_{pqkl}^{\pm}(t') + (i\hbar)^3 \sum_{pqrsuv} \left[\int_{t_0}^{t} d\bar{t} \, \mathcal{U}_{ijrs}^{(2)}(t,\bar{t}) \left(\mathcal{G}_{rspq}^{\mathrm{H},>}(\bar{t}) - \mathcal{G}_{rspq}^{\mathrm{H},<}(\bar{t}) \right) w_{pquv}(\bar{t}) \Omega_{uvkl}^{\mathrm{pp},\gtrless}(\bar{t},t') \right.$$

$$\left. + \int_{t_0}^{t'} d\bar{t} \, \mathcal{U}_{ijrs}^{(2)}(t,\bar{t}) \mathcal{G}_{rspq}^{\mathrm{H},\gtrless}(\bar{t}) w_{pquv}(\bar{t}) \left(\Omega_{uvkl}^{\mathrm{pp},<}(\bar{t},t') - \Omega_{uvkl}^{\mathrm{pp},>}(\bar{t},t') \right) \right], \tag{71}$$

where $\mathcal{U}^{(2)}$ obeys Eqs. (24) and (25). With Eq. (71) we easily find an expression for the time derivative of Ω^{pp},

$$\frac{d}{dt} \Omega_{ijkl}^{\mathrm{pp},\gtrless}(t \geqslant t') = \frac{1}{i\hbar} \sum_{pq} \left(\mathfrak{h}_{ijpq}^{\Omega^{\mathrm{pp}},\mathrm{HF}}(t) + \mathfrak{h}_{ijpq}^{\Omega^{\mathrm{pp}},\mathrm{corr}}(t) \right) \Omega_{pqkl}^{\mathrm{pp},\gtrless}(t \geqslant t'). \tag{72}$$

As for the case of the *GW* self energy, here we introduced two quasi-Hamiltonians,

$$\mathfrak{h}^{\Omega^{pp},\mathrm{HF}}_{ijkl}(t) = h^{(2),\mathrm{HF}}_{ijkl}(t),$$

$$\mathfrak{h}^{\Omega^{pp},\mathrm{corr}}_{ijkl}(t) = (i\hbar)^2 \sum_{pq}\big[\mathcal{G}^{\mathrm{H},>}_{ijpq}(t) - \mathcal{G}^{\mathrm{H},<}_{ijpq}(t)\big] w_{pqkl}(t). \quad (73)$$

Combining these Hamiltonians again into a single one,

$$\mathfrak{h}^{\Omega^{pp}}_{ijkl}(t) = \mathfrak{h}^{\Omega^{pp},\mathrm{HF}}_{ijkl}(t) + \mathfrak{h}^{\Omega^{pp},\mathrm{corr}}_{ijkl}(t), \quad (74)$$

the equation (72) for the Møller operator is transformed into a time-dependent two-particle Schrödinger equation,

$$i\hbar\frac{d}{dt}\Omega^{pp,\gtrless}_{ijkl}(t \geqslant t') = \sum_{pq}\mathfrak{h}^{\Omega^{pp}}_{ijpq}(t)\Omega^{pp,\gtrless}_{pqkl}(t \geqslant t'). \quad (75)$$

This equation is analogous to the Schrödinger equation for the inverse dielectric function, Eq. (57), the main difference being the modified Hamiltonian (74).

2. T^{pp}-G1-G2 equations for a general basis

To derive the G1-G2 scheme for the particle-particle *T* matrix, we have to take the derivative of $\mathcal{G}$, yielding,

$$\frac{d}{dt}\mathcal{G}_{ijkl}(t)$$

$$= \left[\frac{d}{dt}\mathcal{G}_{ijkl}(t)\right]_f + \left[\frac{d}{dt}\mathcal{G}_{ijkl}(t)\right]_{\Omega^{pp}} + \left[\frac{d}{dt}\mathcal{G}_{ijkl}(t)\right]_{\mathcal{U}^{(2)}},$$

The derivative of the integration boundaries results in,

$$\left[\frac{d}{dt}\mathcal{G}_{ijkl}(t)\right]_f$$

$$= \pm\sum_{pq}\big[\Omega^{pp,>}_{ijpq}(t,t)\mathcal{G}^{\mathrm{H},<}_{pqkl}(t) - \Omega^{pp,<}_{ijpq}(t,t)\mathcal{G}^{\mathrm{H},>}_{pqkl}(t)\big]$$

$$= i\hbar\sum_{pqrs}w^{\pm}_{rspq}(t)\big[\mathcal{G}^{\mathrm{H},>}_{ijrs}(t)\mathcal{G}^{\mathrm{H},<}_{pqkl}(t) - \mathcal{G}^{\mathrm{H},<}_{ijrs}(t)\mathcal{G}^{\mathrm{H},>}_{pqkl}(t)\big]$$

$$+ i\hbar\sum_{pqrs}[\mathcal{G}_{rsij}(t)]^* w_{rspq}(t)\big[\mathcal{G}^{\mathrm{H},<}_{pqkl}(t) - \mathcal{G}^{\mathrm{H},>}_{pqkl}(t)\big]$$

$$= \frac{1}{i\hbar}\Psi^{\pm}_{ijkl}(t) - \frac{1}{i\hbar}\sum_{pq}\big[\mathfrak{h}^{\Omega^{pp},\mathrm{corr}}_{klpq}(t)\mathcal{G}_{pqij}(t)\big]^*,$$

while the time derivative of the Møller operator yields

$$\left[\frac{d}{dt}\mathcal{G}_{ijkl}(t)\right]_{\Omega^{pp}}$$

$$= \pm(i\hbar)^2\sum_{pqrs}\int_{t_0}^{t}d\bar{t}\left[\left(\frac{d}{dt}\Omega^{pp,>}_{ijpq}(t,\bar{t})\right)\mathcal{G}^{\mathrm{H},<}_{pqrs}(\bar{t})\right.$$

$$\left. - \left(\frac{d}{dt}\Omega^{pp,<}_{ijpq}(t,\bar{t})\right)\mathcal{G}^{\mathrm{H},>}_{pqrs}(\bar{t})\right]\mathcal{U}^{(2)}_{rskl}(\bar{t},t)$$

$$= \frac{1}{i\hbar}\sum_{pq}\big(\mathfrak{h}^{\Omega^{pp},\mathrm{HF}}_{ijpq}(t) + \mathfrak{h}^{\Omega^{pp},\mathrm{corr}}_{ijpq}(t)\big)\mathcal{G}_{pqkl}(t).$$

The last contribution originates from the derivative of the two-particle propagator,

$$\left[\frac{d}{dt}\mathcal{G}_{ijkl}(t)\right]_{\mathcal{U}^{(2)}}$$

$$= \pm(i\hbar)^2\sum_{pqrs}\int_{t_0}^{t}d\bar{t}\big[\Omega^{pp,>}_{ijpq}(t,\bar{t})\mathcal{G}^{\mathrm{H},<}_{pqrs}(\bar{t})$$

$$- \Omega^{pp,<}_{ijpq}(t,\bar{t})\mathcal{G}^{\mathrm{H},>}_{pqrs}(\bar{t})\big]\left(\frac{d}{dt}\mathcal{U}^{(2)}_{rskl}(\bar{t},t)\right)$$

$$= \frac{1}{i\hbar}\sum_{pq}\mathcal{G}_{ijpq}(t)\mathfrak{h}^{\Omega^{pp},\mathrm{HF}}_{pqkl}(t).$$

Combining the three contributions to the derivative of $\mathcal{G}$ reveals

$$i\hbar\frac{d}{dt}\mathcal{G}_{ijkl}(t) = \Psi^{\pm}_{ijkl}(t) + \sum_{pq}\left\{\mathfrak{h}^{\Omega^{pp}}_{ijpq}(t)[\mathcal{G}_{klpq}(t)]^*\right.$$

$$\left. - \mathcal{G}_{ijpq}(t)\big[\mathfrak{h}^{\Omega^{pp}}_{klpq}(t)\big]^*\right\}, \quad (76)$$

where $\mathfrak{h}^{\Omega^{pp}}(t)$ was introduced in Eq. (74). This is the central equation for the G1-G2 scheme in *T*-matrix approximation for the particle-particle channel [5,71]. Compared to the equation of motion for $\mathcal{G}$ in second-Born approximation, Eq. (29), this equation contains, in addition, the particle-particle ladder terms which are generated by the quasi-Hamiltonian of Eq. (73). Again, for practical use, it is convenient to separate the correlation contributions from the mean-field terms via the introduction of an additional quantity:

$$i\hbar\frac{d}{dt}\mathcal{G}_{ijkl}(t) - \big[h^{(2),\mathrm{HF}}, \mathcal{G}\big]_{ijkl}(t)$$

$$= \Psi^{\pm}_{ijkl}(t) + \Lambda^{pp}_{ijkl}(t) - \big[\Lambda^{pp}_{klij}(t)\big]^*,$$

where the particle-particle ladder term is defined by

$$\Lambda^{pp}_{ijkl}(t) = \sum_{pq}\mathfrak{h}^{\Omega^{pp},\mathrm{corr}}_{ijpq}(t)\mathcal{G}_{pqkl}(t). \quad (77)$$

Without the Λ terms we exactly recover the equation of motion for $\mathcal{G}$ in second-order Born approximation. Inclusion of the Λ terms, on the other hand, allows one to take into account multiple scattering and large-angle scattering effects that are important for strongly correlated systems. These terms correspond to the summation of the infinite Born series.

3. T^{pp}-G1-G2 equations for the Hubbard model

We now apply this result to the Hubbard Hamiltonian and find,

$$i\hbar\frac{d}{dt}\mathcal{G}^{\uparrow\downarrow\uparrow\downarrow}_{ijkl}(t) - \big[h^{(2),\mathrm{HF}}_{\uparrow\downarrow}, \mathcal{G}^{\uparrow\downarrow\uparrow\downarrow}\big]_{ijkl}(t)$$

$$= \Psi^{\uparrow\downarrow\uparrow\downarrow}_{ijkl}(t) + \Lambda^{pp,\uparrow\downarrow\uparrow\downarrow}_{ijkl}(t) - \big[\Lambda^{pp,\uparrow\downarrow\uparrow\downarrow}_{klij}(t)\big]^*,$$

where we introduced the particle-particle ladder term

$$\Lambda^{pp,\uparrow\downarrow\uparrow\downarrow}_{ijkl}(t) = (i\hbar)^2 U(t) \times \sum_{p}\big[G^{>,\uparrow}_{ip}(t)G^{>,\downarrow}_{jp}(t)$$

$$- G^{<,\uparrow}_{ip}(t)G^{<,\downarrow}_{jp}(t)\big]\mathcal{G}^{\uparrow\downarrow\uparrow\downarrow}_{ppkl}(t). \quad (78)$$

In the present case there exists only one distinct spin combination (two when considering $\uparrow \leftrightarrow \downarrow$) of the particle pair that enters the single-particle EOM [cf. Eqs. (34) and (35)] which simplifies the equations. Numerical results for the T^{pp}-G1-G2 scheme are presented in Sec. VII.

4. T^{pp}-G1-G2 equations for jellium

Turning now to the uniform electron gas, Eq. (39), we again use the interaction matrix of Eq. (40) and define

$$\Lambda_{\boldsymbol{p},\bar{\boldsymbol{p}},\boldsymbol{q}}^{\mathrm{pp},\alpha\beta}(t) := \Lambda_{\boldsymbol{p}-\boldsymbol{q},\bar{\boldsymbol{p}}+\boldsymbol{q},\boldsymbol{p},\bar{\boldsymbol{p}}}^{\mathrm{pp},\alpha\beta\alpha\beta}(t).$$

With that, the equation of motion for the time-diagonal two-particle Green function becomes,

$$i\hbar\frac{d}{dt}\mathcal{G}_{\boldsymbol{p}\bar{\boldsymbol{p}}\boldsymbol{q}}^{\alpha\beta}(t) - \mathcal{G}_{\boldsymbol{p}\bar{\boldsymbol{p}}\boldsymbol{q}}^{\alpha\beta}(t)\big(h_{\boldsymbol{p}-\boldsymbol{q}}^{\mathrm{HF},\alpha} + h_{\bar{\boldsymbol{p}}+\boldsymbol{q}}^{\mathrm{HF},\beta} - h_{\boldsymbol{p}}^{\mathrm{HF},\alpha} - h_{\bar{\boldsymbol{p}}}^{\mathrm{HF},\beta}\big)(t)$$
$$= \Psi_{\boldsymbol{p}\bar{\boldsymbol{p}}\boldsymbol{q}}^{\pm,\alpha\beta}(t) + \Lambda_{\boldsymbol{p},\bar{\boldsymbol{p}},\boldsymbol{q}}^{\mathrm{pp},\alpha\beta}(t) - \big[\Lambda_{\boldsymbol{p}-\boldsymbol{q},\bar{\boldsymbol{p}}+\boldsymbol{q},-\boldsymbol{q}}^{\mathrm{pp},\alpha\beta}(t)\big]^*,$$

where the momentum representation of the particle-particle ladder term is given by

$$\Lambda_{\boldsymbol{p},\bar{\boldsymbol{p}},\boldsymbol{q}}^{\mathrm{pp},\alpha\beta}(t) = (i\hbar)^2\big[G_{\boldsymbol{p}-\boldsymbol{q}}^{>,\alpha}(t)G_{\bar{\boldsymbol{p}}+\boldsymbol{q}}^{>,\beta}(t) - G_{\boldsymbol{p}-\boldsymbol{q}}^{<,\alpha}(t)G_{\bar{\boldsymbol{p}}+\boldsymbol{q}}^{<,\beta}(t)\big]$$
$$\times \sum_{\boldsymbol{k}} v_{|\boldsymbol{k}-\boldsymbol{q}|}(t)\mathcal{G}_{\boldsymbol{p}\bar{\boldsymbol{p}}\boldsymbol{k}}^{\alpha\beta}(t). \quad (79)$$

B. Particle-hole T matrix

For the T matrix in the particle-hole channel [28], the derivations of the single-time equations are performed in a similar fashion as for the particle-particle T matrix in Sec. V A. The detailed derivation is given in Appendix C. Here, we summarize the main findings.

1. T^{ph}-G1-G2 equations for a general basis

As for the GW and the TPP approximations, two quasi-Hamiltonians are introduced,

$$\mathfrak{h}_{ijkl}^{\Omega^{\mathrm{ph}},\mathrm{HF}}(t) = \delta_{jl}h_{ik}^{\mathrm{HF}} - \delta_{ik}h_{jl}^{\mathrm{HF}},$$
$$\mathfrak{h}_{ijkl}^{\Omega^{\mathrm{ph}},\mathrm{corr}}(t) = (i\hbar)^2\sum_{pq}\big[\mathcal{G}_{iqlp}^{\mathrm{F},>}(t) - \mathcal{G}_{iqlp}^{\mathrm{F},<}(t)\big]w_{pjkq}(t), \quad (80)$$

and combined into a single quantity,

$$\mathfrak{h}_{ijkl}^{\Omega^{\mathrm{ph}}}(t) = \mathfrak{h}_{ijkl}^{\Omega^{\mathrm{ph}},\mathrm{HF}}(t) + \mathfrak{h}_{ijkl}^{\Omega^{\mathrm{ph}},\mathrm{corr}}(t). \quad (81)$$

The corresponding Møller operator of the particle-hole T matrix again obeys a time-dependent two-particle Schrödinger equation,

$$i\hbar\frac{d}{dt}\Omega_{ijkl}^{\mathrm{ph},\gtrless}(t \geq t') = \sum_{pq}\mathfrak{h}_{ipql}^{\Omega^{\mathrm{ph}}}(t)\Omega_{qjkp}^{\mathrm{ph},\gtrless}(t \geq t'). \quad (82)$$

The time derivative of $\mathcal{G}$ in TPH approximation follows as

$$i\hbar\frac{d}{dt}\mathcal{G}_{ijkl}(t) = \Psi_{ijkl}^{\pm}(t) + \sum_{pq}\bigg\{\mathfrak{h}_{ipql}^{\Omega^{\mathrm{ph}}}(t)[\mathcal{G}_{kpqj}(t)]^*$$
$$- \mathcal{G}_{ipql}(t)\big[\mathfrak{h}_{kpqj}^{\Omega^{\mathrm{ph}}}(t)\big]^*\bigg\}. \quad (83)$$

Again, for practical use, it is convenient to separate the correlation contributions from the mean-field terms via the

introduction of an additional quantity:

$$i\hbar\frac{d}{dt}\mathcal{G}_{ijkl}(t) - [h^{(2),\mathrm{HF}}, \mathcal{G}]_{ijkl}(t)$$
$$= \Psi_{ijkl}^{\pm}(t) + \Lambda_{ijkl}^{\mathrm{ph}}(t) - \big[\Lambda_{klij}^{\mathrm{ph}}(t)\big]^*,$$

where the particle-hole ladder term is defined by

$$\Lambda_{ijkl}^{\mathrm{ph}}(t) = \sum_{pq}\mathfrak{h}_{ipql}^{\Omega^{\mathrm{ph}},\mathrm{corr}}(t)\mathcal{G}_{qjkp}(t). \quad (84)$$

As in the case of the particle-particle T matrix, Sec. V A, neglect of the Λ terms exactly recovers the equation of motion for $\mathcal{G}$ in second-order Born approximation. Inclusion of theses terms, on the other hand, accounts for the entire Born series.

2. T^{ph}-G1-G2 equations for the Hubbard basis

For the Hubbard system (for the definitions, see Sec. III C), we find,

$$i\hbar\frac{d}{dt}\mathcal{G}_{ijkl}^{\uparrow\downarrow\uparrow\downarrow}(t) - \big[h_{\uparrow\downarrow}^{(2),\mathrm{HF}}, \mathcal{G}^{\uparrow\downarrow\uparrow\downarrow}\big]_{ijkl}(t)$$
$$= \Psi_{ijkl}^{\uparrow\downarrow\uparrow\downarrow}(t) + \Lambda_{ijkl}^{\mathrm{ph},\uparrow\downarrow\uparrow\downarrow}(t) - \big[\Lambda_{klij}^{\mathrm{ph},\uparrow\downarrow\uparrow\downarrow}(t)\big]^*,$$

where we introduced the particle-hole ladder term for the Hubbard system

$$\Lambda_{ijkl}^{\mathrm{ph},\uparrow\downarrow\uparrow\downarrow}(t) = (i\hbar)^2 U(t)\sum_{p}\big[G_{ip}^{>,\uparrow}(t)G_{pl}^{<,\downarrow}(t)$$
$$- G_{ip}^{<,\uparrow}(t)G_{pl}^{>,\downarrow}(t)\big]\mathcal{G}_{pjkp}^{\uparrow\downarrow\uparrow\downarrow}(t). \quad (85)$$

Similar to the behavior in the TPP case, only one spin combination (two when considering $\uparrow \leftrightarrow \downarrow$) contributes to the single-particle EOM in Eqs. (34) and (35). The T^{ph}-G1-G2 scheme for the Hubbard model is numerically tested in Sec. VII.

3. T^{ph}-G1-G2 equations for jellium

For the uniform electron gas, Eq. (39), we again use the interaction matrix of Eq. (40), and define

$$\Lambda_{\boldsymbol{p},\bar{\boldsymbol{p}},\boldsymbol{q}}^{\mathrm{ph},\alpha\beta}(t) := \Lambda_{\boldsymbol{p}-\boldsymbol{q},\bar{\boldsymbol{p}}+\boldsymbol{q},\boldsymbol{p},\bar{\boldsymbol{p}}}^{\mathrm{ph},\alpha\beta\alpha\beta}(t).$$

With that, the equation of motion for the time-diagonal two-particle Green function becomes

$$i\hbar\frac{d}{dt}\mathcal{G}_{\boldsymbol{p}\bar{\boldsymbol{p}}\boldsymbol{q}}^{\alpha\beta}(t) - \mathcal{G}_{\boldsymbol{p}\bar{\boldsymbol{p}}\boldsymbol{q}}^{\alpha\beta}(t)\big(h_{\boldsymbol{p}-\boldsymbol{q}}^{\mathrm{HF},\alpha} + h_{\bar{\boldsymbol{p}}+\boldsymbol{q}}^{\mathrm{HF},\beta} - h_{\boldsymbol{p}}^{\mathrm{HF},\alpha} - h_{\bar{\boldsymbol{p}}}^{\mathrm{HF},\beta}\big)(t)$$
$$= \Psi_{\boldsymbol{p}\bar{\boldsymbol{p}}\boldsymbol{q}}^{\pm,\alpha\beta}(t) + \Lambda_{\boldsymbol{p},\bar{\boldsymbol{p}},\boldsymbol{q}}^{\mathrm{ph},\alpha\beta}(t) - \big[\Lambda_{\boldsymbol{p}-\boldsymbol{q},\bar{\boldsymbol{p}}+\boldsymbol{q},-\boldsymbol{q}}^{\mathrm{ph},\alpha\beta}(t)\big]^*,$$

with the momentum representation of the particle-hole ladder term, given by

$$\Lambda_{\boldsymbol{p},\bar{\boldsymbol{p}},\boldsymbol{q}}^{\mathrm{ph},\alpha\beta}(t) = (i\hbar)^2\big[G_{\boldsymbol{p}-\boldsymbol{q}}^{>,\alpha}(t)G_{\bar{\boldsymbol{p}}}^{<,\beta}(t) - G_{\boldsymbol{p}-\boldsymbol{q}}^{<,\alpha}(t)G_{\bar{\boldsymbol{p}}}^{>,\beta}(t)\big]$$
$$\times \sum_{\boldsymbol{k}} v_{|\boldsymbol{k}|}(t)\mathcal{G}_{\boldsymbol{p},\bar{\boldsymbol{p}}-\boldsymbol{k},\boldsymbol{q}+\boldsymbol{k}}^{\alpha\beta}(t). \quad (86)$$

VI. DYNAMICALLY-SCREENED-LADDER APPROXIMATION

So far we have considered three important self-energy approximations: the second-Born approximation, GW, and the particle-particle and particle-hole T matrices. While GW

describes dynamical screening, for weakly coupled systems, the T-matrix self energy accounts for strong coupling but neglects dynamical-screening effects. Therefore, the question arises how to combine strong coupling and dynamical screening into a single model in a computationally feasible way. An approximation to realize this, within NEGF theory, is the fluctuating-exchange approximation (FLEX) that combines T matrix and GW contributions according to $\Sigma = \Sigma_{\mathrm{TPP}} + \Sigma_{\mathrm{TPH}} + \Sigma_{GW} - 2\Sigma_{\mathrm{SOA}}$, where the last term is needed to avoid double counting; for more details, see Ref. [28]. A fully self-consistent treatment of dynamical-screening and strong-coupling effects is provided by the dynamically-screened-ladder approximation that has been studied in the context of the bound-state problem in a plasma medium in equilibrium [72]. For more details, see Ref. [73].

The G1-G2 scheme allows for a straightforward way to combine the GW (including exchange) and both T-matrix approximations in a self-consistent way for arbitrary nonequilibrium situations. This is achieved by including in the EOM of the time-diagonal two-particle Green function the terms with all effective Hamiltonians that were derived for GW, the particle-particle and the particle-hole T matrix, respectively, cf. Eqs. (56), (74), and (81). Then, the EOM for $\mathcal{G}$, in a general basis becomes

$$i\hbar \frac{d}{dt}\mathcal{G}_{ijkl}(t) - \left[h^{(2),\mathrm{HF}}, \mathcal{G}\right]_{ijkl}(t)$$

$$= \Psi^{\pm}_{ijkl}(t) + \sum_{pq}\left\{\mathfrak{h}^{\varepsilon,\mathrm{corr}}_{qjpl}(t)[\mathcal{G}_{qkpi}(t)]^*\right.$$

$$\left. - \mathcal{G}_{qjpl}(t)\left[\mathfrak{h}^{\varepsilon,\mathrm{corr}}_{qkpi}(t)\right]^*\right\} + \sum_{pq}\left\{\mathfrak{h}^{\Omega^{\mathrm{pp}},\mathrm{corr}}_{ijpq}(t)[\mathcal{G}_{klpq}(t)]^*\right.$$

$$\left. - \mathcal{G}_{ijpq}(t)\left[\mathfrak{h}^{\Omega^{\mathrm{pp}},\mathrm{corr}}_{klpq}(t)\right]^*\right\} + \sum_{kl}\left\{\mathfrak{h}^{\Omega^{\mathrm{ph}},\mathrm{corr}}_{ipql}(t)[\mathcal{G}_{kpqj}(t)]^*\right.$$

$$\left. - \mathcal{G}_{ipql}(t)\left[\mathfrak{h}^{\Omega^{\mathrm{ph}},\mathrm{corr}}_{kpqj}(t)\right]^*\right\}. \tag{87}$$

Alternatively, we can rewrite this equation by using the polarization (Π) and ladder (Λ) terms that were defined by Eqs. (61), (77), and (84),

$$i\hbar \frac{d}{dt}\mathcal{G}_{ijkl}(t) - \left[h^{(2),\mathrm{HF}}, \mathcal{G}\right]_{ijkl}(t) = \Psi^{\pm}_{ijkl}(t)$$

$$+ \Pi_{ijkl}(t) - [\Pi_{lkji}(t)]^* + \Lambda_{ijkl}(t) - [\Lambda_{klij}(t)]^*, \quad (88)$$

where we combined both ladder terms into

$$\Lambda_{ijkl}(t) = \Lambda^{\mathrm{pp}}_{ijkl}(t) + \Lambda^{\mathrm{ph}}_{ijkl}(t).$$

Obviously, Eq. (88) is a generalization of all previous cases: It additively includes the contributions of the second-order Born self energy (first line), polarization terms that account for dynamical screening and strong-coupling terms. The SOA term that appears in each of the different approximations is included only once, so no double counting occurs. Since all contributions are treated on the same footing, this equation amounts to a simultaneous full account of dynamical screening and strong binary correlations. Alternatively, this approximation can be obtained from reduced-density-operator theory by neglecting three-particle and higher correlations [5]; an early discussion was presented by Wang and Cassing [74].

TABLE I. Scaling of the CPU time with the number of time steps N_t and basis dimension N_b of the traditional non-Markovian HF-GKBA ("standard") and the present time-local scheme (G1-G2), for three relevant basis sets and the self-energy approximations considered in this paper: the second-Born approximation (SOA), GW approximation (GW), the particle-particle (TPP) and particle-hole (TPH) T matrices, and the dynamically-screened-ladder approximation (DSL). Last column: CPU speedup ratio of the G1-G2 scheme compared to standard HF-GKBA. For DSL, currently no standard HF-GKBA version exists. Note that full two-time NEGF simulations always have cubic scaling with N_t.

| Σ | Basis | HF-GKBA | | Speedup |
		Standard	G1-G2	ratio
SOA	general	$\mathcal{O}(N_b^5 N_t^2)$	$\mathcal{O}(N_b^5 N_t^1)$	$\mathcal{O}(N_t)$
	Hubbard	$\mathcal{O}(N_b^3 N_t^2)$	$\mathcal{O}(N_b^4 N_t^1)$	$\mathcal{O}(N_t/N_b)$
	jellium	$\mathcal{O}(N_b^3 N_t^2)$	$\mathcal{O}(N_b^3 N_t^1)$	$\mathcal{O}(N_t)$
GW	general	$\mathcal{O}(N_b^6 N_t^3)$	$\mathcal{O}(N_b^6 N_t^1)$	$\mathcal{O}(N_t^2)$
	Hubbard	$\mathcal{O}(N_b^3 N_t^3)$	$\mathcal{O}(N_b^4 N_t^1)$	$\mathcal{O}(N_t^2/N_b)$
	jellium	$\mathcal{O}(N_b^3 N_t^3)$	$\mathcal{O}(N_b^3 N_t^1)$	$\mathcal{O}(N_t^2)$
TPP	general	$\mathcal{O}(N_b^6 N_t^3)$	$\mathcal{O}(N_b^6 N_t^1)$	$\mathcal{O}(N_t^2)$
	Hubbard	$\mathcal{O}(N_b^3 N_t^3)$	$\mathcal{O}(N_b^4 N_t^1)$	$\mathcal{O}(N_t^2/N_b)$
	jellium	$\mathcal{O}(N_b^3 N_t^3)$	$\mathcal{O}(N_b^4 N_t^1)$	$\mathcal{O}(N_t^2/N_b)$
TPH	general	$\mathcal{O}(N_b^6 N_t^3)$	$\mathcal{O}(N_b^6 N_t^1)$	$\mathcal{O}(N_t^2)$
	Hubbard	$\mathcal{O}(N_b^3 N_t^3)$	$\mathcal{O}(N_b^4 N_t^1)$	$\mathcal{O}(N_t^2/N_b)$
	jellium	$\mathcal{O}(N_b^3 N_t^3)$	$\mathcal{O}(N_b^4 N_t^1)$	$\mathcal{O}(N_t^2/N_b)$
DSL	general	–	$\mathcal{O}(N_b^6 N_t^1)$	–
	Hubbard	–	$\mathcal{O}(N_b^4 N_t^1)$	–
	jellium	–	$\mathcal{O}(N_b^4 N_t^1)$	–

It is easily verified that the entire Eq. (87) requires a CPU time that has the same linear scaling with N_t as all the special cases that were studied before. On the other hand, the polarization and ladder terms determine the scaling with the basis size N_b. This is summarized in Table I and discussed in more detail in Sec. VII.

VII. ANALYSIS OF THE NUMERICAL SCALING

As was shown in the previous sections, the G1-G2 scheme transforms the time-diagonal KBE within the HF-GKBA to a memory-less, time-local form. This means, the theoretical scaling is first order in the propagation duration. This dramatic acceleration is achieved by propagating, in addition to the single-particle Green function, also the time-diagonal two-particle Green function $\mathcal{G}$. This function has, in general, four basis indices and, thus, a dimensionality of N_b^4, where N_b is the single-particle basis dimension. The total scaling of the G1-G2 scheme with N_b depends on the self energy and on the type of basis. In the following, we investigate this scaling more in detail, extending the analysis of Ref. [39].

A. Second-order Born self energy

We start by analyzing the N_b scaling of the SOA-G1-G2 equation for $\mathcal{G}$, Eq. (29), which we rewrite in a different

form

$$i\hbar\frac{d}{dt}\mathcal{G}_{ijkl}(t) - \left[h^{(2),\mathrm{HF}}, \mathcal{G}\right]_{ijkl}(t)$$

$$= (i\hbar)^2 \sum_p G_{ip}^>(t) \sum_q G_{jq}^>(t) \sum_r G_{rk}^<(t) \sum_s w_{pqrs}^\pm(t) G_{sl}^<(t)$$

$$- (i\hbar)^2 \sum_p G_{ip}^<(t) \sum_q G_{jq}^<(t) \sum_r G_{rk}^>(t) \sum_s w_{pqrs}^\pm(t) G_{sl}^>(t).$$

The r.h.s. of this equation contains four sums of dimensionality N_b which are all independent of each other. They are evaluated by successive execution of the occurring tensor contractions. This means the total scaling of the CPU time, in this case, is of order N_b^5.

For the Hubbard basis a first look at Eqs. (36)–(38) suggests an N_b^5-scaling, due to the commutator term in Eq. (36) and the summation in the Φ term of Eq. (38). However, in the Hubbard model the scaling can be further reduced. Note that the Hartree-Fock Hamiltonian, $h^{\mathrm{HF}}(t)$, is a tridiagonal matrix and, thus, the commutator can be computed with N_b^4 effort:

$$\left[h_{\uparrow\downarrow}^{(2),\mathrm{HF}}, \mathcal{G}^{\uparrow\downarrow\uparrow\downarrow}\right]_{ijkl}(t)$$

$$= \sum_p \left[h_{ip}^{\mathrm{HF},\uparrow}(t)\mathcal{G}_{pjkl}^{\uparrow\downarrow\uparrow\downarrow}(t) + h_{jp}^{\mathrm{HF},\downarrow}(t)\mathcal{G}_{ipkl}^{\uparrow\downarrow\uparrow\downarrow}(t)\right.$$

$$\left. - \mathcal{G}_{ijpl}^{\uparrow\downarrow\uparrow\downarrow}(t)h_{pk}^{\mathrm{HF},\uparrow}(t) - \mathcal{G}_{ijkp}^{\uparrow\downarrow\uparrow\downarrow}(t)h_{pl}^{\mathrm{HF},\downarrow}(t)\right]$$

$$= -i\hbar U(t)\mathcal{G}_{ijkl}^{\uparrow\downarrow\uparrow\downarrow}(t)\left[G_{ii}^\downarrow(t) + G_{jj}^\uparrow(t) - G_{kk}^\downarrow(t) - G_{ll}^\uparrow(t)\right]$$

$$- J \sum_p \left[\delta_{\langle i,p\rangle}\mathcal{G}_{pjkl}^{\uparrow\downarrow\uparrow\downarrow}(t) + \delta_{\langle j,p\rangle}\mathcal{G}_{ipkl}^{\uparrow\downarrow\uparrow\downarrow}(t)\right.$$

$$\left. - \mathcal{G}_{ijpl}^{\uparrow\downarrow\uparrow\downarrow}(t)\delta_{\langle p,k\rangle} - \mathcal{G}_{ijkp}^{\uparrow\downarrow\uparrow\downarrow}(t)\delta_{\langle p,l\rangle}\right].$$

On the other hand, the Φ term can be simplified by using the identity of Eq. (11):

$$\Phi_{ijkl}^{\uparrow\downarrow\uparrow\downarrow}(t)$$

$$= (i\hbar)^4 \sum_p \left\{\left[G_{ip}^{<,\uparrow}(t) + \frac{1}{i\hbar}\delta_{ip}\right]\left[G_{jp}^{<,\downarrow}(t) + \frac{1}{i\hbar}\delta_{jp}\right]\right.$$

$$\times G_{pk}^{<,\uparrow}(t)G_{pl}^{<,\downarrow}(t) - G_{ip}^{<,\uparrow}(t)G_{jp}^{<,\downarrow}(t)$$

$$\times \left.\left[G_{pk}^{<,\uparrow}(t) + \frac{1}{i\hbar}\delta_{pk}\right]\left[G_{pl}^{<,\downarrow}(t) + \frac{1}{i\hbar}\delta_{pl}\right]\right\}$$

$$= (i\hbar)^2(\delta_{ij} - \delta_{kl})G_{ik}^{<,\uparrow}(t)G_{jl}^{<,\downarrow}(t)$$

$$+ (i\hbar)^3[G_{ij}^{<,\uparrow}(t)G_{jk}^{<,\uparrow}(t) - G_{lk}^{<,\uparrow}(t)G_{il}^{<,\uparrow}(t)]G_{jl}^{<,\downarrow}(t)$$

$$+ (i\hbar)^3[G_{ji}^{<,\downarrow}(t)G_{il}^{<,\downarrow}(t) - G_{kl}^{<,\downarrow}(t)G_{jk}^{<,\downarrow}(t)]G_{ik}^{<,\uparrow}(t).$$

$$(89)$$

Here, the leading contribution to the difference, $G^<G^<G^<G^< - G^<G^<G^<G^<$, cancels (contribution with four functions $G^<$) which reduces the complexity. For the Hubbard basis, this reduces the numerical effort of the G1-G2 scheme to a N_b^4 scaling compared to the N_b^5-scaling in the straightforward implementation [39]. In total, an acceleration is achieved for the SOA-G1-G2 scheme, compared to the ordinary HF-GKBA if $N_t \gtrsim N_b$, as summarized in Table I.

The reformulation above that eliminates products of four $G^<$ functions can be made for any basis choice. However, for the general basis this does not result in an improved N_b scaling. For the jellium basis the Eqs. (41)–(43) reveal a particularly favorable scaling with the basis size with N_b^3 for which the above reformulation does not provide further improvement.

B. *GW* self energy

The additional terms of the *GW* approximation can change the N_b scaling compared to the SOA case discussed in the previous section. For the general basis, the leading-order terms for the scaling with the basis size are found in Eqs. (55) and (61) which reveal a N_b^6 scaling. For this case no further reductions are possible, cf. Table I.

For the Hubbard basis the polarization terms [Eqs. (64) and (65)] can be reformulated by again using Eq. (11) to get

$$\Pi_{ijkl}^{\uparrow\downarrow\uparrow\downarrow}(t) = -i\hbar U(t)G_{jl}^{<,\downarrow}(t)[\mathcal{G}_{ijkj}^{\uparrow\uparrow\uparrow\uparrow}(t) - \mathcal{G}_{ilkl}^{\uparrow\uparrow\uparrow\uparrow}(t)],$$

$$\Pi_{ijkl}^{\uparrow\uparrow\uparrow\uparrow}(t) = -i\hbar U(t)G_{jl}^{<,\uparrow}(t)[\mathcal{G}_{ijkj}^{\uparrow\downarrow\uparrow\downarrow}(t) - \mathcal{G}_{ilkl}^{\uparrow\downarrow\uparrow\downarrow}(t)].$$

From this, it is obvious that, compared to the second-order Born approximation, no further complexity is added for *GW* in the Hubbard case, and the scaling with the basis size remains N_b^4.

To explore the N_b scaling for the jellium basis we recall the polarization term, Eq. (66),

$$\Pi_{\mathbf{p},\bar{\mathbf{p}},\mathbf{q}}^{\alpha\beta}(t) = \pm(i\hbar)^2[G_{\bar{\mathbf{p}}+\mathbf{q}}^{>,\beta}(t)G_{\bar{\mathbf{p}}}^{<,\beta}(t) - G_{\bar{\mathbf{p}}+\mathbf{q}}^{<,\beta}(t)G_{\bar{\mathbf{p}}}^{>,\beta}(t)]$$

$$\times v_{|\mathbf{q}|}(t)\sum_{\mathbf{k},\sigma}\mathcal{G}_{\mathbf{p}\mathbf{k}\mathbf{q}}^{\alpha\sigma}(t).$$

As one can see, the tensor contraction over $\mathbf{k}$ can be executed independently of $\bar{\mathbf{p}}$. Thus, the full scaling of the *GW*-G1-G2 scheme for a jellium basis remains of order N_b^3, as in the case of the standard HF-GKBA.

C. *T*-matrix self energies

The *T*-matrix equations [Sec. V] behave very similar to the *GW* equations. For a general basis set with a four-index interaction tensor both, TPP and TPH scale as N_b^6 which can be directly seen from Eqs. (73) and (77), as well as Eqs. (80) and (84).

For the Hubbard basis we can now use Eq. (11) to eliminate contributions that are of second order in $G^<$ from the ladder terms in Eq. (78),

$$\Lambda_{ijkl}^{\mathrm{pp},\uparrow\downarrow\uparrow\downarrow}(t) = \delta_{ij}U(t)\mathcal{G}_{ijkl}^{\uparrow\downarrow\uparrow\downarrow}(t) + i\hbar U(t)[G_{ji}^{<,\downarrow}(t)\mathcal{G}_{iikl}^{\uparrow\downarrow\uparrow\downarrow}(t)$$

$$+ G_{ij}^{<,\uparrow}(t)\mathcal{G}_{jjkl}^{\uparrow\downarrow\uparrow\downarrow}(t)],$$

as well as in Eq. (85),

$$\Lambda_{ijkl}^{\mathrm{ph},\uparrow\downarrow\uparrow\downarrow}(t) = i\hbar U(t)[G_{il}^{<,\downarrow}(t)\mathcal{G}_{ijki}^{\uparrow\downarrow\uparrow\downarrow}(t) - G_{il}^{<,\uparrow}(t)\mathcal{G}_{ljkl}^{\uparrow\downarrow\uparrow\downarrow}(t)].$$

For both cases one can see that the remaining scaling order of the equations is N_b^4 since all internal summations have been eliminated.

In the jellium basis the *T* matrices show a different scaling behavior compared to *GW*. To see this, we reproduce the two

ladder terms of Eqs. (79) and (86),

$$
\Lambda_{\boldsymbol{p},\bar{\boldsymbol{p}},\boldsymbol{q}}^{\mathrm{pp},\alpha\beta}(t) = (i\hbar)^2 \big[G_{\boldsymbol{p}-\boldsymbol{q}}^{>,\alpha}(t) G_{\bar{\boldsymbol{p}}+\boldsymbol{q}}^{>,\beta}(t) - G_{\boldsymbol{p}-\boldsymbol{q}}^{<,\alpha}(t) G_{\bar{\boldsymbol{p}}+\boldsymbol{q}}^{<,\beta}(t) \big]
$$
$$
\times \sum_{\boldsymbol{k}} v_{|\boldsymbol{k}-\boldsymbol{q}|}(t) \mathcal{G}_{\boldsymbol{p}\bar{\boldsymbol{p}}\boldsymbol{k}}^{\alpha\beta}(t) ,
$$

$$
\Lambda_{\boldsymbol{p},\bar{\boldsymbol{p}},\boldsymbol{q}}^{\mathrm{ph},\alpha\beta}(t) = (i\hbar)^2 \big[G_{\boldsymbol{p}-\boldsymbol{q}}^{>,\alpha}(t) G_{\bar{\boldsymbol{p}}}^{<,\beta}(t) - G_{\boldsymbol{p}-\boldsymbol{q}}^{<,\alpha}(t) G_{\bar{\boldsymbol{p}}}^{>,\beta}(t) \big]
$$
$$
\times \sum_{\boldsymbol{k}} v_{|\boldsymbol{k}|}(t) \mathcal{G}_{\boldsymbol{p},\bar{\boldsymbol{p}}-\boldsymbol{k},\boldsymbol{q}+\boldsymbol{k}}^{\alpha\beta}(t) .
$$

Evidently, in both cases the tensor contraction of $\boldsymbol{k}$ depends on all other momenta $\boldsymbol{p}, \bar{\boldsymbol{p}}, \boldsymbol{q}$. Thus, the final scaling with the basis size becomes of order N_b^4. A summary of the numerical scaling with the propagation duration and the basis size is presented in Table I.

At the same time, any practical implementation of the G1-G2 scheme could, in principle, carry a large overhead that prevents us from achieving the theoretical scaling with the simulation duration and the basis dimension within a relevant parameter range. We, therefore, have implemented the G1-G2 scheme for each of the self energies discussed in this paper and present representative numerical results in Sec. VII D.

D. Numerical results for the Hubbard basis

As we have shown above (cf. Table I), the Hubbard basis is the most unfavorable case for the G1-G2 scheme. Therefore, we choose this case for numerical demonstrations. In Ref. [39] we presented the first numerical tests of this scheme and demonstrated that, for finite Hubbard clusters the predicted linear scaling is indeed achieved for SOA and GW self energies, already for rather small values N_t.

Here we extend these simulations to the T-matrix self energies and the DSL approximation. Furthermore, we practically confirm the N_b scaling. As a first test, we verify that the derived formulas of the G1-G2 scheme are equivalent to the original (non-Markovian) HF-GKBA formulation. As a test case we consider, in Fig. 2, the time evolution in a Hubbard dimer for SOA, GW, TPP, and TPH self energies. For both considered methods, the original HF-GKBA and the G1-G2 scheme, a fourth-order Runge-Kutta integration scheme with a time step of $\Delta t = 0.02\hbar/J$ is used. The agreement is excellent, and the deviations are mostly due to the original HF-GKBA, as discussed in Ref. [39].

Next, we demonstrate the scaling with the basis dimension N_b for the SOA self energy. In Fig. 3 we show results for a large number of Hubbard chains of varying length, $N_b = 2 \ldots 100$. We clearly confirm the N_b^5 scaling for the standard implementation of the G1-G2 scheme that uses Eq. (38) [39]. This asymptotic behavior is reached already for $N_b \gtrsim 20$. The second curve is for the same setup but uses the optimization, Eq. (89). Again, the predicted improved scaling according to N_b^4 is clearly identified, at least for $N_b \gtrsim 50$. This confirms the expected speedup of the SOA-G1-G2 scheme compared to the standard HF-GKBA, if $N_t \gtrsim N_b$. Thus, even for the most unfavorable case of a Hubbard basis [cf. Table I] the scaling advantage should be reached already for small simulation durations.
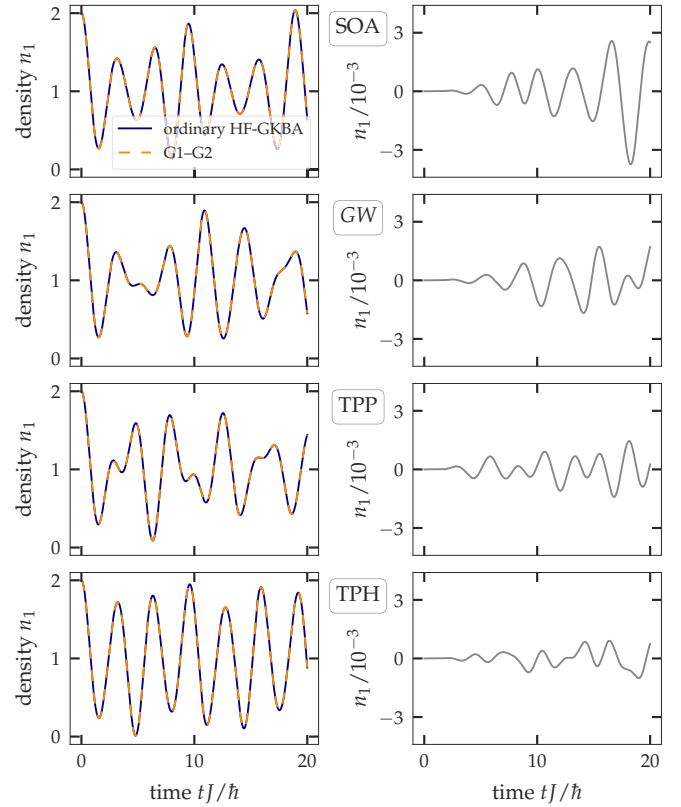
FIG. 2. Comparison of the ordinary HF-GKBA and the G1-G2 scheme for a Hubbard dimer with $U = J$ at half filling. The initial state was uncorrelated with the entire density concentrated at the first lattice site. Rows correspond to SOA, GW, TPP, and TPH self energies. Right column shows the deviation $\Delta n_1(t) = n_1^{\mathrm{G1-G2}}(t) - n_1^{\mathrm{ordinary}}(t)$ of the densities of both schemes on site 1.

To explore the scaling with N_t in more detail we have performed a series of simulations for all self-energy approximations, comparing the standard HF-GKBA to the G1-G2 scheme. The results are shown in Fig. 4 and confirm the quadratic (cubic) scaling of the CPU time with N_t, for the standard HF-GKBA with SOA (GW) self energy. Similar cubic scaling is observed for the two T-matrix approximations
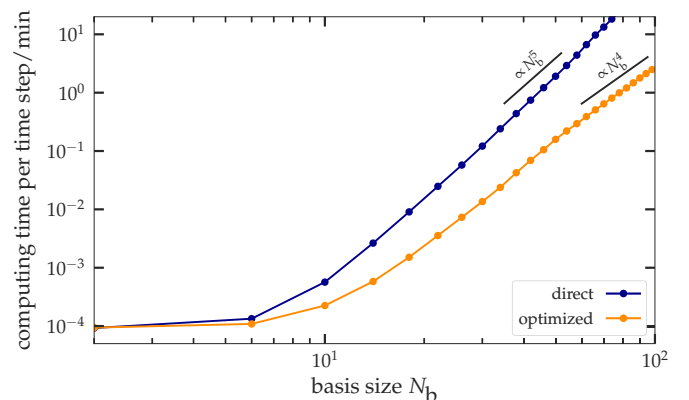
FIG. 3. CPU-time scaling of the SOA-G1-G2 scheme with the basis size N_b comparing the direct, Eq. (39) [39], and the optimized implementation, Eq. (89). Results are for a 1D Hubbard chain.
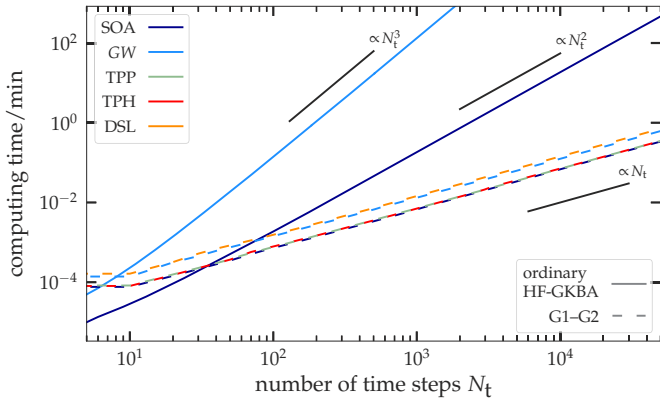
FIG. 4. CPU-time scaling with the simulation duration N_t, comparing the standard HF-GKBA to the G1-G2 scheme. G1-G2 data are shown for five self-energy approximations (indicated in the legend) all of which clearly exhibit linear scaling. In contrast, the standard HF-GKBA scales as N_t^2, for SOA, and N_t^3, for GW. Results are for a 10-site Hubbard chain.

FIG. 5. Density evolution comparing the DSL-G1-G2 scheme to the results of Ref. [75] (WC) and exact-diagonalization simulations. The system is a four-site Hubbard chain at $U = 0.1J$ and half filling; the simulations started from a noninteracting (uncorrelated) initial state, where the first two sites are doubly occupied.

(not shown) whereas simulations with DSL approximation are not possible, at the moment. Let us now turn to the G1-G2 results (dashed lines). Each of the curves exhibits the predicted linear scaling, already for $N_t \gtrsim 20$. Interestingly, in the G1-G2 scheme, the CPU time required for the rather involved T-matrix approximations is only slightly above the time required for the comparatively simple SOA case. Equally remarkable is the observation that the GW and DSL approximations, which, in Hubbard, rely on cross-coupling spin components, are rather close to the former self energies.

Note that, for the present small system (10-site Hubbard chain) "break even" of the G1-G2 scheme is reached for all self energies compared to the ordinary SOA-HF-GKBA (dark blue curve) well below $N_t = 100$ whereas the original GW-HF-GKBA (light blue) is unfavorable, practically from the start. For larger times, the ordinary GW-HF-GKBA quickly turns out unfeasible (e.g., for $N_t \sim 10^3$ it requires 10^4 times longer simulations than GW-G1-G2), and the same applies to the T-matrix self energies. Thus, we conclude that, it is not just a quantitative gain in CPU time that the G1-G2 scheme delivers but, in many cases, highly accurate simulations (beyond the simple SOA self energy) become possible at all that are (currently) impossible otherwise.

In particular, at increased coupling, $U/J \gtrsim 2$, the SOA self energy is known to be inaccurate (for an analysis see Ref. [28]), and for reliable simulations, more advanced approximations are crucial. In that context the DSL approximation is particularly attractive because it contains the dominant correlation effects self consistently. Until now such simulations have only occasionally been reported, for very small systems and short propagation times. An example of a four-site Hubbard chain is shown in Fig. 5. We observe excellent agreement of our DSL-G1-G2 scheme to the Wang-Cassing (WC) approximation simulations of Akbari *et al.* [75] confirming the equivalence of the two approximations. The results show excellent quantitative agreement with exact-diagonalization data (black curve), however, for times $tJ/\hbar \gtrsim 30$ deviations are growing.

VIII. DISCUSSION AND OUTLOOK

In this paper we analyzed the properties of nonequilibrium Green functions in the frame of the generalized Kadanoff-Baym ansatz with Hartree-Fock propagators (HF-GKBA). Due to the non-Markovian structure of the collision integral, HF-GKBA simulations have an unfavorable quadratic (cubic) scaling with the number of time steps, for second-order Born (more complicated) self energies. At the same time, it has been reported earlier that this memory integral can be formally eliminated in favor of coupled time-local differential equations for the single-particle and two-particle density matrix [5,40]. An equivalent formulation in the framework of nonequilibrium Green functions has been established in Ref. [39]—the G1-G2 scheme. The formal equivalence between both approaches is important because it means that the G1-G2 scheme retains all attractive properties of the HF-GKBA: It is total-energy conserving and time reversible [56]. Furthermore, the most prominent self-energy approximations from NEGF theory that have been derived, e.g., using diagrammatic techniques, can be transformed into a time-local form, by applying the HF-GKBA.

The earlier analyses of the time-linear equations [5,40] concentrated mainly on spatially homogeneous systems (jellium) and did not include computational aspects such as the CPU-time requirement. The scaling with the propagation time and basis size have only recently been analyzed in detail in conjunction with the G1-G2 scheme [39], and it was confirmed that the N_t^1 scaling can be achieved in practice. Here, we substantially extended these results, including additional high-level self energies such as the particle-particle and particle-hole T-matrix self energies and the screened-ladder approximation. In each case N_t^1 scaling of the CPU time could be confirmed giving rise to a remarkable N_t^2-scaling advantage compared to the standard HF-GKBA scheme (Fig. 4) which was found to be independent of the single-particle basis used for the simulations. Furthermore, we re-analyzed the CPU-time scaling with the basis dimension N_b and observed that the G1-G2 scheme has an overhead, compared to standard HF-GKBA, that is, *at most*, first order in N_b, cf. Table I.

Even for the most unfavorable basis—the Hubbard basis—the G1-G2 scheme has only a N_b^1 overhead (down from a N_b^2 overhead reported in Ref. [39]) which could be achieved by a reformulation of the scattering term in the G2 equation, cf. Sec. VII A. Thus, we expect that the G1-G2 scheme outperforms the standard HF-GKBA approach, in all cases of practical relevance, which can be seen from the CPU-time scaling ratio summarized in the right column of Table I.

With the G1-G2 scheme NEGF simulations (within the HF-GKBA) have been brought to the same CPU-time scaling as many other time-dependent approaches, including semi-classical molecular dynamics, hydrodynamics, Boltzmann-type kinetic equations, TDDFT (adiabatic approximation), and the time-dependent Schrödinger equation. Most importantly, now long simulations are feasible that were previously prohibited by the memory structure (resulting in the N_t^2 or N_t^3 scaling discussed above) without compromising the quality of the treatment of electronic correlations. We also showed that the inclusion of initial correlations in the G1-G2 scheme is trivial, and their propagation again requires a CPU-time effort that is of order N_t. Also the precomputation of the correlated initial state, e.g., via imaginary-time stepping or adiabatic switching, see, e.g., Ref. [21], can be carried out separately and does not affect the propagation scaling.

While we presented numerical results only for the Hubbard model, even larger gains, compared to the standard HF-GKBA, are predicted for jellium (e.g., electron gas, dense quantum plasmas, electron-hole plasmas etc.) and for more general basis sets where the interaction tensor has four indices (e.g., electron dynamics in atoms and molecules). At the same time, the removal of the memory integral as the main CPU-time bottleneck was achieved by computing the dynamics of an additional quantity—the time-diagonal two-particle Green function $\mathcal{G}_{ijkl}$. Thus, the new bottleneck in the G1-G2 scheme is the memory cost to store this four-dimensional tensor (only the current values are required), but this can be mitigated by suitable parallelization concepts.

By mapping NEGF simulations to a time-local scheme for single-time quantities, it should be expected that close connections exist with reduced-density-operator theory (RDO) [5,39,40]. The latter has been an independent many-body approach that has been successfully applied in many areas, including semiconductor optics, see, e.g., Refs. [76,77], dense plasmas [32], correlated electrons [64,75,78], nuclear matter [79], and cold atoms [80]. Our results indicate the correspondence between important self-energy approximations of NEGF theory to closure relations of RDO and confirm and extend earlier results on the particle-particle T matrix [71] and the GW approximation [64]. We also investigated the simultaneous treatment of strong coupling and dynamical-screening effects by combining ladder and polarization terms in the equation for $\mathcal{G}$. This led us to the dynamically-screened-ladder approximation (DSL) in Sec. VI. This approximation includes all two-particle interaction contributions and is, thus, equivalent to an approximation considered by Wang and Cassing before [74]. The equivalence of the two approximations was confirmed by the excellent agreement with the numerical results of Akbari *et al.* [75] for a small Hubbard cluster, cf. Fig. 5. Consequently, all self-energy contributions that go beyond the DSL correspond to the (partial) account

of three-particle correlations and, thus, additionally require (at least) the propagation of the time-diagonal three-particle Green function, when mapped to a time-linear scheme.

Despite the high quality of the DSL, we also observed that it is in quantitative agreement with exact diagonalization (CI) data (black curve in Fig. 5) only during the initial relaxation phase (for times $tJ/\hbar \lesssim 30$) [75]. So, clearly, more systematic comparisons to CI results, for a broader range of coupling strengths and filling fractions, are desirable to understand the applicability limits of the DSL. While CI simulations are limited to very small particle numbers (basis size N_b) the G1-G2 scheme in DSL and simpler approximations can treat much larger systems. To go beyond those parameters where the DSL approximation is valid, further improved approximations are in high demand. This will require one to partially include three-particle correlations. Examples are the Kirkwood superposition approximation of classical statistical physics [81] (for recent applications see Refs. [82,83]), the approximation by Nakatsuji and Yasuda [84,85], and self-energy corrections to the BBGKY hierarchy [5]. Another route to improvements starts from nonequilibrium Green functions theory where one approach is to apply the GKBA but replace the Hartree-Fock propagators by correlated propagators [21]. Another concept is to replace the GKBA entirely by an improved reconstruction ansatz. In both cases, the procedure outlined in the present paper will allow one to derive the corresponding improved G1-G2 scheme. Since the applicability limits of the GKBA are still not fully explored, full two-time NEGF simulations will remain indispensable for tests and benchmarks, see, e.g., Ref. [86].

In conclusion, let us come back to the remarkable capability of the G1-G2 scheme to efficiently perform long-time simulations of correlated-electron dynamics. With this it should be feasible to reach thermodynamic equilibrium (or a quasistationary or prethermalized state) of the electrons. At the same time, slower processes, such as the equilibration with heavier particles (e.g., with the lattice in solids or with ions in dense plasmas) will make it desirable to develop a multiscale approach. This can be based on approximate solutions of the G1-G2 equations, e.g., by using retardation expansions [5] or the correlation-time approximation [87], eventually approaching the Markovian Boltzmann equation or local thermodynamic equilibrium. In that case a connection of the kinetic simulations to quantum hydrodynamic models, see, e.g., Refs. [88,89], could be a promising approach.

APPENDIX A: PROPERTIES OF THE TIME-EVOLUTION OPERATOR

In the following, we derive important properties of the one- and two-particle propagators.

1. Symmetry relations

The single-particle time-evolution operator $\mathcal{U}$ fulfills the symmetry

$$[\mathcal{U}_{ji}(t', t)]^* = [G^R_{ji}(t', t) - G^A_{ji}(t', t)]^* = -\mathcal{U}_{ij}(t, t'), \quad (A1)$$

where $[G^{A/R}_{ji}(t, t')]^* = G^{R/A}_{ij}(t', t)$ has been used. Likewise, the two-particle propagator obeys,

$$[\mathcal{U}^{(2)}_{klij}(t, t')]^* = [\mathcal{U}_{ki}(t, t')]^*[\mathcal{U}_{lj}(t, t')]^* = \mathcal{U}^{(2)}_{ijkl}(t', t),$$

where Eq. (A1) has been used.

2. Group property

When applying the HF-GKBA the retarded and advanced propagators, $G^R(t, t')$ and $G^A(t, t')$, are used in HF approximation and, thus, obey the group property [36] for $t > \bar{t} > t'$:

$$G^A_{ij}(t', t) = -i\hbar \sum_k G^A_{ik}(t', \bar{t}) G^A_{kj}(\bar{t}, t), \quad (A2)$$

$$G^R_{ij}(t, t') = i\hbar \sum_k G^R_{ik}(t, \bar{t}) G^R_{kj}(\bar{t}, t'). \quad (A3)$$

In the following, the group property for the propagator $\mathcal{U}$ is derived for all relevant time orderings. Starting with

$$i\hbar \sum_k \mathcal{U}_{ik}(t, \bar{t}) \mathcal{U}_{kj}(\bar{t}, t')$$

$$= i\hbar \sum_k [G^R_{ik}(t, \bar{t}) - G^A_{ik}(t, \bar{t})][G^R_{kj}(\bar{t}, t') - G^A_{kj}(\bar{t}, t')],$$

five different cases have to be considered. For $t = \bar{t} = t'$ one gets

$$\sum_k \mathcal{U}_{ik}(t, t) \mathcal{U}_{kj}(t, t) = \sum_k \frac{\delta_{ik}\delta_{kj}}{(i\hbar)^2} = \frac{\delta_{ij}}{(i\hbar)^2} = \frac{1}{i\hbar} \mathcal{U}_{ij}(t, t).$$

For $t = \bar{t}$ one gets

$$\sum_k \mathcal{U}_{ik}(t, t) \mathcal{U}_{kj}(t, t') = \sum_k \frac{1}{i\hbar} \delta_{ik} \mathcal{U}_{kj}(t, t') = \frac{1}{i\hbar} \mathcal{U}_{ij}(t, t'),$$

as well as for $\bar{t} = t'$,

$$\sum_k \mathcal{U}_{ik}(t, t') \mathcal{U}_{kj}(t', t') = \sum_k \mathcal{U}_{ik}(t, t') \frac{1}{i\hbar} \delta_{kj} = \frac{1}{i\hbar} \mathcal{U}_{ij}(t, t').$$

For $t > \bar{t} > t'$, the propagators reduce to $\mathcal{U}_{ij}(t, t') = G^R_{ij}(t, t')$, for which Eq. (A3) is directly applicable. For the analogous case, $t < \bar{t} < t'$, one obtains $\mathcal{U}_{ij}(t, t') = -G^A_{ij}(t, t')$ which, together with Eq. (A2), leads to

$$i\hbar \sum_k \mathcal{U}_{ik}(t, \bar{t}) \mathcal{U}_{kj}(\bar{t}, t') = \mathcal{U}_{ij}(t, t'), \quad (A4)$$

for all t, t'. A direct consequence of this group property is [cf. Eq. (21)],

$$\mathcal{U}^{(2)}_{ijkl}(t, t') = (i\hbar)^2 \sum_{pq} \mathcal{U}^{(2)}_{ijpq}(t, \bar{t}) \mathcal{U}^{(2)}_{pqkl}(\bar{t}, t'), \quad (A5)$$

for the two-particle propagator.

3. Equations of motion

Using the EOM for the retarded/advanced Green functions, Eq. (23), the EOMs for the modified propagator immediately follows, where we separately consider the time evolution along the first and second time arguments:

$$i\hbar \frac{d}{dt} \mathcal{U}_{ij}(t, t') = \sum_k h^{HF}_{ik}(t) G^R_{kj}(t, t') + \delta_{ij}\delta(t, t')$$

$$- \sum_k h^{HF}_{ik}(t) G^A_{kj}(t, t') - \delta_{ij}\delta(t, t')$$

$$= \sum_k h^{HF}_{ik}(t) \mathcal{U}_{kj}(t, t'), \quad (A6)$$

$$i\hbar \frac{d}{dt} \mathcal{U}_{ij}(t', t) = -\sum_k G^R_{ik}(t', t) h^{HF}_{kj}(t) - \delta_{ij}\delta(t, t')$$

$$+ \sum_k G^A_{ik}(t', t) h^{HF}_{kj}(t) + \delta_{ij}\delta(t, t')$$

$$= -\sum_k \mathcal{U}_{ik}(t', t) h^{HF}_{kj}(t). \quad (A7)$$

Obviously, $\mathcal{U}$ has no time-singular term but obeys a Schrödinger-type equation of motion. For the two-particle propagator follows

$$\frac{d}{dt} [\mathcal{U}^{(2)}_{ijkl}(t, \bar{t})] = \frac{d}{dt} [\mathcal{U}_{ik}(t, \bar{t})] \mathcal{U}_{jl}(t, \bar{t})$$

$$+ \mathcal{U}_{ik}(t, \bar{t}) \frac{d}{dt} [\mathcal{U}_{jl}(t, \bar{t})]$$

$$= \left[\frac{1}{i\hbar} \sum_p h^{HF}_{ip}(t) \mathcal{U}_{pk}(t, \bar{t}) \right] \mathcal{U}_{jl}(t, \bar{t})$$

$$+ \mathcal{U}_{ik}(t, \bar{t}) \left[\frac{1}{i\hbar} \sum_p h^{HF}_{jp}(t) \mathcal{U}_{pl}(t, \bar{t}) \right]$$

$$= \frac{1}{i\hbar} \sum_p h^{HF}_{ip}(t) \mathcal{U}^{(2)}_{pjkl}(t, \bar{t})$$

$$+ \frac{1}{i\hbar} \sum_p h^{HF}_{jp}(t) \mathcal{U}^{(2)}_{ipkl}(t, \bar{t}). \quad (A8)$$

To simplify the notation, we use the two-particle Hartree-Fock Hamiltonian [cf. Eq. (26)] so that

$$\sum_{pq} h^{(2),HF}_{ijpq}(t) \mathcal{U}^{(2)}_{pqkl} = \sum_p h^{HF}_{ip}(t) \mathcal{U}^{(2)}_{pjkl}(t, \bar{t})$$

$$+ \sum_p h^{HF}_{jp}(t) \mathcal{U}^{(2)}_{ipkl}(t, \bar{t}),$$

and Eq. (A8) can be rewritten as

$$\frac{d}{dt} [\mathcal{U}^{(2)}_{ijkl}(t, \bar{t})] = \frac{1}{i\hbar} \sum_{pq} h^{(2),HF}_{ijpq}(t) \mathcal{U}^{(2)}_{pqkl}(t, \bar{t}).$$

In the same way the derivative with respect to the second time argument is found,

$$
\begin{aligned}
\frac{d}{dt}\big[\mathcal{U}^{(2)}_{ijkl}(\bar{t},t)\big] &= \frac{d}{dt}[\mathcal{U}_{ik}(\bar{t},t)]\mathcal{U}_{jl}(\bar{t},t) \\
&\quad + \mathcal{U}_{ik}(\bar{t},t)\frac{d}{dt}[\mathcal{U}_{jl}(\bar{t},t)] \\
&= \left[-\frac{1}{i\hbar}\sum_p \mathcal{U}_{ip}(\bar{t},t)h^{\mathrm{HF}}_{pk}(t)\right]\mathcal{U}_{jl}(\bar{t},t) \\
&\quad + \mathcal{U}_{ik}(\bar{t},t)\left[-\frac{1}{i\hbar}\sum_p \mathcal{U}_{jp}(\bar{t},t)h^{\mathrm{HF}}_{pl}(t)\right] \\
&= -\frac{1}{i\hbar}\sum_{pq}\mathcal{U}^{(2)}_{ijpq}(\bar{t},t)h^{(2),\mathrm{HF}}_{pqkl}(t).
\end{aligned}
$$

APPENDIX B: TIME-LINEAR INTEGRAL SOLUTION FOR $\mathcal{G}$

As we show in Sec. III B, the non-Markovian structure of the time-diagonal two-particle Green function, Eq. (22), can be eliminated by converting the problem into two coupled differential equations for $G^<(t)$ and $\mathcal{G}(t)$. Here we show for completeness that, alternatively, time-linear scaling can also be achieved within an integral representation of $\mathcal{G}$. To reveal the time-linear core of Eq. (22) for Hartree-Fock propagators, we consider a time $T+\Delta$ for which the time integral can be split into two intervals $[t_0, T]$ and $[T, T+\Delta]$, resulting in

$$
\begin{aligned}
\mathcal{G}_{ijkl}(T+\Delta) &= \mathcal{G}^{\Delta}_{ijkl}(T) + (i\hbar)^3\sum_{pqrs}\int_{t_0}^{T}d\bar{t} \\
&\quad \times \mathcal{U}^{(2)}_{ijpq}(T+\Delta,\bar{t})\Psi^{\pm}_{pqrs}(\bar{t})\mathcal{U}^{(2)}_{rskl}(\bar{t},T+\Delta),
\end{aligned}
$$

with

$$
\begin{aligned}
\mathcal{G}^{\Delta}_{ijkl}(T) &:= (i\hbar)^3\sum_{pqrs}\int_{T}^{T+\Delta}d\bar{t} \\
&\quad \times \mathcal{U}^{(2)}_{ijpq}(T+\Delta,\bar{t})\Psi^{\pm}_{pqrs}(\bar{t})\mathcal{U}^{(2)}_{rskl}(\bar{t},T+\Delta).
\end{aligned}
$$

Applying the group property of the two-particle propagator, Eq. (A5), leads to

$$
\begin{aligned}
\mathcal{G}_{ijkl}(T+\Delta) &= \mathcal{G}^{\Delta}_{ijkl}(T) + (i\hbar)^7\sum_{pqrsuvxy}\int_{t_0}^{T}d\bar{t} \\
&\quad \times \mathcal{U}^{(2)}_{ijpq}(T+\Delta,T)\mathcal{U}^{(2)}_{pqrs}(T,\bar{t}) \\
&\quad \times \Psi^{\pm}_{rsuv}(\bar{t})\mathcal{U}^{(2)}_{uvxy}(\bar{t},T)\mathcal{U}^{(2)}_{xyjm}(T,T+\Delta),
\end{aligned}
$$

where we identify the two-particle Green function at time T,

$$
\begin{aligned}
\mathcal{G}_{ijkl}(T+\Delta) &= \mathcal{G}^{\Delta}_{ijkl}(T) + (i\hbar)^4\sum_{pqrs}\mathcal{U}^{(2)}_{ijpq}(T+\Delta,T) \\
&\quad \times \mathcal{G}_{pqrs}(T)\mathcal{U}^{(2)}_{rskl}(T,T+\Delta). \quad\quad \text{(B1)}
\end{aligned}
$$

The above expression only contains a time integral of fixed length Δ. Thus, provided that the solution $\mathcal{G}(T)$ is known, the propagation to $T+\Delta$ can be done in a constant amount of time, independent of T. This way Eq. (B1) provides the basis for a time-linear propagation scheme. At the same time, we found that, for current applications, the integral form is less favorable for numerical implementation, compared to the independent approach that uses coupled time-local differential equations (G1-G2 scheme [39]) that is derived in Sec. III B and, therefore, forms the basis of the present paper.

APPENDIX C: PARTICLE-HOLE T MATRIX

For the T matrix in the particle-hole channel [28], the derivation of the G1-G2 scheme is performed in similar fashion as for the particle-particle T matrix in Sec. V A. The self energy has the form,

$$
\Sigma^{\gtrless}_{ij}(t,t') = i\hbar\sum_{kl}T^{\mathrm{ph},\gtrless}_{ikjl}(t,t')G^{\gtrless}_{lk}(t,t'), \quad\quad \text{(C1)}
$$

where now the particle-hole T matrix is expressed as

$$
T^{\mathrm{ph},\gtrless}_{ijkl}(t,t') = \sum_{pq}w_{ipql}(t)\Omega^{\mathrm{ph},\gtrless}_{qjkp}(t,t'), \quad\quad \text{(C2)}
$$

which allows us to rewrite the self energy (C1):

$$
\Sigma^{\gtrless}_{ij}(t,t') = i\hbar\sum_{klpq}w_{ipql}(t)\Omega^{\mathrm{ph},\gtrless}_{qkjp}(t,t')G^{\gtrless}_{lk}(t,t'). \quad\quad \text{(C3)}
$$

In Eqs. (C2) and (C3), Ω^{ph} denotes the nonequilibrium generalization of the Møller operator in the particle-hole channel. The collision integral (10) of the time-diagonal equation then becomes

$$
\begin{aligned}
I_{ij}(t) &= i\hbar\sum_{klpqr}w_{ipqr}(t)\int_{t_0}^{t}d\bar{t}\big[\Omega^{\mathrm{ph},>}_{qlkp}(t,\bar{t})\mathcal{G}^{\mathrm{F},<}_{krlj}(\bar{t},t) \\
&\quad - \Omega^{\mathrm{ph},<}_{qlkp}(t,\bar{t})\mathcal{G}^{\mathrm{F},>}_{krlj}(\bar{t},t)\big] \\
&= \pm i\hbar\sum_{klp}w_{iklp}(t)\mathcal{G}_{lpjk}(t),
\end{aligned}
$$

which results in the following expression for the time-diagonal element of the two-particle Green function,

$$
\begin{aligned}
\mathcal{G}_{ijkl}(t) &= \pm\sum_{pq}\int_{t_0}^{t}d\bar{t}\big[\Omega^{\mathrm{ph},>}_{iqpl}(t,\bar{t})\mathcal{G}^{\mathrm{F},<}_{pjqk}(\bar{t},t) \\
&\quad - \Omega^{\mathrm{ph},<}_{iqpl}(t,\bar{t})\mathcal{G}^{\mathrm{F},>}_{pjqk}(\bar{t},t)\big]. \quad\quad \text{(C4)}
\end{aligned}
$$

By construction, the particle-hole T matrix obeys the following symmetry [cf. Eq. (13)],

$$
T^{\mathrm{ph},\gtrless}_{ijkl}(t,t') = T^{\mathrm{ph},\lessgtr}_{jilk}(t',t).
$$

The particle-hole T matrix sums up the particle-hole collisions via the recursive equation (again the singular part has

been subtracted compared to its standard definition [28])

$$
T_{ijkl}^{\mathrm{ph},\gtrless}(t,t') = \pm i\hbar \sum_{pqrs} w_{iqpl}(t) G_{psqr}^{\mathrm{F},\gtrless}(t,t') w_{rjks}^{\pm}(t') + i\hbar \sum_{pqrs} w_{iqpl}(t) \Bigg[\int_{t_0}^{t} d\bar{t} \left(G_{psqr}^{\mathrm{F},>}(t,\bar{t}) - G_{psqr}^{\mathrm{F},<}(t,\bar{t}) \right) T_{rjks}^{\mathrm{ph},\gtrless}(\bar{t},t')
$$
$$
+ \int_{t_0}^{t'} d\bar{t}\, G_{psqr}^{\mathrm{F},\gtrless}(t,\bar{t}) \left(T_{rjks}^{\mathrm{ph},<}(\bar{t},t') - T_{rjks}^{\mathrm{ph},>}(\bar{t},t') \right) \Bigg],
$$

whereas the Møller operator obeys

$$
\Omega_{ijkl}^{\mathrm{ph},\gtrless}(t,t') = \pm i\hbar \sum_{pq} G_{iplq}^{\mathrm{F},\gtrless}(t,t') w_{qjkp}^{\pm}(t') + i\hbar \sum_{pqrs} \Bigg[\int_{t_0}^{t} d\bar{t} \left(G_{iplq}^{\mathrm{F},>}(t,\bar{t}) - G_{iplq}^{\mathrm{F},<}(t,\bar{t}) \right) w_{qrsp}(\bar{t}) \Omega_{sjkr}^{\mathrm{ph},\gtrless}(\bar{t},t')
$$
$$
+ \int_{t_0}^{t'} d\bar{t}\, G_{iplq}^{\mathrm{F},\gtrless}(t,\bar{t}) w_{qrsp}(\bar{t}) \left(\Omega_{sjkr}^{\mathrm{ph},<}(\bar{t},t') - \Omega_{sjkr}^{\mathrm{ph},>}(\bar{t},t') \right) \Bigg]
$$
$$
= \pm i\hbar \sum_{pq} G_{iplq}^{\mathrm{F},\gtrless}(t,t') w_{qjkp}^{\pm}(t') + i\hbar \sum_{pqrs} \Bigg[\int_{t_0}^{t} d\bar{t} \left(G_{piql}^{\mathrm{F},<}(\bar{t},t) - G_{piql}^{\mathrm{F},>}(\bar{t},t) \right) \Omega_{rqps}^{\mathrm{ph},\lessgtr}(t',\bar{t})
$$
$$
+ \int_{t_0}^{t'} d\bar{t}\, G_{piql}^{\mathrm{F},\lessgtr}(\bar{t},t) \left(\Omega_{rqps}^{\mathrm{ph},>}(t',\bar{t}) - \Omega_{rqps}^{\mathrm{ph},<}(t',\bar{t}) \right) \Bigg] w_{sjkr}(t').
$$

The time-diagonal equation for Ω^{ph} can be further simplified,

$$
\Omega_{ijkl}^{\mathrm{ph},\gtrless}(t,t) = \pm i\hbar \sum_{pq} G_{iplq}^{\mathrm{F},\gtrless}(t) w_{qjkp}^{\pm}(t) + i\hbar \sum_{pqrs} \int_{t_0}^{t} d\bar{t} \left(\mathcal{G}_{piql}^{\mathrm{F},<}(\bar{t},t) \Omega_{rqps}^{\mathrm{ph},>}(t,\bar{t}) - \mathcal{G}_{piql}^{\mathrm{F},>}(\bar{t},t) \Omega_{rqps}^{\mathrm{ph},<}(t,\bar{t}) \right) w_{sjkr}(t)
$$
$$
= \pm i\hbar \sum_{pq} G_{iplq}^{\mathrm{F},\gtrless}(t) w_{qjkp}^{\pm}(t) \pm i\hbar \sum_{pq} \mathcal{G}_{ipql}(t) w_{qjkp}(t).
$$

1. T^{ph} approximation within the HF-GKBA

Applying the HF-GKBA to Eq. (C4) yields

$$
\mathcal{G}_{ijkl}(t) = \pm (i\hbar)^2 \sum_{pqrs} \int_{t_0}^{t} d\bar{t}\, \mathcal{U}_{jr}(t,\bar{t}) \mathcal{U}_{sk}(\bar{t},t) \left[\Omega_{iqpl}^{\mathrm{ph},>}(t,\bar{t}) \mathcal{G}_{prqs}^{\mathrm{F},<}(\bar{t}) - \Omega_{iqpl}^{\mathrm{ph},<}(t,\bar{t}) \mathcal{G}_{prqs}^{\mathrm{F},>}(\bar{t}) \right],
$$

and, for the Møller operator,

$$
\Omega_{ijkl}^{\mathrm{ph},\gtrless}(t \geqslant t') = \pm (i\hbar)^3 \sum_{pqrs} \mathcal{U}_{ir}(t,t') G_{rpsq}^{\mathrm{F},\gtrless}(t') \mathcal{U}_{sl}(t',t) w_{qjkp}^{\pm}(t')
$$
$$
+ (i\hbar)^3 \sum_{pqrsuv} \Bigg[\int_{t_0}^{t} d\bar{t}\, w_{qrsp}(\bar{t}) \mathcal{U}_{iu}(t,\bar{t}) \left(G_{upvq}^{\mathrm{F},>}(t,\bar{t}) - G_{upvq}^{\mathrm{F},<}(t,\bar{t}) \right) \mathcal{U}_{vl}(\bar{t},t) \Omega_{sjkr}^{\mathrm{ph},\gtrless}(\bar{t},t')
$$
$$
+ \int_{t_0}^{t'} d\bar{t}\, \mathcal{U}_{iu}(t,\bar{t}) G_{upvq}^{\mathrm{F},\gtrless}(t,\bar{t}) \mathcal{U}_{vl}(\bar{t},t) w_{qrsp}(\bar{t}) \left(\Omega_{sjkr}^{\mathrm{ph},<}(\bar{t},t') - \Omega_{sjkr}^{\mathrm{ph},>}(\bar{t},t') \right) \Bigg], \tag{C5}
$$

where $\mathcal{U}$ obeys Eqs. (A6) and (A7). With Eq. (C5) we obtain the time derivative,

$$
\frac{d}{dt} \Omega_{ijkl}^{\mathrm{ph},\gtrless}(t \geqslant t') = \frac{1}{i\hbar} \sum_{p} \left\{ h_{ip}^{\mathrm{HF}}(t) \Omega_{pjkl}^{\mathrm{ph},\gtrless}(t \geqslant t') - \Omega_{ijkp}^{\mathrm{ph},\gtrless}(t \geqslant t') h_{pl}^{\mathrm{HF}}(t) \right\}
$$
$$
\pm i\hbar \sum_{pqrs} \left[\mathcal{G}_{iplq}^{\mathrm{F},>}(t) - \mathcal{G}_{iplq}^{\mathrm{F},<}(t) \right] w_{qrsp}(t) \Omega_{sjkr}^{\mathrm{ph},\gtrless}(t \geqslant t')
$$
$$
= \frac{1}{i\hbar} \sum_{pq} \left[\mathfrak{h}_{ipql}^{\Omega^{\mathrm{ph}},\mathrm{HF}}(t) + \mathfrak{h}_{ipql}^{\Omega^{\mathrm{ph}},\mathrm{corr}}(t) \right] \Omega_{qjkp}^{\mathrm{ph},\gtrless}(t \geqslant t'),
$$

where we introduced the Hamiltonians

$$\mathfrak{h}_{ijkl}^{\Omega^{\mathrm{ph}},\mathrm{HF}}(t) = \delta_{jl} h_{ik}^{\mathrm{HF}} - \delta_{ik} h_{jl}^{\mathrm{HF}},$$

$$\mathfrak{h}_{ijkl}^{\Omega^{\mathrm{ph}},\mathrm{corr}}(t) = (i\hbar)^2 \sum_{pq} \left[\mathcal{G}_{iplq}^{\mathrm{F},>}(t) - \mathcal{G}_{iplq}^{\mathrm{F},<}(t) \right] w_{qjkp}(t)$$

that can be combined to

$$\mathfrak{h}_{ijkl}^{\Omega^{\mathrm{ph}}}(t) = \mathfrak{h}_{ijkl}^{\Omega^{\mathrm{ph}},\mathrm{HF}}(t) + \mathfrak{h}_{ijkl}^{\Omega^{\mathrm{ph}},\mathrm{corr}}(t),$$

and the Møller operator obeys a Schrödinger equation,

$$i\hbar \frac{d}{dt} \Omega_{ijkl}^{\mathrm{ph},\gtrless}(t \gtrless t') = \sum_{pq} \mathfrak{h}_{ipql}^{\Omega^{\mathrm{ph}}}(t) \Omega_{qjkp}^{\mathrm{ph},\gtrless}(t \gtrless t').$$

2. T^{ph}-G1-G2 equations for a general basis

Next, we compute the time derivative of $\mathcal{G}$,

$$\frac{d}{dt} \mathcal{G}_{ijkl}(t) = \left[\frac{d}{dt} \mathcal{G}_{ijkl}(t) \right]_{\mathcal{f}} + \left[\frac{d}{dt} \mathcal{G}_{ijkl}(t) \right]_{\Omega^{\mathrm{ph}}} + \left[\frac{d}{dt} \mathcal{G}_{ijkl}(t) \right]_{\mathcal{U}},$$

and obtain for the first part,

$$\left[\frac{d}{dt} \mathcal{G}_{ijkl}(t) \right]_{\mathcal{f}} = \pm \sum_{pq} \left[\Omega_{iqpl}^{\mathrm{ph},>}(t,t) \mathcal{G}_{pjqk}^{\mathrm{F},<}(t,t) - \Omega_{iqpl}^{\mathrm{ph},<}(t,t) \mathcal{G}_{pjqk}^{\mathrm{F},>}(t,t) \right]$$

$$= i\hbar \sum_{pqrs} w_{rqps}^{\pm}(t) \left[\mathcal{G}_{islr}^{\mathrm{F},>}(t) \mathcal{G}_{pjqk}^{\mathrm{F},<}(t) - \mathcal{G}_{islr}^{\mathrm{F},<}(t) \mathcal{G}_{pjqk}^{\mathrm{F},>}(t) \right] + i\hbar \sum_{pqrs} \mathcal{G}_{isrl}(t) w_{rqps}(t) \left[\mathcal{G}_{pjqk}^{\mathrm{F},<}(t) - \mathcal{G}_{pjqk}^{\mathrm{F},>}(t) \right]$$

$$= \frac{1}{i\hbar} \Psi_{ijkl}^{\pm}(t) - \frac{1}{i\hbar} \sum_{pq} \left[\mathfrak{h}_{kqpj}^{\Omega^{\mathrm{ph}},\mathrm{corr}}(t) \right]^* \mathcal{G}_{iqpl}(t),$$

and, for the second part,

$$\left[\frac{d}{dt} \mathcal{G}_{ijkl}(t) \right]_{\Omega^{\mathrm{ph}}} = \pm (i\hbar)^2 \sum_{pqrs} \int_{t_0}^{t} d\bar{t}\, \mathcal{U}_{jr}(t,\bar{t}) \left[\left(\frac{d}{dt} \Omega_{iqpl}^{\mathrm{ph},>}(t,\bar{t}) \right) \mathcal{G}_{prqs}^{\mathrm{F},<}(\bar{t}) - \left(\frac{d}{dt} \Omega_{iqpl}^{\mathrm{ph},<}(t,\bar{t}) \right) \mathcal{G}_{prqs}^{\mathrm{F},>}(\bar{t}) \right] \mathcal{U}_{sk}(\bar{t},t)$$

$$= \frac{1}{i\hbar} \sum_{pq} \left[\mathfrak{h}_{ipql}^{\Omega^{\mathrm{ph}},\mathrm{HF}}(t) + \mathfrak{h}_{ipql}^{\Omega^{\mathrm{ph}},\mathrm{corr}}(t) \right] \mathcal{G}_{qjkp}(t),$$

and, for the third part,

$$\left[\frac{d}{dt} \mathcal{G}_{ijkl}(t) \right]_{\mathcal{U}} = \pm (i\hbar)^2 \sum_{pqrs} \int_{t_0}^{t} d\bar{t} \left(\frac{d}{dt} \mathcal{U}_{jr}(t,\bar{t}) \right) \left[\Omega_{iqpl}^{\mathrm{ph},>}(t,\bar{t}) \mathcal{G}_{prqs}^{\mathrm{F},<}(\bar{t}) - \Omega_{iqpl}^{\mathrm{ph},<}(t,\bar{t}) \mathcal{G}_{prqs}^{\mathrm{F},>}(\bar{t}) \right] \mathcal{U}_{sk}(\bar{t},t)$$

$$\pm (i\hbar)^2 \sum_{pqrs} \int_{t_0}^{t} d\bar{t}\, \mathcal{U}_{jr}(t,\bar{t}) \left[\Omega_{iqpl}^{\mathrm{ph},>}(t,\bar{t}) \mathcal{G}_{prqs}^{\mathrm{F},<}(\bar{t}) - \Omega_{iqpl}^{\mathrm{ph},<}(t,\bar{t}) \mathcal{G}_{prqs}^{\mathrm{F},>}(\bar{t}) \right] \left(\frac{d}{dt} \mathcal{U}_{sk}(\bar{t},t) \right)$$

$$= \frac{1}{i\hbar} \sum_{pq} \mathcal{G}_{ipql}(t) \mathfrak{h}_{jqpk}^{\Omega^{\mathrm{ph}},\mathrm{HF}}(t).$$

Combining the three contributions yields the derivative,

$$i\hbar \frac{d}{dt} \mathcal{G}_{ijkl}(t) = \Psi_{ijkl}^{\pm}(t) + \sum_{kl} \left\{ \mathfrak{h}_{ipql}^{\Omega^{\mathrm{ph}}}(t) [\mathcal{G}_{kpqj}(t)]^* - \mathcal{G}_{ipql}(t) \left[\mathfrak{h}_{kpqj}^{\Omega^{\mathrm{ph}}}(t) \right]^* \right\},$$

which is the result presented in the main part of the paper.

APPENDIX D: INTEGRAL SOLUTION $\mathcal{G}(t)$ AND INITIAL CORRELATIONS FOR HIGHER-ORDER SELF ENERGIES

While initial correlations are trivially added to the differential G1-G2 scheme as an initial condition, as we demonstrated in Sec. III E, for the integral representation of $\mathcal{G}$, this problem is more involved. We, therefore, outline, in this Appendix, the

solution for higher-order self energies by extending our SOA result, Eq. (46). Since the derivations are carried out analogously to Sec. III E and Appendix B, respectively, we only give the resulting equations. Performing the time derivative of the integral expressions recovers the differential equations for the respective self energy, cf. Eqs. (59), (76), and (83).

1. *GW* self energy

In the case of the *GW* self energy Eq. (46) becomes

$$\mathcal{G}_{ijkl}(t) = (i\hbar)^4 \sum_{pqrs} \int_{t_0}^t d\bar{t}\, \mathcal{U}_{lqjs}^{(2),\varepsilon}(t,\bar{t}) \left[\delta(t_0,\bar{t}) \mathcal{G}_{pqrs}^0 + \frac{1}{i\hbar} \Psi_{pqrs}(\bar{t}) \right] \left[\mathcal{U}_{irkp}^{(2),\varepsilon}(t,\bar{t}) \right]^*,$$

where

$$\mathcal{U}_{ijkl}^{(2),\varepsilon}(t,t') = \mathcal{U}_{kj}(t,t') \mathcal{U}_{li}(t',t) + i\hbar \sum_{pqrs} \int_{t'}^t d\bar{t}\, \mathcal{U}_{kp}(t,\bar{t}) \mathcal{U}_{qi}(\bar{t},t) \mathfrak{h}_{rpsq}^{\varepsilon,\mathrm{corr}}(\bar{t}) \mathcal{U}_{rjsl}^{(2),\varepsilon}(\bar{t},t').$$

The equation of motion for these modified propagators can also be brought to a differential form:

$$i\hbar \frac{d}{dt} \mathcal{U}_{ijkl}^{(2),\varepsilon}(t \geqslant t') = \sum_{pq} \mathfrak{h}_{pkqi}^{\varepsilon}(t) \mathcal{U}_{pjql}^{(2),\varepsilon}(t \geqslant t'). \tag{D1}$$

As one observes, $\mathcal{U}^{(2),\varepsilon}$ obeys the same equation as $\varepsilon^{-1,\gtrless}$ itself [cf. Eq. (57)]. They are, however, not identical, since the time-diagonal values differ [cf. Eqs. (18) and (53)].

2. *T* matrix in the particle-particle channel

For the particle-particle *T*-matrix approximation similar equations can be derived. The equivalent of Eq. (46) takes the form,

$$\mathcal{G}_{ijkl}(t) = (i\hbar)^4 \sum_{pqrs} \int_{t_0}^t d\bar{t}\, \mathcal{U}_{ijpq}^{(2),\Omega^{\mathrm{pp}}}(t,\bar{t}) \left[\delta(t_0,\bar{t}) \mathcal{G}_{pqrs}^0 + \frac{1}{i\hbar} \Psi_{pqrs}^{\pm}(\bar{t}) \right] \left[\mathcal{U}_{klrs}^{(2),\Omega^{\mathrm{pp}}}(t,\bar{t}) \right]^*,$$

where

$$\mathcal{U}_{ijkl}^{(2),\Omega^{\mathrm{pp}}}(t,t') = \mathcal{U}_{ijkl}^{(2)}(t,t') + i\hbar \sum_{pqrs} \int_{t'}^t d\bar{t}\, \mathcal{U}_{ijpq}^{(2)}(t,\bar{t}) \mathfrak{h}_{pqrs}^{\Omega^{\mathrm{pp}},\mathrm{corr}}(\bar{t}) \mathcal{U}_{rskl}^{(2),\Omega^{\mathrm{pp}}}(\bar{t},t').$$

The corresponding differential equation for the two-particle propagator mirrors the respective equation for Ω^{pp} [cf. Eq. (75)],

$$i\hbar \frac{d}{dt} \mathcal{U}_{ijkl}^{(2),\Omega^{\mathrm{pp}}}(t \geqslant t') = \sum_{pq} \mathfrak{h}_{ijpq}^{\Omega^{\mathrm{pp}}}(t) \mathcal{U}_{pqkl}^{(2),\Omega^{\mathrm{pp}}}(t \geqslant t'). \tag{D2}$$

As for *GW*, the time-diagonal values of both quantities do, however, not coincide.

3. *T* matrix in the particle-hole channel

Finally, in the particle-hole *T*-matrix approximation Eq. (46) is replaced by

$$\mathcal{G}_{ijkl}(t) = i\hbar \sum_{pqrs} \int_{t_0}^t d\bar{t}\, \mathcal{U}_{ispl}^{(2),\Omega^{\mathrm{ph}}}(t,\bar{t}) \left[\delta(t_0,\bar{t}) \mathcal{G}_{pqrs}^0 + \frac{1}{i\hbar} \Psi_{pqrs}^{\pm}(\bar{t}) \right] \left[\mathcal{U}_{kqrj}^{(2),\Omega^{\mathrm{ph}}}(t,\bar{t}) \right]^*,$$

with

$$\mathcal{U}_{ijkl}^{(2),\Omega^{\mathrm{ph}}}(t,t') = \mathcal{U}_{ik}(t,t') \mathcal{U}_{jl}(t',t) + i\hbar \sum_{pqrs} \int_{t'}^t d\bar{t}\, \mathcal{U}_{iq}(t,\bar{t}) \mathcal{U}_{pl}(\bar{t},t) \mathfrak{h}_{qrsp}^{\Omega^{\mathrm{ph}},\mathrm{corr}}(\bar{t}) \mathcal{U}_{sjkr}^{(2),\Omega^{\mathrm{ph}}}(\bar{t},t').$$

The last equation can again be transformed into its differential form,

$$i\hbar \frac{d}{dt} \mathcal{U}_{ijkl}^{(2),\Omega^{\mathrm{ph}}}(t \geqslant t') = \sum_{pq} \mathfrak{h}_{ipql}^{\Omega^{\mathrm{ph}}}(t) \mathcal{U}_{qjkp}^{(2),\Omega^{\mathrm{ph}}}(t \geqslant t'),$$

which matches Eq. (82) for Ω^{ph} in analogy to Eqs. (D1) and (D2).

---

[1] L. Keldysh, Diagram technique for nonequilibrium processes, Sov. Phys. JETP **20**, 1018 (1965) [Zh. Eksp. Teor. Fiz. **47**, 1515 (1964)].

[2] M. Bonitz, A.-P. Jauho, M. Sadovskii, and S. Tikhodeev, In memoriam Leonid V. Keldysh, Phys. Status Solidi B **256**, 1800600 (2019).

[3] L. Kadanoff and G. Baym, *Quantum Statistical Mechanics* (Benjamin, New York, 1962).

[4] H. Haug and A.-P. Jauho, *Quantum Kinetics in Transport and Optics of Semiconductors* (Springer, Berlin, Heidelberg, 2008).

[5] M. Bonitz, *Quantum Kinetic Theory*, 2nd ed., Teubner-Texte zur Physik (Springer, Cham, 2016).

[6] G. Stefanucci and R. van Leeuwen, *Nonequilibrium Many-Body Theory of Quantum Systems: A Modern Introduction* (Cambridge University Press, Cambridge, 2013).

[7] P. Danielewicz, Quantum theory of nonequilibrium processes II. Application to nuclear collisions, Ann. Phys. **152**, 305 (1984).

[8] H. S. Köhler, Memory and correlation effects in nuclear collisions, Phys. Rev. C **51**, 3232 (1995).

[9] W. Schäfer and M. Wegener, *Semiconductor Optics and Transport Phenomena* (Springer, Berlin, Heidelberg, 2002).

[10] D. Semkat, D. Kremp, and M. Bonitz, Kadanoff-Baym equations with initial correlations, Phys. Rev. E **59**, 1557 (1999).

[11] D. Kremp, T. Bornath, M. Bonitz, and M. Schlanges, Quantum kinetic theory of plasmas in strong laser fields, Phys. Rev. E **60**, 4725 (1999).

[12] N. E. Dahlen and R. van Leeuwen, Solving the Kadanoff-Baym Equations for Inhomogeneous Systems: Application to Atoms and Molecules, Phys. Rev. Lett. **98**, 153004 (2007).

[13] K. Balzer, S. Bauch, and M. Bonitz, Efficient grid-based method in nonequilibrium Green's function calculations: Application to model atoms and molecules, Phys. Rev. A **81**, 022510 (2010).

[14] K. Balzer, S. Bauch, and M. Bonitz, Time-dependent second-order Born calculations for model atoms and molecules in strong laser fields, Phys. Rev. A **82**, 033427 (2010).

[15] M. P. von Friesen, C. Verdozzi, and C.-O. Almbladh, Successes and Failures of Kadanoff-Baym Dynamics in Hubbard Nanoclusters, Phys. Rev. Lett. **103**, 176404 (2009).

[16] M. Puig von Friesen, C. Verdozzi, and C.-O. Almbladh, Kadanoff-Baym dynamics of Hubbard clusters: Performance of many-body schemes, correlation-induced damping and multiple steady and quasi-steady states, Phys. Rev. B **82**, 155108 (2010).

[17] S. Hermanns, N. Schlünzen, and M. Bonitz, Hubbard nanoclusters far from equilibrium, Phys. Rev. B **90**, 125111 (2014).

[18] N. Schlünzen, S. Hermanns, M. Bonitz, and C. Verdozzi, Dynamics of strongly correlated fermions: *Ab initio* results for two and three dimensions, Phys. Rev. B **93**, 035107 (2016).

[19] N. Schlünzen and M. Bonitz, Nonequilibrium green functions approach to strongly correlated fermions in lattice systems, Contrib. Plasma Phys. **56**, 5 (2016).

[20] K. Balzer, M. R. Rasmussen, N. Schlünzen, J.-P. Joost, and M. Bonitz, Doublon Formation by Ions Impacting a Strongly Correlated Finite Lattice System, Phys. Rev. Lett. **121**, 267602 (2018).

[21] M. Bonitz, K. Balzer, N. Schlünzen, M. Rasmussen, and J.-P. Joost, Ion impact induced ultrafast electron dynamics in correlated materials and finite graphene clusters, Phys. Status Solidi B **257**, 1800490 (2019).

[22] N. Schlünzen, K. Balzer, M. Bonitz, L. Deuchler, and E. Pehlke, Time-dependent simulation of ion stopping: Charge transfer and electronic excitations, Contrib. Plasma Phys. **59**, e201800184 (2019).

[23] H. S. Köhler, N.-H. Kwong, and H. A. Yousif, A Fortran code for solving the Kadanoff-Baym equations for a homogeneous fermion system, Comput. Phys. Commun. **123**, 123 (1999).

[24] M. Bonitz and D. Semkat, Generalized quantum kinetic equations, in *Introduction to Computational Methods in Many Body Physics*, edited by M. Bonitz and D. Semkat (Rinton Press, Princeton, 2006), pp. 94–102.

[25] A. Marini, C. Hogan, M. Grüning, and D. Varsano, yambo: An ab initio tool for excited state calculations, Comput. Phys. Commun. **180**, 1392 (2009).

[26] N. Schlünzen, J.-P. Joost, and M. Bonitz, Comment on "On the unphysical solutions of the Kadanoff-Baym equations in linear response: Correlation-induced homogeneous density-distribution and attractors," Phys. Rev. B **96**, 117101 (2017).

[27] N. Schlünzen, J.-P. Joost, F. Heidrich-Meisner, and M. Bonitz, Nonequilibrium dynamics in the one-dimensional Fermi-Hubbard model: Comparison of the nonequilibrium Green-functions approach and the density matrix renormalization group method, Phys. Rev. B **95**, 165139 (2017).

[28] N. Schlünzen, S. Hermanns, M. Scharnke, and M. Bonitz, Ultrafast dynamics of strongly correlated fermions – Nonequilibrium Green functions and selfenergy approximations, J. Phys.: Condens. Matter **32**, 103001 (2020).

[29] E. Gull, A. J. Millis, A. I. Lichtenstein, A. N. Rubtsov, M. Troyer, and P. Werner, Continuous-time Monte Carlo methods for quantum impurity models, Rev. Mod. Phys. **83**, 349 (2011).

[30] P. Lipavský, V. Špička, and B. Velický, Generalized Kadanoff-Baym ansatz for deriving quantum transport equations, Phys. Rev. B **34**, 6933 (1986).

[31] M. Bonitz, D. Kremp, D. C. Scott, R. Binder, W. D. Kraeft, and H. S. Köhler, Numerical analysis of non-Markovian effects in charge-carrier scattering: One-time versus two-time kinetic equations, J. Phys.: Condens. Matter **8**, 6057 (1996).

[32] M. Bonitz and D. Kremp, Kinetic energy relaxation and correlation time of nonequilibrium many-particle systems, Phys. Lett. A **212**, 83 (1996).

[33] K. Balzer and M. Bonitz, *Nonequilibrium Green's Functions Approach to Inhomogeneous Systems* (Springer, Berlin, Heidelberg, 2013).

[34] S. Latini, E. Perfetto, A.-M. Uimonen, R. van Leeuwen, and G. Stefanucci, Charge dynamics in molecular junctions: Nonequilibrium Green's function approach made fast, Phys. Rev. B **89**, 075306 (2014).

[35] A. Marini, Competition between the electronic and phonon–mediated scattering channels in the out–of–equilibrium carrier dynamics of semiconductors: An ab-initio approach, J. Phys.: Conf. Ser. **427**, 012003 (2013).

[36] D. Karlsson, R. van Leeuwen, E. Perfetto, and G. Stefanucci, The generalized Kadanoff-Baym ansatz with initial correlations, Phys. Rev. B **98**, 115148 (2018).

[37] E. Perfetto, A.-M. Uimonen, R. van Leeuwen, and G. Stefanucci, First-principles nonequilibrium Green's-function approach to transient photoabsorption: Application to atoms, Phys. Rev. A **92**, 033419 (2015).

[38] E. V. Boström, A. Mikkelsen, C. Verdozzi, E. Perfetto, and G. Stefanucci, Charge separation in donor-C60 complexes with real-time green functions: The importance of nonlocal correlations, Nano Lett. **18**, 785 (2018).

[39] N. Schlünzen, J.-P. Joost, and M. Bonitz, Achieving the Scaling Limit for Nonequilibrium Green Functions Simulations, Phys. Rev. Lett. **124**, 076601 (2020).

[40] S. Hermanns, K. Balzer, and M. Bonitz, Few-particle quantum dynamics–comparing nonequilibrium Green functions with the generalized Kadanoff–Baym ansatz to density operator theory, J. Phys.: Conf. Ser. **427**, 012008 (2013).

[41] U. Schneider, L. Hackermüller, J. P. Ronzheimer, S. Will, S. Braun, T. Best, I. Bloch, E. Demler, S. Mandt, D. Rasch, and A. Rosch, Fermionic transport and out-of-equilibrium dynamics in a homogeneous Hubbard model with ultracold atoms, Nat. Phys. **8**, 213 (2012).

[42] K. Balzer, M. Bonitz, R. van Leeuwen, A. Stan, and N. E. Dahlen, Nonequilibrium Green's function approach to strongly correlated few-electron quantum dots, Phys. Rev. B **79**, 245306 (2009).

[43] Throughout this work, "±" refers to bosons/fermions.

[44] The commutator of two single-particle quantities $A(t)$ and $B(t)$ is defined as $[A, B]_{ij}(t) = \sum_k [A_{ik}(t)B_{kj}(t) - B_{ik}(t)A_{kj}(t)]$.

[45] The commutator of two two-particle quantities $A(t)$ and $B(t)$ is defined as $[A, B]_{ijkl}(t) = \sum_{pq}[A_{ijpq}(t)B_{pqkl}(t) - B_{ijpq}(t)A_{pqkl}(t)]$.

[46] J. Hubbard and B. H. Flowers, Electron correlations in narrow energy bands, Proc. R. Soc. London A **276**, 238 (1963).

[47] I. Bloch, Probing and controlling quantum matter using ultra-cold quantum gases in optical lattices, in *Quantum Information and Coherence*, edited by E. Andersson and P. Öhberg, Scottish Graduate Series (Springer International Publishing, Cham, 2014), pp. 31–63.

[48] J. Kajala, F. Massel, and P. Törmä, Expansion Dynamics in the One-Dimensional Fermi-Hubbard Model, Phys. Rev. Lett. **106**, 206401 (2011).

[49] T. Dornheim, S. Groth, and M. Bonitz, The uniform electron gas at warm dense matter conditions, Phys. Rep. **744**, 1 (2018).

[50] J. M. Ziman, *Electrons and Phonons: The Theory of Transport Phenomena in Solids* (Oxford University Press, Oxford, 1960).

[51] G. D. Mahan, *Many-Particle Physics* (Springer, Boston, MA, 1990).

[52] D. Semkat, D. Kremp, and M. Bonitz, Kadanoff–Baym equations and non-Markovian Boltzmann equation in generalized T-matrix approximation, J. Math. Phys. **41**, 7458 (2000).

[53] M. Hopjan and C. Verdozzi, Initial correlated states for the generalized Kadanoff-Baym Ansatz without adiabatic switching-on of interactions in closed systems, Eur. Phys. J.: Spec. Top. **227**, 1939 (2019).

[54] D. Semkat, D. Kremp, and M. Bonitz, Generalized T-matrix approximation in quantum kinetic equations, Contrib. Plasma Phys. **42**, 31 (2002).

[55] A. Rios, B. Barker, M. Buchler, and P. Danielewicz, Towards a nonequilibrium Green's function description of nuclear reactions: One-dimensional mean-field dynamics, Ann. Phys. **326**, 1274 (2011).

[56] M. Bonitz, M. Scharnke, and N. Schlünzen, Timereversal invariance of quantum kinetic equations II: Density operator formalism, Contrib. Plasma Phys. **58**, 1036 (2018).

[57] D. Semkat, M. Bonitz, and D. Kremp, Relaxation of a quantum many-body system from a correlated initial state. A general and consistent approach, Contrib. Plasma Phys. **43**, 321 (2003).

[58] D. Gericke, M. Murillo, D. Semkat, M. Bonitz, and D. Kremp, Relaxation of strongly coupled Coulomb systems after rapid changes of the interaction potential, J. Phys. A: Math. Gen. **36**, 6087 (2003).

[59] M. Moeckel and S. Kehrein, Interaction Quench in the Hubbard Model, Phys. Rev. Lett. **100**, 175702 (2008).

[60] M. Eckstein, M. Kollar, and P. Werner, Interaction quench in the hubbard model: Relaxation of the spectral function and the optical conductivity, Phys. Rev. B **81**, 115131 (2010).

[61] M. Bonitz, D. Semkat, D. Gericke, and M. Murillo, Short-time dynamics of quantum many-body systems following a spin statistics switch, in *Progress in Nonequilibrium Green's functions II*, edited by M. Bonitz and D. Semkat (World Scientific Publ., Singapore, 2003), pp. 94–102.

[62] D. Gericke, M. Murillo, M. Bonitz, and D. Semkat, Temperature estimates for quantum systems after an ionization iduced rapid switch of the spin statistics, J. Phys. A: Math. Gen. **36**, 6095 (2003).

[63] L. Hedin, New method for calculating the one-particle Green's function with application to the electron-gas problem, Phys. Rev. **139**, A796 (1965).

[64] U. Hohenester and W. Pötz, Density-matrix approach to nonequilibrium free-carrier screening in semiconductors, Phys. Rev. B **56**, 13177 (1997).

[65] R. Balescu, Irreversible processes in ionized gases, Phys. Fluids **3**, 52 (1960).

[66] A. Lenard, On Bogoliubov's kinetic equation for a spatially homogeneous plasma, Ann. Phys. **10**, 390 (1960).

[67] Y. Klimontovich, *Kinetic Theory of Nonideal Gases and Nonideal Plasmas* (Pergamon, Oxford, 1982).

[68] G. Stefanucci, Y. Pavlyukh, A.-M. Uimonen, and R. van Leeuwen, Diagrammatic expansion for positive spectral functions beyond GW: Application to vertex corrections in the electron gas, Phys. Rev. B **90**, 115134 (2014).

[69] J.-P. Joost, N. Schlünzen, and M. Bonitz, Femtosecond electron dynamics in graphene nanoribbons – a nonequilibrium Green functions approach within an extended Hubbard model, Phys. Status Solidi B **257**, 1800498 (2019).

[70] J. R. Taylor (ed.), *Scattering Theory: The Quantum Theory of Nonrelativistic Collisions* (Dover, Mineola, NY, 1983).

[71] D. Kremp, M. Bonitz, W. Kraeft, and M. Schlanges, Non-Markovian Boltzmann equation, Ann. Phys. **258**, 320 (1997).

[72] R. Zimmermann, K. Kilimann, W. D. Kraeft, D. Kremp, and G. Röpke, Dynamical screening and self-energy of excitons in the electron–hole plasma, Phys. Status Solidi B **90**, 175 (1978).

[73] W. Kraeft, D. Kremp, W. Ebeling, and G. Röpke, *Quantum Statistics of Charged Particle Systems* (Akademieverlag, Berlin, 1986).

[74] W. Shun-jin and W. Cassing, Explicit treatment of n-body correlations within a density-matrix formalism, Ann. Phys. **159**, 328 (1985).

[75] A. Akbari, M. J. Hashemi, A. Rubio, R. M. Nieminen, and R. van Leeuwen, Challenges in truncating the hierarchy of time-dependent reduced density matrices equations, Phys. Rev. B **85**, 235121 (2012).

[76] M. Lindberg and S. W. Koch, Effective Bloch equations for semiconductors, Phys. Rev. B **38**, 3342 (1988).

[77] V. M. Axt and A. Stahl, A dynamics-controlled truncation scheme for the hierarchy of density matrices in semiconductor optics, Z. Phys. B: Condens. Matter **93**, 195 (1994).

[78] D. Lacroix, S. Hermanns, C. M. Hinz, and M. Bonitz, Ultrafast dynamics of finite Hubbard clusters: A stochastic mean-field approach, Phys. Rev. B **90**, 125112 (2014).

[79] P. Schuck and M. Tohyama, Self-consistent RPA and the time-dependent density matrix approach, Eur. Phys. J. A **52**, 307 (2016).

[80] S. Krönke and P. Schmelcher, Born-Bogoliubov-Green-Kirkwood-Yvon hierarchy for ultracold bosonic systems, Phys. Rev. A **98**, 013629 (2018).

[81] J. G. Kirkwood, Statistical mechanics of fluid mixtures, J. Chem. Phys. **3**, 300 (1935).

[82] A. Singer, Maximum entropy formulation of the Kirkwood superposition approximation, J. Chem. Phys. **121**, 3657 (2004).

[83] V. E. Fortov, O. F. Petrov, and O. S. Vaulina, Dusty-Plasma Liquid in the Statistical Theory of the Liquid State, Phys. Rev. Lett. **101**, 195003 (2008).

[84] H. Nakatsuji and K. Yasuda, Direct Determination of the Quantum-Mechanical Density Matrix Using the Density Equation, Phys. Rev. Lett. **76**, 1039 (1996).

[85] F. Lackner, I. Březinová, T. Sato, K. L. Ishikawa, and J. Burgdörfer, High-harmonic spectra from time-dependent two-particle reduced-density-matrix theory, Phys. Rev. A **95**, 033414 (2017).

[86] N. H. Kwong, M. Bonitz, R. Binder, and H. S. Köhler, Semiconductor Kadanoff-Baym equation results for optically excited electron-hole plasmas in quantum wells, Phys. Status Solidi B **206**, 197 (1998).

[87] M. Bonitz, Correlation time approximation in non-Markovian kinetics, Phys. Lett. A **221**, 85 (1996).

[88] Z. A. Moldabekov, M. Bonitz, and T. S. Ramazanov, Theoretical foundations of quantum hydrodynamics for plasmas, Phys. Plasmas **25**, 031903 (2018).

[89] M. Bonitz, Z. A. Moldabekov, and T. S. Ramazanov, Quantum hydrodynamics for plasmas–quo vadis? Phys. Plasmas **26**, 090601 (2019).

3.1.1 Exchange Consistency in the T^{ph}-G1–G2

As shown in Sec. 2.1.4, the GW and TPH approximations in a general single-particle basis can violate physical conservation laws, when the corresponding exchange series are included (cf. Tab. 2.1). Therefore, it is necessary to confine oneself to the direct scattering terms, for both resummation schemes. In Ref. [208] the G1–G2 scheme has been derived for the general form of the particle–hole T matrix—involving exchange. This is particularly problematic since the important symmetry (cf. appendix C of Ref. [208])

$$T_{ijkl}^{\mathrm{ph},\gtrless}(t,t') = T_{jilk}^{\mathrm{ph},\lessgtr}(t',t) \tag{3.1}$$

for T^{ph} is violated, if exchange terms are included.[8] For a more consistent treatment, it is, therefore, indispensable to use a modified EOM for the time-diagonal two-particle Green function in TPH approximation and replace equation (83) of Ref. [208] by the following:

$$
\begin{aligned}
\mathrm{i}\hbar\frac{\mathrm{d}}{\mathrm{d}t}\mathcal{G}_{ijkl}(t) = {}& \Psi_{ijkl}(t) \\
& + \sum_{pq}\left\{\mathfrak{h}_{ipql}^{\Omega^{\mathrm{ph}}}(t)\Big[\mathcal{G}_{kpqj}(t)\Big]^* - \mathcal{G}_{ipql}(t)\Big[\mathfrak{h}_{kpqj}^{\Omega^{\mathrm{ph}}}(t)\Big]^*\right\}.
\end{aligned}
\tag{3.2}
$$

Note that the direct two-particle source term $\Psi(t)$ is used instead of $\Psi^\pm(t)$. See Ref. [208] for the definitions in this context. While the Hubbard formulas for TPH remain unchanged, for jellium (section V.B.3 in Ref. [208]; cf. the definitions therein) one arrives at

$$
\begin{aligned}
& \mathrm{i}\hbar\frac{\mathrm{d}}{\mathrm{d}t}\mathcal{G}_{p\bar{p}q}^{\alpha\beta}(t) - \mathcal{G}_{p\bar{p}q}^{\alpha\beta}(t)\left(h_{\boldsymbol{p-q}}^{\mathrm{HF},\alpha}(t) + h_{\bar{\boldsymbol{p}}+\boldsymbol{q}}^{\mathrm{HF},\beta}(t) - h_{\boldsymbol{p}}^{\mathrm{HF},\alpha}(t) - h_{\bar{\boldsymbol{p}}}^{\mathrm{HF},\beta}(t)\right) \\
& = \Psi_{p\bar{p}q}^{\alpha\beta}(t) + \Lambda_{\boldsymbol{p},\bar{\boldsymbol{p}},\boldsymbol{q}}^{\mathrm{ph},\alpha\beta}(t) - \left[\Lambda_{\boldsymbol{p-q},\bar{\boldsymbol{p}}+\boldsymbol{q},-\boldsymbol{q}}^{\mathrm{ph},\alpha\beta}(t)\right]^*.
\end{aligned}
\tag{3.3}
$$

The same reasoning holds true for the GW-G1–G2 as well, which, therefore, cannot be extended to describe exchange contributions in the suggested way.

Following the above discussion, it becomes necessary to also define a modified DSL approximation within the G1–G2 scheme. To avoid inclusion of terms that violate conservation laws, the source term $\Psi^\pm(t)$ should be replaced in equations (87) and (88) of Ref. [208] as well, leading to

$$
\begin{aligned}
\mathrm{i}\hbar\frac{\mathrm{d}}{\mathrm{d}t}\mathcal{G}_{ijkl}(t) - \big[h^{(2),\mathrm{HF}},\mathcal{G}\big]_{ijkl}(t) = {}& \Psi_{ijkl}(t) \\
& + \sum_{pq}\left\{\mathfrak{h}_{qjpl}^{\varepsilon,\mathrm{corr}}(t)\Big[\mathcal{G}_{qkpi}(t)\Big]^* - \mathcal{G}_{qjpl}(t)\Big[\mathfrak{h}_{qkpi}^{\varepsilon,\mathrm{corr}}(t)\Big]^*\right\} \\
& + \sum_{pq}\left\{\mathfrak{h}_{ijpq}^{\Omega^{\mathrm{pp}},\mathrm{corr}}(t)\Big[\mathcal{G}_{klpq}(t)\Big]^* - \mathcal{G}_{ijpq}(t)\Big[\mathfrak{h}_{klpq}^{\Omega^{\mathrm{pp}},\mathrm{corr}}(t)\Big]^*\right\} \\
& + \sum_{kl}\left\{\mathfrak{h}_{ipql}^{\Omega^{\mathrm{ph}},\mathrm{corr}}(t)\Big[\mathcal{G}_{kpqj}(t)\Big]^* - \mathcal{G}_{ipql}(t)\Big[\mathfrak{h}_{kpqj}^{\Omega^{\mathrm{ph}},\mathrm{corr}}(t)\Big]^*\right\},
\end{aligned}
\tag{3.4}
$$

---

[8]Without the symmetry of Eq. (3.1) the transition to the G1–G2 formulation of the TPH scheme leads to an irresolvable contradiction.

and

$$
\begin{aligned}
i\hbar \frac{\mathrm{d}}{\mathrm{d}t}\mathcal{G}_{ijkl}(t) - \left[h^{(2),\mathrm{HF}}, \mathcal{G}\right]_{ijkl}(t) &= \Psi_{ijkl}(t) \\
&+ \Pi_{ijkl}(t) - \left[\Pi_{lkji}(t)\right]^{*} + \Lambda_{ijkl}(t) - \left[\Lambda_{klij}(t)\right]^{*},
\end{aligned}
\tag{3.5}
$$

respectively (see Ref. [208] for the definitions in this context). Note that this variant of the DSL misses the (valid) exchange terms of the particle–particle T matrix, which may seem artificial but is, nonetheless, required due to the recursive nature of the two-particle EOM. Arguably, the reach of the DSL becomes significantly narrowed by this handling, as already the second-order exchange diagram is omitted. A generalization of the DSL that exceeds the imposed restrictions is presented in the end of Sec. 3.1.2.1 in the context of the third-order approximation. On this occasion, also the link to the RDO theory is discussed.

3.1.2 Extensions for the G1–G2 Scheme: TOA and FLEX

In Refs. [114, 208] the G1–G2 scheme has been introduced for several important selfenergy approximations, i.e. the second-order approximation (SOA), GW, the T-matrix approximation in the particle–particle (TPP), and the particle–hole channel (TPH), as well as the dynamically-screened-ladder (DSL) approximation. Two further common selfenergy choices in NEGF theory are the third-order selfenergy (TOA) and the fluctuating-exchange approximation (FLEX); see, e.g., Refs. [79, 212] for details. To expand the scope of the G1–G2 scheme, the application to TOA and FLEX is a logical next step. Here, the way to derive the TOA result is demonstrated explicitly for the (third-order) particle–particle scattering diagrams in Sec. 3.1.2.1. The derivation for FLEX-G1–G2 is carried out in Sec. 3.1.2.2. The specification of the results to the Hubbard basis and numerical tests are presented in Sec. 3.1.2.3 for both derived methods.

3.1.2.1 G1–G2 Scheme for TOA

In NEGF theory, there are generally ten selfenergy diagrams of third order in the interaction [79]. In the following, the results for the particle–particle scattering terms are derived and discussed. Subsequently, the corresponding results for the third-order diagrams describing particle–hole scattering and dynamical screening are given, followed by the respective expressions for the remaining four diagrams.

Particle–Particle Scattering Terms
The diagrams that describe particle–particle scattering are illustrated in Fig. 3.1. The two diagrams also form the third-order contribution to the TPP selfenergy. For contour-time
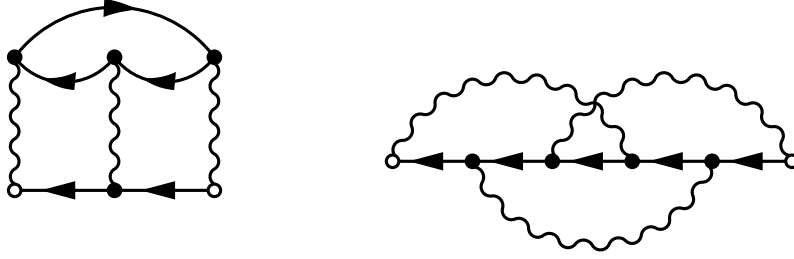
Figure 3.1 – Diagrammatic illustration of the third-order particle–particle selfenergy contributions. The first diagram describes direct particle scattering, while the second one accounts for particle exchange.

arguments, in a general single-particle basis, the selfenergy diagrams can be written in the following combined notation (cf. Refs. [79, 212]):

$$
\Sigma_{ij}(z, z') = \pm (i\hbar)^3 \sum_{\substack{klmnp \\ qrsuv}} \int_{\mathcal{C}} d\bar{z}\, w_{ikmn}(z)\mathcal{G}^{\mathrm{H}}_{mnpq}(z, \bar{z})w_{pqrs}(\bar{z})\mathcal{G}^{\mathrm{H}}_{rsuv}(\bar{z}, z')w^{\pm}_{uvjl}(z')G_{lk}(z', z)\,,
$$

(3.6)

where the two-particle Hartree Green function, $\mathcal{G}^{\mathrm{H}}$, is defined as in Ref. [208] as

$$
\mathcal{G}^{\mathrm{H}}_{ijkl}(z, z') := G_{ik}(z, z')G_{jl}(z, z')\,,
$$

(3.7)

leading to the real-time components

$$
\mathcal{G}^{\mathrm{H}, \gtrless}_{ijkl}(t, t') := G^{\gtrless}_{ik}(t, t')G^{\gtrless}_{jl}(t, t')\,.
$$

(3.8)

The (anti-)symmetrized interaction matrix [cf. Eq. (2.14)]

$$
w^{\pm}_{ijkl}(z) := w_{ijkl}(z) \pm w_{ijlk}(z)
$$

(3.9)

accounts for a particle exchange that leads to the structural difference between the two diagrams. In order to derive the G1–G2 scheme, one has to find a single-time equation for the time-diagonal two-particle Green function, $\mathcal{G}(t)$. The corresponding expression for $\mathcal{G}(t)$ in third order can be identified by comparing two equivalent expressions for the collision integral,

$$
I_{ij}(t) = \pm i\hbar \sum_{klp} w_{iklp}(t)\mathcal{G}_{lpjk}(t)
$$

(3.10)

$$
= \sum_{k} \int_{t_0}^{t} d\bar{t}\, \left[\Sigma^{>}_{ik}(t, \bar{t})G^{<}_{kj}(\bar{t}, t) - \Sigma^{<}_{ik}(t, \bar{t})G^{>}_{kj}(\bar{t}, t) \right]\,,
$$

(3.11)

that enters the EOM for the time-diagonal single-particle Green function,

$$
i\hbar \frac{d}{dt}G^{<}_{ij}(t) - \left[h^{\mathrm{HF}}(t), G^{<}(t) \right]_{ij} = \left[I + I^{\dagger} \right]_{ij}(t)\,.
$$

(3.12)

Here, $h^{\mathrm{HF}}(t)$ denotes the single-particle Hartree–Fock Hamiltonian, that accounts for mean-field effects. The less and greater components of Σ are found to [79]:

$$
\Sigma_{ij}^<(t,t') = \pm (\mathrm{i}\hbar)^3 \sum_{kmn} w_{ikmn}(t) \sum_{lpqrsuv} w_{uvjl}^{\pm}(t') G_{lk}^>(t',t) \times
$$

$$
\times \left[\int_{t_0}^t \mathrm{d}\bar{t}\, \mathcal{G}_{mnpq}^{\mathrm{H},>}(t,\bar{t}) w_{pqrs}(\bar{t}) \mathcal{G}_{rsuv}^{\mathrm{H},<}(\bar{t},t') \right.
$$

$$
+ \int_{t}^{t'} \mathrm{d}\bar{t}\, \mathcal{G}_{mnpq}^{\mathrm{H},<}(t,\bar{t}) w_{pqrs}(\bar{t}) \mathcal{G}_{rsuv}^{\mathrm{H},<}(\bar{t},t')
$$

$$
+ \left. \int_{t'}^{t_0} \mathrm{d}\bar{t}\, \mathcal{G}_{mnpq}^{\mathrm{H},<}(t,\bar{t}) w_{pqrs}(\bar{t}) \mathcal{G}_{rsuv}^{\mathrm{H},>}(\bar{t},t') \right], \tag{3.13}
$$

$$
\Sigma_{ij}^>(t,t') = \pm (\mathrm{i}\hbar)^3 \sum_{kmn} w_{ikmn}(t) \sum_{lpqrsuv} w_{uvjl}^{\pm}(t') G_{lk}^<(t',t) \times
$$

$$
\times \left[\int_{t_0}^{t'} \mathrm{d}\bar{t}\, \mathcal{G}_{mnpq}^{\mathrm{H},>}(t,\bar{t}) w_{pqrs}(\bar{t}) \mathcal{G}_{rsuv}^{\mathrm{H},<}(\bar{t},t') \right.
$$

$$
+ \int_{t'}^{t} \mathrm{d}\bar{t}\, \mathcal{G}_{mnpq}^{\mathrm{H},>}(t,\bar{t}) w_{pqrs}(\bar{t}) \mathcal{G}_{rsuv}^{\mathrm{H},>}(\bar{t},t')
$$

$$
+ \left. \int_{t}^{t_0} \mathrm{d}\bar{t}\, \mathcal{G}_{mnpq}^{\mathrm{H},<}(t,\bar{t}) w_{pqrs}(\bar{t}) \mathcal{G}_{rsuv}^{\mathrm{H},>}(\bar{t},t') \right]. \tag{3.14}
$$

Together with Eqs. (3.10) and (3.11), one can now find an explicit expression for $\mathcal{G}(t)$:

$$
\mathcal{G}_{ijkl}(t) = (\mathrm{i}\hbar)^2 \sum_{\substack{mnpq \\ rsuv}} \int_{t_0}^t \mathrm{d}\bar{t}\, w_{uvmn}^{\pm}(\bar{t}) \left\{ \mathcal{G}_{mnkl}^{\mathrm{H},<}(\bar{t},t) \times \right.
$$

$$
\times \left[\int_{t_0}^{\bar{t}} \mathrm{d}\bar{\bar{t}}\, \mathcal{G}_{ijpq}^{\mathrm{H},>}(t,\bar{\bar{t}}) w_{pqrs}(\bar{\bar{t}}) \mathcal{G}_{rsuv}^{\mathrm{H},<}(\bar{\bar{t}},\bar{t}) + \int_{\bar{t}}^t \mathrm{d}\bar{\bar{t}}\, \mathcal{G}_{ijpq}^{\mathrm{H},>}(t,\bar{\bar{t}}) w_{pqrs}(\bar{\bar{t}}) \mathcal{G}_{rsuv}^{\mathrm{H},>}(\bar{\bar{t}},\bar{t}) \right.
$$

$$
+ \left. \int_{t}^{t_0} \mathrm{d}\bar{\bar{t}}\, \mathcal{G}_{ijpq}^{\mathrm{H},<}(t,\bar{\bar{t}}) w_{pqrs}(\bar{\bar{t}}) \mathcal{G}_{rsuv}^{\mathrm{H},>}(\bar{\bar{t}},\bar{t}) \right] - \mathcal{G}_{mnkl}^{\mathrm{H},>}(\bar{t},t) \times
$$

$$
\times \left[\int_{t_0}^{t} \mathrm{d}\bar{\bar{t}}\, \mathcal{G}_{ijpq}^{\mathrm{H},>}(t,\bar{\bar{t}}) w_{pqrs}(\bar{\bar{t}}) \mathcal{G}_{rsuv}^{\mathrm{H},<}(\bar{\bar{t}},\bar{t}) + \int_{t}^{\bar{t}} \mathrm{d}\bar{\bar{t}}\, \mathcal{G}_{ijpq}^{\mathrm{H},<}(t,\bar{\bar{t}}) w_{pqrs}(\bar{\bar{t}}) \mathcal{G}_{rsuv}^{\mathrm{H},<}(\bar{\bar{t}},\bar{t}) \right.
$$

$$
+ \left. \left. \int_{\bar{t}}^{t_0} \mathrm{d}\bar{\bar{t}}\, \mathcal{G}_{ijpq}^{\mathrm{H},<}(t,\bar{\bar{t}}) w_{pqrs}(\bar{\bar{t}}) \mathcal{G}_{rsuv}^{\mathrm{H},>}(\bar{\bar{t}},\bar{t}) \right] \right\}. \tag{3.15}
$$

As shown in Refs. [114, 208], applying the HF-GKBA is equivalent to the replacement of all time-off-diagonal Green functions according to

$$
G_{ij}^{\gtrless}(t' \le t) = \mathrm{i}\hbar \sum_k G_{ik}^{\gtrless}(t') \mathcal{U}_{kj}(t',t), \tag{3.16}
$$

$$
G_{ij}^{\gtrless}(t \ge t') = \mathrm{i}\hbar \sum_k \mathcal{U}_{ik}(t,t') G_{kj}^{\gtrless}(t'), \tag{3.17}
$$

dependent on the time ordering of the real-time arguments. Here, $\mathcal{U}$ is the time-evolution operator that obeys a Schrödinger equation for the single-particle Hartree–Fock Hamiltonian $h^{\mathrm{HF}}(t)$. The single-time dependent Green functions $G^{\gtrless}(t) := G^{\gtrless}(t, t)$ are related to the system's single-particle density matrix, $n(t)$, via

$$G^{<}_{ij}(t) = G^{>}_{ij}(t) - \frac{1}{\mathrm{i}\hbar}\delta_{ij} = \pm\frac{1}{\mathrm{i}\hbar}n_{ij}(t)\,. \tag{3.18}$$

To describe a particle pair, the corresponding two-particle propagator $\mathcal{U}^{(2)}_{ijkl}(t, t') := \mathcal{U}_{ik}(t, t')\mathcal{U}_{jl}(t, t')$ is introduced, which obeys [208]:

$$\frac{\mathrm{d}}{\mathrm{d}t}\left[\mathcal{U}^{(2)}_{ijkl}(t, t')\right] = \frac{1}{\mathrm{i}\hbar}\sum_{pq} h^{(2),\mathrm{HF}}_{ijpq}(t)\mathcal{U}^{(2)}_{pqkl}(t, t')\,, \tag{3.19}$$

$$\frac{\mathrm{d}}{\mathrm{d}t}\left[\mathcal{U}^{(2)}_{ijkl}(t', t)\right] = -\frac{1}{\mathrm{i}\hbar}\sum_{pq} \mathcal{U}^{(2)}_{ijpq}(t', t)h^{(2),\mathrm{HF}}_{pqkl}(t)\,, \tag{3.20}$$

where $h^{(2),\mathrm{HF}}_{ijkl}(t) := \delta_{jl}h^{\mathrm{HF}}_{ik}(t) + \delta_{ik}h^{\mathrm{HF}}_{jl}(t)$. Using the Eqs. (3.8), (3.16) and (3.17), one finds the HF-GKBA replacements of the two-particle Hartree Green functions:

$$\mathcal{G}^{\mathrm{H},\gtrless}_{ijkl}(t \geq t') = (\mathrm{i}\hbar)^2 \sum_{mn} \mathcal{U}^{(2)}_{ijmn}(t, t')\mathcal{G}^{\mathrm{H},\gtrless}_{mnkl}(t')\,, \tag{3.21}$$

$$\mathcal{G}^{\mathrm{H},\gtrless}_{ijkl}(t' \leq t) = (\mathrm{i}\hbar)^2 \sum_{mn} \mathcal{G}^{\mathrm{H},\gtrless}_{ijmn}(t')\mathcal{U}^{(2)}_{mnkl}(t', t)\,, \tag{3.22}$$

with the single-time dependent $\mathcal{G}^{\mathrm{H},\gtrless}(t) := \mathcal{G}^{\mathrm{H},\gtrless}(t,t)$. Having that, the explicit form of $\mathcal{G}(t)$ [Eq. (3.15)] within the HF-GKBA is readily found[9]:

$$
\begin{aligned}
\mathcal{G}_{ijkl}(t) = (\mathrm{i}\hbar)^8 \sum_{\substack{mnpqrs \\ uvxyabcd}} \int_{t_0}^{t} \mathrm{d}\bar{t}\, w_{uvmn}^{\pm}(\bar{t}) &\Bigg\{ \mathcal{G}_{mnxy}^{\mathrm{H},<}(\bar{t})\mathcal{U}_{xykl}^{(2)}(\bar{t},t) \times \\
\times \Bigg[&\int_{t_0}^{\bar{t}} \mathrm{d}\bar{\bar{t}}\, \mathcal{U}_{ijab}^{(2)}(t,\bar{\bar{t}})\mathcal{G}_{abpq}^{\mathrm{H},>}(\bar{\bar{t}})w_{pqrs}(\bar{\bar{t}})\mathcal{G}_{rscd}^{\mathrm{H},<}(\bar{\bar{t}})\mathcal{U}_{cduv}^{(2)}(\bar{\bar{t}},\bar{t}) \\
&+ \int_{\bar{t}}^{t} \mathrm{d}\bar{\bar{t}}\, \mathcal{U}_{ijab}^{(2)}(t,\bar{\bar{t}})\mathcal{G}_{abpq}^{\mathrm{H},>}(\bar{\bar{t}})w_{pqrs}(\bar{\bar{t}})\mathcal{U}_{rscd}^{(2)}(\bar{\bar{t}},\bar{t})\mathcal{G}_{cduv}^{\mathrm{H},>}(\bar{t}) \\
&- \int_{t_0}^{\bar{t}} \mathrm{d}\bar{\bar{t}}\, \mathcal{U}_{ijab}^{(2)}(t,\bar{\bar{t}})\mathcal{G}_{abpq}^{\mathrm{H},<}(\bar{\bar{t}})w_{pqrs}(\bar{\bar{t}})\mathcal{G}_{rscd}^{\mathrm{H},>}(\bar{\bar{t}})\mathcal{U}_{cduv}^{(2)}(\bar{\bar{t}},\bar{t}) \\
&- \int_{\bar{t}}^{t} \mathrm{d}\bar{\bar{t}}\, \mathcal{U}_{ijab}^{(2)}(t,\bar{\bar{t}})\mathcal{G}_{abpq}^{\mathrm{H},<}(\bar{\bar{t}})w_{pqrs}(\bar{\bar{t}})\mathcal{U}_{rscd}^{(2)}(\bar{\bar{t}},\bar{t})\mathcal{G}_{cduv}^{\mathrm{H},>}(\bar{t}) \Bigg] - \mathcal{G}_{mnxy}^{\mathrm{H},>}(\bar{t})\mathcal{U}_{xykl}^{(2)}(\bar{t},t) \times \\
\times \Bigg[&\int_{t_0}^{\bar{t}} \mathrm{d}\bar{\bar{t}}\, \mathcal{U}_{ijab}^{(2)}(t,\bar{\bar{t}})\mathcal{G}_{abpq}^{\mathrm{H},>}(\bar{\bar{t}})w_{pqrs}(\bar{\bar{t}})\mathcal{G}_{rscd}^{\mathrm{H},<}(\bar{\bar{t}})\mathcal{U}_{cduv}^{(2)}(\bar{\bar{t}},\bar{t}) \\
&+ \int_{\bar{t}}^{t} \mathrm{d}\bar{\bar{t}}\, \mathcal{U}_{ijab}^{(2)}(t,\bar{\bar{t}})\mathcal{G}_{abpq}^{\mathrm{H},>}(\bar{\bar{t}})w_{pqrs}(\bar{\bar{t}})\mathcal{U}_{rscd}^{(2)}(\bar{\bar{t}},\bar{t})\mathcal{G}_{cduv}^{\mathrm{H},<}(\bar{t}) \\
&- \int_{\bar{t}}^{t} \mathrm{d}\bar{\bar{t}}\, \mathcal{U}_{ijab}^{(2)}(t,\bar{\bar{t}})\mathcal{G}_{abpq}^{\mathrm{H},<}(\bar{\bar{t}})w_{pqrs}(\bar{\bar{t}})\mathcal{U}_{rscd}^{(2)}(\bar{\bar{t}},\bar{t})\mathcal{G}_{cduv}^{\mathrm{H},<}(\bar{t}) \\
&- \int_{t_0}^{\bar{t}} \mathrm{d}\bar{\bar{t}}\, \mathcal{U}_{ijab}^{(2)}(t,\bar{\bar{t}})\mathcal{G}_{abpq}^{\mathrm{H},<}(\bar{\bar{t}})w_{pqrs}(\bar{\bar{t}})\mathcal{G}_{rscd}^{\mathrm{H},>}(\bar{\bar{t}})\mathcal{U}_{cduv}^{(2)}(\bar{\bar{t}},\bar{t}) \Bigg] \Bigg\} .
\end{aligned}
\tag{3.23}
$$

Reordering the terms leads to a more compact form:

$$
\begin{aligned}
\mathcal{G}_{ijkl}(t) = (\mathrm{i}\hbar)^8 \sum_{\substack{mnpqrs \\ uvxyabcd}} \int_{t_0}^{t} \mathrm{d}\bar{t}\, w_{uvmn}^{\pm}(\bar{t})\mathcal{U}_{xykl}^{(2)}(\bar{t},t) &\Bigg\{ \Big[\mathcal{G}_{mnxy}^{\mathrm{H},<}(\bar{t}) - \mathcal{G}_{mnxy}^{\mathrm{H},>}(\bar{t}) \Big] \times \\
\times \int_{t_0}^{\bar{t}} \mathrm{d}\bar{\bar{t}}\, \mathcal{U}_{ijab}^{(2)}(t,\bar{\bar{t}})w_{pqrs}(\bar{\bar{t}})\mathcal{U}_{cduv}^{(2)}(\bar{\bar{t}},\bar{t}) &\Big[\mathcal{G}_{abpq}^{\mathrm{H},>}(\bar{\bar{t}})\mathcal{G}_{rscd}^{\mathrm{H},<}(\bar{\bar{t}}) - \mathcal{G}_{abpq}^{\mathrm{H},<}(\bar{\bar{t}})\mathcal{G}_{rscd}^{\mathrm{H},>}(\bar{\bar{t}}) \Big] \\
+ \Big[\mathcal{G}_{cduv}^{\mathrm{H},>}(\bar{t})\mathcal{G}_{mnxy}^{\mathrm{H},<}(\bar{t}) &- \mathcal{G}_{cduv}^{\mathrm{H},<}(\bar{t})\mathcal{G}_{mnxy}^{\mathrm{H},>}(\bar{t}) \Big] \times \\
\times \int_{\bar{t}}^{t} \mathrm{d}\bar{\bar{t}}\, \mathcal{U}_{ijab}^{(2)}(t,\bar{\bar{t}})w_{pqrs}(\bar{\bar{t}})\mathcal{U}_{rscd}^{(2)}(\bar{\bar{t}},\bar{t}) &\Big[\mathcal{G}_{abpq}^{\mathrm{H},>}(\bar{\bar{t}}) - \mathcal{G}_{abpq}^{\mathrm{H},<}(\bar{\bar{t}}) \Big] \Bigg\} .
\end{aligned}
\tag{3.24}
$$

The time derivative of Eq. (3.24) can be carried out by using the derivative relations for the two-particle propagators [cf. Eqs. (3.19) and (3.20)], and accounting for the contributions

---

[9] Compared to Eq. (3.15), some integration boundaries have been flipped to match causal time ordering. To disambiguate the time ordering in the arguments of $\mathcal{G}^{\mathrm{H},\gtrless}$ and $\mathcal{U}^{(2)}$, the integration interval $[t_0, t]$ has been split into two separate intervals $[t_0, \bar{t}]$, $[\bar{t}, t]$.

of the integration boundaries[10]:

$$
\begin{aligned}
\frac{\mathrm{d}}{\mathrm{d}t}\mathcal{G}_{ijkl}(t) &= \frac{1}{\mathrm{i}\hbar}\sum_{mn}h^{(2),\mathrm{HF}}_{ijmn}(t)\mathcal{G}_{mnkl}(t) - \frac{1}{\mathrm{i}\hbar}\sum_{mn}\mathcal{G}_{ijmn}(t)h^{(2),\mathrm{HF}}_{mnkl}(t) \\
&\quad + (\mathrm{i}\hbar)^6 \sum_{\substack{mnpqrs \\ uvabcd}} w^{\pm}_{uvmn}(t)\Big[\mathcal{G}^{\mathrm{H},<}_{mnkl}(t) - \mathcal{G}^{\mathrm{H},>}_{mnkl}(t)\Big] \times \\
&\quad \times \int_{t_0}^{t}\mathrm{d}\bar{t}\, w_{pqrs}(\bar{t})\mathcal{U}^{(2)}_{ijab}(t,\bar{t})\mathcal{U}^{(2)}_{cduv}(\bar{t},t)\Big[\mathcal{G}^{\mathrm{H},>}_{abpq}(\bar{t})\mathcal{G}^{\mathrm{H},<}_{rscd}(\bar{t}) - \mathcal{G}^{\mathrm{H},<}_{abpq}(\bar{t})\mathcal{G}^{\mathrm{H},>}_{rscd}(\bar{t})\Big] \\
&\quad + (\mathrm{i}\hbar)^6 \sum_{\substack{mnpqrs \\ uvxycd}} w_{pqrs}(t)\Big[\mathcal{G}^{\mathrm{H},>}_{ijpq}(t) - \mathcal{G}^{\mathrm{H},<}_{ijpq}(t)\Big] \times \\
&\quad \times \int_{t_0}^{t}\mathrm{d}\bar{t}\, w^{\pm}_{uvmn}(\bar{t})\mathcal{U}^{(2)}_{rscd}(t,\bar{t})\mathcal{U}^{(2)}_{xykl}(\bar{t},t)\Big[\mathcal{G}^{\mathrm{H},>}_{cduv}(\bar{t})\mathcal{G}^{\mathrm{H},<}_{mnxy}(\bar{t}) - \mathcal{G}^{\mathrm{H},<}_{cduv}(\bar{t})\mathcal{G}^{\mathrm{H},>}_{mnxy}(\bar{t})\Big].
\end{aligned}
$$

(3.25)

In the second and third line of the expression, it is convenient to separate the $w^{\pm}_{uvmn}(t) = w_{uvmn}(t) \pm w_{uvnm}(t)$ contribution and rename some indices for the second part ($\pm$), which, together with the symmetry relations for $w(t)$, allows one to regroup the terms in a different way, using $w^{\pm}_{pqrs}(\bar{t})$ instead[11]:

$$
\begin{aligned}
\frac{\mathrm{d}}{\mathrm{d}t}\mathcal{G}_{ijkl}(t) &= \frac{1}{\mathrm{i}\hbar}\sum_{mn}h^{(2),\mathrm{HF}}_{ijmn}(t)\mathcal{G}_{mnkl}(t) - \frac{1}{\mathrm{i}\hbar}\sum_{mn}\mathcal{G}_{ijmn}(t)h^{(2),\mathrm{HF}}_{mnkl}(t) \\
&\quad + (\mathrm{i}\hbar)^6 \sum_{\substack{mnpqrs \\ uvxycd}} w_{pqrs}(t)\Big[\mathcal{G}^{\mathrm{H},>}_{ijpq}(t) - \mathcal{G}^{\mathrm{H},<}_{ijpq}(t)\Big] \times \\
&\quad \times \int_{t_0}^{t}\mathrm{d}\bar{t}\, w^{\pm}_{uvmn}(\bar{t})\mathcal{U}^{(2)}_{rscd}(t,\bar{t})\mathcal{U}^{(2)}_{xykl}(\bar{t},t)\Big[\mathcal{G}^{\mathrm{H},>}_{cduv}(\bar{t})\mathcal{G}^{\mathrm{H},<}_{mnxy}(\bar{t}) - \mathcal{G}^{\mathrm{H},<}_{cduv}(\bar{t})\mathcal{G}^{\mathrm{H},>}_{mnxy}(\bar{t})\Big] \\
&\quad + (\mathrm{i}\hbar)^6 \sum_{\substack{mnpqrs \\ uvabcd}} w_{uvmn}(t)\Big[\mathcal{G}^{\mathrm{H},<}_{mnkl}(t) - \mathcal{G}^{\mathrm{H},>}_{mnkl}(t)\Big] \times \\
&\quad \times \int_{t_0}^{t}\mathrm{d}\bar{t}\, w^{\pm}_{pqrs}(\bar{t})\mathcal{U}^{(2)}_{ijab}(t,\bar{t})\mathcal{U}^{(2)}_{cduv}(\bar{t},t)\Big[\mathcal{G}^{\mathrm{H},>}_{abpq}(\bar{t})\mathcal{G}^{\mathrm{H},<}_{rscd}(\bar{t}) - \mathcal{G}^{\mathrm{H},<}_{abpq}(\bar{t})\mathcal{G}^{\mathrm{H},>}_{rscd}(\bar{t})\Big].
\end{aligned}
$$

(3.26)

In the above expression, the explicit form of the time-diagonal two-particle Green function in second-order Born approximation can be identified, which reads [208]

$$
\mathcal{G}^{\mathrm{SOA}}_{ijkl}(t) = (\mathrm{i}\hbar)^5 \sum_{\substack{pqrs \\ uvxy}} \int_{t_0}^{t}\mathrm{d}\bar{t}\, w^{\pm}_{pqrs}(\bar{t})\mathcal{U}^{(2)}_{ijuv}(t,\bar{t})\Big[\mathcal{G}^{\mathrm{H},>}_{uvpq}(\bar{t})\mathcal{G}^{\mathrm{H},<}_{rsxy}(\bar{t}) - \mathcal{G}^{\mathrm{H},<}_{uvpq}(\bar{t})\mathcal{G}^{\mathrm{H},>}_{rsxy}(\bar{t})\Big]\mathcal{U}^{(2)}_{xykl}(\bar{t},t).
$$

(3.27)

The resulting EOM for $\mathcal{G}(t)$, Eq. (3.26), can be brought to the following time-linear form:

$$
\begin{aligned}
\frac{\mathrm{d}}{\mathrm{d}t}\mathcal{G}_{ijkl}(t) = &\frac{1}{\mathrm{i}\hbar}\Big[h^{(2),\mathrm{HF}}(t),\mathcal{G}(t)\Big]_{ijkl} + \mathrm{i}\hbar\sum_{pqrs}\Big[\mathcal{G}^{\mathrm{H},>}_{ijpq}(t) - \mathcal{G}^{\mathrm{H},<}_{ijpq}(t)\Big]w_{pqrs}(t)\mathcal{G}^{\mathrm{SOA}}_{rskl}(t) \\
&+ \mathrm{i}\hbar\sum_{mnuv}\mathcal{G}^{\mathrm{SOA}}_{ijuv}(t)w_{uvmn}(t)\Big[\mathcal{G}^{\mathrm{H},<}_{mnkl}(t) - \mathcal{G}^{\mathrm{H},>}_{mnkl}(t)\Big].
\end{aligned}
$$

(3.28)

---

[10]The time-diagonal two-particle propagators obey $\mathcal{U}^{(2)}_{ijkl}(t,t) = \frac{1}{(\mathrm{i}\hbar)^2}\delta_{ik}\delta_{jl}$ (cf. Ref. [208]).

[11]The second and third line of Eq. (3.25) have been exchanged with the forth and fifth line.

During the derivation of the G1–G2 scheme for the particle–particle T-matrix approximation in Ref. [208], the effective quasi-Hamiltonian

$$\mathfrak{h}_{ijkl}^{\Omega^{\mathrm{PP}},\mathrm{corr}}(t) := (\mathrm{i}\hbar)^2 \sum_{pq} \left[\mathcal{G}_{ijpq}^{\mathrm{H},>}(t) - \mathcal{G}_{ijpq}^{\mathrm{H},<}(t)\right] w_{pqkl}(t) \tag{3.29}$$

has been introduced, to reveal the Heisenberg character of the EOM of the corresponding two-particle Green function. Using this definition, Eq. (3.28) can be further simplified to the most compact form

$$\mathrm{i}\hbar\frac{\mathrm{d}}{\mathrm{d}t}\mathcal{G}_{ijkl}(t) = \left[h^{(2),\mathrm{HF}}(t), \mathcal{G}(t)\right]_{ijkl} + \sum_{pq}\left\{\mathfrak{h}_{ijpq}^{\Omega^{\mathrm{PP}},\mathrm{corr}}(t)\left[\mathcal{G}_{klpq}^{\mathrm{SOA}}(t)\right]^* - \mathcal{G}_{ijpq}^{\mathrm{SOA}}(t)\left[\mathfrak{h}_{klpq}^{\Omega^{\mathrm{PP}},\mathrm{corr}}(t)\right]^*\right\},$$
$$\tag{3.30}$$

where the symmetry properties of the two-particle Green function and the pair-interaction matrix have been used [208]. Equation (3.30) provides the basis for a time-linear propagation that accounts for third-order particle–particle scattering effects. For a consistent approach, it has to be supplemented with the diagrams of second order in the interaction. The G1–G2 scheme for SOA is derived in Refs. [114, 208]. The resulting expression for the two-particle EOM of the combined selfenergy attains the following form:

$$\mathrm{i}\hbar\frac{\mathrm{d}}{\mathrm{d}t}\mathcal{G}_{ijkl}(t) = \left[h^{(2),\mathrm{HF}}(t), \mathcal{G}(t)\right]_{ijkl} + \Psi_{ijkl}^{\pm}(t)$$
$$+ \sum_{pq}\left\{\mathfrak{h}_{ijpq}^{\Omega^{\mathrm{PP}},\mathrm{corr}}(t)\left[\mathcal{G}_{klpq}^{\mathrm{SOA}}(t)\right]^* - \mathcal{G}_{ijpq}^{\mathrm{SOA}}(t)\left[\mathfrak{h}_{klpq}^{\Omega^{\mathrm{PP}},\mathrm{corr}}(t)\right]^*\right\}, \tag{3.31}$$

where the two-particle source term is defined as

$$\Psi_{ijkl}^{\pm}(t) = (\mathrm{i}\hbar)^2 \sum_{pqrs} w_{pqrs}^{\pm}(t)\left[\mathcal{G}_{ijpq}^{\mathrm{H},>}(t)\mathcal{G}_{rskl}^{\mathrm{H},<}(t) - \mathcal{G}_{ijpq}^{\mathrm{H},<}(t)\mathcal{G}_{rskl}^{\mathrm{H},>}(t)\right]. \tag{3.32}$$

Equation (3.31), together with Eqs. (3.10) and (3.12) for the single-particle Green function, form the G1–G2 scheme for the particle–particle TOA contributions. From a numerical perspective, propagating Eq. (3.31) can only be achieved in a time-linear way, if a separate equation is solved for $\mathcal{G}^{\mathrm{SOA}}(t)$ [which obeys the first line of Eq. (3.31)]. Thus, instead of one, one has to propagate two high-dimensional tensor objects, which doubles the memory effort and significantly increases the CPU time.

Comparing Eq. (3.31) to the result for the TPP approximation from Ref. [208],

$$\mathrm{i}\hbar\frac{\mathrm{d}}{\mathrm{d}t}\mathcal{G}_{ijkl}(t) = \left[h^{(2),\mathrm{HF}}(t), \mathcal{G}(t)\right]_{ijkl} + \Psi_{ijkl}^{\pm}(t)$$
$$+ \sum_{pq}\left\{\mathfrak{h}_{ijpq}^{\Omega^{\mathrm{PP}},\mathrm{corr}}(t)\left[\mathcal{G}_{klpq}(t)\right]^* - \mathcal{G}_{ijpq}(t)\left[\mathfrak{h}_{klpq}^{\Omega^{\mathrm{PP}},\mathrm{corr}}(t)\right]^*\right\}, \tag{3.33}$$

reveals a close connection between both approximations. For the TPP result, the coupling to the second-order two-particle Green function is replaced by the coupling to $\mathcal{G}(t)$ itself, thereby introducing the additional recursive structure of the T matrix. This treatment accounts for particle–particle correlations of higher order, as discussed in Ref. [208].

In the following sections, the results for the remaining third-order selfenergy contributions are discussed. Since the respective G1–G2 schemes are derived in analogous considerations as for the particle–particle diagrams, the derivations will not be repeated.
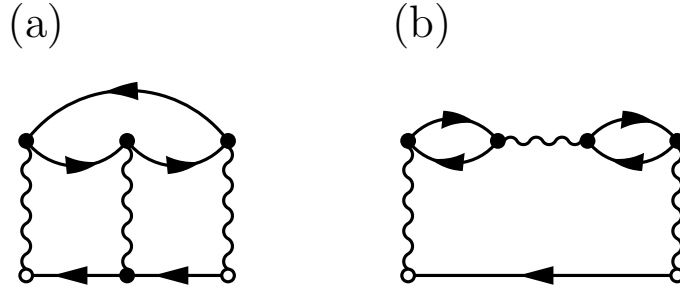
Figure 3.2 – Diagrammatic illustration of different third-order selfenergy contributions. (a) particle–hole scattering diagram (b) dynamical-screening diagram.

Particle–Hole Scattering and Dynamical Screening

The counterpart to the previous particle–particle channel is the particle–hole channel, in which scattering events between particles and holes are described. Such processes are typically included via the TPH approximation. As discussed in Secs. 2.1.4 and 3.1.1, there are exchange diagrams within the third- (and higher-)order contributions of the TPH selfenergy leading to a violation of conservation laws. Hence, when considered isolated, it is expedient to only include the direct third-order particle–hole-scattering term, which is illustrated in Fig. 3.2 (a). For this diagram, the final result for the EOM of the time-diagonal two-particle Green function is the following:

$$
i\hbar \frac{\mathrm{d}}{\mathrm{d}t} \mathcal{G}_{ijkl}(t) = \left[h^{(2),\mathrm{HF}}(t), \mathcal{G}(t) \right]_{ijkl} + \Psi^{\pm}_{ijkl}(t)
$$
$$
+ \sum_{pq} \left\{ \mathfrak{h}^{\Omega^{\mathrm{ph}},\mathrm{corr}}_{ipql}(t) \left[\mathcal{G}^{(2),\mathrm{di}}_{kpqj}(t) \right]^* - \mathcal{G}^{(2),\mathrm{di}}_{ipql}(t) \left[\mathfrak{h}^{\Omega^{\mathrm{ph}},\mathrm{corr}}_{kpqj}(t) \right]^* \right\}, \qquad (3.34)
$$

where the effective quasi-Hamiltonian[12]

$$
\mathfrak{h}^{\Omega^{\mathrm{ph}},\mathrm{corr}}_{ijkl}(t) := (i\hbar)^2 \sum_{pq} \left[\mathcal{G}^{\mathrm{F},>}_{iqlp}(t) - \mathcal{G}^{\mathrm{F},<}_{iqlp}(t) \right] w_{pjkq}(t) \qquad (3.35)
$$

is taken from the derivation of the T^{ph}-G1–G2 scheme in Ref. [208]. In the above equation, only the first part of the second-order two-particle Green function is used that leads to the direct second-order selfenergy diagram, i.e.:

$$
\mathcal{G}^{(2),\mathrm{di}}_{ijkl}(t) = (i\hbar)^5 \sum_{\substack{pqrs \\ uvxy}} \int_{t_0}^{t} \mathrm{d}\bar{t}\, w_{pqrs}(\bar{t}) \mathcal{U}^{(2)}_{ijuv}(t,\bar{t}) \left[\mathcal{G}^{\mathrm{H},>}_{uvpq}(\bar{t}) \mathcal{G}^{\mathrm{H},<}_{rsxy}(\bar{t}) - \mathcal{G}^{\mathrm{H},<}_{uvpq}(\bar{t}) \mathcal{G}^{\mathrm{H},>}_{rsxy}(\bar{t}) \right] \mathcal{U}^{(2)}_{xykl}(\bar{t},t).
$$

$$(3.36)$$

Note that the full two-particle Green function in SOA [cf. Eq. (3.27)] can be expressed as

$$
\mathcal{G}^{\mathrm{SOA}}_{ijkl}(t) = \mathcal{G}^{(2),\mathrm{di}}_{ijkl}(t) \pm \mathcal{G}^{(2),\mathrm{di}}_{ijlk}(t). \qquad (3.37)
$$

---

[12]The time-diagonal two-particle Fock Green function is defined as $\mathcal{G}^{\mathrm{F},\gtrless}_{ijkl}(t) := G^{\gtrless}_{il}(t) G^{\lessgtr}_{jk}(t)$.

Equation (3.34) is again coupled to the EOM for the single-particle Green function, Eq. (3.12), via Eq. (3.10). Similarly to the particle–particle case above, Eq. (3.34) is a less recursive version of the EOM for the two-particle Green function in T-matrix approximation, now for the particle–hole channel [cf. Eq. (3.2)]. As already discussed, the source term

$$\Psi_{ijkl}(t) = (i\hbar)^2 \sum_{pqrs} w_{pqrs}(t) \Big[\mathcal{G}_{ijpq}^{\mathrm{H},>}(t) \mathcal{G}_{rskl}^{\mathrm{H},<}(t) - \mathcal{G}_{ijpq}^{\mathrm{H},<}(t) \mathcal{G}_{rskl}^{\mathrm{H},>}(t) \Big] \tag{3.38}$$

in Eq. (3.2) is defined without exchange contribution to avoid inducing unbalanced diagrams during the recursion. In Eq. (3.34), this is not necessary since $\mathcal{G}^{(2),\mathrm{di}}(t)$ obeys a separate EOM of the form

$$i\hbar \frac{\mathrm{d}}{\mathrm{d}t} \mathcal{G}_{ijkl}^{(2),\mathrm{di}}(t) = \Big[h^{(2),\mathrm{HF}}(t), \mathcal{G}^{(2),\mathrm{di}}(t) \Big]_{ijkl} + \Psi_{ijkl}(t). \tag{3.39}$$

The inclusion of dynamical-screening effects is usually achieved by introducing a renormalized interaction tensor, leading to the well-known GW approximation. The third-order selfenergy contribution, that describes dynamical-screening processes is illustrated in Fig. 3.2 (b). Starting from this diagram and deriving the corresponding G1–G2 scheme leads to the following time-linear EOM for the two-particle Green function:

$$\begin{aligned} i\hbar \frac{\mathrm{d}}{\mathrm{d}t} \mathcal{G}_{ijkl}(t) = {}& \Big[h^{(2),\mathrm{HF}}(t), \mathcal{G}(t) \Big]_{ijkl} + \Psi_{ijkl}^{\pm}(t) \\ & + \sum_{pq} \Big\{ \mathfrak{h}_{qjpl}^{\varepsilon,\mathrm{corr}}(t) \Big[\mathcal{G}_{qkpi}^{(2),\mathrm{di}}(t) \Big]^* - \mathcal{G}_{qjpl}^{(2),\mathrm{di}}(t) \Big[\mathfrak{h}_{qkpi}^{\varepsilon,\mathrm{corr}}(t) \Big]^* \Big\}, \end{aligned} \tag{3.40}$$

where, from the derivation of the GW-G1–G2 scheme in Ref. [208], the effective quasi-Hamiltonian

$$\mathfrak{h}_{ijkl}^{\varepsilon,\mathrm{corr}}(t) := \pm (i\hbar)^2 \sum_{pq} w_{qipk}(t) \Big[\mathcal{G}_{jplq}^{\mathrm{F},>}(t) - \mathcal{G}_{jplq}^{\mathrm{F},<}(t) \Big] \tag{3.41}$$

is used. Again, Eq. (3.40) is solved in conjunction with Eqs. (3.10) and (3.12) for the single-particle Green function. Comparing this result to the two-particle EOM of the GW-G1–G2 scheme [208],

$$\begin{aligned} i\hbar \frac{\mathrm{d}}{\mathrm{d}t} \mathcal{G}_{ijkl}(t) = {}& \Big[h^{(2),\mathrm{HF}}(t), \mathcal{G}(t) \Big]_{ijkl} + \Psi_{ijkl}(t) \\ & + \sum_{pq} \Big\{ \mathfrak{h}_{qjpl}^{\varepsilon,\mathrm{corr}}(t) \Big[\mathcal{G}_{qkpi}(t) \Big]^* - \mathcal{G}_{qjpl}(t) \Big[\mathfrak{h}_{qkpi}^{\varepsilon,\mathrm{corr}}(t) \Big]^* \Big\}, \end{aligned} \tag{3.42}$$

shows that the recursive structure is, once more, reduced for the TOA result due to the explicit usage of the second-order two-particle Green function. The source term $\Psi(t)$ in Eq. (3.42) does not describe exchange processes to maintain, e.g., energy conservation—in line with the insights of Secs. 2.1.4 and 3.1.1.
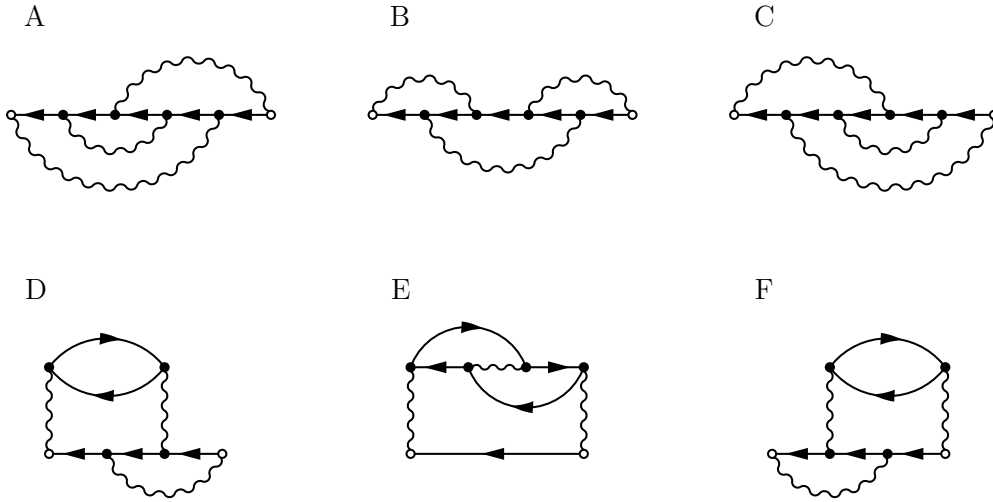
Figure 3.3 – Diagrammatic illustration of the remaining third-order selfenergy contributions that are not included in Fig. 3.1 or Fig. 3.2.

Remaining Terms—Full TOA

In order to complete the description of the selfenergy contributions that are of third order in the interaction now the remaining six diagrams are addressed, four of which are not expressible through common resummation approaches (see Fig. 3.3 for an illustration of the respective terms). While the diagram A can be attributed to the particle–hole T matrix when considering exchange terms [79, 121], diagram D can be assigned to the GW approximation (again, these inclusions will potentially lead to unbalanced energy contributions). The selfenergy parts C and F resemble these diagrams, to which they are mirrored. The diagrams B and E, however, exhibit structural uniqueness, thereby capturing scattering physics that are not accounted for otherwise. For a recent discussion of all third-order selfenergy terms, see, e.g., Ref. [79].

For all terms $X \in \{A, B, C, D, E, F\}$, the derivative of the respective time-diagonal two-particle Green function takes the general form

$$i\hbar \frac{d}{dt} \mathcal{G}^{X}_{ijkl}(t) = \left[h^{(2),\mathrm{HF}}(t), \mathcal{G}^{X}(t) \right]_{ijkl} + \Upsilon^{X}_{ijkl}, \tag{3.43}$$

where the source term Υ^{X} incorporates specific correlations according to

$$\Upsilon^{A}_{ijkl}(t) = \pm (i\hbar)^2 \sum_{mnpq} w_{npqm}(t) \left[\mathcal{G}^{F,>}_{imln}(t) - \mathcal{G}^{F,<}_{imln}(t) \right] \mathcal{G}^{(2),\mathrm{di}}_{qjpk}(t)$$

$$\mp (i\hbar)^2 \sum_{mnpq} w_{nqmp}(t) \left[\mathcal{G}^{F,>}_{mjnk}(t) - \mathcal{G}^{F,<}_{mjnk}(t) \right] \mathcal{G}^{(2),\mathrm{di}}_{ipql}(t), \tag{3.44}$$

$$\Upsilon^{B}_{ijkl}(t) = \pm (i\hbar)^2 \sum_{mnpq} w_{npmq}(t) \left[\mathcal{G}^{F,>}_{imln}(t) - \mathcal{G}^{F,<}_{imln}(t) \right] \mathcal{G}^{(2),\mathrm{di}}_{qjkp}(t)$$

$$\mp (i\hbar)^2 \sum_{mnpq} w_{npqm}(t) \left[\mathcal{G}^{F,>}_{mjnk}(t) - \mathcal{G}^{F,<}_{mjnk}(t) \right] \mathcal{G}^{(2),\mathrm{di}}_{iqlp}(t), \tag{3.45}$$

$$\Upsilon^{\mathrm{C}}_{ijkl}(t) = \pm (\mathrm{i}\hbar)^2 \sum_{mnpq} w_{nqpm}(t) \left[\mathcal{G}^{\mathrm{F},>}_{imkn}(t) - \mathcal{G}^{\mathrm{F},<}_{imkn}(t) \right] \mathcal{G}^{(2),\mathrm{di}}_{jpql}(t)$$

$$\mp (\mathrm{i}\hbar)^2 \sum_{mnpq} w_{npqm}(t) \left[\mathcal{G}^{\mathrm{F},>}_{mjnl}(t) - \mathcal{G}^{\mathrm{F},<}_{mjnl}(t) \right] \mathcal{G}^{(2),\mathrm{di}}_{qikp}(t) , \tag{3.46}$$

$$\Upsilon^{\mathrm{D}}_{ijkl}(t) = (\mathrm{i}\hbar)^2 \sum_{mnpq} w_{nqpm}(t) \left[\mathcal{G}^{\mathrm{F},>}_{imkn}(t) - \mathcal{G}^{\mathrm{F},<}_{imkn}(t) \right] \mathcal{G}^{(2),\mathrm{di}}_{jplq}(t)$$

$$- (\mathrm{i}\hbar)^2 \sum_{mnpq} w_{npmq}(t) \left[\mathcal{G}^{\mathrm{F},>}_{mjnl}(t) - \mathcal{G}^{\mathrm{F},<}_{mjnl}(t) \right] \mathcal{G}^{(2),\mathrm{di}}_{qikp}(t) , \tag{3.47}$$

$$\Upsilon^{\mathrm{E}}_{ijkl}(t) = (\mathrm{i}\hbar)^2 \sum_{mnpq} w_{nqmp}(t) \left[\mathcal{G}^{\mathrm{F},>}_{imkn}(t) - \mathcal{G}^{\mathrm{F},<}_{imkn}(t) \right] \mathcal{G}^{(2),\mathrm{di}}_{jpql}(t)$$

$$- (\mathrm{i}\hbar)^2 \sum_{mnpq} w_{npqm}(t) \left[\mathcal{G}^{\mathrm{F},>}_{mjnl}(t) - \mathcal{G}^{\mathrm{F},<}_{mjnl}(t) \right] \mathcal{G}^{(2),\mathrm{di}}_{qipk}(t) , \tag{3.48}$$

$$\Upsilon^{\mathrm{F}}_{ijkl}(t) = (\mathrm{i}\hbar)^2 \sum_{mnpq} w_{npmq}(t) \left[\mathcal{G}^{\mathrm{F},>}_{imln}(t) - \mathcal{G}^{\mathrm{F},<}_{imln}(t) \right] \mathcal{G}^{(2),\mathrm{di}}_{qjpk}(t)$$

$$- (\mathrm{i}\hbar)^2 \sum_{mnpq} w_{npmq}(t) \left[\mathcal{G}^{\mathrm{F},>}_{mjnk}(t) - \mathcal{G}^{\mathrm{F},<}_{mjnk}(t) \right] \mathcal{G}^{(2),\mathrm{di}}_{iqlp}(t) . \tag{3.49}$$

Equation (3.43) for one specific choice of X should not be used as an EOM on its own; at this point, partial inclusion of selfenergy diagrams can corrupt the approach, being no longer Φ compensated (cf. Sec. 2.1.4). Instead, one can illustrate, how the individual terms counterbalance each other when considered collectively. To this end, four effective quasi-Hamiltonians are introduced:

$$\mathfrak{h}^{(\mathrm{i})}_{ijkl}(t) := (\mathrm{i}\hbar)^2 \sum_{pq} w_{pjkq}(t) \left[\mathcal{G}^{\mathrm{F},>}_{iqlp}(t) - \mathcal{G}^{\mathrm{F},<}_{iqlp}(t) \right] = \mathfrak{h}^{\Omega^{\mathrm{ph}},\mathrm{corr}}_{ijkl}(t) , \tag{3.50}$$

$$\mathfrak{h}^{(\mathrm{ii})}_{ijkl}(t) := \pm (\mathrm{i}\hbar)^2 \sum_{pq} w_{pjqk}(t) \left[\mathcal{G}^{\mathrm{F},>}_{iqlp}(t) - \mathcal{G}^{\mathrm{F},<}_{iqlp}(t) \right] , \tag{3.51}$$

$$\mathfrak{h}^{(\mathrm{iii})}_{ijkl}(t) := \pm (\mathrm{i}\hbar)^2 \sum_{pq} w_{qipk}(t) \left[\mathcal{G}^{\mathrm{F},>}_{jplq}(t) - \mathcal{G}^{\mathrm{F},<}_{jplq}(t) \right] = \mathfrak{h}^{\varepsilon,\mathrm{corr}}_{ijkl}(t) , \tag{3.52}$$

$$\mathfrak{h}^{(\mathrm{iv})}_{ijkl}(t) := (\mathrm{i}\hbar)^2 \sum_{pq} w_{qikp}(t) \left[\mathcal{G}^{\mathrm{F},>}_{jplq}(t) - \mathcal{G}^{\mathrm{F},<}_{jplq}(t) \right] . \tag{3.53}$$

Using the above definitions, the Eqs. (3.44) – (3.49) transform to

$$\Upsilon^{\mathrm{A}}_{ijkl}(t) = \pm \sum_{pq} \mathfrak{h}^{(\mathrm{i})}_{ipql}(t) \left[\mathcal{G}^{(2),\mathrm{di}}_{kpjq}(t) \right]^* - \sum_{pq} \mathcal{G}^{(2),\mathrm{di}}_{ipql}(t) \left[\mathfrak{h}^{(\mathrm{ii})}_{kpqj}(t) \right]^* , \tag{3.54}$$

$$\Upsilon^{\mathrm{B}}_{ijkl}(t) = \sum_{pq} \mathfrak{h}^{(\mathrm{ii})}_{ipql}(t) \left[\mathcal{G}^{(2),\mathrm{di}}_{kpqj}(t) \right]^* \mp \sum_{pq} \mathcal{G}^{(2),\mathrm{di}}_{iplq}(t) \left[\mathfrak{h}^{(\mathrm{i})}_{kpqj}(t) \right]^* , \tag{3.55}$$

$$\Upsilon^{\mathrm{C}}_{ijkl}(t) = \pm \sum_{pq} \mathfrak{h}^{(\mathrm{iv})}_{qjpl}(t) \left[\mathcal{G}^{(2),\mathrm{di}}_{qkip}(t) \right]^* \mp \sum_{pq} \mathcal{G}^{(2),\mathrm{di}}_{qjlp}(t) \left[\mathfrak{h}^{(\mathrm{iv})}_{qkpi}(t) \right]^* , \tag{3.56}$$

$$\Upsilon^{\mathrm{D}}_{ijkl}(t) = \pm \sum_{pq} \mathfrak{h}^{(\mathrm{iii})}_{qjpl}(t) \Big[\mathcal{G}^{(2),\mathrm{di}}_{qkip}(t) \Big]^* - \sum_{pq} \mathcal{G}^{(2),\mathrm{di}}_{qjpl}(t) \Big[\mathfrak{h}^{(\mathrm{iv})}_{qkpi}(t) \Big]^*, \tag{3.57}$$

$$\Upsilon^{\mathrm{E}}_{ijkl}(t) = \sum_{pq} \mathfrak{h}^{(\mathrm{iv})}_{qjpl}(t) \Big[\mathcal{G}^{(2),\mathrm{di}}_{qkpi}(t) \Big]^* \mp \sum_{pq} \mathcal{G}^{(2),\mathrm{di}}_{qjlp}(t) \Big[\mathfrak{h}^{(\mathrm{iii})}_{qkpi}(t) \Big]^*, \tag{3.58}$$

$$\Upsilon^{\mathrm{F}}_{ijkl}(t) = \pm \sum_{pq} \mathfrak{h}^{(\mathrm{ii})}_{ipql}(t) \Big[\mathcal{G}^{(2),\mathrm{di}}_{kpjq}(t) \Big]^* \mp \sum_{pq} \mathcal{G}^{(2),\mathrm{di}}_{iplq}(t) \Big[\mathfrak{h}^{(\mathrm{ii})}_{kpqj}(t) \Big]^*. \tag{3.59}$$

These relations exhibit (or at least resemble) a quasi-commutator form which approaches a Heisenberg-like structure for Eq. (3.43)—similar to the results for the terms considered before [cf. Eqs. (3.31), (3.34) and (3.40)]. However, this time the contributions of each quasi-Hamiltonian are distributed across multiple source terms Υ. Balancing out the quasi-commutator parts is directly linked to energy conservation. Thus, interconnected source terms (and their corresponding selfenergy diagrams) have to be considered in conjunction.

Having transformed all ten third-order diagrams to their respective derivative of the time-diagonal two-particle Green function, it is now convenient to combine all contributions to the full TOA-G1–G2. By gathering Eqs. (3.31), (3.34) and (3.40), as well as Eqs. (3.54) – (3.59) one finds

$$\begin{aligned}
\mathrm{i}\hbar \frac{\mathrm{d}}{\mathrm{d}t} \mathcal{G}_{ijkl}(t) = & \Big[h^{(2),\mathrm{HF}}(t), \mathcal{G}(t) \Big]_{ijkl} + \Psi^{\pm}_{ijkl}(t) \\
& + \sum_{pq} \Big\{ \mathfrak{h}^{\Omega^{\mathrm{PP}},\mathrm{corr}}_{ijpq}(t) \Big[\mathcal{G}^{\mathrm{SOA}}_{klpq}(t) \Big]^* - \mathcal{G}^{\mathrm{SOA}}_{ijpq}(t) \Big[\mathfrak{h}^{\Omega^{\mathrm{PP}},\mathrm{corr}}_{klpq}(t) \Big]^* \Big\} \\
& + \sum_{pq} \Big\{ \mathfrak{h}^{(\mathrm{i})}_{ipql}(t) \Big[\mathcal{G}^{(2),\mathrm{di}}_{kpqj}(t) \Big]^* - \mathcal{G}^{(2),\mathrm{di}}_{ipql}(t) \Big[\mathfrak{h}^{(\mathrm{i})}_{kpqj}(t) \Big]^* \Big\} \\
& + \sum_{pq} \Big\{ \mathfrak{h}^{(\mathrm{iii})}_{qjpl}(t) \Big[\mathcal{G}^{(2),\mathrm{di}}_{qkpi}(t) \Big]^* - \mathcal{G}^{(2),\mathrm{di}}_{qjpl}(t) \Big[\mathfrak{h}^{(\mathrm{iii})}_{qkpi}(t) \Big]^* \Big\} \\
& + \Upsilon^{\mathrm{A}}_{ijkl}(t) + \Upsilon^{\mathrm{B}}_{ijkl}(t) + \Upsilon^{\mathrm{C}}_{ijkl}(t) + \Upsilon^{\mathrm{D}}_{ijkl}(t) + \Upsilon^{\mathrm{E}}_{ijkl}(t) + \Upsilon^{\mathrm{F}}_{ijkl}(t). \tag{3.60}
\end{aligned}$$

Finally, by grouping the quasi-Hamiltonians according to

$$\mathfrak{h}^{\Lambda}_{ijkl}(t) := \mathfrak{h}^{(\mathrm{i})}_{ijkl}(t) + \mathfrak{h}^{(\mathrm{ii})}_{ijkl}(t) = (\mathrm{i}\hbar)^2 \sum_{pq} w^{\pm}_{pjkq}(t) \Big[\mathcal{G}^{\mathrm{F},>}_{iqlp}(t) - \mathcal{G}^{\mathrm{F},<}_{iqlp}(t) \Big], \tag{3.61}$$

$$\mathfrak{h}^{\Pi}_{ijkl}(t) := \mathfrak{h}^{(\mathrm{iii})}_{ijkl}(t) + \mathfrak{h}^{(\mathrm{iv})}_{ijkl}(t) = \pm (\mathrm{i}\hbar)^2 \sum_{pq} w^{\pm}_{qipk}(t) \Big[\mathcal{G}^{\mathrm{F},>}_{jplq}(t) - \mathcal{G}^{\mathrm{F},<}_{jplq}(t) \Big] = \mathfrak{h}^{\Lambda}_{jikl}(t), \tag{3.62}$$

and by using Eq. (3.37), this expression can be transformed to

$$\begin{aligned}
\mathrm{i}\hbar \frac{\mathrm{d}}{\mathrm{d}t} \mathcal{G}_{ijkl}(t) = & \Big[h^{(2),\mathrm{HF}}(t), \mathcal{G}(t) \Big]_{ijkl} + \Psi^{\pm}_{ijkl}(t) \\
& + \sum_{pq} \Big\{ \mathfrak{h}^{\Omega^{\mathrm{PP}},\mathrm{corr}}_{ijpq}(t) \Big[\mathcal{G}^{\mathrm{SOA}}_{klpq}(t) \Big]^* - \mathcal{G}^{\mathrm{SOA}}_{ijpq}(t) \Big[\mathfrak{h}^{\Omega^{\mathrm{PP}},\mathrm{corr}}_{klpq}(t) \Big]^* \Big\} \\
& + \sum_{pq} \Big\{ \mathfrak{h}^{\Lambda}_{ipql}(t) \Big[\mathcal{G}^{\mathrm{SOA}}_{kpqj}(t) \Big]^* - \mathcal{G}^{\mathrm{SOA}}_{ipql}(t) \Big[\mathfrak{h}^{\Lambda}_{kpqj}(t) \Big]^* \Big\} \\
& + \sum_{pq} \Big\{ \mathfrak{h}^{\Pi}_{qjpl}(t) \Big[\mathcal{G}^{\mathrm{SOA}}_{qkpi}(t) \Big]^* - \mathcal{G}^{\mathrm{SOA}}_{qjpl}(t) \Big[\mathfrak{h}^{\Pi}_{qkpi}(t) \Big]^* \Big\}. \tag{3.63}
\end{aligned}$$

Here, $\mathfrak{h}^{\Lambda}(t)$ gives access to mostly the particle–hole ladder diagrams, whereas $\mathfrak{h}^{\Pi}(t)$ incorporates predominantly polarization effects. Note that both $\mathfrak{h}^{\Lambda}(t)$ and $\mathfrak{h}^{\Pi}(t)$ include the anti-symmetrized interaction matrix $w^{\pm}(t)$ [cf. Eqs. (3.61) and (3.62)], while in $\mathfrak{h}^{\Omega^{\mathrm{PP}},\mathrm{corr}}(t)$ only the bare interaction $w(t)$ enters [cf. Eq. (3.29)]. A closer look to the bottom two lines of Eq. (3.63) [and keeping in mind the equivalence of the quasi-Hamiltonians in Eq. (3.62)] reveals that, in fact, both lines show a similar structure, differing only by an index exchange $i \leftrightarrow j$. With the following definitions

$$L_{ijkl}^{\mathrm{SOA}}(t) := \sum_{pq} \left\{ \mathfrak{h}_{ijpq}^{\Omega^{\mathrm{PP}},\mathrm{corr}}(t) \left[\mathcal{G}_{klpq}^{\mathrm{SOA}}(t) \right]^{*} - \mathcal{G}_{ijpq}^{\mathrm{SOA}}(t) \left[\mathfrak{h}_{klpq}^{\Omega^{\mathrm{PP}},\mathrm{corr}}(t) \right]^{*} \right\}, \qquad (3.64)$$

$$P_{ijkl}^{\mathrm{SOA}}(t) := \sum_{pq} \left\{ \mathfrak{h}_{qjpl}^{\Pi}(t) \left[\mathcal{G}_{qkpi}^{\mathrm{SOA}}(t) \right]^{*} - \mathcal{G}_{qjpl}^{\mathrm{SOA}}(t) \left[\mathfrak{h}_{qkpi}^{\Pi}(t) \right]^{*} \right\}, \qquad (3.65)$$

Eq. (3.63) can, thus, be rephrased to

$$i\hbar \frac{\mathrm{d}}{\mathrm{d}t} \mathcal{G}_{ijkl}(t) = \left[h^{(2),\mathrm{HF}}(t), \mathcal{G}(t) \right]_{ijkl} + \Psi_{ijkl}^{\pm}(t) + L_{ijkl}^{\mathrm{SOA}}(t) + P_{ijkl}^{\mathrm{SOA}}(t) \pm P_{jikl}^{\mathrm{SOA}}(t), \qquad (3.66)$$

which shows that, in this context, particle–hole correlations and dynamical-screening effects come out as the (anti-)symmetrized materialization of a shared structural core. The surprisingly compact form of Eq. (3.66) [and Eq. (3.63)] exhibits the desired symmetry with respect to the—now Φ-compensated—Heisenberg-like quasi-commutators between $\mathcal{G}^{\mathrm{SOA}}(t)$ and the quasi-Hamiltonians. This has been achieved, because all interdependent source terms $\Upsilon(t)$ have been included collectively.

Thus, the EOM for the time-diagonal two-particle Green function in TOA is found—the main ingredient for the respective G1–G2 scheme. It has to be solved in conjunction with Eqs. (3.10) and (3.12) and with a separate equation for $\mathcal{G}^{\mathrm{SOA}}(t)$. Having two objects with the size of the two-particle Green function leads to an increased memory consumption compared to the previously derived variants of the G1–G2 scheme, i.e. SOA, GW, TPP, TPH, and DSL. The numerical scaling, however, remains linear with the number of time steps N_{t}. Analyzing Eq. (3.66) with respect to the dimension of the single-particle basis N_{b} reveals a scaling of $\mathcal{O}\left(N_{\mathrm{b}}^{6}\right)$. Hence, the total scaling of TOA-G1–G2 for a general basis is $\mathcal{O}\left(N_{\mathrm{b}}^{6} N_{\mathrm{t}}^{1}\right)$ as opposed to $\mathcal{O}\left(N_{\mathrm{b}}^{6} N_{\mathrm{t}}^{3}\right)$ for the original TOA-HF-GKBA. This confirms the tremendous numerical advantage of the G1–G2 scheme, in line with the results of Refs. [114, 208].

The general structure of Eq. (3.63) resembles the two-particle EOM of the DSL-G1–G2 scheme [208], Eq. (3.4), but with two differences. First, the explicit usage of the second-order $\mathcal{G}^{\mathrm{SOA}}(t)$ leads to a truncated recursiveness for the TOA-G1–G2, as seen for its ingredient terms before. Secondly, the interaction matrix is replaced by its (anti-)symmetrized counterpart in $\Psi(t)$, $\mathfrak{h}^{\Omega^{\mathrm{ph}},\mathrm{corr}}(t)$, and $\mathfrak{h}^{\varepsilon,\mathrm{corr}}(t)$. This is of particular interest, as it hints towards a consistent treatment of exchange terms for both the particle–hole ladder and the dynamically screened interaction (cf. Sec. 3.1.1). Justified by the results in third order, a generalized variant of the DSL-G1–G2 scheme can be proposed. The time-diagonal two-particle Green function within this completed-DSL description obeys

$$i\hbar \frac{\mathrm{d}}{\mathrm{d}t} \mathcal{G}_{ijkl}(t) = \left[h^{(2),\mathrm{HF}}(t), \mathcal{G}(t) \right]_{ijkl} + \Psi_{ijkl}^{\pm}(t) + L_{ijkl}(t) + P_{ijkl}(t) \pm P_{jikl}(t), \qquad (3.67)$$

where the recursive coupling of the two-particle Green function is included in

$$L_{ijkl}(t) := \sum_{pq} \left\{ \mathfrak{h}_{ijpq}^{\Omega^{\text{PP}},\text{corr}}(t) \left[\mathcal{G}_{klpq}(t) \right]^* - \mathcal{G}_{ijpq}(t) \left[\mathfrak{h}_{klpq}^{\Omega^{\text{PP}},\text{corr}}(t) \right]^* \right\}, \tag{3.68}$$

$$P_{ijkl}(t) := \sum_{pq} \left\{ \mathfrak{h}_{qjpl}^{\Pi}(t) \left[\mathcal{G}_{qkpi}(t) \right]^* - \mathcal{G}_{qjpl}(t) \left[\mathfrak{h}_{qkpi}^{\Pi}(t) \right]^* \right\}. \tag{3.69}$$

Again, particle–hole- and polarization contributions differ only by a particle exchange and can be expressed through the same quantity. It is expected, that all higher-order selfenergy terms that emerge during the recursion preserve total-energy conservation by forming Φ-compensated groups (in analogy to the third-order terms). Obviously, the completed-DSL-G1–G2 scheme contains all ten third-order selfenergy contributions. The structure of Eq. (3.67) suggests that even in fourth order 50 out of 82 diagrams are described correctly—beyond any approximation that has been used within the HF-GKBA.

Finally, it should be mentioned that Eq. (3.67) has its equivalent in RDO theory, where it corresponds to the omission of three-particle and higher correlations [96, 261]. In fact, it is possible to deduce a term-by-term correspondence, which will be demonstrated in an upcoming publication [262]. In the RDO framework, there is also a straightforward path to the TOA scheme of Eq. (3.66), which follows as the first-iteration solution of Eq. (3.67) for the two-particle Green function.

The specification of the third-order G1–G2 scheme for the Hubbard basis is specified in Sec. 3.1.2.3. There, also first numerical test results are presented.

3.1.2.2 G1–G2 Scheme for FLEX

There are various developments aiming at a combined treatment of particle–particle and particle–hole scattering, intertwined with dynamical-screening effects [79, 96, 263–266]. An adequate description of this correlation nexus entails the exhilarating promise to capture the predominant physics in quantum systems, even up to the strong-coupling regime. A particularly consistent example of appropriate approximations in this context is the already discussed dynamically-screened-ladder approximation. While it has been successfully integrated in the G1–G2 scheme [208], there is currently no approach to implement the DSL within a two-time NEGF framework. In NEGF theory, however, the linkup of the ladder approximations with the dynamically screened interaction is commonly achieved within the fluctuating-exchange approximation, which implies a slightly smaller degree of selfconsistency.

The idea of the FLEX approximation is to combine the selfenergy contributions of TPP, TPH, and GW, while accounting for the correct handling of the mutual terms. Thus, the selfenergy attains the form [79]

$$\Sigma_{ij}^{\text{FLEX}}(z, z') = \Sigma_{ij}^{\text{H}}(z, z') + \Sigma_{ij}^{\text{F}}(z, z') + \Sigma_{ij}^{GW}(z, z')$$
$$+ \Sigma_{ij}^{\text{TPP}}(z, z') + \Sigma_{ij}^{\text{TPH}}(z, z') - 2\Sigma_{ij}^{(2),\text{di}}(z, z'), \tag{3.70}$$

where the Hartree $\left(\Sigma^{\text{H}}\right)$ and Fock $\left(\Sigma^{\text{F}}\right)$ part describe mean-field effects, and the direct second-order diagram $\Sigma^{(2),\text{di}}$ is subtracted twice to avoid double counting (see, e.g., Ref. [79]

for details). It should be noted that all selfenergy terms in Eq. (3.70) share the same single-particle Green function $G_{ij}(z, z')$, from which their respective expression is evaluated. For all ingredient parts of the FLEX selfenergy, the G1–G2 scheme has a known form, derived in Ref. [208]. Being the sum of said selfenergy parts, Σ^{FLEX} is directly transformed to the following EOM for the time-diagonal two-particle Green function:

$$
\begin{aligned}
i\hbar\frac{\mathrm{d}}{\mathrm{d}t}\mathcal{G}_{ijkl}(t) = {}& \left[h^{(2),\mathrm{HF}}(t), \mathcal{G}(t)\right]_{ijkl} + \Psi^{\pm}_{ijkl}(t) \\
& + \sum_{pq}\left\{\mathfrak{h}^{\Omega^{\mathrm{PP}},\mathrm{corr}}_{ijpq}(t)\left[\mathcal{G}^{\mathrm{TPP}}_{klpq}(t)\right]^* - \mathcal{G}^{\mathrm{TPP}}_{ijpq}(t)\left[\mathfrak{h}^{\Omega^{\mathrm{PP}},\mathrm{corr}}_{klpq}(t)\right]^*\right\} \\
& + \sum_{pq}\left\{\mathfrak{h}^{\Omega^{\mathrm{ph}},\mathrm{corr}}_{ipql}(t)\left[\mathcal{G}^{\mathrm{TPH}}_{kpqj}(t)\right]^* - \mathcal{G}^{\mathrm{TPH}}_{ipql}(t)\left[\mathfrak{h}^{\Omega^{\mathrm{ph}},\mathrm{corr}}_{kpqj}(t)\right]^*\right\} \\
& + \sum_{pq}\left\{\mathfrak{h}^{\varepsilon,\mathrm{corr}}_{qjpl}(t)\left[\mathcal{G}^{GW}_{qkpi}(t)\right]^* - \mathcal{G}^{GW}_{qjpl}(t)\left[\mathfrak{h}^{\varepsilon,\mathrm{corr}}_{qkpi}(t)\right]^*\right\}.
\end{aligned}
\tag{3.71}
$$

Here, each additional $\mathcal{G}$ obeys its own EOM, i.e.,[13]

$$
\begin{aligned}
i\hbar\frac{\mathrm{d}}{\mathrm{d}t}\mathcal{G}^{\mathrm{TPP}}_{ijkl}(t) = {}& \left[h^{(2),\mathrm{HF}}(t), \mathcal{G}^{\mathrm{TPP}}(t)\right]_{ijkl} + \Psi^{\pm}_{ijkl}(t) \\
& + \sum_{pq}\left\{\mathfrak{h}^{\Omega^{\mathrm{PP}},\mathrm{corr}}_{ijpq}(t)\left[\mathcal{G}^{\mathrm{TPP}}_{klpq}(t)\right]^* - \mathcal{G}^{\mathrm{TPP}}_{ijpq}(t)\left[\mathfrak{h}^{\Omega^{\mathrm{PP}},\mathrm{corr}}_{klpq}(t)\right]^*\right\},
\end{aligned}
\tag{3.72}
$$

$$
\begin{aligned}
i\hbar\frac{\mathrm{d}}{\mathrm{d}t}\mathcal{G}^{\mathrm{TPH}}_{ijkl}(t) = {}& \left[h^{(2),\mathrm{HF}}(t), \mathcal{G}^{\mathrm{TPH}}(t)\right]_{ijkl} + \Psi_{ijkl}(t) \\
& + \sum_{pq}\left\{\mathfrak{h}^{\Omega^{\mathrm{ph}},\mathrm{corr}}_{ipql}(t)\left[\mathcal{G}^{\mathrm{TPH}}_{kpqj}(t)\right]^* - \mathcal{G}^{\mathrm{TPH}}_{ipql}(t)\left[\mathfrak{h}^{\Omega^{\mathrm{ph}},\mathrm{corr}}_{kpqj}(t)\right]^*\right\}, \text{ and}
\end{aligned}
\tag{3.73}
$$

$$
\begin{aligned}
i\hbar\frac{\mathrm{d}}{\mathrm{d}t}\mathcal{G}^{GW}_{ijkl}(t) = {}& \left[h^{(2),\mathrm{HF}}(t), \mathcal{G}^{GW}(t)\right]_{ijkl} + \Psi_{ijkl}(t) \\
& + \sum_{pq}\left\{\mathfrak{h}^{\varepsilon,\mathrm{corr}}_{qjpl}(t)\left[\mathcal{G}^{GW}_{qkpi}(t)\right]^* - \mathcal{G}^{GW}_{qjpl}(t)\left[\mathfrak{h}^{\varepsilon,\mathrm{corr}}_{qkpi}(t)\right]^*\right\}.
\end{aligned}
\tag{3.74}
$$

The single-particle Green function enters all four equations [Eqs. (3.71) – (3.74)], but only $\mathcal{G}$ of Eq. (3.71) directly couples to its EOM via Eqs. (3.10) and (3.12). In conclusion, for FLEX-G1–G2, four different two-particle tensors of similar complexity have to be saved and propagated, leading to four times the memory consumption and roughly a factor of four in the CPU runtime for numerical calculations. Comparing Eq. (3.71) to the two-particle equation of DSL-G1–G2 [Eqs. (3.4) and (3.67)], shows a very similar structure of both approximations, differing primarily by the presence of the backcoupling to $\mathcal{G}$ in the bottom three lines. As a consequence, DSL brings in a higher degree of selfconsistency, giving access to possible cross-coupling terms, as stated above. This is opposed to the seemingly artificial separation of the equations in FLEX [cf. Eq. (3.71)]. Therefore, the DSL approximation seems to be the more native treatment for G1–G2. The new-found FLEX-G1–G2 is, nonetheless, of interest due to its one-to-one correspondence to the respective formulation within NEGF theory with HF-GKBA, for which the DSL equivalent

---

[13]To allow for a conserving description, both the particle–hole T matrix and the dynamically screened interaction are considered without exchange terms (cf. Secs. 2.1.4 and 3.1.1).

is, yet, missing. Moreover, it remains to be tested, which treatment can, in practice, lead to more accurate simulations.

For the Hubbard basis, the FLEX-G1–G2 scheme reduces to more compact equations, which is specified in the next section along with first numerical test results.

3.1.2.3 Hubbard Basis and Numerical Demonstration

In order to demonstrate the equivalence between the two novel flavors of the G1–G2 scheme derived above and their counterparts within the HF-GKBA, this section shows simulation results for first numerical test calculations. To this end, first, the central equations of G1–G2 for TOA and FLEX are specified for the Hubbard basis.

Hubbard Basis: TOA-G1–G2

When applying the Hubbard basis, the interaction matrix transforms as follows[14] (explicit Pauli blocking is assumed):

$$w_{ijkl}^{\alpha\beta\gamma\delta}(t) = U(t)\delta_{ij}\delta_{ik}\delta_{il}\delta_{\alpha\gamma}\delta_{\beta\delta}\bar{\delta}_{\alpha\beta}\,, \tag{3.75}$$

with the on-site interaction strength $U(t)$. The matrix of the kinetic energy, $h_{ij}^{(0)} = -J\delta_{\langle i,j\rangle}$, accounts for hopping processes with amplitude J between neighboring lattice sites $\langle i,j\rangle$. This leads to the adjusted single-particle EOM (from here only the spin-up components are explicitly written; the spin-down components follow from the replacement $\uparrow\leftrightarrow\downarrow$)

$$i\hbar\frac{\mathrm{d}}{\mathrm{d}t}G_{ij}^{<,\uparrow}(t) = \left[h^{\mathrm{HF},\uparrow}(t), G^{<,\uparrow}(t)\right]_{ij} + \left[I + I^\dagger\right]_{ij}^\uparrow(t)\,, \tag{3.76}$$

$$I_{ij}^\uparrow(t) = -i\hbar U(t)\mathcal{G}_{iiji}^{\uparrow\downarrow\uparrow\downarrow}(t)\,, \tag{3.77}$$

with the Hartree–Fock Hamiltonian

$$h_{ij}^{\mathrm{HF},\uparrow}(t) = h_{ij}^{(0)} - i\hbar\delta_{ij}U(t)G_{ii}^{<,\downarrow}(t)\,. \tag{3.78}$$

As seen from Eq. (3.77), only one spin component (two, when considering $\uparrow\leftrightarrow\downarrow$) enters the EOM for the single-particle Green function. When the third-order selfenergy is applied, the truncated structure of Eq. (3.63) prevents possible cross-coupling of different spin components (which is seen, e.g., for the GW approximation [208]), leading to a single two-particle EOM. Due to the highly diagonal Hubbard interaction [cf. Eq. (3.75)], only two out of ten third-order diagrams remain—namely the direct particle–particle- and particle–hole-scattering diagram—while all other selfenergy terms vanish [79]. Thus, Eq. (3.63) reduces to

$$i\hbar\frac{\mathrm{d}}{\mathrm{d}t}\mathcal{G}_{ijkl}^{\uparrow\downarrow\uparrow\downarrow}(t) - \left[h_{\uparrow\downarrow}^{(2),\mathrm{HF}}, \mathcal{G}^{\uparrow\downarrow\uparrow\downarrow}\right]_{ijkl}(t) = \Psi_{ijkl}^{\uparrow\downarrow\uparrow\downarrow}(t) + \Lambda_{ijkl}^{\mathrm{SOA},\uparrow\downarrow\uparrow\downarrow}(t) - \left[\Lambda_{klij}^{\mathrm{SOA},\uparrow\downarrow\uparrow\downarrow}(t)\right]^*, \tag{3.79}$$

---

[14]From now on, the spin indices are separated from the single-particle basis indices and, instead, specified explicitly as greek letters.

where the two-particle Hamiltonian for the Hubbard basis becomes

$$h_{ijkl,\uparrow\downarrow}^{(2),\mathrm{HF}}(t) = \delta_{jl} h_{ik}^{\mathrm{HF},\uparrow}(t) + \delta_{ik} h_{jl}^{\mathrm{HF},\downarrow}(t)\,, \tag{3.80}$$

and the two-particle source term transforms to

$$\Psi_{ijkl}^{\uparrow\downarrow\uparrow\downarrow}(t) := (\mathrm{i}\hbar)^2 \, U(t) \sum_p \left[G_{ip}^{>,\uparrow}(t) G_{jp}^{>,\downarrow}(t) G_{pk}^{<,\uparrow}(t) G_{pl}^{<,\downarrow}(t) - G_{ip}^{<,\uparrow}(t) G_{jp}^{<,\downarrow}(t) G_{pk}^{>,\uparrow}(t) G_{pl}^{>,\downarrow}(t) \right]\,. \tag{3.81}$$

The ladder term $\Lambda^{\mathrm{SOA}}(t)$ includes the coupling to the two-particle Green function in second-order approximation and combines the contributions of the two quasi-Hamiltonians $\mathfrak{h}^{\Omega^{\mathrm{PP}},\mathrm{corr}}(t)$ and $\mathfrak{h}^\Lambda(t)$:

$$\Lambda_{ijkl}^{\mathrm{SOA},\uparrow\downarrow\uparrow\downarrow}(t) = (\mathrm{i}\hbar)^2 U(t) \sum_p \left[G_{ip}^{>,\uparrow}(t) G_{jp}^{>,\downarrow}(t) - G_{ip}^{<,\uparrow}(t) G_{jp}^{<,\downarrow}(t) \right] \mathcal{G}_{ppkl}^{\mathrm{SOA},\uparrow\downarrow\uparrow\downarrow}(t)$$
$$+ (\mathrm{i}\hbar)^2 U(t) \sum_p \left[G_{ip}^{>,\uparrow}(t) G_{pl}^{<,\downarrow}(t) - G_{ip}^{<,\uparrow}(t) G_{pl}^{>,\downarrow}(t) \right] \mathcal{G}_{pjkp}^{\mathrm{SOA},\uparrow\downarrow\uparrow\downarrow}(t)\,. \tag{3.82}$$

The separate EOM for $\mathcal{G}^{\mathrm{SOA}}(t)$ attains the form

$$\mathrm{i}\hbar \frac{\mathrm{d}}{\mathrm{d}t} \mathcal{G}_{ijkl}^{\mathrm{SOA},\uparrow\downarrow\uparrow\downarrow}(t) - \left[h_{\uparrow\downarrow}^{(2),\mathrm{HF}}, \mathcal{G}^{\mathrm{SOA},\uparrow\downarrow\uparrow\downarrow} \right]_{ijkl}(t) = \Psi_{ijkl}^{\uparrow\downarrow\uparrow\downarrow}(t)\,. \tag{3.83}$$

From a numerical perspective, Eqs. (3.79), (3.81) and (3.82) suggest a scaling of $\mathcal{O}(N_\mathrm{b}^5)$ with the basis size. It has been shown in the sections VII.A–C of Ref. [208], however, that the general structure of these terms can be rearranged for the Hubbard basis to achieve an $\mathcal{O}(N_\mathrm{b}^4)$ scaling, which is not repeated here. Hence, the total scaling of the TOA-G1–G2 scheme for the Hubbard model is $\mathcal{O}(N_\mathrm{b}^4 N_\mathrm{t}^1)$.

Hubbard Basis: FLEX-G1–G2

When considering the FLEX approximation for the Hubbard model the two-particle EOM of the G1–G2 scheme invokes a coupled system of equations [cf. Eqs. (3.71) – (3.74)]. By applying the Hubbard interaction [Eq. (3.75)] the derivative of the time-diagonal two-particle Green function becomes

$$\mathrm{i}\hbar \frac{\mathrm{d}}{\mathrm{d}t} \mathcal{G}_{ijkl}^{\uparrow\downarrow\uparrow\downarrow}(t) - \left[h_{\uparrow\downarrow}^{(2),\mathrm{HF}}, \mathcal{G}^{\uparrow\downarrow\uparrow\downarrow} \right]_{ijkl}(t) = \Psi_{ijkl}^{\uparrow\downarrow\uparrow\downarrow}(t) + \Lambda_{ijkl}^{\mathrm{PP},\uparrow\downarrow\uparrow\downarrow}(t) - \left[\Lambda_{klij}^{\mathrm{PP},\uparrow\downarrow\uparrow\downarrow}(t) \right]^*$$
$$+ \Lambda_{ijkl}^{\mathrm{ph},\uparrow\downarrow\uparrow\downarrow}(t) - \left[\Lambda_{klij}^{\mathrm{ph},\uparrow\downarrow\uparrow\downarrow}(t) \right]^*$$
$$+ \Pi_{ijkl}^{\uparrow\downarrow\uparrow\downarrow}(t) - \left[\Pi_{lkji}^{\downarrow\uparrow\downarrow\uparrow}(t) \right]^*\,, \tag{3.84}$$

which—together with its counterpart $(\uparrow \leftrightarrow \downarrow)$—is the only spin-component that needs to be considered for $\mathcal{G}(t)$. It is coupled to the single-particle Green function via Eqs. (3.76)

and (3.77). The ladder and polarization terms in Eq. (3.84) obey

$$\Lambda^{\mathrm{TPP},\uparrow\downarrow\uparrow\downarrow}_{ijkl}(t) = (\mathrm{i}\hbar)^2 U(t) \sum_p \left[G^{>,\uparrow}_{ip}(t) G^{>,\downarrow}_{jp}(t) - G^{<,\uparrow}_{ip}(t) G^{<,\downarrow}_{jp}(t) \right] \mathcal{G}^{\mathrm{TPP},\uparrow\downarrow\uparrow\downarrow}_{ppkl}(t) , \tag{3.85}$$

$$\Lambda^{\mathrm{TPH},\uparrow\downarrow\uparrow\downarrow}_{ijkl}(t) = (\mathrm{i}\hbar)^2 U(t) \sum_p \left[G^{>,\uparrow}_{ip}(t) G^{<,\downarrow}_{pl}(t) - G^{<,\uparrow}_{ip}(t) G^{>,\downarrow}_{pl}(t) \right] \mathcal{G}^{\mathrm{TPH},\uparrow\downarrow\uparrow\downarrow}_{pjkp}(t) , \tag{3.86}$$

$$\Pi^{\uparrow\downarrow\uparrow\downarrow}_{ijkl}(t) = -(\mathrm{i}\hbar)^2 U(t) \sum_p \left[G^{>,\downarrow}_{jp}(t) G^{<,\downarrow}_{pl}(t) - G^{<,\downarrow}_{jp}(t) G^{>,\downarrow}_{pl}(t) \right] \mathcal{G}^{GW,\uparrow\uparrow\uparrow\uparrow}_{ipkp}(t) , \tag{3.87}$$

and couple to three additional, self-contained variants of $\mathcal{G}(t)$, each of them obeying its own EOM:

$$\mathrm{i}\hbar \frac{\mathrm{d}}{\mathrm{d}t} \mathcal{G}^{\mathrm{TPP},\uparrow\downarrow\uparrow\downarrow}_{ijkl}(t) - \left[h^{(2),\mathrm{HF}}_{\uparrow\downarrow}, \mathcal{G}^{\mathrm{TPP},\uparrow\downarrow\uparrow\downarrow} \right]_{ijkl}(t) = \Psi^{\uparrow\downarrow\uparrow\downarrow}_{ijkl}(t) + \Lambda^{\mathrm{pp},\uparrow\downarrow\uparrow\downarrow}_{ijkl}(t) - \left[\Lambda^{\mathrm{pp},\uparrow\downarrow\uparrow\downarrow}_{klij}(t) \right]^* , \tag{3.88}$$

$$\mathrm{i}\hbar \frac{\mathrm{d}}{\mathrm{d}t} \mathcal{G}^{\mathrm{TPH},\uparrow\downarrow\uparrow\downarrow}_{ijkl}(t) - \left[h^{(2),\mathrm{HF}}_{\uparrow\downarrow}, \mathcal{G}^{\mathrm{TPH},\uparrow\downarrow\uparrow\downarrow} \right]_{ijkl}(t) = \Psi^{\uparrow\downarrow\uparrow\downarrow}_{ijkl}(t) + \Lambda^{\mathrm{ph},\uparrow\downarrow\uparrow\downarrow}_{ijkl}(t) - \left[\Lambda^{\mathrm{ph},\uparrow\downarrow\uparrow\downarrow}_{klij}(t) \right]^* , \tag{3.89}$$

$$\mathrm{i}\hbar \frac{\mathrm{d}}{\mathrm{d}t} \mathcal{G}^{GW,\uparrow\uparrow\uparrow\uparrow}_{ijkl}(t) - \left[h^{(2),\mathrm{HF}}_{\uparrow\uparrow}, \mathcal{G}^{GW,\uparrow\uparrow\uparrow\uparrow} \right]_{ijkl}(t) = \Pi^{\uparrow\uparrow\uparrow\uparrow}_{ijkl}(t) - \left[\Pi^{\uparrow\uparrow\uparrow\uparrow}_{lkji}(t) \right]^* . \tag{3.90}$$

Within the GW approximation in the Hubbard model, the polarization structure gives rise to a second spin component for $\mathcal{G}^{GW}(t)$ that enters the two-particle EOM [208]. In line with this, Eq. (3.90) is cross-coupled to

$$\mathrm{i}\hbar \frac{\mathrm{d}}{\mathrm{d}t} \mathcal{G}^{GW,\uparrow\downarrow\uparrow\downarrow}_{ijkl}(t) - \left[h^{(2),\mathrm{HF}}_{\uparrow\downarrow}, \mathcal{G}^{GW,\uparrow\downarrow\uparrow\downarrow} \right]_{ijkl}(t) = \Psi^{\uparrow\downarrow\uparrow\downarrow}_{ijkl}(t) + \Pi^{\uparrow\downarrow\uparrow\downarrow}_{ijkl}(t) - \left[\Pi^{\uparrow\downarrow\uparrow\downarrow}_{lkji}(t) \right]^* , \tag{3.91}$$

via the spin-parallel polarization term

$$\Pi^{\uparrow\uparrow\uparrow\uparrow}_{ijkl}(t) = -(\mathrm{i}\hbar)^2 U(t) \sum_p \left[G^{>,\uparrow}_{jp}(t) G^{<,\uparrow}_{pl}(t) - G^{<,\uparrow}_{jp}(t) G^{>,\uparrow}_{pl}(t) \right] \mathcal{G}^{GW,\uparrow\downarrow\uparrow\downarrow}_{ipkp}(t) . \tag{3.92}$$

Albeit the necessity to propagate multiple tensor quantities with their respective EOM, the numerical complexity of the underlying equations is similar to the case of the (Hubbard) TOA-G1–G2 scheme considered above. Thus, the numerical scaling of FLEX-G1–G2 can be brought to $\mathcal{O}\left(N_{\mathrm{b}}^4 N_{\mathrm{t}}^1\right)$ if all occurring expressions are treated as described in Ref. [208].

Numerical Test Calculations

At this point, it is instructive to compare the numerical implementations of the new-found variants of the G1–G2 scheme to their equivalents within the original HF-GKBA. Thereto, short simulations for a convenient test system are presented. It is beyond the scope of this work to give a detailed investigation of the new methods with respect to performance and general accuracy, which is left for future research.

The equations (3.79) for TOA and (3.84) for FLEX form the basis for time-linear
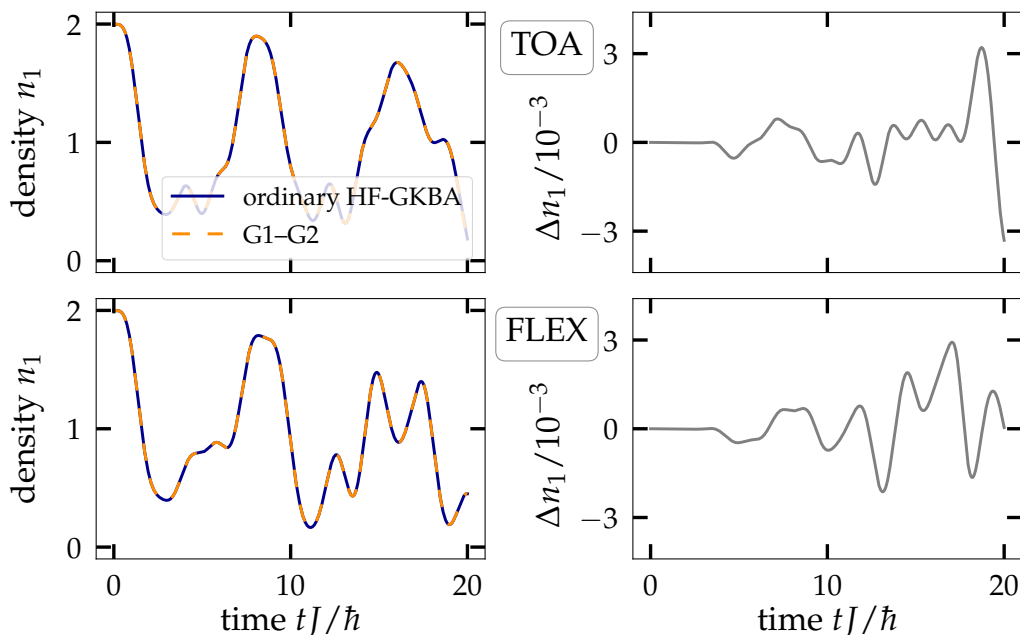
Figure 3.4 – Comparison of the ordinary HF-GKBA and the G1–G2 scheme for a four-site Hubbard chain with $U = J$ at half filling. The initial state was uncorrelated with the entire density concentrated at the two leftmost lattice site. The rows correspond to the TOA and FLEX selfenergies. The right column shows the deviation $\Delta n_1(t)$ of the densities of both schemes on site 1.

propagations of excited Hubbard systems within the G1–G2 scheme. An example for a four-site Hubbard chain is presented in Fig. 3.4. The dynamics starts from an uncorrelated initial state in which all particles of the half-filled system are blocked at the two leftmost sites. Once released, the density starts to oscillate irregularly due to the building up of correlations induced by the interaction strength $U = J$. Apart from numerical uncertainty, the G1–G2 data shows perfect agreement to the reference data of the ordinary HF-GKBA, both for TOA (Fig. 3.4, top left) and FLEX (bottom left). For comparability, a fourth-order Runge–Kutta integration scheme with a time step of $\Delta t = 0.02\hbar/J$ is used for all simulations. The deviations $\Delta n_1(t) = n_1^{\text{G1–G2}}(t) - n_1^{\text{ordinary}}(t)$ grow over time (Fig. 3.4, right column) and are predominantly caused by the original HF-GKBA, as discussed in Ref. [114].

Concluding this supplementary section to the G1–G2 scheme, the capability to describe nonequilibrium Green functions in a time-linear way constitutes a remarkable advancement in NEGF theory. The extension of the G1–G2 scheme to the TOA and FLEX selfenergies further expands the reservoir of corresponding approximations to the HF-GKBA. Of particular interest is the third-order G1–G2 variant, as the TOA has proven to be very successful as an allrounder [79], also when the HF-GKBA is applied [212]. There are several topics for possible future research. Both TOA-G1–G2 and FLEX-G1–G2 need to be tested in a broader context and compared to the previous G1–G2 methods, considering accuracy and numerical behavior. Furthermore, one can specify the derived equations for more single-particle-basis choices, such as the jellium basis. The generalization of the DSL approximation, discussed in Sec. 3.1.2.1, is especially interesting and should

be tested extensively. Being the most in-depth approximation on the two-particle level, which combines its selfenergy constituents in a consistent way, the completed DSL is a particularly promising method for prospective applications.

3.2 Time Reversibility in Quantum-Kinetic Equations

Obviously, every existing tool to describe quantum many-body dynamics is build to reproduce as many characteristics of the exact solution as possible. However, the need to describe increasingly large systems over long periods of time often manifests as a decrease of theoretical depth. Therefore, specific properties such as symmetries and conservation laws are sometimes loosened in favor of efficient and powerful approximations. Examples include the quantum Boltzmann equation, which violates total-energy conservation [96], and also time-dependent Hartree–Fock (TDHF) and NEGF methods, where, in some cases, spin symmetry is broken for half-filled electronic systems (cf. Sec. 3.3). A more subtle yet fundamental property of quantum systems is time-reversal invariance.[15] Following the original notion of Wigner [269], time-reversal invariance is expressed by reversing the (wavefunction) trajectory $|\Psi(t)\rangle \mapsto \hat{T}|\Psi(-t)\rangle$ for $t \mapsto -t$, where $\hat{T}$ is an anti-unitary time-reversal operator. The fact that, by this definition, also instantaneous states ($t = 0$) are affected by $\hat{T}$ has given rise to an expansive, still ongoing (and quite entertaining) philosophical debate [270–274] about whether or not Wigner's representation is the justified translation to the quantum realm.[16] This shows that the concept of time reversibility is not entirely intuitive. Accepting the time-dependent Schrödinger equation and the Heisenberg equation as being time-reversal invariant, it is not immediately clear that all many-body approximations preserve this property. Instead, e.g., Boltzmann-type equations of motion are known to be irreversible, thereby giving rise to relaxation processes towards a thermalized equilibrium state [53].

Given the fact that time reversibility is not only of theoretical relevance but also opens the path to advanced numerical testing opportunities (see, e.g., Refs. [130, 202, 211]), it is surprising that there has been no rigorous discussion in the context of generalized quantum-kinetic equations. The following publications,[17,18] Refs. [209] and [210], form a two-part analysis on time-reversal invariance considering—in part I—the NEGF framework and—in part II—the RDO method.

As a first outcome of Ref. [209] an analytical proof of the expected time reversibility of the exact Martin–Schwinger hierarchy is given. To this end, the respective derivations for the Schrödinger and the Heisenberg equation are redone first. Both relations are reversible if the commutator between the time-reversal operator $\hat{T}$ and the Hamiltonian $\hat{H}$ vanishes. Subsequently, $\hat{T}$ is applied to the field operators and, eventually, the n-particle correlator and the n-particle nonequilibrium Green function to demonstrate the desired symmetry.

---

[15]It should be noted that time-reversal symmetry (or T symmetry) can be violated under the influence of the weak interaction. A direct observation of such a T violation has been presented in Ref. [267] for the decay of entangled neutral B mesons. Instead, the—more general—CPT theorem is widely believed to remain valid under all conditions [268], which, for every physical process, predicts the existence of the time-reversed process under charge conjugation and parity inversion.

[16]Quoting from Ref. [271]: "David Albert, forthcoming, argues – rightly in my opinion – that the traditional definition of [time-reversal invariance], which I have just given, is in fact gibberish. It just doesn't make sense to time-reverse a truly instantaneous state of a system".

[17]M. Scharnke, N. Schlünzen, and M. Bonitz, J. Math. Phys., **58**, 061903 (2017). Copyright by AIP Publishing. Reproduced with permission.

[18]M. Bonitz, M. Scharnke, and N. Schlünzen, Contrib. Plasma Phys., **58**, 1036 (2018). Copyright Wiley-VCH Verlag GmbH & Co. KGaA. Reproduced with permission.

While the result for the hierarchy is mostly of theoretical interest, the corresponding statement for frequently used many-body approximations has great practical relevance. For this reason, a time-reversibility condition for the selfenergy is derived in Ref. [209] using the Kadanoff–Baym equations. It is shown that this condition is fulfilled—and, thus, time-reversal invariance is preserved—for any Φ-derivable selfenergy. This result, on the one hand, reinforces the importance of the Φ functional and, on the other hand, accounts for the inner consistency of the NEGF framework. Finally, the application of the GKBA and the associated implications for time-reversal invariance are discussed.

The central result of Ref. [209] lifts NEGF theory on a more solid foundation. At the same time, it substantiates an important tool to ensure numerical stability via backwards-propagation consistency in NEGF calculations. Practically, this has already been applied in Refs. [130, 202, 211]. It is important to note that the need for numerical convergence tests can hardly be overstated. For example, such numerical pitfalls have been at the heart of the recent controversy around a paper by Adrian Stan [202], which is addressed in detail in Ref. [211] included in Sec. 4.1.

In the second part of the time-reversibility analysis, Ref. [210], the RDO theory (see, e.g., Ref. [96]) is addressed, which shares its theoretical foundation with the NEGF theory, but focuses on single-time-dependent density-matrix objects, instead. The first major result of Ref. [210] is the proof of time-reversal invariance for the Bogolyubov–Born–Green–Kirkwood–Yvon (BBGKY) hierarchy which depends on a more general condition—not just the full Hamiltonian $\hat{H}$, but also the single-particle, two-particle, and higher contributions have to commute individually with the operator $\hat{T}$. In exact calculations, this constitutes no further restriction, since the n-particle dynamics are always consistent to each other. Subsequently, a general reversibility condition for closure relations is derived and it is demonstrated that all common many-body approximations for density operators fulfill this condition. The final part of Ref. [210] discusses the successive transition from the density-operator equations to the quantum Boltzmann equation, which is not time-reversal invariant. It is shown that the crucial approximation that leads to the violation of time reversibility is, in fact, the Markov limit that effectively shifts the initial time t_0 to $-\infty$, thereby breaking the unitary character of the dynamics.

These important results close a gap in the theoretical basis of the RDO method. Beyond that, time-reversal symmetry is of direct practical use for numerical consistency tests in RDO calculations. The outcome of Ref. [210] is also relevant for the recently developed G1–G2 scheme (cf. Sec. 3.1), which is closely related to RDO theory.

Time reversal invariance of quantum kinetic equations: Nonequilibrium Green functions formalism

Miriam Scharnke, Niclas Schlünzen, and Michael Bonitz
*Institut für Theoretische Physik und Astrophysik, Christian-Albrechts-Universität Kiel,
Leibnizstraße 15, 24098 Kiel, Germany*

Time reversal symmetry is a fundamental property of many quantum mechanical systems. The relation between statistical physics and time reversal is subtle and not all statistical theories conserve this particular symmetry, most notably hydrodynamic equations and kinetic equations such as the Boltzmann equation. In this article, it is shown analytically that quantum kinetic generalizations of the Boltzmann equation that are derived using the nonequilibrium Green functions formalism as well as all approximations that stem from Φ-derivable self-energies are time reversal invariant. *Published by AIP Publishing.* [http://dx.doi.org/10.1063/1.4989684]

I. INTRODUCTION

The nonequilibrium Green functions (NEGFs) formalism provides an *ab initio* description of strongly interacting quantum many-particle systems far from equilibrium. It has gained much importance in the last two decades mainly because it is now possible to solve the two-time Keldysh–Kadanoff–Baym (KBE) equations numerically. NEGFs have been successfully used to describe a huge variety of systems and phenomena, such as Bose condensation, quantum and molecular transport[1] and femtosecond spectroscopy, carrier dynamics in quantum dots and quantum wells,[2,3] laser excitation of small atoms,[4,5] nuclear collisions,[6] intense laser-plasma interaction,[7] baryogenesis in cosmology,[8] and much more. Within the Green functions formalism, there exists an elegant diagrammatic method for constructing approximations that conserve energy, momentum, angular momentum, and particle number, by using the so-called Φ-derivable self-energies. It is the purpose of this paper to show that those approximations as well as the exact equations of motion of the Green functions formalism are invariant under time reversal.

The relation between time reversal symmetry and statistical physics is subtle and not all statistical theories are invariant under time reversal, the most famous counterexample being the Boltzmann equation of classical statistical mechanics and its quantum generalization. Therefore, extensive work has been done over the recent seven decades to derive non-Markovian generalizations of the Boltzmann equation that are time-reversal invariant as the underlying quantum mechanical system. Among the well established approaches, we mention density operator concepts, see, e.g., Ref. 9 for an overview, and nonequilibrium Green functions,[10] for a recent text book discussion, see Ref. 11. Despite recent activities in this field, we are not aware of a general analysis of the time reversal properties of the resulting generalized quantum kinetic equations. Since these equations are usually solved with the help of certain many-body approximations, it is even more important to understand under which conditions time reversal invariance is retained.

It is the goal of the present article to solve these questions for the NEGF formalism which we briefly recall in Sec. II. Since the Kadanoff–Baym equations can be directly derived from the equations of motion of the field operators in second quantization which are time-reversal invariant, it should be expected that the KBE equations have the same symmetry properties. It is, nonetheless, not trivial to show this directly in full generality, and a successful procedure is presented in Sec. IV. We then demonstrate in Sec. V that an important class of approximations—the so-called Φ-derivable approximations—also preserve time reversal symmetry. We conclude with a summary in Sec. VI where we also outline the time reversal invariance conditions of the generalized Kadanoff–Baym ansatz.[12]

II. NONEQUILIBRIUM GREEN FUNCTIONS

The n-particle Green function $G^{(n)}$ is defined element-wise as the ensemble average of the n-particle correlator in second quantization

$$G^{(n)}_{i_1\ldots i_n;j_1\ldots j_n}(z_1\ldots z_n; z'_1\ldots z'_n) = \left\langle \hat{G}^{(n)}_{i_1\ldots i_n;j_1\ldots j_n}(z_1\ldots z_n; z'_1\ldots z'_n) \right\rangle$$

$$= \left(-\frac{i}{\hbar}\right)^n \left\langle \hat{\mathcal{T}}_\mathcal{C}\, \hat{c}_{i_1}(z_1)\ldots \hat{c}_{i_n}(z_n)\hat{c}^\dagger_{j_n}(z'_n)\ldots \hat{c}^\dagger_{j_1}(z'_1) \right\rangle, \tag{1}$$

where $\hat{c}^\dagger_{j_k}$ and $\hat{c}_{i_k}$ are second quantization creation and annihilation operators with respect to a complete orthonormal basis of single-particle states $\{|\phi_i\rangle\}$ obeying the (anti-)commutation relations for bosons (fermions),

$$[\hat{c}_{i_k}, \hat{c}_{i_l}]_\mp = [\hat{c}^\dagger_{i_k}, \hat{c}^\dagger_{i_l}]_\mp = 0,$$
$$[\hat{c}_{i_k}, \hat{c}^\dagger_{i_l}]_\mp = \delta_{i_k,i_l}. \tag{2}$$

Further, $\hat{\mathcal{T}}_\mathcal{C}$ is the time ordering operator on the Keldysh time contour $\mathcal{C}$, as illustrated in Fig. 1.

The dynamics of the n-particle Green function are described by the Martin–Schwinger hierarchy—a coupled hierarchy of equations of motion (we leave out the orbital indices for brevity),

$$\left[i\hbar\partial_{z_k} - h^{(0)}(z_k)\right] G^{(n)}(z_1\ldots z_n; z'_1\ldots z'_n) =$$

$$\pm i\hbar \int_\mathcal{C} d\bar{z}\, W(z_k\bar{z})\, G^{(n+1)}(z_1\ldots z_n\bar{z}; z'_1\ldots z'_n\bar{z}^+)$$

$$+ \sum_{p=1}^n (\pm 1)^{k+p}\delta_\mathcal{C}(z_k z'_p) G^{(n-1)}(z_1\ldots \cancel{z}_k\ldots z_n; z'_1\ldots \cancel{z}_p{}'\ldots z'_n), \tag{3}$$

and

$$G^{(n)}(z_1\ldots z_n; z'_1\ldots z'_n)\left[-i\hbar\overleftarrow{\partial}_{z'_k} - h^{(0)}(z'_k)\right] =$$

$$\pm i\hbar \int_\mathcal{C} d\bar{z}\, G^{(n+1)}(z_1\ldots z_n\bar{z}^-; z'_1\ldots z'_n\bar{z})W(\bar{z}z'_k)$$

$$+ \sum_{p=1}^n (\pm 1)^{k+p}\delta_\mathcal{C}(z_p z'_k) G^{(n-1)}(z_1\ldots \cancel{z}_p\ldots z_n; z'_1\ldots \cancel{z}_k{}'\ldots z'_n), \tag{4}$$

where $W(z_1, z_2) = \delta_\mathcal{C}(z_1, z_2)w(z_1)$ and $w(z_1)$ is the instantaneous two-particle interaction operator. The Dirac delta function $\delta_\mathcal{C}$ acts on contour times z, and $h^{(0)}$ denotes the matrix element of the single-particle Hamiltonian. The first-order hierarchy equations can be formally closed by introducing the self-energy Σ, reducing the description to the dynamics of the single-particle Green function $G^{(1)}$,

$$[i\hbar\partial_z - h(z)]\, G^{(1)}(zz') = \delta_\mathcal{C}(zz')\, \mathbb{1} + \int_\mathcal{C} d\bar{z}\, \Sigma(z\bar{z})\, G^{(1)}(\bar{z}z'), \tag{5}$$

and its adjoint

$$[-i\hbar\partial_{z'} - h(z)]\, G^{(1)}(zz') = \delta_\mathcal{C}(zz')\mathbb{1} + \int_\mathcal{C} d\bar{z}\, G^{(1)}(z\bar{z})\Sigma(\bar{z}z'). \tag{6}$$
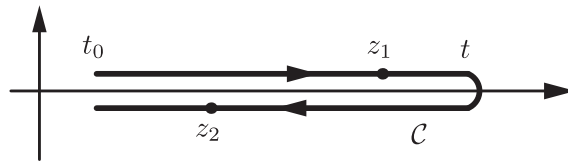
FIG. 1. Illustration of the two real-time branches of the Keldysh contour. z_1 on the causal branch $\mathcal{C}_-$ is earlier on the contour than z_2 on the anti-causal branch $\mathcal{C}_+$, although the physical time t_1 corresponding to z_1 is later than the physical time t_2 corresponding to z_2.

$$(a) \qquad\qquad (b)$$
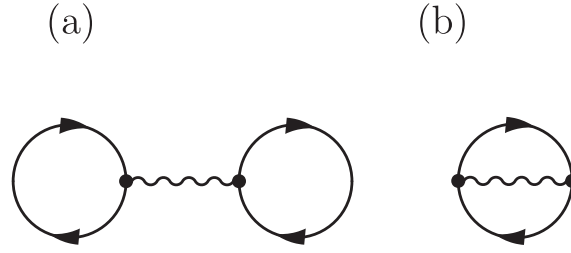
FIG. 2. The Hartree (a) and Fock (b) diagrams contributing to the Hartree–Fock potential Φ^{HF}. A full (wiggly) line corresponds to a Green function (interaction potential).

These equations are the Keldysh–Kadanoff–Baym equations. It is theoretically possible to write Σ as a functional of $G^{(1)}$ such that Eqs. (5) and (6) are still exact. The main challenge of the Green functions formalism is to find suitable approximations for the self-energy. One important class of self-energy approximations is constructed as the functional derivative of a scalar function Φ ("Φ-derivable approximations"),

$$\Sigma(z_1, z_2) = \frac{\delta \Phi[G]}{\delta G(z_2, z_1^+)}. \tag{7}$$

These approximations conserve particle number, momentum, energy, and angular momentum if Φ is invariant under gauge transformations, space and time translations, and rotations, respectively. This is satisfied if Φ is the amplitude of a scattering process (since every scattering process satisfies these conservation requirements). Therefore, it is possible to construct conserving scalar potentials diagrammatically. For example, the potential Φ^{HF} corresponding to the Hartree–Fock approximation consists of two diagrams, as illustrated in Fig. 2,

$$\Phi^{HF}[G] = \pm \frac{i\hbar}{2} \Phi^{(a)}[G] + \frac{i\hbar}{2} \Phi^{(b)}[G], \tag{8}$$

$$\Phi^{(a)}[G] = \int_{\mathcal{C}} dz_1 dz_2 \, G(z_1; z_1^+) W(z_1; z_2) G(z_2; z_2^+), \tag{9}$$

$$\Phi^{(b)}[G] = \int_{\mathcal{C}} dz_1 dz_2 \, G(z_1; z_2^+) W(z_1; z_2) G(z_2; z_1^+). \tag{10}$$

resulting in the Hartree–Fock self-energy

$$\Sigma^{HF}(zz') = \pm i\hbar \delta_{\mathcal{C}}(zz') \int_{\mathcal{C}} d\bar{z} \, W(z\bar{z}) G^{(1)}(\bar{z}\bar{z}^+) + i\hbar G^{(1)}(zz') W(z^+z'). \tag{11}$$

Other Φ-derivable approximations are the second order and third order Born approximations, the GW-approximation, and the T-matrix (ladder) approximation, e.g., Ref. 11.

III. TIME REVERSAL INVARIANCE IN QUANTUM MANY-BODY THEORY

Here, we briefly recall the notion of time reversibility introducing the time reversal operator $\hat{T}$. We first illustrate this for the N-particle Schrödinger equation and then extend the concept to many-body theory within second quantization.

A. Time reversal invariance of the Schrödinger equation

The Schrödinger equation is called symmetric with regard to time reversal if (i) for any solution $|\psi(t)\rangle$, there exists another solution $|\psi'(t')\rangle$ with $t' = -t$, and if (ii) there exists a unique relation between the two, $|\psi'\rangle = \hat{T}|\psi\rangle$, for some operator $\hat{T}$.[13] It can be shown that $\hat{T}$ must not only be a linear operator but also an anti-unitary one. Thus, it can be expressed as the product of complex conjugation and some unitary operator $\hat{U}$. The quantum mechanical equivalent to classical conventional time reversal is obtained by choosing $\hat{U} = \mathbb{1}$, so that $|\psi\rangle \to |\psi\rangle^*$.

Let us illustrate this for the time-dependent Schrödinger equation

$$i\hbar\,\partial_t|\psi\rangle = \hat{H}|\psi\rangle. \tag{12}$$

Applying $\hat{T}$ to both sides yields

$$\hat{T}\,i\hbar\,\partial_t|\psi\rangle = \hat{T}\,\hat{H}|\psi\rangle$$
$$\Longleftrightarrow \underbrace{-i\hbar\,\partial_t\,\hat{T}|\psi\rangle}_{i\hbar\partial_{(-t)}} = \hat{T}\hat{H}\hat{T}^{-1}\hat{T}|\psi\rangle, \tag{13}$$

which means that $\hat{T}|\psi\rangle$ solves the time-reversed Schrödinger equation

$$i\hbar\,\partial_{(-t)}|\psi'\rangle = \hat{H}|\psi'\rangle \tag{14}$$

if (and only if) $\hat{H} = \hat{T}\hat{H}\hat{T}^{-1}$. This result is valid for an arbitrary interacting many-particle system.

B. Time reversal invariance of the Heisenberg equation

The Heisenberg equation for an operator $\hat{A}_{\mathrm{H}}$ is equivalent to the Schrödinger equation and should, therefore, possess the same reversibility properties. This is straightforwardly shown applying the $\hat{T}$-operator introduced above from left and right,

$$i\hbar\,\partial_t\hat{A}_{\mathrm{H}} = \left[\hat{A}_{\mathrm{H}}, \hat{H}\right], \tag{15}$$

$$\Longleftrightarrow \hat{T}\,i\hbar\,\partial_t\hat{A}_{\mathrm{H}}\,\hat{T}^{-1} = \hat{T}\left(\hat{A}_{\mathrm{H}}\hat{H} - \hat{H}\hat{A}_{\mathrm{H}}\right)\hat{T}^{-1}$$

$$\Longleftrightarrow -i\hbar\,\partial_t\hat{T}\hat{A}_{\mathrm{H}}\hat{T}^{-1} = \hat{T}\hat{A}_{\mathrm{H}}\hat{T}^{-1}\,\hat{T}\hat{H}\hat{T}^{-1} - \hat{T}\hat{H}\hat{T}^{-1}\,\hat{T}\hat{A}_{\mathrm{H}}\hat{T}^{-1}, \tag{16}$$

which is equivalent to

$$i\hbar\,\partial_{-t}\hat{T}\hat{A}_{\mathrm{H}}\hat{T}^{-1} = \left[\hat{T}\hat{A}_{\mathrm{H}}\hat{T}^{-1}, \hat{H}\right] \tag{17}$$

if and only if $\hat{H} = \hat{T}\hat{H}\hat{T}^{-1}$. This means that, if a Heisenberg operator $\hat{A}_{\mathrm{H}}(t)$ solves the Heisenberg equation, then $\hat{T}\hat{A}_{\mathrm{H}}\hat{T}^{-1}$ solves the time-reversed Heisenberg equation.

C. Time reversal invariance of the equations of motion of the field operators of second quantization

The equation of motion of the annihilation operator in an arbitrary single-particle basis $\{|\phi_i\rangle\}$ [cf. Sec. II] reads[14]

$$i\hbar\,\partial_t\hat{c}_i(t) = \sum_k \left(t_{ik} + v_{ik}(t)\right)\hat{c}_k(t) + \sum_{jkl} w_{ijkl}(t)\,\hat{c}_j^\dagger(t)\hat{c}_l(t)\hat{c}_k(t), \tag{18}$$

where t_{ik} and v_{ik} (w_{ijkl}) are the matrix elements computed with the respective single-particle (two-particle product) basis states. For the purpose of analyzing time reversal symmetry, it is convenient to consider that Eq. (18) is derived from and equivalent to the Heisenberg equation for $\hat{c}_i(t)$,

$$i\hbar\,\partial_t\hat{c}_i(t) = \left[\hat{c}_i, \hat{H}\right], \tag{19}$$

and, as such, possesses the same symmetry properties that $\hat{H}$ does. The same obviously holds for the creation operator $\hat{c}_j^\dagger$.

IV. TIME REVERSAL INVARIANCE OF THE MARTIN–SCHWINGER HIERARCHY

The Martin–Schwinger hierarchy (3) follows from taking the ensemble average of the formally equivalent hierarchy of equations of motion of the n-particle correlators $\hat{G}^{(n)}$. The latter, in turn, follows from the equations of motion of field operators (3) and (4) and, therefore, must satisfy the same symmetry properties as the field operators. Nonetheless, it is instructive to prove the time reversal invariance of the Martin–Schwinger hierarchy directly. To this end, it is important to understand how the contour-δ-distribution behaves under time reversal. Since δ is even with respect to its argument,

i.e., $\delta(z) = \delta(-z)$, it might be expected that $\tilde{\delta}_{\mathcal{C}} := \delta_{\mathcal{C}}^{z \to -z} = \delta_{\mathcal{C}}$. That, however, cannot be true, as the following considerations show

$$\int_{\mathcal{C}} \mathrm{d}z \, \delta_{\mathcal{C}}(z) = 1 \xrightarrow{z \to -z} 1 = \int_{\mathcal{C}} \mathrm{d}(-z) \, \tilde{\delta}_{\mathcal{C}}(z),$$

$$\iff \delta_{\mathcal{C}} \xrightarrow{z \to -z} \tilde{\delta}_{\mathcal{C}} = -\delta_{\mathcal{C}}. \tag{20}$$

This means that the δ-distribution with respect to contour time arguments changes its sign under time reversal, in analogy to differential and integral operators.

Component-wise, the nth order hierarchy equations for the correlators read

$$\sum_{l} \left[\mathrm{i}\hbar \frac{\partial}{\partial z_k} \delta_{i_k l} - h_{i_k l}^{(0)}(z_k) \right] \hat{G}_{i_1 \ldots l \ldots i_n; j_1 \ldots j_n}^{(n)} (z_1 \ldots z_n; z_1' \ldots z_n')$$

$$= \pm \, \mathrm{i}\hbar \sum_{lmn} \int_{\mathcal{C}} \mathrm{d}\bar{z} \left\{ W_{i_k lmn}(z_k \bar{z}) \hat{G}_{i_1 \ldots m \ldots i_n n; j_1 \ldots j_n l}^{(n+1)} (z_1 \ldots z_n \bar{z}; z_1' \ldots z_n' \bar{z}^+) \right\}$$

$$+ \sum_{p=1}^{n} \left\{ (\pm 1)^{k+p} \delta_{i_k j_p} \delta_{\mathrm{C}}(z_k z_p') \hat{G}_{i_1 \ldots \not{i}_k \ldots i_n; j_1 \ldots \not{j}_p \ldots j_n}^{(n-1)} (z_1 \ldots \not{z}_k \ldots z_n; z_1' \ldots \not{z}_p' \ldots z_n') \right\}. \tag{21}$$

Since $W(zz') = w(z)\delta_{\mathcal{C}}(zz')$, it immediately follows that $W^{z^{(\prime)} \to -z^{(\prime)}} = -W$. Therefore, the time-reversed equations read

$$\sum_{l} \left[-\mathrm{i}\hbar \frac{\partial}{\partial z_k} \delta_{i_k l} - h_{i_k l}^{(0)}(z_k) \right] \hat{G}_{i_1 \ldots l \ldots i_n; j_1 \ldots j_n}^{(n)} (z_1 \ldots z_n; z_1' \ldots z_n')$$

$$= \pm \mathrm{i}\hbar \sum_{lmn} \int_{\mathcal{C}} \mathrm{d}\bar{z} \left\{ W_{i_k lmn}(z_k \bar{z}) \, \hat{G}_{i_1 \ldots m \ldots i_n n; j_1 \ldots j_n l}^{(n+1)} (z_1 \ldots z_n \bar{z}; z_1' \ldots z_n' \bar{z}^+) \right\}$$

$$- \sum_{p=1}^{n} \left\{ (\pm 1)^{k+p} \delta_{i_k j_p} \delta_{\mathrm{C}}(z_k z_p') \, \hat{G}_{i_1 \ldots \not{i}_k \ldots i_n; j_1 \ldots \not{j}_p \ldots j_n}^{(n-1)} (z_1 \ldots \not{z}_k \ldots z_n; z_1' \ldots \not{z}_p' \ldots z_n') \right\}. \tag{22}$$

The question remains whether these reversed equations have a solution and what the relation between this solution and the solution of the original (non-reversed) equations is. Applying $\hat{T}$ from the left and $\hat{T}^{-1}$ from the right on both sides of Eq. (21), and omitting the time arguments for brevity, yields

$$\sum_{l} \left[-\mathrm{i}\hbar \frac{\partial}{\partial z_k} \delta_{i_k l} - h_{i_k l}^{(0)}(z_k) \right] \hat{T} \hat{G}_{i_1 \ldots l \ldots i_n; j_1 \ldots j_n}^{(n)} \hat{T}^{-1}$$

$$= \mp \mathrm{i}\hbar \sum_{lmn} \int_{\mathcal{C}} \mathrm{d}\bar{z} \, W_{i_k lmn}(z_k \bar{z}) \hat{T} \hat{G}_{i_1 \ldots m \ldots i_n n; j_1 \ldots j_n l}^{(n+1)} \hat{T}^{-1}$$

$$+ \sum_{p=1}^{n} (\pm 1)^{k+p} \delta_{i_k j_p} \delta_{\mathrm{C}}(z_k z_p') \hat{T} \hat{G}_{i_1 \ldots \not{i}_k \ldots i_n; j_1 \ldots \not{j}_p \ldots j_n}^{(n-1)} \hat{T}^{-1}. \tag{23}$$

This is not equivalent to Eq. (22), and therefore $\hat{T} \hat{G}_{i_1 \ldots l \ldots i_n; j_1 \ldots j_n}^{(n)} \hat{T}^{-1}$ does not solve the reversed equations.

We, therefore, use a different approach which takes advantage of the fact that $\hat{G}_{i_1 \ldots l \ldots i_n; j_1 \ldots j_n}^{(n)}$ can be interpreted as a functional of $\hat{c}_{i_1}, \ldots, \hat{c}_{i_n}, \hat{c}_{j_1}^{\dagger}, \ldots, \hat{c}_{j_n}^{\dagger}$. Considering that $\hat{T}\hat{c}_i\hat{T}^{-1}$ and $\hat{T}\hat{c}_j^{\dagger}\hat{T}^{-1}$ solve the reversed equations of motion compared to $\hat{c}_i$ and $\hat{c}_j^{\dagger}$, it could be expected that the solution to the reversed hierarchy equations is given by the same functional $\hat{G}_{i_1 \ldots l \ldots i_n; j_1 \ldots j_n}^{(n)}$ of $\hat{T}\hat{c}_i\hat{T}^{-1}$. This is, in fact, the case because

$$\hat{T}\hat{G}^{(n)}_{i_1\ldots l\ldots i_n;j_1\ldots j_n}\hat{T}^{-1}$$

$$= \hat{T}\left\{\left(-\frac{i}{\hbar}\right)^n \hat{\mathcal{T}}_\mathcal{C}\hat{c}_{i_1}(z_1)\ldots\hat{c}_{i_n}(z_n)\hat{c}^\dagger_{j_n}(z'_n)\ldots\hat{c}^\dagger_{j_1}(z'_1)\right\}\hat{T}^{-1}$$

$$= (-1)^n\left(-\frac{i}{\hbar}\right)^n\left\{\hat{\mathcal{T}}_\mathcal{C}\hat{T}\hat{c}_{i_1}(z_1)\hat{T}^{-1}\ldots\hat{T}\hat{c}_{i_n}(z_n)\hat{T}^{-1}\hat{T}\hat{c}^\dagger_{j_n}(z'_n)\hat{T}^{-1}\ldots\hat{T}\hat{c}^\dagger_{j_1}(z'_1)\hat{T}^{-1}\right\}$$

$$= (-1)^n\hat{G}^{(n)}_{i_1\ldots l\ldots i_n;j_1\ldots j_n}\left\{\hat{T}\hat{c}_{i_1}(z_1)\hat{T}^{-1}\ldots\hat{T}\hat{c}_{i_n}(z_n)\hat{T}^{-1}\hat{T}\hat{c}^\dagger_{j_n}(z'_n)\hat{T}^{-1}\ldots\hat{T}\hat{c}^\dagger_{j_1}(z'_1)\hat{T}^{-1}\right\}$$

$$=: (-1)^n\tilde{\hat{G}}^{(n)}_{i_1\ldots l\ldots i_n;j_1\ldots j_n}. \tag{24}$$

Inserting this into Eq. (23) yields

$$(-1)^n\sum_l\left[-i\hbar\frac{\partial}{\partial z_k}\delta_{i_k l} - h^{(0)}_{i_k l}(z_k)\right]\tilde{\hat{G}}^{(n)}_{i_1\ldots l\ldots i_n;j_1\ldots j_n} \tag{25}$$

$$= \mp(-1)^{n+1}i\hbar\sum_{lmn}\int_\mathcal{C}\mathrm{d}\bar{z}\,W_{i_k lmn}(z_k\bar{z})\tilde{\hat{G}}^{(n+1)}_{i_1\ldots m\ldots i_n n;j_1\ldots j_n l} + (-1)^{n-1}\sum_{p=1}^n(\pm 1)^{k+p}\delta_{i_k j_p}\delta_\mathrm{C}(z_k z'_p)\tilde{\hat{G}}^{(n-1)}_{i_1\ldots \cancel{k}\ldots i_n;j_1\ldots \cancel{p}\ldots j_n},$$

which, when divided by $(-1)^n$, is equivalent to Eq. (22). From this it follows directly, by taking the ensemble average of both sides, that $G^{(n)}\left[\hat{T}\hat{c}\hat{T}^{-1}, \hat{T}\hat{c}^\dagger\hat{T}^{-1}\right]$ satisfies the reversed nth-order equations of the Martin–Schwinger hierarchy in the same way. Thus, we have demonstrated that the exact Martin–Schwinger hierarchy is time reversal invariant, as expected.

V. TIME REVERSAL INVARIANCE OF Φ-DERIVABLE APPROXIMATIONS

Since the solution of the Martin–Schwinger hierarchy is usually possible only with suitable approximations, the important question arises as which approximations retain the time reversal properties of the exact system. In the following, we demonstrate that any Φ-derivable self-energy leads to time reversal invariance. Thereby we will restrict ourselves to real-valued Hamiltonians, $\hat{H}^* = \hat{H}$.

A. Time reversal symmetry condition for the self-energy

Let us recall the first Kadanoff–Baym equation,

$$[i\hbar\partial_z - h(z)]\,G_{[\hat{c}]}(zz') = \delta_\mathcal{C}(zz')\mathbb{1} + \int_\mathcal{C}\mathrm{d}\bar{z}\,\Sigma_{[G_{[\hat{c}]}]}(z\bar{z})G_{[\hat{c}]}(\bar{z}z'), \tag{26}$$

and take the complex conjugate of both sides,

$$[-i\hbar\partial_z - h(z)]\,G^*_{[\hat{c}]}(zz') = \delta_\mathcal{C}(zz')\mathbb{1} + \int_\mathcal{C}\mathrm{d}\bar{z}\,\Sigma^*_{[G_{[\hat{c}]}]}(z\bar{z})G^*_{[\hat{c}]}(\bar{z}z'), \tag{27}$$

where $G^*_{[\hat{c}]}(zz') = -G_{[\hat{c}^*]}(zz')$ and, therefore,

$$-[-i\hbar\partial_z - h(z)]\,G_{[\hat{c}^*]}(zz') = \delta_\mathcal{C}(zz')\mathbb{1} - \int_\mathcal{C}\mathrm{d}\bar{z}\,\Sigma^*_{[G_{[\hat{c}]}]}(z\bar{z})G_{[\hat{c}^*]}(\bar{z}z'). \tag{28}$$

This means that $G_{[\hat{c}^*]}$ solves the reversed equation

$$[-i\hbar\partial_z - h(z)]\,G_{[\hat{c}^*]}(zz') = -\delta_\mathcal{C}(zz')\mathbb{1} - \int_\mathcal{C}\mathrm{d}\bar{z}\,\Sigma^{z^{(\prime)}\to -z^{(\prime)}}_{[G_{[\hat{c}^*]}]}(z\bar{z})G_{[\hat{c}^*]}(\bar{z}z') \tag{29}$$

if the following holds true for the self-energy Σ:

$$\Sigma^*_{[G_{[\hat{c}]}]} = -\Sigma^{z^{(\prime)}\to -z^{(\prime)}}_{[G_{[\hat{c}^*]}]}, \tag{30}$$

where the superscript denotes that the sign of both z and z' is inverted.

B. Φ-derived self-energies

Consider the important case of self-energies that are expressed as a functional derivative of a scalar potential Φ. Complex conjugation of both sides of Eq. (7) yields

$$\Sigma^* = \frac{\delta \Phi^*[G]}{\delta G^*} = -\frac{\delta \Phi^*[G_{[\hat{c}]}]}{\delta G_{[\hat{c}^*]}}, \tag{31}$$

and, therefore, condition (30) for the self-energy translates into the following condition for the functional Φ:

$$\Phi^*[G_{[\hat{c}]}] = \Phi^{z^{(\prime)} \to -z^{(\prime)}}[G_{[\hat{c}^*]}]. \tag{32}$$

The rules governing the construction of valid functionals Φ dictate[11] that an nth-order diagram includes $2n$ contour-time integrals, $2n$ single-particle Green functions G, n interparticle interactions W, and a factor $(i\hbar)^n$. This means that

$$\Phi^*[G_{[\hat{c}]}] = (-1)^n \Phi[G_{[\hat{c}]}^*] = (-1)^n \Phi[-G_{[\hat{c}^*]}]$$
$$= (-1)^{3n} \Phi[G_{[\hat{c}^*]}] = \Phi^{z^{(\prime)} \to -z^{(\prime)}}[G_{[\hat{c}^*]}]. \tag{33}$$

The last equivalence is true because of the delta-functions in the n interparticle interactions and the $2n$ contour-time integrals that lead to $3n$ sign changes under time-reversal. Thus we have shown that any Φ-derivable NEGF approximation is time reversal invariant.

C. Example: Hartree–Fock self-energy

The simplest example of a Φ-derivable self-energy is Hartree–Fock. Nevertheless, it is instructive to explicitly verify that Σ^{HF} satisfies Eq. (30). To this end, we take the complex conjugate of both sides of Eq. (11),

$$\Sigma^{\mathrm{HF},*}(zz') = \pm (-i)\hbar \delta_{\mathcal{C}}(zz') \int_{\mathcal{C}} \mathrm{d}\bar{z}\, W(z\bar{z}) \left[-G^{(1)}_{[\hat{c}^*]}(\bar{z}\bar{z}^+) \right] + (-i)\hbar \left[-G^{(1)}_{[\hat{c}^*]}(zz') \right] W(z^+z')$$

$$= \pm i\hbar \delta_{\mathcal{C}}(zz') \int_{\mathcal{C}} \mathrm{d}\bar{z}\, W(z\bar{z})\, G^{(1)}_{[\hat{c}^*]}(\bar{z}\bar{z}^+) + i\hbar G^{(1)}_{[\hat{c}^*]}(zz')\, W(z^+z')$$

$$= \pm i\hbar \left[-\tilde{\delta}_{\mathcal{C}}(zz') \right] \int_{\mathcal{C}} \mathrm{d}(-\bar{z}) \left[-\tilde{W}(z\bar{z}) \right] G^{(1)}_{[\hat{c}^*]}(\bar{z}\bar{z}^+) + i\hbar G^{(1)}_{[\hat{c}^*]}(zz') \left[-\tilde{W}(z^+z') \right]$$

$$= -\Sigma^{\mathrm{HF},\, z^{(\prime)} \to -z^{(\prime)}}_{[G_{[\hat{c}^*]}]}, \tag{34}$$

where $\tilde{\delta} = \delta^{z^{(\prime)} \to -z^{(\prime)}}$ and $\tilde{W} = W^{z^{(\prime)} \to -z^{(\prime)}}$. Equivalently, it can be checked that Φ^{HF} satisfies Eq. (33),

$$\Phi^{\mathrm{HF},*} = \pm \frac{(-i)}{2} \int_{\mathcal{C}} \int_{\mathcal{C}} \mathrm{d}z_1 \mathrm{d}z_2 \left[-G_{[\hat{c}^*]}(z_1; z_1^+)\, W(z_1; z_2) \right] \left[-G_{[\hat{c}^*]}(z_2; z_2^+) \right]$$

$$+ \frac{(-i)}{2} \int_{\mathcal{C}} \int_{\mathcal{C}} \mathrm{d}z_1 \mathrm{d}z_2 \left[-G_{[\hat{c}^*]}(z_1; z_2^+) \right] W(z_1; z_2) \left[-G_{[\hat{c}^*]}(z_2; z_1^+) \right]$$

$$= \mp \frac{i}{2} \int_{\mathcal{C}} \int_{\mathcal{C}} \mathrm{d}z_1 \mathrm{d}z_2\, G_{[\hat{c}^*]}(z_1; z_1^+)\, W(z_1; z_2)\, G_{[\hat{c}^*]}(z_2; z_2^+)$$

$$- \frac{i}{2} \int_{\mathcal{C}} \int_{\mathcal{C}} \mathrm{d}z_1 \mathrm{d}z_2\, G_{[\hat{c}^*]}(z_1; z_2^+)\, W(z_1; z_2)\, G_{[\hat{c}^*]}(z_2; z_1^+)$$

$$= \pm \frac{i}{2} \int_{\mathcal{C}} \int_{\mathcal{C}} \mathrm{d}(-z_1)\mathrm{d}(-z_2)\, G_{[\hat{c}^*]}(z_1; z_1^+) \left[-\tilde{W}(z_1; z_2) \right] G_{[\hat{c}^*]}(z_2; z_2^+)$$

$$+ \frac{i}{2} \int_{\mathcal{C}} \int_{\mathcal{C}} \mathrm{d}(-z_1)\mathrm{d}(-z_2)\, G_{[\hat{c}^*]}(z_1; z_2^+) \left[-\tilde{W}(z_1; z_2) \right] G_{[\hat{c}^*]}(z_2; z_1^+)$$

$$= \Phi^{\mathrm{HF},\, z^{(\prime)} \to -z^{(\prime)}}[G_{[\hat{c}^*]}]. \tag{35}$$

VI. SUMMARY AND DISCUSSION

In this paper, it has been explicitly shown that the governing equations of the nonequilibrium Green functions formalism, the exact Martin–Schwinger hierarchy, and the associated quantum-kinetic equations are time reversible. This is in striking contrast to conventional Boltzmann-type kinetic equations, where irreversibility is introduced by the "Stoßzahlansatz" or similar procedures. The existence of generalized quantum kinetic equations that retain the reversibility of the underlying quantum-mechanical equations is known for a long time. Here we have presented a simple procedure that allows us to verify this property. It is based on use of the anti-unitary time-reversal operator $\hat{T}$ that translates the solution of the Schrödinger equation into the time-reversed equation.

We then turned to approximate solutions to the NEGF formalism that are based on approximations of the self-energy. We have demonstrated that any self-energy that is Φ-derivable is symmetric with respect to time reversal, as long as the (single-particle) Hamiltonian possesses an anti-unitary symmetry $\hat{H} = \hat{T}\hat{H}\hat{T}^{-1}$. These approximations include the well-known Hartree–Fock, second Born, and T-matrix approximations as well as many others.

Aside from the Φ-derivable self-energy approximations discussed above, in recent years, another class of approximations has attracted high interest: the generalized Kadanoff–Baym ansatz (GKBA). It replaces the two-time Green function by a single-time approximation. The GKBA was originally derived by Lipavský *et al.*,[12] and a rigorous derivation from density operator theory was given in Ref. 9. In a detailed investigation by Hermanns *et al.*,[15] it was shown that the GKBA retains the conservation properties of the original two-time equations if the approximation for the retarded Green function G^R is conserving as well. The same reasoning can be applied to the issue of time reversal invariance. The result is that use of a Φ-derivable approximation for G^R (which may differ from the approximation for the self-energy) will retain the time reversal properties of the original two-time approximation. Using the GKBA it is also straightforward to perform the transition to conventional "Boltzmann-type" kinetic equations that are known to be irreversible. The analysis shows that reversibility is lost upon performing the Markov limit and by neglecting initial correlations. This issue is studied in detail in Ref. 16.

An interesting outcome of our analysis is that Φ-derivable approximations for the self-energy are both conserving and time reversible. It remains to investigate whether this applies also to other classes of approximations. Finally, proof of time-reversibility of an approximation is also of a high practical value in numerical solutions of the KBE, as this provides a sensitive test for the numerical accuracy and convergence, e.g., Ref. 17.

[1] A.-M. Uimonen, E. Khosravi, A. Stan, G. Stefanucci, S. Kurth, R. van Leeuwen, and E. K. U. Gross, Phys. Rev. B **84**, 115103 (2011).
[2] P. Gartner, J. Seebeck, and F. Jahnke, Phys. Rev. B **73**, 115307 (2006).
[3] M. Lorke, T. R. Nielsen, J. Seebeck, P. Gartner, and F. Jahnke, Phys. Rev. B **73**, 085324 (2006).
[4] N. E. Dahlen and R. van Leeuwen, Phys. Rev. Lett. **98**, 153004 (2007).
[5] K. Balzer, S. Bauch, and M. Bonitz, Phys. Rev. A **81**, 022510 (2010).
[6] A. Rios, B. Barker, M. Buchler, and P. Danielewicz, Ann. Phys. **326**, 1274 (2011).
[7] M. Bonitz, T. Bornath, D. Kremp, M. Schlanges, and W. D. Kraeft, Contrib. Plasma Phys. **39**, 329 (1999).
[8] M. Garny, A. Kartavtsev, and A. Hohenegger, Ann. Phys. **328**, 26 (2013).
[9] M. Bonitz, *Quantum Kinetic Theory*, Volume 33 of Teubner-Texte zur Physik (B. G. Teubner, 1998) (Springer, 2016), 2nd ed.
[10] L. P. Kadanoff and G. Baym, *Quantum Statistical Mechanics* (Addison-Wesley Publishing Company, 1989).
[11] G. Stefanucci and R. van Leeuwen, *Nonequilibrium Many-Body Theory of Quantum Systems* (Cambridge University Press, 2013).
[12] P. Lipavský, V. Špička, and B. Velický, Phys. Rev. B **34**, 6933 (1986).
[13] F. Haake, *Quantum Signatures of Chaos* (Springer-Verlag, 2001).
[14] N. Schlünzen and M. Bonitz, Contrib. Plasma Phys. **56**, 5 (2016).
[15] S. Hermanns, N. Schlünzen, and M. Bonitz, Phys. Rev. B **90**, 125111 (2014).
[16] M. Bonitz, N. Schlünzen, and M. Scharnke, "Time reversal invariance of quantum kinetic equations II: Density operator formalism," Contrib. Plasma Phys. (submitted); e-print arXiv:1705.04566 (2017).
[17] N. Schlünzen, J.-P. Joost, and M. Bonitz, "Comment on "On the unphysical solutions of the Kadanoff–Baym equations in linear response: Correlation-induced homogeneous density-distribution and attractors"," Phys. Rev. B (submitted); e-print arXiv:1605.04588.

ORIGINAL ARTICLE

Time-reversal invariance of quantum kinetic equations II: Density operator formalism

Michael Bonitz | **Miriam Scharnke** | **Niclas Schlünzen***

Christian-Albrechts-University Kiel, Institute for Theoretical Physics and Astrophysics, Kiel, Germany

*Correspondence
Niclas Schlünzen, Christian-Albrechts-University Kiel, Institute for Theoretical Physics and Astrophysics, Leibnizstraße 15, 24098 Kiel, Germany.
Email: schluenzen@theo-physik.uni-kiel.de

Time-reversal symmetry is a fundamental property of many quantum mechanical systems. The relation between statistical physics and time reversal is subtle, and not all statistical theories conserve this particular symmetry—most notably, hydrodynamic equations and kinetic equations such as the Boltzmann equation. Here, we consider quantum kinetic generalizations of the Boltzmann equation using the method of reduced density operators, leading to the quantum generalization of the Bogolyubov-Born-Green-Kirkwood-Yvon (BBGKY) hierarchy. We demonstrate that all commonly used approximations, including Vlasov; Hartree-Fock; and the non-Markovian generalizations of the Landau, T-matrix, and Lenard-Balescu equations, are originally time-reversal invariant, and we formulate a general criterion for time reversibility of approximations to the quantum BBGKY hierarchy. Finally, we illustrate, through the example of the Born approximation, how irreversibility is introduced into quantum kinetic theory via the Markov limit, making the connection with the standard Boltzmann equation. This paper is a complement to paper I (Scharnke et al., *J. Math. Phys.*, **2017**, *58*, 061903), where the time-reversal invariance of quantum kinetic equations was analysed in the frame of the independent non-equilibrium Green functions formalism.

KEYWORDS
BBGKY-hierarchy, density operators, quantum dynamics, quantum kinetic theory, time reversibility

1 | INTRODUCTION

The time evolution of quantum many-body systems is of great interest currently in many areas of modern physics and chemistry, for example, in the context of laser–matter interaction, non-stationary transport, or dynamics following an interaction or confinement quench. The theoretical concepts used to study these dynamics are fairly broad and include (but are not limited to) wave function-based approaches, density functional theory, and quantum kinetic theory. The latter treats the time dynamics of the Wigner distribution or, more generally, the density matrix and captures the relaxation towards an equilibrium state (see, e.g., Refs. 1–4). The most famous example of a kinetic equation is the Boltzmann equation, along with quantum generalization, but this equation is known to not be applicable to the short-time dynamics. For this reason, generalized quantum kinetic equations were derived that are non-Markovian in nature (e.g., Refs. 1, 3, 5–9) and that have a number of remarkable properties, including the conservation of total energy, in contrast to kinetic energy conservation in the Boltzmann equation. It was recently demonstrated that these generalized quantum kinetic equations are well suited to study the relaxation dynamics of weakly and moderately correlated quantum systems, in very good agreement with experiments with ultra-cold atoms (e.g., Refs. 10, 11) and first-principle density matrix renormalization group methods.[12]

This success of generalized quantum kinetic equations warrants a more detailed theoretical analysis of their properties. Despite extensive work over recent decades, the aspect of time reversibility was not studied in detail. The relation between time-reversal symmetry and statistical physics is generally subtle, and not all statistical theories are invariant under time reversal, the most famous counterexample being the above-mentioned Boltzmann equation of classical statistical mechanics and its quantum generalization. In contrast, the non-Markovian generalizations of the Boltzmann equation, which can be used to improve the Boltzmann equation and reduce to the latter as a limiting case, are expected to be time-reversal invariant because of the underlying quantum mechanical system. But then, questions arise about where exactly time-reversal invariance is lost, how this is related to common many-body approximations, and so on.

Among the well-established approaches to derive these generalized quantum kinetic equations, we mention density operator concepts—see, for example, Ref. 3 for an overview—and non-equilibrium Green functions (NEGF). We recently analysed the question of time-reversal invariance within the NEGF formalism in paper I.[13] It is the goal of the present article to complement the NEGF results of that paper with an analysis of the independent and technically very different density operator formalism. In this paper, we briefly recall the derivation of the quantum Bogolyubov-Born-Green-Kirkwood-Yvon (BBGKY) hierarchy in section 2. As the BBGKY hierarchy can be directly derived from the Heisenberg equation (von Neumann equation) for the N-particle density operator, which is time-reversal invariant, it should be expected that this hierarchy has the same symmetry properties. Nevertheless, general proof is usually missing in the literature, for example, Refs. 1–4, and a successful procedure is presented in section 4. We then demonstrate, in section 5, that important standard closure approximations to the BBGKY hierarchy also preserve time-reversal symmetry. In section 6, we demonstrate, as an example, the transition from a time-reversal invariant generalized kinetic equation to an irreversible equation of the Boltzmann type by performing the Markov limit and the weakening of initial conditions. We conclude with a summary in section 7.

2 | BBGKY HIERARCHY FOR THE REDUCED-DENSITY OPERATORS

Here, we briefly recall the basic equations of the density operator theory following Ref. 3. The generic Hamiltonian of an interacting N-particle system is given by a sum of a single particle and an interaction term

$$\widehat{H} = \sum_{i=1}^{N} \widehat{H}_i + \sum_{1 \le i < j \le N} \widehat{V}_{ij}, \tag{1}$$

$$\widehat{H}_i(t) = \frac{\widehat{p}_i^2}{2m_i} + \widehat{U}_i(t). \tag{2}$$

The solutions of the time-dependent N-particle Schrödinger equation with this Hamiltonian are denoted by $|\psi^{(1)}\rangle \ldots |\psi^{(M)}\rangle$ and form a complete orthonormal basis:

$$\langle \psi^{(k)}|\psi^{(l)}\rangle = \delta_{k,l}, \tag{3}$$

$$\sum_{k=1}^{M} |\psi^{(k)}\rangle\langle \psi^{(k)}| = 1. \tag{4}$$

The central quantity for the construction of quantum kinetic equations is the N-particle density operator:

$$\widehat{\rho} = \sum_{k=1}^{M} W_k |\psi^{(k)}\rangle\langle \psi^{(k)}|, \tag{5}$$

where W_k are positive real probabilities, and $0 \le W_k \le 1$, with $\sum_{k=1}^{M} W_k = 1$, and we restrict ourselves to the case of time-independent probabilities. The density operator obeys the von Neumann equation

$$i\hbar \frac{\partial}{\partial t} \widehat{\rho} - [\widehat{H}, \widehat{\rho}] = 0. \tag{6}$$

In order to derive the quantum BBGKY hierarchy, we introduce the reduced s-particle density operator ($s = 1 \ldots N - 1$)

$$\widehat{F}_{1\ldots s} = C_s^N \text{Tr}_{s+1\ldots N} \, \widehat{\rho}, \qquad \text{Tr}_{1\ldots s} \widehat{F}_{1\ldots s} = C_s^N, \tag{7}$$

where $C_s^N = \frac{N!}{(N-s)!}$. The equations of motion for the reduced density operators follow directly from the von Neumann Equation 6 and the definition 7:

$$i\hbar \frac{\partial}{\partial t} \widehat{F}_{1\ldots s} - [\widehat{H}_{1\ldots s}, \widehat{F}_{1\ldots s}] = \text{Tr}_{s+1} \sum_{i=1}^{s} [\widehat{V}_{i,s+1}, \widehat{F}_{1\ldots s+1}], \tag{8}$$

where $\widehat{H}_{1\dots s}$ is the s-particle Hamilton operator, which follows from the N-particle Hamiltonian, Equation 1, by substituting $N \to s$. The system 8 with $s = 1\dots N-1$ constitutes the quantum generalization of the BBGKY hierarchy.

In order to specify decoupling approximations to the hierarchy, we introduce the correlation operators:

$$\widehat{F}_{12} = \widehat{F}_1\widehat{F}_2 + \widehat{g}_{12}, \tag{9}$$

$$\widehat{F}_{123} = \widehat{F}_1\widehat{F}_2\widehat{F}_3 + \widehat{g}_{23}\widehat{F}_1 + \widehat{g}_{13}\widehat{F}_2 + \widehat{g}_{12}\widehat{F}_3 + \widehat{g}_{123}, \tag{10}$$

where $\widehat{g}_{12}$ describes pair correlations, $\widehat{g}_{123}$ three-particle correlations, and so on, which are due to interaction effects beyond the mean field. In contrast, mean field (Vlasov, Hartree-Fock) terms are contained in the products of single-particle density operators and appear via the mean field potential $\widehat{U}_i^{\mathrm{H}} = \mathrm{Tr}_j\widehat{V}_{ij}\widehat{F}_j$, leading to the renormalization of the single-particle and two-particle Hamiltonians $\widehat{H}_i \to \overline{\widehat{H}}_i = \widehat{H}_i + \widehat{U}_i^{\mathrm{H}}, \widehat{H}_{ij} \to \overline{\widehat{H}}_{ij} = \overline{\widehat{H}}_i + \overline{\widehat{H}}_j + \widehat{V}_{ij}$, and so on. The BBGKY hierarchy, rewritten in terms of the correlation operators, then becomes:

$$i\hbar\frac{\partial}{\partial t}\widehat{F}_1 - [\overline{\widehat{H}}_1, \widehat{F}_1] = \mathrm{Tr}_2[\widehat{V}_{12}, \widehat{g}_{12}], \tag{11}$$

$$i\hbar\frac{\partial}{\partial t}\widehat{g}_{12} - [\overline{\widehat{H}}_{12}, \widehat{g}_{12}] = [\widehat{V}_{12}, \widehat{F}_1\widehat{F}_2] +$$
$$+ \mathrm{Tr}_3\{[\widehat{V}_{13}, \widehat{F}_1\widehat{g}_{23}] + [\widehat{V}_{23}, \widehat{F}_2\widehat{g}_{13}] + [\widehat{V}_{13} + \widehat{V}_{23}, \widehat{g}_{123}]\}, \tag{12}$$

and this is also applicable for the higher-order operators. Standard many-body approximations are easily identified from Equations 11 and 12, cf. for example, Ref. 3:

1. The *mean field (Hartree or Hartree-Fock) approximation* that leads to the non-linear Vlasov equation (or to the time-dependent Hartree-Fock) follows from letting $\widehat{g}_{12} \to 0$ in Equation 11.
2. The *second-order Born approximation,* leading to the Landau equation, follows from neglecting $\widehat{V}_{12}$ in $\overline{\widehat{H}}_{12}$ on the left and $\widehat{g}_{23} = \widehat{g}_{13} = \widehat{g}_{123} \to 0$ on the right side in Equation 12.
3. The *T-matrix or ladder approximation* follows from setting $\widehat{g}_{23} = \widehat{g}_{13} = \widehat{g}_{123} \to 0$ on the right side in Equation 12.
4. The *polarization approximation* that is related to the GW approximation of Green functions theory and leads to the Lenard-Balescu equation follows from neglecting $\widehat{V}_{12}$ in $\overline{\widehat{H}}_{12}$ on the left and $\widehat{g}_{123} \to 0$ on the right side in Equation 12.
5. The *screened ladder approximation* that is related to the parquet approximation (or "FLEX") in Green functions theory follows from $\widehat{g}_{123} \to 0$ on the right side in Equation 12.

In a similar manner, higher-order decoupling schemes for the BBGKY hierarchy are introduced on the level of the equation of motion for g_{123}. Typically, approximations are derived by omitting terms of the form $[\widehat{A}, \widehat{B}]$, where $\widehat{A}$ is a contribution to the full Hamiltonian 1 (typically an interaction potential), and $\widehat{B}$ are contributions to the cluster expansion 10. This will be discussed in more detail in section 5.

Finally, we note that the cluster expansion 10 is written without an explicit account of the spin statistics. A direct (anti-)symmetrization of the hierarchy, for the case of bosons (fermions), is straightforwardly achieved by replacing the density operators according to[14] (Figure 1)

$$\widehat{F}_{1\dots s} \to \widehat{F}_{1\dots s}\Lambda_{1\dots s}^{\pm}, \tag{13}$$

where the (anti-)symmetrization operators are given by

$$\Lambda_{12}^{\pm} = 1 \pm P_{12},$$
$$\Lambda_{123}^{\pm} = 1 \pm P_{12} \pm P_{13} \pm P_{23} + P_{12}P_{13} + P_{12}P_{23},$$

and so on, where P_{ij} is the permutation operator of particles i and j, and the upper (lower) sign refers to bosons (fermions). (Anti-)symmetrization is then achieved by applying the s-particle operator $\Lambda_{1\dots s}^{\pm}$ to the s-th equation of the BBGKY hierarchy, term by term. We illustrate this procedure for the (anti-)symmetrization of the Hartree mean field term on the l.h.s. of
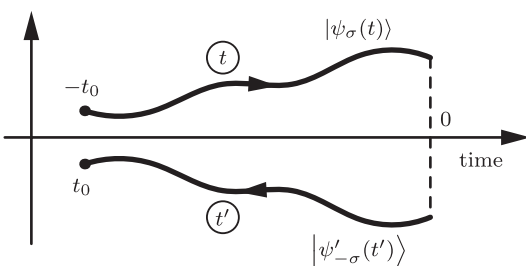
FIGURE 1 Illustration of the forward and backward solutions of the time-dependent Schrödinger equation. Upper trajectory: forward solution $|\psi_\sigma(t)\rangle$. Lower trajectory: backward solution $|\psi'_{-\sigma}(t')\rangle$. Note that we choose the limits of the forward trajectory as $t = -t_0$ and $t = 0$, whereas the backward one runs from $t' = 0$ to $t' = t_0$. The time reversal occurs at $t = 0$

Equation 11, which is obtained by replacing $\widehat{F}_1\widehat{F}_2 \rightarrow \widehat{F}_1\widehat{F}_2\Lambda^{\pm}_{12}$:

$$[\widehat{U}^H_1, \widehat{F}_1] \rightarrow [\widehat{U}^{HF}_1, \widehat{F}_1] = \mathrm{Tr}_2[\widehat{V}_{12}, \widehat{F}_1\widehat{F}_2\Lambda^{\pm}_{12}],$$

$$\text{with} \quad \widehat{U}^{HF}_i = \mathrm{Tr}_j \widehat{V}_{ij}\widehat{F}_j\Lambda^{\pm}_{ij}, \tag{14}$$

The full (anti-)symmetrized equations are given in Ref. [3]. However, we will not need these equations below. This is because the (anti-)symmetrization operators commute with the time-reversal operator $\widehat{T}$, cf. section 3. Therefore, (anti-)symmetrization does not affect the time-reversal properties of the resulting equations and approximations, allowing us to restrict ourselves to the simpler Equations 11, 12 in this study.

3 | TIME-REVERSAL INVARIANCE IN QUANTUM MANY-BODY THEORY

3.1 | Time-reversal invariance of the equations of motion of quantum mechanics

Let us recall the concept of time reversibility as was discussed in Ref. 13; for text book discussions, see Refs. 15, 16. Consider the time-dependent N-particle Schrödinger equation on an arbitrary finite interval of time, $-t_0 \leq t \leq 0$, with a given initial condition $|\psi_0\rangle$:

$$i\hbar\partial_t \mid \psi(t)\rangle = \widehat{H} \mid \psi(t)\rangle \ , \tag{15}$$

$$\mid \psi(-t_0)\rangle = \mid \psi_0\rangle. \tag{16}$$

This equation is called time-reversal invariant if:

i. for any solution $|\psi(t)\rangle$, there exists another solution $|\psi'(t')\rangle$ with $t' \in [0, t_0]$ and $t' = -t$ and
ii. there exists a unique relation between the two:

$$\mid \psi'(t')\rangle = \widehat{T} \mid \psi(t)\rangle, \tag{17}$$

for which the time-reversal operator $\widehat{T}$ will be specified below. Both solutions describe the same physical state; therefore, the associated probability densities must coincide:

$$||\psi_\sigma(t)\rangle|^2 = ||\psi'_{-\sigma}(-t)\rangle|^2, \tag{18}$$

where we indicated explicitly that, on the backward trajectory $|\psi'(t')\rangle$, the spin projections σ of all particles are inverted. Analogously, momenta and angular momenta (their eigenvalues) are inverted, as in classical mechanics. To motivate the choice of $\widehat{T}$, we rewrite the Schrödinger dynamics 15 in terms of the standard time-evolution operator $\widehat{U}$:

$$\mid \psi(t)\rangle = \widehat{U}(t, -t_0) \mid \psi_0\rangle, \tag{19}$$

$$\widehat{U}(t, t') = T e^{-\frac{i}{\hbar}\int_{t'}^{t} d\bar{t}\widehat{H}(\bar{t})}. \tag{20}$$

Backward evolution in time is, obviously, achieved by the complex conjugation of U. This brings us to the following choice of the time-reversal operator $\widehat{T}$, which is originally due to Wigner[17]:

$\widehat{T}$ is an anti-unitary operator, that is, $\widehat{T} = \widehat{K}\widehat{W}$, where $\widehat{W}$ is a unitary operator that assures the spin flip in Equation 18, and $\widehat{K}$ performs complex conjugation. Here, we will not treat the spin explicitly and will, therefore, use $\widehat{W} \rightarrow 1$. As a result, Equation 17 becomes:

$$\mid \psi'(t')\rangle = \widehat{T} \mid \psi(t)\rangle = \mid \psi(-t)\rangle^*, \tag{21}$$

An operator $\widehat{A}'$ acting on the time-reversed solution is obtained from the original operator $\widehat{A}$ via

$$\widehat{A}' = \widehat{T}\widehat{A}\widehat{T}^{-1} \tag{22}$$

$\widehat{T}$ is anti-linear, that is,

$$\widehat{T}\{|\psi_1\rangle + i|\psi_2\rangle\} = \widehat{T} \mid \psi_1\rangle - i\widehat{T} \mid \psi_2\rangle, \tag{23}$$

$$\widehat{T}\{\widehat{A} + i\widehat{B}\}\widehat{T}^{-1} = \widehat{T}\widehat{A}\widehat{T}^{-1} - i\widehat{T}\widehat{B}\widehat{T}^{-1}, \tag{24}$$

for any two states and any two operators.
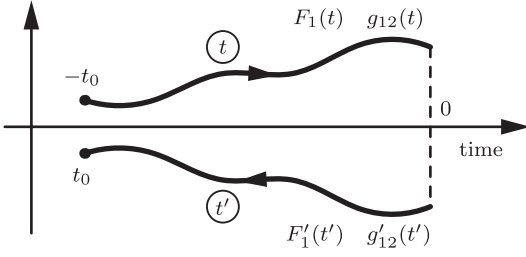
FIGURE 2 Illustration of the forward and backward solutions of the quantum BBGKY hierarchy. Upper trajectory: forward solution $\{F_1(t), g_{12}(t), \dots\}$ on the interval $-t_0 \le t \le 0$. Lower trajectory: backward solution $\{F'_1(t'), g'_{12}(t'), \dots\}$ on the same interval with $0 \le t' \le t_0$, Time reversal occurs at $t = 0$, cf. Figure 1

As a test, we apply the operator $\widehat{T}$ to both sides of Equation 15:

$$\widehat{T} i\hbar\partial_t \mid \psi\rangle = \widehat{T}\widehat{H} \mid \psi\rangle$$

$$\Longleftrightarrow \quad \underbrace{-i\hbar\partial_t \, \widehat{T} \mid \psi\rangle}_{i\hbar\partial_{(-t)}} = \widehat{T}\widehat{H}\widehat{T}^{-1}\widehat{T} \mid \psi\rangle \ , \tag{25}$$

which means that, indeed, $\mid \psi'\rangle = \widehat{T} \mid \psi\rangle$ solves the time-reversed Schrödinger equation

$$i\hbar\partial_{(-t)} \mid \psi'\rangle = \widehat{H} \mid \psi'\rangle \tag{26}$$

if and only if

$$\widehat{H} = \widehat{T}\widehat{H}\widehat{T}^{-1}. \tag{27}$$

This is equivalent to $[\widehat{T}, \widehat{H}] = 0$, and we obtain a result found in many text books. However, we will see in section 4 that condition 27 is, in fact, not sufficient.

Next, we find the time-reversed values of the coordinate and momentum operators using the coordinate representation:

$$\widehat{r}' = \widehat{T}\widehat{r}\widehat{T}^{-1} = \widehat{r}\widehat{T}\widehat{T}^{-1} = \widehat{r}, \tag{28}$$

as $\widehat{r}$ is real, and

$$\widehat{p}' = \widehat{T}\widehat{p}\widehat{T}^{-1} = -\widehat{p}, \tag{29}$$

as $\widehat{p} = \frac{\hbar}{i}\nabla$ is purely imaginary. This is again consistent with the time-reversal properties of classical mechanics. Furthermore, Equation 29 also shows that relation 27 excludes certain classes of Hamiltonians, such as those containing odd powers of the momentum (Figure 2).

4 | TIME-REVERSAL INVARIANCE OF THE BBGKY HIERARCHY

The N-particle density operator $\widehat{\rho}$, defined by Equation 5, extends the concept of the time-dependent Schrödinger equation to a thermodynamic ensemble while containing the dynamics of a pure state $\mid \psi^{(l)}\rangle$ as a special case, when $W_k = \delta_{k,l}$.

Let us now analyse the time-reversal symmetry of the von Neumann Equation 6 by applying the $\widehat{T}$ operator, introduced above, from the left and its inverse from the right:

$$\widehat{T} i\hbar\partial_t\widehat{\rho}\widehat{T}^{-1} = \widehat{T}(\widehat{\rho}\widehat{H} - \widehat{H}\widehat{\rho})\widehat{T}^{-1}$$

$$-i\hbar\partial_t\widehat{T}\widehat{\rho}\widehat{T}^{-1} = \widehat{T}\widehat{\rho}\widehat{T}^{-1}\widehat{T}\widehat{H}\widehat{T}^{-1} - \widehat{T}\widehat{H}\widehat{T}^{-1}\widehat{T}\widehat{\rho}\widehat{T}^{-1} \ ,$$

which is equivalent to the time-reversed equation

$$i\hbar\partial_{-t}\widehat{\rho}' = [\widehat{\rho}', \widehat{H}], \tag{30}$$

again, if and only if condition 27 is fulfilled, as in the case of the Schrödinger equation. Here, we introduced the solution of the time-reversed von Neumann equation:

$$\widehat{\rho}'(-t) = \widehat{T}\widehat{\rho}(t)\widehat{T}^{-1}$$

$$= \sum_k W_k\widehat{T} \mid \psi^{(k)}(t)\rangle\langle\psi^{(k)}(t) \mid \widehat{T}^{-1}$$

$$= \sum_k W_k \mid \psi^{(k)'}(-t)\rangle\langle\psi^{(k)'}(-t) \mid, \tag{31}$$

which is consistent with the definition of the density operator 5 in terms of the solutions of the time-reversed Schrödinger equation. Let us now return to the BBGKY hierarchy 8. Its time reversibility follows immediately from the reversibility of the von Neumann Equation 6 that was demonstrated above. Nevertheless, it is instructive to verify the time reversibility explicitly

as this will be useful for the analysis of approximations to the hierarchy in section 5. Applying the operators $\widehat{T}$ and $\widehat{T}^{-1}$ from the left and right, respectively, we obtain:

$$i\hbar\frac{\partial}{\partial(-t)}\widehat{F}'_{1\ldots s} - [\widehat{H}'_{1\ldots s}(-t), \widehat{F}'_{1\ldots s}(-t)]$$

$$= \text{Tr}_{s+1}\sum_{i=1}^{s}[\widehat{V}'_{i,s+1}, \widehat{F}'_{1\ldots s+1}(-t)], \tag{32}$$

where we used the fact that the definition 7 is a real linear operation

$$\widehat{T}\widehat{F}_{1\ldots s}(t)\widehat{T}^{-1} = C_s^N \text{Tr}_{s+1\ldots N}\widehat{T}\widehat{\rho}(t)\widehat{T}^{-1} =$$

$$= C_s^N \text{Tr}_{s+1\ldots N}\widehat{\rho}'(-t) = \widehat{F}'_{1\ldots s}(-t), \tag{33}$$

such that $\widehat{F}'_{1\ldots s}(-t)$ is, indeed, the solution of the time-reversed hierarchy equation if the following conditions hold:

$$\widehat{H}'_{1\ldots s}(-t) \equiv \widehat{T}\widehat{H}_{1\ldots s}(t)\widehat{T}^{-1} = \widehat{H}_{1\ldots s}(t), \tag{34}$$

$$\widehat{V}'_{ij} \equiv \widehat{T}\widehat{V}_{ij}\widehat{T}^{-1} = \widehat{V}_{ij}, \tag{35}$$

for all $i \neq j \in [1, N]$ and all $s = 1\ldots N-1$, simultaneously. While for typical distance-dependent real potentials, Equation 35 is always fulfilled, Equation 34 places clear restrictions on the contributions to the system Hamiltonian.

Based on these results, we conclude that time-reversal invariance of the exact BBGKY hierarchy requires not only the time reversal symmetry of the full N-particle Hamiltonian 1, as in the case of the Schrödinger equation, cf. condition 27, but also that each of the contributions to the Hamiltonian have to obey this symmetry separately. This is, of course, a much stronger condition than 27.

5 | TIME-REVERSAL INVARIANCE OF APPROXIMATIONS TO THE HIERARCHY

As the solution of the BBGKY hierarchy is usually possible only with suitable approximations, the important question is which approximations retain the time-reversal properties of the exact system. We subsequently demonstrate that a very broad class of approximations retains time-reversal invariance. Therefore, we will restrict ourselves to real-valued Hamiltonians, $\widehat{H}^* = \widehat{H}$.

We start by rewriting the first two equations of the BBGKY hierarchy in terms of the correlation operators, Equations 11, 12, in a different form:

$$i\hbar\frac{\partial}{\partial t}\widehat{F}_1 = \widehat{J}_1 = \widehat{J}_1^{\text{app}} + \widehat{O}_1, \tag{36}$$

$$i\hbar\frac{\partial}{\partial t}\widehat{g}_{12} = \widehat{J}_{12} = \widehat{J}_{12}^{\text{app}} + \widehat{O}_{12}, \tag{37}$$

where $\widehat{J}_1$ and $\widehat{J}_{12}$ comprise all the remaining terms in Equations 11, 12. A decoupling approximation to the hierarchy can then be defined by specifying approximate expressions, $\widehat{J}_1^{\text{app}}$ and $\widehat{J}_{12}^{\text{app}}$, where the remainders, $\widehat{O}_1$ and $\widehat{O}_{12}$, are being omitted. The same procedure can be applied to decoupling approximations on the level of the third or higher-order hierarchy equations. To answer the question of whether a given decoupling approximation, $\widehat{J}^{\text{app}} = \{\widehat{J}_1^{\text{app}}, \widehat{J}_{12}^{\text{app}}, \ldots\}$, is time reversible, we either have to analyse the resulting equations directly or, alternatively, investigate the time-reversal properties of the omitted operators, $\widehat{O} = \{\widehat{O}_1, \widehat{O}_{12}, \ldots\}$, as the exact equations are known to be time-reversal invariant. Here, it will be advantageous to use the latter approach.

In the following, we answer this question for the approximations that were introduced in section 2, starting by specifying the corresponding operators $\widehat{O}$.

1. The *mean field approximation* is given by the choice $\widehat{O} \equiv \widehat{O}_1^{\text{HF}} = \text{Tr}_2[\widehat{V}_{12}, \widehat{g}_{12}]$.
2. The *second-order Born approximation* is given by $\widehat{O} \equiv \widehat{O}_{12}^{\text{2B}} = [\widehat{V}_{12}, \widehat{g}_{12}] + Tr_3\{[\widehat{V}_{13}, \widehat{F}_1\widehat{g}_{23}] + [\widehat{V}_{23}, \widehat{F}_2\widehat{g}_{13}] + [\widehat{V}_{13} + \widehat{V}_{23}, \widehat{g}_{123}]\}$.
3. The *T-matrix or ladder approximation* is given by $\widehat{O} \equiv \widehat{O}_{12}^{\text{T}} = Tr_3\{[\widehat{V}_{13}, \widehat{F}_1\widehat{g}_{23}] + [\widehat{V}_{23}, \widehat{F}_2\widehat{g}_{13}] + [\widehat{V}_{13} + \widehat{V}_{23}, \widehat{g}_{123}]\}$.
4. The *polarization approximation* is given by $\widehat{O} \equiv \widehat{O}_{12}^{\text{POL}} = [\widehat{V}_{12}, \widehat{g}_{12}] + \text{Tr}_3[\widehat{V}_{13} + \widehat{V}_{23}, \widehat{g}_{123}]$.
5. The *screened ladder approximation* is given by $\widehat{O} \equiv \widehat{O}_{12}^{\text{SCT}} = \text{Tr}_3[\widehat{V}_{13} + \widehat{V}_{23}, \widehat{g}_{123}]$.

Aside from their different physical characters, all these approximations have a common mathematical structure. They are given by a functional relation of the form

$$\widehat{O}(t) = R[\widehat{V}_{ij}, \widehat{F}_k(t), \widehat{g}_{lm}(t), \widehat{g}_{nop}(t), \ldots], \qquad R \in \mathcal{R}, \tag{38}$$

where the indices are i, j, k, l, m, n, o, $p \in 1 \ldots N$, and R is a real function. The properties of expression 38 under time reversal are easily obtained. First, due to its real character, the functional form of R obviously does not change, that is, $\widehat{T}R\widehat{T}^{-1} = R$. Second, the properties of the arguments of R are known: as we have discussed above, standard pair potentials are always time-reversal invariant, $\widehat{T}\widehat{V}_{ij}\widehat{T}^{-1} = \widehat{V}_{ij}$. Next, the time-reversal invariance of the single-particle density operator was demonstrated in Equation 33. Finally, based on property 33, together with the cluster expansion $(9, 10, \ldots)$, which is a real functional relation, we easily conclude (iteratively) that all correlation operators are time-reversal invariant:

$$\widehat{T}\widehat{g}_{1\ldots s}(t)\widehat{T}^{-1} = \widehat{g}_{1\ldots s}(-t), \qquad s = 1 \ldots N - 1. \tag{39}$$

Summarizing these results, we conclude that the operator 38 is time-reversal invariant:

$$\widehat{T}\widehat{O}(t)\widehat{T}^{-1} = \widehat{O}(-t). \tag{40}$$

This means that each of the approximations that were listed above (and the corresponding non-Markovian quantum kinetic equations)—time-dependent Hartree-Fock (non-linear quantum Vlasov equation), second-order Born approximation (quantum Landau equation), T-matrix (quantum Boltzmann equation), polarization approximation (quantum Lenárd-Balescu equation), and the screened ladder approximation—are time-reversal invariant. We emphasize that condition 38 is much more general than those approximations, including a broad range of decoupling schemes of the hierarchy that were proposed in the literature.

6 | BREAKING THE TIME-REVERSAL SYMMETRY: EXAMPLE OF THE BORN APPROXIMATION

The emergence of time irreversibility, starting from reversible quantum dynamics, has been discussed in great detail since the appearance of the Boltzmann kinetic Equation 18. Using our formalism, we can trace this emergence particularly clearly for the case of the quantum Landau equation that corresponds to the following first two hierarchy equations:

$$i\hbar \frac{\partial}{\partial t}\widehat{F}_1 - [\overline{\widehat{H}}_1, \widehat{F}_1] = \mathrm{Tr}_2[\widehat{V}_{12}, \widehat{g}_{12}], \tag{41}$$

$$i\hbar \frac{\partial}{\partial t}\widehat{g}_{12} - [\overline{\widehat{H}}_{12}, \widehat{g}_{12}] = [\widehat{V}_{12}, \widehat{F}_1\widehat{F}_2]^{\pm} = \widehat{J}_{12}^{2B}(t), \tag{42}$$

$$\widehat{F}_1(-t_0) = \widehat{F}_1^0, \qquad \widehat{g}_{12}(-t_0) = \widehat{g}_{12}^0, \qquad t \in [-t_0, 0], \tag{43}$$

where we added the initial conditions for both operators. These coupled, time-local equations can be numerically solved directly. The alternative route that leads to a quantum kinetic equation consists of, first, formally solving the equation for $\widehat{g}_{12}$ analytically and then inserting the result into the r.h.s. of Equation 41. This is the approach we will use here. The solution of the initial value problem 41–43 is easily found[3] and consists of an initial value term (solution of the homogeneous equation) and a collision term

$$\widehat{g}_{12}(t) = \widehat{g}_{12}^{\mathrm{IC}}(t) + \widehat{g}_{12}^{\mathrm{coll}}(t), \tag{44}$$

$$\widehat{g}_{12}^{\mathrm{IC}}(t) = \widehat{U}_{12}^0(t, -t_0)\widehat{g}_{12}^0\widehat{U}_{12}^{0\dagger}(t, -t_0), \tag{45}$$

$$\widehat{g}_{12}^{\mathrm{coll}}(t) = \frac{1}{i\hbar} \int_{-t_0}^{t} \mathrm{d}\bar{t}\,\widehat{U}_{12}^0(t, \bar{t})\widehat{J}_{12}^0(\bar{t})\widehat{U}_{12}^{0\dagger}(t, \bar{t}), \tag{46}$$

where the two-particle propagator factorizes into single-particle Hartree-Fock propagators, $\widehat{U}_{12}^0(t, t') = \widehat{U}_1(t, t')\widehat{U}_2(t, t')$, with

$$\left\{ i\hbar \frac{\partial}{\partial t} - \overline{\widehat{H}}_1(t) \right\} \widehat{U}_1(t, t') = 0, \qquad \widehat{U}_1(t, t) = 1, \tag{47}$$

the solution for which is analogous to that of the Schrödinger equation, cf. Equation 20. The quantum kinetic equation that is associated with the solution 44 contains two collision integrals: the first, involving $\widehat{g}_{12}^{\mathrm{IC}}(t)$, is due to correlations existing in the system at the initial time moment, whereas the second is due to correlations being formed as a result of two-particle collisions while being absent at the initial moment. The characteristic feature of the latter collision integral is its non-Markovian character (i.e., the presence of the time integral), which is in striking contrast to the traditional Boltzmann equation that involves only distribution functions taken at the current time t.

To analyse the transition from the former to the latter and, thereby, from time reversibility to irreversibility, we switch from the operator form of the solution 44 to an instantaneous Hartree-Fock basis $\{|n\rangle\}$, given by $\hat{\bar{H}}_1 \mid n\rangle = E_n \mid n\rangle$. Then, the first hierarchy Equation 41 becomes

$$i\hbar\frac{\partial}{\partial t}F_{n_1,n_{1'}} - (E_{n_1} - E_{n'_1})F_{n_1,n_{1'}} =$$

$$= \sum_{n_2}\sum_{\bar{n}_1\bar{n}_2}\{V_{n,\bar{n}}g_{\bar{n},n'} - g_{n,\bar{n}}V_{\bar{n},n'}\}\Bigg|_{n_{2'}=n_2}, \tag{48}$$

where we introduced the short notations $n \equiv (n_1, n_2)$, $n' \equiv (n_1', n_2')$, and $\bar{n} \equiv (\bar{n}_1, \bar{n}_2)$. This is a generalized quantum kinetic equation that describes the probability of transitions between different single-particle states (dynamics of $F_{n_1,n_{1'}}$ with $n_1 \neq n_{1'}$), as well as the dynamics of the occupations of state n_1 (given by $F_{n_1} \equiv F_{n_1,n_1}$). Here, we focus on the latter as it is directly related to the evolution towards an equilibrium state. Furthermore, the emergence of irreversibility in the dynamics of F_n is sufficient for the transition of the whole system of coupled equations from reversible to irreversible.

The corresponding dynamics of the diagonal matrix elements are given by

$$i\hbar\frac{\partial}{\partial t}F_{n_1}(t) = 2i\sum_{n_2}\sum_{\bar{n}_1\bar{n}_2}V_{n,\bar{n}}Im\ g_{\bar{n},n}(t), \tag{49}$$

where we used $g_{n,n'} = g^*_{n',n}$ and $V_{n,n'} = V_{n',n}$. To compute $Im\,g_{\bar{n},n}(t)$, we first write down the solution of Equation 47, which is given by a diagonal matrix:

$$\langle n_1|\hat{U}(tt')|n'_1\rangle = U_{n_1}(t - t')\delta_{n_1,n_{1'}},$$

$$U_{n_1}(\tau) = e^{-\frac{i}{\hbar}E_{n_1}\tau}, \tag{50}$$

and the matrix of the pair correlation operator 44 becomes

$$Im\ g_{n,n'}(t) = Im\ g^{IC}_{n,n'}(t) + Im\ g^{coll}_{n,n'}(t), \tag{51}$$

$$Im\ g^{IC}_{n,n'}(t) = Im\{e^{-i\omega_{n,n'}[t-(-t_0)]}g^0_{n,n'}\} \tag{52}$$

$$Im\ g^{coll}_{n,n'}(t) = -\frac{1}{\hbar}\int_{-t_0}^{t}d\bar{t}\cos[\omega_{n,n'}(t - \bar{t})]J^{2B}_{n,n'}(\bar{t}) \tag{53}$$

where we defined $\hbar\omega_{n,n'} \equiv E_{n1} + E_{n2} - E_{n1'} - E_{n2'}$ and used $J^{2B*}_{n,n'} = J^{2B}_{n,n'}$.

Let us now investigate the time-reversal symmetry of the kinetic Equation 48, that is, we apply the time-reversal operators $\hat{T}$ and $\hat{T}^{-1}$ from the left and right, respectively, as before:

$$i\hbar\frac{\partial}{\partial(-t)}F'_{n_1,n_{1'}}(t) - (E_{n_1} - E_{n'_1})F'_{n_1,n_{1'}}(t) =$$

$$= \sum_{n_2}\sum_{\bar{n}_1\bar{n}_2}\{V_{n,\bar{n}}g'_{\bar{n},n'}(t) - g'_{n,\bar{n}}(t)V_{\bar{n},n'}\}\Bigg|_{n_{2'}=n_2},$$

where F' is the solution of the time-reversed equation. Time-reversal symmetry again requires fulfilment of $F'_{n_1,n_{1'}}(t) \equiv \hat{T}F_{n_1,n_{1'}}(t)\hat{T}^{-1} = F_{n_1,n_{1'}}(-t)$ and is observed only when the time-reversed solution of the second equation obeys

$$Im\ g'_{n,n'}(t) \equiv \hat{T}Im\ g_{n_1,n_{1'}}(t)\hat{T}^{-1} = Im\ g_{n,n'}(-t). \tag{54}$$

This is easily verified by writing down the solution $g'(t)$ noticing that application of the operators $\hat{T}$ and $\hat{T}^{-1}$, from the left and right, to the second hierarchy equation again changes the sign of the time derivative, which is equivalent to replacing $\omega_{n,n'} \rightarrow -\omega_{n,n'}$, and $J^{2B}_{n,n'} \rightarrow J^{2B}_{n,n'}$, and the solution 52, 53 changes into

$$Img^{IC'}_{n,n'}(t) = Im\{e^{+i\omega_{n,n'}[t-(-t_0)]}g^0_{n,n'}\} \tag{55}$$

$$Im\ g^{coll'}_{n,n'}(t) = -\frac{1}{\hbar}\int_{-t_0}^{t}d\bar{t}\cos[-\omega_{n,n'}(t - \bar{t})][-J^{2B}_{n,n'}(\bar{t})]$$

$$= -\frac{1}{\hbar}\int_{-t}^{t_0}d\bar{t}\cos[\omega_{n,n'}(-t - \bar{t})]J^{2B}_{n,n'}(-\bar{t}). \tag{56}$$

It is obvious that the solutions g and g' fulfil 54, which can be seen by changing $(t, -t_0) \rightarrow (-t, t_0)$, in $g^{IC'}$, and $(t, -t_0, \bar{t}) \rightarrow (-t, t_0, -\bar{t})$, in $g^{coll'}$.

The mathematical transition to the conventional (quantum) Boltzmann collision integral that contains a delta function, $\delta(E_{n_1} + E_{n_2} - E_{n_1'} - E_{n_2'})$, of the single-particle energies before and after the collision involves three steps:

Decoupling of the time scales of the single-particle and two-particle dynamics. The argument here is that, during a collision, when the two-particle correlations are formed (during the correlation time τ_{cor}), the occupation of the single-particle states changes only weakly. Its relaxation towards an equilibrium distribution involves many collisions and, therefore, requires a relaxation time that is much larger

$$t_{\text{rel}} \gg \tau_{\text{cor}}. \tag{57}$$

This justifies the expansion of $F_n(\bar{t})$, and with it $J_{n,n'}^{\text{2B}}(\bar{t})$, under the time integral in 53 around its value at the upper limit (the current time),

$$J_{n,n'}^{\text{2B}}(\bar{t}) = J_{n,n'}^{\text{2B}}(t) + \sum_{k=1} \frac{(\bar{t}-t)^k}{k!} \frac{\mathrm{d}^k}{\mathrm{d}t^k} J_{n,n'}^{\text{2B}}(t). \tag{58}$$

Truncating this retardation expansion 3 at the first term (0-th-order retardation approximation) leads to the following result for the pair correlations:

$$\begin{aligned} Img_{n,n'}^{\text{coll}(0)}(t) &= -\frac{J_{n,n'}^{\text{2B}}(t)}{\hbar} \frac{\sin[\omega_{n,n'}(t - (-t_0))]}{\omega_{n,n'}} \\ &= Img_{n,n'}^{\text{coll}(0)}(t, [F(t)]). \end{aligned} \tag{59}$$

This expression is, of course, a drastic distortion of the original result, and its accuracy depends on the fulfilment of condition 57. In fact, it is well known that, for weakly coupled systems, the two times are related by $\frac{\tau_{\text{cor}}}{t_{\text{rel}}} \sim \Gamma \ll 1$, where Γ is the relevant coupling parameter. In the second line of 59, we noted explicitly that the pair correlation functions have a twofold time dependence: an explicit one (via the sine function, which is fast, for increasing time, particularly for high frequencies) and a slow one via the evolution of $F(t)$.

Note that this is still a proper (although distorted) solution of the initial value problem. It is also consistent with an (arbitrary) initial condition $g_{n,n'}^0(-t_0)$ because the collision term exactly vanishes for $t \to -t_0$. Interestingly, despite the approximate character of $g_{n,n'}^{\text{coll}(0)}(t)$, it is easily seen (by performing the retardation expansion in 56) that it still satisfies the time-reversal invariance condition 54.

Markov limit. The limit of an infinitely remote initial state, $-t_0 \to -\infty$, is usually motivated by the assumption that two particles enter a scattering process in an uncorrelated manner. The result for the Markovian pair correlations is then:

$$\begin{aligned} Img_{n,n'}^{\text{coll}(M)}(t) &\equiv \\ -\frac{J_{n,n'}^{\text{2B}}(t)}{\hbar} &\lim_{-t_0 \to -\infty} \frac{\sin[\omega_{n,n'}(t - (-t_0))]}{\omega_{n,n'}} \\ &= -\frac{J_{n,n'}^{\text{2B}}(t)}{\hbar} \delta(\omega_{n,n'}). \end{aligned} \tag{60}$$

Note that it is assumed that the single-particle operators (i.e., the slow time dependence of $g^{\text{coll}[0]}$) are not affected by the limit, which means that the limit $\Gamma \to 0$ has been considered first.

Weakening of initial correlations. Motivated by the argument that the state of the system cannot remember (and, hence, be influenced by) its infinitely remote history, particularly its correlations, the Markov limit is accompanied by the suppression of initial correlations:

$$\lim_{-t_0 \to -\infty} g_{n,n'}^0(-t_0) \to 0. \tag{61}$$

This is consistent with the Markov limit because, after the procedure leading to 61, $g_{n,n'}[F(t)]$ does not obey an initial value problem that starts from an arbitrary initial state anymore but only adiabatically follows the dynamics of $F(t)$, according to the prescription 60. This concept is due to Bogolyubov[4] ("functional hypothesis"; "weakening of initial correlations") and has been generalized to situations where there exists a subclass of long-living correlations (such as those related to bound states or long range order; *partial weakening of initial correlations*) by Kremp et al.[18]

With the result 61, the collision integral due to initial correlations (the term g^{IC}) vanishes, and only the collision integral involving Im $g_{n,n'}^{\text{coll}(M)}$, Equation 60, remains, which is of the conventional Boltzmann-type form.

To summarize, time-reversal symmetry is lost at step 2. While the result of step 1, Im $g_{n,n'}^{\text{coll}(0)}(t)$, is time-reversal invariant *for any finite value* $-t_0$, no matter how far back in the past, this property vanishes with the limit $-t_0 \to -\infty$. With this limit, the unitary operator structure that is still present in the sine function is lost together with the explicit time dependence of the pair correlations (this is particularly clear when the single-particle operators F are exactly stationary.)

7 | SUMMARY AND DISCUSSION

In this paper, we analysed the question of the time reversibility of generalized quantum kinetic equations that are derived within the reduced density operator formalism. The governing equations of the density operator theory are given by the quantum BBGKY hierarchy. Here, we demonstrated that the exact BBGKY hierarchy and the associated quantum kinetic equations are time reversible. This behaviour is in striking contrast to the conventional Boltzmann-type kinetic equations that are known to be irreversible and describe the relaxation of a many-body system to an equilibrium state, which is accompanied by an increase of its entropy (H-theorem). This is traditionally achieved by means of ad hoc assumptions, such as about "molecular chaos",[19] via Boltzmann's "Stoßzahlansatz"[20] or by similar procedures.

Although the derivation of generalized non-Markovian quantum kinetic equations goes back almost seven decades, in many communities, the existence of a systematic kinetic theory beyond the Boltzmann equation is poorly known, which warrants a detailed reconsideration of some mathematical aspects on the way from a reversible to an irreversible kinetic theory. Here, we have presented a simple procedure that allows one to directly verify the time-reversal property of the exact BBGKY hierachy and of important closure relations, as well as the transition to the conventional Boltzmann equation. Our approach is based on the use of Wigner's anti-unitary time-reversal operator $\widehat{T}$[17] that translates the solution of the Schrödinger equation into the time-reversed equation and is a mathematically well-controlled procedure that replaces the traditional heuristic arguments mentioned above.

Let us summarize our main results:

1. Our proof of time-reversal invariance of the exact quantum BBGKY hierarchy revealed a much stronger condition, Equations 34 and 35, than the commonly used condition for time reversibility of the N-particle Schrödinger equation, that is, Equation 27. We have shown that not only does the total Hamiltonian have to obey $\widehat{T}\widehat{H}\widehat{T}^{-1} = \widehat{H}$, but in addition, each of its single-particle, two-particle, and higher contributions, have this property separately. This might seem surprising as Equation 27 is known to be necessary and sufficient for the Schrödinger and von Neumann equations. However, the N-particle dynamics have to always be consistent with the quantum dynamics of sub-complexes (of $N-1\ldots1$ particles), which follow directly from the partial integration of the N-particle equations. It is clearly impossible that the N-particles dynamics are reversible, whereas the N-s-particle dynamics are not.

2. We presented a very general condition for time-reversal invariance of approximate solutions to the BBGKY hierarchy, Equation 38, and demonstrated that it applies to many of the commonly used many-body approximations. Moreover, this condition goes far beyond those approximations, including a broad range of additional decoupling schemes of the hierarchy. This is not limited to approximations that are motivated by physical considerations and violate conservation laws. For example, the choice of the omitted term $\widehat{O} = \widehat{O}_{12} \neq \widehat{O}_{21}$ would violate the conservation of total energy, cf. Ref. 3, while still being time-reversal invariant.

3. Our results allow us to analyse the interesting question posed in Ref. 13 of how total energy conservation and time reversibility are related. While in most cases of practical relevance, both phenomena are fulfilled (or violated) simultaneously, their areas of validity are not equivalent. As shown above, there exist time-reversible models that violate energy conservation. On the other hand, there exist model Hamiltonians (e.g., those that contain odd powers of the momentum) that conserve energy but violate condition 27 and, therefore, time-reversal symmetry.

4. Our analysis of the transition to the conventional Boltzmann equation involved three successive approximations. The first one—the decoupling of the relaxation time scales of single-particle $t_{\rm rel}$ and two-particle dynamics ($\tau_{\rm cor}$) by means of a retardation expansion—allowed us to perform the memory integral and obtain a time-local result for the pair correlations, Equation 59. This result ("completed collision approximation" or "energy broadening approximation") not only conserves total energy,[3] but, here, we also demonstrated that it preserves time-reversal symmetry. The same analysis also applies to higher-order approximations in the retardation expansion 58.

5. We have demonstrated that time reversibility is lost only at the second step—the Markov limit, that is, with the shift of the initial time to the infinitely remote past, $-t_0 \to -\infty$. This destroys the unitary character of the dynamics of the pair correlations and introduces a preferred "arrow" of time because there is no possibility of the system ever returning to this state.

6. Our analysis also shows that the commonly used argument, that irreversibility is introduced into the theory via the assumption of "molecular chaos"[19] or the "Stoßzahlansatz",[20] has to be stated with some care. The requirement that the two-particle probabilities factorize and particles enter the collision uncorrelatedly—that is, in our notation, $F_{12} = F_1 F_2$ or $g_{12} \equiv 0$—is not sufficient. First, transition to irreversibility is also possible in a strongly correlated system where this factorization is not possible, for example, Ref. 3. Second, the example of the Born approximation that we discussed in section 5 applied to a weakly coupled system. Choosing, as the initial condition, an uncorrelated system, that is, $g(-t_0) = g^0 = 0$, we would formally satisfy those assumptions. Nevertheless, the resulting dynamics would still be given by Equation 44 without the

initial correlation term, but it would be perfectly time reversible. The crucial point for the emergence of irreversibility is again that the factorization is introduced not at a finite initial time but in the infinitely remote past.

With the generalized quantum kinetic equations that were discussed above at our disposal, one may ask whether it is necessary at all to force the transition to conventional irreversible Boltzmann-type kinetic equations given the rather crude approximations involved. The argument for the latter has always been that macroscopic many-particle dynamics, such as transport (diffusion, heat conduction, viscosity, fluid dynamics etc.), is dissipative, and the dynamics are expected to approach thermodynamic equilibrium—the state of maximum entropy. The answer is clearly "No". Experience in solving the generalized quantum kinetic equations (e.g., Ref. 3), which are derived either from the BBGKY hierarchy or from non-equilibrium Green functions, for a sufficiently long time clearly reveals that these solutions exhibit an irreversible trend towards an asymptotic state that is consistent with thermodynamic equilibrium. However, this state is different from a Maxwellian, Fermi, or Bose momentum distribution as a result of correlations. Certainly, the present reversible dynamics will return to the initial state; however the associated Poincaré recurrence time increases exponentially with particle number. This behaviour is in complete agreement with simulation results for classical systems: solutions of the reversible equations of classical mechanics of a many-particle system by means of microcanonical molecular dynamics show perfect relaxation trends to (correlated) thermodynamic equilibrium.

Therefore, the choice between the irreversible Boltzmann-type kinetic equations and reversible generalized kinetic equations is mainly governed by the substantially increased computational effort involved in the solution of the latter. Here, in fact, proof of time reversibility of the relevant approximations that was given in this paper is of high practical value as it provides a sensitive test for the numerical accuracy and convergence, for example, Ref. 21. Time reversibility is also of importance for "echo"-type experiments (e.g., Loschmidt echo,[22] spin echo, Rabi flop etc.) where time reversal is being forced by an external pulse. The analysis of the forward and backward dynamics gives important insights into the internal properties (e.g., dissipation channels) of a many-body system, and the present generalized quantum kinetic equations are well suited for such investigation. For a recent theoretical analysis, see Ref. 23.

REFERENCES

[1] Y. L. Klimontovich, *Kinetic Theory of Nonideal Gases and Nonideal Plasmas*, Pergamon Press, Oxford **1982**.
[2] K.-H. Spatschek, *Theoretische Plasmaphysik*, B.G. Teubner, Stuttgart **1990**.
[3] M. Bonitz, *Quantum Kinetic Theory, vol. 33 of Teubner-Texte zur Physik (B. G. Teubner, Leipzig 1998)*, 2nd ed., Springer, Cham **2016**.
[4] N. N. Bogolyubov, *Lectures on Quantum Statistics*, Vol. 2, Gordon and Breach, New York **1970**.
[5] A. Akbari, M. J. Hashemi, A. Rubio, R. M. Nieminen, R. van Leeuwen, *Phys. Rev. B* **2012**, *85*, 235121.
[6] P. Schuck, M. Tohyama, *Phys. Rev. B* **2016**, *93*, 165117.
[7] M. Bonitz, D. Kremp, *Phys. Lett. A* **1996**, *212*, 83.
[8] D. Lacroix, S. Hermanns, C. M. Hinz, M. Bonitz, *Phys. Rev. B* **2014**, *90*, 125112.
[9] S. Hermanns, N. Schlünzen, M. Bonitz, *Phys. Rev. B* **2014**, *90*, 125111.
[10] N. Schlünzen, S. Hermanns, M. Bonitz, C. Verdozzi, *Phys. Rev. B* **2016**, *93*, 035107.
[11] N. Schlünzen, M. Bonitz, *Contrib. Plasma Phys.* **2016**, *56*, 5.
[12] N. Schlünzen, J.-P. Joost, F. Heidrich-Meisner, M. Bonitz, *Phys. Rev. B* **2017**, *95*, 165139.
[13] M. Scharnke, N. Schlünzen, M. Bonitz, *J. Math. Phys.* **2017**, *58*, 061903.
[14] D. B. Boercker, J. W. Dufty, *Ann. Phys. (N.Y.)* **1979**, *119*, 43.
[15] F. Haake, *Quantum Signatures of Chaos*, Springer-Verlag, Berlin **2001**.
[16] D. Zubarev, V. Morozov, G. Röpke, *Statistical Mechanics of Nonequilibrium Processes*, Vol. *1*, Akademie Verlag, Berlin, Germany **1996**.
[17] E. P. Wigner, *Math.-Phys. Kl.* **1932**, *31*, 546.
[18] Y. L. Klimontovich, D. Kremp, *Physica* **1981**, *109 A*, 517.
[19] J. C. Maxwell, *Philosophical Transactions of the Royal Society of London* **1867**, *157*, 49.
[20] L. Boltzmann, *Math.-Naturwiss. Classe Bd.* **1872**, *66*, 275.
[21] N. Schlünzen, J.-P. Joost, M. Bonitz, *Phys. Rev. B* **2016**, *97*, 117101.
[22] J. Loschmidt, *Sitzungsber Kais. Akad. Wiss. Wien Math. Naturwiss. Classe* **1876**, *73*, 128.
[23] M. Schmitt, S. Kehrein, *EPL* **2016**, *115*, 50001.

3.3 Löwdin's Symmetry Dilemma in the Hubbard Model

There is one question that has been controversially discussed in recent years, particularly between Verdozzi and Coworkers (Lund University, Sweden) on the one side, and members of the Bonitz group (Kiel University, Germany) on the other side: "Can Green-function approaches produce a Mott-Hubbard (correlation) gap?" The existence of the gap is fundamental for understanding the Mott transition between a paramagnetic metal and a correlated insulator [245]. The former group considered respective methods conceptually ill-suited to describe this feature and published results with a vanishing gap for the infinite 1D and 3D Hubbard system [111, 275]. The group from Kiel, however, has found several NEGF results for correlation gaps that go beyond the simple finite-size effects [216, 276]. Following the KBEt^2 workshop in Kiel that took place in march 2019, both groups collaborated to analyze the seemingly contradictory results in more detail. Both previous results could be identified as the multiple solutions of the KBE/Dyson equation corresponding to different symmetry constraints.

A related kind of behavior was first described by Löwdin (published in Ref. [277]) who observed for the Hartree–Fock approximation that the adaption of all exact symmetries can prevent one from obtaining the minimum possible total energy. Similar "dilemma" and symmetry-breaking scenarios have been observed for several systems, including the homogeneous electron gas [10, 278, 279], the electronic structure of molecules [280], quantum dots [281–286], and ultracold Bose gases [284]. For the Hubbard model, the loss of the exact symmetries within mean-field descriptions was explored decades ago [287, 288]. For more sophisticated approximations that include electronic correlations, only little effort was put into the analysis of symmetry breaking in Hubbard systems.

Independently, recent developments regarding the Green-functions technique have shown the existence of solution multiplicity under certain conditions for different model systems [196–201]. This is usually traced back to the multivaluedness of the Φ functional (cf. Sec. 2.1.4) and questions the general validity of perturbative many-body approaches for such cases.

The above-mentioned results for the correlation gap by the Kiel–Lund collaboration initiated the preparation of the following publication,[19] Ref. [118], which links multiple solutions for the one-dimensional Hubbard model to different degrees of symmetry in the system. Thereto, an equilibrium Green-functions description in the frequency space is used which is explained in detail. Using the example of the SOA selfenergy, three different framing conditions are compared: (I) the uniformity constraint, which forces the system to be translationally invariant, (II) the restricted-spin constraint, which only enforces spin symmetry, and (III) the unrestricted treatment, which allows for asymmetric (spin-)density distributions. The approaches are then analyzed regarding the spectral properties—particularly the Mott gap—and the spin-dependent density matrix. To estimate the quality, exact-diagonalization calculations as well as DMRG simulations are used as reference data. In this course, it is demonstrated that the successive relaxation

of symmetry constraints drastically improves the quality of the spectral information, while the density matrices diverge from the exact behavior. Hence, considering the equilibrium groundstates corresponding to (I)–(III), Löwdin's original symmetry dilemma manifests—in the strict word sense—as a trilemma for the Green-function method in Hubbard systems, although even further states are conceivable. Additionally, it is shown that both groundstates of (I) and (II) are also solutions for the unrestricted treatment (III). In fact, during the respective iteration procedure of the equilibrium Dyson equation, the results for (I) and (II) appear as long-living metastable states. Thus, the multiple solutions in this context can be characterized and attributed to specific structural properties.

Coming back to the question from the beginning, Green-functions approaches do indeed constitute a reliable tool to predict and estimate the Mott-Hubbard gap—presumed that no (or few) symmetries are enforced onto the system.

ORIGINAL ARTICLE

Löwdin's symmetry dilemma within Green functions theory for the one-dimensional Hubbard model

J.-P. Joost[1] | **N. Schlünzen[1]** | **S. Hese[1]** | **M. Bonitz[1]** | **C. Verdozzi[2]** |
P. Schmitteckert[3] | **M. Hopjan[4]**

[1]Institute of Theoretical Physics and Astrophysics, Kiel University, Kiel, Germany

[2]Physics Department and ETSF, Lund University, Lund, Sweden

[3]HQS Quantum Simulations GmbH, Karlsruhe, Germany

[4]Institute for Theoretical Physics, Göttingen University, Göttingen, Germany

Correspondence

N. Schlünzen, Institut für Theoretische Physik und Astrophysik, Christian-Albrechts-Universität zu Kiel, Leibnizstraße 15, 24098 Kiel, Germany.
Email: schluenzen@theo-physik.uni-kiel.de

Funding information

Christian-Albrechts-Universität zu Kiel

Abstract

The energy gap of correlated Hubbard clusters is well studied for one-dimensional systems using analytical methods and density-matrix-renormalization-group (DMRG) simulations. Beyond 1D, however, exact results are available only for small systems by quantum Monte Carlo. For this reason and, due to the problems of DMRG in simulating 2D and 3D systems, alternative methods such as Green functions combined with many-body approximations (GFMBA), that do not have this restriction, are highly important. However, it has remained open whether the approximate character of GFMBA simulations prevents the computation of the Hubbard gap. Here we present new GFMBA results that demonstrate that GFMBA simulations are capable of producing reliable data for the gap which agrees well with the DMRG benchmarks in 1D. An interesting observation is that the accuracy of the gap can be significantly increased when the simulations give up certain symmetry restriction of the exact system, such as spin symmetry and spatial homogeneity. This is seen as manifestation and generalization of the "symmetry dilemma" introduced by Löwdin for Hartree–Fock wave function calculations.

KEYWORDS

DMRG simulations, Green functions, Hubbard model, symmetry breaking

1 | INTRODUCTION

Symmetry and its possible violation or breaking are basic notions in our understanding of physical phenomena. In essence, this is because the symmetry transformations in a physical system relate to conservation laws of specific observables.

Around six decades ago, Löwdin introduced the term *symmetry dilemma*[1][1] to portray a situation where imposing symmetry constraints in a Hartree–Fock (HF) calculation of the eigenfunction of a given electronic system gives an energy eigenvalue higher than in absence of such constraints. In other words, the removal of constraints increases the variational

---

[1]Quoting Löwdin from that reference, p. 498: "In my opinion, the Hartree–Fock scheme based on a single Slater determinant D is in a dilemma with respect to the symmetry properties and the normal constants of motion Λ. The assumption that D should be symmetry-adapted or an eigenfunction to Λ. leads to an energy $\langle H \rangle$ high above the absolute minimum,..."

flexibility of the HF wavefunction, giving an approximate energy value closer to the exact one, but typically does not preserve the system's good quantum numbers and symmetry properties. Well-known examples are HF simulations of the ground state of the uniform electron gas, e.g., Refs. [2–4]. From Löwdin's original insight, extensive research has spurred, to develop approaches where symmetries in a single-determinant wavefunction are deliberately broken, and subsequently reintroduced via symmetry projection operators, to attain a variationally improved multi-determinant state (see, e.g., Ref. [5] for a recent discussion).

Ambivalence in the use of symmetry is in fact of very general occurrence, and concerns both finite and infinite systems. An interesting example is provided by spontaneous symmetry breaking (SSB).[6] In a rigorous sense, SSB only takes place in the thermodynamic limit. However, exact numerical evidence from finite systems shows that the "disjointness" (typical of macroscopic sizes) of phases or different values/orientations of the order parameter is replaced by a crossover behaviour across finite barriers in Hilbert space, whose sharpness and strength increases on enlarging the system's size. An example is Wigner crystallization in finite electron systems, such as quantum dots, e.g., Refs. [7–9], for which also SSB in HF calculations was investigated;[10] other examples are found in ultracold bosons in traps, nuclear matter, and quantum chemistry; for an overview, see Ref. [11]. It can thus be methodologically expedient to artificially break the symmetry in a finite system, to gain insight about the system behaviour in the thermodynamic limit. An often used prescription is the addition of small external sources lowering the symmetry,[12,13] but under the stipulation that it is understood that true SSB occurs only asymptotically.

Another central element to consider in addressing the symmetry-related behaviour of a system is electronic or inter-particle correlations. These have deep influence in various situations, e.g. condensed-matter systems and materials, plasmas, nuclear matter, and cold atoms, to mention a few.[14–17] Clearly, the interplay of electronic interactions and symmetry constraints affects the system's properties in a way that is not accountable for within a free-particle or mean-field picture. It should be noted, though, that already within a wavefunction framework, some theories going beyond the mean-field picture can mimic the effect of strong electronic correlations with wavefunctions that do not respect the expected symmetry (see, e.g., Ref. [18]).

In this work, we take a different route from wavefunctions, and we study the effect of lifting/breaking symmetry in the presence of significant electronic correlations within many-body perturbative Green functions theory. As the system of choice with strong correlations, we consider the Hubbard model[14,19,20] which via a minimum-complexity Hamiltonian, describes the key trends in the behaviour of interacting electrons in the energy bands of a solid. For this reason, Hubbard-like models have been applied in many contexts and to a wide typology of systems, both in and out of equilibrium, see, e.g., Refs. [21–37].

Even though the Hubbard Hamiltonian is considerably simpler than that of a realistic material, exact solutions for the Hubbard model are only known in special cases: in one dimension, an exact analytical treatment is possible via Bethe-ansatz techniques,[38] and exact numerical solutions for finite samples can be obtained via the density-matrix-renormalization-group (DMRG) method[39–41] (including spin-charge separation effects[42–44]). Using configuration interaction (CI)[45] or quantum Monte Carlo methods,[46–49] exact solutions can be obtained for any dimensionality, but only for small clusters. Finally, an exact description is possible in the limit of infinite dimensionality via dynamical-mean-field theory (DMFT).[50–52] In all other cases (notably, in two and three dimensions), some level of approximation must be introduced. Yet, high accuracy can be attained, for example, via the diagrammatic Monte Carlo technique,[53] or by extensions of DMFT via cluster[54] or diagrammatic approaches.[55,56]

A premier method traditionally applied to the Hubbard model is the Green functions formalism combined with many-body perturbation theory (GFMBA).[57,58] The GFMBA method is a general framework that can be used in any dimension (i.e. also for 2D and 3D Hubbard models), scales not too unfavourably with system's size, can deal with both static and time-dependent regimes,[17,59] and is also practically viable for implementation for realistic systems. Furthermore, a very recent reformulation of the method in terms of coupled one- and two-particle propagators[60,61] has considerably increased its scope and range of applicability. In the case of the GFMBA method, correlation effects are included via selected classes (possibly infinite sums) of diagrams in the selfenergy, or via truncated iterative functional-derivative schemes. This leads to different perturbative treatments,[57,58] e.g. HF, second-order Born approximation (SOA), third-order approximation,[62,63] GW, and the particle–particle and particle–hole T-matrix approximation.[17,63] Comparisons against exact benchmarks for finite systems have shown that the GFMBA method works well for not too strong interactions.[62–65]

The GFMBA approach has recently been under extensive scrutiny in relation to the existence of multiple solutions in the ground state and a potential convergence to nonphysical ones[66–68] (for an example from out-of-equilibrium systems, see e.g. Ref. [69]). However, in the discussion the multiplicity of GFMBA solutions, little or no attention has been given

so far in the literature to the explicit role of symmetry, particularly in relation to the Hubbard model (for some discussion of broken symmetry in the case of an isolated Hubbard dimer, see Refs. [70, 71]). For the exact solution of this model, important ground-state properties and symmetries are well known[72,73] and in common practice, these symmetries are granted by default also to the approximate solutions.

There is scarce knowledge on how these symmetries affect approximate treatments beyond mean-field theory. For example, for Hartree–Fock treatments of the Hubbard model, it is well known that a phase transition from a paramagnetic ground state to an antiferromagnetic one of unphysical nature occurs at a critical interaction, U_c, where the specific value depends on the system size and geometry.[47,74] Yet, at the same time, the (unphysical) broken spin-symmetry solutions result in a ground-state energy closer to the exact one, as well as in the emergence of a band gap (the latter is absent within spin-symmetric/spin-restricted mean-field schemes). This raises the question whether selfenergy approximations beyond Hartree–Fock can be found that violate the symmetry properties of the exact solution as well, and yet provide "improved" values of relevant observables, such as the ground-state energy or the Hubbard gap. In other words,

1. Is there a Löwdin symmetry dilemma for the Hubbard model within many-body perturbation theory?
2. And in case, how is this related to solution multiplicity?

Our answer to the first question is in the affirmative: By considering the Hubbard model in the one-dimensional case, and comparing GFMBA, CI, and DMRG results, we find that, lifting the symmetry constraints artificially, simulates the effect of having more correlation effects in the system, and leads to a significant improvement of observables like the system's ground-state energy or the spectral functions, even at fairly large interactions. In particular, our discussion will be especially focussed on the charge energy gap Δ (also known as Mott-Hubbard gap). For a system containing N particles, it depends on the ground-state energies of the N, $N+1$ and $N-1$ systems,

$$\Delta = E_{GS}(N+1) + E_{GS}(N-1) - 2E_{GS}(N). \tag{1}$$

This is a central quantity of the Hubbard model, related to the metal–insulator transition at a characteristic interaction strength.[2]

For the second question, we find that the occurrence of multiple (metastable) solutions is central to the connection between symmetry lifting and improved values of certain observables in the Hubbard model. Besides looking at what happens when lifting symmetry and why, we will also consider the possible implications in physical terms. However, due to the explorative nature of this initial study, we will not explore/discuss strategies to restore symmetry. This is left to future work.

The paper is organized as follows: in Section 2, we introduce the Hubbard Hamiltonian and the Green functions formalism for HF and SOA treatments within the three self-consistency protocols with different levels of symmetry constraints. Section 3 presents results from a mean-field treatment, specifically for the ground-state energy, the Hubbard gap, and the magnetic moment as function of the interaction strength U. In Section 4, we consider the SOA, discussing at the same time the ground-state density matrix and equilibrium spectral function for all the three self-consistency prescriptions. The multiple solutions in SOA are further analysed in Section 5 in terms of ground-state energy values and self-consistency convergence errors. Finally, Section 6 focuses on a characterization of the Hubbard gap, where HF and SOA results are compared to DMRG ones, and the dependence on system size, L, is taken into account. Our conclusions and a brief outlook are presented in Section 7.

2 | GREEN FUNCTIONS THEORY

We consider the Fermi-Hubbard model which is described by the Hamiltonian

$$\hat{H} = -J \sum_{\langle i,j \rangle} \sum_{\sigma=\uparrow,\downarrow} \hat{c}_{i,\sigma}^\dagger \hat{c}_{j,\sigma} + U \sum_i \hat{n}_{i,\uparrow} \hat{n}_{i,\downarrow}, \tag{2}$$

---

[2]The characteristics of the MIT (and thus of the gap) depend on dimensionality (see, e.g., Refs. [14, 75]). For $D=1$, the exact solution shows that the insulating phase (and the charge gap) exist for any $U > 0$ (i.e. no MIT occurs).[38] For infinite dimensions, where the model is exactly solvable via DMFT, the MIT occurs at finite interaction values[52] (however, there is coexistence of metallic and insulating solutions in an interval $U_{c_2} < U < U_{c_1}$). This picture qualitatively remains in three dimensions, with however quantitative modifications, due to antiferromagnetic fluctuations.[48] However, antiferromagnetic correlations appear to play an even more dramatic role in two dimensions, where it has been recently also proposed in Ref. [76] that the system is gapped for any $U > 0$. For a recent review of the situation in 2D see e.g. Ref. [77].

where J is the hopping amplitude between adjacent lattice sites, and U is the on-site interaction strength. The operators $\hat{c}^\dagger_{i,\sigma}$ and $\hat{c}_{j,\sigma}$ create and annihilate an electron with spin projection σ at site i and j, respectively, and the density operator is given by $\hat{n}_{i,\sigma} = \hat{c}^\dagger_{i,\sigma} \hat{c}_{i,\sigma}$.

The one-body nonequilibrium Green function of the system is defined by the canonical operators for complex times z on the Keldysh contour $\mathcal{C}$,[78,79]

$$G_{ij,\sigma}\left(z, z'\right) = \frac{1}{i\hbar} \left\langle \mathcal{T}_\mathcal{C} \left\{ \hat{c}_{i,\sigma}\left(z\right) \hat{c}^\dagger_{j,\sigma}\left(z'\right) \right\} \right\rangle, \tag{3}$$

where $\mathcal{T}_\mathcal{C}$ is the time-ordering operator on the contour, and the averaging is performed with the correlated unperturbed density operator of the system. In the rest of this work, we specialize to the equilibrium regime, i.e. when the system is not acted upon by external fields. In that case, the real-time components[17,59] of the Green function depend only on the difference of the two time arguments. Further, the retarded (R) component for the spin projection σ obeys the Dyson equation

$$\boldsymbol{G}^R_\sigma\left(\omega\right) = \boldsymbol{G}^R_0\left(\omega\right) + \boldsymbol{G}^R_0\left(\omega\right) \boldsymbol{\Sigma}^R_\sigma\left(\omega\right) \boldsymbol{G}^R_\sigma\left(\omega\right), \tag{4}$$

where all quantities are matrices in the orthonormal single-particle basis $\{|i\rangle\}$. For spin-compensated situations, the noninteracting retarded Green function $\boldsymbol{G}^R_0\left(\omega\right)$ is independent of the spin projection and given by

$$G^R_{0,ij}\left(\omega\right) = \left\langle i \left| \left(\omega - \hat{h}_0 + i\eta\right)^{-1} \right| j \right\rangle, \qquad \eta \to 0^+, \tag{5}$$

depending only on the single-particle contribution to the Hamiltonian

$$\hat{h}_0 = -J \sum_{\langle i,j \rangle} |i\rangle\langle j|, \tag{6}$$

where the sum over $\langle i, j \rangle$ ensures only nearest neighbour hopping. For numerical reasons, a finite value of $\eta = 10^{-2}$ is used throughout this work. If the exact selfenergy $\Sigma^R_\sigma\left(\omega\right)$ of the system was known, Equation (4) would provide the exact single-particle Green function. However, in practice many-body approximations to the selfenergy have to be used.

In this work, we employ the time-diagonal Hartree–Fock as well as the time-non-local second-order Born approximation. The retarded component of the HF selfenergy is defined as[3]

$$\boldsymbol{\Sigma}^{R,HF}_\sigma\left(t\right) = \delta\left(t, 0\right) \; U \; \mathrm{diag}\left(n_{1,\bar{\sigma}}, \, \dots, n_{L,\bar{\sigma}}\right), \tag{7}$$

where δ is the Dirac delta function for the relative time t in equilibrium and diag($\cdot$) represents a diagonal matrix with the given arguments as diagonal entries. Further, $\bar{\sigma}$ denotes the spin-projection opposite to σ, L the number of lattice sites, and $n_{i,\sigma} = \left\langle \hat{n}_{i,\sigma} \right\rangle$. The density matrix is given by the less component of the Green function,

$$\boldsymbol{n}_\sigma = -i\hbar \int_{-\infty}^{\infty} \frac{d\omega}{2\pi} \boldsymbol{G}^<_\sigma\left(\omega\right). \tag{8}$$

For the correlated Green function, the less ($<$) and greater ($>$) components can be determined by

$$\boldsymbol{G}^<_\sigma\left(\omega\right) = -f_F\left(\omega - \mu\right)\left[\boldsymbol{G}^R_\sigma\left(\omega\right) - \boldsymbol{G}^A_\sigma\left(\omega\right)\right], \tag{9}$$

$$\boldsymbol{G}^>_\sigma\left(\omega\right) = \bar{f}_F\left(\omega - \mu\right)\left[\boldsymbol{G}^R_\sigma\left(\omega\right) - \boldsymbol{G}^A_\sigma\left(\omega\right)\right], \tag{10}$$

with the Fermi function $f_F(\omega) = 1/(e^{\beta\omega} + 1)$, $\bar{f}_F\left(\omega\right) = 1 - f_F\left(\omega\right)$, the inverse temperature β, and $\boldsymbol{G}^A_\sigma\left(\omega\right) = \left[\boldsymbol{G}^R_\sigma\left(\omega\right)\right]^\dagger$.

---

[3]Mind that in the Hubbard model all exchange contributions vanish and only the direct diagrams remain.

For the SOA selfenergy, the retarded component is given by

$$\Sigma_\sigma^{R,SOA}(t) = \Sigma_\sigma^{R,HF}(t) + \Theta(t)\left[\Sigma_\sigma^{>,SOA}(t) - \Sigma_\sigma^{<,SOA}(t)\right],\tag{11}$$

with the Heaviside step function $\Theta(t)$ and the greater and less components of the selfenergy

$$\Sigma_\sigma^{\gtrless,SOA}(t) = -(i\hbar)^2 U^2 G_\sigma^{\gtrless}(t) \circ G_{\bar{\sigma}}^{\gtrless}(t) \circ \left[G_\sigma^{\lessgtr}(t)\right]^\dagger.\tag{12}$$

Here, $\circ$ denotes the Hadamard product between matrices, and the $G^{\gtrless}(t)$ are determined by the inverse Fourier transform,

$$G_\sigma^{\gtrless}(t) = \mathcal{F}^{-1}\left[G_\sigma^{\gtrless}(\omega)\right] := \int_{-\infty}^{\infty} \frac{d\omega}{2\pi}\ e^{-i\omega t} G_\sigma^{\gtrless}(\omega).\tag{13}$$

Finally, using the Fourier transform, $\Sigma_\sigma^R(\omega) = \mathcal{F}\left[\Sigma_\sigma^R(t)\right]$, the selfenergies, Equations (7) and (11), can be included in Equation (4).

Since the selfenergy, in general, is a functional of the single-particle Green function, Equation (4) has to be solved iteratively for both spin components until a self-consistent solution is found. The choice of a suitable initial value is crucial and can affect the final result of the iteration. Here, if not mentioned otherwise, $G_0^R(\omega)$ is chosen as the starting point.

In summary, for the self-consistent solution of Equation (4) the following scheme is iterated until convergence is achieved:

1. Diagonalize the single-particle Hamiltonian $\hat{h}_0$, cf. Equation (6), set $G_0^R(\omega)$ via Equation (5) and choose an initial value to start the iteration, e.g. $G_\sigma^R(\omega) = G_0^R(\omega)$
2. Calculate $G_\sigma^{\gtrless}(\omega)$ from $G_\sigma{}^R(\omega)$, using Equations (9) and (10)
3. Perform the inverse Fourier transform $G_\sigma^{\gtrless}(t) = \mathcal{F}^{-1}\left[G_\sigma^{\gtrless}(\omega)\right]$, cf. Equation (13)
4. Calculate $\Sigma_\sigma^{\gtrless}(t)$ and $\Sigma_\sigma^R(t)$ using Equations (7), (11) and (12)
5. Perform the Fourier transform $\Sigma_\sigma^R(\omega) = \mathcal{F}\left[\Sigma_\sigma^R(t)\right]$
6. Solve the Dyson equation for $G_\sigma^R(\omega)$, Equation (4), using the new $\Sigma_\sigma^R(\omega)$
7. If $G_\sigma^R(\omega)$ is not yet converged start again at (1)

To improve the convergence of the above scheme, the input Green function at iteration k, $G_{k,in}^R$ (the spin index is neglected here), is determined by mixing the solutions of the two previous iterations

$$G_{k,in}^R(\omega) = \alpha G_{k-1,out}^R(\omega) + (1-\alpha)G_{k-1,in}^R(\omega),\tag{14}$$

where a mixing parameter of $\alpha = 0.05$ is used. The error at iteration k is given by

$$\epsilon_k = \frac{1}{\alpha L}\int_{-\infty}^{\infty}\frac{d\omega}{2\pi}\mid D_k(\omega) - D_{k-1}(\omega)\mid,\tag{15}$$

where $D(\omega)$ is the density of states (DOS) of the system,

$$D(\omega) = i\hbar\sum_{\sigma=\uparrow,\downarrow}\mathrm{tr}\left[G_\sigma^>(\omega) - G_\sigma^<(\omega)\right].\tag{16}$$

During the calculations, it is verified that the sum rules for the spectral function hold, i.e. that the DOS remains positive and integrates to the number of lattice sites L within numerical accuracy. To ensure the convergence of the iteration scheme an error threshold of $\epsilon_{thr} = 10^{-12}$ is used in this work. In addition to spectral properties, the single-particle Green function gives access to the total energy of the system.[17,57]

$$E_{tot} = \frac{1}{2}E_{kin} + E_{GM},\tag{17}$$

which combines the kinetic part

$$E_{\mathrm{kin}} = \sum_{\sigma} \mathrm{tr}\,(\boldsymbol{h}_0 \boldsymbol{n}_\sigma)\,, \tag{18}$$

and the Galitskii–Migdal interaction energy

$$E_{\mathrm{GM}} = -\frac{\mathrm{i}\hbar}{2} \sum_{\sigma=\uparrow,\downarrow} \int_{-\infty}^{\infty} \frac{\mathrm{d}\omega}{2\pi}\,(\omega - \mu)\;\,\mathrm{tr}\left[\boldsymbol{G}_\sigma^< (\omega)\right], \tag{19}$$

where, in the GFMBA simulations of the present paper, the chemical potential is set to $\mu = 0$.

In this paper, we consider three distinct cases for which different symmetry restrictions are imposed on the Green function during the solution of the Dyson equation:

1. "uniform" (uni): the system is required to be translationally invariant. In this case, the iteration scheme is solved in momentum space where the Green function and selfenergy are diagonal, i.e. $G_{ij,\sigma}^{\mathrm{R}}(\omega) \to G_{p,\sigma}^{\mathrm{R}}(\omega)$.
2. "restricted spin" (rs): the system is required to be spin-symmetric. In this case, the iteration scheme is solved for one spin projection only since the Green function and selfenergy are spin-independent, i.e. $\boldsymbol{G}_\uparrow^{\mathrm{R}}(\omega) = \boldsymbol{G}_\downarrow^{\mathrm{R}}(\omega)$.
3. "unrestricted spin" (us): no restrictions regarding both, the translation and spin symmetry are imposed. In this case, an antiferromagnetic state is chosen to start the iteration.[4]

3 | SPIN SYMMETRY IN THE MEAN-FIELD APPROXIMATION

Since the exact ground state of the half-filled 1D Hubbard Hamiltonian is known to be spin-symmetric (i.e. paramagnetic) for systems with an even number of particles,[72,73] a logical prescription is to introduce spin symmetry also for approximate solutions like HF and SOA. However, it is well known that, beyond a critical interaction strength U_{c}, unrestricted-spin HF (usHF) spontaneously breaks spin symmetry resulting in an antiferromagnetic ground state. In the following, we quantify the influence of this artificial phase transition on important ground-state properties by comparing the performance of restricted-spin (rs) and unrestricted-spin (us) HF for finite one-dimensional Hubbard chains with open (hard-wall) boundary conditions. In Figure 1a the ground-state energy of three Hubbard clusters containing $L = 2$, 4, 6 sites is plotted vs. the interaction strength U for rsHF, usHF, and the result obtained by exact diagonalization of the Hamiltonian. The qualitative observations are similar for all three systems. In the limit of vanishing on-site interaction all three methods agree perfectly and show a linear increase of the ground-state energy with U. For interactions beyond $U \gtrsim 1J$, the exact energy is reduced due to increasing correlations giving rise to mounting differences compared to the two HF solutions. In the case of rsHF, which by design fulfils the exact spin symmetry of the system, the linear increase of the ground-state energy is present for all values of U resulting in a strong deviation from the exact result, for $U \gtrsim 1J$. Most notably, since correlations are not included in rsHF, no Mott regime is observed in the presence of the on-site interaction.

By contrast, removing the requirement of spin-symmetry (usHF) results in a lower ground-state energy for interactions beyond $U_{\mathrm{c}} \approx 2\,J$ which approaches the exact value for $U \to \infty$. Additionally, the usHF density of states, shown in Figure 1c for a Hubbard chain of 10 sites, is indicative that a correlation gap in the spectrum (corresponding to a Mott transition) emerges for a critical interaction U_{c}. However, since the usHF selfenergy accounts only for mean-field effects, the improved results for the Hubbard gap and the ground-state energy cannot be attributed to the effects of correlations. Instead, they are connected to the emergence of the antiferromagnetic state. This becomes apparent when looking at the local magnetic moment on the outermost site of finite Hubbard chains depicted in Figure 1b. The local magnetic moment is defined as

$$\left\langle \widehat{m}_i^2 \right\rangle = \left\langle \left(\widehat{n}_{i,\uparrow} - \widehat{n}_{i,\downarrow} \right)^2 \right\rangle = n_i - 2d_i, \tag{20}$$

with $n_i = n_{i,\uparrow} + n_{i,\downarrow}$ and the local double occupancy d_i which contains a mean-field and a correlation part,

$$d_i = n_{i,\uparrow} n_{i,\downarrow} + d_i^{\mathrm{corr}}. \tag{21}$$

---

[4]When choosing the spin-symmetric $\boldsymbol{G}_0^{\mathrm{R}}(\omega)$ as the initial value, the iteration will not break spin symmetry.
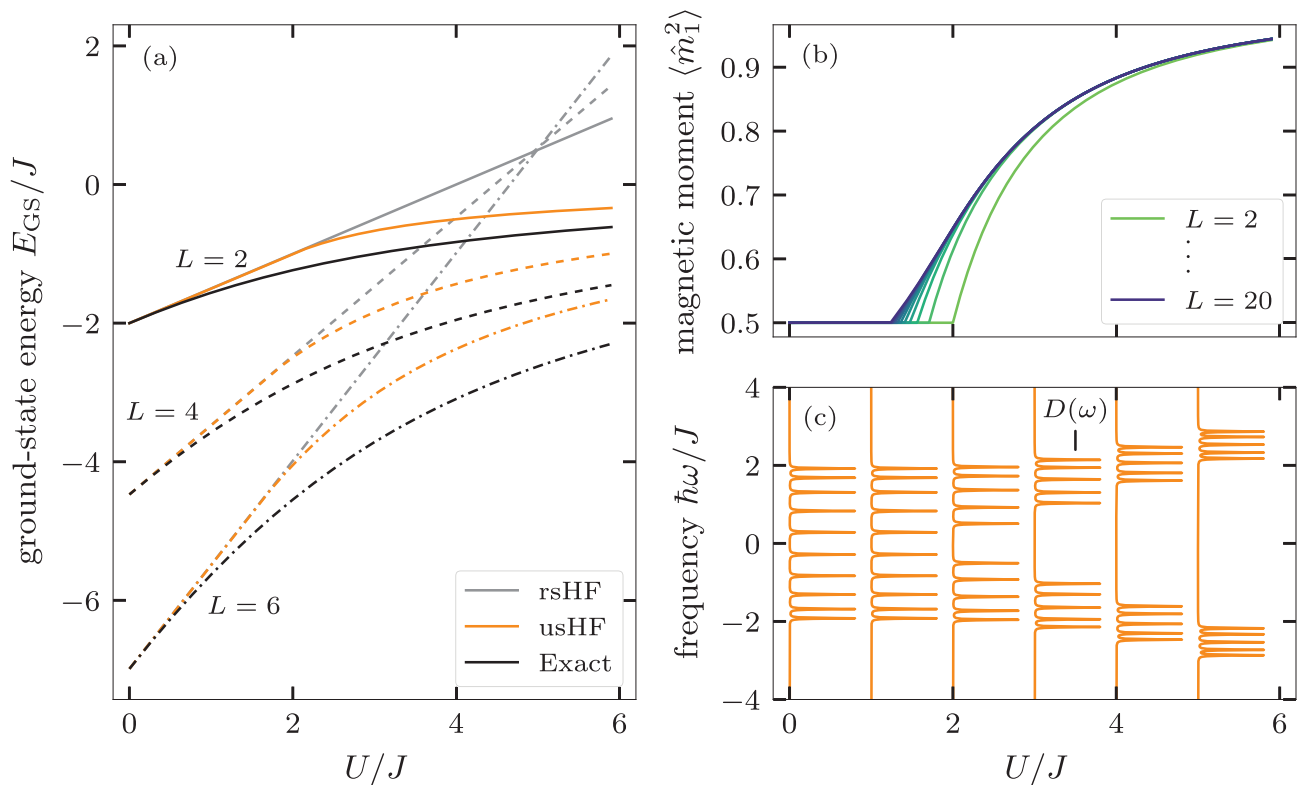
FIGURE 1 (a) Comparison of the ground-state energy E_{GS} vs. interaction strength U for rsHF, usHF, and the exact solution of the Hubbard Hamiltonian. Three finite Hubbard chains of length $L = 2, 4, 6$ with open boundary conditions at half filling are considered. (b) Interaction dependence of the local magnetic moment $\langle \hat{m}^2 \rangle$, Equation (20), on the first site of finite Hubbard chains of length $L = 2, \dots, 20$ with open boundary conditions at half filling for usHF. (c) Interaction dependence of the DOS for a finite Hubbard chain of length $L = 10$ with open boundary conditions at half filling for usHF. A sudden opening of the correlation gap occurs at $U \approx 2J$

In the exact case, where the spin densities are homogeneous, an increasing magnetic moment at high interaction strengths is caused by an increase of electronic correlations leading to a negative d_i^{corr} and, thus, a decrease in the double occupancy. However, for usHF, where $d_i^{\text{corr}} \equiv 0$, the inhomogeneous spin-density distribution of the antiferromagnetic spin state mimics the effect of additional correlations.[5] To summarize, removing the requirement of a homogeneous spin-symmetric ground state, as observed in the exact solution, allows HF simulations to achieve results for ground-state energies closer to the exact ones and gives rise to a Hubbard gap of reasonable magnitude.

4 | SYMMETRIES IN SECOND-BORN APPROXIMATION

We next analyse the effect of imposing symmetry restrictions when including selfenergies with correlation effects (beyond HF). The first correction beyond HF that takes into account interparticle scattering is the second-order Born approximation (SOA). We thus consider, within SOA, the behaviour of finite Hubbard chains with periodic boundary conditions for which the exact ground state is known to be both, spin symmetric and invariant under space translations.[72,73,80] The effect of relaxing the aforementioned symmetry constraints is quantified by comparing results from the three SOA approaches I, II, and III, (i.e. for the uniform, restricted-spin, and unrestricted-spin treatments) introduced in Section 2; we will refer to these three treatments as uniSOA, rsSOA, and usSOA, respectively. For all three cases, we compare in Figure 2 the spin-up density matrix (a–d), the DOS (e–g) and the ground-state energy (h) to the exact results for an 8-site Hubbard chain with periodic boundary conditions at $U = 4J$. In the uniform case, the density matrix by design exhibits perfect

---

[5]Note that the critical interaction U_c for which the symmetry-broken state emerges decreases with increasing length of the chain. An in-depth analysis on the exact value of U_c goes beyond the scope of this work.
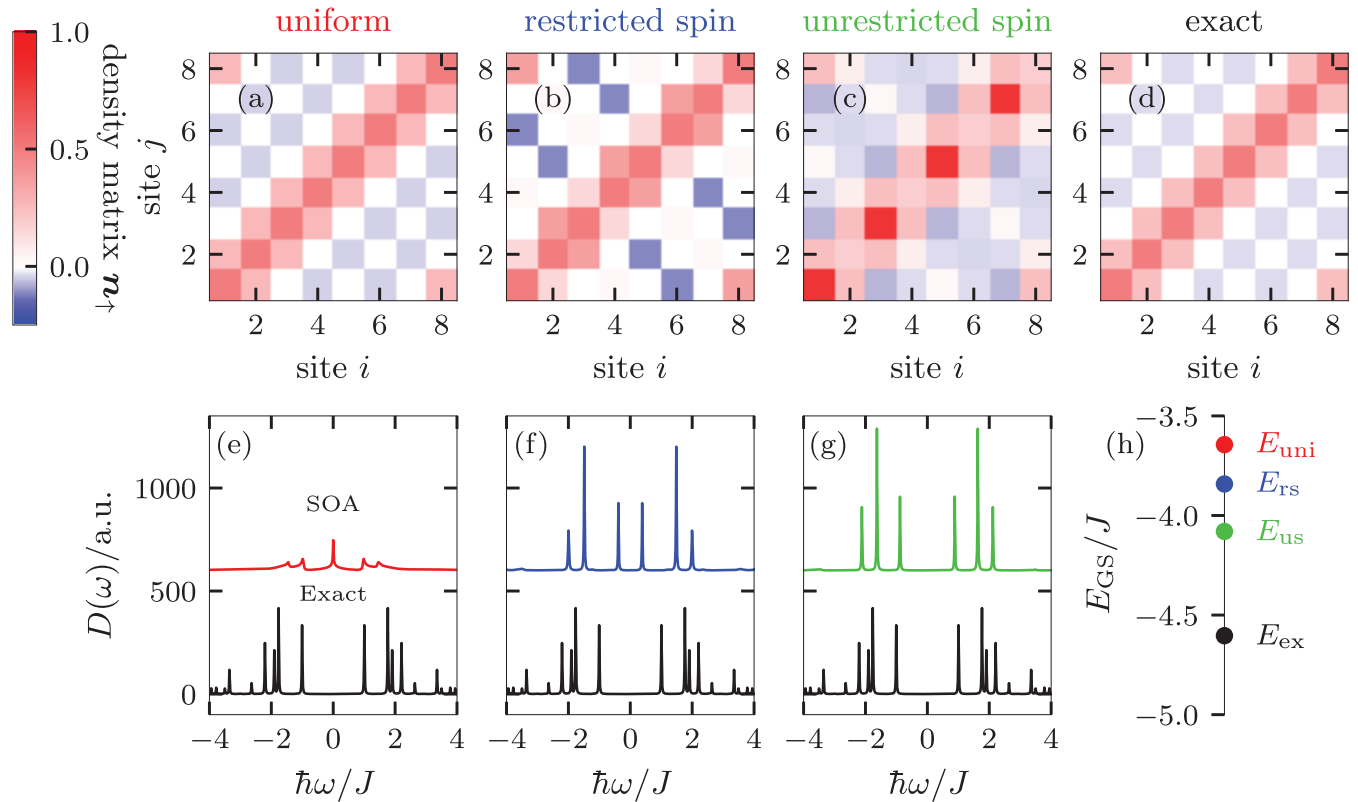
FIGURE 2 Ground-state properties of a periodic, half-filled Hubbard chain of length $L = 8$ and $U = 4\,J$, within second-order Born approximation. (a)–(d) Density matrix for a translationally invariant system (red), without imposing homogeneity but spin symmetry (blue), without both, homogeneity and spin restriction (green), and exact configuration interaction (CI) solution without restrictions (black). (e)–(g) Spectral function (density of states) of the three approximations compared to CI results ("Exact"). (h) Total ground-state energy for the three cases, compared to the exact result

translational symmetry and the resulting checkerboard structure closely resembles the exact solution (cf. Figure 2a,d). At the same time, the ground-state energy of $-3.64\,J$ for uniSOA does not agree with the exact value of $-4.60\,J$. Similarly, the DOS shows poor qualitative agreement with the exact result, failing to reproduce the correct position of the peaks and, above all, the existence of a band gap.

Relaxing the requirement of translational symmetry (rsSOA) leads to unphysical inhomogeneities in the odd minor diagonals of the spin-up density matrix which is in contrast to the exact solution.[6] However, the ground-state energy is improved, to $-3.84\,J$, closer to the exact result. Additionally, in the DOS, a correlation-induced gap emerges at the Fermi energy in conjunction with an, in general, better qualitative agreement with the exact spectrum. Still, the rsSOA gap of $0.77\,J$ is less than half the size of the exact result of $2.01\,J$.

As a next step, we no longer enforce spin symmetry (usSOA) which results in an antiferromagnetic ground state indicated by the spin-density wave on the diagonal and the inhomogeneities on the even minor diagonals of the spin-up density matrix, shown in Figure 2c. This Néel state has an energy of $-4.08\,J$ which is in much better agreement with the exact value. In this case, the DOS nicely reproduces the position of the main peaks and the Hubbard gap of $1.77\,J$ is much closer to the exact value.[7]

Similar to the findings for the HF selfenergy presented in Section 3, removing the requirement of translation and spin symmetry for the SOA leads to a significant improvement for the ground-state energy and the DOS. This way the exact Mott gap can be remarkably well reproduced, even for relatively large interactions such as $U = 4\,J$.

---

[6]Note that, while the translational symmetry is broken, the spin symmetry is still fulfilled.
[7]The remaining differences to the exact DOS, namely, the missing high-energy satellites and the degenerate peak at $\sim\pm1.8\,J$, can be attributed to the shortcoming of the SOA at the large interaction $U = 4\,J$.

5 | MULTIPLE SOLUTIONS OF THE DYSON EQUATION IN SECOND-BORN APPROXIMATION

The possibility of multiple solutions is a well-known feature of self-consistent treatments of the Dyson equation.[67,68,81] Usually, a self-consistency requirement is employed in approximate treatments via e.g. perturbation theory. The existence of a self-consistent solution to the Dyson equation was shown to depend on the choice of the selfenergy approximation, in particular its positive semi-definiteness (PSD). The SOA selfenergy used in this work is known to be conserving and PSD,[82] and is thus suitable to study the emergence of multiple solutions. With a specific choice of the translational invariance, and without addressing the role of broken symmetry, this was done before in a specific case.[83] Here, the effect of artificially breaking specific symmetries is brought to the foreground, and explicitly connected to the insurgence of multiple approximate self-consistent solutions. To this end, we solve Equation (4) with no symmetries enforced (usSOA), for a half-filled Hubbard chain of length $L = 8$ with periodic boundary conditions and $U = 4\,J$, i.e., for the same system as in Section 4. The initial state of the iteration scheme is chosen to be the homogeneous, spin-restricted HF ground state where the density is modified by a small random perturbation of the order 10^{-5}.[8]

In Figure 3, the DOS (a,b), ground-state energy (c), and iteration error (d) are shown during the iterative procedure. The calculation starts from the slightly disturbed rsHF ground state with energy $-1.52\,J$ (not shown in Figure 3c). Within the first 170 iterations, the system converges into the homogeneous state (cf. the DOS in Figure 2e), as the relative iteration error drops to 10^{-3}. However, at around 300 iterations the error increases and the system transitions into the inhomogeneous but spin-symmetric state (cf. the DOS in Figure 2f). This state appears to be even more stable, with the relative iteration error temporarily dropping to 10^{-5}. However, after 3000 iterations, a final transition sets in, and the system arrives in the spin-asymmetric state (cf. the DOS in Figure 2g). The system remained in this state for the remainder of the iteration process, and the relative error of the calculation eventually reached the order of machine precision.[9]

While, during the iteration, the DOS evolves through the three states shown in Figure 2, the total energy passes through the values of the respective states that are depicted in Figure 2h. This is shown in detail, as a function of the iteration number, in Figure 3c, cf. the coloured lines. This shows that the three states, corresponding to the different symmetry restrictions discussed in Section 4, can be reached by a single iterative solution of the Dyson equation when no symmetries are enforced. During the iteration, in the vicinity of each of the three states, the iteration error drops significantly (reaching a high degree of self-consistency). This suggests that all of them are solutions of the same Dyson equation, with only the unrestricted-spin state being absolutely numerically stable. A well-conditioned iteration scheme will, ultimately, reach this minimum-energy state. Of course, the sequence of states reached on the way to the minimum depends on the choice of the initial state of the iteration and on details of the numerical procedure.

The present example is a direct illustration of Löwdin's symmetry dilemma discussed above and shows that a successive reduction of the symmetry of explored states may allow one to improve certain target properties of a system, such as the ground-state energy, also in a many-body calculation with the SOA selfenergy. The behaviour just discussed here is expected to be a specific facet of a general scenario underlying the search for multiple solutions of the Dyson equation that are a consequence of the nonlinear dependence of the collision integrals on the Green functions which is a general property of selfenergies beyond Hartree–Fock. These observations should give useful hints how to improve iterative solutions of the Dyson equation or similar nonlinear equations.

6 | BENCHMARKING AGAINST DMRG

The existence of a Mott gap for large on-site interactions is one of the most important features of the Hubbard model. After analysing the general properties of GFMBA simulations with HF and SOA selfenergies for the three methods (I)–(III), we now focus on their performance regarding the Hubbard gap, Equation (1), in particular. Since we are considering finite systems we are interested in the correlation part of the band gap which we define as

$$\Delta_{\mathrm{corr}} = \Delta - \Delta_{\mathrm{rsHF}}, \tag{22}$$

---

[8]Recall that, without this small initial inhomogeneity, no broken spin symmetry would occur, even in spin-resolved calculations.
[9]It should be noted that there is a little dip/kink in the relative error at around iteration 3500. This could hint to a possible forth viable state that we did not reach in our calculation.
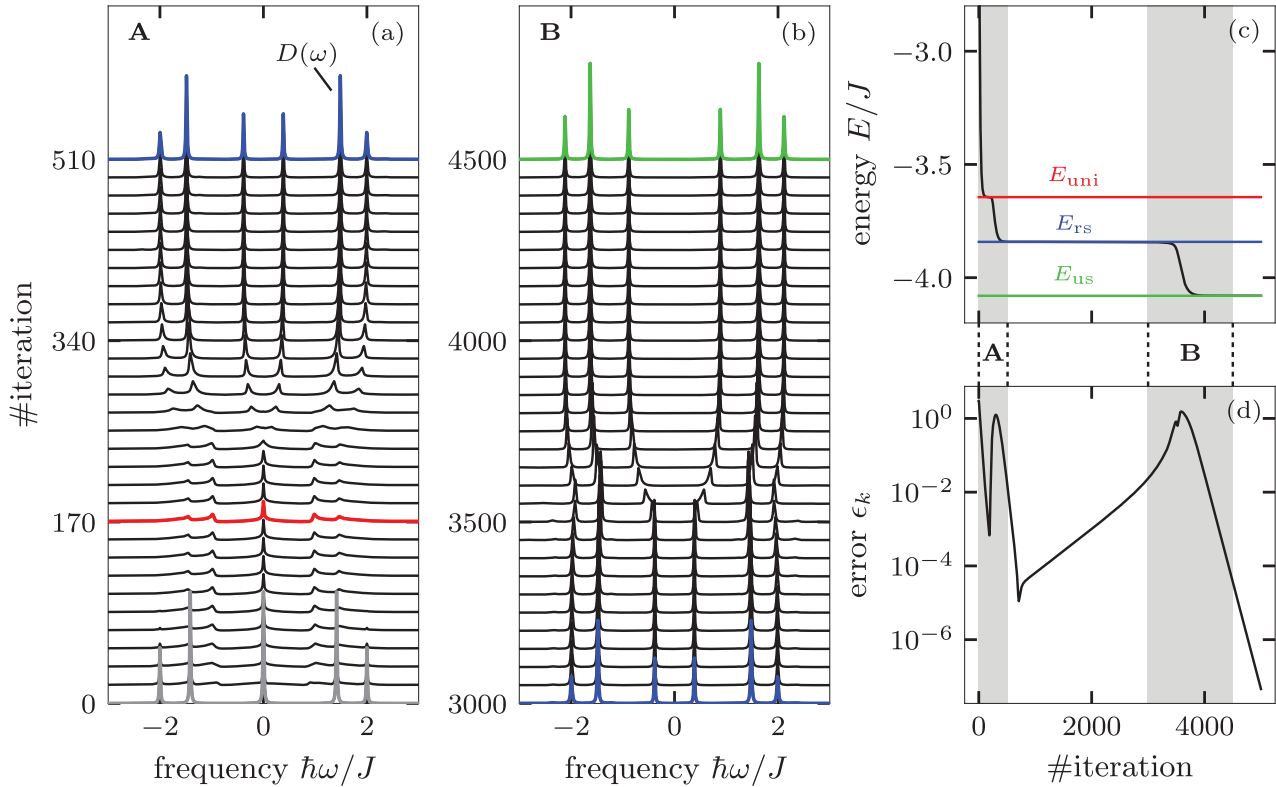
FIGURE 3 Ground-state properties of a half-filled Hubbard chain of length $L = 8$ and $U = 4\,J$ for usSOA during the iteration procedure. The initial state is the rsHF solution of the system modified by a small deviation to initiate the symmetry breaking. (a),(b) Evolution of the density of states during the iteration procedure, for two stages **A** and **B** of the iteration that are highlighted by the grey areas in (c) and (d). The coloured spectra correspond to the respective states in Figure 2. (c) Ground-state energy during the iteration procedure. The energies corresponding to the states of Figure 2 are shown with their respective colour. (d) Relative error during the iteration procedure

where Δ_{rsHF} is the band gap obtained from a rsHF calculation that contains only the finite-size contribution. In the thermodynamic limit Δ_{rsHF} vanishes, and $\Delta_{\mathrm{corr}} = \Delta$. In Figure 4, we compare the correlation gap of finite Hubbard chains of varying length at $U = 4\,J$ to the (exact) result obtained by DMRG (we employed the size-increasing scheme as in Refs. [84, 85]). Additionally, we extrapolate the data to $L \rightarrow \infty$ where the DMRG result agrees with the Bethe-ansatz solution.[86] In the case of the restricted-spin HF and the homogeneous SOA (uniSOA) state the Hubbard gap vanishes, cf. Figure 2d for the latter.

In contrast, starting with open boundary conditions, rsSOA shows a finite gap and correctly predicts its qualitative dependence on the length of the system. However, since SOA captures only part of the correlation effects, the correct band gap is underestimated by $\sim 0.7\,J$ for all system sizes. As discussed for the local magnetic moment in Section 3, the antiferromagnetic ground state of the unrestricted-spin methods can compensate shortcomings of the selfenergy approximations in treating correlations. In the case of usHF, this results in the opening of a correlation gap on the mean-field level. However, for the large interaction of $U = 4\,J$, the size of the gap is severely overestimated, especially, in the thermodynamic case, where usHF predicts a size of $3.073\,J$, as opposed to the exact value of $1.287\,J$. In contrast to the exact case, the correlated gap is monotonically increasing with the system length for the unrestricted-spin methods. Nevertheless, usSOA shows the best agreement with the exact gap out of all selfenergies and symmetry restrictions considered here. Especially for large system sizes, including the case of the infinite Hubbard chain, the deviation does not exceed $\sim 0.25\,J$.

The results for periodic boundary conditions (shown as dashed lines in Figure 4) differ only slightly from the above observations. While, for small systems ($L < 40$), there is a noticeable difference between both cases, the size of the correlated gap converges to the same value for larger systems. The speed of this convergence is considerably faster for the unrestricted-spin methods which possess an antiferromagnetic ground state.

Independent of the type of boundary conditions, giving up on the symmetries of the exact solution, the description of the Hubbard gap in finite systems, especially for the selfenergy in SOA, improves dramatically, even for large interaction strengths, again confirming Löwdin's symmetry dilemma.
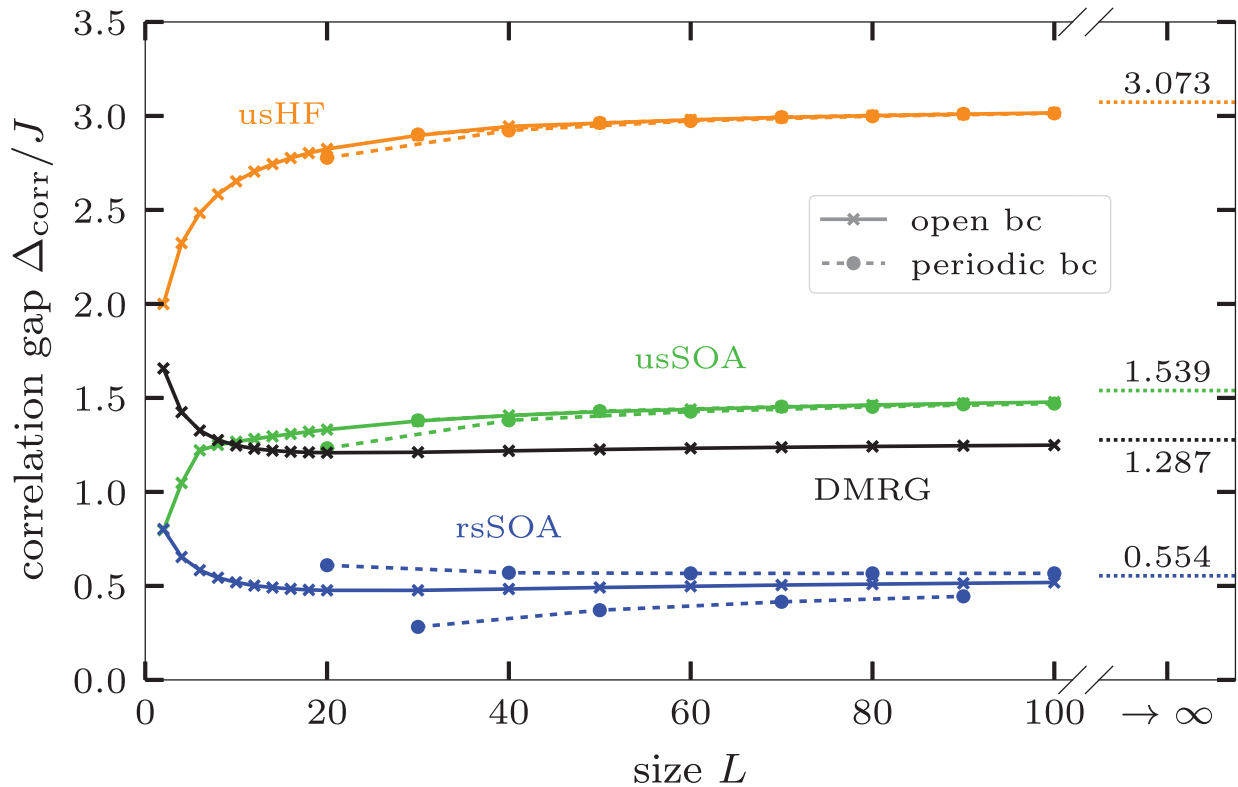
FIGURE 4 Correlation band gap of a half-filled, one-dimensional Hubbard chain of finite length L and $U = 4J$ with open (full lines with crosses) and periodic (dashed lines with circles) boundary conditions. Density-matrix-renormalization-group results are compared to different restricted-spin (rs) and unrestricted-spin (us) selfenergy approximations. The extrapolated results for the limit of the infinite Hubbard chain are shown as dotted lines on the right

To further assess the quality of not only the correlation gap but the total DOS, in Figure 5 we compare the results of the rsSOA and usSOA methods to the spectral function obtained by Nocera et al.[87] using the time-dependent DMRG (tDMRG) method for an open Hubbard chain of 40 sites for $U = 4J$. The finite real-time window of the tDMRG approach results in an artificial broadening of the peaks in the spectral function. For a better comparison, we emulate this effect by performing on our much sharper DOS a convolution with a Gaussian that corresponds to a time-window size of $15J^{-1}$. The general trends observed in Figure 2f,g for a short chain of eight sites are confirmed also for this larger system of length $L = 40$. The main characteristics of the tDMRG spectrum are the major peaks at $\pm 1J$ and $\pm 2J$, the satellites at $\pm 4.5J$ and a slowly descending slope between those features. According to the observations of Figure 4, rsSOA severely underestimates the size of the Hubbard gap since the spectrum in general is shifted toward the Fermi energy resulting in a poor overall agreement with tDMRG. On the contrary, usSOA reproduces the position of the major peaks and the satellites remarkably well, whereas only the slope between them is not described correctly. The spectral weight that is missing in the slope is, instead, transferred to the oversized major peaks. Nevertheless, the agreement of usSOA with the tDMRG results is striking, considering the high on-site interaction of $U = 4J$.

7 | CONCLUSION

Currently, there is great interest in the theoretical condensed-matter community in devising approaches for strongly correlated systems, i.e. for those systems where a description based on an independent-particle picture is qualitatively inadequate.

In this work, we have looked at a certain aspect of the problem, namely, the interplay of symmetry constraints and electronic correlations. Specifically, using finite Hubbard chains at half filling as a case study for strongly correlated systems, we investigated the role of symmetry requirements in many-body perturbation Green function theory (GFMBA), where approximations of increasing complexity can be systematically devised for the many-body selfenergy.
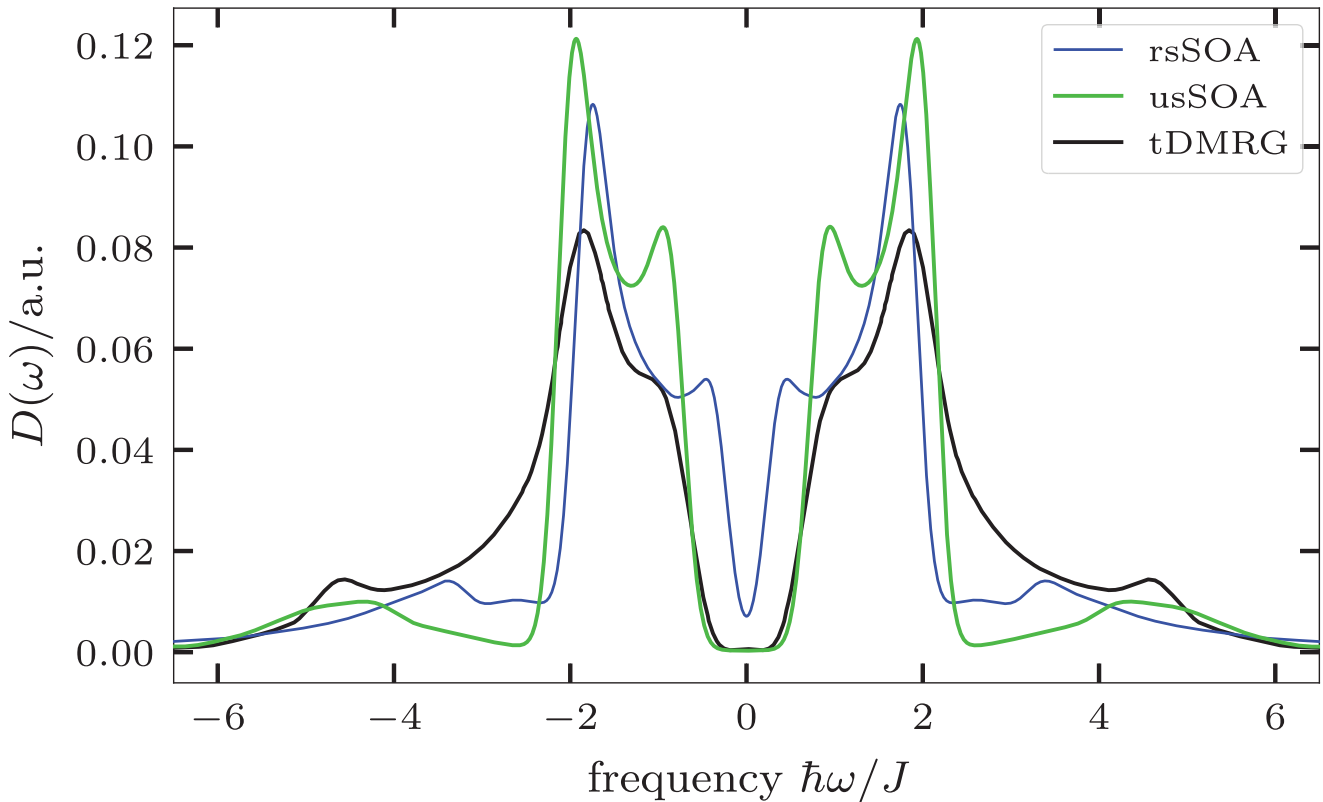
FIGURE 5 Density of states of a half-filled Hubbard chain of length $L = 40$ and $U = 4J$ with open boundary conditions. The tDMRG data are taken from Ref. [87]. The rsSOA and usSOA spectra are broadened using a Gaussian corresponding to a real-time window of size $15J^{-1}$ that matches the width in Ref. [87]

In the literature, GFMBA is often seen as an ill-suited conceptual paradigm to describe strong correlations, because of, e.g., possible multiple self-consistent approximate solutions, or uncertainty about the convergence radius of the perturbation expansion. While not calling into question this point of view, in this study we have used GFMBA to address the interplay of symmetry and correlation effects. To our knowledge this is a point that, irrespective of the methodology used, has received little systematic attention so far. For our GFMBA description of Hubbard systems, we used the second-Born approximation which accounts for electronic correlations at lowest perturbative order in a "skeleton-diagram" sense. However, for the sake of comparison we also presented results from an Hartree–Fock treatment.

Already at the HF level, our comparison of spin-symmetry-restricted and unrestricted self-consistent solutions indicates that one is facing a so-called *Löwdin symmetry dilemma* for the one-dimensional Hubbard model: namely, the violation of spin-symmetry can lead to a spectral function and ground-state energy that are closer to the exact ones than those obtained when spin symmetry is imposed.

Our results suggest that this behaviour is robust against the inclusion of electronic correlations within GFMBA. For our self-consistent SOA treatment of finite periodic Hubbard chains at half-filling, in addition to spin symmetry we also considered translation symmetry. While the exact solution corresponds to densities which are both spin-projection symmetric and translationally invariant, the violation of these properties in SOA leads to results for the ground-state energy and the local spectral function which are remarkably close to the exact ones. This is particularly so when using the unrestricted-spin symmetry SOA: in this case, the exact value of the Hubbard energy gap is surprisingly well produced, within ∼15%, also for strong on-site interaction $U = 4J$. Finally, an interesting overall trait of our results is that the symmetry-restricted states are in fact solutions (albeit metastable) to the unrestricted Dyson equation: starting from a specifically crafted initial state, the self-consistency iteration dynamics passes through the symmetry-constrained states before reaching the unrestricted ground state.

Thus, altogether our work illustrates a direct connection between symmetry constraints and solution multiplicity in GFMBA, adding to the already available body of knowledge on the behaviour of multiple solutions for the Dyson equation. As possible future directions, an obvious point to address is if more complex selfenergy approximations, such as the

T matrix and *GW* approximations, would give improved results in symmetry-lifted treatments as well. Other straightforward extensions would be the exploration of the case of higher dimensions (where, however, an increased complexity is expected due to a richer structure of the phase diagram) and electron occupancies different from half filling.

More in general (and very much in the spirit of Löwdin's original lines of thought), it could be of some interest to see if it is possible (and what happens) when concretely profiting from the symmetry dilemma within GFMBA, by restoring symmetry at the end via projection techniques. This procedure, in different variants and extensions, has been already used in the literature for wavefunctions, typically starting from HF symmetry-unrestricted states, e.g., Ref. [11]. Pursuing the same strategy within GFMBA would allow one to explore the feasibility of convenient ways to access some important physical quantities in strongly correlated systems.

ACKNOWLEDGMENTS

DATA AVAILABILITY STATEMENT
Research data are not shared

REFERENCES
[1] P. Lykos, G. W. Pratt, *Rev. Mod. Phys.* **1963**, *35*, 496.
[2] A. W. Overhauser, *Phys. Rev. Lett.* **1960**, *4*, 462.
[3] B. Bernu, F. Delyon, L. Baguet, M. Holzmann, *Contrib. Plasma Phys.* **2017**, *57*(10), 524.
[4] T. Dornheim, S. Groth, M. Bonitz, *Phys. Rep.* **2018**, *744*, 1.
[5] G. E. Scuseria, C. A. Jiménez-Hoyos, T. M. Henderson, K. Samanta, J. K. Ellis, *J. Chem. Phys.* **2011**, *135*(12), 124108.
[6] P. W. Anderson, Basic Notions of Condensed Matter Physics, Benjamin/Cummings, Menlo Park, CA **1984**.
[7] A. V. Filinov, M. Bonitz, Y. E. Lozovik, *Phys. Rev. Lett.* **2001**, *86*, 3851.
[8] A. V. Filinov, Y. E. Lozovik, M. Bonitz, *Phys. Status Solidi B* **2000**, *221*(1), 231.
[9] J. Böning, A. Filinov, P. Ludwig, H. Baumgartner, M. Bonitz, Y. E. Lozovik, *Phys. Rev. Lett.* **2008**, *100*, 113401.
[10] C. Yannouleas, U. Landman, *Phys. Rev. Lett.* **1999**, *82*, 5325.
[11] C. Yannouleas, U. Landman, *Rep. Prog. Phys.* **2007**, *70*(12), 2067.
[12] J. G. Kirkwood, I. Oppenheim, F. H. Stillinger, Quantum Statistics and Cooperative Phenomena, Vol. 1, Gordon and Breach, New York **1965**.
[13] N. N. Bogoliubov, *Lectures on Quantum Statistics*, Vol. 1 of *Lectures on Quantum Statistics*, Gordon and Breach, New York **1967**.
[14] F. Gebhard, The Mott Metal-Insulator Transition, Springer, Berlin Heidelberg **1997**.
[15] M. Bonitz, C. Henning, D. Block, *Rep. Prog. Phys.* **2010**, *73*, 066501.
[16] K. Balzer, M. Bonitz, R. van Leeuwen, A. Stan, N. E. Dahlen, *Phys. Rev. B* **2009**, *79*, 245306.
[17] G. Stefanucci, R. van Leeuwen, Nonequilibrium Many-Body Theory of Quantum Systems, Cambridge University Press, Cambridge **2013**.
[18] C. B. Mendl, F. Malet, P. Gori-Giorgi, *Phys. Rev. B* **2014**, *89*, 125106.
[19] M. C. Gutzwiller, *Phys. Rev. Lett.* **1963**, *10*, 159.
[20] J. Hubbard, B. H. Flowers, *Proc. R. Soc. London, Ser. A* **1963**, *276*(1365), 238.
[21] Editorial, *Nat. Phys* **2013**, *9*, 523.
[22] L. Tarruell, L. Sanchez-Palencia, *C. R. Phys.* **2018**, *19*, 365.
[23] M. Eckstein, M. Kollar, P. Werner, *Phys. Rev. Lett.* **2009**, *103*, 056403.
[24] N. Schlünzen, S. Hermanns, M. Bonitz, C. Verdozzi, *Phys. Rev. B* **2016**, *93*, 035107.
[25] K. Balzer, N. Schlünzen, M. Bonitz, *Phys. Rev. B* **2016**, *94*, 245118.
[26] K. Balzer, M. R. Rasmussen, N. Schlünzen, J.-P. Joost, M. Bonitz, *Phys. Rev. Lett.* **2018**, *121*, 267602.
[27] N. Schlünzen, K. Balzer, M. Bonitz, L. Deuchler, E. Pehlke, *Contrib. Plasma Phys.* **2019**, *59*, e201800184.
[28] J.-P. Joost, N. Schlünzen, M. Bonitz, *Phys. Status Solidi B* **2019**, *257*, 1800498.
[29] E. V. Boström, A. Mikkelsen, C. Verdozzi, E. Perfetto, G. Stefanucci, *Nano Lett.* **2018**, *18*, 785.
[30] M. Hopjan, G. Stefanucci, E. Perfetto, C. Verdozzi, *Phys. Rev. B* **2018**, *98*, 041405.
[31] E. Viñas Boström, C. Verdozzi, *Phys. Status Solidi B* **2019**, *256*, 1800590.
[32] J.-P. Joost, A.-P. Jauho, M. Bonitz, *Nano Lett.* **2019**, *19*(12), 9045.
[33] F. Covito, E. Perfetto, A. Rubio, G. Stefanucci, *Phys. Rev. A* **2018**, *97*, 061401.
[34] G. Cohen, M. Galperin, *J. Chem. Phys.* **2020**, *152*, 090901.
[35] A. Kalvová, B. Velický, V. Špička, *EPL (Europhysics Letters)* **2018**, *121*, 67002.
[36] A. Kalvová, B. Velický, V. Špička, *Phys. Status Solidi B* **2019**, *256*, 1800594.
[37] R. Rodríguez-Guzmán, C. A. Jiménez-Hoyos, R. Schutski, G. E. Scuseria, *Phys. Rev. B* **2013**, *87*, 235129.
[38] E. H. Lieb, F. Y. Wu, *Phys. Rev. Lett.* **1968**, *20*, 1445.
[39] A. J. Daley, C. Kollath, U. Schollwöck, G. Vidal, *J. Stat. Mech.: Theory Exp.* **2004**, *2004*, P04005.

[40] G. Vidal, *Phys. Rev. Lett.* **2004**, *93*, 040502.

[41] S. R. White, A. E. Feiguin, *Phys. Rev. Lett.* **2004**, *93*, 076401.

[42] T. Ulbricht, P. Schmitteckert, *EPL* **2009**, *86*, 57006.

[43] T. Ulbricht, P. Schmitteckert, *EPL* **2010**, *89*, 47001.

[44] B. Schoenauer, P. Schmitteckert, D. Schuricht, *Phys. Rev. B* **2017**, *95*, 205103.

[45] E. Dagotto, *Rev. Mod. Phys.* **1994**, *66*, 763.

[46] E. Gull, A. J. Millis, A. I. Lichtenstein, A. N. Rubtsov, M. Troyer, P. Werner, *Rev. Mod. Phys.* **2011**, *83*, 349.

[47] J. E. Hirsch, *Phys. Rev. B* **1985**, *31*, 4403.

[48] R. Staudt, M. Dzierzawa, A. Muramatsu, *Eur. Phys. J. B* **2000**, *17*, 411.

[49] P. Hamann, T. Dornheim, J. Vorberger, Z. Moldabekov, M. Bonitz, *Contrib. Plasma Phys.* **2020**, *60*, e202000147.

[50] W. Metzner, D. Vollhardt, *Phys. Rev. Lett.* **1989**, *62*, 324.

[51] M. Jarrell, *Phys. Rev. Lett.* **1992**, *69*, 168.

[52] A. Georges, G. Kotliar, W. Krauth, M. J. Rozenberg, *Rev. Mod. Phys.* **1996**, *68*, 13.

[53] E. Kozik, K. Van Houcke, E. Gull, L. Pollet, N. Prokof'ev, B. Svistunov, M. Troyer, *EPL* **2010**, *90*(1), 10004.

[54] T. Maier, M. Jarrell, T. Pruschke, M. H. Hettler, *Rev. Mod. Phys.* **2005**, *77*, 1027.

[55] A. N. Rubtsov, M. I. Katsnelson, A. I. Lichtenstein, *Ann. Phys.* **2012**, *327*, 1320.

[56] T. Ayral, O. Parcollet, *Phys. Rev. B* **2015**, *92*, 115109.

[57] A. L. Fetter, J. D. Walecka, Quantum Theory of Many-Particle Systems, McGraw-Hill, Boston **1971**.

[58] A. A. Abrikosov, L. P. Gorkov, I. Dzyaloshinskii, R. A. Silverman, Methods of Quantum Field Theory in Statistical Physics, Dover, New York **1975**.

[59] K. Balzer, M. Bonitz, *Nonequilibrium Green's Functions Approach to Inhomogeneous Systems* (*Lecture* Notes in Physics), Springer, Berlin, Heidelberg **2013**.

[60] N. Schlünzen, J.-P. Joost, M. Bonitz, *Phys. Rev. Lett.* **2020**, *124*, 076601.

[61] J.-P. Joost, N. Schlünzen, M. Bonitz, *Phys. Rev. B* **2020**, *101*, 245101.

[62] M. Puig von Friesen, C. Verdozzi, C.-O. Almbladh, *Phys. Rev. Lett.,* **2009**, *103*(17), 176404.

[63] N. Schlünzen, S. Hermanns, M. Scharnke, M. Bonitz, *J. Phys. Condens. Matter* **2020**, *32*, 103001.

[64] N. Schlünzen, J.-P. Joost, M. Bonitz, *Phys. Rev. B* **2017**, *96*, 117101.

[65] N. Schlünzen, J.-P. Joost, F. Heidrich-Meisner, M. Bonitz, *Phys. Rev. B* **2017**, *95*, 165139.

[66] G. Lani, P. Romaniello, L. Reining, *New J. Phys.* **2012**, *14*(1), 013056.

[67] F. Tandetzky, J. K. Dewhurst, S. Sharma, E. K. U. Gross, *Phys. Rev. B* **2015**, *92*(11), 115125.

[68] O. Gunnarsson, G. Rohringer, T. Schäfer, G. Sangiovanni, A. Toschi, *Phys. Rev. Lett.* **2017**, *119*, 056402.

[69] C. D. Spataru, M. S. Hybertsen, S. G. Louie, A. J. Millis, *Phys. Rev. B* **2009**, *79*, 155110.

[70] S. Di Sabatino, J. A. Berger, L. Reining, P. Romaniello, *J. Chem. Phys.* **2015**, *143*, 024108.

[71] N. Säkkinen, Y. Peng, H. Appel, R. van Leeuwen, *The Journal of Chemical Physics* **2015**, *143*, 234102.

[72] E. H. Lieb, *Phys. Rev. Lett.* **1989**, *62*(10), 1201.

[73] E. H. Lieb, M. Loss, R. J. McCann, *J. Math. Phys.* **1993**, *34*, 891.

[74] D. R. Penn, *Phys. Rev.* **1966**, *142*, 350.

[75] W. F. Brinkman, T. M. Rice, *Phys. Rev. B* **1970**, *2*, 4302.

[76] T. Schäfer, F. Geles, D. Rost, G. Rohringer, E. Arrigoni, K. Held, N. Blümer, M. Aichhorn, A. Toschi, *Phys. Rev. B* **2015**, *91*, 125109.

[77] A. Mukherjee, S. Lal, *New J. Phys.* **2020**, *22*, 063007.

[78] L. V. Keldysh, *Soviet Phys. JETP* **1965**, *20*, 1018 (Zh. Eksp. Teor. Fiz. **47**, 1515 (1964)).

[79] M. Bonitz, A.-P. Jauho, M. Sadovskii, S. Tikhodeev, *Phys. Status Solidi B* **2019**, *256*, 1800600.

[80] D. Baeriswyl, D. K. Campbell, J. M. P. Carmelo, F. Guinea, E. Louis, *The Hubbard Model: Its Physics and Mathematical Physics*, of *Nato Science Series B*, Springer, New York **2013**.

[81] A. Stan, P. Romaniello, S. Rigamonti, L. Reining, J. A. Berger, *New J. Phys.* **2015**, *17*, 093045.

[82] G. Stefanucci, Y. Pavlyukh, A.-M. Uimonen, R. van Leeuwen, *Phys. Rev. B* **2014**, *90*(11), 115134.

[83] A. A. Rusakov, D. Zgid, *J. Chem. Phys.* **2016**, *144*, 054106.

[84] R. Korytár, D. Xenioti, P. Schmitteckert, M. Alouani, F. Evers, *Nat. Commun.* **2014**, *5*(1), 5000.

[85] P. Schmitteckert, R. Thomale, R. Korytár, F. Evers, *J. Chem. Phys.* **2017**, *146*, 092320.

[86] F. H. L. Essler, H. Frahm, F. Göhmann, A. Klümper, V. E. Korepin, The One-Dimensional Hubbard Model, Cambridge University Press, Cambridge **2005**.

[87] A. Nocera, F. H. L. Essler, A. E. Feiguin, *Phys. Rev. B* **2018**, *97*, 045146.

Chapter 4

Applications to Correlated Lattice Systems Out of Equilibrium

Based on the theoretical improvements of the last chapters, the NEGF approach is well qualified to describe nonequilibrium phenomena in experimentally relevant correlated lattice systems. Chpt. 4 contains NEGF simulation results to examine the underlying physics under such conditions. First, the predictive power of the method for state-of-the-art applications is brought to proof to further validate the approach (I). Subsequently, the NEGF technique is applied to ultracold atoms in optical lattices, where an unprecedented agreement with recent experiments is obtained. Furthermore, ion-stopping dynamics in graphene nanostructures are investigated, where a new mechanism to induce stable double occupation in the material is identified.

4.1 Numerical Studies: Benchmark and Stability

Historically, it was a long way from the theoretical foundation of the NEGF technique by Baym, Kadanoff and Keldysh in the early 60s to the first numerical applications in the mid 80s [106]. Since then, the NEGF framework has proven many times to be a competitive method in practice. In the new millennium, the application to lattice models has been particularly successful (see, e.g., the pioneering publications of Refs. [109, 130, 136]). The combination of the simplicity of lattice Hamiltonians on the one hand and the general rise of computer power on the other hand has spawned a well-suited, controllable environment to compare different NEGF approaches. This makes it all the more surprising that a systematic accuracy test for different NEGF approximations has been lacking—particularly in the mesoscopic realm, where finite-size effects become less important.

   In addition, it was found that under the influence of strong external fields the Kadanoff–Baym dynamics suffer from an unphysical damping behavior that eventually leads to a steady-state solution for finite systems [109, 130]. This behavior was identified as a correlation-induced effect caused by unbalanced n-particle correlations due to the partial summation schemes within the selfconsistent many-body approximations. Several attempts

have been made to mitigate this artificial damping property. Among them, a more promising candidate has been the application of the GKBA [134, 136] (cf. Secs. 2.2 and 3.1). In Ref. [202], Adrian Stan further analyzed the unphysical damping behavior earlier found for strongly excited, finite lattice systems. His observations have driven him to make a series of rather drastic statements. Additional to the previous findings, he claimed to have found the artificial damping also for small excitations, i.e., in the linear-response regime. Furthermore, not only a steady state should be approached in all these cases, but (after a sufficiently long time) even a homogeneous density distribution (HDD), indicating the existence of an attractor. Lastly, the damping behavior should appear even for selfenergies on the mean-field level (Hartree/Hartree–Fock), although without reaching the HDD. With all these claims, Stan seriously questioned the NEGF framework as a whole. As this would drastically narrow the repertoire of quantum many-body tools, a thorough reevaluation of Stan's analysis is indispensable.

The above-mentioned shortcomings regarding the missing benchmark analysis and the reexamination to Ref. [202] are remedied in the following publications,[1,2] Refs. [211] and [212].

Regarding the serious claims by Stan, the author has carefully redone all critical calculations of Ref. [202] with a strikingly different outcome. Ref. [211] is, therefore, written as a comment to Ref. [202], and in it the above statements by Stan are unambiguously proven wrong. The reasoning in this comment is twofold. In the first part, the numerical foundation of the above claims—the HDD, the damping in linear response, and the mean-field damping—is refuted. It is shown on the basis of three representative example calculations that by using thoroughly converged numerics the resulting dynamics differ significantly from the ones presented in Ref. [202]. The converged results, instead, show no sign for any of the described behaviors. This observation is in striking difference to the well-described artificial damping for strongly excited systems, which manifests in any converged description. Thus, there is no foundation to draw the far-reaching conclusions of Ref. [202]. In the second part of Ref. [211], it is demonstrated that the above-mentioned trends observed by Stan are not an intrinsic numerical property of the KBE, but crucially depend on the choice of the numerical integration method. A general tendency towards damped oscillations can be generated if the collision integral is evaluated with a low-order integration rule combined with an insufficiently small time step, which is the most probable explanation for Stan's observations. It is also demonstrated, that, in an equally likely scenario, the opposite behavior can be induced by using a low-order time-stepping scheme with a too large step, leading to monotonically growing—and eventually diverging—oscillations. If there is a lesson to learn for NEGF simulations, it is the great importance of numerical accuracy checks, such as convergency tests, fulfilling the conservation laws (cf. Sec. 2.1.4), and time reversibility (cf. Sec. 3.2).

Ref. [212] provides a thorough benchmark analysis that compares Green-functions methods utilizing more advanced selfenergy approximations to the quasi-exact density-matrix-renormalization-group (DMRG) theory. The concept of the paper has been devel-

[1] N. Schlünzen, J.-P. Joost, and M. Bonitz, Phys. Rev. B, **96**, 117101 (2017). Copyright by the American Physical Society. Reproduced with permission.

[2] N. Schlünzen, J.-P. Joost, F. Heidrich-Meisner, and M. Bonitz, Phys. Rev. B, **95**, 165139 (2017). Copyright by the American Physical Society. Reproduced with permission.

oped in collaboration with Fabian Heidrich-Meisner, who also provided all DMRG data and wrote the corresponding theoretical part. Ref. [212] focuses on electron dynamics following strong nonequilibrium conditions for Hubbard chains and a two-dimensional ladder setup. The author's work on the NEGF implementation has decisively facilitated the applicability of the used many-body approximations on the Green-function side, comprising the T-matrix and the third-order approximation with and without the additional adaption of the GKBA. The analysis led to several key observations. Above all, the presented simulation data confirm the excellent quality of the NEGF approach in the regime of small to moderate coupling strengths. It is, however, of great importance to use every selfenergy approximation in its appropriate context, as the system's requirements such as the filling ratio favor specific classes of many-body scattering processes. Furthermore, it is demonstrated that the quasi-exact DMRG data are typically enclosed between the results of the two-time NEGF and the GKBA description. This property can be utilized to estimate the accuracy of NEGF calculations when no reference data is available, i.e., for systems that are out of reach for other quantum-dynamical methods. Lastly, it is shown that DMRG and NEGF have complementary applicability ranges with respect to the two-particle interaction strength. While DMRG simulations significantly slow down in the weak-coupling regime due to the more versatile dynamics and the concomitant exponential spreading of entanglement, the NEGF method loses its predictive power in the strong-coupling regime due to the perturbative nature of the selfenergy approximations. Thus, an accurate description in the full interaction range can be achieved with a combination of both methods.

The numerical studies in this section have demonstrated that the NEGF technique is indeed a reliable tool to describe time-dependent correlated nonequilibrium systems. For this reason, it is applied to various experimentally relevant setups in the next sections.

Comment on "On the unphysical solutions of the Kadanoff-Baym equations in linear response: Correlation-induced homogeneous density-distribution and attractors"

N. Schlünzen, J.-P. Joost, and M. Bonitz

Institut für Theoretische Physik und Astrophysik, Christian-Albrechts-Universität zu Kiel, D-24098 Kiel, Germany

In a recent Rapid Communication [A. Stan, Phys. Rev. B **93**, 041103(R) (2016)], the reliability of the Keldysh-Kadanoff-Baym equations (KBE) using correlated self-energy approximations applied to linear and nonlinear response has been questioned. In particular, the existence of a universal attractor has been predicted that would drive the dynamics of any correlated system towards an unphysical homogeneous density distribution regardless of the system type, the interaction, and the many-body approximation. Moreover, it was conjectured that even the mean-field dynamics would be damped. Here, by performing accurate solutions of the KBE for situations studied in that paper, we prove these claims wrong, being caused by numerical inaccuracies.

The dynamics of correlated quantum many-body systems has been in the focus of experimental and theoretical studies over the recent two decades. Applications span (but are not limited to) nuclear physics, semiconductor optics and transport, dense plasmas and, more recently, strongly correlated materials and ultracold atoms [1]. A very popular tool to describe these systems theoretically has been the method of nonequilibrium Green functions (NEGF) [2,3] due to their internal consistency and conserving properties. For recent textbook discussions see Refs. [4–7]. Direct numerical solutions of their equations of motion—the Keldysh-Kadanoff-Baym equations (KBE)—have been performed for macroscopic, spatially homogeneous systems such as nuclear matter [8], dense plasmas and electron-hole plasmas (e.g., Refs. [9,10]), or the correlated electron gas [11]. More recently, finite spatially inhomogeneous systems were treated, including atoms and small molecules [12–14], electrons in quantum dots [15], or finite Hubbard clusters [16–18]. For an overview see Ref. [7].

Given the high success of numerical solutions of the KBE, which includes excellent agreement with time-resolved optical experiments in semiconductor optics, excitonic features and transport [4] and, recently, with experiments on the expansion dynamics of fermionic atoms [19,20], it came as a surprise when unphysical behaviors were reported in applications to small systems. Von Friesen, Verdozzi, and Almbladh demonstrated [16,17] that, in small Hubbard clusters, cf. Eq. (1), subjected to a strong external potential, the nonlinear density evolution suffers from an unphysical damping, eventually leading to a steady state, in striking contrast to the exact solution. The authors explained this behavior by the highly nonlinear structure of the correlation self energies entering the KBE giving rise to an infinite sum of diagrams during a self-consistent solution of the KBE. Due to the partial summation schemes of the many-body approximations, the order-by-order balance of the exact solution can be violated which leads to an artificial energy reservoir that can cause damping. This explanation was supported by modified approximations where the degree of self consistency was reduced [17]. Another confirmation and, at the same time, a more systematic approach to this problem is the application of the generalized Kadanoff-Baym ansatz (GKBA) [21] that practically eliminates the artificial damping [22].

In view of the importance and popularity of the KBE, a detailed investigation of the issue of unphysical solutions and a clear mapping out of the range of validity of the KBE is, of course, of high interest. Such an analysis has been attempted by Stan [23] who concludes that unphysical solutions are universal when solving the KBE with a correlation self energy, thereby "[...]drastically restricting the parameter space for which the method can give physically meaningful insights." It is the purpose of this Comment to analyze these far-reaching statements.

The author of Ref. [23] considers a one-band Hubbard model with the Hamiltonian [24]

$$
H(t) = -\sum_{\langle s,s'\rangle}\sum_{\sigma=\uparrow,\downarrow}\hat{c}^{\dagger}_{s,\sigma}\hat{c}_{s',\sigma} + U\sum_{s}\hat{c}^{\dagger}_{s,\uparrow}\hat{c}_{s,\uparrow}\hat{c}^{\dagger}_{s,\downarrow}\hat{c}_{s,\downarrow}
$$
$$
+ \sum_{s}\sum_{\sigma=\uparrow,\downarrow} f_s(t)\hat{c}^{\dagger}_{s,\sigma}\hat{c}_{s,\sigma}, \tag{1}
$$

with $\langle s,s'\rangle$ being the summation over next neighbors and U being the on-site Hubbard interaction. As a second example, he considers a Hubbard lattice with Coulomb interaction. The analysis focuses on a simple system: two lattice sites occupied by two electrons (Hubbard dimer), except for one case where a four-site system is simulated. Furthermore, the interaction strength U (in units of the hopping rate) is varied between 0 and 5 and the system is treated using weak coupling many-body approximations: the second Born self energy (2B, except for one case where also GW results are shown). To study the electron dynamics following an external excitation, the author considers two variants of the time-dependent single-particle field $f_s(t)$: first, a steplike form, $f_s(t) = w_0\delta_{s,1}\theta(t)$, and, second, an instantaneous excitation: $f_s(t) = k_0\delta_{s,1}\delta(t)$, both acting only on site 1. Varying the field amplitude between 0.01 and 5 the linear and nonlinear response are investigated.

Based on the simulation results for this limited set of systems and situations, the author draws the following conclusions that are termed "universal," i.e., are claimed to be valid *regardless of the system size, the interaction type, the interaction strength, and the many-body approximation*:

(1) The density dynamics obtained from the KBE in the case of strong excitation is damped, in agreement with previous studies [16,17].
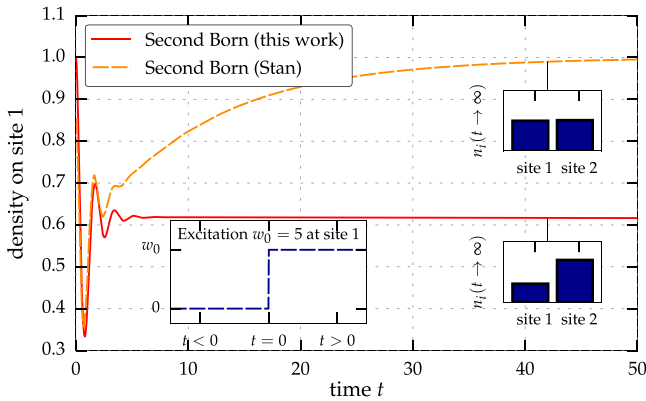
FIG. 1. Density evolution on the first Hubbard site of the dimer with $U = 4$ after the switch-on of a constant excitation with $w_0 = 5$ at site 1, which is shown in the lower left inset. The insets on the right-hand-side show the asymptotic density distributions of Ref. [23] (top) and the present work (bottom). Solutions of the KBE in self-consistent second Born approximation. The time step in our simulation is $\Delta t = 10^{-3}$.

(2) For sufficiently long propagation time, a state with artificial homogeneous density distribution (HDD) is reached, indicating the existence of an attractor.

(3) In addition to previous observations, the unphysical damping occurs also for weak excitation (linear response regime).

(4) For an uncorrelated system (Hartree or Hartree-Fock self energies), damping occurs as well, although no artificial HDD is approached.

We underline that item (1) is relevant only for small finite systems, i.e., the damping effect vanishes quickly with increasing system size. According to the author of Ref. [23], the reason why the new points (2)–(4) have been "missed" by previous studies is due to the insufficient propagation durations in the latter. In the remainder of this Comment, we carefully test the above new claims for several relevant cases.

Let us start with item (2) and analyze the results presented in Fig. 1 of Ref. [23]. There the author studies the nonlinear response of a correlated dimer ($U = 4$) to a strong steplike excitation ($w_0 = 5$). His result for the density on site 1 is reprinted in our Fig. 1 by the dashed line [25] indicating that the density approaches unity (the same value as on the other site, cf. upper inset), i.e., the dynamics approach a spatially homogeneous state (HDD). Now, compare this to our result [26] shown by the full line. Both simulations are in agreement for short times, $t \lesssim 2$, after which we observe a qualitatively different behavior. Even though we also find the unphysical damping known from Refs. [16,17], the asymptotic value is very different from the one of Stan. Regardless of how far the simulations are continued, no alleged HDD state emerges. We note that the time step in our simulations is $\Delta t = 10^{-3}$ whereas Stan reports the value [23] $\Delta t \simeq 10^{-2}$. [A precise value for the time step is missing from his paper.] We underline that this is a typical case. In converged simulations we never found a homogeneous density.

Item (3) concerns the case of a very weak external excitation (linear response). Results for a two-site system were presented in Fig. 2 of Ref. [23]. Here, we concentrate on the example of
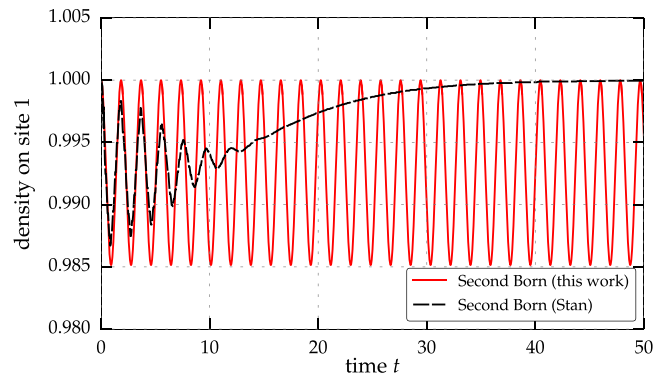
FIG. 2. Density evolution at site 1 of a Hubbard dimer ($U = 3$), following a very weak ($w_0 = 0.05$) steplike excitation at site 1. Black dashed line: result of Ref. [23]. Full red line: present result, using a time step of $\Delta t = 10^{-3}$.

a Hubbard system at $U = 3$ excited by a weak external field (amplitude $w_0 = 0.05$) that is turned on at time $t = 0$ at site 1. While the exact dynamics show undamped oscillations [cf. Figs. 2(a) and 2(b) of Ref. [23]], Stan's second order Born result for the density at site 1 shows strong damping initially and, after $t \sim 10$, approaches the homogeneous density value $n = 1$, cf. the black dashed curve in Fig. 2. Our result is shown by the full red line and shows undamped oscillations as the exact solution. We note that the amplitude and frequency of our result show small deviations from the exact data which is a consequence of the failure of the second Born approximation for U exceeding unity [19,22].

Let us now turn to item (4) of the above list, which concerns the mean-field dynamics. In Fig. 5 of Ref. [23], a strongly interacting ($U = 5$) dimer is considered in Hartree and Hartree-Fock (HF) approximations. The corresponding results of Stan for the densities on the two sites are reproduced in Fig. 3 (cf. the red and black curves) and exhibit a damping towards constant (slightly different) values. This relaxation behavior is very surprising since mean-field dynamics are nondissipative [27]. We, therefore, repeated the Hartree simulations with our
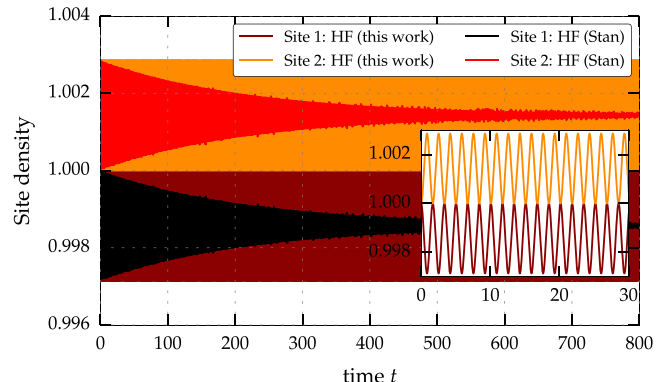
FIG. 3. Mean field (Hartree) density evolution of a Hubbard dimer with $U = 5$ following the switch-on of a constant excitation with $w_0 = 0.01$ on site 1. The results of Ref. [23] are shown by the red and black lines and exhibit damping, whereas our results are undamped (orange and brown lines). The high-frequency oscillations of the density are illustrated in the inset (the resolution of the results of Ref. [23] does not allow to resolve these oscillations).

code for the same parameters. The results are plotted by the orange and brown curves and show no damping. We also note that in our simulations the density exhibits high-frequency oscillations (see inset).

Summarizing our numerical simulations (cf. Figs. 1–3) we found that the statements (2)–(4) of the above list cannot be reproduced within converged calculations. By "converged" we denote simulations the result of which does not change anymore upon further reduction of the time step in the discretization of the KBE. To understand possible sources of damping in the linear response regime and the emergence of an artificial HDD state we now analyze the convergence behavior in detail. The numerical solution of the KBE basically invokes two time integration procedures [20,28]:

(A) the evaluation of the collision integral [cf. integral expression in Eq. (1) of Ref. [23]] and

(B) the time propagation of the entire (integro)differential equations (time stepping).

Obviously, for any discretization procedure, the exact integrodifferential equation will be recovered when the time step Δt vanishes. For practical simulations, however, a finite value Δt has to be used, so the question arises, which values are acceptable. For converged solutions, all values Δt less or equal to some threshold Δt_c are expected to yield the same result, at least for a given propagation duration T (Δt_c may depend on T). A key question is how to determine the threshold Δt_c. Since the answer to these questions strongly depends on the specific scheme used to perform the integrations (A) and (B), we consider two typical cases:

(I) The collision integral (A) is evaluated in the lowest possible order using the trapezoidal rule whereas the integration (B) is performed by a fourth order Runge-Kutta method.

(II) The integral evaluation (A) is performed using a higher order scheme (see Ref. [20] for details), and the integration (B) is done with an explicit Euler method which is known to be less accurate than Runge-Kutta.

In both cases convergence can be achieved, however, the threshold values Δt_c may be different.

In the following, we analyze these issues for the setup presented in Fig. 2 [i.e., a dimer ($U = 3$) with a weak steplike excitation ($w_0 = 0.05$) at site 1], but the results are representative for all examples considered in this paper. Figure 4(a) shows the density evolution using method I and different time steps Δt ranging from $\Delta t = 0.3$ to $\Delta t = 0.01$. In (b) the convergence behavior for the density is shown for method II for time steps in the range $\Delta t = 6 \times 10^{-5} \ldots 0.01$. In both cases convergence is observed: undamped density oscillations that are in exact agreement with each other (see also our result in Fig. 2) and are depicted by the green curve. Since the two implementations are independent of each other, this provides a strong test of the numerics. At the same time, both methods have a very different numerical efficiency that is reflected by the threshold time steps: In the case of method I, $\Delta t_c^I \approx 0.01$, whereas for method II, $\Delta t_c^{II} \approx 6 \times 10^{-5}$.

Let us now analyze the behavior of the simulations when the time step exceeds Δt_c. The figure clearly demonstrates that then the dynamics strongly deviate from the converged behavior where the type of density response and of deviation from the converged result is very different for methods I and II. In case II [Fig. 4(b)] not-converged simulations lead to an
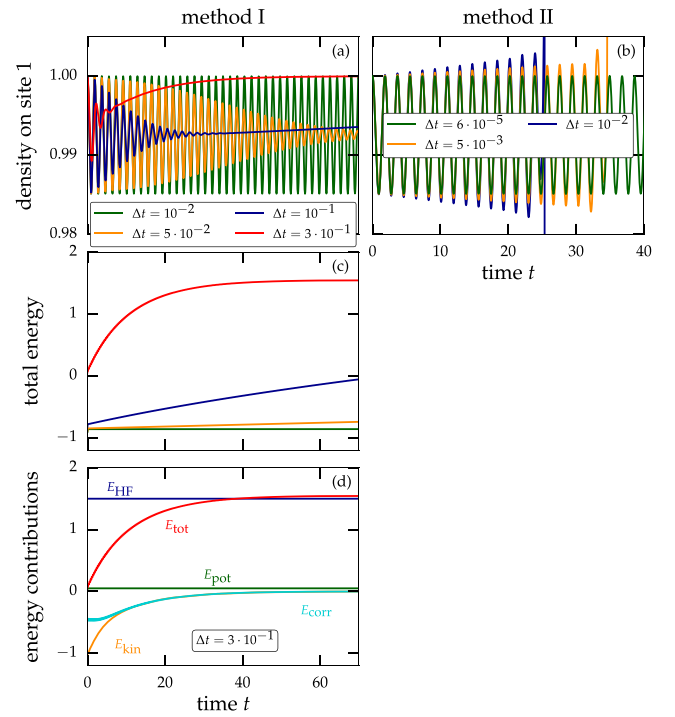
FIG. 4. Demonstration of the convergence behavior for a Hubbard dimer ($U = 3$), following a very weak ($w_0 = 0.05$) steplike excitation at site 1. (a)/(b): density evolution at site 1 for different time steps Δt. Simulations in (a) [(b)] are done with method I (method II). (c) Quality of energy conservation corresponding to the results in (a). (d). Different energy contributions for $\Delta t = 3 \times 10^{-1}$ in (a) and (c). We note that in (b) the time steps only refer to the integration (B). The collision integral (A) is solved with $\Delta t = 10^{-2}$.

increase of the oscillation amplitude in time and, eventually, the simulations become unstable. Increasing the time step leads to an earlier onset of the instability and a more rapid density increase. In case of method I [Fig. 4(a)], we observe the opposite behavior, for $\Delta t > \Delta t_c^I$: The density rapidly decays (cf. the yellow and green curves), a trend that sets in earlier when Δt increases. If Δt is increased to 0.1 or beyond, however, the behavior changes: After a short decay interval the density increases again and approaches a constant value $n_1 = n_2 = 1$, i.e., we exactly recover the trends reported by Stan in Ref. [23] and that he termed "emergence of the HDD" or of a "universal attractor."

From the above observations, we conclude that, indeed, an artificial HDD can be found, however, only if the time step significantly exceeds the critical time step and only for certain discretization schemes. Therefore, this observation is clearly a consequence of nonconverged simulation and is not an inherent property of the KBE.

One may now ask how such erroneous simulations can be avoided. The final test is always a verification of convergence, i.e., a repetition of the simulations with systematic reduction of the time step Δt. In case of the KBE, fortunately, this procedure may be simplified essentially by monitoring the conservation laws of density and total energy. While the former is usually well maintained, the latter is quickly violated if the time step is chosen too large. We, therefore, present in

Fig. 4(c) the time dependence of total energy for method I, for different time steps (the behavior is similar for method II). While for $\Delta t \leqslant \Delta t_c$ energy is perfectly conserved (green curve), for larger time steps this conservation is violated, and the deviations increase with Δt. Comparison with figure (a) clearly shows that an occurrence of damping goes together with a crucial violation of energy conservation [29]. We also observe that the emergence of the artificial HDD is connected to a convergence of the total energy to an unphysical value (cf. red curve). This can be understood from the fact that the trapezoidal rule systematically underestimates the result of the integration of oscillating functions, such as the integrand of the collision integral (see Appendix A for details). Together with the self-consistent structure of the KBE, this results in an ongoing damping, up to the point when the collision integral completely vanishes. This is explored in more detail in Fig. 4(d) where the different contributions to the energy are shown for the time step $\Delta t = 3 \times 10^{-1}$. The potential and the HF energy are stable since they only depend on the density which is conserved due to the accurate solution of the differential equation (B). However, the kinetic and correlation energy, which are connected to the collision integral, tend to zero, leaving the system in a completely uncorrelated stationary state that has nothing to do with the Hamiltonian. Thus, for practical purposes, monitoring total energy conservation is a strong quality test giving a necessary (though not sufficient) criterion of convergence.

Another useful test of the accuracy of the simulations is the verification of time reversal symmetry—a known property of the KBE. This can be done in two ways. First, if after a propagation duration t_1, the times are inverted, $t \to -t$, a numerically correct scheme will return to the initial state after a time $2t_1$. This behavior was verified by Stan in the Supplemental Material to Ref. [23], but this only proves that the time step for integrating the differential equation (B) is sufficiently small, but it is independent of the accuracy of evaluation of the collision integral (A), as we show in Appendix B. Therefore, a more sensitive approach to time reversal is to change, at time t_1, instead, the sign of the Hamiltonian, $H(t) \to -H(-t)$ and of all its contributions. Any converged solution will return to the initial state at $t = 2t_1$. In contrast, in case of a nonconverged evaluation of the collision integral (A), time reversal symmetry is violated (there is a loss of information). This is demonstrated in Appendix B where we also show that the damped dynamics in the case of strong excitation of a small system (a known property of the KBE, cf. Refs. [16,17]) are completely time reversible, if the simulation is converged.

Let us summarize our results. We have repeated a representative part of the simulations of Ref. [23] and presented the results in Figs. 1–3. Our results are in disagreement with Ref. [23] on all the above points, (2)–(4). In particular, we do not observe the alleged HDD state in any of our simulations. Our results have been obtained by two independent methods (method I and II) and have also been confirmed by another program [30]. In the second part of the paper we have analyzed possible reasons of the disagreement with Ref. [23]. A detailed analysis of the convergence behavior of numerical solutions of the KBE has been summarized in Figs. 4, 5, and 6. We presented numerical evidence that our results are converged. In

contrast, the author of Ref. [23] did not present such evidence. The data for the density conservation and time reversal in that paper are not conclusive and the crucial checks of total energy conservation and convergence with respect to the time step are missing. Finally, by analyzing various numerical schemes and their convergence properties we were, indeed, able to recover the emergence of an artificial HDD state of Ref. [23], however, only if we use method I together with a substantially too large time step. Thus, the predictions of Stan are wrong, being a numerical artifact (most likely arising from an inaccurate time integration of the collision integral, cf. Fig. 4). The impressive properties of the Keldysh-Kadanoff-Baym equations remain fully intact.

Note added in proof. Recently, two papers have been published that confirm the results of our Comment: A detailed comparison of NEGF simulations with *ab initio* density matrix renormalization group calculations [31] confirmed the excellent accuracy of our results; and the time-reversal invariance of NEGF theory was proven directly for phi-derivable approximations in Ref. [32].

APPENDIX A: DETAILS ON THE NUMERICAL ERROR OF THE TRAPEZOIDAL RULE

To understand the fact that numerical integration applying the trapezoidal rule can lead to an artificial damping in the solution of the KBE, it is instructive to look at the shape of the collision integral and its integrand, respectively. Figure 5 shows a typical $\bar{t}$ dependence of $\text{Im}[\Sigma(t,\bar{t})G(\bar{t},t')]$ (red). As one can see the integrand oscillates around zero alternating between concave and convex pieces, depending on the sign. The blue line shows how the integrand is approximated with the trapezoidal rule integration. It is apparent that the absolute
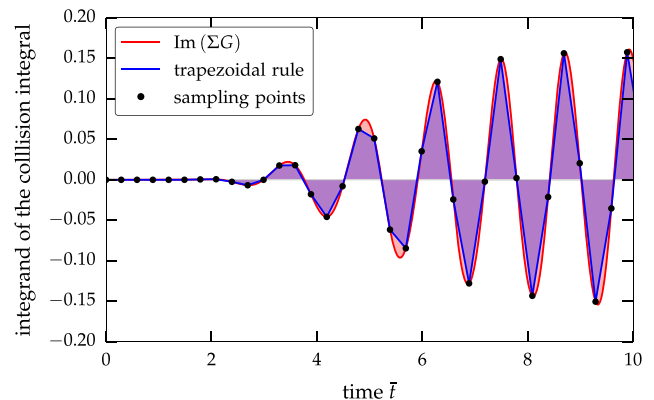
FIG. 5. Illustration of the trapezoidal rule for a typical calculation of the collision integral. The red line shows a realistic example of the integrand in Eq. (1) of Ref. [23] during a converged simulation. The blue curve corresponds to the respective approximation of the trapezoidal rule for a large time step $\Delta t = 0.3$.

value of the integrand is systematically underestimated for every $\bar{t}$. During the evaluation of the integral, after the cancellation of the areas with opposite sign, this leads to an underestimation of the collision integral. Due to the self-consistent structure of the KBE this systematic numerical error results in a progressive damping during the time evolution eventually leading to vanishing kinetic and correlation energy, cf. Fig. 4(d).

The damping property for the integration of oscillating functions can also be understood from a mathematical point of view. The error of the extended trapezoidal rule, $E(I)$, for the integral $\int_a^b f(x)\mathrm{d}x$ is given by [33]

$$E(I) = -\frac{h^2}{12}[f'(b) - f'(a)] + \mathcal{O}(h^3), \qquad (A1)$$

where h is the integration step. The behavior of oscillating integrands can be easily demonstrated for the example of a cosine function. For $I(x) = \int_0^x \cos(\bar{x})\mathrm{d}\bar{x}$ it immediately follows that

$$I_{\text{trapez}}(x) = \sin(x)\left[1 - \frac{h^2}{12}\right] + \mathcal{O}(h^3), \qquad (A2)$$

where the reduction of the amplitude is evident. We note that this systematic underestimation of the oscillations is inherent only for the trapezoidal rule. Higher order interpolation polynomials do not have this clear trend and, therefore, never result in an "amplitude death."

APPENDIX B: TIME REVERSIBILITY

Beside the conservation of the particle number and the total energy, a very important accuracy test for the propagation of the KBE is provided by the time reversal symmetry. As mentioned in the main text, time reversal can be realized either by changing the direction of time or by changing the sign of the Hamiltonian at some time t_1.

In Figs. 6(a) and 6(b) time reversibility tests are performed for linear response, cf. Figs. 2 and 4(a). In Fig. 6(a) method I is used, with a time step of $\Delta t = 3 \times 10^{-1}$ which was shown to result in a nonconverged density evolution associated with damping and emergence of the artificial HDD. While in the case of the backwards propagation ($t \to -t$, dashed brown curve), time reversal symmetry holds due to the accurate treatment of the time-stepping (B), this symmetry is completely broken if one applies the sign change of the Hamiltonian (solid yellow curve). This is a clear indication of a too large time step in the integral (A). In Fig. 6(b) the behavior is shown for a converged calculation with $\Delta t = 10^{-2}$, resulting in an undamped density evolution. As expected, the results for
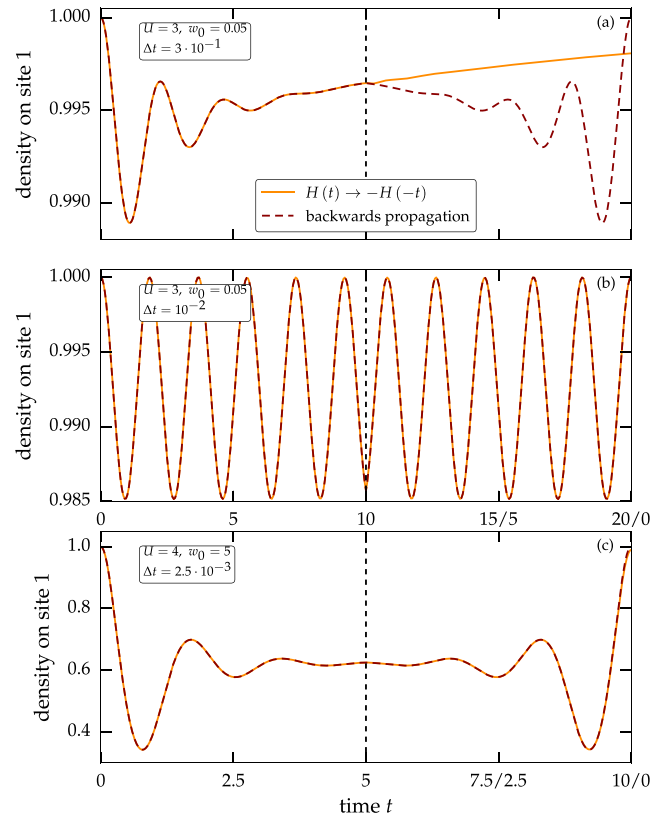
FIG. 6. Time reversal properties of the density on the first site for a Hubbard dimer with steplike excitation. Solid yellow (dashed brown) lines correspond to simulations where $\hat{H}(t) \to -\hat{H}(-t)$ ($t \to -t$) is being applied. All calculations are performed via method I. Parts (a) and (b) show the density for linear response ($w_0 = 0.05$) and $U = 3$. The time step in (a) is $\Delta t = 3 \times 10^{-1}$ (not converged), while in (b) it is $\Delta t = 10^{-2}$ (converged). Part (c) shows the time reversal behavior for a strong excitation ($w_0 = 5$) with $U = 4$ and a time step of $\Delta t = 2.5 \times 10^{-3}$ (converged).

both ways of performing the time reversal coincide and the system properly returns to the initial state.

Finally, in Fig. 6(c) we analyze the case of a strong excitation ($w_0 = 5$), where unphysical damping of the density occurs in a converged solution (cf. Fig. 1). As one can see, even though the oscillation amplitude is drastically reduced, the propagation is entirely time reversal symmetric, even if the sign of the Hamiltonian is changed. Compared to Fig. 6(a), this again confirms the substantial difference between the artificial damping for strongly excited systems (which is inherent to the KBE) and the damping caused by numerical inaccuracies.

[1] Edited by C. Verdozzi, A. Wacker, C.-O. Almbladh, and M. Bonitz, *Progress in Non-Equilibrium Green's Functions (PNGF VI)* (IOP Publishing, Bristol, 2016) [J. Phys.: Conf. Ser. **696** (2016)].

[2] L. P. Kadanoff and G. Baym, *Quantum Statistical Mechanics* (Benjamin, New York, 1962).

[3] L. V. Keldysh, Zh. Eksp. Teor. Fiz. **47**, 1515 (1964) [Sov. Phys. JETP **20**, 1018 (1965)].

[4] H. Haug and A.-P. Jauho, *Quantum Kinetics in Transport and Optics of Semiconductors* (Springer, Berlin, 2008).

[5] M. Bonitz, *Quantum Kinetic Theory*, 2nd ed. (Springer, Cham, 2016).

[6] G. Stefanucci and R. van Leeuwen, *Nonequilibrium Many-body Theory of Quantum Systems* (Cambridge University Press, Cambridge, 2013).

[7] K. Balzer and M. Bonitz, *Nonequilibrium Green's Functions Approach to Inhomogeneous Systems*, Lecture Notes Physics, Vol. 867 (Springer, Heidelberg, 2013).

[8] P. Danielewicz, Ann. Phys. (NY) **152**, 305 (1984).

[9] M. Bonitz, D. Kremp, D. C. Scott, R. Binder, W. D. Kraeft, and H. S. Köhler, J. Phys.: Condens. Matter **8**, 6057 (1996).

[10] N. H. Kwong, M. Bonitz, R. Binder, and S. Köhler, Phys. Status Solidi B **206**, 197 (1998).

[11] N. H. Kwong and M. Bonitz, Phys. Rev. Lett. **84**, 1768 (2000).

[12] N. E. Dahlen and R. van Leeuwen, Phys. Rev. Lett. **98**, 153004 (2007).

[13] K. Balzer, S. Bauch, and M. Bonitz, Phys. Rev. A **81**, 022510 (2010).

[14] K. Balzer, S. Bauch, and M. Bonitz, Phys. Rev. A **82**, 033427 (2010).

[15] K. Balzer, M. Bonitz, R. van Leeuwen, A. Stan, and N. E. Dahlen, Phys. Rev. B **79**, 245306 (2009).

[16] M. P. v. Friesen, C. Verdozzi, and C.-O. Almbladh, Phys. Rev. Lett. **103**, 176404 (2009).

[17] M. P. v. Friesen, C. Verdozzi, and C.-O. Almbladh, Phys. Rev. B **82**, 155108 (2010).

[18] M. Bonitz, S. Hermanns, and N. Schlünzen, Contrib. Plasma Phys. **55**, 152 (2015).

[19] N. Schlünzen, S. Hermanns, M. Bonitz, and C. Verdozzi, Phys. Rev. B **93**, 035107 (2016).

[20] N. Schlünzen and M. Bonitz, Contrib. Plasma Phys. **56**, 5 (2016).

[21] P. Lipavský, V. Špička, and B. Velický, Phys. Rev. B **34**, 6933 (1986).

[22] S. Hermanns, N. Schlünzen, and M. Bonitz, Phys. Rev. B **90**, 125111 (2014).

[23] A. Stan, Phys. Rev. B **93**, 041103(R) (2016).

[24] The Hamiltonian in Ref. [23] online, Eq. (2), is wrong, missing the interaction matrix element.

[25] We use the common units for the density—the number of particles. This means, in all figures, our densities are larger by a factor of two, compared to Ref. [23] online.

[26] If not stated otherwise, our simulations are obtained using a fourth order Runge-Kutta scheme for the time stepping (B) and a higher order integral evaluation (see Ref. [20] online for details) for the collision integral (A).

[27] We underline that this has nothing to do with the Kadanoff-Baym equations because in the absence of a correlation self energy the KBE reduce to standard time-dependent Hartree-Fock.

[28] A. Stan, N. E. Dahlen, and R. van Leeuwen, J. Chem. Phys. **130**, 224101 (2009).

[29] We note that the particle number is conserved within machine precision due to the accurate treatment of the time stepping (B).

[30] A.-M. Uimonen (private communication, 2016).

[31] N. Schlünzen, J.-P. Joost, F. Heidrich-Meisner, and M. Bonitz, Phys. Rev. B **95**, 165139 (2017).

[32] M. Scharnke, N. Schlünzen, and M. Bonitz, J. Math. Phys. **58**, 061903 (2017).

[33] K. E. Atkinson, *An Introduction to Numerical Analysis*, Second edition (Wiley, Hoboken, NJ, 1989).

Nonequilibrium dynamics in the one-dimensional Fermi-Hubbard model: Comparison of the nonequilibrium Green-functions approach and the density matrix renormalization group method

N. Schlünzen,[1] J.-P. Joost,[1] F. Heidrich-Meisner,[2] and M. Bonitz[1]

[1]*Institut für Theoretische Physik und Astrophysik, Christian-Albrechts Universität Kiel, Leibnizstr. 15, Germany*
[2]*Department of Physics and Arnold Sommerfeld Center for Theoretical Physics,*
Ludwig-Maximilians-Universität München, D-80333 München, Germany

The nonequilibrium dynamics of strongly-correlated fermions in lattice systems have attracted considerable interest in the condensed matter and ultracold atomic-gas communities. While experiments have made remarkable progress in recent years, there remains a need for the further development of theoretical tools that can account for both the nonequilibrium conditions and strong correlations. For instance, time-dependent theoretical quantum approaches based on the density matrix renormalization group (DMRG) methods have been primarily applied to one-dimensional setups. Recently, two-dimensional quantum simulations of the expansion of fermions based on nonequilibrium Green functions (NEGF) have been presented [Schlünzen *et al.*, Phys. Rev. B **93**, 035107 (2016)] that showed excellent agreement with the experiments. Here we present an extensive comparison of the NEGF approach to numerically accurate DMRG results. The results indicate that NEGF are a reliable theoretical tool for weak to intermediate coupling strengths in arbitrary dimensions and make long simulations possible. This is complementary to DMRG simulations which are particularly efficient at strong coupling.

I. INTRODUCTION

Experiments addressing the nonequilibrium dynamics of quantum many-body systems have made remarkable progress in recent years, both probing ultrafast dynamics in strongly correlated materials [1,2] and quantum quenches in interacting quantum gases (see Refs. [3–5] for a review). Among the many ultracold quantum-gas experiments with fermions we mention the study of the expansion dynamics of strongly-correlated fermions in a two-dimensional optical lattice [6], the collapse and revival dynamics of Fermi-Bose mixtures [7], and the real-time decay of a density wave in one-dimensional lattices [8]. Very recently, several experimental groups reported the successful implementation of fermionic quantum-gas microscopes [9–17], which will give unprecedented access to both equilibrium and nonequilibrium properties of the Fermi-Hubbard model. Given the tremendous success of the earlier bosonic quantum-gas microscopes in exploring the nonequilibrium realm [18–22], a considerable experimental activity in studying quantum-quench dynamics in the Fermi-Hubbard model can be expected in the near future. Quantum-gas microscopes operate with two-dimensional systems which will push the efforts into this most challenging regime (see also Ref. [23]) while also allowing one to study one-dimensional systems [17].

A large body of theoretical work has concentrated on one-dimensional systems, the reason being both experiments [18,24–29] as well as the availability of powerful theoretical tools based on field theory [30], integrability [31], or numerical methods. While exact diagonalization (ED) is still an indispensable tool (see, e.g., Refs. [32–34]), it is limited to small systems. Nonetheless, for problems restricted to the dynamics of a single charge carrier coupled to spin or phonon degrees of freedom, there exist Krylov-space approaches that operate in a subspace of the full Hilbert space constructed by selecting only those states accessible by the Hamiltonian dynamics [35]. Such an exact diagonalization in a limited functional space has

been applied quite extensively to two-dimensional problems as well (see, e.g., Refs. [36–39]).

Time-dependent density matrix renormalization group (DMRG) methods [40–42] have been very widely applied to nonequilibrium problems and yield numerically accurate results but are limited by the accessible timescales and are primarily useful for one-dimensional systems. A recent variant of the method [43] has been tailored for long-range interactions and is thus better suited for coupled one-dimensional and two-dimensional systems [43,44] but cannot overcome the exponential scaling of a matrix-product states ansatz with the number of coupled chains. The application of time-dependent tensor network approaches that are based on ansatz states suitable for two-dimensional systems such as the projected entangled pair states has been very little explored [45–47].

Apart from time-dependent DMRG methods, there are other many-body methods for the real-time evolution including continuous-time quantum Monte Carlo [48] and time-dependent dynamical mean-field theory approaches [49–51]. The former, while being able to achieve essentially exact results for short evolution times, can suffer from a dynamical sign problem [48]. The latter method often utilizes continuous-time quantum Monte Carlo as an impurity solver, while in more recent developments, time-dependent DMRG has also been successfully used for this purpose [52,53]. Time-dependent DMFT methods are not exact in two dimensions either but are argued to capture better the physics of strongly-correlated systems in higher dimensions, leading to a wide range of applications in the context of nonequilibrium dynamics in the Hubbard model (see, e.g., Ref. [51]). Finally, the iterative equation-of-motion method for operators provides an alternative approach [54], which has also been applied to quantum quench problems in the 2D Fermi-Hubbard model [55].

Despite all these efforts, there still is a significant gap between the rapidly progressing experiments in the field of ultracold atoms and accurate quantum dynamics simulations

when it comes to correlated systems in two dimensions. To contribute towards closing this gap, two of us have applied an alternative approach to the quantum simulation of the nonequilibrium mass transport of correlated fermions studied in the experiment of Ref. [6]: nonequilibrium Green functions (NEGF). Previously, this theory has been successfully applied to a variety of many-particle systems including the correlated electron gas [56], electron-hole plasmas [57], nuclear matter [58], and electrons in quantum dots [59,60], for a recent overview, see Ref. [61]. Extensive applications to finite Hubbard clusters were presented in Ref. [62] and first applications of NEGF to mass transport in small lattice systems of correlated fermions were shown in Ref. [63]. Finally, in Ref. [64] these simulations were extended to strong coupling by using T-matrix self energies as well as to substantially larger systems. Applying an extrapolation to the thermodynamic limit the nonequilibrium correlated quantum mass transport in two-dimensional fermion ensembles could be directly compared to the experiments of Ref. [6] and excellent agreement was observed. For an overview on the NEGF approach and its application to inhomogeneous Hubbard clusters, see Ref. [65].

Even though NEGF simulations are computationally demanding, they have a number of remarkable advantages. First, they do not exhibit an exponential scaling with system size, as is the case for exact diagonalization, and they do not have a dynamical sign problem as continuous time QMC methods. Second, they are not limited with respect to the system dimensionality, as opposed to matrix-product state methods. At the same time, in contrast to ED, NEGF simulations are not a first-principle method since they involve a many-body approximation—the self energy—which determines the accuracy and the quality of the results, similar to the approximate exchange-correlation energy in density functional theory. DMRG, on the other hand, also involves an approximation but the numerical errors depend on a control parameter, the discarded weight, and whenever this can be made sufficiently small, the results can become essentially exact for system sizes larger than what is accessible to ED [66,67].

The accuracy of NEGF simulations of spatially inhomogeneous fermion systems was tested before for few-electron atoms [68] and small Hubbard clusters [69] where exact diagonalization results are available. This analysis was extended to larger Hubbard systems, on the order of 10 sites in Refs. [62,70], revealing a high accuracy of simulations with second-order Born self energies, for weak coupling and moderate times (on the order of 20 inverse hopping times). However, the quality of the results for larger systems has remained open until now, due to the lack of reliable benchmark data. On the other hand, for small Hubbard clusters, also problems were reported: In the case of a strong excitation, two-time NEGF simulations were found to exhibit an unphysical damping of the dynamics [69,71]. The origin of this behavior has been traced back to the self-consistent nature of the used approximations. These deficiencies could be removed to a large extent by making the transition to single-time dynamics with the help of the generalized Kadanoff-Baym ansatz [72] with Hartree-Fock propagators (HF-GKBA) [62].

Thus, there is a clear need to further study the question of accuracy and predictive capability of NEGF simulations,
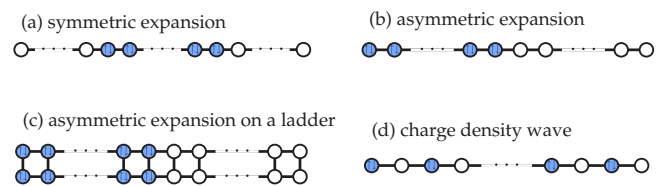
FIG. 1. Initial states of the nonequilibrium problems studied in this paper: (a) Symmetric 1D sudden expansion from a band insulator (BI). (b) Asymmetric 1D expansion from a BI. (c) Sudden expansion on a two-leg ladder. (d) Relaxation dynamics from a charge-density wave state $|\psi_0\rangle = |2,0,2,0,2,0,\dots\rangle$ in 1D. The open circles indicate empty sites, the filled circles represent an initial occupation with two fermions, i.e., a doublon.

in particular, for systems larger than those studied so far, for longer simulation times and beyond the weak-coupling limit. The goal of this paper is to present such an analysis by benchmarking NEGF results using a variety of different self-energy approximations, in a two-time as well as in a single-time formalism (i.e., using the GKBA), against DMRG results. Due to the inherent properties of matrix-product states [67], these comparisons have to focus on 1D fermion systems. We choose a set of four nontrivial cases of nonequilibrium dynamics in the Fermi-Hubbard model for which correlations play a crucial role.

The Hamiltonian of the Fermi-Hubbard chain is

$$H = -J \sum_{\langle s,s' \rangle} \sum_{\sigma=\uparrow,\downarrow} (\hat{c}_{s,\sigma}^{\dagger} \hat{c}_{s',\sigma} + \text{H.c.}) + U \sum_s \hat{n}_s^{\uparrow} \hat{n}_s^{\downarrow}, \quad (1)$$

where $\hat{c}_{s,\sigma}^{\dagger}$ creates a fermion with spin $\sigma = \uparrow, \downarrow$ in site s and $\hat{n}_s^{\sigma} = \hat{c}_{s,\sigma}^{\dagger} \hat{c}_{s,\sigma}$. J is the hopping matrix element (set to unity in our simulations), U denotes the onsite interaction, and L is the number of sites (the lattice spacing and $\hbar$ are set to unity). The cases studied include (i) the symmetric and (ii) asymmetric expansion from a band insulator into an empty lattice, (iii) the expansion from a band insulator in a quasi-1D situation on a two-leg ladder, and (iv) the decay of an ideal charge-density wave state. These four initial situations are sketched in Fig. 1.

As a result of this analysis, the applicability range of NEGF simulations and relevant approximations is being mapped out. Our main results are the following: NEGF simulations with the HF-GKBA are reliable also for moderate coupling, $U/J \lesssim 4$, if the proper self energies are being used. These are the T-matrix self energy—for small or large filling—and the third-order self energy (including all diagrams of third order, cf. Sec. II A)—close to half filling. In all cases, two-time simulations are less accurate (due to the unphysical damping mentioned above) but they can be used to estimate the deviations of the HF-GKBA from the exact result as typically the latter is enclosed between single-time and two-time NEGF results. Finally, NEGF simulations fill the gap left open by DMRG by being capable to treat large systems (of any dimensionality) and to achieve long simulation times, for weak and moderate coupling, whereas the DMRG is advantageous and more efficient for strong coupling.

The remainder of this paper is as follows: in Sec. II we give a brief introduction into NEGF and time-dependent DMRG simulations. This is followed in Sec. III by numerical results.

There we study the four cases introduced above and depicted in Fig. 1: a symmetric and asymmetric sudden expansion (confinement quench) in 1D, Secs. III A and III B, respectively, the sudden expansion in a two-leg ladder, Sec. III C, and a charge-density-wave initial state, Sec. III D.

II. METHODS

A. Nonequilibrium Green functions (NEGF)

The central quantity in the nonequilibrium Green functions theory is the (single-particle) Green function G. It is defined on the Schwinger-Keldysh contour [73,74] $\mathcal{C}$ via the time-ordering operator $T_{\mathcal{C}}$,

$$G_{ss'}^{\sigma}(z,z') = -\frac{i}{\hbar}\langle T_{\mathcal{C}}\hat{c}_{s,\sigma}(z)\hat{c}_{s',\sigma}^{\dagger}(z')\rangle, \qquad (2)$$

where $\langle\ldots\rangle$ denotes the ensemble average. The Green function can be understood as a generalization of the nonequilibrium single-particle density matrix, $n_{s,s'}^{\sigma} = \langle\hat{n}_{s,s'}^{\sigma}\rangle$, onto the two-time plane. Therefore, G provides easy access not only to the observables related to $n_{s,s'}^{\sigma}$ but, in addition, also to the spectral properties of the system. However, the full N-particle information is not directly available from G, although, for example, the pair correlation function can be reconstructed from G [75].

The equations of motion for the single-particle Green function are the Keldysh-Kadanoff-Baym equations [76],

$$\left(i\hbar\frac{\partial}{\partial z}\delta_{s,\bar{s}} - h_{s\bar{s}}^{\sigma}\right)G_{\bar{s}s'}^{\sigma}(z,z')$$
$$= \delta_{\mathcal{C}}(z-z')\delta_{s,s'} + \int_{\mathcal{C}}d\bar{z}\,\Sigma_{s\bar{s}}^{\sigma}(z,\bar{z})G_{\bar{s}s'}^{\sigma}(\bar{z},z'), \qquad (3)$$

together with the adjoint equation (h denotes the matrix element of the single-particle Hamiltonian). Σ denotes the self energy which is the only unknown of the theory, and with an exact Σ the method would be exact. In practice, the self energy has to be approximated for which systematic many-body schemes (e.g., Feynman diagrams) exist that are applicable in equilibrium as well as in nonequilibrium, via the use of the time contour.

In the following we list the self energies that are used in the present paper. The contribution of the first order in the interaction is given by the Hartree-Fock (mean field) self energy,

$$\Sigma_{ss'}^{\text{HF},\uparrow(\downarrow)}(z,z') = U\delta_{\mathcal{C}}(z-z')\delta_{s,s'}n_s^{\downarrow(\uparrow)}(z), \qquad (4)$$

which is contained in each of the approximations used below. Many-body approximations that go beyond the mean field level (that are of higher than first order in U) contain, in addition, a correlation self energy, i.e., $\Sigma_{ss'}^{\sigma} =: \Sigma_{ss'}^{\text{HF},\sigma} + \Sigma_{ss'}^{\text{cor},\sigma}$.

The first correlation correction is of second order and works well for weak coupling, i.e., $U \lesssim J$, for a discussion see Ref. [62]. Here we want to go beyond the weak coupling regime. Therefore, we focus on two higher order many-body approximations. The first is the T-matrix approximation (TMA) in the particle-particle channel and yields a self energy $\Sigma_{ss'}^{\text{cor},\sigma}$ which accounts for scattering processes up to infinite order (see Ref. [65] for a detailed discussion). This is realized by the self-consistent, recursive structure of the T matrix which
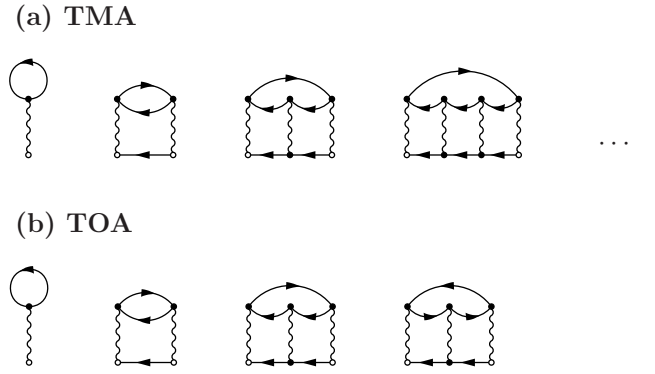
FIG. 2. Feynman diagrams of the considered self-energy approximations: (a) Diagram series of the particle-particle T-matrix approximation (TMA). (b) Diagrams contained in the third-order approximation (TOA), see text.

can be understood as an effective interaction that obeys its own equation of motion (the Lippmann-Schwinger equation), Eq. (6),

$$\Sigma_{ss'}^{\text{TMA},\uparrow(\downarrow)}(z,z') = i\hbar\,T_{ss'}(z,z')\,G_{s's}^{\downarrow(\uparrow)}(z',z), \qquad (5)$$

$$T_{ss'}(z,z') = -i\hbar\,U^2\,G_{ss'}^{\uparrow}(z,z')\,G_{ss'}^{\downarrow}(z,z')$$
$$+ i\hbar\,U\int_{\mathcal{C}}d\bar{z}\,G_{s\bar{s}}^{\uparrow}(z,\bar{z})\,G_{s\bar{s}}^{\downarrow}(z,\bar{z})T_{\bar{s}s'}(\bar{z},z'). \qquad (6)$$

The corresponding Feynman diagrams are shown in Fig. 2(a). The TMA is known to perform best in the limit of small (or large) density [65,71,77], i.e., when the interaction in the system is dominated by electron-electron or hole-hole scattering events. Around half filling, however, electron-hole scattering gains in importance which is not captured by the particle-particle TMA. Therefore, we introduce, in addition, the third-order approximation (TOA) which contains all self-energy contributions up to $\mathcal{O}(U^3)$. In this approximation the correlation self energy, $\Sigma_{ss'}^{\text{cor},\sigma}$, attains the following form [77],

$$\Sigma_{ss'}^{\text{TOA},\uparrow(\downarrow)}(z,z')$$
$$= -(i\hbar)^2\,U^2 G_{ss'}^{\uparrow}(z,z')\,G_{ss'}^{\downarrow}(z,z')\,G_{s's}^{\downarrow(\uparrow)}(z',z)$$
$$- (i\hbar)^3\,U^3\int_{\mathcal{C}}d\bar{z}\,G_{s\bar{s}}^{\uparrow}(z,\bar{z})\,G_{s\bar{s}}^{\downarrow}(z,\bar{z})$$
$$G_{\bar{s}s'}^{\uparrow}(\bar{z},z')\,G_{\bar{s}s'}^{\downarrow}(\bar{z},z')\,G_{s's}^{\downarrow(\uparrow)}(z',z)$$
$$- (i\hbar)^3\,U^3\int_{\mathcal{C}}d\bar{z}\,G_{s\bar{s}}^{\uparrow(\downarrow)}(z,\bar{z})\,G_{\bar{s}s}^{\downarrow(\uparrow)}(\bar{z},z)$$
$$G_{\bar{s}s'}^{\uparrow(\downarrow)}(\bar{z},z')\,G_{s'\bar{s}}^{\downarrow(\uparrow)}(z',\bar{z})\,G_{ss'}^{\downarrow(\uparrow)}(z,z'). \qquad (7)$$

The corresponding diagrams are shown in Fig. 2(b). In the TOA, particle-particle and electron-hole scattering processes are considered on equal footing, yet only to third order inclusively. Both the TMA and TOA approach have been found to perform well for weak to moderate coupling strengths as long as the respective density conditions are fulfilled [62–65,69,71,71,77,78].

Finally, we introduce the generalized Kadanoff-Baym ansatz (GKBA) which is an approximation that reduces the complexity of the time structure of NEGF theory by separating the time-diagonal Green functions from the off-diagonal ones. The full KBE of Eq. (3) is solved only for $z = z'$, while, for $z \neq z'$, the Green function is reconstructed from its time-diagonal values, i.e., from the single-particle density matrix. For the latter, the less and greater component of G which originate from the mapping of the time contour onto the real time axis [79] are reconstructed according to [72],

$$G_{ss'}^{\gtrless,\sigma}(t,t') \approx -\left[G_{s\bar{s}}^{R,\sigma}(t,t')\mathfrak{n}_{\bar{s}s'}^{\gtrless,\sigma}(t') - \mathfrak{n}_{s\bar{s}}^{\gtrless,\sigma}(t)G_{\bar{s}s'}^{A,\sigma}(t,t')\right], \quad (8)$$

where $\mathfrak{n}_{ss'}^{<,\sigma}(t) = n_{s,s'}^{\sigma}(t)$ and $\mathfrak{n}_{ss'}^{>,\sigma}(t) = n_{s,s'}^{\sigma}(t) - \delta_{s,s'}$. The GKBA does not violate the attractive properties of the NEGF method, as it retains density and energy conservation, as well as time reversibility [80]. When using the GKBA, still the question remains how the retarded and advanced propagators $G^{R/A}$ [81] are approximated. Here, we concentrate on Hartree-Fock propagators—the resulting approximation will be called HF-GKBA [62]. This approximation has been shown to eliminate (or drastically reduce) the artificial damping properties of two-time simulations for strongly excited systems and, at the same time, substantially improving the computational performance.

B. Time-dependent density matrix renormalization group method (DMRG)

The density matrix renormalization group method [66,67,82] relies on approximating many-body wave functions $|\psi\rangle$ via matrix-product states of a finite bond dimension m. A matrix-product state can be written as

$$|\psi\rangle = \sum_{\sigma_1 \dots \sigma_L} A^{\sigma_1} A^{\sigma_2} \dots A^{\sigma_L} |\sigma_1 \dots \sigma_L\rangle, \quad (9)$$

where σ_ℓ are the local degrees of freedom at site ℓ and A^{σ_ℓ} are matrices of dimensions $m \times m$ (for details and the role of boundary conditions, see Ref. [67]). Any wave function $|\psi\rangle$ can be brought into the form Eq. (9) by a sequence of singular value decompositions where in general, the bond dimension of the matrices will scale exponentially in system size. To illustrate this procedure, consider a one-dimensional system that is cut into two parts A and B. By denoting complete basis sets in the parts A and B by $|a\rangle_A$ and $|b\rangle_B$, we can express a many-body wave function as

$$|\psi\rangle = \sum_{a,b} \psi_{a,b} |a\rangle_A |b\rangle_B. \quad (10)$$

By means of a singular value decomposition of the rectangular matrix $\psi_{a,b}$, this can be reexpressed in terms of new basis sets in A and B with a single index α

$$|\psi\rangle = \sum_{\alpha=1}^{s} s_\alpha |\alpha\rangle_A |\alpha\rangle_B, \quad (11)$$

where the s_α are the singular values and s is the Schmidt number, which in general scales exponentially with system size. At the heart of the approximation used in DMRG and matrix-product states methods in general is a truncation in the number of states used to represent $|\psi\rangle$ by keeping only those

m states $|\alpha\rangle_A$ with the largest Schmidt coefficients $s_1^2 \geqslant s_2^2 \geqslant s_m^2 \geqslant \cdots \geqslant s_s^2$, i.e.,

$$|\psi\rangle \approx \sum_{\alpha=1}^{m} s_\alpha |\alpha\rangle_A |\alpha\rangle_B. \quad (12)$$

This is equivalent to diagonalizing the reduced density matrix of part A and truncating in its eigenspectrum, which was White's original formulation [82]

$$\rho_A = \mathrm{tr}_B |\psi\rangle\langle\psi| = \sum_\alpha s_\alpha^2 |\alpha\rangle_{AA}\langle\alpha|. \quad (13)$$

While actual algorithms are described comprehensively in Ref. [67], we here want to explain for which many-body states Eq. (12) provides a useful approximation in the sense that few states (order of $m \sim 100, 1000$) suffice to obtain numerically accurate results for observables $\langle \hat{O} \rangle = \langle \psi | \hat{O} | \psi \rangle$. This obviously depends on how quickly the eigenvalues s_α^2 of the reduced density matrix decay. A correct intuition can be gained from relating the decay of s_α^2 to the entanglement entropy

$$S_{\mathrm{vN}} = -\mathrm{tr}[\rho_A \log \rho_A] = -\sum_\alpha s_\alpha^2 \log s_\alpha^2. \quad (14)$$

A fast decay of s_α^2 translates into a weakly entangled wave function and vice versa. The crucial question is the scaling of the entanglement entropy with the system size. For ground states of gapped Hamiltonians with short-range interactions, an area law holds [83]

$$S_{\mathrm{vN}} \propto L_A^{D-1}, \quad (15)$$

where L_A is the linear dimension of subsystem A and D is the dimension. Scaling in L_A translates directly into scaling in L, i.e., the linear dimension of the full system. In $D = 1$, we obtain $S_{\mathrm{vN}} = \mathrm{const}$ for $L \gg \xi$ where ξ is the correlation length and this implies that the numerical effort (i.e., the number of states m used to approximate $|\psi\rangle$) does not increase with system size since $m \lesssim \exp(S_{\mathrm{vN}}(L))$ [67]. For critical systems in one dimension, the entanglement entropy acquires a logarithmic correction (see Refs. [67,83] and references therein). This reasoning explains why matrix-product states based techniques work primarily for one-dimensional systems since in 2D, even if an area law holds, the scaling is exponential in the width of the system [84]. The other important issue is whether an efficient algorithm can be formulated based on matrix-product states. It turns out that most matrix-product state methods including DMRG scale as m^3 and linearly in L [67].

For real-time evolutions $|\psi(t)\rangle = \exp(-iHt)|\psi(t=0)\rangle$, the application of the time-evolution operator can be efficiently implemented via a Trotter-Suzuki decomposition (using $H = \sum_\ell h_{\ell,\ell+1}$) into operators $\exp(-ih_{\ell,\ell+1}\delta t)$ which is just a local two-site gate affecting two A matrices in Eq. (9) (δt is the time step) [40–42]. In general, a time-propagated many-body state $|\psi(t)\rangle$ will develop volume law like entanglement even if the initial state was a product state [67]. For global quantum quenches [such as the time evolution from a product state such as our case (iv), see Fig. 1(d)], the entanglement grows linearly in time $S_{\mathrm{vN}} \propto t$, implying that the number of states m needed to maintain the same quality of approximation to the true

$|\psi(t)\rangle$ will increase exponentially. This limits the accessible times in global quenches to about $t \lesssim \mathcal{O}(10/J)$, while in local quenches, geometric quenches such as the sudden expansion considered in examples (i)–(iii) or for slow parameter changes, a milder entanglement increase occurs.

The two main parameters that control the accuracy of time-dependent DMRG simulations are the time step δt and the discarded weight $\delta\rho$ [67,85]. The latter is defined as

$$\delta\rho = \sum_{\alpha=m+1}^{s} s_\alpha^2, \tag{16}$$

which is a measure for the error made per truncation. The quality of DMRG data has to be analyzed as a function of both δt and $\delta\rho$, with the latter the dominant parameter since the dependence of the error on δt can be reduced by using higher-order Trotter-Suzuki decompositions [67]. In this work, we use a time-dependent DMRG implementation as introduced in Refs. [41,42] and we varied the time step between $0.02/J \leqslant \delta t \leqslant 0.1/J$ and the discarded weight $10^{-7} \leqslant \delta\rho \leqslant 10^{-4}$ with a maximum number of 2000 states.

III. NUMERICAL RESULTS

In our simulations we consider four different nonequilibrium setups. The corresponding initial states are depicted in Fig. 1. In all cases, the incipient configuration consists of both doubly occupied and empty Hubbard sites. In the first setup, the occupied sites are arranged on a straight line to form a one-dimensional band insulator (BI). During time propagation, and in the absence of any further potential, the density starts to expand symmetrically towards the left and right edges of the Hubbard chain, cf. Fig. 1(a). Next, in order to also investigate an asymmetric expansion dynamics the initial BI is placed onto the leftmost sites of the chain allowing the density to escape only to the right, see Fig. 1(b). Further, to analyze the effect of the dimensionality of the system we extend the asymmetric setup to a two-leg Hubbard ladder the leftmost rungs of which are initially doubly occupied, Fig. 1(c). The dynamics on such ladders is often used to investigate the 1D-to-2D crossover. Finally, we consider a setup that generates a final state at a constant and large density where correlation effects are expected to manifest themselves even stronger, cf. Fig. 1(d). Here, the initial state consists of a one-dimensional Hubbard chain with alternating occupation $n_s = 0,2$. During the evolution from this charge-density wave (CDW), the particles quickly form an entangled many-body state in which correlations play a crucial role. These four setups will be analyzed in detail in Secs. III A–III D.

A. Sudden expansion in 1D: symmetric case

We start the numerical analysis by considering a confinement quench giving rise to a sudden symmetric expansion of an ensemble of fermions into an empty lattice [see Fig. 1(a)]. This setup has been studied in many papers, including experimental studies [6,29,86,87], and theoretically using DMRG methods [44,88–94] and NEGF [64]. We exclusively study an initial density of $n = 2$ on the sites that are occupied at $t = 0$, which was previously considered in Refs. [64,90,95] such that the general properties are well understood.
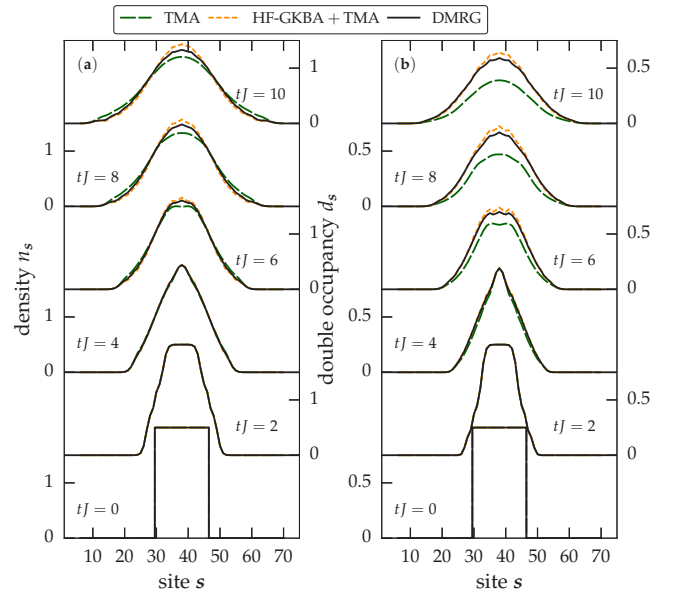
FIG. 3. Symmetric 1D sudden expansion of a Hubbard chain of $N = 34$ fermions at $U = J$. Time evolution of (a) density n_s and (b) double occupancy d_s for six times (from bottom to top): $tJ = 0,2,4,6,8,10$. Solid lines: DMRG, long dashes: NEGF (two-time T matrix), dashed lines: T matrix with HF-GKBA.

Here, we focus on the quantitative details of the time dynamics and compare our NEGF results to DMRG. We consider a chain of length $L = 75$ with $N = 34$ particles for $U = J$. The evolution of the respective density profiles is shown in Fig. 3(a) for six consecutive times $tJ = 0,2,4,6,8,10$. The solid black lines correspond to the DMRG results and the dashed green lines belong to the NEGF calculations using the T-matrix approximation (TMA) while the orange lines are obtained by additionally invoking the HF-GKBA, cf. Sec. II A. As expected, the general trend of the density is to propagate outwards resulting in a bell-shaped profile which can be seen from all considered descriptions. For times exceeding $5J^{-1}$, the site occupations start to deviate slightly in the three simulations. In the full two-time NEGF calculation the fermion expansion is slightly faster than in the DMRG, while in the HF-GKBA simulation the particles stay closer to the center and are in very good agreement with the DMRG.

A quantity more sensitive to correlations is the double occupancy,

$$d_s := n_s^{\uparrow\downarrow} = \langle \hat{c}_{s,\uparrow}^\dagger \hat{c}_{s,\uparrow} \hat{c}_{s,\downarrow}^\dagger \hat{c}_{s,\downarrow} \rangle, \tag{17}$$

the dynamics of which are displayed in Fig. 3(b). It is evident that it follows the trend of the density by which it is dominated. Again, in the full two-time NEGF calculation d_s expands faster than in the DMRG result, where the deviations are larger than for the density. In contrast, the HF-GKBA is again very close to the latter.

To better quantify the discrepancies between DMRG and the two NEGF approaches we introduce the total density deviation between the two methods in the following way,

$$\Delta n(t) := \sum_s \left| n_s^{\mathrm{I}}(t) - n_s^{\mathrm{II}}(t) \right|, \tag{18}$$
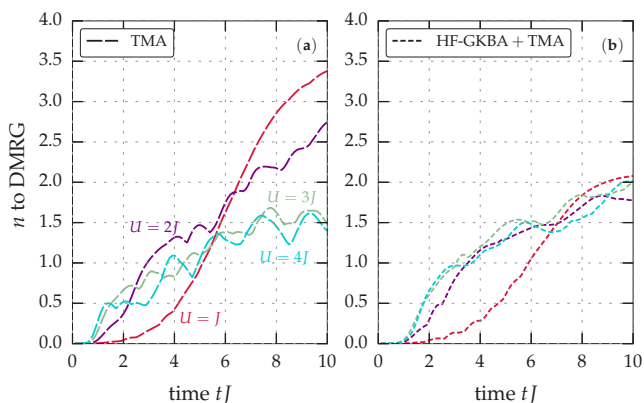
FIG. 4. Total density deviation, Eq. (18), between (a) DMRG and NEGF and (b) DMRG and HF-GKBA, for the symmetric 1D sudden expansion. Simulations as in Fig. 3 with $N = 34$ particles, but for four different values of U indicated in the figure.

FIG. 5. *Symmetric 1D sudden expansion.* Total deviation of (a) the density and (b) the double occupancy between DMRG and NEGF (long dashed lines) and DMRG and HF-GKBA (dashed lines) at $tJ = 1$ and $tJ = 9$, for $N = 34$.

where I and II denote the respective method. This quantity allows us to analyze the time dependent difference of the density profiles. It should be noted that the quantitative value of Δn has no direct interpretation. Instead, by dividing by the total number of Hubbard sites L, one gets the average deviation per site. Adopting DMRG as the reference method, we investigate the dependence of the deviation on the interaction strength U and time by calculating the total deviations for the two-time TMA simulation and the HF-GKBA results which are displayed in Figs. 4(a) and 4(b), respectively. As expected, the total deviation grows in time for all cases. Interestingly, however, the deviations saturate around $t = 10J^{-1}$. A closer look reveals that, during the early propagation period, the growth appears to be superlinear, followed by a receding phase after which the growth becomes more fluctuating. The lengths of these time periods strongly depends on the interaction strength, as they become shorter for larger U. As a consequence, for times around $tJ = 1$ the total deviation increases with the interaction strength while for times around $tJ = 9$ it decreases with U. The overall trend is common between the full TMA results and the HF-GKBA simulations. The only noticeable difference is that Δn remains a little smaller for larger times and small U in the HF-GKBA calculations.

To better understand how the density deviations vary with U and t, we replot these quantities in Fig. 5(a) for the two time points, $tJ = 1$ and $tJ = 9$. In addition, we compute the total deviation of the double occupancy which is defined, by analogy to Eq. (18), as

$$\Delta d(t) := \sum_s \left| d_s^{(1)}(t) - d_s^{(2)}(t) \right|, \tag{19}$$

which is shown in Fig. 5(b). While for $tJ = 1$ all results confirm the trend that the deviations grow with increasing U, for $tJ = 9$ the dependence is more irregular. In the latter case, the deviations between HF-GKBA and DMRG, in particular, are nearly independent of the interaction strength. The two-time NEGF results for the double occupancy, however, show large deviations for small U. The decrease of Δn and Δd with increasing U for later times can be understood from the direct
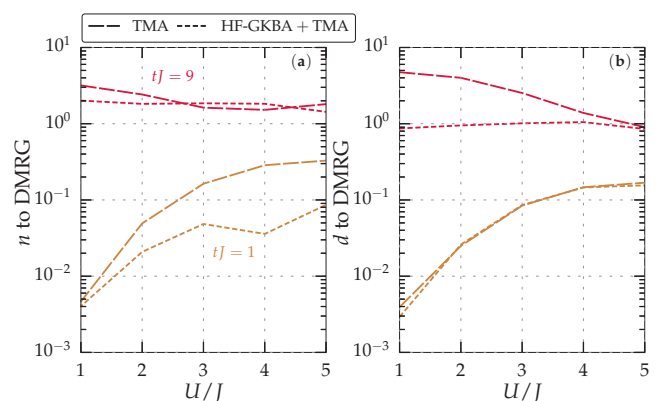
dynamics of the density profiles. Since for large U the particles predominantly remain in the center of the system the growth of the deviations is limited due to the absence of moving particles.

From the presented results, it turns out that the DMRG result is typically enclosed between the HF-GKBA and the two-time NEGF result in T-matrix approximation. At the same time the HF-GKBA data are slightly closer to the DMRG results.

To further analyze the expansion behavior following a 1D sudden confinement switch, it is instructive to analyze the expansion velocity of the fermion cloud which is defined according to [64]

$$v_{\exp}(t) = \frac{d}{dt} D(t), \quad \text{with} \quad D(t) = \sqrt{R^2(t) - R^2(0)},$$

$$R^2(t) = \frac{1}{N} \sum_s n_s(t) \|s - s_0\|^2, \quad s_0 = \frac{1}{N} \sum_s n_s(0) s. \tag{20}$$

This quantity measures the temporal growth of the particle cloud which has a mean square radius $R(t)$ from which the initial size is subtracted. This quantity was analyzed in detail for 1D, 2D, and 3D systems and a broad range of system size N in Ref. [64]. Here we focus on the time evolution of $v_{\exp}$ for 1D systems and compare again DMRG, two-time NEGF simulations, and HF-GKBA. The results are shown in Fig. 6 for $U/J = 1, 2, 5$. As one can see, for all cases $v_{\exp}$ starts from the same value $v_{\exp}(0) = v_{\max} = \sqrt{2D}J = \sqrt{2}J$ which is the largest expansion velocity in an empty lattice (cf. Refs. [6,64,91]). A noninteracting gas expands with a constant $v_{\exp}(0) = v_{\max} = \sqrt{2D}J$ [6]. For $U > 0$, $v_{\exp}$ decreases from its initial value until it slowly converges to an approximately constant value once U/J becomes comparable to the bandwidth.

This behavior is explained by the large effective mass of doublons in the limit $U \gtrsim 4J$, where perturbation theory results in an effective hopping matrix elements $J_{\text{doublon}} \propto J^2/U$ for $U \gg J$ (see, e.g., Ref. [96]). As a consequence, the doublons become inert on the accessible time scales and the system remains largely in a weakly-correlated state that is essentially a product state in the core region [89,90,92]
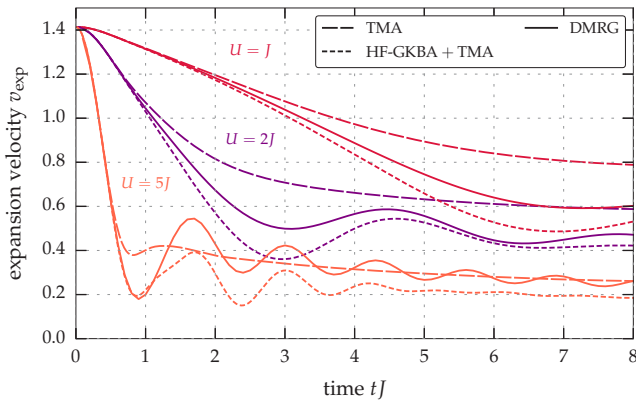
FIG. 6. Symmetric 1D sudden expansion. Evolution of the expansion velocity versus time for $U/J = 1, 2, 5$ for three simulation methods.

(see also Refs. [97–99]). Therefore, v_{exp} is dominated by the few atoms that expand after some doublons have dissolved into single particles [90] and at long times, the expansion velocity is dominated by these fast atoms while the slow doublons do not contribute [93].

For the applicability of the NEGF methods, this dynamical freezing of a build-up of correlations as $U/J \gtrsim 4$ implies that the methods become more accurate again, since the wave functions acquire a simpler structure than at weak U/J. This explains the *a priori* counterintuitive observation that the numerical deviations of the NEGF methods compared to DMRG (see the discussion of Figs. 4 and 5) become smaller as U/J increases, even though the NEGF techniques are by construction weak-coupling methods [100]. The regime of $U/J \gg 4$ can much easier be accessed by DMRG with longer times becoming accessible [89], demonstrating the usefulness of NEGF and DMRG as complementary approaches for weak and strong coupling, respectively.

Interestingly, for large interaction strength both DMRG and the HF-GKBA propagation show oscillations in the expansion velocity with similar frequency. In contrast, for the two-time TMA calculations an onset of oscillations is seen only for $U/J = 5$, in all other cases the expansion velocity quickly decays monotonically approaching an asymptotic value. This is consistent with earlier observations that two-time propagations of the KBEs for strongly excited small Hubbard systems can be accompanied by an unphysical damping in the density evolution [62,69,71], as was noted in the introduction Sec. I. Since the initial confinement quench in our simulations constitutes such a strong excitation it is very likely that the missing of the oscillations of the expansion velocity in the two-time simulations are associated with this artificial damping.

On the other hand, the HF-GKBA is known to remove the artificial damping in strongly excited small systems [62]. Therefore, it is not surprising that in the present setup, the HF-GKBA simulations exhibit better agreement with the DMRG for intermediate times, including the reproduction of the oscillations of the expansion velocity. This is particularly the case for small and moderate couplings, $U \lesssim 3J$. For larger couplings, the long-time asymptotics of the expansion velocity of the two-time simulations is closer to the DMRG

than the HF-GKBA result. This behavior is also consistent with the earlier observations for the evolution of the density profile and the double occupancy. This complementarity of the performance of the two-time and the HF-GKBA NEGF simulations are a particularly attractive feature.

Therefore, having both NEGF results at hand, allows one to estimate, e.g., the value of the asymptotic expansion velocity. For all U, the DMRG solution of this asymptotic value lies within the NEGF results. Utilizing this observation, one can extract the exact value of $\lim_{t \to \infty} v_{exp}(t)$ with a relative error of $\lesssim 30\%$, for all U.

The experiment [6] used a different measure for the expansion velocity derived from the time evolution of the half width at half maximum, called core expansion velocity. In Ref. [64], a direct comparison of numerical results for this core expansion velocity to experimental data of Ref. [6] was presented, with a very good agreement. Our analysis of the errors of densities as a function of U/J and time in the different NEGF schemes further corroborates the validity of the NEGF data used in that comparison.

It should be mentioned that, in the present case, the choice of the TOA self energy in the NEGF description leads to an overestimation of the expansion by a factor of $\lesssim 2$ (not shown). This indicates that the stability of the correlated doublon cloud at the center of the system is only sufficiently described if higher order scattering diagrams are considered, as in TMA. Additionally, throughout the early dynamics the lattice sites are predominantly either empty or nearly fully occupied which supports the validity of the TMA (cf. Sec. II A).

We close this discussion by noting that in principle, it should be possible to compute the asymptotic expansion velocities from the Bethe ansatz, along the lines of Refs. [92,94]. For instance, $\lim_{t \to \infty} v_{exp}(t)$ was computed for $n \leqslant 1$ with an excellent agreement with DMRG results [94]. The extension of Ref. [94] to initial densities $n \gtrsim 1$ is left for future research.

B. Sudden expansion in 1D: asymmetric case

It is now interesting to further investigate whether the observed accuracy and the complementary behavior of single-time and two-time NEGF simulations is just a special case of the symmetric expansion. To this end we now consider a modified setup [cf. Fig. 1(b)] where the confinement quench gives rise to a density expansion in only one direction. The results are presented in Fig. 7(a) for $N = 20$ fermions and $U = J$. The respective evolution of the double occupancy is shown in Fig. 7(b). As one can see, the results obtained by all considered methods lie very close to each other. To better distinguish between the particular profiles, we show the deviations to the DMRG results in Fig. 8. The subfigures Figs. 8(a)–8(d) correspond to different interaction strengths $U/J = 1, 2, 4, 8$. As in the symmetric 1D setup we observe a complementary behavior of the two-time result and the HF-GKBA. First, it is striking that again both approximations exhibit opposite deviations from the DMRG: While the two-time results show a slightly too fast expansion, the HF-GKBA results are retarded. Correspondingly, the deviations of the local densities from the DMRG results have opposite signs: The HF-GKBA (two-time TMA) densities are above (below) the DMRG result, on the originally doubly occupied sites,
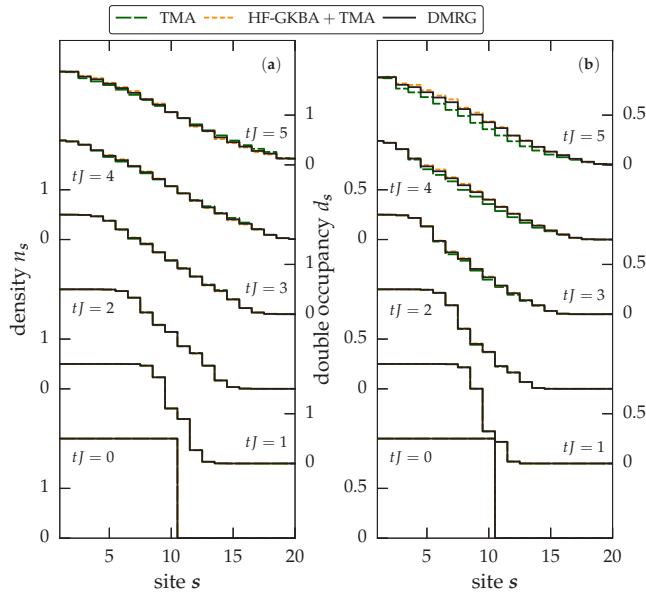
FIG. 7. *Asymmetric 1D sudden expansion.* Time evolution of (a) density n_s and (b) double occupancy d_s for $U = J$, $N = 20$ for $tJ = 0,1,2,3,4,5$. Solid lines: DMRG, long dashes: NEGF (two-time T matrix), dashed lines: T matrix with HF-GKBA.

FIG. 9. Asymmetric 1D sudden expansion. Reduced radius $D(t)$ defined by Eq. (20) as a function of time for four values of the interaction strength. (a): $L_0 = L/2$, cf. Fig. 8 and (b): $L_0 = 2/5L$.

FIG. 8. Asymmetric 1D sudden expansion for $N = 20$ fermions, initially doubly occupying the $L_0 = 10$ leftmost sites labeled $0, \ldots, 9$. Total system length is 30 sites, cf. Fig. 1(b). Deviation of the density profiles between DMRG and NEGF and DMRG and HF-GKBA for different time steps and (a) $U = J$, (b) $U = 2J$, (c) $U = 4J$, (d) $U = 8J$. Successive times are (from bottom to top) $tJ = 1,2,3,4,5$ (each curve is vertically shifted by 0.2). For better visibility, the HF-GKBA curves are horizontally displaced by one site.

and, vice versa, for the unoccupied sites. Also, the deviations have a similar dependence on the coupling strength as in the symmetric case, Sec. III A: For the HF-GKBA that exhibits smaller density deviations than the two-time result for all considered U, the maximum deviation is found for intermediate coupling strengths ($2J \leqslant U \leqslant 4J$). In contrast, for $U = 8J$, the two-time result shows large deviations at the edge of the occupied region.

After considering the densities we again compute the width of the expanding particle cloud, using Eq. (20) [see Fig. 9(a)]. This quantity confirms the observations made before for the density: Compared to the DMRG, the expansion of the particle cloud is slightly accelerated (decelerated) for the two-time (GKBA) simulations. With increasing U the two-time result becomes more accurate than the HF-GKBA. For large couplings, $U \gtrsim 6J$, the deviations between two-time and single-time approximations vanish. In this limit, also the two-time result for the expansion is retarded, in comparison to the DMRG. This analysis indicates that for $U \lesssim 6J$ a combination of two-time and single-time simulations is able to reproduce the cloud size with a relative error not exceeding 20%. However, for large couplings, the inaccuracies grow and appear to arise from the inadequacy of the underlying T-matrix approximation in the particle-particle channel. This makes it necessary to study additional many-body approximations.

The considered system of $L = 20$ sites and $L_0 = L/2 = 10$ initially doubly occupied sites obeys a high symmetry [101] between the electron (hole) density on site s and the hole (electron) density on site $L - s$. To generalize our findings, we also present results for a system of $L_0 = 2L/5 = 8$ initially occupied sites, for which this symmetry is broken. The corresponding widths of the particle cloud are shown in Fig. 9(b). As one can see, all trends agree with the previous results and especially the enclosing behavior of the NEGF methods seems not to depend on the symmetry of the system.

C. Asymmetric sudden expansion on a two-leg ladder

As mentioned before, the generalization to higher system dimensions constitutes a challenging problem to DMRG due
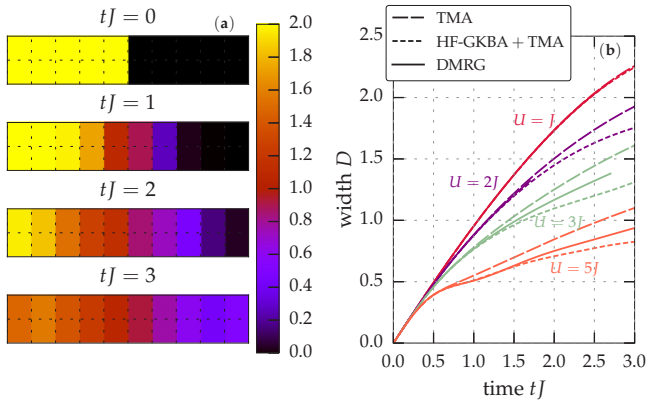
FIG. 10. Asymmetric sudden expansion on a two-leg ladder. (a) Density distribution for four times $tJ = 0, 1, 2, 3$ of the HF-GKBA+TMA simulation for $U = J$. (b) Reduced radius $D(t)$ defined by Eq. (20) as a function of time for four values of the coupling parameter.

FIG. 11. *Relaxation of CDW state* of doublons for $U/J = 0.5, 1, 2, 3, 4$ (each curve is vertically shifted by 0.5) and $L = 20$, $N = 20$. (a) Density imbalance, Eq. (21). (b) Total double occupancy $\sum_s d_s(t)$.

to the additional degrees of freedom in the correlation growth. Therefore, only simple 2D toy models have been simulated so far with time-dependent DMRG, including the expansion of strongly interacting bosons on few-leg ladders and in small 2D clusters [44]. Since the NEGF method is not restricted with respect to dimensionality it is very interesting to compare the performance of both methods on a two-leg ladder to see if the good agreement of the previous 1D analysis can be confirmed for higher dimension.

As in Sec. III B, we consider an asymmetric expansion setup, now with a ladder of ten rungs, the leftmost five of which are initially doubly occupied [cf. Fig. 1(c)]. The resulting density evolution is illustrated in Fig. 10(a) where the density distributions for several times $tJ = 0, 1, 2, 3$ are shown in a simulation using the HF-GKBA+TMA approach with $U = J$. As in the 1D case, the particles tend to move to the right. To quantify the growth of the width of the particle cloud we again use the reduced radius $D(t)$ of Eq. (20) the time evolution of which is shown in Fig. 10(b) for all considered methods and $U/J = 1, 2, 3, 5$. As one can see, the behavior is very similar to the 1D case (cf. Fig. 9). The slowing down of the expansion for increasing interaction strength is well predicted by all considered methods for small interaction strengths, whereas for larger U, the DMRG curve lies between the NEGF results.

It should be mentioned that the evolutions of the reduced radius for all U share a common short-time phase (this is also present in 1D but becomes more apparent on the ladder), for which $D(t)$ behaves like the ideal system. This phase shortens with increasing interaction strength, which is due to the build-up of correlations. The behavior is similar for the symmetric expansion setup (cf. Sec. III A) for which the dependence of the early expansion phases and the connection to the onset of correlations are analyzed in detail in Refs. [64,65].

D. Relaxation of charge-density-wave state of doublons

We now turn to the fourth setup that is depicted in Fig. 1(d), an alternating sequence of doubly occupied and empty states
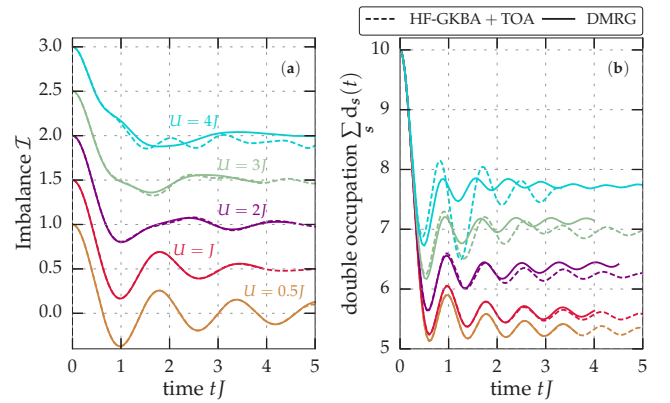
corresponding to a charge-density wave. There have been a number of experiments starting from similar initial states with both fermions [8] or bosons [28], but mostly of the $|\psi_0\rangle = |1, 0, 1, 0, \dots\rangle$ type. Theoretically, there is much interest in the decay of charge-density waves or initial states with perfect Néel order in the Fermi-Hubbard model, with previous work on both its 1D version [102,103] and for higher-dimensional systems (see, e.g., Ref. [104]). The decay from the bosonic version of our initial state $|\psi_0\rangle = |2, 0, 2, 0, \dots\rangle$ was studied in Ref. [105].

Here the dynamics is governed by a short-time process in which particles move into the empty sites, provided that $U < 4J$, which is the bandwidth. After that, a spreading and build-up of correlations sets in, for which the relevant velocity is typically strongly dependent on U/J [18,102,103].

A useful quantity for the dynamics is the density imbalance which is defined as the difference of the densities on all even and all odd sites,

$$\mathcal{I}(t) = \frac{N_{\text{even}}(t) - N_{\text{odd}}(t)}{L}, \qquad (21)$$

where N_{even} (N_{odd}) sums up all densities of the even (odd) sites. The imbalance starts from N/L and is then expected to decay. The results for $N = 20$ fermions and five different couplings are shown in Fig. 11(a). In the figure we compare DMRG results to NEGF simulations using a third-order approximation for the self energy. We show results for the single-time limit, i.e., after applying the HF-GKBA [106]. The agreement is excellent for small and moderate couplings. Only once the interaction strength becomes as large as $U/J = 3$, small deviations are visible which grow for $U = 4J$. This is not surprising because the third-order approximation does not capture higher order corrections. It contains, however, the third-order electron-hole diagram (cf. Fig. 2) which becomes essentially important at half filling. Therefore, TOA simulations are superior to the T-matrix calculations with respect to the description of CDW dynamics. Similar trends are seen in the total double occupancy which is displayed in Fig. 11(b). The dependence of errors of the NEGF methods on U/J (i.e., an increase as U/J becomes order of the bandwidth)

in this example is the expected generic behavior since these methods are by construction weak-coupling approaches. DMRG works particularly well for $U/J > 4$ in such problems [102], illustrating the complementary strength of NEGF versus DMRG time evolutions.

IV. SUMMARY AND OUTLOOK

A. Summary of main results

In this paper we thoroughly investigated the accuracy and applicability range of NEGF-based approaches in the description of the complex and correlated electron dynamics in strongly excited large Hubbard chains. The basis for this benchmark analysis were DMRG simulations performed for the same setups. Based on this analysis for the selected four setups we may conclude that NEGF simulations are reliable and accurate, thereby fully confirming earlier comparisons to exact diagonalization results for small clusters. Thus, NEGF simulations have predictive power, far beyond the present systems and situations. More precisely, our conclusions can be summarized as follows:

(1) The quality of the NEGF results crucially depends on the choice of the self energy, Σ, which is clearly dictated by the physical situation. For weak coupling, $U < J$ (not studied here, cf. [62]), the second Born approximation is adequate. For moderate coupling, $U \lesssim 2J$, proper approximations are the particle-particle T-matrix (TMA) and the third-order approximation (TOA).

(2) For $U \lesssim 2J$, the choice of Σ depends on the local densities (filling): For densities close to zero (or close to one), TMA is appropriate, confirming earlier results for small clusters [71], whereas near half filling TOA is significantly more accurate, as it contains contributions neglected in TMA.

(3) For the present system sizes the HF-GKBA (with the relevant self energy) yields more accurate results compared to the corresponding two-time simulations (due to the artificial damping observed in the latter). While the envelopes of global dynamical quantities (energies, cloud size, expansion velocity, density imbalance, etc.) are captured very accurately, oscillations of these quantities are reproduced only qualitatively, for $U \lesssim 2J$.

(4) Full two-time NEGF simulations can be used as a support of the HF-GKBA data, as typically the exact result is enclosed between the single-time and two-time simulations. One half of the difference of the two yields a (conservative) estimate of the numerical error, at least for couplings $U \lesssim 6J$.

Based on this analysis of the NEGF capabilities, the main outcome of this paper is that NEGF and DMRG have, to a large degree, complementary strengths and limitations, with respect to the interaction strength. If U does not exceed the bandwidth of the system, the NEGF approach has predictive power even for long-time propagations, and it is directly applicable to 2D and 3D systems [64]. In contrast, the exponential spreading of entanglement narrows the DMRG approach to very short 1D simulations (somewhat larger times can be reached than presented here by using more states and possibly also by using variants of the algorithm [46,102]). On the other hand, if U is larger than the bandwidth, the NEGF approach, in its present form, does not describe the dynamics properly, due to the
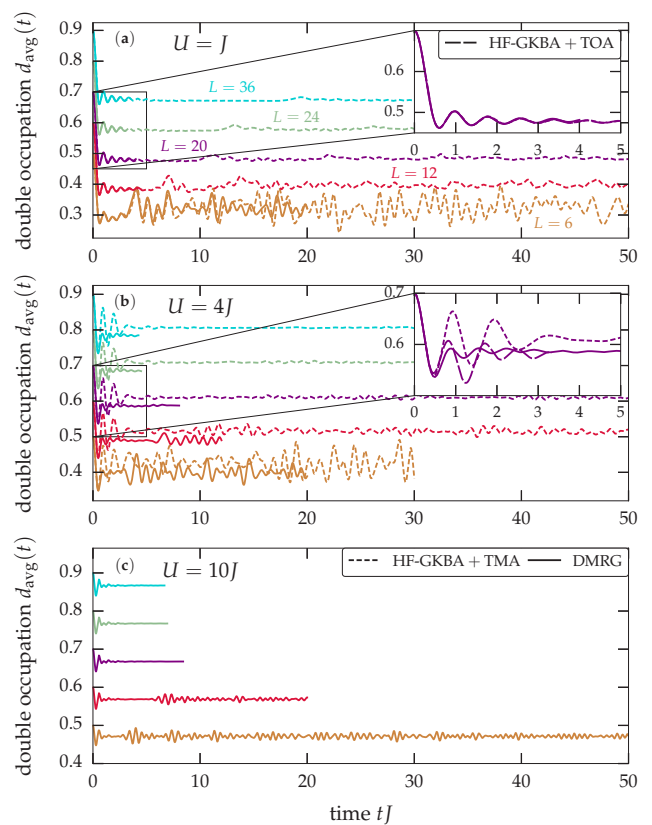
FIG. 12. *Relaxation of a CDW state of doublons.* System-size dependence and long-time evolution of the average double occupancy, Eq. (22), for (a) $U = J$, (b) $U = 4J$, and (c) $U = 10J$ (DMRG results only) for chains of length $L = 6,12,20,24,36$. Full lines: DMRG, short dashes: HF-GKBA+TMA. The insets, in addition, show HF-GKBA+TOA results (long dashes). For better visibility, curves for different L are shifted vertically by 0.1.

built-in perturbative character of the approximations, whereas the DMRG method provides the exact dynamics for rather long times, although being limited to 1D and small 2D systems.

B. Complementarity of NEGF and DMRG simulations: A case study

To illustrate this complementarity and the reach of the two methods, we have performed additional long-time simulations and investigated the system-size dependence of the simulations, for the CDW setup (cf. Sec. III D). As a particularly sensitive quantity, we introduce the average double occupation

$$d_{\mathrm{avg}}(t) = L^{-1} \sum_s d_s(t). \tag{22}$$

The time evolution of d_{avg} is shown in Fig. 12 for different chain lengths L, ranging from 6 to 36, corresponding to $6, \ldots, 36$ particles, for (a) $U = J$, (b) $U = 4J$, and (c) $U = 10J$. The NEGF simulations use the HF-GKBA with T-matrix self energies. TOA simulations had a stability problem and are included only for shorter times (see insets).

Starting from the case of $U = J$ [cf. Fig. 12(a)], one can see that the short-time dynamics ($tJ < 3$) of all considered chains

are very similar. After the transient oscillations have decayed a quasistationary regime is observed. However, at some time the double occupation abruptly increases again [cf. Fig. 12(a)]. These revivals occur periodically, becoming weaker with increasing system size L, and their periods increase nearly linearly with L. This indicates particles with a critical velocity that pass through the entire system. It should be noted that, after the revivals, d_{avg} starts to fluctuate inhomogeneously with an amplitude that decreases with L. We note that similar revivals and system-size dependencies were reported in Ref. [107]. While for $U = J$ the DMRG simulations are restricted to very short times, e.g., $tJ \sim 20$ for $L = 6$ ($tJ \sim 5$ for $L = 12$), the NEGF simulations easily allow us to reach $tJ = 50$ and more, for all chain lengths. The excellent agreement with DMRG is striking, suggesting that also the long time results are reliable.

Consider now the case $U = 4J$, Fig. 12(b). Here the complementary behavior of the two approaches becomes particularly obvious. While DMRG simulations show an improved performance compared to $U = J$ and reach times of the order of $tJ \sim 20$, for $L = 6$ ($tJ \sim 12$, for $L = 12$), NEGF simulations still reach times of the order of $tJ = 50$, however, it is more difficult to achieve convergence. Simulations with the most accurate TOA self energy are stable only for short times, on the order of $tJ \sim 4$, for $L = 20$, similar to DMRG, and are in good agreement with the latter [cf. inset of Fig. 12(b)]. Long-time simulations are presently possible only with T-matrix self energies which, however, exhibit a small upshift, compared to DMRG. Interestingly, the L-dependent revivals that were observed in the NEGF simulations for $U = J$ are confirmed here as well by the NEGF results and, even more clearly in the DMRG runs.

Finally, in Fig. 12(c) we show results for $U = 10J$. Here, accurate long-time evolutions for small systems can be easily performed with the DMRG method. In contrast, the available NEGF approximations are not accurate enough and show poor convergence for long times (results from NEGF simulations not included in the figure).

C. Outlook

After this analysis of the NEGF approach and the illustration of the interesting complementarity with DMRG we briefly discuss questions that will be of interest for future developments. First, it will be very important to extend the arsenal of self energies. One important improvement will be achieved by extending the T-matrix approximation by including electron-hole contributions and by including dynamical screening effects (FLEX approximation [77]). These choices for the self energy will help to extend the interaction range where NEGF properly describes the dynamics. Another way to access larger U is to derive novel self energies via a perturbation expansion with respect to U^{-1}, i.e., by starting from a Hamiltonian that includes doublons directly. Finally, it would be interesting to further improve the GKBA. While it was found to cure the artificial damping problems of two-time simulations, the dynamics is often too weakly damped. This behavior should improve if one uses correlated propagators instead of HF-propagators [57,81].

While in this paper, 1D and small quasi-1D systems have been investigated for uncorrelated initial states, it will be interesting to extend the present method comparison to more complex, correlated initial states (including the ground states) as well as to larger 2D and 3D systems. It will also be interesting to analyze the dependence of the dynamics on the sign of the interaction [6,64], to investigate disordered setups [108–111] and to compare the fermionic simulations to those for bosonic lattice systems. Finally, the access of long simulation times by NEGF and DMRG for weak and strong coupling, respectively, should allow one to study interesting features of the quantum-quench dynamics such as prethermalization [112–114].

[1] C. Giannetti, M. Capone, D. Fausti, M. Fabrizio, F. Parmigiani, and D. Mihailovic, Adv. Phys. **65**, 58 (2016).

[2] M. Gandolfi, G. L. Celardo, F. Borgonovi, G. Ferrini, A. Avella, F. Banfi, and C. Giannetti, Phys. Scr. **92**, 034004 (2017).

[3] T. Langen, R. Geiger, and J. Schmiedmayer, Annu. Rev. Condens. Matter Phys. **6**, 201 (2015).

[4] J. Eisert, M. Friesdorf, and C. Gogolin, Nat. Phys. **11**, 124 (2015).

[5] C. Gogolin and J. Eisert, Rep. Prog. Phys. **79**, 056001 (2016).

[6] U. Schneider, L. Hackermüller, J. P. Ronzheimer, S. Will, S. Braun, T. Best, I. Bloch, E. Demler, S. Mandt, D. Rasch, and A. Rosch, Nat. Phys. **8**, 213 (2012).

[7] S. Will, D. Iyer, and M. Rigol, Nat. Commun. **6**, 6009 (2015).

[8] D. Pertot, A. Sheikhan, E. Cocchi, L. A. Miller, J. E. Bohn, M. Koschorreck, M. Köhl, and C. Kollath, Phys. Rev. Lett. **113**, 170403 (2014).

[9] L. W. Cheuk, M. A. Nichols, M. Okan, T. Gersdorf, V. V. Ramasesh, W. S. Bakr, T. Lompe, and M. W. Zwierlein, Phys. Rev. Lett. **114**, 193001 (2015).

[10] M. F. Parsons, F. Huber, A. Mazurenko, C. S. Chiu, W. Setiawan, K. Wooley-Brown, S. Blatt, and M. Greiner, Phys. Rev. Lett. **114**, 213002 (2015).

[11] E. Haller, J. Hudson, A. Kelly, D. Cotta, B. Peaudecerf, G. Bruce, and S. Kuhr, Nat. Phys. **11**, 738 (2015).

[12] G. J. A. Edge, R. Anderson, D. Jervis, D. C. McKay, R. Day, S. Trotzky, and J. H. Thywissen, Phys. Rev. A **92**, 063406 (2015).

[13] A. Omran, M. Boll, T. A. Hilker, K. Kleinlein, G. Salomon, I. Bloch, and C. Gross, Phys. Rev. Lett. **115**, 263001 (2015).

[14] L. W. Cheuk, M. A. Nichols, K. R. Lawrence, M. Okan, H. Zhang, and M. W. Zwierlein, Phys. Rev. Lett. **116**, 235301 (2016).

[15] L. W. Cheuk, M. A. Nichols, K. R. Lawrence, M. Okan, H. Zhang, E. Khatami, N. Trivedi, T. Paiva, M. Rigol, and M. W. Zwierlein, Science **353**, 1260 (2016).

[16] D. Greif, M. F. Parsons, A. Mazurenko, C. S. Chiu, S. Blatt, F. Huber, G. Ji, and M. Greiner, Science **351**, 953 (2016).

[17] M. Boll, T. A. Hilker, G. Salomon, A. Omran, J. Nespolo, L. Pollet, I. Bloch, and C. Gross, Science **353**, 1257 (2016).

[18] M. Cheneau, P. Barmettler, D. Poletti, M. Endres, P. Schauß, T. Fukuhara, C. Gross, I. Bloch, C. Kollath, and S. Kuhr, Nature (London) **481**, 484 (2012).

[19] T. Fukuhara, A. Kantian, M. Endres, M. Cheneau, P. Schauß, S. Hild, D. Bellem, U. Schollwöck, T. Giamarchi, C. Gross, I. Bloch, and S. Kuhr, Nat. Phys. **9**, 235 (2013).

[20] T. Fukuhara, P. Schauß, M. Endres, S. Hild, M. Cheneau, I. Bloch, and C. Gross, Nature (London) **502**, 76 (2013).

[21] S. Hild, T. Fukuhara, P. Schauß, J. Zeiher, M. Knap, E. Demler, I. Bloch, and C. Gross, Phys. Rev. Lett. **113**, 147205 (2014).

[22] P. M. Preiss, R. Ma, M. E. Tai, A. Lukin, M. Rispoli, P. Zupancic, Y. Lahini, R. Islam, and M. Greiner, Science **347**, 1229 (2015).

[23] E. Cocchi, L. A. Miller, J. H. Drewes, M. Koschorreck, D. Pertot, F. Brennecke, and M. Köhl, Phys. Rev. Lett. **116**, 175301 (2016).

[24] T. Kinoshita, T. Wenger, and S. D. Weiss, Nature (London) **440**, 900 (2006).

[25] S. Hofferberth, I. Lesanovsky, B. Fisher, T. Schumm, and J. Schmiedmayer, Nature (London) **449**, 324 (2007).

[26] T. Langen, R. Geiger, M. Kuhnert, B. Rauer, and J. Schmiedmayer, Nat. Phys. **9**, 640 (2013).

[27] M. Gring, M. Kuhnert, T. Langen, T. Kitagawa, B. Rauer, M. Schreitl, I. Mazets, D. A. Smith, E. Demler, and J. Schmiedmayer, Science **337**, 1318 (2012).

[28] S. Trotzky, Y.-A. Chen, A. Flesch, I. P. McCulloch, U. Schollwöck, J. Eisert, and I. Bloch, Nat. Phys. **8**, 325 (2012).

[29] J. P. Ronzheimer, M. Schreiber, S. Braun, S. S. Hodgman, S. Langer, I. P. McCulloch, F. Heidrich-Meisner, I. Bloch, and U. Schneider, Phys. Rev. Lett. **110**, 205301 (2013).

[30] T. Giamarchi, *Quantum Physics in One Dimension* (Clarendon Press, Oxford, 2004).

[31] F. Essler, H. Frahm, F. Göhmann, A. Klümper, and V. E. Korepin, *The One-Dimensional Hubbard Model* (Cambridge University Press, New York, 2005).

[32] S. R. Manmana, A. Muramatsu, and R. M. Noack, AIP Conf. Proc. **789**, 269 (2005).

[33] M. Rigol, V. Dunjko, and M. Olshanii, Nature (London) **452**, 854 (2008).

[34] P. Prelovsek and J. Bonca, Springer Ser. Solid-State Sci. **176**, 1 (2013).

[35] J. Bonča, S. A. Trugman, and I. Batistić, Phys. Rev. B **60**, 1633 (1999).

[36] L. Vidmar, J. Bonča, M. Mierzejewski, P. Prelovšek, and S. A. Trugman, Phys. Rev. B **83**, 134301 (2011).

[37] M. Mierzejewski, L. Vidmar, J. Bonča, and P. Prelovšek, Phys. Rev. Lett. **106**, 196401 (2011).

[38] J. Bonča, M. Mierzejewski, and L. Vidmar, Phys. Rev. Lett. **109**, 156404 (2012).

[39] D. Golež, J. Bonča, M. Mierzejewski, and L. Vidmar, Phys. Rev. B **89**, 165118 (2014).

[40] G. Vidal, Phys. Rev. Lett. **93**, 040502 (2004).

[41] A. Daley, C. Kollath, U. Schollwöck, and G. Vidal, J. Stat. Mech. (2004) P04005.

[42] S. R. White and A. E. Feiguin, Phys. Rev. Lett. **93**, 076401 (2004).

[43] M. P. Zaletel, R. S. K. Mong, C. Karrasch, J. E. Moore, and F. Pollmann, Phys. Rev. B **91**, 165112 (2015).

[44] J. Hauschild, F. Pollmann, and F. Heidrich-Meisner, Phys. Rev. A **92**, 053629 (2015).

[45] J. J. Dorando, J. Hachmann, and G. K.-L. Chan, J. Chem. Phys. **130**, 184111 (2009).

[46] J. Haegeman, J. I. Cirac, T. J. Osborne, I. Pižorn, H. Verschelde, and F. Verstraete, Phys. Rev. Lett. **107**, 070601 (2011).

[47] M. Lubasch, V. Murg, U. Schneider, J. I. Cirac, and M.-C. Bañuls, Phys. Rev. Lett. **107**, 165301 (2011).

[48] E. Gull, A. J. Millis, A. I. Lichtenstein, A. N. Rubtsov, M. Troyer, and P. Werner, Rev. Mod. Phys. **83**, 349 (2011).

[49] P. Schmidt and H. Monien, arXiv:cond-mat/0202046.

[50] J. K. Freericks, V. M. Turkowski, and V. Zlatić, Phys. Rev. Lett. **97**, 266408 (2006).

[51] M. Eckstein, A. Hackl, S. Kehrein, M. Kollar, M. Moeckel, P. Werner, and F. A. Wolf, Eur. Phys. J. Special Topics **180**, 217 (2010).

[52] F. A. Wolf, I. P. McCulloch, and U. Schollwöck, Phys. Rev. B **90**, 235131 (2014).

[53] M. Ganahl, M. Aichhorn, H. G. Evertz, P. Thunström, K. Held, and F. Verstraete, Phys. Rev. B **92**, 155132 (2015).

[54] G. S. Uhrig, Phys. Rev. A **80**, 061602 (2009).

[55] S. A. Hamerla and G. S. Uhrig, Phys. Rev. B **89**, 104301 (2014).

[56] N.-H. Kwong and M. Bonitz, Phys. Rev. Lett. **84**, 1768 (2000).

[57] N. Kwong, M. Bonitz, R. Binder, and H. Köhler, Phys. Status Solidi (b) **206**, 197 (1998).

[58] A. Rios, B. Barker, M. Buchler, and P. Danielewicz, Ann. Phys. **326**, 1274 (2011).

[59] K. Balzer, M. Bonitz, R. van Leeuwen, A. Stan, and N. E. Dahlen, Phys. Rev. B **79**, 245306 (2009).

[60] M. Lorke, T. R. Nielsen, J. Seebeck, P. Gartner, and F. Jahnke, Phys. Rev. B **73**, 085324 (2006).

[61] *Progress in Non-Equilibrium Green's Functions (PNGF VI)*, edited by C. Verdozzi, A. Wacker, C.-O. Almbladh, and M. Bonitz, J. Phys.: Conf. Ser. (IOP Publishing, Bristol, 2016), Vol. 696.

[62] S. Hermanns, N. Schlünzen, and M. Bonitz, Phys. Rev. B **90**, 125111 (2014).

[63] M. Bonitz, N. Schlünzen, and S. Hermanns, Contrib. Plasma Phys. **55**, 152 (2015).

[64] N. Schlünzen, S. Hermanns, M. Bonitz, and C. Verdozzi, Phys. Rev. B **93**, 035107 (2016).

[65] N. Schlünzen and M. Bonitz, Contrib. Plasma Phys. **56**, 5 (2016).

[66] U. Schollwöck, Rev. Mod. Phys. **77**, 259 (2005).

[67] U. Schollwöck, Ann. Phys. (NY) **326**, 96 (2011).

[68] K. Balzer, S. Bauch, and M. Bonitz, Phys. Rev. A **81**, 022510 (2010).

[69] M. P. von Friesen, C. Verdozzi, and C.-O. Almbladh, Phys. Rev. B **82**, 155108 (2010).

[70] D. Lacroix, S. Hermanns, C. M. Hinz, and M. Bonitz, Phys. Rev. B **90**, 125112 (2014).

[71] M. P. von Friesen, C. Verdozzi, and C.-O. Almbladh, Phys. Rev. Lett. **103**, 176404 (2009).

[72] P. Lipavský, V. Špička, and B. Velický, Phys. Rev. B **34**, 6933 (1986).

[73] J. Schwinger, J. Math. Phys. **2**, 407 (1961).

[74] L. V. Keldysh, Zh. Eksp. Teor. Fiz. **47**, 1515 (1964) [Sov. Phys. JETP **20**, 1018 (1965)].

[75] M. Bonitz, S. Hermanns, K. Kobusch, and K. Balzer, J. Phys.: Conf. Ser. **427**, 012002 (2013).

[76] L. Kadanoff and G. Baym, *Quantum statistical mechanics*, Frontiers in physics (W.A. Benjamin, New York, 1962).

[77] S. Hermanns, Ph.D. dissertation, Kiel University (2016).

[78] K. Balzer, N. Schlünzen, and M. Bonitz, Phys. Rev. B **94**, 245118 (2016).

[79] K. Balzer and M. Bonitz, *Nonequilibrium Green's Functions Approach to Inhomogeneous Systems*, Vol. 867 of Lecture Notes in Physics (Springer, Heidelberg, 2013).

[80] M. Scharnke, N. Schlünzen, and M. Bonitz, arXiv:1612.08033.

[81] S. Latini, E. Perfetto, A.-M. Uimonen, R. van Leeuwen, and G. Stefanucci, Phys. Rev. B **89**, 075306 (2014).

[82] S. R. White, Phys. Rev. Lett. **69**, 2863 (1992).

[83] J. Eisert, M. Cramer, and M. B. Plenio, Rev. Mod. Phys. **82**, 277 (2010).

[84] E. Stoudenmire and S. R. White, Annu. Rev. Condens. Matter Phys. **3**, 111 (2012).

[85] D. Gobert, C. Kollath, U. Schollwöck, and G. Schütz, Phys. Rev. E **71**, 036102 (2005).

[86] L. Xia, L. A. Zundel, J. Carrasquilla, A. Reinhard, J. M. Wilson, M. Rigol, and D. S. Weiss, Nat. Phys. **11**, 316 (2014).

[87] L. Vidmar, J. P. Ronzheimer, M. Schreiber, S. Braun, S. S. Hodgman, S. Langer, F. Heidrich-Meisner, I. Bloch, and U. Schneider, Phys. Rev. Lett. **115**, 175301 (2015).

[88] F. Heidrich-Meisner, M. Rigol, A. Muramatsu, A. E. Feiguin, and E. Dagotto, Phys. Rev. A **78**, 013620 (2008).

[89] F. Heidrich-Meisner, S. R. Manmana, M. Rigol, A. Muramatsu, A. E. Feiguin, and E. Dagotto, Phys. Rev. A **80**, 041603 (2009).

[90] J. Kajala, F. Massel, and P. Törmä, Phys. Rev. Lett. **106**, 206401 (2011).

[91] S. Langer, M. J. A. Schuetz, I. P. McCulloch, U. Schollwöck, and F. Heidrich-Meisner, Phys. Rev. A **85**, 043618 (2012).

[92] C. J. Bolech, F. Heidrich-Meisner, S. Langer, I. P. McCulloch, G. Orso, and M. Rigol, Phys. Rev. Lett. **109**, 110602 (2012).

[93] L. Vidmar, S. Langer, I. P. McCulloch, U. Schneider, U. Schollwöck, and F. Heidrich-Meisner, Phys. Rev. B **88**, 235117 (2013).

[94] Z. Mei, L. Vidmar, F. Heidrich-Meisner, and C. J. Bolech, Phys. Rev. A **93**, 021607 (2016).

[95] S. Keßler, I. P. McCulloch, and F. Marquardt, New J. Phys. **15**, 053043 (2013).

[96] K. Winkler, G. Thalhammer, F. Lang, R. Grimm, J. H. Denschlag, A. J. Daley, A. Kantian, H. P. Bahler, and P. Zoller, Nature (London) **441**, 853 (2006).

[97] F. Hofmann and M. Potthoff, Phys. Rev. B **85**, 205127 (2012).

[98] D. Muth, D. Petrosyan, and M. Fleischhauer, Phys. Rev. A **85**, 013615 (2012).

[99] R. Rausch and M. Potthoff, Phys. Rev. B **95**, 045152 (2017).

[100] For completeness, we note that there are certain limiting cases, in which NEGF are valid regardless of the interaction strength, e.g., the TMA in full/empty bands (cf. Ref. [115]).

[101] This symmetry is only fulfilled by the density and not necessarily by other local quantities, as can be seen, e.g., from the double occupation [cf. Fig. 7(b)].

[102] T. Enss and J. Sirker, New J. Phys. **14**, 023008 (2012).

[103] A. Bauer, F. Dorfner, and F. Heidrich-Meisner, Phys. Rev. A **91**, 053628 (2015).

[104] K. Balzer, F. A. Wolf, I. P. McCulloch, P. Werner, and M. Eckstein, Phys. Rev. X **5**, 031039 (2015).

[105] G. Carleo, F. Becca, M. Schiró, and M. Fabrizio, Sci. Rep. **2**, 243 (2012).

[106] For NEGF, we leave out the full two-time propagation results due to the artificial damping (cf. Fig. 6) that completely cancels out all occurring oscillations in the CDW setup.

[107] T. Kiendl and F. Marquardt, Phys. Rev. Lett. **118**, 130601 (2017).

[108] D. M. Basko, I. L. Aleiner, and B. L. Altshuler, Ann. Phys. **321**, 1126 (2006).

[109] I. V. Gornyi, A. D. Mirlin, and D. G. Polyakov, Phys. Rev. Lett. **95**, 206603 (2005).

[110] R. Nandkishore and D. A. Huse, Annu. Rev. Condens. Matter Phys. **6**, 15 (2015).

[111] E. Altman and R. Vosk, Annu. Rev. Condens. Matter Phys. **6**, 383 (2015).

[112] J. Berges, S. Borsányi, and C. Wetterich, Phys. Rev. Lett. **93**, 142002 (2004).

[113] M. Moeckel and S. Kehrein, Phys. Rev. Lett. **100**, 175702 (2008).

[114] M. Eckstein, M. Kollar, and P. Werner, Phys. Rev. Lett. **103**, 056403 (2009).

[115] J. Kanamori, Prog. Theor. Phys. **30**, 275 (1963).

4.2 Dynamics of Ultracold Atoms

When ultracold quantum gases are brought into particular configurations of counterpropagating laser beams they can be forced to rearrange in what can be fittingly described as artificial crystals of light. The interfering light beams create spatially periodic polarization patterns resulting in lattice-like potentials. Adequately cooled neutral atoms can then be trapped within this elaborate laser field via the Stark shift. The development of these optical lattices for ultracold atoms has laid the foundation of an extremely versatile and productive experimental field (an overview can be found, e.g., in Refs. [42–45]). The strength of this technique is the high degree of controllability as the system's parameters can be tuned in such a way that the atoms simulate the electrons of a condensed-matter state with adjustable characteristics. For this reason, cold gases in optical lattices are considered a promising realization of a *quantum simulator* [45]. Likewise, the lattice dimension can be modified to create effective 1D, 2D, or 3D systems. Due to the high accessibility of the laser optics, it is possible to design arbitrary potentials and even dynamical excitations. Another major breakthrough in the field of ultracold atoms in optical lattices has been the development of the quantum-gas microscopes for bosons [144, 145] and six years later for fermions [146–150]. They allow for single-site-resolved observations of the atoms in the lattice. With all these features the technique is well suited to experimentally simulate bosons or fermions in the Hubbard model and even realize nonequilibrium states.

Due to the possibility to make time-resolved observations of particle dynamics within optical lattices, it is of particular interest to investigate transport phenomena. A specific setup that has been successfully studied is the expansion of an initially confined particle cloud for bosons [151–153] and fermions [140, 154]. For numerical methods the reliable prediction of bosonic and fermionic expansion is heavily demanding. Therefore, numerically accurate reference data provided by, e.g., DMRG calculations are usually limited to 1D setups [154, 156]. This conjuncture has caused a drastic imbalance between the experiment and the theoretical description [44, 140, 218]. However, the system dimension is no conceptional barrier for the NEGF method and the recent developments in the author's group [136, 289] have rendered the application of the NEGF technique to practically relevant, correlated nonequilibrium systems possible. For this reason, the author focused on the prediction of fermionic 2D expansion in his master's thesis [290]. The result was a convincingly close agreement with the experimental data by Schneider *et al.* in Ref. [140]. During the author's PhD studies, the previous findings have been complemented and generalized to be published in the following paper,[3] Ref. [213].

The time evolution of an expanding fermionic particle cloud crucially depends on the strength of the on-site interaction. Ref. [213] focuses on the different limiting cases of the expansion and, in particular, the crossover regime in between. In the noninteracting limit—starting from a doubly occupied lattice center—the particles can move ballistically towards the outer region of the system, unaffected by the surrounding fermions. In the strong-coupling regime, however, one finds a phenomenon called *quantum distillation* [155]— the separation between independent single particles and effective doublons (correlated

---

[3]N. Schlünzen, S. Hermanns, M. Bonitz, and C. Verdozzi, Phys. Rev. B, **93**, 035107 (2016). Copyright by the American Physical Society. Reproduced with permission.

particle pairs), both with a characteristic expansion velocity. With increasing interaction, the doublon fraction becomes larger and more stable. The crossover between both cases, i.e., the region of intermediate interaction strengths, is governed by various scattering processes and a complex correlation interplay, with an overall reducing expansion velocity for increasing coupling. In Ref. [213], an NEGF approach with the (particle–particle) T-matrix selfenergy, which has been developed by the author, is applied to study the expansion in finite 1D, 2D, and 3D lattices. An analysis of the particle-number dependence reveals a universal scaling of the expansion velocity that can be used for an extrapolation to the macroscopic limit. The resulting data match the experiments of Ref. [140] with an unprecedented accuracy. Furthermore, the short-time behavior is specified with three characteristic phases that correspond to the time scales of the mean-field effects, the (slower) correlation build-up, and the eventual saturation, respectively. Apart from the single-particle observables, the NEGF approach gives also access to more involved quantities, such as the double occupation and the entanglement entropy, which give additional insights to the dynamical behavior.

Finally, it is mentioned that the results have already impacted the community and Fig. 1 of Ref. [213] has been reprinted in the reviews [122],[79] and [291].

Dynamics of strongly correlated fermions: *Ab initio* results for two and three dimensions

N. Schlünzen, S. Hermanns, and M. Bonitz

Institut für Theoretische Physik und Astrophysik, Christian-Albrechts-Universität zu Kiel, D-24098 Kiel, Germany

C. Verdozzi

Department of Physics and ETSF, Lund University, Box 118, S-22100 Lund, Sweden
(Received 13 August 2015; revised manuscript received 16 December 2015; published 11 January 2016)

Quantum transport of strongly correlated fermions is of central interest in condensed matter physics. While the stationary expansion dynamics have recently been measured with cold atoms in 2D optical lattices, *ab initio* simulations have been limited to 1D setups so far. Here, we present the first precise fermionic quantum dynamics simulations for 2D and 3D. The simulations are based on nonequilibrium Green functions and incorporate strong correlations via T-matrix self-energies. The simulations predict the short-time dynamics, and we discover a universal scaling of the expansion velocity with the particle number. Our predictions can be verified experimentally using the recently developed fermionic atom microscopes.

I. INTRODUCTION

Particle, momentum, and energy transport of strongly correlated quantum systems are of growing interest in condensed matter [1–3], ultracold quantum gases [4–8], and dense plasmas [9]. Direct measurements of quantum transport have been accomplished in Hubbard-type one- and two-dimensional (1D, 2D) optical lattices by monitoring the expansion of ultracold atoms following a confinement quench [4,6–8], for an illustration see Fig. 1. Also, the dynamics following a quench in lattice depth have been measured [11–14], and very recently, three groups reported the development of an atomic microscope for fermions [15–17] opening the way for experiments with unprecedented single-site resolution. In contrast to the experiment, theoretical studies of these transport processes for fermions face fundamental difficulties. While, in 1D, the expansion of fermions can be accurately simulated with time-dependent density matrix renormalization group (DMRG) methods, e.g., Refs. [5,6], currently higher dimensions are not accessible [18].

The authors of Ref. [4] also presented 2D numerical results from a semiclassical Boltzmann equation (SC-BE) model with a collision integral in the relaxation-time approximation (RTA). One important feature of the experiment—the reduction of the expansion velocity C_{exp} of the central part (the "core," defined as half width at half maximum [HWHM]) of the density with the Hubbard coupling strength U (see Sec. II A) and, eventually, shrinkage of the core—is qualitatively captured by RTA, see lower part of Fig. 1. However, additional observations, such as the zero crossing of C_{exp} around $U = 3$ are missed, the value of C_{exp} at large $|U|$ is off by several $100\%s$, and even the value for the ideal case ($U = 0$) is not reproduced. This is, of course, not unexpected [4] due to the known defects of the SC-BE that include the violation of total energy conservation and an incorrect asymptotic state [20,21]. Also, the experimental system is well isolated so the dynamics should be unitary (reversible), which is in contrast to the Boltzmann equation. The RTA, in addition, assumes that the system is close to local thermal equilibrium, which may be adequate only at a late stage of the expansion.

It is the purpose of this paper to present a theory that overcomes all these problems. We present the first *ab initio* quantum simulations for correlated fermions that apply not only to one-dimensional systems but also to two and three dimensions. We capture not only the final stage of hydrodynamic expansion but also the early period where the system is far from equilibrium, and correlations and entanglement emerge. The method of choice are first-principles nonequilibrium Green functions (NEGF) simulations—a theory long established in quantum statistical mechanics, e.g., Refs. [21,22]—and demonstrate that it is capable to accurately simulate correlated fermions in Hubbard lattices, in general, and fermionic atoms in optical lattices under realistic experimental conditions, in particular.

A first confirmation is shown in the lower part of Fig. 1 where we report excellent *quantitative agreement with the experiment* [4] *for all U* without any free parameters. Furthermore, we present extensive additional predictions of quantum dynamics not yet observed experimentally: (a) the early stage of the evolution of the expansion velocity $v_{exp}(t)$, of pair correlations and of entanglement, (b) the change of the dynamics with the system dimensionality D, (c) the momentum distribution of the expanding correlated fermions, and (d) the approach of the thermodynamic limit, $N \to \infty$. Here, a striking universal behavior is discovered: for all U and D, the expansion velocity decreases with system size according to $v_{exp}^{\infty}(N) - V_{exp} \sim N^{-1/2}$, where we denoted the long-time asymptotics by $v_{exp}^{\infty} \equiv v_{exp}(t \to \infty)$ and $V_{exp} \equiv v_{exp}^{\infty}(N \to \infty)$.

This paper is organized as follows. In Sec. II, we introduce the D-dimensional Hubbard model and summarize the basic formulas of the nonequilibrium Green functions approach. In Sec. III, we present the numerical results. In Sec. IV, we conclude with a summary and a discussion of our results.

II. THEORY

A. Hubbard model

We consider the *D*-dimensional Hubbard model with N_s sites that are labeled by a *D*-dimensional index $s =$
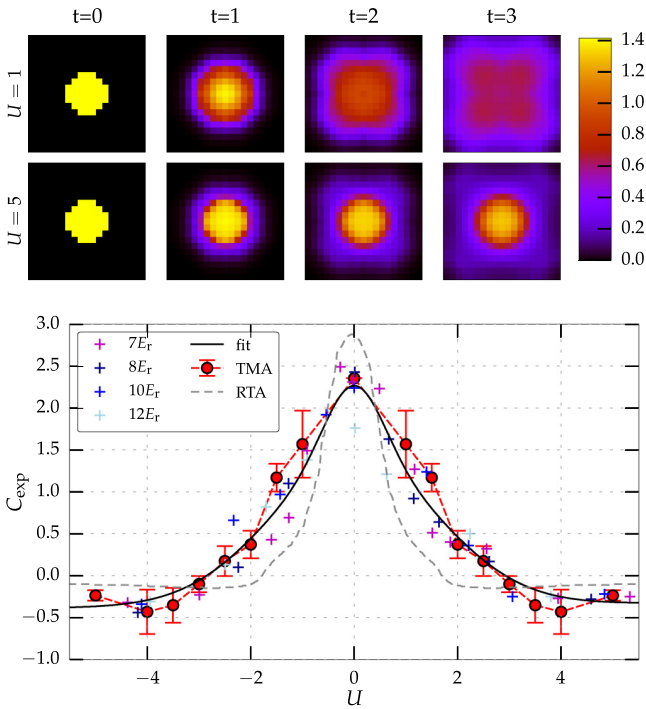
FIG. 1. (Top) Expansion dynamics of 74 circularly confined fermions in a 2D 19×19 Hubbard lattice (1) following the removal of the confinement at time $t = 0$, for $U = 1(5)$, first (second) row. Snapshots of the density n_s for four time points during the early stage of the expansion (t in units of the inverse hopping rate, color code: $\sqrt{n_s}$). (Bottom) Asymptotic core [defined as density HWHM] expansion velocity C_{exp}. Plus signs: experimental results for different lattice depths in units of the recoil energy E_r [10]; gray dashed line: RTA model [4]; red circles: present NEGF results. The black line is a fit through the experimental points to guide the eye.

$(s_1, \ldots, s_D)$ and the local spin projection is denoted by $\sigma \in \{\uparrow, \downarrow\}$. The Hamiltonian is, in second quantization, expressed in terms of creation and annihilation operators $\hat{c}_{s,\sigma}^\dagger$ and $\hat{c}_{s,\sigma}$:

$$H(t) = -\sum_{\langle s,s' \rangle} \sum_{\sigma=\uparrow,\downarrow} \hat{c}_{s,\sigma}^\dagger \hat{c}_{s',\sigma} + U \sum_s \hat{c}_{s,\uparrow}^\dagger \hat{c}_{s,\uparrow} \hat{c}_{s,\downarrow}^\dagger \hat{c}_{s,\downarrow}$$

$$+ \sum_s \sum_{\sigma=\uparrow,\downarrow} V_s^R(t) \hat{c}_{s,\sigma}^\dagger \hat{c}_{s,\sigma}, \quad (1)$$

and, in the first (hopping) term, $\langle s, s' \rangle$ denotes nearest-neighbor sites. The second term describes on-site interactions of electrons with opposite spin, which has the strength U. In the third term, $V_s^R(t)$ is a circular potential of radius R that initially confines N fermions occupying $N/2$ sites in the trap center. In the present paper, we consider the dynamics that are initiated by a potential quench, i.e., at time $t = 0$, V^R is switched off what initiates a diffusion process, as, e.g., in the experiment [4].

B. Nonequilibrium Green functions

Our goal is to study the correlated expansion dynamics of spatially inhomogeneous finite Hubbard clusters with a single-site resolution. We are interested in the dynamics on all time scales while exactly fulfilling the many-particle conservation

laws of particle number, momentum, and total energy. This can be achieved using NEGF that are defined on the Keldysh time contour $\mathcal{C}$ with the contour-time-ordering operator $T_\mathcal{C}$ as

$$G_{ss'}^\sigma(z,z') = -\frac{i}{\hbar} \langle T_\mathcal{C} \hat{c}_{s,\sigma}(z) \hat{c}_{s',\sigma}^\dagger(z') \rangle. \quad (2)$$

The Green functions can be understood as generalized time-dependent single-particle density matrices on the lattice where the presence of two time arguments allows to incorporate spectral information, and $\langle \ldots \rangle$ denotes the ensemble average. The equations of motion for the NEGF are the Keldysh–Kadanoff–Baym equations (KBE) [21,22],

$$\left(i\hbar \frac{\partial}{\partial z} \delta_{s,\bar{s}} - h_{s\bar{s}}^\sigma \right) G_{\bar{s}s'}^\sigma(z,z')$$

$$= \delta_\mathcal{C}(z - z') \delta_{s,s'} + \int_\mathcal{C} d\bar{z} \, \Sigma_{s\bar{s}}^\sigma(z,\bar{z}) G_{\bar{s}s'}^\sigma(\bar{z},z'), \quad (3)$$

and its adjoint (summation over $\bar{s}$ is implied). In order to account for correlation effects in the dynamics, the self-energy Σ includes, in addition to mean-field (Hartree-Fock), also correlation contributions. For weak to moderate coupling ($|U| \lesssim 1$), the second-order Born approximation is appropriate [23], which includes all irreducible diagrams of second order in the interaction (second order in U). However, for the case of strong correlations (large $|U|$), the next orders (third, fourth powers of U) become comparable and perturbation theory fails. Therefore one has to sum up the entire Born series, i.e., diagrams of all orders in U. This is equivalent to the T-matrix approximation to the correlation self-energy (TMA) [24], which reads, for the Hubbard model [25],

$$\Sigma_{ss'}^{\text{cor},\uparrow(\downarrow)}(z,z') = i\hbar \, T_{ss'}(z,z') \, G_{s's}^{\downarrow(\uparrow)}(z',z), \quad (4)$$

$$T_{ss'}(z,z') = -i\hbar \, U^2 \, G_{ss'}^\uparrow(z,z') \, G_{ss'}^\downarrow(z,z')$$

$$+ i\hbar \, U \int_\mathcal{C} d\bar{z} \, G_{s\bar{s}}^\uparrow(z,\bar{z}) \, G_{s\bar{s}}^\downarrow(z,\bar{z}) T_{\bar{s}s'}(\bar{z},z'). \quad (5)$$

Here, T can be understood as an effective interaction obeying the Lippmann-Schwinger equation (5), e.g., Refs. [20,22,27]. The first term in (5) alone describes the interaction of a single fermion pair and corresponds to the second-order Born approximation, whereas the integral term adds interaction contributions of all orders (in U).

We underline the conserving character of this approximation [22] and, in fact, conservation of particle number and *total energy* is observed to high accuracy in all our simulations. Further, time-reversal symmetry is guaranteed (as it should be since the system is isolated). Also, our simulations yield the same time-dependent densities when U is replaced by $-U$ confirming the dynamical symmetry demonstrated in Refs. [4,28].

The two-time KBE have been solved for a variety of spatially homogeneous systems, including dense plasmas and optically excited semiconductors [29–31] or the uniform electron gas [32]. More recently, spatially inhomogeneous systems were studied, in particular, the ionization dynamics of few-electron atoms [33–35] and quantum dots [2]. All these simulations used self-energies on the level of the static second Born approximation. Only recently the use of the two-time TMA, under full nonequilibrium conditions, has

become possible for the Hubbard model in Refs. [23,25,36]. However, only very small 1D systems ($N \leqslant 6, U \leqslant 4$) could be simulated for rather short times. Here, we report a dramatic extension of TMA simulations in terms of particle number, simulation duration, and dimensionality. With this, it is possible, for the first time, to access experimentally relevant situations. We systematically study up to $N = N^\uparrow + N^\downarrow = 2N^\uparrow = 114$ fermions in a broad range of coupling parameters, $0 \leqslant |U| \leqslant 8$, in a one-, two-, and three-dimensional lattice.

III. RESULTS

The initial state of our simulations is a doubly occupied spherical central region in the ground state [4] that is confined by a properly chosen potential V^R which is turned off at $t = 0$. In our simulations we use a steplike potential. We show in Sec. III E that the precise functional form has a negligible effect on the expansion dynamics. The KBE (3) are then solved with this initial condition for the two-time correlation function $G^{\sigma, <}_{ss'}(t, t')$ (the less component of the NEGF (2)[21,37]) yielding the time dependence of all observables.

Figure 1 shows snapshots of the site-resolved particle density $n_s(t) = n_s^\uparrow(t) + n_s^\downarrow(t)$ with $n_s^\sigma(t) = -iG^{\sigma, <}_{ss}(t, t)$, for two couplings, $U = 1, 5$. For $U = 1$, the density rapidly evolves towards the square symmetry of the lattice, whereas for $U = 5$ the core region remains circular over the entire simulation duration, in agreement with experimental observations [4].

A. Time evolution of the expansion velocity

The density evolution is quantified by the diameter $d(t) = \sqrt{R^2(t) - R^2(0)}$, corrected for its starting value $R(0)$,

$$R^2(t) = \frac{1}{N} \sum_s^{N_s} n_s(t) \|s - s_0\|^2, \quad s_0 = \frac{1}{N} \sum_s^{N_s} n_s(0) s,$$

where the center of mass s_0 is immobile in the present case. The left part of Fig. 2 shows the dynamics of the instantaneous expansion velocity

$$v_{\exp}(t) = \frac{d}{dt} d(t), \quad (6)$$
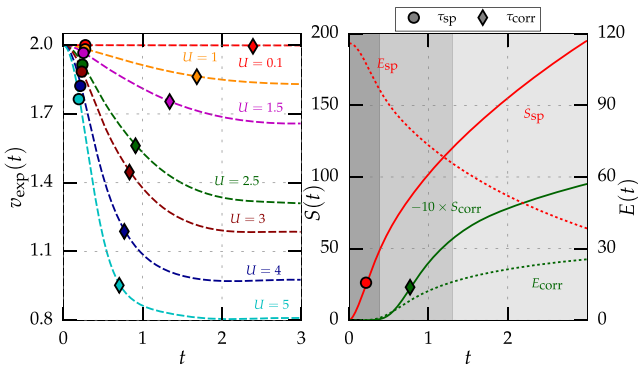
FIG. 2. (Left) Time evolution of the expansion velocity for $N = 58$ in 2D and various U. (Right) Evolution of the independent-particle and correlation parts of the entropy and energy, for $U = 4$. Symbols mark the respective inflection points. Shaded areas correspond to the three phases of the evolution (see text).

for various U, for a typical case, $N = 58$ in 2D. As the system is initially uncorrelated, the expansion starts ballistically from the ideal value, $v_{\exp}(0) = v^{id} = \sqrt{2D} = 2$, and converges to a smaller asymptotic value, $v_{\exp}^\infty$. These asymptotics monotonically decrease with increasing coupling strength U. This trend is well known and easily understood: the diffusion front forms at the cluster edge since particles in the "bulk" cannot move due to the Pauli principle, since all neighboring lattice sites are occupied. When $|U|$ grows, the expansion of the outermost particles is slowed down due to the growing interaction with the bulk particles. Here, we can quantify this trend, for the first time, for two- and three-dimensional systems.

B. Short-time dynamics. Build-up of correlations and entanglement

The time evolution of $v_{\exp}(t)$ is not trivial and results from the interplay between independent-particle and correlation effects. To quantify this, we decompose the double occupation [38] of each site s into a factorized part ("fac") and a correlation part ("corr," the reminder)

$$n_s^{\uparrow\downarrow} = \langle \hat{c}^\dagger_{s,\uparrow} \hat{c}_{s,\uparrow} \hat{c}^\dagger_{s,\downarrow} \hat{c}_{s,\downarrow} \rangle =: n_s^{\uparrow\downarrow,\text{fac}} + n_s^{\uparrow\downarrow,\text{corr}}, \quad (7)$$

$$n_s^{\uparrow\downarrow,\text{fac}} = n_s^\uparrow n_s^\downarrow. \quad (8)$$

The factorized contribution is formally equivalent to the contribution of independent particles. Note, however, that the single-particle densities entering $n_s^{\uparrow\downarrow,\text{fac}}$ are obtained from a fully correlated calculation and, thus, the factorized term also contains interaction effects.

With this, we identify the corresponding components of the energy ($E_{\text{fac}}, E_{\text{corr}}$) [23] as well as the entanglement entropy [38,39],

$$S = S_{\text{fac}} + S_{\text{corr}} = \sum_s S_s, \quad (9)$$

$$S_s = -2\left(\frac{n_s}{2} - n_s^{\uparrow\downarrow}\right)\log_2\left(\frac{n_s}{2} - n_s^{\uparrow\downarrow}\right),$$
$$- n_s^{\uparrow\downarrow}\log_2 n_s^{\uparrow\downarrow} - (1 - n_s + n_s^{\uparrow\downarrow})\log_2(1 - n_s + n_s^{\uparrow\downarrow}). \quad (10)$$

Here, the factorized contribution, S_{fac} follows from the total entropy by the replacement Eq. (8).

The dynamics of these two energy and entropy contributions are dominated by single-particle and correlation effects, respectively, and it is well known from the dynamics of uniform systems [21,29,40] that they proceed on rather different time scales: typically pair correlations relax substantially faster than single-particle quantities. In the expansion dynamics of the present Hubbard clusters we also observe a sequence of time scales, however, the details are very different. We identify three characteristic phases: during the *first phase*, S_{fac} (E_{fac}) is being built up (destroyed), resulting in a decrease of $v_{\exp}$, see Fig. 2. Here, the increase of S_{fac} measures the transition from a state of independent particles ($S = 0$) to an interacting many-body state. The inflection point τ_{fac} (circles) of S_{fac} (and E_{fac}) is representative for the time scale of this phase. The *second phase* is characterized by the saturation of E_{fac} and $v_{\exp}$. The simultaneous build-up of correlations partly prolongs
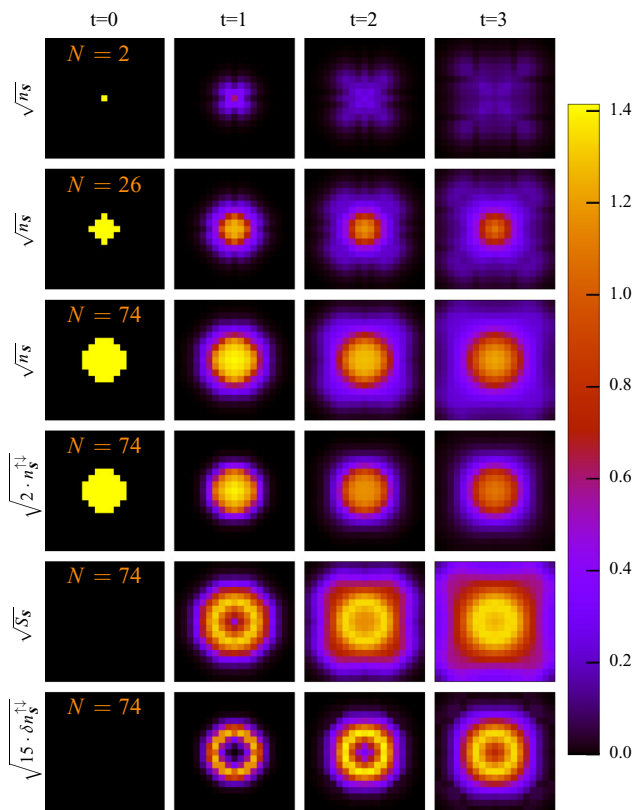
FIG. 3. Fermion expansion dynamics in a 2D 19×19 Hubbard lattice (1) at $U = 4$. Top three rows: square root of density n_s for $N = 2$, 26, and 74, respectively. Rows 4–6: square root of double occupation, entropy density S_s, and the pair correlation function $\delta n_s^{\uparrow\downarrow} = n_s^{\uparrow\downarrow} - n_s^{\uparrow} n_s^{\downarrow}$.

the saturation and determines the final value, $v_{\exp}^{\infty}$. The time scale of these processes is the correlation time τ_{corr} [21,40], which is estimated by the inflection point of S_{corr} (and E_{corr}, diamonds). Both phases become shorter when U is increased, i.e., correlations accelerate the early dynamics, cf. left part of Fig. 2, It is evident that τ_{corr} is one order of magnitude larger than τ_{fac}—in striking contrast to homogeneous systems as discussed above. The main difference here is the strong inhomogeneity leading to a spatially localized formation of correlations and entanglement [see Sec. III C] and the formation of a diffusion front.

C. Single-site resolved expansion and correlation dynamics

Additional insight into the physics is gained from a site-resolved analysis which is presented in Fig. 3. The top three rows show the dynamics in 2D for a fixed U and three particle numbers. Quantum interference effects are evident for small N. Further, the dynamics are slowing down with increasing N, because only fermions at the cluster edge are mobile, in the beginning, due to the Pauli principle. The fourth row displays the spatial distribution of the double occupation $n_s^{\uparrow\downarrow}$. It originally coincides with the single-particle density (third row) but then the two decouple. The much slower doublon expansion is the first indication of "quantum distillation"[41] of fermions in 2D. Finally, the emergence of entanglement and
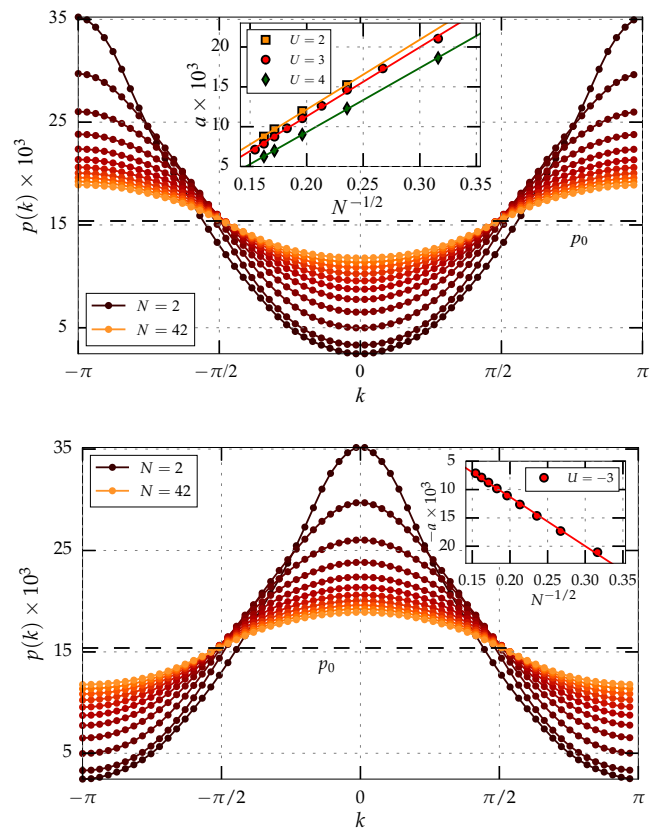
FIG. 4. Momentum distribution $p(k)$, Eq. (11) at $t = 9.5$, for a 1D system of $N_s = 65$ for $N = 2, \ldots, 42$. (Top) $U = 3$. (Bottom) $U = -3$. The dashed lines denotes the uniform initial distribution $p_0(k)$. (Insets) N-dependence of amplitude a. Symbols: data points, lines: linear fits.

of pair correlations is shown in rows 5 and 6. Both start from zero everywhere and emerge first at the cluster boundary from where they propagate inward and outward. These processes are accelerated (slowed down) with increasing U (N), which explains the corresponding behavior of the characteristic time scales τ_{fac} and τ_{corr}.

D. Hydrodynamic expansion phase. Momentum distribution

The *third and final phase* is the hydrodynamic expansion where $v_{\exp}$, the correlations and the momentum distribution have become stationary, see Fig. 4, whereas the independent-particle energy and entropy continue to evolve, cf. Fig. 2. Figure 4 shows the normalized momentum distribution, $p(\mathbf{k}) = n(\mathbf{k})/N$ [obtained from the site occupations], of a 1D system for $U = 3$ at the end of the simulation. For all N, $p(\mathbf{k})$ is oscillatory with an amplitude a that monotonically decreases with N. For large N, it is very well described by the function

$$p(\mathbf{k}) = p(k) = N_s^{-1} - a\cos(k), \qquad (11)$$

where the value of $a(U,N)$ is shown in the inset of Fig. 4 for different U. It is obvious that, for positive U, $p(k)$ is peaked at $\pm\pi$ while the maximum of the occupation is around $k = 0$, for negative U. We note that these results are in agreement with the qualitative predictions in Ref. [28]. A striking observation is
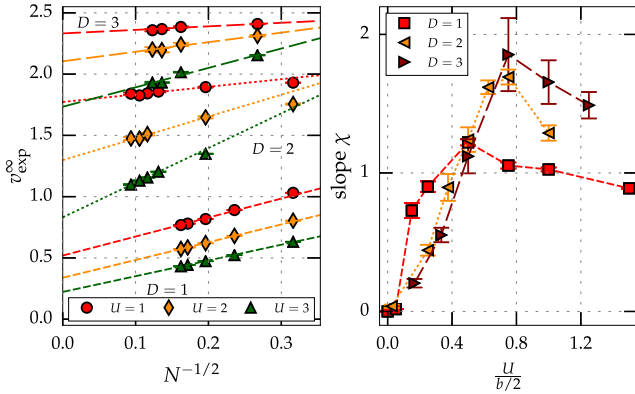
FIG. 5. (Left) Asymptotic expansion velocity vs particle number for $D = 1, \ldots, 3$ and $U = 1, \ldots, 3$. Symbols correspond to data points, errors are smaller than symbol size. Dashed lines: linear extrapolation $N \to \infty$ according to Eq. (13). (Right) Corresponding slope χ vs bandwidth-normalized interaction.

the particle number dependence of the momentum distribution. We observe that the amplitude of the oscillations scales as $a \sim N^{-1/2}$. The origin of this scaling is presently an open question but this behavior was observed in all cases and appears to be universal.

To quantify the stationary hydrodynamic expansion we extrapolate the expansion velocity to $t \to \infty$, denoting the result by $v_{\mathrm{exp}}^{\infty}$. It is obtained from $v_{\mathrm{exp}}(t)$ by averaging over all times exceeding t_{avg} where saturation is reached (cf. Fig. 2) and which is given by

$$\left| \frac{1}{v_{\mathrm{exp}}(t)} \frac{dv_{\mathrm{exp}}}{dt}(t) \right| < \epsilon \,, \tag{12}$$

for all $t > t_{\mathrm{avg}}$ and a given small parameter ($\epsilon \ll 1$). To quantify the error of $v_{\mathrm{exp}}^{\infty}$, we use the standard deviation $\sigma(v_{\mathrm{exp}}^{\infty})$ of the averaging process.

An interesting question is how the expansion of a group of N fermions depends on the value of N and the system dimensionality D. The results of the extrapolation are shown in the left part of Fig. 5. Again, we observe a monotonic decrease with U and, furthermore, a systematic increase of $v_{\mathrm{exp}}^{\infty}$ with D, that is due to the enlarged number of degrees of freedom.

E. Influence of particle number and dimensionality. Extrapolation to the macroscopic limit

The most striking observation is the N dependence of $v_{\mathrm{exp}}^{\infty}$ and its approach to the macroscopic limit: for any fixed U and D and sufficiently large N, we observe the scaling

$$v_{\mathrm{exp}}^{\infty}(U; N; D) - V_{\mathrm{exp}}(U; D) = \chi(U; D) N^{-1/2} \,, \tag{13}$$

$$V_{\mathrm{exp}}(U; D) \equiv \lim_{N \to \infty} v_{\mathrm{exp}}^{\infty}(U; N; D). \tag{14}$$

Interestingly, this N dependence is the same as in the momentum distribution (11), cf. Fig. 4 and is caused by the latter.

For the extrapolation, V_{exp} and the slope χ are used as fit parameters. Only particle numbers N larger than a cutoff value
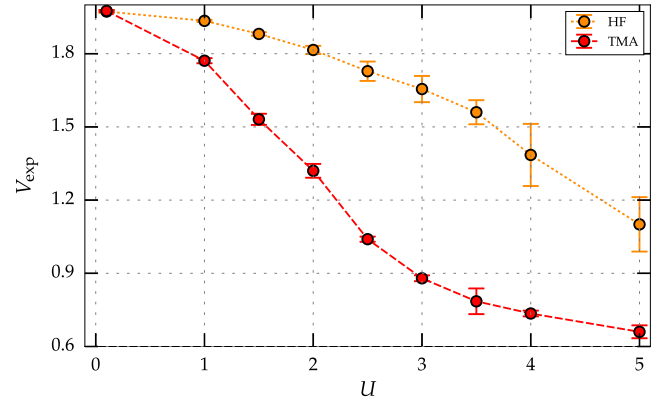
FIG. 6. Macroscopic expansion velocity V_{exp} for varying U. Comparison between Hartree-Fock (HF) and the correlated T-matrix (TMA) results.

$N^{\star}$ are taken into account. The errors $\sigma(v_{\mathrm{exp}}^{\infty})$ are also included in the fit process, resulting in the final statistical uncertainty, $\sigma(V_{\mathrm{exp}})$. We note that our procedure is very similar to the one applied for the diffusion of a Mott insulator and Néel state in a 1D fermionic system in Ref. [42].

The right-hand part of Fig. 5 shows the dependency of the slope χ on the bandwidth-normalized interaction strength $U/(b/2)$ with the effective bandwidth $b = 4D$. For all D and N, χ starts from zero, at $U = 0$, which is a consequence of ballistic expansion of noninteracting particles. When U is increased further, χ reaches a maximum slightly below $U = (b/2)$ and then decreases again. The reason for the latter is that fermions on doubly occupied sites are effectively frozen, at large U, regardless of N. In-between these two limits, the slope shows a qualitatively similar behavior for all D: a steep rise (slow decrease) for small (large) U.

We now turn to the analysis of the macroscopic limit of the expansion velocity, V_{exp}. In Fig. 6, we show V_{exp} as a function of U and confirm the monotonic reduction that was observed before for finite N, cf. Fig. 2. The error bars show the total statistical error resulting from the time averaging and the extrapolation with respect to N. We also show, for comparison, the Hartree-Fock approximation, which exhibits strong deviations, which underlines the key role of correlations in the present quench dynamics.

Similar to our procedure of obtaining the asymptotic expansion velocity $v_{\mathrm{exp}}^{\infty}$ and its macroscopic limit, we can proceed with the core expansion velocity $c_{\mathrm{exp}}^{\infty}$ and its macroscopic limit, C_{exp}. The experimental results of Schneider et al. [4] for a 2D Hubbard system and our T-matrix results were displayed in Sec. I, in Fig. 1. We now explain how our results were obtained. For the case $D = 2$, the density distribution is averaged azimuthally for each time step. The half width at half maximum of the resulting density profile, $R_{\mathrm{HWHM}}(t)$, is used to measure the "core" width. Adjusted for the initial core width, R_{HWHM}^{0}, $c_{\mathrm{exp}}^{\infty}$ is determined by fitting the resulting $R_{\mathrm{HWHM}}(t)$ to

$$R_{\mathrm{HWHM}}(t) = \sqrt{\left(R_{\mathrm{HWHM}}^{0} \right)^{2} + \left(c_{\mathrm{exp}}^{\infty} t \right)^{2}} \tag{15}$$

for all $t > t_{\mathrm{avg}}$ with R_{HWHM}^{0} and $c_{\mathrm{exp}}^{\infty}$ as free fitting parameters. Since the core of the density distribution starts to shrink for
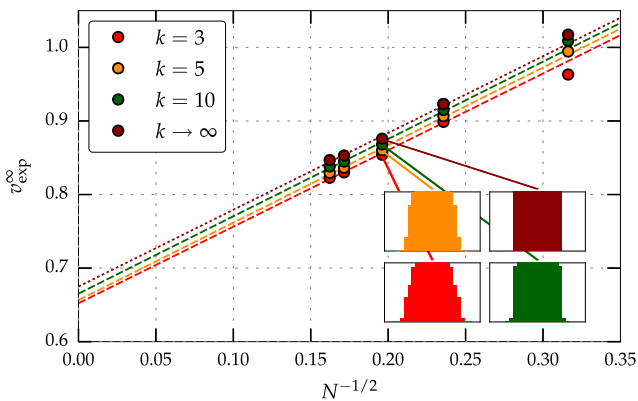
FIG. 7. Dependence of the asymptotic expansion velocity on N for confinement potentials of different curvature $\gamma_k(N)$. Insets show the shape of the initial density profile.

sufficiently large interaction strength U, we apply

$$R_{\text{HWHM}}(t) = \sqrt{\left(R_{\text{HWHM}}^0\right)^2 - \left(c_{\text{exp}}^\infty t\right)^2} \quad (16)$$

instead, following Ref. [4], and consider c_{exp}^∞ the speed of contraction of the core region.

The extrapolation of c_{exp}^∞ is done as in Eq. (13), resulting in the macroscopic core expansion velocity C_{exp}, confirming the scaling with $N^{-1/2}$. This robust scaling with N allows us to perform the thermodynamic limit, $N \to \infty$. This yields the results that were presented in Fig. 1, and that exhibit excellent agreement with the experiment over the entire U range, including the zero crossing of C_{exp} around $U = 3$.

One may wonder whether the results depend on the chosen steep confinement, cf. Figs. 1 and 3. Here, we demonstrate that the shape of the initial confinement has only a minor effect on the asymptotic expansion velocity, in agreement with the observations in Ref. [43]. To this end, we use a harmonic confinement

$$V(R) = \gamma_k R^2, \quad (17)$$

with curvature γ_k. To achieve a similar shape for different N, we choose

$$\gamma_k(N) = k/N, \quad (18)$$

for three strengths $k = 3, 5, 10$. Together with the steplike potential ($k \to \infty$), the results are shown in Fig. 7. Even though the initial density profile is affected by the curvature (see inset), the expansion velocity is not. In particular, the macroscopic limit, V_{exp} changes by less than 10%.

IV. DISCUSSION

To summarize, we have introduced T-matrix NEGF simulations into the field of fermion dynamics in Hubbard lattices providing the first accurate quantum dynamics results [24] for two and three dimensions [44]. While the magnitude of the error of NEGF simulations with T-matrix self-energies for the present large systems is not exactly known, for the cases where the exact results are available (small N, 1D) the agreement is excellent [23,25,26]. It is expected that the accuracy will further improve when N increases, as well as in higher dimensions. The largest uncertainty is expected for Hubbard clusters at half-filling and for small integrable systems. Further tests are needed to verify and quantify this behavior.

Our results for 2D fermionic Hubbard clusters exhibit excellent quantitative agreement with recent experiments that investigated the final stage of the expansion dynamics following a confinement quench [4]. They, moreover, yield detailed information on the early stages of the dynamics of correlated fermions, including the buildup and propagation of correlations and entanglement and on the effect of the system dimensionality. Furthermore, we uncovered a universal scaling of macroscopic quantities with N. Our predictions, including the site-resolved results for the pair correlations and entanglement entropy, can be directly tested experimentally using the novel quantum-gas microscopes [15–17].

[1] *The LDA+DMFT Approach to Strongly Correlated Materials*, edited by E. Pavarini, E. Koch, D. Vollhardt and A. Lichtenstein (Forschungszentrum Jülich GmbH, Zentralbibliothek, Verlag 2011).

[2] K. Balzer, M. Bonitz, R. van Leeuwen, A. Stan, and N. E. Dahlen, Phys. Rev. B **79**, 245306 (2009).

[3] A.-M. Uimonen, E. Khosravi, A. Stan, G. Stefanucci, S. Kurth and R. van Leeuwen, and E. K. U. Gross, Phys. Rev. B **84**, 115103 (2011).

[4] U. Schneider, L. Hackermüller, J. P. Ronzheimer, S. Will, S. Braun, T. Best, I. BlochE. Demler, S. Mandt, D. Rasch, A. Rosch, Nat. Phys. **8**, 213 (2012).

[5] J. Kajala, F. Massel, and P. Törmä, Phys. Rev. Lett. **106**, 206401 (2011).

[6] J. P. Ronzheimer, M. Schreiber, S. Braun, S. S. Hodgman, S. Langer, I. P. McCulloch, F. Heidrich-Meisner, I. Bloch, and U. Schneider, Phys. Rev. Lett. **110**, 205301 (2013).

[7] L. Vidmar, J. P. Ronzheimer, M. Schreiber, S. Braun, S. S. Hodgman, S. Langer, F. Heidrich-Meisner, I. Bloch, and U. Schneider, Phys. Rev. Lett. **115**, 175301 (2015).

[8] L. Xia, L. A. Zundel, J. Carrasquilla, A. Reinhard, J. M. Wilson, M. Rigol, and D. S. Weiss, Nat. Phys. **11**, 316 (2015).

[9] H. D. Whitley, Ch. R. Scullard, L. X. Benedict, J. I. Castor, A. Randles, J. N. Glosli, D. F. Richards, M. P. Desjarlais, and F. R. Graziani, Contrib. Plasma Phys. **55**, 192 (2015).

[10] We include all values E_r shown in Ref. [4] in the comparison.

[11] S. Trotzky, Y.-A. Chen, A. Flesch, I. P. McCulloch, U. Schollwöck, J. Eisert, and I. Bloch, Nature (London) **8**, 484 (2012).

[12] M. Cheneau, P. Barmettler, D. Poletti, M. Endres, P. Schauß, T. Fukuhara, C. Gross, I. Bloch, C. Kollath, and S. Kuhr, Nature (London) **481**, 484 (2012).

[13] S. Will, D. Iyer, and M. Rigol, Nat. Comm. **6**, 6009 (2015).

[14] X. Zhang, C.-L. Hung, S.-K. Tung, and C. Chin, Science **335**, 1070 (2012).

[15] L. W. Cheuk, M. A. Nichols, M. Okan, T. Gersdorf, V. V. Ramasesh, W. S. Bakr, T. Lompe, and M. W. Zwierlein, Phys. Rev. Lett. **114**, 193001 (2015).

[16] M. F. Parsons, F. Huber, A. Mazurenko, C. S. Chiu, W. Setiawan, K. Wooley-Brown, S. Blatt, and M. Greiner, Phys. Rev. Lett. **114**, 213002 (2015).

[17] E. Haller *et al.*, Nat. Phys. **11**, 738 (2015).

[18] For completeness, we mention recent simulations of the expansion dynamics in 3D Hubbard systems with time-dependent DFT [19]. However, they used the adiabatic local density approximation, the reliability of which is still under debate, and considered coupling strengths which are larger than the ones studied in Ref. [4].

[19] A. Kartsev, D. Karlsson, A. Privitera, and C. Verdozzi, Sci. Rep. **3**, 2570 (2013).

[20] D. Kremp, M. Bonitz, W. D. Kraeft, and M. Schlanges, Ann. Phys. (N. Y.) **258**, 320 (1997).

[21] M. Bonitz, *Quantum Kinetic Theory*, 1st ed. (B. G. Teubner, Leipzig, Germany, 1998); *Quantum Kinetic Theory*, 2nd ed. (Springer International Publishing, Cham, Switzerland, 2015).

[22] L. P. Kadanoff and G. Baym, *Quantum Statistical Mechanics* (Benjamin, New York, 1962).

[23] S. Hermanns, N. Schlünzen, and M. Bonitz, Phys. Rev. B **90**, 125111 (2014).

[24] The T-matrix approximation shows very good agreement with exact diagonalization results where available (small N) [23, 25, 26]. Since it is a low-density approximation, small systematic errors are expected around half-filling.

[25] M. Puig von Friesen, C. Verdozzi and C.-O. Almbladh, Phys. Rev. Lett. **103**, 176404 (2009).

[26] M. Puig von Friesen, C. Verdozzi and C.-O. Almbladh, Phys. Rev. B **82**, 155108 (2010).

[27] D. Semkat, D. Kremp, and M. Bonitz, J. Math. Phys. **41**, 7458 (2000).

[28] U. Schneider, Ph.D. Dissertation, University Mainz, 2010.

[29] M. Bonitz, D. Kremp, D. C. Scott, R. Binder, W. D. Kraeft, and H. S. Köhler, J. Phys. Condens. Matter **8**, 6057 (1996).

[30] R. Binder, H. S. Köhler, M. Bonitz, and N. Kwong, Phys. Rev. B **55**, 5110 (1997).

[31] N. H. Kwong, M. Bonitz, R. Binder and S. Köhler, Phys. Stat. Sol. **206**, 197 (1998).

[32] N. H. Kwong, and M. Bonitz, Phys. Rev. Lett. **84**, 1768 (2000),

[33] N. E. Dahlen, and R. van Leeuwen, Phys. Rev. Lett. **98**, 153004 (2007).

[34] K. Balzer, S. Bauch, and M. Bonitz, Phys. Rev. A **81**, 022510 (2010).

[35] K. Balzer, S. Bauch, and M. Bonitz, Phys. Rev. A **82**, 033427 (2010).

[36] M. Bonitz, S. Hermanns, and N. Schlünzen, Contrib. Plasma Phys. **55**, 152 (2015).

[37] G. Stefanucci and R. van Leeuwen, *Nonequilibrium Many-Body Theory of Quantum Systems* (Cambridge University Press, Cambridge UK, 2031).

[38] M. Puig von Friesen, C. Verdozzi and C.-O. Almbladh, Europ. Phys. Lett. **95**, 27005 (2011).

[39] D. Larsson and H. Johannesson, Phys. Rev. Lett. **95**, 196406 (2005).

[40] M. Bonitz, and D. Kremp, Phys. Lett. A. **212**, 83 (1996); M. Bonitz, *ibid*. **221**, 85 (1996).

[41] F. Heidrich-Meisner, S. R. Manmana, M. Rigol, A. Muramatsu, A. E. Feiguin, and E. Dagotto, Phys. Rev. A **80**, 041603 (2009).

[42] L. Vidmar, S. Langer, I. P. McCulloch, U. Schneider, U. Schollwöck, and F. Heidrich-Meisner, Phys. Rev. B **88**, 235117 (2013).

[43] S. Langer, M. J. A. Schuetz, I. P. McCulloch, U. Schollwöck, and F. Heidrich-Meisner, Phys. Rev. A **85**, 043618 (2012).

[44] For more details, see N. Schlünzen, and M. Bonitz, Contrib. Plasma Phys. **56** (to be published in 2016).

4.3 Ion Stopping in Hexagonal Lattices

The mechanism of ion stopping is a fundamental concept in physics and has important applications in such diverse fields as medicine [292–294], astrophysics [295–297], astro-biology[4] [298–300], warm dense matter [301–304], and in laboratory research [40, 244, 301, 305]. In particular, the impact of energetic ions on solid surfaces (see, e.g., Refs. [38, 306–315]) is of high relevance for modern applications including magnetic fusion as well as inertial confinement fusion [40, 316], and ion-sputtering experiments [40]. Moreover, ion stopping is generally at the heart of plasma–solid-interface scenarios (see, e.g., Ref. [246]). An important characteristic describing ion-stopping processes is the energy-loss function, or *stopping power*, of the incident charged particles. Measuring the stopping power is a valuable diagnostic tool to investigate the electronic structure of materials [244]. A particularly interesting target material with a unique ion-radiation response is the acclaimed carbon allotrope graphene [157]. It has a number of intriguing and exotic properties that follow from its two-dimensional, hexagonal configuration [157, 163–166, 317]. For this reason, graphene-based structures are on the verge of revolutionizing nanoelectronics permanently [186–188] (see also Sec. 5.1). While in planar graphene[5] electronic correlation effects are only of minor importance, they significantly shape the physics of finite graphene fragments due to the induced quantum confinement. Therefore, graphene clusters provide a unique opportunity to study the nontrivial interplay of nonequilibrium and correlations. In the context of ion-impact excitations, however, previous first-principle studies of graphene fragments [38, 310, 311] involved adiabatic approximations. This contradicts the true nature of the complex nonequilibrium state that arises from the redistribution of the correlated mobile electrons due to the rapidly evolving ionic field. To fully understand the electronic response to ionic radiation and its impact on the stopping power, a highly accurate description of nonequilibrium correlations is therefore indispensable.

This demanding challenge can be met by using the NEGF technique, which allows one to systematically describe electronic correlations via the choice of the selfenergy (cf. Sec. 2.1). Therefore, the author (in close collaboration with Karsten Balzer and others) focused on the description of ion stopping in finite hexagonal lattices via NEGF and further complementing quantum-dynamics tools. The results of these efforts have been published in the three following papers,[6,7,8] Refs. [214], [41] and [215], as well as in the topical review [207] that is discussed and included in Sec. 2.2. Within these publications, two important key observations are made:

---

[4]The interaction of solar-wind ions with ice surfaces in space is believed to trigger the evolution of certain prebiotic organic materials [298–300].

[5]For planar graphene, the exposition to ion radiation has been studied both experimentally and in theory [39, 318–320].

[6]K. Balzer, N. Schlünzen, and M. Bonitz, Phys. Rev. B, **94**, 245118 (2016). Copyright by the American Physical Society. Reproduced with permission.

[7]K. Balzer, M. Rodriguez Rasmussen, N. Schlünzen, J.-P. Joost, and M. Bonitz, Phys. Rev. Lett., **121**, 267602 (2018). Copyright by the American Physical Society. Reproduced with permission.

[8]N. Schlünzen, K. Balzer, M. Bonitz, L. Deuchler, and E. Pehlke, Contrib. Plasma Phys., **59**, e201800184 (2019). Copyright Wiley-VCH Verlag GmbH & Co. KGaA. Reproduced with permission.

- It is demonstrated that electronic correlations in finite graphene have important consequences for the stopping power of the incident ion (Refs. [214], [215] and [207]).

- It is proposed that the excitation by ion impact constitutes an efficient mechanism to induce the formation of doublons—bound pairs of correlated electrons with opposite spin—in graphene fragments (Refs. [41], [215] and [207]).

In Ref. [214], the effect of electronic correlations on the stopping power of fully ionized hydrogen and helium atoms passing through finite segments of hexagonal lattices is investigated. To this aim, time-dependent simulations have been performed with a combined Ehrenfest–NEGF approach, i.e., the projectiles are treated classically with Newton's equations for the Coulomb interaction, whereas quantum-many-body effects are considered between the lattice electrons via a Hubbard Hamiltonian. Within this description, for sufficiently fast ions, the stopping power is bounded by two opposing effects: if the time scales of the system's components differ drastically, the lattice electrons either adiabatically follow the potential landscape caused by the atom in a completely symmetric and reversible process, or the effective interaction time becomes too small to cause any energy transfer at all. This leads to a typical bell shape for the stopping power with a maximum at a certain velocity. The paper compares different perturbation degrees for the correlation treatment, ranging from the (mean-field) Hartree approximation, and the local second-order selfenergy (both provided by Karsten Balzer) to full two-time selfenergies in second-order, third-order and T-matrix approximation (cf. Sec. 2.1), as well as the application of the GKBA (all provided by the author). From mean-field calculations, one can easily deduce that strong interactions in the lattice have the effect of reducing the maximum in the stopping-power curve. This qualitatively correct trend is due to the decreased mobility of collective electrons. The analysis of Ref. [214] shows that this effect becomes even more pronounced for more accurate treatments of correlations. Furthermore, it is found that in a certain low-energy range the energy loss is slightly increased compared to the mean-field prediction, which goes together with an altered scaling behavior in this regime. Another connection that is explored in Ref. [214] concerns the influence of finite temperatures on the stopping power. Here, it is demonstrated that increased thermal fluctuations in the electronic system hamper a coherent response and, thus, cause an overall reduced energy loss for the projectile. The simulations also indicate that correlations can gain relative importance for larger temperatures, but the particular reason for this effects remains an interesting topic for future research. There are certain classes of processes that cannot be accounted for within the used theoretical model in Ref. [214], such as lattice phonons, charge transfer between both components and electronic excitations of the energetic atom. Recent attempts to consistently include charge transfer into NEGF calculations can be found in Refs. [207, 246, 247]. Though it is clear that such processes become negligible for sufficiently fast ions, it is important to examine the validity of the considered approximations. To this end, the final section of Ref. [214] contains benchmark calculations for protons and alpha particles penetrating through single-layer graphene. With some model adjustments to ensure the applicability to real graphene, it is possible to achieve convincing agreement with the experimentally supported SRIM results [315].

Having found that electronic correlations in the lattice can have a profound impact

on the slowing down of the incident projectile, it was reasonable to further investigate the characteristics of the emerging many-body states. As elaborated in, e.g., Secs. 2.1.1 and 4.2, the decreased mobility in strongly interacting Hubbard systems goes together with the formation of correlated doublons. Since the double occupation is expected to be minimal in the (half-filled) groundstate of electronic lattices, this suggests that the exposition of energetic ions could favor the emergence of doublons. Upon closer analysis, this turned out to be well quantifiable not only during the impact of the projectile; the double occupation remains at an increased level even after the field of the ion has vanished—corresponding to the existence of stable doublons. This came as a surprise since comparable observations of doublon manifestation processes involved mainly spatially delocalized excitation scenarios [321–328]. Ref. [41] demonstrates and discusses this novel doublon-formation protocol on several levels. An exactly solvable twelve-site Hubbard cluster that represents a simplified honeycomb flake is used to show the substantial growth in the double occupation when exposed to fast protons and alpha particles. The effect is then quantified in terms of the projectile's velocity. Interestingly, the local densities of the lattice quickly go back to a homogeneous distribution after the impact. This implies that the system is driven into a so called "prethermalized" [329, 330] doublon state. To shine more light on the underlying mechanism, a carefully selected minimal two-site model is analyzed regarding its energy levels during the excitation. With this, the doublon formation is successfully explained by a Landau–Zener transition [331, 332]—a driven transition at the point of an avoided energy crossing [328, 333]—between a single-particle state and a doublon state. The remainder of Ref. [41] is dedicated to the question how the described excitation protocol can be used to generate stable doublons in larger 1D and 2D systems. Obviously, the effect of a single energetic ion becomes progressively insignificant when the system size is gradually increased. Multiple sequential excitations, however, allow for a successively increased average double occupation up to $d_{\mathrm{av}} = 0.25$, as is demonstrated for Hubbard chains and hexagonal lattices up to $N_{\mathrm{b}} = 54$. These calculations only became possible with an efficient NEGF description involving the GKBA and the second-order Born selfenergy and its massively parallelized implementation, which has been provided by the author. It should be noted that the subsequently developed G1–G2 scheme (see Sec. 3.1) is able to push the limits even further. This will be demonstrated in an upcoming publication [256].

As elaborated in Sec. 2.1, the NEGF method gives access to a variety of observables including detailed information about the individual energy contributions. In the context of ion stopping, this is further explored in Ref. [215] where the results of the previous two papers are complemented and an additional perspective with TDDFT calculations is added. The TDDFT part has been conceptualized by Lukas Deuchler and Eckhard Pehlke. Based on earlier analyses of different stopping scenarios [309, 310, 334–338] they applied a TDDFT description to the impact of neutral and ionized hydrogen atoms on an Al(111) surface which captures charge transfer and energy dissipation. Additional investigations following this ansatz can be found in Ref. [339]. The NEGF part of Ref. [215] again focuses on proton stopping in finite honeycomb clusters. Ehrenfest–Green-functions calculations are used to give a detailed breakdown of several energy contributions and the average double occupation. The extensive parameter scan that was provided by the author allows for a fully time-dependence analysis covering a wide range of initial projectile velocities.

Comparable NEGF simulations with a local selfenergy (provided by Karsten Balzer) are used to take a closer look at the occurrences of correlation-enhanced stopping power for impact energies below 1 keV, that were already mentioned in the description of Ref. [214]. Finally, Ref. [215] discusses the benefits and disadvantages of the considered TDDFT and NEGF approaches on ion stopping and explores how both methods can be combined to refine the predictive capability.

Stopping dynamics of ions passing through correlated honeycomb clusters

Karsten Balzer,[1,*] Niclas Schlünzen,[2] and Michael Bonitz[2]

[1]*Rechenzentrum, Christian-Albrechts-Universität zu Kiel, Ludewig-Meyn-Strasse 4, 24118 Kiel, Germany*
[2]*Institut für Theoretische Physik und Astrophysik, Christian-Albrechts-Universität zu Kiel, Leibnizstrasse 15, 24098 Kiel, Germany*

A combined nonequilibrium Green functions–Ehrenfest dynamics approach is developed that allows for a time-dependent study of the energy loss of a charged particle penetrating a strongly correlated system at zero and finite temperatures. Numerical results are presented for finite inhomogeneous two-dimensional Fermi-Hubbard models, where the many-electron dynamics in the target are treated fully quantum mechanically and the motion of the projectile is treated classically. The simulations are based on the solution of the two-time Dyson (Keldysh-Kadanoff-Baym) equations using the second-order Born, third-order, and T-matrix approximations of the self-energy. As application, we consider protons and helium nuclei with a kinetic energy between 1 and 500 keV/u passing through planar fragments of the two-dimensional honeycomb lattice and, in particular, examine the influence of electron-electron correlations on the energy exchange between projectile and electron system. We investigate the time dependence of the projectile's kinetic energy (stopping power), the electron density, the double occupancy, and the photoemission spectrum. Finally, we show that, for a suitable choice of the Hubbard model parameters, the results for the stopping power are in fair agreement with *ab initio* simulations for particle irradiation of single-layer graphene.

I. INTRODUCTION

The interaction of particles with matter is a fundamental aspect of physics and allows one to measure their properties in colliding-beam or beam-target experiments. Conversely, the irradiation of matter by particles can be used also as a diagnostic tool to probe the static and dynamic properties of matter itself. In soft collisions of heavy charged particles, such as ions, with a solid, typically the electrostatic force, i.e., the Coulomb interaction, has the largest impact, leading to excitation and ionization of electrons in the target material and thus to the loss of kinetic energy of the projectile [1]. For nonrelativistic projectile velocities of the order of or larger than the Fermi velocity ($\sim 10^6$ m/s in metals), theoretical approaches based on scattering theory [2] or on the response functions of the homogeneous electron gas [3], can give a quantitative description of the energy transferred during the collision process but neglect the precise atomic composition of the target.

Regarding first-principles modeling in the same velocity regime, recent theoretical progress is due to time-dependent density functional theory (TDDFT), which has been applied to describe the slowing down of charged particles in a variety of solids, including metals [4–6], semimetals [7,8] and clusters [9,10], narrow-band-gap semiconductors [11], and insulators [12,13]. Taking into account primarily the excitation of valence electrons, these simulations yield satisfactory results for the electronic stopping power (the transfer of energy to the electronic degrees of freedom per unit length traveled by the projectile) and work for a wide range of impact energies. On the other hand, one can quite generally determine the stopping power of energetic ions in matter using the SRIM code [14], which uses the binary collision approximation in combination with an averaging over a large range of experimental situations

to provide energy loss and range tables for many materials and gaseous targets. In principle, TDDFT and SRIM can include effects of electron-electron correlations on the stopping behavior, either by using exchange-correlation potentials beyond the local density approximation in TDDFT, e.g., [15,16], or by including static exchange and correlation contributions to the interaction energy between overlapping electron shells in SRIM. Despite these capabilities, both methods have, however, difficulties to approach *strong* Coulomb correlations, which are crucial, e.g., in transition-metal oxides [17] or specific organic materials [18]. In addition, we note that SRIM does account neither for the exact crystal structure of the material nor dynamic (i.e., time-dependent) changes in the target during the collision process, which limits its applicability.

It is, therefore, interesting to consider an alternative approach to the stopping power that does not have these limitations: nonequilibrium Green functions (NEGF) [19,20]. This method allows one to systematically include electron-electron correlations via a time-dependent many-body self-energy, and it has recently successfully been applied to strongly correlated lattice systems as well [21]. Particular advantages of the NEGF approach are that it is not limited to either weak or strong coupling and that it is particularly well suited to study finite-sized clusters and spatially inhomogeneous systems on a self-consistent footing. While the NEGF approach is computationally very demanding, in recent years efficient numerical schemes have been developed to solve the underlying Keldysh-Kadanoff-Baym equations (KBE) [22–29].

Here, we extend the NEGF approach by including the interaction with a classical projectile using an Ehrenfest-type approach that is well established in TDDFT simulations. Our goal is to develop a full time-dependent and space-resolved description, which is necessary as the projectile induces local time-dependent changes to the electron density and to the local band structure. This allows us, in particular, to consider finite clusters of size L, which are of substantial current interest. Furthermore, we study the size dependence of the response

---

*balzer@rz.uni-kiel.de

to the projectile. At the same time, the thermodynamic limit of the stopping power (cluster size L approaching infinity) is more difficult and expansive to obtain, as it requires an extrapolation of results for different L. Nevertheless, we obtain good agreement with existing results for macroscopic systems.

To implement this approach, we choose, as a first application, the energy deposition of simple ions (protons and alpha particles), where there is no interatomic electron dynamics, in planar two-dimensional honeycomb clusters, in which the electron dynamics is well described in terms of a Fermi-Hubbard model. To investigate the importance of electronic correlation effects, we vary the coupling strength from small to moderate values (up to $U/J = 4$) and test various self-energy approximations, such as the second Born and the much more involved T-matrix approximation. The results are compared to mean-field (Hartree) results, which are provided by the same NEGF program.

The paper is organized as follows. In Sec. II, we define the model Hamiltonian, discuss the interaction potential between projectile and target, and describe the self-consistent computational scheme, which allows us to calculate the correlated electron dynamics on the honeycomb clusters. In Sec. III, we review the equilibrium properties of the target system, which are sensitive to correlations, and then present the main results for the stopping dynamics in Sec. IV. Here, we primarily focus on the effect of electron-electron correlations on the energy transfer, analyze the time-dependent collision process for a wide range of projectile velocities, and consider different initial states and temperatures. In Sec. V, we finally discuss the application of the used model to graphene and conclude the paper with Sec. VI, outlining possible future work.

II. COMPUTATIONAL SETUP

A. Model

To study the stopping dynamics of a classical charged particle which passes through a (strongly) correlated system, we consider a finite lattice of electrons described by a single-band Fermi-Hubbard model and monitor the transfer of energy during the collision process. Taken as a whole, the lattice system is electrically neutral, i.e., the electronic charges are compensated by corresponding opposite charges located at the site coordinates $\mathbf{R}_i$. The general stopping mechanism is mediated by the bare Coulomb interaction between the projectile, the fixed background charges, and the target electrons which are initially in equilibrium. Throughout, we focus on positively charged ions as projectiles, which, when approaching the lattice, induce a confinement potential to the electrons and thus initiate a nonequilibrium electron dynamics. In turn, the ions (of mass m_p and charge $Z_\mathrm{p}e$) react to any charge redistribution on the lattice and change their position and kinetic energy accordingly.

As lattice systems, we choose circular honeycomb clusters, which are oriented in the xy plane and have a finite number of honeycombs, yielding in total L sites (see Fig. 1 for an illustration). We consider a half-filled system in the paramagnetic phase and, to generate realistic results, set the lattice spacing to $a_0 = 1.42$ Å, which corresponds to the carbon-carbon bond length in graphene [30]. Using a nearest-neighbor hopping J
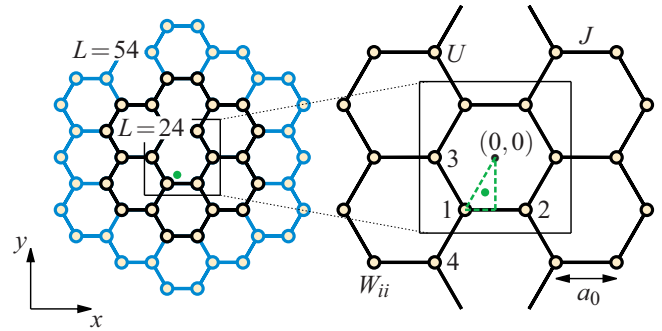
FIG. 1. Lattice structure of circular honeycomb clusters with $L = 24$ (black) and 54 sites (blue). The green point indicates the position where the projectile hits the lattice plain. For further reference, we label four sites in the center of the clusters, where we will monitor the time-dependent electron density in Sec. IV B. Furthermore, a_0 denotes the lattice spacing, J (U) is the nearest-neighbor hopping (the onsite interaction), and W_{ii} is the local energy defined in Eq. (2).

and an onsite Coulomb repulsion U, the Hamiltonian for the lattice electrons is then given by

$$H_\mathrm{e}(t) = -J \sum_{\langle i,j \rangle, \sigma} c_{i\sigma}^\dagger c_{j\sigma} + U \sum_i \left(n_{i\uparrow} - \frac{1}{2} \right) \left(n_{i\downarrow} - \frac{1}{2} \right) + \sum_{ij,\sigma} W_{ij}(t) c_{i\sigma}^\dagger c_{j\sigma}, \tag{1}$$

where the operator $c_{i\sigma}^\dagger$ ($c_{i\sigma}$) creates (annihilates) an electron with spin σ on site i, $n_{i\sigma} = c_{i\sigma}^\dagger c_{i\sigma}$ denotes the electron density, and W_{ij} are the matrix elements of the confinement potential induced by the projectile. In Sec. IV, we imply localized electronic wave functions $\varphi_i(\mathbf{r}) \propto \delta(\mathbf{r} - \mathbf{R}_i)$, for which we can resort to the diagonal components of this potential:

$$W_{ii}(t) = -\frac{e^2}{4\pi \epsilon_0} \frac{Z_\mathrm{p}}{|\mathbf{r}_\mathrm{p}(t) - \mathbf{R}_i|}, \tag{2}$$

where $\mathbf{r}_\mathrm{p}(t)$ denotes the time-dependent position of the projectile, $-e$ is the electron charge, and ϵ_0 the vacuum permittivity. Moreover, in Sec. V, we improve this model by including also terms $W_{ij}(t)$ with $|i - j| = 1$, which locally renormalize the nearest-neighbor hopping [cf. Eq. (14)].

For convenience, we measure J and U in electron volts, define U/J as the interaction strength for the electrons, and use $t_0 = \hbar/J$ as the unit of time. Unless otherwise stated, we use $J = 2.8$ eV (which is typical for graphene [31]) to fix the time scale.

B. Computational method

To compute the classical motion of the projectile with an initial velocity $d\mathbf{r}_\mathrm{p}/dt = (0,0,v_z)$, we solve Newton's equation with the total potential

$$V(\mathbf{r}_\mathrm{p}, t) = \frac{e^2}{4\pi \epsilon_0} \sum_i \frac{Z_\mathrm{p} Z_i(t)}{|\mathbf{r}_\mathrm{p}(t) - \mathbf{R}_i|} \tag{3}$$

created by all lattice charges [here, $Z_i(t) = 1 - \sum_\sigma \langle n_{i\sigma} \rangle(t)$ denotes the net charge on the lattice site i]. For the solution we

use a three-dimensional velocity-Verlet algorithm. Motivated by TDDFT calculations [7], we set the initial position of the incident ion to $\mathbf{r}_\mathrm{p} = (-\frac{1}{6}a_0, -\frac{\sqrt{3}}{3}a_0, -z)$ (see the centroid point of the green dashed triangle in Fig. 1). These coordinates have been found to give similar stopping results for the highly symmetric honeycomb lattice compared to calculations, where one averages over many different collision sites. This allows us to avoid averaging over many trajectories and to directly compare to previous TDDFT results (Sec. V). Furthermore, the initial z position is chosen such that the measured energy transfer becomes independent of the initial conditions (typically $z \gtrsim 10a_0$).

To compute the correlated time evolution of the lattice electrons, we use a quantum statistical approach based on the one-particle nonequilibrium Green function (NEGF)

$$G_{ij\sigma}(t,t') = -\frac{\mathrm{i}}{\hbar} \langle T_{\mathcal{C}} c_{i\sigma}(t) c_{j\sigma}^\dagger(t') \rangle, \qquad (4)$$

which is defined on the Keldysh time contour $\mathcal{C}$ [32] and can be interpreted as a two-time generalization of the one-particle density matrix

$$\langle \rho_{ij\sigma} \rangle(t) = \langle c_{i\sigma}^\dagger c_{j\sigma} \rangle = -\mathrm{i}\hbar\, G_{ji\sigma}(t,t^+). \qquad (5)$$

On the contour, $T_{\mathcal{C}}$ furthermore denotes the time-ordering operator, $\langle T_{\mathcal{C}} \ldots \rangle = \mathrm{tr}[T_{\mathcal{C}} \exp(S) \ldots]/\mathrm{tr}[T_{\mathcal{C}} \exp(S)]$ with $S = -\mathrm{i}/\hbar \int_{\mathcal{C}} ds\, H_\mathrm{e}(s)$ defines the ensemble average, and the notation t^+ means that the time t^+ is infinitesimally larger along $\mathcal{C}$ than t. The equations of motion of the greater and less components of the NEGF (4),

$$
\begin{aligned}
G_{ij\sigma}^{>}(t,t') &= -\frac{\mathrm{i}}{\hbar} \langle c_{i\sigma}(t) c_{j\sigma}^\dagger(t') \rangle, \\
G_{ij\sigma}^{<}(t,t') &= \frac{\mathrm{i}}{\hbar} \langle c_{j\sigma}^\dagger(t') c_{i\sigma}(t) \rangle,
\end{aligned}
\qquad (6)
$$

follow from the time evolution of the creation and annihilation operators in the Heisenberg representation and are known as the two-time Keldysh-Kadanoff-Baym equation (KBE) [19,20,23]:

$$\sum_k [\mathrm{i}\hbar\, \partial_t \delta_{ik} - h_{ik\sigma}(t)] G_{kj\sigma}^{\gtrless}(t,t')$$
$$= \delta_{\mathcal{C}}(t,t')\delta_{ij} + \sum_k \left\{ \int_{\mathcal{C}} ds\, \Sigma_{ik\sigma}(t,s) G_{kj\sigma}(s,t') \right\}^{\gtrless}. \qquad (7)$$

Here, $\delta_{\mathcal{C}}$ denotes the delta function on the contour, and $h_{ij\sigma}(t)$ is the time-dependent effective one-particle Hamiltonian, which explicitly includes the Hartree contribution to the electron-electron interaction, i.e.,

$$h_{ij\sigma}(t) = \underbrace{-J\delta_{\langle i,j \rangle}}_{=J_{ij}} + \left\{ W_{ii}(t) + U\big[\langle n_{i\bar\sigma} \rangle(t) - \tfrac{1}{2}\big] \right\}\delta_{ij}, \qquad (8)$$

with the density $\langle n_{i\sigma} \rangle(t) = -\mathrm{i}\hbar G_{ii\sigma}^{<}(t,t)$. On the right-hand side of Eq. (7), the contour integral defines the memory kernel of the KBE, in which $\Sigma_{ij\sigma}(t,t')$ denotes the correlation part of the self-energy [i.e., the mean-field part is excluded as it is contained in Eq. (8)]. Systematic expressions for the self-energy can be constructed by many-body perturbation theory, e.g., using diagram techniques [20,33]. Below, we treat the

correlation self-energy Σ in different approximations, which conserve particle number, momentum, and energy.

C. Many-body approximations

We consider the correlation self-energy Σ in the following approximations:

(1) As the simplest self-energy beyond the (Hartree) mean-field level, we consider the second-order Born approximation (2B),

$$\Sigma_{ij\sigma}^{\mathrm{2B},\gtrless}(t,t') = \hbar^2 U^2 G_{ji\sigma}^{\gtrless}(t,t') G_{ji\bar\sigma}^{\gtrless}(t,t') G_{ij\bar\sigma}^{\lessgtr}(t',t), \qquad (9)$$

which includes all irreducible diagrams of second order in the interaction U. Aside from the full evaluation of this self-energy, we will consider, in addition, the *local* (in space) second Born approximation, which includes only the diagonal components $\Sigma_{ii\sigma}^{\mathrm{2B}}$ of the self-energy (9). This approximation substantially reduces the numerical complexity, as it allows to solve the KBE via particularly efficient schemes [34–36]. We note that the 2B approximation is a perturbation theory result and, therefore, becomes less accurate when U increases.

(2) We consider the particle-particle T-matrix (TM) self-energy, which sums up the whole Born series including diagrams of all orders in U and is given by [37]

$$\Sigma_{ij\sigma}^{\mathrm{TM}}(t,t') = \mathrm{i}\hbar\, T_{ij}(t,t') G_{ji\bar\sigma}(t',t), \qquad (10)$$

with the effective interaction

$$
\begin{aligned}
T_{ij}(t,t') = {}&-\mathrm{i}\hbar\, U^2 G_{ij\sigma}(t,t') G_{ij\bar\sigma}(t,t') \\
&+ \mathrm{i}\hbar\, U \sum_k \int_{\mathcal{C}} ds\, G_{ik\sigma}(t,s) G_{ik\bar\sigma}(t,s) T_{kj}(s,t').
\end{aligned}
$$

The T-matrix approximation has been found to perform very well in the regime of small (or large) density, i.e., away from half-filling [33,37,38]. If the number of electrons and holes become comparable, however, particle-hole interaction processes gain in importance, which are not captured by the particle-particle T-matrix.

(3) In order to accurately treat strongly correlated systems, we also consider the third-order approximation [38], which exactly takes into account all self-energy contributions up to $\mathcal{O}(U^3)$. This approximation has been found advantageous around half-filling, in particular, for small to moderate interaction strengths [38].

(4) We also consider the generalized Kadanoff-Baym ansatz (GKBA) of Lipavský *et al.* [39], which has recently attracted growing attention [28,29,33,40]. By reconstructing the two-time Green function $G_{ij\sigma}(t,t')$ from its time-diagonal value, the GKBA provides a way to substantially reduce the numerical effort of the computation of the NEGF, while still accurately accounting for particle number and energy conservation and correlations. Here, we will apply the GKBA to the second-order Born self-energy using mean-field type propagators (HF-GKBA) (for details see Refs. [29,33]). This allows us to increase the simulation duration and extend the calculations to lower projectile energies (see Sec. IV D).

With these self-energies, the KBE (7) is solved together with its adjoint equation by a self-consistent time propagation scheme in the two-time plane, starting from a given initial-state Green function at $t,t' = 0$. For details on the numerical

solution of the two-time KBE including the above approximations, we refer the reader to Refs. [23,25,27,33]. To investigate the influence of the initial state of the many-electron system on the dynamics and the energy loss of the projectile, we consider two relevant cases. For the example of the system being initially in the ground state (we set $k_B T = \beta^{-1} = 0.01$ eV and note that the case of finite temperature is discussed separately in Sec. IV E), we consider the following:

(A) The stationary correlated equilibrium state, which is formed via a relaxation that starts in the Hartree ground state (see Sec. III for details). This is, of course, only an approximation to the true ground state but it substantially reduces the computation time.

(B) The fully correlated ground state. It is obtained via a time-dependent procedure (adiabatic switch-on of the interaction U) (see, e.g., Refs. [33,41] for details).

For the case of half-filling (chemical potential $\mu = 0$), the Hartree ground state of Hamiltonian (1) (with $W_{ij} \equiv 0$) is independent of U and is given by the density matrix

$$\langle \rho_{ij\sigma} \rangle(t=0) = -i\hbar\, G_{ji\sigma}^<(0,0)$$

$$= -i\hbar \sum_k v_{ki}^* v_{kj}\, f_\beta(\epsilon_k, \mu), \qquad (11)$$

where ϵ_k (v_k) are the eigenvalues (eigenvectors) of the hopping matrix $(\mathbf{J})_{ij} = J\delta_{\langle i,j \rangle}$, and $f_\beta(\epsilon, \mu) = 1/(e^{\beta(\epsilon-\mu)} + 1)$ is the Fermi-Dirac distribution.

III. LATTICE PROPERTIES PRIOR TO THE IMPACT

In this section, we solve the KBE (7) without the incident projectile and compute central equilibrium properties of the honeycomb clusters primarily in the local second Born approximation. First, we analyze the double occupations

$$\langle d_i \rangle = \langle n_{i\uparrow} n_{i\downarrow} \rangle = -\frac{i\hbar}{U} \sum_k \int_{\mathcal{C}} ds\, \Sigma_{ik\sigma}(t,s) G_{ki\sigma}(s,t^+) \quad (12)$$

on the lattice sites i, which contain important information about the correlations in the system.

In Fig. 2, we show results for the average double occupation $\langle d \rangle_{\mathrm{av}} = \frac{1}{L} \sum_i \langle n_{i\uparrow} n_{i\downarrow} \rangle$ on clusters of different size L, which is established over time, when the system is prepared in the Hartree ground state [Eq. (11), case (A)]. We find that the emerging double occupation is practically independent of the system size, which is even the case for larger values of the interaction strength. The value $\langle d \rangle_{\mathrm{av}}$ is, up to $U/J \lesssim 4$, in reasonable agreement with exact quantum Monte Carlo data (black triangles) for the extended honeycomb lattice [42]. The right panel of Fig. 2 gives details on the time dependence of the double occupation during this (fictitious) relaxation. Clearly, the sudden switch-on of the correlation part of the self-energy at $t = 0$ leads to an oscillatory transient response, after which the double occupation rapidly reaches a new (correlated) stationary value. The site densities ($\langle n_{i\sigma} \rangle = 0.5$) remain constant during this relaxation because we consider an undoped system with particle-hole symmetry. We note that this final state is a stationary correlated state, which slightly differs from the correlated ground state as it has a slightly larger total energy (due to correlation-induced heating [43,44]) (cf. the
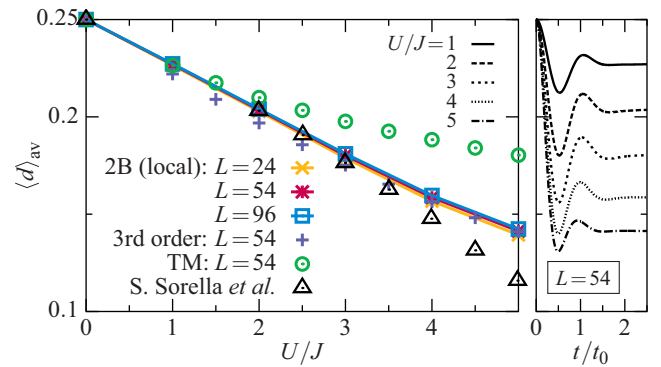
FIG. 2. Left panel: average double occupation $\langle d \rangle_{\mathrm{av}}$ on the honeycomb clusters with $L = 24$, 54, and 96 sites for different interaction strengths U/J in the local second Born, third-order, and T-matrix approximations, using the initial state (A). The black triangles correspond to exact data for the extended honeycomb lattice (taken from Ref. [42]). Right panel: time evolution of $\langle d \rangle_{\mathrm{av}}$ for the local second Born calculations starting from the Hartree ground state [Eq. (11)], for which $\langle d \rangle_{\mathrm{av}} = \langle d_i \rangle = \langle n_{i\uparrow} \rangle \langle n_{i\downarrow} \rangle = 0.25$.

spectral weight discussed below). Nevertheless, the excellent agreement with the reference data confirms the reliability of this procedure, which is computationally efficient as it requires comparatively few time steps.

Finally, the stationary values of the double occupations allow us to test the accuracy of the different approximations for the self-energy. The T-matrix result is accurate up to about $U/J = 1.5$ but for larger coupling starts to deviate from the reference. The third-order approximation and the local second Born result are very close to each other and work substantially better up to $U/J = 3.5$. Since the correlated states (A) and (B) are particle-hole symmetric, in an exact calculation, the third-order contributions to the self-energy would perfectly cancel each other [21,38,45]. Therefore, in the T-matrix approximation, the leading term beyond second order becomes unbalanced, which explains the poor performance in Fig. 2. For the same reason, both a full second Born calculation and a third-order simulation would be exact up to $\mathcal{O}(U^3)$, which also is the origin for the high accuracy of the local second Born results. These findings give us confidence to use the comparatively simple local second Born approximation for most simulations below [46].

Second, we study the photoemission spectrum, which is directly obtained from the less component $G_{ii\sigma}^<(t,t')$ of the nonequilibrium Green function (for details, see the Appendix). In Fig. 3, we present the photoemission signal $I_1(\omega)$ of the cluster with $L = 54$ sites recorded at the central site 1 (as labeled in Fig. 1). We show results for different values of U/J with a probe pulse arriving at some time after the transient regime (for the computational details and the specific probe pulse parameters, see Appendix A). In the case of half-filling, the Hartree approximation ($\Sigma = 0$) yields a photoemission signal with a few pronounced peaks which are independent of U/J. On the other hand, correlations lead to an essential broadening of the whole spectrum and, in particular, to single-particle energies beyond the cutoff energy $\omega_{\mathrm{cutoff}} = -3J$ of the
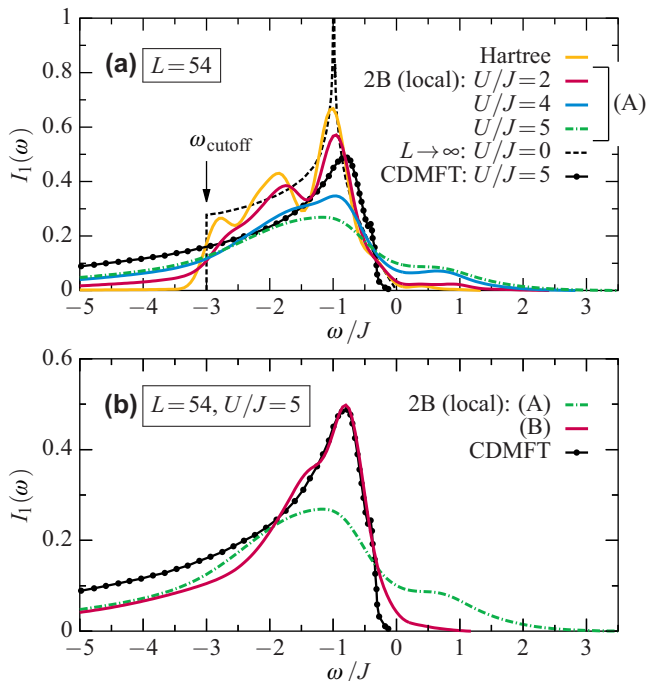
FIG. 3. (a) Photoemission signal $I_1(\omega)$ for the honeycomb cluster with $L = 54$ sites in Hartree approximation (U independent) and in local second Born approximation for different U/J, using the initial state (A) of Sec. II C. Black dashed line: spectrum of the extended lattice at $U/J = 0$ (e.g., Refs. [48,49]), black solid line: spectrum for $U/J = 5$, as obtained from a cluster-DMFT calculation [from Ref. [47] and also shown in panel (b)]. (b) Comparison of the photoemission signal $I_1(\omega)$ at $U/J = 5$ for local second Born calculations with different initial states. Green line: spectrum [as in panel (a)] for the initial state (A). Red line: correlated ground state (B).

noninteracting system (see the black dashed line and compare also with Fig. 11 in Appendix A). Moreover, this broadening is accompanied by a shift of the main peak (around $\omega = -J$) towards the Fermi energy, $\omega_F = 0$, as a function of the interaction strength. For $U/J = 5$ (green dashed-dotted line), we finally observe that the photoemission spectrum becomes rather flat due to enhanced occupations of single-particle energies above the Fermi level. These occupations originate from the fact that the equilibrated state is not the ground state of the system. On the contrary, if we first prepare the correlated ground state (B) (recall Sec. II C) and then propagate the nonequilibrium Green functions in time, we obtain a photoemission spectrum as shown by the red solid line in Fig. 3(b). If we compare it, for example, to a cluster-DMFT (CDMFT) study [47] for the extended honeycomb lattice (black solid line), we find a very good agreement. However, the finite spectral resolution introduced by the probe pulse does not allow us to recover the emergence of a small energy gap [48], which exists at finite onsite interactions U/J.

In summary, we conclude from Figs. 2 and 3 that already the local second Born approximation is able to capture important electron correlation properties of the honeycomb clusters. As the considered equilibrium properties are adequately described up to $U/J \approx 3 \ldots 4$, we will likewise analyze the stopping dynamics in Sec. IV up to this regime of interaction strengths.

IV. STOPPING DYNAMICS

A. Energy loss of the projectile

We now simulate collisions of protons ($Z_p = 1$) with honeycomb clusters of size $L = 24$ and 54. To characterize the stopping dynamics, we consider different impact kinetic energies $E_{\mathrm{kin}} = \frac{1}{2}m_p \dot{\mathbf{r}}_p^2(t = 0)$, ranging from below 1 keV to about 0.5 MeV, and measure the energy loss S_e, defined as the change of the projectile's kinetic energy after passing through the lattice:

$$S_e = E_{\mathrm{kin}}(t = 0) - E_{\mathrm{kin}}(t \to \infty). \qquad (13)$$

As function of $E_{\mathrm{kin}}(t = 0)$, this quantity yields the energy loss spectrum, which is similar to the stopping power spectrum (spectrum of dissipated power per length) for the case of homogeneous media. Below, we specify the kinetic energy of the proton in units of keV/u, where u denotes the unified atomic mass unit.

We begin with the analysis of S_e for the smaller cluster [see Fig. 4(a)]. In Hartree approximation (black lines), we find a pronounced maximum of the energy loss in the regime of considered energies, which is the behavior known from the stopping power of nonrelativistic ions (we note, however, that the position of the maximum is typically at larger energies, compare with Sec. V). When U is increased, the peak height decreases and, at the same time, the peak slightly shifts towards larger proton energies. At large impact energies, the curves for different interaction strength approach each other, leading to a rather generic scaling of the energy loss as $\propto v_z^{-a} \ln(b v_z^2)$ (with fit parameters $a, b > 0$). Thus, the high-energy tail is consistent with predictions from the nonrelativistic Bethe formula [1]. On the other hand, for low energies, the change of the energy loss is closer to $\sim v_z$.

Next, we examine the influence of electron-electron correlations [cf. the red curves in Fig. 4(a)], which represent local second Born calculations for the initial state (A) of Sec. II C, where the lattice system has equilibrated before the impact of the proton. For small interactions $U/J \lesssim 2$, we find that corrections to the Hartree approximation are rather small. On the contrary, for $U/J = 4$, we observe clear deviations from the mean-field picture, with a decrease of S_e over a large energy window and a slight increase around $E_{\mathrm{kin}} \approx 1$ keV/u.

In Fig. 4(b), we present the same analysis for the larger honeycomb cluster with $L = 54$ sites, including results for various approximations of the self-energy. While S_e becomes generally larger compared to the smaller cluster, we notice that correlations have the same effect of reducing the energy loss for proton energies of $E_{\mathrm{kin}} \gtrsim 5$ keV/u, as was observed for $L = 24$. At the same time, the low-energy tail behaves differently: here we find a scaling $\propto \ln(v_z)$. Moreover, we observe that all considered self-energies lead to very similar stopping results. In particular, there is very good agreement between the local and full second-order Born approximation, which indicates that here it is sufficient to treat correlations locally. We emphasize again that a nonlocal self-energy (with $\Sigma_{ij} \neq 0$) or a more complex self-energy (including higher-order diagrams) generally brings about a drastic increase of the computation time, particularly on a large time grid, which is required to study the impact of slow projectiles. For this reason,
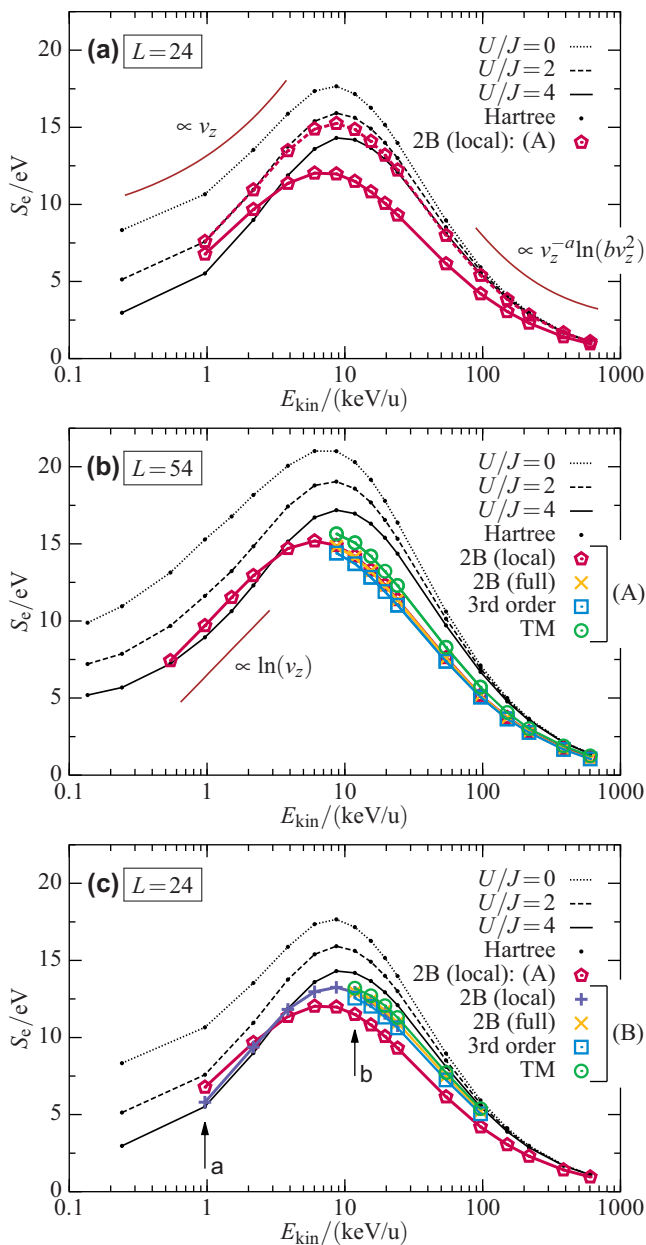
FIG. 4. Energy loss S_e for protons passing through honeycomb clusters of size $L = 24$ [panels (a) and (c)] and $L = 54$ [panel (b)]. In all panels, the value of the onsite interaction U/J is encoded in the line style, and the black lines indicate the results of the Hartree approximation. In panel (a), the red curves show the energy loss in the local second Born approximation with initial state (A). In panel (b), we present the same analysis for the larger cluster, including results of the full second Born (yellow), the third-order (blue), and the T-matrix approximation (green). Panel (c) shows the influence of initial correlations, comparing the second Born results of panel (a) to local and full second Born, third-order, as well as T-matrix calculations for the initial state (B). The arrows in panel (c) indicate the two situations analyzed in more detail in Fig. 5.

we show results beyond the local second Born approximation in Fig. 4(b) only for correspondingly large proton energies.

Standard stopping power calculations of a charged particle usually consider the target material in the ground state before

the collision. This is, however, not the case for our simulations with the initial condition (A) and self-energies beyond mean field. To quantify the effect of this systematic inconsistency, we repeat some of the simulations with the initial state (B) [see Fig. 4(c) for $L = 24$ and $U/J = 4$]. As a result, we observe that the form of the correlated initial state has a non-negligible influence on the energy loss of the projectile. In fact, we find that the self-consistent correlated ground state [case (B)] yields energy losses which are overall closer to those of the Hartree approximation. Nevertheless, there remain significant differences between correlated and mean-field calculations, most importantly around the maximum of the curves.

B. Time-dependent density response of the electron system

To gain insight into the effect of correlations on S_e and the physical mechanisms, we now analyze the response of the lattice electrons to the approaching projectile for a fixed value of the interaction strength $U/J = 4$. The general scenario is as follows. During the early stage of the dynamics, the electrons (initially distributed uniformly over the cluster with $\langle n_{i\sigma} \rangle = 0.5$) start to accumulate close to the impact point and, thus, create a negative net space charge, which attracts and accelerates the proton towards the cluster. After passing through the lattice plane, the proton then loses kinetic energy, depending on the nonadiabatic response of the electron density. For two different proton energies [indicated by arrows labeled a and b in Fig. 4(c)], the precise dynamics is shown in Fig. 5. There, we compare the Hartree approximation to the local second Born approximation for both considered initial states (A) and (B).

The difference in the time scale on which the observables change during the collision process is evident: While at a kinetic energy around 1 keV/u, the electron density and the double occupation in the center of the honeycomb cluster change on a time scale of a few inverse hopping times, $t_0 = \hbar/J$, they change on a time scale comparable to t_0 for the much faster proton ($\sim$10 keV/u). This difference has immediate consequences for the energy transfer to the lattice: From Fig. 5(b) (fast proton), we find that the exchange of energy between projectile and target occurs mainly during the stage of electron accumulation. Together with a retarded response of the electron density in the second Born approximation [dotted and solid lines in panel (b)], this translates into a faster proton (of a few eV) after the collision, as compared to the mean-field calculation (dashed line). On the contrary, for the slow proton, the energy loss is defined by both the buildup *and* the removal stage of the charge-induced confinement potential. For this reason it, is not *a priori* obvious how S_e is altered by correlations. This is also confirmed by the difference of the two second Born calculations [cf. in particular the center panel in Fig. 5(a)]. Here, the calculation which starts from the correlated ground state (dotted line) shows a density response rather close to the Hartree approximation [50], whereas the simulation which uses the equilibrated Hartree ground state as initial state (solid line) yields an energy transfer that is clearly larger than the mean-field result. The time evolution of the double occupation is, however, almost identical in both correlated cases, but significantly different from the mean-field approximation [see the bottom panel in Fig. 5(a)].
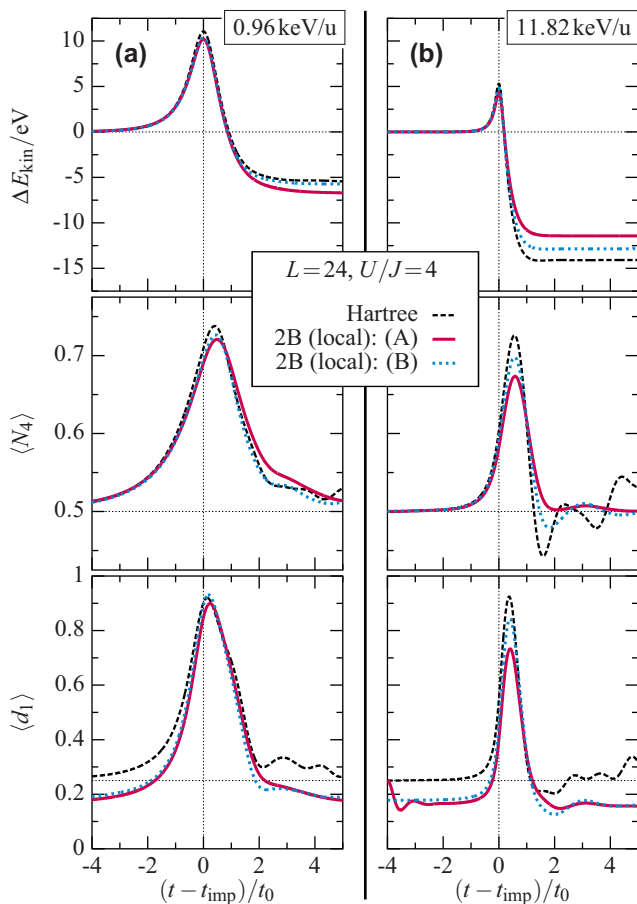
FIG. 5. Coupled proton-electron dynamics for the honeycomb cluster with $L = 24$ sites for two different proton energies, $E_{\mathrm{kin}} = 0.96$ keV/u (left panels) and 11.82 keV/u (right panels), corresponding to the arrows shown in Fig. 4(c). The coupling strength is fixed, $U/J = 4$, and three many-body approximations are compared (see inset). Top panels: change of the projectile's kinetic energy $\Delta E_{\mathrm{kin}}(t) = E_{\mathrm{kin}}(t) - E_{\mathrm{kin}}(t = 0)$ as function of time. Center panels: time evolution of the electron density averaged over the central sites labeled 1 to 4 in Fig. 1, i.e., $\langle N_4 \rangle(t) = \frac{1}{4}\sum_{i=1}^{4}\langle n_{i\sigma}\rangle(t)$. Bottom panels: time evolution of the double occupation $\langle d_1 \rangle(t) = \langle n_{1\uparrow}n_{1\downarrow}\rangle(t)$ on the site 1, which is closest to the impact point of the projectile.

C. Time-dependent electron spectral properties

An even closer look at the electronic excitations during the collision process is provided by the time-resolved photoemission spectrum $I(\omega,t_{\mathrm{p}}) = I_0^{-1}\sum_{i=1}^{L} I_i(\omega,t_{\mathrm{p}})$, with normalization factor I_0. Our NEGF approach directly yields this quantity (see Appendix), and we present the results in Fig. 6 for two different probe times t_{p}. Prior to the impact of the proton ($t_{\mathrm{p}} = 0$), the spectrum corresponds to the correlated ground state [we use initial state (B)] of the system and is, thus, analogous to the one discussed in Fig. 3(b). Note, however, that here we use $U/J = 4$, and we average over the whole cluster and use a different probe pulse. At a later time, when the projectile just passes the lattice plane ($t_{\mathrm{p}} \sim 4.1 t_0$), we observe a spectrum which indicates a strong redistribution of electrons in the lower Hubbard band, particularly towards lower energies
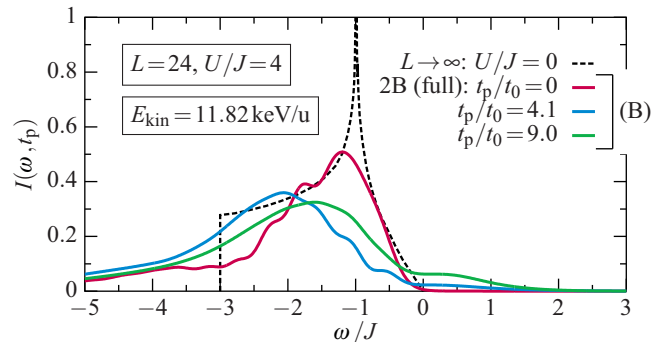
FIG. 6. Time-resolved photoemission spectrum $I(\omega,t_{\mathrm{p}}) = I_0^{-1}\sum_{i=1}^{L} I_i(\omega,t_{\mathrm{p}})$ of a cluster with $L = 24$ and $U/J = 4$ for the stopping dynamics of a proton with energy $E_{\mathrm{kin}} = 11.82$ keV/u [the scenario is similar to Fig. 5(b)]. The calculations are performed in full second Born approximation with a correlated initial state [case (B)]. Red curve: initial state, black dashes: ground state of an infinite system at $U/J = 0$. Blue line: spectrum when the projectile passes through the lattice plane. Green line: "final" state after the collision. To resolve the spectrum at the different stages of the dynamics, we have set the probe pulse width here to $\tau = 2t_0$ (cf. Appendix A).

(blue line in Fig. 6). This redistribution is, obviously, a result of the negative electronic confinement potential induced to the lattice electrons by the projectile and corresponds to a net energy loss of the electron system. Finally, at time $t_{\mathrm{p}} \gtrsim 9t_0$, the proton has passed through the lattice and is located far enough such that it does not affect the electrons anymore. We, therefore, measure a state of the electrons that is close to the "final" state. This state is characterized by a net energy gain of the electron system [as was shown in the top panel of Fig. 5(b)]. Here, we can resolve the spectral distribution of this energy: a substantial amount of electrons is being excited (above the Fermi level, $\omega_{\mathrm{F}} = 0$) into the upper Hubbard band. Of course, on a longer time scale (part of) this energy will be transferred from the electrons to lattice vibrations (phonons), but this is beyond the present model.

D. Projectile energy loss within the generalized Kadanoff-Baym ansatz

In this section, we analyze the generalized Kadanoff-Baym ansatz (GKBA) that was discussed in Sec. II C. This approximation has recently attracted growing attention [28,29,33,40] because it provides a way to significantly reduce the numerical effort of the computation of the NEGF, while still preserving the conservation laws of the chosen many-body approximations. Here, we apply the GKBA to reconstruct the two-time Green function $G_{ij\sigma}(t,t')$ for second Born self-energies from its time-diagonal value by using Hartree propagators (see Ref. [33] for details). For the present setup, the GKBA allows us to extend the full second Born calculations of Fig. 4(b) towards significantly longer times and, thus, to lower proton impact energies. We also note that, for finite systems which are strongly excited, the GKBA has been found to be free of certain artifacts of the two-time simulations [29], while being of comparable accuracy than the latter.
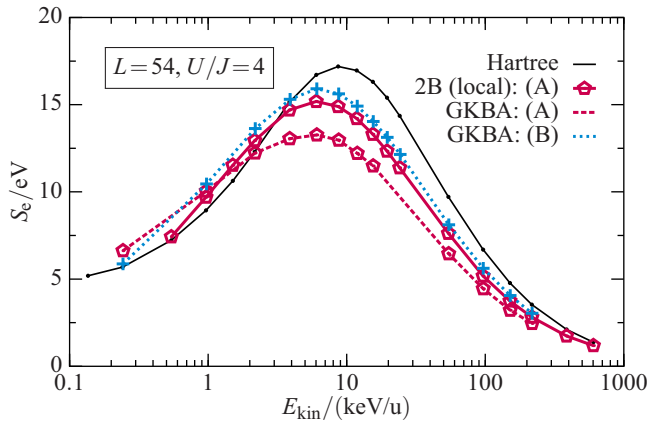
FIG. 7. Energy loss for the honeycomb cluster with $L = 54$ sites in second Born approximation. Comparison of the full two-time simulation and the GKBA (see text for details). Black and red solid lines are the same as in Fig. 4(b); red dashed and blue dotted curves: GKBA results for the initial states (A) and (B), respectively.

In Fig. 7, we present such GKBA simulations for both initial states, (A) and (B), as discussed above. For the initial state (A), we find a qualitative agreement with the analogous two-time calculations. At the same time, the GKBA simulations yield a systematically lower energy loss S_e for proton energies of $E_{kin} \gtrsim 5$ keV/u than the two-time simulations. In the present case, the projectile induces a rather strong and nonlocal perturbation, which is typically well described by the GKBA [29]. Whether the GKBA or two-time results for the stopping power are more accurate is presently unknown, as there are no exact results available, and this remains to be resolved in future studies.

Finally, we perform GKBA simulations with the fully correlated initial state (B). This leads to significantly increased results for the energy loss spectrum of the protons (blue dotted curve), which are closer to the mean-field result. The most striking achievement is that the GKBA simulations can be extended towards projectile energies around 200 eV. Interestingly, for these energies, the stopping power is significantly increased, as compared to the mean-field result. At the same time, with the use of Hartree propagators, we lose direct access to the correlated spectral functions.

E. Finite temperatures

For slow projectiles, we have seen in Secs. IV A and IV D that the inclusion of electron-electron correlations can lead to a slight increase of the energy loss in comparison to the mean-field treatment of the collision process. As this effect seems to be larger for a lattice system which is initially not in the self-consistent ground state [and thus has a nonzero effective temperature, cf. initial state (A)], it is worthwhile to discuss in more detail the influence of a finite electron temperature on the stopping dynamics.

In contrast to other approaches, the effect of finite temperature is straightforwardly incorporated in the NEGF formalism, where temperature effects enter the KBE via the initial state defined in Eq. (11). In Fig. 8, we perform Hartree and second Born calculations for $L = 24$ and different inverse
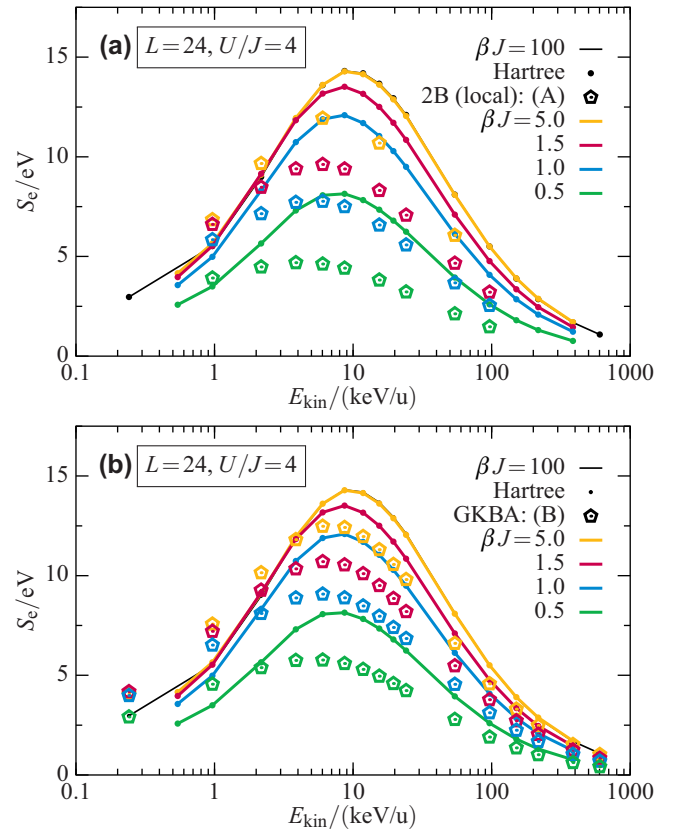
FIG. 8. Temperature dependence of the energy loss S_e for the honeycomb cluster with $L = 24$ sites and $U/J = 4$. Black lines: zero-temperature Hartree calculations, as in Fig. 4(a). Colored lines: Hartree results for different temperatures. Symbols: local second Born results for the same temperatures $\beta J = 5$, 1.5, 1, and 0.5. (a) Local second Born calculations with initial state (A). (b) GKBA calculations as in Sec. IV D with initial state (B).

temperatures $\beta J \ll 100$. For $\beta J = 5$, which corresponds to an electron temperature of $k_B T = 0.56$ eV (or about $T = 6500$ K) for a hopping amplitude of $J = 2.8$ eV, we measure energy loss spectra (cf. the yellow curves) that are still very close to the ground-state results of Fig. 4(a). For higher temperatures, $\beta J < 5$, on the other hand, we observe that the energy loss systematically decreases with temperature, whereas the maximum of the spectrum shifts to slightly lower energies. These trends continue even for higher electron temperatures (obviously, this refers to a nonequilibrium state, where the electron temperature is decoupled from the lattice) (see the red, blue, and green solid curves).

To understand the origin of the reduction of the energy loss with temperature, we investigate in Fig. 9 the time dependence of the proton energy and of the local electron density computed in mean-field approximation. Obviously, a temperature increase reduces the local enhancement of the electron density, as thermal fluctuations reduce the coherent response of the electrons to the projectile.

Finally, electron correlations are important even at the highest temperature considered [$\beta J = 0.5$ ($T \approx 65000$ K for $J = 2.8$ eV)], where the interaction energy U is still twice as large as the thermal energy. Here, compared to the mean-field
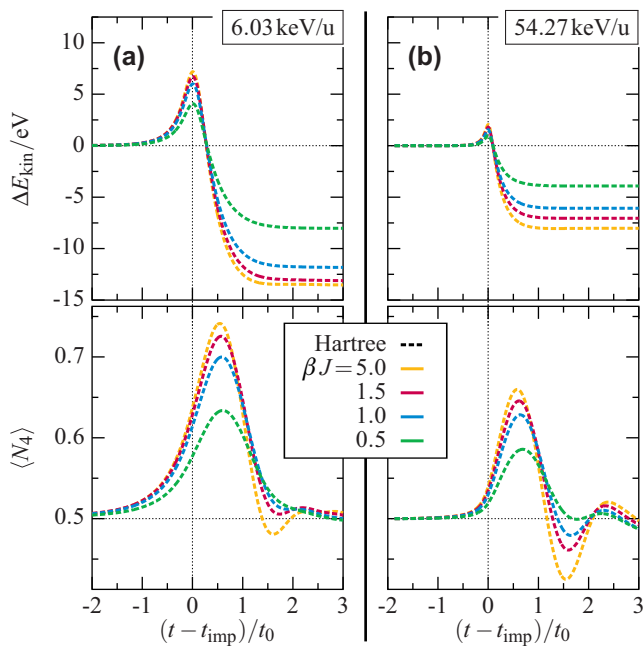
FIG. 9. Time-dependent energy change $\Delta E_{\text{kin}}(t) = E_{\text{kin}}(t) - E_{\text{kin}}(t=0)$ of the proton (upper panels) and electron density $\langle N_4 \rangle(t) = \frac{1}{4} \sum_{i=1}^{4} \langle n_{i\sigma} \rangle(t)$ at the four sites around the impact point (lower panels) for four different temperatures. Same cases (Hartree dynamics, $U/J = 4$) as shown in Fig. 8.

model, we observe that the local second Born calculations yield a clear shift of the whole spectrum towards smaller energies. Furthermore, the maximum energy loss is substantially reduced (with a peak value of the second Born calculation that is only about half of the mean-field result, Fig. 8(a)], which shows that the relative importance of correlations seems to increase with reduction of the temperature βJ. This unexpected behavior is due to the reduction of quantum diffraction effects with temperature, leading to an increased electron localization, which will be investigated in more detail elsewhere.

V. APPLICATION TO GRAPHENE

As a supplementary investigation, we examine, in this section, whether the coupled NEGF-Ehrenfest approach can be applied also to study the collision of charged particles with real (low-dimensional) materials. As example, we consider a two-dimensional sheet of graphene. As was shown in Refs. [51,52], the equilibrium properties of graphene [30,49] are well described through an extended Hubbard model with a nearest-neighbor hopping J on the honeycomb lattice using, beyond the onsite interaction U, additional nonlocal Coulomb interactions V_{ij}, that are known to stabilize the Dirac semimetallic phase [53]. However, it is not clear *a priori* whether this model holds also out of equilibrium. In particular, the present situation of the impact of a charged particle corresponds to a (locally) very strong excitation, driving the system far away from equilibrium. This question can only be answered by direct simulations of this process

and by comparison to reliable reference data for the stopping power.

In order to map this extended Hubbard model to the Hamiltonian of the form (1) with purely local interactions, we follow Ref. [31] and use an effective onsite interaction $U' = U - \bar{V} = 1.6J$, where $\bar{V}$ denotes a weighted average over the nonlocal contributions. Although this approximation has limitations, e.g. [52], it is agreed to be, at least, qualitatively correct. Moreover, we extend the Hamiltonian of Sec. II in two regards:

(i) We take into account the existence of four valence electrons per site. This means we consider (instead of a single-band model) a system with four independent Hubbard bands of equal hopping and interaction parameters, which together describe the dynamics of the four electrons provided by each sp^2-hybridized carbon atom in the graphene sheet. We are aware of the fact that such an approach excludes the specific nature of the σ and π bonds as well as possible (sp-)interband transitions. The main advantage of this model is, however, that it can be straightforwardly implemented by setting the local net charges Z_i in Eq. (3) to $Z_i = 4(1 - \sum_{\sigma} \langle n_{i\sigma} \rangle)$, leaving open a single parameter, the hopping amplitude J, which we will use below to adjust the maximum energy transfer.

(ii) We account for the fact that the incident projectile can influence the electron mobility on the lattice. This includes local changes to the electron's kinetic energy which originate from the presence of the off-diagonal matrix elements of the interaction potential W_{ij} between the projectile and the electrons on the lattice. Below, we approximate such a renormalization of the hopping to be proportional to the average potential energy between neighboring sites, i.e., we define an effective time- and site-dependent hopping amplitude

$$J_{ij}(t) = \begin{cases} -J + W_{ij}(t), & |i - j| = 1 \\ 0, & \text{otherwise} \end{cases} \qquad (14)$$

where

$$W_{ij}(t) = \gamma \frac{W_{ii}(t) + W_{jj}(t)}{2}. \qquad (15)$$

The proportionality factor γ can be interpreted as the strength of the orbital overlap and will be used as a second fit parameter below (see Appendix B for details).

We note that the ansatz (14) neglects corrections of the form W_{ij} with $|i - j| > 1$, which is justified because the wave functions of next-nearest and more distant neighbors have in general a much smaller overlap. Nevertheless, a further improved treatment of the off-diagonal components may be important for future studies since the projectile induces strong perturbations to the system.

In Fig. 10, we present stopping results for protons and alpha particles ($Z_p = 2$) for the model parameters $J = 3.15$ eV and $\gamma = 0.55$. To obtain reasonable agreement with *ab initio* TDDFT and SRIM data for the planar *infinitely extended* graphene sheet [7,8], we consider cluster sizes as large as $L = 384$, which are easily treated in Hartree approximation. The neglect of correlations is justified due to the relatively small onsite interaction strength of $U/J = 1.6$ (recall Sec. IV A). This expectation is confirmed by performing additional local second Born simulations for $L = 54$ (green circles) that lie on top of the Hartree curves [cf. Figs. 10(a) and 10(b)]. Generally,
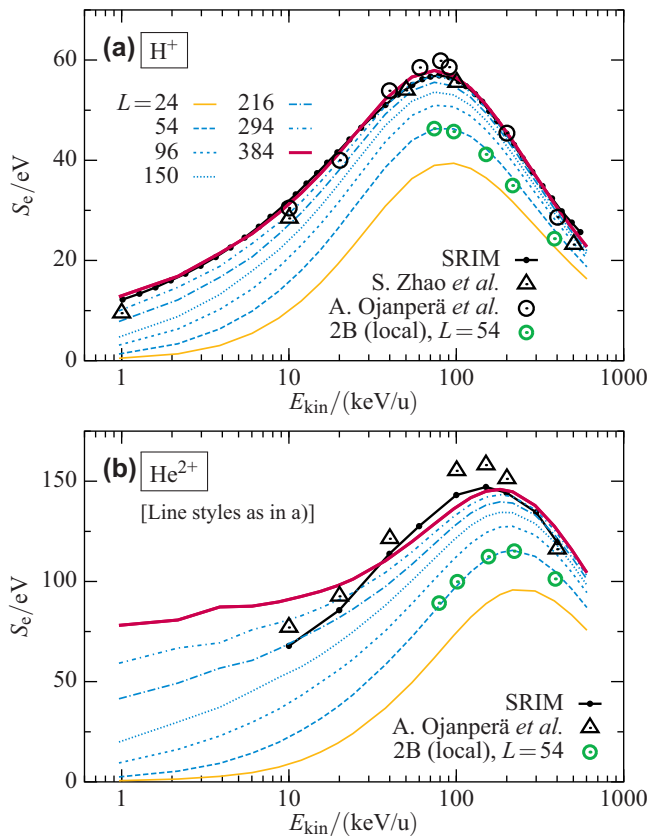
FIG. 10. Energy loss of (a) hydrogen ions (H$^+$) and (b) alpha particles (He^{2+}) penetrating through a single layer of graphene. In both panels, the strength of the Coulomb interaction is $U/J = 1.6$, the fit parameters are $J = 3.15$ eV and $\gamma = 0.55$, and the initial z position of the projectile is $z = 20a_0$. The Hartree results for different cluster sizes, ranging from $L = 24$ (bottom) to $L = 384$ (top), are shown by different line styles. For the cluster with $L = 54$ sites, we also performed second Born calculations (green circles) showing that correlation corrections are rather small in this case. For a detailed discussion of the U, J, and γ dependence, see Appendix B. The black symbols and lines correspond to *ab initio* TDDFT calculations and SRIMdata, respectively (taken from Refs. [7,8]).

we find that the energy transfer increases with the cluster size, which is consistent with results for graphene clusters discussed in Ref. [9]. In Fig. 10(a), the curves $S_e(E_{kin})$ tend to converge for large L and, for practically all considered proton energies, well approach the energy loss given by the reference data.

Finally, an important test of the model is provided by Fig. 10(b). There, we use exactly the same model parameters J and γ to simulate the energy loss for collisions of single-layer graphene with bare helium nuclei (He^{2+}). Without further adjustments, we recover good agreement with the available reference data, including the increase of the overall magnitude of S_e compared to the case of protons and, in addition, the shift of the maximum energy loss towards larger kinetic energies.

Given the simplicity of the model Hamiltonian, it is interesting that our NEGF-based approach reveals the correct trends for a fairly realistic system. On the other hand, however, we have to note also problems of the model. In particular, at the low-energy tail of the energy loss curve, we observe

significantly larger values compared to the TDDFT simulation in the case of alpha particles [cf. the red curve in Fig. 10(b)]. The origin of these discrepancies is not fully clear yet, and, therefore, in this range, additional correlated simulations as well as improvements to the model are required in the future.

VI. CONCLUSIONS

In summary, we have presented a combined nonequilibrium Green functions and classical Ehrenfest dynamics approach to the interaction of a nonrelativistic charged particle with a (strongly) correlated system. Our approach allows for a fully time-dependent treatment and is, thus, able to resolve nonadiabatic processes in the electronic subsystems. To explore the role of electronic correlations, we performed solutions of the two-time Keldysh-Kadanoff-Baym equations using different many-body approximations for the self-energy: the second Born, third-order, and the T-matrix approximations. This enabled us to demonstrate that electron-electron correlations do significantly influence the slowing down of a charged projectile in, both, the low and high-energy limits. The high computational effort of the NEGF simulations has limited us to projectile energies of 1 keV, as lower impact energies increase the interaction time with the lattice and, in turn, the computing time. To extend the simulations to lower energies, we have applied the generalized Kadanoff-Baym ansatz (GKBA), which is substantially more efficient. Interestingly, these simulations predict an energy loss well above the mean-field model, indicating that correlations can enhance the slowing down of a (slow) projectile. How accurate these results are is not known at the moment. This requires further analysis via full two-time simulations, the use of improved self-energies such as T-matrix self-energies, as well as independent TDDFT simulations.

Of particular current interest is the energy loss of low-energy (below 1 keV) charged particles in solid materials. An important field of applications are low-temperature plasmas. Questions of interest include the stopping power in materials with very strong electronic correlations (e.g., lattice models with $U/J \gtrsim 10$) or for magnetically ordered systems or insulators, where the stopping power can vanish below a certain threshold [54]. Furthermore, it will be important to extend the model beyond the Hubbard model to better capture realistic material properties, e.g., by using a Kohn-Sham basis. This, however, will drastically increase the computational requirements.

Additional questions of interest at low energies concern the inclusion of all relevant dissipation mechanisms, in particular, inelastic mechanisms such as phonons, impact excitation, and ionization or reemission of particles. Further relevant processes include neutralization of the ion before impact and capture (sticking), which is expected to cause deviations from the linear velocity scaling. Finally, it will be important to also consider more complex charged projectiles that are different from bare ionic cores. Here, intraionic electronic excitations play an important role in the stopping dynamics, e.g., [55].

From a technological point of view, it would furthermore be interesting to explore whether the energy deposition can be externally controlled, e.g., by time-dependent (laser) fields, which excite the target material before or during the impact. The potential effect of such an out-of-equilibrium situation

was demonstrated by an analysis of an increased temperature of the electronic subsystem. For such kinds of nonequilibrium investigations, our NEGF-based approach represents an optimal toolbox, as it handles external fields self-consistently and nonperturbatively and can include arbitrary scattering processes in a systematic way.

ACKNOWLEDGMENTS

We thank A. Marini and D. Sangalli for stimulating discussions and L. Wulff for performing simulations during the early stage of this work.

APPENDIX A: TIME-RESOLVED PHOTOEMISSION SPECTRUM

As an essential test for the numerics and the time propagation of the KBE (7), we verify here whether the correct spectrum and bandwidth are recovered from the two-time NEGF in the limit of an infinite honeycomb lattice. To this end, we compute the photoemission spectrum for vanishing onsite interaction [$U = 0$ in Hamiltonian (1)] and consider clusters of different size L.

We consider the photoemission signal of a reference site i, which is given by [56]

$$I_i(\omega, t_p) = -i \int dt \int dt'\, s(t - t_p) s(t' - t_p) e^{i\omega(t - t')} G_{ii\sigma}^<(t, t')$$

(A1)

at some probe time t_p. The function $s(t)$ thereby describes the envelope of the probe pulse and is chosen to be of Gaussian form, i.e.,

$$s(t) = \frac{1}{\tau \sqrt{2\pi}} e^{-t^2/(2\tau^2)},$$

(A2)

where we set $\tau = 4t_0$ with $t_0 = \hbar/J$ and $J = 2.8$ eV.

Figure 11 shows the spectrum $I_1(\omega)$ for honeycomb clusters with up to $L = 216$ sites at a probe time $t_p = 8t_0$, where, to evaluate the integral in Eq. (A1), we have computed the nonequilibrium Green function up to $t, t' = 15t_0$. Aside from some pulse-induced peak broadening, we observe that the
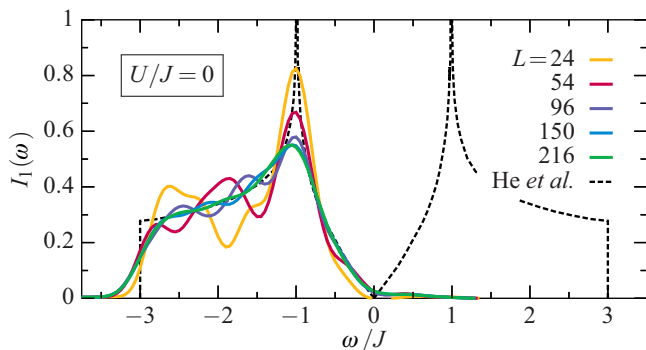
FIG. 11. Photoemission spectrum $I_1(\omega)$ for different uncorrelated honeycomb clusters of size L, measured at a probe time $t_p = 8t_0$ with $\tau/t_0 = 4$ [cf. Eq. (A1)]. The black dashed line shows the density of states in the valence and conduction band of the extended honeycomb lattice at half-filling, e.g., Refs. [48,49].

smaller clusters reveal only a few single-particle states, which are due to the finite system size. On the other hand, the spectra of the larger clusters ($L > 96$ sites) approach already well the density of states in the lower (valence) band of the extended honeycomb lattice (cf. the black dashed line).

APPENDIX B: ADAPTATION OF THE MODEL TO GRAPHENE

In order to model the impact of protons on a single sheet of graphene, we have tuned in Sec. V the hopping amplitude J and the orbital overlap parameter γ [defined in Eq. (14)] such that the energy loss spectrum is in good agreement with first-principles and SRIM data. By performing Hartree calculations, we show in Fig. 12 in more detail how the energy transfer S_e varies when these parameters are changed. Moreover, we discuss the influence of the ratio of the onsite Coulomb interaction U to the hopping J.

From Fig. 12(a), we observe that the interaction strength mainly influences the energy transfer below about 20 keV/u, whereas the high-energy tail remains unchanged. In the course of this, the low-energy tail as well as the maximum energy loss increase fairly linearly with U/J. Figure 12(b) shows that the hopping amplitude and the overlap parameter γ
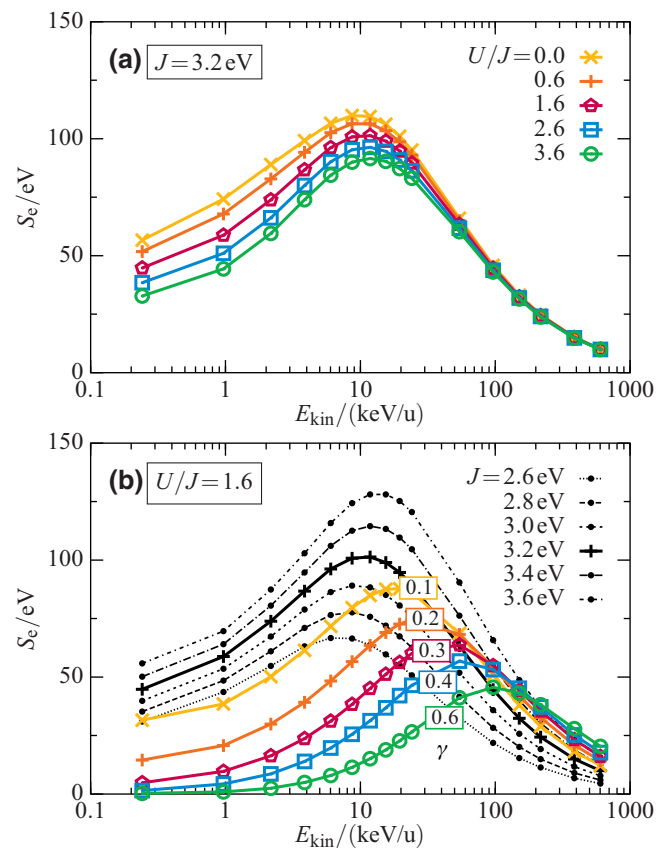
FIG. 12. Proton stopping dynamics as in Sec. V, but for different parameters U, J, and γ in Hartree approximation. The system size is $L = 54$. (a) Influence of the onsite interaction U for fixed $J = 3.2$ eV and $\gamma = 0$. (b) Influence of the hopping amplitude J and the orbital overlap γ for fixed interaction strength of $U/J = 1.6$.

affect the energy transfer substantially more than the Coulomb interaction. For a fixed value $U/J = 1.6$, a larger value of J (i.e., an increase of the general electron mobility on the lattice) leads to a larger energy loss, independently of the initial kinetic energy of the projectile. On the other hand, if we increase the hopping locally by choosing $\gamma > 0$, we find that the energy transfer becomes considerably smaller, which is accompanied by a shift of the maximum of S_e towards larger kinetic energies.

---

[1] P. Sigmund, *Particle Penetration and Radiation Effects* (Springer, Berlin, 2006).

[2] I. Nagy and B. Apagyi, Phys. Rev. A **58**, R1653(R) (1998).

[3] J. M. Pitarke, R. H. Ritchie, and P. M. Echenique, Phys. Rev. B **52**, 13883 (1995).

[4] M. Quijada, A. G. Borisov, I. Nagy, R. Díez Muiño, and P. M. Echenique, Phys. Rev. A **75**, 042902 (2007).

[5] M. A. Zeb, J. Kohanoff, D. Sánchez-Portal, A. Arnau, J. I. Juaristi, and E. Artacho, Phys. Rev. Lett. **108**, 225504 (2012).

[6] A. Schleife, Y. Kanai, and A. A. Correa, Phys. Rev. B **91**, 014306 (2015).

[7] S. Zhao, W. Kang, J. Xue, X. Zhang, and P. Zhang, J. Phys.: Condens. Matter **27**, 025401 (2015).

[8] A. Ojanperä, A. V. Krasheninnikov, and M. Puska, Phys. Rev. B **89**, 035120 (2014).

[9] S. Bubin, B. Wang, S. Pantelides, and K. Varga, Phys. Rev. B **85**, 235435 (2012).

[10] F. Mao, C. Zhang, C.-Z. Gao, J. Dai, and F.-S. Zhang, J. Phys.: Condens. Matter **26**, 085402 (2014).

[11] R. Ullah, F. Corsetti, D. Sánchez-Portal, and E. Artacho, Phys. Rev. B **91**, 125203 (2015).

[12] M. A. Zeb, J. Kohanoff, D. Sánchez-Portal, and E. Artacho, Nucl. Instrum. Methods Phys. Res., Sect. B **303**, 59 (2013).

[13] J. M. Pruneda, D. Sánchez-Portal, A. Arnau, J. I. Juaristi, and E. Artacho, Phys. Rev. Lett. **99**, 235501 (2007).

[14] J. F. Ziegler, M. D. Ziegler, and J. P. Biersack, Nucl. Instrum. Meth. B **268**, 1818 (2010); J. F. Ziegler, J. P. Biersack, and U. Littmark, *The Stopping and Range of Ions in Solids* (Pergamon, New York, 1985).

[15] V. U. Nazarov, J. M. Pitarke, C. S. Kim, and Y. Takada, Phys. Rev. B **71**, 121106(R) (2005).

[16] V. U. Nazarov, J. M. Pitarke, Y. Takada, G. Vignale, and Y.-C. Chang, Phys. Rev. B **76**, 205103 (2007).

[17] V. I. Anisimov, F. Aryasetiawan, and A. I. Lichtenstein, J. Phys.: Condens. Matter **9**, 767 (1997).

[18] R. Singla, G. Cotugno, S. Kaiser, M. Först, M. Mitrano, H. Y. Liu, A. Cartella, C. Manzoni, H. Okamoto, T. Hasegawa, S. R. Clark, D. Jaksch, and A. Cavalleri, Phys. Rev. Lett. **115**, 187401 (2015).

[19] L. P. Kadanoff and G. Baym, *Quantum Statistical Mechanics* (W. A. Benjamin, New York, 1962).

[20] G. Stefanucci and R. van Leeuwen, *Nonequilibrium Many-Body Theory of Quantum Systems: A Modern Introduction* (Cambridge University Press, Cambridge, 2013).

[21] N. Schlünzen, S. Hermanns, M. Bonitz, and C. Verdozzi, Phys. Rev. B **93**, 035107 (2016).

[22] N. E. Dahlen and R. van Leeuwen, Phys. Rev. Lett. **98**, 153004 (2007).

[23] A. Stan, N. E. Dahlen, and R. van Leeuwen, J. Chem. Phys. **130**, 224101 (2009).

[24] K. Balzer, S. Bauch, and M. Bonitz, Phys. Rev. A **81**, 022510 (2010).

[25] K. Balzer, S. Bauch, and M. Bonitz, Phys. Rev. A **82**, 033427 (2010).

[26] M. Garny and M. M. Müller, *High Performance Computing in Science and Engineering, Garching/Munich 2009* (Springer, Berlin, 2010).

[27] K. Balzer and M. Bonitz, Lect. Notes Phys. **867** (2013).

[28] S. Latini, E. Perfetto, A.-M. Uimonen, R. van Leeuwen, and G. Stefanucci, Phys. Rev. B **89**, 075306 (2014).

[29] S. Hermanns, N. Schlünzen, and M. Bonitz, Phys. Rev. B **90**, 125111 (2014).

[30] M. I. Katsnelson, *Graphene: Carbon in Two Dimensions* (Cambridge University Press, Cambridge, 2012).

[31] M. Schüler, M. Rösner, T. O. Wehling, A. I. Lichtenstein, and M. I. Katsnelson, Phys. Rev. Lett. **111**, 036601 (2013).

[32] L. V. Keldysh, Zh. Eksp. Teor. Fiz. **47**, 1515 (1964) [Sov. Phys.–JETP **20**, 1018 (1965)].

[33] N. Schlünzen and M. Bonitz, Contrib. Plasma Phys. **56**, 5 (2016).

[34] K. Balzer and M. Eckstein, Phys. Rev. B **89**, 035148 (2014).

[35] K. Balzer, J. Phys.: Conf. Ser. **696**, 012001 (2016).

[36] C. Gramsch and M. Potthoff, Phys. Rev. B **92**, 235135 (2015).

[37] M. Puig von Friesen, C. Verdozzi, and C.-O. Almbladh, Phys. Rev. Lett. **103**, 176404 (2009).

[38] S. Hermanns, Ph.D. dissertation, Kiel University, 2016.

[39] P. Lipavský, V. Špička, and B. Velický, Phys. Rev. B **34**, 6933 (1986).

[40] E. Perfetto, A.-M. Uimonen, R. van Leeuwen, and G. Stefanucci, Phys. Rev. A **92**, 033419 (2015).

[41] A. Rios, B. Barker, M. Buchler, and P. Danielewicz, Ann. Phys. **326**, 1274 (2011).

[42] S. Sorella and E. Tosatti, Europhys. Lett. **19**, 699 (1992).

[43] M. Bonitz and D. Kremp, Phys. Lett. A **212**, 83 (1996).

[44] D. Semkat, D. Kremp, and M. Bonitz, Phys. Rev. E **59**, 1557 (1999).

[45] F. Gebhard, E. Jeckelmann, S. Mahlert, S. Nishimoto, and R. M. Noack, Eur. Phys. J. B **36**, 491 (2003).

[46] We note that in the case of an external excitation (as the field of a charged projectile) the particle-hole symmetry breaks and the second Born self-energy becomes $\mathcal{O}(U^2)$. Nevertheless, the Hubbard sites remain predominantly half-filled which makes the error in $\mathcal{O}(U^3)$ small.

[47] A. Liebsch, Phys. Rev. B **83**, 035113 (2011).

[48] R.-Q. He and Z.-Y. Lu, Phys. Rev. B **86**, 045105 (2012).

[49] A. H. C. Neto, F. Guinea, N. M. R. Peres, K. S. Novoselov, and A. K. Geim, Rev. Mod. Phys. **81**, 109 (2009).

[50] We note that the density matrix $\langle \rho_{ij\sigma} \rangle$ of the correlated ground state [e.g., in the local second Born approximation, case (B)] is more similar to that of the Hartree ground state than to that of the equilibrated Hartree ground state [case (A)].

[51] T. O. Wehling, E. Şaşıoğlu, C. Friedrich, A. I. Lichtenstein, M. I. Katsnelson, and S. Blügel, Phys. Rev. Lett. **106**, 236805 (2011).

[52] H.-K. Tang, E. Laksono, J. N. B. Rodrigues, P. Sengupta, F. F. Assaad, and S. Adam, Phys. Rev. Lett. **115**, 186602 (2015).

[53] W. Wu and A.-M. S. Tremblay, Phys. Rev. B **89**, 205128 (2014).

[54] S. N. Markin, D. Primetzhofer, and P. Bauer, Phys. Rev. Lett. **103**, 113201 (2009).

[55] M. Pamperin, F. X. Bronold, and H. Fehske, Phys. Rev. B **91**, 035440 (2015).

[56] M. Eckstein and M. Kollar, Phys. Rev. B **78**, 245113 (2008).

Doublon Formation by Ions Impacting a Strongly Correlated Finite Lattice System

Karsten Balzer,[1] Maximilian Rodriguez Rasmussen,[2] Niclas Schlünzen,[2] Jan-Philip Joost,[2] and Michael Bonitz[2,*]

[1]*Rechenzentrum, Christian-Albrechts-Universität zu Kiel, D-24098 Kiel, Germany*
[2]*Institut für Theoretische Physik und Astrophysik, Christian-Albrechts-Universität zu Kiel, D-24098 Kiel, Germany*

Strongly correlated systems of fermions have a number of exciting collective properties. Among them, the creation of a lattice that is occupied by doublons, i.e., two quantum particles with opposite spins, offers interesting electronic properties. In the past a variety of methods have been proposed to control doublon formation, both, spatially and temporally. Here, a novel mechanism is proposed and verified by exact diagonalization and nonequilibrium Green functions simulations—fermionic doublon creation by the impact of energetic ions. We report the formation of a nonequilibrium steady state with homogeneous doublon distribution. The effect should be particularly important for strongly correlated finite systems, such as graphene nanoribbons, and directly observable with fermionic atoms in optical lattices.

Strongly correlated systems are attracting increasing interest in many fields including dense plasmas [1], warm dense matter [2], dusty plasmas [3], and ultracold atoms [4]. Among the most intriguing phenomena in strongly correlated quantum systems of both fermions and bosons is the formation of doublons—pairs of repulsively bound particles occupying the same lattice site [5]. In recent years, there have been many attempts to study the dynamics of doublons after a correlated system is driven out of equilibrium leading to many surprising results. "Quantum distillation"—the spatial separation of doublons and single fermions—was observed in Refs. [6,7]. The nonequilibrium expansion dynamics of a fermionic particle cloud following a confinement quench and its slowing down due to doublon formation has been studied experimentally in a 2D optical lattice [4] and theoretically by 2D quantum simulations using nonequilibrium Green functions (NEGF) [8]. Also, the external control of doublons by an interaction quench [9], by periodically modulating an optical lattice [10–12], by external electric fields [13–18] or by optical excitation [19] has been proposed. Furthermore, the dynamics of heteronuclear doublons [20] and the spatial transfer of doublons via topological edge states [21] have been studied.

Previous setups of doublon manipulation involved spatially homogeneous systems containing a large number of fermions triggering their collective response to a spatially delocalized excitation. In contrast, in this Letter we predict a novel mechanism to induce and control the formation of doublons in a finite system where the excitation is localized in space and time. The most interesting examples are finite graphene clusters (e.g., "nanoribbons," GNR) that are fabricated in a controlled way, e.g., Refs. [22–24], and are accurately characterized experimentally [25–27]. In contrast to graphene, GNR have a finite band gap [28–30]

that can be tuned by varying the system size and geometry [31], giving rise to exciting electronic correlation effects and optical and transport properties [32]. The doublon excitation mechanism we are proposing is driven by energetic ions penetrating a strongly correlated finite system and depositing energy ("stopping power," e.g., Refs. [33–36]). We demonstrate the mechanism by exact diagonalization simulations, and a physical explanation is given with an analytical model in terms of the Landau-Zener effect [37]. We then investigate how the doublon number depends on the cluster size in one and two dimensions by performing NEGF simulations and demonstrate the emergence of a stationary nonequilibrium state with homogeneous doublon distribution. Finally, we show that the effect can be further enhanced by using a sequence of excitations.

Model.—We consider strongly correlated electrons in a single-band finite Hubbard model containing L sites with nearest-neighbor hopping J and on-site interaction U,

$$\hat{H} = -J \sum_{\langle i,j \rangle \sigma} \hat{c}_{i\sigma}^\dagger \hat{c}_{j\sigma} + U \sum_i \hat{n}_{i\uparrow} \hat{n}_{i\downarrow} + \sum_{i\sigma} W_i(t) \hat{n}_{i\sigma}, \quad (1)$$

where $\hat{n}_{i\sigma} = \hat{c}_{i\sigma}^\dagger \hat{c}_{i\sigma}$ is the density, σ denotes the spin, and $W_i(t) = -Ze^2/[4\pi\epsilon_0|\mathbf{r}(t) - \mathbf{r}_i|]$ describes the interaction of the electron at lattice site $\mathbf{r}_i$ with a positive ion of charge Ze moving on a classical trajectory $\mathbf{r}(t)$, neglecting nonlocal contributions, $W_{ij} = \delta_{ij} W_i$. We denote $W_0 = e^2/(4\pi\epsilon_0 a)$ and measure energies, times, and lengths in units of J, $\hbar J^{-1}$, and the lattice constant a, respectively. The quantities of central interest are the site-resolved density, $n_{i\sigma}$, and double occupation d_i, the cluster average of d, and its long-time limit after passing of the projectile:

$$n_{i\sigma}(t) = \langle \hat{n}_{i\sigma}(t) \rangle, \qquad d_i(t) = \langle \hat{n}_{i\uparrow}(t) \hat{n}_{i\downarrow}(t) \rangle, \quad (2)$$
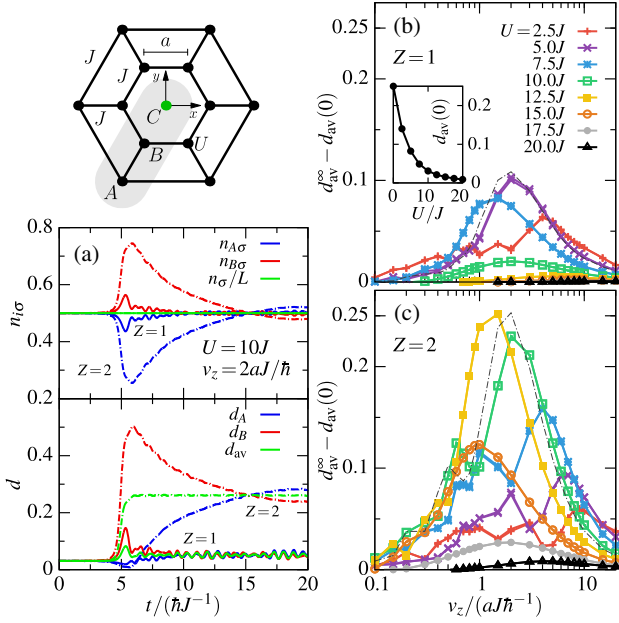
FIG. 1. Ion impact-induced doublon formation in a two-dimensional Hubbard nanocluster (top left, black points) with $L = 12$ sites, nearest-neighbor hopping J and on-site interaction U. (a) Time evolution of the electron density $n_{i\sigma}$ (top) and double occupation d_i (bottom) on sites A (blue) and B (red) for a positive charge with $Z = 1$ (solid lines) and $Z = 2$ (dash-dotted lines) impacting the system at $U = 10J$ with velocity $v_z = 2aJ/\hbar$ in point $C = (0,0,0)$. The green curves show the mean density, $n_\sigma(t)/L = (1/L)\sum_i n_{i\sigma}(t) = 0.5$, and double occupation $d_{av}(t)$, Eq. (3), respectively. (b) and (c) Increase of the double occupation, $d_{av}^\infty - d_{av}(0)$ [inset in (b) shows $d_{av}(0)$], as a function of v_z for different U and $Z = 1$ ($Z = 2$), where the thin dash-dotted gray curves correspond to $U = U^* = 5.4J$ ($U = U^* = 10.8J$), as derived from the dimer model below.

$$d_{av}(t) = \frac{1}{L}\sum_{i=1}^{L} d_i(t), \quad d_{av}^\infty = \lim_{t\to\infty}\frac{1}{\Delta t}\int_t^{t+\Delta t} d\bar{t}\, d_{av}(\bar{t}). \quad (3)$$

Results for a finite 2D cluster.—In Figure 1, we present solutions of the system (1) for an exemplary 2D half-filled Hubbard nanocluster with $L = 12$ sites, obtained by time-dependent exact diagonalization (CI) starting at $t = 0$ from the ground state. The trajectory of the ion is set to $r(t) = (0,0,z + v_z t)$ with velocity v_z and initial z position such that $W_i(t = 0) \to 0$, $\forall$ i. We use $W_0 = 14.4J$, which corresponds to a force $J/a = 1$ eV/Å. Figure 1(a) shows the time evolution for an on-site interaction $U = 10J$, $v_z = 2aJ/\hbar$, and $Z = 1$ and 2, where the expectation values are computed as $\langle\hat{\mathcal{O}}\rangle(t) = \langle\psi(t)|\hat{\mathcal{O}}|\psi(t)\rangle$, with the many-electron wave function $|\psi(t)\rangle = \{T\exp[-(i/\hbar)\int_0^t ds\hat{H}(s)]\}|\psi(0)\rangle$ and time-ordering operator T. During the time of impact ($t = 5\hbar/J$), both $n_{B\sigma}$ and d_B ($n_{A\sigma}$ and d_A) increase (decrease). After departure of the projectile the electron densities return (close) to their initial value $n_{i\sigma} = 0.5$.

In contrast, the spatiotemporal evolution of the double occupation [38] is such that $d_{A,B}$ remain above their initial value, particularly for $Z = 2$. Thus, the projectile has created a significant number of stable doublons, indicating the emergence of a stationary nonequilibrium ("prethermalized" [39,40]) state. This is quantified in Figs. 1(b) and 1(c) by the asymptotic value of the average double occupation, d_{av}^∞ (3). A striking result is the nonmonotonic dependence of d_{av}^∞ on the projectile velocity with a maximum around $v_z \sim (1\ldots3)aJ/\hbar$. Moreover, also the dependence on U is nonmonotonic: d_{av}^∞ exhibits a single maximum which is in the range of $U \sim 5J$, for $Z = 1$, and $U \sim 12J$, for $Z = 2$. Further, d_{av}^∞, increases with the projectile charge. We note that in the present setup we consider a projectile with constant kinetic energy; for a discussion on the energy transfer see Ref. [35]. Also, reducing the hopping J between the A sites (along the edges of the cluster), does not significantly change the results [41].

Analytical model.—To understand the main mechanism of the doublon formation, we consider a Hubbard dimer at half-filling and develop a Landau-Zener (LZ) description [9,18,37]. The dimer is excited by a time-dependent energy $W(t) = -W_0\exp[-t^2/(2\tau^2)]$ on one site, which well mimics the projectile. Here the interaction duration with the projectile $\tau > 0$ is inversely proportional to the projectile velocity v_z, and we use $W_0 = 2U$. In the basis $\{|\uparrow,\downarrow\rangle, |\downarrow,\uparrow\rangle, |\uparrow\downarrow,0\rangle, |0,\uparrow\downarrow\rangle\}$, the Hamiltonian

$$\hat{H}_{dimer}(t) = \begin{pmatrix} W(t) & 0 & -J & -J \\ 0 & W(t) & J & J \\ -J & J & U + 2W(t) & 0 \\ -J & J & 0 & U \end{pmatrix}, \quad (4)$$

is straightforwardly diagonalized for all times.

Figure 2(a) shows the evolution of all four eigenenergies, $E_0 \leq E_1 \leq E_U \leq E_2$, (the explicit expressions are given in the Supplemental Material [41]) for $U = 10J$ as function of $W(t)$. Starting in the triplet ground state (E_0), for $t = -\infty$, the dimer undergoes a transition to the second excited state (E_U) via an avoided crossing with probability p when $W(t)$ is switched on sufficiently fast. Using a reduced two-level Landau-Zener picture, the probability that the dimer, for $t = +\infty$, remains in state E_U can be approximated by a twofold (forward-backward) passage of the avoided level crossing:

$$P_{E_0 \to E_U} = 2p(1 - p), \quad (5)$$

with the LZ transition probability for a single diabatic passage of the crossing (for details see Ref. [41]),

$$p(\tau; U) = \exp\left(-\frac{\pi e^{1/2}[\min_{W(t)}(E_U - E_0)]^2\tau}{2\hbar W_0|d(E_U - E_0)/dW|}\right). \quad (6)$$
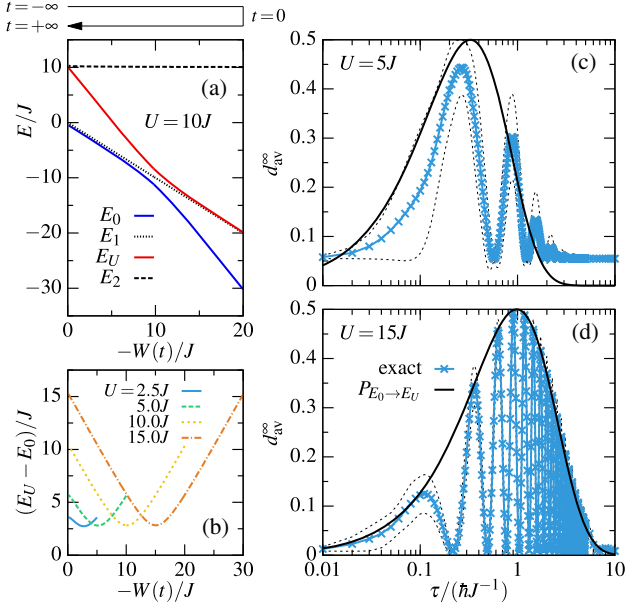
FIG. 2. Hubbard dimer of Eq. (4). (a) Evolution of the eigenenergies as a function of $W(t)$, for $U = 10J$. The initial and final state corresponds to $W = 0$, and the impact of the projectile to $-W/J = 20$; its trajectory is sketched above the figure. (b) Eigenenergy difference, $E = E_U - E_0$, as function of $W(t)$ for $W_0 = 2U$ and different values of U. (c) and (d) Asymptotic double occupation, for $U = 5J$ and $15J$ as function of τ. Blue: CI data [using $\Delta t = 50\hbar J^{-1}$ in Eq. (3)], black line: Landau-Zener result based on Eq. (5), thin dashed lines: exact minimum and maximum values of $d_{av}(t)$.

From Fig. 2(b), we observe that, around $W(t) = -W_0$, the level spacing and its derivative are almost independent of U; therefore, the probabilities p and $P_{E_0 \to E_U}$ only depend (for fixed U) on the duration τ of the excitation.

Figures 2(c) and 2(d) show d_{av}^∞, in the dimer, for $U = 5J$ and $15J$ (black curves), together with the exact solution of Eq. (4). The most striking result is that d_{av}^∞ can reach (and remain at) 0.5, for an optimal choice of τ, which is well captured by the LZ picture where this corresponds to the probability (6), $p = 1/2$, of creating a doublon on site one. Overall we observe that, for $U \gtrsim 10J$, our model (5) reproduces the envelope of $d_{av}^\infty(\tau)$ very well, although it does not capture the oscillations that are proportional to the field W_0 and are due to transient Bloch oscillations [43].

With insight from the dimer model, we find the parameters that maximize d_{av}^∞, in the 12-site cluster of Fig. 1: (i) the optimal interaction strength is $U^*/J \approx Z \times 5.4$; (ii) for $U = U^*$, the optimal velocity v_z^* decreases linearly with Z [41]. The result is shown by the thin gray dash-dotted line in Fig. 1(b) [Fig. 1(c)]. The striking agreement of the peak height and position with the CI result for $L = 12$ confirms that our model captures the correct physics: local doublon formation via a twofold passage of an avoided level crossing.

Maximizing the doublon number in larger 1D and 2D systems.—We now turn to finite Hubbard clusters with lower symmetry than the one in Fig. 1 starting with a 1D half-filled chain with $L = 8$ sites, $U = 20J$ and periodic boundary conditions which we solve exactly. To investigate how the spreading of the doublons along the chain changes compared to the dimer case we use the same local excitation, $W(t)$, applied only to site 1. As shown in Fig. 3(b), now the average doublon number reaches only $d_{av}^\infty \approx 0.08$, at $t \approx 15\hbar J^{-1}$. To increase d_{av}^∞ further, we apply a second identical excitation to site one which indeed raises d_{av}^∞ to 0.145. Repeating this procedure periodically allows for a successive increase until a value $d_{av}^\infty \approx 1/4$ is reached. This final value is consistent with the time evolution of the many-particle energy spectrum

$$S(\hbar\omega, t) = \sum_i |\langle \psi(t)|E_i\rangle|^2 e^{-\{(\hbar\omega - [E_i - UL/4])^2/2(\hbar\omega_0)^2\}}, \quad (7)$$

where $|E_i\rangle$ denote the energy eigenstates, which is shown in Fig. 3(c) for a level broadening $\hbar\omega_0 = J$. The final energy spectrum ($t > 200\hbar J^{-1}$) becomes symmetric around $\omega = 0$, therefore providing on average two doublons in the system, corresponding to $d_{av}^\infty \to 1/4$. Moreover, we observe that the double occupation (just as the density) becomes homogeneous along the chain, cf. Fig. 3(b), and
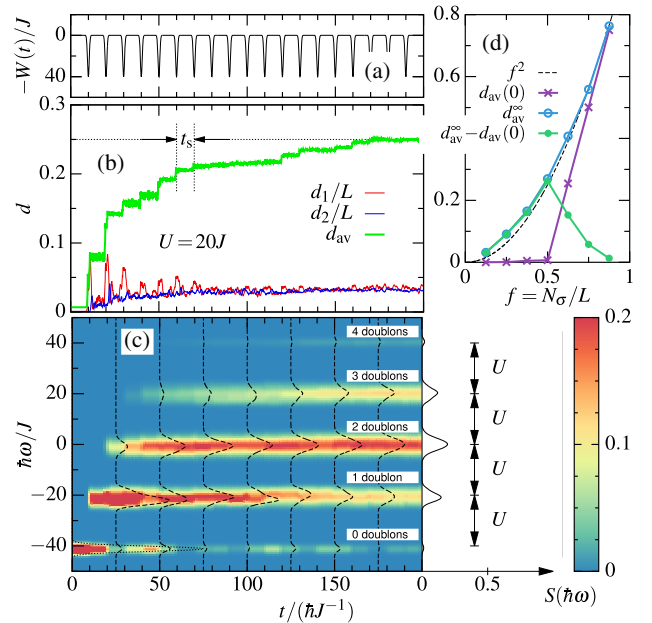
FIG. 3. Evolution of a half-filled Hubbard chain with $L = 8$ sites and $U = 20J$ subject to multiple excitations at site 1. (a) Applied field, $W(t)$, with $\tau = 0.5\hbar J^{-1}$ and peak separation $t_s = 10\hbar J^{-1}$. (b) Dynamics of the mean double occupation $d_{av}(t)$ of Eq. (3). (c) Time evolution of the energy spectrum $S(\hbar\omega, t)$, Eq. (7) with $\hbar\omega_0 = J$. (d) Doublon formation process for different filling fractions $f = N_\sigma/L$, where N_σ denotes the number of electrons of spin σ.
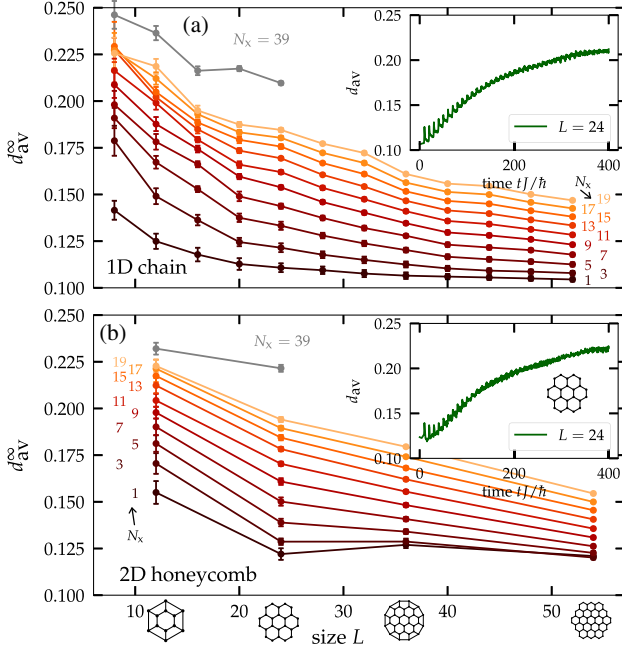
FIG. 4. Asymptotic double occupation (3) for (a) 1D chains and (b) 2D half-filled honeycomb clusters of different size L and $U = 4J$ from NEGF simulations. The number of excitations, N_x, which are performed on one of the innermost sites, is indicated in the figure. Insets show $d_{av}(t)$, for $L = 24$ and $N_x = 40$.

that the correlation part of the interaction energy vanishes almost completely [not shown], indicating the approach of a mean-field state. In Fig. 3(d), we furthermore investigate the same scenario for different fillings [44] ($N_\sigma = \sum_i n_{i\sigma} = 1, 2, \ldots, 7$), which shows that the change of double occupation with respect to the initial ground state is largest for half-filling.

In order to test whether our doublon production protocol can be realized also in larger systems and 2D setups as well, we have performed extensive NEGF simulations for L up to 54 of long duration, $t \leq 400\hbar J^{-1}$, which enables us to consider up to $N_x = 39$ localized excitations of the same form as in Fig. 3(a). We used second-order Born self-energies within the generalized Kadanoff-Baym ansatz with Hartree-Fock propagators (HF-GKBA), as explained in detail in Refs. [8,35,45,46]. From benchmarks against density matrix renormalization group simulations [47] we expect that these simulations are reliable for $U/J \lesssim 4$. Tests against our present CI data for small systems confirm the high quality of the NEGF results and indicate that they yield a lower bound to d_{av}^∞, the exact result being 5%–15% higher.

In Fig. 4 we show the asymptotic double occupation, d_{av}^∞, for $W_0 = 2U = 8J$, for 1D chains, Fig. 4(a), and 2D honeycomb lattice fragments, Fig. 4(b). Clearly, the successive increase of d_{av}^∞ with N_x is confirmed for larger systems. Also, for fixed N_x, we observe a decrease of d_{av}^∞ with L, as expected. Extrapolating to larger values of N_x we expect that for all systems d_{av}^∞ will reach at least 0.25.

Summary and discussion.—We have presented a novel scenario for the production of doubly occupied electronic states in correlated finite 1D and 2D Hubbard clusters that is based on the impact of energetic ions. We have reported CI results for system sizes $L \leq 12$ that were complemented by nonequilibrium Green functions simulations for $L \leq 54$. The physical mechanism has been made transparent by analytically solving the relevant dimer problem in the presence of an ion impact: it is the formation of avoided level crossings between bands of different doublon number, cf. Fig. 3, and it is straightforwardly extended to multiple sequential excitations. For the case that the system is not coupled to a bath [as in our simulations] we observed formation of a stationary homogeneous doublon population which provides another example for pre-thermalization phenomena [17,40,48,49] that recently have attracted high interest. More generally, we have presented a new scenario of nonequilibrium dynamics without thermalization [50,51] that is driven by a rapid, spatially localized single-particle potential quench instead of an interaction quench. While in the homogeneous state we observe doublon occupations up to 0.25, as in previous homogeneous excitation scenarios, e.g., Refs. [11–18], we have shown [cf. Figs. 2(c) and 2(d)] that, for inhomogeneous states in finite systems, significantly higher final values can be achieved. Moreover, the flexibility of the excitation protocol should allow for further optimization. We have verified (see Fig. 1 and Ref. [41]) that the same protocol can be realized also with Coulomb interaction where the long range interaction even enhances the doublon number.

Our results are directly applicable to finite correlated solid state systems, such as graphene nanoribbons [23–31], that are exposed to energetic ions [36]. For moderately correlated systems with typical parameters $J = 1$ eV and $a = 1$ Å, ion velocities $v_z \sim 1aJ/\hbar$ are required which translates into kinetic energies of 120 eV (480 eV) for protons (alpha particles). These values are well feasible with ion guns or in low-temperature high-pressure plasmas [52], where the present effect should have a strong influence on the stopping power [33–35] and may offer new optical and transport applications. Of course, for the case of multiple excitations, one would need to consider spatial variations of the impact point, energy, and time delay between impacts. These issues are easily studied within the dimer model and with our NEGF approach as well. Furthermore, for these systems the coupling to the environment (bath) and the associated dissipation effects will have to be included, which sets an upper limit for the lifetime of the nonequilibrium doublon state in the range of several hundred femtoseconds. Since the timescale of the doublon formation is of the order of 1–10 fs we expect that the presented scenario of multiple ion impacts can be realized.

Suitable candidates to verify this scenario experimentally are fermionic atoms in optical lattices. While direct ion impact will be less efficient, due to the weaker short range

charge-atom interaction [53], a promising approach is to mimic the projectile dynamics via suitable time-dependent local variation of the lattice potentials [54]. This would open the way to simulate, with cold atoms, ion stopping in condensed matter, including correlated materials.

---

[*]bonitz@theo-physik.uni-kiel.de

[1] V. E. Fortov, R. I. Ilkaev, V. A. Arinin, V. V. Burtzev, V. A. Golubev, I. L. Iosilevskiy, V. V. Khrustalev, A. L. Mikhailov, M. A. Mochalov, V. Ya. Ternovoi, and M. V. Zhernokletov, Phase Transition in a Strongly Nonideal Deuterium Plasma Generated by Quasi-Isentropical Compression at Megabar Pressures, Phys. Rev. Lett. **99**, 185001 (2007).

[2] T. Dornheim, S. Groth, T. Sjostrom, F. D. Malone, W. M. C. Foulkes, and M. Bonitz, *Ab Initio* Quantum Monte Carlo Simulation of the Warm Dense Electron Gas in the Thermodynamic Limit, Phys. Rev. Lett. **117**, 156403 (2016).

[3] M. Bonitz, C. Henning, and D. Block, Complex plasmas—A laboratory for strong correlations, Rep. Prog. Phys. **73**, 066501 (2010).

[4] U. Schneider, L. Hackermüller, J. P. Ronzheimer, S. Will, S. Braun, T. Best, I. Bloch, E. Demler, S. Mandt, D. Rasch, and A. Rosch, Fermionic transport and out-of-equilibrium dynamics in a homogeneous Hubbard model with ultracold atoms, Nat. Phys. **8**, 213 (2012).

[5] K. Winkler, G. Thalhammer, F. Lang, R. Grimm, J. Hecker Denschlag, A. J. Daley, A. Kantian, H. P. Büchler, and P. Zoller, Repulsively bound atom pairs in an optical lattice, Nature (London) **441**, 853 (2006).

[6] F. Heidrich-Meisner, S. R. Manmana, M. Rigol, A. Muramatsu, A. E. Feiguin, and E. Dagotto, Quantum distillation: Dynamical generation of low-entropy states of strongly correlated fermions in an optical lattice, Phys. Rev. A **80**, 041603(R) (2009).

[7] L. Xia, L. A. Zundel, J. Carrasquilla, A. Reinhard, J. M. Wilson, M. Rigol, and D. S. Weiss, Quantum distillation and confinement of vacancies in a doublon sea, Nat. Phys. **11**, 316 (2015).

[8] N. Schlünzen, S. Hermanns, M. Bonitz, and C. Verdozzi, Dynamics of strongly correlated fermions—*Ab initio* results for two and three dimensions, Phys. Rev. B **93**, 035107 (2016).

[9] M. Schecter and A. Kamenev, Forming doublons by a quantum quench, Phys. Rev. A **85**, 043623 (2012).

[10] D. Greif, L. Tarruell, T. Uehlinger, R. Jördens, and T. Esslinger, Probing Nearest-Neighbor Correlations of Ultracold Fermions in an Optical Lattice, Phys. Rev. Lett. **106**, 145302 (2011).

[11] A. Tokuno, E. Demler, and T. Giamarchi, Doublon production rate in modulated optical lattices, Phys. Rev. A **85**, 053601 (2012).

[12] A. Dirks, K. Mikelsons, H. R. Krishnamurthy, and J. K. Freericks, Theoretical description of coherent doublon creation via lattice modulation spectroscopy, Phys. Rev. A **89**, 021602(R) (2014).

[13] M. Eckstein, T. Oka, and P. Werner, Dielectric Breakdown of Mott Insulators in Dynamical Mean-Field Theory, Phys. Rev. Lett. **105**, 146404 (2010).

[14] M. Eckstein and P. Werner, Dielectric breakdown of Mott insulators—Doublon production and doublon heating, J. Phys. Conf. Ser. **427**, 012005 (2013).

[15] K. Balzer and M. Eckstein, Field-assisted doublon manipulation in the Hubbard model: A quantum doublon ratchet, Europhys. Lett. **107**, 57012 (2014).

[16] M. Genske and A. Rosch, Directed motion of doublons and holes in periodically driven Mott insulators, Phys. Rev. A **90**, 043637 (2014).

[17] A. V. Joura, J. K. Freericks, and A. I. Lichtenstein, Long-lived nonequilibrium states in the Hubbard model with an electric field, Phys. Rev. B **91**, 245153 (2015).

[18] A. R. Kolovsky and D. N. Maksimov, Mott-insulator state of cold atoms in tilted optical lattices: Doublon dynamics and multilevel Landau-Zener tunneling, Phys. Rev. A **94**, 043630 (2016).

[19] M. Ligges, I. Avigo, D. Golež, H. Strand, L. Stojchevska, M. Kalläne, P. Zhou, K. Rossnagel, M. Eckstein, P. Werner, and U. Bovensiepen, Ultrafast Doublon Dynamics in Photo-Excited $1T - TaS_2$, Phys. Rev. Lett. **120**, 166401 (2018).

[20] J. P. Covey, S. A. Moses, M. Gärttner, A. Safavi-Naini, M. T. Miecnikowski, Z. Fu, J. Schachenmayer, P. S. Julienne, A. M. Rey, D. S. Jin, and J. Ye, Doublon dynamics and polar molecule production in an optical lattice, Nat. Commun. **7**, 11279 (2016).

[21] M. Bello, C. E. Creffield, and G. Platero, Sublattice dynamics and quantum state transfer of doublons in two-dimensional lattices, Phys. Rev. B **95**, 094303 (2017).

[22] L. Jiao, L. Zhang, X. Wang, G. Diankov, and H. Dai, Narrow graphene nanoribbons from carbon nanotubes, Nature (London) **458**, 877 (2009).

[23] J. Cai, P. Ruffieux, R. Jaafar, M. Bieri, T. Braun, S. Blankenburg, M. Muoth, A. P. Seitsonen, M. Saleh, X. Feng, K. Müllen, and R. Fasel, Atomically precise bottom-up fabrication of graphene nanoribbons, Nature (London) **466**, 470 (2010).

[24] A. Kimouche, M. M. Ervasti, R. Drost, S. Halonen, A. Harju, P. M. Joensuu, J. Sainio, and P. Liljeroth, Ultra-narrow metallic armchair graphene nanoribbons, Nat. Commun. **6**, 10177 (2015).

[25] B. V. Senkovskiy, D. Haberer, D. Yu. Usachov, A. V. Fedorov, N. Ehlen, M. Hell, L. Petaccia, G. Di Santo, R. A. Durr, F. R. Fischer, and A. Grüneis, Spectroscopic characterization of $N = 9$ armchair graphene nanoribbons, Phys. Status Solidi RRL **11**, 1700157 (2017).

[26] S. Wang, L. Talirz, C. A. Pignedoli, X. Feng, K. Müllen, R. Fasel, and P. Ruffieux, Giant edge state splitting at atomically precise graphene zigzag edges, Nat. Commun. **7**, 11507 (2016).

[27] L. Talirz, H. Söde, T. Dumslaff, S. Wang, J. R. Sanchez-Valencia, J. Liu, P. Shinde, C. A. Pignedoli, L. Liang, V. Meunier, N. C. Plumb, M. Shi, X. Feng, A. Narita, K. Müllen, R. Fasel, and P. Ruffieux, On-surface synthesis and characterization of 9-atom wide armchair graphene nanoribbons, ACS Nano **11**, 1380 (2017).

[28] K. Nakada, M. Fujita, G. Dresselhaus, and M. S. Dresselhaus, Edge state in graphene ribbons: Nanometer size effect and edge shape dependence, Phys. Rev. B **54,** 17954 (1996).

[29] Y.-W. Son, M. L. Cohen, and S. G. Louie, Energy Gaps in Graphene Nanoribbons, Phys. Rev. Lett. **97,** 216803 (2006).

[30] P. Ruffieux, J. Cai, N. C. Plumb, L. Patthey, D. Prezzi, A. Ferretti, E. Molinari, X. Feng, K. Müllen, C. A. Pignedoli, and R. Fasel, Electronic structure of atomically precise graphene nanoribbons, ACS Nano **6,** 6930 (2012).

[31] L. Yang, C.-H. Park, Y.-W. Son, M. L. Cohen, and S. G. Louie, Quasiparticle Energies and Band Gaps in Graphene Nanoribbons, Phys. Rev. Lett. **99,** 186801 (2007).

[32] D. Prezzi, D. Varsano, A. Ruini, A. Marini, and E. Molinari, Optical properties of graphene nanoribbons: The role of many-body effects, Phys. Rev. B **77,** 041404 (2008).

[33] A. Ojanperä, A. V. Krasheninnikov, and M. Puska, Electronic stopping power from first-principles calculations with account for core electron excitations and projectile ionization, Phys. Rev. B **89,** 035120 (2014).

[34] S. Zhao, W. Kang, J. Xue, X. Zhang, and P. Zhang, Comparison of electronic energy loss in graphene and BN sheet by means of time-dependent density functional theory, J. Phys. Condens. Matter **27,** 025401 (2015).

[35] K. Balzer, N. Schlünzen, and M. Bonitz, Stopping dynamics of ions passing through correlated honeycomb clusters, Phys. Rev. B **94,** 245118 (2016).

[36] E. Gruber, R. A. Wilhelm, R. Petuya, V. Smejkal, R. Kozubek, A. Hierzenberger, B. C. Bayer, I. Aldazabal, A. K. Kazansky, F. Libisch, A. V. Krasheninnikov, M. Schleberger, S. Facsko, A. G. Borisov, A. Arnau, and F. Aumayr, Ultrafast electronic response of graphene to a strong and localized electric field, Nat. Commun. **7,** 13948 (2016).

[37] L. D. Landau, Zur theorie der Energieübertragung. II, Phys. Z. Sowjetunion **2,** 46 (1932); G. Zener, Non-adiabatic crossing of energy levels, Proc. R. Soc. A **137,** 696 (1932).

[38] F. Hofmann and M. Potthoff, Doublon dynamics in the extended Fermi-Hubbard model, Phys. Rev. B **85,** 205127 (2012).

[39] M. Moeckel and S. Kehrein, Interaction Quench in the Hubbard Model, Phys. Rev. Lett. **100,** 175702 (2008).

[40] M. Eckstein and M. Kollar, Nonthermal Steady States After an Interaction Quench in the Falicov-Kimball Model, Phys. Rev. Lett. **100,** 120404 (2008).

[41] See Supplemental Material at http://link.aps.org/supplemental/10.1103/PhysRevLett.121.267602 for additional information on the time-dependent Landau–Zener dimer model and additional simulation results that analyze the influence of reduced hopping rates at the edge of finite honeycomb clusters, as well as the effect of long range Coulomb interaction, which includes Ref. [42].

[42] T. Wassmann, A. P. Seitsonen, A. M. Saitta, M. Lazzeri, and F. Mauri, Structure, Stability, Edge States, and Aromaticity of Graphene Ribbons, Phys. Rev. Lett. **101,** 096402 (2008).

[43] M. Eckstein and P. Werner, Damping of Bloch Oscillations in the Hubbard Model, Phys. Rev. Lett. **107,** 186406 (2011).

[44] R. Rausch and M. Potthoff, Filling-dependent doublon dynamics in the one-dimensional Hubbard model, Phys. Rev. B **95,** 045152 (2017).

[45] K. Balzer and M. Bonitz, *Nonequilibrium Green's Functions Approach to Inhomogeneous Systems*, Lecture Notes in Physics Vol. 867 (Springer, Heidelberg, 2013).

[46] N. Schlünzen and M. Bonitz, Nonequilibrium Green functions approach to strongly correlated fermions in lattice systems, Contrib. Plasma Phys. **56,** 5 (2016).

[47] N. Schlünzen, J.-P. Joost, F. Heidrich-Meisner, and M. Bonitz, Nonequilibrium dynamics in the one-dimensional Fermi-Hubbard model: A comparison of the nonequilibrium Green functions approach and the density matrix renormalization group method, Phys. Rev. B **95,** 165139 (2017).

[48] M. Kollar, F. A. Wolf, and M. Eckstein, Generalized Gibbs ensemble prediction of prethermalization plateaus and their relation to nonthermal steady states in integrable systems, Phys. Rev. B **84,** 054304 (2011).

[49] E. Canovi, M. Kollar, and M. Eckstein, Stroboscopic prethermalization in weakly interacting periodically driven systems, Phys. Rev. E **93,** 012130 (2016).

[50] M. Rigol, V. Dunjiko, and M. Olshanii, Thermalization and its mechanism for generic isolated quantum systems, Nature (London) **452,** 854 (2008).

[51] M. Cramer, C. M. Dawson, J. Eisert, and T. J. Osborne, Exact Relaxation in a Class of Nonequilibrium Quantum Lattice Systems, Phys. Rev. Lett. **100,** 030602 (2008).

[52] I. Adamovich, S. D. Baalrud, A. Bogaerts, P. J. Bruggeman, M. Cappelli, V. Colombo, U. Czarnetzki, U. Ebert, J. G. Eden, P. Favia *et al.*, The 2017 plasma roadmap: Low temperature plasma science and technology, J. Phys. D **50,** 323001 (2017).

[53] Z. Idziaszek, T. Calarco, P. S. Julienne, and A. Simoni, Quantum theory of ultracold atom-ion collisions, Phys. Rev. A **79,** 010702(R) (2009).

[54] C. Weitenberg, M. Endres, J. F. Sherson, M. Cheneau, P. Schauß, T. Fukuhara, I. Bloch, and S. Kuhr, Single-spin addressing in an atomic Mott insulator, Nature (London) **471,** 319 (2011).

Supplementary material for manuscript "Doublon formation by ions impacting a strongly correlated finite lattice system"

K. Balzer, M.R. Rasmussen, N. Schlünzen, J.-P. Joost, and M. Bonitz

October 22, 2018

This supplement contains additional information on 1. the Landau–Zener dimer model, 2. additional simulation results that analyze the influenc of reduced hopping rates at the edge of finite honeycomb clusters, and 3. additional simulation results for the case of long range Coulomb interaction.

1 Time-dependent Landau–Zener model for a dimer interacting with a projectile

The Landau–Zener (LZ) model [1] has been applied to doublon formation in optical lattices where the lattice depth or interaction strength were changed adiabatically [2, 3]. Here we extend the model to a different situation: the interaction of a classical projectile with a strongly correlated dimer. In this case, the external potential varies non-monotonically (see Fig. 2.a of the main text) reaching its (negative) maximum when the projectile is in the cluster plane. Therefore, a LZ transition will occur only if the system remains in the upper state after a *two-fold (forward and backward) passage of the avoided level crossing.*

As explained in the paper this problem can be solved exactly by diagonalizing the time-dependent hamiltonian. The four energy eigenvalues of the dimer, $E_0 \leq E_1 \leq E_U \leq E_2$, before the impact are well known and given by

$$
\begin{aligned}
E_0 &= \frac{1}{2}\left(U - \sqrt{16J^2 + U^2}\right) \\
E_1 &= 0 \\
E_U &= U \\
E_2 &= \frac{1}{2}\left(U + \sqrt{16J^2 + U^2}\right)
\end{aligned}
$$

Furthermore, in the presence of the potential $W(t)$ the solutions become

$$
\begin{aligned}
E_0(t) &= R_1(t) \\
E_1(t) &= W(t) \\
E_U(t) &= R_2(t) \\
E_2 &= \frac{1}{2}\left(U + \sqrt{16J^2 + U^2}\right)
\end{aligned}
$$

where R_1 and R_2 are the first and second root of the third-order polynomial equation

$$
R^3 + (-2U - 3W)R^2 + (-4J^2 + U^2 + 2W^2 + 4UW)R - 2UW^2 + 4J^2U + 4J^2W - U^2W = 0. \tag{S1}
$$

The four solutions are shown in Figure 2.a of the main text versus $W(t)$. Starting in the triplet ground state (E_0), for $t = -\infty$, the dimer undergoes a transition to the second excited state (E_U) via an avoided crossing when $W(t)$ is switched on sufficiently fast. Using a reduced two-level Landau–Zener picture, the probabilities to find the system at maximum field $W(t)$ in states E_U and E_0 can be approximated by p and $(1 - p)$, respectively, where p denotes the LZ transition probability for a single diabatic passage of the crossing,

$$
p = \exp\left(-\frac{2\pi V^2}{\hbar|dE/dt|}\right), \quad V = \frac{1}{2}\min_{W(t)} E, \tag{S2}
$$

and $E = E_U - E_0$. To evaluate Eq. (S2) we use $\frac{dE}{dt} = \frac{dE}{dW}\frac{dW}{dt} = -\frac{dE}{dW}\frac{tW(t)}{\tau^2}$, set $t = \pm\tau$ [turning points of $W(t)$] and obtain

$$p = \exp\left(-\frac{2\pi\, e^{1/2}\, V^2 \tau}{\hbar W_0 |dE/dW|}\right). \tag{S3}$$

From Fig. 2.b of the main text, we furthermore observe that V and dE/dW are almost independent of U: $2V \approx 2.826J$ and $|dE/dW| \approx 0.976$, around $W(t) = -W_0$, therefore, the probability p only depends (for fixed U) on the duration τ of the excitation.

When the projectile is leaving the dimer, the system is then transferred via another avoided level crossing from E_0 at maximum field to E_U at zero field with a conditional probability $(1-p)p$ and from E_U at maximum field to E_U at zero field with a conditional probability $p(1-p)$. The overall probability that the dimer, for $t = +\infty$, remains in state E_U after the twofold (forward and backward) passage of the avoided level crossing can therefore be approximated by:

$$P_{E_0 \to E_U} = 2p(1-p), \tag{S4}$$

With insight from the dimer model, we find parameters for particularly efficient doublon formation in the 12-site cluster of Fig. 1 of the main text: (i) the optimal on-site interaction is $U^* \approx \frac{1}{2}W^*$, where $W^* = Z \cdot 10.8J$ denotes the maximum induced potential averaged over the sites A and B; thus $U^* = 5.4J$ for $Z = 1$ ($U^* = 10.8J$ for $Z = 2$), cf. the thin grey dash-dotted line in Fig. 2.b (2.c). (ii) For $U = U^*$, the velocity v_z^*, that maximizes d_{av}^∞, decreases linearly with Z. This follows from the Landau–Zener condition, $\frac{d}{d\tau}P_{E_0 \to E_U}(\tau) = 0$, which is solved by

$$(\tau^*)^{-1} = \frac{2\pi\, e^{1/2}\, V^2}{\hbar W_0 |dE/dt| \log(2)} \propto v_z^*. \tag{S5}$$

2 Impact of reduced hopping rates at the cluster edge

In the main text, we considered the intra-cluster hopping to be uniform and isotropic. However, it is well known that sites at the cluster edges may have a different connectivity or a specific saturation [4], leading to a modified hopping to neighboring sites. In Fig. S1, we analyze the effect of anisotropy on the doublon formation mechanism by reducing the hopping parameter between the A sites in the 12-site cluster of Fig. 1 of the main text to a value $J' < J$, according to a larger, spatial separation of the A sites compared to the distance AB. We find similar results for d_{av}^∞ as a function of the ion velocity v_z for a charge with $Z = 1$, where the doublon yield is rather low. On the other hand, for $Z = 2$, the doublon number appears even larger, as the reduction of the hopping makes the system more similar to the Hubbard dimer, where a maximum double occupation of 0.5 can be achieved by our excitation protocol as shown in Fig. 2.c, d.

3 NEGF results for Coulomb interaction. Correlation effects

In the main text, we presented in Fig. 4 results of nonequilibrium Green functions (NEGF) simulations for the asymptotic mean doublon number as a result of a sequence of excitations with Gaussian time-dependence that all occurred on one site. While this protocol is the easiest to test in an optical lattice setup, for ion stopping in a correlated finite condensed matter system the projectile-electron interaction is, of course, Coulombic. To test what is the effect of the long-range Coulomb interaction on the doublon formation scenario here we repeat the simulations using the Coulomb potential between ion and the electrons. The quantitative results depend on a large variety of parameters including the impact point (and its possilble variation) and the timing of the subsequent impacts. For better comparison with the results in the main text we retain equal time intervals between impacts and use the same impact point – in the cluster center, as in Fig. 1. The NEGF simulations used second order Born selfenergies within the generalized Kadanoff-Baym ansatz as described in Refs. [5, 6]. The high accuracy of these simulations was verified by benchmarks against DMRG results in Ref. [7]. The comparison with the results presented in Fig. 4 reveals that all trends reported in the main text remain valid also for Coulomb interaction. In fact, the long-range character of the projectile-electron interaction even enhances doublon production since the projectile interacts simultaneously with many electrons and thereby deposits more energy.

The figure also contains results of a time-dependent Hartree–Fock calculation (inset of lower figure) that exhibits completely wrong behavior as it neglects correlation effects that are of crucial importance for the present dynamics. Already the initial state (half filling) reveals the incorrect mean doublon number, $d_{\text{av}}^{\text{HF}}(0) = 0.25$ because, in Hartree–Fock, $d_i^{\text{HF}} = \langle \hat{n}_{i\uparrow}\rangle\langle \hat{n}_{i\downarrow}\rangle$, cf. Eq. (2). Thus, $d_{\text{av}}^{\text{HF}}$ only follows the one-particle density which
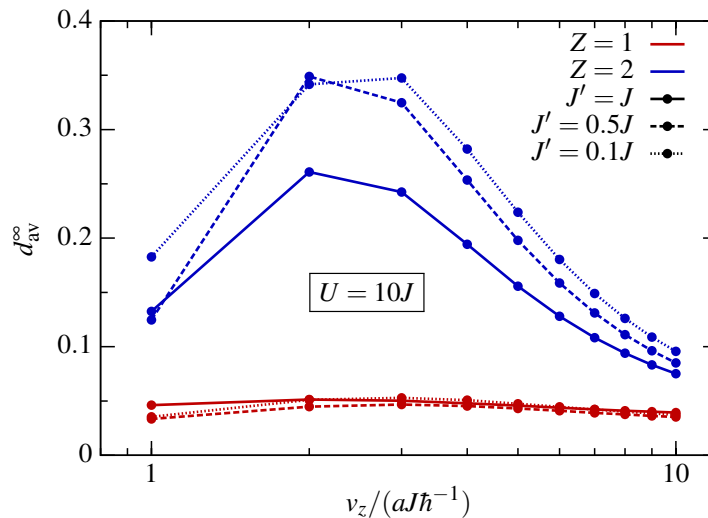
Figure S1: Ion-impact induced doublon formation in the two-dimensional Hubbard nano-cluster of Fig. 1 of the main text at $U = 10J$, where we have reduced the hopping amplitude between the A sites (along the edges of the 12-site cluster) from J to $J' = 0.5J$ (dashed) and $J' = 0.1J$ (dotted), respectively. The red (blue) lines show d_{av}^{∞} as function of the projectile's velocity v_z for a positive charge of $Z = 1$ ($Z = 2$). A reduced hopping at the edges favors doublon excitation in finite clusters, in particular for high projectile charge, except for very small velocities.

exhibits a completely different time dependence than the correlated doublon number, cf. Fig. 1.a. This confirms that the present scenario, in particular, the Landau–Zener transition (see above) is a correlation effect.

References

[1] L.D. Landau, Zur Theorie der Energieübertragung. II, Phys. Z. Sowjetunion **2**, 46 (1932); G. Zener, Non-adiabatic crossing of energy levels, Proc. R. Soc. A **137**, 696 (1932).

[2] M. Schecter and A. Kamenev, Forming doublons by a quantum quench, Phys. Rev. A **85**, 043623 (2012).

[3] A.R. Kolovsky and D.N. Maksimov, Mott-insulator state of cold atoms in tilted optical lattices: Doublon dynamics and multilevel Landau-Zener tunneling, Phys. Rev. A **94**, 043630 (2016).

[4] T. Wassmann, A.P. Seitsonen, A.M. Saitta, M. Lazzeri, and F. Mauri, Structure, Stability, Edge States, and Aromaticity of Graphene Ribbons, Phys. Rev. Lett. **101**, 096402 (2008).

[5] K. Balzer and M. Bonitz, Nonequilibrium Green's Functions Approach to Inhomogeneous Systems, Lecture Notes in Physics, Springer, vol. 867 (2013).

[6] N. Schlünzen, S. Hermanns, M. Bonitz, and C. Verdozzi, Dynamics of strongly correlated fermions – ab initio results for two and three dimensions, Phys. Rev. B **93**, 035107 (2016).

[7] N. Schlünzen, J.-P. Joost, F. Heidrich-Meisner, and M. Bonitz, Nonequilibrium dynamics in the one-dimensional Fermi-Hubbard model: A comparison of the nonequilibrium Green functions approach and the density matrix renormalization group method, Phys. Rev. B **95**, 165139 (2017).
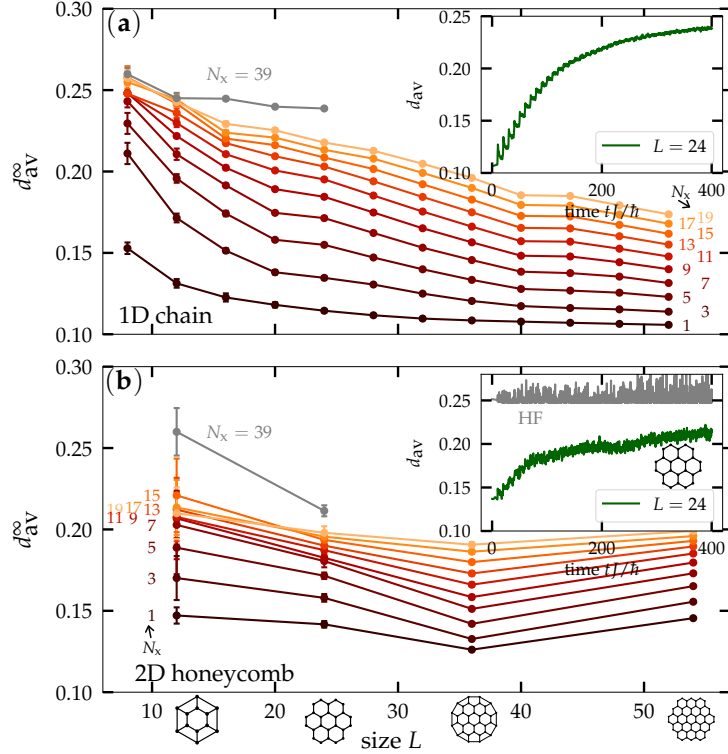
Figure S2: Asymptotic mean double occupation for a charged projectile interacting by a Coulomb potential with all electrons of the system for $U = 4J$. **a)** 1D chains and **b)** 2D half-filled honeycomb clusters of different size L. The number of excitations, N_x, which are performed in the cluster center, is indicated in the figure. All main trends are as for Gaussian-type excitation on a single site (Fig. 4), but the doublon number is enhanced. Results of NEGF simulations (second order Born selfenergies) with the HF-GKBA, for details see Refs. [5, 6]. Insets show the time-dependence $d_{av}(t)$, for $L = 24$ and $N_x = 40$. The grey curve in the lower picture corresponds to a time-dependent Hartree–Fock calculation.
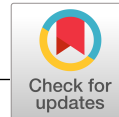
Contributions to
Plasma Physics

Time-dependent simulation of ion stopping: Charge transfer and electronic excitations

N. Schlünzen[1] | **K. Balzer[2]** | **M. Bonitz[1]** | **L. Deuchler[1]** | **E. Pehlke[1]**

[1]Institut für Theoretische Physik und Astrophysik, Christian-Albrechts-Universität zu Kiel, Kiel, Germany

[2]Rechenzentrum, Christian-Albrechts-Universität zu Kiel, Kiel, Germany

*Correspondence
N. Schlünzen, Institut für Theoretische Physik und Astrophysik, Christian-Albrechts-Universität zu Kiel, Leibnizstraße 15, 24098 Kiel, Germany.
Email: schluenzen@theo-physik.uni-kiel.de

The energy loss of charged particles in matter has been studied for many decades, both, analytically and via computer simulations. While the regime of high projectile energies is well understood, low energy stopping in solids is more challenging due to the importance of non-adiabatic effects and electronic correlations. Here we consider two problems: the charge transfer between substrate and projectile and the role of electronic correlations, specifically formation of doubly occupied lattice sites in the material during the stopping process. The former problem is treated by time-dependent density functional theory simulations and the latter by non-equilibrium Green functions.

KEYWORDS
charge transfer, doublon formation, nonequlibrium Green functions, stopping power, TDDFT simulations

1 | INTRODUCTION

The impact of ions on a solid surface is of prime importance for plasma physics and surface science and has been studied for decades, both, experimentally and theoretically. The theoretical approaches include scattering theory[1] or uniform electron gas models.[2] Here the primary input is the dynamic inverse dielectric function (or dynamic structure factor, DSF) for which electron gas models or recently developed quantum Monte Carlo methods[3] can be applied. Recently, also ab initio simulations of ion stopping based on time-dependent density functional theory (TDDFT) were reported for metals,[4] semimetals,[5] or boron nitride and graphene sheets[6] and other materials. These simulations account primarily for valence–electron excitation. Good results for the stopping power of high energy ions in matter are also provided by the SRIM code[7] that uses the binary collision approximation in combination with an averaging over a large range of experimental situations. Stopping power simulations have also been extensively applied for plasmas using kinetic equations. Here, again, the energy loss is usually computed by integrating of the DSF of the plasma which can be understood as a linear-response approach. At the same time, time-resolved simulations have been performed based on quantum kinetic theory[8,9] which allow one to go beyond the linear response approximation. This is of particular importance in case of strong excitation or for the treatment of fast non-adiabatic processes in the target.

Aside from high-density plasmas (warm dense matter), for example, Zylstra et al.[10] and Kremp et al.,[11] ion stopping is also of central relevance for low-temperature plasmas in contact with a solid surface. This latter system is in the focus of the present paper. In these plasmas most of the ions are usually in equilibrium with the neutral gas and are at room temperature. In addition, close to the surface (in the plasma sheath) ions may be accelerated by the sheath electric field up to keV energies, for a recent overview on plasma–surface simulations see Bonitz et al.[12] Even though the overall behavior of the stopping power as a function of ion impact energy is understood, for low-temperature plasmas special questions remain open. This includes: how does charge transfer between substrate and ion occur (neutralization of projectile)? How does it depend on the impact energy

and on the substrate material? In what distance from the target does it occur? Furthermore, how does the stopping behavior change in the case of nontrivial targets that either have a complicated surface morphology, nanostructuring or exhibit strong electronic correlations? Answers to these questions are not only of fundamental interest but are also important for applications as they may give rise to new plasma–surface combinations with non-traditional properties.

The goal of the present paper is to address some of these questions that are of relevance for low-temperature plasmas. We present time-resolved non-adiabatic simulations of ion stopping that are capable of resolving the electronic processes in the projectile and in the target. In particular, we concentrate on two questions. The first is the charge transfer between a metallic substrate and an incoming proton which we treat via TDDFT (c.f., Section 2). The second question is the change of stopping power in correlated nano-scale materials. Here we apply non-equilibrium Green functions (NEGF)–Ehrenfest simulations, extending the recent work of Balzer et al.[13,14] The NEGF approach is introduced in Section 3 and applied to finite honeycomb Hubbard clusters. Finally, in Section 4 we discuss how the two complementary approaches might be combined in the future in order to achieve a comprehensive description of ion and electron dynamics at the plasma–solid interface.

2 | TDDFT SIMULATIONS OF CHARGE TRANSFER AND ION STOPPING

In this section we present ab initio molecular dynamics (MD) simulations for the neutralization of an ion, H^+, incident on a simple metal surface, Al(111), which we have carried through using the Octopus code.[15–17] The metal substrate is represented by a cluster. The coupled system of the ions and the electrons is described in an approximate way by using Ehrenfest dynamics.[15,18] The Al atomic coordinates will be kept fixed during the time-dependent simulation, but this restriction could easily be lifted without any significant additional computational effort. The electrons are described within TDDFT.[15,19,20] The time-dependent Kohn–Sham equations, which in case of a local potential v read (in atomic units)

$$i\frac{\partial \psi_j(\mathbf{r}, t)}{\partial t} = -\frac{1}{2}\nabla^2 \psi_j(\mathbf{r}, t) + \left(v(\mathbf{r}, t) + \int d^3\mathbf{r}' \frac{n(\mathbf{r}', t)}{|\mathbf{r} - \mathbf{r}'|} + v_{XC}(\mathbf{r}, t)\right)\psi_j(\mathbf{r}, t),\tag{1}$$

are integrated together with the Ehrenfest equation of motion. The electron density is calculated from the sum over the probability densities of the time-dependent Kohn–Sham states that are occupied in the initial state, which itself is constructed by combining the separately calculated electronic Kohn–Sham ground-states of the metal atom cluster and the incident particle. The adiabatic approximation is applied to the exchange–correlation (XC) potential v_{XC}, and, in addition, an approximate XC functional from ground-state DFT is used:

$$v_{XC}(\mathbf{r}, t) \approx v_{XC}^{approx}([n(.,t)], \mathbf{r}) .\tag{2}$$

In case of a proton incident on a metal surface, the electronic system is initially strongly locally excited. This is different from the case of an atom, for example H^0, scattered at the surface.[21] The adiabatic approximation of the XC potential will be a more serious approximation in case of the strongly locally electronically excited system. In particular, Auger transitions are not expected to be accounted for.[22,23] However, this is not a major restriction in case of the present simulations, because Merino et al.[24] have concluded from their study using a model Hamiltonian that at the low H^+ kinetic energies considered here (below keV) the charge transfer is dominated by resonant processes. Finally, we note that the TDDFT–MD simulations we present below refer to the valence electrons only. The core electronic states of the metal atoms have been incorporated into an ionic pseudopotential. Moreover, also the *s*-wavefunction of the H-atom is pseudoized.

Important insight into proton neutralization at Al surfaces has been achieved by various authors using rate equations[25,26] or (Newns–Anderson-type) model Hamiltonians.[24,27–30] While strong correlation effects can be incorporated into model Hamiltonians, the advantage of the direct simulation of the charge transfer process using a TDDFT code like Octopus lies in the ab initio determination of the time-dependent electron density (i.e., screening and charge transfer), the effective potential, and hence the time-dependent electron tunnelling probabilities.

TDDFT–MD simulations of ions accounting for resonant charge transfer have been carried out by other authors before, for example, for the interaction of Li^+ with an Al_{58}-cluster by Moss et al.,[31] for a proton scattered at a Li_4-cluster by Castro et al.,[32] and collisions with carbon nanostructures by Krasheninnikov et al.,[33] or DNA fragments by Seraide et al.,[34] or graphene fragments by Bubin et al.,[35] or graphene and boron nitride by Zhao et al.,[6] and for Cl^- incident on a $MoSe_2$ monolayer by Wang et al.[36] This has lead to many significant scientific advances. However, there are open questions concerning, for example, the resonant charge transfer in particular at low kinetic energies and the effect of the approximation to the XC-potential.[37,38] Moreover, technological advances allow for the treatment of more extended systems. Here we present a TDDFT-MD simulation of the charge transfer and energy dissipation for an H^+ ion with initial kinetic energy 2 eV ... 50 eV incident on an Al(111) metal surface (modelled by a cluster), and compare to the energy dissipation in case of an incident H-atom.

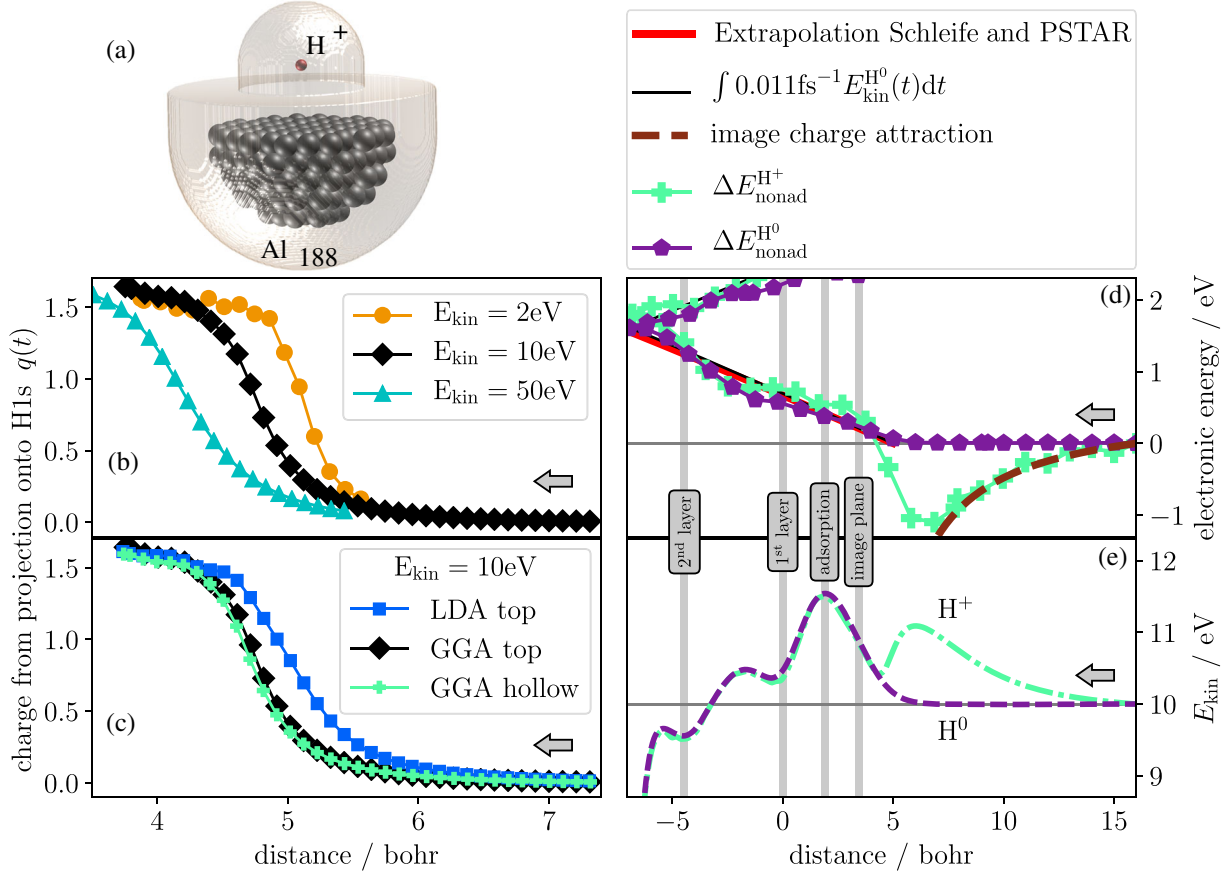Technical details of the TDDFT-MD simulations are summarized below.

FIGURE 1 (a) Visualization of Al-cluster and simulation box in case of H–Al on-top collision; graphic produced using the vmd software.[40] (b) Charge transfer from the Al(111) target to the H$^+$ projectile incident on an Al on-top site as obtained from the TDDFT-MD simulations (Equation (3)). The uppermost Al-layer is located at $z = 0$ bohr. (c) Comparison of charge transfer for H$^+$-projectile incident on an Al-hollow or on-top site and comparison between GGA and LDA results. (d) Comparison of the variation of the electronic excitation energy (Equations (4) and (5)) and (e) the kinetic energy of the H$^+$ or H^0 projectile incident on the Al(111) fcc hollow-site. The H penetrates the surface and propagates through the first two layers inside the Al-cluster until it is reflected at the third Al-layer

2.1 | Computational details

The Octopus code (version 6) by Rubio et al.[15–17] has been employed for all TDDFT-MD simulations presented in this paper. The adiabatic approximation is applied to v_{xc}, together with the Perdew–Burke–Ernzerhof (PBE) generalized gradient approximation (GGA) for exchange and correlation from ground-state DFT (PBE-GGA)[39]. The Al(111) surface is modelled by a cluster containing either 172 Al-atoms (for H$^+$ incident at the Al(111) hollow site) or 188 Al-atoms (for H$^+$ incident at the on-top site). The Al-clusters have been created by cutting out half-spheres from a (111)-oriented substrate with lattice constant of 4.047 Å as determined from ground-state DFT calculations with the convergence parameters and pseudopotential as described below. The uppermost Al-layer has been fixed and an ionic relaxation of the remaining Al-atoms has been performed. The simulation has been performed inside a user-defined region (see Figure 1a) that fits into a cube with edge size 60 bohr, and a minimum distance between atoms and the boundary of the user-defined region of 12 bohr. The FFT for solving the Poisson equation requires a box with twice the edge length of the cube described above. Ions are represented by norm-conserving Troullier–Martins pseudopotentials[41] created with FHIPP.[42] In case of the Al atom, 10 electrons are treated as frozen-in core states. The non-local pseudopotential is p-local in case of Al and s-local in case of H. The following cut-off radii have been used for the creation of the pseudopotentials: $r_{1s}^{Al} = 1.791$ bohr, $r_{2p}^{Al} = 1.974$ bohr, $r_{3d}^{Al} = 2.124$ bohr, $r_{1s}^{H} = 1.276$ bohr, $r_{2p}^{H} = 1.276$ bohr. Fourier components of the pseudopotentials beyond the cut-off determined by the real-space mesh size are filtered using the method of Tafipolsky and Schmid[43] as supplied within Octopus. The Kohn–Sham wavefunctions are sampled on a real-space grid. We have used a spacing $\Delta x = 0.5$ bohr. As a test, we have carried through simulations with either smaller spacings ≥ 0.4 bohr or larger cluster (302 atoms for H$^+$ towards the on-top position). The electronic ground state of the Al-cluster has been determined using a Methfessel–Paxton smearing[44] with a small smearing parameter of 20 meV.

In case of the H$^+$ projectile, the bare H-pseudopotential has been added to the simulation box. In case of the H^0 projectile, in addition the spin-polarized ground-state Kohn–Sham wavefunction of the H-atom has been calculated and added to the set of wavefunctions. The initial distance between target and projectile is set to 16 bohr. An initial velocity has been assigned to the

projectile, corresponding to a kinetic energy of 2, 10, or 50 eV. The initial-state Kohn–Sham wavefunction of the H-atom has been multiplied with a boost phase factor.[22,45] The Al atomic positions were kept fixed during the simulations. A time step of 0.02 atomic time units (0.5 attoseconds) has been used for the propagation of the Kohn–Sham wavefunctions. The exponent in the propagator is approximated using the exponential midpoint rule, and a fourth-order Taylor expansion of the exponential is used as implemented in Octopus[46].

2.2 | Charge transfer H$^+$/Al(111)

The charge transfer from the Al-substrate to the H$^+$ projectile as derived from the TDDFT-MD simulations is shown in Figure 1b for the initial condition that the projectile is incident on the on top-site of the Al(111) surface. Only the incoming part of the trajectory—before the H–Al head-on collision—is analysed. As the eigenvalue of the hydrogen 1 s level is located inside the valence band of bulk Al, resonant neutralization via elastic tunnelling of the electron from the metal to the proton is possible.[24] In order to quantify the charge transfer $q(t)$ to the incident H$^+$ ion we project the time-dependent Kohn–Sham wavefunctions $|\psi_j(t)\rangle$ onto the H1s-orbital $|1\,s\rangle$. Including the occupation f_j this yields the local charge of the H-ion

$$q(t) = \sum_j f_j \, |\langle 1s|\psi_j(t)\rangle|^2 \,. \tag{3}$$

In Figure 1b the transferred charge is plotted as a function of the distance of the projectile from the Al-surface. The neutralization of the proton occurs at a distance between 4 and 6 bohr in front of the surface, depending on proton velocity. This is consistent with the respective distance obtained by Jouin and Gutierrez.[26] The H$^+$ neutralization has been reported in the literature[29] to be very efficient. As the slower projectile spends a longer time at a certain separation in front of the metal surface, the neutralization of the slower particle occurs at larger separation from the surface. The charge on the H finally exceeds a value of 1.0. Negatively charged hydrogen is well known, for example, in case of metal hydrides.[47] The quantitative value (as compared to other definitions of local ionic charges) may be partially affected by the overlap of the H1s wavefunction with the electronic states of the Al-cluster. The data may be useful for the parametrization of the H–Al interaction in many-particle model Hamiltonians.

As can be read from the results for the charge transfer to a proton with initial kinetic energy of 10 eV shown in Figure 1c, the charge-transfer dynamics is rather insensitive to the point of incidence on the Al-surface. This was to be expected in view of the small corrugation of the effective potential and electron density far above the metal surface layer. However, we note a significant sensitivity of the charge-transfer dynamics on the choice of the approximation—here local-density approximation (LDA) versus PBE-GGA—applied to the electronic ground-state XC-energy functional. We suggest that this may be due to differences in the description of the electronic ground state of the H-atom.

There is a well-known difficulty to describe long-range correlations with semilocal approximations for the XC energy functional in ground-state calculations[48]. For example, when describing the dissociation of H$_2$ with a semilocal XC-functional, an artificial transition to a spin-polarized system is in general used to describe total energies at large atom separation.[48,49] In time-dependent simulations of H^0 incident on a metal surface, the H^0 atom has been assumed to be electronically spin-polarized at large separations from the surface and loses spin polarization when interacting with the surface.[50,51] We also use an initially spin-polarized H^0-atom in the present simulations in Section 2.3. In case of H$^+$ incident on the Al-cluster in the present calculation the initial configuration is spin-unpolarized and there is no term in the Hamiltonian that could break this symmetry during time evolution. We therefore suspect that the exchange-correlation effects are not well accounted for by the present spin-unpolarized semilocal approximation to v_{XC}, and more advanced approximations would be desirable.[48] For the model-Hamiltonian calculations, the problem of correlation has been approached using, for example, as approximation for the correlation in multiple-level systems $U \to \infty$.[30]

It is argued that no electron–electron relaxation (Auger effect) occurs when the present adiabatic XC-functionals are employed.[22,23] Theoretical work on the He$^+$/Al system shows that in case of the projectile velocity range applied here, the Auger channel is the relevant one in order to be able to describe the experiment.[52–55] First test calculations within the framework described above for a He$^+$ ion ($E_{kin} = 2$ H) incident on an Al(111) surface, confirm that Auger processes do not show in the calculations performed using an adiabatic GGA XC-functional. Hence, other methods beyond the TDDFT-MD with adiabatic GGA have to be used if Auger transitions are to be considered.

2.3 | Energy dissipation for H$^+$, H^0 projectiles penetrating the Al-surface

TDDFT-MD simulations of an H$^+$ or an H^0 projectile starting 16 bohr above the hollow site of the Al(111) surface facet of the Al-cluster with an initial kinetic energy of 10 eV show—in agreement with similar previous TDDFT-MD simulations for H^0 by Lindenblatt et al.[21,56]—that the projectile (in case of H$^+$ after neutralization) penetrates the Al-surface. It propagates

through the top two metal layers before it is reflected at the third atomic layer in a head-on collision. In Figure 1d the variation of the electronic excitation energy with respect to its initial value is plotted versus the distance of the projectile from the surface (defined by the position of the top layer Al atoms). In case of the uncharged H^0 this equals the electronically nonadiabatic energy, which is defined by the difference between the electronic energy in the time-dependent simulation and the energy of the electronic ground state at frozen-in atomic coordinates $R(t) = (\mathbf{R}_1(t), ..., \mathbf{R}_N(t))$:

$$\Delta E_{\text{nonad}}^{H^0} := E_{\text{td}}(t) - E_{\text{gs}}(R(t)). \tag{4}$$

In case of a proton incident on the surface, in addition the energy needed to ionize an H-atom, i.e. to transfer one electron from the H^0-atom to the Al-cluster, has been subtracted for the sake of easier comparison to the case of H^0:

$$\Delta E_{\text{nonad}}^{H^+} := E_{\text{td}}(t) - E_{\text{gs}}(R(t)) - (E_{\text{ion}}(H) - W_A(\text{Al-cluster})). \tag{5}$$

All energies refer to DFT calculations with PBE-GGA applied to v_{XC}. In Figure 1e the kinetic energies of the H^+ and H^0 projectiles are visualized. The neutral H^0 projectile approaches the surface, accelerates inside the chemisorption well and transverses the adsorption position (at 1.89 bohr) where it gains the adsorption energy of 1.93 eV. This results in an increase of the kinetic energy of the projectile, however, part of the kinetic energy of the projectile is dissipated into electron–hole pair excitations.[21] The charged projectile H^+ is accelerated towards the surface due to the image-charge attraction.[57] The image plane of Al(111) is located at $z_{\text{image}} = 3.49$ bohr in front of the surface, according to Chulkov and Silkin.[58] The image-charge potential $1/(4[z - z_{\text{image}}])$ that would be induced in case of an infinitely large surface slab is included in Figure 1d by the brown dashed curve. In case of the finite cluster utilized here, the attractive potential will deviate from the simple image-potential form. The kinetic energy gain of about 0.54 eV due to attraction by the image charge of a proton starting infinitely far away from a plane surface and reaching a surface separation of 16 bohr is not accounted for in our calculation. As can be seen by comparing Figure 1d and e, while the kinetic energy increases due to image-charge attraction, the electronic excitation energy decreases by about the same amount (brown dashed curve in Figure 1d). This is in line with the conservation of total energy. Note that E_{gs} in Equation (5) refers to the electronic ground state, that is, an uncharged H^0. Thus the change of electrostatic energy due to polarization of the Al-cluster by the proton is included in $\Delta E_{\text{nonad}}^{H^+}$. At a surface separation between 4.5 and 6.0 bohr, the partially charged H^+ loses kinetic energy. This region coincides with the region where the charge transfer occurs (see Figure 1c). The deacceleration of the projectile is ascribed to Coulomb repulsion between the projectile and the Al-cluster. In case of an infinitely large substrate and in the adiabatic limit the charge transferred to the projectile will, in the electrostatic case, come from infinity. Hence we have to be aware that the above Coulomb repulsion effect will be limited to the finite-size clusters. The cluster-size convergence is expected to be slow. Thus we cannot easily generalize the result of the rather similar variation of the kinetic energy of the H^+ and H^0 projectile at distances smaller than 4.5 bohr from our cluster calculation to the case of a metallic half space. However, as far as the interaction with the Al-cluster used in the simulations is concerned, the H^+ loses its charge in front of the surface and the variation of the electronic excitation energy comes out very similar when the projectile propagates within the metal cluster. This is in line with the observation that final projectile charges do not depend on the charge state of the incident particle for the given H^+/Al system and velocity range by, for example, Zimny et al.,[25] Jouin et al.,[26] and Torralba et al.[29] The similar behavior between H^+ and H^0 incident on, for example, a graphene sheet has been noted before in TDDFT-MD calculations by Krasheninnikov et al.[33]

For clarity we point out that, while not immediately deducable from Figure 1d and e, the neutralization of the H^+ in front of the surface is associated with a strong energy transfer into hole excitations of the metal substrate as the hole tunnels from the proton into the metal.

Stopping power for protons in bulk Al has been discussed and analysed in detail by several authors using TDDFT-dynamics[4,59,60] or linear-response theory.[61,62] A neutral hydrogen atom impinging on the Al(111) surface and penetrating into the crystal has been studied before in Lindenblatt et al.[21,56] Theory for bulk electronic stopping agrees with experimental data, especially in the low-energy range subject to the present investigation. For comparison, in Figure 1d we include the stopping power derived from a linear-friction ansatz[21] (black curve) as well as an extrapolation of data from Schleife et al.[60] and PSTAR[63] (red curve). The starting point of both curves is chosen to coincide with the commencing electron–hole pair creation. Thus we agree with previous work[4,21,59–62] that electronic stopping of hydrogen (after neutralization) within the Al-metal can reliably be simulated by TDDFT. At the same time, many questions remain to be solved, for a discussion see Section 4.

3 | NEGF–EHRENFEST APPROACH TO ION STOPPING IN CORRELATED MATERIALS

3.1 | Theory overview

A method that allows for a systematic treatment of electronic correlations in a solid-state material and, at the same time, of inhomogeneity effects induced by an external excitation are (real-time) NEGF.[64–67] The central quantity is the one-particle

NEGF

$$G_{ij\sigma}(t,t') = -i\hbar\langle T_C c_{i\sigma}(t)c_{j\sigma}^\dagger(t')\rangle \tag{6}$$

which appears as a two-time generalization of the one-particle density matrix $\rho_{ij\sigma}(t) = -\frac{i}{\hbar}G_{ji\sigma}(t,t^+)$, where the notation t^+ means $t = t + \varepsilon$ with $\varepsilon_{>0} \to 0$, and G determines all time-dependent one-particle observables. In the definition of the NEGF, $c_{i\sigma}^\dagger$ ($c_{i\sigma}$) are creation (annihilation) operators in the Heisenberg picture for electrons in a single-particle orbital $|i\rangle$ with spin projection σ, and the expectation value is computed with the equilibrium density operator of the system. Furthermore, times are running along the Keldysh contour C, with T_C denoting ordering of operators on C.[65,68,69] The equations of motion for the NEGF are the two-time Keldysh–Kadanoff–Baym equations (KBE)[65]

$$\sum_k [i\hbar\partial_t\delta_{ik} - \bar{h}_{ik\sigma}(t)]G_{kj\sigma}(t,t') = \delta_C(t-t')\delta_{ij} + \sum_k \int_C ds \Sigma_{ik\sigma}(t,s)G_{kj\sigma}(s,t') \tag{7}$$

$$\sum_k G_{ik\sigma}(t,t')[-i\hbar\overleftarrow{\partial}_{t'}\delta_{kj} - \bar{h}_{kj\sigma}(t')] = \delta_C(t-t')\delta_{ij} + \sum_k \int_C ds G_{kj\sigma}(t,s)\Sigma_{ik\sigma}(s,t') \tag{8}$$

a set of two integro-differential equations, where the Hamiltonian $\bar{h}(t)$ contains the one-particle kinetic, potential and mean-field energy, whereas correlation effects are contained in the two-time selfenergy $\Sigma(t,t')$ that can be approximated as a functional of the NEGF according to a diagrammatic many-body perturbation expansion. Note, that in the given form of the KBE we do not consider spin changes and assume a paramagnetic system.

As an approximation for the selfenergy beyond the Hartree–Fock (HF) level (for which $\Sigma = 0$ and mean-field contributions are incorporated in $\bar{h}(t)$), we consider in the present work the second-order Born (2B) approximation,[64,65] which conserves total energy, particle number and momentum and is specified in Equation (12) below for the case of a local Hubbard-type interaction. For more advanced expressions for the selfenergy, such as GW, T matrix or third order, for example, Schlünzen et al.[70,71] In addition to the use of the 2B approximation, we simplify the solution of the KBE in one of two ways:

i we apply the generalized Kadanoff–Baym ansatz (GKBA) with HF propagators, as proposed in Ref. [72], to reduce the computational effort of solving the KBE (7) and (8) from a scaling $\sim T_{\text{tot}}^3$ with the total simulation duration to $\sim T_{\text{tot}}^2$, see Lipavský et al.[73] for details,

ii we consider the selfenergy to be local in space, $\Sigma_{ij\sigma}(t,t') = \delta_{ij}\Sigma_{i\sigma}(t,t')$, for which the KBE can be solved very efficiently using the auxiliary-Hamiltonian representation introduced in Hermanns et al.[74]

Both strategies allow us to reach sufficiently long propagation times that are needed to treat electronic excitations during charged-particle stopping scenarios with sub-keV impact energies. To include an external moving charge (projectile) into the KBE simulations, we choose an NEGF–Ehrenfest approach which was first presented in Balzer et al.[13] and applied in Balzer et al.[14] and Bonitz et al.[75] In the course of this, the trajectory $r(t)$ of the projectile is calculated on the fly by Ehrenfest dynamics using a classical potential that is derived from the Coulomb interaction between the projectile's charge Ze and the time-dependent total charge density $\rho(R,t)$ of all constituents of the material.

As a prototype model for a correlated material, we consider single-band Hubbard nano clusters with a 2D honeycomb structure, the interparticle distance $a_0 = 1.42$ Å and L sites that have spatial coordinates R_i. With a nearest-neighbour hopping J and an on-site Coulomb interaction U, the cluster Hamiltonian reads

$$H = -J\sum_{\langle i,j\rangle\sigma} c_{i\sigma}^\dagger c_{j\sigma} + U\sum_i \left(n_{i\uparrow} - \frac{1}{2}\right)\left(n_{i\downarrow} - \frac{1}{2}\right) + \sum_{i\sigma} W_i(t)c_{i\sigma}^\dagger c_{i\sigma} \tag{9}$$

where $n_{i\sigma} = c_{i\sigma}^\dagger c_{i\sigma}$ is the electron density, and $\langle i,j\rangle$ indicates summation over nearest neighbours. In our calculations, we chose the hopping parameter as $J = 2.8$ eV, which results from a mapping of ab initio calculations to graphene-type systems in the tight-binding approximation.[76,77] This choice provides a typical setting with a realistic synchronization of the projectile–lattice time scales. Furthermore, the last term of Equation (9) describes the Coulomb interaction of the lattice electrons with the projectile in terms of a time-dependent on-site energy

$$W_i(t) = -\frac{1}{4\pi\varepsilon_0}\frac{Ze^2}{|r(t) - R_i|}. \tag{10}$$

Throughout, we consider the case of half filling and measure times in units of $t_0 = \hbar/J$. Inside the KBE, the many-body Hamiltonian (9) translates into a one-particle Hamiltonian

$$\bar{h}_{ij\sigma}(t) = -J\delta_{\langle i,j\rangle} + \left[U\left(\langle n_{i\sigma}(t)\rangle - \frac{1}{2}\right) + W_i(t)\right]\delta_{ij}. \tag{11}$$

Note that, for Hubbard systems, the Fock terms of the mean field are absent. In addition, we employ the second Born (2B) selfenergy of the form

$$\Sigma_{ij\sigma}^{2B}(t, t') = \hbar^2 U^2 [G_{ij\sigma}(t, t')]^2 G_{lj\sigma}(t', t) \tag{12}$$

where, in the special case of a "local" selfenergy (local 2B), the site-off-diagonal components are neglected, as mentioned above. The trajectory along which the projectile passes through the cluster is calculated from the potential

$$V(t) = \frac{Ze^2}{4\pi\varepsilon_0} \sum_i \frac{\rho(R_i, t)}{|r(t) - R_i|} \tag{13}$$

where $\rho(R_i, t) = -\sum_\sigma \left(\langle n_{i\sigma}(t) \rangle - \frac{1}{2} \right)$ is the total charge density on the cluster, assuming a positive background that results from the atomic cores in a real material. As initial conditions we use $r(t_{-\infty}) = (x_0, y_0, -z_0)$, where z_0 is chosen such that the projectile penetrates the cluster at half the simulation time, and $dr/dt(t_{-\infty}) = (0, 0, v_0)$, performing calculations for a perpendicular incidence, with the honeycomb cluster located in the xy-plane.

A central observable which characterizes the stopping process is the energy loss of the projectile (P),

$$S = E_{kin}^P(t_{+\infty}) - E_{kin}^P(t_{-\infty}) \tag{14}$$

where $E_{kin}^P(t_{-\infty}) \equiv E_{kin,0}^P = \frac{1}{2}mv_0^2$ and $E_{kin}^P(t_{+\infty})$ denote the initial and final kinetic energies, before and after passing through the cluster, respectively. Further important observables are the different energy contributions on the cluster, that is, the kinetic, potential, and interaction energy:

$$E_{kin}(t) = \Re \left[-J \sum_{ij} \delta_{\langle i,j \rangle} \rho_{ji}(t) \right], \qquad E_{pot}(t) = \Re \left[\sum_i W_i(t) \rho_{ii}(t) \right] \qquad \text{and} \tag{15}$$

$$E_{int}(t) = \frac{i\hbar}{2} \Im \left[\sum_{ij} \int_C ds \Sigma_{ij}(t, s) G_{ji}(s, t^+) \right] \tag{16}$$

where the latter is decomposed into mean field (Hartree–Fock) and correlation energy according to $E_{HF}(t) = \Re[\sum_i U \rho_{ii}(t)]$ and $E_{corr}(t) = E_{int}(t) - E_{HF}(t)$. Furthermore, we analysed the evolution of the local and cluster-averaged double occupation,

$$d_i(t) = \langle n_{i\uparrow}(t) n_{i\downarrow}(t) \rangle = -\frac{i\hbar}{U} \sum_k \int_C ds \Sigma_{ik}(t, s) G_{ki}(s, t^+), \quad d_{avg}(t) = \frac{1}{L} \sum_{i=1}^L d_i(t) \tag{17}$$

where spin indices are omitted.

3.2 | Time-resolved energy exchange between projectile and cluster

Below we present numerical results of the KBE coupled to the semiclassical projectile dynamics, as introduced in Balzer et al.[13] We consider two honeycomb clusters that are described by the Hubbard model (9) containing $L = 24$ and $L = 54$ sites, respectively, see Figure 4 for a sketch of the former. We start by giving an overview of the general dynamical behavior of correlated 2D systems during the impact of a charged particle. For the 54-site cluster, the results are shown in Figure 2 for the case of a proton, penetrating the lattice at the centroid point C with $\mathbf{R}_C = \left(-\frac{1}{6}a_0, -\frac{\sqrt{3}}{3}a_0, 0 \right)$. We apply the NEGF approach including the GKBA, as introduced in Section 3.1, to study the coupled projectile–lattice dynamics. Thereto, we first generate the correlated ground state of the electrons on the lattice via an adiabatic-switching procedure, where the interaction U of the system is slowly ramped to its final value during the initial time-propagation interval (see Schlünzen and Bonitz[67] for details). We consider the case of $U = 4\,J$—a configuration that allows for the build-up of correlations. Once the interacting ground state is reached, the projectile dynamics starts by solving the coupled Equations (9) to (13). For a broad range of projectile energies, 10^{-1} keV/u $< E_{kin,0}^P < 10^3$ keV/u, we compute the dynamical evolution of relevant energies of both, the lattice electrons and the proton. The results are shown in Figure 2. For better comparability, all quantities are plotted as a function of the time-dependent projectile position $z^P(t)$. To further illustrate the dependence of the relevant observables on the ion impact energy we show slices for three different ion–surface distances, $z^P/a_0 = 0, 2.5, 5$, corresponding to the impact time ($z^P = 0$) and two slightly later times, in Figure 3.

Consider first the *kinetic energy of the projectile* that is shown in part (e) of Figures 2 and 3. The energy loss of the projectile to the cluster can be seen from a vertical cut through Figure 2e at large z^P. One clearly recognizes the familiar bell-shaped dependence on the impact energy with a single peak around 10 keV/u. On the other hand, looking at horizontal cuts provides the time dependence of the proton energy: before the impact (negative z^P) the proton gains energy because it is attracted by the electrons of the cluster, whereas after the impact the proton loses energy to the electrons (more than it had gained before), see
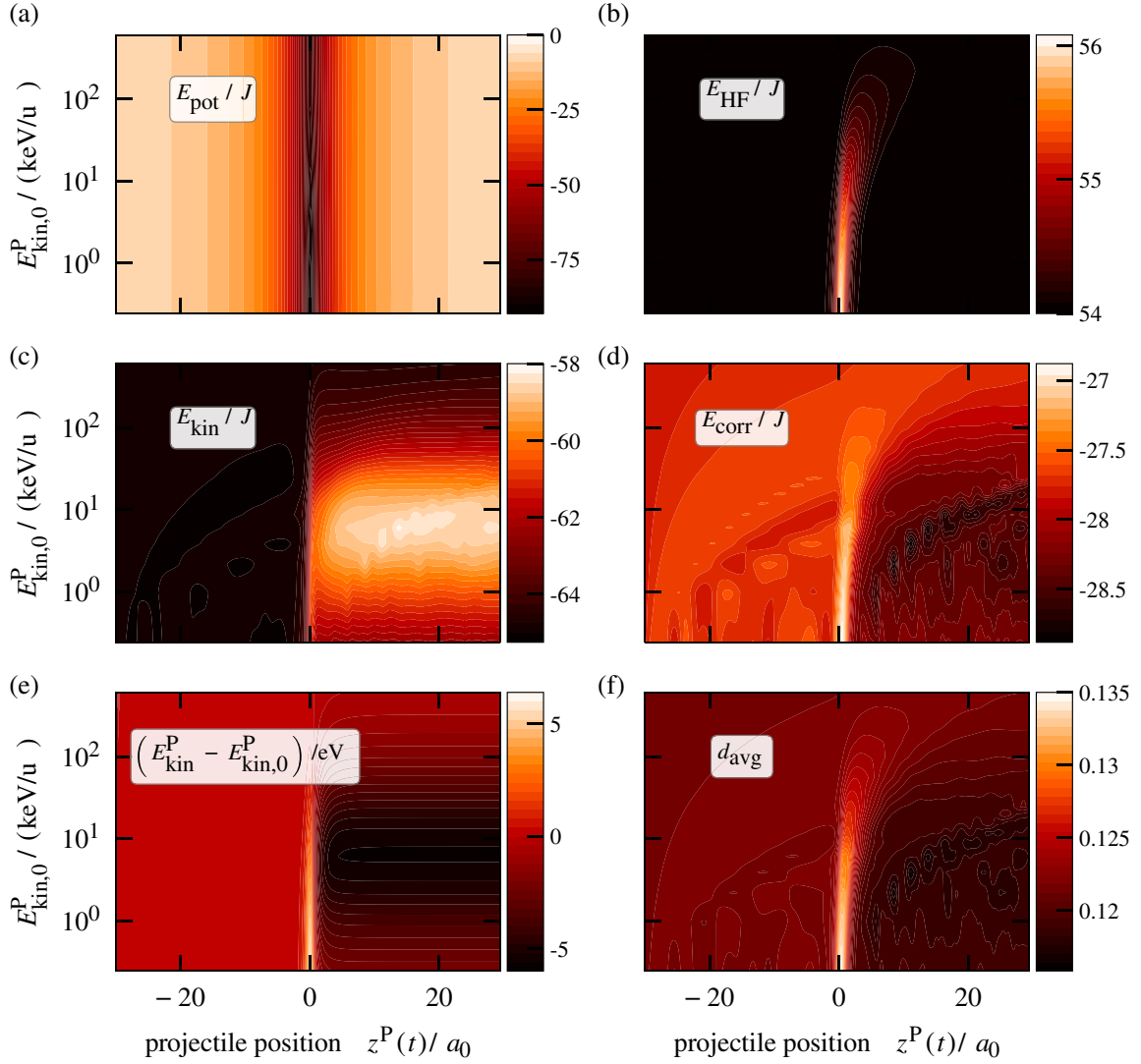
FIGURE 2 Evolution of relevant energies during the impact of a proton at point C (c.f., Figure 4) on a 54-site honeycomb cluster at correlation strength $U = 4\,J$ for different initial kinetic energies in the range 10^{-1} keV/u $< E_{kin,0}^{P} < 10^{3}$ keV/u, indicated on the y-axis. The x-axis contains the current height of the proton, $z^{P}(t)$, (impacting from the left) above the cluster plane. Since the projectile velocity is almost constant, the height is a measure of time. (a): potential energy, (b): Hartree–Fock energy, (c): kinetic energy, (d): correlation energy, and (f): average double occupation of the lattice electrons; (e): kinetic energy loss of the projectile. The colour scale is shown to the right of each figure. To ease the analysis of the data, three vertical cuts at $z^{P} = 0$; 2.5; 5 through each graph are shown in Figure 3

also Figure 3e. A general discussion of this behavior has been given in Balzer et al.[13] Here we provide more details of the physics including a breakup of the energy gain of the electrons into different contributions: potential energy in the field of the projectile, kinetic energy, mean-field energy, and correlation energy.

The *potential energy of the cluster electrons* in the Coulomb field of the projectile, Equation (15), is shown in Figure 2a. While, in the absence of the projectile this energy is zero, during the impact the attraction of the electrons towards the projectile impact point gives rise to a large (negative) energy—electrons are confined in a potential well centred at the impact point. For each projectile energy, $E_{kin,0}^{P}$, the potential energy is perfectly symmetric with respect to the impact point $z^{P} = 0$. This demonstrates that there is no drift of the ion in x- and y-direction during the penetration process. Next consider the *kinetic energy* of the electrons, Figure 2c, and compare it to the kinetic energy of the projectile, Figure 2e. For any vertical cut through the figures (constant $z^{P} > 0$) the two energies are essentially mirror images of each other. The maximum energy reduction of the projectile (maximal stopping) is observed slightly below $E_{kin,0}^{P} = 10$ keV/u, exactly where the electrons experience the highest kinetic-energy gain. This is even more clearly visible in blue and green curves in Figure 3c and e. Figure 2b shows the *Hartree–Fock part of the interaction energy* of the electrons. It is directly proportional to the electron density, compare Equation (16) and, thus, illustrates the density response to the projectile. Note the striking difference in the two limiting cases of low and high ion energy, respectively: for low $E_{kin,0}^{P}$, the electron density adiabatically follows the external excitation, leading to a symmetric bell-shaped curve, similar to E_{pot}. In contrast, for high-energy ions, the interaction time is too short for the electronic system to respond, therefore the
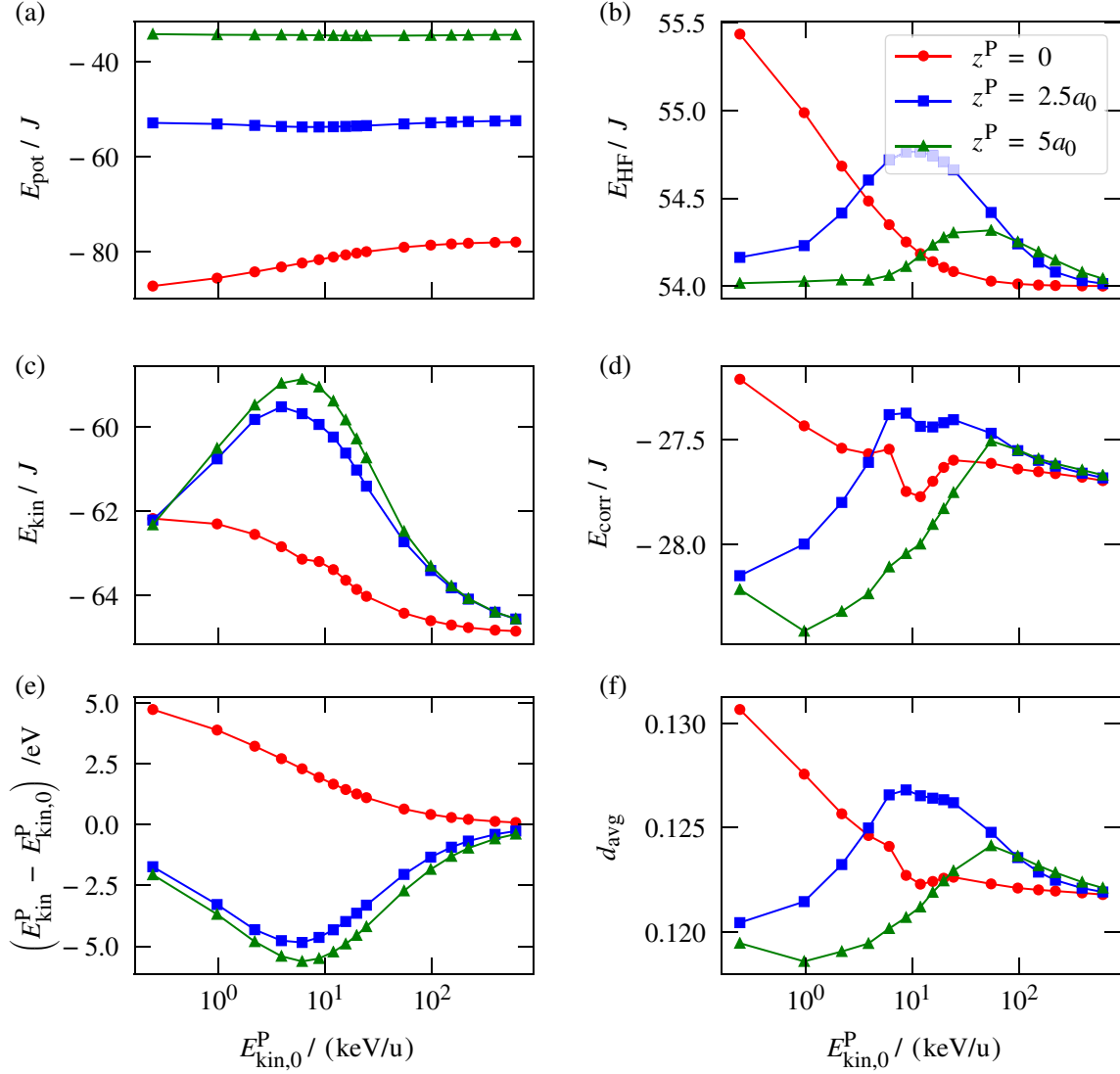
FIGURE 3 Same as Figure 2, but for three cuts at fixed values z^P of the proton coordinate (height above the plane): in the cluster plane ($z^P = 0$, red line) and two distances after the impact (blue and green), see inset of top right figure

density and, thus, E_{HF} do not change significantly—even during the particle impact. The physics inbetween these two limits is dominated by an increasingly delayed and broadened response of the electron density, due to the build up of electron–electron correlations. The same trends are seen also in Figure 3c: for example, the red curve demonstrates the reduction of the electronic density response with increasing projectile speed. Consider now the *correlation energy* of the electrons, E_{corr}, Equation (16), and the closely related average doublon number, d_{avg}, Equation (17), that are displayed in Figures 2(d) and (f), respectively. Both quantities show a very similar behavior that resembles that of the Hartree–Fock energy, E_{HF}, compare figure part (b). Thus, both quantities mainly following the evolution of the density, as well, which is also seen in Figure 3, compare parts (d, f) to part (b).

The time-dependent re-distribution of the energy gained by the electrons between kinetic, mean-field and correlation energy can be clearly seen in Figure 3(b-d), compare the red and green curves. When the projectile departs towards positive z^P, the kinetic energy always increases because the potential well that has trapped the electrons is removed. At the same time, Hartree–Fock and correlation energy decrease, for impact energies below 10 keV/u, compare Figure 3b and d. In contrast, for impact energies exceeding approximately 10 keV/u (25 keV/u) the Hartree–Fock (correlation) energy increase.

3.3 | Correlated-energy dissipation for impact energies below 1 keV

In this section, we perform additional simulations for an $L = 24$-site honeycomb cluster (c.f., visualization in Figure 4), where we focus, in particular, on correlation effects at small proton energies. To reach sufficiently long simulation times, in this case, we do not perform an adiabatic switching on of the interaction U but start from the Hartree ground state, for the inclusion of a correlated initial state, see Semkat et al.[78,79]. In this case the proton impact should occur only after the initial transient
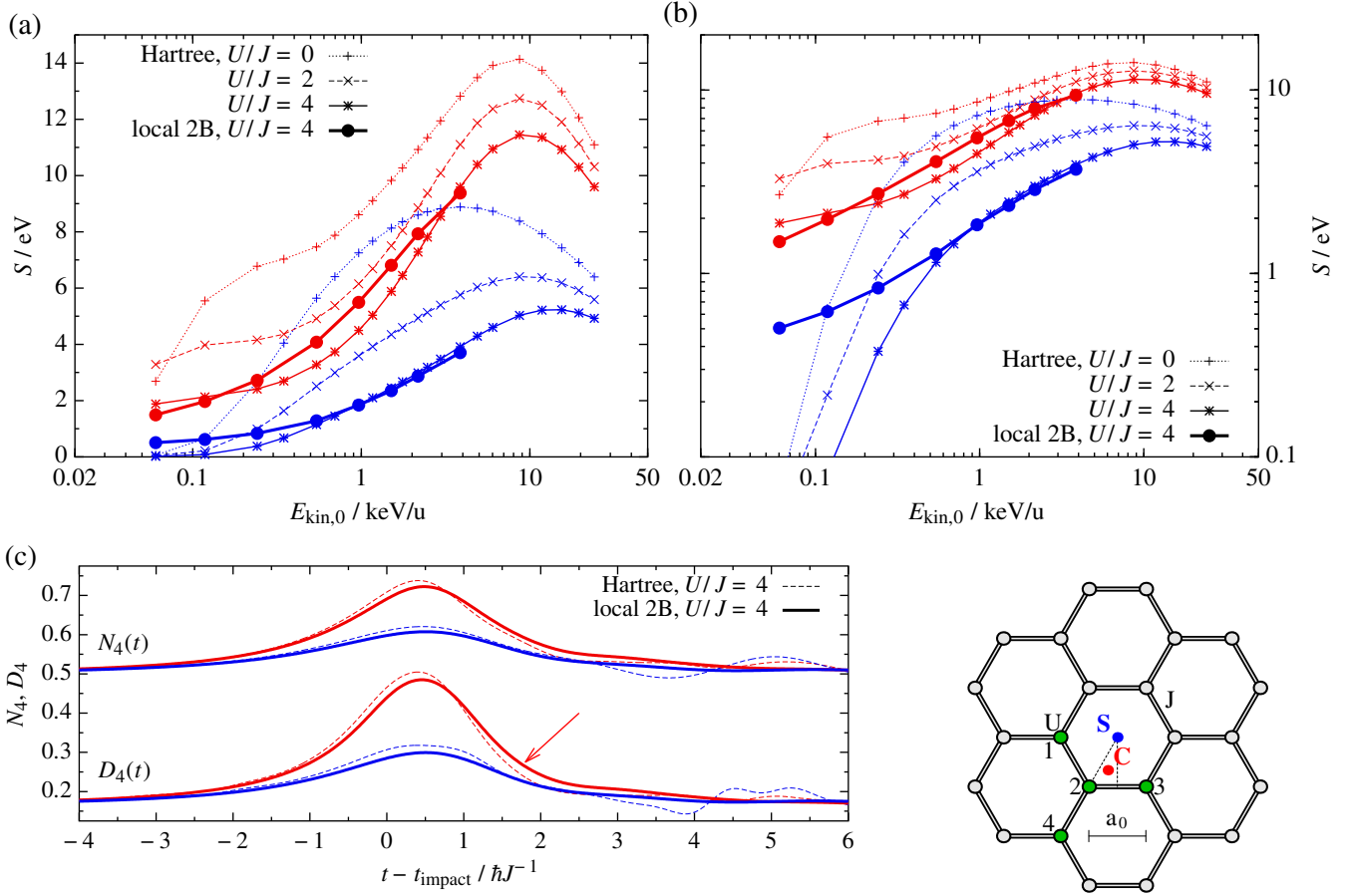
FIGURE 4   (a) and (b): Energy loss $S(E_{\mathrm{kin},0}^{\mathrm{P}})$ of a proton passing through a 24-site honeycomb cluster ($J = 2.8$ eV, $a_0 = 1.42$ Å.) at three correlation strengths $U/J = 0, 2, 4$, for two different impact points marked in the bottom right figure: C ($-a_0/6, -a_0/\sqrt{3}, 0$), red lines) and S (cluster center, blue lines). (b) The same data as (a) on a logarithmic scale to better resolve the low-energy behaviour. For $U/J = 4$, we include, in addition to the Hartree calculations, results obtained in the local second-order Born approximation (local 2B). Note that, at impact energies below 2 keV, electron–electron correlations tend to increase the energy loss compared to the mean-field result. (c): Time evolution of the density $N_4(t)$ and double occupation $D_4(t)$, as defined in the text (averages over the four green sites in the bottom right figure), for the impact energy $E_{\mathrm{kin},0}^{\mathrm{P}} = 1$ keV. The red arrow marks the ion-induced doublon excitation that is observed in the correlated simulations

dynamics which are caused by the sudden (nonadiabatic) switch on of the 2B selfenergy. These transient dynamics also change the initial Hartree double occupation $d_{\mathrm{avg}}(t_{-\infty}) = \frac{1}{2L}\sum_{i\sigma}\langle n_{i\sigma}(t_{-\infty})\rangle = 0.25$ to some smaller value (for details see Balzer et al.[13]). Extending the work of Balzer et al.,[13] we consider in the following two different initial positions of the proton: the points S (cluster center, blue) and C (centroid point, red) as sketched in Figure 4.

Figure 4a and b shows the energy loss in a broad range of proton energies between 0.05 and 25 keV/u for three different values of the interaction strength $U/J \leq 4$. For the point C (red curves), the peak position of the energy loss is located roughly around 10 keV/u, while, for the point S (blue curves), the maximum of the stopping power varies between 4 keV/u ($U = 0$) and 15 keV/u ($U/J = 4$). Generally, we observe that, in the investigated regime, an increase of the interaction strength U leads to a smaller energy loss for fixed impact parameters. Moreover, when the energy is decreased below 0.1 keV/u, the energy loss rapidly vanishes, in a mean-field description, due to a rather instantaneous change of the charge density on the cluster, which we attribute to the onset of the adiabatic-response regime.

In the next step, we examine the influence of electron–electron correlations on the energy loss. In the 2B approximation for a moderate interaction strength of $U/J = 4$, we find clear deviations from the Hartree results. Around $E_{\mathrm{kin},0}^{\mathrm{P}} = 1$ keV, the correlated result for the stopping power significantly exceeds the Hartree result, for the starting point C, while for the point S the correlated results remain close to the mean-field result. When the impact energy is further reduced the situation changes. For the impact point C correlated and uncorrelated simulations do not differ systematically. In contrast, for impact point S the correlated calculation leads to a significantly increased energy loss compared to the mean-field simulation. Moreover, at and below 0.2 keV/u, the energy loss seems to be dominated by correlation effects, as the mean-field results rapidly vanish, for point S. This low-energy behavior needs further investigation since here also effects beyond the second-Born approximation might become important.

Let us now return to the impact energy $E_{\text{kin},0}^{\text{P}} = 1$ keV/u. We expect that the increased energy loss obtained in the local 2B calculations for the starting point C, is a consequence of enhanced doublon formation on the cluster, triggered by the interaction with the proton along the excitation protocol discussed in Balzer et al.[14] This protocol connects single-electron and doublon states in a strongly correlated Hubbard model via nonadiabatic Landau–Zener transitions. As an indication that such excitations play a crucial role, we mention that, for the case C, the maximum value of the interaction energy with the proton at the nearest lattice site, $|W_{i=2}(t)|$, is about twice as large as the electron–electron interaction strength U, which was found to be the optimum condition for ion-induced doublon excitation in Balzer et al.[14] In contrast, this energy is of the order of U, for the impact point S. For cases where the maximum value of the interaction with the proton is smaller, $|W| \lesssim U$, doublon production should be not as efficient as for on-site energies $W \gtrsim 2U$, compare Balzer et al.[14] and Bonitz et al.[75]

Additional support for these arguments is obtained from an analysis of the time evolution of the electron density and double occupation on the cluster. In Figure 4c, we show two quantities: $N_4(t) = \frac{1}{4} \sum_{\alpha=1}^{4} \langle n_{\alpha\sigma}(t) \rangle$ and $D_4(t) = \frac{1}{4} \sum_{\alpha=1}^{4} d_\alpha(t)$, that is, the density and doublon number averaged over the four sites that are nearest to the impact point C, compare the green sites labelled 1 to 4 in the cluster sketch of Figure 4. We observe that, after the impact, the relaxation of the density towards the equilibrium value $N_4 = \langle n_{i\sigma} \rangle = 0.5$ is slightly different for the cases C and S. In the former case, the density in 2B approximation remains larger than the Hartree result whereas, in the latter case the second-Born result is slightly lower, at least up to the time $t - t_{\text{impact}} \approx 2.5 \hbar J^{-1}$. From the quantity D_4 we find that this difference in the evolution of the densities is associated with a larger doublon number after the impact, in a correlated simulation, for the case C, see the red arrow. Also, note, that we have computed D_4 in Hartree approximation with the full mean-field NEGF $G(t, t')$ according to Equation (17) instead of evaluating just the uncorrelated part $D_4^{\text{uncorr}} = \frac{1}{4} \sum_{\alpha=1}^{4} \langle n_{\alpha\sigma}(t) \rangle^2$, that has the equilibrium limit $D_4(t_{-\infty}) = 0.25$.

Even though the effect of doublon excitation is not strong, in the present case, recent simulations have confirmed the importance of this effect, as will be discussed in Section 4.

4 | CONCLUSIONS AND OUTLOOK

In this article we presented new results of time-dependent quantum simulations for the dynamics of ions near a solid surface. Such processes are of prime importance for the interaction of plasmas with solids where many questions remain poorly understood. We focused on two important aspects of ion stopping in nanoscale solid systems exposed to low-energy projectiles: (a) the charge transfer from the surface to the projectile and (b) the modification of the projectile energy loss in case of a target material with strong electronic correlations. While the former problem was studied using time-dependent DFT simulations, the latter one was studied using NEGF simulations for small honeycomb Hubbard clusters. The results for the two problems are summarized below before we discuss future developments.

In our TDDFT simulations we have used an adiabatic GGA for the exchange–correlation potential and, thus, restricted ourselves to a resonant charge-transfer process. A proton incident on an Al(111) surface serves as a well-established model system, which has been studied intensely for a long time using model Hamiltonians.[24,27–30] The strength of TDDFT-MD lies in the ab initio material-specific description of the time-dependent charge and energy transfer and the screening. Tunnelling rates differ from estimates from electronic ground-state theory. Limitations of the approach are due to the adiabatic approximation for exchange and correlation plus the semilocal approximation applied to the exchange–correlation energy functional of ground-state DFT, and improvements pose an open problem.

In our NEGF simulations we have concentrated on electronic correlation effects in the stopping of ions. We have confirmed that, at impact energies below 1 keV correlations tend to increase the energy transfer to the target, compared to an uncorrelated (Hartree) simulation. Among the possible mechanisms is the excitation of doublons in the target. In Bonitz et al.[75] it was shown that, for a proper choice of impact energy, and for a more strongly coupled hexagon cluster ($U/J \geq 10$) of size $L = 12$ an ion impacting in the cluster center may excite a large doublon number that does not decay after the projectile has left. Moreover, it was shown in Balzer et al.[14] and Bonitz et al.[75] that, in the case of multiple ion impacts, the doublon number can be increased further.

Let us now discuss the combined treatment of the two effects. Even though charge transfer is most likely not relevant for the kinetic energy loss of the projectile, it may well affect the electronic processes in the target, including doublon excitations. Answering these questions, though, requires a combination of the two simulation methods. However, presently none of the two methods is capable of incorporating the missing effect. Present approximations to the exchange–correlation potential in TDDFT simulations do not describe strongly correlated systems and, thus, cannot treat doublon formation in the target. On the other hand, NEGF simulations of charge transfer have recently been attempted for simple model systems (1D Hubbard chains) in Bonitz et al.[12,75]. However, these simulations did not include a realistic treatment of the impacting ion. Here, a combination with TDDFT could be the basis for major progress. A possible combination could be via a Newns–Anderson model for the projectile where TDDFT provides selfconsistent model parameters. A second promising combination of the two

methods consists in the derivation of improved exchange–correlation functionals for TDDFT that include finite-temperature effects[80,81] and their benchmarking by NEGF simulations. This will be particularly important for the treatment of Auger-type processes in the interaction of an ion or atom with the surface which are straightforwardly described within NEGF already with second-order Born selfenergies, for example, Bonitz et al.[12] and Covito et al.[82] These combinations of TDDFT and NEGF are expected to be of high importance for the development of accurate simulations of low-temperature plasma–surface interaction. Moreover, such combinations should also be of high interest for other fields including surface physics and chemistry.

REFERENCES

[1] I. Nagy, B. Apagyi, *Phys. Rev. A* **1998**, *58*, R1653.
[2] J. M. Pitarke, R. H. Ritchie, P. M. Echenique, *Phys. Rev. B* **1995**, *52*, 13883.
[3] T. Dornheim, S. Groth, J. Vorberger, M. Bonitz, *Phys. Rev. Lett.* **2018**, *121*, 255001.
[4] M. Quijada, A. G. Borisov, I. Nagy, R. Díez Muiño, P. M. Echenique, *Phys. Rev. A* **2007**, *75*, 042902.
[5] A. Ojanperä, A. V. Krasheninnikov, M. Puska, *Phys. Rev. B* **2014**, *89*, 035120.
[6] S. Zhao, W. Kang, J. Xue, X. Zhang, P. Zhang, *J. Phys. Condens. Matter* **2015**, *27*, 025401.
[7] F. James, M. D. Ziegler, J. P. B. Ziegler, *Nucl. Instrum. Methods Phys. Res. B* **2010**, *268*(11), 1818 19th International Conference on Ion Beam Analysis.
[8] M. Bonitz, D. Kremp, S. Kosse, D. C. Scott, W. D. Kraeft, presented at *Proceedings of the XXII. Int. Conf. on Phenomena in Ionized Gases*, Hoboken, NJ, **1995**.
[9] M. Bonitz, D. Kremp, S. Kosse, D. C. Scott, W. D. Kraeft, *Physics of Strongly Coupled Plasmas*, World Scientific, Singapore, **1996**, p. 117.
[10] A. B. Zylstra, J. A. Frenje, P. E. Grabowski, C. K. Li, G. W. Collins, P. Fitzsimmons, S. Glenzer, F. Graziani, S. B. Hansen, S. X. Hu, M. Gatu Johnson, P. Keiter, H. Reynolds, J. R. Rygg, F. H. Séguin, R. D. Petrasso, *Phys. Rev. Lett.* **2015**, *114*, 215002.
[11] D. Kremp, M. Schlanges, W. D. Kraeft, *Quantum Statistics of Nonideal Plasmas*, Springer, Berlin, Heidelberg, **2005**.
[12] M. Bonitz, A. V. Filinov, J. W. Abraham, K. Balzer, H. Kaehlert, E. Pehlke, F. X. Bronold, M. Pamperin, M. Becker, D. Loffhagen, H. Fehske, *Front. Chem. Sci. Eng.* **2018** in press, arXiv:1809.02473.
[13] K. Balzer, N. Schlünzen, M. Bonitz, *Phys. Rev. B* **2016**, *94*, 245118.
[14] K. Balzer, M. Rasmussen, N. Schlünzen, J. P. Joost, M. Bonitz, *Phys. Rev. Lett.* **2018** *121*, 267602. DOI:10.1103/PhysRevLett.121.267602.
[15] M. A. L. Marques, A. Castro, G. F. Bertsch, A. Rubio, *Comput. Phys. Commun.* **2003**, *151*(1), 60.
[16] A. Castro, H. Appel, M. Oliveira, C. A. Rozzi, X. Andrade, F. Lorenzen, M. A. L. Marques, E. K. U. Gross, A. Rubio, *Phys. Status Solidi B Basic Solid State Phys.* **2006**, *243*(11), 2465.
[17] X. Andrade, D. Strubbe, U. De Giovannini, A. H. Larsen, M. J. T. Oliveira, J. Alberdi-Rodriguez, A. Varas, I. Theophilou, N. Helbig, M. J. Verstraete, L. Stella, F. Nogueira, A./'a. Aspuru-Guzik, A. Castro, M. A. Marques, A. Rubio, *Phys. Chem. Chem. Phys.* **2015**, *17*, 31371.
[18] D. Marx, J. Hutter, *Ab Initio Molecular Dynamics: Basic Theory and Advanced Methods*, Cambridge University Press, Cambridge, **2009**.
[19] M. A. L. Marques, C. A. Ullrich, F. Nogueira, A. Rubio, K. Burke, E. K. U. Gross Eds., *Time-Dependent Density Functional Theory. Lecture Notes in Physics*, Vol. *706*, Springer, Berlin, Heidelberg, **2006**.
[20] M. A. L. Marques, N. T. Maitra, F. M. S. Nogueira, E. K. U. Gross, A. Rubio Eds., *Fundamentals of Time-Dependent Density Functional Theory. Lecture Notes in Physics*, Vol. *837*, Springer, Berlin, Heidelberg, **2012**.
[21] M. Lindenblatt, E. Pehlke, A. Duvenbeck, B. Rethfeld, A. Wucher, *Nucl. Instrum. Methods Phys. Res., Sect. B* **2006**, *246*(2), 333.
[22] R. Nagano, K. Yabana, T. Tazawa, Y. Abe, *Phys. Rev. A* **2000**, *62*, 062721.
[23] V. Kapoor, *Phys. Rev. A* **2016**, *93*, 063408.
[24] J. Merino, N. Lorente, M. Y. Gusev, F. Flores, M. Maazouz, L. Guillemot, V. A. Esaulov, *Phys. Rev. B* **1998**, *57*, 1947.
[25] R. Zimny, Z. L. Mišković, N. N. Nedeljković, L. D. Nedeljković, *Surf. Sci.* **1991**, *255*(1), 135.
[26] H. Jouin, F. A. Gutierrez, *Phys. Rev. A* **2011**, *84*, 014901.
[27] J. Merino, N. Lorente, P. Pou, F. Flores, *Phys. Rev. B* **1996**, *54*, 10959.
[28] J. Merino, N. Lorente, F. Flores, M. Y. Gusev, *Nucl. Instrum. Methods Phys. Res., Sect. B* **1997**, *125*(1), 288.
[29] M. C. Torralba, P. G. Bolcatto, E. C. Goldberg, *Phys. Rev. B* **2003**, *68*, 075406.
[30] C. David, P. N. Langreth, *Phys. Rev. B* **1991**, *43*, 2541.
[31] C. L. Moss, C. M. Isborn, X. Li, *Phys. Rev. A* **2009**, *80*, 024503.
[32] A. Castro, M. Isla, J. I. Martínez, J. A. Alonso, *Chem. Phys.* **2012**, *399*, 130.
[33] A. V. Krasheninnikov, Y. Miyamoto, D. Tománek, *Phys. Rev. Lett.* **2007**, *99*, 016104.
[34] R. Seraide, M. A. Bernal, G. Brunetto, U. de Giovannini, A. Rubio, *J. Phys. Chem. B.* **2017**, *121*(30), 7276.
[35] S. Bubin, B. Wang, S. Pantelides, K. Varga, *Phys. Rev. B* **2012**, *85*, 235435.
[36] Z. Wang, S.-S. Li, L.-W. Wang, *Phys. Rev. Lett.* **2015**, *114*, 063004.
[37] N. T. Maitra, *J. Phys. Condens. Matter* **2017**, *29*(42), 423001.
[38] S. Zhao, W. Kang, J. Xue, X. Zhang, P. Zhang, *Phys. Lett. A* **2015**, *379*, 319.
[39] J. P. Perdew, K. Burke, M. Ernzerhof, *Phys. Rev. Lett.* **1996**, *77*, 3865.
[40] W. Humphrey, A. Dalke, K. Schulten, *J. Mol. Graph.* **1996**, *14*, 33.
[41] N. Trouiller, J. L. Martins, *Phys. Rev. B* **1991**, *43*, 1993.
[42] M. Fuchs, M. Scheffler, *Comput. Phys. Commun.* **1999**, *119*(1), 67.
[43] M. Tafipolsky, R. Schmid, *J. Chem. Phys.* **2006**, *124*(17), 174102.
[44] M. Methfessel, A. T. Paxton, *Phys. Rev. B* **1989**, *40*, 3616.
[45] G. A. Franco, *Ph.D. Thesis*, Université Catholique de Louvain (Ottignies-Louvain-la-Neuve), **2013**.
[46] A. Castro, M. A. L. Marques, A. Rubio, *J. Chem. Phys.* **2004**, *121*(8), 3425.
[47] T. Noritake, M. Aoki, S. Towata, Y. Seno, Y. Hirose, E. Nishibori, M. Takata, M. Sakata, *Appl. Phys. Lett.* **2002**, *81*(11), 2008.
[48] M. Fuchs, Y.-M. Niquet, X. Gonze, K. Burke, *J. Chem. Phys.* **2005**, *122*(9), 094116.

[49]   O. Gunnarsson, B. I. Lundqvist, *Phys. Rev. B* **1976**, *13*, 4274.

[50]   M. Lindenblatt, E. Pehlke, *Phys. Rev. Lett.* **2006**, *97*, 216101.

[51]   M. S. Mizielinski, D. M. Bird, M. Persson, S. Holloway, *J. Chem. Phys.* **2005**, *122*, 084710.

[52]   M. A. Cazalilla, N. Lorente, R. Díez Muiño, J.-P. Gauyacq, D. Teillet-Billy, P. M. Echenique, *Phys. Rev. B* **1998**, *58*, 13991.

[53]   E. C. Diego Valdés, J. M. Goldberg, R. C. M. Blanco, *Phys. Rev. B* **2005**, *71*, 245417.

[54]   N. P. Wang, E. A. García, R. Monreal, F. Flores, E. C. Goldberg, H. H. Brongersma, P. Bauer, *Phys. Rev. A* **2001**, *64*, 012901.

[55]   M. Pamperin, F. X. Bronold, H. Fehske, *Plasma Sources Sci. Technol.* **2018**, *27*(8), 084003.

[56]   M. Lindenblatt, J. van Heys, E. Pehlke, *Surf. Sci.* **2006**, *600*(18), 3624.

[57]   H. Winter, *J. Phys. Condens. Matter* **1996**, *8*(49), 10149.

[58]   E. V. Chulkov, V. M. Silkin, P. M. Echenique, *Surf. Sci.* **1999**, *437*(3), 330.

[59]   A. A. Correa, J. Kohanoff, E. Artacho, D. Sánchez-Portal, A. Caro, *Phys. Rev. Lett.* **2012**, *108*, 213201.

[60]   A. Schleife, Y. Kanai, A. A. Correa, *Phys. Rev. B* **2015**, *91*, 014306.

[61]   I. Campillo, J. M. Pitarke, A. G. Eguiluz, *Phys. Rev. B* **1998**, *58*, 10307.

[62]   A. Atef Shukri, F. Bruneval, L. Reining, *Phys. Rev. B* **2016**, *93*, 035128.

[63]   M. J. Berger, J. S. Coursey, M. A. Zucker, J. Chang, *Stopping-Power and Range Tables for Electrons, Protons, and Helium Ions*, Physical Measurement Laboratory, Gaithersburg, **1999**. https://dx.doi.org/10.18434/T4NC7P.

[64]   G. Stefanucci, R. van Leeuwen, *Nonequilibrium Many-Body Theory of Quantum Systems*, Cambridge University Press, Cambridge, UK **2013**.

[65]   L. P. Kadanoff, G. Baym, *Quantum Statistical Mechanics*, Benjamin, New York, NY **1962**.

[66]   K. Balzer, M. Bonitz, *Nonequilibrium Green's Functions Approach to Inhomogeneous Systems*, Springer, Berlin, Germany **2013**.

[67]   N. Schlünzen, M. Bonitz, *Contrib. Plasma Phys.* **2016**, *56*(1), 5.

[68]   L. V. Keldysh, *J. Exp. Theor. Phys.* **1965**, *20*, 1018 (*Zh. Eksp. Teor. Fiz.* **1964**, *47*, 1515).

[69]   M. Bonitz, A. P. Jauho, M. Sadovskii, S. Tikhodeev, *Phys. Status Solidi B Basic Solid State Phys.* **2018** in press, arXiv:1901.01065.

[70]   N. Schlünzen, S. Hermanns, M. Bonitz, C. Verdozzi, *Phys. Rev. B* **2016**, *93*, 035107.

[71]   N. Schlünzen, J.-P. Joost, F. Heidrich-Meisner, M. Bonitz, *Phys. Rev. B* **2017**, *95*, 165139.

[72]   P. Lipavský, V. Špička, B. Velický, *Phys. Rev. B* **1986**, *34*, 6933.

[73]   S. Hermanns, K. Balzer, M. Bonitz, *Phys. Scr.* **2012**, *2012*(T151), 014036.

[74]   K. Balzer, M. Eckstein, *Phys. Rev. B* **2014**, *89*, 035148.

[75]   M. Bonitz, K. Balzer, N. Schlünzen, M. Rasmussen, J.-P. Joost, *Phys. Status Solidi B Basic Solid State Phys.* **2018**, 1800490. https://doi.org/10.1002/pssb.201800490.

[76]   S. Reich, J. Maultzsch, C. Thomsen, P. Ordejón, *Phys. Rev. B* **2002**, *66*, 035412.

[77]   J.-P. Joost, N. Schlünzen, M. Bonitz, *Phys. Status Solidi B Basic Solid State Phys.* **2019**, 1800498, https://doi.org/10.1002/pssb.201800498.

[78]   D. Semkat, D. Kremp, M. Bonitz, *Phys. Rev. E* **1999**, *59*, 1557.

[79]   D. Semkat, D. Kremp, M. Bonitz, *J. Math. Phys.* **2000**, *41*(11), 7458.

[80]   T. Dornheim, S. Groth, T. Sjostrom, F. D. Malone, W. M. C. Foulkes, M. Bonitz, *Phys. Rev. Lett.* **2016**, *117*, 156403.

[81]   T. Dornheim, S. Groth, M. Bonitz, *Phys. Rep.* **2018**, *744*, 1.

[82]   F. Covito, E. Perfetto, A. Rubio, G. Stefanucci, *Phys. Rev. A* **2018**, *97*, 061401.

Chapter 5

Other Works

The key ambition of the present thesis is the further development of the NEGF method in theory and application. Indeed, the author's extensive theoretical improvements presented in Sec. 2.1 have rendered the potential of hitherto untapped selfenergy approximations practically accessible, thereby opening up new avenues for future research. The following section discusses a particularly interesting example that focuses on light-driven graphene nanoribbons (GNRs)—a material that has attracted wide attention but is notoriously hard to describe.

5.1 Optical Properties of Graphene Nanoribbons

Graphene [157] exhibits an astonishingly high carrier mobility following from its unique band structure and its two-dimensional configuration [161]. In order to utilize its potential in modern nanoelectronics, it is essential to find a way to manufacture a finite band gap in graphene. A particularly encouraging realization has been the usage of the quantum confinement in finite graphene fragments [173, 174]. A systematical way to control the confinement-induced band gap is provided by GNR structures (straps of graphene with a finite width in the direction of one symmetry axis), which can be reliably fabricated in different sizes [173, 174, 180–185]. Recent laser experiments with graphene-based structures have revealed the existence of the so-called carrier-multiplication (CM) or impact-excitation effect [31–35]—an Auger-type process where one excited electron can raise another electron above the band gap—in monolayer graphene [194, 195] and graphene nanotubes [192, 193]. This is especially interesting for photovoltaic applications of graphene, as it might improve the achievable efficiency beyond the Shockley–Queisser limit [340, 341]. For GNRs the experimental confirmation has not yet been achieved. While CM effects have been theoretically predicted for GNRs on a conceptual level [35] a rigorous correlated nonequilibrium-dynamics description has been missing. The proper characterization of time-dependent nonequilibrium situations in finite GNRs imposes great challenges to any theoretical method due to the increased electronic coupling. The NEGF approach that was advanced by the author does not only meet these challenges in an efficient way but gives

access to the important time-resolved spectral information as well. With large contribution of Jan-Philip Joost the author's NEGF implementation was adapted to simulate laser-excited GNR systems. The results are published in the following publication,[1] Ref. [216].

As shown in Ref. [342], GNRs are accurately described in an extended Hubbard model that additionally incorporates hopping processes to second- and third-nearest neighbor sites and a finite orbital overlap. In Ref. [216] this model is combined with the *GW* selfenergy to capture electron–hole correlations that are important at and near half filling.[2] The first-order (HF) and second-order (SOA) selfenergies are applied for comparison as well. To further adjust the approach the theoretical band gap for nanoribbons with up to 112 carbon atoms is matched to experimental data [344, 345]. In benchmark calculations for the spectral quantities it is demonstrated that the resulting description conceptually improves the equilibrium dispersion relation compared to existing DFT+LDA results [345]. As a proof of concept, the approach is then applied to a 30-site GNR which is excited by a linearly polarized laser pulse. It is shown that the photoemission spectrum exhibits an energetic redistribution of the electrons in the upper Hubbard band, even after the laser field has vanished. As this is not visible in mean-field calculations, the observed behavior is clearly caused by Auger-type electron–electron scattering effects—such as the above-mentioned carrier multiplication—which again confirms the necessity of a correlated nonequilibrium description. The detailed characterization of the correlation effects at hand is left open for an upcoming publication. The observations are highly relevant for future experiments, which can be guided by the theoretical predictions of Ref. [216]. Finally, Green-function studies of GNRs are further developed in Ref. [119] where a groundstate formalism is used to predict topological effects that match experimental results.

---

[1]J.-P. Joost, N. Schlünzen, and M. Bonitz, Phys. Status Solidi B, **256**, 1800498 (2019). Copyright Wiley-VCH Verlag GmbH & Co. KGaA. Reproduced with permission.

[2]A comparable approach on the mean-field level has been successfully applied to GNRs in Ref. [343]

Femtosecond Electron Dynamics in Graphene Nanoribbons – A Nonequilibrium Green Functions Approach Within an Extended Hubbard Model

Jan-Philip Joost,* Niclas Schlünzen, and Michael Bonitz

A new approach to study the correlated femtosecond electron dynamics in finite graphene clusters, such as nanoribbons, is presented here. The systems are described by an extended Hubbard model that takes into account the overlap of adjacent orbitals and hopping between up to third-nearest neighbors. The model is solved by the nonequilibrium Green functions approach combined with different self-energy approximations, including the second-Born and *GW* self-energy, to take into account electronic correlations. The description allows us to predict the correlated nonequilibrium dynamics of excited graphene nanostructures of arbitrary geometry containing up to 100 carbon atoms for up to 25 fs.

1. Introduction

Since the first experimental discovery of its unique features in 2004[1] the interest in graphene has grown rapidly. As the first truly two-dimensional material it exhibits a number of unique mechanical, optical, and electronic properties which make graphene a promising candidate for various technological applications of the future.[2–6] However, as graphene is a semimetal, the absence of a band gap prevents the realization of next-generation graphene-based nanoelectronics.[7] Therefore, large effort was put into creating semiconducting graphene materials that retain its remarkable transport properties. While some methods focus on substrate-induced[8,9] or strain-induced[10,11] band gaps, the most promising approach, at the moment, is obtaining a band gap through the effect of quantum confinement in finite graphene nanostructures[12,13] such as graphene nanoribbons (GNRs). The electronic properties and especially the low energy spectrum of the π-electrons are strongly influenced by the edge structure of the nanoribbons. Depending on the shape of the edges one distinguishes between armchair graphene nanoribbons (AGNR) and zigzag graphene nanoribbons (ZGNR).

A detailed understanding of these finite graphene nanostructures is of high importance for current research. Due to the recently developed new synthetization methods of graphene nanoribbons,[14–18] the number of exciting experiments increased drastically over the last years.[19–25] Therefore, an accurate theoretical description of these systems in nonequilibrium and particularly of their time-resolved spectral properties is needed. However, finite graphene nanostructures, especially in nonequilibrium, are extremely complex, inhomogeneous systems that put high requirements on any theory that attempts to describe them accurately. A proper theory has to describe finite systems that are experimentally accessible. Such systems typically include up to 100 carbon atoms.[17,26,27] Further, the approach has to take into account the finite overlap of the atomic orbitals and describe moderate electronic correlations. Additionally, the two-dimensional geometry of the graphene honeycomb lattice has to be modeled. Finally, the theory has to be able to describe the correlated nonequilibrium dynamics of the system for up to several femtoseconds within a reasonable amount of computational time. In conclusion, one has to find a model that allows for an accurate description of these systems while at the same time remains numerically manageable.

A method that fulfills all these requirements is the theory of real-time nonequilibrium Green functions (NEGF) due to Keldysh.[28,29] It allows for a self-consistent dynamics of correlated electrons fully obeying conservation laws. The method contains a single input quantity – the self-energy Σ, see Section 3 – and would be exact if the exact $\Sigma = \Sigma[G]$ was used. But in practice, of course, approximations are used. Nevertheless, the accuracy of NEGF simulations has been carefully tested in recent years, for example, refs. [30,31], and – with the appropriate choice of the self-energy – allows for reliable and predictive simulations. At the same time, NEGF simulations are computationally demanding and the effort scales cubically with the basis dimension. A link between accuracy and low numerical effort is provided by using Hubbard-type lattice models, for example, ref. [32], and we will, therefore, follow this strategy in the present paper as well. At the same time we will improve the model compared to earlier simulations, by using an extended Hubbard model where the model parameters are provided by ab initio approaches as discussed in Section 2. Using this approach we obtain accurate ground-state results for graphene

J.-P. Joost, N. Schlünzen, Prof. M. Bonitz
Institut für Theoretische Physik und Astrophysik
Christian-Albrechts-Universität zu Kiel
24098 Kiel, Germany
E-mail: joost@theo-physik.uni-kiel.de

The ORCID identification number(s) for the author(s) of this article can be found under https://doi.org/10.1002/pssb.201800498.

nanoribbons including the band gap, the momentum dispersion and the spectral function. Further the first nonequilibrium results for the electron dynamics following a short laser pulse are presented and demonstrate the strength of the NEGF approach.

This paper is organized as follows. In Section 2, we introduce the extended Hubbard model and formulate a systematic many-body description on the mean-field level. This is extended to correlation effects in Section 3 where the NEGF approach is introduced. Our numerical results are presented in Section 4 starting with ground-state properties and concluding with correlated electron dynamics in response to a short laser pulse. We conclude with an outlook in Section 5.

2. Extended Hubbard Model

The elementary constituent of graphene is carbon, the sixth element of the periodic table. As such, it contains six electrons that are in the configuration $1s^2 2s^2 2p^2$ if the carbon is in the ground state. That is, two electrons are close to the nucleus and occupy the innermost 1s-shell while the other four fill the outer shells of the 2s and 2p orbitals. However, in the presence of other carbon atoms one electron from the 2s orbital is excited to the 2p orbital and forms covalent σ-bonds between the atoms. The quantum-mechanical superposition of the remaining 2s electron with n of the 2p states is called sp^n hybridization.[33]

The structure of graphene is obtained by the planar sp^2 hybridization. The three hybridized orbitals are oriented in a plane and have mutual angles of $120°$. This lets the carbon atoms arrange in a hexagonal structure, the so-called honeycomb lattice. The remaining unhybridized $2p_z$ orbital is oriented perpendicular to the plane. Due to the non-negligible overlap between these orbitals of adjacent atoms, they form the so-called π-bonds.[34] These half-filled bands are responsible for most of graphene's interesting electronic properties.

2.1. Tight-Binding Model

A commonly used model when describing graphene-based systems is the tight-binding approximation (TB) which is easy to solve due to its simplistic nature.[35] In this model, the aforementioned $2p_z$ atomic orbitals are a common choice for the underlying basis set $|\tilde{i}\rangle$ which, in general, is non-orthogonal. The non-vanishing overlap of these single-particle orbitals is taken into account by the overlap matrix

$$\tilde{S}_{ij} = \langle \tilde{i} | \tilde{j} \rangle \tag{1}$$

where the special case of an orthonormal basis is equivalent to $\tilde{S}_{ij} = \delta_{ij}$.

In the TB approximation the graphene system is described by the single-particle Hamiltonian

$$\hat{H}^{TB} = \sum_{ijkl} \tilde{S}_{ik}^{-1} \tilde{h}_{kl}^{TB} \tilde{S}_{lj}^{-1} |\tilde{i}\rangle \langle \tilde{j}| \tag{2}$$

with the corresponding matrix elements $\tilde{h}_{kl}^{TB} = \langle \tilde{k} | \hat{H}^{TB} | \tilde{l} \rangle$ which in general include the kinetic part and the on-site potential as

well as any possible external single-particle excitations. The Hamiltonian $\hat{H}^{TB}$ possesses a complete set of orthonormal eigenstates $|\Psi_n\rangle$, which are given by a linear combination of the atomic orbitals $|\tilde{i}\rangle$,

$$|\Psi_n\rangle = \sum_i \tilde{a}_i^n |\tilde{i}\rangle \tag{3}$$

These eigenstates and the corresponding eigenvalues E_n of the Hamiltonian are determined by the stationary Schrödinger equation

$$\hat{H}^{TB} |\Psi_n\rangle = E_n |\Psi_n\rangle \tag{4}$$

which can be transformed into a generalized eigenvalue problem by multiplying from the left with the bra vector $\langle \tilde{j} |$ resulting in

$$\sum_i \langle \tilde{j} | \hat{H}^{TB} | \tilde{i} \rangle \tilde{a}_i^n = \sum_i \langle \tilde{j} | \tilde{i} \rangle \tilde{a}_i^n E_n \tag{5}$$

This set of linear equations can be written in matrix form as

$$\tilde{\mathbf{H}}^{TB} \tilde{\mathbf{A}} = \tilde{\mathbf{S}} \tilde{\mathbf{A}} \mathbf{E} \tag{6}$$

where $\tilde{\mathbf{H}}^{TB}$, $\tilde{\mathbf{A}}$, and $\tilde{\mathbf{S}}$ contain the matrix elements $\tilde{h}_{ji}^{TB}$, $\tilde{a}_i^n$, and $\tilde{S}_{ji}$, respectively. $\mathbf{E}$ is a diagonal matrix with the eigenvalues $\mathbf{E}_n$.

To solve Equation (6) one can apply the symmetric Löwdin orthogonalization[37] which leads to a standard eigenvalue problem

$$\mathbf{H}^{TB} \mathbf{A} = \mathbf{A} \mathbf{E} \tag{7}$$

that is defined in a new orthogonal basis $|i\rangle$ which are denoted without a tilde. Both basis sets are connected by the square root of the overlap matrix via

$$|i\rangle = \sum_k |\tilde{k}\rangle \tilde{S}_{ki}^{-\frac{1}{2}} \tag{8}$$

Further, the matrices containing the matrix elements of the Hamiltonian and the expansion coefficients of the eigenstates transform as

$$\mathbf{H}^{TB} = \tilde{\mathbf{S}}^{-\frac{1}{2}} \tilde{\mathbf{H}}^{TB} \tilde{\mathbf{S}}^{-\frac{1}{2}} \tag{9}$$

$$\mathbf{A} = \tilde{\mathbf{S}}^{\frac{1}{2}} \tilde{\mathbf{A}} \tag{10}$$

Thus, in the TB approximation the system is defined by the matrix elements of the single-particle Hamiltonian $\tilde{h}_{ij}^{TB}$ and the overlap matrix $\tilde{S}_{ij}$.

A common way to get a set of parameters that closely reproduce the electronic properties of graphene and graphene nanostructures is to fit the resulting TB band structure against ab initio results of DFT calculations.[35,36,38] In practice, often only the orbital overlap of up to the third-nearest-neighbor atoms is considered which results in seven fitting parameters. An illustration of the three nearest neighbors of a single site in a

graphene lattice is depicted in **Figure 1**. The resulting matrix elements of the Hamiltonian are then given by

$$\tilde{h}_{ij}^{\mathrm{TB}} = -J\big(\delta_{ij}\tilde{E}_{2\mathrm{p}} + \tilde{t}_{ij}\big) \tag{11}$$

where J is the hopping amplitude which is used for normalization, $\tilde{E}_{2\mathrm{p}}$ is the $2\mathrm{p}_z$ on-site energy of a carbon atom and $\tilde{t}_{ij}$ are the hopping matrix elements defined as

$$\tilde{t}_{ij} = \begin{cases} \tilde{t}_1, & \text{if } (i,j) \text{ is 1 NN} \\ \tilde{t}_2, & \text{if } (i,j) \text{ is 2 NN} \\ \tilde{t}_3, & \text{if } (i,j) \text{ is 3 NN} \\ 0, & \text{else} \end{cases} \tag{12}$$

In a similar fashion, the elements of the overlap matrix are given by three parameters as

$$\tilde{S}_{ij} = \delta_{ij} + \begin{cases} \tilde{s}_1, & \text{if } (i,j) \text{ is 1 NN} \\ \tilde{s}_2, & \text{if } (i,j) \text{ is 2 NN} \\ \tilde{s}_3, & \text{if } (i,j) \text{ is 3 NN} \\ 0, & \text{else} \end{cases} \tag{13}$$

In **Table 1**, some parameter sets are presented that have shown to reliably reproduce the DFT band structure of different graphene systems.

However, while this approach is reasonable for infinite graphene sheets where electronic correlations are commonly thought to be weak, it provides insufficiently accurate results for finite graphene structures such as nanoribbons. For the latter, it
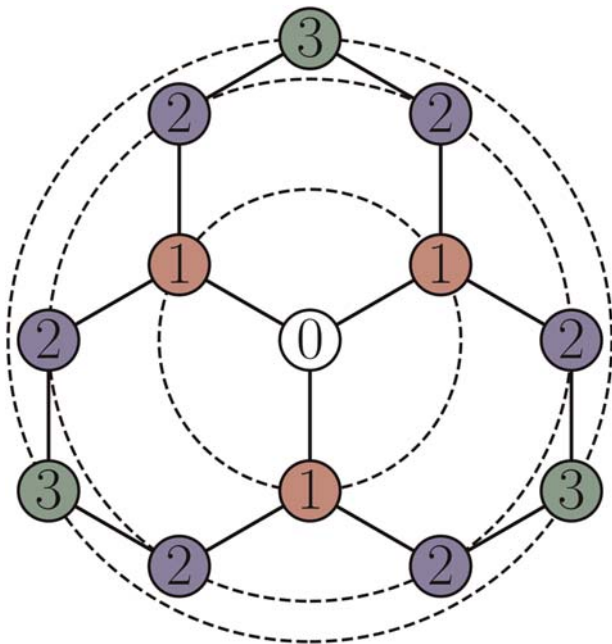
Figure 1. Illustration of the positions of neighboring sites in the graphene honeycomb lattice. The three nearest neighbors (1NN) of the white site are marked in red, the six second-nearest neighbors (2NN) in blue and the three third-nearest neighbors (3NN) in green.

is known that the reduction of screening that is due to the quantum confinement, results in stronger electron–electron correlations and the emergence of a band gap which cannot be described sufficiently well by DFT (LDA) calculations.[12,39] Instead, it was found that including quasiparticle corrections using the G_0W_0 approximation results in a larger band gap that is in better agreement with experimental findings.[26,40] Thus, the tight-binding approach presented above that is able to reproduce DFT band structures has to be extended to include correlations.

2.2. Extension to Hartree–Fock

In a first step electron interactions can be included on the Hartree–Fock (HF) level. Since this case can still be described by an effective single-particle Hamiltonian, only the matrix elements $\tilde{h}_{ji}^{\mathrm{TB}}$ in Equation (6) have to be replaced by the ones of the new Hamiltonian containing mean-field interactions while the rest of the derivation in Section 2.1 remains untouched.

To derive the HF Hamiltonian it is convenient to express it in second quantization. The creation and annihilation operators obey the same transformation relation between the two basis sets as the single-particle orbitals, *cf.* Equation (8). Thus, in the nonorthogonal basis the generalized operators, *cf.* Equation (18), that create and annihilate an electron with spin σ on site i can be written as

$$\tilde{\hat{c}}_{i,\sigma}^{\dagger} = \sum_k \hat{c}_{k,\sigma}^{\dagger} \tilde{S}_{ki}^{\frac{1}{2}} \tag{14}$$

$$\tilde{\hat{c}}_{i,\sigma} = \sum_k \tilde{S}_{ik}^{\frac{1}{2}} \hat{c}_{k,\sigma} \tag{15}$$

Since the overlap matrix S is real and symmetric it follows immediately from Equations (14) and (15) that the creation and annihilation operators fulfill the known involutivity condition

$$\left(\tilde{\hat{c}}_{i,\sigma}^{\dagger}\right)^{\dagger} = \tilde{\hat{c}}_{i,\sigma} \tag{16}$$

Additionally, as is the case of the orthonormal basis, two creation and two annihilation operators anticommute

$$\left\{\tilde{\hat{c}}_{i,\sigma}^{\dagger}, \tilde{\hat{c}}_{i,\tau}^{\dagger}\right\} = \left\{\tilde{\hat{c}}_{i,\sigma}, \tilde{\hat{c}}_{i,\tau}\right\} = 0 \tag{17}$$

However, the anticommutation relation between a creation operator and an annihilation operator is modified and contains the overlap matrix

$$\left\{\tilde{\hat{c}}_{j,\sigma}^{\dagger}, \tilde{\hat{c}}_{i,\tau}\right\} = \delta_{\sigma\tau}\tilde{S}_{ij} \tag{18}$$

which for $\tilde{S}_{ij} = \delta_{ij}$ reduces to the familiar anticommutator in an orthonormal basis.

Table 1. Various parameter sets for the hopping (*cf.* Equation (12)) and overlap (*cf.* Equation (13)) matrix in the extended Hubbard model.

Structure	Set	J [eV]	$\tilde{E}_{2p}$ [J]	$\tilde{t}_1$ [J]	$\tilde{t}_2$ [J]	$\tilde{t}_3$ [J]	$\tilde{S}_1$	$\tilde{S}_2$	$\tilde{S}_3$
2D Graphene	1NN	2.7	0	1	–	–	–	–	–
	3NN[35](Reich2002)	2.97	0.094	1	0.025	0.111	0.073	0.018	0.026
Graphene nanoribbons	3NN[36](Tran2017)	2.756	0.068	1	0.026	0.138	0.093	0.079	0.070

For homogeneous graphene the parameters are taken from Reich et al.[35] and for GNRs from Tran et al.[36]

The action of a creation operator $\tilde{\tilde{c}}_{i,\sigma}^{\dagger}$ and annihilation operator $\tilde{\tilde{c}}_{i,\sigma}$ on an arbitrary N-particle state $|\{n\}\rangle$ is defined as

$$\tilde{\tilde{c}}_{i,\sigma}^{\dagger}|\{n\}\rangle = (1 - n_{i,\sigma})(-1)^{a_{i,\sigma}}|\{n\}^{i,\sigma}\rangle,$$

$$\tilde{\tilde{c}}_{i,\sigma}|\{n\}\rangle = \sum_k n_{k,\sigma}(-1)^{a_{k,\sigma}}\,\tilde{S}_{ik}|\{n\}k,\sigma\rangle \quad (19)$$

where the notation $|\{n\}^{i,\sigma}\rangle$ and $|\{n\}_{i,\sigma}\rangle$ denotes that a particle with spin σ was added or removed at site i, respectively, $n_{i,\sigma}$ is the occupation number of the orbital corresponding to site i and spin σ and $a_{k,\sigma} = \sum_{l<k} n_{l,\sigma}$.

In the basis of these canonical operators given in Equations (14) and (15), a Hamiltonian including single-particle and two-particle contributions has the form

$$\hat{H} = \sum_{\substack{ijkl \\ \sigma \in \{\uparrow,\downarrow\}}} \tilde{S}_{ik}^{-1} \tilde{h}_{kl}^{\mathrm{TB}} \tilde{S}_{lj}^{-1} \tilde{\tilde{c}}_{i,\sigma}^{\dagger} \tilde{\tilde{c}}_{j,\sigma}$$

$$+ \frac{1}{2} \sum_{\substack{ijklmnpq \\ \sigma,\tau \in \{\uparrow,\downarrow\}}} \tilde{S}_{im}^{-1} \tilde{S}_{jn}^{-1} \tilde{w}_{mnpq}^{\sigma\tau\sigma\tau} \tilde{S}_{pk}^{-1} \tilde{S}_{ql}^{-1} \tilde{\tilde{c}}_{i,\sigma}^{\dagger} \tilde{\tilde{c}}_{j,\tau}^{\dagger} \tilde{\tilde{c}}_{l,\tau} \tilde{\tilde{c}}_{k,\sigma} \quad (20)$$

where the matrix elements of the interaction $\tilde{w}_{mnpq}^{\sigma\tau\sigma\tau}$ do not allow for spin flips and the single-particle contribution $\tilde{h}_{kl}^{\mathrm{TB}}$ is assumed to be spin independent. Further, the matrix elements of the effective single-particle Hartree–Fock Hamiltonian, the so called Fock matrix $\tilde{h}_{ij}^{\mathrm{eff}}$, are given by[41]

$$\tilde{h}_{ij}^{\mathrm{eff}} = \tilde{h}_{ij}^{\mathrm{TB}} + \sum_{\substack{klmn \\ \sigma,\tau \in \{\uparrow,\downarrow\}}} \left(\tilde{w}_{imjn}^{\tau\sigma\tau\sigma} - \tilde{w}_{imnj}^{\sigma\sigma\sigma\sigma} \right) \tilde{S}_{nl}^{-1} \tilde{\rho}_{lk,\sigma} \tilde{S}_{km}^{-1} \quad (21)$$

where $\tilde{\rho}_{lk,\sigma} = \langle \tilde{\tilde{c}}_{k,\sigma}^{\dagger} \tilde{\tilde{c}}_{l,\sigma} \rangle$ is the element of the reduced density matrix in the nonorthogonal basis.[42]

Inserting these matrix elements in Equation (6) for $\tilde{H}$ results in the well-known Roothaan–Hall equations[43–45]

$$\tilde{\mathbf{F}}\tilde{\mathbf{A}} = \tilde{\mathbf{S}}\tilde{\mathbf{A}}\mathbf{E} \quad (22)$$

with $\tilde{\mathbf{F}}$ containing the matrix elements $\tilde{h}_{ij}^{\mathrm{eff}}$. Again, a Löwdin orthogonalization results in a standard eigenvalue problem in the orthonormal basis

$$\mathbf{FA} = \mathbf{AE}, \quad (23)$$

with

$$\mathbf{F} = \tilde{\mathbf{S}}^{-\frac{1}{2}} \tilde{\mathbf{F}} \tilde{\mathbf{S}}^{-\frac{1}{2}} \quad (24)$$

Since the Fock matrix contains the elements of the density matrix, Equation (23) has to be solved self consistently until convergence is reached.

A similar approach was already successfully applied by Hancock et al.[46] for transport calculations in graphene nanoribbons using a Hubbard type on-site interaction of the form

$$\tilde{w}_{ijkl}^{\sigma\tau\sigma\tau} = U\delta_{ij}\delta_{ik}\delta_{il}\overline{\delta}_{\sigma\tau} \quad (25)$$

where $\overline{\delta}_{\sigma\tau} = 1 - \delta_{\sigma\tau}$ enforces Pauli blocking and U is a free parameter that corresponds to the strength of the interaction. For these interaction elements the Fock matrix becomes

$$\tilde{h}_{ij}^{\mathrm{eff}} = \tilde{h}_{ij}^{\mathrm{TB}} + \delta_{ij} U \sum_{kl} \tilde{S}_{il}^{-1} \tilde{\rho}_{lk} \tilde{S}_{ki}^{-1} \quad (26)$$

with $\tilde{\rho}_{lk} := \tilde{\rho}_{lk,\uparrow} + \tilde{\rho}_{lk,\downarrow}$. However, as discussed in Section 2.1, a pure mean-field approach is not sufficient to correctly describe finite graphene nanosystems. For an accurate treatment one has to take into account electronic correlations. Therefore, we will extend the description systematically using the formalism of nonequilibrium Green functions (NEGF) that is described in the next section. Since it is convenient to treat the NEGF approach in an orthonormal basis, it is useful to also express the Fock matrix in this basis. Using Equations (21) and (24) results in

$$h_{ij}^{\mathrm{eff}} = h_{ij}^{\mathrm{TB}} + \sum_{\substack{kl \\ \sigma,\tau \in \{\uparrow,\downarrow\}}} \left(w_{ikjl}^{\tau\sigma\tau\sigma} - w_{iklj}^{\sigma\sigma\sigma\sigma} \right) \rho_{lk,\sigma} \quad (27)$$

with the matrix elements in the orthonormal basis given by

$$h_{ij}^{\mathrm{TB}} = \sum_{kl} \tilde{S}_{ik}^{-\frac{1}{2}} \tilde{h}_{kl}^{\mathrm{TB}} \tilde{S}_{lj}^{-\frac{1}{2}} \quad (28)$$

$$\rho_{ij,\sigma} = \sum_{kl} \tilde{S}_{ik}^{-\frac{1}{2}} \tilde{\rho}_{kl,\sigma} \tilde{S}_{lj}^{-\frac{1}{2}} \quad (29)$$

$$w_{ijkl}^{\sigma\tau\sigma\tau} = \sum_{mnpq} \tilde{S}_{im}^{-\frac{1}{2}} \tilde{S}_{jn}^{-\frac{1}{2}} \tilde{w}_{mnpq}^{\sigma\tau\sigma\tau} \tilde{S}_{pk}^{-\frac{1}{2}} \tilde{S}_{ql}^{-\frac{1}{2}} \tag{30}$$

In the special case of an on-site Hubbard interaction, *cf.* Equation (25), the interaction elements in the orthonormal basis reduce to

$$w_{ijkl}^{\sigma\tau\sigma\tau} = U\bar{\delta}_{\sigma\tau} \sum_m \tilde{S}_{im}^{-\frac{1}{2}} \tilde{S}_{jm}^{-\frac{1}{2}} \tilde{S}_{mk}^{-\frac{1}{2}} \tilde{S}_{ml}^{-\frac{1}{2}} =: w_{ijkl}\bar{\delta}_{\sigma\tau} \tag{31}$$

Finally, the spin-resolved Fock matrix is then given by

$$h_{ij,\uparrow(\downarrow)}^{\text{eff}} = h_{ij}^{\text{TB}} + \sum_{kl} w_{ikjl}\rho_{lk,\downarrow(\uparrow)} \tag{32}$$

which will later on be used in the propagation of the nonequilibrium Green functions, see Section 3.1.

3. Nonequilibrium Green Functions Approach

The single-particle Green function G is the central property in the nonequilibrium Green functions approach. It is defined on the Keldysh time contour C as[47,48]

$$G_{ij}^{\sigma}(z, z') = -\frac{i}{\hbar} \langle T_C \hat{c}_{i,\sigma}(z)\hat{c}_{j,\sigma}^{\dagger}(z')\rangle \tag{33}$$

where $\langle\dots\rangle$ is the ensemble average and the creation and annihilation operator are defined in an orthonormal basis. Due to the spin symmetry of the considered systems the spin indices will be neglected in the further discussion and the Green function will be simplified to[49]

$$G_{ij}(z, z') := G_{ij}^{\uparrow}(z, z') = G_{ij}^{\downarrow}(z, z') \tag{34}$$

In order to make the complex-time Green function numerically accessible, it is useful to define real-time contour components of the Green function based in the relative positions of the complex times z and z' on the contour, namely the less ($G^<$), greater ($G^>$), retarded (G^R), and advanced (G^A) component that are defined as

$$G_{ij}^<(t, t') = -\frac{1}{i\hbar} \langle \hat{c}_j^{\dagger}(t')\hat{c}_i(t)\rangle \tag{35}$$

$$G_{ij}^>(t, t') = \frac{1}{i\hbar} \langle \hat{c}_i(t)\hat{c}_j^{\dagger}(t')\rangle \tag{36}$$

$$G_{ij}^R(t, t') = \Theta(t, t')\left(G_{ij}^>(t, t') - G_{ij}^<(t, t')\right) \tag{37}$$

$$G_{ij}^A(t, t') = \Theta(t', t)\left(G_{ij}^<(t, t') - G_{ij}^>(t, t')\right) \tag{38}$$

where $\Theta(t, t')$ denotes the Heaviside step function.

As a generalization of the single-particle density matrix, $\rho_{ij} = \langle\hat{c}_j^{\dagger}\hat{c}_i\rangle$, onto the two-time plane the Green function carries all information about the single-particle density on the time diagonal

$$\rho_{ij}(t) = -i\hbar G_{ij}^<(t, t) \tag{39}$$

With this, one gets access to the time-dependent expectation value of any single-particle operator $\hat{A}_1$, such as the single-particle energy, via

$$\langle\hat{A}_1\rangle(t) = -i\hbar \sum_{ij} A_{ij} G_{ji}^<(t, t) \tag{40}$$

One should note that when combined with the TB approach presented in Section 2.1 the orthonormal basis of the Green function does not correspond to the nonorthogonal basis of the $2p_z$ atomic orbitals of the carbon lattice. For the density matrix the transformation to the physical basis can be performed by the inverse of Equation (29) which leads to

$$\tilde{\rho}_{ij} = \sum_{kl} \tilde{S}_{ik}^{\frac{1}{2}} \rho_{kl} \tilde{S}_{lj}^{\frac{1}{2}} \tag{41}$$

In this basis the occupation on a single lattice site i is then given by

$$\langle\hat{\rho}_{ii}\rangle = \sum_k \tilde{S}_{ik}^{-1} \tilde{\rho}_{ki} \tag{42}$$

Since the Green function is defined as a two-time quantity (*cf.* Equation (33)), it also gives access to the spectral properties of the system. The local spectral function is given by a Fourier transform with respect to the relative time,

$$A_i(\omega) = i\hbar \int dt\, dt' e^{-i\omega(t-t')}\left[G_{ii}^>(t, t') - G_{ii}^<(t, t')\right] \tag{43}$$

The sum over all local contributions of the spectral function results in the density of states (DOS) of the system. Combining the temporal transform in Equation (43) with a spatial one results in an expression for the full energy dispersion relation

$$A(\omega, k) = \frac{i\hbar}{N_s} \sum_{ij} e^{-ik(i-j)} \int dt\, dt' e^{-i\omega(t-t')}$$
$$\times \left[G_{ij}^>(t, t') - G_{ij}^<(t, t')\right] \tag{44}$$

Another important quantity is the time-resolved photoemission spectrum[50,51]

$$A^<(\omega, T) = -i\hbar \sum_i \int dt\, dt' S_\kappa(t - T) S_\kappa(t' - T)$$
$$\times e^{-i\omega(t-t')} G_{ii}^<(t, t') \tag{45}$$

as it allows for direct comparison with photoemission experiments. Here, S is a Gaussian function to simulate the probe pulse that is used in corresponding experiments

$$S_\kappa(t) = \frac{1}{\kappa\sqrt{2\pi}}\exp\left(-\frac{t^2}{2\kappa^2}\right) \tag{46}$$

with a given pulse width κ.

3.1. Equations of Motion

The time evolution of the Green function on the Keldysh contour is given by the Kadanoff–Baym equations (KBEs),[52]

$$\sum_l \left[i\hbar\frac{d}{dz}\delta_{il} - h_{il}^{TB}(z)\right]G_{lj}(z,z')$$
$$= \delta_{ij}\delta_C(z,z') + \sum_l \int_C dz\, \Sigma_{il}(z,\overline{z})G_{lj}(\overline{z},z') \tag{47}$$

and the adjoint equation. The KBEs would be formally exact if the self-energy Σ in the collision integral on the right hand side of the equation was known. However, for most system the exact self-energy is not accessible. Hence, approximations to the NEGF scheme are introduced via proper choices of the self-energy. A more detailed discussion on the approximations used here is given in Section 3.2. The self-energy can be separated into a time-diagonal mean-field contribution and a correlation part

$$\Sigma(z,z') = \delta_C(z,z')\Sigma^{HF}(z) + \Sigma^{corr}(z,z') \tag{48}$$

Due to the contour delta distribution $\delta_C(z,z')$ the Hartree–Fock part of the self-energy can be included into the Hamiltonian on the left side of Equation (47) resulting in an effective single-particle Hamiltonian that is equivalent to the Fock matrix in Equation (27). Now the KBE can be written as

$$\sum_l \left[i\hbar\frac{d}{dz}\delta_{il} - h_{il}^{eff}(z)\right]G_{lj}(z,z')$$
$$= \delta_{ij}\delta_C(z,z') + \sum_l \int_C d\overline{z}\, \Sigma_{il}(z,\overline{z})G_{lj}(\overline{z},z') \tag{49}$$

where the self-energy $\Sigma(t,t') := \Sigma^{corr}(t,t')$ only contains the correlation part.

In practice, the KBEs are solved for the less and greater real-time components of the Green function. In order to get access to the full single-particle information of the system, it is necessary to obtain $G^>(t,t')$ and $G^<(t,t')$ in the complete (t,t')-plane. However, due to the symmetry relation $G_{ij}^{\lessgtr}(t,t') = -\left[G_{ji}^{\lessgtr}(t',t)\right]^*$ each of the two KBEs (Equation (49) and the adjoint) has to be solved for only one real-time argument and component of the Green function. One possible choice of equations is:

$$\sum_l \left[i\hbar\frac{d}{dt}\delta_{il} - h_{il}^{eff}(t)\right]G_{lj}^>(t,t') = I_{ij}^{(1),>}(t,t') \tag{50}$$

$$\sum_l G_{il}^<(t,t')\left[-i\hbar\frac{\overleftarrow{d}}{dt'}\delta_{il} - h_{lj}^{eff}(t')\right] = I_{ij}^{(2),<}(t,t') \tag{51}$$

where on the right-hand side the collision integrals $I^{(1),>}$ and $I^{(2),<}$ are introduced. They are defined as

$$I_{ij}^{(1),>}(t,t') := \sum_l \int_{t_s}^\infty d\overline{t}\left\{\Sigma_{il}^R(t,\overline{t})G_{lj}^>(\overline{t},t') + \Sigma_{il}^>(t,\overline{t})G_{lj}^A(\overline{t},t')\right\} \tag{52}$$

$$I_{ij}^{(2),<}(t,t') := \sum_l \int_{t_s}^\infty d\overline{t}\left\{G_{il}^R(t,\overline{t})\Sigma_{lj}^<(\overline{t},t') + G_{il}^<(t,\overline{t})\Sigma_{lj}^A(\overline{t},t')\right\} \tag{53}$$

with the starting time t_s, see Section 3.3 for a discussion. This way, $G^<(t,t')$ is propagated above and $G^>(t,t')$ below the time diagonal. For $t = t'$ either one of them can be calculated while the other one can be accessed by the symmetry relation on the time diagonal

$$G_{ij}^>(t,t) - G_{ij}^<(t,t) = -\frac{i}{\hbar}\delta_{ij} \tag{54}$$

Likewise, the collision integrals $I^{(1),>}(t,t')$ and $I^{(2),<}(t,t')$ have to be calculated for times $t > t'$ and $t < t'$ only, respectively. To this end a new notation is introduced for a general contour quantity A,

$$A(t \gtreqless t') := A(t,t')\big|_{t \gtreqless t'} \tag{55}$$

This results in three equations of motion for the full two-time propagation of the real-time components of the Green function:

$$i\hbar\frac{d}{dt}G_{ij}^>(t \geq t') = \sum_l h_{il}^{eff}(t)G_{il}^>(t \geq t')$$
$$+ I_{ij}^{(1),>}(t \geq t') \tag{56}$$

$$-i\hbar\frac{d}{dt'}G_{ij}^<(t \leq t') = \sum_l G_{il}^<(t \leq t')h_{lj}^{eff}(t')$$
$$+ I_{ij}^{(2),<}(t \leq t') \tag{57}$$

$$i\hbar\frac{d}{dt}G_{ij}^<(t,t) = \left[h^{eff}(t), G^<(t,t)\right]_{ij}$$
$$+ I_{ij}^{(1),>}(t,t) - I_{ij}^{(2),<}(t,t) \tag{58}$$

In order to solve these equations of motion, the collision integrals that appear in Equations (56)–(58) have to be expressed in terms of $G^<(t < t')$ and $G^>(t > t')$. Using the definition of the advanced and retarded Green function and self-energy (cf. Equations (37) and (38)) one arrives, after some calculations, at the following expressions for the collision integrals at a given time step T:

$$I_{ij}^{(1),>}(T > t') = \int_{t_s}^{t'} d\bar{t} \sum_k \left\{ \Sigma_{ik}^>(T > \bar{t}) G_{kj}^<(\bar{t} < t') \right.$$
$$\left. - \left(\Sigma_{ki}^<(\bar{t} < T) G_{jk}^>(t' > \bar{t}) \right)^* \right\}$$
$$+ \int_{t'}^{T} d\bar{t} \sum_k \left\{ \Sigma_{ik}^>(T > \bar{t}) G_{kj}^>(\bar{t} > t') \right.$$
$$\left. + \left(\Sigma_{ki}^<(\bar{t} < T) \right)^* G_{kj}^>(\bar{t} > t') \right\} \tag{59}$$

$$I_{ij}^{(2),<}(t < T) = \int_{t_s}^{t} d\bar{t} \sum_k \left\{ G_{ik}^>(t > \bar{t}) \Sigma_{kj}^<(\bar{t} < T) \right.$$
$$\left. - \left(G_{ki}^<(\bar{t} < t) \Sigma_{jk}^>(T > \bar{t}) \right)^* \right\}$$
$$+ \int_{t}^{T} d\bar{t} \sum_k \left\{ G_{ik}^<(t < \bar{t}) \Sigma_{kj}^<(\bar{t} < T) \right.$$
$$\left. + G_{ik}^<(t < \bar{t}) \left(\Sigma_{jk}^>(T > \bar{t}) \right)^* \right\} \tag{60}$$

for the off-diagonal elements and

$$I_{ij}^{(1),>}(T, T) = \int_{t_s}^{T} d\bar{t} \sum_k \left\{ \Sigma_{ik}^>(T > \bar{t}) G_{kj}^<(\bar{t} < T) \right.$$
$$\left. - \left(\Sigma_{ki}^<(\bar{t} < T) G_{jk}^>(T > \bar{t}) \right)^* \right\} \tag{61}$$

$$I_{ij}^{(2),<}(T, T) = \int_{t_s}^{T} d\bar{t} \sum_k \left\{ G_{ik}^>(T > \bar{t}) \Sigma_{kj}^<(\bar{t} < T) \right.$$
$$\left. - \left(G_{ki}^<(\bar{t} < T) \Sigma_{jk}^>(T > \bar{t}) \right)^* \right\}$$
$$= - \left(I_{ji}^{(1),>}(T, T) \right)^* \tag{62}$$

for the time diagonal. These equation do only depend on $G^<(t < t')$, $G^>(t > t')$, $\Sigma^<(t < t')$, and $\Sigma^>(t > t')$. Therefore, if it is possible to express the self-energy in terms of the less and greater components of the Green function – which is possible for all relevant approximations, *cf.* Section 3.2 – the propagation scheme will be closed. Examples for application of this NEGF scheme to Hubbard clusters can be found for example, in refs. [32,53–55]. Computational details will be presented in Section 3.3.

3.2. Self-Energy Approximations

The exact self-energy Σ contains the full N-particle information of the system. However, since in most cases the exact solution is not known one has to develop many-body approximations (MBA) to the self-energy. For this, as shown in Equation (48), the self-energy can be separated into a Hartree–Fock and a correlation contribution. The time-diagonal mean-field part can be included in an effective single-particle Hamiltonian and the remaining self-energy contains only the correlation part, *cf.* Equation (49).

The mean-field Hamiltonian was derived in Section 2.2 and its elements are given by the Fock matrix, *cf.* Equation (32). For a Hubbard-type on-site interaction that is considered here, the matrix elements of the interaction in the orthonormal basis are defined in Equation (31). The corresponding diagram is depicted in **Figure 2**. Due to the spin delta $\bar{\delta}_{\sigma\tau}$ the exchange contribution vanishes and only the direct mean-field diagram remains.

While in the nonorthogonal basis the strength of the on-site interaction is defined by the parameter U, in the orthonormal basis this leads to a local interaction, *cf.* Equation (31)

$$w_{ijkl} = U \sum_m \tilde{S}_{im}^{-\frac{1}{2}} \tilde{S}_{jm}^{-\frac{1}{2}} \tilde{S}_{mk}^{-\frac{1}{2}} \tilde{S}_{ml}^{-\frac{1}{2}} \tag{63}$$

For higher-order approximations to the correlation self-energy this would result in a high numerical complexity. In order to reduce the numerical effort, here, only the diagonal contribution to the interaction

$$U_i := w_{iiii} U \sum_m \tilde{S}_{im}^{-\frac{1}{2}} \tilde{S}_{im}^{-\frac{1}{2}} \tilde{S}_{mi}^{-\frac{1}{2}} \tilde{S}_{mi}^{-\frac{1}{2}} \tag{64}$$

is taken into account. This approximation is valid if the overlap matrix $\tilde{S}$ – and consequently $\tilde{S}^{-\frac{1}{2}}$ – has mainly diagonal contributions which is the case for the considered parameter set, *cf.* Table 1 and Equation (13). Further, it allows for a fast calculation of higher-order self-energy contributions. The two approximations specifically used in this work are presented in the following using a generalized time-dependent $U(t)$ for the adiabatic switching procedure, *cf.* Section 3.3.

The second-Born (2B) approximation is the most simple approach to add correlations to the self-energy. The idea is to describe the scattering event between two particles by considering only the first term in the Born series.[47] This results in the following expression for the 2B self-energy

$$\Sigma_{ij}^{2B,>}(T > t') = \hbar^2 U_i(T) U_j(t') G_{ij}^>(T > t') G_{ij}^>(T > t') G_{ji}^<(t' < T) \tag{65}$$
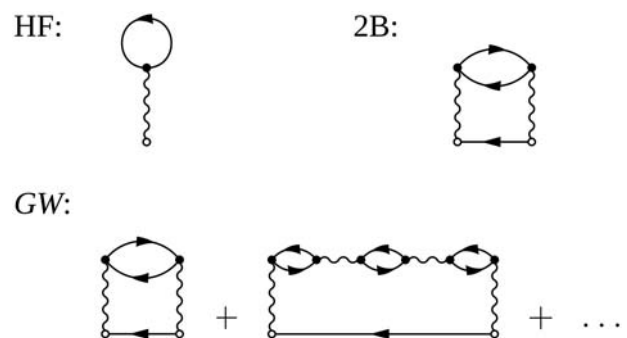

Figure 2. Feynman diagrams for the self-energy approximations used in this work: Hartree–Fock (HF), second-order Born approximation (2B), and Hedin's *GW* approximation.

$$\Sigma_{ij}^{2B,<}(t < T) = \hbar^2 U_i(t) U_j(T) G_{ij}^<(t < T) G_{ij}^<(t < T) G_{ji}^>(T > t) \tag{66}$$

It includes all terms up to second order in the interaction U but no higher-order terms. Thus, it is a reasonable approach when the interaction strength is low. From a numerical point of view the 2B self-energy is easy to calculate since no integration over a time argument has to be performed. A diagrammatic representation is shown in Figure 2. More details can be found in refs. [47,56,57].

The GW approximation is a more sophisticated approach that takes the dynamically screened interaction between particles into account. The real-time components of the self-energy are given by

$$\Sigma_{ij}^{GW,>}(T > t') = i\hbar W_{ji}^{<,\uparrow\uparrow}(t' < T) G_{ij}^>(T > t') \tag{67}$$

$$\Sigma_{ij}^{GW,<}(t < T) = i\hbar W_{ij}^{<,\uparrow\uparrow}(t < T) G_{ij}^<(t < T) \tag{68}$$

The less component of the same-spin screened interaction $W^{<,\uparrow\uparrow}$ has to be calculated in an iterative manner. For this, it is convenient to define the retarded and advanced component of the two-particle Fock-like Green function

$$G_{ij}^{F,R}(t > t') = G_{ij}^>(t > t') G_{ji}^<(t' < t) - \left(G_{ji}^<(t' < t)\right)^* \left(G_{ij}^>(t > t')\right)^* \tag{69}$$

$$G_{ij}^{F,A}(t < t') = G_{ij}^<(t < t') G_{ji}^>(t' > t) - \left(G_{ji}^>(t' > t)\right)^* \left(G_{ij}^<(t < t')\right)^* \tag{70}$$

Now, the same-spin screened interaction is given by

$$W_{ij}^{<,\uparrow\uparrow}(t < T) = -i\hbar U_i(t) G_{ij}^{F,<}(t < T) U_j(T)$$
$$-i\hbar U_i(t) \sum_k \int_{t_s}^t d\bar{t} G_{ik}^{F,R}(t > \bar{t}) W_{kj}^{<,\uparrow\downarrow}(\bar{t} < T)$$
$$-i\hbar U_i(t) \sum_k \int_{t_s}^t d\bar{t} \left(G_{ki}^{F,<}(\bar{t} < t)\right)^* W_{kj}^{A,\uparrow\downarrow}(\bar{t} < T)$$
$$-i\hbar U_i(t) \sum_k \int_t^T d\bar{t} G_{ik}^{F,<}(t < \bar{t}) W_{kj}^{A,\uparrow\downarrow}(\bar{t} < T) \tag{71}$$

It depends on the different-spin screened interaction

$$W_{ij}^{<,\uparrow\downarrow}(t < T) = -i\hbar U_i(t) G_{ij}^{F,<}(t < T) U_j(T)$$
$$-i\hbar U_i(t) \sum_k \int_{t_s}^t d\bar{t} G_{ik}^{F,R}(t > \bar{t}) W_{kj}^{<,\uparrow\uparrow}(\bar{t} < T)$$
$$-i\hbar U_i(t) \sum_k \int_{t_s}^t d\bar{t} \left(G_{ki}^{F,<}(\bar{t} < t)\right)^* W_{kj}^{A,\uparrow\uparrow}(\bar{t} < T)$$
$$-i\hbar U_i(t) \sum_k \int_t^T d\bar{t} G_{ik}^{F,<}(t < \bar{t}) W_{kj}^{A,\uparrow\uparrow}(\bar{t} < T) \tag{72}$$

that, again, contains the same-spin screened interaction $W^{<,\uparrow\uparrow}$. Additionally, these two coupled equations depend on the advanced components of the same- and different-spin screened interaction that are given by

$$W_{ij}^{A,\uparrow\uparrow}(t < T) = -i\hbar U_i(t) G_{ij}^{F,A}(t < T) U_j(T)$$
$$+i\hbar U_i(t) \sum_k \int_t^T d\bar{t} G_{ik}^{F,A}(t < \bar{t}) W_{kj}^{A,\uparrow\downarrow}(\bar{t} < T) \tag{73}$$

$$W_{ij}^{A,\uparrow\downarrow}(t < T) = i\hbar U_i(t) \sum_k \int_t^T d\bar{t} G_{ik}^{F,A}(t < \bar{t}) W_{kj}^{A,\uparrow\uparrow}(\bar{t} < T) \tag{74}$$

In order to solve this system of coupled equations numerically, first, the two advanced components of the screened interaction are calculated. On the time diagonal a solution can be immediately found for both:

$$W_{ij}^{A,\uparrow\uparrow}(T, T) = -i\hbar U_i(T) G_{ij}^{F,A}(T, T) U_j(T) \tag{75}$$

$$W_{ij}^{A,\uparrow\downarrow}(T, T) = 0 \tag{76}$$

Next, Equations (73) and (74) can be solved simultaneously in an iterative manner for every time t starting from the diagonal. After that, Equations (71) and (72) are iterated until convergence for every time step t, this time starting at t_s. This way, the less and greater component of the GW self-energy can be computed according to Equations (67) and (68).

Due to its integral (Dyson) equation structure the GW approach contains contributions up to infinite order in U. Therefore, it is much more challenging than the 2B approximation, from a numerical perspective. But this effort is warranted because the GW approximation has shown very good results for systems near half filling, where screening effects are important.[58] Furthermore, it is frequently used for band structure and photoemission calculations.[59,60] The first three diagrams of the GW approximation are depicted in **Figure 3**. A detailed derivation of these equations and the corresponding expressions for other self-energies can be found in ref. [61].

With the self-energies given in Equations (65)–(68) the propagation scheme for the real-time components of the Green function is closed.

3.3. Numerical Solution of the Keldysh–Kadanoff–Baym Equations for GNR

Despite the application of the diagonal Hubbard interaction the numerical solution of the KBEs remains a challenging task. For a given time step T, first, the effective single-particle Hamiltonian h_{ij}^{eff} (*cf.* Equation (32)) and the chosen self-energy (*cf.* Equations (65)–(68)) have to be calculated from the Green functions. Now all quantities are known that are needed to determine the collision integrals $I^{(1),>}$ and $I^{(2),<}$ via Equations (59)–(62). Next, the components of the Green function can be propagated one
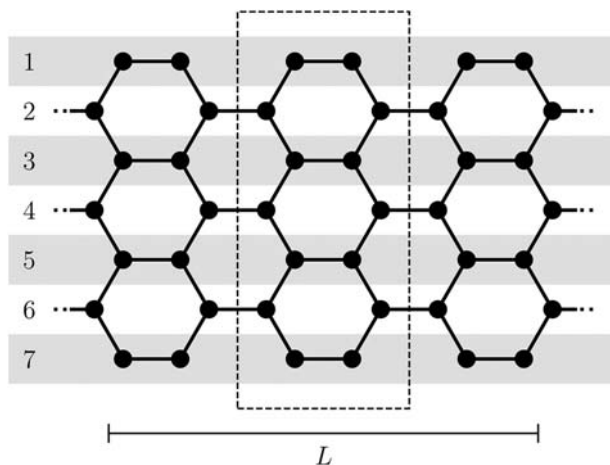
Figure 3. Illustration of the structure of an armchair graphene nanoribbon (AGNR). The width $N(=7)$ and the length $L(=7)$ of the graphene ribbon is defined as the number of dimer and zigzag lines of carbon atoms, respectively. Here, a 7-AGNR is shown. The dashed rectangle defines the unit cell of the ribbon. In Figure 1 the positions of the nearest neighbors in a GNR are depicted.

time step further to $T + \Delta$ using Equations (56)–(58), where Δ is the time step size. Before the actual propagation is started the ground state of the system has to be calculated, which is done via adiabatic switching. A detailed description of this procedure is given in ref. [32]. An alternative procedure to obtain the ground state is the inclusion of the imaginary-time branch in the Keldysh time contour.[47,62] Both methods have their advantages, adiabatic switching results in additional propagation time while the imaginary branch leads to the occurrence of extra terms in the collision integrals.[63]

Since the calculation of the self-energies and collision integrals require the Green function on the complete two-time plane, the computational memory demand and calculation time of the propagation algorithm show a quadratic and cubic scaling, respectively, with respect to both, the basis size and the number of time steps.

In order to nevertheless keep the numerical challenges in check a lot of sophisticated improvements have been made to the propagation techniques of the NEGF scheme. For the solution of the KBEs a fourth-order Runge–Kutta method is used while the time integrals occurring in the calculation of the self-energies and the collision integrals are determined using high-order Newton–Cotes and Fourier extension algorithms.

From a performance perspective, another crucial part of the propagation scheme is the huge number of matrix multiplications which can be parallelized with respect to the spatial and temporal indices. In theory, this can be utilized to massively speed-up the simulation on an appropriate architecture. Therefore, all calculations in this work have been performed using graphics processing units (GPUs) that are known to greatly outperform CPUs when it comes to parallel calculations.[64]

In the past, our NEGF simulations have been carefully tested for convergence with respect to the time step where, among others, particle number and total energy conservation are monitored, for example, Ref. [31], and also time reversibility[65,66] is verified. For small systems tests against exact diagonalization

calculation are performed. Additionally, comparisons with 2D cold atom experiments[32,67] and 1D density-matrix renormalization group (DMRG) calculations[30] showed excellent accuracy of our simulations.

4. Results

The system of interest in this paper are so-called graphene nanoribbons (GNR) which are quasi-one-dimensional slices of graphene. Because of their typical width of only a few nanometers they exhibit various remarkable properties such as enhanced electron correlations due to quantum confinement effects.[39]

The electronic properties and especially the low energy spectrum of the π-electrons is strongly influenced by the edge structure of the nanoribbons. Depending on the shape of the edges one distinguishes between armchair (AGNR) and zigzag graphene nanoribbons (ZGNR). While the model presented in Sections 2 and 3 is applicable to both types of nanoribbons, here we will focus our attention on hydrogen-passivated AGNRs. The width N of the ribbons is defined as the number of dimer lines while the length L is given by the number of zigzag lines as illustrated in Figure 3.

4.1. Ground-State Results: Band Gap, Dispersion, and Spectral Function

The extended Hubbard model introduced in Sections 2 and 3 contains eight free parameters. For the seven tight-binding parameters we choose the set proposed by Tran et al.[36], *cf.* Table 1, that has been created to accurately reproduce the LDA band structure for a wide range of GNRs including different edge structures and various widths. The final free parameter of the model, the on-site interaction U, has to be adjusted to best reproduce the band structure and band gap of GNRs observed in experiments and theory that goes beyond LDA by including quasiparticle corrections. A convenient choice for the system for which the value of U can be fit is the GNR with an armchair edge and a width of seven dimer lines (7-AGNR) which is depicted in **Figure 4**. On the one hand this system has a small width which reduces the numerical effort of our calculations and, on the other hand, its ground-state properties such as the band structure and band gap have been explored in detail both theoretically and experimentally.[12,26,68–70]

However, most experiments and theoretical works study long 7-AGNRs the band gaps of which are converged toward the value of the respective GNR for $L \to \infty$. Since our calculations are for ribbons of finite length L we have to consider the influence of finite-size effects on our results before comparing with theoretical and experimental values for the band gap. For this reason in Figure 4, we plot the size of the band gap E_g for 7-AGNRs of different lengths L within our model with the interaction set to $U = 0$ which is equivalent to the extended tight-binding model. The high numerical costs allow for calculations up to a length of $L = 16$ which corresponds to a basis size of $N_s = 112$. The band gap is given by calculating the energy dispersion, *cf.* Equation (44), and determining the difference
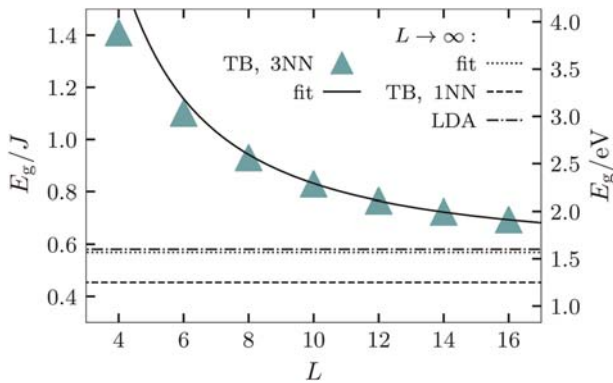
Figure 4. Band gap E_g for 7-AGNRs of different length L. The results of our model for $U = 0$ are shown as triangles. The black solid line corresponds to an exponential fit through the data points for $L = 10, \ldots, 16$ and its asymptotic value for $L \to \infty$ is marked by the dotted line. As a comparison the band gap for an infinite 7-AGNR predicted by the nearest-neighbor tight-binding model and LDA are shown as dashed lines.[68]

between the lowest peak in the upper subband and the highest peak in the lower subband at the high symmetry point K in the first Brillouin zone of graphene.

Since the band gap of the shorter ribbons $L = 4, \ldots, 8$ is highly modified due to finite-size effects we perform an exponential fit through the data of the longer ribbons $L = 10, \ldots, 16$ which is shown as the solid black line in Figure 4. The value of the fit for $L \to \infty$ is shown as dotted line and shows excellent agreement with the LDA gap of ≈ 1.6 eV for the 7-AGNR with infinite length. This is not surprising since the parameter set used was fit to match the LDA band structure of GNRs. As a comparison, the band gap predicted by the tight-binding model considering only nearest-neighbor hopping is considerably smaller with $E_g = 1.25$ eV. In the following, we adjust the value of U for a system of length $L = 16$. For this size the deviation of the band gap compared to the infinite system is about $0.1\,J$. Thus, when comparing our results for $U > 0$ we expect the observed gap to be $\approx 0.1\,J$ larger due to finite-size effects than it would be for an infinite ribbon.

In order to obtain a reasonable value for the interaction U, in **Figure 5** we compare the band gap of our HF, 2B and GW calculations using $U = 0, \ldots, 3.5\,J$ for a 7-AGNR of length $L = 16$ against various theoretical and experimental results for similar 7-AGNRs in the form of horizontal lines. As already mentioned, these reference data describe the converged band gap for long ribbons ($L \to \infty$) on top of different interacting substrates.

Setting $U = 0$ the HF, 2B and GW self-energies produce the same band gap of $E_g \approx 0.7\,J$ which is equal to the data of Figure 4 for $L = 16$. As a result it is roughly $0.1\,J$ above the LDA result for free-standing ribbons with $L \to \infty$ due to finite-size effects as established in Figure 4. For HF the band gap is nearly independent of U and only slightly decreases by $\approx 0.025\,J$ from $U = 0$ to $U = 3.5\,J$. The 2B self-energy on the other hand shows an opening of the band gap starting at $U \approx 2\,J$ which results in a band gap at $U = 3.5\,J$ that is about $0.02\,J$ larger than for $U = 0$. Using the GW self-energy the band gap also starts to open at $U \approx 2\,J$. However, at $U = 3.5\,J$ the gap already has a size of $\approx 1\,J$, which is an increase of $0.3\,J$ compared to $U = 0$. A similar
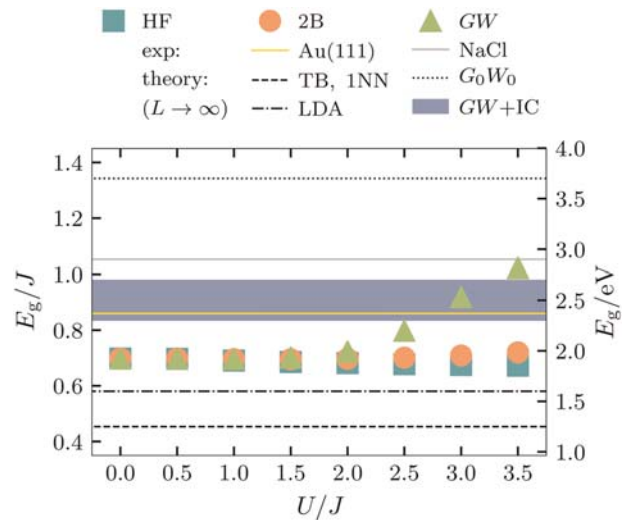

Figure 5. Band gap E_g of 7-AGNRs with a length of $L = 16$ within the extended Hubbard model using the HF (teal squares), 2B (orange circles), and GW (green triangles) self-energy as a function of the on-site interaction U. As a reference various theoretical and experimental band gaps for infinite 7-AGNRs are added. The results for free-standing GNRs are marked by dashed lines for the nearest-neighbor tight-binding model and LDA,[68] and by a dotted line for G_0W_0.[12] The blue rectangle shows the area considering image-charge corrections[69] and the gold and gray solid lines correspond to measurements for GNRs on Au(111)[70] and NaCl,[26] respectively.

dependence of the band gap on the on-site interaction has been observed for the one-dimensional Hubbard chain.[71] However, here the band gap increase due to correlations in the case of 2B and GW is not as strong as in the 1D case. This is likely due to the larger bandwidth of the graphene honeycomb lattice ($6J$) compared to the one-dimensional chain lattice ($4J$) which is why an interaction of $U = 3.5\,J$ is less significant in the former case than in the latter.

In order to assess the quality of our results for the size of the band gap we compare to various reference data in Figure 5. While LDA calculations produce good results for weakly correlated homogeneous graphene,[72] for graphene nanoribbons it was found that electronic correlation effects are more important and that quasiparticle corrections (G_0W_0) to LDA greatly increase the band gap to $E_g = 3.7$ eV.[12] However, in the presence of a substrate that influences the band structure of the ribbons through screening effects smaller band gaps are observed. Measurements of 7-AGNRs on a Au(111) and NaCl surface revealed a band gap of $E_g = 2.37$ eV and $E_g = 2.9$ eV, respectively, which are between the prediction of LDA and G_0W_0.[26,70] Taking into account screening effects theoretically through image-charge corrections ($GW + \mathrm{IC}$) leads to a reduced band gap of $E_g = 2.3 - 2.7$ eV compared to G_0W_0.[69]

Considering finite-size effects the GW self-energy for an interaction strength of $U = 3.5\,J$ nicely reproduces the band gap found including image-charge corrections ($GW + \mathrm{IC}$) and measured for 7-AGNRs on Au(111).

To highlight the influence of the interaction U in the left two panels of **Figure 6**, we show the band structure (cf. Equation (44) for the energy dispersion) of the 7-AGNR of length $L = 16$

**ADVANCED
SCIENCE NEWS**

www.advancedsciencenews.com

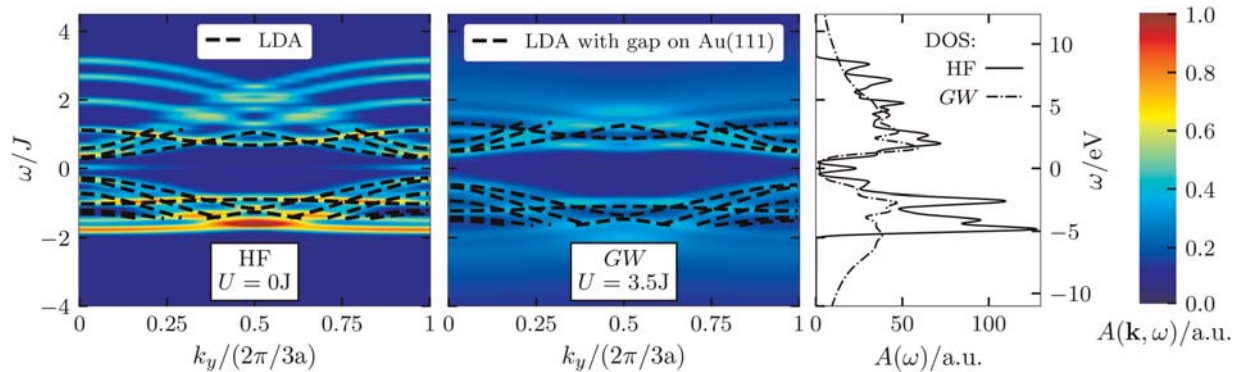**pss b**
physica status solidi b

www.pss-b.com

Figure 6. The left and middle panel show the energy dispersion of a 7-AGNR with a length of $L = 16$. The colormap corresponds to NEGF calculations using the HF (left) and GW (middle) self-energy with $U = 0$ and $U = 3.5J$, respectively. The dashed black lines mark the LDA band structure with the original LDA band gap (left)[26] and shifted to obtain the band gap measured for 7-AGNRs on Au(111) (middle).[70] The right panel shows the DOS for the NEGF results.

considered in Figure 5 for a HF calculation with $U = 0$ and a GW calculation using $U = 3.5J$. In the right panel, we plot the corresponding DOS, *cf.* Equation (43). The HF result is compared to the LDA band structure marked by the dashed black lines. As expected they match up nicely with some small deviations due to finite-size effects, one of them is the peak at $\omega = 0J$ which was found to vanish for $L \to \infty$. In the middle panel the dashed lines again show the LDA band structure, but shifted in such a way that the band gap corresponds to the experimental result of $E_g = 2.37$ eV for 7-AGNRs on Au(111). As found in Figure 5, the GW self-energy with $U = 3.5J$ nicely reproduces the band gap. Thus, in the vicinity of the band gap the shifted LDA result agrees with the GW band structure. However, the higher energy regions are strongly affected by correlation effects which is especially noticeable in the DOS where satellites appear for $\omega < -2J$ and $\omega > 3J$ which is outside the scope of the LDA. Therefore, the shifted LDA band structure is not accurate outside of the direct vicinity of the band gap.

In conclusion, we choose $U = 3.5J$ for the on-site interaction of the extended Hubbard model. It should be mentioned that despite only fit to 7-AGNRs, the model presented here is able to accurately describe a broad range of AGNRs. On the one hand, the set of TB parameters by Tran et al.[36] was created to perform well for all kinds of nanoribbons with different width and edge structure and, on the other hand, it was found by Yang et al.[12] that the influence of quasiparticle corrections results in a similar increase of the band gap compared to LDA calculations for all small AGNRs. Thus, the introduced parameter set combined with an on-site interaction of $U = 3.5J$ should be applicable to a broad range of AGNRs. Of course the value of U can be changed and determined in similar fashion if other geometries or edge shapes are to be described.

4.2. Laser-Pulse-Excited Electron Dynamics in GNR

In the following we evaluate the performance of the different self-energy approximations in the non-equilibrium regime using a 5-AGNR with a length of $L = 6$. Nanoribbons of this type and size can be produced through bottom-up synthesis.[17] The system starts in the ground state and is subsequently excited by a laser pulse of the form

$$E_{\text{laser}}(t) = E_0 \cos[\omega_0(t - t_0)]e^{-\frac{(t-t_0^2)}{2\sigma^2}} \qquad (77)$$

with a laser amplitude of $E_0 = 0.1Je^{-1}a^{-1}$, where e is the elementary charge and $a = 0.142$ nm is the lattice constant of the system. Furthermore, a laser frequency of $\omega_0 = 2J$ is used and the standard deviation of the Gaussian is set to $\sigma = 4.35J^{-1}$. The shape of the laser pulse at $t_0 = 0$ is depicted as a solid black line in the upper panel of **Figure 7**. The laser excitation is treated within the dipole approximation resulting in a single-particle excitation

$$f_i(t) = -\mathbf{r}_i \cdot e\mathbf{E}_{\text{laser}}(t) \qquad (78)$$

which is justified because the wavelength $\lambda_0 = 224.9$ nm of the laser pulse is a lot larger than the size $l \approx 1$ nm of the system. The excitation enters in Equation (11) as an additional time-dependent local on-site energy. In the following the direction of the electric field is set to be parallel to the armchair edge of the ribbons.

In order to study the response of the nanocluster to the laser excitation, we consider the time- and energy-resolved occupation of carriers in the conduction band. For that reason, we determine the time-dependent photoemission spectrum, *cf.* Equation (45), using a probe pulse width of $\kappa = 2.5J^{-1}$ at four different times, $tJ = -30, 0, 20, 50$, that are sketched in the upper panel of Figure 7 by the Gaussians of different colors. The different snapshots show the system in the ground state, during the laser interaction, directly after the laser pulse decayed and long after the laser excitation (≈ 12 fs), respectively.

In the lower panel of Figure 7, the photoemission spectrum around the Fermi energy $\omega_F = 0$ is depicted for all four times for the HF, 2B, and GW self-energies. In the ground state only states below the Fermi energy are occupied. The small spectral weight above $\omega = 0$ is due to the broadening of the highest occupied state in the valence band ($\omega < 0$) because of the finite width κ of the probe pulse. In general, during the interaction with the laser pulse with a frequency of $\omega_0 = 2J$ electrons are excited from $\omega \approx -1J$ to $\omega \approx 1J$. The precise shape of the excited carrier
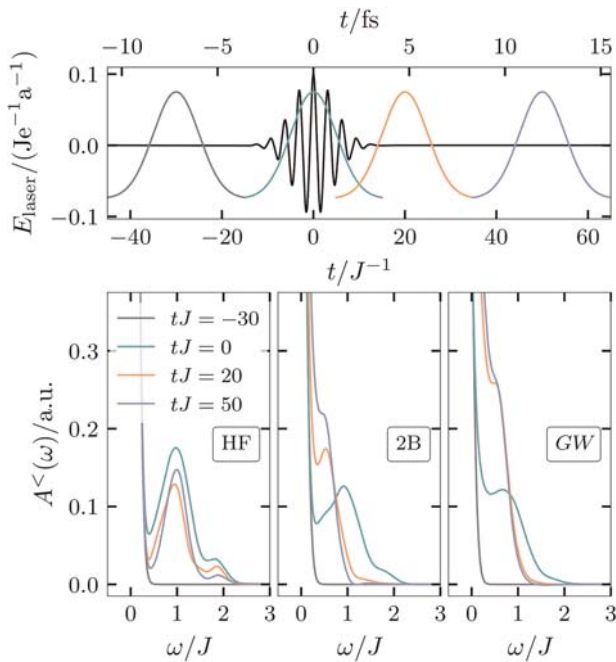
Figure 7. The lower panels show the time-dependent photoemission spectrum for a 5-AGNR with a length of $L = 6$ at four different times before, during and after a laser excitation for the HF (left), 2B (middle), and GW (right) self-energy at $U = 3.5J$. In the upper panel, the four times are marked, with respect to the pump laser pulse (black line), by Gaussian functions that correspond to the probe pulse.

distribution differs slightly for the distinct self-energies which is likely due to the different descriptions of the band structure and the resulting possible single-particle transitions. Nevertheless, the direct single-particle excitation by the laser pulse is already well reproduced by the HF self-energy.

However, for the correct description of the electron dynamics after the laser pulse correlation effects have to be included. For the HF self-energy the total spectral weight in the conduction band ($\omega > 0$) decreases slightly after the laser-pulse amplitude vanishes. However, the general shape of the distribution remains the same because collision processes that could lead to a redistribution of the occupation are not contained in the mean-field description. In contrast, using the 2B self-energy that takes into account collision events between electrons a considerable shift of the excited carrier occupation can be observed after the laser-pulse interaction. Even for long times ($\approx 12\,\text{fs}$) after the excitation the system has not reached a steady state yet. Instead, the number of particles in the valence band seems to increase. One possible explanation for this are carrier multiplication effects that were predicted[73–76] and experimentally observed[20,22,77,78] for various graphene structures. In this mechanism, highly-excited electrons can excite additional electrons from the valence to the conduction band through collisions. In total this results in an increase of the carrier density in the conduction band but a decrease of their mean energy. This effect will be studied in greater detail in a forthcoming paper.

The GW approximation observes a similar redistribution of the excited carriers toward lower energies with a simultaneous increase in the electron density. However, between $tJ = 20$ and

$tJ = 50$ this effect is considerably smaller than for the 2B self-energy. Nonetheless, both the 2B and the GW self-energy contain electron–electron collision effects which lead to the increase of carriers in the conduction band. Since HF does not include these kind of scattering events, going beyond the mean-field level is essential for the correct description of the observed electron dynamics. Therefore, previously developed extended TB and mean-field models[46,79,80] are not suitable for the electron dynamics considered here.

5. Conclusions and Outlook

In this paper, we have developed a new approach to describe the time-resolved nonequilibrium dynamics and spectral properties of finite graphene nanoclusters. Our description is based on an extension of the standard Hubbard model that is solved by the nonequilibrium Green functions (NEGF) approach to include correlations. Due to its concise nature the Hubbard model greatly reduces the computational demands of the description of finite systems. For the correct description of finite graphene nanostructures the standard Hubbard model has to be extended to take into account the overlap of the π-orbitals in the graphene honeycomb lattice. Here, hopping and overlap between up to third-nearest neighbors is included. The parameter set is taken from Tran et al.[36] that was created to accurately describe finite graphene systems. Additionally, to determine the on-site interaction U the band gap and band structure of a 7-AGNR has been compared to various theoretical and experimental results.[12,26,68–70] It was found that the width of the band gap of 7-AGNRs on Au(111) is well reproduced using the GW self-energy and an interaction of $U = 3.5J$.

Furthermore, we investigated the response of a 5-AGNR with a length of $L = 6$ to a laser-pulse excitation and compared the results of the HF, 2B, and GW self-energies. Taking correlation effects into account appeared to be mandatory for the correct description of the electron dynamics in the nanoribbon following the laser pulse interaction. On the mean-field level the general shape of the electron distribution in the conduction band did not change for long times ($\approx 12\,\text{fs}$) after the laser pulse excitation. In contrast for the 2B and GW self-energy an increase of the particle number in the upper band was observed even after the interaction with the laser has vanished. This could indicate the presence of carrier multiplication effects that will be further investigated in an upcoming paper.

The flexibility of the presented approach allows us to describe not only GNRs but finite graphene structures in general with any possible lattice geometry. In fact, there is a variety of systems with different edge structures that exhibit intriguing properties[7,81–83] that could be analyzed using this model in the future. One interesting system is carbon nanotubes (CNTs) which have a similar structure to GNRs.[84] In the presented approach of the extended Hubbard model and the NEGF method CNTs can be described as GNRs with periodic boundary conditions perpendicular to the ribbon axis. Therefore, it is easy to also extend the investigations to CNTs. Of course, the parameter set might have to be adjusted if the systems differ strongly from the GNRs considered here.

Conflict of Interest

The authors declare no conflict of interest.

Keywords

correlated dynamics, graphene nanoribbons, Hubbard model, nonequilibrium Green functions

[1] K. S. Novoselov, A. K. Geim, S. V. Morozov, D. Jiang, Y. Zhang, S. V. Dubonos, I. V. Grigorieva, A. A. Firsov, *Science* **2004**, *306*, 666.

[2] P. Avouris, Z. Chen, V. Perebeinos, *Nat. Nanotechnol.* **2007**, *2*, 605.

[3] X. Wang, L. Zhi, K. Müllen, *Nano Lett.* **2008**, *8*, 323.

[4] Y. H. Hu, H. Wang, B. Hu, *ChemSusChem* **2010**, *3*, 782.

[5] I. V. Lightcap, P. V. Kamat, *Acc. Chem. Res.* **2013**, *46*, 2235.

[6] Y. Song, S. Chang, S. Gradecak, J. Kong, *Adv. Energy Mater.* **2016**, *6*, 1600847.

[7] M. Dvorak, W. Oswald, Z. Wu, *Sci. Rep.* **2013**, *3*, 2289.

[8] S. Y. Zhou, G. H. Gweon, A. V. Fedorov, P. N. First, W. A. de Heer, D. H. Lee, F. Guinea, A. H. Castro Neto, A. Lanzara, *Nat. Mater.* **2007**, *6*, 770.

[9] C. Jeon, H. C. Shin, I. Song, M. Kim, J. H. Park, J. Nam, D. H. Oh, S. Woo, C. C. Hwang, C. Y. Park, J. R. Ahn, *Sci. Rep.* **2013**, *3*, 2725.

[10] F. Guinea, M. I. Katsnelson, A. K. Geim, *Nat. Phys.* **2009**, *6*, 30.

[11] S. M. Choi, S. H. Jhi, Y. W. Son, *Phys. Rev. B* **2010**, *81*, 081407.

[12] L. Yang, C. H. Park, Y. W. Son, M. L. Cohen, S. G. Louie, *Phys. Rev. Lett.* **2007**, *99*, 186801.

[13] M. Y. Han, B. Özyilmaz, Y. Zhang, P. Kim, *Phys. Rev. Lett.* **2007**, *98*, 206805.

[14] J. Bai, X. Duan, Y. Huang, *Nano Lett.* **2009**, *9*, 2083.

[15] L. Jiao, X. Wang, G. Diankov, H. Wang, H. Dai, *Nat. Nanotechnol.* **2010**, *5*, 321.

[16] O. V. Yazyev, *Acc. Chem. Res.* **2013**, *46*, 2319.

[17] A. Kimouche, M. M. Ervasti, R. Drost, S. Halonen, A. Harju, P. M. Joensuu, J. Sainio, P. Liljeroth, *Nat. Commun.* **2015**, *6*, 10177.

[18] R. M. Jacobberger, B. Kiraly, M. Fortin-Deschenes, P. L. Levesque, K. M. McElhinny, G. J. Brady, R. Rojas Delgado, S. Singha Roy, A. Mannix, M. G. Lagally, P. G. Evans, P. Desjardins, R. Martel, M. C. Hersam, N. P. Guisinger, M. S. Arnold, *Nat. Commun* **2015**, *6*, 8006.

[19] S. A. Jensen, R. Ulbricht, A. Narita, X. Feng, K. Müllen, T. Hertel, D. Turchinovich, M. Bonn, *Nano Lett.* **2013**, *13*, 5925.

[20] I. Gierz, J. C. Petersen, M. Mitrano, C. Cacho, I. C. E. Turcu, E. Springate, A. Stöhr, A. Köhler, U. Starke, A. Cavalleri, *Nat. Mater.* **2013**, *12*, 1119.

[21] R. Denk, M. Hohage, P. Zeppenfeld, J. Cai, C. A. Pignedoli, H. Söde, R. Fasel, X. Feng, K. Müllen, S. Wang, D. Prezzi, A. Ferretti, A. Ruini, E. Molinari, P. Ruffieux, *Nat. Commun.* **2014**, *5*, 5253.

[22] I. Gierz, F. Calegari, S. Aeschlimann, M. Chávez Cervantes, C. Cacho, R. T. Chapman, E. Springate, S. Link, U. Starke, C. R. Ast, A. Cavalleri, *Phys. Rev. Lett.* **2015**, *115*, 086803.

[23] G. Soavi, S. D. Conte, C. Manzoni, D. Viola, A. Narita, Y. Hu, X. Feng, U. Hohenester, E. Molinari, D. Prezzi, K. Müllen, G. Cerullo, *Nat. Commun.* **2016**, *7*, 11010.

[24] B. V. Senkovskiy, A. V. Fedorov, D. Haberer, M. Farjam, K. A. Simonov, A. B. Preobrajenski, N. Mårtensson, N. Atodiresei, V. Caciuc, S. Blügel, A. Rosch, N. I. Verbitskiy, M. Hell, D. V. Evtushinsky, R. German, T. Marangoni, P. H. M. van Loosdrecht, F. R. Fischer, A. Grüneis, *Adv. Electron. Mater.* **2017**, *3*, 1600490.

[25] I. Ivanov, Y. Hu, S. Osella, U. Beser, H. I. Wang, D. Beljonne, A. Narita, K. Müllen, D. Turchinovich, M. Bonn, *J. Am. Chem. Soc.* **2017**, *139*, 7982.

[26] S. Wang, L. Talirz, C. A. Pignedoli, X. Feng, K. Müllen, R. Fasel, P. Ruffieux, *Nat. Commun.* **2016**, *7*, 11507.

[27] D. J. Rizzo, G. Veber, T. Cao, C. Bronner, T. Chen, F. Zhao, H. Rodriguez, S. G. Louie, M. F. Crommie, F. R. Fischer, *Nature* **2018**, *560*, 204.

[28] L. Keldysh, *Soviet Phys. JETP* **1965**, *20*, 1018 [Zh. Eksp. Teor. Fiz. **1964**, *47*, 1515].

[29] M. Bonitz, A. Jauho, M. Sadovskii, S. Tikhodeev, *Phys. Status Solidi B* **2019**, *256*, 1800600 (this issue).

[30] N. Schlünzen, J. P. Joost, F. Heidrich-Meisner, M. Bonitz, *Phys. Rev. B* **2017**, *95*, 165139.

[31] N. Schlünzen, J. P. Joost, M. Bonitz, *Phys. Rev. B* **2017**, *96*, 117101.

[32] N. Schlünzen, M. Bonitz, *Contrib. Plasma Phys.* **2016**, *56*, 5.

[33] R. Saito, G. Dresselhaus, M. Dresselhaus, *Physical Properties of Carbon Nanotubes*. Imperial College Press, **1998**.

[34] J. Munárriz Arrieta, *Modelling of Plasmonic and Graphene Nanodevices*. Springer International Publishing, Cham **2014**, Ch 2.

[35] S. Reich, J. Maultzsch, C. Thomsen, P. Ordejón, *Phys. Rev. B* **2002**, *66*, 035412.

[36] V. T. Tran, J. Saint-Martin, P. Dollfus, S. Volz, *AIP Adv.* **2017**, *7*, 075212.

[37] P. O. Löwdin, *J. Chem. Phys.* **1950**, *18*, 365.

[38] R. Kundu, *Mod. Phys. Lett. B* **2011**, *25*, 163.

[39] D. Neilson, A. Perali, M. Zarenia, *J. Phys.: Conf. Ser.* **2016**, *702*, 012008.

[40] D. Prezzi, D. Varsano, A. Ruini, A. Marini, E. Molinari, *Phys. Rev. B* **2008**, *77*, 041404.

[41] T. Helgaker, P. Jørgensen, J. Olsen, *Molecular Electronic-Structure Theory*. John Wiley & Sons Ltd, Chichester **2000**.

[42] P. R. Surján, *Second Quantized Approach to Quantum Chemistry*. Springer-Verlag, Berlin **1989**.

[43] C. C. J. Roothaan, *Rev. Mod. Phys.* **1951**, *23*, 69.

[44] G. G. Hall, *Proc. R. Soc. London, Ser. A* **1951**, *205*, 541.

[45] K. I. Ramachandran, G. Deepa, K. Namboori, *Computational Chemistry and Molecular Modeling*. Springer-Verlag, Berlin **2008**.

[46] Y. Hancock, A. Uppstu, K. Saloriutta, A. Harju, M. J. Puska, *Phys. Rev. B* **2010**, *81*, 245402.

[47] G. Stefanucci, R. v. Leeuwen, *Nonequilibrium Many-Body Theory of Quantum Systems: A Modern Introduction*. Cambridge University Press, Cambridge **2013**.

[48] K. Balzer, M. Bonitz, *Nonequilibrium Green's Functions Approach to Inhomogeneous Systems*. Lect. Notes Phys., Vol. *867*, Springer, Berlin, Heidelberg **2013**.

[49] Of course there are experimental observations[26] and mean field level calculations[85,86] that exhibit spin asymmetries in the form of so-called edge states. However, those are only single measurements in the case of the experiments and (known but often times ignored) shortcomings of the HF approach which breaks the SU(2)-symmetry of the Hubbard model. The Green function is ensemble averaged and provides the expectation value instead of single measurements of observables such as the density which is clearly symmetric with respect to the spin.[87]

[50] M. Eckstein, M. Kollar, *Phys. Rev. B* **2008**, *78*, 245113.

[51] R. C. Albers, N. E. Christensen, A. Svane, *J. Phys.: Condens. Matter* **2009**, *21*, 343201.

[52] G. Baym, L. P. Kadanoff, *Phys. Rev.* **1961**, *124*, 287.

[53] M. Bonitz, S. Hermanns, K. Balzer, *Contrib. Plasma Phys.* **2013**, *53*, 778.

[54] S. Hermanns, N. Schlünzen, M. Bonitz, *Phys. Rev. B* **2014**, *90*, 125111.

[55] D. Lacroix, S. Hermanns, C. M. Hinz, M. Bonitz, *Phys. Rev. B* **2014**, *90*, 125112.

[56] M. P. von Friesen, C. Verdozzi, C. O. Almbladh, *Phys. Rev. Lett.* **2009**, *103*, 176404.

[57] M. P. von Friesen, C. Verdozzi, C. O. Almbladh, *Phys. Rev. B* **2010**, *82*, 155108.

[58] P. Romaniello, F. Bechstedt, L. Reining, *Phys. Rev. B* **2012**, *85*, 155131.

[59] M. Gatti, F. Bruneval, V. Olevano, L. Reining, *Phys. Rev. Lett.* **2007**, *99*, 266402.

[60] A. N. Chantis, M. van Schilfgaarde, T. Kotani, *Phys. Rev. B* **2007**, *76*, 165126.

[61] S. Hermanns, Phd thesis, Christian-Albrechts-Universität zu Kiel **2016**.

[62] N. E. Dahlen, R. van Leeuwen, *J. Chem. Phys.* **2005**, *122*, 164102.

[63] A. Stan, R. van Leeuwen, *J. Chem. Phys.* **2009**, *130*, 224101.

[64] The most demanding simulations performed in the scope of this work have been done for systems of 30 Hubbard sites and a propagation time of $110J^{-1}$ using a time step of $\Delta 0.01 J^{-1}$. For the *GW* self-energy such simulations would typically take around seven days to complete on a single NVIDIA Tesla P100 and use up to 300GB of RAM each. Using the 2B self-energy reduces the time of the calculation to about two days while the memory consumption stays the same.

[65] M. Scharnke, N. Schlünzen, M. Bonitz, *J. Math. Phys.* **2017**, *58*, 061903.

[66] M. Bonitz, M. Scharnke, N. Schlünzen, *Contrib. Plasma Phys.* **2018**, *58*, 1036.

[67] N. Schlünzen, S. Hermanns, M. Bonitz, C. Verdozzi, *Phys. Rev. B* **2016**, *93*, 035107.

[68] Y. W. Son, M. L. Cohen, S. G. Louie, *Phys. Rev. Lett.* **2006**, *97*, 216803.

[69] P. Ruffieux, J. Cai, N. C. Plumb, L. Patthey, D. Prezzi, A. Ferretti, E. Molinari, X. Feng, K. Müllen, C. A. Pignedoli, R. Fasel, *ACS Nano* **2012**, *6*, 6930.

[70] H. Söde, L. Talirz, O. Gröning, C. A. Pignedoli, R. Berger, X. Feng, K. Müllen, R. Fasel, P. Ruffieux, *Phys. Rev. B* **2015**, *91*, 045429.

[71] J. P. Joost, Master's thesis, Christian-Albrechts-Universität zu Kiel **2017**.

[72] P. E. Trevisanutto, C. Giorgetti, L. Reining, M. Ladisa, V. Olevano Ab Initio, *Phys. Rev. Lett.* **2008**, *101*, 226405.

[73] T. Winzer, A. Knorr, E. Malic, *Nano Lett.* **2010**, *10*, 4839.

[74] R. Baer, E. Rabani, *Nano Lett.* **2010**, *10*, 3277.

[75] S. Konabe, N. Onoda, K. Watanabe, *Phys. Rev. B* **2010**, *82*, 073402.

[76] F. Schulze, M. Schoth, U. Woggon, A. Knorr, C. Weber, *Phys. Rev. B* **2011**, *84*, 125318.

[77] N. M. Gabor, Z. Zhong, K. Bosnick, J. Park, P. L. McEuen, *Science* **2009**, *325*, 1367.

[78] S. Wang, M. Khafizov, X. Tu, M. Zheng, T. D. Krauss, *Nano Lett.* **2010**, *10*, 2381.

[79] Y. Wu, P. Childs, *Nanoscale Res. Lett.* **2010**, *6*, 62.

[80] T. Stegmann, J. A. Franco-Villafañe, U. Kuhl, F. Mortessagne, T. H. Seligman, *Phys. Rev. B* **2017**, *95*, 035413.

[81] D. G. de Oteyza, A. García-Lekue, M. Vilas-Varela, N. Merino-Díez, E. Carbonell-Sanromà, M. Corso, G. Vasseur, C. Rogero, E. Guitián, J. I. Pascual, J. E. Ortega, Y. Wakayama, D. Peña, *ACS Nano* **2016**, *10*, 9000.

[82] G. D. Nguyen, H. Z. Tsai, A. A. Omrani, T. Marangoni, M. Wu, D. J. Rizzo, G. F. Rodgers, R. R. Cloke, R. A. Durr, Y. Sakai, F. Liou, A. S. Aikawa, J. R. Chelikowsky, S. G. Louie, F. R. Fischer, M. F. Crommie, *Nat. Nanotechnol.* **2017**, *12*, 1077.

[83] C. Bronner, R. A. Durr, D. J. Rizzo, Y. L. Lee, T. Marangoni, A. M. Kalayjian, H. Rodriguez, W. Zhao, S. G. Louie, F. R. Fischer, M. F. Crommie, *ACS Nano*, **2018**, *12*, 2193.

[84] J. C. Charlier, X. Blase, S. Roche, *Rev. Mod. Phys.* **2007**, *79*, 677.

[85] H. Feldner, Z. Y. Meng, A. Honecker, D. Cabra, S. Wessel, F. F. Assaad, *Phys. Rev. B* **2010**, *81*, 115416.

[86] M. Golor, C. Koop, T. C. Lang, S. Wessel, M. J. Schmidt, *Phys. Rev. Lett.* **2013**, *111*, 085504.

[87] T. Hikihara, X. Hu, H. H. Lin, C. Y. Mou, *Phys. Rev. B* **2003**, *68*, 035432.

Chapter 6

Summary and Outlook

6.1 Summary and Discussion

The description of correlated many-body quantum systems under nonequilibrium conditions is among the most formidable challenges of statistical physics. Due to the lack of small parameters in this context, any approach has to capture the full complexity of the intricate interplay between quantum correlations and the irreducible disorder of general nonequilibrium. On the other hand, correlated nonequilibrium systems are at the heart of many modern experiments that constantly push the envelope of technological progress.

The primary goal of the present thesis is the rigorous description of correlated lattice systems out of equilibrium. Quantum lattice system are remarkably scalable—from minimal test-bed examples to isolate driving mechanisms and do benchmark analyses up to larger clusters of direct practical relevance. Hence, lattice systems provide a unique environment to investigate dynamical correlation effects. The NEGF method is specifically constructed to meet the challenging demands of the arising complex states in such systems. However, there were severe limitations and methodological weaknesses that had to be overcome for the effective applicability of the framework. In this regard, the present thesis displays a number of theoretical breakthroughs that have significantly increased the consistency, the accuracy, and the computational reach of the NEGF method. These game-changing methodological advances have rendered the implementation of different modern applications possible for the first time. On this footing, remarkable new predictions of interesting nonequilibrium effects for ultracold atoms in optical lattices and finite graphene nanostructures are presented in this thesis.

6.1.1 Methodological Improvements Towards a Rigorous Description of Correlated Finite Systems Out of Equilibrium

The improvements of the NEGF method within this thesis eradicate three substantive central flaws to achieve the primary goal and to put NEGF theory in an overall better

position. Concretely, these flaws are the insufficient theoretical foundation for the steep demands of state-of-the-art applications, the accurate higher-order selfenergy approximations being practically inaccessible, and the notoriously unfavorable cubic time scaling.

6.1.1.1 Improving the Theoretical Foundation (I)

As part of his master's studies, the author has started the development of more precise numerical integration schemes for NEGF simulations in Ref. [290]. Building on this foundation, these higher-order techniques were subsequently further refined by the author in cooperation with Jan-Philip Joost (see, e.g., Sec. 2.1.1 and Ref. [346]). Early in 2016, a much-noticed publication by Adrian Stan [202] seriously questioned the credibility of the NEGF technique by predicting the existence of a universal unphysical attractor. The considerable experience with the numerical behavior of the KBE put N.S. and J.-P.J. in the position to carefully reexamine Stan's analysis. As a result, his observations could be identified as numerical artifacts of the used integration techniques with insufficient resolution (Sec. 4.1). The rather drastic claims considering the inherent structure of the KBE were unambiguously proven wrong, which constitutes an important verification of the consistency of the NEGF framework. The concomitant controversy clearly demonstrates the prime importance of numerical stability and reliable convergence checks.

Motivated by this, the author and Miriam Scharnke established time-reversal symmetry as an additional stability test for NEGF calculations. To this end—and for the first time—a formal proof for time-reversibility in the KBE was given, which depends on a single general condition: Φ derivability of the selfenergy (Sec. 3.2). This legitimizes the use as a numerical convergence check, i.e. reversing the sign of the Hamiltonian and propagating back to the initial state, which is extremely sensitive to numerical errors and, thus, constitutes a valuable tool for succeeding NEGF studies. Furthermore, a similar condition was derived for time-reversal symmetry in the related RDO technique.

On the basis of these theoretical developments, the author was confident to close another gap pertaining the practicability of the NEGF method. Prior to the PhD studies of the author, there has been no reliable specification of the accuracy of the NEGF method, particularly in the context of experimentally relevant lattice systems. This shortcoming was remedied in Ref. [212] (Sec. 4.1). Here, NEGF simulations for nonequilibrium situations in large correlated lattice systems were compared to quasi-exact DMRG data. Beyond that, the influence of the GKBA was analyzed and various higher-order selfenergy approximations were applied. The results show an overall close agreement between both methods. DMRG and NEGF exhibit complementary applicability ranges with respect to the interaction strength, which can be gaplessly connected within a combined description. Finally, the exact DMRG result is typically enclosed between the full NEGF curve and the GKBA data. This behavior can be used as a powerful accuracy check for simulations of larger 2D or 3D systems, where no DMRG data can be generated.

Another potential weakness of Green-function techniques, which has been observed frequently, is the occurrence of artificial solution multiplicity [196–201]. The multivaluedness of specific many-body approximations under certain conditions can—when left

unanalyzed—cause significant accuracy drops in the prediction of some observables. For this reason, the author and others studied a conclusive example of solution multiplicity for correlated lattice systems (Sec. 3.3). It was shown that in such a case, different stable equilibrium states link to different degrees of spatial symmetry. By enforcing specific symmetry constraints, these states could be distinctly reproduced. Furthermore, it was demonstrated for the SOA selfenergy that the accuracy of the spectral function drastically improves by allowing asymmetry in the system, whereas the density matrix becomes inaccurate. Thus, a "dilemma" situation is present, much in the sense of Löwdin's original symmetry dilemma [277]. These theoretical insights into the inherent structure of Green-function approaches are highly valuable for practical applications, as deliberate symmetry constraints can be utilized to optimize the method's performance with respect to specific desired observables.

6.1.1.2 Improving the Selfenergy Accessibility (II)

Within the framework of NEGF theory, the selfenergy terms are generally constructed with respect to orders of the interaction strength. When it comes to the description of strong-coupling effects, the inclusion of higher-order terms to the selfenergy becomes indispensable. Unfortunately, more sophisticated many-body approximations significantly increase the computational effort of the simulations. Hence, the research for practically relevant systems was predominantly limited to only the HF and SOA selfenergies [101]. The author provided the theoretical foundation to expand these boundaries in his master's thesis and early PhD studies (Sec. 2.1.1), where the TMA (TPP) was set up and implemented for considerably large lattice systems. The TPP approximation accounts for particle–particle scattering terms, which are particularly important in the description of nonequilibrium expansion dynamics (cf. Sec. 4.2). In order to predict the dynamics in more general strong-coupling situations, the author further generalized the NEGF approach by additionally invoking the TPH for particle–hole scattering terms, the GWA for dynamical-screening effects, as well as the FLEX selfenergy that combines all previous contributions (Sec. 2.1.2). Furthermore, a novel selfenergy approximation was established in this context: the TOA that includes all terms up to the third order in the interaction strength (Secs. 2.1.2 and 4.1). The extensive review article [79] contains in-depth derivations for all previous approximations and shows how the equations are efficiently set up for bosons and fermions in several representative basis choices. For optimal accessibility, N.S., S.H., and J.-P.J. implemented all mentioned selfenergies and provided a GPU-accelerated high-performance code for fermionic lattice systems.

Having multiple (differently constructed) many-body approximations at hand raises the question of the best performance and accuracy. One pivotal outcome of the author's studies is the characterization of specific applicability ranges for these approximations in the context of lattice systems. By specifically taking into account the respective preconditions of the system of interest, this allows for an optimal choice within the NEGF framework. Relevant parameters in this process include the density of the system and the interaction strength. For an overall reliable performance, the TOA has proven to be

a suitable selection throughout the parameter space (Secs. 2.1.2 and 4.1). Within this thesis, an additional important observation was made for the TPH approximation, namely the violation of physical conservation laws following from the inclusion of particle–hole exchange terms (Sec. 2.1.4).

6.1.1.3 Achieving the Scaling Limit (III)

The methodological pinnacle of this thesis is the development of the G1–G2 scheme (Sec. 3.1). It provides a convincing solution to the problem of unfavorable computational scaling properties within NEGF theory, which raises the framework onto the next level. In particular, the G1–G2 scheme is an exact reformulation of the HF-GKBA in terms of the time-diagonal elements of the single-particle and two-particle Green functions. By this approach, the $\mathcal{O}\left(N_{\mathrm{t}}^2\right)$ scaling of the HF-GKBA with the SOA selfenergy can be reduced to $\mathcal{O}\left(N_{\mathrm{t}}^1\right)$, which constitutes the universal scaling limit for time-propagation schemes. Remarkably, even the inherently more complex resummation selfenergies that feature a cubic time scaling within the HF-GKBA translate into a time-linear G1–G2 form. This was initially derived for the GWA in Ref. [114], and later also demonstrated for the TPP, and TPH approximations in Ref. [208]. In line with the central goal of this thesis, the G1–G2 scheme was adapted to the Hubbard model in order to render the description of correlated lattice systems possible. It is important to note that the G1–G2 scheme is in no way limited to lattice systems. A particularly promising future application is given by the uniform electron gas (UEG), for which the scheme has already been set up.

As the new-found approach features a single-time differential equation for the two-particle Green function, inevitably also the numerical scaling with the basis size is changed in comparison the original HF-GKBA. However, this drawback is convincingly compensated by the time-scaling advantage, so that the overall numerical scaling is far superior for all practically relevant systems; it is demonstrated in Ref. [114] that speed-up factors of 10^4 are easily attainable for representative simulations. Furthermore, the scaling with the basis size for the Hubbard model could be further improved from $\mathcal{O}\left(N_{\mathrm{b}}^5\right)$ to $\mathcal{O}\left(N_{\mathrm{b}}^4\right)$ in Ref. [208] by analytically accounting for the cancellation of specific terms.

As described above, different many-body approximations such as the T matrices and GWA capture specific types of scattering processes. This leads to the situation that the nature of the many-body state determines the accuracy of the applied approach. Therefore, it is expedient to search for universal approximations that unify several classes of scattering terms. Within the G1–G2 scheme, the TPP, TPH and GWA approaches can be combined in a remarkably simple, but selfconsistent way. This results in the DSL approximation—the most consistent portrayal of dynamical correlation effects in this context. The DSL-G1–G2 approach is implemented and tested in Ref. [208] with promising outcome. Beyond that, the novel TOA selfenergy that has proven to provide accurate results in the context of two-time NEGF simulations is combined with the G1–G2 scheme in Sec. 3.1.2, alongside with the DSL-related FLEX approximation. With these developments, the G1–G2 scheme now exhibits the same (or even a larger) versatility as the ordinary NEGF framework within the KBE formulation.

For these reasons, the time-linear G1–G2 scheme is particularly well suited to meet the challenges of the investigation of nonequilibrium phenomena in correlated finite systems. A first practical demonstration of this new paradigm is presented in the subsequent outlook (Sec. 6.2), which also includes an overview of further possible applications for future research. In addition, it is noted that the methodological advances from Sec. 3.1 have already been embraced by other groups and form the basis for new avenues of developments and applications [205, 206].

6.1.2 Application to Correlated Lattice Systems Under Nonequilibrium Conditions

The abovementioned methodological breakthroughs have successively introduced new possibilities for the accurate simulation of excited lattice systems on experimentally relevant parameter scales. With accordingly refined NEGF tools, the author accomplished significant advances in the description of interesting many-body phenomena in ultracold-atom lattices and excited graphene fragments. Both systems are notoriously hard to describe due to the interplay of electronic correlations and nonequilibrium effects.

6.1.2.1 Ultracold Atoms in Optical Lattices

An important outcome of the author's work is the analysis and prediction of fermionic expansion scenarios in multi-dimensional lattice systems that can be realized in experiments with ultracold atoms in periodic optical traps (Secs. 2.1.1 and 4.2). In the respective NEGF studies, the driving mechanisms for the characteristic expansion dynamics was identified and a convincingly close agreement with recent experiments for 2D systems could be achieved. In particular, a two-time NEGF approach based on the TPP selfenergy was used to describe the time evolution of initially confined particle clouds in 1D, 2D, and 3D lattices. The author showed that the expansion dynamics undergoes several ultrafast characteristic phases, which are linked with the build-up of correlation. In the final (saturated) phase, the dynamical separation between single particles and effectively bound particle pairs was observed, which confirms the effect of quantum distillation.

Overall, the simulation results exhibited the exact same behavior as has been found in experiments for fermionic 2D expansion in optical lattices [140]. To enable a direct comparison, an extensive system-size study was carried out that ultimately allowed the author to extrapolate the data to the macroscopic limit. The respective results fully match the measurements within the given experimental accuracy. This convincing agreement is unmatched by any other applicable approach in this context.

Beyond that, it was possible to spatially resolve the fermionic correlations in the system: the entanglement emerges at the edges of the particle cloud and spreads towards the center and the outer region of the lattice. These insights are important for the understanding of expansion experiments in optical lattices and can even guide future measurements with the recently developed quantum-gas microscopes [146–150].

6.1.2.2 Finite Graphene Nanostructures

The most relevant and far-reaching predictions within this thesis are made in the context of finite graphene nanostructures that are excited by impacting energetic ions. To be precise, it was found that a) the presence of electronic correlations in the material significantly influences the energy exchange to the projectile and b) that the incident ions can induce the formation of stable doublons (Secs. 2.2 and 4.3). This was achieved by applying the NEGF approach to hexagonal Hubbard lattice systems. In a first feasibility study [214], the effects of strong lattice interactions and finite temperature on the stopping power of the projectile was investigated using several selfenergy approximations within two-time and GKBA calculations. It was demonstrated that the coupling of the lattice electrons decreases their mobility and thus significantly reduces the amount of transferred energy from the incident ion. Therefore, it leads to a generally decreased stopping power. This effect even gains relative importance for finite temperatures. The applied model was verified by a comparison with experimentally supported benchmark data.

The interesting backcoupling effect between the ion and the lattice raises the question of the precise nature of the ensuing many-body state in the material. In a thorough analysis [41], the author and others discovered a fascinating new phenomenon: the ion-impact-induced formation of stable correlated doublons. This effect was predicted on different length scales by applying analytic calculations, exact computations, and NEGF simulations. Furthermore it was demonstrated that multiple sequential excitations constitute an efficient mechanism to successively increase the number of doublons even further. This remarkable result stands out in comparison with other observations for doublon manifestation that depend on spatially delocalized excitations [321–328]. The properties of the doublon-production effect by projectile excitation have been further explored in two subsequent publications. In a topical review [207], the previous results were complemented by measurements of the spatially resolved double occupation and the time evolution of the spectral function. An extensive parameter study for the velocity of the incident ions was published in Ref. [215] were the time-dependent change of the separate energy contributions was analyzed in detail. As a result, the parameter space for the optimal effectiveness of doublon formation was successfully narrowed down. This is not only highly relevant for ion-sputtering experiments with graphene-based materials, but could also directly be conveyed to ultracold atoms in optical lattices, were the ion impact can be simulated by the highly versatile laser optics (cf. Sec. 4.2).

As an additional outcome of the developments of this thesis, the NEGF approach was also used to describe laser-excited GNRs (Sec. 5.1). By applying the GW selfenergy to an extended Hubbard model it was possible to predict the appearance of electronic Auger effects after the laser beam has vanished. These results clearly surpass the predictive power of mean-field approaches, which were included for comparison. The observations serve as a potential reference for future experimental photoemission-spectroscopy studies of GNRs.

6.2 Outlook

The extensive theoretical developments and subsequent practical applications presented in this thesis have opened up new avenues for interesting future research. This includes further studies in the scope of the discussed topics, as well as subjects going substantially beyond. A selection of particularly promising research applications is listed below.

- As demonstrated within this thesis, the NEGF method is able to accurately predict the dynamics of experiments with ultracold atoms in optical lattices. In the continuously ongoing refinement process of optical lattices as quantum simulators, the NEGF approach is therefore a well-suited candidate to provide valuable reference data. Since a large fraction of cold-gas experiments is performed with effectively bosonic atoms [144, 145, 151–153], it would be highly beneficial to expand the approach accordingly. In this regard, an NEGF implementation for the Bose-Hubbard model is most expedient. The required selfenergy equations for this basis choice are already included in Ref. [79] (Sec. 2.1.2). With this description, a different class of exciting collective phenomena is within reach, such as Bose–Einstein condensation in optical lattices.

- Much in the spirit of Ref. [246], the NEGF approach to ion stopping can be used as part of a joint description of plasma–solid interface scenarios. This would include other computational tools, such as PIC or fluid simulations on the plasma side, to combine with. A more direct interaction process between the energetic plasma ions and the solid system could be simulated by including charge transfer via an embedding-selfenergy scheme [207, 246, 247]. Furthermore, one would need to describe larger materials than considered in this thesis. A practicable pathway to approach this problem has been opened by the drastic scaling advantages of the G1–G2 scheme (see also Secs. 6.2.1 and 6.2.2).

- The NEGF description of laser-driven GNR systems has revealed the occurrence of Auger effects after the excitation has vanished. These effects can be studied in more detail by considering more observables provided by the two-time Green functions. Furthermore, this approach can easily be generalized to carbon nanotubes (CNTs) by applying periodic boundary conditions to the edges of the ribbons. Auger effects in CNTs are of great interest both in theory [347, 348] and experiments [192, 193, 349].

- The most auspicious result of this thesis is the development of the G1–G2 scheme with its game-changing linear time scaling. This method is particularly promising in conjunction with the in-depth DSL approximation in its exchange-corrected form (i.e. completed DSL, see Sec. 3.1.2.1). In fact, elaborate long-time DSL calculations for Hubbard systems have revealed a new kind of stability issues, in the form of gradually off-drifting eigenvalues of the two-particle Green function. Albeit being equally present in previous GKBA calculations, these issues have not been

observed before for Green functions due to the limited propagation times. For RDO simulations, a similar behavior has been investigated, e.g., in Refs. [100, 259]. In this context, the methods of *trace consistency* and *purification* (see, e.g., Refs. [100, 350, 351]) have been proposed as promising solutions to the problem. Therefore, a consequent next step for the G1–G2 scheme is to apply these concepts to Green functions, which will be discussed in an upcoming publication [262]. Both ideas rely on small gradual corrections in every time step to keep the calculations within the physically expected range. Inevitably, such procedures slowly start to alter the intrinsic memory of the simulation. The validity of these approximations can then be adequately tested with the numerical verification of time-reversal symmetry (cf. Sec. 3.2).

- The G1–G2 scheme is well-suited to describe atoms and molecules in a spatially continuous basis. As shown in Ref. [114], a tremendous speed-up is expected compared to previous NEGF studies in this context [124–126]. Concretely, the description of irradiated krypton with the DSL-G1–G2 method is particularly promising. It is conjectured in Ref. [126] that a many-body approximation on the level of DSL should be sufficient to predict the experimentally validated transition to Kr^{3+}, which previously used approaches failed to describe.

- The uniform electron gas (UEG) is a versatile model for many-body physics in general, as it is applied to a wide range of systems ranging from quantum plasmas [117] to warm–dense matter [10] and electrons in metals [352]. Specifically for WDM systems, a proper description of nonequilibrium effects is indispensable [30]. Moreover, dynamical observables, such as the dynamic structure factor, are of key importance for WDM diagnostics [10]. This plays to the strengths of the NEGF technique in general. The description of the UEG within the G1–G2 scheme in particular is expected to provide a speed-up factor of up to $\mathcal{O}\left(N_{\mathrm{t}}^2\right)$ in comparison to previous NEGF studies [353]. This will potentially allow for analyses on a larger, experimentally relevant scale.

The G1–G2 scheme is expected to shift the boundaries of NEGF applications in many ways. Indeed, it has already opened up new possibilities for the description of correlated finite lattice systems that are currently investigated in the author's group. The following two sections include early-stage G1–G2 results for excited graphene nanostructures that have been previously out of reach.

6.2.1 G1–G2 Approach to Ion Stopping in Large Graphene Fragments

By means of the NEGF technique and the HF-GKBA in combination with the SOA selfenergy, the author managed to predict ion-impact-induced doublon production in graphene-like honeycomb flakes of up to $L = 54$ atoms (Ref. [41], Sec. 4.3). The G1–G2 scheme allows one to generalize these results to higher-order many-body approximations,

larger systems and longer time evolutions. Very recently, these perspectives have been partially explored in two bachelor's theses by Franziska Reiser [354] and Lotte Borkowski [355]. Here, the author includes impressive results from Ref. [355] that demonstrate the new possibilities in this context.

In Ref. [355], the SOA-G1–G2 approach is applied for multiple-impact scenarios in honeycomb flakes. As a starting point, Ref. [355] successfully reproduces the results of Figs. 4 and S2 in Ref. [41]. Subsequently, the analysis focuses on a larger hexagonal lattice of $L = 96$ sites. An overview of the system can be found in Fig. 6.1. The results for this lattice are included in Fig. 6.2. First, the system is excited with a sequence of 50 ion impacts at a fixed impact point. The results are illustrated as golden curves for the total energy E (top left) and the average double occupation d_{av} (bottom left). As one can see, both quantities share an overall increasing trend with growing number of excitations. This confirms the predictions of Ref. [41] as the increase of d_{av} corresponds to the formation of correlated doublons. Interestingly, the double occupation initially exhibits a minimum after few excitations. For smaller systems this behavior could not be observed due to overlay effects with finite-size-induced fluctuations. As d_{av} is expected to be minimal in the groundstate [41], it would be interesting to verify and analyze this trend in the future. The blue curves in Fig. 6.2 refer to the results for randomly distributed impact points within a circle of radius $r = a_0$. These variations can be regarded as a first step towards more realistic ion-stopping descriptions for plasma–solid interface situations or ion-sputtering experiments. Clearly, all previous observations are confirmed for random impact points—albeit in attenuated form as less energy is transferred to the lattice. This is due to an overall-reduced average potential since the impact points are statistically more distant to the lattice electrons.

In this particular example, the G1–G2 scheme has allowed to study systems of nearly twice the size as before for three times as long propagation times. The large system size is indispensable to distinguish real physical behaviour from artificial finite size effects. The results will be included in an upcoming publication [256].

6.2.2 G1–G2 Approach to Laser-Excited GNR Heterostructures

Within this thesis, the NEGF approach has been successfully applied to light-driven finite GNR structures (Sec. 5.1). In this study, the graphene fragments have been modeled with an extended Hubbard Hamiltonian. An even more realistic description for graphene nanostructures can be achieved with the so-called Pariser–Parr–Pople (PPP) model [356, 357]. This lattice model was developed in 1953 [358–360] and relies on a full interaction matrix V_{ij} as opposed to the scalar Hubbard U. There are different possible choices for the matrix V_{ij}, all of which can be understood as an interpolation between the on-site Hubbard U and a long-range Coulomb interaction. The most common choices are the
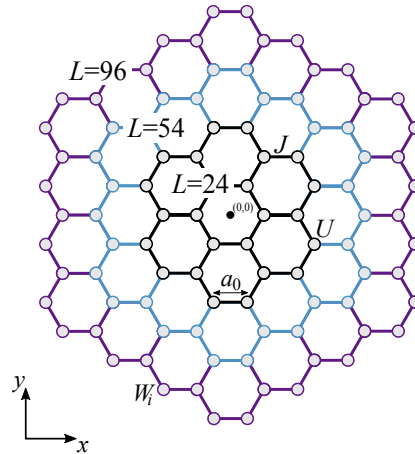
Figure 6.1 – Overview of honeycomb clusters of different sizes. The lattices of 24, 54, and 96 sites are colored in black, blue, and violet, respectively. J and U denote the parameters of the Hubbard Hamiltonian for nearest-neighbor hopping and on-site interaction. The lattice constant a_0 describes the distance between two lattice atoms. W_i denotes the Coulomb interaction with the charged projectile acting on the lattice site i. More details on the model can be found in Sec. 4.3. The figure is taken from Ref. [355] with permission from the author.
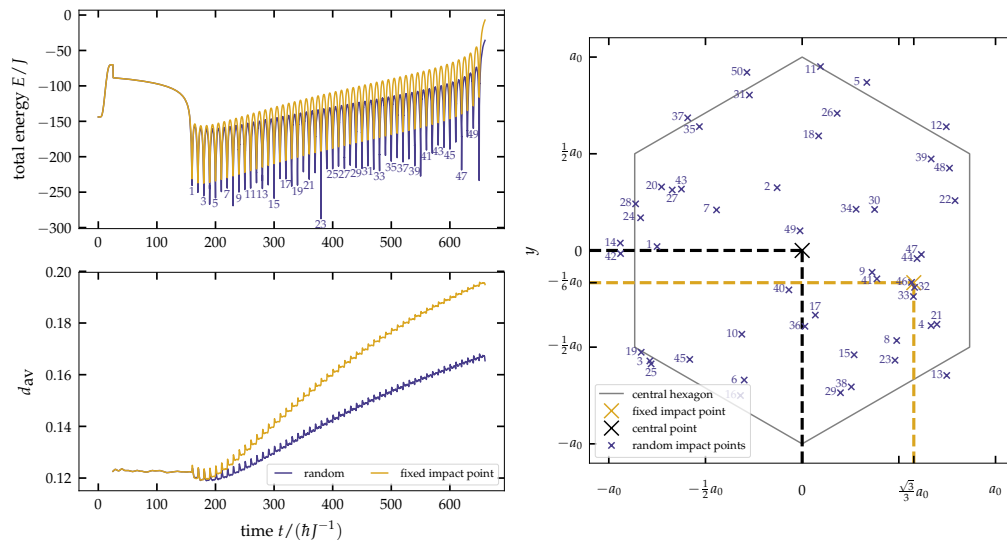
Figure 6.2 – Multiple ion impact for fixed and random positions on a 96-site honeycomb cluster. Results for the fixed (random) impact point are depicted in gold (blue). Top left: time evolution of the total energy of the lattice including the adiabatic-switching procedure. Bottom left: time evolution of the average double occupation. Right: illustration of the impact points within the innermost hexagon of the lattice. The random impact points are labeled chronologically in ascending order. The calculations are performed for $U = 4J$ and an initial projectile velocity of $v_p = 3a_0/t_0$ with $t_0 = \hbar/J$. The figure is taken from Ref. [355] with permission from the author.

Ohno parametrization [361]

$$V_{ij} = \frac{U}{\left[1 + \left(\frac{r_{ij}}{r_0}\right)^2\right]^{1/2}}, \tag{6.1}$$

the Mataga–Nishimoto parametrization [362, 363]

$$V_{ij} = \frac{U}{1 + \frac{r_{ij}}{r_0}}, \tag{6.2}$$

and the exponential[1] form [364]

$$V_{ij} = U \exp\left(-\frac{r_{ij}}{r_0}\right). \tag{6.3}$$

Here, $r_{ij} = |\boldsymbol{r}_i - \boldsymbol{r}_j|$ is the absolute distance between the lattice-site positions $\boldsymbol{r}_i$ and $\boldsymbol{r}_j$, and $r_0 = \frac{e^2 k_e}{U}$ is a characteristic unit length with the Coulomb constant k_e. The increased complexity of the interaction matrix results in an unfavorable numerical scaling in comparison to the Hubbard model. This conjuncture renders the PPP model unfeasible for two-time NEGF approaches.[2] With the new-found G1–G2 scheme, however, this hurdle is compensated by the immense time-scaling advantages. It is therefore most desirable to apply the PPP model in a G1–G2 description of excited graphene nanostructures.

In order to derive the G1–G2 equations for the PPP model, one starts from the EOMs in the general basis and substitutes the interaction tensor as $w_{ijkl} = V_{ij}\delta_{ik}\delta_{jl}$. For the completed DSL approximation, this applies to the Eqs. (3.10), (3.12) and (3.67). For spin-up electrons, the single-particle EOM attains the form (again, the spin-down components follow from the replacement $\uparrow \leftrightarrow \downarrow$)

$$i\hbar\frac{\mathrm{d}}{\mathrm{d}t}G_{ij}^{<,\uparrow}(t) - \left[h^{\mathrm{HF},\uparrow}(t), G^{<,\uparrow}(t)\right]_{ij} = \left[I^\uparrow + \left(I^\uparrow\right)^\dagger\right]_{ij}(t), \tag{6.4}$$

where the Hartree–Fock Hamiltonian becomes[3]

$$h_{ij}^{\mathrm{HF},\uparrow}(t) = h_{ij}^{(0)}(t) - i\hbar\delta_{ij}\sum_k V_{ik}(t)\left[G_{kk}^{<,\uparrow}(t) + G_{kk}^{<,\downarrow}(t)\right] + i\hbar V_{ij}(t)G_{ij}^{<,\uparrow}(t), \tag{6.5}$$

and the collision integral is given by

$$I_{ij}^\uparrow(t) = -i\hbar\sum_k V_{ik}(t)\left[\mathcal{G}_{ikjk}^{\uparrow\downarrow\uparrow\downarrow}(t) + \mathcal{G}_{ikjk}^{\uparrow\uparrow\uparrow\uparrow}(t)\right]. \tag{6.6}$$

Obviously, the solution of single-particle EOM requires the knowledge of two spin components for the two-particle Green function. In the following, the EOMs for $\mathcal{G}$ are given in

---

[1]This interaction is not motivated from the Coulomb potential but is related to a Yukawa screening instead.

[2]Exceptions to this are the SOA and GWA approaches, for which a comparable scaling can be achieved [79].

[3]Here, the interaction matrix is given a time dependence to account for adiabatic-switching procedures.

the most practical form for numerical applications. With the two-particle Hartree–Fock Hamiltonians,

$$h_{\uparrow\downarrow,ijkl}^{(2),\mathrm{HF}}(t) = \delta_{jl}h_{ik}^{\mathrm{HF},\uparrow}(t) + \delta_{ik}h_{jl}^{\mathrm{HF},\downarrow}(t) \quad \text{and} \tag{6.7}$$

$$h_{\uparrow\uparrow,ijkl}^{(2),\mathrm{HF}}(t) = \delta_{jl}h_{ik}^{\mathrm{HF},\uparrow}(t) + \delta_{ik}h_{jl}^{\mathrm{HF},\uparrow}(t)\,, \tag{6.8}$$

the two-particle EOMs become

$$i\hbar\frac{\mathrm{d}}{\mathrm{d}t}\mathcal{G}_{ijkl}^{\uparrow\downarrow\uparrow\downarrow}(t) = \left[h_{\uparrow\downarrow}^{(2),\mathrm{HF}}(t), \mathcal{G}^{\uparrow\downarrow\uparrow\downarrow}(t)\right]_{ijkl} + \Psi_{ijkl}^{-,\uparrow\downarrow\uparrow\downarrow}(t) + \Pi_{ijkl}^{\uparrow\downarrow\uparrow\downarrow}(t) - \left[\Pi_{lkji}^{\downarrow\uparrow\downarrow\uparrow}(t)\right]^{*}$$
$$+ \Lambda_{ijkl}^{\mathrm{pp},\uparrow\downarrow\uparrow\downarrow}(t) - \left[\Lambda_{klij}^{\mathrm{pp},\uparrow\downarrow\uparrow\downarrow}(t)\right]^{*} + \Lambda_{ijkl}^{\mathrm{ph},\uparrow\downarrow\uparrow\downarrow}(t) - \left[\Lambda_{klij}^{\mathrm{ph},\uparrow\downarrow\uparrow\downarrow}(t)\right]^{*} \quad \text{and} \tag{6.9}$$

$$i\hbar\frac{\mathrm{d}}{\mathrm{d}t}\mathcal{G}_{ijkl}^{\uparrow\uparrow\uparrow\uparrow}(t) = \left[h_{\uparrow\uparrow}^{(2),\mathrm{HF}}(t), \mathcal{G}^{\uparrow\uparrow\uparrow\uparrow}(t)\right]_{ijkl} + \Psi_{ijkl}^{-,\uparrow\uparrow\uparrow\uparrow}(t) + \Pi_{ijkl}^{\uparrow\uparrow\uparrow\uparrow}(t) - \left[\Pi_{lkji}^{\uparrow\uparrow\uparrow\uparrow}(t)\right]^{*}$$
$$+ \Lambda_{ijkl}^{\mathrm{pp},\uparrow\uparrow\uparrow\uparrow}(t) - \left[\Lambda_{klij}^{\mathrm{pp},\uparrow\uparrow\uparrow\uparrow}(t)\right]^{*} + \Lambda_{ijkl}^{\mathrm{ph},\uparrow\uparrow\uparrow\uparrow}(t) - \left[\Lambda_{klij}^{\mathrm{ph},\uparrow\uparrow\uparrow\uparrow}(t)\right]^{*}\,. \tag{6.10}$$

In these equations, the two-particle source terms are given as

$$\Psi_{ijkl}^{-,\uparrow\downarrow\uparrow\downarrow}(t) = \; G_{ik}^{<,\uparrow}(t)G_{jl}^{<,\downarrow}(t)\left[V_{ij}(t) - V_{kl}(t)\right]$$
$$+ i\hbar G_{ik}^{<,\uparrow}(t)\sum_{p}V_{ip}(t)G_{jp}^{<,\downarrow}(t)G_{pl}^{<,\downarrow}(t) - i\hbar G_{ik}^{<,\uparrow}(t)\sum_{p}V_{kp}(t)G_{jp}^{<,\downarrow}(t)G_{pl}^{<,\downarrow}(t)$$
$$+ i\hbar G_{jl}^{<,\downarrow}(t)\sum_{p}V_{pj}(t)G_{ip}^{<,\uparrow}(t)G_{pk}^{<,\uparrow}(t) - i\hbar G_{jl}^{<,\downarrow}(t)\sum_{p}V_{pl}(t)G_{ip}^{<,\uparrow}(t)G_{pk}^{<,\uparrow}(t) \tag{6.11}$$

and

$$\Psi_{ijkl}^{-,\uparrow\uparrow\uparrow\uparrow}(t) = \; G_{ik}^{<,\uparrow}(t)G_{jl}^{<,\uparrow}(t)\left[V_{ij}(t) - V_{kl}(t)\right] - G_{il}^{<,\uparrow}(t)G_{jk}^{<,\uparrow}(t)\left[V_{ij}(t) - V_{lk}(t)\right]$$
$$+ i\hbar G_{ik}^{<,\uparrow}(t)\sum_{p}V_{ip}(t)G_{jp}^{<,\uparrow}(t)G_{pl}^{<,\uparrow}(t) - i\hbar G_{ik}^{<,\uparrow}(t)\sum_{p}V_{kp}(t)G_{jp}^{<,\uparrow}(t)G_{pl}^{<,\uparrow}(t)$$
$$+ i\hbar G_{jl}^{<,\uparrow}(t)\sum_{p}V_{pj}(t)G_{ip}^{<,\uparrow}(t)G_{pk}^{<,\uparrow}(t) - i\hbar G_{jl}^{<,\uparrow}(t)\sum_{p}V_{pl}(t)G_{ip}^{<,\uparrow}(t)G_{pk}^{<,\uparrow}(t)$$
$$- i\hbar G_{il}^{<,\uparrow}(t)\sum_{p}V_{ip}(t)G_{jp}^{<,\uparrow}(t)G_{pk}^{<,\uparrow}(t) + i\hbar G_{il}^{<,\uparrow}(t)\sum_{p}V_{lp}(t)G_{jp}^{<,\uparrow}(t)G_{pk}^{<,\uparrow}(t)$$
$$- i\hbar G_{jk}^{<,\uparrow}(t)\sum_{p}V_{pj}(t)G_{ip}^{<,\uparrow}(t)G_{pl}^{<,\uparrow}(t) + i\hbar G_{jk}^{<,\uparrow}(t)\sum_{p}V_{pk}(t)G_{ip}^{<,\uparrow}(t)G_{pl}^{<,\uparrow}(t)\,. \tag{6.12}$$

The polarization contributions in Eqs. (6.9) and (6.10) become

$$\Pi_{ijkl}^{\uparrow\downarrow\uparrow\downarrow}(t) = - \, i\hbar G_{jl}^{<,\downarrow}(t)\sum_{p}V_{jp}(t)\left[\mathcal{G}_{ipkp}^{\uparrow\downarrow\uparrow\downarrow}(t) + \mathcal{G}_{ipkp}^{\uparrow\uparrow\uparrow\uparrow}(t)\right]$$
$$+ i\hbar G_{jl}^{<,\downarrow}(t)\sum_{p}V_{lp}(t)\left[\mathcal{G}_{ipkp}^{\uparrow\downarrow\uparrow\downarrow}(t) + \mathcal{G}_{ipkp}^{\uparrow\uparrow\uparrow\uparrow}(t)\right]$$
$$+ i\hbar\sum_{p}V_{jp}(t)G_{pl}^{<,\downarrow}(t)\mathcal{G}_{ijkp}^{\uparrow\downarrow\uparrow\downarrow}(t) - i\hbar\sum_{p}V_{pl}(t)G_{jp}^{<,\downarrow}(t)\mathcal{G}_{ipkl}^{\uparrow\downarrow\uparrow\downarrow}(t) \quad \text{and} \tag{6.13}$$

$$\Pi_{ijkl}^{\uparrow\uparrow\uparrow\uparrow}(t) = - \, \mathrm{i}\hbar G_{jl}^{<,\uparrow}(t) \sum_p V_{jp}(t) \left[\mathcal{G}_{ipkp}^{\uparrow\downarrow\uparrow\downarrow}(t) + \mathcal{G}_{ipkp}^{\uparrow\uparrow\uparrow\uparrow}(t) \right]$$

$$+ \, \mathrm{i}\hbar G_{jl}^{<,\uparrow}(t) \sum_p V_{lp}(t) \left[\mathcal{G}_{ipkp}^{\uparrow\downarrow\uparrow\downarrow}(t) + \mathcal{G}_{ipkp}^{\uparrow\uparrow\uparrow\uparrow}(t) \right]$$

$$+ \, \mathrm{i}\hbar \sum_p V_{jp}(t) G_{pl}^{<,\uparrow}(t) \mathcal{G}_{ijkp}^{\uparrow\uparrow\uparrow\uparrow}(t) - \mathrm{i}\hbar \sum_p V_{pl}(t) G_{jp}^{<,\uparrow}(t) \mathcal{G}_{ipkl}^{\uparrow\uparrow\uparrow\uparrow}(t) \,. \tag{6.14}$$

The particle–particle scattering terms of Eqs. (6.9) and (6.10) are included via

$$\Lambda_{ijkl}^{\mathrm{pp},\uparrow\downarrow\uparrow\downarrow}(t) = V_{ij}(t)\mathcal{G}_{ijkl}^{\uparrow\downarrow\uparrow\downarrow}(t) + \mathrm{i}\hbar \sum_p G_{ip}^{<,\uparrow}(t) V_{pj}(t) \mathcal{G}_{pjkl}^{\uparrow\downarrow\uparrow\downarrow}(t)$$

$$+ \, \mathrm{i}\hbar \sum_p G_{jp}^{<,\downarrow}(t) V_{ip}(t) \mathcal{G}_{ipkl}^{\uparrow\downarrow\uparrow\downarrow}(t) \quad \text{and} \tag{6.15}$$

$$\Lambda_{ijkl}^{\mathrm{pp},\uparrow\uparrow\uparrow\uparrow}(t) = V_{ij}(t)\mathcal{G}_{ijkl}^{\uparrow\uparrow\uparrow\uparrow}(t) + \mathrm{i}\hbar \sum_p G_{ip}^{<,\uparrow}(t) V_{pj}(t) \mathcal{G}_{pjkl}^{\uparrow\uparrow\uparrow\uparrow}(t)$$

$$+ \, \mathrm{i}\hbar \sum_p G_{jp}^{<,\uparrow}(t) V_{ip}(t) \mathcal{G}_{ipkl}^{\uparrow\uparrow\uparrow\uparrow}(t) \,. \tag{6.16}$$

Finally, the particle–hole scattering terms of Eqs. (6.9) and (6.10) are given as

$$\Lambda_{ijkl}^{\mathrm{ph},\uparrow\downarrow\uparrow\downarrow}(t) = - \, \mathrm{i}\hbar \sum_p G_{ip}^{<,\uparrow}(t) V_{pl}(t) \mathcal{G}_{pjkl}^{\uparrow\downarrow\uparrow\downarrow}(t) + \mathrm{i}\hbar \sum_p G_{pl}^{<,\downarrow}(t) V_{ip}(t) \mathcal{G}_{ijkp}^{\uparrow\downarrow\uparrow\downarrow}(t) \quad \text{and} \tag{6.17}$$

$$\Lambda_{ijkl}^{\mathrm{ph},\uparrow\uparrow\uparrow\uparrow}(t) = - \, \mathrm{i}\hbar \sum_p G_{ip}^{<,\uparrow}(t) V_{pl}(t) \mathcal{G}_{pjkl}^{\uparrow\uparrow\uparrow\uparrow}(t) + \mathrm{i}\hbar \sum_p G_{pl}^{<,\uparrow}(t) V_{ip}(t) \mathcal{G}_{ijkp}^{\uparrow\uparrow\uparrow\uparrow}(t)$$

$$- \, \mathrm{i}\hbar G_{il}^{<,\uparrow}(t) \sum_p V_{ip}(t) \left[\mathcal{G}_{pjkp}^{\uparrow\uparrow\uparrow\uparrow}(t) - \mathcal{G}_{pjpk}^{\uparrow\downarrow\uparrow\downarrow}(t) \right]$$

$$+ \, \mathrm{i}\hbar G_{il}^{<,\uparrow}(t) \sum_p V_{lp}(t) \left[\mathcal{G}_{pjkp}^{\uparrow\uparrow\uparrow\uparrow}(t) - \mathcal{G}_{pjpk}^{\uparrow\downarrow\uparrow\downarrow}(t) \right] \,. \tag{6.18}$$

These equations account for all terms of the completed DSL approximation [Eq. (3.67)]. Other approximations that have been discussed in this thesis can be obtained by neglecting specific terms. The results have been derived and implemented by the author and Jan-Philip Joost.

As discussed in Sec. 5.1, GNRs feature interesting electronic characteristics due to the confinement-enhanced correlations. Recently, an exciting class of GNR systems has raised particular attention: GNR heterostructures [365–371]. The characteristic geometries of these system cause the existence of topological states that can fundamentally change the electronic properties of the GNRs. A specific example of these heterostructures—namely an alternating sequence of 7- and 9-armchair GNRs (AGNRs)—was recently analyzed in theory [119] and experiment [251]. Here, the theoretical study [119] involved equilibrium Green functions to predict the spatially resolved groundstate-energy distribution. The introduced G1–G2 approach using the PPP model allows one to directly describe ultrafast nonequilibrium dynamics in this heterostructure system. As a proof of concept, Fig. 6.3 contains results by Jan-Philip Joost for the 96-site unit cell [251]. Here, the system is driven by a circularly polarized laser (top right). From the single-particle Green function one has access to the spatially resolved kinetic energy E_{kin}, which is shown for the groundstate

Initial kinetic energy: $E_{\text{kin}}(0)/J$

Laser-induced change in local kinetic energy: $E_{\text{kin}}(t)/J - E_{\text{kin}}(0)/J$

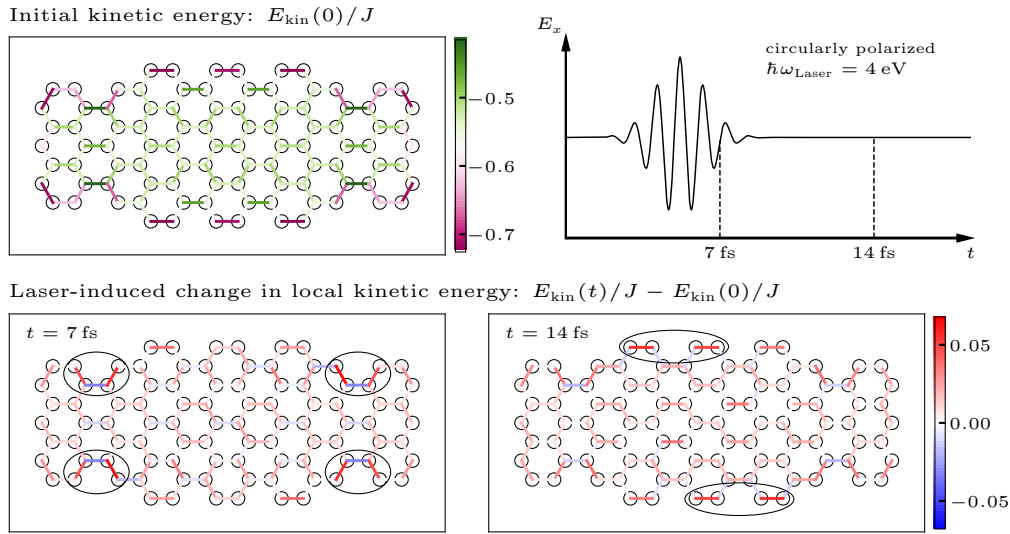$t = 7\,\text{fs}$ $t = 14\,\text{fs}$

Figure 6.3 – Snapshots of the spatially resolved kinetic energy in a 96-site GNR heterostructure during a laser excitation. Top left: initial (groundstate) distribution of E_{kin} in the interatomic orbitals. Bottom: laser-induced change of the kinetic energy after $t = 7\,\text{fs}$ (left) and $t = 14\,\text{fs}$ (right). Top right: time evolution of the laser amplitude in x direction. The circularly polarized laser has a frequency of $\hbar\omega_{\text{Laser}} = 4\,\text{eV}$ and a maximal amplitude of $E_0 = 0.1$. The PPP model uses the Ohno parametrization [cf. Eq. (6.1)] with $U = J$. The figure has been created by Jan-Philip Joost.

of the ribbon (top left). One can see that it is most pronounced on the edges of the system due to the reduced number of neighboring atoms to distribute the energy. The bottom of Fig. 6.3 shows two snapshots ($t = 7\,\text{fs}$ and $t = 14\,\text{fs}$) of the kinetic-energy change relative to the initial state. Overall, the laser excitation leads to a non-localized redistribution of E_{kin}. Interestingly, one can observe small energy excesses at the edges and—remarkably—at the junctions between the 7-AGNR and the 9-AGNR segments. This conjuncture emphasizes the special role of the junction regions within the heterostructure system. A precise characterization of the observed behavior is an interesting topic for future investigations.

To summarize, the DSL-G1–G2 scheme for the PPP model that has been presented in this outlook provides a systematic and efficient way to predict ultrafast dynamics in finite graphene nanostructures. The promising application of light-driven GNR heterostructures has been demonstrated to be within reach of the new approach. Other interesting applications are finite graphene fragments exposed to ionic radiation (cf. Sec. 4.3) and current-signal transmission through GNR systems [372–374], which is relevant for, e.g., next-generation DNA-sequencing methods [372, 375–377].

Appendix A

List of Acronyms

AGNR armchair graphene nanoribbon

BBGKY Bogolyubov–Born–Green–Kirkwood–Yvon

CM carrier multiplication

CNT carbon nanotube

CPT charge–parity–time

CPU central processing unit

DFT density-functional theory

DiagMC diagrammatic Monte Carlo

DMFT dynamical mean-field theory

DMRG density-matrix renormalization group

DNA deoxyribonucleic acid

DSL dynamically screened ladder

EOM equation of motion

FLEX fluctuating-exchange approximation

GKBA generalized Kadanoff–Baym ansatz

GNR graphene nanoribbon

GPU graphics processing unit

GWA GW approximation

HDD homogeneous density distribution

HF Hartree–Fock

HF-GKBA Hartree–Fock generalized Kadanoff–Baym ansatz

IIT integrated-information theory

KBE Keldysh–Kadanoff–Baym equations

LDA local-density approximation

NEGF nonequilibrium Green functions

PIC particle in cell

PPP Pariser–Parr–Pople

RDO reduced density operators

RTQMC real-time quantum Monte Carlo

SOA second-order Born approximation

SRIM the stopping and range of ions in matter

TDDFT time-dependent density-functional theory

TDHF time-dependent Hartree–Fock

TMA T-matrix approximation

TOA third-order approximation

TPH particle–hole T-matrix

TPP particle–particle T-matrix

trARPES time-resolved, angle-resolved photoemission spectroscopy

UEG uniform electron gas

WDM warm dense matter

Appendix B

List of Contributions to International Conferences

2014

- **Dresden, Germany, DPG spring meeting (poster):**
  Green functions approach to Hubbard nano–clusters with the GKBA and T–matrix approximation
  – Niclas Schlünzen, Sebastian Hermanns, and Michael Bonitz

2015

- **Berlin, Germany, DPG spring meeting (poster):**
  Nonequilibrium Green functions approach to transport properties in strongly coupled finite quantum systems
  – Niclas Schlünzen, Sebastian Hermanns, and Michael Bonitz

- **Lund, Sweden, Progress in Non-equilibrium Green's Functions (PNGF VI) (contributed talk):**
  Nonequilibrium Green functions approach to transport and diffusion in strongly coupled finite quantum systems
  – Niclas Schlünzen, Sebastian Hermanns, Michael Bonitz, and Claudio Verdozzi

- **Bad Honnef, Germany, WEH seminar: Isolated Quantum Many-Body Systems out of Equilibrium (poster):**
  Dynamics of strongly correlated fermions—first principle results for two and three dimensions
  – Niclas Schlünzen, Sebastian Hermanns, Michael Bonitz, and Claudio Verdozzi
  → This contribution has been awarded the *Best Poster Prize.*

- **Bad Honnef, Germany, WEH seminar: Isolated Quantum Many-Body Systems out of Equilibrium (shared lecture with Michael Bonitz):**
  Ultrafast dynamics of strongly correlated fermions – a Nonequilibrium Green functions approach
  – Michael Bonitz and Niclas Schlünzen

2016

- **Hannover, Germany, DPG spring meeting (contributed talk):**
  Dynamics of strongly correlated fermions—first principle results for two and three dimensions
  – Niclas Schlünzen, Sebastian Hermanns, Jan-Philip Joost, and Michael Bonitz

- **Lausanne, Switzerland, CECAM workshop: Ultra-fast phenomena in quantum physics: a challenge for theory & experiment (shared talk with Michael Bonitz):**
  Ultrafast Dynamics of Strongly Correlated Fermions - a Nonequilibrium Green Functions Approach
  – Michael Bonitz, Niclas Schlünzen, Sebastian Hermanns, Karsten Balzer, and Jan-Philip Joost

2017

- **Dresden, Germany, DPG spring meeting (poster):**
  Nonequilibrium dynamics of correlated fermions in lattice systems: A benchmark analysis of the nonequilibrium Green functions approach
  – Niclas Schlünzen, Jan-Philip Joost, Fabian Heidrich-Meisner, and Michael Bonitz

- **Kiel, Germany, Strongly Coupled Coulomb Systems 2017 (invited talk):**
  Ab initio simulations of the transport of strongly correlated fermions
  – Niclas Schlünzen, Jan-Philip Joost, and Michael Bonitz

2018

- **Berlin, Germany, DPG spring meeting (poster):**
  Doublon Formation by Ions Impacting a Strongly Correlated System
  – Karsten Balzer, Niclas Schlünzen, Maximilian Rodriguez Rasmussen, and Michael Bonitz

2019

- **Regensburg, Germany, DPG spring meeting (poster):**
  Nonequilibrium Green Functions for Excited Lattice Systems—A Case Study of the
  Artificial Damping
  – Niclas Schlünzen, Jan-Philip Joost, and Michael Bonitz

- **Kiel, Germany, KBEt^2 workshop: Solving the Two-time Kadanoff-Baym
  Equations. Status and Open Problems (invited talk):**
  A Selfenergy Cookbook — State-of-the-Art Computing for the NEGF Key Ingredient
  – Niclas Schlünzen, Jan-Philip Joost, and Michael Bonitz

2020

- **Virtual, 62nd Annual Meeting of the APS Division of Plasma Physics
  (contributed talk):**
  Quantum Dynamics of Electrons Made Fast: Achieving Linear Time-Scaling for
  Nonequilibrium Green Functions
  – Niclas Schlünzen, Jan-Philip Joost, Christopher Makait, and Michael Bonitz

Appendix C

Full List of Publications

1. S. Hermanns, **N. Schlünzen**, and M. Bonitz, *Hubbard nanoclusters far from equilibrium*, Phys. Rev. B, **90**, 125111 (2014)

2. M. Bonitz, **N. Schlünzen**, and S. Hermanns, *Toward a Nonequilibrium Green Functions Approach to Diffusion in Strongly Coupled Finite Quantum Systems*, Contrib. Plasma Phys., **55**, 152 (2015)

3. **N. Schlünzen**, S. Hermanns, M. Bonitz, and C. Verdozzi, *Dynamics of strongly correlated fermions: Ab initio results for two and three dimensions*, Phys. Rev. B, **93**, 035107 (2016)

4. **N. Schlünzen** and M. Bonitz, *Nonequilibrium Green Functions Approach to Strongly Correlated Fermions in Lattice Systems*, Contrib. Plasma Phys., **56**, 5 (2016)

5. K. Balzer, **N. Schlünzen**, and M. Bonitz, *Stopping dynamics of ions passing through correlated honeycomb clusters*, Phys. Rev. B, **94**, 245118 (2016)

6. **N. Schlünzen**, J.-P. Joost, F. Heidrich-Meisner, and M. Bonitz, *Nonequilibrium dynamics in the one-dimensional Fermi-Hubbard model: Comparison of the nonequilibrium Green-functions approach and the density matrix renormalization group method*, Phys. Rev. B, **95**, 165139 (2017)

7. M. Scharnke, **N. Schlünzen** and M. Bonitz, *Time reversal invariance of quantum kinetic equations: Nonequilibrium Green functions formalism*, J. Math. Phys., **58**, 061903 (2017)

8. **N. Schlünzen**, J.-P. Joost, and M. Bonitz, *Comment on "On the unphysical solutions of the Kadanoff-Baym equations in linear response: Correlation-induced homogeneous density-distribution and attractors"*, Phys. Rev. B, **96**, 117101 (2017)

9. M. Bonitz, M. Scharnke, and **N. Schlünzen**, *Time-reversal invariance of quantum kinetic equations II: Density operator formalism*, Contrib. Plasma Phys., **58**, 1036

(2018)

10. K. Balzer, M. Rodriguez Rasmussen, **N. Schlünzen**, J.-P. Joost, and M. Bonitz, *Doublon Formation by Ions Impacting a Strongly Correlated Finite Lattice System*, Phys. Rev. Lett., **121**, 267602 (2018)

11. **N. Schlünzen**, K. Balzer, M. Bonitz, L. Deuchler, and E. Pehlke, *Time-dependent simulation of ion stopping: Charge transfer and electronic excitations*, Contrib. Plasma Phys., **59**, e201800184 (2019)

12. J.-P. Joost, **N. Schlünzen**, and M. Bonitz, *Femtosecond Electron Dynamics in Graphene Nanoribbons – A Nonequilibrium Green Functions Approach Within an Extended Hubbard Model*, Phys. Status Solidi B, **256**, 1800498 (2019)

13. M. Bonitz, K. Balzer, **N. Schlünzen**, M. Rodriguez Rasmussen, and J.-P. Joost, *Ion Impact Induced Ultrafast Electron Dynamics in Finite Graphene-Type Hubbard Clusters*, Phys. Status Solidi B, **256**, 1800490 (2019)

14. **N. Schlünzen**, S. Hermanns, M. Scharnke, and M. Bonitz, *Ultrafast dynamics of strongly correlated fermions - Nonequilibrium Green functions and selfenergy approximations*, J. Phys. Condens. Matter, **32**, 103001 (2020)

15. **N. Schlünzen**, J.-P. Joost, and M. Bonitz, *Achieving the Scaling Limit for Nonequilibrium Green Functions Simulations*, Phys. Rev. Lett., **124**, 076601 (2020)

16. J.-P. Joost, **N. Schlünzen**, and M. Bonitz, *G1-G2 scheme: Dramatic acceleration of nonequilibrium Green functions simulations within the Hartree-Fock generalized Kadanoff-Baym ansatz*, Phys. Rev. B, **101**, 245101 (2020)

17. J.-P. Joost, **N. Schlünzen**, S. Hese, M. Bonitz, P. Schmitteckert, C. Verdozzi, and M. Hopjan, *Löwdin's symmetry dilemma within Green functions theory for the one-dimensional Hubbard model*, Contrib. Plasma Phys., **Early View**, DOI: 10.1002/ctpp.202000220 (2021)

References

[1] K.-C. Chao and R. A. Greenkorn, *Thermodynamics of Fluids : An Introduction to Equilibrium Theory* (M. Dekker, New York, 1975).

[2] J. Prausnitz, R. Lichtenthaler, and E. de Azevedo, *Molecular Thermodynamics of Fluid-Phase Equilibria* (Prentice Hall PTR, New Jersey, 1999).

[3] D. Young, B. Munson, T. Okiishi, and W. Huebsch, *A Brief Introduction to Fluid Mechanics* (Wiley, 2010).

[4] P. Simon and Y. Gogotsi, "Materials for electrochemical capacitors", Nanoscience and technology: a collection of reviews from Nature journals, 320–329 (2010).

[5] M. V. Fedorov and A. A. Kornyshev, "Ionic Liquids at Electrified Interfaces", Chemical Reviews **114**, 2978–3036 (2014).

[6] B. Parida, S. Iniyan, and R. Goic, "A review of solar photovoltaic technologies", Renewable and Sustainable Energy Reviews **15**, 1625–1636 (2011).

[7] N. Vogel, *Surface Patterning with Colloidal Monolayers*, Springer Theses (Springer, Berlin, 2012).

[8] F. Chen, *Introduction to Plasma Physics* (Springer US, New York, 2012).

[9] F. Graziani, M. Desjarlais, R. Redmer, and S. Trickey, *Frontiers and Challenges in Warm Dense Matter*, Lecture Notes in Computational Science and Engineering (Springer International Publishing, Cham, 2014).

[10] T. Dornheim, S. Groth, and M. Bonitz, "The uniform electron gas at warm dense matter conditions", Physics Reports **744**, 1–86 (2018).

[11] M. Bonitz, T. Dornheim, Z. A. Moldabekov, S. Zhang, P. Hamann, H. Kählert, A. Filinov, K. Ramakrishna, and J. Vorberger, "Ab initio simulation of warm dense matter", Physics of Plasmas **27**, 042710 (2020).

[12] I. H. Hutchinson, "Principles of Plasma Diagnostics: Second Edition", Plasma Physics and Controlled Fusion **44**, 2603–2603 (2002).

[13] S. X. Hu, B. Militzer, V. N. Goncharov, and S. Skupsky, "Strong Coupling and Degeneracy Effects in Inertial Confinement Fusion Implosions", Phys. Rev. Lett. **104**, 235003 (2010).

[14] J. Kondo, "Resistance Minimum in Dilute Magnetic Alloys", Progress of Theoretical Physics **32**, 37–49 (1964).

[15] K. G. Wilson, "The renormalization group: Critical phenomena and the Kondo problem", Rev. Mod. Phys. **47**, 773–840 (1975).

[16] R. Bulla, T. A. Costi, and T. Pruschke, "Numerical renormalization group method for quantum impurity systems", Rev. Mod. Phys. **80**, 395–450 (2008).

[17] K. v. Klitzing, G. Dorda, and M. Pepper, "New Method for High-Accuracy Determination of the Fine-Structure Constant Based on Quantized Hall Resistance", Phys. Rev. Lett. **45**, 494–497 (1980).

[18] R. Prange, M. Cage, K. Klitzing, S. Girvin, A. Chang, F. Duncan, M. Haldane, R. Laughlin, A. Pruisken, and D. Thouless, *The Quantum Hall Effect*, Graduate Texts in Contemporary Physics (Springer, New York, 2012).

[19] W. K. A. Salem, "Nonequilibrium quantum statistical mechanics and thermodynamics", arXiv:math-ph/0601047 (2006).

[20] G. Giuliani and G. Vignale, *Quantum Theory of the Electron Liquid* (Cambridge University Press, Cambridge, 2005).

[21] J. Schwinger, "Brownian Motion of a Quantum Oscillator", J. Math. Phys. **2**, 407–432 (1961).

[22] L. V. Keldysh, "Diagram Technique for Nonequilibrium Processes", Sov. Phys. JETP **20**, 1018–1026 (1965).

[23] G. Stefanucci and R. v. Leeuwen, *Nonequilibrium many-body theory of quantum systems: a modern introduction* (Cambridge University Press, Cambridge, 2013).

[24] M. P. Bircher, E. Liberatore, N. J. Browning, S. Brickel, C. Hofmann, A. Patoz, O. T. Unke, T. Zimmermann, M. Chergui, P. Hamm, U. Keller, M. Meuwly, H.-J. Woerner, J. Vaníček, and U. Rothlisberger, "Nonadiabatic effects in electronic and nuclear dynamics", Structural Dynamics **4**, 061510 (2017).

[25] A. W. Jasper, S. Nangia, C. Zhu, and D. G. Truhlar, "Non-Born–Oppenheimer Molecular Dynamics", Accounts of Chemical Research **39**, 101–108 (2006).

[26] L. Perfetti, P. A. Loukakos, M. Lisowski, U. Bovensiepen, H. Berger, S. Biermann, P. S. Cornaglia, A. Georges, and M. Wolf, "Time Evolution of the Electronic Structure of $1T-\text{TaS}_2$ through the Insulator-Metal Transition", Phys. Rev. Lett. **97**, 067402 (2006).

[27] J. K. Freericks, H. R. Krishnamurthy, and T. Pruschke, "Theoretical Description of Time-Resolved Photoemission Spectroscopy: Application to Pump-Probe Experiments", Phys. Rev. Lett. **102**, 136401 (2009).

[28] C. L. Smallwood, R. A. Kaindl, and A. Lanzara, "Ultrafast angle-resolved photoemission spectroscopy of quantum materials", EPL (Europhysics Letters) **115**, 27001 (2016).

[29] A. F. Kemper, M. A. Sentef, B. Moritz, T. P. Devereaux, and J. K. Freericks, "Review of the Theoretical Description of Time-Resolved Angle-Resolved Photoemission Spectroscopy in Electron-Phonon Mediated Superconductors", Annalen der Physik **529**, 1600235 (2017).

[30] L. Waldecker, R. Bertoni, R. Ernstorfer, and J. Vorberger, "Electron-Phonon Coupling and Energy Flow in a Simple Metal beyond the Two-Temperature Approximation", Phys. Rev. X **6**, 021003 (2016).

[31] E. Malic and A. Knorr, *Graphene and Carbon Nanotubes: Ultrafast Optics and Relaxation Dynamics* (Wiley, Weinheim, Germany, 2013).

[32] T. Winzer, A. Knorr, and E. Malic, "Carrier Multiplication in Graphene", Nano Letters **10**, 4839–4843 (2010).

[33] F. Schulze, M. Schoth, U. Woggon, A. Knorr, and C. Weber, "Ultrafast dynamics of carrier multiplication in quantum dots", Phys. Rev. B **84**, 125318 (2011).

[34] R. Baer and E. Rabani, "Can Impact Excitation Explain Efficient Carrier Multiplication in Carbon Nanotube Photodiodes?", Nano Letters **10**, 3277–3282 (2010).

[35] S. Konabe, N. Onoda, and K. Watanabe, "Auger ionization in armchair-edge graphene nanoribbons", Phys. Rev. B **82**, 073402 (2010).

[36] C. Birdsall and A. Langdon, *Plasma Physics via Computer Simulation*, Series in Plasma Physics and Fluid Dynamics (Taylor & Francis, New York, 2004).

[37] T. D. Arber, K. Bennett, C. S. Brady, A. Lawrence-Douglas, M. G. Ramsay, N. J. Sircombe, P. Gillies, R. G. Evans, H. Schmitz, A. R. Bell, and C. P. Ridgers, "Contemporary particle-in-cell approach to laser-plasma modelling", Plasma Physics and Controlled Fusion **57**, 113001 (2015).

[38] A. Ojanperä, A. V. Krasheninnikov, and M. Puska, "Electronic stopping power from first-principles calculations with account for core electron excitations and projectile ionization", Phys. Rev. B **89**, 035120 (2014).

[39] E. Gruber, R. A. Wilhelm, R. Pétuya, V. Smejkal, R. Kozubek, A. Hierzenberger, B. C. Bayer, I. Aldazabal, A. K. Kazansky, F. Libisch, A. V. Krasheninnikov, M. Schleberger, S. Facsko, A. G. Borisov, A. Arnau, and F. Aumayr, "Ultrafast electronic response of graphene to a strong and localized electric field", Nature Communications **7**, 13948 (2016).

[40] I. Adamovich, A. Anders, S. Baalrud, M. Bonitz, A. Brizard, T. Carter, J. Cary, J. Daligault, J. Danielson, F. Doss, J. Drake, R. P. Drake, N. Fisch, C. Forest, D. Froula, G. Ganguli, S. P. Gary, S. Glenzer, J. Goree, D. Graves, G. Gregori, G. Hebner, W. Heidbrink, J. Hopwood, G. Howes, C. Joshi, I. Kaganovich, M. Keidar, T. Killian, K. Krushelnick, M. Kunz, M. Kushner, D. Lamb, M. Laming, M. Mauel, J. Mikhailova, P. Morrison, B. Remington, J. Rocca, R. Rudd, D. Ryutov, A. Safronova, J. Sarff, T. Schenkel, V. Shiltsev, U. Shumlak, G. Shvets, D. B. Sinars, F. Skiff, R. Smith, J. Stone, E. Thomas, G. Tynan, A. White, J. Wurtele, S. Zweben, and E. Zweibel, "Plasma: at the frontier of scientific discovery", Technical Report, U.S. Department of Energy, Office of Sciences **1615243**, 1–106 (2017).

[41] K. Balzer, M. R. Rasmussen, N. Schlünzen, J.-P. Joost, and M. Bonitz, "Doublon Formation by Ions Impacting a Strongly Correlated Finite Lattice System", Phys. Rev. Lett. **121**, 267602 (2018).

[42] I. Bloch, "Ultracold quantum gases in optical lattices", Nature physics **1**, 23–30 (2005).

[43] I. M. Georgescu, S. Ashhab, and F. Nori, "Quantum simulation", Rev. Mod. Phys. **86**, 153–185 (2014).

[44] I. Bloch, J. Dalibard, and S. Nascimbene, "Quantum simulations with ultracold quantum gases", Nature Physics **8**, 267–276 (2012).

[45] C. Gross and I. Bloch, "Quantum simulations with ultracold atoms in optical lattices", Science **357**, 995–1001 (2017).

[46] R. Kosloff, "Propagation methods for quantum molecular dynamics", Annual Review of Physical Chemistry **45**, 145–178 (1994).

[47] J. Zhang, *Theory And Application Of Quantum Molecular Dynamics* (World Scientific Publishing Company, 1998).

[48] M. Ben-Nun and T. J. Martínez, "Ab initio quantum molecular dynamics", Advances in chemical physics **121**, 439–512 (2002).

[49] M. Bonitz and D. Semkat, eds., *Introduction to Computational Methods in Many Body Physics* (Rinton Press, Paramus, New Jersey, 2006).

[50] W. G. Hoover, "Nonequilibrium Molecular Dynamics", Annual Review of Physical Chemistry **34**, 103–127 (1983).

[51] W. G. Hoover and C. G. Hoover, "Nonequilibrium molecular dynamics", Condensed Matter Physics **8**, 247–260 (2005).

[52] B. Todd and P. Daivis, *Nonequilibrium Molecular Dynamics: Theory, Algorithms and Applications* (Cambridge University Press, Cambridge, 2017).

[53] L. Boltzmann, "Weitere Studien über das Wärmegleichgewicht unter Gasmolekülen", Sitzungsber. Kais. Akad. Wiss. Wien Math. Naturwiss. Classe **66**, 275–370 (1872).

[54] L. Boltzmann, *Vorlesungen über Gastheorie: Theorie der Gase mit einatomigen Molekülen, deren Dimensionen gegen die mittlere Weglänge verschwinden*, Vol. 1 (J. A. Barth, Leipzig, 1896).

[55] R. Lehe, M. Kirchen, I. A. Andriyash, B. B. Godfrey, and J.-L. Vay, "A spectral, quasi-cylindrical and dispersion-free Particle-In-Cell algorithm", Computer Physics Communications **203**, 66–82 (2016).

[56] B. Goplen, L. Ludeking, D. Smith, and G. Warren, "User-configurable magic for electromagnetic pic calculations", Computer Physics Communications **87**, Particle Simulation Methods, 54–86 (1995).

[57] R. A. Fonseca, L. O. Silva, F. S. Tsung, V. K. Decyk, W. Lu, C. Ren, W. B. Mori, S. Deng, S. Lee, T. Katsouleas, and J. C. Adam, "Osiris: a three-dimensional, fully relativistic particle in cell code for modeling plasma based accelerators", in Computational science — iccs 2002, edited by P. M. A. Sloot, A. G. Hoekstra, C. J. K. Tan, and J. J. Dongarra (2002), pp. 342–351.

[58] K. J. Bowers, B. J. Albright, L. Yin, B. Bergen, and T. J. T. Kwan, "Ultrahigh performance three-dimensional electromagnetic relativistic kinetic plasma simulation", Physics of Plasmas **15**, 055703 (2008).

[59] C. Nieter and J. R. Cary, "VORPAL: a versatile plasma simulation code", Journal of Computational Physics **196**, 448–473 (2004).

[60] D. Welch, D. Rose, B. Oliver, and R. Clark, "Simulation techniques for heavy ion fusion chamber transport", Nuclear Instruments and Methods in Physics Research Section A: Accelerators, Spectrometers, Detectors and Associated Equipment **464**, Pfoc. of the 13th Int. Symp. on Heavy Ion Intertial Fusion, 134–139 (2001).

[61] H. Burau, R. Widera, W. Hönig, G. Juckeland, A. Debus, T. Kluge, U. Schramm, T. E. Cowan, R. Sauerbrey, and M. Bussmann, "PIConGPU: A Fully Relativistic Particle-in-Cell Code for a GPU Cluster", IEEE Transactions on Plasma Science **38**, 2831–2839 (2010).

[62] A. Gonoskov, S. Bastrakov, E. Efimenko, A. Ilderton, M. Marklund, I. Meyerov, A. Muraviev, A. Sergeev, I. Surmin, and E. Wallin, "Extended particle-in-cell schemes for physics in ultrastrong laser fields: review and developments", Phys. Rev. E **92**, 023305 (2015).

[63] A. Sgattoni, L. Fedeli, S. Sinigardi, A. Marocchino, and M. Chandra, *piccante: 2016 with Poisson solver and quite start*, version v1.5.0, Mar. 2016.

[64] D. L. Freeman, "Coupled-cluster expansion applied to the electron gas: Inclusion of ring and exchange effects", Phys. Rev. B **15**, 5512–5521 (1977).

[65] R. J. Bartlett, "Many-Body Perturbation Theory and Coupled Cluster Theory for Electron Correlation in Molecules", Annual Review of Physical Chemistry **32**, 359–401 (1981).

[66] P. E. M. Siegbahn, "The Configuration Interaction Method", in *Lecture notes in quantum chemistry: european summer school in quantum chemistry*, edited by B. O. Roos (Springer Berlin Heidelberg, Berlin, Heidelberg, 1992), pp. 255–293.

[67] C. David Sherrill and H. F. Schaefer, "The Configuration Interaction Method: Advances in Highly Correlated Approaches", in , Vol. 34, edited by P.-O. Löwdin, J. R. Sabin, M. C. Zerner, and E. Brändas, Advances in Quantum Chemistry (Academic Press, 1999), pp. 143–269.

[68] J. Olsen, B. O. Roos, P. Jørgensen, and H. J. A. Jensen, "Determinant based configuration interaction algorithms for complete and restricted configuration interaction spaces", The Journal of Chemical Physics **89**, 2185–2192 (1988).

[69] D. Hochstuhl and M. Bonitz, "Time-dependent restricted-active-space configuration-interaction method for the photoionization of many-electron atoms", Phys. Rev. A **86**, 053424 (2012).

[70] S. Bauch, L. K. Sørensen, and L. B. Madsen, "Time-dependent generalized-active-space configuration-interaction approach to photoionization dynamics of atoms and molecules", Phys. Rev. A **90**, 062508 (2014).

[71] J. Caillat, J. Zanghellini, M. Kitzler, O. Koch, W. Kreuzer, and A. Scrinzi, "Correlated multielectron systems in strong laser fields: A multiconfiguration time-dependent Hartree-Fock approach", Phys. Rev. A **71**, 012712 (2005).

[72] D. Hochstuhl, S. Bauch, and M. Bonitz, "Multiconfigurational time-dependent Hartree-Fock calculations for photoionization of one-dimensional Helium", Journal of Physics: Conference Series **220**, 012019 (2010).

[73] D. Hochstuhl and M. Bonitz, "Two-photon ionization of helium studied with the multiconfigurational time-dependent Hartree–Fock method", The Journal of Chemical Physics **134**, 084106 (2011).

[74] D. Hochstuhl, C. M. Hinz, and M. Bonitz, "Time-dependent multiconfiguration methods for the numerical simulation of photoionization processes of many-electron atoms", The European Physical Journal Special Topics **223**, 177–336 (2014).

[75] G. Vidal, "Efficient Simulation of One-Dimensional Quantum Many-Body Systems", Phys. Rev. Lett. **93**, 040502 (2004).

[76] A. J. Daley, C. Kollath, U. Schollwöck, and G. Vidal, "Time-dependent density-matrix renormalization-group using adaptive effective Hilbert spaces", Journal of Statistical Mechanics: Theory and Experiment **2004**, P04005 (2004).

[77] S. R. White and A. E. Feiguin, "Real-Time Evolution Using the Density Matrix Renormalization Group", Phys. Rev. Lett. **93**, 076401 (2004).

[78] U. Schollwöck, "Matrix product state algorithms: DMRG, TEBD and relatives", in Strongly Correlated Systems (Springer, Berlin, 2013), pp. 67–98.

[79] N. Schlünzen, S. Hermanns, M. Scharnke, and M. Bonitz, "Ultrafast dynamics of strongly correlated fermions—nonequilibrium Green functions and selfenergy approximations", J. Phys. Condens. Matter **32**, 103001 (2020).

[80] E. Gross and W. Kohn, "Time-Dependent Density-Functional Theory", in Density functional theory of many-fermion systems, Vol. 21, edited by P.-O. Löwdin, Advances in Quantum Chemistry (Academic Press, 1990), pp. 255–291.

[81] M. Marques and E. Gross, "Time-dependent density functional theory", Annual Review of Physical Chemistry **55**, 427–455 (2004).

[82] K. Burke, J. Werschnik, and E. K. U. Gross, "Time-dependent density functional theory: past, present, and future", The Journal of Chemical Physics **123**, 062206 (2005).

[83] C. Ullrich, Time-Dependent Density-Functional Theory: Concepts and Applications, Oxford Graduate Texts (Oxford University Press, New York, 2012).

[84] A. N. Rubtsov, V. V. Savkin, and A. I. Lichtenstein, "Continuous-time quantum Monte Carlo method for fermions", Phys. Rev. B **72**, 035122 (2005).

[85] E. Gull, A. J. Millis, A. I. Lichtenstein, A. N. Rubtsov, M. Troyer, and P. Werner, "Continuous-time Monte Carlo methods for quantum impurity models", Rev. Mod. Phys. **83**, 349–404 (2011).

[86] N. V. Prokof'ev and B. V. Svistunov, "Polaron Problem by Diagrammatic Quantum Monte Carlo", Phys. Rev. Lett. **81**, 2514–2517 (1998).

[87] P. Werner, T. Oka, and A. J. Millis, "Diagrammatic Monte Carlo simulation of nonequilibrium systems", Phys. Rev. B **79**, 035320 (2009).

[88] E. Kozik, K. V. Houcke, E. Gull, L. Pollet, N. Prokof'ev, B. Svistunov, and M. Troyer, "Diagrammatic Monte Carlo for correlated fermions", EPL (Europhysics Letters) **90**, 10004 (2010).

[89] K. Van Houcke, E. Kozik, N. Prokof'ev, and B. Svistunov, "Diagrammatic Monte Carlo", Physics Procedia **6**, Computer Simulations Studies in Condensed Matter Physics XXI, 95–105 (2010).

[90] K. Byczuk and D. Vollhardt, "Correlated bosons on a lattice: Dynamical mean-field theory for Bose-Einstein condensed and normal phases", Phys. Rev. B **77**, 235106 (2008).

[91] M. Eckstein, A. Hackl, S. Kehrein, M. Kollar, M. Moeckel, P. Werner, and F. A. Wolf, "New theoretical approaches for correlated systems in nonequilibrium", The European Physical Journal Special Topics **180**, 217–235 (2009).

[92] T. Ayral, S. Biermann, and P. Werner, "Screening and nonlocal correlations in the extended Hubbard model from self-consistent combined GW and dynamical mean field theory", Phys. Rev. B **87**, 125149 (2013).

[93] S. Biermann, "Dynamical screening effects in correlated electron materials—a progress report on combined many-body perturbation and dynamical mean field theory: 'GW + DMFT'", Journal of Physics: Condensed Matter **26**, 173202 (2014).

[94] P.-O. Löwdin, "Quantum Theory of Many-Particle Systems. I. Physical Interpretations by Means of Density Matrices, Natural Spin-Orbitals, and Convergence Problems in the Method of Configurational Interaction", Phys. Rev. **97**, 1474–1489 (1955).

[95] F. Bopp, "Ableitung der Bindungsenergie von N-Teilchen-Systemen aus 2-Teilchen-Dichtematrizen", Zeitschrift für Physik **156**, 348–359 (1959).

[96] M. Bonitz, *Quantum Kinetic Theory*, 2nd ed. (Springer, Cham, 2016).

[97] D. A. Mazziotti, "Realization of Quantum Chemistry without Wave Functions through First-Order Semidefinite Programming", Phys. Rev. Lett. **93**, 213001 (2004).

[98] Z. Zhao, B. J. Braams, M. Fukuda, M. L. Overton, and J. K. Percus, "The reduced density matrix method for electronic structure calculations and the role of three-index representability conditions", The Journal of Chemical Physics **120**, 2095–2104 (2004).

[99] D. A. Mazziotti, "Anti-Hermitian Contracted Schrödinger Equation: Direct Determination of the Two-Electron Reduced Density Matrices of Many-Electron Molecules", Phys. Rev. Lett. **97**, 143002 (2006).

[100] F. Lackner, I. Březinová, T. Sato, K. L. Ishikawa, and J. Burgdörfer, "Propagating two-particle reduced density matrices without wave functions", Phys. Rev. A **91**, 023412 (2015).

[101] K. Balzer and M. Bonitz, *Nonequilibrium Green's Functions Approach to Inhomogeneous Systems*, Vol. 867, Lect. Notes Phys. (Springer, Berlin, Heidelberg, 2013).

[102] L. V. Keldysh, "Ionization in the field of a static electromagnetic wave", Sov. Phys. JETP **20**, 1307 (1965).

[103] L. Kadanoff and G. Baym, *Quantum statistical mechanics: Green's function methods in equilibrium and nonequilibrium problems*, Frontiers in physics (W.A. Benjamin, 1962).

[104] L. V. Keldysh, "Real-time Nonequilibrium Green's Functions", in *Progress in Nonequilibrium Green's Functions II*, edited by M. Bonitz and D. Semkat (World Scientific, Singapore, 2003), pp. 4–17.

[105] M. Bonitz, A.-P. Jauho, M. Sadovskii, and S. Tikhodeev, "In Memoriam Leonid V. Keldysh", physica status solidi (b) **256**, 1800600 (2019).

[106] P. Danielewicz, "Quantum theory of nonequilibrium processes II. Application to nuclear collisions", Annals of Physics **152**, 305–326 (1984).

[107] P. Lipavský, V. Špička, and B. Velický, "Generalized Kadanoff-Baym ansatz for deriving quantum transport equations", Phys. Rev. B **34**, 6933–6942 (1986).

[108] N. E. Dahlen and R. van Leeuwen, "Solving the Kadanoff-Baym Equations for Inhomogeneous Systems: Application to Atoms and Molecules", Phys. Rev. Lett. **98**, 153004 (2007).

[109] M. P. von Friesen, C. Verdozzi, and C.-O. Almbladh, "Successes and Failures of Kadanoff-Baym Dynamics in Hubbard Nanoclusters", Phys. Rev. Lett. **103**, 176404 (2009).

[110] E. A. A. Pogna, M. Marsili, D. De Fazio, S. Dal Conte, C. Manzoni, D. Sangalli, D. Yoon, A. Lombardo, A. C. Ferrari, A. Marini, G. Cerullo, and D. Prezzi, "Photo-Induced Bandgap Renormalization Governs the Ultrafast Response of Single-Layer MoS2", ACS Nano **10**, 1182–1188 (2016).

[111] M. Hopjan, D. Karlsson, S. Ydman, C. Verdozzi, and C.-O. Almbladh, "Merging Features from Green's Functions and Time Dependent Density Functional Theory: A Route to the Description of Correlated Materials out of Equilibrium?", Phys. Rev. Lett. **116**, 236402 (2016).

[112] A. Molina-Sánchez, D. Sangalli, L. Wirtz, and A. Marini, "Ab Initio Calculations of Ultrashort Carrier Dynamics in Two-Dimensional Materials: Valley Depolarization in Single-Layer WSe2", Nano Letters **17**, 4549–4555 (2017).

[113] E. V. Boström, A. Mikkelsen, C. Verdozzi, E. Perfetto, and G. Stefanucci, "Charge Separation in Donor–C60 Complexes with Real-Time Green Functions: The Importance of Nonlocal Correlations", Nano Lett. **18**, 785–792 (2018).

[114] N. Schlünzen, J.-P. Joost, and M. Bonitz, "Achieving the Scaling Limit for Nonequilibrium Green Functions Simulations", Phys. Rev. Lett. **124**, 076601 (2020).

[115] P. C. Martin and J. Schwinger, "Theory of Many-Particle Systems. I", Phys. Rev. **115**, 1342–1373 (1959).

[116] G. Green, *An Essay on the Application of Mathematical Analysis to the Theories of Electricity and Magnetism* (T. Wheelhouse, Nottingham, 1828).

[117] D. Kremp, T. Bornath, M. Schlanges, and W. Kraeft, *Quantum statistics of nonideal plasmas*, Springer Series on Atomic, Optical, and Plasma Physics (Springer, Berlin, Heidelberg, 2005).

[118] J.-P. Joost, N. Schlünzen, S. Hese, M. Bonitz, C. Verdozzi, P. Schmitteckert, and M. Hopjan, "Löwdin's symmetry dilemma within Green functions theory for the one-dimensional Hubbard model", Contrib. Plasma Phys. **Early View**, DOI: 10.1002/ctpp.202000220 (2021).

[119] J.-P. Joost, A.-P. Jauho, and M. Bonitz, "Correlated Topological States in Graphene Nanoribbon Heterostructures", Nano Letters **19**, 9045–9050 (2019).

[120] L. Hedin, "New Method for Calculating the One-Particle Green's Function with Application to the Electron-Gas Problem", Phys. Rev. **139**, A796–A823 (1965).

[121] P. Romaniello, F. Bechstedt, and L. Reining, "Beyond the *GW* approximation: Combining correlation channels", Phys. Rev. B **85**, 155131 (2012).

[122] N. Schlünzen and M. Bonitz, "Nonequilibrium Green Functions Approach to Strongly Correlated Fermions in Lattice Systems", Contrib. Plasma Phys. **56**, 5–91 (2016).

[123] J. Kanamori, "Electron Correlation and Ferromagnetism of Transition Metals", Progress of Theoretical Physics **30**, 275–289 (1963).

[124] K. Balzer, S. Bauch, and M. Bonitz, "Time-dependent second-order Born calculations for model atoms and molecules in strong laser fields", Phys. Rev. A **82**, 033427 (2010).

[125] D. Hochstuhl, K. Balzer, S. Bauch, and M. Bonitz, "Nonequilibrium Green function approach to photoionization processes in atoms", Physica E: Low-dimensional Systems and Nanostructures **42**, Proceedings of the international conference Frontiers of Quantum and Mesoscopic Thermodynamics FQMT '08, 513–519 (2010).

[126] E. Perfetto, A.-M. Uimonen, R. van Leeuwen, and G. Stefanucci, "First-principles nonequilibrium Green's-function approach to transient photoabsorption: Application to atoms", Phys. Rev. A **92**, 033419 (2015).

[127] K. Balzer, M. Bonitz, R. van Leeuwen, A. Stan, and N. E. Dahlen, "Nonequilibrium Green's function approach to strongly correlated few-electron quantum dots", Phys. Rev. B **79**, 245306 (2009).

[128] K. Balzer, S. Hermanns, and M. Bonitz, "Electronic double excitations in quantum wells: Solving the two-time Kadanoff-Baym equations", EPL (Europhysics Letters) **98**, 67002 (2012).

[129] S. Hermanns, K. Balzer, and M. Bonitz, "The non-equilibrium Green function approach to inhomogeneous quantum many-body systems using the generalized Kadanoff–Baym ansatz", Phys. Scr. **T151**, 014036 (2012).

[130] M. von Friesen, C. Verdozzi, and C.-O. Almbladh, "Kadanoff-Baym dynamics of Hubbard clusters: Performance of many-body schemes, correlation-induced damping and multiple steady and quasi-steady states", Phys. Rev. B **82**, 155108 (2010).

[131] A.-M. Uimonen, E. Khosravi, G. Stefanucci, S. Kurth, R. van Leeuwen, and E. K. U. Gross, "Real-time switching between multiple steady-states in quantum transport", Journal of Physics: Conference Series **220**, 012018 (2010).

[132] N. Säkkinen, M. Manninen, and R. van Leeuwen, "The Kadanoff–Baym approach to double excitations in finite systems", New Journal of Physics **14**, 013032 (2012).

[133] K. Balzer, S. Hermanns, and M. Bonitz, "The generalized Kadanoff-Baym ansatz. Computing nonlinear response properties of finite systems", Journal of Physics: Conference Series **427**, 012006 (2013).

[134] S. Hermanns, K. Balzer, and M. Bonitz, "Few-particle quantum dynamics–comparing nonequilibrium Green functions with the generalized Kadanoff–Baym ansatz to density operator theory", J. Phys.: Conf. Ser. **427**, 012008 (2013).

[135] R. Tuovinen, E. Perfetto, G. Stefanucci, and R. van Leeuwen, "Time-dependent Landauer-Büttiker formula: Application to transient dynamics in graphene nanoribbons", Phys. Rev. B **89**, 085131 (2014).

[136] S. Hermanns, N. Schlünzen, and M. Bonitz, "Hubbard nanoclusters far from equilibrium", Phys. Rev. B **90**, 125111 (2014).

[137] D. Jaksch, C. Bruder, J. I. Cirac, C. W. Gardiner, and P. Zoller, "Cold Bosonic Atoms in Optical Lattices", Phys. Rev. Lett. **81**, 3108–3111 (1998).

[138] T. Stöferle, H. Moritz, C. Schori, M. Köhl, and T. Esslinger, "Transition from a Strongly Interacting 1D Superfluid to a Mott Insulator", Phys. Rev. Lett. **92**, 130403 (2004).

[139] C. D. Fertig, K. M. O'Hara, J. H. Huckans, S. L. Rolston, W. D. Phillips, and J. V. Porto, "Strongly Inhibited Transport of a Degenerate 1D Bose Gas in a Lattice", Phys. Rev. Lett. **94**, 120403 (2005).

[140] U. Schneider, L. Hackermüller, J. P. Ronzheimer, S. Will, S. Braun, T. Best, I. Bloch, E. Demler, S. Mandt, D. Rasch, et al., "Fermionic transport and out-of-equilibrium dynamics in a homogeneous Hubbard model with ultracold atoms", Nat. Phys. **8**, 213–218 (2012).

[141] L. W. Cheuk, M. A. Nichols, K. R. Lawrence, M. Okan, H. Zhang, and M. W. Zwierlein, "Observation of 2D Fermionic Mott Insulators of ^{40}K with Single-Site Resolution", Phys. Rev. Lett. **116**, 235301 (2016).

[142] M. Köhl, H. Moritz, T. Stöferle, K. Günter, and T. Esslinger, "Fermionic Atoms in a Three Dimensional Optical Lattice: Observing Fermi Surfaces, Dynamics, and Interactions", Phys. Rev. Lett. **94**, 080403 (2005).

[143] R. Jördens, N. Strohmaier, K. Günter, H. Moritz, and T. Esslinger, "A Mott insulator of fermionic atoms in an optical lattice", Nature **455**, 204–207 (2008).

[144] W. S. Bakr, J. I. Gillen, A. Peng, S. Fölling, and M. Greiner, "A quantum gas microscope for detecting single atoms in a Hubbard-regime optical lattice", Nature **462**, 74–77 (2009).

[145] J. F. Sherson, C. Weitenberg, M. Endres, M. Cheneau, I. Bloch, and S. Kuhr, "Single-atom-resolved fluorescence imaging of an atomic Mott insulator", Nature **467**, 68–72 (2010).

[146] L. W. Cheuk, M. A. Nichols, M. Okan, T. Gersdorf, V. V. Ramasesh, W. S. Bakr, T. Lompe, and M. W. Zwierlein, "Quantum-Gas Microscope for Fermionic Atoms", Phys. Rev. Lett. **114**, 193001 (2015).

[147] E. Haller, J. Hudson, A. Kelly, D. A. Cotta, B. Peaudecerf, G. D. Bruce, and S. Kuhr, "Single-atom imaging of fermions in a quantum-gas microscope", Nature Physics **11**, 738–742 (2015).

[148] M. F. Parsons, F. Huber, A. Mazurenko, C. S. Chiu, W. Setiawan, K. Wooley-Brown, S. Blatt, and M. Greiner, "Site-Resolved Imaging of Fermionic ^{6}Li in an Optical Lattice", Phys. Rev. Lett. **114**, 213002 (2015).

[149] A. Omran, M. Boll, T. A. Hilker, K. Kleinlein, G. Salomon, I. Bloch, and C. Gross, "Microscopic Observation of Pauli Blocking in Degenerate Fermionic Lattice Gases", Phys. Rev. Lett. **115**, 263001 (2015).

[150]G. J. A. Edge, R. Anderson, D. Jervis, D. C. McKay, R. Day, S. Trotzky, and J. H. Thywissen, "Imaging and addressing of individual fermionic atoms in an optical lattice", Phys. Rev. A **92**, 063406 (2015).

[151]J. P. Ronzheimer, M. Schreiber, S. Braun, S. S. Hodgman, S. Langer, I. P. McCulloch, F. Heidrich-Meisner, I. Bloch, and U. Schneider, "Expansion Dynamics of Interacting Bosons in Homogeneous Lattices in One and Two Dimensions", Phys. Rev. Lett. **110**, 205301 (2013).

[152]L. Vidmar, J. P. Ronzheimer, M. Schreiber, S. Braun, S. S. Hodgman, S. Langer, F. Heidrich-Meisner, I. Bloch, and U. Schneider, "Dynamical Quasicondensation of Hard-Core Bosons at Finite Momenta", Phys. Rev. Lett. **115**, 175301 (2015).

[153]L. Xia, L. A. Zundel, J. Carrasquilla, A. Reinhard, J. M. Wilson, M. Rigol, and D. S. Weiss, "Quantum distillation and confinement of vacancies in a doublon sea", Nature Physics **11**, 316–320 (2015).

[154]S. Scherg, T. Kohlert, J. Herbrych, J. Stolpp, P. Bordia, U. Schneider, F. Heidrich-Meisner, I. Bloch, and M. Aidelsburger, "Nonequilibrium Mass Transport in the 1D Fermi-Hubbard Model", Phys. Rev. Lett. **121**, 130402 (2018).

[155]F. Heidrich-Meisner, S. R. Manmana, M. Rigol, A. Muramatsu, A. E. Feiguin, and E. Dagotto, "Quantum distillation: Dynamical generation of low-entropy states of strongly correlated fermions in an optical lattice", Phys. Rev. A **80**, 041603 (2009).

[156]J. Kajala, F. Massel, and P. Törmä, "Expansion Dynamics in the One-Dimensional Fermi-Hubbard Model", Phys. Rev. Lett. **106**, 206401 (2011).

[157]K. S. Novoselov, A. K. Geim, S. V. Morozov, D. Jiang, Y. Zhang, S. V. Dubonos, I. V. Grigorieva, and A. A. Firsov, "Electric Field Effect in Atomically Thin Carbon Films", Science **306**, 666–669 (2004).

[158]E. Gerstner, "Nobel prize 2010: Andre Geim & Konstantin Novoselov", Nature Physics **6**, 836–836 (2010).

[159]K. S. Novoselov, A. K. Geim, S. V. Morozov, D. Jiang, M. I. Katsnelson, I. Grigorieva, S. Dubonos, Firsov, and AA, "Two-dimensional gas of massless Dirac fermions in graphene", Nature **438**, 197–200 (2005).

[160]Y. Zhang, Y.-W. Tan, H. L. Stormer, and P. Kim, "Experimental observation of the quantum Hall effect and Berry's phase in graphene", Nature **438**, 201–204 (2005).

[161]K. Bolotin, K. Sikes, Z. Jiang, M. Klima, G. Fudenberg, J. Hone, P. Kim, and H. Stormer, "Ultrahigh electron mobility in suspended graphene", Solid State Communications **146**, 351–355 (2008).

[162]F. Xia, T. Mueller, Y.-m. Lin, A. Valdes-Garcia, and P. Avouris, "Ultrafast graphene photodetector", Nature nanotechnology **4**, 839–843 (2009).

[163]X. Wang, L. Zhi, and K. Müllen, "Transparent, Conductive Graphene Electrodes for Dye-Sensitized Solar Cells", Nano Letters **8**, 323–327 (2008).

[164]Y. H. Hu, H. Wang, and B. Hu, "Thinnest Two-Dimensional Nanomaterial—Graphene for Solar Energy", ChemSusChem **3**, 782–796 (2010).

[165] I. V. Lightcap and P. V. Kamat, "Graphitic Design: Prospects of Graphene-Based Nanocomposites for Solar Energy Conversion, Storage, and Sensing", Accounts of Chemical Research **46**, 2235–2243 (2013).

[166] Y. Song, S. Chang, S. Gradecak, and J. Kong, "Visibly-Transparent Organic Solar Cells on Flexible Substrates with All-Graphene Electrodes", Advanced Energy Materials **6**, 1600847 (2016).

[167] S. Y. Zhou, G.-H. Gweon, A. Fedorov, d. First PN, W. De Heer, D.-H. Lee, F. Guinea, A. C. Neto, and A. Lanzara, "Substrate-induced bandgap opening in epitaxial graphene", Nature materials **6**, 770–775 (2007).

[168] C. Jeon, H.-C. Shin, I. Song, M. Kim, J.-H. Park, J. Nam, D.-H. Oh, S. Woo, C.-C. Hwang, C.-Y. Park, et al., "Opening and reversible control of a wide energy gap in uniform monolayer graphene", Scientific reports **3**, 1–6 (2013).

[169] F. Guinea, M. Katsnelson, and A. Geim, "Energy gaps and a zero-field quantum Hall effect in graphene by strain engineering", Nature Physics **6**, 30–33 (2010).

[170] S.-M. Choi, S.-H. Jhi, and Y.-W. Son, "Effects of strain on electronic properties of graphene", Phys. Rev. B **81**, 081407 (2010).

[171] Y. Zhang, T.-T. Tang, C. Girit, Z. Hao, M. C. Martin, A. Zettl, M. F. Crommie, Y. R. Shen, and F. Wang, "Direct observation of a widely tunable bandgap in bilayer graphene", Nature **459**, 820–823 (2009).

[172] E. Gibney, "How 'magic angle' graphene is stirring up physics", Nature **565**, 15–19 (2019).

[173] L. Yang, C.-H. Park, Y.-W. Son, M. L. Cohen, and S. G. Louie, "Quasiparticle Energies and Band Gaps in Graphene Nanoribbons", Phys. Rev. Lett. **99**, 186801 (2007).

[174] M. Y. Han, B. Özyilmaz, Y. Zhang, and P. Kim, "Energy Band-Gap Engineering of Graphene Nanoribbons", Phys. Rev. Lett. **98**, 206805 (2007).

[175] S. A. Jensen, R. Ulbricht, A. Narita, X. Feng, K. Müllen, T. Hertel, D. Turchinovich, and M. Bonn, "Ultrafast Photoconductivity of Graphene Nanoribbons and Carbon Nanotubes", Nano Letters **13**, 5925–5930 (2013).

[176] R. Denk, M. Hohage, P. Zeppenfeld, J. Cai, C. A. Pignedoli, H. Söde, R. Fasel, X. Feng, K. Müllen, S. Wang, et al., "Exciton-dominated optical response of ultra-narrow graphene nanoribbons", Nature communications **5**, 1–7 (2014).

[177] G. Soavi, S. Dal Conte, C. Manzoni, D. Viola, A. Narita, Y. Hu, X. Feng, U. Hohenester, E. Molinari, D. Prezzi, et al., "Exciton–exciton annihilation and biexciton stimulated emission in graphene nanoribbons", Nature communications **7**, 1–7 (2016).

[178] B. V. Senkovskiy, A. V. Fedorov, D. Haberer, M. Farjam, K. A. Simonov, A. B. Preobrajenski, N. Mårtensson, N. Atodiresei, V. Caciuc, S. Blügel, A. Rosch, N. I. Verbitskiy, M. Hell, D. V. Evtushinsky, R. German, T. Marangoni, P. H. M. van Loosdrecht, F. R. Fischer, and A. Grüneis, "Semiconductor-to-Metal Transition and Quasiparticle Renormalization in Doped Graphene Nanoribbons", Advanced Electronic Materials **3**, 1600490 (2017).

[179] I. Ivanov, Y. Hu, S. Osella, U. Beser, H. I. Wang, D. Beljonne, A. Narita, K. Müllen, D. Turchinovich, and M. Bonn, "Role of Edge Engineering in Photoconductivity of Graphene Nanoribbons", Journal of the American Chemical Society **139**, 7982–7988 (2017).

[180] J. Bai, X. Duan, and Y. Huang, "Rational Fabrication of Graphene Nanoribbons Using a Nanowire Etch Mask", Nano Letters **9**, 2083–2087 (2009).

[181] J. Cai, P. Ruffieux, R. Jaafar, M. Bieri, T. Braun, S. Blankenburg, M. Muoth, A. P. Seitsonen, M. Saleh, X. Feng, et al., "Atomically precise bottom-up fabrication of graphene nanoribbons", Nature **466**, 470–473 (2010).

[182] L. Jiao, X. Wang, G. Diankov, H. Wang, and H. Dai, "Facile synthesis of high-quality graphene nanoribbons", Nature nanotechnology **5**, 321–325 (2010).

[183] O. V. Yazyev, "A Guide to the Design of Electronic Properties of Graphene Nanoribbons", Accounts of Chemical Research **46**, 2319–2328 (2013).

[184] A. Kimouche, M. M. Ervasti, R. Drost, S. Halonen, A. Harju, P. M. Joensuu, J. Sainio, and P. Liljeroth, "Ultra-narrow metallic armchair graphene nanoribbons", Nature communications **6**, 1–6 (2015).

[185] R. M. Jacobberger, B. Kiraly, M. Fortin-Deschenes, P. L. Levesque, K. M. McElhinny, G. J. Brady, R. R. Delgado, S. S. Roy, A. Mannix, M. G. Lagally, et al., "Direct oriented growth of armchair graphene nanoribbons on germanium", Nature communications **6**, 1–8 (2015).

[186] A. K. Geim, "Graphene: Status and Prospects", Science **324**, 1530–1534 (2009).

[187] K. S. Novoselov, V. Fal, L. Colombo, P. Gellert, M. Schwab, K. Kim, et al., "A roadmap for graphene", Nature **490**, 192–200 (2012).

[188] S. K. Tiwari, S. Sahoo, N. Wang, and A. Huczko, "Graphene research and their outputs: Status and prospect", Journal of Science: Advanced Materials and Devices **5**, 10–29 (2020).

[189] D. C. Bell, M. C. Lemme, L. A. Stern, J. R. Williams, and C. M. Marcus, "Precision cutting and patterning of graphene with helium ions", Nanotechnology **20**, 455301 (2009).

[190] J. Buchheim, R. M. Wyss, I. Shorubalko, and H. G. Park, "Understanding the interaction between energetic ions and freestanding graphene towards practical 2D perforation", Nanoscale **8**, 8345–8354 (2016).

[191] P. Zhao, J. Wang, and Q. Wang, "Damage mechanism of graphene nanoribbons field effect transistors during focused ion beam etching", Materials Today Communications **26**, 101778 (2021).

[192] N. M. Gabor, Z. Zhong, K. Bosnick, J. Park, and P. L. McEuen, "Extremely Efficient Multiple Electron-Hole Pair Generation in Carbon Nanotube Photodiodes", Science **325**, 1367–1371 (2009).

[193] S. Wang, M. Khafizov, X. Tu, M. Zheng, and T. D. Krauss, "Multiple Exciton Generation in Single-Walled Carbon Nanotubes", Nano Letters **10**, 2381–2386 (2010).

[194] I. Gierz, J. C. Petersen, M. Mitrano, C. Cacho, I. E. Turcu, E. Springate, A. Stöhr, A. Köhler, U. Starke, and A. Cavalleri, "Snapshots of non-equilibrium Dirac carrier distributions in graphene", Nature materials **12**, 1119–1124 (2013).

[195] I. Gierz, F. Calegari, S. Aeschlimann, M. Chávez Cervantes, C. Cacho, R. T. Chapman, E. Springate, S. Link, U. Starke, C. R. Ast, and A. Cavalleri, "Tracking Primary Thermalization Events in Graphene with Photoemission at Extreme Time Scales", Phys. Rev. Lett. **115**, 086803 (2015).

[196] G. Lani, P. Romaniello, and L. Reining, "Approximations for many-body Green's functions: insights from the fundamental equations", New J. Phys. **14**, 013056 (2012).

[197] F. Tandetzky, J. K. Dewhurst, S. Sharma, and E. K. U. Gross, "Multiplicity of solutions to GW-type approximations", Phys. Rev. B **92**, 115125 (2015).

[198] R. Rossi and F. Werner, "Skeleton series and multivaluedness of the self-energy functional in zero space-time dimensions", J. Phys. A: Math. Theor. **48**, 485202 (2015).

[199] A. Stan, P. Romaniello, S. Rigamonti, L. Reining, and J. A. Berger, "Unphysical and physical solutions in many-body theories: from weak to strong correlation", New J. Phys. **17**, 093045 (2015).

[200] E. Kozik, M. Ferrero, and A. Georges, "Nonexistence of the Luttinger-Ward Functional and Misleading Convergence of Skeleton Diagrammatic Series for Hubbard-Like Models", Phys. Rev. Lett. **114**, 156402 (2015).

[201] O. Gunnarsson, G. Rohringer, T. Schäfer, G. Sangiovanni, and A. Toschi, "Breakdown of Traditional Many-Body Theories for Correlated Electrons", Phys. Rev. Lett. **119**, 056402 (2017).

[202] A. Stan, "On the unphysical solutions of the Kadanoff-Baym equations in linear response: Correlation-induced homogeneous density-distribution and attractors", Phys. Rev. B **93**, 041103 (2016).

[203] S. Latini, E. Perfetto, A.-M. Uimonen, R. van Leeuwen, and G. Stefanucci, "Charge dynamics in molecular junctions: Nonequilibrium Green's function approach made fast", Phys. Rev. B **89**, 075306 (2014).

[204] J. Hubbard and B. H. Flowers, "Electron correlations in narrow energy bands", Proceedings of the Royal Society of London. Series A. Mathematical and Physical Sciences **276**, 238–257 (1963).

[205] D. Karlsson, R. van Leeuwen, Y. Pavlyukh, E. Perfetto, and G. Stefanucci, "Fast Green's Function Method for Ultrafast Electron-Boson Dynamics", Phys. Rev. Lett. **127**, 036402 (2021).

[206] Y. Pavlyukh, E. Perfetto, and G. Stefanucci, "Photoinduced dynamics of organic molecules using nonequilibrium Green's functions with second-Born, GW, T-matrix, and three-particle correlations", Phys. Rev. B **104**, 035124 (2021).

[207] M. Bonitz, K. Balzer, N. Schlünzen, M. R. Rasmussen, and J.-P. Joost, "Ion Impact Induced Ultrafast Electron Dynamics in Finite Graphene-Type Hubbard Clusters", physica status solidi (b) **256**, 1800490 (2019).

[208] J.-P. Joost, N. Schlünzen, and M. Bonitz, "G1-G2 scheme: Dramatic acceleration of nonequilibrium Green functions simulations within the Hartree-Fock generalized Kadanoff-Baym ansatz", Phys. Rev. B **101**, 245101 (2020).

[209] M. Scharnke, N. Schlünzen, and M. Bonitz, "Time reversal invariance of quantum kinetic equations: Nonequilibrium Green functions formalism", Journal of Mathematical Physics **58**, 061903 (2017).

[210] M. Bonitz, M. Scharnke, and N. Schlünzen, "Time-reversal invariance of quantum kinetic equations II: Density operator formalism", Contrib. Plasma Phys. **58**, 1036–1046 (2018).

[211] N. Schlünzen, J.-P. Joost, and M. Bonitz, "Comment on "On the unphysical solutions of the Kadanoff-Baym equations in linear response: Correlation-induced homogeneous density-distribution and attractors"", Phys. Rev. B **96**, 117101 (2017).

[212] N. Schlünzen, J.-P. Joost, F. Heidrich-Meisner, and M. Bonitz, "Nonequilibrium dynamics in the one-dimensional Fermi-Hubbard model: Comparison of the nonequilibrium Green-functions approach and the density matrix renormalization group method", Phys. Rev. B **95**, 165139 (2017).

[213] N. Schlünzen, S. Hermanns, M. Bonitz, and C. Verdozzi, "Dynamics of strongly correlated fermions: Ab initio results for two and three dimensions", Phys. Rev. B **93**, 035107 (2016).

[214] K. Balzer, N. Schlünzen, and M. Bonitz, "Stopping dynamics of ions passing through correlated honeycomb clusters", Phys. Rev. B **94**, 245118 (2016).

[215] N. Schlünzen, K. Balzer, M. Bonitz, L. Deuchler, and E. Pehlke, "Time-dependent simulation of ion stopping: charge transfer and electronic excitations", Contributions to Plasma Physics **59**, e201800184 (2019).

[216] J.-P. Joost, N. Schlünzen, and M. Bonitz, "Femtosecond Electron Dynamics in Graphene Nanoribbons – A Nonequilibrium Green Functions Approach Within an Extended Hubbard Model", physica status solidi (b) **256**, 1800498 (2019).

[217] M. Pourfath, *The Non-Equilibrium Green's Function Method for Nanoscale Device Simulation* (Springer, Vienna, 2014).

[218] M. Greiner and I. Bloch, "Quantengase unter dem Mikroskop", Physik Journal **14**, 33 (2015).

[219] A. Fetter and J. Walecka, *Quantum theory of many particle systems* (McGraw Hill, New York, 1971).

[220] C. D. Sherrill and H. F. Schaefer, "The configuration interaction method: Advances in highly correlated approaches", in *Advances in quantum chemistry*, Vol. 34 (Academic Press, Cambridge, 1999), pp. 143–269.

[221] F. Jensen, *Introduction to Computational Chemistry* (Wiley, Chichester, 2007).

[222] A. Szabo and N. Ostlund, *Modern quantum chemistry: introduction to advanced electronic structure theory*, Dover Books on Chemistry (Dover Publications, Mineola, New York, 2012).

[223] P. Myöhänen, A. Stan, G. Stefanucci, and R. van Leeuwen, "Kadanoff-Baym approach to quantum transport through interacting nanoscale systems: From the transient to the steady-state regime", Phys. Rev. B **80**, 115107 (2009).

[224] A. Stan, N. E. Dahlen, and R. van Leeuwen, "Levels of self-consistency in the GW approximation", The Journal of Chemical Physics **130**, 114105 (2009).

[225] G. Baym, "Self-Consistent Approximations in Many-Body Systems", Phys. Rev. **127**, 1391–1401 (1962).

[226] C.-O. Almbladh, U. v. Barth, and R. v. Leeuwen, "Variational total energies from Φ- and Ψ- derivable theories", International Journal of Modern Physics B **13**, 535–541 (1999).

[227] N. E. Dahlen and R. van Leeuwen, "Self-consistent solution of the dyson equation for atoms and molecules within a conserving approximation", The Journal of Chemical Physics **122**, 164102 (2005).

[228] U. von Barth, N. E. Dahlen, R. van Leeuwen, and G. Stefanucci, "Conserving approximations in time-dependent density functional theory", Phys. Rev. B **72**, 235109 (2005).

[229] J. M. Luttinger and J. C. Ward, "Ground-State Energy of a Many-Fermion System. II", Phys. Rev. **118**, 1417–1427 (1960).

[230] G. Tononi, *Phi: A Voyage from the Brain to the Soul* (Knopf Doubleday Publishing Group, 2012).

[231] G. Tononi, "Consciousness as integrated information: a provisional manifesto", The Biological Bulletin **215**, PMID: 19098144, 216–242 (2008).

[232] M. Oizumi, L. Albantakis, and G. Tononi, "From the phenomenology to the mechanisms of consciousness: integrated information theory 3.0", PLOS Computational Biology **10**, 1–25 (2014).

[233] G. Tononi, M. Boly, M. Massimini, and C. Koch, "Integrated information theory: from consciousness to its physical substrate", Nature Reviews Neuroscience **17**, 450–461 (2016).

[234] H. Kleinert, *Particles and quantum fields* (World Scientific, Singapore, 2016).

[235] H. D. Cornean, V. Moldoveanu, and C. A. Pillet, "A Dyson Equation for Non-Equilibrium Green's Functions in the Partition-Free Setting", physica status solidi (b) **256**, 1800447 (2019).

[236] N. W. Talarico, S. Maniscalco, and N. Lo Gullo, "A Scalable Numerical Approach to the Solution of the Dyson Equation for the Non-Equilibrium Single-Particle Green's Function", physica status solidi (b) **256**, 1800501 (2019).

[237] R. Tuovinen, D. Golež, M. Schüler, P. Werner, M. Eckstein, and M. A. Sentef, "Adiabatic Preparation of a Correlated Symmetry-Broken Initial State with the Generalized Kadanoff–Baym Ansatz", physica status solidi (b) **256**, 1800469 (2019).

[238] A. Kalvová, B. Velický, and V. Špička, "Beyond the Generalized Kadanoff–Baym Ansatz", physica status solidi (b) **256**, 1800594 (2019).

[239] M. Hyrkäs, D. Karlsson, and R. van Leeuwen, "Diagrammatic Expansion for Positive Spectral Functions in the Steady-State Limit", physica status solidi (b) **256**, 1800615 (2019).

[240] E. Perfetto and G. Stefanucci, "The Dissection Algorithm for the Second-Born Self-Energy", physica status solidi (b) **256**, 1800573 (2019).

[241] E. Viñas Boström and C. Verdozzi, "Steering Magnetic Skyrmions with Currents: A Nonequilibrium Green's Functions Approach", physica status solidi (b) **256**, 1800590 (2019).

[242] U. Aeberhard, "Challenges in the NEGF Simulation of Quantum-Well Photovoltaics Posed by Non-Locality and Localization", physica status solidi (b) **256**, 1800500 (2019).

[243] I. Adamovich, S. D. Baalrud, A. Bogaerts, P. J. Bruggeman, M. Cappelli, V. Colombo, U. Czarnetzki, U. Ebert, J. G. Eden, P. Favia, D. B. Graves, S. Hamaguchi, G. Hieftje, M. Hori, I. D. Kaganovich, U. Kortshagen, M. J. Kushner, N. J. Mason, S. Mazouffre, S. M. Thagard, H.-R. Metelmann, A. Mizuno, E. Moreau, A. B. Murphy, B. A. Niemira, G. S. Oehrlein, Z. L. Petrovic, L. C. Pitchford, Y.-K. Pu, S. Rauf, O. Sakai, S. Samukawa, S. Starikovskaia, J. Tennyson, K. Terashima, M. M. Turner, M. C. M. van de Sanden, and A. Vardelle, "The 2017 Plasma Roadmap: Low temperature plasma science and technology", Journal of Physics D: Applied Physics **50**, 323001 (2017).

[244] P. Sigmund, "Particle penetration and radiation effects volume 2", in *Springer series in solid-state sciences*, Vol. 179 (Springer, 2014).

[245] F. H. Essler, H. Frahm, F. Göhmann, A. Klümper, and V. E. Korepin, *The one-dimensional Hubbard model* (Cambridge University Press, Cambridge, 2005).

[246] M. Bonitz, A. Filinov, J.-W. Abraham, K. Balzer, H. Kählert, E. Pehlke, F. X. Bronold, M. Pamperin, M. Becker, D. Loffhagen, and H. Fehske, "Towards an integrated modeling of the plasma-solid interface", Frontiers of Chemical Science and Engineering **13**, 201–237 (2019).

[247] K. Balzer and M. Bonitz, "Neutralization dynamics of slow highly charged ions passing through graphene nanoflakes: an embedding self-energy approach", Contrib. Plasma Phys. **Early View**, DOI: 10.1002/ctpp.202100041.

[248] G. Pal, Y. Pavlyukh, W. Hübner, and H. C. Schneider, "Optical absorption spectra of finite systems from a conserving Bethe-Salpeter equation approach", Eur. Phys. J. B **79**, 327–334 (2011).

[249] D. Sangalli, S. Dal Conte, C. Manzoni, G. Cerullo, and A. Marini, "Nonequilibrium optical properties in semiconductors from first principles: A combined theoretical and experimental study of bulk silicon", Phys. Rev. B **93**, 195205 (2016).

[250] E. Perfetto, D. Sangalli, A. Marini, and G. Stefanucci, "Ultrafast Charge Migration in XUV Photoexcited Phenylalanine: A First-Principles Study Based on Real-Time Nonequilibrium Green's Functions", J. Phys. Chem. Lett. **9**, 1353–1358 (2018).

[251] D. J. Rizzo, G. Veber, T. Cao, C. Bronner, T. Chen, F. Zhao, H. Rodriguez, S. G. Louie, M. F. Crommie, and F. R. Fischer, "Topological band engineering of graphene nanoribbons", Nature **560**, 204–208 (2018).

[252] E. Goulielmakis, Z.-H. Loh, A. Wirth, R. Santra, N. Rohringer, V. S. Yakovlev, S. Zherebtsov, T. Pfeifer, A. M. Azzeer, M. F. Kling, et al., "Real-time observation of valence electron motion", Nature **466**, 739–743 (2010).

[253] D. Karlsson, R. van Leeuwen, E. Perfetto, and G. Stefanucci, "The generalized Kadanoff-Baym ansatz with initial correlations", Phys. Rev. B **98**, 115148 (2018).

[254] M. Hopjan and C. Verdozzi, "Initial correlated states for the generalized Kadanoff–Baym Ansatz without adiabatic switching-on of interactions in closed systems", Eur. Phys. J. Spec. Top. **227**, 1939–1948 (2019).

[255] R. O. Jones and O. Gunnarsson, "The density functional formalism, its applications and prospects", Rev. Mod. Phys. **61**, 689–746 (1989).

[256] L. Borkowski, F. Reiser, N. Schlünzen, J.-P. Joost, and M. Bonitz, *Doublon production in correlated materials by multiple ion impacts*, in preparation.

[257] D. Kremp, M. Bonitz, W. Kraeft, and M. Schlanges, "Non-Markovian Boltzmann Equation", Ann. Phys. **258**, 320–359 (1997).

[258] J. Taylor, *Scattering Theory: The Quantum Theory of Nonrelativistic Collisions* (Dover, Mineola, New York, 2006).

[259] A. Akbari, M. J. Hashemi, A. Rubio, R. M. Nieminen, and R. van Leeuwen, "Challenges in truncating the hierarchy of time-dependent reduced density matrices equations", Phys. Rev. B **85**, 235121 (2012).

[260] F. Colmenero, C. Pérez del Valle, and C. Valdemoro, "Approximating q-order reduced density matrices in terms of the lower-order ones. I. General relations", Phys. Rev. A **47**, 971–978 (1993).

[261] W. Shun-jin and W. Cassing, "Explicit treatment of n-body correlations within a density-matrix formalism", Ann. Phys. **159**, 328–350 (1985).

[262] H. Ohldag, J.-P. Joost, N. Schlünzen, M. Bonitz, and I. Brezinova, *Correlated electron dynamics in finite Hubbard clusters: Testing the G1–G2 scheme*, in preparation.

[263] H. A. Gould and H. E. DeWitt, "Convergent kinetic equation for a classical plasma", Phys. Rev. **155**, 68–74 (1967).

[264] R. Balescu, "Irreversible processes in ionized gases", The Physics of Fluids **3**, 52–63 (1960).

[265] W. Kraeft, D. Kremp, W. Ebeling, and G. Röpke, *Quantum statistics of charged particle systems* (Akademieverlag, Berlin, 1986).

[266] H. D. Whitley, A. Alastuey, J. Gaffney, R. Cauble, W. Kraeft, and M. Bonitz, "A tribute to pioneers of strongly coupled plasmas: Hugh E. DeWitt, Bernard Jancovici, and Forrest J. Rogers", Contrib. Plasma Phys. **55**, 102–115 (2015).

[267] J. P. Lees et al. (The BABAR Collaboration), "Observation of time-reversal violation in the B^0 meson system", Phys. Rev. Lett. **109**, 211801 (2012).

[268] C. Kiefer, "CPT Theorem", in *Compendium of Quantum Physics*, edited by D. Greenberger, K. Hentschel, and F. Weinert (Springer, Berlin, Heidelberg, 2009), pp. 138–139.

[269] E. Wigner, "Über die Operation der Zeitumkehr in der Quantenmechanik", Nachrichten von der Gesellschaft der Wissenschaften zu Göttingen, Mathematisch-Physikalische Klasse **1932**, 546–559 (1932).

[270] D. Z. Albert, *Time and Chance*, English (Harvard University Press Cambridge, Mass, 2000).

[271] C. Callender, "Is time 'handed' in a quantum world?", Proceedings of the Aristotelian Society (Hardback) **100**, 247–269 (2000).

[272] J. Earman, "What time reversal invariance is and why it matters", International Studies in the Philosophy of Science **16**, 245–264 (2002).

[273] D. Wallace, "The arrow of time in physics", in *A companion to the philosophy of time* (John Wiley & Sons, Ltd, 2013) Chap. 16, pp. 262–281.

[274] B. W. Roberts, "Three Myths about Time Reversal in Quantum Theory", Philosophy of Science **84**, 315–334 (2017).

[275] E. Boström, M. Hopjan, A. Kartsev, C. Verdozzi, and C.-O. Almbladh, "Nonequilibrium Green's functions and atom-surface dynamics: Simple views from a simple model system", J. Phys.: Conf. Ser. **696**, 012007 (2016).

[276] N. Schlünzen, "A Selfenergy Cookbook — State-of-the-Art Computing for the NEGF Key Ingredient", presented at the KBEt^2 workshop, Kiel, 2019.

[277] P. Lykos and G. W. Pratt, "Discussion on The Hartree-Fock Approximation", Rev. Mod. Phys. **35**, 496–501 (1963).

[278] A. W. Overhauser, "Giant Spin Density Waves", Phys. Rev. Lett. **4**, 462–465 (1960).

[279] B. Bernu, F. Delyon, L. Baguet, and M. Holzmann, "Periodic ground states of the electron gas in two and three dimensions", Contrib. Plasma Phys. **57**, 524–531 (2017).

[280] G. E. Scuseria, C. A. Jiménez-Hoyos, T. M. Henderson, K. Samanta, and J. K. Ellis, "Projected quasiparticle theory for molecular electronic structure", The Journal of Chemical Physics **135**, 124108 (2011).

[281] C. Yannouleas and U. Landman, "Spontaneous Symmetry Breaking in Single and Molecular Quantum Dots", Phys. Rev. Lett. **82**, 5325–5328 (1999).

[282] A. Filinov, Y. Lozovik, and M. Bonitz, "Path Integral Simulations of Crystallization of Quantum Confined Electrons", physica status solidi (b) **221**, 231–234 (2000).

[283] A. V. Filinov, M. Bonitz, and Y. E. Lozovik, "Wigner Crystallization in Mesoscopic 2D Electron Systems", Phys. Rev. Lett. **86**, 3851–3854 (2001).

[284] C. Yannouleas and U. Landman, "Symmetry breaking and quantum correlations in finite systems: studies of quantum dots and ultracold Bose gases and related nuclear and chemical methods", Reports on Progress in Physics **70**, 2067–2148 (2007).

[285] J. Böning, A. Filinov, P. Ludwig, H. Baumgartner, M. Bonitz, and Y. E. Lozovik, "Melting of Trapped Few-Particle Systems", Phys. Rev. Lett. **100**, 113401 (2008).

[286] C. B. Mendl, F. Malet, and P. Gori-Giorgi, "Wigner localization in quantum dots from Kohn-Sham density functional theory without symmetry breaking", Phys. Rev. B **89**, 125106 (2014).

[287]D. R. Penn, "Stability Theory of the Magnetic Phases for a Simple Model of the Transition Metals", Phys. Rev. **142**, 350–365 (1966).

[288]J. E. Hirsch, "Two-dimensional Hubbard model: Numerical simulation study", Phys. Rev. B **31**, 4403–4419 (1985).

[289]M. Bonitz, N. Schlünzen, and S. Hermanns, "Toward a Nonequilibrium Green Functions Approach to Diffusion in Strongly Coupled Finite Quantum Systems", Contributions to Plasma Physics **55**, 152–158 (2015).

[290]N. Schlünzen, "Nonequilibrium Green functions analysis of electron dynamics in strongly correlated lattice systems", MA thesis (Christian-Albrechts-Universität zu Kiel, Kiel, Sept. 2015).

[291]M. R. Hirsbrunner, T. M. Philip, B. Basa, Y. Kim, M. J. Park, and M. J. Gilbert, "A review of modeling interacting transient phenomena with non-equilibrium Green functions", Reports on Progress in Physics **82**, 046001 (2019).

[292]W. Levin, H. Kooy, J. S. Loeffler, and T. F. Delaney, "Proton beam therapy", British journal of Cancer **93**, 849–854 (2005).

[293]M. Jermann, "Particle Therapy Statistics in 2013", International Journal of Particle Therapy **1**, 40–43 (2014).

[294]T.-Z. Yuan, Z.-J. Zhan, and C.-N. Qian, "New frontiers in proton therapy: applications in cancers", Cancer Communications **39**, 61 (2019).

[295]R. C. Elphic, H. O. Funsten III, B. L. Barraclough, D. J. McComas, M. T. Paffett, D. T. Vaniman, and G. Heiken, "Lunar surface composition and solar wind-induced secondary ion mass spectrometry", Geophysical Research Letters **18**, 2165–2168 (1991).

[296]A. Barghouty, F. Meyer, P. Harris, and J. Adams, "Solar-wind protons and heavy ions sputtering of lunar surface materials", Nuclear Instruments and Methods in Physics Research Section B: Beam Interactions with Materials and Atoms **269**, 1310–1315 (2011).

[297]E. Kallio, P. Wurz, R. Killen, S. McKenna-Lawlor, A. Milillo, A. Mura, S. Massetti, S. Orsini, H. Lammer, P. Janhunen, and W.-H. Ip, "On the impact of multiply charged heavy solar wind ions on the surface of Mercury, the Moon and Ceres", Planetary and Space Science **56**, 1506–1516 (2008).

[298]C. Anders and H. M. Urbassek, "Solar wind ion impacts into ice surfaces: A molecular-dynamics study using the REAX force field", Icarus **282**, 351–362 (2017).

[299]R. Saladino, E. Carota, G. Botta, M. Kapralov, G. N. Timoshenko, A. Y. Rozanov, E. Krasavin, and E. Di Mauro, "Meteorite-catalyzed syntheses of nucleosides and of other prebiotic compounds from formamide under proton irradiation", Proceedings of the National Academy of Sciences **112**, E2746–E2755 (2015).

[300]G. Horneck, N. Walter, F. Westall, J. L. Grenfell, W. F. Martin, F. Gomez, S. Leuko, N. Lee, S. Onofri, K. Tsiganis, R. Saladino, E. Pilat-Lohinger, E. Palomba, J. Harrison, F. Rull, C. Muller, G. Strazzulla, J. R. Brucato, P. Rettberg, and M. T. Capria, "AstRoMap European Astrobiology Roadmap", Astrobiology **16**, 201–243 (2016).

[301] C. Deutsch and G. Maynard, "Ion stopping in dense plasmas: A basic physics approach", Matter and Radiation at Extremes **1**, 277–307 (2016).

[302] J. A. Frenje, R. Florido, R. Mancini, T. Nagayama, P. E. Grabowski, H. Rinderknecht, H. Sio, A. Zylstra, M. Gatu Johnson, C. K. Li, F. H. Séguin, R. D. Petrasso, V. Y. Glebov, and S. P. Regan, "Experimental Validation of Low-Z Ion-Stopping Formalisms around the Bragg Peak in High-Energy-Density Plasmas", Phys. Rev. Lett. **122**, 015002 (2019).

[303] B. Y. Sharkov, D. H. Hoffmann, A. A. Golubev, and Y. Zhao, "High energy density physics with intense ion beams", Matter and Radiation at Extremes **1**, 28–47 (2016).

[304] S. Kodanova, M. Issanova, S. Amirov, T. Ramazanov, A. Tikhonov, and Z. Moldabekov, "Relaxation of non-isothermal hot dense plasma parameters", Matter and Radiation at Extremes **3**, 40–49 (2018).

[305] G. Zwicknagel, C. Toepffer, and P.-G. Reinhard, "Stopping of heavy ions in plasmas at strong coupling", Physics Reports **309**, 117–208 (1999).

[306] M. Quijada, A. G. Borisov, I. Nagy, R. D. Muiño, and P. M. Echenique, "Time-dependent density-functional calculation of the stopping power for protons and antiprotons in metals", Phys. Rev. A **75**, 042902 (2007).

[307] M. A. Zeb, J. Kohanoff, D. Sánchez-Portal, A. Arnau, J. I. Juaristi, and E. Artacho, "Electronic Stopping Power in Gold: The Role of d Electrons and the **H**/He Anomaly", Phys. Rev. Lett. **108**, 225504 (2012).

[308] A. Schleife, Y. Kanai, and A. A. Correa, "Accurate atomistic first-principles calculations of electronic stopping", Phys. Rev. B **91**, 014306 (2015).

[309] S. Zhao, W. Kang, J. Xue, X. Zhang, and P. Zhang, "Comparison of electronic energy loss in graphene and BN sheet by means of time-dependent density functional theory", Journal of Physics: Condensed Matter **27**, 025401 (2014).

[310] S. Bubin, B. Wang, S. Pantelides, and K. Varga, "Simulation of high-energy ion collisions with graphene fragments", Phys. Rev. B **85**, 235435 (2012).

[311] F. Mao, C. Zhang, C.-Z. Gao, J. Dai, and F.-S. Zhang, "The effects of electron transfer on the energy loss of slow He^{2+}, C^{2+}, and C^{4+}ions penetrating a graphene fragment", Journal of Physics: Condensed Matter **26**, 085402 (2014).

[312] R. Ullah, F. Corsetti, D. Sánchez-Portal, and E. Artacho, "Electronic stopping power in a narrow band gap semiconductor from first principles", Phys. Rev. B **91**, 125203 (2015).

[313] M. A. Zeb, J. Kohanoff, D. Sánchez-Portal, and E. Artacho, "Electronic stopping power of H and He in Al and LiF from first principles", Nuclear Instruments and Methods in Physics Research Section B: Beam Interactions with Materials and Atoms **303**, Proceedings of the 11th Computer Simulation of Radiation Effects in Solids (COSIRES) Conference Santa Fe, New Mexico, USA, July 24-29, 2012, 59–61 (2013).

[314] J. M. Pruneda, D. Sánchez-Portal, A. Arnau, J. I. Juaristi, and E. Artacho, "Electronic Stopping Power in LiF from First Principles", Phys. Rev. Lett. **99**, 235501 (2007).

[315] J. F. Ziegler, M. Ziegler, and J. Biersack, "SRIM – The stopping and range of ions in matter (2010)", Nuclear Instruments and Methods in Physics Research Section B: Beam Interactions with Materials and Atoms **268**, 19th International Conference on Ion Beam Analysis, 1818–1823 (2010).

[316] E. Zarkadoula, S. L. Daraszewicz, D. M. Duffy, M. A. Seaton, I. T. Todorov, K. Nordlund, M. T. Dove, and K. Trachenko, "Electronic effects in high-energy radiation damage in iron", Journal of Physics: Condensed Matter **26**, 085401 (2014).

[317] P. Avouris, Z. Chen, and V. Perebeinos, "Carbon-based electronics", Nature nanotechnology **2**, 605 (2007).

[318] W. He, C. Chen, and Z. Xu, "Electronic excitation in graphene under single-particle irradiation", Nanotechnology **32**, 165702 (2021).

[319] Z. Li and F. Chen, "Ion beam modification of two-dimensional materials: Characterization, properties, and applications", Applied Physics Reviews **4**, 011103 (2017).

[320] M. Schleberger and J. Kotakoski, "2D Material Science: Defect Engineering by Particle Irradiation", Materials **11**, 1885 (2018).

[321] A. Tokuno, E. Demler, and T. Giamarchi, "Doublon production rate in modulated optical lattices", Phys. Rev. A **85**, 053601 (2012).

[322] A. Dirks, K. Mikelsons, H. R. Krishnamurthy, and J. K. Freericks, "Theoretical description of coherent doublon creation via lattice modulation spectroscopy", Phys. Rev. A **89**, 021602 (2014).

[323] M. Eckstein, T. Oka, and P. Werner, "Dielectric Breakdown of Mott Insulators in Dynamical Mean-Field Theory", Phys. Rev. Lett. **105**, 146404 (2010).

[324] M. Eckstein and P. Werner, "Dielectric breakdown of Mott insulators – doublon production and doublon heating", Journal of Physics: Conference Series **427**, 012005 (2013).

[325] K. Balzer and M. Eckstein, "Field-assisted doublon manipulation in the Hubbard model: A quantum doublon ratchet", EPL (Europhysics Letters) **107**, 57012 (2014).

[326] M. Genske and A. Rosch, "Directed motion of doublons and holes in periodically driven Mott insulators", Phys. Rev. A **90**, 043637 (2014).

[327] A. V. Joura, J. K. Freericks, and A. I. Lichtenstein, "Long-lived nonequilibrium states in the Hubbard model with an electric field", Phys. Rev. B **91**, 245153 (2015).

[328] A. R. Kolovsky and D. N. Maksimov, "Mott-insulator state of cold atoms in tilted optical lattices: Doublon dynamics and multilevel Landau-Zener tunneling", Phys. Rev. A **94**, 043630 (2016).

[329] M. Moeckel and S. Kehrein, "Interaction Quench in the Hubbard Model", Phys. Rev. Lett. **100**, 175702 (2008).

[330] M. Eckstein and M. Kollar, "Nonthermal Steady States after an Interaction Quench in the Falicov-Kimball Model", Phys. Rev. Lett. **100**, 120404 (2008).

[331] L. D. Landau, "Zur Theorie der Energieubertragung II", Z. Sowjetunion **2**, 46–51 (1932).

[332] C. Zener, "Non-adiabatic crossing of energy levels", Proceedings of the Royal Society of London. Series A, Containing Papers of a Mathematical and Physical Character **137**, 696–702 (1932).

[333] M. Schecter and A. Kamenev, "Forming doublons by a quantum quench", Phys. Rev. A **85**, 043623 (2012).

[334] C. L. Moss, C. M. Isborn, and X. Li, "Ehrenfest dynamics with a time-dependent density-functional-theory calculation of lifetimes and resonant widths of charge-transfer states of Li^+ near an aluminum cluster surface", Phys. Rev. A **80**, 024503 (2009).

[335] A. Castro, M. Isla, J. I. Martínez, and J. Alonso, "Scattering of a proton with the Li_4 cluster: Non-adiabatic molecular dynamics description based on time-dependent density-functional theory", Chemical Physics **399**, New trends in atomic and molecular clusters, 130–134 (2012).

[336] A. V. Krasheninnikov, Y. Miyamoto, and D. Tománek, "Role of Electronic Excitations in Ion Collisions with Carbon Nanostructures", Phys. Rev. Lett. **99**, 016104 (2007).

[337] R. Seraide, M. A. Bernal, G. Brunetto, U. de Giovannini, and A. Rubio, "TDDFT-Based Study on the Proton–DNA Collision", The Journal of Physical Chemistry B **121**, 7276–7283 (2017).

[338] Z. Wang, S.-S. Li, and L.-W. Wang, "Efficient Real-Time Time-Dependent Density Functional Theory Method and its Application to a Collision of an Ion with a 2D Material", Phys. Rev. Lett. **114**, 063004 (2015).

[339] L. Deuchler and E. Pehlke, "Energy transfer during resonant neutralization of hyperthermal protons at an aluminum surface studied with time-dependent density functional theory", Phys. Rev. B **102**, 235421 (2020).

[340] W. Shockley and H. J. Queisser, "Detailed Balance Limit of Efficiency of p-n Junction Solar Cells", Journal of Applied Physics **32**, 510–519 (1961).

[341] A. Nozik, "Quantum dot solar cells", Physica E: Low-dimensional Systems and Nanostructures **14**, 115–120 (2002).

[342] V.-T. Tran, J. Saint-Martin, P. Dollfus, and S. Volz, "Third nearest neighbor parameterized tight binding model for graphene nano-ribbons", AIP Advances **7**, 075212 (2017).

[343] Y. Hancock, A. Uppstu, K. Saloriutta, A. Harju, and M. J. Puska, "Generalized tight-binding transport model for graphene nanoribbon-based systems", Phys. Rev. B **81**, 245402 (2010).

[344] H. Söde, L. Talirz, O. Gröning, C. A. Pignedoli, R. Berger, X. Feng, K. Müllen, R. Fasel, and P. Ruffieux, "Electronic band dispersion of graphene nanoribbons via Fourier-transformed scanning tunneling spectroscopy", Phys. Rev. B **91**, 045429 (2015).

[345] S. Wang, L. Talirz, C. A. Pignedoli, X. Feng, K. Müllen, R. Fasel, and P. Ruffieux, "Giant edge state splitting at atomically precise graphene zigzag edges", Nature communications **7**, 1–6 (2016).

[346] J.-P. Joost, "Spectral Properties of Excited Hubbard Clusters: A Nonequilibrium Green Functions Approach", MA thesis (Christian-Albrechts-Universität zu Kiel, Kiel, Dec. 2017).

[347] T. Koyama, Y. Miyata, H. Kishida, H. Shinohara, and A. Nakamura, "Photophysics in Single-Walled Carbon Nanotubes with (6,4) Chirality at High Excitation Densities: Bimolecular Auger Recombination and Phase-Space Filling of Excitons", The Journal of Physical Chemistry C **117**, 1974–1981 (2013).

[348] S. Pal, D. Casanova, and O. V. Prezhdo, "Effect of Aspect Ratio on Multiparticle Auger Recombination in Single-Walled Carbon Nanotubes: Time Domain Atomistic Simulation", Nano Letters **18**, 58–63 (2018).

[349] F. Wang, G. Dukovic, E. Knoesel, L. E. Brus, and T. F. Heinz, "Observation of rapid Auger recombination in optically excited semiconducting carbon nanotubes", Phys. Rev. B **70**, 241403 (2004).

[350] F. Lackner, I. Březinová, T. Sato, K. L. Ishikawa, and J. Burgdörfer, "High-harmonic spectra from time-dependent two-particle reduced-density-matrix theory", Phys. Rev. A **95**, 033414 (2017).

[351] F. Lackner, "Time-dependent two-particle reduced density matrix theory: application to multi-electron atoms and molecules in strong laser pulses", PhD thesis (Technische Universität Wien, 2017).

[352] B. Y. Mueller and B. Rethfeld, "Relaxation dynamics in laser-excited metals under nonequilibrium conditions", Phys. Rev. B **87**, 035139 (2013).

[353] N.-H. Kwong and M. Bonitz, "Real-Time Kadanoff-Baym Approach to Plasma Oscillations in a Correlated Electron Gas", Phys. Rev. Lett. **84**, 1768–1771 (2000).

[354] F. Reiser, "Stopping Power in Graphen-Nanoclustern im Rahmen des G1-G2-Schemas", Bachelor thesis (Christian-Albrechts-Universität zu Kiel, Mar. 2021).

[355] L. Borkowski, "Electronic Correlations in Lattice Systems Induced by Multiple Ion Impacts: A Nonequilibrium Description via the G1-G2 Scheme", Bachelor thesis (Christian-Albrechts-Universität zu Kiel, May 2021).

[356] K. Gundra and A. Shukla, "Band structure and optical absorption in multilayer armchair graphene nanoribbons: A Pariser-Parr-Pople model study", Phys. Rev. B **84**, 075442 (2011).

[357] K. Gundra and A. Shukla, "A Pariser–Parr–Pople Model Hamiltonian-Based Approach to the Electronic Structure and Optical Properties of Graphene Nanostructures", in *Topological Modelling of Nanostructures and Extended Systems*, edited by A. R. Ashrafi, F. Cataldo, A. Iranmanesh, and O. Ori (Springer Netherlands, Dordrecht, 2013), pp. 199–227.

[358] R. Pariser and R. G. Parr, "A Semi-Empirical Theory of the Electronic Spectra and Electronic Structure of Complex Unsaturated Molecules. I.", The Journal of Chemical Physics **21**, 466–471 (1953).

[359] R. Pariser and R. G. Parr, "A Semi-Empirical Theory of the Electronic Spectra and Electronic Structure of Complex Unsaturated Molecules. II", The Journal of Chemical Physics **21**, 767–776 (1953).

[360] J. A. Pople, "Electron interaction in unsaturated hydrocarbons", Trans. Faraday Soc. **49**, 1375–1385 (1953).

[361] K. Ohno, "Some remarks on the Pariser-Parr-Pople method", Theoretica chimica acta **2**, 219–227 (1964).

[362] K. Nishimoto and N. Mataga, "Electronic Structure and Spectra of Some Nitrogen Heterocycles: " Zeitschrift für Physikalische Chemie **12**, 335–338 (1957).

[363] N. Mataga and K. Nishimoto, "Electronic Structure and Spectra of Nitrogen Heterocycles: " Zeitschrift für Physikalische Chemie **13**, 140–157 (1957).

[364] K. Schulten, I. Ohmine, and M. Karplus, "Correlation effects in the spectra of polyenes", The Journal of Chemical Physics **64**, 4422–4441 (1976).

[365] J. Cai, C. A. Pignedoli, L. Talirz, P. Ruffieux, H. Söde, L. Liang, V. Meunier, R. Berger, R. Li, X. Feng, et al., "Graphene nanoribbon heterojunctions", Nature nanotechnology **9**, 896–900 (2014).

[366] Y.-C. Chen, T. Cao, C. Chen, Z. Pedramrazi, D. Haberer, D. G. De Oteyza, F. R. Fischer, S. G. Louie, and M. F. Crommie, "Molecular bandgap engineering of bottom-up synthesized graphene nanoribbon heterojunctions", Nature nanotechnology **10**, 156–160 (2015).

[367] T. Cao, F. Zhao, and S. G. Louie, "Topological phases in graphene nanoribbons: junction states, spin centers, and quantum spin chains", Phys. Rev. Lett. **119**, 076401 (2017).

[368] P. H. Jacobse, A. Kimouche, T. Gebraad, M. Ervasti, J. Thijssen, P. Liljeroth, and I. Swart, "Electronic components embedded in a single graphene nanoribbon", Nature communications **8**, 1–7 (2017).

[369] C. Ma, L. Liang, Z. Xiao, A. A. Puretzky, K. Hong, W. Lu, V. Meunier, J. Bernholc, and A.-P. Li, "Seamless Staircase Electrical Contact to Semiconducting Graphene Nanoribbons", Nano Letters **17**, 6241–6247 (2017).

[370] S. Wang, N. Kharche, E. Costa Girão, X. Feng, K. Müllen, V. Meunier, R. Fasel, and P. Ruffieux, "Quantum Dots in Graphene Nanoribbons", Nano Letters **17**, 4277–4283 (2017).

[371] D. J. Rizzo, M. Wu, H.-Z. Tsai, T. Marangoni, R. A. Durr, A. A. Omrani, F. Liou, C. Bronner, T. Joshi, G. D. Nguyen, G. F. Rodgers, W.-W. Choi, J. H. Jørgensen, F. R. Fischer, S. G. Louie, and M. F. Crommie, "Length-Dependent Evolution of Type II Heterojunctions in Bottom-Up-Synthesized Graphene Nanoribbons", Nano Letters **19**, 3221–3228 (2019).

[372] M. Puster, A. Balan, J. A. Rodríguez-Manzo, G. Danda, J.-H. Ahn, W. Parkin, and M. Drndić, "Cross-Talk Between Ionic and Nanoribbon Current Signals in Graphene Nanoribbon-Nanopore Sensors for Single-Molecule Detection", Small **11**, 6309–6316 (2015).

[373] S. Ganguly, S. Basu, and S. K. Maiti, "Unconventional charge and spin-dependent transport properties of a graphene nanoribbon with line-disorder", EPL (Europhysics Letters) **124**, 57003 (2018).

[374]L. Martini, Z. Chen, N. Mishra, G. B. Barin, P. Fantuzzi, P. Ruffieux, R. Fasel, X. Feng, A. Narita, C. Coletti, K. Müllen, and A. Candini, "Structure-dependent electrical properties of graphene nanoribbon devices with graphene electrodes", Carbon **146**, 36–43 (2019).

[375]S. J. Heerema, L. Vicarelli, S. Pud, R. N. Schouten, H. W. Zandbergen, and C. Dekker, "Probing DNA Translocations with Inplane Current Signals in a Graphene Nanoribbon with a Nanopore", ACS Nano **12**, 2623–2633 (2018).

[376]A. Wasfi, F. Awwad, and A. I. Ayesh, "Electronic signature of DNA bases via Z-shaped graphene nanoribbon with a nanopore", Biosensors and Bioelectronics: X **1**, 100011 (2019).

[377]A. Wasfi, F. Awwad, and A. I. Ayesh, "DNA sequencing via z-shaped graphene nano ribbon field effect transistor decorated with nanoparticles using first-principle transport simulations", New Journal of Physics **22**, 063004 (2020).

Acknowledgements

Selbstständigkeitserklärung

Ich erkläre, dass die vorliegende Dissertation - abgesehen von der Beratung durch den Betreuer - nach Inhalt und Form meine eigene Arbeit darstellt und unter Einhaltung der Regeln guter wissenschaftlicher Praxis der Deutschen Forschungsgemeinschaft entstanden ist. Ausgewählte Ergebnisse wurden in den in Abschnitt 1.5 angegebenen Fachartikeln publiziert, was an entsprechender Stelle in dieser Arbeit gekennzeichnet wurde. Weiterhin bestätige ich, dass diese Arbeit weder ganz noch in Teilen in einem anderen Prüfungsverfahren zur Begutachtung vorgelegen hat. Es wurde kein akademischer Grad entzogen.

Kiel, den _____   _____
                                                      Niclas Schlünzen